Electronic Engineering and Information Science

Edited by Jinghua Yin, Bo Su and Dongxing Wang

TRANS TECH PUBLICATIONS

Electronic Engineering and Information Science

Edited by Jinghua Yin Bo Su Dongxing Wang

Electronic Engineering and Information Science

Selected, peer reviewed papers from the 2014 International Conference on Electronic Engineering and Information Science (ICEEIS 2014), June 21-22, 2014, Harbin, China

Edited by

Jinghua Yin, Bo Su and Dongxing Wang



Copyright © 2014 Trans Tech Publications Ltd, Switzerland

All rights reserved. No part of the contents of this publication may be reproduced or transmitted in any form or by any means without the written permission of the publisher.

Trans Tech Publications Ltd Churerstrasse 20 CH-8808 Pfaffikon Switzerland http://www.ttp.net

Volume 981 of Advanced Materials Research ISSN print 1022-6680 ISSN cd 1022-6680 ISSN web 1662-8985

Full text available online at http://www.scientific.net

Distributed worldwide by

Trans Tech Publications Ltd Churerstrasse 20 CH-8808 Pfaffikon Switzerland

Fax: +41 (44) 922 10 33 e-mail: sales@ttp.net

and in the Americas by

Trans Tech Publications Inc. PO Box 699, May Street Enfield, NH 03748 USA

Phone: +1 (603) 632-7377 Fax: +1 (603) 632-5611 e-mail: sales-usa@ttp.net

Preface

2014 International Conference of Electronic Engineering and Information Science (ICEEIS 2014) will be held 21-22 June in Harbin, China. The ICEEIS 2014 is sponsored by Harbin University of Science and Technology.

The main role of ICEEIS 2014 is to bring together innovators from engineering researchers, scientists, practitioners to provide a forum to discuss ideas, concepts, and experimental results related to all aspects of electronic engineering and information science. In order to meet high standard of TTP, Advanced Materials Research, the organization committee has made their efforts to do the following things. Firstly, poor quality papers have been refused after reviewing course by anonymous referee experts. Secondly, periodically review meetings have been held around the reviewers about six times for exchanging reviewing suggestions. Finally, the conference organization had several preliminary sessions before the conference. Through efforts of different people and departments, the conference will be successful and fruitful.

ICEEIS 2014 is co-sponsored by Harbin University. In addition, the conference organizer will invite some keynote speakers to deliver their speech in the conference. All participants will have chance to discuss with the speakers face to face, which is very helpful for participants.

We hope that you will enjoy the conference and find the ICEEIS 2014 exciting. We are looking forward to seeing more friends at the next conference.

Jinghua Yin

Table of Contents

Preface

Chapter 1: Electronic Engineering

Phasor Analysis Based Fault Modeling and Fault Diagnosis Methods for Linear Analog Circuits	
Y. Gao, C.L. Yang and S.L. Tian	3
Methods of Handling the Aliasing and Tolerance Problem for a New Unified Fault Modeling Technique in Analog-Circuit Fault Diagnosis Y. Gao, C.L. Yang and S.L. Tian	11
Designing of New Intelligent Music Electro-Acupuncture Apparatus S.Z. Bi, Y. Liu and C.H. Wang	17
Research of Low Power Design Strategy Based on IEEE 1801 Unified Power Format S.P. Cui and C. Xie	21
The Key Technology of Designing the Universal Programmer for Freescale HCS12 Serial MCUs	
J. Zhang and Z.L. Nie	25
A Design of High Performance CMOS Folded Cascode Operational Amplifier Z.F. Wang, Y.J. Cao and J.M. Feng	31
The Research of Programmable Equivalent Capacitor Circuit X. Sheng, Q.H. Shang, Z. Huang and B.S. Wang	36
The Nonlinearities of Memoryless Power Amplifier and Model of Predistorter H. Yang and Y.Z. He	40
Low-Cost and Modularized Test Bench for Focal Plane Array X.Q. Chen and Q. Lv	46
Design of Music Prescription for Music Electroacupuncture Instrument C.H. Wang, J.Q. Du and H.L. Zhang	50
The Analysis of Institutional Factors for Gain of EDFA L.L. Liu, T. Shen, S. Meng, H.Y. Yang, P.Y. Nie and X. Zhang	54
Design and Implementation of a RISC Processor on FPGA H.J. Yang, H. Fan and H.G. Dong	58
The Modeling of OTFT and the Measuring of Small Signal Detection Circuit X.C. Liu, M. Zhu and Z.H. Jing	62
A Bandgap Reference with Temperature Coefficient of 13.2 ppm/°C M.Y. Ren and E.M. Zhao	66
CMOS Low Power Ring VCO Design M.X. Song, S.S. Wang and G.D. Sun	70
The Dual Sine Signal Generator Design Based on the Principle of Difference Frequency Filtering	
C.Z. Zhang, Y. Zhu and J.N. Han	74
Full Scan Structure Application in the Design of 16 Bit MCU H.B. Pan, M.X. Song, X. Jin and J.H. Yin	78
The Design and Verification of VGA Controller B. Yu and Y. Guang	82
Particle Filter Approach for IGBT Remaining Useful Life M. Li, J.J. Zhu and B. Long	86
Design of a High Performance CMOS Bandgap Voltage Reference Y. Guang, B. Yu and H. Hai	90
A Novel Strategy of Area Cost Estimation for Custom Instruction Based on FPGA	
Architecture H.M. Liu and Q. Wu	94
A Circuit Design for Portable Cooling and Heating System Based on STC89C52RC MCU J. Long, X.D. Wang and Y. Song	99

External Memory Interface Verification Based on VMM R. Xu, Z.P. Jiang, C.C. Dong and X.B. Lu	103
Noise Analysis and Characterization of a CMOS Interface Circuit for Fluxgate Sensor C.C. Dong and Z.P. Jiang	107
Design of a Three-Stage Amplifier with Single Miller Capacitor Feedforward Compensation L.H. Cui, X.B. Lu and Y. Guang	111
The Design of the Sinusoidal Signal Generator G.D. Sun, M.X. Song, S.S. Wang and Y. Zhao	116
A Sigma-Delta Modulator System Design with 2-2 Mash Structure Y. Yang, G.D. Sun, M.X. Song and Z.M. Wang	121
The Nonlinear Analysis of Readout Circuit for Microgyroscope G.S. Wang and X.W. Liu	125
The Research of Noise Figure for EDFA Performance Impact Q.R. Yang, T. Shen, C.L. Tan, Q.Y. Zhao, X. Zhang, L. Zhao and Y. Feng	129
Research on Matlab Simulation Output of Optical Current Transformer T. Shen, C. Hu, Q.R. Yang, M.X. Song and X.L. Wei	133
Numerical Simulation of Rapid Solidification Process for Micrometer Level Solder Ball Used in BGA Packaging	
S. Li, J.W. Huang, F. Wang and W. Liu	137
Flatness Improvement of FRA with Multi-Wavelength Pump Y. Ma, Y.C. Li, C.X. Liu, X.Y. Meng and J.R. Yang	141

Chapter 2: Information Science and Information Technologies

Semantic Feature Modeling Based on the Decomposition of Feature Dependent Graph X.Y. Gao, C.X. Zhang and X.Y. Yu	149
Word Sense Disambiguation for Improving the Quality of Machine Translation C.X. Zhang, L. Deng, X.Y. Gao and L.L. Guo	153
Word Sense Disambiguation Based on Center Window C.X. Zhang, L.L. Guo and X.Y. Gao	157
Nipdroid: An Enhanced Detection Mechanism for Android IPC C. Chen, J.X. Song and W.D. Liu	161
A Novel XML Document Retrieval Method J.X. Chen and L.Y. Wan	167
Selecting Filter Range of Hybrid Brain-Computer Interfaces by Mutual Information L. Wang, X. Zhang, X.F. Zhong and Z.W. Fan	171
A New Quadtree-Based Skyline Query Algorithm R.T. Liu, Y.J. Chen, D.Y. Cao and D.Y. Liu	175
Research on Reusable Software Process Model Based on Petri Net G.Y. Tang, D.J. Yao and L.J. Cui	179
Research on Service Model Combination Method Based on Colored Petri Net G.Y. Tang, D.J. Yao and L.J. Cui	183
Web Pages Mining Based on Terms and Formal Concept Analysis B. Yu, D.J. Yao and G.Y. Tang	187
The Research and Design of the Intelligence Application Platform in Public Security E- Government	
Y. Wang, S.Y. Guan and W.H. Li	192
VEET: 3D Virtual Electrical Experimental Tool Supporting Multi-Modal User Interfaces and Platforms	
B.W. Sun, B. Shen, W.W. Chen, Y.P. Zhang and J.Q. Lin	196
A Kind of Distributed Simulation Runtime Infrastructure Based on Grid Y. Liu, J.W. Hu and P.Z. Cui	200
New Solution for Small File Storage of Hadoop Based on Prefetch Mechanism H.X. Zhou and Q.Y. Wen	205
A Game Theoretic Analysis of Resource Pricing and Sharing in P2P Networks Q.F. Zhang, S. Wang and D. Liao	209

Using Untiy 3D Game Development Platform to Develop Low Cost Online Real Estate Display System R. Jiang	213
A Design of IT Enterprise Information Platform in Cloud Environment L. Wei, W.X. Zhang and X.P. Guo	218
Algorithm for Discovering Community in Multi-Relational Social Network Based on Modified Common Neighbors Similarity L.Q. Qiu, Y.Q. Liang, J.J. Xu and Z.Y. Chen	222
WIFI Network Analysis and Transplantation on Android Platform Y. Wang, H.G. Dong and G.Q. Wang	227
The Research of Information Monitoring System for Whole Producing Process Model Z. Min, W.Z. Huang and H.X. Li	231
Research of Intelligent Mobile Inspection System Based IT H.X. Li, Y.P. Wang, Z.X. Jin and J. Qian	235
Study on Self-Configuration Model and Environment Awareness Algorithm for Mission- Critical Systems J. Wang and G.S. Zhao	240
A Research and Exploration of Established Public Service Network Information Platform of University-Enterprise Cooperation	210
J. Wu The Performance Evaluation of Enterprise Informatization Research Based on Dynamic	244
Balanced Scorecard L. Wei, W.X. Zhang and W.Z. Xu	249

Chapter 3: Computational Mathematics and Data Mining

On Normal Sequence in Abelian Group C _n C _n H.Y. Zhang and X.S. Yang	255
The Application of Boosting Algorithm in Data Mining J.L. Du and Y. Qian	258
Massive Data Analysis Based MapReduce Structure on Hadoop System Y.Q. Xu	262
Modified Proportional 2-Tuple and its Application in Uncertainty Environment A.P. Zhang and T.J. Zhan	267
Based on Non-Redundant Electronic Scale Engineering Development Theory R. Li and P. Li	275
L _p - Type of Weighted Fuzzy Number Metrics Induced by Fuzzy Structured Element F. Zhao and S.Z. Guo	279
An Improved Voice Activation Detection Method Based on Energy Acceleration Parameters and Support Vector Machine	
Q. Liu, J.X. Wang, M.J. Wang and P.P. Jiang	287

Chapter 4: Image Processing and Computer Vision

Athermalization Design of Wide Field Medium Wave Infrared Optical System L. Zhao, Z.H. Luan, Y.L. Xiong and L.J. He	295
General Digital Image Processing Circuit and its Applications Y.J. Fan and H. Chen	299
Study of Fiber Gyroscope Fiber Defects Image Enhancement Based on Bias-Normal and Fuzzy Processing	
L.J. Shan, Y.C. Liang and W.Q. Ge	304
Adaptive Pixel Crosstalk Compensation for CMOS Image Sensor C.R. Zhao, X.M. Chi, Z.Y. Wang, W. Yan and D. Li	310
A Clock Optimization Method in the Digital Zooming of the Image Signal Processing	
System D. Li, X.L. Wang, S.M. Chi, C.R. Zhao and B. Yang	315

A Novel Rapid Full-View Measuring Method by Coded Structured Light H.B. Wu, L. Tian, B.Y. Wang, C. Liu, Y. Wang and Z.Y. Wang	319
Design and Implementation of Unified DCT/IDCT Architecture Based on FPGA H. Huang, J.M. Liu, X.B. Lu and B. Yu	323
Diffusion-Substitution Mechanism for Color Image Encryption Based on Multiple Chaotic Systems	327
T.J. Zhang, A.A.A. El-Latif, M. Amin and A. Zaghloul Detecting Human Actions by 3D Deformable Parts Models	527
M. Yang and Y. Yang	331
Video Segmentation Algorithm Based on Improved Kirsch Edge Operator and Three- Frame Difference C.Y. Chen and M.Y. Zhao	335
Denoise PET Images Based on a Combining Method of EMD and ICA Q. Wei and Q. Liu	340
An Improved C-Means Clustering for Image Segmentation T.F. Zhang	344
Coded-Structured Light System Calibration Using Orthogonal Phase Shift Coding Combined with Zhang's Method X.Y. Yu, X.L. Meng, H.B. Wu, X.M. Sun and L. Wang	348
Stereo Matching Algorithm Based on Pyramid Double Dynamic Programming	540
J.Z. Wei, S.C. Yu, W.F. Dong, C. Feng and B. Xie	352
Accurate Calibration Method for a Computer Vision System J.Z. Wei, S.C. Yu, H.B. Wu, Y.W. Zhang and Y.M. Feng	356
A Image Retrival Method with Multi-Features Based on Dempster-Shafer Theory M. Ji, X.M. Sun, X. Chen, L.J. Qi, L. Bao and L. Huang	360
The Projector Calibration Based on ZHANG's Self-Calibration Method G. Yu, B.Y. Yu, S.C. Yang, L. Wen, W.F. Dong and H. Wang	364
Sonar Image Segmentation Using the Level Set Method without Re-Initialization G.Y. Liu, Y.J. Pang, H.Y. Bian and E.M. Zhao	368
Cryptanalysis of Elementary Cellular Automata Based Image Encryption T.J. Zhang, I.M. Manhrawy, A.A. Abdo, A.A.A. El-Latif and R. Rhouma	372
Analysis of the Tongue Body Fat and Thin Based on the Neural Net K. Zhang, C.H. Ding, J.Q. Du, C.H. Wang and J. Shi	376
Chapter 5: Communication and Signal Processing	
The Beidou Satellite High-Precision Timing Applied Research Z.P. Hu, Y. Hua and S.F. Li	381
A New Method of Time Domain Coherency for Radar Emitter Signal Sorting L.R. Guo, M.H. He, C.L. Yu and B.Q. Wang	386
Design and Implementation of GPS L2C Signal Tracking Algorithm X.F. Zhu, F. Shen, Y. Yang, D.R. Yang and X.Y. Chen	392
Design and Implementation of Digital Communication Platform Based on FPGA/DSP S.G. Zhou, W.J. Shang, N. Wang and V. Rublev	398
The Research of Multi-Points Sources Signal Power Synthesis Technology Q.B. Liu, F.L. Zeng and Q.J. Chen	402
A Flat Fiber Raman Amplifier by Optimizing a Single-Wavelength Laser Diode Y. Ma, Y.C. Li, C.Y. Liu and J.R. Yang	409
Simulation of FBG Wavelength Signal Demodulation Based on Sideband Filter N.K. Ren, Y.L. Xiong, M.Z. Wu, H. Xu, Z.Y. Ma and J.Y. Zou	413
Research on the Method of CPM Signal Phase Smoothing Based on Different Power Sine Function	
W.J. Shang, S.G. Zhou, N. Wang and V. Rublev	417
Corrected Differential Evolution Particle Filter for Nonlinear Filtering C.Z. Zhang and L. Li	422
Implementation of FFT Algorithm Based on IP Core C. Ma and Z.L. He	426

Design of Router Supporting Multiply Routing Algorithm for NoC Z.P. Jiang, R. Xu, C.C. Dong and L.H. Cui	431
Research on Signal Aliasing in Long Baseline Positioning System J. Cao, D.J. Sun and D.L. Zhang	435
A Novel Algorithm for Multiuser Resource Allocation of OFDM Z.N. Zhao, J. Wang and H.W. Guo	440
A Modified DFE-MMSE Equalization Algorithm Y. Xia, F. Ye, Y.B. Li and L. Wang	444
Power Allocation Algorithm Based on QoS Strategy in Power-Line Communication K. Zhou, Y. Deng, W. He and X. Zhang	450
A Novel DFT-Based Channel Estimation for LTE-A Uplink L. Wang, F. Ye, Y.B. Li and Y. Xia	457
Based on the Jerk System Phase Space Division of the Study of the Method J. Yi, L.M. An, D.H. Li, J.Y. Tian, X.H. Wang and C.X. Liu	463
Design of an Ultra-Wideband Four Arms Sinuous Antenna W. Wang, X.T. Wang, Y. Li and S. Song	469
The Wireless Sensor Networks Based on Adjacent Strong Edge Chromatic Number Z.J. Sun and J. Chen	474
The Effects of RB Usage on Single User Rate in TD-LTE T. Li	478
Effects of Energy Harvesting Rate on Lifetime and Throughput Capacity in Wireless Sensor	
Networks Y. Zeng, X.D. Zhang and Y.H. Dong	482
Modified Fast Directional Multilevel Algorithm for Analysis of Scattering of Microstrip Patch	
H. Chen and F.Y. Jie	486
The Analysis on Research Progress of the Typical Hybrid Routing Protocol in Ad Hoc Networks	
J. Wu, G.Z. Hou, Z.G. Chen and L.Q. Tian	490
Mobile Prediction Idea Based Clustering Algorithm and Related Mathematical Quantitative Description	
J. Wu, T.J. Shao, Z.G. Chen and D.S. Cao	494

Chapter 6: Mechatronics, Control and Automation

Design of Coal Mine Main-Fan Automatic Monitoring System Based on ZigBee H.Q. Zhang and Z.H. Zhang	501
Chaotic Decision Model in the Collaborative Decision of Command and Control System Y.J. Xiao, D.X. Zhang and Z.S. Shi	505
Effectiveness Evaluation Model for Collaborative Command and Control System Y.J. Xiao, Z.M. Qiu and Z.S. Shi	509
Design the PCI Bus Servo Control Card Based on the PCI9052 W.L. Guo, H.J. Xing and X.N. Dong	513
Study of Nonlinear Observer for Dynamic Friction Compensation of High-Accuracy Servo-	
System L.Z. Wang	517
Solar Tracking Device Based on Electronic Compass and Accelerometer Z.R. Zhang, Y. Ma, B. Jiao and T.L. Liu	522
The Analysis of the Phase Noise of the Closed-Loop Driver Circuit in Micromechanical Gyroscope Based on the Phase-Locked Principle	
G.S. Wang and X.W. Liu	526
Development and Research of Open CNC System Based on Motion Controller H.W. Zhang and C.J. Chen	530
Application of the K-Means Immune Particle Swarm Optimization Algorithm in the Steam Generator Water Level Control	
G.M. Sheng, Y.C. Xue and B.Y. Zhang	534
The Application of Medical Robotics in the MRI-Guided Invention W.L. Guo, Z.J. Huang and Y. Zhang	538

Key Technology Research Based on the Smart Home BSNs C.Y. Wang and J. Zhang	542
Database Design of NC Cutting Tool Matching and Management System X.L. Sui, D. Wang, X.Y. Liu and Y. Teng	546
Exponentially Stable Sampled-Data Control for Uncertain Systems L.Y. Fan	551
Simulation Research on Fuzzy Control of Main Steam Temperature in Power Series S.Q. Tian, Q. Wei and X.F. Mu	555
Impact Velocity Analysis of Capacitive RF-MEMS Switch R. Wu and M.X. Song	560
Microwave Performance Simulation of RF-MEMS Switch R. Wu and M.X. Song	564

Chapter 7: Methods, Devices and Systems for Measurement and Monitoring

The Design of Wind Control LED Display System Applied on Ice Lantern L. Lan, Y.J. Cao and J.M. Cao	571
Design of the Pulse Wave Digital Filters Based on MATLAB H.L. Zhang, G.L. Zhang and K. Zhang	576
Measuring the Submarine's Induced Magnetic Field by Geomagnetic Simulation Method Z.Y. Zhang and J. Yi	579
Design of Induced Power Supply System for On-Line Monitoring Device of Power Cable X.L. Wei, B. Zhu, B. Pang, T. Liu, S. Wang and R.H. Li	585
Research on PCB Rogowski Current Transformer Based on AD7742 X.L. Wei, B. Zhu, B. Pang, T. Liu, S. Wang and R.H. Li	589
Research on Small-Capacity Capacitor Type Sensor Detection Method W.T. Hu, Y.X. Zhang, Y. Sun, W.S. Liu and L.Z. Zhang	594
The Measurement of DC Electric Field for Transformer Oil System Based on the Kerr Electro-Optic Effect	
T. Shen, C. Hu, M.X. Song, X.L. Wei and Q.R. Yang	598
Research on a Liquid Color Detecting Device Z. Zhou, D.X. Li, Y. Qin and L.F. Liu	602
Coal Mine Safety Monitoring System Based on ZigBee X. Liu, H.Q. Zhang and Z.H. Zhang	608
The Design of Wireless Video Monitoring System Based on FPGA Y.J. Yue, X.J. Zhang and C.M. Sha	612
Hydrogel Coated Long Period Grating Sensor for High Relative Humidity Measurement X.J. Yu, J.T. Zhang, X.F. Chen and S.C. Liu	616
A New Sensor for the Electrical Equipment Leakage Current X.L. Wei and W.L. Zheng	620
Evanescent Field Absorption Sensor Based on Special U Shaped Optical Fiber C.L. Liu, E.M. Zhao, E.T. Li, A. Zhou and X.H. Yang	624
A Measuring Method of Liquid Food Conductivity Based on Pulse Response Measurement	
Method X.L. Wei and Y.L. LI	628
Piezoelectric Resonant Temperature Sensor	020
Y. Yu, J. Xu, J. Ma and H.Y. Chen	632
Research on the On-Line Measuring Method of Transformer Short-Circuit Reactance Y.B. Wei and D. Zhang	636
Analysis of Data Mining Method for Near Infrared Spectral Data of Dairy Products Based Orthogonality	
L.J. Wang, Z. Zhou, Y. Qin, J.Y. Yin, J.Y. Guo, W.N. Dong and D. Wang	641
The Equal Precision Measurement Data Processing System Based on Virtual Instrument L.F. Zhang and S.Y. Wang	647

A Synchronous Sampling System of On-Line Monitoring for Long-Distance Cable	
Insulation Based on DSP and GPS	(5)
X.L. Wei, B. Zhu, B. Pang, T. Liu, S. Wang and R.H. Li	653
Design of Wireless Sensor Network for Fire Detection N. Du, Z.L. Liu and H.G. Dong	657
N. Du, Z.L. Liu and H.O. Dong	037
Chapter 8: Power Engineering and Power Supply	
Chapter 6: I ower Engineering and I ower Suppry	
Study on Low Frequency Oscillation of Wind Power System Based on HHT	
H.L. Xie and T. Yue	663
CHP Microgrid Optimized Operation Based on Bacterial Foraging Optimization Algorithm	
R. Li and P. Li	668
Community Based of CHP Microgrid Optimal Operation R. Li and P. Li	673
	075
Power Supply Efficiency Analysis and Techno-Economic Evaluation of IGCC Projects C.S. Xie, C.C. Zhao, P.Y. Zhong and C.Y. Zhou	677
Study on Relationships between High-Frequency High-Voltage Pulse Breakdown Voltage of	
Air-Gaps and Pulse Delay Time L.L. Li, Y.L. Wang and H.D. Yang	683
	085
The Control Technology of the Z-Source Three-Phase Four-Leg Inverter Based on Computer Simulation	
M. Su, X.Y. Ma and Y. Sun	688
Power System Probabilistic Production Simulation Including Efficiency Power Plant	
C.S. Xie, P.Y. Zhong, C.C. Zhao and C.Y. Zhou	695
Study on Fault Diagnosis Method for Nuclear Power Plant Based on Fuzzy Rough Sets and	
Decision Tree Y. Mu, G.M. Sheng, H. Xia, P.N. Sun and Y. Qian	701
	701
Chapter 9: Engineering of Weapons Systems	
Chapter 7. Engineering of Weapons Systems	
Research on Temporal Fire Distribution of Shipboard-Gun Neutralization Firing Anti-	
Shore D.O. Liong, V.W. Sup, H.C. Wong, D.H. Wong and F. Tion	700
D.Q. Liang, X.W. Sun, H.C. Wang, D.H. Wang and F. Tian	709
Operational Capability of Ship-to-Air Missile Weapon System	

Y.H. Lu, J.H. Dou, X.B. Yang and C.W. Zhu **The Research of Conventional Weapons Proving Ground Information System Construction** X.Y. Zhang, K. Lu, H.J. Wang and H.H. Ma **Research on Armored Mechanized Forces' Equipment Support Simulation Training System** X.Y. Zhang, K. Lu, H.J. Wang and H.H. Ma

Detection Performance Analysis of Space-Based Radar to near Space Hypersonic Target S. Xiao, X.S. Tan, H. Wang and Z.F. Zuo 730 **Cooperative Path Planning of Jammer Formation in Penetration Attack** J.J. Ou, A. Zhang and Z.Q. Chen 735 Study on a New Algorithm for Tracking Ballistic Missile in Free Flight Phase C.X. Chen and D.Y. Zhou 743 Conceptual Model of Information Naval Gun Weapon System Using Weapon System **Engineering Method** X.W. Sun, F. Tian, D.Q. Liang, H.Y. Shan and X.J. Zhang 754 Research on the Simulation of Naval Gun Exterior Trajectory Differential Equations in **Real-Time Solution** F. Tian, X.W. Sun, X. Zhang, H.Y. Shan and L.J. Wang 758

Chapter 10: Mechanical Engineering

713

717

724

Energy Efficiency Analysis of Piston Type Air Compressor S.L. Zheng, Y.Y. Mao, X.P. Wang, Z.Y. Zheng, S.X. He, Z.Y. Huang and D.D. Wang	769
The Optical Design of Achromatic Phase Matching System Based on ZEMAX L.Y. Zhang, Y.J. Liu and J.Z. Huang	774
Mechanical Design of End Support in Coal Mine H.W. Zhou	778
System Precision of Thermal Insulating Door in Environmental Laboratory H.W. Zhou	782
Study on Feature Extraction of Ship Radiated Noise Based on Cepstrum and Anti-Noise	
Property S. Zhan	786

Chapter 11: Material Science and Technologies of Processing

Digital Henon Sequences Generation and its Analysis B.B. Song, J. Pan and Q. Ding	793
Fluorescence from the Compound System of PVK Molecules and SiO ₂ Nanoparticles with Different Sizes	
L.M. An, Y.F. Duan, H. Liu, J. Yi, C.X. Liu, X.G. Li, L.Z. He, L.S. Zhou, P.Y. Wang and W.Y. An	797
Charge Transfer and Energy Transfer between CdSe Semiconductor Nano Crystals and Polyaniline Molecule	801
W.L. Zhou, T. Cai, J. Xiao, X.T. Han, J.B. Liu, L. Xu, J.G. Chi, S.H. Gao, X.P. Cai and L.M. An Synthesis of CdS-Capped CdSe Nanocrystals without any Poisonous Materials	801
W.L. Zhou, T. Cai, Y. Chen, X.L. Chen, Y.Q. Qu, X.B. Huang, W.J. Dai, D.H. Xiao, C.B. Yu, H. Wei and L.M. An	806
Advantages and Challenges Analyzed Utilizing MMA as the Printable Material to Fabricate Optical Waveguides	
H.B. Li, H. Liu and E.M. Zhao	810
Electrical Conductivity and Breakdown Characteristics of SiC/LSR Nanocomposites at Different Temperatures	
N.Q. Shang, Q.G. Chen, Y.J. Qin, M.H. Chi and X.L. Wei	814
Pre-Mixed Abrasive Water Jet Cutting in the Marble J.S. Xia, Q.Z. Jia and Z.Z. Sun	818
MgAl/PbPc/Cu Organic Thin-Film Diode Preparation and Gas-Sensing Characteristics Analysis	
J.B. Chen, P. Yu, Y. Zhang, Y. Shan and D.X. Wang	822
The Fabrication and Characteristics of CuPc Thin Film Phototransistor Y.S. Zhang, M. Zhu, D.X. Wang, Z.Y. Wang, Y.Y. Wang and J.H. Yin	826
The Dynamic Characteristics of Al Gate CuPc Thin Film Transistor Z.Y. Wang, D.X. Wang, Y.S. Zhang, Y.Y. Wang, J.H. Yin and H. Zhao	830
The Preparation and Characteristics Analysis of ZnO/Ni/ZnO Schottky Junction TFTs Y. Shan, Y.H. Wu, D.X. Wang, Y. Zhang, J.B. Chen, J.H. Yin and H. Zhao	834
The Analysis of Photocurrent Multiplication in Organic Dye CuPc Transistor with Wide	
Wavelength Light Y.Y. Wang, D.X. Wang, Y.S. Zhang and Z.Y. Wang	838
Research of Silicon-Based Micro Direct Methanol Fuel Cell S.S. Cao	842
The Design and Characterization of Three-Dimension Metamaterial for Terahertz	
Frequencies Q. Wang, Y. Wang, Y.L. He, W.C. Zhang and X. Wang	846
The Effect of Components Based on Synchronous Radiation SAXS on Micro-Structure of BI/TiO_None Composite Film	
PI/TiO ₂ Nano-Composite Film L. Yao, J.H. Yin, G.Y. Li, X.X. Liu and G. Mo	851
The Research of Trap Level Distribution of PI/AIN (Treated)-MMT Films with Different	
Contents Based on Decay Charge Theory Y.Y. Liu, J.H. Yin and Y. Lei	855

PIC/MCC Simulations for the Oxygen Microwave Breakdown at Atmospheric Conditions H.H. Wang, D.G. Liu, L.Q. Liu and L. Meng	859
The Preparation of Alq₃/CuPc Heterojunction Organic Electroluminesence Diodes Y.H. Wu, Y. Shan, D.X. Wang, C.M. Meng, Y.W. Yang, J. Fu and S.K. Deng	863
Solute Field in Liquid Ahead of the Solid-Liquid Interface during Dendritic Solidification Incorporating Relaxation Effect	
X.Z. Jin, H.Y. Wang, N. Wang, X.G. Lan and S. Li	867
Study on Preparation and Refining Efficiency of Al-5Ti-1C Master Alloy Refiner F.W. Kang, Y. Xiong, X. Bai, D.D. Zhang, P. Liu, T.L. Yang and Y.C. Feng	871
Optimized Technical Characteristics of Polysilicon Nanofilm X.B. Lu, L.H. Cui and M.Y. Ren	875
Effect of Charge Transferring Materials on Photoluminescence Properties of CdSe/ZnS	
Quantum Dots X.L. Chen, Y.Q. Qu, G.F. Li, H. Wei, L.Y. Zhang and L.M. An	879
Study on Photoluminescence Quenching of CdSe Core/Shell Quantum Dots with Organic Charge Transferring Material	002
Y.Q. Qu, L.Y. Zhang, L.M. An, H. Wei and G.F. Li	883
Self-Propagating High-Temperature Synthesis of Ni-Cu-Zn Ferrites with Alternative Fuel of Carbon Powder Z.H. Wang, J.X. Jiang, C.L. Tan, Z.H. Zhu and F. Xu	887
Effect of PVP Hydrophilic Additive on the Morphology and Properties of PVDF Porous	867
Membranes Y.W. Guo, W.W. Cui, W.H. Xu, Y. Jiang, H.H. Liu, J.Y. Xu, Z.Q. Gao and L.Z. Liu	891
Analysis to Milling Force Base on AdvantEdge Finite Element Analysis	691
F.C. Zhang, Q. Wang and R. Yang	895
Research on the Effects of Ultraviolet Aging of Polyethylene Trap Distribution L.J. He, C. Zhu, H.C. Huang, S. Wang, H.P. Xie and C.T. Chen	899
Characteristics Research of New Type Silicon Magnetic Sensitivity Transistor Differential	
Structure by ATLAS X.F. Zhao, H.Y. Guan, H. Sui and D.Z. Wen	903
Fast Solidification and Electrical Conductivity of Apatite-Type Nanoceramics Q. Li and L.M. Dong	909
Particle Size Effect on the Corona Resistant Properties of PI/TiO ₂ Composite Films G.Y. Li, J.H. Yin, L. Yao and X. Zhao	914
Structure and Property Stability of Rapidly Solidified In-Sn γ-Phase Alloy J.Z. Wang, M.L. Liu and D.Y. Li	918
Influcing Factor Research of Kerr Effect R.L. Guo, N.N. Sun, M.X. Song and Q. Liu	923
Type Conversion of Undoped NiO Thin Films Fabricated by Electron Beam Evaporation	20
Technique	
Q.C. Liang, M. Zhao, D.Y. Jiang, X. Wang, J.X. Zhao, S. Gao, J.M. Qin, J.H. Hou and Y. Cui	927
A New Type of EO Polymer Based on Polyphosphazenes Y. Zhang, C.J. QIU, Y. Li, W.L. Zhang and X. Wang	932
The Stress Distribution and Influence of VDMOS Device Based on ANSYS J.H. Yin, S.T. Gao and M.H. Chen	936
Analysis of Electric Field Homogenization of Converter Transformer Barrier System Based on Nano Modification of Pressboard	
Q.G. Chen, H.Q. Liu, X.L. Zhuge, M.H. Chi and X.L. Wei	940
Experimental Investigation of Emulsifying Viscosity Reduction of a New Viscosity Breaker F. Wang, C. Ai, D.D. Yuan, S. Liang and G.M. Qu	946
The Photocurrent Characteristic Analysis of the Copper Phthalocyanine Organic Thin Film Transistor Irradiated by 700 nm Monochromatic Light	
Y. Zhang, D.X. Wang, J.B. Chen, Y. Shan, J.H. Yin and H. Zhao	

Chapter 12: Engineering Management and Logistics

Order Batching Picking Based on Activity Based Classification Storage L. Guo and X.J. Yang

Analysis of Financial Agglomeration Effect on Corporate Financing Behavior F.F. Li and J.Y. Huang	961
Research on Seasonal Index Based on Dynamic Clustering of the Daily Railway Passenger Flow Title	
Z.Z. Wei and F.Z. Wang	966
Evolving Model Research of Layered Agri-Food Supply Chains Weighted Complex Networks Y. Li, Z.P. Du and L. Zhang	972
Affective Identification Motivation Mechanism of Sino-Japanese Bi-Cultural Teleworking	12
Teams B. He, S.Y. Li, H. Zheng, C.Z. Ma and X. Tang	976

CHAPTER 1:

Electronic Engineering

Phasor Analysis Based Fault Modeling and Fault Diagnosis Methods for Linear Analog Circuits

Yuan Gao^{1,a}, Chenglin Yang^{1,b} and Shulin Tian^{1,c} ¹University of Electronic Science and Technology of China Xiyuan Ave, West Hi-Tech Zone, Chengdu, Sichuan, P.R.China,611731 ^ac4isrmm@sohu.com, ^byangclin@uestc.edu.cn, ^cShulin@uestc.edu.cn

Keywords: Analog Fault Diagnosis, Fault modeling, Fault Feature, Tolerance.

Abstract. Soft fault diagnosis and tolerance are two challenging problems in linear analog circuit fault diagnosis. To solve these problems, a phasor analysis based fault modeling method and its theoretical proof are presented at first. Second, to form fault feature data base, the differential voltage phasor ratio (DVPR) is decomposed into real and imaginary parts. Optimal feature selection method and testability analysis method are used to determine the optimal fault feature data base. Statistical experiments prove that the proposed fault modeling method can improve the fault diagnosis robustness. Then, Multi-class support vector machine (SVM) classifiers are used for fault diagnosis. The effectiveness of the proposed approaches is verified by both simulated and experimental results.

Introduction

The catastrophic faults are handled in Ref.[4]. Methods proposed in literatures [5], [6] are used to diagnosis discretized parameter faults. Both catastrophic and discretized parameter fault diagnosis problem are discussed in papers [7]. Local spot defect is handled in reference [8]. The author also point out that the local spot defect are often modeled by open and short circuits. Aiming at linear Switched-Capacitor Circuit fault, Hao-Chiao Hong [9] proposes a static linear behavior modeling method. By using this method, the CUT is partitioned into several functional macros. Each functional macro has specified design parameters which constitute the parameter set and determine the transfer function of the CUT. If frequency responses are out of the design specification, the parameter set is supposed to be faulty. This method falls into functional test method.

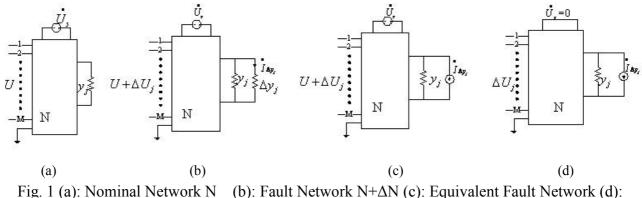
A high level fault modeling method proposed in Ref.[10] is used to model transistor level analog faults. In Ref. [11], a node-voltage sensitivity sequence dictionary method is established. Whether a fault is hard or soft, only one fault characteristic code is needed to detect any fault of a component. Based on the ideas in Ref.[11], Ref.[12] and [13] developed methods for diagnosing soft faults of tolerance analog circuits and nonlinear circuits. A slope fault feature based soft fault diagnosis method is proposed in Ref.[14]. It is a uniform fault modeling method for both hard and soft fault in linear circuit. By using fuzzy math to replace ambiguity sets to handle tolerance issue, Wang and Yang [15] propose an equivalent faults model to handle test node selection problem. However, all the mentioned methods do not model fault on complex domain, and do not handle tolerance well.

This paper focuses on component level fault modeling and fault diagnosis problem. First, the modeling idea is to establish the relationship between the DVPR and fault component by using phasor analysis. This kind of relationship is independent from the value of fault component and can be served as fault feature. The feature can be easily obtained by using simulation. Second, the optimal test selection method proposed in [16] are used to determine the optimal fault feature data

base. Based on this data base, Multi-class SVM classifiers are trained and used to future fault diagnosis.

Principle of The Proposed Fault Model

A. Theoretical Foundation



Differential Network ΔN

Suppose that CUT *N* shown in Fig.1(a) is a linear time-invariant passive circuit. The admittance of passive element is $y_j \cdot U$ is voltage phasor vector of measurable nodes {1, 2,...,M} in *N*. U_s is independent source. Without loss of generality, assume that the admittance is shifted to $y_j + \Delta y_j$ when a fault occurs to x_j . As a result, the fault voltage phasor vector of measurable nodes is $U + \Delta U_j$. Suppose that the current in Δy_j is $I_{\Delta y_j}$, according to the substitution theorem [16], the passive element Δy_j can be replaced with independent current source $I_{\Delta y_j}$, as shown in Fig. 1(c). According to the superposition theorem [16], the voltage vector on measurable nodes in Fig. 1(c) equals the algebraic sum of the responses caused by U_s and $I_{\Delta y_j}$ acting alone. Fig. 1(a) shows that U_s acts alone, and Fig. 1(d) shows that $I_{\Delta y_j}$ acts solely. In Fig.1(d)

$$\Delta U_{j} = Z_{j} I_{\Delta y_{j}}$$
⁽¹⁾

where Z_j is the transfer impedance vector from fault port to measurable nodes. It can be seen from this figure that Z_j is independent from the value of $I_{\Delta y_j}$; hence, it is independent from the fault magnitude Δy_j . Additionally, Z_j is uniquely determined by the nominal CUT and the location of fault component. Totally, there are M measurable nodes in Fig. 1(a). Hence, vector ΔU_j can be obtained. By using ΔU_{1j} to divide ΔU_j , differential voltage phasor ratio (DVPR) vector k_j is obtained.

$$k_{j} = \frac{\Delta U_{j}}{\Delta U_{1j}} = \begin{pmatrix} 1 \\ Z_{2j} / Z_{1j} \\ Z_{3j} / Z_{1j} \\ \vdots \\ Z_{Mj} / Z_{1j} \end{pmatrix} = \begin{pmatrix} k_{1j} \\ k_{2j} \\ k_{3j} \\ \vdots \\ k_{Mj} \end{pmatrix}$$
(2)

Obviously, k_j is uniquely determined by Z_j ; hence, it is uniquely determined by the nominal CUT and the location of fault component y_j . Hence, k_j can act as fault feature of y_j . More importantly, k_j is independent from the fault magnitude of y_j . Regardless of what kind of fault it is and how much the fault magnitude is, k_j are fixed. It is a uniform fault feature for both hard (open or short) and soft (parametric) faults. Based on formula (2), the following simulation steps are proposed to calculate k_j .

B. Simulation Based Fault Model Acquisition

From formula (2), the vector k_i is calculated by using following equation.

$$k_{j} = \frac{\Delta U_{j}}{\Delta U_{1j}} \tag{3}$$

Based on this formula and Fig. 1(b), the vector k_j can be computed by using following simulation steps.

Step 1) The CUT is stimulated by independent source U_s . Fault free voltage U on measurable nodes is stored.

Step 2) Component y_j is randomly adjusted to any value other than fault free. Voltage on measurable nodes is recorded as U_j .

Step 3) Calculating differential voltage $\Delta U_j = U_j - U$. k_j is calculated by using (3).

C. Construction of the Optimal Fault Database

If there are N potential fault components in the CUT, the DVPR K is a M×N matrix. In this matrix, columns represent different fault sources and the rows show the available test nodes. There might be identical columns in matrix K, viz., $k_i = k_j (i \neq j)$. It means that the corresponding fault sources have the same fault feature. Faults with the same fault feature form an ambiguity set. Identical rows represent redundant test nodes. The test nodes selection algorithm proposed in [16] is used to select optimal test nodes.

Based on equation (2), $k_{1j} = 1$. Hence, all the elements in the first row of matrix K is equal to 1. It means that the first test node cannot distinguish any fault. This row should be removed from matrix K. Due to that impedance Z_j is complex vector, $k_{ij} = Z_{ij}/Z_{1j}$ is complex number too. Suppose that the real and imaginary parts of k_{ij} are $\operatorname{Re} k_{ij}$ and $\operatorname{Im} k_{ij}$ respectively. A matrix \tilde{K} derived from K is as follows.

$$\tilde{K} = \begin{bmatrix} \tilde{k}_{1} & \tilde{k}_{2} & \cdots & \tilde{k}_{N} \end{bmatrix} = \begin{bmatrix} \operatorname{Re} k_{21} & \operatorname{Re} k_{22} & \cdots & \operatorname{Re} k_{2N} \\ \operatorname{Im} k_{21} & \operatorname{Im} k_{22} & \cdots & \operatorname{Im} k_{2N} \\ \operatorname{Re} k_{31} & \operatorname{Re} k_{32} & \cdots & \operatorname{Re} k_{3N} \\ \operatorname{Im} k_{31} & \operatorname{Im} k_{32} & \cdots & \operatorname{Im} k_{3N} \\ \vdots & \vdots & \vdots & \vdots \\ \operatorname{Re} k_{M1} & \operatorname{Re} k_{M2} & \cdots & \operatorname{Re} k_{MN} \\ \operatorname{Im} k_{M1} & \operatorname{Im} k_{M2} & \cdots & \operatorname{Im} k_{MN} \end{bmatrix}$$
(4)

where $\tilde{k}_j \in R^{2(M-1)}$ is column vector, and fault feature database \tilde{K} is $2(M-1) \times N$ matrix. *M* is the number of optimal test nodes, and *N* is the number of representative faults.

SVM Classifier Based Fault Diagnosis

In an actual analog circuit, a parameter of a circuit element may vary within a range around its nominal value without treating it as a fault. This is termed as "tolerance." Hence, when a fault occurs to circuit element y_i , the measured fault feature \tilde{k}_f may not be equal to the nominal fault feature \tilde{k}_i exactly. Under this circumstance, fault diagnosis is much more a fault classification problem. Support Vector Machine (SVM) is a powerful solution to the classification problems [18]. The simplest linear SVM classifier is adopted in this paper.

Step1) The fault free CUT is simulated, and the voltage vector on M selected test nodes $\overset{\bullet}{U}$ is stored. The number of Monte Carlo simulation N_M is preset.

Step 2) Suppose that there are N representative fault components. For every representative fault component y_i , the following simulations are run for N_M times.

Step2.1) The faulty parameter $\Delta y_j \in (0, (1-a)y_j) \cup ((1+a)y_j, \infty)$ is randomly generated by computer, where *a* is the tolerance limit.

Step2.2) Within the tolerance range $((1-a)y_i,(1+a)y_i)$, all other fault free components' parameters are randomly generated by computer too.

Step2.3) The simulated fault voltage vector is recorded as U_f .

Step 2.4) The differential voltage is $\Delta U_i = U_f - U$. Fault feature $\tilde{k}_j \in R^{2(M-1)}$ is calculated by using formula (2) and (4).

Step 3) The training data is $\{\tilde{k}_j, y_j\}$, $j = 1, \dots, N_M \times N$, $y_j \in \{-1, 1\}$, $\tilde{k}_j \in R^{2(M-1)}$. There are *N* representative fault components; hence, the training data is classified into *N* groups, and N(N-1)/2 individual SVM networks are trained.

Totally, there are three phases in the proposed fault modeling and diagnosis procedure. The first phase includes fault modeling, testability analysis and fault feature database optimization. Fault modeling is to establish the optimal fault feature database \tilde{K} . The second phase is Multi-class SVMs training. All the involved simulations are executed by using Pspice under the supervision of Matlab. Except for the Monte Carlo simulations, all the faulty parameters are set by Matlab. Hence, the whole simulation process is automatically accomplished. The third phase is fault diagnosis. In

this phase, the trained Multi-class SVM classifiers are used to classify the simulated or actual fault data. All the algorithm and data process are realized by using Matlab.

Experimental Results

In this section, not only the tolerance but also measurement error is taken into consideration. The following parameters are used in all the experiments.

—resistance tolerance limit $a_R=\pm5\%$;

- —capacitance tolerance limit $a_C = \pm 10\%$;
- —measurement error limit $e=\pm 5\%$.

The CUT is shown in Fig.2. Totally, there are six available test nodes. The first phase is fault modeling and fault feature database optimization. The CUT is stimulated by a 1-kHz 1-V sinusoidal

wave. The simulated faulty and fault free voltage vector U are recorded in Table 1. Due to page limitation, only parts of the results are listed.

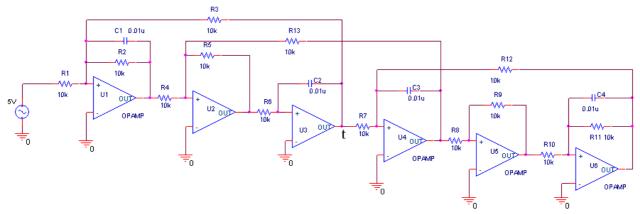


Fig.2. Leapfrog filter

	Fault free	R1=5[kΩ]	R2=[5kΩ]	 C3=10[nF]	C4=5[nF]		U5 fail	U6 fail
	\dot{U}	$\overset{\bullet}{U}_{1}$	U_2	 $\overset{ullet}{U}_{16}$	$\overset{ullet}{U}_{17}$		• U 22	• U ₂₃
n1	-0.5262 -	-1.0525 -	-0.3455 -	 -0.6431 +	-0.5802 -		-0.3757-	-0.4380-
	0.0504 <i>i</i>	0.1007i	0.0216i	0.1150i	0.1029i		0.1645i	0.1857i
n2	0.4788 +	0.9576 +	0.3271 +	 0.3633 +	0.5874 +	•••	0.5034+	0.5792+
	0.6351 <i>i</i>	1.2703i	0.4054i	0.3577i	0.6088i		0.9145i	0.8529i
n3	-0.5054+	-1.0108 +	-0.3226 +	 -0.2847 +	-0.4845 +		-0.7277+	-0.6787+
	0.3810 <i>i</i>	0.7620i	0.2603i	0.2891i	0.4675i		0.4006i	0.4609i
n4	0.0474-	0.0949 -	0.0184 -	 0.2798 -	-0.0072 -		-0.1277-	-0.1413-
	0.5848 <i>i</i>	1.1695i	0.3838i	0.4727i	0.5059i		0.7500i	0.6672i
n5	-0.0474+	-0.0949 +	-0.0184 +	 -0.2798 +	0.0072 +		0.0639+	0.1413+
	0.5848 <i>i</i>	1.1695i	0.3838i	0.4727i	0.5059i		0.3750i	0.6672i
n6	-0.2294-	-0.4588 -	-0.1597 -	 -0.0123 -	-0.1512 -		-0.2147-	-0.1597-
	0.4406 <i>i</i>	0.8812i	0.2834i	0.4649i	0.4584i		0.2401i	0.2834i

Table 1 Simulated voltage vector (in volt)

Based on the data shown in Table 1, the DVPRs are calculated. The results are saved in Table 2. The optimized fault features are shown in Table 3. It can be seen from this table that there are six ambiguity sets. The first component in each set is selected as representative. By using the optimization method proposed in former section, features on nodes n2, n5 and n6 are selected to diagnose fault.

	R1	R2		C3	C4		U5 fail	U6 fail
	k_1	k_2		k_{16}	k_{17}		<i>k</i> ₂₂	k_{23}
nl	1	1		1	1		1	1
n2	-1.0161-	-1.0161-		-0.7896+	-0.7896+		-0.7896+	-0.7896+
	1.1097i	1.1097i		1.2566i	1.2566i		1.2566i	1.2566i
n3	0.8831-	0.8831-		-1.0000-	-1.0000-		-1.0000-	-1.0000-
	0.8086i	0.8086i		0.6283i	0.6283i		0.6283i	0.6283i
n4	0.0161+	0.0161+		-0.2104-	-0.2104-		-0.2104-	-0.2104-
	1.1097i	1.1097i		1.2566i	1.2566i		1.2566i	1.2566i
n5	-0.0161-	-0.0161-		0.2104 +	0.2104+		1.1401-	0.2104 +
	1.1097i	1.1097i		1.2566i	1.2566i		0.5289i	1.2566i
n6	0.5114+	0.5114+		-0.7170-	-0.5791+		-0.5791+	-0.5791+
	0.7884i	0.7884i		0.8062i	0.8928i		0.8928i	0.8928i
			Table 2	Ontimal	fault faatu	ro		

Table 2 DVPR vector kj

Table 3 Optimal fault feature

		<i>R1</i> ,R2,R3,C1	R4 ,R5,R13,	R6 ,C2,	R7 ,R12,C3,	R8 ,R9,	<i>R10</i> ,R11,C4
		,U1	U2	U3	U4	U5	,U6
		$ ilde{k_1}$	$ ilde{k}_2$	\tilde{k}_3	$ ilde{k}_4$	\tilde{k}_5	\tilde{k}_6
	Real part	-1.0161	-0.7896	-2.0512	-0.7896	-0.7896	-0.7896
n2	Imaginary part	-1.1097	1.2566	0.3056	1.2566	1.2566	1.2566
	Real part	-0.0161	-1.0512	-1.0512	0.2104	1.1401	0.2104
n5	Imaginary part	-1.1097	0.3056	0.3056	1.2566	-0.5289	1.2566
	Real part	0.5114	0.6160	0.6160	-0.7170	-0.5791	-0.5791
n6	Imaginary part	0.7884	-0.6926	-0.6926	-0.8062	0.8928	0.8928

It can be seen from Table 3 that fault feature $\tilde{k}_j \in R^6$. The second phase is Multi-class SVMs training. Totally, 6(6-1)/2=15 individual SVM networks are needed to classify 6 ambiguity sets. For each representative component y_j , Monte Carlo simulation is run for 80 iterations. In each iteration, its faulty parameter is randomly generated within the range of $(0, 0.9y_j) \cup (1.1y_j, \infty)$. At the same time, all other components' parameter is randomly generated within the tolerance limit. Based on the simulated features $\tilde{k}_j \in R^6$, the Multi-class SVM classifiers are trained. The results, viz., weight vectors w_j and bias b, are shown in Table 4.

Table 4 Multi-class SVM training results

	(R1,R4)	(R1,R6)	 (R1,R10)	(R4,R6)		(R4,R10)	(R6,R7)		(R6,R10)	(R7,R8)	(R7,R10)	(R8,R10)
	<i>w</i> ₁	w_2	 W5	W6	•••	Wg	<i>w</i> ₁₀		<i>w</i> ₁₂	<i>w</i> ₁₃	<i>w</i> ₁₄	<i>w</i> 15
	-0.1298	0.2826	 -0.0455	1.1511	•••	0.0530	-0.4834	•••	-0.3402	0.0763	0.1376	-0.1382
	-0.5522	-0.4724	 -0.4621	0.9577	•••	0.0123	-0.3478	•••	-0.2713	-0.1902	-0.2186	0.2339
	0.1948	0.3013	 -0.0705	-0.1511		-0.4550	-0.4518		-0.3227	-0.4154	0.2311	0.6444
W	-0.3151	-0.4874	 -0.4584	-0.1090		-0.3454	-0.3535		-0.2450	0.6479	-0.3237	-0.9906
	0.0048	0.0074	 0.1749	0.0890		0.3947	0.4548		0.2799	0.0208	-0.0357	-0.2550
	0.3097	0.4791	 -0.0819	0.0064		-0.6508	0.0519		-0.4616	-0.6452	-1.3881	-0.2492
b	-0.0618	0.2864	 0.1239	0.6568	•••	0.1834	-0.1739		-0.1339	0.3968	0.8128	-0.3997

Fault diagnosis is realized by using the training results shown in Table 4. In actual application, the accuracy of the proposed fault diagnosis method is affected by the tolerance problem and measurement error. To check the accuracy, statistical simulations are carried out. For each representative fault component, its fault range is classified into three ranges.

$$R_{f} = \begin{cases} (0.8R_{o}, 0.9R_{o}) \cup (1.1R_{o}, 1.2R_{o}) \\ (0.7R_{o}, 0.8R_{o}) \cup (1.2R_{o}, 1.3R_{o}) \\ (0.0.7R_{o}) \cup (1.3R_{o}, \infty) \end{cases}$$
(5)

where R_f is the fault parameter and R_0 represents fault free parameter. Within each fault range, simulation is run for 100 iterations. Faulty parameter is randomly generated within the predefined fault range. The other components are varied within the tolerance limit. Because there are six representative faults; hence, there are $6\times3\times100=1800$ simulations, and there are 1800 fault features to be diagnosed. Random measurement errors are added to fault voltage vectors, and the fault features are calculated. Classifiers shown in Table 4 are used to diagnosis faults. The results are shown in Table 5. For small parameter shifting errors, the fault diagnosis accuracy is 90%. Take R6 for example. If R6 varies within the range of $(0, 7k\Omega) \cup (13k\Omega, \infty)$, it is diagnosed properly. When $R6 = (7k\Omega, 8k\Omega) \cup (12 k\Omega, 13 k\Omega)$, there are 5 percent of faults is not diagnosed. If its fault range is $(8k\Omega, 9k\Omega) \cup (11 k\Omega, 12 k\Omega)$, the fault diagnosis accuracy is decreased to 90%. Therefore, we can conclude that the proposed fault diagnosis method is not affected by tolerance problem. But the accuracy of small parameter shifting is susceptible to measurement error. The reason is that small parameter shifting incurs small differential voltage. Small differential voltage information is more likely covered by measurement errors. Therefore, the fault diagnosis accuracy is decreased. Even though, 90% fault diagnosis accuracy is acceptable.

	fau	faulty parameter range							
	$(0.8R_0, 0.9R_0)$ U	$(0.7R_0, 0.8R_0)$ U	$(0, 0.7R_0)U$						
	$(1.1R_0, 1.2R_0)$	$(1.2R_0, 1.3R_0)$	(1.3R ₀ , ∞)						
R1	100%	100%	100%						
R4	94%	98%	100%						
R6	90%	95%	100%						
R7	93%	100%	100%						
R8	94%	100%	100%						
R10	97%	100%	100%						

	T 1.		
Table 5	Fault	diagnosis	accuracy

Conclusions

The slope-based modeling method has solved the soft-fault diagnosis problem. However, the tolerance problem remains unsolved. The proposed phasor analysis and complex number decomposition based method can accurately model analog fault and is immune from tolerance problem. When combined with the Multi-class SVM technique, the proposed fault diagnosis method can accurately locate the fault component, even in the presence of a soft fault and tolerance. When a low magnitude parameter shifting happens, the component parameter shift just out of the tolerance limit for example, the measurement error might incur false diagnosis result. Even though, the accuracy is at least 90%. Additionally, the proposed method can readily be extended to multiple-fault situations. For example, to modeling and diagnosis double faults, all possible combinations of any two faults are listed. Same as single fault, for every pair of faults, the proposed simulation method is used to obtain fault voltage vector. Then the fault feature database is optimized and the Multi-class SVM technique can also be used to Multi-fault diagnosis.

Acknowledgements

This work was supported in part by the NSFC (No. 61201009, No. 61271035).

References

- [1] W. Hochwald and J. D. Bastian: IEEE Trans. Circuits Syst., vol. CAS-26(1979), p. 523.
- [2] P. M. Lin and Y. S. Elcherif: Inl. J. Circuit Theory Appl., vol. 13(1985), p. 149.
- [3] Janusz A. Starzyk, Dong Liu, Zhi-Hong Liu, Dale E. Nelson and Jerzy O Rutkowski: *IEEE Trans. Instrum. Meas.*, vol. 53 (2004), p. 754.
- [4] Shangcong Feng and Xiaofeng Wang, "Research on Fault Diagnosis of Mixed-Signal Circuits Based on Genetic Algorithms," 2012 International Conference on Computer Science and Electronics Engineering (ICCSEE), vol.3(2012), pp.12-15,.
- [5] Yong Deng, Yibing Shi and Wei Zhang: IEEE Trans. Instrum. Meas., vol. 61, no.2(2012), p. 358.
- [6] Sai Sarathi Vasan, A., Long B. and Pecht, M: *IEEE Transactions on Industrial Electronics*, vol.60 (2013), p.1,.
- [7] Xiang Li, Yang Zhang, Shujuan Wang and Guofu Zha:2012 International Symposium on Instrumentation & Measurement, Sensor Network and Automation (IMSNA), vol. 1(2012), p.236,.
- [8] Ke Huang, Stratigopoulos H.G., Mir S., Hora C., Yizi Xing and Kruseman B.:*IEEE Trans. Instrum. Meas.*, vol. 61 (2012), no.10, p. 2701.
- [9] Hao-Chiao Hong, "A Static Linear Behavior Analog Fault Model for Switched-Capacitor Circuits," *IEEE Trans. Comput.-Aided Design Integr. Circuits Syst.*, vol.31, no.4(2012), p.597.
- [10]Farooq M.U., Likun Xia, Hussin F.A. and Malik A.S, "High level fault modeling and fault propagation in analog circuits using NLARX automated model generation technique," *4th International Conference on Intelligent and Advanced Systems (ICIAS)*, vol.2(2012), p. 846.
- [11] Feng Li and Peng-Yung Woo: IEEE Trans. Circuits Sys. I, vol.46 (1999), p.1222.
- [12]Zhou Longfu and Shi Yibin, "A Novel Method of Single Fault Diagnosis in Linear Resistive Circuit based on Slope", *ICCCAS*, p.1350,(2008).
- [13] Yanjun Li, Houjun Wang, and Rueywen Liu:*IEEE Circuits and Systems International Conference on Testing and Diagnosis*, p.1 (2009).
- [14]Hu Mei, Wand Hong, Hu Geng and Yang Shiyuan: *Tsinghua Science And Technology*, vol.12(2007), p.26.
- [15] Wang Peng and Yang Shiyuan: *IEEE Trans. on Circuits and Systems-I: Regular Papers*, vol. 52(2005), p.2118,.
- [16] Chenglin Yang, Shulin Tian, Bing Long, and Fang Chen: *IEEE Trans. Instrum. Meas.*, vol. 60, no.1(2011), p. 176.
- [17]Robert L. Boylestad, "Introductory Circuit Analysis (10th Edition)", Prentice Hall, p.354, (2002).
- [18]Koley C., Purkait P., Chakravorti S.:*IEEE Transactions on Dielectrics and Electrical Insulation*, vol.14, no.6(2007), p. 1538.
- [19] Christopher j.c. Burges: Data Mining and Knowledge Discovery, vol. 2(1998), p.121.
- [20]C.W. Hsu and C. J. Lin: IEEE Trans. Neural Netw., vol. 13, no. 2(2002), p. 415.

Methods of Handling the Aliasing and Tolerance Problem for a New Unified Fault Modeling Technique in Analog-Circuit Fault Diagnosis

Yuan Gao^{1,a}, Chenglin Yang^{1,b} and Shulin Tian^{1,c}

¹University of Electronic Science and Technology of China, Xiyuan Ave, West Hi-Tech Zone, Chengdu, Sichuan, P.R.China,611731

^ac4isrmm@sohu.com, ^byangclin@uestc.edu.cn, ^cShulin@uestc.edu.cn

Keywords: Analog fault diagnosis, fault modeling, tolerance, aliasing problem.

Abstract. Soft fault diagnosis and tolerance are two challenging problems in analog circuit fault diagnosis. This paper proposes approaches to solve these two problems. First, a complex field modeling method and its theoretical proof are presented. This fault modeling method is applicable to both hard (open or short) and soft (parametric) faults. It is also applicable to either linear or nonlinear analog circuits. Then, the parameter tolerance is taken into consideration. A frequency selection method is proposed to maximize the difference between the faults fault signature. Hence, the aliasing problem arise from tolerance can be mitigated. The effectiveness of the proposed approaches is verified by simulated results.

Introduction

Among various fault diagnosis methods, one of the most widely used SBT methods is the fault dictionary method[1,2,3,4]. The fault dictionary technique is initially used in catastrophic faults diagnosis 0. Recently, it is extended to both hard-fault and soft-fault detection. In reference 0, a node-voltage sensitivity sequence dictionary method is established. Whether a fault is hard or soft, only one fault characteristic code is needed to detect any fault of a component. However, such a sequence is simples a qualitative signature and cannot explain the difference between any two signatures quantitatively, so it is unable to determine whether the real state of the circuits is within the tolerance range or under a fault state. Based on the ideas in Ref. 0, Ref. 0 developed a method for diagnosing soft faults of tolerance analog circuits and nonlinear circuits; while Ref. 0 constructed a new dictionary method based on a theorem referred to as "the conservation of node voltage sensitivity weight sequence". Wang and Yang 0 improved the method in Ref. 0, and then the fault dictionary method could theoretically achieve both single and multiple fault diagnosis, and handle tolerance. All the mentioned fault diagnosis methods and fault models can not properly solve the influence of tolerance on fault diagnosis.

A unified fault modeling method is proposed in this paper, and frequency selection method is proposed to solve the aliasing problem.

Aliasing Problem of The Proposed Fault Model

It is proved0 that in a linear time-invariant circuit under test(CUT), the real and image parts of fault voltage must satisfy the following quadratic equation.

$$\Delta U_{or}^2 + \Delta U_{oj}^2 + \left(\frac{R_0}{X_0}n - m\right)\Delta U_{or} - \left(\frac{R_0}{X_0}m + n\right)\Delta U_{oj} = 0$$
⁽¹⁾

where ' R_0 ', ' X_0 ', 'a' and 'b' are independent from the value of fault component x and are uniquely determined by the fault free components in N and the location of the fault element x; hence, formulation (1) always hold regardless of what kind of fault occurs to x, and can be used as the fault model. If x is a dynamic element, the same conclusion is reached. Therefore, the equation (1) is a unified fault modeling method. It is need to point out that equation (1) is also the function of frequency.

$$f_x\left(U_{or}, U_{oj}, \boldsymbol{\omega}\right) = 0 \tag{2}$$

For lumped, linear, time-invariant circuits, the frequency response function is rational function in the frequency variable ω and the circuit elements x_i .

$$H(\omega) = \frac{N(\omega, x_1, x_2, \cdots, x_m)}{D(\omega, x_1, x_2, \cdots, x_m)}$$
(3)

Without loss of generality, suppose that the fault source is x_i and all the other components kept constant, the frequency response function is the function of x_i

$$H_i(\boldsymbol{\omega}) = F_i(\boldsymbol{\omega}, \mathbf{x}_i) \tag{4}$$

Because equation (1) is quadratic, the loci of any two different fault source on the complex plane might have intersections besides the fault free point, viz., for any two fault sources x_i and x_k , there might be x_{fi} and x_{fk} such that the following equation established.

$$F_{i}\left(\boldsymbol{\omega}_{0},\boldsymbol{x}_{fi}\right) = F_{k}\left(\boldsymbol{\omega}_{0},\boldsymbol{x}_{fk}\right)$$

$$\tag{5}$$

where ω_0 is the operation frequency of CUT. It means that different faults may have the same output U_{ik} even if the fault sources are distinguishable.

Take Fig. 2 for example. R1 (signature curve ①) and C3 (signature curve ①) have different signature curves governed by equation(1). But besides the fault free point, either R1=3728 Ω or C3=73.5*n* induce the same output $\dot{U}_f = -4.9 + 2.6j$. Hence, these two specific parameter faults are undistinguishable at current frequency. It is referred to as aliasing problem in this paper. Methods are provided in the following section to solve such problem.

Methods of Eliminating Aliasing and Tolerance Problem

In analog circuit, a parameter of a circuit element may vary within a range around its nominal value, without treating it as a fault. This is termed "tolerance". As we know, due to the tolerance of analog components, the fault free voltage \dot{U}_o in an actual circuit is definitely not equal to those obtained from simulation. That means the fault free point is shifted; hence, all signature curves are shifted and induce fault diagnosis failure. To mitigate these influences on fault diagnosis, this paper proposes three approaches:

[1] To eliminate the influence on the fault free point

When the circuit works steadily, voltage \dot{U}_0 is measured. The fault free point is shifted by

$$U_{shift} = U_0 - U_0 \tag{6}$$

If a CUT fails and the corresponding output voltage is \dot{U}_{t} , the standardized fault voltage \dot{U}_{st} is

$$U_{sf} = U_f - U_{shift} \tag{7}$$

[2] To eliminate the aliasing problem

A frequency selection method is proposed to select the optimum frequency to distinguish this kind of faults. In equation (5), there may be \mathscr{O} such that $F_i(\mathscr{O}, x_{fi}) \neq F_k(\mathscr{O}, x_{fk})$. The idea is to select an optimum frequency \mathscr{O}_{ik} such that $\max_{\mathscr{O}} \left\{ abs \left[F_i(\mathscr{O}_{ik}, x_{fi}) - F_k(\mathscr{O}_{ik}, x_{fk}) \right] \right\}$ is achieved. At this frequency, faults xfi and xfk induce different outputs \dot{U}_{fi} and \dot{U}_{fk} respectively. At fault diagnosis phase, if the faulty output is around \dot{U}_{ik} , the frequency of the stimuli is adjusted to \mathscr{O}_{ik} , and the faulty output \dot{U}_f is measured. If \dot{U}_f is more close to \dot{U}_{fi} , viz. $abs(\dot{U}_f - \dot{U}_{fi}) < abs(\dot{U}_f - \dot{U}_{fk})$, the fault source is xi and vice versa.

Process of The Proposed Fault Diagnosis Method

[3] Construction of fault dictionary

Step 1) The CUT is stimulated at selected frequency ω_0 and **fault dictionary figure** such as Fig. 2 is constructed.

Step 2) For any pair of faults (xi, x_k) that can be distinguished, except for the fault free scenario, finding the intersection points \dot{U}_{ik} of the fault signature curves on complex plane. Output \dot{U}_{ik} and corresponding fault values (x_{fi}, x_{fk}) that incur such intersection point are recorded.

For each pair of faults (x_{fi}, x_{fk}) , the following frequency selection steps are executed.

Step 3.1) Except for that $x_i=x_{fi}$, all other components are fault free. By using the frequency sweeping function of PSPICE, $F_i(\omega, x_{fi})$ is obtained. $F_k(\omega, x_{fk})$ is achieved by using the same method.

Step 3.2) Frequency ω_{ik} that maximize $abs[F_i(\omega, x_{fi}) - F_k(\omega, x_{fk})]$ is calculated. ω_{ik} , \dot{U}_{fi} and \dot{U}_{ik} obtained at frequency ω_{ik} are saved in a fault dictionary table for future fault diagnosis.

[4] Fault diagnosis

Step 1) The same stimuli, sinusoidal signal with frequency ω_0 , as that used in constructing the dictionary is applied to the CUT. The output \dot{U} at selected test point is measured and saved.

Step 2) Standardized fault voltage \dot{U}_{sf} is calculated

Step 3) If \dot{U}_{sf} close to any intersection point \dot{U}_{ik} , go to step 5), else go to step 4).

Step 4) The stimuli frequency is adjusted to ω_{ik} . Output voltage at this frequency is measured. Looking up the fault source in fault dictionary table.

Step 5) On fault dictionary figure, looking up the signature curve that close to \dot{U}_{sf} . The component corresponding to the signature curve is the fault source.

Experimental Results

The circuit is shown in Fig. 1. The excitation (input) signal is a 1kHz, 5V sinusoidal wave, and 't' is the test point.

Constructing fault dictionary

By using the parameter sweeping function, all components' feature loci are simulated and shown in Fig. 2. The fault free voltage is $\dot{U}_o = -1.84 + 0.98j$. Simulated results show that the components in this CUT fall into several ambiguity groups, as shown in Table 1.

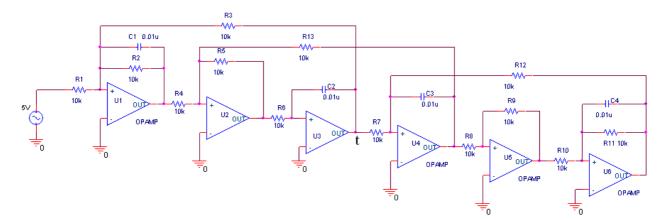
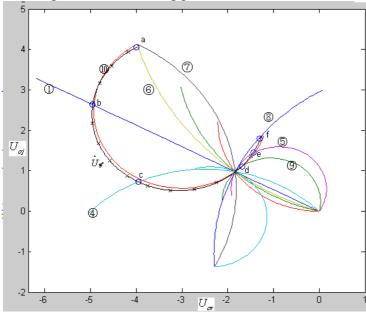
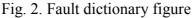


Fig. 1. Leapfrog filter

Table 1	Ambiguity Group of the CUT
Ambig	uity Fault component
group	i duit component
\bigcirc	R1
2	R2
3	R3
4	R4
5	R5,R6,C2
6	R7, R13
$\overline{7}$	R8,R9,R10,R12
8	R11
9	C1
(10)	C3
(11)	C4

Each ambiguity group has a signature curve as shown in Fig. 2. This figure is saved as fault dictionary for future fault diagnosis. The aliasing problems, are solved as follows.





Take R1 (signature curve (1)) and C3 (signature curve (10)) for example. R1=3728 Ω and all other components kept fault free. By using the AC sweeping function of Pspice, the output voltage $\dot{U}_{R1}(\omega)$ from 1 Hz through 10kHz are saved. C3=73.5n and all other components kept fault free, $\dot{U}_{C3}(\omega)$ is obtained. It can be calculated that $\max_{\omega} \left\{ abs \left[\dot{U}_{R1}(\omega) - \dot{U}_{C3}(\omega) \right] \right\} = 11.32$ is achieved at 2381Hz, and $\dot{U}_{R1=3728} = -4.2 + 11.9j$ and $\dot{U}_{C3=73.5n} = 1.7 + 2.2j$ at this frequency.

In fault dictionary Table 2, \dot{U}_f , $\dot{U}_{R1=3728}$, $\dot{U}_{C3=73.5n}$ and f=2381Hz are recorded for future fault diagnosis. All other intersection points marked as black circles shown in Fig. 2 are handled by using the same method, and the results are shown in Table 2.

Inter	section point	Faults ir	nvolved	ω_{ik}	Output vol	tage at f_{ik}
Ů	at 1kHz	X_i	$x_i \qquad x_k$		$\overset{\bullet}{U}_{fi}$	$\overset{ullet}{U}_{fk}$
1	-4.93+2.62j	R1=3728	C3=73.5 n	2381	-4.20+11.86j	1.72+2.22j
2	-1.40+0.62j	R2=6061	C4=17.3 n	2319	-1.55+2.96j	-2.25+6.00j
3	-2.21+2.30j	R3 open	R8=4339	2133	0.35+5.53j	-0.55+1.82j
4	-1.26+0.39j	R3=4007	C4=21.4n	2339	-2.04+1.03j	-1.31+6.65j
5	-3.87+0.76j	R4=2172	C3=29.7 n	3636	-3.66+11.14j	0.99+0.55j
6	-2.80+1.03j	R4=5104	C4 ≈ 0	2696	-3.07+6.80j	1.32+2.29j
7	-1.40+1.46j	R5=4908	C3=4.3 n	3462	0.52+0.28j	-0.51+2.95j
8	-1.49+0.73j	R7=7235	C4=15.3 n	2441	-2.94+3.09j	-0.28+5.78j
9	-2.12+0.22j	R11=5265	C1 ≈ 0	2531	0.85 + 4.21j	-2.96+1.88j
1 0	-1.68+1.11j	C1=12.9n	C3=8.2n	2532	-0.35+4.43j	-2.35+2.77j
1 1	-1.18+1.98j	R11=25.3k	C3 ≈ 0	2474	-2.33+5.34j	0.48+0.78j

Table2 Fault Dictionary Table

Fault diagnosis

Within the tolerance limit, $R_i \pm 5\% R_i$, $C_i \pm 10\% C_i$, all fault free components' parameter are randomly computer-generalized. The fault free voltage is $U_a^{\dagger} = -1.75 + 1.02j$.

As an example, all possible parameter shifting faults occur to C3 is considered, viz. C3={ $0.001n \sim 9n$ } \cup { $11n \sim 10^5 n$ }. The simulated faulty voltages are recorded and the standardized faulty voltage \dot{U}_{sf} is calculated. Marked by '×', the faulty voltage \dot{U}_{sf} is drawn in Fig. 2. It can be seen that far from the fault free and intersection points, signature curve of C3 (curve 10) is the sole curve that most close to \dot{U}_{sf} . On these conditions, fault source C3 can be diagnosed correctly.

When C3=30*n*, the simulated \dot{U}_f =-3.75+0.71j falls into circle 'c'. In the first column of Table 2, -3.87+0.76j shown in the 5th row is more close to \dot{U}_f than others are. -3.87+0.76j is the common fault future of C3 and R4. To realize fault diagnosis, the corresponding frequency 3636Hz is applied to the CUT, and the output voltage 0.99+0.56j is obtained. From the 5th row of Table 2, it can be seen clearly that 0.99+0.56j is the fault signature of C3 at 3636Hz.

Conclusion

The complex field fault modeling method introduced in this paper can handle both soft and hard fault diagnosis. Hence, it is a unified fault modeling method. This method needs only one test point, usually the output point, to diagnose fault component. Hence, it is especially applicable to CUT which has no inner accessible test points. Additionally, a frequency sensitivity method is proposed to solve the aliasing problem.

Acknowledgements

This work was supported in part by the NSFC (No. 61201009, No. 61271035).

References

[1]J. W. Bandler and A. E. Salama: Proc. IEEE, vol. 73 (1985), p. 1279.
[2]W. Hochwald and J. D. Bastian: IEEE Trans. Circuits Syst., vol. CAS-26 (1979), p. 523.
[3]P. M. Lin and Y. S. Elcherif: Inl. J. Circuit Theory Appl., vol. 13(1985), p. 149.
[4]Janusz A. Starzyk, Dong Liu, Zhi-Hong Liu, Dale E. Nelson, and Jerzy O, Rutkowski:*IEEE Trans. Instrum. Meas.*, vol. 53 (2004), p. 754.
[5]Feng Li and Peng-Yung Woo:*IEEE Trans .Circuits Sys. I*, vol. 46(1999), p. 1222.
[6]Tan Yanghong, He Yigang:*Microelectronics*, vol. 31(2001), p. 252.(in Chinese)
[7]Zhang Wei, Xu Aiqiang, Chen Zhenlin:*Journal of Electronic Measurement andInstrument*, vol. 20(2006), p. 46. (in Chinese)

[8] Wang Peng, Yang Shiyuan: Control and Automation, vol.22, no. 6 (2006), p. 1.

[9]Wang Peng, Yang Shiyuan: *IEEE Trans. on Circuits and Systems-I: Regular Papers*, vol. 52(2005), p2118.

[10]Robert L. Boylestad. Introductory Circuit Analysis (10th Edition)", Prentice Hall, p. 354-356, (2002).

[11]Giulio Fedi, Stefano Manetti, Maria Cristina Piccirilli, and Janusz Starzyk:IEEE Transactions on Circuits and Systems-I:Fundamental Theory and Applications, vol. 46, no. 7(1999), p. 779.

[12]Chenglin Yang, Shulin Tian, Zhen Liu, Jianguo Huang, and Fang Chen:IEEE Transactions On Instrumentation And Measurement, vol. 62, no. 10(2013), p. 2730.

Designing of New Intelligent Music Electro-acupuncture Apparatus

Shengzhao BI^{1,a}, Ye LIU^{1,b}, Canhua WANG^{2,c}

¹Department of Electronic Information Engineering Nanchang University, Nanchang, China ²School of Computer Jiangxi University of Traditional Chinese Medical, Nanchang, China ^ashengzhaobi@sina.com, ^bliuye@ncu.edu.cn, ^ccanhuawang2007@sina.com

Keywords: Music Electro-acupuncture Apparatus, electrical-stimulation adaptability, 1/f fluctuation, ARM

Abstract. The phenomenon of acupoint electrical-stimulation adaptability is common while traditional Pulse Electro-acupuncture (EA) Apparatus is used for treatment. To solve this problem, we designed an intelligent Music Electro-acupuncture (EA) Apparatus base on ARM9 and Linux. We analyzed power spectrum of music and put forward a possible screening technique for effective treatment music based on "1/f fluctuation" therapy. This system has excellent Qt user interface and touch screen. It is good for physical and psychological rehabilitation to listen to our music during treatment.

Introduction

The waveform output from traditional Pulse EA Apparatus is repetitive pulse with fixed frequency and intensity, it is very easy to result in acupoint electrical-stimulation adaptability, which means that patients' needling sensation will be weakened and even disappeared with time, only by increasing the strength of electrical simulation can needling sensation be re-felt by patients. Acupoint electrical-stimulation adaptability has badly affected EA efficacy, hindered the development and promotion of EA. In this context, The Intelligent Music EA Apparatus avoided the effect of electrical-stimulation adaptability by applying Musical Electro-therapy and "1/f fluctuation" theory.

Musical Electro-therapy

Musical Electro-therapy, using specific music signal acting on human body to treat diseases, is a new method which combines musical therapy with electrical therapy of traditional medicine. Experiments verify that Musical Electro-therapy has more advantages than traditional Pulse EA in some ways.

From the comparative observation of analgesic action of Music EA and Pulse EA on behavioristic and electro-neurophysiology, Hongsheng Dong [1] have confirmed that music EA had superiority on the analgesic action of rats, Musical Electro-therapy can overcome electrical-stimulation adaptability and played better acupoint function. From observation of the influence of the Music EA on the depression model rat hypothalamus and colonic mucosa β -endorphins (β -EP), Jinyan Teng [2] have concluded that Music EA can regulate the imbalance of brain-gut peptide in different regions, which provided practical approach to the clinical treatment of depression.

"1/f fluctuation" theory

According to the corresponding relations between the Power Spectral Density (PSD) and Frequency (f), the fluctuation in the nature can be divided into three categories [3] as shown in Fig. 1. The first is white noise which is called $1/f^0$ fluctuation, its PSD parallels to the horizontal axis and has no link with f; The second is brown noise which is called $1/f^2$ fluctuation, its PSD is inversely proportional to f^2 ; The last noise, called 1/f fluctuation, is a disordered state locally while has certain relevance in the macro level, its PSD is inversely proportional to f.

If we use x(t) to represent 1/f fluctuation, the Fourier transform is

$$X_{T}(f) = \int_{-T}^{T} x(t) e^{-j2\pi ft} dt .$$
 (1)

The PSD of x(t) is

$$S(f) = \lim_{T \to \infty} \frac{1}{2T} E\left[\left| X_T(f) \right|^2 \right].$$
⁽²⁾

The relationship [4] between PSD and f is

$$S(f) = A / \left| f \right|^{\lambda}.$$
(3)

In Eq.3, S (f) is PSD, A is a constant, f is the frequency and λ is the index of frequency. Take the logarithm of both ends of Eq.3, we will get

$$\lg S(f) = \lg A - \lambda \lg f.$$
⁽⁴⁾

In Eq.4, there is a linear relationship between lgS (f) and lg f, $-\lambda$ is slope, when λ is 0,1 and 2, it is corresponding to $1/f^0$, 1/f and $1/f^2$ as shown in Fig.1.

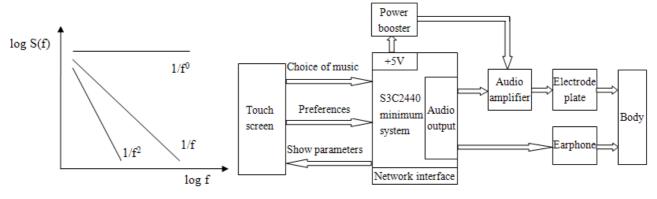


Fig.1 Spectral characteristic

Fig.2 Hardware system block diagram

"1/f fluctuation" widely exists in the nature, such as refreshing breeze, the waves of the sea and the murmur stream; it also exists in the changing strength and rhythms of music. Studies [5] have shown that human being's heartbeat cycle in a comfortable state and α brainwaves' variation cycle are in accordance with "1/f fluctuation". "1/f fluctuation" of outside world can also inspire human being's α brainwaves to produce "1/f fluctuation" and make us comfortable. Based on above research, we can use "1/f fluctuation" theory to analyze music, screen out comfortable and harmonious music for Musical Electro-therapy.

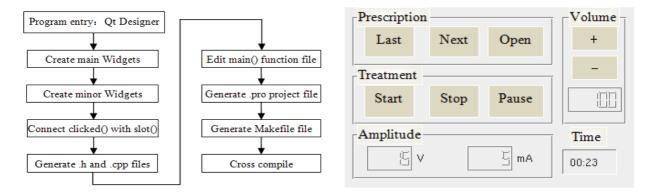
Hardware system design

The hardware system of Music EA Apparatus was composed of S3C2440 (ARM9 processor chip) minimum system, Power booster circuit, Audio amplifier circuit and Touch screen. As shown in Fig.2, the audio signal output from S3C2440 minimum system was \pm 500mV; one signal can be zoomed into \pm 7.5V to be applied to Musical Electro-therapy through Audio amplifier circuit, another signal provided patients of music appreciation through earphone; the +15V working voltage of Audio amplifier circuit was provided by Power booster circuit; by the graphical user interface, we can controll the therapeutic process. The network functions can be extended by Network interface and we

can build the doctor workstation to perform many other functions, such as information input and management of patients.

Software system design

The software design of Music EA Apparatus was based on Qt, a cross-platform C++ graphical user interface library developed by the Norwegian TrollTech company. Qt has three notable features, one is that its cross-platform enable it can be run on Unix, Linux, Windows and many other platforms; two, Qt is based on C++ structure, thus enjoying all the advantages of object-oriented programming; besides, using underlying graphics functions from different platforms, Qt can simulate different styles of the platform, which is easy to use and with fast running speed. With Qt development interface and software flow chart shown in Fig.3, we realized functions such as open music files, display the list of songs, play music, select song playing order and the volume. Music EA Apparatus interface is shown in Fig.4.



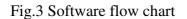


Fig.4 Music EA apparatus interface

Test of electrical-stimulation adaptability

According to reference [6], in randomized controlled trial, we divided 20 volunteers into Pulse EA group and Music EA group equably. Then we used Visual Analogue Scale, VAS, to record the needling sensation values (0~50). At the beginning of test (0min), volunteers felt the needling sensation and set the value at the center of the VAS scale (5cm). Scale decrease meant the weakness of needling sensation and increase meant enhancement. The left boundary (0cm) stood for "no sense" and the right (10cm) was 2 times of the original value. During the test, volunteers were invited to point out the needling sensation at the 5, 10, 15, 20, 25, 30min of the test and the corresponding values were recorded. After that, we used SPSS17.0 to process recorded data and get a chart of needling sensation values(Table 1). variance approach was taken between groups to analyze repeated measurement data, and results are shown by mean ±standard deviation ($\bar{x} \pm s$).

Table 1 Needling sensation changes of two groups $(\bar{x} \pm s, \text{mm}, \text{n}=10)$

Needling sensation values (mm)							
Group	0min	5min	10min	15min	20min	25min	30min
Pulse EA	50.0	47.7±6.3	43.3±7.9	34.8±8.7	27.0±11.3	19.3±12.1	15.5±11.6
Music EA	50.0	51.2±1.6	53.8±3.1	53.3±2.4	53.7±1.6	53.8±1.7	53.3±2.7 [#]

PS: compared to Pulse EA group, ${}^{\#}P < 0.05$

P < 0.05 meant difference of needling sensation values was statistically significant between Pulse EA group and Music EA group. In Table 1, values of pulse EA group decreased gradually with time, a clear decreasing trend arises after 10min, suggested the emergence of electrical-stimulation adaptability; on the contrary, values of music EA group shown trend of increase with time, the value

at 30min increased by 3.3 than that at 0min, suggested that music EA avoid electrical-stimulation adaptability.

Test of "1/f fluctuation" law

We used MATLAB to analyze "1/f fluctuation" law of music signals and get PSD trend of different music [7]. Take two songs, 《My heart will go on》 and 《Rock On the New Long March》, for example. The former was a lingering melodious song whose PSD was shown in Fig.5; and the latter was a rock song whose PSD was shown in Fig.6. Compared the two figures we can know that PSD in Fig.5 was inversely proportional to f and lgS (f) was approximately linear with lgf, this coincided with 1/f fluctuation law. But in Fig.6, the relationship between PSD and f was complicated, and it does not meet 1/f fluctuation law. In this way, we picked out the music whose PSD had 1/f fluctuation characteristic from those had not, and took them as prescription of Musical EA apparatus.

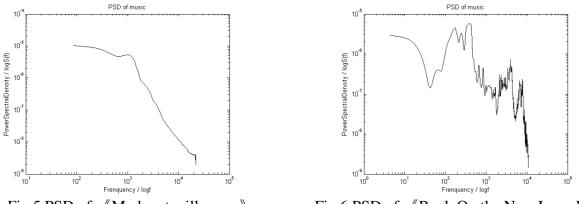


Fig.5 PSD of 《My heart will go on》

Fig.6 PSD of 《Rock On the New Long March》

Conclusions

In this paper, Embedded ARM technology was used to devise an intelligent Music EA Acupuncture. Experiment verified that it could avoid the effect of electrical-stimulation adaptability. We analyzed music power spectrum by MATLAB, and put forward a possible screening technique for effective treatment music. We find that it's theoretical reasonable for music with character of "1/f fluctuation" to be a treatment. Compared with Pulse EA Acupuncture, intelligent Music EA Acupuncture has high efficient Linux systems and Qt graphical user interface which is easy to operate. It has great practical significance as medical equipment for clinical study and home health care.

Acknowledgements

This work was financially supported by the project: Key Technology Research and Development Program of Jiangxi province (NO. 20133BBG70087).

References

- Hongsheng Dong, Hao Pei, Guirong Dong. Acupuncture Research, 2005,30(2):83-87. In Chinese
- [2] Jinyan Teng, Zhigang Li, Yan Bai. World Journal of Integrated Traditional and Western Medicine, 2013,8(4):348-350. In Chinese.
- [3] Xia Mao, Yukuan Ding, Muta Itsuya. Acta Electronica Sinica, 2001,29(12A):1923-1927.
- [4] Shaobing Wu, Shi Chen, Hai Li. Acta Physica. Sinica, 2012, 61(9):1-10.
- [5] T Musha, M Yamamoto. 1/f Fluctuations in Biological Systems. Proc.of 19th International Conference IEEE/EMBS, 1997[C] Chicago,IL,USA.
- [6] Xiaoqing Huang, Xun Chen, Zhifang Yao. China Association for Acupuncture and Moxibustion annual meeting memoir, 2011. In Chinese.
- [7] Hao Zhang. Communications Technology, 2009, 42(1):280-281. In Chinese.

Research of Low Power Design Strategy Based on IEEE 1801 Unified Power Format

ShuPing Cui^{1, a}, Chuang, Xie^{1, b}

¹Lab of Industrial Control Network and System Shenyang Institute of Automation, Chinese Academ y of Sciences, Liaoning Shenyang, China

^acuisp@sia.cn, ^bxiechuang@sia.cn

Keywords: IEEE 1801, UPF, low power, power consumption

Abstract. Power consumption is becoming an increasingly important aspect of circuit design. High power consumption can lead to high machine temperature, short battery life which makes laptop electronics difficult to be widely used. IEEE 1801 Unified Power Format (UPF) is designed to express power intent for electronic systems and components .This paper first introduces the power principles, puts forward the approaches to reduce power consumption according to UPF, and then demonstrates the Synopsys design flow based on UPF, finally gives the power report and makes a conclusion.

Introduction

In recent years, the device densities and clock frequencies have been higher and higher, at the same time, the supply voltages and transistor threshold voltages have been lowered in CMOS devices, so power consumption has been dramatically increased. Increased power consumption can lead to a series of headache problems such as high machine temperature which makes users uncomfortable and requires expensive cooling systems, low battery life which restrict the widely use of laptop electronics. For millions of computers, servers, and other electronic devices used on a large scale, even a little rise of power consumption can cause enormous electrical energy waste. At the same time, even a small reduction in power consumption can result in large aggregate cost savings and can provide significant benefits to the environment as well^[1].

The Unified Power Format (UPF) is a standard set of Tcl-like commands used to specify the low-power design intent for electronic systems. The official Unified Power Format, version 1.0,was approved in February 2007 by Accellera. Accellera is an electronics industry organization focused on creating electronic design automation standards that can be used throughout the industry. Accellera transferred the UPF copyright to the IEEE P1801 Working Group for further expansion and refinement of the power specification standards and for formal approval as an IEEE standard. IEEE 1801TM-2013 ", the newest revised version, was announced at 30 May 2013^[2].

1. The types of power

There are two types power that we must consider during chip operation, dynamic and static power. **1.1. Dynamic power**

Dynamic power is the energy consumed during logic transitions on nets, consisting of two components, switching power and internal power.

Switching power results from the charging and discharging of the external capacitive load on the output of a cell. Switching power consumption depends on the clock frequency (possible transitions per second) and the switching activity (presence or absence of transitions actually occurring on the net in successive clock cycles).

Internal power results from the short-circuit current that flows through the PMOS-NMOS stack during a transition. When the input signal is at an intermediate voltage level, the PMOS and NMOS transistors can be conducting both. This condition results in a nearly short-circuit conductive path

from VSS to ground. Lower threshold voltages and slower transitions result in more internal power consumption.

1.2. Static power

Static power is also called leakage power which is caused by leakage current including reverse-bias p-n junction diode leakage, subthreshold leakage, and gate leakage. Leakage power is becoming increasingly significant with shrinking device geometries and reduced threshold voltages. Leakage currents occur whenever power is applied to the transistor, irrespective of the clock speed or switching activity. Leakage cannot be reduced by slowing or stopping the clock.

However, it can be reduced or eliminated by lowering the supply voltage or by switching off the power to the transistors entirely.

Low power design strategy 2.

There are many kinds of ways to reduce power, such as clock gating, dynamic voltage, and frequency scaling etc. And most of these strategies can be implemented using UPF commands.

2.1. Clock gating and power switching

Clock gating has been used widely and successfully for a long time. In some circumstance registers need to maintain the same logic values over many clock cycles. Reloading the registers with the same value on each clock cycle causes power waste. If the clock is gated, the power will be reduced. According to the design, clock gating can be inserted intently during RTL design. Synthesis tool for example design compiler (DC) can also find low-throughput data paths and automatically done this work. This kind of work can be checked from the command log file.

Power switching is different from clock gating because parts of the chip are shut down completely during periods of inactivity by cutting the supply voltage which is called power down mode. Before they are in use, they must be "wake up". In power down mode, there is no leakage and switching power, which can dramatically reduce power consumption. The implementation of power switching needs the help of a power controller, a power-switching network, isolation cells, and retention registers. A power controller is a logic block that determines when to power down and power up a specific block. The network connects the power to or disconnected the power from the logic gates in the block. Isolation cells are used to connect power on module and power down module. When both modules are on, they like wires. When one is off, they can provide a known, constant logic value to an always-on block. Before power down, the value of registers should be saved and restored after power on by retention register. The relevant commands of UPF are create_power_switch, map_power_switch, set_isolation, and set_retention etc.

2.2. Dealing with voltage

Supply voltage reduction can reduce power effectively. According to the formula Power = IV = V2/R, A 50 percent reduction in the supply voltage results in a 75 percent reduction in power. But lower voltage can cause low speed and some other problems, such as, noise immunity, crowbar currents, and sub-threshold leakage. Of course, different parts in a chip might have different speed. So multivoltage can be implemented to save power. Even the voltage can be changed dynamically according the operating status. So is the clock's frequency. The relevant commands of UPF are create_power_domain, create_supply_net, create_supply_port, set_domain_supply_net, and so on.

2.3. Using Multiple-Vt Library Cells

Some CMOS technologies support the fabrication of transistors with different threshold. The cells have the same logic function but different transistor threshold. Low-Vt leads to higher speed, and higher sub-threshold leakage current. High-Vt leads to low leakage current, but less speed. Synthesis' tool can decide which cell to use. When timming is critical, low-Vt cells are used. When timing is loose, High-Vt cells are chosen. High-Vt transistors are used as power switches and retention register because they minimize leakage and their switching speed is not critical.

3. The Synopsys low power flow

The Synopsys low-power flow is shown in Figure1. First Design Compiler reads in the RTL and UPF1 files, and synthesizes a gate-level net list and a UPF2 file. The DC commands are Load_upf and save_upf. Then IC Compiler reads in the gate-level net list and the UPF2 file, after physical implementation produces a modified gate-level net list, a complete power and ground (PG) netlist, and an updated UPF file. VCS and MVSIM can be used for functional verification of the multivoltage design. MVRC checks for adherence to multivoltage rules and reports any problems related to power. PrimeRail performs voltage drop and electro migration analysis for gate-level and transistor-level designs. PrimeTime does timing analysis with UPF information.

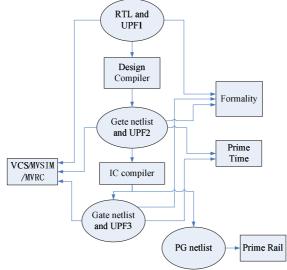


Figure1 Synopsys low-power flow

4. Report analysis

TSMC is the world's largest dedicated semiconductor foundry. It supplies 180nm CE018FG ULL (ultra low leakage) technology library to support ultra low power design. Synthesis base on UPF using ULL (ultra low leakage) technology library and normal flow using base technology library are done respectively, and two different power reports are got. The contrast between them is shown in table1.

с	ategory	ULL fl	ow	Normal flow		
total	cell internal	nternal 4.4750 mW		6.5583 mW		
dynamic	power		9 1 4 2 4 W		12 2461 mW	
power	net switching	3.6673 mW	8.1424 mW	5.6879 mW	12.2461 mW	
	power					
static	Cell leakage	1.9220 uW		13.2836 uW		
power	power					

Table1 Contrasts between two design flows

From the data of table, both the static and dynamic power is reduced. DC is not expert power analyzer. Comprehensive power analysis should be performed by Primetime PX after physical implementation.

5. Conclusions

With the improvement of science, plenty of electric devices consume enormous energy. Energy consumption causes the worse environment on the earth. Reduction power consumption becomes extremely urgent. Low power strategy base on IEEE 1801 Unified Power Format can reduce power consumption of chips dramatically. With the wide application of this technology, the problems will be solved finally.

Acknowledgements

This work was financially supported by the National High Technology Research and Development Program of China (863 Program) under grant 2011AA040102 and 2012AA041701.

References

- [1] Synopsys® Low-Power Flow User Guide, Version B-2008.09, September 2008
- [2] Erich Marschner, The Evolution of UPF: What's Next?verification horizons,www.mentor.com
- [3] ZHONG T ao, Optimization and Design for Power Techniques for CMOS IC's, Microelectronics, Vo 1. 30, № 2
- [4] Apr. 2000,p107-112.
- [5] The information on www.arm.com
- [6] The information on www.tsmc.com

The Key Technology of Designing the Universal Programmer for Freescale HCS12 Serial MCUs

Jing Zhang^{1,a}, Zhanglong Nie^{1,b}

¹Changzhou College of Information Technology Changzhou, Jiangsu, China ^anzjing78@sohu.com,^bniezhanglong@sohu.com

Keywords: Programmer, Freescale HCS12, BDM, high-speed downloading, Erase, Write

Abstract. For implementing on-line programming of Freescale HCS12 series MCU, designing a common downloading programmer which functions include chip selection, erase and write operations. Designing a database where Freescale HCS12 MCU Flash difference parameter values placed, so achieving HCS12 MCU family online programming versatility. Erase and write machine codes are provided in the RAM area of Flash memory, these codes will be run at high voltage, these codes are relocated from Flash to RAM area for improving flash operation stability during the high voltage. According to BDM communication theory, we have developed a separate BDM serial communication program, the target device only receives the user code from the programmer, programmer does not need send opcode and the address information, not waiting for a command, so, increasing the erase and write speed. the programmer has the versatility and easily using.

Introduction

Now, the CodeWarrior is the integrated development environment(ie,.IDE) for the Freescale HCS12 serial MCUs and is largely impacting on the market, it is functional, stable performance, but expensive, so it is not suitable to teaching and development for the embedded area. The universal programmer for the Freescale S12 MCU in this paper is the BDM debuger tool which supporting the Freescale MC9S12 series, MC9S12X MCU, it could implement the writing and erasing operations for all 16-bit Freescale MCUs. through studying the common and difference features of the Freescale HCS12 series MCUs, the key technology of the versatility and high-speed downloading of the programmer are given.

Overview

The universal programmer for Freescale S12 serial MCUs is the BDM debugging tool for the 16-bit MCU of Freescale, the core chip of the programmer is MC68HC908JB8^[1], communicates with the target board by the BDM way^[2], and communicates with the PC by the USB interface, and the USB interface can provide working power of the target board, the system block diagram is shown in Fig.1 to implement the BDM way communication, the programmer also needs the BDM driver module.

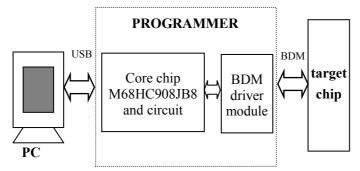


Fig. 1. Programmer system diagram

System design

The design of system software including: communication program interface design, PC programming, MCU flash programming. When the flash erasing and writing operations of the target chip is runing, Firstly, PC needs to get the user instructions, and then call the corresponding erasing and writing codes of MCU, and these codes are writen to the Specified RAM area of the target chip. Finally, PC program run the command of turnnig to erasing-writing address in the RAM area, and execute the erasing-writing codes. When the PC communicates with the MCU, communications program need to call the appropriate dynamic-link library files:TBDML.DLL, which provided by Freescale company^[3].

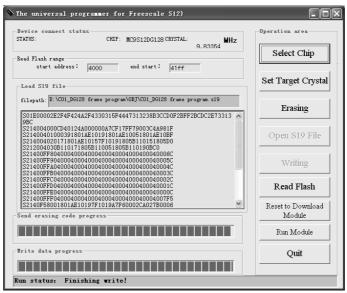


Fig 2. Programmer PC operation screen

PC software design

1) main module

The view chart of PC program running^[4]as shown in Fig.2, the module's main flow chart is shown in Fig.3.

Programmer communication process is as follows:

(1) PC sends the command of entering the BDM, then the target chip is into the BDM mode;

(2) PC sends the command of completely erase, the target chip Flash is erased, and checked, then returning checkedcode;

③ PC sends the commands of downloading the write subprogram code into the target chip memory, the function of write subprogram is that the user target codes stored in the chip memory are written to ROM Flash;

(4) PC analysis S19 files, extracting the target code being sent, combining 512 bytes into one page, sending to the target chip memory via paging, and then running the writing subprogram stored in the RAM area, the user object codes are written to ROM Flash area;

(5) PC could detect whether or not to send the next page, and receive a check code to determine correctness of the sending data.

After starting the program, at first, detecting device connection, if unconnected, returning error message ,and prohibiting the following erasing and writing operations.

If the initialization process is completed and the chip successfully enter the BDM mode ,then,the system is waiting for the user operating instructions,which is as shown in Fig.3. After completing the necessary operations, the user can execute quit to turn off the device and exit the main program.

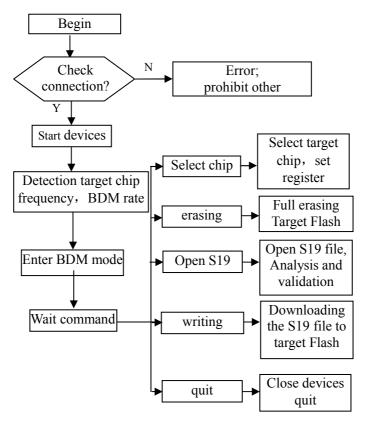


Fig.3. Main program flow chart

Programmer universal design

It is important for the key technology of universal design to deal with the FLASH parameters of HCS12 series MCU^[5]. It is necessary to in-depth understanding, comparing and summarizing the FLASH parameters of different chips before you will design the program downloading module. When the different FLASH parameters of the different chips are obtained, they should be put into the database, so,when downloading program, the related chip parameters could be read from the database.Now, PC software can read the parameter values from the configuration file and database according to the selected MCU type these parameter values are necessary to design the erasing-writing program of the target chip The following table shows some important parameters of the several chips of the HCS12 series MCUs, these parameters value may be different for different MCU. When the user data of one page is written to the RAM area, the start address of user data stored in RAM area will be different, so it is variable parameters, and can be read from the database.

			<u>.</u>	
chip name	user data start address	flag bit start address	writing file path	erasing file path
MC9S12DB128	0x1A00	0x19FE	.\DB128Write	.\DB128Erase
MC9S12DG128	0x1800	0x16FE	.\DG128Write	.\DG128Erase
MC9S12DJ128	0x1800	0x16FE	.\DJ128Write	.\DJ128Erase
MC9S12NE64	0x3000	0x2FFE	.\NE64Write	.\NE64Erase
MC9S12UF32	0x1800	0x16FE	.\UF32Write	.\UF32Erase
MC9S12xDP512	0x2800	0x27FE	.\S12XWrite	.\S12XErase

Table 1 Some MCU parameter

Flag bit start address: the parameter is an address of RAM area, the flag sign of the success or error of erasing-writing operation is stored here, two bytes. After one page user data is writen completely,

PC must read a word from this address to judge the success or failure of Flash writing operation, only success, the next page user data could be writen.

Writing and erasing file path: because the FLASH parameters and space of each MCU are different, their erasing and writing program code are different, therefore, PC need to call writing program code files (* Write.s19) or erasing program code files (* Erase.s19) according to the currently selected chip name and operation type.PC calls the * Write.s19 file when the writing operation is executed the erasing operation is too.the two file path could be read from the database.

b) Programmer high-speed downloading design

By optimizing the communication subfunction code, the time spending on sending data from the JB8 chip memory to the target chip memory can be greatly reduced, but when executing BDM command, in addition to sending 2 bytes of user data, but also sending some extral bytes, and the completion of the command will require a longer delay.Because the single-pin BDM serial communication is used, you can design the function which simulating BDM serial communication, the target MCU only receives user object code from the programmer, so improving communication speed.

Furthermore, the PTB.0 pin of JB8 connect with PTA.0 pin of the target MCU, BKGD pin is unaffected during the data communication. Communication process is as follows:

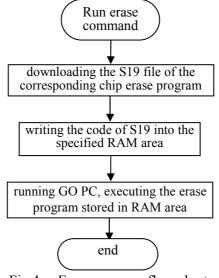


Fig.4. Erase program flow chart

(1) in accordance with the sequence that programmer sends a bit data, the function sending byte via PTB.0 pin are designed;

(2) in according to the process of receiving a bit data of the target chip, the function receiving byte via PTA.0 pin, and then designing target chip receive function;

(3) the target chip receive function are compiled into object code, then the code is sent to the target MCU RAM area by executing BDM command.

(4) executing the target chip receive function, the bytes received will be written to the specified ROM area of the target MCU.

Since the target chip receive function is own definition, the programmer need not to send opcode and address information, and need not wait for command completion. The code size of the target chip receive function less than 50 bytes, the time speding on sending them is very short. Thus, if the programmer sends the100KB data to the target MCU RAM, the time spent is calculated as follows:

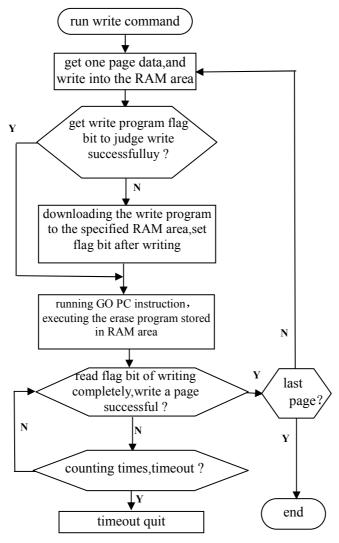


Fig.5. Write operation flow chart

 (100×1024) bytes $\times 809$ cycles $\div (24 \times 106) = 3.45$ s

After using the function, the downloading speed of the programmer is increased by 8 times.

2) Erase module

The flow chart of erase function is shown in Fig.4. After obtaining the erase command, at first, the main module loads erase file of the corresponding chip, then,writing the S19 code of erase function to the target MCU RAM area, and executing GO PC instruction, so the target MCU turned to the address where the erase function code stored ,and run the function, and the corresponding Flash area is erased^[6].

3) Open and analysis S19 module

Executing the operation, firstly the main module read the open S19 file by line and save the data to a string array, at the same time, verify the checksum, the array element contains the line data of S19 file. Then the data are recombinated in pages and saved to a new string array, but the space of previous array should been released.

4) Write module

The flow chart of write function is shown in Fig.5. After obtaining the write command, t firstly the main module get a page data, and writing it to the corresponding RAM area, then judge the success or failure of write operation, if it is failure, then writing again. then executing GO PC instruction, so the target MCU turned to the address where the write function code stored and run the function, and

waiting for the completion of one page data writed, if the wait time is too long, and quit the operaton, otherwise, could write the next page, the write operation is all completion until the last page.

MCU flash programming

MCU erasing-writing funciton is to erase and write the target chip Flash area ^[7]. Flash could not be read during executing erase and write process of Flash, , so the erase and write function code shuld to be placed in Flash RAM, that is, before erasing or writing Flash, the PC software should take the erase or write executable code into RAM, and run them in RAM.

The step of Flash erase and write operation is as follows.

(1) clearing the ACCERR and PVIOL, which is the error flag bit of the FSTAT that is the Flash status register;

(2) writing the b1 and b0 bit of FCNFG that is the Flash configuration register, for example, the the two bit value of MC9S12DP256 determine to use which 64KB of the 256KB Flash;

(3) writing PPAGE register;

(4) Checking the last Flash operation command is finished or not, if not, couldn't write a new command;

(5) writing the data word to the appropriate address, the address must be an even address;

6 writing the command word to the FCMD register, the 0x41 is the command word of the overall erase, the 0x20 is the command word of the single-byte write;

⑦ writing 1 for clearing to CBEIF bit of FSTAT that is the Flash Status Register then the CCIF bit in the status register will be set, which indicating a successful clearing operation.

Conclusion

This paper design a universal programmer, which can program a serie MCUs of Freescale S12. The programmer Use MC68HC908JB8 as the core chip, and communicating with the high-end by USB, and communicating with the MCU by BDM. Not only the MC68HC908JB8 MCU selected is cost-effective, but also the operation of its own USB module is convenient and reliable. The programmer is reliable and low cost, the user can design the programmer of other series MCU by modeling on this programmer, but the MCU must support the BDM standard.

References

- [1] "Freescale. Technical Data-MC68HC908JB8,".2005.
- [2] "Background Debug Module(BDM)V4," 2003.
- [3] Daniel Malík. "Turbo BDM Light interface," 2005.
- [4] CAO Jin-hua, LIU Xiao-sheng and WANG Yi-huai, "Design of An Integrated Development Environment For MCUs of Freescale HC08," Microcomputer Information, vol 9,2009, pp.77-79.
- [5] Yingzhen Jiang, "The Design of Universal Programmer and Software for M68HC08 MCUs," Soochow University, October. 2004.
- [6] LIU Xiao-sheng, CAO Jing-hua and SHEN An-dong, "Universal Design of Programmer & Debugger Based on HC08 Family MCU,". Computer Engineering, Dec 2008, pp. 253-255.
- [7] WANG Yan-chun and WANG Yi-huai, "Design and Implementation of Universal Programmer for M68HC08 MCU," Automation & Instrumentation., September. 2008, pp. 58-60.

A Design of High Performance CMOS Folded Cascode Operational Amplifier

Zhefei Wang^a, Yijiang Cao, Jumeng Feng

Department of Electronic Science and Technology, College of Applied Science, Ministry of Education Harbin University of Science and Technology, Heilongjiang Harbin 150080, China

^awzff8909@163.com

Keywords: high performance; folded cascode; amplifie

Abstract. This paper describes a kind of folded cascode amplifier, which not only has high gain, large output swing characteristics, and its outputs can be self-compensation, it has a strong suppression capability with voltage noise. Based on a 0.5μ m CMOS process uses two operational amplifiers. Through software emulation corrected the error which was caused by theoretical calculation. Has good performance in gain, noise, swing, phase margin, common mode rejection ratio and other parameters.

Introduction

With the rapid development of very large scale integrated, analog integrated circuits have been developed by leaps and bounds as well. Amplifiers, filters, feedback circuits, reference circuits, switched capacitor circuits and many other circuits could be constituted by analog integrated circuits though its different forms. It was applied in radar, aerospace, surveying, storage and many other areas. So the requirements of accuracy, speed and efficiency is increasing. With the improvement of the level of technology, a new epoch is waiting for analog integrated circuits. Operational amplifiers as one of the most common units of analog integrated circuits. Depend on its large bandwidth, large swings and high speed, folded cascode amplifier get more attention by people [1]. The paper design a kind amplifier circuit of folded cascade for integrated CMOS, realization of high gain and voltage noise suppression by two cascaded op-amp, and be verified through software emulation.

Principle And Structure of Circuit

Folded cascode amplifier can overcome the small output voltage swing disadvantages of telescopic cascode amplifier. Folded cascode amplifier is constituted by common source tube and common gate tube parallel transverse [2]. The basic design idea of folded cascode amplifier is transform input voltage to current, then as the input terminal of common source tube. The basic structure of folded cascode amplifier as is shown in picture 1.

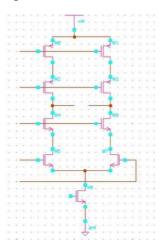


Figure 1 The basic structure of folded cascode amplifier

The folded cascode amplifier can be divided into two parts, the first portion of the circuit provides a low noise input stage. The noise from the back of the circuit will be amplified by the first stage, we have to reduce the noise in the first stage circuit. So we will choice differential input amplifier circuit structure. Meanwhile adopts cascode circuit structure in order to improve the circuit gain and output swing. The second part is an inverter structure, swing and gain will be controlled within a desired range. The overall structure of the operational amplifier is shown in Figure 2.

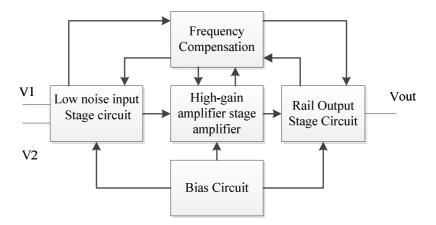


Figure 2 The overall structure of the amplifier

Circuit Design

The Overall Design. Folded cascode amplifier design is shown in Figure 3. M_0 , M_1 provides a paranoid current for amplifier circuit. M_2 , M_3 are NMOS input common-source amplifier tubes, and make the input common-mode voltage range greater. M_4 provides tail current for differential amplifier. M5 and M_6 are PMOS cascode amplifier tubes. M_7 , M_8 , M_9 , M_{10} is the low-voltage NMOS wide-swing cascode current mirror. They are used as the active load of the differential amplifier, and converted the differential current to a single-ended output voltage. M_{15} and M_{17} constitute the structure of the output stage. Wherein the M_{15} selected PMOS as input pipe and M_{17} was used as a current load.

DC Gain. DC gain is one of the most important indicators of amplifier design, affects the precision of operational amplifier system [3]. With open-loop gain increases, may reduce voltage swing. Generally, we take to reduce the paranoid current approach to improve open-loop gain [4]. The amplifier gain is expressed as:

AV=Gm*Rout

(1)

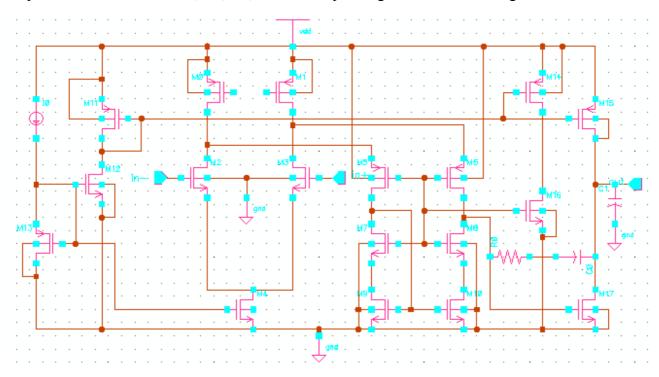
Gm is the trans conductance of the input differential stage, Rout is the output resistance. For the folded cascode amplifier we know that, the output Resistance of cascode current mirror parallel the output Resistance of cascode amplifier is the small signal output resistance:

$$R_{out} \approx \left[(g_{m6} + g_{mb6}) (r_{ds3} \| r_{ds1}) r_{ds6} \right] \left[(g_{m8} + g_{mb8}) r_{d8} r_{d10} \right]$$
(2)

 g_{m6} , g_{m8} are the transconductance value of M_6 , M_8 . g_{mb6} , g_{mb8} are the transconductance value which caused by bulk effect. r_{ds8} , r_{ds10} are the internal resistance value of M_8 , M_{10} . rds_1 , r_{ds3} are the output resistance value of M_1 , M_3 when operating in the saturation region.

If we ignore the bulk effect, the single-ended small-signal voltage gain is:

$$A_{vd} = \left| \frac{V_{out}}{V_{id}} \right| = g_{m2,3} \{ [g_{m6} r_{ds6} (r_{ds3} \| r_{ds1})] \| g_{m8} r_{ds8} r_{ds10} \}$$
(3)



 g_{m2} , g_{m3} , g_{m6} , g_{m8} are the transconductance value of M_2 , M_3 , M_6 , M_8 . r_{ds1} , r_{ds3} , r_{ds6} , r_{ds10} are the output resistance value of M_1 , M_3 , M_6 , M_{10} when operating in the saturation region.

Figure 3 The amplifier circuit diagrams of folded cascode

Output Swing. Operational amplifier output swing to represent the greatest undistorted voltage at the output range. It is related to output stage circuit structure, size and paranoid current. We managed to improve the output voltage swing by increasing the width to length ratio of MOS, but note that this will also increase the parasitic capacitance, and make the frequency characteristic of the system drops.

To make the output swing is large enough, we will let the input common source tube and the output a total of cascade tubes respectively the NMOS and PMOS, then the input and output shorted to play a role in increasing the swing. The same time as the permissible range of input vcm increases, select the input vcm value becomes much easier [5].

Common Mode Rejected Ratio. The ratio of difference-mode voltage gain and common mode voltage gain is common mode rejected ratio, it represents the ability of which the op amp suppress common mode voltage [6]. For the ideal operational amplifier, $A_{vc} = 0$, so the CMSS should be infinite. However, the actual circuit will decrease due process limitations. It expression is:

CMSS= | Avd/Avc | Avd is difference-mode voltage gain, Avc is common mode voltage gain.

Phase margin. Pm size determines the stability and transient response of the entire system, generally for the integrated circuit amplifier designs [7], 60° PM best meet the design requirements.

Slewing Rate. SR of a system is determined by tail current differential amplifier and phase compensation capacitor, although the increase in tail current can be increase SR, but also make the system power consumption increases, so we should adjust the appropriate tail current and phase compensation value, and make the circuit reach the design standards what we want. When operational amplifiers processing high speed and large signal swing, we need to increase the value of the SR to prevent the output signal distortion [8]. Slew rate expressions are as follows:

(4)

SR=I/Cc

I is tail current differential amplifier, C_c is Phase compensation capacitor.

(5)

As folded cascode amplifier has high output impedance characteristics, the output capacitance is also usually relatively large. Its main poles are generally located in the output of the circuit affected by output resistance and load capacitance. We all know that load capacitance has a phase compensation effect, increasing the load capacitance can make larger phase margin. If the load capacitance is too small, it will lead to the main poles and other poles cannot be separated, the phase margin may not meet the requirements. If the load capacitance is too large it will affect the bandwidth and speed of the system, so we need to choose an appropriate compensation capacitor to meet the design requirements [9].

The Results of Simulation Analysis

To test the correctness of folded cascode amplifier design, through analysis and calculation. The size of each MOS transistor and related parameters were designed which based $0.5 \,\mu$ m CMOS process. Applying simulation software circuit to carry out multiple simulations, making the corresponding adjustment for the ratio of width and length of every MOS tube. In the end get the output waveform of the circuit.

Figure 4 is open loop gain of the op-amp and the curve of phase margin. Through simulation we can see that the open-loop gain of the amplifier reaches 92dB, meets the design requirements. And the phase margin of the amplifier is 76° , with good stability. However, as previously mentioned, Its Time response speed is relatively slow.

Figure 5 is input noise graph of the op-amp, in this paper, equivalent voltage of input noise is $9.256^{nV/\sqrt{Hz}}$, as to the mill volt level change of the input signal, its influence is very small, which Shows the differential structure can efficiently reduce the noise effect to the circuit.

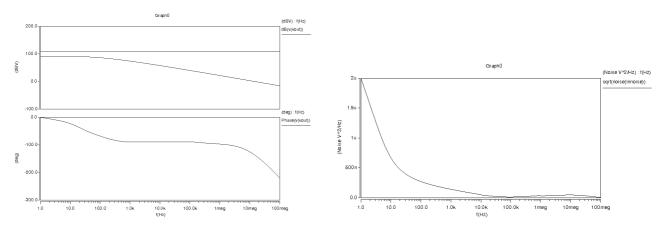


Figure 4 Op amp's open-loop gain and phase margin

Figure 5 Characteristic curve of input noise

Figure 6 is a characteristic curve of op-amp common-mode rejection ratio, common mode rejection ratio is 82.3 dB, and the greater common mode rejection ratio shows that the design of amplifier has a high stability.

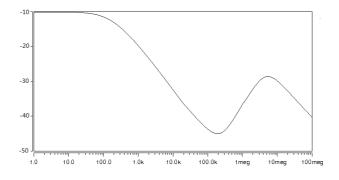


Figure 6 Op-amp common-mode rejection ratio.

Conclusion

This paper studies High-performance folded cascode amplifier, overcomes the shortcomings of the Traditional folded cascode amplifiers and telescopic cascode amplifier, and it Has a high gain, low noise, high common mode rejection ratio and so on. To simulate and modulate by using simulation software, and consider with a number of design specifications, adjust width to length ratio of each MOS transistor, the simulation results meet the design requirements. This structure of folded cascode amplifier is simple and easy to implement, and suitable in the field of ADC interface circuit.

Acknowledgment

During the period of researching, we greatly thank the Department of Electronic Science and Technology of Harbin University of science and technology and the MEMS Centre of Harbin Institute of Technology for strongly support.

References

- [1] A. Younis, M. Hassoun, "A high speed fully differential CMOS op-amp," Proceedings of the 43rd IEEE Midwest Symposium, vol. 2, pp. 780 783, (2000).
- [2] S. Mallya, J. H. Nevin, "Design procedures for a fully differential folded-cascode CMOS operational amplifier," IEEE Journal of Solid-State Circuits, vol. 24, pp. 1737 1740, (2002).
- [3] S. A. Enche Ab, I. M. Azmi, "A CMOS single stage fully differential folded cascode amplifier employing gain boosting technique," 13th International Symposium of Integrated Circuits, pp. 234 - 237, (2011).
- [4] T. Singh, T. Sasther, T. Ytterdal, "Common source amplifier with feedback biasing in 90nm CMOS," Research in Microelectronics and ElectronicS, pp. 161 164, (2006).
- [5] S. Mallya, J. H. Nevin, "A high DC-gain folded-cascode CMOS operational amplifier," Southeastcon . Proceedings. IEEE, pp. 167 - 177, (2008).
- [6] W. I. W. Fuad, A. H. Ali, "Analysis of CMOS differential input to increase ICMR of folded cascode operational amplifier," Industrial Electronics & Applications (ISIEA) on 2010 IEEE Symposium, pp. 711 - 715, (2010).
- [7] Jui-Lin Lai, Ting-You Lin, Cheng-Fang Tai, Yi-Te Lai, "Design a low-noise operational amplifier with constant-gm," Proceedings of SICE Annual Conference, vol. 24, pp. 322 - 326, (2010).
- [8] S. Mallya, J. H. Nevin, "Slew rate enhancement method for folded-cascode amplifiers," Electronics Letters, pp. 1226 - 1228, (2008).
- [9] N. Bako, Z. Butkovic, A. Baric, "Design of fully differential folded cascode operational amplifier by the gm/ID methodology," 2010 Proceedings of the 33rd International Convention, pp. 89 - 94, (2010).

The research of programmable equivalent capacitor circuit

Xia Sheng^{1, a}, Qinghua Shang^{1,b} Zhen Huang^{1,c} Bangshao Wang^{1,d} ¹Harbin University of Science and Technology, Harbin, Heilongjiang,China ^a735014862@gg.com ^b13804561689@139.com ^c765927062@gg.com

Keywords:programmable;impedance transformation;equivalent capacitance

Abstract: Resistors, inductors and capacitors are indispensable components in modern electronics field. While digital potentiometer is capable of conducting digital adjustments on resistances, the flexibility of adjusting the capacitance of most capacitors is still very limited even until now. This paper introduced a digital capacitor circuit based on impedance transformations. The impedance transformation circuit was set up by assembling an integrated operational amplifier and small amounts of resistors and capacitors. The capacitance of this circuit can be adjusted by controlling the resistance of a certain resistor using a digital potentiometer. Simulation results showed this circuit has many advantages including great flexibility if controlled with a single chip, wide capacitance adjustment range, insensitivity to temperature and pressure, and the size of the circuit remaining the same while the capacitance increases.

Introduction

As the electronic technology develops, there are significantly increasing needs of digital programmable devices in this field. Now days, there are few digital adjustable capacitor products in the market. Most of available capacitors use simple analog switches to control the capacitance. This kind of capacitor has many disadvantages including size limitation and narrow adjustment range (only several to less than 20 pF). Also, most equivalent capacitor circuits consist of capacitors and resistors connecting in series or parallel instead of just capacitors alone. This narrows the freedom of the resistor in the circuit and subsequently limits the range of the equivalent capacitance. The digital capacitor introduced in this paper, using impedance changing circuit, yields pure capacitance equivalent outputs. In order to make the integration of the circuit easy, the traditional method of directly using analog switches to control the capacitance in the circuit. Using this method, the equivalent capacitance has large adjustable range and high accuracy, and the size of the equivalent circuit remains the same regardless the value of the capacitance output. This circuit, if adding a single chip to control the output capacitance, has the potential to be widely used in many different kinds of electronic devices.

1. Impedance generator principle

By impedance transformation of operational amplifier circuit is shown in figure 1.

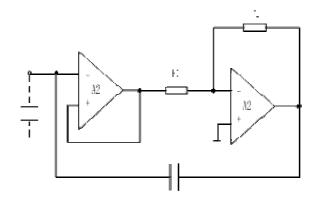


Figure1. Impedance converting circuit

Set the operational amplifier in figure 1 as the ideal, the node voltage of e1, e2 and e3.In figure 1, according to the operational knowledge and the kirchhoff's current law, we can get the following equation:

$$e_1 = e_2 \tag{1}$$

$$e_3 = -\frac{R_2}{R_1} e_2 \tag{2}$$

$$\frac{e_1}{Z_{in}} = \frac{e_1 - e_3}{1/jwC}$$
(3)

According to $(1) \sim (3)$ to the expression of equivalent impedance Z_{in} of figure 1 are as follows:

$$Z_{in} = \frac{1}{jw(1 + \frac{R_2}{R_1})C}$$
(4)

Thus, we can see the equivalent impedance of $\frac{1}{jw(1 + \frac{R_z}{R_1})C}$. This is a capacitor for equivalent capacitance impedance. In other words, the circuit is composed of a electric capacitance of capacitor of $\left(1 + \frac{R_z}{R_1}\right)C$. Through changing the value of C, R₁ and R₂ can get the equivalent capacitance value of C_E .

2. Equivalent Capacitor Circuit

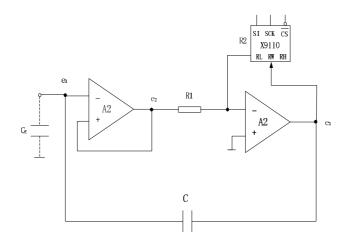
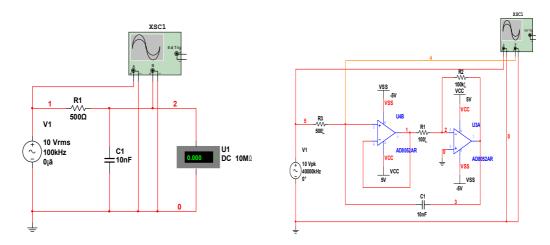


Figure2. Programmable capacitor equivalent circuit

The programmable capacitance circuit as shown in figure 2.We can replace the R₂ by digital potentiometer X9110 in figure 1.The selected X9110 is a 1024 tap with serial SPI interface (10 digits) of 100 K digital potentiometer.By the principle of digital potentiometer we can know $R_2 = \frac{D}{1024} \times 100K$, D in 0~1023, and $R_1 = \frac{100K}{1024} \approx 97.66\Omega$. The R₁ and R₂ into formula (4) available C_E= (1+D) C.

When the capacitance C equal 1 pf, D in $0 \sim 998$. We can achieve the equivalent capacitance range from 1pf to 999 pf. Similarly, when capacitance C equal 1nf, the equivalent capacitance value can range from 1nf to 999 nf. If selected capacitance C value is 1pf, 1 nf, 1 uf and 1mf, and use analog switch to switch, the equivalent capacitance is from 1 pf to 999 uF.

3. Comparison of experimental and simulation results



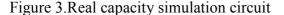


Figure 4.Equivalent capacitance simulation circuit

The low pass filtering circuits of a real capacity and resistances Figure 3 and the equivalent capacitance and resistances Figure 4 are shown below. The cut-off frequency is 318.42kHZ. Figure 5 shows the frequency amplitude characteristics curve of the real capacitor. Figure 6 shows the frequency amplitude characteristics curve of the equivalent capacitance. The simulation results showed that the amplitude frequency characteristic curves of the equivalent capacitor and the real capacitor fit very well.

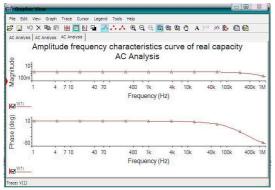


Figure 5. Curve of real capacity

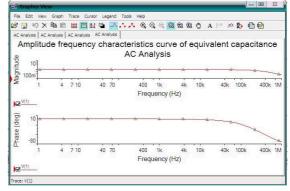


Figure 6. Curve of equivalent capacitance

4.Conclusion

The simulation and experimental results showed that the amplitude frequency characteristics of the equivalent capacitor and real capacitor were basically the same. The differences between the simulation and experimental results can be explained by the non-ideality of the experimental devices such as the operational amplifier. Those differences could be minimized if considering this factor while setting up the circuit. With different amplifiers or circuit settings, different types (e.g. with high power, high frequency, high voltage or high precision etc.) of equivalent capacitance circuits can be obtained. Using single chips to control the value of the equivalent capacitance is able to make the equivalent capacitor programmable. This design has the potential to bring great convenience to electronic product designs and scientific researches. Integrating the programmable equivalent capacitor circuit into a single chip as shown in Figure 2, a new programmable capacitor chip will be obtained, which will greatly benefit the field of digital electronic circuit.

References

- [1] Yang Suxing. Analog electronic technology basic introductory tutorial .Higher education press.(2005).
- [2] NiuMan, YuHongyun. Electronic circuit analysis and design. Tsinghua university press.(2009).
- [3] far prefer jun zhao. Measurement of electronic circuit design. Beijing: science press.(2006).
- [4] Dao Ye Bao. Oscillation circuit design and application. Beijing: science press.(2005).
- [5] ShaZhanYou The design principle and application of digital potentiometer. Mechanical industry press.(2007).

The Nonlinearities of Memoryless Power Amplifier and Model of Predistorter

Huan Yang ^{1,a}, Yuanzhi He ^{2,b}

¹The Institute of Communication Engineering, PLA University of Science and Technology, Nanjing Jiangsu Province, China

²China Electronic Equipment Systems Engineering Company, Beijing, China

^ayanghuan_mc@163.com; ^bYuanzhi1974@gmail.com

Keywords: Nonlinearities; power amplifier; predistortion; LS and adaptive LMS

Abstract. By analyzing the input and output data of memoryless power amplifier (PA), we construct the polynomial model and study the nonlinearities characteristics of it. Based on that the mathematic model of predistorter is gained, Least-square (LS) and adaptive LMS are used respectively to solve the question. Simulation results demonstrate predistortion can effectively correct the nonlinearities and both LS and LMS work well depending on different conditions.

Introduction

Power amplifiers (PA) are important segments for communication systems and are inherently nonlinear. When modulated signals go through a nonlinear PA, spectral regrowth appears in the PA output, which in turn causes adjacent channel interference (ACI). Stringent limits on the ACI are imposed by regulatory bodies, and thus the extent of the PA nonlinearity must be controlled. PA linearization is often necessary to suppress spectral regrowth, contain adjacent channel interference, and to reduce bit error rate (BER).^[1]

Prediction of spectral regrowth for a prescribed level of PA nonlinearity can be very helpful for designing communication systems. Since more linear PAs are less efficient, practitioners may wish to use the PA in a configuration that allows for maximum PA efficiency while still stay below the spectral emission limits. ^[2]Among all techniques, digital baseband predistortion is one of the most cost effective,^[3] and generally, we often gain the model of PA by data calculation and then use the PA model to realize the predistortion.

Model of Memoryless Power Amplifier

From the perspective of the generalized system identification, power amplifiers, according to the type of data extraction, model into physical model and black-box model.^[4] Physical models need to know electronic devices consist of a power amplifier and the relationship between them, and then use the theory to describe it; black-box models, however, just learn the input and output data to study the characteristics of amplifier power amplifier. Typically, the black box model is more complicated and used more widely in engineering practice.

There are three mathematical models to describe the characteristics of the power amplifier: Saleh model, Rapp model and polynomial model. Relatively the application range of polynomial model is wider and it could be used to describe both TWTA and SSPA^[5]. In this paper, we assume the input and output data of a PA are known and a polynomial model is employed to describe the PA as:

$$\hat{z}(n) = \sum_{k=1}^{K} h_k x^k(n)$$
(1)

where k is the order of nonlinearity (i.e. the order of polynomial), $\hat{z}(n)$ is output of the model, h_k is power of the coefficient and x(n) is input of memoryless PA. Make z(n) an observed value of the model and for every $\hat{z}(n)$, the target is to make the overall deviation between z(n) and $\hat{z}(n)$ minimum in time domain. To solve such kind of problem, the most common solution is the method of Least-squares^[6].

$$\Delta = \min\left\{\sum_{n=1}^{N} (z(n) - \hat{z}(n))^2\right\} = \min\left\{\sum_{n=1}^{N} (z(n) - \sum_{i=1}^{K} h_i x^i(n))^2\right\}$$
(2)

For equation (3), find the partial derivative with respect to h_k

$$\sum_{n=1}^{N} \left[z(n) - \sum_{i=1}^{K} h_i x^i(n) \right] x^k(n) = 0$$

$$\sum_{n=1}^{N} z(n) x^k(n) = \sum_{n=1}^{N} \left[\sum_{i=1}^{K} h_i x^i(n) \right] x^k(n) = \sum_{i=1}^{K} h_i \left[\sum_{n=1}^{N} x^i(n) x^k(n) \right]$$
(3)

then we could get the optimal coefficient.

Model of Memoryless Predistorter

The basic idea of predistortion compensation technology is add an additional nonlinear segment which has the opposite characteristics in front of the PA, making the nonlinear segment cascaded the PA perform linear amplification characteristics so that the output power of the devices can be used fully^[6]. Figure 1 shows the Block diagram of nonlinear compensation.

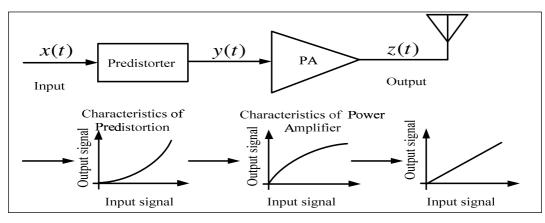


Figure 1. Block diagram of nonlinear compensation.

We assume x(t) and z(t) are input signal and output signal of PA respectively while y(t) is the output signal of predistorter. Use G to represent the transfer function of PA and F to represent the transfer function of predistorter then predistortion processing principle can be expressed as:

$$z(t) = G(y(t)) = G(F(x(t))) = G \circ F(x(t)) = L(x(t))$$
(4)

where $G \circ F = L$ is the composite function of G and F. Usually the linearization is required for the PA is:

$$z(t) = L(x(t)) = g \cdot x(t)$$
(5)

constant g is the ideal amplitude magnification of PA (g>1).

Predistorter is essentially the inverse of the power amplifier, therefore, its structure model is essentially the same with a power amplifiers' and can be described by the same mathematical model as: $y(n) = \sum_{k=1}^{K} a_k x(n)^{k-1}$.

as:
$$y(n) = \sum_{k=1}^{k} a_k x(n)^{k-1}$$

Memoryless predistorter and PA use the same mathematical model, then the method above-mentioned can also be used directly for solving the problem. The method of Least-squares algorithm is simple, fitting high precision, but this advantage is limited to a small amount of data

processing and calculation of static data. Considering the large amount of computation Least-squares method, we consider the use of LMS adaptive algorithm for solving calculations.

LMS algorithm is a recursive method for solving minimum of multi-variable function which is used to solve the optimal value by iterative search. Assuming ξ_M is a known function with coefficient of h(n), where $0 \le n \le M - 1$. Generally the algorithm which is used to recursively calculate the minimum of ξ_M often has a form as:

$$\mathbf{h}_{M}(n+1) = \mathbf{h}_{M}(n) + \frac{1}{2}\Delta(n)\mathbf{S}(n), \qquad n = 0, 1, ...$$
 (6)

where $\mathbf{h}_{M}(n)$ represents filter coefficient vector of the n-th iteration, $\Delta(n)$ is the step length of n-th iteration and $\mathbf{S}(n)$ is direction vector of n-th iteration what's more the initial vector $\mathbf{h}_{M}(n)$ could chose arbitrary value.

The simplest method of searching for minimum is based on Steepest-descent Search, which is defined as:

$$\mathbf{g}(n) = \frac{d\xi_{M}}{d\mathbf{h}_{M}(n)} = 2\left[\mathbf{\Gamma}_{M}\mathbf{h}_{M}(n) - \boldsymbol{\gamma}_{d}\right] \qquad n = 0, 1, 2, \dots$$
(7)

where $\mathbf{g}(n)$ is the grad vector of n-th iteration and $\mathbf{S}(n) = -\mathbf{g}(n)$, Γ_M is autocorrelation matrix and γ_d is cross-correlation vector. Thus In each iteration, the gradient is calculated at all times, and in the opposite direction of gradient to modify the $\mathbf{h}_M(n)$. Such recursive equation based on steepest gradient algorithm is:

$$\mathbf{h}_{M}(n+1) = \left[\mathbf{I} - \Delta(n)\mathbf{\Gamma}_{M}\right]\mathbf{h}_{M}(n) + \Delta(n)\mathbf{\gamma}_{d}$$
(8)

Simulation Results and Analysis

1 Least-square algorithm simulation results

We use the input and output data of a PA to compute. Considering that the increasing of K will make the calculation increase faster and usually the polynomial 5-order or 6-oeder could meet the accuracy requirements,^[7] so we set K=6 to fit the data. And by calculating we get the coefficients of the PA model displayed in the Table 2.

h_1	h_2	h ₃	h_4	h_5	h ₆			
3.0317	-0.7245	5.1929	-15.1075	13.5094	-3.9904			

Table 2. Coefficients of the PA model

The expression of the memoryless PA is :

$$\hat{z}(n) = -3.9964x^6 + 13.5094x^5 - 15.1075x^4 + 5.1929x^3 - 0.7245x^2 + 3.0317x$$
(8)

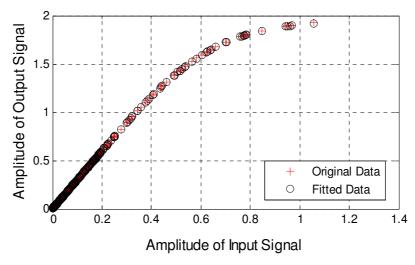


Figure 2. AM/AM characteristics of PA

Compared with the original value of the actual observations we can see the sixth-order polynomial fit the original data well both in linear and saturated zone as showing in Figure 2. The coefficients of predistorter displayed in the table below:

h ₁	h_2 h_3 h_4		h ₄	h ₅	h ₆	
0.3659	3.1307	-14.7018	31.0756	-30.1624	11.0822	

Table 3. Coefficients of the predistorter model by LS

Thus the predistorter analytical formula is:

$$y(n) = 11.0822x^{6} - 30.1624x^{5} - 31.0756x^{4} - 14.7018x^{3} + 3.1307x^{2} + 0.3659x$$
(9)

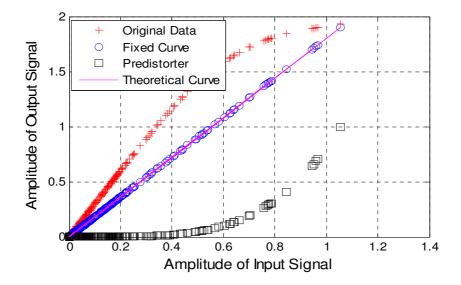


Figure 3. AM/AM characteristics by LS

From the fitting results, we can find that compared to the output without correction, the nonlinearities of output corrected by predistorter is improved greatly and there is no distortion occurs situation in the data range.

LMS algorithm simulation results

Taking K = 6 to get the coefficients of predistorter displayed in the table below:

h_1	h ₂	h ₃ h ₄		h ₅	h ₆
0.5963	0.0085	0.0234	0.0326	0.0376	0.0403

Table 3. Coefficients of the predistorter model by LMS

Thus the predistorter analytical formula is:

$$y(n) = 0.0403x^{6} + 0.0376x^{5} + 0.0326x^{4} + 0.0234x^{3} + 0.0085x^{2} + 0.5963x$$
(10)

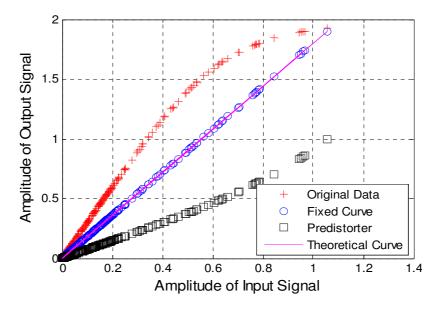


Figure 4. AM/AM characteristics by LMS

We can find that compared to the output without correction, the nonlinearities of output corrected by predistorter is improved greatly and there is no distortion occurs situation in the data range.

Conclusions

Usually the standard used to evaluate fitting result is Normalized Mean Square Error (NMSE); NMSE could be treated as a kind of deformation of Mean Square Error (MSE) and reflect the degree that the mathematic model approximate the physical reality model and can be used to judge how approximately the model output approaches the ideal output after a predistorter added to the PA. Furthermore, the smaller NMSE is, the better the effect of compensation is. Combine the memoryless PA model and the calculation data, the NMSE of PA fitting is -63.9962dB, and that shows the polynomial can fit the memoryless PA model perfectly.

The fitting accuracy of predistorter is displayed in the Table 4, and we can find that both Least-square algorithm and LMS adaptive algorithm could fit the model data effectively, except that the Least-square algorithm is about 8dB better than LMS adaptive algorithm in accuracy.

Table 4. NMSE of LMS and LS

LMS adaptive algorithm	-34.3758 (dB)
Least-square algorithm	-41.3178 (dB)

The excellence of Least-square algorithm, however, is not absolute while the high fitting accuracy of Least-square algorithm is paid for a large amount of calculation which will occupy a large number of resources, especially when need to do inverse calculation for a matrix or deal with massive dynamic data and that will obviously reduce the calculate efficiency. On the other hand, LMS adaptive algorithm is based on iteration has a faster compute speed and is easy to realize in engineering practice. Thus to weigh the accuracy and the complexity, it is worth to use accuracy exchanging for compute speed. Both of the two algorithms have advantages and disadvantages and we could make our choice depending on the actual conditions.

Acknowledgement

This work is supported by China National Natural Science Foundation under grant 61231011.

Reference

- [1] Park J S, Gelfand S B and Fitz M P. Joint optimization of data pre-distortion and baseband pulse shaping in high speed transmission nonlinear systems[C]//IEEE International Conference on Microwaves, Communications, Antennas and Electronics Systems, Tel Aviv, Israel: IEEE Press, 2009:9-11
- [2] Cripps, S. C., Advanced Techniques in RF Power Amplifier Design. Norwood, MA: Artech House, 2002.
- [3] Alasady H, Ibnkahla M, Rahman Q. Symbol error rate calculation and data pre-distortion for 16-QAM transmission over nonlinear memory-less satellite channels, Wireless Communications and Mobile Computing,2008,8:137-153
- [4] Karam G, Sari H. Analysis of pre-distortion, equalization and ISI cancellation techniques in digital radio systems with nonlinear transmit amplifiers. IEEE Transactions on Communication, 1989,37(12):1245-1253
- [5] Chen H H, Lin C H, Huang P C, et al. Joint polynomial and lookup table pre-distortion power amplifier linearization. IEEE Transactions on Circuits and Systems,2006, 53(8):612-616
- [6] Raviv Raich, Nonlinear system identification and analysis with applications to power amplifier modeling and power amplifier predistortion. School of Electrical and Computer Engineering Georgia Institute of Technology,2004
- [7] Sunmin Lim, Chung Nam etc. Predistorter design for a memory-less nonlinear high power amplifier using the pth-order inverse method for OFDM systems, 2003 vol.6- 689-692

Low-cost and Modularized Test Bench for Focal Plane Array

Xiqu Chen^{1, a} and Qiang Lv^{1,b}

¹ School of Electrical & Electronic Engineering, Wuhan Polytechnic University, Wuhan, China ^acxqdhl@sina.cn, ^bcaeolus@gmail.com

Keywords: Test bench, Microbolometer, focal plane array

Abstract. In this paper, a low-cost and modularized test bench for microbolometric focal plane array is proposed. Based on the analysis of driving microbolometric focal plane array, we have set up the simple test bench. The test bench consists of four major modules: optical part, driving sequence timer, power supply and signal processing board, and data analyzer. Each module in the test bench is reconfigurable and the driving sequence timer is programmable in system. The proposed test bench is low-cost and has been applied to practical microbolometric focal plane arrays in our laboratory.

Introduction

With the improvement of micro fabricating technology, the performance of microbolometric focal plane array (FPA) is more and more stable and excellent. However, there are still some challenging factors including non-constant fabricating process parameters which will lead to the inconsistent performance of microbolometric FPAs of same model. Thus, the strict and fast characteristic parameter measurement and test of microbolometric FPA are necessary in manufacturing factories of microbolometric FPA. Additionally, testing systems for experimental microbolometric FPA prototypes in laboratories or research institutes are also indispensable to judge the performance characteristics of these prototypes.

Some conventional testing systems for microbolometric FPA are complex and expensive like the FPA testing system in Sofradir in France, and other special testing systems such as the testing module in INO in Canada are simple and low-cost but inflexible to be applied to different kinds of microbolometric FPAs [1]. We have referred some kinds of testing benches for measuring and testing VO₂-based FPA prototypes in our laboratory, and this has been reported in one of our previous published papers [2]. Although these kinds of testing benches are adequate to measure and test normal microbolometric FPA, there are still some requirements in the areas of flexibility, reconfiguration, and modularization.

In this paper, we designed and set up a new test bench for microbolometric FPA, and this test bench has a kind of simple structure and contains only four modules. One of four modules in this test bench is programmable in system to be utilized for different types of microbolometric FPAs. At the same time, all these four modules can be reconfigured according to the practical requirements of measurement and test. This low-cost test bench has successfully been used for measuring and testing several different kinds of VO₂-based FPAs in our laboratory and can be easily reconfigured to test normal different microbolometric FPAs.

Test Bench Analysis

The basic structure of normal microbolometric FPA is shown in Fig. 1, in which the infrared (IR) radiation is focused on the bolometer through some infrared optical parts and the resistance value of the microbolometer is changed. When the microbolometric FPA works, the changed resistance is transformed into voltage signal and selected to be output to the column amplifier by the row select driving signal. All the column pixel signals of one row are selected to be output by the column select driving signal. A test bench for the microbolometric FPA should provide row and column select driving signals and power supplies for the microbolometric FPA. In addition, the test bench must have

a signal processing unit that realizes signal acquisition, post-processing, and communication. Furthermore, the output data from the signal processing unit in the test bench should be processed by a data analyzer within the test bench.

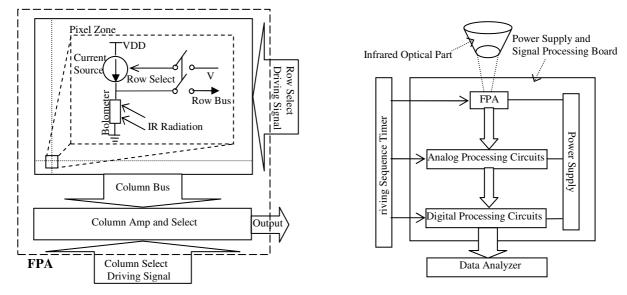


Fig. 1. Schematic representation of microbolometric FPA.

Fig. 2. Schematics of the proposed test bench.

From above analysis, it can be found that a test bench for microbolometric FPA should contain four basic sections: infrared optical part, driving and power supply unit, signal processing unit, and data analyzer. Based on this kind of idea, we propose the test bench in this paper which is schematically shown in Fig. 2. In the proposed test bench, the power supply part to provide power supplies for both the microbolometric FPA and the signal processing unit is merged into the signal processing circuit board. The test bench has four modules: infrared optical part, driving sequence timer, power supply and signal processing board, and data analyzer. The module of infrared optical part is mainly composed of several infrared optical lenses, and the module of driving sequence timer is a circuit board which is based on a FPGA chip providing a sequence of driving pulse signals to the module of power supply and signal processing board. The analog processing circuits in the power supply and signal processing board amplify and preprocess the analog output signal from the FPA to the digital processing circuits into digital signal and further process the digital signal to be output to the data analyzer in the test bench.

The integrated FPGA chip in the module of driving sequence timer is programmable in system and can provide different driving signals for all microbolometers of different families. The digital processing circuits in the module of power supply and signal processing board is majorly based on an integrated DSP chip, and the integrated DSP chip is also programmable in system. The data analyzer is a data processing and analyzing system being composed of a universal computer and special operation software, and the special operation software in the computer can process the data originating from the FPA and give out the performance characteristics of the tested microbolometric FPA according to the need and possibility. At the same time, the module of infrared optical part is reconfigurable to agree with practical test requirements. Then, it can be said that all these four modules in the test bench are flexible to be reconfigured.

Test Bench Application

In order to verify the proposed test bench, a practical test bench for a 128×128 element microbolometric FPA is configured on the base of the proposed test bench. The driving sequence signals for the 128×128 element FPA include column select driving signal and row select driving signal, and the frequency of row select driving signal is

$$F_R = \frac{F_C}{128},\tag{1}$$

where F_c is the frequency of column select driving signal. Then, the output video frame frequency of the 128×128 element FPA is

$$F_F = \frac{F_C}{128 \times 128}.$$
 (2)

To get the row and column driving sequence signals, programs are implemented in the integrated FPGA chip with a 4MHz crystal oscillator in the test bench. The frequency of column select driving signal is obtained through the eight frequency divisions of the 4MHz crystal oscillator output and is

$$F_C = \frac{4}{9} = 0.5M$$
 Hz. (3)

The column and row driving sequence signal waveforms generated by the module of driving sequence timer in the test bench are respectively shown in Fig. 3 and Fig. 4, and the frequencies of column and row driving signals are consistent with Eq. 1 and 3. Additionally, the corresponding output frame frequency signal and pixel signal waveforms of the tested microbolometric FPA are shown in Fig. 5 and Fig. 6. From the waveform in Fig. 5, it can be approximately found that the output frame frequency of the tested microbolometric FPA is about

$$F_F = \frac{F_C}{128 \times 128} = \frac{4M}{8 \times 128 \times 128} = 30.52 \,\mathrm{Hz},\tag{4}$$

which can be deduced from Eq. 2. From Fig. 6, it can be seen that the pixel output period of 2µS is the same as the column driving sequence signal period in Fig. 3. Thus, it can be said that the programmable driving sequence timer in the practical test bench can correctly perform its driving function for the 128×128 element microbolometric FPA.

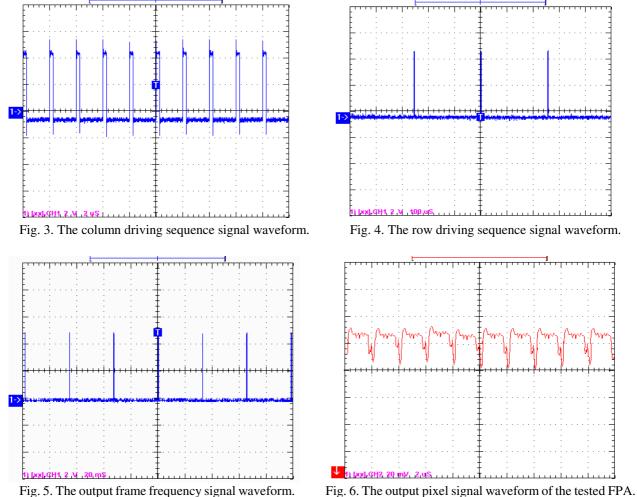


Fig. 5. The output frame frequency signal waveform.

In order to compare tested parameters with nominal parameters, the module of infrared optical part is configured with infrared optical lens with an f/1 aperture. Besides, the module of power supply and signal processing board can provide 5V power voltage to the microbolometric FPA and preliminarily process and transform the output analog voltage signal of the test FPA.

The module of data analyzer in the test bench is a portable computer equipped with an acquisition and analysis software. The output digital signals from the module of power supply and signal processing board are acquired by the computer and analyzed by the software to display the performance characteristics of the tested microbolometric FPA. The algorithms of necessary performance parameters of the tested microbolometric FPA are contained within the analysis software of data analyzer, in which for example the average responsivity and non-uniformity of the FPA can respectively be expressed as

$$\overline{R} = \frac{1}{128 \times 128 - (d+h)} \sum_{i=1}^{128} \sum_{j=1}^{128} R(i,j) , \qquad (5)$$

and

$$N = \frac{1}{R} \cdot \sqrt{\frac{1}{128 \times 128 - (d+h)} \sum_{i=1}^{128} \sum_{j=1}^{128} \left[R(i,j) - \overline{R} \right]^2} ,$$
(6)

where *d* is dead pixel number, *h* is hot pixel number, and R(i, j) is the microbolometer responsivity of the *j*th column in the *i*th row.

Some tested performance parameters of the tested microbolometric FPA are finally given out by the analysis software of data analyzer, and part key tested and nominal performance characteristics of the 128×128 element FPA are summarized in Table 1, from which it can be found that the tested performance characteristics are almost the same as the nominal performance characteristics. Therefore, it can be said that the proposed test bench is feasible and can be applied to practical tested system for microbolometric FPA.

Table 1 Summary of performance charatenstics						
Performance	Tested	Nominal				
Terrormanee	parameter	parameter				
Spectral Response (µm)	8~14	8~14				
Output Noise (mV RMS)	0.3	0.3				
Responsivity \overline{R} (VW ⁻¹)	14970	15000				
Detectivity D^* (cmHz ^{1/2} W ⁻¹)	1.5×10 ⁸	1.5×10 ⁸				
NETD (°C)	0.2	0.2				
Non-uniformity N (p-p)	14.8%	<15%				

Table 1 Summary of performance charateristics

Conclusions

The basic driving principle of universal microbolometric FPA is theoretically analyzed, and a new low-cost and modularized test bench for microbolometric FPA is proposed based on the analysis of driving principle. With the proposed test bench, we have configured a practical test bench for a 128×128 element microbolometric FPA in our laboratory. Tested results by using the practical test bench indicate that the proposed test bench is programmable in system and reconfigurable according to practical testing requirements. Furthermore, the practical test bench has successfully been reconfigured to be used for measuring and testing several different kinds of VO₂-based FPAs in our laboratory, which proves that the proposed test bench is feasible and potential to be applied to different kinds of normal microbolometric FPAs.

References

- [1] A. Bergeronl, H. Jerominek, C. Chevalier, et al, Journal of Physics Vol. 276 (2011), p. 1.
- [2] X. Chen, Optical Engineering Vol. 47 (2008), p. 104402-1.

Design of Music Prescription for Music Electroacupuncture Instrument

Canhua Wang¹, Jianqiang Du¹, Helin Zhang^{1,a}

¹School of Computer, JiangXi University of Traditional Chinese Medicine, Nanchang, China ^a390921890@qq.com

Keywords: Music therapy, 1/f fluctuation, Electroacupuncture, Embedded

Abstract. As a physical therapy way,music therapy has been widely used. The choice of music is very important during treatment because different music has different curative effect. However, the choice of music often come to depend on people's subjective feeling and the theoretical foundation why the music is chosen is unknown. In this paper, the choice of music,i.e. music prescription, is considered from the following three aspects. Firstly, the power spectral density of the music must satisfy the 1/f fluctuation law. Secondly, the relationship must be ascertained between the frequency of the music and symptoms. Thirdly, melody and rhythm of the music should be choosen for different symptoms. Clinical test show that the scheme in this paper is feasible and the treatment effect is significant.

Introduction

A lot of research show that music signal has a better therapeutic effect on the human body. At first, the music has a direct effect on the nervous system and can affect the cardiovascular system. Secondly, Listening music can resonate in the emotional psychologic.Thirdly, in the course of treatment, the current can penetrae ones skin and reach the depths of the body.This can administer to the remission of muscular tension. The local blood circulation is improved too[1,2]. However, the music is different for different patients because different music has different curative effect.Therefore, The choice of music i.e. music prescription, play a direct role in the treatment of disease.

Design of music prescription

The music signal can be considered as a stochastic process[3]. If x(t) represents music signal, the Fourier transform can be calculated by following formulas(1):

$$X_{T}(f) = \int_{-T}^{T} x(t) e^{-j2\pi ft} dt .$$
 (1)

The Power Spectral Density (PSD) of x(t) can be calculated by following formulas(2):

$$S(f) = \lim_{T \to \infty} \frac{1}{2T} E\left[\left| X_T(f) \right|^2 \right].$$
⁽²⁾

The relationship between PSD and f can be determined by fllowing Eq.(3):

$$S(f) = A / \left| f \right|^{\lambda}.$$
(3)

In Eq.3, S(f) is PSD, A is a constant, f is the frequency, λ is the index of frequency. Take the logarithm of both ends of Eq.3, Eq.4 can be drawn up:

$$\lg S(f) = \lg A - \lambda \lg f.$$
⁽⁴⁾

In Eq.4, there is a linear relationship between $\lg S(f)$ and $\lg f$, $-\lambda$ is slope. The x(t) is called 1/f fluctuation when λ is 1. As shown in Fig.1.

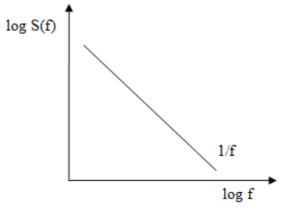
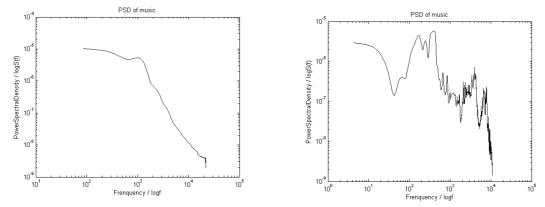


Fig.1 Spectral characteristic of 1/f fluctuation

Studies have shown that human being's heartbeat cycle and α brainwaves' variation cycle are in accordance with the regular of "1/f fluctuation" in a comfortable state. "1/f fluctuation" of outside world can also inspire human being's α brainwaves, prompt it produce "1/f fluctuation" and make us comfortable^[4]. To make the patient easily to accept music electrical stimulation, the music with 1 / f fluctuation law can be choosen as the prescription.

Take two songs, (My heart will go on) and (Rock On the New Long March), for example. The former is a lingering melodious song, whose PSD is shown in Fig.2; and the latter is a rock song whose PSD is shown in Fig.3. In Fig.2, PSD is inversely proportional to f and lgS(f) is approximately linear with lgf, which coincided with 1/f fluctuation law; but in Fig.3, the relationship between PSD and f is complicated, which does not meet 1/f fluctuation law. So 《My heart will go on may be choosen as a prescription, but 《Rock On the New Long March》 not.



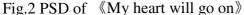


Fig.3 PSD of 《Rock On the New Long March》 Take cervical spondylotic radiculopathy for example, the design of music prescription should be taken acoount as follows.Firstly, the music whose PSD have 1/f fluctuation characteristic should be picked up.Secondly, the energy of music must focus on 2Hz and 100Hz because the clinical test show the effect is better on the two frequency points[5]. Thirdly, the characteristics of music should

Music electroacupuncture instrument based on ARM

The authors developed a music electroacupuncture instrument based on ARM by the support of science and technology project of Jiangxi Province. The hardware system of music electroacupuncture instrument was composed of S3C2440, Audio decoding circuit, Audio amplifier circuit,USB interface circuit and Touch screen,etc. As shown in Fig.4. In order to avoid the permanent damage for human nervous tissue by charge accumulation[6], the instrument output bipolar pulse so that the total charge obtained by human nervous tissue is zero. That is, the range of voltage amplitude is form -7.5V to +7.5V, the range of current amplitude is from -2mA to +2mA.In addition,the software design of music electroacupuncture instrument was based on Qt and Linux. The functions such as open music files, display the list of songs, play music, select song playing order and the volume all be realized.

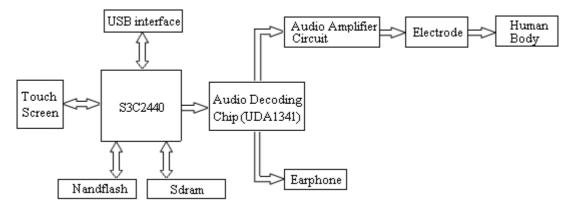


Fig.4 Hardware system block diagram of the music electroacupuncture instrument

The music electroacupuncture instrument can play music from USB storage device by clicking on the touch screen. The audio signal is applied to the body by the electrode after decoding and amplification. In addition, the patient can enjoy music at the same time of treatment.

Efficacy assessment

A total of 60 cervical spondylotic radiculopathy patients were randomly divided into music1 group, music2 group and pulse group, with 20 cases in each group. Ordinary electric pulse therapeutic instrument was used in pulse group and the music electroacupuncture instrument was used in music 1 group and music 2 group.Music prescription mentioned above was choosen in music 2 group,but the music not meeting 1/f fluctuation law was choosen in music 1 group. The three therapies were applied to jingjiaji,jianjing,jianyu,quchi and waiguan once daily for 20 days.

We used visual analogue scale (VAS) to record the pain sensation values[7]. SPSS was used to process recorded data and get a chart of pain sensation values. Results are shown by mean \pm standard deviation ($\overline{x} \pm s$). There was significant statistical difference if P<0.05. If the P<0.01, with a very significant difference[8].As shown in Table 1.

Table 1. Comparison of VAS before and after treatment among three groups $(\bar{x} \pm s)$

Groups	Cases	Pretherapy	10 days after treatment	20 days after treatment
Pulse	20	6.89±0.36	4.16±0.50	2.86±0.32
Music 1	20	6.91±0.35	3.85±0.25	2.05 ± 0.56
Music 2	20	6.90±0.37	3.50±0.15	0.82±0.15

Note: P<0.01 show that the music 2 group has obvious advantages in erasing pain

The scoring table for symptoms and signs was designed to evaluate therapeutic effect[9]. As shown in Table 2.

	Table 2. Comparison of cultarive effect before and after treatment among three groups										
Groups	Cases	Cured	Markedly efective	Effective	Failed	Totally effective rate					
Pulse	20	4	5	5	6	70%					
Music 1	20	6	5	6	3	85%					
Music 2	20	9	6	4	1	95%					

Table 2. Comparison of curative effect before and after treatment among three groups

Note: P<0.05 show that it is statistically significant.

Summary

In this paper, a new music electroacupuncture instrument based on ARM is introduced and a new method to design music prescription is put forward. It makes good use of the 1/f fluctuation theory. And experiences verify the effect. In the same way, other music prescription also can be designed for mental illness such as insomnia.

Acknowledgements

This work was financially supported by the project: Science and technology project of Jiangxi Province (NO. 20133BBG70087).

References

- [1] Weimin Zhou. Musicology in China, 2007,01:117-121. In Chinese.
- [2] Jinyan Teng, Zhigang Li,Yan Bai. World Journal of Integrated Traditional and Western Medicine, 2013,8(4):348-350. In Chinese.
- [3] T Musha, M Yamamoto. 1/f Fluctuations in Biological Systems. Proc.of 19th International Conference IEEE/EMBS, 1997[C] Chicago,IL,USA.
- [4] Xia Mao, Yukuan Ding, Muta Itsuya. Acta Electronica Sinica, 2001,29(12A):1923-1927.
- [5] Shaobing Wu, Shi Chen, Hai Li. Acta Physica. Sinica, 2012,61(9):1-10. In Chinese.
- [6] Yuxia Yang, Mingchao Yong. Chinese Acupuncture & Moxibustion. 2009, 29(4): 339-341.
- [7] Xiaoqing Huang, Xun Chen, Zhifang Yao. China Association for Acupuncture and Moxibustion annual meeting memoir, 2011. In Chinese.
- [8] Hao Zhang. Communications Technology, 2009,42(1):280-281. In Chinese.
- [9] Hua Xie, Mi Liu, etc. Acupuncture Research. 2012, 4(37): 318-323. In Chinese.

Advanced Materials Research Vol. 981 (2014) pp 54-57 © (2014) Trans Tech Publications, Switzerland doi:10.4028/www.scientific.net/AMR.981.54

The Analysis of Institutional Factors for Gain of EDFA

Lianlian Liu, Tao Shen^a, Suai Meng, Hanyu Yang, Pingyu Nie, Xin Zhang College of Applied Sciences, Harbin University of Science and Technology, Harbin, China ^ataoshenchina@163.com

Keywords: optical fiber communication systems; fiber amplifier; small-signal gain; erbium-doped fiber amplifier; fiber length

Abstract: Small signal gain of fiber amplifier has been measurement using a small signal broadband light source of simple and more accurate. And through the numerical simulation for test condition and experimental results of this method are discussed. The factors influencing of the erbium-doped fiber amplifier gain has been simulation and analysis, and effect of fiber length on the gain of the test. A new method is proposed for measuring optical fiber amplifier gain spectrum.

Introduction

Fiber amplifier optical fiber communication from breaking the constraints of fiber loss, to achieve all-optical communication distance is extended to thousands of kilometers of optical fiber communication has to make a revolutionary change. This paper analyzes the theoretical model of erbium-doped fiber amplifier (EDFA), emanating from the steady-state rate equation theory, such as the transmission equation, analysis of EDFA gain characteristics. Through simulation testing software OASIX fiber length, pump power forward, the impact of the pump power, signal power, temperature, and the gain structure of the different pump[1-2], and measure the gain spectrum, conclusions can be provide a reference for the design of the personnel engaged in EDFA[3].

A measurement principle

Set the pump light and signal light with regard to the background to the loss of doped fiber transmission while there:

$$\frac{dI_{p}}{dz} = (N_{2}\sigma_{p}^{(e)} - N_{1}\sigma_{p}^{(a)})I_{p} - \alpha_{p}^{(a_{0})}I_{p}$$
(1)

$$\frac{dI_s}{dz} = (N_2 \sigma_s^{(e)} - N_1 \sigma_s^{(a)}) I_s - \alpha_s^{(s_0)} I_s$$
(2)

Among them, $\alpha_p^{(a_0)}$ Said pump light in the background loss, $\alpha_s^{(s_0)}$ Background loss of said signal light, I_p and I_s The pump light and signal light, respectively, of the optical power in Z.B Establish measurement system

Due to the impact of the working substance EDFA erbium ion energy level structure, EDFA optical amplification characteristics of the signal also has its inherent flaws: EDFA gain of optical signals of different wavelengths are not identical, in the performance parameters of the optical fiber amplifier, The gain is one of the most basic and the most important indicator of its, how quickly and accurately test out this parameter will directly affect the practical application of optical fiber amplifiers[4].

The following factors will be used based on Giles, model Lucent's OASIX software simulation analyze the impact of EDFA gain. In the computer simulation, the erbium-doped fiber choice in the software EDF-HE980 and EDF-HG980 two models fiber in the 1525nm-1565nm wavelength range, input 41-channel signal, channel spacing of 1nm, strength 0.001mw.

Fiber amplifier gain is defined as the ratio of the signal output power and input power, which reflects the ability of the amplifier to enlarge. Can be expressed as:

$$G = p_1 / p_0 \tag{3}$$

Logarithmic coordinates is expressed as:

$$G(dB) = 10log(G)G \tag{4}$$

Experimental results and analysis

Experiments were conducted to test the fiber length, pump power forward, the impact of the pump power, signal power, temperature, and the different structure of the pump on the gain, and mathematically smoothed curve obtained in Fig.1, Fig.2, Fig.3. And Fig.4, Fig.5, Fig.6, gain spectrum under different conditions vary, but are generally on the rise, and the final size of the gain is roughly the same.

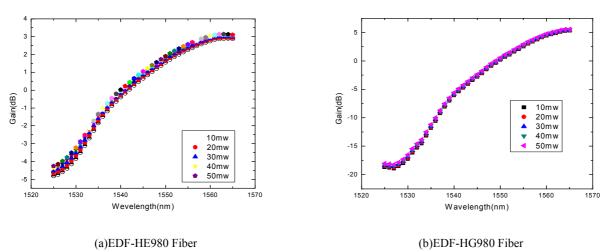
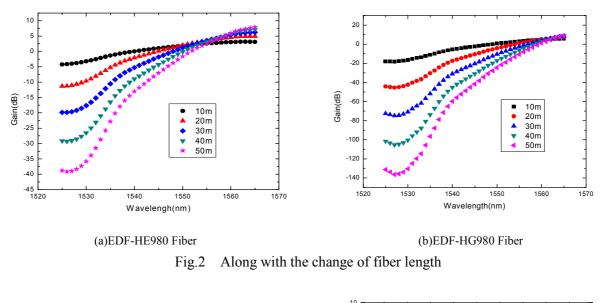


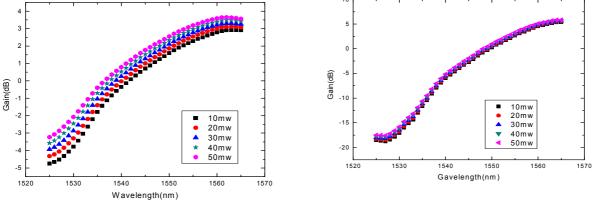
Fig.1 Along with the change of the forward pump power gain

From Fig.1(a), (b) two figures also clearly seen, both gain significant differences also exist in the wavelength 1525-1540nm wavelength range, EDF-HE980 fiber remains with the pump power increases, the gain increases the law, However, within this range, EDF-HG980 fiber prior gain increases with the pump power but slightly decreased at around the wavelength of 1528 rebounded to rise within a range. And both in the same wavelength range, the range is not the same gain value, the gain range of the optical fiber EDF-HG980 5-4dB, EDF-HG980 gain value in the range 20-5dB.

However, the fiber length as a variable in the numerical simulation, in which a single variable, the growth rate in both the wavelength range 1525-1540nm was significantly higher in the wavelength range 1540-1565nm growth. In the wavelength 1525-1530nm wavelength range, both have increased with the length of the fiber gain but slightly reduced phenomenon.

The pump power after the numerical simulation as a variable, in which case a single variable, both the growth rate in the wavelength range 1525-1540nm was significantly higher than in 1540-1565nm. Signal power as a variable in the numerical simulation of both the growth rate in the wavelength range of 1525-1540nm was significantly higher than in the 1540-1565nm wavelength range growth.

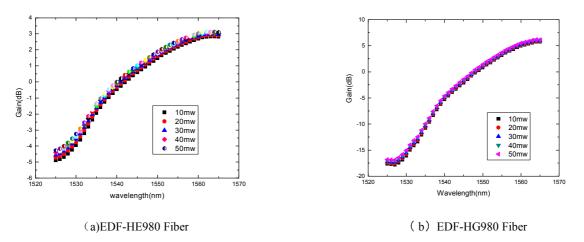


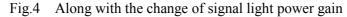


(a)EDF-HE980 Fiber

(b)EDF-HG980 Fiber

Fig.3 Gain subsequent to the change of the pump power





Temperature as a variable in the numerical simulations, the growth in the wavelength range of the gain in the 1525-1540nm range slope than the 1540-1565m range, at around 1540nm wavelength, the gain reaches 0dB, the gain range for this wavelength range -4-3dB, and at a wavelength of 1560nm at a gain value peaked, then began to decrease gain.

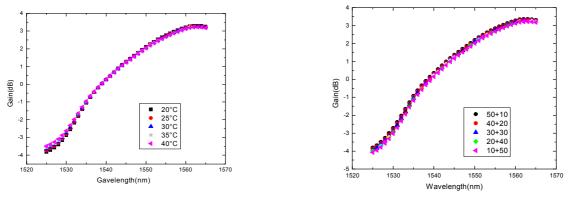


Fig.5 Gain change with temperature

Fig.6 Gain change with the structure of the pump

As a variable in the pump structure of the numerical simulation, the gain of the pump changes with corresponding changes in the structure before the pump is reduced, and then increases to the pump, the gain also increases. Increasing the gain slope is within the range of 1525-1540nm in the ratio in the range 1540-1565nm wavelength range, at a wavelength around 1540nm, the gain reaches 0dB, the gain range of the wavelength range of-4-3dB, and the wavelength of 1560nm Department reached a peak gain value, and then began to decrease gain.

Conclusion

Lucent's OASIX use software to simulate different types of fiber grouping, select a different independent variables such as the length of the optical fiber, the forward pump power, the pump power to get through the array, the signal light power, temperature and pumping structure The origin of data points plotted in Fig type, obtained under different conditions, as are the large gain increase, but the strength in different conditions, the gain is somewhat different.

Acknowledgements

This work was financially supported by the Science and Technology Research Project of Heilongjiang Province Education Bureau (No.12531134).

References

- [1] Lanlan Zhao, in:Research and numerical simulation EDFA gain slope factors experiments, Jiangnan University PhD thesis, 7, (2010).
- [2] Chushan Lin, Dapeng Deng, Xiaomin Liao and Zhang Bin: Industrial Control and Electronics Engineering, Vol. 264 (2012), p. 995.
- [3] Pengyu Wang and Ning Yan: Information Security and Technology, Vol. 4-7 (2013), p. 63.
- [4] Uiara C. de Moura, Juliano R. F. Oliveira and J'ulio C. R. F. Oliveira: Microwave & Optoelectronics Conference, Vol. 64-69 (2013), p. 1.

Design and Implementation of a RISC Processor on FPGA

Yang huijing¹, Fan hao^{1,a}, and Dong huaiguo¹

¹ School of Software, Harbin University of Science and Technology, Harbin, Heilongjing, China

^a yhj_833@163.com

Keywords: CPU, Verilog HDL, Control Unit, RISC, Processor.

Abstract. This paper targets the computer architecture courses and presents an Field Programmable Gate Array implementation of a RISC Processor via Verilog HDL design. It has 8-bit instruction words and 4 general purpose registers. It have two instruction formats. And it has been designed with Verilog HDL, synthesized using Quatus II 12.0, simulated using ModelSim simulator, and then implemented on Altera Cyclone IV FPGA that has 484 available Input/Output pins and 50MHz clock oscillator. The final overall simulation's experimental data verify the correctness of the processor.

Introduction

Reduced Instruction Set Computer (RISC) focuses on reducing the number and complexity of instructions in the machine[1]. Field Programmable Gate Arrays (FPGAs) are growing fast with cost reduction compared to ASIC design[2,3]. The goal of this project is to enhance the simulator based approach by integrating some hardware design to help the computer architecture students gain a hands-on experience in hardware-software integration and achieve a better understanding of both the single-cycle and pipelined processors[4].

Instruction Set

The first step in design of a RISC processor is the design of instruction set. An instruction set contains instructions supported by the processor. Each instruction is assigned a unique code, known as operation code (Opcode). For 16 instructions 4 bits opcode field is required. Instruction is divided into double-byte and single-byte. Mainly consists of the following four formats, the format is shown in Figure 1.

Format 1:	ų.										
7 6	5 4	4	3	2		1	0	 ↓(
0	₽₽		Rx.	ρ			Ry₊	i é	,		
Format 2:	el III										
15 14 13 12	11 10) 9	8	7	6	5	4	3	2	1	0 ⊷
O₽↔J	OP ₊ ∂ immedia			null@				÷			
Format 3:	ų										
76	5 4	1	3		2	1		0 ⊷	_		
0	P₽			nu	11 ₽				÷		
Format 4: 🗸											
15 14 13 12	11 10	9	8	7 (5 5	4	3	2	1	() ⊷
O₽↔		4	ADD	R₽							ę

Figure 1 The Instruction format

Table 1 lists the instructions supported by this processor. 16 instructions in the instruction set architecture that individual to handle Operation, Read memory, Writer memory, etc.

Opcode	Instruction Format	Function
0000	Format 3	Idle
0001	Format 2	Load Data
0010	Format 1	Move Rx, Ry
0011	Format 1	Add Rx, Ry
0100	Format 1	Sub Rx, Ry
0101	Format 1	AND Rx, Ry
0110	Format 1	OR Rx, Ry
0111	Format 1	XOR Rx, Ry
1000	Format 1	Shr Rx
1001	Format 1	Shl Rx
1010	Format 1	Swap Rx, Ry
1011	Format 4	Jmp Addr
1100	Format 4	Jz Addr
1101	Format 4	Read Addr
1110	Format 4	Write Addr
1111	Format 3	Stop

Table 1: Instruction Set

Architecture of the Processor

The processor in this paper has 8-bit instruction words and 4 general purpose registers. It have two instruction formats. An external clock is used as the timing mechanism for the control unit and datapath units. The processor presented in this paper consists of three components as shown in Figure 2.these components are ALU, Registers and Control Unit.

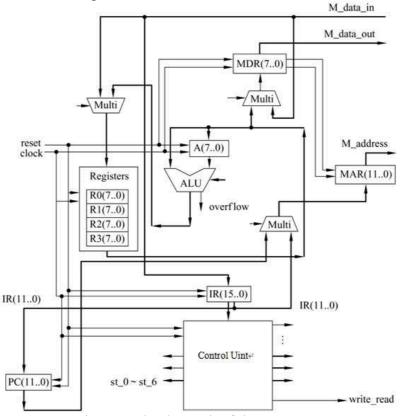


Figure 2 The datapath of the processor

The micro-architecture refers to a view of the machine that exposes the registers, buses and all other important functional units such as ALUs and counters. The datapath and the control unit interact to do the actual processing task. The control unit receives signals from the data path and sends control

signals to the data oath. These signals control the data flow within the CPU and between the CPU and the main memory and Input/Output.

Design and Implementation of Control Unit

The Control Unit is the brain of the CPU, It needs to generate signals for each register transfer action and other operations specified, and to be able to sequence through the steps for fetching/executing the instructions in the program.

The control unit design is based on using FSM (Finite State Machine) and we designed it in a way that has nine distinct states that determine the operation of the processor, and allows each state to run at one clock cycle, the first state is the reset which is initializes the CPU internal registers and variables. the control unit state diagram is shown in Figure 3. The machine goes to the reset state by enabling the reset signal for a certain number of clocks. Following the reset state would be the instruction fetching and decoding states which will enable the appropriate signals for reading instruction data from the memory then decoding the parts of the instruction. The decoding state will also select the next state depending on the instruction, since every instruction has its own set of states, the control unit will jump to the correct state based on the instruction given. After all states of a running instruction are finished, the last one will return to the fetch state which will allow us to process the next instruction in the program.

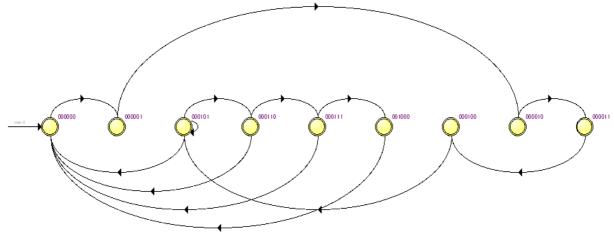


Figure 3 The control unit state diagram

Design and Implementation of ALU Unit

The ALU for this CPU performs only five functions: adds its two inputs, subtract its two inputs, logically ORs its two inputs, logically XORs its two inputs, and logically ANDs its two inputs. The circuit interface diagram for the ALU is shown in Figure 4.

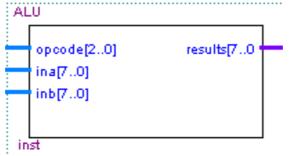


Figure 4 The circuit interface diagram of the ALU

The simplest way to design this ALU is to create separate hardware to perform each function and then use a multiplexer to output one of the five results. The addition is implemented using a standard 8-bit parallel adder. The Subtraction is implemented using a standard 8-bit parallel Subtractor. The

logical OR, XOR, AND operations are implemented using individual eight 2-input OR, XOR, AND gates. The outputs of the operation results are input to an 8-bit 5 to 1 multiplexer.

Simulation and Results Analysis

The 8-bit RISC processor functional implementation was perform on cyclone IV EP4CE15. Design a program that calculate cumulative from one to ten. Run the program in the RISC processor. The simulation results of control uint is shown in figures 5.

SIII	iuiuiioii i						•							
		0 ps	40.0 ns	80.0 ns	120. 0 ns	160.0 ns	200.0 ns	240. 0 ns	280. 0 ns	320. 0 ns	360.0 ns	400.0 ns	440.0 ns	480.0 ns
	Name	30	.3 ns											
i 🖗	🗷 R0							00						
9	si													
≥ 1.	rst													
≥ 1.	clk	LT.T.		unn			ىرىرىر	uuuu	uunu			uuuuu	uuuu	ىىيىر
	state	(. 0) (Xe. 0	0.0%.0%.0	X. 0X. 0X. 0X. 0	<u>X. 0X. 0X. 0X.</u>	0%.0%.0%.0%.0	<u>. 0)(. 0)(. 0)(. (</u>	X. 0X. 0X. 0X. 0	<u>X. 0X. 0X. 0X.</u>	0X.0X.0X.0X.0	(. 0)(. 0)(. 0)	stat	e.000101	
iiii 1.	🗉 op_in		000100	11	X 0	0100100	X 00	110001	X	1100000	X	111100	000	
@ 2.	🗏 rx			0		X 1 X	0 X1	X			0			
🔊 2.	-rx[1]													
	rx[0]													
 2. 2. 2. 2. 	🗷 Reg		0	X 2 X	0	$\chi_1\chi$	0	χ1χ			0			
👁 2. J	IR_ena													
2.	PC_load													
@ 3. @ 3. @ 3.	PC_add													
🕑 3.	R_wr													
🞯 3.	M_wr													
@ 3.	MAR													
Figure 5 Simulation results of control unit														

Figure 5 Simulation results of control unit

Throughout the results of simulation, we can see that the Execution process of the processor. we can also see that the transmission of the data in all registers in an instruction execution process.

Summary

In this paper describes a functional FPGA implementation design of a RISC processor designed using Verilog HDL. to help the computer architecture students gain a better understanding of the RISC processor. the FPGA implementation of the RISC processor and tools involved presented in this paper represent my goal of introducing FPGAs to help teach computer architecture courses by presenting the students with an enriching hands-on experience. I am convinced that if professors where to integrate these tools into their classes the students would display a better understanding of the class lessons as well as an increased enthusiasm about the work being performed.

Acknowledgements

In this paper, the research was sponsored by the Natural Science Foundation of Heilongjiang Province (Project NO. F201314).

References

- [1] Michael Gschwind, Valentina Salapura, and Dietmar Maurer "FPGA prototyping of a RISC Processor Core For Embedded Applications" IEEE transaction on VLSI systems, vol 9, no.2, April 2001.
- [2] Rainer Ohlendorf, Thomas Wild, Michael Meitinger, Holm Rauchfuss, Andreas Herkersdorf, "Simulated and measured performance evaluation of RISCbased SoC platforms in network processing applications", Journal of Systems Architecture 53, 2007, P 703–718.
- [3] John L. Hennessy, and David A. Patterson, "Computer Architecture A Quantitative Approach", 4th Edition; 2006.
- [4] K. Vlachos, T. Orphanoudakis, Y. Papaeftathiou, N. Nikolaou, D. Pnevmatikatos, G. Konstantoulakis, J.A. SanchezP., "Design and performance evaluation of a Programmable Packet Processing Engine (PPE) suitable for highspeed network processors units", Microprocessors and Microsystems 31, 2007, p 188–199.

The Modeling of OTFT and the Measuring of Small Signal Detection Circuit

Xin-cheng Liu^a, Min Zhu and Zhi-hui Jing

Department of Electronic Science and Technology, School of Applied Science, Key Laboratory of Engineering Dielectrics and Its Application, Ministry of Education Harbin University of Science and Technology, Harbin 150080, China

^a1096221992@qq.com

Keywords: OTFT; dynamic characteristics; micro-current detection; transistor modeling.

Abstract: In order to detect OTFT small signal dynamic characteristics of weak current, we designed the detection circuit. The current detection range of the circuit is $10^{-9} \sim 10^{-6}$ A, circuit bandwidth reaches 10kHz. According to the data tested by copper pthalocyanine thin organic static induction transistor we prepared, an equivalent circuit for simulating its dynamic performances was built and the factors influencing the performance of the device was investigated. The simulation results and actual test results are basically identical, which show the reliability of organic thin film transistor equivalent circuit model. In addition, through analyzing the model structure and the simulation results, the grid schottky junction capacitance and the device current intensity are the important factors in determining the dynamic properties of organic thin film transistor.

Introduction

In the past several decades, organic thin film transistor was paid attention to more and more people because of its high application potential and the value in the display, sensors, radio frequency identification tags and smart cards and other fields. Especially in the field of display application of organic thin film transistor compared with silicon transistors has the following advantages: low processing temperature, generally at 180 °C, decreasing significantly the energy consumption , it'ssuitable for flexible substrate; it greatly simplifies the process and greatly reduces the cost, two kinds of methods of vapor deposition and printing are suitable for large area processing; wide material source, great potential for development, at the same time, environmental friendly^[1].

But because the carrier concentration and mobility of organic semiconductor rate are very small, the performance is not ideal, such as low switching speed ,high driving voltage make it difficult to be practical, from magnifying multiple parameters of the switching speed and voltage of electronic it's difficult to make devices be practical. This paper is to test the dynamic characteristics to design the circuit and construct the equivalent model, providing the basis for the performance improvement of organic thin film transistors.

Since the detection of dynamic characteristics of organic thin film transistor is weak current signal and the signal processing circuit is voltage as signal processing. Therefore, how to maximize the current signal into voltage signal without distortion is the focus of current detection circuit. In this paper, the frequency of the detection circuit is within 10 kHz, detecting the current is 1nA-1uA.

In the past we commonly used static high input impedance meter tube current amplifier to measure, but the electrometer tube has the disadvantages of short service life, large volume, long stable time and power complex. With the advent of high impedance, high performance operational amplifier, development of micro current integrated amplifier has become possible.

The micro current amplifier

The micro current signal source can be regarded as current source I_S with very large the internal resistance, a grounding end micro current measurement principle is as shown in Fig.1. For the ideal operational amplifier that input impedance and magnification are infinite, output voltage Vo=- $I_S \times R_f$. In theory as long as the resistance R_f made large enough, even if the current I_S is very small, the large output voltage of V_O can be gotten such as $R_f = 10^9 \Omega$, $I_S = 10^{-10} A$, $V_O = -I_S \times R_f = 0.1 V$.

In fact, the input impedance of amplifier is not infinite, increase of resistance R_f is limited by input impedance amplifier. Considering the bias current I_B on the current to be measured I_S shunt, V_O =- (I_S - I_B) R_f , if I_B is greater than I_S , the I_S cannot measure ^[2].

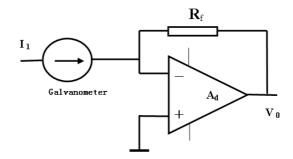


Fig.1. Micro current amplifier.

The primary factors affecting the micro current measurement sensitivity is bias current I_B of operational amplifier, followed by the noise voltage and zero drift. In order to realize the micro current measurement, operational amplifier should meet these demands: the bias current of I_B is less than the measured current I_S ; the input impedance of the R_i is greater than the feedback resistor R_f lot; the gain, common mode rejection ratio; the offset voltage and drift is small; the noise is small.

Design of micro current detection circuit

Choice of operational amplifier. Because the measured object is the weak current signal amplification, and it is easy to cause the offset voltage and current, and the zero drift, self interference, to test the accuracy of above factors n micro current will have an impact, so that ordinary operational amplifier has been unable to meet the accuracy requirements because their amplification, input offset voltage of typically a few hundred microvolt, imbalance current is larger also, to achieve amplification of micro current amplifier, the selection is the key, according to the following points to select ^[3]:Input impedance amplifier to, bias current should be small, low offset, low offset drift, gain and common mode rejection ratio to be high, low noise.

Circuit design using OPA128 operational amplifier, the OPA128 is a monolithic operational amplifier with a very low bias current. It is called the dielectric isolation process to achieve insulation, there is no PN junction diode, in order to achieve a small bias current. Even the cheapest of J version also can reach 150 (300) fA. The input impedance of $10^{13} \Omega$, open loop gain and common mode rejection ratio of the minimum values were 110dB and 90dB, and its low noise, and other performances are very superior.

Circuit design. In this paper, the design of the micro current amplifier requires the measurement range is $10^{-9} \sim 10^{-6}$ A, current is small and has a large range, so the circuit is composed of OPA128 pre amplifier and voltage amplifier is composed of two parts, as shown in Fig. 2.

The circuit used a total of two operational amplifiers, the first operational amplifier for I-V conversion, second for the voltage amplification and phase output. In I-V conversion part, R_{11} for the protection of resistance, the 1K. R_8 - R_{10} is a negative feedback resistance R_f , used for switching

range. There is no use of T resistor network as a negative feedback, because although T resistor network can indirectly improve the feedback resistor R_f value, but it also makes the offset voltage amplification factor. At the same time, ratio of signal to noise ratio is reduced accordingly, so here as far as possible to choose the larger $R_f^{[4]}$. Figure C4-C6 for power supply filtering device, C4 is used to attenuate the differential mode interference, C5 and C6 are used to attenuate common mode interference. C7~C14 as the power supply decoupling capacitor, C8, C9 two and a small capacitor in parallel, large capacity capacitor itself has inductance, current pulse filtering effect on the speed of change is not ideal, in parallel with a small capacitance can achieve good results, they are composed of R_{11} with LC filter^[5]. R_7 is output protection resistance, and it has the current limiting effect. Relationship between the output voltage and input current of the circuit is: $V_{out}=I_{in}\times R_f \times (1+R_6/R_5)$.

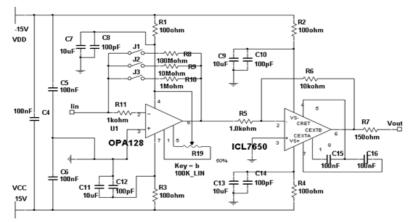


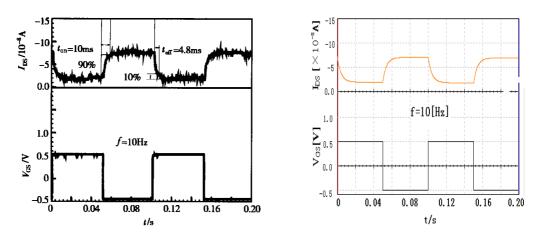
Fig.2 Schematic diagram of micro current amplifier

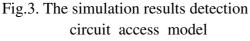
From the experiment the upper limit frequency of the amplification circuit is 10K Hz, output voltage can be maintained at more than 1V in the frequency range, which can directly output for A/D conversion or oscillograph, meet the measurement requirements.

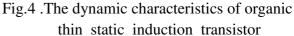
Method for improving circuit performance. There are many methods to improve circuit performance, for example reducing the operational amplifier working temperature, as far as possible from the heating device of the amplifier; balance resistance is not connected with the operational amplifier; reducing the PCB leakage current, we use high insulation board, PTFE wiring column and the protective ring; and improve the signal-to-noise ratio, using practical and high performance resistance and capacitance, and one point grounding.

Organic thin film transistor model simulation

In this paper, in view of the trial production of the organic semiconductor Copper Phthalocyanine Thin film aluminum gate static induction transistor, which is composed of a Au / CuPc / Al / CuPc / Au five layer. The dynamic properties for the detection and study of I_{DS} varies with the gate source voltage transistor small signal, is established based on the experimental data of static equivalent circuit model of thin films of organic static induction transistor equivalent circuit model ^[6].the V_{GS} between Gaga voltage frequency is 10Hz, \pm 0.5V amplitude rectangular wave AC signal to detect the dynamic characteristics of triode. The current source Iq is static current voltage of V_{DS} plus -3V. The micro current detection circuit access equivalent circuit measurement of I_{DS}, the simulation results are shown in Fig.3.







The actual test results of the experiment is shown in Fig.4 ,and comparison of Fig.4 and Fig.3 can be seen the results of simulation and the actual test results are basically the same. The correctness of the model is validated, but it also fully proves the feasibility and practicality of the amplifier to detect thin organic static induction transistor.

Forming the model of the structure can be seen, because the organic material has higher resistivity, the signal current is very small, and because the comb grid used in experiments, increasing the film area, the capacitance increases^[7]. The above factors make the capacitor charge and discharge time lengthen, dynamic characteristics and transistor is worse. In order to improve the dynamic characteristics of the transistor, it can reduce the device electrode area to reduce the interelectrode capacitance, or the carrier mobility, low resistivity material.

Conclusion

This paper aimed at the measurement of dynamic characteristics of organic thin film transistor, designing a detection circuit. By constructing the equivalent circuit of organic static induction transistor, we had a good performance analog device. And the simulation model and the detection circuit, to verify the feasibility of small signal detection circuit design. According to the simulation results, analyzing the reason of triode poor dynamic characteristics is the interelectrode capacitance too large and small signal current. This is the future of dynamic characteristics of organic thin film transistors improved, providing a theoretical basis for.

Reference

- Mittal. P., Kumar. Brijesh and Negi. Y.S.: Communication Systems and Network Technologies (2011),p.436
- [2] Zhang. Ming, Llaser.Nicolas and Mathias. H.:ISCAS(2008) ,p.2094
- [3] Picos.R., Garcia.E. and Roca.M.: 2012 8th International Conference(2012).p.1
- [4] Linrun Feng, Xiaoli Xu and Xiaojun Guo: Electron Devices(2012), p.3382
- [5] Bonea.A., Hassinen.T.and Ofrim.B.A.: Semiconductor Conference(CAS), Vol.2(2012), p.399
- [6] Castro-Carranza.A., Cheralathan.M.and Iniguez.B.: Electron Devices (CDE)(2013), p.49
- [7] Zaki.T., Scheinert.S. and Horselmann.I.: Electron Devices, Vol.61(2014), p.98

A Bandgap Reference with Temperature Coefficient of 13.2 ppm/°C

Mingyuan Ren^{1, a}, Enming Zhao^{2,b}

¹School of software, Harbin University of Science and Technology, Harbin, 150000, China

²Harbin Engineering University, Harbin, 150000, China ^army2000@qq.com, ^bzhaoenming@hrbeu.edu.cn

Keywords: Bandgap reference, PTAT, CMOS

Abstract. This paper presents a design and analysis method of a bandgap reference circuit. The Bandgap design is realized through the 0.18um CMOS process. Simulation results show that the bandgap circuit outputs 1.239V in the typical operation condition. The variance rate of output voltage is $0.016 \text{mV/}^{\circ}\text{C}$ with the operating temperature varying from -60°C to 160°C. And it is 3.27mV/V with the power supply changes from 1.8V to 3.3V.

Introduction

Voltage references are used in many types of analogcircuits for signal processing, such as A-D converters, smart sensors, D-A converters, etc.[1~2]. A bandgap reference with high PSRR and low temperature coefficient is desired for high performance analog-digital systems. The bandgap with an Opamp (operational amplifier) has good performance; however, it depends on the OpAmp characteristics, and, in the specific, on the PSRR of the OpAmp. For example, a good PSRR can easily be achieved by increasing the loop gain, at low frequencies, while these circuits present strong limitations at higher frequencies because of drastically decreasing of the loop gain[3]. In these cases, techniques to improve PSRR of OpAmp should be adopted. On the contrary, Brokaw bandgap exhibits good behavior over a wide range of frequencies (up to 1 GHz), and the PSRR of a single Brokaw bandgap is about 40dB, which can be improved at higher frequency by adding a compensation capacitor. The temperature stability of the bandgap reference has been continuously improved via new circuit and technology innovations such as curvature compensation. To obtain a good PSRR as well as better temperature stability, we propose a Bandgap circuit made up of two Brokaw Cells, without OpAmp. The PSRR at low frequency is improved by adding a Brokaw bandgap as compensation. Both a high PSRR at a wide range of frequency and a low temperature coefficient are achieved without complex high-order curvature-compensated.

Proposed circuit

Fig.1 shows the proposed bandgap reference, which is composed of an operational amplifier, resistors, and diodes. In CMOS technology, the diode is formed by collector. Neglecting base current, the emitter-base voltage of a forward active operation diode can be expressed as

$$V_T = \frac{kT}{q} \tag{1}$$

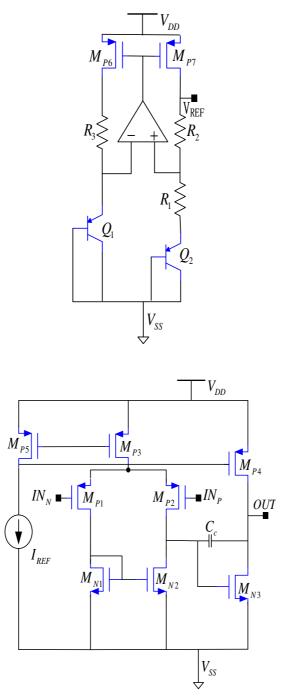
where k is Boltzmann's constant and q is electronic charge. The input voltage for the op-amp is forced to be the same. Let the size of Q_1 N times the size of Q_2 , the emitter-base voltage difference between Q_1 and Q_2 is

$$\Delta V_{BE} = V_{BE2} - V_{BE1} = \frac{kT}{q} \ln N \tag{2}$$

The current through R_1 equals the current through R_2 , and is formed to be PTAT, and an output voltage is obtained as

$$V_{REF} = V_{BE1} + \frac{kT}{q} \ln N \frac{R_1}{R_2}$$
(3)

The two-stage opamp utilized in this design is shown in Fig. 2, which consists of a PMOS differential pair operating in weak inversion and a common source stage with a diode-connected PMOS transistor load which inherently arises from the fact that the output is fed back via M_{P1} and M_{P2} in order to generate the current of the first and second stages. Therefore, a high power supply rejection (PSRR) is achieved at the cost of a low second-stage gain, which can be set by device and current scaling. The following analysis with respect to the loop dynamics and stability is conducted for the general case where a 2-stage opamp is used. The BGR circuit consists of two loops; one with



negative feedback (through M_{P2}) and one with positive feedback (through M_{P1}). This may lead to instability especially if the positive feedback dominates over the negative feedback.

Fig.1 The proposed bandgap reference circuit

Fig.2 Opamp circuit with compensation network

Simulation Results

Fig. 3 shows the temperature dependent with different supply voltages of 1.8 V, 2.5 V, and 3.3 V. As shown in Figure 3 the output voltage varies between 1.2371 V and 1.2418 V over a temperature range from -60 to 160 °C.

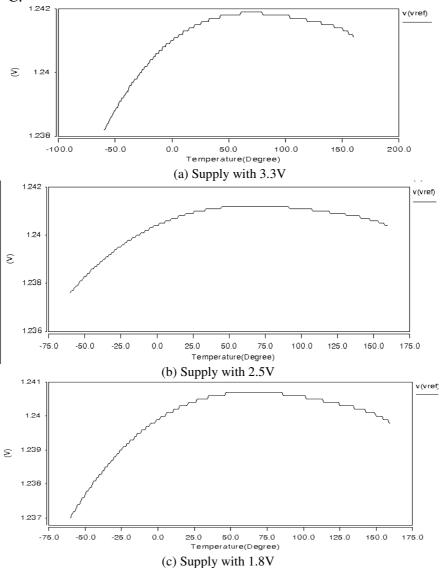


Fig.3 Simulated temperature dependence of output reference voltage

When V_{DD} is 3.3V, the ratio of temperature drift of the bandgap is about 13.19648ppm/°C with the operating temperature varying from -60°C to 160°C.

$$T_{c} = \frac{1.2418 - 1.2382}{0.5 \times (1.2418 + 1.2382) \times (60 + 160)} \times 10^{6} = 13.19648 \binom{ppm/}{^{\circ}C}$$
(4)

When V_{DD} is 2.5V, the ratio of temperature drift of the bandgap is about 12.88361ppm/°C with the operating temperature varying from -60°C to 160°C.

$$T_{c} = \frac{1.2411 - 1.2376}{0.5 \times (1.2411 + 1.2376) \times (60 + 160)} \times 10^{6} = 12.88361 \binom{ppm}{^{\circ}C} \tag{5}$$

When V_{DD} is 1.8V, the ratio of temperature drift of the bandgap is about 13.20713ppm/°C with the operating temperature varying from -60°C to 160°C.

$$T_{c} = \frac{1.2407 - 1.2371}{0.5 \times (1.2407 + 1.2371) \times (60 + 160)} \times 10^{6} = 13.20713 \binom{ppm}{^{\circ}C}$$
(6)

Fig. 3 is the output voltage drift with the supply voltage change. From the result we know when supply voltage change form $1.8V \sim 3.3V$, the reference voltage change only 1.1mV, the drift rate is about 3.27mV/V.

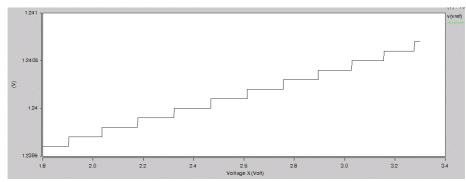


Fig.3 Simulated supply voltage dependence of output reference voltage

Summary

A complete analysis of a CMOS bandgap reference voltage was presented. A complete stability analysis, including a 2-stage opamp, was conducted and an area efficient compensation method was demonstrated. Several important tradeoffs between area, loop-gain, stability and offset sensitivity were discussed and a high-performance design in a 0.18µm CMOS process was presented. Simulation results show that the bandgap circuit outputs 1.239V in the typical operation condition. The variance rate of output voltage is 0.016mV/°C and the ratio of temperature drift of the bandgap is about 13.2ppm/°C with the operating temperature varying from -60°C to 160°C. And it is 3.27mV/V with the power supply changes from 1.8V to 3.3V. The design has a wide working voltage range, stability, good performance which can used in AD converter

Acknowledgment

This work is supported by Natural Science Foundation of Heilongjiang Province under Grant No. F201205, the National Natural Science Foundation of China (NSFC, 61377085).

References

- [1] A. Brokaw: IEEE J. of Solid-State Circuits Vol.SC-9 (1974), p.388.
- [2] M. Gunawan, G. Meijer, and J. Fonderie: IEEE J. of Solid-State Circuits Vol.28 (1993), p. 667.
- [3] G. Giustolisi, and G. Palumbo: Circuits and Systems I: Fundamental Theory and Applications, IEEE Transactions on, Vol.50 (2003), p.185.

CMOS Low Power Ring VCO Design

Mingxin Song^{1,a}, Shanshan Wang^{1,b}, Guodong Sun^{1,c}

¹Department of Electronic Science and Technology, College of Applied Science, Key Laboratory of Engineering Dielectrics and Its Application, Ministry of Education Harbin University of Science and Technology, Heilongjiang Harbin 150080, China

^asongmingxin@126.com, ^b83849800@qq.com, ^c519473312@qq.com

Keywords: ring voltage controlled oscillator, phase-locked loop, phase noise

Abstract. A design project of voltage controlled oscillator which is the central component of the low voltage phase locked loop (PLL) is proposed in this paper. The VCO adopted the folding differential voltage controlled oscillator.Simulation results in Cadence Hspice indicate that the VCO proposed behaves in good linearity, simple structure, small phase noise.The frequency range from 125 to 787 MHz, the power consumption of this oscillator is only 6mW at central frequency is 480MHz with 3V power supply.

Introduction

Recently, as the widely use of phase-locked loop in the field of medical, aviation, communications and electronics, voltage-controlled oscillator as a core part of phase-locked loop has been paid welled attention. Low power consumption and low noise have been committed to the direction of the IC. The voltage-controlled oscillator provided in this paper refers to the integrated voltage-controlled oscillator.

LC oscillator and ring vco are two main structures of modern voltage-controlled oscillator. But in an integrated circuit LC oscillator is difficult to be made ,as it has low Q value, large chip area and difficult to tune. nd the ring vco has the advantage of simple structure , easy to integrate, small chip area and good linearity. It has been widely applied in practice. The standard CMOS process folding differential structureVCO was used in this article. The oscillator is adjusted by adjusting the current flowing through the control tube. The circuit has the very good linearity, wide linear range and high working frequency under low voltage_{\circ}

Definition and Performance Parameters of the VCO

The working state and element parameters of the oscillation circuit is controlled by the input voltage, that is to say, the input control voltage adjusts the output frequency. In different application environments, the performance requirements of the VCO will be different. Various performance of analog circuits will limit each other, so it is necessary for them to compromise. It will achieve some ideal parameters at the expense of some performance conditions.

Usually we will consider the following performance indicators:

The center frequency, the center value of the adjustment range, which is determined by the usage environment of the VCO.

Linearity adjustment: ideal VCO output frequency is a linear function of the input control voltage, relationship as follows:

$$V_{out} = V_o + K_{vco} \cdot V_{ctrl} \tag{1}$$

However, in practice the VCO regulation characteristics will exhibit nonlinear, that is to say, K_{vco} is not constant, it will affect the stability of PLL. So we would hope K_{vco} remains unchanged in the adjustment range. Output amplitude: output waveform is not sensitive when the output oscillation is larger. However, if the output amplitude changes in the entire adjustment range, the circuit will be severely affected.

Circuit Design

Work principle of ring oscillator

As long as Barkhausen criteria and the conditions of stable oscillation are meeted, the ring oscillator can work properly.Figure (1) is a ring oscillator circuit which composed of N gain stage,Each gain stage corresponds to a inverter in the signal circuit principle, We call it a delay unit.

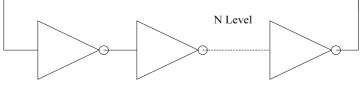


Fig. 1 A ring oscillator

 $-A_0/(1+s/w_0)$ represents the transfer function of each delay stage, loop gain of N-stage ring oscillator inverted is:

$$H(s) = (-1)^{N} A_{0}^{N} / (1 + \frac{s}{w_{0}})^{N}$$
(2)

Wherein w_0 is a 3dB bandwidth of each stage of the circuit, A_0 is the DC gain. When N is an even number, it occurs a "deadlock"; N is an odd number, only when the frequency-dependent phase shift is equal to 180du ,the circuit can oscillate, that each stage should provide a phase shift of $180^o/N$.Let $s = jw_{asc}$, above equation becomes:

$$H(s) = (-1)^{N} A_{0}^{N} (-1)^{N} A_{0}^{N} / (1 + \frac{j w_{osc}}{w_{0}})^{N}$$
(3)

 w_{osc} is called the oscillation frequency, the size can be obtained from the formula:

$$\arctan\frac{w_{osc}}{w_o} = \frac{\pi}{N} \tag{4}$$

Therefore trigonometric relationship is:

$$w_{osc} = w_o \tan \frac{\pi}{N} \tag{5}$$

If the loop gain at the same time satisfy the following formula, a ring oscillator can generate and maintain a stable oscillation.

$$\frac{A_0^N}{\left[\sqrt{1 + \left(\frac{W_{osc}}{W_0}\right)}\right]^N} > 1$$
(6)

A differential delay unit

Figure (2) is the delay unit of traditional differential structure oscillator. The delay is changed by changing the difference of tail current, thereby changing the frequency of oscillation. Generally, tail current has a variety of forms, but considering the simple structure, ease of integration, usually with mirror voltage controlled current source or a single MOS tube as a current source. As shown in figure (2), Vc controls the tail current to provide difference of current, but when Vc gradually increased, the oscillation frequency is gradually increased. Because the frequency is largely sensitive to the change of voltage, in practice the voltage can not be precisely controlled, the linearity is not high, and it has larger voltage swing across the voltage control range, we do not want to see.

Fig. 2 A differential delay unit

Fig. 3 Folding Differential VCO Structure

Folding Differential VCO Structure

Figure (3) is a standard CMOS process folding difference structure VCO. The characteristics of this circuit are simple structure, high voltage controlled linear degree and the small phase noise. The delay unit consists of a pair of difference tubes (M6 and M7), a pair of positive feedback tubes (M3 and M4), a pair of diode connected load tubes (M2 and M5), and a current sink (M1). The function of the tubes M3 and M4 are to maintain the oscillation of oscillator when Vc is too low to open the M1. Tubes M2 and M5 are connected by diode, and they are always in a saturated state, so they may be regarded as active load. Vc controls tube M1 grid electrode voltage, and adjust current of current sink. By changing the current through the tube M1 (that is the sum of the current through tubes M2 and M5) to change the transconductance between M2 and M5, so as to realize the delay unit time adjustment, and control the oscillation frequency.

In order to eliminate the limit of current in output node and make the magnitude of the oscillator output voltage gets maximum, so the source electrode of the tubes M3 and M4 do not directly connected with the source electrode of other transistors, but directly connected to the power supply, so it can increase the current through the tubes M3 and M4, thereby increasing the current in output node and maximizing the swing of output voltage. Increase the swing amplitude not only can improve the driving ability of the circuit, but also can achieve periodic shut off of tubes M1, M2, M3, M4 and M5, so as to reduce the influence of noise. By changing the current through the tubes M1 and M2, the change of the transconductance between M5 and M2 can range from zero to close to the value of transconductance between M3 and M4, therefore, the frequency tuning range of this structure is about 50%.

Simulation results and analysis

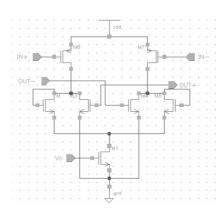
The operating frequency of the VCO (Voltage Controlled Oscillator) is:

$$f_{osc} = \frac{1}{2\pi} \sqrt{\frac{g_1^2 - (g_3 - g_2)^2}{c_L^2}}$$
(7)

Where g_1 is the input differential transconductance between M_6 and M_7 , g_2 is the transconductance between M_3 and M_4 , g_3 is the transconductance between M_2 and M_5 , c_L is the equivalent capacitance equivalent from the output node. As can be seen from the above equation, we can control the output frequency of the VCO by changing g_3 , (the transconductance between M_2 and M_5) When g_2 and g_3 are equal, the oscillation frequency of VCO achieve maximum:

$$f_{\max} \approx \frac{g_1}{2\pi c_I} \tag{8}$$

When NMOS tube M_2 and M_5 connected by diode is off, I.e., g_3 =0,the oscillation frequency of VCO achieve minimum:



$$f_{\min} = \frac{1}{2\pi} \sqrt{\frac{g_1^2 - g_2^2}{c_L^2}}$$
(9)

Next we conduct the circuit simulation. Figure (3) is the output waveform when the input voltage is 1.5V. Figure(4) is VOC frequency - voltage variation relations.

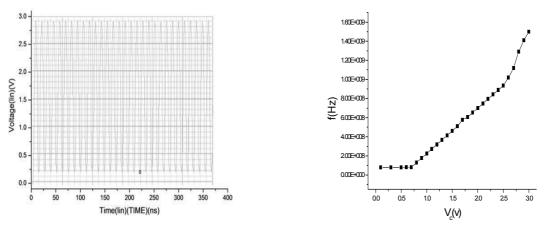




Fig. 5 The voltage controlled characteristic of VCO

It can be seen from Figure (4) and Figure (5) the VOC output waveform is approximately square wave with 50% duty cycle. When the input voltage is 1.5V, the center frequency is 480MHz. And compared with the previous two VCOs, when control voltage is from 0.8v to 2.2v, the output frequency varies from 125MHz to 787MHz and has better linearity. The gain of VCO is:

$$K_{vco} = \frac{f_{\text{max}} - f_{\text{min}}}{v_2 - v_1} = \frac{787 - 125(MHz)}{2.2 - 0.8(V)} = 472.8MHz/V.$$
(10)

Conclusion

This article designed a low-power voltage-controlled oscillator Cadence Hspice.Compared with traditional delay unit, we made some improvements.By using a folding differential structure maked power lower, and improved linearity of the circuit.Under 1.5 voltage, voltage controlled oscillator output frequency range is from 125MHz to 787MHz, frequency gain is 472.8MHz/V. It got a better frequency gain in a wide frequency range.

References

- [1] Behzad Razavi, :Solid-State Circuit. Vol. 31(1996), p.331
- [2] Lin T H,Lai Y J,:Solid-State Circuit. Vol. 2(2007), p.340
- [3] Lin Yijing, Sheng Shimin,: Acta Scientiarum Naturalium Universitatis Pekinensis.Vol. 38(2002), p.467
- [4] Demir A,: Circuits and systems 1: Fundamental Theroy and Applications. Vol. 49(2002), p.1782
- [5] One Jiarong,: Journal of Computer and Information Science. Vol. 14(1986), p.421
- [6] K M B,:IEEE custom integrated circuits conference. Vol. 35(2005), p.31

The Dual Sine Signal Generator Design Based on the Principle of Difference Frequency Filtering

Chaozhu Zhang, Yue Zhu^a and Jinan Han

College of information and communication engineering, Harbin Engineering University

^azhuyue@hrbeu.edu.cn

Keywords: signal generator;MSP430 microcontroller;CPLD;low pass filter

Abstract. The paper attempts to realize the processing scheme of low cost dual sine wave generator. It used single-chip microcomputer and CPLD(Complex Programable Logic Device) as the control core. It maked use of CPLD and discrete component simulations to implement DDS principle. It utilized the filter circuit, integrated op-amp circuit and multiplier circuit instead of DAC chip. The range of frequency, amplitude and phase difference are 1Hz~1000Hz, 1V~3V and 0°~359°, respectively. The results show that a 2-channel sine signal generator can be designed with adjustable frequency, amplitude and phase difference.

Introduction

As a kind of widely used signal source, sine signal source plays a very important role in the laboratory and in the design of electronic engineering[1]. Currently, there are lots of people have designed and implemented a sinusoidal signal generator through making use of frequency synthesis technology[2,3,4,5,6]. In this paper, it uses the "MSP430 MCU + CPLD + analog discrete component" instead of a DDS chip to design a low-cost dual sine signal generator, which could be used as a analog signal source in the laboratory or a signal source in the teaching demonstration. The system provides a higher level of integration and simple operation, which makes it possible to be overhauled fast and accurately[7,8].

The Theoretical Principles of System Design

DDS Principle. The working principle of DDS is shown in Fig. 1.

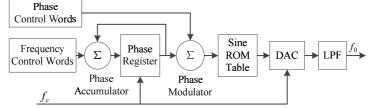


Fig. 1 The working principle of DDS

In Fig. 1, DDS consists of a phase accumulator, a phase modulator, a sine ROM lookup table, a digital to analog converter (DAC) and a low pass filter (LPF). At every clock, N-bit phase accumulator is accumulated with the feedback value. The result of the high L-bit is the address of the sine ROM table, and from the sine ROM table it reads the amplitude value to the DAC, and finally by a low-pass filter to convert a continuous sine signal output[9].

Adjusting Amplitude Accuracy Principle. The PWM signal is the periodic square wave signal with adjustable duty ratio. The trigonometric form of its Fourier series is shown in Eq. 1,.

$$f(t) = \frac{E\tau}{T_1} + \frac{2E\tau}{T_1} \sum_{n=1}^{\infty} Sa(\frac{n\pi\tau}{T_1}) \cos(n\omega_1 t).$$
(1)

Where f(t) denotes the PWM signal; *E* expresses the rectangular wave amplitude; τ shows the pulse width; T_1 is denoted as the period of the signal f(t); Sa(x) is expressed as sampling function.

From (1), it could obtain a DC voltage when making the PWM signal through a low pass filter. So the size of the DC component can be fully adjusted by the duty ratio of the PWM signal.

Difference Frequency Filtering Principle. After a sine signal multiplies a square wave signal, the result is given in Eq. 2.

$$f(t) = -\frac{AE}{\pi} \{ \cos[2\pi(f_2 + f_1)t + \varphi] - \cos[2\pi(f_2 - f_1)t + \varphi] - \frac{1}{3} \cos[2\pi(3f_2 + f_1)t + \varphi] + \frac{1}{3} \cos[2\pi(3f_2 - f_1)t + \varphi] + \dots \}$$
(2)

Where A denotes the amplitude of the sine signal and E expresses the amplitude of the square signal. It can be designed to filter the components with $f_2+f_1,3f_2+f_1,3f_2-f_1$...frequendies out and restain the component with f_2 - f_1 frequency. With this method it could get the signal with frequency f_2 - f_1 , phase φ , and amplitude AE/π .

The Overall System Design Solutions

The overall system design includes the minimum single-chip system unit, CPLD control logic unit, analog circuit unit and waveform output section. Wherein, in DDS principle, the DAC part is entirely replaced by amplification circuit and filter which is make up of simulation of discrete component unit. The overall system design is shown in Fig. 2.

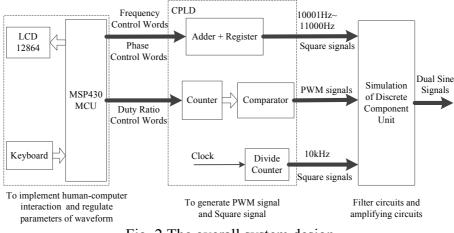


Fig. 2 The overall system design

Hardware Design and Implementation

Multiplier Circuits. In analog circuits, the core component is 74HCT4053, which is a triple 2-channel analog multiplexer / demultiplexer. The multiplier circuit connection design is shown in Fig. 3.

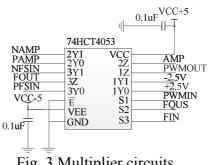


Fig. 3 Multiplier circuits

Standard Voltage Circuits. In order to generate a stable ± 2.5 V DC voltage, a DC voltage is applied to the ends of 5V circuit through the voltage-regulator diode and the phase inverter. The design is presented in Fig. 4.

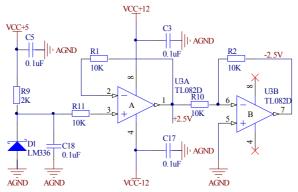
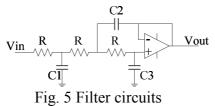


Fig. 4 Standard voltage circuit

Filter Circuits.In analog circuits. As the frequency characteristics of the system have no special requirements, it considers to use a third-order Butterworth I type low-pass filter[10]. The design is presented in Fig. 5.



Software Design and Implementation

MSP430 Microcontroller Programming. In this design, it changes the size of the frequency, amplitude and phase through the keyboard input. MSP430 MCU makes use of LCD12864 to display values for each set, which achieves human-computer interaction, making the operation more convenient and faster.

CPLD Programming. In Fig. 2, it inputs control commands from the matrix keyboard (ie, to adjust the value of the amplitude, frequency and phase difference). Then it transfers duty ratio control words, frequency control words and phase control words from MSP430 MCU to CPLD. After analyzing the words, CPLD generated PWM signals with adjustable duty ratio, square signals ranging from 10001Hz to 11000Hz and 10kHz square signals[11].

Index Test

The system outputs A and B, respectively connect to CH1 and CH2 of a digital oscilloscope to test the index of the system. The amplitude, frequency, and phase test results are shown in Fig. 6, Fig. 7 and Fig. 8, respectively.

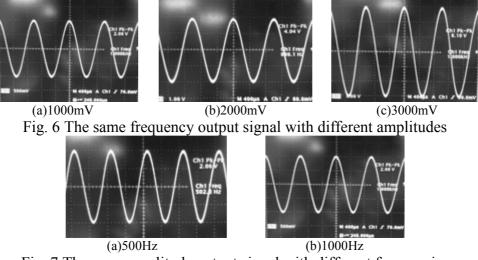


Fig. 7 The same amplitude output signal with different frequencies

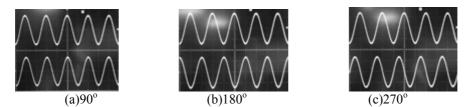


Fig. 8 The same amplitude and frequency output signal with different phase differences

From Fig. 8, when the frequency is constant, the amplitude error is small.From Fig. 9, when the amplitude is constant, the frequency error is small.From Fig. 10, when the amplitude and frequency are constant, the phase error is small.

Conclusions

The system has completed the design and implementation of dual sinusoidal signal generator.

1. It has studied the digital direct frequency synthesis technology in both the theoretical and practical aspects.

It has used CPLD and analog discrete components instead of a DDS chip to achieve DDS principle.
 In particular, it has used analog filters, operational amplifiers and multipliers instead of a DAC chip to complete digital to analog conversion.

Acknowledgements

This paper is funded by the International Exchange Program of Harbin Engineering University for Innovation-oriented Talents Cultivation.

References

- [1] Zhiqi Lin, Huiping Jiang: Signal Generating Circuit Theory and Practical Design(In Chinese). Posts & Telecom Press. (2010), p.273
- [2] Xu Feng, Wei Zhong, Liang Hu, Weicong Lu: Foreign Electronic Measurement Technology. Vol.29-1 (2010), p. 39
- [3] Juan Wang, Xibao Guo: Electronic Technology. 9 (2011), p.51
- [4] Daolin Li, Xupeng Han, Chunfang Xiao: Electronic Design Engineering. Vol.18-12 (2010), p.165
- [5] Qiuju Li: Computer & Telecommunication. 4 (2010), p.57
- [6] Qun Mao, Shixu Wang: Modern Electronics Technique. 9 (2010), p.118
- [7] Yongqing Lu: Sichuan University of Arts and Science Journal. Vol.19-5 (2009), p.37
- [8] Xiaorong Chen: Electronic Instrumentation Customer. 4 (2006), p.53
- [9] Yanfei Liu, Suoli Guo, Xiaorong Wang: The Electronic System Design and Engineering Practice Based on Altera FPGA / CPLD(In Chinese). Posts & Telecom Press. 2009, p.229
- [10] Jianping Wu, Yu Zhou, Guoshuai Chen: Popular Science & Technology. Vol.14-151 (2012), p.8
- [11]Xin Su, Xibin Xu: Principles and Techniques of Software Radio(In Chinese). Posts & Telecom Press. 2010, p.105

Full Scan Structure Application in the Design of 16 Bit MCU

Hongbo Pan^{1,2,a}, Mingxin Song^{1,b}, Xing Jin^{2,c} and Jinghua Yin^{1,d}

¹Dept. Electronics and Science Institute of Applied Science and Technology Harbin University of Science and Technology Harbin, China

²Shanghai institute of microsystem and information technology, Chinese academy of sciences, China

^apphongbo@126.com, ^bsongmingxin@126.com, ^cjinxing@mail.sim.ac.cn, ^dyinjinghua1@126.com

Keywords: testability design; full scan structure; MCU

Abstract. A design project of 16 bit RISC MCU with full scan structure by the tool of SYNOPSYSTM DFT COMPILER. The flip-flops can be linked into the chains; the memory modules in the MCU were tested by the technology of BIST; and the circuits were tested by the test vectors by ATPG. The chip test circuit include 8 chains, and cover rate can reach at 99.20%.

Introduction

With the rapid development of semiconductor technology and design automation tools, the chip complexity rising dramatically, VLSI need to give a wide range of testability features. Accuracy is very important in IC design and manufacturing. In order to adapt to the needs of the development of technology, the design team manage to shorten design period, and make sure the successful tape-out, which depends on the design test in the design^[1].

DFT Design

Definition of DFT

DFT is short for Design for Testability. DFT testing is the way of the detection circuit of the control signal and observation in the circuit signal to test the circuit^[2, 3].

The processes of scanning structure

Full scan technology refers to change flip-flops to scanning flip-flops in the circuit, making all flip-flops link into several flip-flop chains, called scan chain. The test circuit can be divided into the testing circuit of pure combinational logic and the testing circuit of shift flip-flop chain. All the state in circuit based on the DFT test method can be gotten directly from the original input port and output port end under controllability, observability, and predictability, to ensure that a device is testable.

Full scan testability design process is shown in Fig. 1. The circuit signal Scan_En can decide that the circuit is working in the scanning mode or in normal working mode. Scan_En set 1, chosing signal Scan_in, the state of circuit is in scanning input mode. When the clock pulse is arriving, test vector shifting into the scan chain, loading to the combinational circuit, meanwhile, circuit will start in parallel test phase. When enabled signal is set 0, the state of circuit is in normal working mode. When CLK pulse arrives, test response can be into the storage unit. Then, Scan_En set 1, the response data with the clock pulse is shifted to Scan_out port.

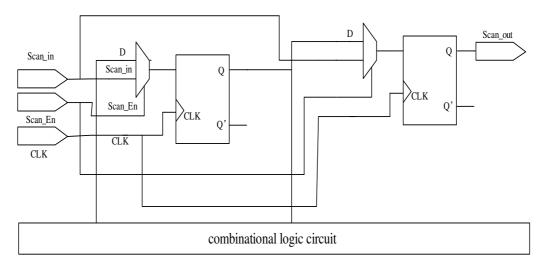


Fig. 1 The processes of scan flip-flop

Simulation Module and Memory Module Processing Method

The project contains ADC module and memory module. The modules will be treated as a black box processed in DFT testing, and the observerable and controllable combination circuit will disappear around modules, which is called shadow logic. Fig. 2 shows to deal with the shadow logic is that increase test package around the memory. The modules boundary should be made BIST, which is the function that detects read and reads BIST data to increase the observation point, and the accuracy of detection circuit^[4].

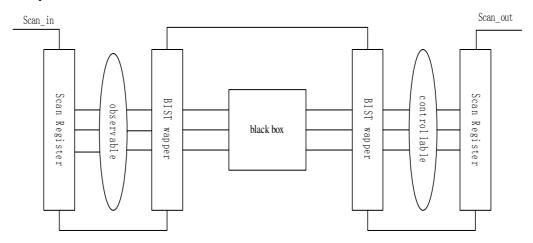


Fig. 2 Processing method for black box

Internal Clock Processing Method

In the 16 bit MCU design, internal core modules are used the clock signal clkcpu, peripheral modules are used the clock signal clkper. The two clock signals are clock frequency demultiplication signal. Because the flip-flops are replaced by the scanning units, and the test data input port and output port speed is different, which increase the difficulty of the test.

Fig. 3 shows the way to solve this problem is to change the circuit structure that the gate controls method. Gate control method is that every clock in own way adds a selector circuit structure to control the signal clock. When circuit is in scanning state, test_se set 1, the scanning unit clock synchronization is realized, and the data of scanning shift and test response can be got in the same time.

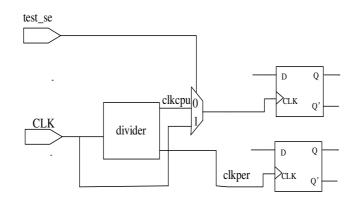


Fig.3 Frequency demultiplication circuit with gate control

Bidirectional port processing

In this design a lot of port is the reuse, including both I/O port as many as 34, that ports input function and output function is controlled by the port controlling register. In the scanning mode, the data of controlling port register is constantly changing, causing bus contention in the way that the port data flow direction is changing. It is difficult too control to increase the difficulty of the sweep test^[5].

According to the DFT COMPILER software using rules, in command prompt dc_shell >, write down the script that set_atuofix_configuration - type bidirectional - method input, it will make bidirectional I/O ports designated to be as a single input port, which can avoid conflict from both the input and output data.

Results and Analysis

According to the above mentioned, units strung into scan chain are composed by most of the combinational logic units and sequential logic units. Fig. 4 shows the circuit report.

Number of chains: 8	
Scan methodology: full_scan	
Scan style: multiplexed_flip_flop	
Clock domain: mix_clocks	
Scan enable: DFT_SS (hookup pin: PAD_DFTSS,	/Y, sense: non_inverted)
Scan chain '1' (port02> port03) contains	5 638 cells:
Scan chain '2' (port04> port05) contains	5 638 cells:
Scan chain '3' (port06> port07) contains	5 638 cells:
Scan chain '4' (port10> port11) contains	
Scan chain '5' (port30> port31) contains	
Scan chain '6' (port32> port33) contains	
Scan chain '7' (port34> port35) contains	5 637 cells:
Scan chain '8' (port36> port37) contains	5 637 cells:

Uncollapsed Stuck Fault Summary fault class	Report code	#faults
Detected	DT	418184
Possibly detected	РТ	162
Undetectable	UD	2076
ATPG untestable	AU	2952
Not detected	ND	334
total faults test coverage		423708 98.20%

a) Scan_chains contain cells

b) Test coverage report

Fig. 4 DFT circuit report

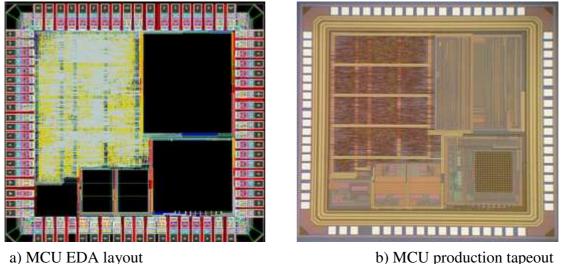
The full scan test circuit is accomplished by the two steps. One is that testing data is from shifting into the sweep test unit. A scan chain is the depth of NSFF + 4, where NSFF is representative of the sum number of the flip-flop with scan chain, and 4 is representative of 4 clock cycles. The testing data is shifted to the observable output signal by the NSFF + 4 steps, which covers most of flip-flops and is able to verify the correctness of the circuit in this step. The other is test vector generated in Automatic Test Pattern Generation (ATPG) processing. The depth of the scan chain can be gotten, according to the formula, expressed as:

$$N_{SFF} + 4 + (N_{SFF} + 1) n_{comb} + N_{SFI}$$

(1)

Where ncomb is representative of the number of the combination test vector, and NSFF is representative of the number of is the flip-flop in scanning flip-flops. To reduce the time of scanning test, the scanning unit is arranged into multiple paratactic scan chain .Setting the number of the scan chain is n, so that each scanning test length is NSFF /n (ncomb + 2) + ncomb + 4 clock.

Due to the number of scanning unit in set of scan chain is average distribution, which reduces the filling of registers from the instrument, makes full use of the test storage and reduces the cost. The production layout of the chip is shown in Fig.5.



b) MCU production tapeout

Fig. 5 The layout of MCU chip

Conclusion

The article puts forward full scan structure design problems and corresponding solution from the specific project In GSMC 0.18 um process library, which has the very strong pertinence. Experimental results show that the circuits set 8 scan chains and scanning unit number is 5104, so that each scanning chain has 638 units on average, the test coverage rate can reach at 99.20%, which will reduce the test cost.

Reference

- [1] Margulis, A. Akselrod, D; Rentschler, E; et al. : Evolution of Graphics Northbridge Test and Debug Architectures Across Four Generations of AMD ASICs[J]. Design & Test. Vol. 30, p. 16-25. (2013)
- [2] Reznicek, F: Mixed-Signal DFT for fully testable ASIC[C]. Design and Diagnostics of Electronic Circuits and Systems, Bratislava. p. 1-4. (2008)
- [3] Pant, P; Amodeo, M; Vora, S; et al. Innovative practices session 10C: Delay test[C]. VLSI Test Symposium, Berkeley, CA, USA, p. 1. (2013)
- [4] Parekhji, R: Innovative practices session 1C: Innovative practices in RF test[C]. VLSI Test Symposium, Santa Cruz, CA, USA. p. 39. (2010)
- [5] Deutsch, S; Keller, B; Chickermane, V; et al. : DfT architecture and ATPG for Interconnect tests of JEDEC Wide-I/O memory-on-logic die stacks[C]. Test Conference, Anaheim, CA, p. 1-10. (2012)

The Design and Verification of VGA Controller

Yu Bin^{1, a}, Yang Guang^{1,b}

¹Harbin University of Science and Technology,Harbin,150040, China. ^a277768267@qq.com,^b3802080@qq.com

Keywords: VGA controller; timing sequence; FPGA.

Abstract: CORDIC Algorithm is widely applicable to the hardware implementation of DSP, and it attaches a great importance in many hardware implementations of DSP for a lot of arithmetic operations are simplified to simple addition operations and shifting operations. The FPGA implement of sine and cosine functions are achieved through CORDIC Algorithm in the paper, and the input and output data of the entire structure complies with IEEE754 standards. The basic theory of CORDIC Algorithm is introduced first in the paper, then the hardware iterative formula and the flow chart get out of basic formulas are given, and the structure of the design is introduced in detail, at last synthesis and simulation results are given.

Introduction

VGA is short for Video Graphic Array. It is a video transmission standard launched by IBM which is characterized by high resolution, fast display speed, rich colors and other advantages. It has been widely applied in monochrome and color image display. By now, the technical indexes of VGA color display system have been adopted and standardized by the industrial community. Before loading their unique drivers, personal computers must support VGA standard first.

In this paper, based on the industrial standard, a VGA controller with a simple framework was designed which not only can well meet people's requirements for the fast processing speed and real-time signal, but also increases the color type displayed to make the images more close to the real situation.

Display Principles

A standard VGA interface has 15 D-subs which must be designed in accordance to the standard. The industrial standard is not listed here because it has been very popular. After hardware has reached the standard, priority should be given to the design of VGA sequential control signal. The display of VGA scan depends on two pulse signals: horizontal sync pulse and vertical sync pulse. The combination of these two is called composite sync pulse.

Horizontal timing sequence includes the following sequence parameters:

Thsync: the width of the horizontal sync pulse.

Thgdel: the width between the finish of the horizontal sync pulse and the start of the horizontal door. The images can be shuffled horizontally in the display by modifying the value of this variable. In the video sequence diagram, this variable is often regarded as the back porch.

Thgate: the width of the visual area of a video; in the video sequence diagram, this variable is regarded as the effective time of horizontal sync signal.

Thlen: the width of a complete video row, from the start of a horizontal sync pulse to the start of the next one (time of horizontal flyback included).

The vertical timing sequence has similar signals; the combination of the two can form up the scanning image of the video frame. It is shown as Fig.1.

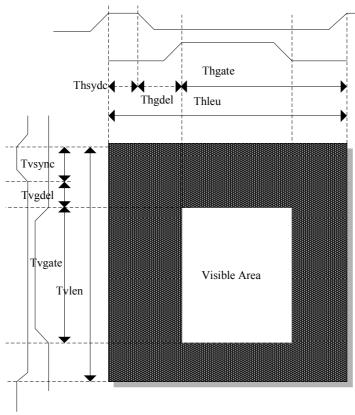


Fig.1 Scanning image

The Division and Design of Module

The peripheral circuit controlled by VGA was designed according to the basic principles of VGA display and FPGA was adopted as the main logic device of hardware implementation. FPGA includes two modules: VGA controller and SRAM controller. Data in SRAM read through SRAM controller was transmitted to VGA controller which then forwarded it to DA chip for processing and then the data was transmitted to the screen for display. In this way, the block diagram of the hardware in this design has been determined as Fig.2.

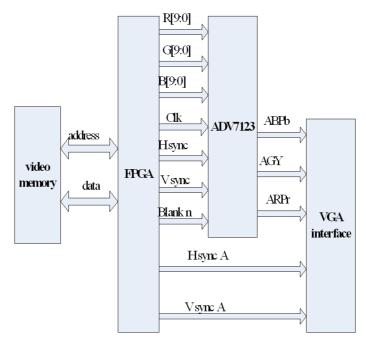


Fig.2 Block diagram of the hardware

In this design, crystal oscillator and phase-locked loop were combined to construct the clock control module of the system. The clock with a frequency of 50M was produced by crystal oscillator, and then the phase-locked loop increased it to 65M by frequency multiplication for the use of VGA controller. The clock module of this design realized frequency multiplication through PLL in FPGA. The module configuration of PLL was realized mainly through the Mega Wizard tools in Quartus. The circuit symbol diagram is shown as Fig.3.

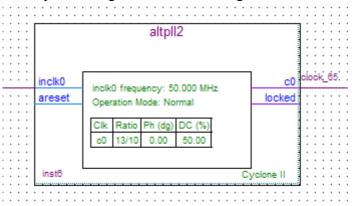
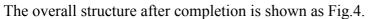


Fig.3 Circuit symbol diagram



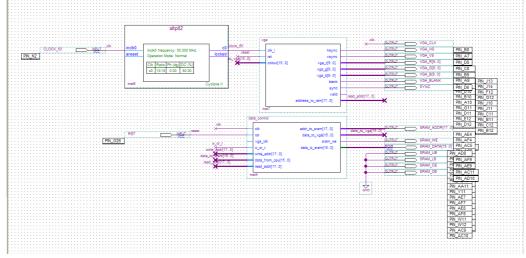
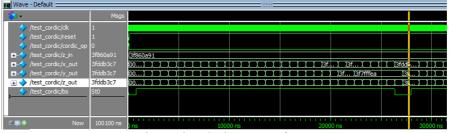
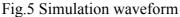


Fig.4 The overall structure

Simulation Results

This design realized simulation with the simulation tools of Quartus. The simulation excitation was input through establishing vector wave file which can output simulation waveforms after being started. The waveform is shown sa Fig.5.





The simulation process can be carried out in the DE-II development board by connecting VGA interface of DE2 development board to VGA display and the final effects can be seen on the screen.

Conclusion

This paper designed the VGA controller, presented the overall structure of the VGA controller, implemented hardware modeling of various modules by using the HDL language and debugged the hardware by using the DE-II development platform. All the research results were proved correct and the expected design effects were achieved.

References

- [1] 1 S. Sarkar, C. G Subash, S. Shinde. VGA controller hardware module design. VGA controller, USA, 2005: 25-28
- [2] 2 R. B. Jones, J. W. OLeary. C. H. Seger et al. The ADV7123 timing chip configuration. ADV7123 Design and Test of Computers, 2001, 18(4): 16-25
- [3] 3 J. M. Ludden, W. Roesner, G. VGA controller design and verication. 2001, 12
 (4): 44-56
- [4] 18 U. Ko, P. T. Balsara, A. K. Nanda. Digital signal processing and circuit simulation. 2002, 30(4): 56-58

Particle Filter Approach for IGBT Remaining Useful Life

Min Li^{1,a}, Jiongjiong Zhu^{1,b} and Bing Long^{1,c}

¹School of Automation, University of Electronic Science and Technology of China ^aliminuestc@163.com, ^bamolinzhu@126.com, ^clongbing@uestc.edu.cn

Key words: Failure Prognosis; IGBT; RUL; Particle Filter

Abstract: With the increasingly widespread application, the requirement for PHM of IGBT is becoming gradually urgent. Based on particle filter theory, a method for remaining useful life(RUL) prediction of IGBT is proposed. Firstly, the deterioration parameters on-state V_{CE} and I_{CE} are extracted by temperature cycling test, then a model is developed based on the degradation trend exhibited by deterioration parameters. In the end, PF approach is applied to the IGBT's RUL prediction with the mentioned model. The results show that the proposed prediction method can achieve high prediction accuracy.

1 Introduction

Insulated gate bipolar transistors (IGBT) have switching characteristics similar to a MOSFET and the high current and voltage capabilities of a BJT, which are commonly used in hybrid cars, motion control systems and high power switch mode power supplies due to their robust short-current capability, large current density, availability and relatively low cast [1]. This is of great importance for safety critical applications where an unpredicted failure may trigger a catastronphic accident or unscheduled maintenance may result in high penalty cost. Hence, Prognostic and Health Management (PHM) has recently been developed that required to monitor the health and predict reliability of these devices to prevent system downtime and costly failures. In this study, we aged the IGBTs by temperature cycling test to acquire on-state V_{CE} and I_{CE} as the deterioration parameters. Then a method based on particle filter theory was proposed to predict the remaining useful life (RUL) of IGBTs under test.

2 IGBT Failure Analysis

The failure modes for the IGBT include short circuits, increased leakage current, or loss of gate control (inability to turn-off). One of the failure causes can be due to high electric field when the device works in the operating conditions that beyond ratings. Overvoltage contains gate-voltage, stray-voltage and surge-voltage. It will lead to failure when IGBT works with high current that exceeds the SOA.

Thermal stress is also the most common failure cause of power modules. Through repetitive thermal stress, the mismatch between the thermal expansion coefficients of the aluminum wire and the silicon chip creates a shear stress on the bonding interface concentrating on the heel and toe of the aluminum wire bond. Therefore, cracks propagete from there to the center of the bonding area, grow along the boundary of fine and coarse grains and lead to the lifting off of aluminum wire. The composition of the solder and the operating temperature conditions strongly affect fatigue in the solder which in turn accelerates the crack propagation of the aluminum wire bonds, so these factors also reduce the lifetime of the device[2].

Drive circuit and RC absorb circuit not fitted the device, the gate-drain parasitic capacitance and parasitic inductance which from emitter, collector and the bus loop would lead to IGBT working in harsh environment to bring about failure.

3 Temperature Cycling Experiment

IGBT would result in failure or fatigue under repeated thermal shocking when it turns on and off repeatedly, whose reliability will affect the normal operation of the device or system. Statistics

show that the 55% reasons for the failure of the electronic device approximately is due to overheating and heat-related problems.

In this experiment, IGBT devices (600V/6A) packaged in a TO-220A package along with a soft recovery diode from International Rectifier were evaluated. For the aging of IGBTs, the gate signal was chosen to be a Pulse Width Modulated (PWM) signal with amplitude of 15V, a frequency of 1 or 5 KHz. During the experiment, the IGBT under test were switched on and off repeatedly until the case-temperature reached the max value T_{max} which was set before. When T_{max} was attained, the device was powered off until the temperature drop to T_{min} . Then the device was cycled between the temperatures T_{max} and T_{min} while the average was set to 175 °C with an optional swing. The experiment condition setting was shown in Table 1.

Number	frequency(Hz)	swing $\Delta T(^{\circ}C)$
F1	5k	100
F2	5k	50
F3	5k	50
F4	1k	50
F5	1k	50
F6	1k	100

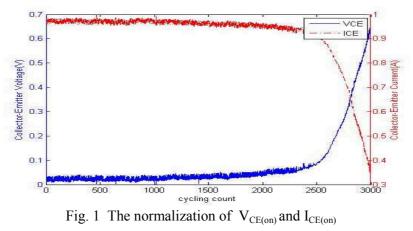
 Table 1 Frequency and temperature swing of cycle test

The Collector Emitter ON voltage, Collector Emitter ON current and case temperature were insitu measured and preserved by data acquisition system until failure of the IGBT under test, which was observed as a large increase in Collector Emitter ON current caused by latch-up [3].

4 Prognosis

4.1 data preprocessing

In order to facilitate a more accurate prediction of RUL of IGBT, we need to compress and convert the raw data extracted to get the best features in a low-dimensional space. Firstly, we used 3σ criterion to exclude the bad points. Secondly, we obtained the average of collection data each cycle, which was seen as characteristic of cycle. Then make normalization to bring the entire probability distributions of the average into alignment. The normalization result was shown in Fig 1.



4.2 particle filter

Particle filter methods are a set of on-line posterior density estimation algorithms that estimate the posterior density of the state-space by directly implementing the Bayesian recursion equations. The particles are generated and recursively updated from a non-linear process model that describes the evolution in time of the system under analysis, a measurement model, and a set of available measurements and priori estimate of the state probability density function [4].

4.3 parameter degradation model

In the previous section, IGBT degradation performance can be reflected by the Collector Emitter ON voltage. In order to predict the remaining life of the IGBT, a model for the trend by Collector Emitter ON voltage needs to developed, which is significantly consist of robustness.

To find such a model, we used the curve fitting tool in Matlab toolbox to fit the trend exhibited by Collector Emitter ON voltage for experiment F4 and F5. And it was found that the following model can meet the needs of fitting the trend.

 $Q = a \cdot e^{b \cdot k} + c \cdot e^{d \cdot k}$

Here, a, b, c and d were the model parameters, and k is the time index. The fitting result was shown in Fig. 2. The goodness-of-fit statistics was given in Table 2. The R^2 and Adjusted R^2 were near to 1 while the root mean squared err (RMSE) was close to 1. The statistical parameters indicated that the proposed model can characterize the trend exhibited by Collector Emitter ON voltage.

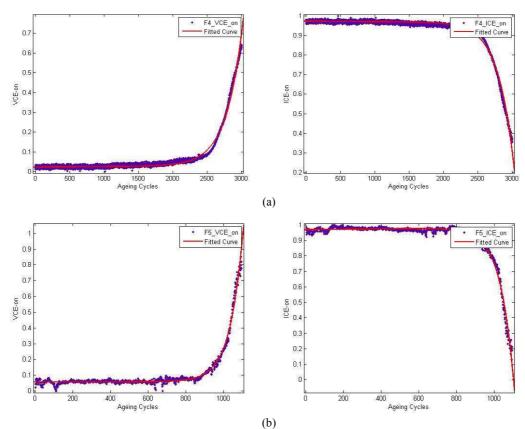


Fig. 2 Matlab curve fitting result

Table 2 Goodness-of-fit statistics

$V_{\text{CE(on)}}$	R ²	Adjusted R ²	RMSE
F4	0.9906	0.9906	0.01202
F 5	0.985	0.985	0.0176
I _{CE(on)}	R ²	Adjusted R ²	RMSE
F4	0.9912	0.9912	0.0114
F 5	0.9847	0.9847	0.01885

4.4 experiment result

According to prognostic procedure, Fig. 3 shows the prediction results for the Experiment F4 at cycle index 2400 and 2700 respectively. It can be seen that the accuracy of the model in predicting RUP improves as more data become available.

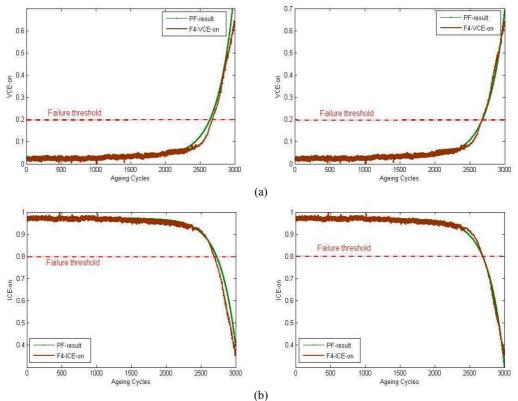


Fig. 3 (a)The prediction result at cycle 2400. (b)The prediction result at cycle 2700.

5 Conclusion

In this paper, IGBT failure causes and mechanism were analyzed. Aging IGBTs by temperature cycling test could obtain on-state voltage and current as deterioration parameters. Then we established a corresponding exponential model for fitting the parameters. Based on this model, PF was used to predict the RUL of IGBTs. The experiment results show that it is particularly useful for achieving IGBT condition-based maintenance with a high prediction accuracy of RUL.

References

- H Lu, C Bailey, C Yin. Design for reliability of power electronics modules. Microelectronics Reliability, vol. 49 (2009), pp. 1250-1255.
- [2] G Sonnenfeld, K Goebel, JR.Celaya. An Agile Accelerated Aging, Characterization and Scenario Simulation System for Gate Controlled Power Transistors. IEEE Autotestcon, 2008, 8-11.
- [3] J.Dai, D. Das, M. Pecht. Prognostics Based Risk Mitigation for Telecom Equipment under Free Air Cooling Conditions. Applied Energy, vol. 99(2012), pp. 423-429.
- [4] Gordon NJ, Salmond DJ, Smith AFM (1993) Novel approach to nonlinear/non-Gaussian Bayesian state estimation, IEE Proceedings F. Radar and Signal Processing 140(2), pp. 107-113

Design of a High performance CMOS Bandgap voltage Reference

Yang Guang^{1, a}, Yu Bin^{1,b} and Huang Hai^{1,c} ¹Harbin University of Science and Technology,Harbin,150040, China. ^A3802080@qq.com, ^b277768267@qq.com, ^chusthh@yahoo.com.cn

Keywords: Bandgap reference; Amplifier; Temperature coefficient; PSRR

Abstract. Bandgap voltage reference, to provide a temperature and power supply insensitive output voltage, is a very important module in the analog integrated circuits and mixed-signal integrated circuits. In this paper, a high performance CMOS bandgap with low-power consumption has been designed. It can get the PTAT (Proportional to absolute temperature) current, and then get the reference voltage. Based on 0.35µm CMOS process, using HSPICE 2008 software for circuit simulation, the results showed that , when the temperature changes from -40 to 80 °C, the proposed circuit's reference voltage achieve to 1.2V, temperature coefficient is 3.09ppm/°C. Adopt a series of measures, like ESD protection circuit, in layout design. The ultimately design through the DRC and LVS verification, and the final layout size is 700µm * 560µm.

Introduction

In recent years, with the decrease of the threshold voltage by the progress in the CMOS fabrication technology, low voltage and low power analog circuit design method are become more and more important. Although digital technology has become the development trend of modern electronic products. The original signals generated by most electronic devices, such as electromagnetic records and microphone, are analog [1]. The analog signals must be processed before digital processing. Meanwhile, after digital processing, the signal must be converted to analog to be accepted by the real world. Analog circuits, like amplifiers, filters, A/D converter, become the key factors of performance of modern integrated circuits.

The research on low-voltage analog circuit design using CMOS technology becomes more and more important. As a way of generating high precision voltage reference, bandgap voltage reference is a common module in the analog integrated circuits. How to design a suitable low-voltage bandgap circuit to meet the low-power requirements is a new task for designers to perform. In this paper, a bandgap voltage reference circuit has been implemented. First, we designed an op-amp, The circuit design is realized in 0.35 μ m CMOS technology and use HSPICE 2008 as the simulation tools. The simulation results show that the low frequency gain of the op-amp is 69.8dB, the phase margin is 64° and the PSRR (power supply rejection ratio) is 87dB. Second, based on the op-amp we designed bandgap reference circuit. Simulation results show that from -40°C to 80°C, the temperature coefficient of the proposed circuit is 3.09ppm/°C. Finally, the overall structure of the circuit layout has been optimized.

Circuit design

The basic principle of the bandgap reference circuit is to make temperature compensation for the voltage which is independent of the power supply voltage. The temperature compensation, in accordance with the compensation principle, can be divided into first-order temperature compensation and high-order (usually second) temperature compensation [3].

A typical CMOS bandgap circuit is designed based upon the PTAT unit. Using op-amp in the design can make the current of PTAT more accurate. The principle of designing a bandgap reference either in CMOS technology or in BICMOS technology is the same.As shown in Fig.1[4], where:

$$V_{REF} = V_{EB2} + \frac{R_2 V_T \ln N}{R_3}$$
(1)

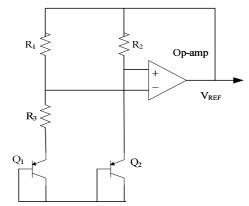


Fig.1. A typical CMOS bandgap reference circuit

The operational amplifier is the core unit of the bandgap reference circuit. The precision and stability of the op-amp determines the performances of the whole system[2,3]. Precision is one of the most important indicators of a bandgap reference circuit. It is mainly affected by the noise and the circuit mismatch. In order to improve the precision of bandgap voltage, two measures are usually taken: One approach is to optimize the structure of the traditional first-order temperature compensation bandgap voltage reference circuit to minimize the offset error of mismatch [6]. Another method is to make a high-order (usually second-order) temperature compensate on the bandgap voltage reference circuit using BiCMOS technology[5]. In this paper, the overall circuit of the bandgap circuit were shown in Fig.2. According to this circuit, where:

$$V_{REF} = V_{EB3} + \frac{R_2 V_T \ln N}{R_1}$$
(2)

Positive and negative temperature coefficient obtained by two transistors which were working at different current density, and the PTAT current generated by an operational amplifier. The resistor R2 and transistor Q3 composition is the load of the circuit, once the current flow through the load, a reference voltage will be generated. The area ratio of the transistor Q1, Q2 and Q3 are 1:8:8.

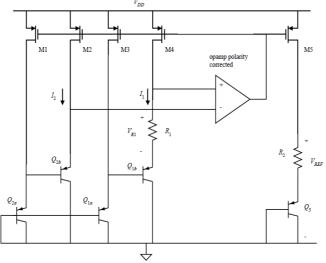


Fig.2. The overall structure of the bandgap reference circuit

Simulation results and analysis

The overall circuit simulation use 0.35um CMOS process model and Hspice2008 as simulation tools. Amplitude-frequency and phase-frequency characteristic of the proposed circuit has been shown in Figure 3. The circuit's open loop gain is 69.8dB, the phase margin is 64.5 degrees.

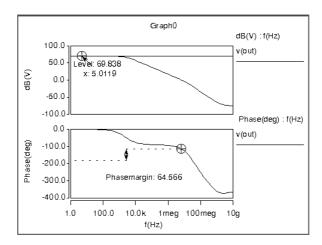


Fig.3. Open-loop frequency response of the Op-amp

The power cord of the integrated circuit often contain noise. AC power supply rejection ratio is actually under the linear small signal adjustment rate, which changes the power output of small-signal voltage changes. It reflects the ability of power supply noise suppression circuit. Simulation results shown that the designed circuit PSRR is 87.5dB (Fig.4).

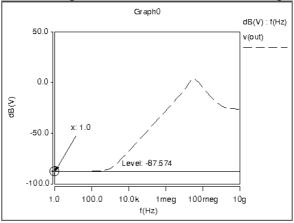


Fig.4. PSRR of the Op-amp

In order to verify the performance of the circuit, the simulation conditions is: temperature range of $-40 \sim 80$ degrees centigrade, simulation results is shown in Fig.5. It can be seen from the simulation results that the reference voltage is relatively stable and less affected by the temperature. The precision is about 3.09 ppm/°C. Simulation results of the all circuit are shown in Table.1.

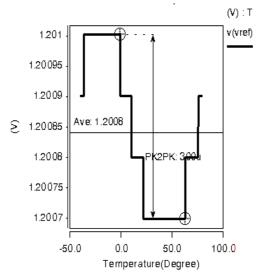


Fig.5. Temperature Coefficient of the bandgap circuit

Table.1. Performance summary of the bandgap reference cil		
Parameter	Result	
Supply voltage	3.3[V]	
Output voltage	1.2[V]	
temperature range	-40~ 80[°C]	
Temperature Coefficient	3.09[ppm/°C]	

A layout of the designed circuit has been shown in Fig.6. Using the 0.35um CMOS process, the layout design has taken some preventive measures to minimize the effects of crosstalk, mismatch and noise. The important module has been protected by isolation ring. The right side of the layout is the ESD protection circuit.

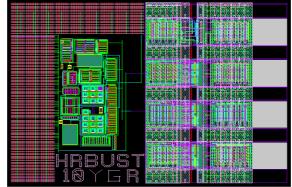


Fig.6. The layout of the overall bandgap reference circuit

Conclusion

A high-precision bandgap reference circuit is presented in this paper. First, we designed a op-amp circuit. As the basic component in bandgap reference circuit, the open-loop gain of the op-amp is 69.8dB, phase margin is 64 degrees and the PSRR of the circuit is 87dB. Second the bandgap reference circuit has been designed. The temperature coefficient is 3.09ppm /°C from -40 °Cto 80°C. The design indicates that the circuit performs well and it can be used for high precision analog integrated circuits.

Acknowledgment

This work was supported by Natural Science Foundation of Heilongjiang Province of China, (Grant No. F201314)

References

- [1] Tajalli A, Atarodi M, Khodaverdi A, et al. Proceedings of the 2004 International Symposium on Circuits and Systems. Montreal, 2004: 45~48.
- [2] P.E.Allen and D.R.Holberg, "CMOS Analog Circuit design-2nd Ed"., Oxford University Press, 2002.
- [3] Behzad Razavi "Design of analog CMOS integrated circuits". McGraw-Hill; 2001.
- [4] Najafizadeh L, Filanovsky L.Towards a sub-1V CMOS voltage reference, IEEE, 2004: 53-56J.
- [5] Banba H, Shiga H, Umerawa A, et al. IEEE Journal of Solid-State Circuits, 1999, 34(5): 670~674.
- [6] Lin Hong chin, Liang Chao-Jui. Proceedings of the 2005 IEEE International Symposium on Circuits and Systems. IEEE, 2005.: 4253~4256.

A Novel Strategy of Area Cost Estimation for Custom Instruction Based on FPGA Architecture

Haiming Liu^{1, a}, Qiang Wu^{1, b}

¹College of Information Science and Engineering, Hunan University, Changsha 410082, China ^aliuhm87@163.com, ^b wuqiang2000@gmail.com

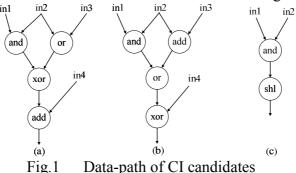
Keywords: custom instruction, Area estimation, FPGA

Abstract-Area cost estimation model is important for accurate measurement of area on reconfigurable processor. However, in the process of CI (Custom Instruction), traditional model can't accurately estimate area cost of CI candidates. In the paper, we propose a novel strategy of area cost estimation. According to island-style FPGA (Field Programmable Gate Array) structure, the strategy firstly enumerated all BCs (Basic Cells) from data-path of CI candidates. Then checked all the validity of BCs enumerated, and selected the unique BC set to overlap original data-paths. We lastly used the effective estimation model based on BC to accurately measure area cost of CI candidates. Experimental results show that novel strategy can accurately estimate area cost of CI candidates, which is very close to actual result from a HLS (High Level Synthesis) tool, and deviation is less than 6%.

Introduction

With development of embedded system technology and increase in demand of complexity in the application, high computing performance and programmability become more important for system design. However, traditional ASIC (Application Specific Integrated Circuit) needs long design cycle and has bad programmability. The defects result in that ASIC has higher design cost and lower Nonrecurring Engineering (NRE) cost. However, reconfigurable processors can overcome the shortcomings by using CI (Custom Instruction). CI can extend code segments that have the highest execution frequency as specific instruction set. Therefore, not only CI can improve system's computing performance, but meet requirements of programmability and flexibility.

Future embedded systems need to meet the shrinking time-to-market windows, reconfigurable processors based on FPGA (Field Programmable Gate Array) can meet the demand. Reconfigurable processors consist of a microprocessor core and a RU (Reconfigurable Unit) based on FPGA, and they communicate each other by register file. Lots of FPGA products currently contain embedded processors. For example, Virtex-II Pro/Pro X serials in Xilinx seamlessly embedded PowerPC405 processors. Not only reconfigurable processors can meet demand of high computing performance and programmability, but shrink time-to-mark window and reduce design cost.



Custom instruction can extend the original instruction to a set of special instructions, which can observably improve system performance and be easily realized on reconfigurable processor. CI process is divided into two stages of identification and generation. Identification chiefly explores subgraphs from IR (Intermediary Representation) as CI candidates, which satisfy all constraints of system architecture. IR is extracted from some compiler (e.g. Trimaran, Spark). In [1] [2] [3] [4],

various identification algorithms are used to rapidly indentify a set of CI candidates from DFG (Data Flow Graph). Generation stage mainly selects lesser subgraphs as CI set from candidates. Criterions of selection are mainly about performance enhancement and area cost. Performance enhancement is estimated by measuring reduction of execution cycle. Based on characterizing of basic blocks to explore CI candidates, Liang proposed an efficient custom instruction generation algorithm in [5]. Meanwhile Liang adopted CDFG (Control Data Flow Graph) as IR.

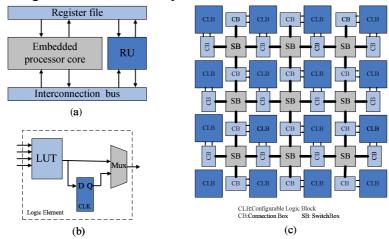
However, in $[1 \sim 5]$, area cost estimation is based on linear accumulation of the certain values of nodes in the IR. For reconfiguration processor based on FPGA, the measure approach can't accurately estimate area cost of RU (Reconfigurable Unit) CI candidates used. For example, data-paths that Fig.1a and Fig.1b depicted have the equal area value for area cost model in [5], because they have same operations and interconnections. But they need different number (1 and 2) of LEs (Logic Elements) to implement their function. In addition, one logic element can implement the function of Fig.1b or Fig.1c, but their area values are different in [5].

The contribution of paper is:

- For reconfigurable processor based on island-style FPGA, proposed a framework of novel strategy to quickly enumerate all basic cells from data-path of CI candidates, which can be realized on one logic element of FPGA, and optimally select least amount of valid BCs to overlap original data-path.
- On the basis of basic cell, which is the most critical factor for area cost estimation, we adopted an effective area cost model to accurately estimate area cost of CI candidates, and delivered estimation values to generation algorithm. Experimental results show that novel strategy can accurately estimate area cost of CI candidates, which is very close to actual results from a high level synthesis tool, and deviation is less than 6%.

FPGA-based Reconfigurable Processor

Differed from general processor, reconfigurable processors mainly consist of an embedded processor core and a RU (Reconfiguration Unit). RU implements custom functions of users, and accelerates the computing performance of total system. Therefore, the reconfigurable processor can satisfy demands of custom function and high performance. In Fig.2a, an embedded processor core was extended with a RU based on FPGA to implement custom instruction. RU can gain input data from register file and output computing results to interconnection bus. The way of communication may facilitate data sharing between embedded processor and RU.



Architecture of FPGA-based Reconfigurable Processor Fig.2

FPGA structure generally contains programmable IOBs (Input Output Blocks) that connect to input/output pins, abundant routing resource and CLB (Configurable Logic Block). CLBs connect routing bus with CB (Connection Box) and communication other CLBs with SB (Switch Box). As basic logic units of FPGA, CLBs can implement combination logic function and timing function by a certain number of inner LEs (Logic Elements), in which number is different according to different devices. Fig.2c represents a structure of island-style FPGA.

Fig2b illustrates an inner structure of LE. LEs mainly contain LUT (Look-Up Table), D flip-flop and multiplexers. LUT mainly implements combination logic function of up to k inputs, k is generally four or six. When want to finish combination logic function, the Mux select the result of LUT to out. If want to finish timing logic function, Mux needs to output the result of D flip-flop. Meanwhile LE can finish arithmetic operation (e.g. addition, subtraction) by using inner fast carry chains of FPGA.

Framework of novel strategy

Based on off-the-shelf island-style structure of FPGA, we proposed a novel strategy to accurately estimate area cost of CI candidates. Framework of the strategy is divided to 4 stages: (1) BC enumeration, (2) BC validity checking, (3) BC overlapping, (4) Area cost estimation. First, we enumerate all BCs (Basic Cells) from CI candidates. Then BCs validity checking can make sure that each valid BC can be implemented on one LE of FPGA. In third stage, select unique BC set to overlap original data-path of CI candidates. Lastly we measure area cost of CI candidates by using effective model of area estimation.

BC enumeration

According to the features of island-style FPGA structure, LE can implement combination logic function of up to k inputs by using LUTs. Meanwhile, LEs may realize the functions of some arithmetic operations by exploiting fast carry chain of FPGA. It is worth mentioning that RU can realize complex arithmetic operation (e.g. multiplication, division) by inside multiplier. RU may implement shift operation by configuring routing resource to gain the suitable value after shift operation. Therefore, primitive operations (e.g. $1 \sim 6$ in Fig.3a) were classified firstly to logic operations (e.g. and, xor, or), shift operations (e.g. shr, shl), arithmetic operations (e.g. add, sub). Then we adopted graph partitioning algorithm to enumerate all subgraphs as BC examples (e.g. BC₁, BC₂ in Fig.3a). Although runtime of algorithm is exponential increase according to number of operations, the algorithm is still adopted because the number of operations of CI candidates can't generally beyond 10.

BC validity checking

A basic cell is valid if it can be mapped onto one logic elements of FPGA. In other words, only one logic element can realize the function of entire subgraph of basic cell (e.g. $(1) \sim (16)$ in Fig.3b). Therefore, BCs must comply with a set of rules, which include checking of operations and external inputs/outputs. Operation checking is used to decide whether an operation may be included in the basic cell.

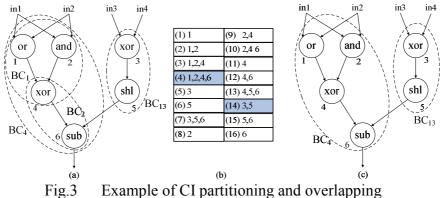
- There is only one arithmetic operation in the DFG of one BC. Because one LE of FPGA can only implement the function of one arithmetic operation (e.g. sub, add) by using inner fast carry chain.
- If there are shift operation and arithmetic operation simultaneously in the BC, condition that shift operation executed after arithmetic operation is allowed. Because shifted value of arithmetic operation can be implemented by configuring FPGA's routing resource.
- If there are logic operation and arithmetic operation simultaneously in one BC, logic operation must be executed before arithmetic operation. Because logic elements use result of LUT as partial value to realize arithmetic operation.

Another rule is used to check external inputs/outputs of the BCs. The rule makes sure that basic cell can't violate the constraints about number of inputs/outputs. We suppose that input pin of k-LUT is k:

- Maximum number of input and maximum output is *k* and 1 respectively. Because a LUT only realizes combination logic of up to k inputs. Moreover there is one output pin of LE.
- One input of arithmetic operation (e.g. add, sub) must be external input. In other words, one input to arithmetic operation must be directly connected to one of external inputs to BC. Because carry-out comes from carry-in or one input of LUT when LE realize function of arithmetic operation.

BC overlapping

We selected a unique set of valid BCs (e.g. BC_4 and BC_{14} in Fig.3c) to overlap original DFGs of CI candidates by using a heuristic algorithm of graph overlapping. The objective function is to minimize the number of BCs selected. Therefore the final BCs selected will be realized by using least number of LEs.



Area cost estimation

Based on island-style FPGA architecture, area of RU CI candidates used may be categorized to area of LEs and area of routing resource. We use Eq.1to estimate area of LE, in which N represents the number of BCs (e.g. N=2 in Fig.3). In addition, we use 32 as factor because we assume that data

width of RU is 4 bytes. Parameter A_b represents the area to store 1 bit. Parameter 2^k indicates

that a LUT of k inputs can store 2^{k} bit information. A represents the remaining area of LE.

$$A_{LE} = N \cdot 32 \cdot (2^k \cdot A_b + A_f). \tag{1}$$

$$A_{R} = N \cdot 32 \cdot \left(2 \cdot \sqrt{A_{LE}} \cdot \sqrt{A_{b}} \cdot W_{r} + A_{b} \cdot W_{r}^{2}\right).$$
⁽²⁾

We use Eq.2 to evaluate area of routing resource. A routing track width is approximated to the square root of the area of single bit [6], because each routing track needs at least 1 bit to control opening and closing of switch. In addition, ^W represents the routing channel width of RU based FPGA.

Experimental Results

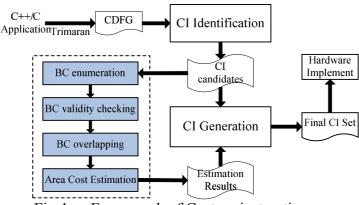


Fig.4 Framework of Custom instruction

For validating our strategy, we use benchmark of Trimaran and gain CI candidates by using identification algorithm in [5] as inputs to strategy. Then output estimation results to CI generation as a selection criteria. The final CI set is realized on RU based on FPGA of 4-LUT (e.g. Virtex-4 in Xilinx). The whole strategy is described by C++, and machine configuration is: AMD Athlon(tm) 64 X2 Dual core processor, 2G memory. Fig.4 shows whole framework of custom instruction.

Benchmark	Num	HLS Results		Strategy Results	
		LUT	Time[s]	LUT	Time[s]
adpcm	5	62	3	64	0.031
cjpeg_int	4	33	2	32	0.015
bmm	7	60	3	64	0.093
bitcount_int	6	91	4	96	0.078
fir	3	60	3	64	0.016
idct	9	90	5	96	0.391
mm_dyn	4	59	2	64	0.015
sqrt	11	119	6	128	2.157

Table1 Comparing strategy results with HLS results

For 8 CI candidates from different benchmarks, table 1 shows that strategy results compare with High Level Synthesis (HLS) results with a hardware synthesis tool. Column 1 represents benchmark name, column 2 represents the number of nodes in a CI candidates. Column 3 and column 5 represent areas (the number of LUTs) of HLS and strategy respectively. Their runtime are column 4 and column6 respectively. From comparing results, we find that area value of strategy is very close to actual value of high level synthesis, and deviation is less than 6%. But execution time is less evidently than time of HLS.

Summary

In the paper, we proposed a strategy to strategy to quickly enumerate a set of basic cells from data-path of CI candidates, and optimally select least number of basic cells to overlap original data-path. Based on basic cell, strategy use an effective area cost model to accurately estimate area cost of CI candidates. Experimental results shows that the estimation value of strategy is very close to actual value of a high level synthesis tool, but execution time is less evidently than time of HLS.

References

- [1] K. Atasu, L. Pozzi, and P. Ienne: Automatic application-specific instruction-set extensions under microarchitectural constrains. DAC, 2003, pp.256-261.
- [2] Cong J, Fan Y, Han G, and Zhang Z: Application-specific instruction generation for configurable processor architectures". FPGA, 2004, PP.183-189.
- [3] L. Pozzi, K. Atasu, and P. Ienne, "Exact and approximate gorithms for the extension of embedded processor instruction sets". IEEE Trans. on CAD of Integrated Circuits and Systems, 2006, pp.1209-1229.
- [4] I-Wei Wu, Cheng-Ping Chung, Jean Jyn-Jium Shann, "Area Effificent Instruction Set Extension Exploration with Hardware Design Space Exploration". Journal of inforation science and engineering 27, 2011, pp.1641-1657.
- [5] Guoqiang Liang, Yuchun Ma, Kang Zhao, Jinan Bian, "Efficient Custom Instruction Generation Based on Characterizing of Basic Blocks". 17th IEEE International Conference on Computer Supported Cooperative Work in Design, 2013.
- [6] H. Gao, Y. Yang, X. Ma, G. Dong, Analysis of the effect of LUT size on FPGA area and delay using theoretical derivations, in: Proceedings of the Sixth International Symposium on Quality of Electronic Design, March 2005, pp.370-374.

[7] http://www.trimaran.org/

A Circuit Design for Portable Cooling and Heating System based on STC89C52RC MCU

Jiang Long^{1,a}, Xudong Wang^{1,b} and Yu Song^{2,c}

¹College of Electrical and Electronic Engineering, Harbin University of Science and Technology, Harbin, 150080, China

²State Grid Nan Yang Power Supply Company, Nan Yang, 473000, China

^avolkswage.n@163.com, ^bwxd6158@163.com, ^cskybox12345@163.com

Keywords: Temperature, Real-time monitoring, MCU, Thermoelectric Cooler

Abstract. Thermoelectric Cooler (TEC), with typical advantages such as low acoustic noise, small volume, lightness, high performance and high reliability, is a compact device widely used in fields like military applications and cooling or heating small spaces. Circuit design of a real-time controlled, LED displayed and monitored cooling and heating system is presented in this paper. The system is consisted of STC89C52RC MCU, TEC1-12706, temperature monitoring chip DS18B20, LED temperature display unit etc. Five kinds of functions like heating or cooling automatically adjustable, temperature controlling, temperature real-time displaying and monitoring and limitation value settings are achieved. A high cooling/heating efficiency has been obtained. The test result shows that the temperature rise/decrease can be 6,83°C/2.18°C per minute in the early 5 operation process of this system.

Introduction

The traditional cooling and heating devices have been existed for decades and have been proven to be helpful with a high performance in our everyday life. However, the large volume and relatively high electric consuming rate can not be accepted when concerned about fields like office room, accurate uses and in car applications. Thus, researchers have been trying to develop portable cooling and heating devices for years and have found medias like Freon, refrigerant 22 etc. But due to drawbacks like having mechanical driving parts, the existence of pollution elements or their potential harm to atmospheric ozone layer, people are always reluctant to use them or afraid of the bad effects these devices may brought about. In order to tackle with these issues, some environment friendly and harmless cooling or heating devices, medias and materials are being developed by researchers recently. Thermoelectric Cooler (TEC) is a newly developed cooling/heating device with advantages like small volume, lightness, good performance, high reliability, low acoustic noise and no extra refrigerant [1-3]. It has been chosen as the best material for manufacture the portable cooling or heating devices. Considering these merits of TEC, researchers have been focused on the development and research of it and have developed lots of relevant devices [2-4]. However, the use of TEC to realize cooling a space or heating a space with two-direction function has rarely been reported and been yet. This paper demonstrates circuit designs of a portable temperature real-time monitoring system, combined with MCU STC89C52RC, thermoelectric cooler, temperature sensor and other hardwares. The system uses one chip of thermoelectric cooler to realize both cooling and heating functions by automatically change the direction of the current. It is not only an optimal way of utilizing thermoelectric cooler, but also a new approach to design portable cooling and heating devices.

Circuit design of system

1. The system hardware composition

The hardware of the system contains MCU STC89C52RC, TEC1-12706, NPN transistor S8050, temperature monitoring chip DS18B20, separated button input unit, alarm buzzer, LED temperature display unit, 5V relay, double-pole-double-throw switch, thermal conductivity fan and cold conductivity fan. The system schematic is shown in Fig. 1.

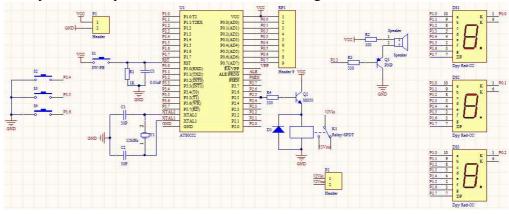


Fig. 1 System schematic

2. Signal separation between 12V and 5V

Because of the voltage standard difference between control part (STC89C52RC and DS18B20: 5V) and operative part (TEC1-12706, cold and hot conductivity fans: 12V) of the system, a coupling device needs to be added to avoid the destructive high voltage leakage from operative part to control part. Traditionally, optical coupling devices are served as a switch to connect and disconnect the high voltage part by deciphering the optical signals from the low voltage part, but these optical devices are often used in higher voltage standards and have relatively high prices.

In this system, the two parts are coupled by a 5V relay instead of devices. An NPN transistor is applied to control the relay. When a high (low) level signal is conducted from STC89C52RC P2.5 I/O port to the base of the transistor, the transistor stays at saturation (cut-off) state. Then the coil of the relay will be activated (deactivated) to accomplish a connection (disconnection) in the 12V circuit. In this way, the signals from the 5V circuit are capable of controlling the 12V circuit.

Hardware design of system

1. Central processing unit

As central processing unit (CPU), STC89C52RC has advantages like easily software programming and high reliability. It can connect a digital temperature sensor (DTS) DS18B20 directly without any extra components. Temperature data could be sent to/from the DS18B20 over a 1-wire interface, so that only one wire (and ground) needs to be connected from the central processing unit to a DS18B20. Power for reading, writing and performing temperature conversions can be derived from the data line itself with no need for an external power source [5]. It greatly simplifies the connections between CPU and DTS. The schematic of CPU is shown in Fig. 2.

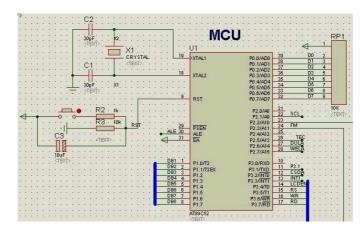


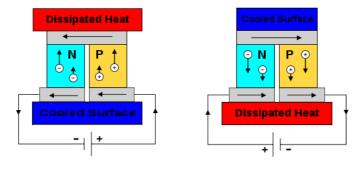
Fig. 2: CPU schematic

2. Temperature monitoring chip

The 1-wire digital DS18B20 is chosen as the temperature monitoring chip in this system. It can measure temperatures from -55°C to 125°Cand will achieve a ± 0.5 °C accuracy within the range of -10°C to +85°C which can easily meet the test requirements. Meanwhile, because each DS18B20 contains one unique silicon serial number, multiple DS18B20s can exist simultaneously on the same 1-Wire bus. This allows for placing temperature sensors in many different places, which provide a potential probability for the refit like multiple DS18B20s with one MCU controlling system in the future.

3. The function of TEC

The Peltier effect is a presence of heating or cooling at an electrified junction of two different conductors and TEC is a production of it. When current flows through a junction between two conductors, heat may be generated (or removed) at the junction. The heat generating work condition is shown in Fig. 3 (a), with the current goes from the right side to left side, by forcing P (hole) and N (electron) move to separated sizes and remove the heat from one side to another, and Fig. 3 (b) shows backwards of the current direction. A TEC1-12706 was chosen as heating and cooling executive part in this paper. Its maximum cooling power is 51.4W, rated current is 6A, maximum voltage is 15.4V, a much higher heating efficiency its dimension is 40mm(L)×40mm(W)×3.8 mm (H) and its highest temperature difference between the two sides is 67°C. The two-way adjustable function was achieved automatically in this system. The TEC can change its hot and cold side fluently by the changing of current direction through it.



(a) TEC heating work condition

(b) TEC cooling work condition

Fig. 3: Peltier effect schematic representation of a single thermocouple for two-direction uses

Experimental results and analysis

PCB is drawn according to Fig. 1. The main control panel is shown in Fig. 4:

The performance of the system is tested in a test box which has an effective volume of 8512cm³. It is made of 2cm thick cystosepiment. A real-time measure temperature result is shown in Fig. 4.

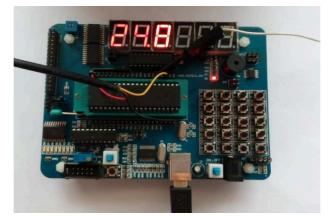


Fig. 4: Main control panel

A high cooling/heating efficiency has been obtained. The result shows that the temperature rise/decrease can be 6,83°C/2.18°C per minuute in this system in the early 5 minute operation process. The efficiency of heating is higher than that of cooling. It is because the heat for heating comes from two parts: one is from the cold side; the other is generated by the current. The test results show that this system can conveniently replace the traditional heating (cooling) devices by controlling the direction of current which successfully meets our requirements.

Conclusions

1. The circuit design for a portable cooling and heating two-way adjustable semiconductor system was successfully presented in this paper. The system is mainly composed of MCU STC89C52RC, TEC1-12706, temperature monitoring chip DS18B20, LED display unit and fan of cold and heat conductivity.

2. The system can achieve a high heating/cooling efficience at a rate about 6.83°C/2.18°C per minute in the early 5 minutes' operation process.

References

- [1] M. Ikeda, T. Nakamura and Y. Kimura et. al: *Thermal Performance of Thermoelectric Cooler* (*TEC*) *Integrated Heat Sink and Optimizing Structure for Low Acoustic Noise / Power Consumption* 22nd IEEE SEMI-THERM Symposium (2006) p.144.
- [2] S. W. Karng, J. Shin, H. S. Han, Y. H. Kim and S. Y. Kim, *Thermal performance of a thermoelectric air-cooling system with heat sinks*, Thermal and Thermomechanical Phenomena in Electronic Systems (ITherm), 12th IEEE Intersociety Conference (2010) p1-7.
- [3] J. Kim, K. H. Lee et. al *A Study on the Application of Micro TEC for Hot Spot Cooling,* International Conference on Thermoelectrics, (Jeju Island, 2007) p339-342.
- [4] L. Sauciuc et. al: *Thermal Performance and Key Challenges for Future CPU Cooling Technologies*, International Electronic Packaging Technical Conference and Exhibition (San Francisco, 2005).
- [5] L. Ping, Z. Yucai, et.al: A Design of the Temperature Test System Based on Grouping DS18B20, ICIEA. 2nd IEEE Conference on Industrial Electronics and Applications, (Harbin, 2007) p188-191.

External Memory Interface Verification Based on VMM

Rui Xu^{1, a}, Zhanpeng Jiang^{1,b}, Changchun Dong^{1,c}, Xuebin Lu^{1,d}

¹Department of Integrated circuits design and integrated systems, Harbin University of Science and Technology, Harbin, Heilongjiang, China

^aruirui@163.com, ^bjzpp@vip.qq.com, ^cdcc@163.com, ^d luxuebin@126.com

Keywords: SystemVerilog VMM. Transaction. Verification. Coverage. EMI

Abstract. With the growth of the scale of SoC, function verification becomes more and more complicated. Traditional functional verification method is confronted with some challenges. This paper achieves coverage-driven, constrained-randomization and assertion verification methodology based on SystemVerilog and VMM, to build verification platform by taking example of EMI (external memory interface). As result of verification, we can monitor coverage, control the platform, optimize testbench and testcase, finish function coverage 100%. These applications can simplify complex function verification, improve the platform reuse, and meet the needs of chip verification.

Introduction

VMM is a hierarchical verification methodology, it will validate the step stratified divided into transaction layer, functional layer, the command level, the signal level four levels, will verify the work in the transaction layer, verification need only be concerned the pins of DUV, Figure 1 is a VMM hierarchical verification model: Generator directly or randomized affairs; Transactor generates a specific bus transaction for EMI issued for memory read and write; Driver achieves functional model of bus and conversion between signals transaction and the underlying level; Scoreboard get the expected output from Transactor, then compare with the actual output, automatically check for DUV function correctly; Functional Coverage collect functional coverage rate, and give it back to the Generator, and if the rate can not satisfy expectation, Generator will generate new test vectors for further tests to improve coverage; Assertion inserted assertion inside and interface of EMI, check EMI behavior is consistent with the specification.

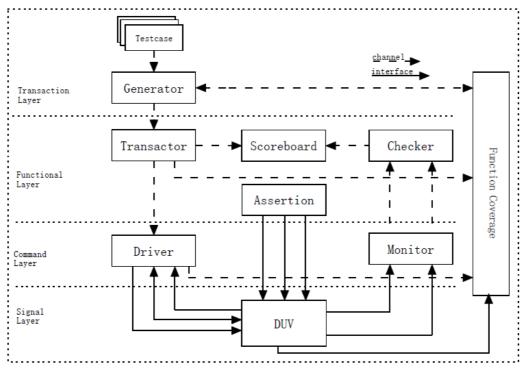


Fig. 1 VMM hierarchical verification model

This verification platform uses the following core techniques of VMM verification:constrained random transaction, Coverage drive, assert.

SoC verification platform with a chip external memory interface (EMI), for example, discusses the application of SoC design verification based coverage-driven features, using VMM and Synopsys DesignWare Verification IP design verification environment, combined with the external memory model functional verification, given the specific and detailed verification steps Code and functional coverage points report.

Design of the VMM verification platform

Interface of external memory.EMI is a SoC chip with ARCA3 processor core provided by ARCA company, which is designed for network on chip, the bus of which meets AMBA2.0 bus standard, memory outside of the chip including: SRAM, SDRAM, ROM. The functions of EMI is to provide the interface for all the memory, and complete the decoding of address in the AHB manner, and give other signals to control the data transmission. Fig. 2 is the internal structure of EMI, EMI includes the following sections: HIU (Host Interface Unit) which receives address and data from the bus and MIU (Memory Interface Unit), which identifies read and write requests from the register or a memory t; MIU is a common interface of SRAM and SDRAM, it generates the appropriate address, data, control commands associated with the memory read / write transmission.

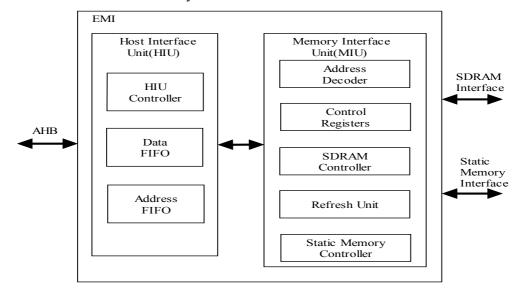


Fig. 2 Structure of EMI

Design of EMI verification platform

VMM base classes and object-oriented will be used to design the hierarchical verification platform, which is the most direct method of VMM verification method, that can efficiently build all levels of the platform. Verification environment is that , using an extension of the base class from vmm_env to implement Generator and Transactor, Driver is an extension from the base class of Verification IP; Scoreboard is an extension from the vmm_xactor base class; Channel can be extended from the VIP class group, can also be extended from vmm_channel; assertion is jointly implemented by the SystemVerilog and VMM assertion libraries, Function Coverage was extended from vmm_callbacks base class. The gray area in Figure 3, is extended from AHB VIP slash shaded vmm_xactor extend from the base class.

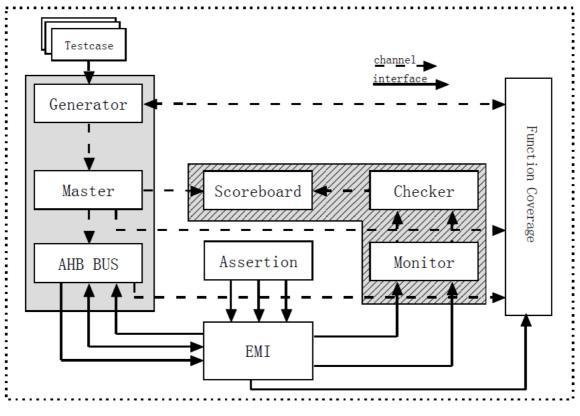


Fig. 3 Verification platform of EMI

Judging from the implementation platform, we can see that using VMM approach is not necessarily in strict accordance with Figure. 1. as Figure. 3 shown, in the EMI verification platforms, Generator, Master and AHB BUS are extensions from VIP meets AHB protocol, Scoreboard, Checker and Monitor will be implemented as part of the expansion of cross-layer, in the same manner, Assertion[5] will be implemented using a variety of methods.

Results and analysis of the verification

Verification results were shown in Figure. 4, the verification was divided into three parts, the first one is the basic verification including verification for register and basic operation of memory, as shown by case0 in Fig. 5, the second one was to inject errors, case1-2 injected into the validation testcase, case1 injected errors into EMI address space, case2 was the error outside of address space, the third part is random verification for the coverage driven, the coverage rate of random function of case3, case4, case5, case6, case7, case8 was set as 80%, 85%, 90%, 95%, 98% and 100%, the platform will stop verification as while as functional coverage rate reaches the set value, then export the report of coverage. Meanwhile uses real-time code coverage report, which you can see the quality of testcase to help optimize the verification platform.

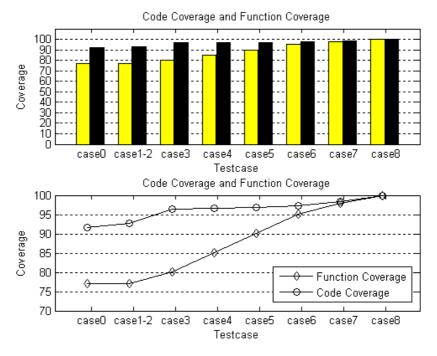


Fig. 4 Report of code and functional coverage

In Figure 5, the yellow bar represent the functional coverage, the black ones represent the code coverage. The abscissa represents the type of authentication testcase, the ordinate indicates the coverage, such as 90 represent 90%. Code coverage and functional coverage in the first part were 91.70% and 76.99%, from the line chart in Figure. 5, we can see that h functional coverage and code coverage increasing with the testcase until to 100%.

Summary

Completed the verification platform with SystemVerilog and VMM verification method, and took advantage of random incentive constrained, coverage-driven, assertions and other means of verification to complete verification of the external memory controller, got detailed functional coverage and code coverage reports. Results shows that the method can simplify the design of verification platform and improve the code and functional coverage, and get an efficient verification of complex chips, which greatly improve the reliability.

References

- [1] Janick Bergeron, Eduard Cerny, Alan Hunter, et al. Verification Methodology Manual for System Verilog[M]. Springer:2006.
- [2] Ben Cohen, Srinivasan Venkataramanan, Ajeetha Kumari. SystemVerilog Testbench by Example[C], SNUG, San Jose: VhdlCohen Publishing, 2006.
- [3] Kausik Datta, P P Das, Assertion Based Verification Using HDVL[C], the 17th International Conference on VLSI Design, Austin Texas: VLSI, 2004.
- [4] Rui Xu,Zhanpeng Jiang.Design of a 6502-compatibable microprocessor. Applied Mechanics and Materials Vols.380-384(2013) pp 3279-3282

Noise Analysis and Characterization of a CMOS Interface Circuit for Fluxgate Sensor

Changchun Dong^{1,a}, Jiang Zhanpeng¹

¹Department of Integrated circuits design and integrated systems, Harbin University of Science and Technology, Harbin, Heilongjiang, China

^ahitdongcc@163.com

Keywords: fluxgate sensor, interface circuit, CMOS

Abstract. In this paper, noise analysis and characterization of a 5V CMOS interface circuit for the fluxgate is presented, which is based on second-harmonic detection of the output voltage. The circuit consists of oscillator, band pass filter, phase sensitive demodulation, low pass filter. The chip is fabricated in the 0.5 μ m two–metal and two-poly n-well CMOS process with an area of 4 mm2. Experimental results shows, the system exhibits a sensitivity of 16.5 μ V/nT for a magnetic field range of ±90 μ T in open-loop with 5kHz excitation frequency. Using 5V supply voltage, the power consumption of the system is measured to be 35 mW.

1. Introduction

Magnetic sensors represent an essential block in several industrial and research applications, such as environmental monitoring, current measurements [1], electronic compasses [2] and proximity detection systems. Fluxgate sensors are typically used to measure low values of magnetic field, such as the Earth magnetic field or the magnetic field induced by low currents. When fluxgate magnetic sensors are used for current measurements, the electronic interface circuit plays an important role, since it must guarantee high linearity, low-power consumption (for portable applications), reliable results and high magnetic noise rejection. Many research efforts have recently been made to design CMOS interface circuit for fluxgate sensor to reduced sensor size [3,4]. However, few efforts have been focused on analysis of noise of the overall system and increase performance by circuit's design.

In this work, a low noise CMOS integrated circuit (IC) for a fluxgate sensor that is suitable for weak magnetic field measurement was presented. A detailed noise analysis of the fluxgate and interface circuit also presented.

2. Interface circuits of fluxgate interface circuit

Figure 1 illustrates the block diagram of the proposed CMOS interface circuit for the fluxgate. The circuits can be divided into two sections, driving and readout. The driving section provides alternate current that can periodically saturate the sensor's magnetic core, producing the desired fluxgate effect. The readout section employs second harmonic principle to accurately convert the AC induction voltage on the sensing coils into DC value linearly proportional to the applied field.

3. Noise analysis for fluxgate

There are several noise sources affecting the overall system resolution of the fluxgate sensor. These noise sources can be classified in two main groups: probe and electrical [5-8].

- At least three known noise sources exist in the probe of the fluxgate, namely
- (a) Modulated thermal agitation noise.
- (b) Direct thermal agitation noise.
- (c) Barkhausen effect.

The modulated thermal agitation noise relates to the noise generated by the flow of nearly zero-frequency currents in the driving winding due to thermal agitation effect, which is given by:

$$V_m^2 = 4KTR_{driving} \tag{1}$$

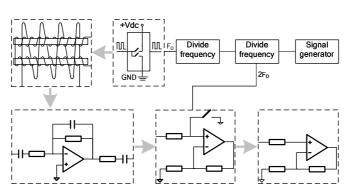


Fig.1. Schematic of interface circuit for fluxgate sensor

Direct thermal agitation noise, which is quite separate, is that due to thermal agitation in the resistance of the readout winding near the second-harmonic frequency, which is passed on to the amplifier without an intermediate modulation process, which is given by:

$$V_D^2 = 4KTR_{readout} \tag{2}$$

The Barkhausen noise is used to designate noise arising from the randomly timed impulses which make up the essentially noise from this source will be expressed in terms of the input signal necessary to yield an output of equal r.m.s. value [9, 10].

$$R_{c}(0) = 32\pi^{2}B_{sat}^{2}(\frac{A}{M})^{2}(Mf)(\sigma f)^{2}(1-\frac{\sin x}{x})$$
(3)

Bandpass filter's noise is dominant noise source for the interface electronics. Hence bandpass filter's noise should be analyzed [11]. Figure 2 shows the simplified noise model of the bandpass filter. V_n is the input referred noise of the amplifier; V_{t1} and V_{t2} are the thermal noises of R_1 and R_2 . By writing KCL at node A and finding the output voltage for each of the circuits, the total input referred noise is calculated as follow:

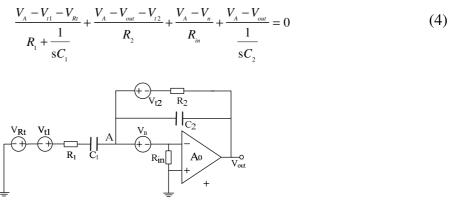


Fig.2. Simplified noise model of the bandpass filter

For large op amp gain (A_V) and large CMOS input resistance (R_{IN}) , the input referred noise is simplified to

$$V_{ni}(s) = -\left[1 + \frac{(1 + sC_1R_1)(1 + sC_2R_2)}{sC_1R_2}\right]V_n + (V_{i1} + V_{R_i}) + \frac{(1 + sC_1R_1)}{sC_1R_2}V_{i2}$$
(5)

Another major noise source for the interface electronics is the noise generated by thermal noise of the switches of phase sensitive [12].

$$V_{sw}^2 = 4KTR_{sw} \tag{6}$$

In order to decrease noise of overall system, drive waveform has to transition into saturation in a very short time for reducing Barkhausen noise, all operational amplifiers employ the PMOS transistor to realize the input stage, and its noise is given by equation (7). Figure 3 shows Noise of the operational amplifier.

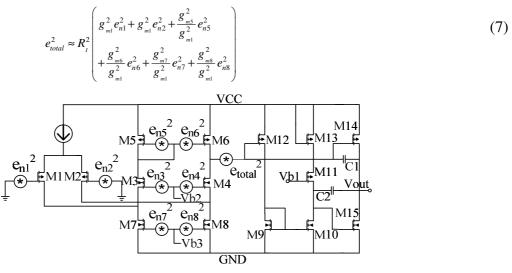


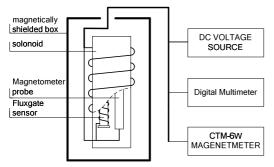
Fig.3. Noise of the operational amplifier

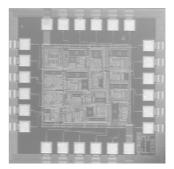
4. EXPERIMENTAL RESULT

The interface chip was designed in $0.5\mu m$ dual-metal dual poly n-well CMOS process and a micrograph is shown in Figure 5. All critical individual blocks of the interface chip were tested extensively and the functionality was verified. The power dissipation is 35mW at a supply voltage of 5V. And the area is $4mm^2$.

The magnetic field to be measured was produced from a solenoid, whose dimensions and electrical and magnetic characteristics are precisely known.

In order to measure a wide range of magnetic fields, two different solenoids were used with different number of turns. By precisely controlling the current in the solenoids, we could produce external magnetic fields in the range of $0-\pm0.2$ mT. The fluxgate sensor was placed in the center of the solenoid, where the magnetic field was assumed homogeneous and constant. As shown in Figure 4, the measurements were performed in a magnetically shielded box to minimize external noise.





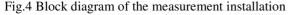


Fig.5. Chip micrograph of the fluxgate interface circuit

In order to estimate the sensor output signal, selective measurements of the second harmonic component were used. The measurements were performed using a pulse excitation field. The sensitivity was determined from the transfer characteristics obtained in the field range from -90 μ T to +90 μ T with 20 μ T step. Figure 6 shows the measurement results of the overall system. We found a sensitivity of the system of 16.5 μ V/T. The data of the system summarized in table1.

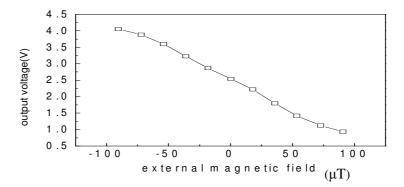


Fig.6. Output signal of the system vs. magnetic field.

TABLE I Data of Fluxgate Interface ASIC Circuit				
Technology	0.5µm DPDM CMOS			
Voltage supply	5V			
Excitation frequency	5kHz			
Measurement range	±90µT			
System sensitivity	16.5µV/nT			
Power consumption	35mW			
Chip area	$2 \times 2 \text{mm}^2$			

5. Conclusion

The newly proposed CMOS ASIC reduces the size of interface circuit for fluxgate sensor, achieving favorable characteristics as a integrated interface circuit of the fluxgate sensor. The chip is suitable for high accuracy requiring fluxgate sensors and it can work in open-loop mode. The result of the fabrication of the CMOS chip indicated that, with the power voltage supply of 5V, the system has a consumption power of 35mw, a linear range of $\pm 90\mu$ T, a sensitivity of 16.5μ V/T. The chip is fabricated in the 0.5 μ m two–metal and two-poly n-well CMOS process with an area of 4mm².

References

- [1] L. D. Rienzo, R. Bazzocchi, and A. Manara, IEEE Trans. Instrum. Meas., 50, 1093(2001).
- [2] A. Baschirotto, A. Cabrini, E. Dallago, P. Malcovati, M. Marchesi, and G. Venchi, IEEE Sensors J., 6,365(2006).
- [3] X. Qian, X. Li, Y. Ping, and J. Fan, IEEE Trans. Magn. 41, 3715(2005).
- [4] C. C. Dong, W. P. Chen and Z. P. Zhou, Opt Precision Eng., 17, 1651 (2009).
- [5] F. C. Williams and S. W. Noble, Proc. Inst. Elect. Engineers, 97, 445(1950).
- [6] P. Ripka, J. Magn. Magn. Mater. 157, 427(1996).
- [7] C. Hinnrichs, C. Pels, and M. Schilling, J. Appl. Phys. 87, 7085(2000).
- [8] R. H. Kocha) and J. R. Rozen, Appl. Phys. Lett. 78, 1897 (2001).
- [9] P. D. Dimitropoulos, Int. J. Electron. 92, 499(2005).
- [10] P. D. Dimitropoulos, Int. J. Electron. 92, 561(2005).
- [11]J. Kubik and P. Ripka, Sens. Actuators, A 132, 236(2006).
- [12] P. Ripka, and M. Janosek, IEEE Sens. J. 10, 108(2010).

Design of a Three-Stage Amplifier with Single Miller Capacitor Feedforward Compensation

Cui Linhai^{1, a}, Lu Xuebin^{1, b}, Yang Guang^{1, c}

¹Software School, Harbin University of Science and Technology, Harbin, China 150040 ^acuilinhai@hrbust.edu.cn, ^blxbsw@126.com, ^c3802080@qq.com

Keywords: Single Miller capacitor feedforward compensation, Frequency compensation, Multi-stage amplifier

Abstract An efficient three-stage amplifier with a new compensation method called single Miller capacitor feedforward compensation (SMFFC) which is suitable for large capacitive load applications are introduced in this paper. The overall layout area of the amplifier can be significantly reduced without influencing their stability by using a single Miller compensation capacitor in a three-stage amplifier. Pole-splitting and feedforward techniques are effectively combined in this compensation method to achieve a better performance.

Introduction

Because the traditional two-stage amplifier can not meet the requirements of high gain and high output swing, three-stage amplifiers have become important as they can provide high gain. In three-stage amplifiers, frequency compensation is required to ensure the stability. Therefore, many frequency-compensation methods have been reported to stabilize the multistage amplifiers. As the bandwidth and the slew rate of a three-stage amplifier are limited by using the existing compensation techniques, special frequency compensation measures must be taken to ensure stability of multistage amplifier.

Related Work

In recent years, a variety form of compensation methods has been developed, of which the most common one is Nested Miller capacitor compensation (NMC)[1]. This structure requires two compensation capacitors. However, the Miller capacitors are often larger than usual, taking up a considerable area of the layout due to the uncertainty of the load. In addition, the nested Miller capacitors increase the loading at the output of the amplifier, resulting in bandwidth reduction [2].

Based on pole-splitting compensation approach, three-stage amplifiers with single Miller capacitor compensation (SMC) [3], multipath nested Miller compensation (MN-MC) [4], multipath nested Miller compensation (MNMC) [5, 6], nested compensation (NGCC) [7], and NMC with feedforward transconductance stage and nulling resistor (NMCFNR) [8] have been developed too.

Single Miller Capacitor Feedforward Compensation (SMFFC)

The structure of the proposed single Miller capacitor feedforward compensation approach (SMFFC) is shown in Fig.1. The feedforward path adds current at the second stage output pushing the second non-dominant pole to higher frequencies. The left half plane (LHP) zero is placed near the second pole which provides a positive phase shift and compensates for the negative phase shift due to the non-dominant poles.

Small Signal Analysis On solving the small signal circuit model with the same assumptions as that of SMC, the approximately educed transfer function is given by Eq. 1, and the amplifier has two non-dominant poles and two zeros.

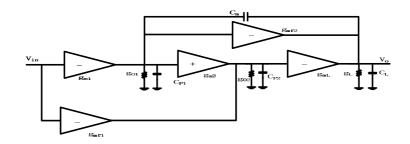


Figure 1. Structure of the SMFFC

$$Av(s) \approx \frac{\left(1 + s \frac{C_m g_{mf1}}{g_{m1} g_{m2}} - s^2 \frac{C_{p2} C_m}{g_{m2} g_{mL}}\right)}{s \frac{C_m}{g_{m1}} \left(1 + s \frac{C_L}{G_{meff}} + s^2 \frac{C_{p2} C_L}{g_{m2} g_{mL}}\right)}$$
(1)

Stability Analysis The stability analysis of the amplifier is done using the separate pole approach. Since the s² term is negative and the s term is positive, this implies that there is a LHP zero and a right half plane (RHP) zero and the LHP zero occurs at a lower frequency than the RHP zero, which does not pose any threat to the stability of the amplifier, instead it helps improving the frequency response. From the transfer function the zeroes of the amplifier are obtained as Eq. 2 and Eq. 3.

$$z_1 = \frac{g_{m1}g_{m2}}{C_m g_{mf1}}$$
(2)

$$z_{2} = \left(\frac{g_{mf1}g_{mL}}{g_{m1}C_{p2}} + \frac{g_{m1}g_{m2}}{C_{m}g_{mf1}}\right) \approx \frac{g_{mf1}g_{mL}}{g_{m1}C_{p2}}(C_{m} \gg C_{p2})$$
(3)

The RHP zero is at very high frequency and hence does not cause stability problems. We use a feedforward path to provide a LHP zero z1 to compensate the second pole p2, shown as Eq. 4

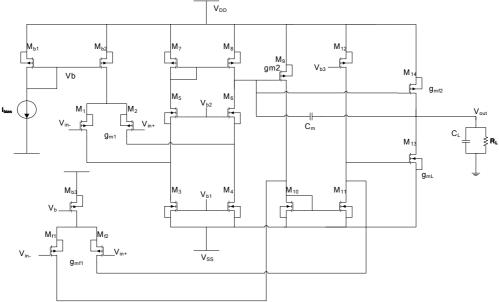
$$p_2 = z_1 \Rightarrow g_{mf1} = \frac{1}{A_{v2}} \frac{g_{m1}g_{m2}C_L}{g_{mL}C_m}$$
(4)

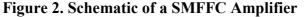
Implementation of the Proposed Structure

A judicious distribution of gain among the three stages is the most important consideration in the design of these amplifiers. For high gain amplifiers (>100 dB) the gain is distributed such that $A_{v1} \ge A_{v2} > A_{v3}$. The gain of the first stage is maximized, with the second stage having moderate gain and the final stage having a very small gain. This results in the second and third pole of the amplifier to be located at higher frequencies due to the high output conductance of the second and third stages and thereby resulting in a single pole system. In order to achieve this, the first stage uses a folded cascode topology to enhance the output impedance.

A moderate gain at the second stage helps in reducing the required compensation capacitor to a great extent. For example a 100dB gain from three stages can be distributed as 50dB, 30 dB and 20 dB for first, second and third stage respectively. Thus, $A_{v2} = 30$ dB resulting in the reduction of the

required C_m by a factor of 30 as compared to that of NMC while ensuring stability. The circuit implementations of the SMFFC amplifiers are shown in Fig.2. Transistors $M_1 - M_8$ form the first gain stage. Transistors M_{f1} and M_{f2} form the feedforward transconductance stage, gmf1 in the SMFFC amplifier. The second gain stage of the amplifiers comprises of transistors $M_9- M_{12}$. The output stage comprises of a feedforward stage, g_{mf2} in SMFFC and the third gain stage g_{mL} forming a push-pull stage. The third gain stage is realized by transistor M_{13} whereas the feedforward stage is realized by transistor M_{14} . Transistors $M_{b1} - M_{b3}$ are used for biasing. The bias voltages V_{b1} and V_{b2} were realized using a cascode current mirror. Each of the other bias voltage sources was realized using a simple current mirror.





The performances of the amplifier are tabulated in Table 1. Four figures of merit, FOM_S , FOM_L , FOM_S^* and FOM_L^* , are defined for small-signal and large-signal performances, as shown in Eq. 5, Eq. 6, Eq. 7, and Eq. 8.

$$FOM_S = \frac{GBW * C_L}{Power}$$
(5)

$$FOM_L = \frac{SR * C_L}{Power}$$
(6)

$$FOM_{S}^{*} = \frac{GBW * C_{L}}{Power * C_{Total}}$$
⁽⁷⁾

$$FOM_{L}^{*} = \frac{SR^{*}C_{L}}{Power^{*}C_{Total}}$$
(8)

An average SR is used in the calculation. A larger figure of merit implies a better frequency compensation topology.

Table 1. Amplifier 1 erformance Summary				
Quiescent Power Dissipation	0.3m[W]			
DC Gain(C _L =100pf)	115.9 [dB]			
Unity Gain Bandwidth	3.2325[MHz]			
Phase Margin	77.882			
Slew Rate	2[V/µs]			
Power Supply Rejection (f=1KHz)	>90[dB]			
FOM _S	1077.5[MHz.pF/mW]			
FOML	667[V/µs.pF/mW]			
FOM _s *	269[MHz.pF/mW.pF]			
FOM _L *	167[V/µs.pF/mW.pF]			
Area	0.007[mm ²]			
Technology	0.35[µm] CMOS			

Table 1. Amplifier Performance Summary

Conclusions

This paper presents a better type frequency compensation method, single Miller capacitor feedforward compensation(SMFFC), for three-stage amplifiers based on a analytically investigation of several frequency-compensation topologies. This approach is well suited for driving large capacitive loads. The simulation results show that the new compensation structure has a high gain, good phase margin, and good bandwidth.

Acknowledgment

This work is supported by the Science and Technology Research Funds of Education Department in Heilongjiang Province under Grant Nos. 12531132.

Reference

- [1] R. G. H. Eschauzier, L. P. T. Kerklaan, and J. H. Huijsing, A 100-MHz 100-dB operational amplifier with multipath nested Miller compensation structure, *IEEE Journal of Solid-State Circuits*, 27 (1992), 1709-1717.
- [2] H. T. Ng, R. M. Ziazadeh, and D. J. Allstot, A multistage amplifier Technique with embedded frequency compensation, *IEEE Journal of Solid-State Circuits*, 34(1999), 339–347.
- [3] X. Fan, C. Mishra, and E. Sánchez-Sinencio, Single Miller capacitor compensated multistage amplifiers for large capacitive load applications, in *Proc. IEEE International Symposium on Circuits and Systems*, Vancouver, Canada, 2004,493-496.
- [4] J. H. Huijsing, Multi-stage amplifier with capacitive nesting for frequency compensation, U.S. Patent Appl. Ser. 602234, filed Apr.19 1984.
- [5] Philip K.T, Analysis of Multistage Amplifier Frequency Compensation, *IEEE Transactions on Circuits and Systems* I: 48(2001), 1-56.

- [6] Leung K N, Mok P K T. Analysis of Multistage Amplifier Frequency Compensation [J]. *IEEE Trans Circuit Syst* I, 48(2001), 1041.
- [7] B. K. Ahuja, "An improved frequency compensation technique for CMOS operational amplifiers," *IEEE Journal of Solid-State Circuits*, vol. SC-18, 6(1983), 629–633.
- [8] K. N. Leung and P. K. T. Mok, Nested Miller compensation in low-power CMOS design, *IEEE Trans. Circuits Syst.* II, 48(2001), 388–394.

Advanced Materials Research Vol. 981 (2014) pp 116-120 © (2014) Trans Tech Publications, Switzerland doi:10.4028/www.scientific.net/AMR.981.116

The Design of the Sinusoidal Signal Generator

Guodong Sun¹, Mingxin Song^{1, a}, Shanshan Wang¹and Yu Zhao¹

¹ College of Applied Science, Harbin University of Science and Technology, Harbin 150080, China

^asongmingxin@126.com

Keywords Sine wave generator; Wien bridge oscillation circuit; Open loop gain; Distortion

Abstract. Sinusoidal signal generator is common electronic equipment. In this paper, the writer designed a kind of integrated CMOS sine signal generator, which generator uses wien bridge oscillation circuit. This generator circuit mainly constitutes by amplifier, leveled and low-pass filter circuit, which uses Cadence software to simulate and analysis its amplification circuit, in order to get a sine wave which has high performance accuracy and stability. Through simulating this generator, we can get a kind of sine wave which includes the frequency as the 1.109 kHz, the center potential as 2.5V, the amplitude as 2.58V, distortion is less than 2%, and this sine wave is more practical for the lower voltage supply system.

Introduction

With the continuous development of electronic information industry, more and more electronic systems need sinusoidal signal, which always used for reference signal and the carrier signal, and requires it is easy to adjust the amplitude and frequency. Typically, sinusoidal signal is generated in two ways, analog sine wave signal circuit [1-2] and DDS [3-4] (direct digital synthesis). Although DDS technology has many advantages, such as: the fast rate of conversion signal, high stability of output signal, the continuous of output waveform, etc., its high price makes it overqualified in some areas. Therefore, in this paper, we describe a method using analog circuitry to generate a sine wave.

The System Structure

The paper introduces a RC oscillator circuit based on Wien bridge circuit. The circuit diagram is shown in Fig. 1. The circuit has three parts: the positive feedback which is composed by amplifier circuit and RC oscillator circuit, negative feedback which is made up of integral amplifier circuit, and the structure to fix amplitude which consists of two parallel diodes. The RC matching in the positive feedback circuit is the key to the quality of output sine wave.

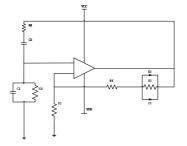


Figure 1 Wien bridge sine signal generator

Operational Amplifier Circuit

In the Wien bridge circuit, it's important to design the amplifying circuit which determines the quality of the waveform. In the amplifying circuit, some parameters, for example, the gain, frequency bandwidth, CMRR, PSRR and slew rate, directly influence the frequent, continuity and degree of distortion of the output wave. The reason why the Wien-bridge circuit demands for unity

gain bandwidth less is that the frequent of sine signal which is generated by the Wien bridge circuit is relatively low, typically in a few KHz, or even lower. However, the circuit is strict in the output swing and open loop gain. Under normal conditions, to ensure the output signal with low distortion, we gain the magnification of the circuit. In the meantime, the output swing of the operational amplifier and the amplitude of the sine output signal becomes more lager.

Table1 Operational amplifier parameters		
supply	5V	
gain	>100dB	
unity gain bandwidth	>38MHz	
phase margin	>55°	
slew rate	>100V/us	
outswing	0.3-4.7V	
CMRR	>80dB	
PSRR	≥80dB	
load capacitance	1pf	
load resistance	10KΩ	

According to the operational requirements of the input common mode range of 0-2.4V, for the circuit configuration of the MOS differential, Usually use the PMOS input device as a circuit, In order to get a greater gain this design uses the source circuit common gate structure, so the first level amplifying circuit are presented in this paper for the fully differential folded cascode amplifier. The structure shown in figure 2. The gain of the circuit is expressed as:

 $A_v = G_m R_{out}$

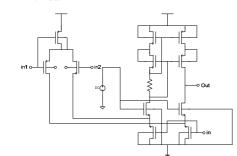


Figure 2 Input differential transconductance

vb o M11 vin o M12 gnd

Figure 3 Output stage structure diagram

stage structure diagram For the output stage, the second stage is concerned, The output swing is an important indicator, In order to obtain the greatest possible output swing, In this paper using cascode amplifier, the cascode amplifier both simple and practical. The output stage circuit configuration shown in Figure 3. In the circuit shown in Figure 3, the conditions of M11 and M12 are able to work properly so that

they are in the saturation region, watching from the output node to see the output impedance. The $r \parallel r$

output impedance is seen $r_{O11} || r_{O12}$, the gain of the circuit is:

$$A_{v} = -g_{m12} \left(r_{O11} \| r_{O12} \right) \tag{2}$$

In the operational amplifier circuit a 1 v bias is need to design, its design idea is that according to the 5V voltage source Obtain bias voltage by way of partial pressure. The way of partial pressure is using structure of 3 same NMOS transistor in series. Of course, when source swing 0.5V, the bias



(1)

voltage swing is 0.1V, this swing of value is can be accepted in this circuit, since there are some variation margin in source-drain voltage of the bias transistor, thus can ensure the smaller change in the bias voltage. Biasing circuit is shown in figure 4.

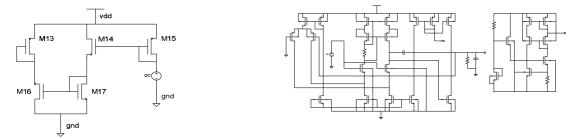


Figure 4 Bias circuit Figure 5 The overall operational amplifier circuit Figure 5 shows 15 PMOS tubes, 11 NMOS tubes, 5 resistors and 2 capacitors. the major difference between the design of two-stage amplifier and that of fully differential operational amplifier is that the former need internal compensation. It can use simple framework in this design because the requirements of specification were not strict. The design of MOS operational amplifiers was similar to the design of bipolar operational amplifiers, it considered from gain , unity gain bandwidth, phase margin, slew rate, outswing, CMRR, PSRR, etc.

Frequency Selection Circuit

The role of frequency-selective network is normalizing the frequency of the output signal and generate sinusoidal signal which has uniqueness frequency as shown in Figure 6.

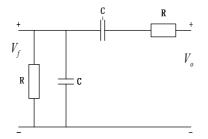


Figure 6 Frequency selection circuit

In Figure 6, Vo is the output quantity of operational amplifier and Vf is feedback quantity of operational amplifier. To be able to form a oscillation circuit, it must select parameters, which is determined the frequency, and Vo and Vf has same phase at a frequency. If the signal frequency were low,

$$\frac{1}{\omega C} >> R \tag{3}$$

there would be the phase of Vf leads the phase of Vo and the phase lead near 90-degree when the frequency close to 0. By contrast, when the signal frequency were higher or tends to infinite, it is clear from this is that the phase of Vf lag the fhase of Vo which is nearly -90-degrees. So, in this changing processes, it must have a certain frequency which make the output quantity same phase with feedback quantity and than forms the positive feedback.

Feedback Circuit And Stability Of The Circuit

Feedback networks: amplifier, the capacitance and the resistor constitute the positive feedback circuit, for the purpose of supplying some feedback signals to the input of the circuit. The

proportional - integral circuit also called a proportional - integral control, as shown in figure 7,the relationship between the input voltage level and output voltage level of the circuit as shown in equation below:

$$u_{sc} = K_p U_{st}(t) + K_p \int_0 u_{st}(t) dt / \tau_1$$
(4)

$$K_{F}(s) = U_{sc}(s) / U_{sr}(s) = K_{p}(1 + \tau_{1}s) / (\tau_{1}s)$$
(5)

In the equation: Kp is a proportional gain; S is the integration time. Kp and S are adjustable, and S requires great value. This make the proportional - integral circuit is a phase-inverted structure that it could turned 180 degree.

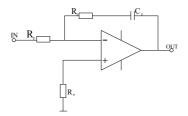


Figure 7 Feedback circuit

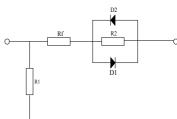


Figure 8 Amplitude stabilization circuit

Amplitude stabilization part: that is the nonlinear part, make the output signal amplitude stability. The specific realization of the circuit is shown in Figure 8.

Cadence Spectre Simulation Analysis

Through the above analysis we can see , to get a larger amplification factor, it is necessary to make a lower frequency; To make CMRR decline , the frequency should be remained at intermediate frequency; to make the PSRR value low, the frequency must be high enough. After the repeated simulation and verification, Sinusoidal signal waveform simulation results are showed in Figure 10. As can be seen from the Figure , the diode limiting method required a certain amount of time from the beginning of the sine wave to signal amplitude reaching stability, as shown in the figure is about 5ms, which can meet the requirement about the time. This Sinusoidal signal generator with the Wien bridge structure can produce the low frequency distortion (harmonic distortion is less than 2 %), stable amplitude and single frequency sine wave with frequency 1.109kHz, center potential 2.5V and amplitude 2.58V.

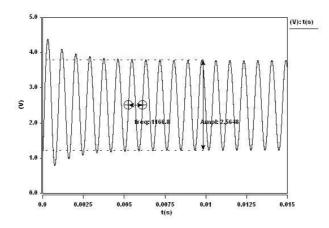


Figure 10. The output of sinusoidal waveform

Conclusion

This design presents a sinusoidal signal generator generated by the wien bridge oscillator circuit. Power supply voltage of the design circuit is 5V voltage, when the simulation is 0.5 μ m process, and the simulation software is Cadence. This design is to make the output waveform as smooth as possible, and to achieve the lowest total output signal distortion through designing and simulating the amplifier circuit based on the wien bridge circuit. Its structure is both simple and practical. And it can produce a single frequency waveform. The waveform of output signal is clear. It has the supply mode of dual voltage power , low distortion, high waveform stability, large output swing, high gain and lower power consumption, etc. It is more practical for system which needs low power supply.

Acknowledgment

This work is supported by the Natural Science Foundation of Heilongjiang Province of China (Grant No. QC2011C087).

Reference

- LE Xiang, QIN Shi, QIAN Qiang. Frequency modulation pulsegenerator based on the phase-locked loop[J]. Journal of TsinghuaUniversity: Science and Technology, 1997, 37 (10): 34-36.
- [2] LI Wei, GAO Zhi-hong. High stability of high frequency sine-wave generator based on phase-locked loop[J]. Journal of Test and Measurement Technology, 2005, 19 (1) :75-78.
- [3] LIU Ping, LAI Xin-quan, LOU Shun-tian, et al. Low frequency function generator based on phase-locked loop [J]. Electronic Design Engineering, 2007 (12) :36-39.
- [4] CHEN Peng. Design of waveform generator based on the DDS[J]. Modern Electronics Technique, 2009 (9) :103-105.
- [5] Behzad Razavi, "Design of Analog CMOS Integrated Circuits", McGraw-Hill, International Edition 2001.
- [6] HE Yong, CHEN Lei. A Novel Design of Wien Bridge Sine Wave Generator [J]. Journal of Donghua University (Natural Science),2009,35(2):P194-200 (Ch).

A Sigma-Delta Modulator System Design with 2-2 Mash Structure

Yang Yang¹, Guodong Sun¹, Mingxin Song^{1,a}, and Zhiming Wang¹

¹College of Applied Science, Harbin University of Science and Technology, Harbin 150080, China

^asongmingxin@126.com

Keywords: Σ-Δ modulator; ADC; Non-ideal factors; 2-2 Mash; Cascade structure

Abstract. Σ - Δ modulator structure is increasingly becoming complex, it is very necessary to improve the design efficiency by the level of behavior model in the simulation. The paper discussed several important Σ - Δ modulators with ideal factors, and gives corresponding behavior model. Then, the paper shows a behavior level design with non-ideal factors. Under the condition that sample rate is 256 and input signal frequency is 250 KHz, the SNR can get 105 dB, the effective bit can get 16 bit. It can be used in audio and electronic equipment.

Introduction

As mixed-signal circuit need of high quality, high performance audio and video for people, this leads to the development of high precision, high conversion rate of the AD converter. AD converter develops gradually from the traditional development to the present that has the noise plastic modulus converter, quantization, band pass modulation structure technology. Σ - Δ modulator can be divided into single and cascade (mash) structure, there is only a quantitative unit in one ring structure, so in the higher order structure the system is not stable due to output effect of the dynamic range of integrator quantize. Then mash structure was conducted on the basis of the low order monocyclic cascade, because the ring is stable, so system stability is improved after the cascade [1]. Behavioral level simulation method of Σ - Δ ADC is proposed, the most popular method is to use the SIMULINK toolbox in MATLAB. It makes some important non-ideal factors in modeling, and the designer can well forecast in time domain Σ - Δ modulator performance and greatly improve the design efficiency. First of all, this article discusses several important Σ - Δ modulators of non-ideal factors and behavior model [2]. Secondly, the article introduces an example of the behavioral level design method on the base of the Σ - Δ mash structure.

Analysis

Sigma Delta modulator will exist instability problem in the high order structure. It can makes performance sharply decline compared to the theoretical ideal modulator. This is the result each designer does not want to see. Cascade structure can avoid unstable phenomenon and can implement high-order noise shaping. So its performance tends to be an ideal higher-order modulator. It can achieve greater dynamic range, higher effective digits when they are in the same order number [3]. Therefore, cascade structure has been widely used. Different from one ring structure, cascade structures has both analog circuits and digital circuits, and digital circuits have the effect of the noise cancellation. Cascade structure is cascade of a few low orders (order1or2). Each level of low-order modulators is stable, so system is stable after the cascade.

The cascaded modulator can be represented by a string of Numbers. For example, a 2-2 cascade structure of Sigma Delta modulator makes two second-order modulators linked together. Generally speaking, we call number of integrator order number. Fig.1 is a typical structure of Sigma Delta N structure.

In Sigma-Delta modulator of N level, quantization noise generated by the former level is the input signal of the next level. Each level of output Yi through proper processing and integrating cancels out all the quantization noise except the last level, which makes it only include the level of the quantization noise in the final output of the modulator [4].

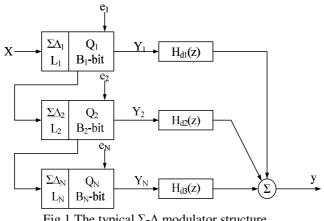


Fig.1 The typical Σ - Δ modulator structure

System Design

System structure of Sigma Delta ADC is shown in Fig.2, it includes the anti aliasing filter, loop filter, quantize, DAC and digital filter. Loop filter is the core of the modulator part and generally can be achieved by the switch electricity capacity. Loop filter, quantize and feedback DAC constitute the Delta Sigma modulator and module the input signal pulse width.

Sine wave in single frequency is as a test signal and the output is PWM digital code stream. The integrator ideally have unlimited dc gain, so feedback make the average of the discrete-time integrator input be exactly equal to zero. It implements that output tracks the input signal change .

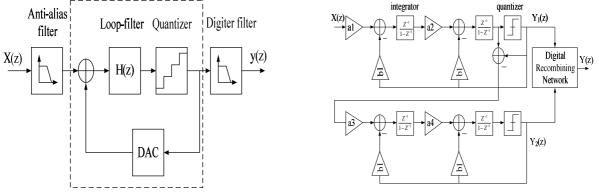


Fig.2 One ring Sigma Delta structure diagram

Fig.3 Mash 2-2 structure diagram

Relative to the one ring structure, 2-2 mash structure is cascade of two second-order ring structure. Each level of output eliminates noise by noise shaping units; at last noise of the quantization tends to white noise. It greatly improves the performance. Above is 2-2 mash structure.

To analysis of mash structure in Fig.3, the output signal is set for the x1, quantitative gain is for the g1. L1(z) is the first level of loop filter function, the output of the modulator is Y(z), the secondary output is $Y_2(z)$, modulator output is Y(z). According to control theory it can be obtained [5]:

$$x_1 = \frac{g_1' y_1}{z - 1}$$
(1)

$$x_2 = \frac{g_1(x_1g_2 - g_2'y_1)}{z - 1} \tag{2}$$

To the above three formulas, we get the first level loop filtering function L1 (z),

$$L_{1}(z) = \frac{g_{1}'g_{2}g_{3} + (z-1)g_{2}'g_{3}}{(z-1)^{2}}$$
(3)

So we can get modulator (NTF) noise transfer function and transfer function (STF),

$$NTF = \frac{1}{1 - L_1(z)} = \frac{(z - 1)^2}{(z - 1)^2 + g_1 g_2 g_3 + (z - 1) g_2' g_3}$$
(4)

$$STF = \frac{L_0(z)}{1 - L_1(z)} = \frac{g_1 g_2}{(z - 1)^2 + g_1' g_2 + (z - 1)g_2'}$$
(5)

According to above analysis, we can get the modulator output Y(z),

$$Y(Z) = STF \bullet X(Z) + NTF \bullet E(Z)$$

= $\frac{g_1g_2g_3Z^{-2}X(Z) + (1 - z^{-1})E(Z)}{1 + (g'_2g_3 - 2)z^{-1} + (1 + g_1g_2g_3 - g''_2g_3)Z^{-2}}$ (6)

To sum up, in an ideal case, after a comprehensive parameters and manual debugging, we get the parameters listed in Table 1. It can counteract the quantization noise of the first level completely and makes the output of the modulator only contain the second quantization noise.

Table 1 Modulator system parameters						
a1	a2	a3	a4	b1		
0.0061	0.0647	0.3085	0.8056	0.0000174		

Behavioral Level Simulation

The following is to simulate systems in Fig.3 by use of parameter in Table 1.

If signal bandwidth is 1 KHz, the input signal is 250Hz and the sampling rate is 256. Simulation results is shown in Fig.4, the SNR is 125.7 dB, effective digits of 20.59, this greatly can meet the design requirements of 16 bit precision.

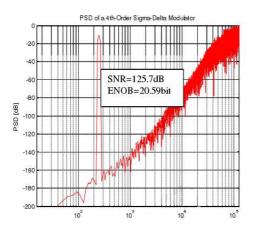


Fig.4 Ideal 2-2 mash behavioral level simulation structure

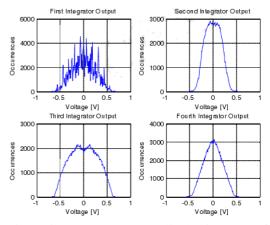


Fig.5 Four integrator output amplitude histogram of the simulation

It can be seen from the diagram four integrator output swing is small in Fig.5, all between [-1, +1], and each other are close, the output does not appear overload phenomenon.

A Non-Ideal Factors Analysis

Because the modulator system analysis is based on ideal circumstances of system model, but in practical applications there are a lot of non-ideal factors, they will affect this system. In the progress of CMOS design, there are two kinds of noise, one is the flicker noise, and another is the thermal noise. Flicker noise is principal component in low frequency, it has inverse relationship with frequency, we can limit the size of it by oversampling techniques; thermal noise plays a dominant position at high frequencies. Under the consideration of thermal noise ands sampling clock, we simulate non-ideal module of the system. Non-ideal module of the system are shown in Fig.6. We can compare the simulation results with ideal system model simulation results.

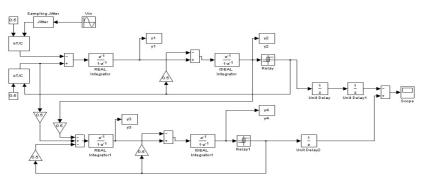


Fig.6 Non-ideal 2-2 mash behavioral level diagram

Simulation results are shown in Fig.7. After adding the non-ideal factors of system, when the input is 250 Hz sinusoidal signal, signal bandwidth is 1 KHz, sampling rate is 256, the SNR of the system can get 105.7 dB, and effective digit can get 17.27. So the modulator with non-ideal factors still meets the design requirements of 16 bit precision.

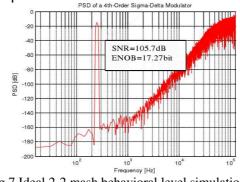


Fig.7 Ideal 2-2 mash behavioral level simulation

Conclusion

In this paper a 2-2 mash structure is analyzed. The system model is set up respectively to the ideal and non-ideal factors. Through scientific analysis and demonstration, we get non-ideal factors that can affect the performance of mash modulator; the final design for 4 order mash modulator structure is designed. From design results, we conclude that the s/n ratio is 105.7 dB, effective bit is to 16 bit, and this can meet the design requirements, and can be used in audio and other electronic equipment.

Acknowledgements

The work is supported by the Major Project of Graduate Innovation Fund in Heilongjiang Province of China (YJSCX2012-103HLJ) and the Natural Science Foundation of Heilongjiang Province of China (Grant No. QC2011C087).

References

- Raf Schoofs, Michiel S. J. Steyaert and Willy M. C. Sansen, IEEE T. Circuits and Systems-I: Regular Papers, vol. 54, NO. 1, January, (2007), p. 209-217
- [2] Y. I. Park, S. Karthikeyan, W. M. Koe, etc, IEEE Custom Integrated Circuits Conference, (2003), p. 115-118
- [3] Yuqing Yang, Terry Sculley and Jacob Abraham. IFIP International Conference on Very Large Scale Integration, (2007), p. 248-251
- [4] M. Dessouky and A. Kaiser. IEEE CICC, pp. May, (2000), p. 13-16
- [5] Liyuan Liu, Dongmei Li, Liangdong Chen, Yafei Ye and Zhihua Wang. IEEE J. Solid-State Circuits, (2011), p. 510-513

The nonlinear analysis of readout circuit for microgyroscope

Wang Guanshi^{1, a}, Liu Xiaowei^{1, b} ¹Harbin Institute of Technology,Harbin, China ^aohno1999@126.com, ^blxw@hit.edu.cn

Keywords: micromechanical gyroscope; readout circuit; nonlinear.

Abstract. In a vibratory microgyroscope, the nonlinear of the readout circuit is a critical part of the signal processing. This is because nonlinear can corrupt the resulting signals, including the angular velocity information. In this paper, issues related to nonliear are discussed. A detailed analysis of the effects caused by various nonidealities is provided. The nonlinear considered are as follows: the distance between the active comb and the fixed comb at the static modal and the equivalent capacitance at sensitive modal. In addition to the analysis of the nonlinear, which is necessary for a successful system-level design is provided.

Introduction

MEMS gyroscope is an inertial sensor to measure the angular velocity which is an important aspect of MEMS technology^[1-3]. It have been widely used in the defense, military and civilian aspects^[4,5]. As the gyroscope structure is very complex, and the performance is vulnerable for some non-ideal characteristics of the interference. For some micromechanical gyroscope with high sensitivity, the nonlinear relationship between the capacitance and the displacement will cause a greater sensitivity third harmonic at the output terminal^[6,7]. Therefore, the theoretical analysis for the nonlinear micromechanical gyroscope to improve the overall performance of micromechanical gyroscope is very meaningful.

Nonlinear analysis of the detection circuit

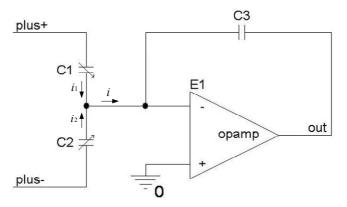


Fig.2 Principle of frequency modulation

In the sensitive mode, the equivalent capacitance C1 and C2 of the respective fixed plates are loaded in high frequency signal of opposite phase, equal frequency and amplitude[8]. They are assumed as sinusoidal signal $+V_{sin}$ and $-V_{sin}$. Since the opamp is "virtual short", the current flowing through C1 and C2 and the total current can be expressed as follows:

$$i_1 = V_{plus} \cdot j\omega C_1 \tag{1}$$

$$i_2 = -V_{plus} \cdot j\omega C_2 \tag{2}$$

$$i = i_1 + i_2 = j\omega(C_1 - C_2) \cdot V_{plus} = 2j\omega\Delta C \cdot V_{plus}$$
(3)

The integrator output voltage is:

$$V_{out} = -i \times \frac{1}{j\omega C_3} = -\frac{2\Delta C}{C_3} \cdot V_{plus}$$
(4)

$$V_{plus} = \frac{4}{\pi} V_{amp} \left(\sin \omega_d t + \frac{1}{3} \sin 3\omega_d t + \frac{1}{5} \sin 5\omega_d t + \cdots \right)$$
(5)

The integrator output is:

$$V_{I} \approx \frac{2C_{0}}{C_{3}d_{0}^{3}} (d_{0}^{2}C_{1}\cos\omega_{d}t \cdot \cos(\omega t + \frac{\varphi_{s2} - \varphi_{s1}}{2} - \varphi_{s}) + C_{1}^{3}(\cos\omega_{d}t)^{3} \cdot (\cos(\omega t + \frac{\varphi_{s2} - \varphi_{s1}}{2} - \varphi_{s}))^{3})V_{phus}$$

$$= \frac{2C_{0}}{C_{3}d_{0}^{3}} (d_{0}^{2}C_{1}\cos\omega_{d}t \cdot \cos(\omega t + \varphi_{1}) + \frac{C_{1}^{3}}{16} (\cos 3\omega_{d}t + 3\cos\omega_{d}t) \cdot (\cos(3\omega t + 3\varphi_{1}) + 3\cos(\omega t + \varphi_{1})))V_{phus}$$

$$= \frac{2C_{0}}{C_{3}d_{0}^{3}} [(d_{0}^{2}C_{1} + \frac{9}{16}C_{1}^{3})\cos\omega_{d}t \cdot \cos(\omega t + \varphi_{1}) + \frac{C_{1}^{3}}{16} (3\cos\omega_{d}t \cdot \cos(3\omega t + 3\varphi_{1}) + 3\cos 3\omega_{d}t \cdot \cos(\omega t + \varphi_{1}))$$

$$+ \cos 3\omega_{d}t \cdot \cos(3\omega t + 3\varphi_{1}))]V_{phus}$$

$$\varphi_{1} = \frac{\varphi_{s2} - \varphi_{s1}}{2} - \varphi_{3}.$$
(6)

where $\varphi_1 = \frac{\varphi_{s2} - \varphi_{s1}}{2} - \varphi_3$.

The reference signal of the first phase sensitive demodulation is a square wave at the amplitude 1, and the frequency is the same as V_{plus} .

$$K = -\frac{4}{\pi} \left(\sin \omega_{\rm d} t + \frac{1}{3} \sin 3\omega_{\rm d} t + \frac{1}{5} \sin 5\omega_{\rm d} t + \cdots \right) \tag{7}$$

The first demodulated signal is:

$$V_{I1} = V_I \cdot K \cdot V_{plus} = -\frac{16}{\pi^2} V_{amp} \cdot V_I \left(\sin \omega_d t + \frac{1}{3} \sin 3\omega_d t + \frac{1}{5} \sin 5\omega_d t + \cdots \right)^2$$

$$= -\frac{16}{\pi^2} V_{amp} \cdot \frac{2C_0}{C_3 d_0^3} \left(\frac{\pi^2}{16} + B \cos 2\omega_d t + C \cos 4\omega_d t + D \cos 6\omega_d t + \cdots \right) [(d_0^2 C_1 + \frac{9}{16} C_1^3) \cos \omega_d t \cdot \cos(\omega_d t + \varphi_1) + \frac{C_1^3}{16} (3 \cos \omega_d t \cdot \cos(3\omega_d t + 3\varphi_1) + 3 \cos 3\omega_d t \cdot \cos(\omega_d t + \varphi_1) + \cos 3\omega_d t \cdot \cos(3\omega_d t + 3\varphi_1))]$$

$$= -\frac{16}{\pi^2} V_{amp} \cdot \frac{2C_0}{C_3 d_0^3} \cdot \frac{\pi^2}{16} ((d_0^2 C_1 + \frac{9}{16} C_1^3) \cos \omega_d t \cdot \cos(\omega_d t + \varphi_1) + \frac{C_1^3}{16} (3 \cos \omega_d t \cdot \cos(3\omega_d t + 3\varphi_1)) + B' \cos 2\omega_d t \cdot (\varphi(\omega_d \pm \omega_d)) + \varphi(\omega_d \pm 3\omega_d) + \varphi(3\omega_d \pm \omega_d) + \varphi(3\omega_d \pm 3\omega_d) + \varphi(3\omega_d \pm 3\omega_d) + \dots$$

(8)

where $\varphi(\omega)$ is a cosine function about ω_d and ω_i .

Because $\omega_d \gg \omega_d$, after a cut-off low-pass filter of the frequency between ω_d and $2\omega_d$, the above equation becomes:

$$V_{I1}' = a_1 \cos \omega_d t \cdot \cos(\omega_i t + \varphi_1) + a_2 \cos \omega_d t \cdot \cos(3\omega_i t + 3\varphi_1) \quad (9)$$

where $a_1 = -V_{amp} \cdot \frac{2C_0}{C_3 d_0^3} (d_0^2 C_1 + \frac{9}{16} C_1^3), \quad a_2 = -V_{amp} \cdot \frac{C_0}{C_3 d_0^3} \cdot \frac{3C_1^3}{8}$

High frequency signal is filtered before the second demodulation, the demodulated signal is:

$$K' = -\frac{4}{\pi} \left(\cos \omega_d t + \frac{1}{3} \cos 3\omega_d t + \frac{1}{5} \cos 5\omega_d t + \cdots \right)$$
(10)

The demodulated output is:

$$V_{I2} = V_{I1} \cdot K = -\frac{4}{\pi} (a_1 \cos \omega_d t \cdot \cos(\omega_i t + \varphi_1) + a_2 \cos \omega_d t \cdot \cos(3\omega_i t + 3\varphi_1))$$

$$\times \left(\cos \omega_d t + \frac{1}{3} \cos 3\omega_d t + \frac{1}{5} \cos 5\omega_d t + \cdots \right)$$

$$= -\frac{4}{\pi} a_1 (\frac{1}{2} + \frac{1}{2} \cos 2\omega_d t) \cos(\omega_i t + \varphi_1) - \frac{4}{\pi} a_2 (\frac{1}{2} + \frac{1}{2} \cos 2\omega_d t) \cos(3\omega_i t + 3\varphi_1)$$

$$+ \frac{1}{3} \cos 3\omega_d t \cdot (\varphi(\omega_d \pm \omega_i) + \varphi(\omega_d \pm 3\omega_i)) + \cdots$$
(11)
$$= -\frac{2}{\pi} (a_1 \cos(\omega_i t + \varphi_1) + a_2 \cos(3\omega_i t + 3\varphi_1)) + \varphi(2\omega_d \pm \omega_i) + \varphi(2\omega_d \pm 3\omega_i)$$

$$+ \frac{1}{3} \cos 3\omega_d t \cdot (\varphi(\omega_d \pm \omega_i) + \varphi(\omega_d \pm 3\omega_i)) + \cdots$$

This signal is filtered by a low pass filter of a corner frequency much less than $2\omega_d$, the output is:

$$V_{12}' = -\frac{2}{\pi} (a_1 \cos(\omega t + \varphi_1) + a_2 \cos(3\omega t + 3\varphi_1))$$
(12)

As can be seen from the above equation, the output signal contains not only by the input angular velocity signal, but also comprising a third harmonic component^[9].

The ratio of the amplitude of the third harmonic component and the magnitude of the fundamental is

$$\frac{a_2}{a_1} = -V_{amp} \cdot \frac{C_0}{C_3 d_0^3} \cdot \frac{3C_1^3}{8} / \left(-V_{amp} \cdot \frac{2C_0}{C_3 d_0^3} \left(d_0^2 C_1 + \frac{9}{16} C_1^3\right)\right) = \frac{3C_1^2}{16d_0^2 + 9C_1^2} \quad (13)$$

where: $C_1 = \sqrt{K_1^2 + K_2^2} = \sqrt{B_{s1}^2 + B_{s2}^2 + 2B_{s1}B_{s2}\cos(\varphi_{s1} + \varphi_{s2} + 2\varphi_d)}$
 $\varphi_3 = \operatorname{arctg} \frac{K_2}{K_1} = \operatorname{arctg} \left[\frac{B_{s1} - B_{s2}}{B_{s1} + B_{s2}} \cdot \tan\left(\frac{\varphi_{s1} + \varphi_{s2}}{2} + \varphi_d\right)\right]$

As can be seen from the above equation, reducing C_1 and increasing d_0 can be reduce the third harmonic distortion components of the output signal, and improving the micro mechanical gyroscope sensitive signal output.

Conclusion

In this paper, issues related to the nonlinear of the readout circuit for a vibratory microgyroscope were studied. First, non-linear relationship between the capacitance variation of the angular velocity caused by external detection of the presence and direction of displacement was considered. After that, nonlinear from the distance between the active comb and the fixed comb, and the nonlinear from the equivalent capacitance of the sense modal were analyzed one by one. Finally, an expression for nonlinear from readout circuit of microgyroscope was written.

References

- [1] Mrigank Sharma, Elie H Sarraf, Edmond Cretu. Parametric Amplification/Damping in Mems Gyroscopes[C]. MEMS 2011, Cancun, Mexico, 2011: 617-620
- [2] Hongzhi Sun, Kemiao Jia, Xuesong Liu, Guizhen Yan, Yu-Wen Hsu, Robert M. Fox, Huikai Xie. A CMOS-MEMS Gyroscope Interface Circuit Design With High Gain and Low Temperature Dependence[J], IEEE Sensors Journal, 2011, 11(11):2740-2747
- [3] S. Sonmezoglu, S.E.Alper, and T. Akin, An Automatically Mode-Matched Mems Gyroscope With 50 Hz Bandwidth[C], MEMS 2012, Paris, France, 2012:523-526
- [4] Chunhua He, Qiancheng Zhao, Jian Cui, Zhenchuan Yang, Guizhen Yan, A Research of the Bandwidth of a Mode-Matching MEMS Vibratory Gyroscope[C], NEMS 2012, Kyoto, Japan,2012:738-741
- [5] J. Seok, H. F. Tiersten, H. A. Scarton. An Analysis of a Vibratory Angular-rate Gyroscope Using Polarized Piezoceramic Bimorph Plates[J]. Part 2: Solution Procedure for the Gyroscope with Superposed Angular Velocity. IEEE Sound and Vibration. 2005, 280(1-2):289-310
- [6] T. Rogers, N. Aitken, K. Stribley, J. Boyd. Improvements in MEMS Gyroscope Production as a Result of Using in Situ, Aligned, Current-limited Anodic Bonding[J]. IEEE Sensors and Actuators. 2005,123-124:106-11
- [7] W. A. Clark, R. T. Howe, R. Horowitz. Surface Micromachined Z-axis Vibratory Rate Gyroscope[C]. Tech. Dig. Solid-state Sensors and Actuators Workshop. Los Angeles, United States, 1996:283-287
- [8] X. Xiong, D. Lu, W. Wang. A Bulk-micromachined Comb Vibratory Microgyroscope Design[J]. Circuits and Systems. 2005, 1(7) 7: 151-154
- [9] McCluskey, P., Lemus, D. Performance and reliability of mems gyroscopes at high temperatures[C]. Thermal and Thermomechanical Phenomena in Electronic Systems (ITherm).2010:1-5

The Research of Noise Figure for EDFA Performance Impact

Qianru Yang, Tao Shen^a, Changlong Tan, Qiuyu Zhao, Xin Zhang, Li Zhao, Yue Feng

College of Applied Sciences, Harbin University of Science and Technology, Harbin, China

^ataoshenchina@163.com

Key words: optical fiber communication systems; erbium-doped fiber amplifier; noise figure

Abstract. Erbium-doped fiber amplifiers is a signal light amplification of optical devices. This paper analyzes the impact of various fiber parameters on the noise figure, and characteristic of noise index has been simulated by means of OASIX software. The relationship between the pump power and noise figure, and fiber length and noise figure are obtained.

Introduction

Erbium-doped fiber amplifier (EDFA) is a new device in the 1990s began to use fiber-optic transmission systems, erbium-doped fiber is mainly developed in the research base 1550nm band applications on the active fiber. EDFA optical attenuation to solve the network transmission rate and distance limitations, completely abandon the expensive based on the photoelectric conversion of light repeater. EDFA with real-time, broadband, online, all low-loss optical zoom function is an important milestone in the history of the development of optical communication. EDFA applications can be divided functionally as long distance transmission line amplifiers, the power amplifier output used as the optical transmitter and receiver front-end preamplifier used[1].

Noise and noise figure: The so-called noise is a random variation in the current or voltage amplification circuit, the output of electronic devices exist in the useful signal, the useful signal when it is not present[2]. Noise figure is the input and the output signal to noise ratio SNR ratio, which reflects the extent of the signal light after the fall of the amplifier signal to noise ratio is an important indicator to measure the characteristics of the erbium-doped fiber amplifier, which directly react with the efficiency of EDFA, noise figure, the greater the fiber loss.

Principle

From the erbium-doped fiber amplifier as shown in Fig. 1 in principle, mainly by erbium-doped optical fiber, a pump light source, an isolator, a coupler, and an optical filter composed of a control circuit. EDFA erbium-doped fiber is the main body of the bait ion incorporation into the interstitial quartz. Pumping light energy for supplying the fiber erbium doped erbium particles to absorb the energy transition to the metastable level. Means for coupling the signal light and the pump light is coupled into the erbium doped fiber[3-4]. Extracting a signal from the control circuit monitoring the output of the amplifier, the pump light power of the amplifier input signal light and the like is adjusted to control the size of the gain to ensure stability of the output signal. The optical filter bandwidth of 1nm or less is a narrow band optical filter is used to eliminate the amplifier spontaneous emission, to reduce the noise of the amplifier.

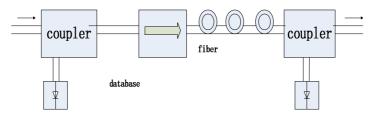


Fig. 1 Constitute the schematic fiber amplifiers

Research and analysis

The fig.2(a) show different pump power, the noise characteristics of the index changes with wavelength. Be seen from the pump power increases, the noise index decreased, which is due to the principle of EDFA amplification is dependent on the distribution of the population inversion, and the pump power changes mainly affecting the distribution of the number of inversion. The EDFA pump power to provide energy for the particles absorb energy to achieve amplification. Fig.2(b) show different fiber lengths, noise figure characteristic changes with wavelength. Be seen from the fiber length increases, the noise figure increases, which is due to the fiber length variation may cause a change of the scattering loss of the fiber, and these changes may cause changes in the output signal to noise ratio, thereby affecting the noise figure changes. Fig.2(c) show illustrates different fiber, the noise figure versus wavelength characteristics. This has largely affected the EDFA amplification effect, and the direct impact on the characteristics of the noise index. Fig.2(d) show different temperatures, noise figure characteristics change with wavelength. Seen from the diagram, the noise increases as the temperature fell, regardless of the temperature at a wavelength of about 1645nm, followed by the increase of temperature rise to reduce the noise figure, which shows the change in ambient temperature can affect to some extent the performance of the optical fiber However, since small changes in the ambient temperature range of the practical application of the noise figure of the EDFA may be limited.

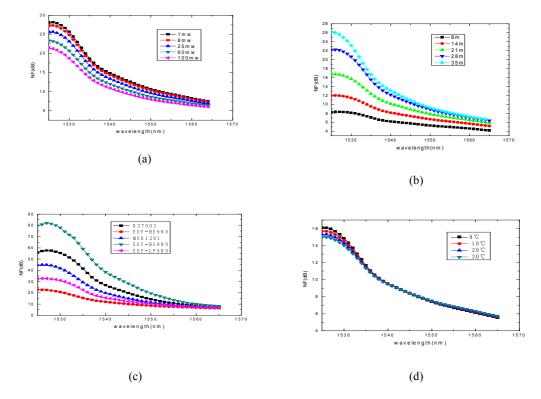


Fig.2 The related parameters of noise index I

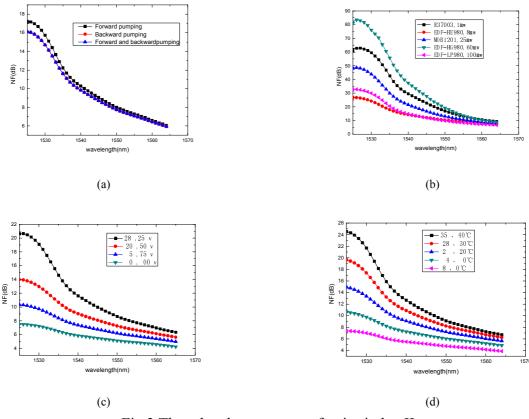


Fig.3 The related parameters of noise index II

The Fig.3(a) show different pump structure, the noise figure characteristics change with wavelength. The basic structure of the EDFA pump. In relatively short EDFA, three signal gain and noise figure is almost the difference is small, and the three ways can make fiber-pumped erbium ions completely inverted state, so the same degree of deterioration of the signal to noise ratio, but EDFA is longer, with the lowest noise figure to the pump in the form of; bidirectional pumping center; reverse pumping highest. Different ways of pumping, there are different EDFA lengths, so that to achieve the best performance of the EDFA. So that changes in the structure will change so that the noise index. The Fig.3(b) show icon transform the pump power and fiber type, change the noise index. Changes resulting noise power spectrum of the entire pitch change, you can not know the impact between the two parameters can even say no. However, the fiber can be seen in the pump power is greater than the influence of the type. Fig.3(c) show illustrates the fiber length is reduced and the pump power is increased, the noise index changes. The two together can be better optimized noise figure, both mutual promotion and mutual influence, and the noise index flat a lot. Fig.3(d) show lowering the temperature and reducing the variation illustrated fiber length, the noise figure. Effect of temperature on the noise figure is small, the combination of temperature together affect the noise figure of the EDFA has been enhanced, in particular in the temperature of 30 $^{\circ}$ C -40 $^{\circ}$ C within this range can be reduced to some extent on the noise figure. At the same time it can be seen the two together so that the entire spectrum of the noise decreased 1-2dB, ie a combination of both can be better optimized EDFA noise figure.

Conclusion

This paper studies the erbium-doped fiber amplifier research background, including features, applications development prospects necessity of erbium-doped fiber amplifier composition, as well as research. Erbium-doped fiber studied the basic concepts and parameters, erbium ion energy transition between the principle of erbium-doped fiber amplifier basic principles, but on this basis, the erbium-doped fiber amplifier parameters are described in detail. The use of simulation analysis OASIX will combine theory and practice targeted more detailed characteristics of the EDFA noise figure studies, and summarizes the effects of several parameters on the EDFA and size, the results can be designed to provide for EDFA reference.

Acknowledgements

This work was financially supported by the Science and Technology Research Project of Heilongjiang Province Education Bureau (No.12531134).

- [1] Hongyun Meng, in:ultrawideband theoretical and experimental study of the optical fiber amplifier", Nankai University PhD thesis, 7, (2003).
- [2] Yanfei Du: Journal of Liaocheng University, Vol. 18-3 (2005), p. 36
- [3] Xueda Huang, in: Works and development trend of Wong EDFA optical communications", A Dissertation Submitted to China University of Geosciences, 21, (2003).
- [4] Pengyu Wang, Ning Yan: Information Security and Technology, Vol. 4-7 (2013), p. 63

Research on Matlab Simulation Output of Optical Current Transformer

Tao Shen^{1,2,a}, Chao Hu^{2,b}, Qianru Yang^{2,c}, Mingxin Song^{1,2,d}, Xinlao Wei^{1,e}

¹ College of Electrical and Electronic Engineering, Harbin University of Science and Technology, Harbin, China

² College of Applied Sciences, Harbin University of Science and Technology, Harbin, China

^ataoshenchina@163.com, ^bhuchaokobe123@163.com, ^cyangwenlong1983@163.com, ^dsongmingxin@126.com, ^eweixinlao@163.com

Key words: fiber-optic transformer; Faraday effect; correlation deltection; signal simulation

Abstract: The theory model of the reflective optical current transformer (OCT) has been established using Jones matrix method, and the proper devices have been chose. According to the characteristics of the transformer's output, signal processing circuits including photoelectric translating circuit, preamplifier, correlation detector, lowpass filter and ARM processor have been designed. The simulation mode was established in the Matlab environment. The simulation analysis as well as the noise analysis was carried out. Finally, the analysis of the relationship between transformer's input and output was analyzed by using function fitting method. The fitting coefficients and error were given and quadratic or quartic curve fitting was proposed.

Introduction

OCT technology is developing rapidly along with the development of the optical fiber and the optical fiber communication technology[1]. Optical fiber as a medium and it's a new transformer technology of perception and outside signal transmission[2]. OCT has a lot of advantages compared to other types of transformers, such as electrically insulation, anti-electro-magnetic interference, corrosiveness resistance etc. And it's received widespread attention and application. Now OCT has been applied to measure current[3]. OCT has advantages unmatched by electromagnetic current transformer, it is a relatively ideal current transformer and its market demand and economic benefit is very considerable. Other departments, such as the current electricity demand for OCT and use a large amount, while in some special occasions only use OCT. Research output OCT to have important academic value.

OCT model design

The basic structure of reflective OCT design is shown in Fig.1[4]. In the configuration of light retro reflected by the mirror returns to the coil, the Faraday effect is non-reciprocity, so it is twice the positive and negative waves by the fiber loop, so this structure is not only possible to reduce the linear birefringence fiber. The Faraday effect is also possible to double. Two-beam interference optical reflection structure in the same transmission optical fiber, it is possible to reduce the external factors of the interference, and is not affected Sganac effects. In addition device of reflection structure using relatively few, and polarization rotation and phase modulation structure compared with the reflective structure has the advantages of high sensitivity[5-6].

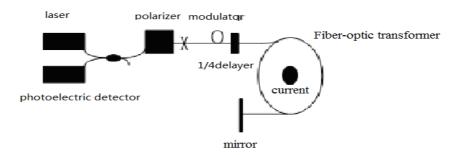


Fig.1 The basic structure of reflective all-fiber current transformer

The establishment of simulation model

OCT model is establish using Matlab simulation as shown in Fig.2. For a more realistic simulation environment, the simulation system noise added band-limited white noise module 0.001Db in Fig.3, while the output of each module via different oscilloscope display, we can always observe the different stages of the signal waveform.

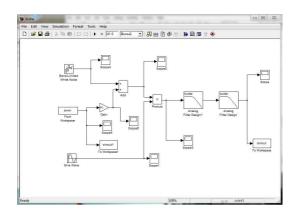


Fig.2 System Simulation Model

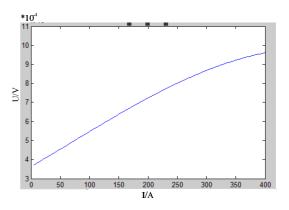


Fig.3 Relationship between the output voltage and input current

The simulation results and the processing analysis

In order to find the relationship between the input current and the output voltage, the use of simulation software to prepare M file and run the file can be plotted input current and output voltage relationship diagram, prepared as part of the M file.

```
I=[5:5:400];
t=3;
V=4.68*10^(-6);
N=200;
thi=V.*N.*I;
a=(0.99*10^(-3))/2;
b=1+cos(4*thi)*cos(1.84*cos(pi.*t));
c=-sin(4.*thi)*sin(1.84*cos(pi.*t));
f=a.*(b+c);
u=1980*f;
plot(I,u);
```

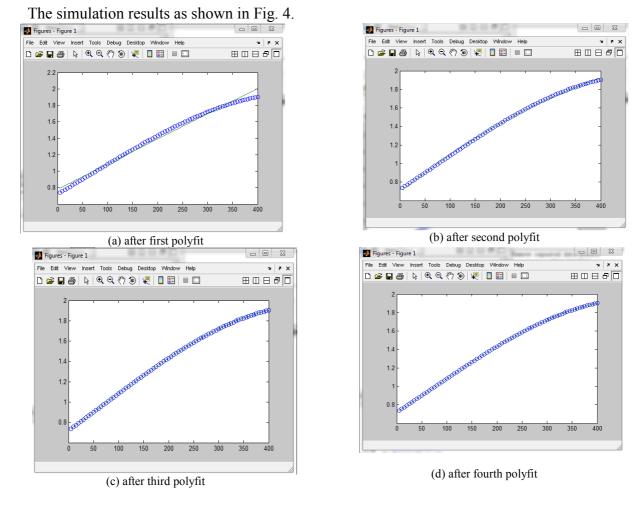


Fig.4 The output voltage and input current relationship

Polyfit the image shown in Fig.4, wherein the abscissa represents the current (A) in polyfit image, and the ordinate represents the voltage (U), d = polyfit (I, u, 2) in the figures represent the polyfit coefficients, '2 'represents the quadratic polyfit, the simulation data is in the optical fiber coil of N = 200 the data can be seen from the simulation. When the linearity of 0 to 250A is very good, if you want to measure larger current can only reduce the number of turns. By fitting also know that when current is less than 250A. The transformer has good linearity, when the current continue increasing, the voltage-current curve to flatten and reduce linearity. Visible output value and the current is not a simple proportional relationship.

After processing the transformer output signal, the output of the linear relationship between voltage and current when found in only a small current, for the entire measurement range. There is a high relative error after the first polyfit. When using a quadratic polyfit, more consistent with the measurement, in order to obtain input-output relationship of the transformer, generally require the use of a quadratic polyfit. To find the input and output more accurate results, we need to use a higher order polyfit, polyfit can select four times, four times after the relative error of the improvement has not been seen.

Conclusion

OCT simulation model is established by using simulation software, the results of OCT establishing reflective model simulation indicate when the current is less than 250A. The transformer has well linearity. When the current continues increasing, the voltage current curves to flatten, reduce linearity, output value and the current is not seen as a simple proportional relationship. By using polyfit, observing the simulation results with a consistent level of statistical figures corresponding

numerical group, to get the input-output relationship of the transformer, for the entire measurement range, a higher relative error after first polyfit. When using a quadratic polyfit, more in line with the measurement conditions.

Acknowledgements

The authors thank National Natural Science Foundation of China (51307036), Natural Science Foundation of Heilongjiang Province of China (E201303, F201131), the Education Department of Heilongjiang province of China (12531134) and National Undergraduate Training Programs for Innovation and Entrepreneurship of China (201310214010).

- C. Li, X. Cui, I. Yamaguchi, Y. Masayuki, and Y. Toshihiko: IEEE Trans. Instr. Meas., Vol. 54 (2005), p. 273.
- [2] J. Dakin and B. Culshaw: Artech House, Vol.4 (1997), p. 437.
- [3] H. d. Pei, J. Zu and H. Chen, in: A Novel Demodulation Method for the Sagnac Interferometric Fiber Current Sensor, IEEE, 4, 208. (2007).
- [4] V. P. Gubin and V. A. Isaev: Lasers for Measurements and Information Transfer, (2005), p. 98.
- [5] J. H. Haywood, I. M. Bassett and M. Matar, in:Restoring reciprocity to the 3X3 Sagnac interferometer using the NIMI technique, 17th International Conference on Optical Fibre Transformers, 953(2005).
- [6] D. C. Ericksan: Power Apparaus and Systems, Vol. 99-3 (1980), p. 105.

Numerical Simulation of Rapid Solidification Process for Micrometer Level Solder Ball Used in BGA Packaging

Shu Li^{1,a}, Jianwei Huang¹, Fei Wang¹ and Wei Liu¹

¹College of Applied Science, Harbin University of Science and Technology, Harbin, Heilongjiang 150080, People's Republic of China

^alishu@hrbust.edu.cn

Keywords: Ball grid array, Solder ball, Microelectronic packaging, Microstructure, Simulation, Sn-5mass%Pb

Abstract. We numerically simulated the containerless rapid solidification for micrometer level solder ball used in BGA packaging, based on prior models for heterogeneous droplet nucleation and non-equilibrium solidification, to predict the solidification microstructure of solder ball. Results of simulations for Sn-5mass%Pb solder ball produced under different conditions are discussed.

Introduction

A ball grid array (BGA) is a type of surface-mount packaging used for integrated circuits. BGA packages are used to permanently mount devices such as microprocessors. A BGA can provide more interconnection pins than can be put on a dual in-line or flat package. The whole bottom surface of the device can be used, instead of just the perimeter. The leads are also on average shorter than with a perimeter-only type, leading to better performance at high speeds.

Soldering of BGA devices requires micrometer level solder ball. Quality of solder ball, such as alloy composition, melting point and microstructure, determines final soldering joint quality, such as mechanical and electrical properties. Material properties are closely related to preparation process of the material. Therefore research on the preparation process of solder ball and further obtaining the solder ball with high quality are very meaningful.

The present main work was to numerically simulate the containerless rapid solidification for micrometer level solder ball used in BGA packaging, by adopting previous models developed by the first author of the present paper and his previous co-authors, to predict the solidification microstructure of solder ball. The used models include the model for heterogeneous droplet nucleation [1,2] and the model for non-equilibrium solidification [3].

Simulation Method

The present section describes the basic scheme of assembling the prior models into the simulation method. The in-flight nucleation of droplet may be caused by surface oxide or a catalyst in the melt. Li *et al.* modeled the two modes of nucleation for gas-atomized droplets and obtained CCT curves [1]. Based on their work, we can calculate the nucleation temperature T_N for a given set of atomizing gas, residual oxygen content (P_{O_2}) in the atomizing gas and initial gas velocity $(V_{g0}, exponential decay)$ for a droplet of selected diameter (d_d) . Here, the simulated values of undercooling (from the liquidus temperature of 497.7 K) are shown in Table 1 for Sn-5mass%Pb droplets for the selected four GA conditions. It is clear that the droplet undercooling depends strongly on the mode of nucleation, which depends on both cooling rate and oxygen potential in the atomizing gas, in a complex way.

Once a droplet nucleates, solidification immediately sets in. During the solidification, the droplet temperature T is determined by the convective heat transfer to the atmosphere and the latent heat

generation due to crystallization, while the radiation heat transfer is negligible for the Sn-5mass%Pb alloy so that [2]:

$$\frac{dT}{dt} = \frac{\Delta H_f}{C_p} \frac{df_s}{dt} - \frac{h}{\rho_d C_p} \left(\frac{6}{d_d}\right) \left(T - T_g\right). \tag{1}$$

where f_s is the fraction solid in the droplet, df_s/dt is the fractional rate of solidification, ΔH_f is the latent heat of fusion of the alloy per unit mass, C_p is the specific heat, h is the heat transfer coefficient, ρ_d is the density of the alloy, T_g is the temperature of the gas (assumed to be constant, 298 K). The df_s / dt in Eq. 1 can be represented by:

$$\frac{df_s}{dt} = \frac{V_i A_i^s}{V_d}.$$
(2)

where V_i is the migration velocity of solid-liquid interface, A_i^s is the area of the solid-liquid interface and V_d is the droplet volume. In the early stage of solidification, V_i is so large that the second term in Eq. 1 has little effect on dT/dt, causing the droplet temperature to rise sharply (recalescence). For the calculation of V_i , a free dendritic growth model (DA model) [3], is adopted. For a given droplet temperature, the dendritic growth model predicts the V_i , the tip radius r_{iin} , and the compositions of the liquid and the solid at the tip, C_i^s and C_i^L .

	1401			
Simulation results for gas-atomiz	zed Sn-5mass	%Pb drople	ts under sele	ected four condition
Droplet No.	GA 1	GA 2	GA 3	GA 4
Atomizing gas	helium	argon	helium	nitrogen
Nucleation mode	internal	surface	internal	internal
d_d (µm)	750	500	350	150
V_{g0} (m/s)	1700	200	200	200
<i>P</i> _{<i>O</i>₂} (ppm)	500	10	500	500
Undercooling (K)	102.9	36.7	144.3	187.3
t_r (µs)	1449.1	492.1	489.9	257.7
V_i at t_r (m/s)	0.006	0.005	0.013	0.025
r_{tip} at t_r (µm)	0.315	0.351	0.204	0.138
C_i^s at t_r (mass%Pb)	1.06	1.03	1.19	1.35
f_s at t_r	0.390	0.129	0.561	0.699
Plateau duration (s)	0.072	0.271	0.011	0.010

Table 1 S ms.

Results and Discussion

In this section we present the simulation results for gas-atomized Sn-5mass%Pb droplets. Four typical conditions (GA 1-4) are selected to discuss the effect of processing conditions on the solidification path and resultant microstructure. Table 1 also shows the recalescence behavior and post-recalescence duration Δt_{pl} of the droplets defined under conditions GA 1-4, which include the V_i , r_{iin} , C_i^s and f_s at the recalescence time (t_r) , defined as the time after nucleation at which the droplet heating rate decreases to 1000 K/s. The cooling curve of the droplet GA 1 is shown in Fig.1, in which Δt_{pl} and t_r are denoted and the initial droplet temperature is assumed to be 545 K.

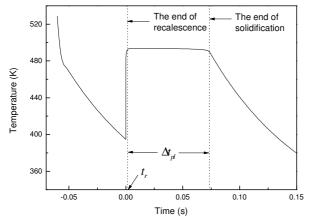


Fig. 1. The relationship between droplet temperature (K) and solidification time (s). Zero point of the time represents the beginning of solidification.

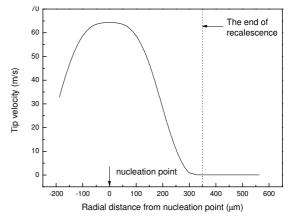


Fig. 2. Primary dendrite tip velocity (m/s) as a function of the radial distance from nucleation point for the 750 μm droplet GA 1.

GA 1 and GA 3 (Table 1) indicate that a 750 μ m droplet and a 350 μ m droplet, when atomized with helium gas in the presence of 500 ppm of oxygen, would undercool by 102.9 K and 144.3 K, respectively. Although larger undercoolings normally occur at higher atomizing gas velocities, here the droplet size has stronger effects on the undercooling. In fact, a 50 μ m droplet, atomized with argon gas containing 20,000 ppm oxygen, would get around nucleation by surface oxidation or the internal catalyst of concern, even at a low atomizing gas velocity of 200 m/s. Such a small droplet may, however, nucleate on yet another catalyst that may be present in the melt, although homogeneous nucleation should not be excluded. Even if residual oxygen is reduced to as low as 10 ppm, i.e., GA 2, 500 μ m droplets atomized with nitrogen gas would still nucleate on surface oxide at a low undercooling of 36.7 K. This is because the heat capacity and thermal conductivity of argon gas are much lower than those of helium gas [2]. Atomizing with nitrogen gas, which has even lower heat capacity and thermal conductivity, would further promote oxidation-catalyzed surface nucleation, but 150 μ m droplets atomized under GA 4, because of their high cooling rate, would nonetheless undercool by 187.3 K and nucleate internally, even in the presence of 500 ppm oxygen.

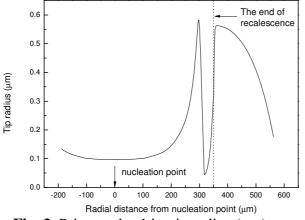


Fig. 3. Primary dendrite tip radius (μm) as a function of the radial distance from nucleation point for the 750 μm droplet GA 1.

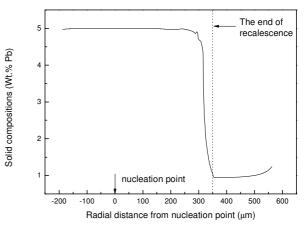


Fig. 4. Primary dendrite tip composition (mass%Pb) as a function of the radial distance from nucleation point for the 750 μm droplet GA 1.

Figs. 2-4 show the solidification behavior of an internally nucleated 750 μ m droplet produced under condition GA 1, including primary dendrite tip velocity, tip radius and tip composition. In the present paper, for the mode of internal nucleation it is assumed that the distance of nucleation point

from the centre of sphere is $d_d/4$. Three stages of solidification are identified: the initial thermal dendritic solidification, the thermal-to-solutal transition (where the undercooling ranges between about 20 K and 30 K for Sn-5mass%Pb alloy [3] and the final solutal dendritic solidification.

The initial thermal dendritic solidification prevails for a large part of recalescence at an initial growth rate exceeding 60 m/s with little solute partitioning at the dendrite tips. The growth rate quickly decreases while the dendrite tip radius initially increases from 0.097 μ m to about 0.6 μ m. The tip radius then decreases toward the end of recalescence as the droplet temperature rises further (thermal to solutal transition). By the time the recalescence ends (doted lines in Figs. 2-4), solutal dendritic solidification has established, with the growth rate decreased to 0.006 m/s, the tip radius increased to 0.315 μ m and the solute concentration at the tip decreased to 1.06 mass%Pb. At this point, the droplet temperature reaches about 490 K, just a few degrees below the equilibrium liquidus, and, 39.0% of the droplet volume has solidified, Table 1.

Beyond this point, the growth is controlled essentially by the rate of heat removal from the droplet and the droplet temperature decreases slightly (see Fig. 1). This leads to the variation in tip radius and solute concentration (Fig. 3 and Fig. 4), while the tip velocity stay almost constant near the values reached at the end of recalescence throughout the post-recalescence plateau stage which lasts for 0.072 s. However, it is still the solute diffusion-controlled growth, i.e., the solutal dendritic solidification.

Because nearly adiabatic conditions prevails during the recalescence stage, the fraction solid at t_r is essentially proportional to the undercooling (0.13 for the droplet GA 2 that undercools by 36.7 K and 0.56 for the droplet GA 3 that undercools by 144.3 K). In addition, for the droplet GA 2 the post-recalescence plateau stage lasts as long as 0.271 s, limiting the rapid solidification effects. In contrast, the post-recalescence solidification of the droplet GA 3 takes only 0.01 s because of the high cooling capacity of helium gas as well as the small droplet mass and the small fraction of the liquid left to solidify during the post-recalescence plateau stage, assuring a high level of rapid solidification. Thus, the heat capacity and thermal conductivity of the atomizing gas have strong effects on the post-recalescence plateau duration and hence on the solidification microstructure of gas-atomized droplets.

Summary

Adopting prior models for heterogeneous droplet nucleation and non-equilibrium solidification, the containerless rapid solidification for micrometer level solder ball used in BGA packaging was numerically simulated, to predict the solidification microstructure of solder ball. Results of simulations for Sn-5mass%Pb solder ball produced under different conditions are discussed. Both internal nucleation and surface nucleation are considered. For a given set of atomizing gas, residual oxygen content in the atomizing gas and initial gas velocity, the present method predicts the entire course of solidification, which includes the tip velocity, the primary dendrite tip radius, tip composition and post-recalescence duration etc.

Acknowledgments

The authors acknowledge the support of Scientific Research Fund of Heilongjiang Provincial Education Department (NO: 12511073).

- [1] S. Li, P. Wu, W. Zhou and T. Ando: Mater. Sci. Eng. A Vol. 473 (2008), p. 206.
- [2] S. Li, P. Wu, H. Fukuda and T. Ando: Mate. Sci. Eng. A, Vol. 499 (2009), p. 396.
- [3] A.G. Divenuti and T. Ando: Meta. Mater. Tran. A, Vol. 29 (1998), p. 3047.

Flatness Improvement of FRA with Multi-Wavelength Pump

Yu Ma¹, Yanchao Li², Changxing Liu¹, Xiangyu Meng¹, Jiuru Yang^{1,a}

¹College of Electronic Engineering, Heilongjiang University, Harbin, P.R. China;

²Key lab of Electronics Engineering, College of Heilongjiang Province, Heilongjiang University, P.R.

China

^ayangjr@hlju.edu.cn

Key words: Fiber Raman amplifier, gain-flatness, multi-wavelength pump, simulation

Abstract: A fiber Raman amplifier (FRA) based on the properties of silica fiber can not only get a wideband gain spectrum by using multiple pumps, but also has the nature of low noise and cost. In the study of FRA, gain-flatness is one of the most key and hot issues. In this paper, we focus on the gain flatness of fiber Raman amplifier by multi-pump, and various parameters in term if power and number of pump source are analyzed comprehensively. According to the numerical results obtained, the optimized within power and number of the pump source are determined. And we controlled the gain-flatness of FRA within ± 1 dB from 1512nm to 1566nm in a dense wavelength division multiplexing system with 67 channels.

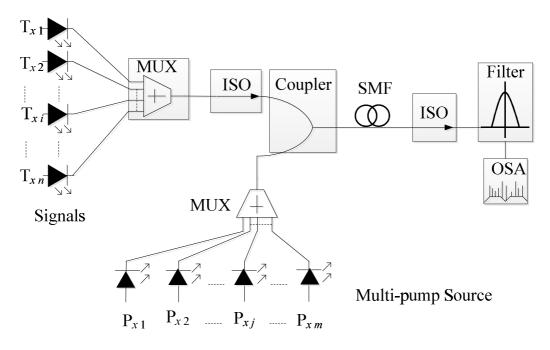
Introduction:

Undoubtedly the performance of optical amplifier is significant with respects of cost, energy consumption, signals quality, etc, for a high speed optical communication system. So far, erbium doped fiber amplifier (EDFA) has been still one of the most widely-used devices due to high gain and bandwidth. However, with huge traffic increase, the demand of users on bandwidth is rising astonishingly. As a substitute, fiber Raman Amplifier (FRA) is receiving much attention and has already been widely used in long distance large capacity transmission system recently because of a much broader and flatter bandwidth [1-4]. And the technology with multi-wavelength pump is widely used In order to get a more than 100 nm flat gain spectrum [5-7]. Some typical results such as ± 0.5 dB gain-flatness within 80 nm and ± 1 dB gain-flatness within 100 nm are presented in [8]. But its penalty is the huge complexity of the combination of genetic algorithm to determine the optimized parameters of pump sources. To improve it, the authors had taken some studies on gain-flatness of FRA through single-wavelength pump technology [9-10]. In this paper, with the premise of low complexity, the features of gain-flatness of a FRA system based multi-wavelength pump technology are investigated by simulation. And we then obtain about ±1 dB flatness in the range of 1512 nm~1566 nm by applying the optimized multi-pump sources in a dense wavelength division multiplexing system with 67 channels.

Model

Fig. 1 demonstrates a typical multi-wavelength fiber Raman amplifier system. It includes six parts: (1) signals, (2) gain fiber, (3) filter and isolator, (4) analyzer, (5) multi-pump source. As shown in Fig. 1, the signals (i.e. transmitters) is made from several DFB-type laser diodes which is denoted by Tx *i*, and the maximum of *i* is *n*. In this section, we set the n=6 and the interval of center wavelength for each laser diode is the same 10 nm which can cover the band of 1510 nm~1560 nm. Furthermore, we design the input power of Tx *i* is equal to -10 dBm. Then such six signals will be amplified in FRA after they go through multiplexer (MUX) and isolator (ISO). For FRA, we choose a 25km single mode fiber (SMF) as gain fiber and the energy of pump source will be transformed into the input signals in such SMF. Then the amplified signals go through ISO and optical Filter again. Finally, they are received by an optical spectrum analyzer (OSA) at output end. In our paper,

the key to get gain-flatness is the optimization of the pump source with multi-wavelength. It includes several DFB-type laser diodes with high output power. We denote each of them by Px *j*, where *j*=1, 2,..., *m*. And the corresponding center wavelengths are $\lambda_1, \lambda_2, ..., \lambda_m$, respectively. Our work then focuses on optimizing the parameters of multi-pump source in terms of wavelength and power (denoted by P_j).



Tx *i*: the *ith* Transmitter Px *j*: the *jth* Pump Sources

OSA: Optical Spectrum Analyzer SMF: Single Mode Fiber ISO: Isolator MUX: Multiplexer

Fig. 1 Experimental model of a FRA system based forward multi-pump

Simulation and Analysis

We define the fluctuation of gain spectrum is $\Delta G = G_{max} - G_{min}$, where G_{max} and G_{min} are the maximum and minimum of gain power, respectively. The average of gain-flatness is defined as $G_{ave} = \sum_{i=1}^{n} G_i / n$, where G_i is gain of the *ith* signal light. According to the aforementioned two parameters, we

where G_i is gain of the *ith* signal light. According to the aforementioned two parameters, we evaluate and optimized the gain-flatness of FRA by varying wavelengths and power of multi-pump source.

a. Dual-wavelength pump

In this situation, m=2. Aiming to get a gain-flatness spectrum, we adjust the power of wavelength of two laser diodes as pump. This process comprises four *Steps*. The parameters chosen and results on the gain of signals are shown in Table 1. From Table 1, we find the worst results occur in the case *Step* 1 and *Step* 3 in which the pump power of two laser diodes are the same and the values of ΔG reaches more than ± 2 dB. Comparatively, in *Step* 2 and *Step* 4, the unequal pump power is adopted and it brings an improvement on gain-flatness. From the obtained result in *Step* 4, the minimum ΔG by dual-wavelength pump will be about ± 1.25 dB in whole waveband. Honestly, such results on gain-flatness are not satisfied though the adjustment of tow pumps is easy to be achieved.

			Signals (nm)					
			1510	1520	1530	1540	1550	1560
Gain (dB)	Step 1	$\lambda_1 = 1420$ nm, $P_1 = 150$ mW, $\lambda_2 = 1440$ nm, $P_2 = 150$ mW	-1	-4	-0.5	-1	-5	0
	Step 2	$\lambda_1 = 1420$ nm, $P_1 = 160$ mW, $\lambda_2 = 1440$ nm, $P_2 = 150$ mW;	0.5	-1.5	-2	-1.5	-3.5	-1
	Step 3	$\lambda_1 = 1420$ nm, $P_1 = 150$ mW, $\lambda_2 = 1445$ nm, $P_2 = 150$ mW;	-0.5	-1	-1	-2	-4.5	-2
	Step 4	λ_1 = 1420nm, P_1 =168mW, λ_2 =1445nm, P_2 =158mW;	0	-0.5	-1	-0.5	-2.5	-0.5

Table 1 Gain with dual-wavelength pump

b. Triple-wavelength pump

In order to further improve gain-flatness, we add the third pump source in the FRA system and seek its optimized parameters in terms of power and wavelength. Specially, for comparison, we select the multi-pump source with the parameters (λ_1 =1415 nm, λ_2 =1425 nm, λ_3 =1435 nm, $P_1=P_2=P_3=100$ mW) as a baseline. In Fig. 2(a), we fix the pump wavelengths and keep the power of any two laser diodes, and observe the fluctuation of gain by varying the third pump power. A similar result with baseline is presented in the range of 1510 nm~1560 nm. By calculating, the value of ΔG maintains in the level of ±1 dB. Moreover, in Fig. 2(b), we vary the center wavelength of all three diodes under the condition $P_1=P_2=P_3=100$ mW and a different result on gain-flatness is shown. Compare to baseline, the flatness is improved about ±0.3 dB, especially in the field near 1560 nm. This result proves that both power and wavelength of multi-pump source have an effect on gain-flatness of FRA. But note that, the optimized interval of power and wavelength of pump source may be not uniform. It adds the designing complexity of the FRA system definitely.

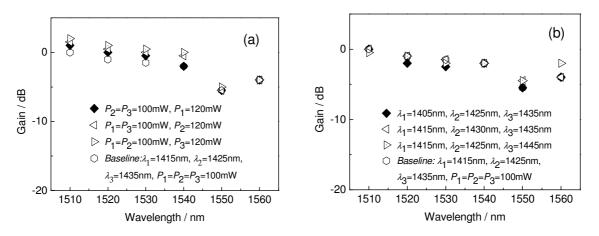


Fig. 2 Comparison on gain-flatness by triple-wavelength pump, (a) varying pump power, (b) varying pump wavelength

c. Quad-wavelength pump

Then, similar to triple-wavelength pump, we continue to add the fourth laser diode into pump source to improve gain-flatness of FRA. By adjusting the power and wavelengths of multi-pump source, two groups of parameters are obtained for the case m=3 and m=4, respectively (see Table 2).

And the numerical results on gain are also shown in Table 2. Comparatively, we find the better flatness takes place in the case of m=4 because the value of ΔG may be less than ± 0.5 dB. Nevertheless, it is clear that the optimized parameters of multi-pump source are gotten difficultly. In some lectures, more pump source in number is advised to flat the gain spectrum of FRA [11]. But in the authors eyes, from the point of view of application, m=4 is enough and advisable.

Signals	Gain (dB)		Ordinaired Demonstration	
(nm)	<i>m</i> =3	<i>m</i> =4	Optimized Parameters	
1510	0	0	1 1420 1 1424 1 1446	
1520	-0.5	0	$\lambda_1 = 1420 \text{ nm}, \lambda_2 = 1434 \text{ nm}, \lambda_3 = 1446 \text{ nm}, \lambda_3 = 1446 \text{ nm}, \lambda_4 = 1266 \text{ cm}, \lambda_5 = 1266 $	
1530	-0.5	-0.5	$P_{\lambda 1}$ =98.6mW, $P_{\lambda 2}$ =136.6mW, $P_{\lambda 3}$ =95.3mV	
1540	0	-1	λ_1 =1410 nm, λ_2 =1419 nm, λ_3 =1434 nm	
1550	-1	0	$m=4$ $\lambda_4=1452$ nm, $P_{\lambda 1}=50$ mW, $P_{\lambda 2}=90$ mW	
1560	-0.5	-0.5	$P_{\lambda 3}$ =100.82 mW, $P_{\lambda 4}$ =131.1 mW.	

Table 2 Comparison on gain-flatness between m=3 and m=4

Finally, we let the optimized FRA system with m=4 serve to a dense wavelength division multiplexing (DWDM) system with 67 channels and the interval is the same and equal to 0.8 nm. The gain spectrums of signals are then shown in Fig. 3. It is obvious that the worst gain-flatness is presented in Fig. 3(a) in which the FRA system is pumped by a single-wavelength laser diode (λ =1500nm, P=250mW). In contrast, when multi-wavelength pump (m=4) is adopted, the nature of gain-flatness is improved clearly within the band of 1512nm~1566.2nm (see Fig. 3(b) and (c)). Especially in Fig. 3(c), the value of both G_{max} and G_{min} are controlled in ±1 dB with the optimized parameters (λ_1 =1410 nm, λ_2 =1427 nm, λ_3 =1441 nm, λ_4 =1454 nm and the corresponding power are P_1 =141.8 mW, P_2 =76 mW, P_3 =81.8 mW, P_4 =160 mW).

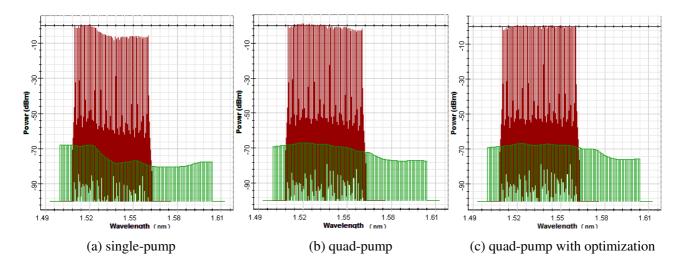


Fig. 3 Flatness improvement of FRA with *m*=4 in a DWDM case

Summary

In this paper, we develop a performance analysis of a FRA system with forward multi-wavelength pump on gain-flatness. According to gain-spectrum shown in OSA, we optimize the parameters in terms of power and wavelengths of multi-pump source. Simulation results show that the gain-flatness can be controlled within ± 1 dB by using our optimized quad-pump FRA system.

Acknowledgement

This work is supported by National Natural Science Foundation of China (61302075, 61205071, 61177079), Science Foundation of Heilongjiang Province of China (F201009), China Postdoctoral Science Foundation funded project (2012M520779).

- K. Rottwitt, H. Kidorf. A 92 nm Bandwidth Raman Amplifier[C]. IEEE/OSA OFC, Vol.1 (1997), PD 6.
- [2] H. Masuda, S. Kawai, K. Suzuki, et al. Wide-band and Low Noise Optical Amplification Using Distributed Raman Amplifiers and Erbium-Doped Fiber Amplifiers[C]. ECOC, Vol. 1(1998), p. 51-52.
- [3] A. C. Rasmussen, J. T. Fjeled, J Bennike, et al. DWDM 40G Transmission over Trans-Pacific Distance (10000km) Using CSRZ-DPSK, Enhanced FEC, and A Raman-Amplified 100-km Ultra-wave Fiber Spans[J]. Journal of Lightwave Technol., Vol. 22(2004), p. 203-207.
- [4] P. Xiao, Zeng Q, Huang J, et al. A New Optimal Algorithm for Multi-pump Sources of Distributed Fiber Raman Amplifier[J]. IEEE Photon. Technol. Lett., Vol. 15(2003), p. 206-208.
- [5] S. Cui, J. Liu, X. Ma. A Novel Efficient Optimal Design Method for Gain-flattened Multi-Wavelength Pumped Fiber Raman Amplifier[J]. IEEE Photon. Technol. Lett., Vol. 16(2004), p. 2451-2453.
- [6] S. Namiki, Y. Emori. Ultra Broad-band Raman Amplifier Pumped and Gain-equalized by Wavelength Division-multiplexed High-power Laser Diodes[J]. IEEE J on Selected Topics in Quantum Electronics, Vol. 7(2001), p. 3-16.
- [7] J. Zhou, J. Chen. Optimal Design of Raman Amplifier Pumped by Multi-wavelength Low Power Dioxides[J]. Journal of Optoelectronics Laser, Vol. 16(2005), p. 286-288, 293.
- [8] X. An. Analysis and Design of Multi-pumped Broadband Fiber Raman Amplifiers[D]. Beijing: Beijing Jiaotong University, 2011, p. 44-52.
- [9] L. Liu, Y. Ma, J. Yang. Performance Optimization based Spectrum Analysis on OFRA and EDFA Devices[J]. TELKOMNIKA, Vol.11 (2013), p. 3742-3749.
- [10] Y. Ma, Y. C. Li, C. Liu, J. R. Yang. A Flat Fiber Raman Amplifier by Optimizing a Single-Wavelength Laser Diode [C], ICEEIS, (2014), accepted.
- [11]B. Wu. The Computer Simulation and Research of Optical Fiber Raman Amplifier[D]. Shandong: Shandong University, 2005, p. 58-60.

CHAPTER 2:

Information Science and Information Technologies

Semantic Feature Modeling Based on the Decomposition of Feature Dependent Graph

Xue-Yao Gao^{1,a}, Chun-Xiang Zhang^{2,b} and Xiao-Yang Yu^{3,c}

¹School of Computer Science and Technology, Harbin University of Science and Technology, Harbin 150080, China

²School of Software, Harbin University of Science and Technology, Harbin 150080, China

³School of Measurement–Control Technology and Communications Engineering, Harbin University of Science and Technology, Harbin 150080, China

^agaoxueyao@hotmail.com, ^bz6c6x666@163.com, ^czcxbysj2006@aliyun.com

Keywords: Semantic feature modeling; geometric constraints; feature dependent graph

Abstract. Semantic feature modeling is an important research topic in CAD, in which geometric constraints in model are solved automatically. A semantic feature modeling method is given in this paper. Firstly, the feature dependent graph is built based on geometric constraints. Secondly, the feature dependent graph is decomposed according to the complexity of subgraphs and the whole problem of solving geometric constraints is divided into several small ones. Thirdly, these small problems are solved. At the same time, the modeling architecture based on the decomposition of feature dependent graph is given. Experimental results show that when the proposed method is applied, the modeling performance is improved.

Introduction

In semantic feature modeling, to solve geometric constraints between objects and parameters is an important problem. The task is always a topic for many researchers in CAD field. Shi investigates a united modeling method of the generalized geometric constraint system and codes it as a directed geometric constraint graph in a prototype system WhutVAS[1]. Cao proposes a novel network framework which combines the immune mechanism with the immune neural network for solving the geometric constraint problems. At the same time, the characteristic information of the problem is used and the transcendental knowledge is applied to simplify the network[2]. Michelucci gives a new method for detecting all dependencies between constraints based on the vector space of the free infinitesimal motions with a typical witness[3]. Then, these dependencies are used to decompose geometric constraints. Kale uses a graph-based constraint solving algorithm in CAD system. It is also called as the modified frontier algorithm with solution selection. In this research, he investigates whether the frontier algorithm can be extended to solve geometry positioning problems and inequality based declarations[4]. Hanniel gives a new method to construct global constraints on free-form curves in a constraint-based framework, in which sufficient conditions on the curves are defined in terms of an inequality expression [5]. Cao changes the constraint problem into an optimization problem and solves the problem with quantum particle swarm. At the same time, a novel quantum-behaved particle swarm optimization is presented[6]. Van Der Meiden gives a new constructive solving algorithm for systems of 3D geometric constraints based on the cluster rewriting approach, which rewrites a system of constraints with various internal degrees of freedom[7]. Zhang integrates the improved differential evolution algorithm and the multi-mutation competition algorithm to solve the geometric constraint optimization problem. Experimental results indicate that the searching ability and stability are very good[8]. Yuan gives a new method to solve geometric constraints which uses the genetic algorithm to search the area where the best solution may exist. At the same time, tabu search strategy is used to enhance the performance of the genetic algorithm[9]. He transforms the problem of solving geometric constraint into the problem of function optimization and the election-survey optimization algorithm is used to find the optimal result[10].

In this paper, a semantic feature modeling method is proposed where feature dependent graph is decomposed for solving geometric constraints. The whole problem of solving geometric constraints is divided into several small ones and the solving complexity is decreased. At the same time, the frame of the modeling system based on the decomposition of geometric constraint graphs is given. In experiments, an example modeled by the proposed method is given.

The Modeling Architecture Based on the Decomposition of Feature Dependent Graph

Feature dependent graph (FDG) is an acyclic digraph which describes all dependent relationships between features in a model. It is denoted as FDR=(E, R), where E={feature | feature \in model}, R \subseteq E×E\{(u, u) | u \in E}. In the feature dependent graph, the node is a feature in the model. FDG is used to decrease the complexity of solving geometric constraints in this paper. The modeling frame based on decomposing the feature dependent graph is shown in Fig. 1. The set of geometric constraints is input into feature dependent graph constructor. Feature dependent graph constructor builds FDG based on features and the relationships between features in geometric constraints. From FDG, the dependent degree between features can be computed, which is changed into the computation of the subgraph's complexity. If a subgraph has more nodes whose in-degrees and out-degrees are high, it is more complex. The complexity CP(g) of the subgraph g is computed as formula(1) described. Here, m is the number of nodes in g and the nodes of g are respectively n_1 , n_2 , ..., n_m . The deg (n_i) is the in-degrees of node n_i and deg (n_i) is the out-degrees of node n_i .

$$CP(g) = \frac{\sum_{i=1}^{m} \deg_{-}(n_{i}) + \deg_{+}(n_{i})}{m}$$
(1)

Feature dependent graph decomposer breaks the FDG into several parts and makes the complexity of every subgraph highest. In this kind of subgraphs, dependent relationships between nodes are strong. It means that when a feature correspondent to a node is edited, features correspondent to other nodes in this subgraph are influenced. But features correspondent to nodes which are not in this subgraph will be not influenced. Then, the set of simple feature dependent graphs are gotten. Geometric constraint solver divides the set of geometric constraints into several subsets based on the set of simple feature dependent graphs. A subset of geometric constraints corresponds with a simple feature dependent subgraph. Geometric constraint solver will solve every subset of geometric constraints and give their solutions.

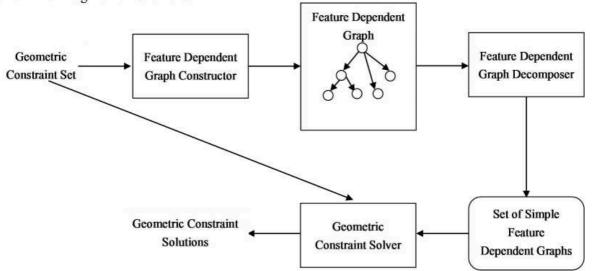


Fig. 1. The modeling frame based on decomposing geometric constraint graphs

The Process of Semantic Feature Modeling

In the modeling process, the user input all geometric constraints. In geometric constraints, features and relationships between features are given. Because the 3D modeling problem is very complex, there are always many features in a geometric constraint. In order to simplify the modeling process, a geometric constraint including many features will be rewritten into some constraints in which 2 features are only included. Then the geometric constraint set is gotten. Feature dependent graph is built. After that, the feature dependent graph is decomposed into subgraphs according to formula(1). The geometric constraint set is divided into several parts according to these feature dependent subgraphs. The size of geometric constraints correspondent to a feature dependent subgraph will be small and the solving complexity becomes decreased. The problem of solving geometric constraints is changed into several small problems. The subset of geometric constraints is corresponded with a group of algebraic equations. The newton iteration method is used to solve every group of algebraic equations are gotten. When all groups of algebraic equations are solved, their solutions are combined. Then, the solutions of geometric constraints in the whole model will be gotten.

Experiments

In order to evaluate the performance of the proposed method in this paper, experiments have been conducted. We apply the proposed method to a computer-aided design system HUST-CAID developed by Harbin University of Science and Technology. In this system, we input all geometric constraints in interfaces. These geometric constraints are described that there are two slots in the model. They are respectively slot1 and slot2. These two slots are created in base block. A tube is located on slot2. At the same time, the tube is not intersected with slot1. The system will solve these geometric constraints as described in Fig. 1 and the solutions are gotten. Then the model is built according to the solutions. Fig.2 shows the result model.

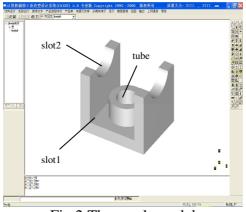


Fig.2 The result model

Conclusions

In this paper, a new semantic feature modeling method based on the decomposition of feature dependent graph is proposed. The method has been applied to HUST-CAID system. In the modeling system, the user input all geometric constraints. The feature dependent graph is built based on these geometric constraints. Then the feature dependent graph is divided into many small subgraphs. At the same time, these geometric constraints correspondent to every subgraph are solved. After that, all solutions are combined and the result model is built. Experimental results show that the modeling performance is increased.

Acknowledgments

This work is supported by Science and Technology Research Funds of Education Department in Heilongjiang Province under Grant Nos. 12511095.

- [1] Zhiliang Shi, Zhongquan Zhang and Yi Chen. A united modeling method of generalized geometric constraint system. In Proceedings of the 3rd International Conference on Intelligent System Design and Engineering Applications. 2013: 204~208.
- [2] Chunhong Cao, Bin Zhang, Limin Wang and Wenhui Li. On geometric constraint solving based on the immune neural network. In Proceedings of the 27th Chinese Control Conference. 2008: 536~540.
- [3] Dominique Michelucci and Sebti Foufou. Interrogating witnesses for geometric constraint solving. In Proceedings of SPM 2009 SIAM/ACM Joint Conference on Geometric and Physical Modeling. 2009: 343~348.
- [4] Vaibhav Kale, Vikram Bapat and Bernie Bettig. Geometric constraint solving with solution selectors. In Proceedings of the ASME International Design Engineering Technical Conferences and Computers and Information in Engineering Conference. 2009: 353~365.
- [5] Iddo Hanniel and Kirk Haller. Solving global geometric constraints on free-form curves. In Proceedings of SPM 2009 SIAM/ACM Joint Conference on Geometric and Physical Modeling. 2009: 307~312.
- [6] Chunhong Cao, Limin Wang and Wenhui Li. The geometric constraint solving based on the quantum particle swarm. In Proceedings of the 5th International Conference RSKT. 2010: 582~587.
- [7] Hilderick A Van Der Meiden. Solving systems of 3D geometric constraints with non-rigid clusters. In Proceedings of the 2008 Advances in Geometric Modeling and Processing. 2008: 423~436.
- [8] Youhua Zhang, Kunqi Liu and Gang Liu. A concurrent-hybrid evolutionary algorithm for geometric constraint solving. In Proceedings of Computational Intelligence and Intelligent Systems. 2010: 1~10.
- [9] Hua Yuan and Chunjiang Yu. Optimization genetic algorithm for geometric constraint solving. In Proceedings of 2010 International Conference on Artificial Intelligence and Education. 2010: 590~593.
- [10] Chunhua He, Xiangwei Zhang and Wenge Lv. A new approach for solving geometric constraint based on election-survey algorithm. In Proceedings of 2010 International Conference on Computer, Mechatronics, Control and Electronic Engineering. 2010: 427~430.

Word Sense Disambiguation for Improving the Quality of Machine Translation

Chun-Xiang Zhang^{1,a}, Long Deng^{2,b}, Xue-Yao Gao^{2,c} and Li-Li Guo^{3,d}

¹School of Software, Harbin University of Science and Technology, Harbin 150080, China

²School of Computer Science and Technology, Harbin University of Science and Technology, Harbin 150080, China

³College of Information and Communication Engineering, Harbin Engineering University, Harbin 150001, China

^az6c6x666@163.com, ^bwudixihalong@163.com, ^cgaoxueyao@hotmail.com, ^dguolili@hrb.cdu.cn

Keywords: machine translation; output translation; classification labels; translation quality

Abstract. Word sense disambiguation is key to many application problems in natural language processing. In this paper, a specific classifier of word sense disambiguation is introduced into machine translation system in order to improve the quality of the output translation. Firstly, translation of ambiguous word is deleted from machine translation of Chinese sentence. Secondly, ambiguous word is disambiguated and the classification labels are translations of ambiguous word. Thirdly, these two translations are combined. 50 Chinese sentences including ambiguous words are collected for test experiments. Experimental results show that the translation quality is improved after the proposed method is applied.

Introduction

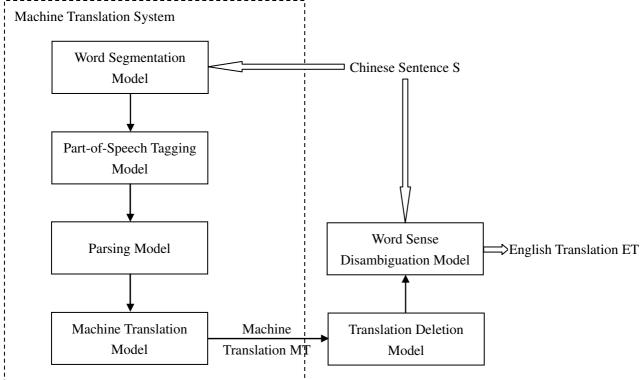
Word sense disambiguation is an important problem in natural language processing, in which a correct sense of a word is determined in a sentence when it has multiple meanings. The task is always a topic for many researchers. Prokofyev proposes a semi-supervised method of word sense disambiguation, in which the graph structure that connects different terms and their definitions is used to identify the correct sense[1]. Experimental results show that the proposed method's performance outperforms state-of-the-art approaches based on term co-occurrences. Li identifies the optimal local context window for word and part of speech separately. At the same time, an experiment is conducted on Senseval-3 Chinese data set. The experiments show that when the gap is smaller, the performance is better[2]. Wimmer uses social media as a dynamic context for word sense disambiguation and gives the preliminary evidence for the efficacy of the proposed method[3]. Broda does some experiments of word sense disambiguation with 6 clustering algorithms in order to evaluate their performances. The experiments show that the precision of the best clustering algorithm is close to that of the supervised method on the same data set[4]. Diego adapts the PageRank algorithm to finish the task of word sense disambiguation. It preserves the disambiguation accuracy and reduces the high computational time[5]. At the same time, experimental analysis over well-known benchmarks is given. Szumlanski uses lexical co-occurrences in Wikipedia to evaluate the network of semantically related noun senses and concepts. When semantical networks are built, the metadata and links from the encyclopedia are not needed. The inventory of WordNet3.0 is only used[6]. Zhong estimates sense distributions for short queries and incorporates word senses of the documents into the language modeling approach for IR. Experimental results show that the improvements over a state-of-the-art IR system are obtained on standard TREC collections[7]. Aung solves the ambiguity of Myanmar words for Myanmar-English machine translation, in which the nearest neighbor cosine classifier is used to finish the task of word sense disambiguation with part-of-speech and co-occurring words[8]. Chan integrates a word sense disambiguation model into Hiero which is a phrase-based machine translation system. The experiments show that the performance of statistical machine translation systems is improved when all senses of ambiguous

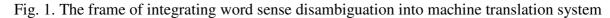
words are determined[9]. Carpuat finishes a task of multi-word disambiguation with a new strategy in a statistical machine translation system and redefines the task of word sense disambiguation[10].

In this paper, word sense disambiguation is used as the post-processing step of machine translation system. At the same time, the architecture of machine translation based on word sense disambiguation is given. The quality of the output translation is improved after the new method is used.

The Architecture of Machine Translation Based on Word Sense Disambiguation

Ambiguity is an important phenomenon in Chinese. In Chinese dictionary, 14.8 percent of words are ambiguous. Although the number of ambiguous words is little, they are always common words and occur frequently in corpus. In machine translation system, the translation of ambiguous words is a difficult task, which influences the output translation. For example, Chinese word 'da' is an ambiguous word. When it is labeled as a verb, there are two kinds of senses. One is 'play' and the other is 'hit'. Chinese sentence including word 'da' is input into machine translation system, in which the dictionary is used. In dictionary entry of word 'da', the translation 'play' is located before the translation 'hit'. So, word 'da' is always translated into 'play'. Sometimes they are correct and sometimes they are incorrect. Here, we use the technology of word sense disambiguation to select senses of ambiguous words in machine translation. The process of integrating word sense disambiguation into machine translation system is shown in Fig. 1.





In machine translation system, there are four models including word segmentation model, part-of-speech tagging model, parsing model and machine translation model. After Chinese sentence S including polysemous words is processed step by step with these four models, its machine translation MT is obtained. Because it is difficult to translate polysemous words, machine translation MT of Chinese sentence S is transferred to the translation deletion model. Translations of Chinese ambiguous words are deleted from machine translation MT and MT is gotten. At the same time, polysemous words in Chinese sentence S are processed in word sense disambiguation model and correct senses are selected based on its context. After MT is combined with the correct translation of the polysemous word, English translation ET is obtained.

The Process of Translation Based on Disambiguation

For Chinese sentence $S=c_1, c_2, ..., c_m, c_i$ is a polysemous word. After S is translated by machine translation system, its machine translation MT is gotten. For $MT=e_1, e_2, ..., e_n$, string $PT=e_1, ..., e_k$ is machine translation of c_i . Maybe, j equals to k. String PT is deleted from MT and string MT = $e_1, ...,$ $e_{i-1}, e_{k+1}, \ldots, e_n$ is obtained.

Chinese sentence $S=c_1, c_2, ..., c_m$ is input into word sense disambiguation model. Chinese word c_i is disambiguated based on its context. The contexts are string $CT_1=c_1, \ldots, c_{i-1}$ and string $CT_2=c_{i+1}, \ldots, c_{i-1}$ $c_{\rm m}$. Based on CT₁ and CT₂, the classifier of word sense disambiguation is used to select the correct sense of Chinese word c_i . Here, a specific classifier is used. When the classifier is built, the machine translation dictionary is used. For ambiguous word c_i , a disambiguation classifier is constructed. The classification labels are its translation in machine translation dictionary. If there are three kinds of English translations $WT_1=e_{11}, e_{12}, ..., e_{1p}, WT_2=e_{21}, e_{22}, ..., e_{2q}$, and $WT_3=e_{31}, e_{32}, ..., e_{3r}$, the classification labels of the disambiguation classifier are 3. Here, $WT_2=e_{21}, e_{22}, \dots, e_{2q}$ is selected as the sense of word c_i .

The combination of translations is shown in Fig. 2. The combination process is satisfied with a large of language phenomenon. But there are few Chinese words, their English translations are strings whose words are not continuous. For example, Chinese word 'zhi fu' has an English translation 'bring ... under control'. According to translations, we get these Chinese ambiguous words from machine translation dictionary and process these special language phenomena.

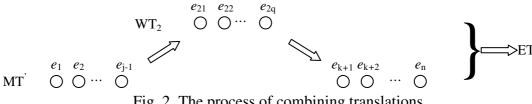


Fig. 2. The process of combining translations

Experiments

In order to evaluate the proposed method, 50 Chinese sentences including polysemous word 'da' are collected. Two groups of experiments are conducted. In experiment 1, these 50 Chinese sentences are translated by machine translation system. In experiment 2, the proposed method is used. These 50 Chinese sentences are translated into English and polysemous word 'da' in every sentence is disambiguated based on its context. Two human annotators evaluate the output translation. The evaluation grades are respectively A, B, C and D. If the translation is fluent and there is no error, it is evaluated as A. If the translation expresses meanings of Chinese sentence and there are few errors, it is evaluated as B. If the translation expresses basic meanings of Chinese sentence and there are lots of errors, it is evaluated as C. If the translation does not express meanings of Chinese sentence, it is evaluated as D. The evaluation results of two experiments are shown in Table 1. From Table 1, we can find that the performance of experiment 2 surpasses that of experiment 1. In experiment 2, the number of English translations evaluated as A, B and C is improved. The translation quality is increased.

	А	В	С	D
Experiment 1	7	5	11	27
Experiment 2	10	7	18	15

Table 1. The evaluation results in two experiments

Conclusions

In this paper, a new method of integrating word sense disambiguation into machine translation is proposed. The frame of machine translation based on word sense disambiguation is described. 50 Chinese sentences including ambiguous words are collected and comparative experiments are

conducted. Experimental results show that the proposed method can improve the translation quality of machine translation system.

Acknowledgments

This work is supported by Science and Technology Research Funds of Education Department in Heilongjiang Province under Grant Nos. 12531106.

- Roman Prokofyev, Gianluca Demartini and Alexey Boyarsky. Ontology-based word sense disambiguation for scientific literature. In Proceedings of the 35th European Conference on IR Research. 2013: 594~605.
- [2] Gang Li, Guangzeng Kou and Ercui Zhou. Symmetric trends: optimal local context window in chinese word sense disambiguation. In Proceedings of the 9th International Conference on Hybrid Intelligent Systems. 2009: 151~154.
- [3] Hayden Wimmer and Lina Zhou. Word sense disambiguation for ontology learning. In Proceedings of the 19th Americas Conference on Information Systems. 2013: 4036~4045.
- [4] Bartosz Broda and Wojciech Mazur. Evaluation of clustering algorithms for Polish word sense disambiguation. In Proceedings of the International Multiconference on Computer Science and Information Technology. 2010: 25~32.
- [5] De Cao Diego, Basili Roberto and Luciani Matteo. Robust and efficient page rank for word sense disambiguation. In Proceedings of 2010 Workshop on Graph-Based Methods for Natural Language Processing. 2010: 24~32.
- [6] Sean Szumlanski and Fernando Gomez. Evaluating a semantic network automatically constructed from lexical co-occurrence on a word sense disambiguation task. In Proceedings of Fifteenth Conference on Computational Natural Language Learning. 2011: 190~199.
- [7] Zhi Zhong and Hwee Tou Ng. Word sense disambiguation improves information retrieval. In Proceedings of the 50th Annual Meeting of the Association for Computational Linguistics. 2012: 273~282.
- [8] Nyein Thwet Thwet Aung and Ni Lar Thein. Word sense disambiguation system for Myanmar word in support of Myanmar-English machine translation. In Proceedings of the SICE Annual Conference. 2011: 2835~2840.
- [9] Yee Seng Chan, Hwee Tou Ng and David Chiang. Word sense disambiguation improves statistical machine translation. In Proceedings of the 45th Annual Meeting of the Association for Computational Linguistics. 2007: 33~40.
- [10] Marine Carpuat and Dekai Wu. Improving statistical machine translation using word sense disambiguation. In Proceedings of the 2007 Joint Conference on Empirical Methods in Natural Language Processing and Computational Natural Language Learning. 2007: 61~72.

Word Sense Disambiguation Based on Center Window

Chun-Xiang Zhang^{1,2,a}, Li-Li Guo^{1,b} and Xue-Yao Gao^{3,c}

¹College of Information and Communication Engineering, Harbin Engineering University, Harbin 150001, China

²School of Software, Harbin University of Science and Technology, Harbin 150080, China

³School of Computer Science and Technology, Harbin University of Science and Technology, Harbin 150080

^az6c6x666@163.com, ^bguolili@hrb.cdu.cn, ^cgaoxueyao@hotmail.com

Keywords: Natural language processing; center window; ambiguous word; accuracy rate

Abstract. Word sense disambiguation is widely applied to information retrieval, semantic comprehension and automatic summarization. It is an important research problem in natural language processing. In this paper, the center window is determined from the target ambiguous word. The words in the center window are extracted as discriminative features. At the same time, a new method of word sense disambiguation is proposed and the disambiguation classifier is given. The classifier is optimized and tested on SemEval-2007 #Task5 corpus. Experimental results show that the accuracy rate of disambiguation arrives at 64.2%.

Introduction

Today, the task of automatically determining the correct sense of a polysemous word has remained a challenge. Wang applies the exponential kernel to word sense disambiguation, which models semantic similarity by means of a diffusion process on a graph defined by lexicon and co-occurrence information[1]. Raviv introduces the method of concept-based disambiguation. It is a novel framework that utilizes recent semantic analysis techniques to represent both the context of the word and its senses in a high-dimensional space of natural concepts. The concepts are retrieved from a vast encyclopedic resource and more comprehensive measures can be applied in order to pick the right sense^[2]. Hulpus gives a HITS-inspired method that attempts to optimize the score for the entire sense combination rather than one word at a time[3]. Li proposes a new method of feature selection and initial parameter estimation, which is applied to reduce the noise jamming and the dimensionality of the models in order to solve the problem of supervised learning that sense-tagged text is not available for most domains and is expensive to create[4]. Akkaya investigates firstly methods to utilize it to improve word sense discrimination and word sense disambiguation. He relies on a previously proposed multiplicative model of composition to extend this model in order to exploit richer contexts. Context vectors are built from the word representations based on the extended compositional model[5]. Kobylinski presents a new method of improving the results of word sense disambiguation by generalizing nouns appearing in a disambiguated context to concepts, in which the corpus-based semantic similarity function is used, by substituting appearances of particular nouns with a set of the most closely related similar words[6]. Pohl uses Jaccard coefficient inspired measure and takes into account additional features in word sense disambiguation. Its performance is improved[7]. Naskar gives an extended WordNet for disambiguating nouns, verbs and adjectives based on word sense disambiguation algorithm. The algorithm is to find overlaps between the context of a word in a sentence and contexts constructed from the WordNet[8]. Yu uses information gain to calculate the weight of different position's context, which affects the performance of word sense disambiguation. The ahead and back six position's context of ambiguous words are extracted as the feature vectors. The feature vectors are endued with different value of weight in bayesian model[9]. Fan presents a word sense disambiguation method in which the context of an ambigous word is reconstructed based on the correlation between words[10].

In this paper, left word and right word around the target ambiguous word is viewed as the center window. The center window is extracted as discriminative features. The bayesian model is used to build the classifier of word sense disambiguation.

The Center Window of Word Sense Disambiguation

The frame of extracting the center window is shown in Fig. 1. There are two steps for extracting the center window.

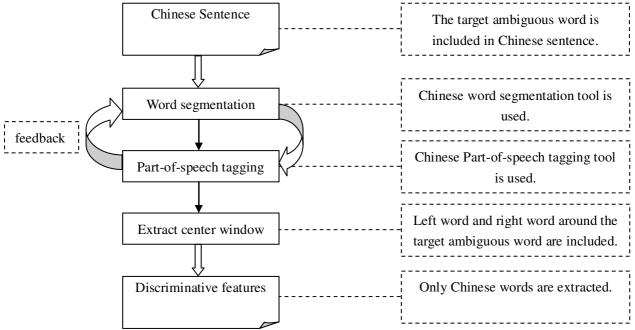


Fig. 1. The frame of extracting the center window

Firstly, Chinese sentence including the target polysemous word is segmented into words by Chinese word segmentation tool. This is because that there are no blanks between Chinese words, from which any discriminative features can not be acquired. Secondly, every Chinese word is tagged with its syntax tag by Chinese part-of-speech tagging tool. There are ambigous phenomena in natural language including Chinese. The results of word segmentation may be uncertain. Part-of-speech tagging may be also uncertain. But there are some information in part-of-speech tagging which can help to correct errors in results of word segmentation. So, there are feedbacks which start from part-of-speech tagging results to Chinese word segmentation tool in Fig. 1. After several iterations, the performance of word segmentation is better and its results can be used to extract the center window. The center window only contains the left words and the right words around the target polysemous word. If the size of center window is larger, it will provide more discriminative information for word sense disambiguation. However, there are data sparse problem in natural language. Although some language phenomena are very important, the probability that they occur is low. This is because that we could not collect enough data for this language phenomenon. If these features are used to build the disambiguation model, the performance of word sense disambiguation will be decreased. So, we can often find that although more word units are selected, the classification performance is low. In this paper, the left word and the right word around the target polysemous word are selected as the center window, which can decrease the effect of data sparsity and provide more discriminative information. Maybe, it is a tradeoff. After the center window is determined, the words are selected as discriminative features. Other factors are not considered.

For the following Chinese sentence in which ambiguity word 'meng2' is included, the process of extracting the center window is shown as follows:

Chinese sentence: zuo4 an4 ren2 meng2 zhe1 mian4 pao2 le1.

Word segmentation: zuo4 an4 ren2/ meng2/ zhe1/ mian4/ pao2/ le1/ ./

Part-of-speech tagging: zuo4 an4 ren2/ng meng2/vg zhe1/used mian4/ng pao2/vg le1/y ./wj

Center window: zhe1+pao2

Here, 'meng2' is an ambiguity word. Its left Chinese word is zhe1. Its part-of-speech is 'used' which means that Chinese word zhe1 is an auxiliary verb. Its right Chinese word is pao2. Its part-of-speech is 'vg' which means that Chinese word pao2 is a verb. The center window contains Chinese word zhe1 and Chinese word pao2. Theses two Chinese words are used for word sense disambiguation.

The Classifier of Word Sense Disambiguation

The idea of a bayesian classifier is that the role of a class is to predict the values of features for members of that class. It means that if we know the class, we can predict the values of other features. We can build a probabilistic model of the features and use it to predict the classification of a new example. The bayesian model is adopted to build the classifier of word sense disambiguation, in which the left word and the right word around the target polysemous word are used as discriminative features. The discriminative model is shown in formula (1).

$$S = \underset{i=1,2,\dots,m}{\operatorname{arg\,max}} P(S_i \mid w_l, w_r)$$

$$\approx \underset{i=1,2,\dots,m}{\operatorname{arg\,max}} P(w_l, w_r \mid S_i) \cdot P(S_i)$$

$$\approx \underset{i=1,2,\dots,m}{\operatorname{arg\,max}} P(w_l \mid S_i) \cdot P(w_r \mid S_i) \cdot P(S_i)$$
(1)

There are two parameters in models which are class priors and feature probability distributions. The class prior is $P(S_i)$ (*i*=1, 2, ..., m). Feature probability distributions are $P(w_l|S_i)$ (*i*=1, 2, ..., m) and $P(w_r|S_i)$ (*i*=1, 2, ..., m). They can be approximated with relative frequencies from the training set. The principle of maximum likelihood is used to estimate these two parameters. Then the optimized classifier is used to determinate the correct sense of the target polysemous word.

Experiments

In order to evaluate the performance of the proposed method in this paper, an experiment is conducted, in which SemEval-2007 #Task5 is used as training corpus and test corpus. 39 Chinese sentences including polysemous word 'qi4 xi1' have been collected as training corpus and 14 Chinese sentences including polysemous word 'qi4 xi1' have been collected as test corpus. Firstly, they are segmented into Chinese words. Secondly, every word is labeled with its part-of-speech. Word segmentation tool and part-of-speech tagging tool are developed by Ministry of Education-Microsoft Key Laboratory of Natural Language Processing and Speech in Harbin Institute of Technology. Two human annotators are asked to manually annotate semantic categories of the ambiguous word 'qi4 xi1' according to TongYiCi CiLin. The bayesian classifier is trained as shown in formula (1) on the training corpus. Then the optimized classifier is used to classify the test corpus. We use accuracy to evaluate the performance of the optimized classifier. Its performance is shown in Table 1. Its accuracy is 64.2%.

Name of classifier	Accuracy(%)
Bayesian classifier	64.2%

 Table 1. The performance of the classifier on test corpus

Conclusions

In this paper, the method for finding the center window of the target polysemous word is given. Discriminative features are extracted form the center window and Chinese words are only selected. Based on the center window, the bayesian model is used to build the disambiguation classifier. SemEval-2007 #Task5 is applied to train and test the classifier. Experimental results show that the accuracy of the optimized classifier is 64.2%.

Acknowledgments

This work is supported by Science and Technology Research Funds of Education Department in Heilongjiang Province under Grant Nos. 12531106 and National Natural Science Foundation of China under Grant Nos. 61103149.

- [1] Tinghua Wang, Junyang Rao and Dongyan Zhao. Using exponential kernel for word sense disambiguation. In Proceedings of the 23rd International Conference on Artificial Neural Networks. 2013: 545~552.
- [2] Ariel Raviv and Shaul Markovitch. Concept-based approach to word-sense disambiguation. In Proceedings of the 26th AAAI Conference on Artificial Intelligence and the 24th Innovative Applications of Artificial Intelligence Conference. 2012: 807~813.
- [3] Ioana Hulpus and Conor Hayes. An eigenvalue-based measure for word-sense disambiguation. In Proceedings of the 25th International Florida Artificial Intelligence Research Society Conference. 2012: 226~231.
- [4] Xu Li, Xiuyan Zhao and Fenglong Fan. An improved unsupervised learning probabilistic model of word sense disambiguation. In Proceedings of the 2012 World Congress on Information and Communication Technologies. 2012: 1071~1075.
- [5] Cem Akkaya, Janyce Wiebe and Rada Mihalcea. Utilizing semantic composition in distributional semantic models for word sense discrimination and word sense disambiguation. In Proceedings of IEEE 6th International Conference on Semantic Computing. 2012: 45~51.
- [6] Lstrok Ukasz Kobylinski and Mateusz Kopec. Semantic similarity functions in word sense disambiguation. In Proceedings of the 15th International Conference on Text, Speech and Dialogue. 2012: 31~38.
- [7] Aleksander Pohl. Improving the Wikipedia Miner word sense disambiguation algorithm. In Proceedings of the 2012 Federated Conference on Computer Science and Information Systems. 2012: 241~248.
- [8] Sudip Kumar Naskar and Sivaji Bandyopadhyay. Word sense disambiguation using extended WordNet. In Proceedings of International Conference on Computing: Theory and Applications. 2007: 446~450.
- [9] Zhengtao Yu, Bin Deng and Bo Hou. Word sense disambiguation based on Bayes model and information gain. In Proceedings of the 2nd International Conference on Future Generation Communication and Networking. 2008: 153~157.
- [10]Xinhua Fan, Bingjun Zhang and Dong Zhou. A word sense disambiguation method based on reconstruction of context by correlation. In Proceedings of the 2011 WASE Global Conference on Science Engineering. 2012: 160~166.

Nipdroid: an enhanced detection mechanism for Android IPC

Chen Chen^{1,a}, Jiaxing Song^{1,b} and Weidong Liu^{1,c}

¹Department of Computer Science and Technology, Tsinghua University, Beijing, China ^aallanchen007@163.com, ^bjxsong@tsinghua.edu.cn, ^cliuwd@tsinghua.edu.cn

Keywords: Android, IPC, enhanced detection

Abstract. As one of the most popular mobile operating system, Android has been troubled by privilege escalation attacks. This is because that the original Android ignores the inspection of transmitted data in *intent*. It only checks the permission of *intent* to determine whether the Inter-Process Communication (IPC) could continue. We developed Nipdroid to solve the mentioned defect in Android IPC detection. Nipdroid is based on the technology of marking and tracking sensitive data. After the original Android detection, Nipdroid extracts the sensitive tags from *intent*, and matches them with the permission lists of both communication apps, and then checks whether there is unreasonable data transmission in IPC. Experiments show that Nipdroid is effective on both preventing privilege escalation attacks and protecting user's sensitive data.

Introduction

Since Android appeared, its characteristics of open source have won the favor of numerous users. Android is quickly beyond iOS and Symbian, and becomes the mobile OS with the most market share. Meanwhile, the powerful development technical support and the lax censorship of Android Market breed a large number of non-standard apps. They apply for permissions excessively and expose sensitive interfaces. Malicious attackers can make use of the non-standard apps or sign up to develop malicious apps to steal user's sensitive data through privilege escalation attacks.

We studied *binder* which is the mechanism used in Android IPC, and analyzed the four types of communication in *binder*, and then developed Nipdroid in order to solve the defect that Android lacks the ability to prevent privilege escalation attacks. Nipdroid extracts the sensitive tags from *intent*, and matches them with the permission lists of both communication apps, and then checks whether there is unreasonable data transmission in IPC. Nipdroid can prevent privilege escalation attacks and protect user's sensitive data.

As the implementation, we deployed Nipdroid on Android with Taintdroid [1]. Experiments show that Nipdroid captures all sensitive tags in IPC with a low rate of false positives. The performance overhead imposed by Nipdroid is below human perception and the user will not notice any performance delays.

Related Works

Access control mechanism of Android mainly focuses on the middleware layer. During IPC, *ActivityManager* manages the lifecycle of applications, and verifies whether the caller has requested permissions to access target object. The security enhancement of Android framework layer mainly depends on the improvement of *PackageManager* and *ActivityManager*.

XMandroid [2] is based on Android permission mechanism. It develops IPC strategies to implement communication data isolation. But it uses the one-size-fits-all method on strategy

formulation which leads to a higher rate of false positives. Quire [3] provides a lightweight system in order to prevent privilege escalation attacks. Quire solves the vulnerable trust interface issues which easily exploited by privilege escalation attacks. But it can't prevent coordinated attacks caused by malware. Apex [4] allows the user to manually selectively grant and deny permissions requested by applications at install-time. Unfortunately, it fully depends on users to take security decisions, so it may cause application crash. Moreover, privilege escalation attacks where permissions are split over multiple applications are not addressed by Apex. Taintdroid provides system-wide dynamic taint tracking for Android and detects unauthorized leakage of sensitive data. However, it only has monitoring function, and lacks of control measures.

Except for the dynamic solutions mentioned above, there are also some static solutions, such as Comdroid [5],SCandroid [6] and Saint [7].But these static analysis solutions are likely to be incomplete, because they cannot completely predict the actual application communication that will occur at runtime.

To summarize, existing security extensions for Android do not provide universal solutions against all kinds of security threats. These representative research results, to a great extent, improve the Android security mechanism. But, there is no ideal solution to address privilege escalation attacks.

Defect of Access Control Mechanism

Android uses a component-based model which provides convenience for application development. But it also brings some security issues. Malicious attackers can get dangerous permissions and obtain user's sensitive information by combining multiple applications or using exposed interfaces in other applications. In general, such attacks exist in Android system programs and third-party apps. Fig.1 shows a typical privilege escalation attacks: application A indirect accesses the system resource C through application B.

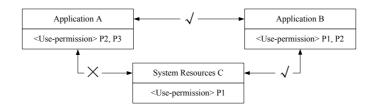


Fig. 1: Privilege escalation attacks

Inter-Components Communication (ICC) which is based on *binder* mechanism is the main form of Android IPC. Application initiates ICC and sends *intent*, the structure of *intent* is described in Fig.2. The *intent* contains transmitted data, required permissions, process id and user id. During ICC, *ActivityManager* checks required permissions, but it ignores the inspection of transmitted data in *intent*. Malicious attacker could make use of this defect, and combine multiple applications into a logical application to complete the attack.



Fig. 2: The intent in ICC

Nipdroid is based on the technology of marking and tracking sensitive data offered by Taintdroid. It exploits the adjacent store properties of Dalvik and inserts a 32-bit tag behind the 32-bit sensitive data. Sensitive data and tag are classified as a group. The transfer of sensitive tags start from the data source, after several applications, eventually arrives at the destination. During the whole process, tags are transmitted in the same time with sensitive dates.

Nipdroid

ICC Procedure with Nipdroid. We have modified the original Android ICC procedure, add Nipdroid to check the sensitive data transmission in ICC. Fig.3 describes the new ICC procedure in brief.

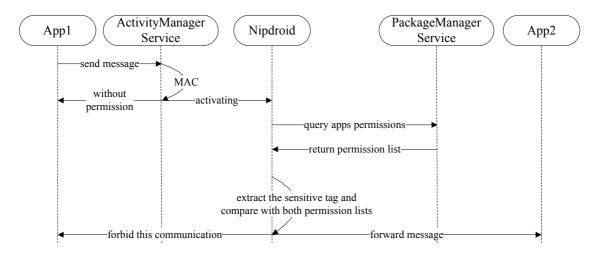


Fig. 3: ICC procedure with Nipdroid

As shown in Fig.3, when the app1 sends a request message (such as calling Activity request, sending broadcast information request, etc), *ActivityManager* parses out relevant information from the message (such as message type, object, and permissions, etc). First of all, *ActivityManager* compares required permissions in the message with the caller's permission list. If it finds out that the caller doesn't have the corresponding permissions, it throws an exception and returns. Otherwise, Nipdroid will be activated. Firstly, Nipdroid collects relevant information including caller UID, target object UID and *intent* object. Secondly, it inquiries *PackageManager* to obtain permission lists of both the caller and target object, and parses message to extract sensitive tag. Finally, Nipdroid compares sensitive tag with permission list, and estimates whether there is unreasonable transmission.

Information Collection Procedure. ICC is based on *binder* mechanism in Android [8]. *Binder* with distributed component architecture provides RPC function. All objects based on *binder* for transmission must implement *Parcelable* interface. It converts transmitted data to a serialization format called *Parcel*. Nipdroid modifies *Parcel* class in order to parse out the sensitive tag from *Parcel*.

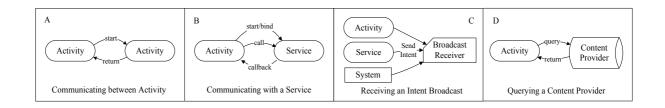


Fig. 4:ICC types in Android

As shown in Fig.4, there are four types of ICC in Android. We analyze each type of communication, and place monitoring function at different locations in order to monitor ICC.

A. We place monitoring function in *ActivityStack.startActivityLocked*. After ICC passed the original detection, the monitoring function is activated. It is responsible for collecting relevant information for the next operation. It fetches out target UID from *intent*, and obtains calling UID by *binder.getCallingUid*. According to UID, it obtains permission list from *PackageManager*. Then it calls permission comparison function in *PackageManager* to execute the next operation.

B. There are two kinds of communication between activity and service. One is *startService*, and the other one is *bindService*. In *startService*, we place monitoring function in *ActivityManagerService.startServiceLocked*. In *bindService*, we place monitoring function in *ActivityManagerService.bindService*. The rest of the operations are similar to A.

C. We place monitoring function in *ActivityManagerService.broadcastIntentLocked* for broadcast. In Broadcast, there are two kinds of broadcast receivers, specific receiver and interested receivers. For the specific receiver, we obtain the receiver information according to component attribute values of *intent*. For the interested receivers, we need to estimate each receiver in the receiver list. We filter out the unreasonable receives, and remove them from the receiver list.

D. Android use anonymous shared memory approach to query *ContentProvider*. In this case, it is difficult to parse sensitive tag directly from the *Parcel*. As an alternative, we parse the *cursor* generated by querying *ContentProvider*. We use relevant *cursor* function to obtain the elements contains sensitive tags from *cursor*, and then extract sensitive tags from the elements. However, the efficiency for extracting tag from *cursor* is poorer than from *intent*.

Permission Comparison Procedure. Permission comparison function is located in PackageManagerService. We convert sensitive permission set to the corresponding hexadecimal number according to Taintdroid. Then we compare it with sensitive tag obtained from *intent* or cursor to estimate the rationality of communication.

Consider two applications A and B. Let C denote the sensitive data transferred between A and B. $P_A = \{a_1, a_2, ..., a_i\}$ and $P_B = \{b_1, b_2, ..., b_j\}$ are the sensitive permission sets of A and B, respectively, where a_i and b_i are sensitive permissions defined by Android.

Let t_{ai} (or t_{bj}) denote the sensitive tag defined by Taintdroid, where each bit corresponds to one kind of sensitive permission. Each sensitive permission a_i (or b_j) corresponds to a sensitive tag t_{ai} (or t_{bj}). For example, sensitive permission a_i (or b_j) = *android.permission.READ_CONTACTS* corresponds to sensitive tag t_{ai} (or t_{bj}) = 0x00000002. Let $T_A = \{t_{a1}, t_{a2}, ..., t_{ai}\}$ and $T_B = \{t_{b1}, t_{b2}, ..., t_{bj}\}$

be the sensitive tag sets of A and B. Let $t_A = t_{a1} |t_{a2}| ... |t_{ai}, t_B = t_{b1} |t_{b2}| ... |t_{bj}$ (symbol | represents OR operation). The sensitive tag of C obtained from *intent* or *cursor* is t_C .

If $t_C \& (t_A \uparrow t_B) \neq 0$ (symbol & represents AND operation, and symbol \land represents XOR operation), then there exists unreasonable sensitive data transmission between A and B.

Experiment and Result

Effectiveness of Nipdroid. In order to test the effectiveness of Nipdroid, we have designed some malwares to execute privilege escalation attacks. As shown in Table 1, in scenarios 1-2, two colluding malicious applications execute privilege escalation attacks. In scenarios 3-4, malwares make use of insecure service or broadcast to obtain user's sensitive data.

	1st App	2nd App
1	Malware with READ_CONTACTS	Malware with INTERNET
2	Malware with ACCESS_FINE_LOCATION	Malware with INTERNET no ACCESS_FINE_LOCATION
3	Malware with READ_PHONE_STATE	Malicious broadcast receiver with INTERNET
4	Vulnerable browser	Malicious information manager with READ_SMS and READ_CONTACTS

Table 1: Malware test suite

Experimental results as shown in Table 2, Nipdroid captured all the sensitive tags in IPC. All attacks were successfully detected and prevented by Nipdroid. Nipdroid has about 5% of the false positive rate due to the tag diffusion problem of Taintdroid. The rate could be lower by solving the tag diffusion problem effectively.

Table 2: Communication interception situation

Num of capturing tag	Num of unreasonable communication	Num of intercepting communications	The rate of false positives
50	37	39	5.1%
100	83	87	4.6%
150	117	123	4.9%

Performance Overhead. In order to assess the performance loss of Nipdroid, we used the traceview tool to test the four types of Android ICC. As shown in Fig.5, the performance overhead imposed by Nipdroid is below human perception and the user will not notice any performance delays. We can see that the time for querying ContentProvider increased more than the others. This is because the efficiency for extracting tag from cursor is lower than from *intent*.

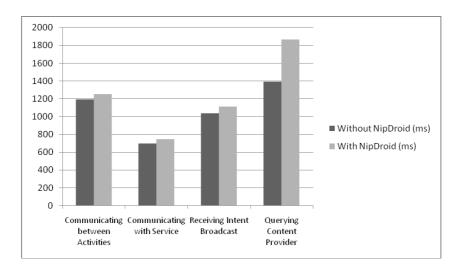


Fig. 5: Performance of Nipdroid

Conclusion

Currently, the enhanced solutions for access control mechanism of Android are mainly focused on the middleware layer. Various access control strategies are proposed to enhance Android security. Nipdroid is based on the technology of marking and tracking sensitive data, it checks unreasonable transmission in IPC and prevents the privilege escalation attacks. We expect that our research will be particularly useful in protecting Android OS.

- [1] W. Enck, P. Gilbert, B.G. Chun, L.P. Cox, J. Jung, P. McDaniel and A.N. Sheth. TaintDroid: An information-flow tracking system for realtime privacy monitoring on smartphones. In 9th USENIX Symposium on Operating Systems Design and Implementation (OSDI), 2010.
- [2] S. Bugiel, L. Davi, A. Dmitrienko, T. Fischer and A.R. Sadeghi. Xmandroid: A new android evolution to mitigate privilege escalation attacks[J]. Technische Universität Darmstadt, Technical Report TR-2011-04, 2011.
- [3] M. Dietz, S. Shekhar, Y. Pisetsky, A. Shu and D.S. Wallach. QUIRE: Lightweight Provenance for Smart Phone Operating Systems[C]//USENIX Security Symposium. 2011.
- [4] M. Nauman, S. Khan and X. Zhang. Apex: extending android permission model and enforcement with user-defined runtime constraints[C]//Proceedings of the 5th ACM Symposium on Information, Computer and Communications Security. ACM, 2010: 328-332.
- [5] E. Chin, A.P. Felt, K. Greenwood and D. Wagner. Analyzing inter application communication in Android. In 9th Annual International Conference on Mobile Systems, Applications, and Services (MobiSys),2011.
- [6] A.P. Fuchs, A. Chaudhuri and J.S. Foster. SCanDroid: Automated security certication of Android applications. Technical report, University of Maryland, 2009.
- [7] M. Ongtang, S. McLaughlin, W. Enck and P. McDaniel. Semantically rich application centric security in Android[J]. Security and Communication Networks, 2012, 5(6): 658-673.
- [8] Information on Google Android. http://www.android.com/.

A Novel XML Document Retrieval Method

Jianxin Chen^{1, a}, Liyong Wan^{2, b*}

¹Computer Science Department of Pinghu Campus, Jiaxing University, Jiaxing 314200,China ²School of Information , Nanchang Institute of science & Technology , NanChang 330108,China ^acsuzju@163.com; ^b wanliyong@163.com

Keywords: XML Retrieval; Information Retrieval; Extension of Structure Query; Query of Content and Structure

Abstract. XML is a new standard for data representation and exchange, which has been widely used on the Internet. XML retrieval has caused more and more researchers concern. How to improve the retrieval efficiency has become an important study field, this paper proposes the retrieval method based on keyword weight and structure extension, which can get the middle retrieval results in accordance with calculating the keyword weight, and further to retrieval by implementing structural extension of middle retrieval results, then can get the final query results. The experiment results show that the retrieval method has high accuracy and the recall rate compared with the traditional retrieval method.

Introduction

Because XML has the characteristics of structure, easy expansibility and crossing-platform, which has gradually become the main format of information storage and exchange, and XML document has also rapidly grown accompany with it [1]. At present, XML document has been widely used in the field of scientific databases, digital libraries, the internet and other field, how to efficiently and accurately query massive data has become the very meaningful research topic in information retrieval field [2-4]. The accuracy of retrieval results depends on whether query expression of information retrieval or not. XML document is a semi-structure document, which has content features of text document besides structural characteristics [5-7]. Therefore query expression of expressive query intent when implementing XML document retrieval not only includes query keyword, but also includes structure at the present time, they need learn the corresponding grammar and good command of the document structure. That is much difficult for most users. So it is a good method for improving the retrieval accuracy of document by query expression of feedback help users.

The Types and Characteristics of the Retrieval

According to the characteristic of XML retrieval, XML retrieval is two types of content retrieval and content & structure retrieval [8]. The content retrieval search XML document by keyword, which is similar to text retrieval. The content & structure retrieval means that the query expression includes retrieval of keyword content expression and structural expression. Users only need input query keyword in the content retrieval, which has good users' interface, but query results of the content retrieval have many irrelative results because that the content retrieval doesn't make the best of XML document information, so it is accurate. The content & structure retrieval includes the query content expression and structural expression. In addition users also need the grammar of Xpath, Query and Xsearch, etc and know structure of object document. This paper has analyzed the problems that exist in the searching of unfriendly users interface, and has proposed the retrieval method based on keyword weight and structure extension. The retrieval method can get middle results by calculating the keyword weight, then further to search the middle result, get the final results in the end.

The Calculation of Keyword Weight and Extension of Query Structure.

The Calculation of Keyword Weight. The retrieval key problem is that the relative element of user query and weight calculation of keyword of relative document. The traditional text retrieval mainly considers the factors of document size and keyword frequency, such as TF*IDF method [9]. The XML document is structural document, and structural information of XML document can significantly affect the query result. So this paper takes the structural information as important factor of affecting the keyword weight, The method combines the level position of keyword, semantic constraints of keyword with document size, get calculated formula of the XML document in accordance with modifying the TF*IDF.

Influence of Keyword Level Positions to Weight. There is a lot of inserted words in XML documents, so the same as the query keyword may exist in different tag hierarchy. It is obviously unsuitable that the query keyword of different level is taken as the same weight in traditional text retrieval. Some researcher extracted sample documents on random and found out that in XML document the higher of keyword level, the greater of its weight. A XML document tree is shown in Figure 1. There are both nodes "*title*" in the second level and the fourth level, whose important are obviously different in document topic. Generally speaking, nodes of high level are more important than nodes of low level in the importance of document topic.

Influence of Document Nodes Semantics to Weight. There are some different node elements, which may be includes the same keywords. This paper think the more important of node elements, the more important of it contains the keyword in document topic. In XML document of figure 1, words of node *"title"* is more important than words of *"paragraph"* in topic relative contribution. Therefore, this paper will set the semantics weight of node element to reflect the importance of the elements and judge the important degree in accordance with semantic weight of node elements.

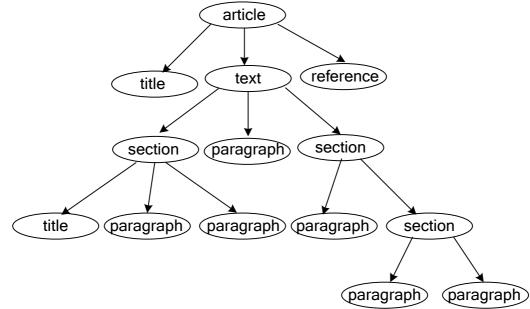


Fig.1. A XML document tree

Influence of Document Size to Weight. In this paper, influence of document size query weight is called the length factor, which is decided by total length of a word in document. The more of words, the smaller of length factor in XML document, and the weight of the word which document will be reduced. For example, a XML document of size 15K which a keyword is searched only one, while another XML document of length 15K is searched only one too, but keyword of the former document can better reflect the document topic.

The Calculation Formula of Keyword Weight. The calculation of keyword weight is mainly decided by term frequency and inverse document frequency in traditional text retrieval. The occurrence frequency of keyword t_j is f_{ij} in XML document d_i , in addition, words of high occurrence frequency must be excluded. The inverse document frequency of keyword t_j is df_j ,

whose calculation method is $idf_j = \ln(N/n_j) + 1$, where N represents document amount of document

set, nj represents the document amount of keyword i_j .

The calculation method of weight $f^* idf$ is applied in text retrieval, this paper adjust the formula f^{*idf} in accordance with the factor of influencing keyword weight, and gives a formula to calculate keyword weight:

$$\boldsymbol{\omega}_{qt} = \sum_{q \in t} \frac{c_q}{h_q} \times t f_{qt} \times i d f_{qt} \times l_t$$
(1)

Where ω_{qt} represents the weight of keyword q in document t; cq represents semantic constraint factor of query keyword q; h_q represents level which query keyword lies in XML document tree; l_t represent length factor, which is decided by total length of query keyword q in document t. $l_t = \sqrt{1/L_t}$; f_{qt} and idf_q is same meaning as traditional text retrieval.

The content expression is closely related with structural expression is in XML document retrieve. That is to say, the query of content expression is closely related with element information of words. This paper proposes method of the query structural extension is shown as follows:

(1) For query extension keyword in relative document, finding the maximal weight element tag in relative document, and tag-keyword is extended as structural query;

(2) For content expression with many keywords, the relation expression based on multiple tag-keyword is extended.

This paper expresses query extension expression by query language of INEX, the expression of structural query extension is shown:

// Doc[about(.//tag1, keyword1) and about (.// tag2, keyword2) and...]

According to above the Description, the retrieval method of this paper can be described as follows:

- (1) Calculating the weight of words in document in accordance with formula 1;
- (2) Getting the query keyword set of extension in accordance with retrieval keyword.

(3) Producing the *tag-keyword* set in accordance with retrieval keyword and extensible query keyword:

(4) Producing the query expressions in accordance with feedback of users;

(5) Returning to retrieval results;

Experiment and Result

Experiment Platform. Hardware:Intel E4400 2GHZ CPU, RAM 1.0G; Operation System: Windows XP sp3; Programming Tools: Java language; Data Set :Wikipedia XML data set. The retrieval keywords are sorted by TopX sorted method in the experiment.

Table 1 Query Keywords and extensible query					
Number	Initialized qurey	Query extension			
1	dragon	//article[about(.//title, "dragon")and about(.//p, "dragon"]			
2	zhouqiu festival	//article[about(.//p, "zhongqiu Festival")]			
3	Video	//article[about(.//p, "video")]			
4	open source	<pre>//article[about(.//p, "open source")]</pre>			
5	language	// article[about(.// title, "dragon") and about(.// p, "program")]			
6	retrieval	//article[about(.//p, "retrieval search")]			
7	software	//article[about(.//p, "software")]			

Table1 Ouerv keywords and extensible query

In experiment, owing to consider users do not open all the retrieval result to view, but only hope to search the retrieval result in the first page(or 10 results), so the experimental evaluation index are p (a)10, that is to say, return the accuracy of the top 10 results. In the experiment, seven keywords are

selected and compared randomly, whose initial query keyword and query expression of extension are shown in table 1, retrieval results of extensible before and after is shown in Fig 2.

Analysis of Experiment Results. In the experiment, we select randomly severn query keywords to test from data set. It can be seen from the figure 2 that the retrieval accuracy after being extended are more than before being extended.

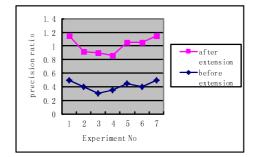


Fig.2. Query accuarcy of before and after extension

Conclusions

In order to improve retrieval accuracy and the recall rate, this paper proposes the retrieval method of XML document based on keyword weight and structural extension. The retrieval method can not only help users to reflect the query intent of users, but also its retrieval accuracy is better after users select the feedback.

Acknowledgment

The author wishes to express thanks to corresponding author *Liyong Wan* in conducting this study. The study work is supported by Major Development Program of Visiting Scholars under Grant no.FX2013113.

- L.B.Kong, S.W.Tang, D.Q.Yang, et, in: *Querying Techniques for XML Data*, Journal of Software Vol. 18(2007), p. 1401-1407.
- [2] J.B. Li, X.H.Li, in: *Research* on *Feedback Information Retrieval System Based on XML*, Journal of Information, Vol.10(2005), p.72-74.
- [3] X.P.Liu, C.X.Wan, D.X.Liu, in: *Effective XML Vague Content and Structure Retrieval and Scoring*, Journal of Computer Research and Development, Vol.47(2010), P.1070-1078.
- [4] C.X.Wan, Y.Nu, in: *XML Structural Query Extension Based on Query Keyword Weight*, Journal of Software, Vol.19(2008).2611-2619.
- [5] Y.T.Li, Z.Y.Cao, J.W.Li, in: XML Query Based the Weight of the Edit Distance, Journal of Lanzhou Jiaotong University, Vol.29(2010),P.108-111.
- [6] L.P.Li, Q.Y.Wang, S.Wang, in: *The Feedback Algorithm of XML Element*, Computer Engineering and Aplications, Vol.46(2010), P.131-134.
- [7] J.Huang, J.H.Lu, X.F.Meng, in: *Efficient XML Keyword Query Refinement with Meaningful Results Generation*, Journal of Computer Research and Development, Vol.47(2010),p.841-848.
- [8] Saadia. M, Andrew T, Mounia L, et al, in: Overview of INEX (2006).
- [9] Y.Wang, S.F.Gong. in: Research on Quadratic TF*IDF-Based Mutual Information Text Feature Selection Algorithms, Computer Applications and Software, Vol.28(2011), P.129-131.

Selecting Filter Range of Hybrid Brain-Computer Interfaces by Mutual Information

Li Wang^{1, a}, Xiong Zhang^{1, b}, Xuefei Zhong^{1, c} and Zhaowen Fan^{1, d}

¹ School of Electronic Science and Engineering, Southeast University, Nanjing 210096, China

^a230119219@seu.edu.cn, ^bzxbell@seu.edu.cn, ^czxf@seu.edu.cn, ^dzhaowenfan@seu.edu.cn,

Keywords: Brain-computer interface (BCI), common spatial patterns (CSP), mutual information (MI), support vector machine (SVM).

Abstract. The hybrid brain-computer interface (BCI) based on electroencephalography (EEG) become more and more popular. Motor imagery, steady state visual evoked potentials (SSVEPs) and P300 are main training Paradigms. In our previous research, BCI systems based on motor imagery can be extended by speech imagery. However, noise and artifact may be produced by different mental tasks and EEG signals are also different among users, so the classification accuracy can be improved by selecting optimum frequency range for each user. Mutual information (MI) is usually used to choose optimal features. After extracted the features from each narrow frequency range of EEG by common spatial patterns (CSP), the features are assessed by MI. Then, the optimum frequency range can be acquired. The final classification results are calculated by support vector machine (SVM). The average result of optimum frequency range from seven subjects is better than the result of a fixed frequency range.

Introduction

In recent years, with the rapid development of electronic technology and biomedical technology, bio-potential signals of mankind can be extracted to aid human assisted living and entertainment. Brain-computer interfaces (BCIs) can directly translate brain activity into commands [1]. Bypassing the peripheral nerve and muscle tissue, BCIs effectively improve the quality and convenience of patients' life. Most of BCIs, especially based on electroencephalography (EEG), are noninvasive systems, as they are safer and cheaper than invasive systems [2]. These brain activities are typically used to control BCIs: Event-related (de)synchronization (ERD/ERS), steady state visual evoked potentials (SSVEPs) and P300 evoked potentials [3-5]. These control methods have advantages and disadvantages, so two or more brain activities are merged as a hybrid BCI to improve the efficiency, e.g. combining P300 and SSVEP to control the wheelchair [6].

In our previous papers [7, 8], the EEG signals from reading two Chinese characters in mind have been analyzed and classified, and BCI systems based on motor imagery can be extended by speech imagery. As a state-of-the-art feature extraction method, the common spatial pattern (CSP) algorithm has been successfully applied to extract discriminant spatial features in these papers. Especially, motor imagery and speech imagery are processed by different cerebral cortex. However, CSP is very sensitive to noise and artifact, inappropriate filter range can directly affect the classification accuracy. In this paper, an appropriate filter range will be selected by mutual information (MI) for the hybrid BCI based on motor imagery and speech imagery.

Methods

Data Acquisition. Seven healthy, right-handed, Chinese subjects (five males and two females, 22-27 years old with the average of 23.72 years and the standard deviation of 1.54 years) participated in the no feedback experiment. After explained the purpose and procedure of the study, they signed the Informed Consent that was approved by the Academic Ethics Committee. The subjects sat one meter away from a LCD monitor. As shown in Fig. 1 (a), an electrode cap corresponding to the international 10-20 system is placed on the head to record the EEG signals from 35 channels. The EEG signals are

recorded by a SynAmps 2 system (Neuroscan Co., Ltd.). The reference electrode is attached to left mastoid and the grounding electrode to forehead. EEG signals are recorded after passed through a 0.1-100Hz band-pass filter, and the sampling frequency is set as 250Hz. The skin impedance is maintained below $5k\Omega$.

Experimental paradigm. The training paradigm is shown in Fig. 1 (b). The background of LCD monitor is black all the time. To start with each trial, the ready period is 1 s with displaying a fixed cross. After it, a "Cue" appears for 1 s. In the next 4 s, if the "Cue" is "move" in Chinese, the subjects are required to keep reading it in mind. If the "Cue" is the right arrow, they imagine their hands movement. After the imagery period, they can have a rest for 2-3 s with a fixed asterisk. In each run, each of two cues is randomly displayed 15 times. For each subject, he/she is trained by 5 runs, and he/she can have sufficient time to rest between each run.

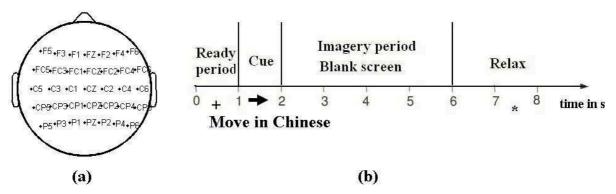


Fig. 1. (a) Electrode positions of the EEG setup. 35 channels are distributed over the scalp according to the international 10-20 system. (b) Timing of a trial of the training paradigm.

Common Spatial Patterns (CSP). According to the result of simultaneous diagonalization of two corresponding covariance matrices, the spatial filter matrix W can be designed by CSP. Therefore, EEG signals from two different mental tasks can be respectively projected into low-dimensional subspace by CSP spatial filters. As it is a supervised algorithm, the useful feature of EEG signals will be effectively extracted. For more details of CSP, please refer to [9]. The decomposition of each trial E is given as Z=WE. For each trial, the variances of only a small number vectors from Z are suitable to construct the eigenvector. Thus, the first m and last m columns of Z_p (p=1,...,2m) can be calculated the feature vectors by the following changes:

$$f_p = \log\left(\frac{\operatorname{var}(Z_p)}{\sum_{i=1}^{2m} \operatorname{var}(Z_i)}\right).$$
(1)

The variance is marked as $var(\bullet)$ and *m* is set as 2 in the paper. As CSP algorithm is particularly sensitive for the noise and artifact of EEG, selection of filter range for each subject is very crucial.

Mutual Information (MI). Feature selection is a special point in pattern classification, as it can improve classification accuracy and save computing time. There are two main methods for feature selection: wrapper approach and filter approach. MI is the filter approach that selects the features independent from the classifier [10]. Although MI may not obtain better results than the wrapper approach, it does not need much computational effort. MI is extremely suited for BCI systems [11], especially for the online systems. The basic method to calculate MI from two variables *X* and *Y* is:

$$I(X;Y) = H(Y) - H(Y \mid X)$$
⁽²⁾

H(Y) is the entropy of Y, and H(Y | X) is the conditional entropy of X and Y.

Feature Classification. In this paper, support vector machine (SVM) is selected to classify the feature vectors. SVM specializes in classifying the small sample and high dimensional model, and SVM is calculated by LIBSVM [12] with radial basis kernel.

Results

Each trial lasts at least 8s, and EEG signals of imagery period contain useful information. Thence, the EEG signals from 3-5s of Fig. 1(b) can properly estimate the classification accuracy. After filtered by sixth order Butterworth bandpass filter (filter range: 4-7Hz, 5-8Hz,...,44-47Hz), the feature values of signals are calculated by Eq. 1. These values are assessed by MI at first. Hereafter, the frequency ranges will be selected, if their values of MI are greater than the mean of all values. If these ranges are continuous, they will be joined together. At last, the widest frequency range must be chosen as the optimum frequency range (OFR) for each subject. The raw EEG signals are re-filtered according to the selected frequency range. To properly estimate the CSP spatial filters and classification accuracy, the final results of filtered signals are calculated by 10×10 cross-validation [7]. The flowchart of experimental algorithm is shown in Fig 2(a).

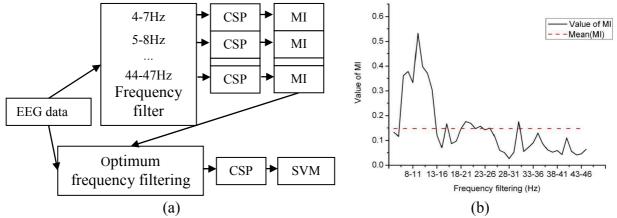


Fig. 2. (a) Flowchart of experimental algorithm. (b) The result of MI for Subject S6. The full line is values of MI for each narrow frequency range and the line of dashes is the mean of these values.

Fig 2(b) shows the result of MI for Subject S6, and his optimum frequency range is identified as 6-15Hz according to the red line of dashes. The curve is not smooth for the nonstationarity of EEG, but the trend of these values is obvious with the change of frequency filtering. As EEG signals mainly include α -rhythm (8-12Hz) and β -rhythm (14-30Hz), 6-30Hz is chosen as the fixed frequency range to compare with the optimum frequency range. The final results are shown in Table 1.

_	Accuracy [%]						
Subject:	S 1	S2	S3	S4	S5	S6	S7
6-30Hz	74.63	81.35	82.87	85.73	72.89	71.79	80.89
Std	± 3.37	±3.16	±1.54	±1.75	±2.24	± 2.82	±2.39
OFR	79.96	87.43	81.56	87.67	80.74	76.83	83.57
Std	± 2.48	±1.31	± 2.06	±1.49	±1.63	±1.56	± 1.72
Optimum frequency range (OFR) [Hz]							
	7-19	13-24	6-21	6-14	7-15	6-15	13-23

Table 1. The classification results of 10×10 cross-validation and optimum frequency range.

The average accuracy of optimum frequency range for seven subjects is 82.54%, which is better than the result of fixed frequency range (78.59%). Except for S3, the results of others have been improved by chosen the optimum frequency range. The optimum ranges of all subjects are different, and it implies that EEG signals have great diversity among subjects. MI is an adaptive algorithm to choose the range, and the classification results get better after filtered by the optimum range.

Conclusions

It is the tendency to utilize hybrid BCI systems in the future. The different mental tasks may pull-in more noise and artifact, and then the classification accuracy of systems will be deteriorated. The selection of appropriate filter range is a great method to reduce the influence of noise and artifact. As MI is an excellent feature selection approach, it is also successfully applied to define the optimum frequency range of users in this paper.

Acknowledgments

This work was supported by the National Key Basic Research Program of China (No. 2010CB327705), the National High Technology Research and Development Program of China (No. 2012AA03A302), and the Fundamental Research Funds for the Central Universities under Grant CXLC12_0095, and this work was also supported by Shenzhen China Star Optoelectronics Technology Co. Ltd.

- [1] J. R. Wolpaw, N. Birbaumer, D. J. McFarland, G. Pfurtscheller and T. M. Vaughan: Clin. Neurophysiol., Vol. 113 (2002), p. 767–791.
- [2] D. McFarland, D. Krusienski, W. Sarnacki and J. Wolpaw: J. Neural Eng., Vol. 5 (2008), p. 101-110.
- [3] G. Pfurtscheller, C. Brunner, A. Schlögl and F. H. Lopes da Silva: NeuroImage, Vol. 31 (2006), p. 153-159.
- [4] P. Lee, C. Yeh, J. Y. Cheng, C. Yang and G. Lan: IEEE Trans. Biomed. Eng., Vol. 58 (2011), p. 3350-3359.
- [5] M. Salvaris, C. Cinel, L. Citi and R. Poli: IEEE Trans. Neural Syst. Rehabil. Eng., Vol. 20 (2012), p. 8-17.
- [6] Y. Li, J. Pan, F. Wang and Z. Yu: IEEE Trans. Biomed. Eng., Vol. 60(11) (2013), p. 3156-3166.
- [7] L. Wang, X. Zhang, X. Zhong and Y. Zhang: Biomedical Signal Processing and Control, Vol. 8 (2013), p. 901-908.
- [8] L. Wang, X. Zhang and Y. Zhang, in: Proceedings of the 35rd Annual Conference of the IEEE Engineering in Medicine and Biology Society, Osaka, Japan (2013), p. 7056-7059.
- [9] H. Ramoser, J. Müller-Gerking and G. Pfurtscheller: IEEE Trans. Rehabil. Eng., Vol. 8 (2000), p. 441-446.
- [10]R. Battiti: IEEE Trans. Neural Networks, Vol. 5(4) (1994), p. 537-550.
- [11]H. Zhang, Z. Y. Chin, K. K. Ang, C. Guan and C. Wang: IEEE Trans. Neural Networks, Vol. 22(1) (2011), p. 52-63.
- [12]Information on http://www.csie.ntu.edu.tw/cjlin/libsvm.

A New Quadtree-based Skyline Query Algorithm

Liu Runtao^{1,a}, Chen Yuanjing^{2,b*}, Cao Dayong^{3,c}, Liu Deyu^{3,d}

¹Institute of Information and Scientific Computing Technology, Harbin University of Science and Technology, Harbin, China

²Harbin University of Science and Technology, Harbin, ChinaCollege of Applied Science, Harbin University of Science and Technology, Harbin, China(corresponding author)

³College of Applied Science, Harbin University of Science and Technology, Harbin, China

^aliurt@hrbust.edu.cn, ^bchenyjhar@163.com, ^ccaodyhar@163.com, ^dliudy321@163.com

Keywords: Skyline query, PR-quadtree, domination

Abstract. In this paper, the index structure, PR-quadtree for spatial data, is used to store data for a database. The properties of the quadtree are studied. With the properties prunning rules are set up for searching the Skyline set of the data stored in the quadtree. Through detailed analysis for the tree the method of finding some approximate skyline points is designed, by which a new skyline searching algorithm is given. The new algorithm is more effective.

1. Introduction

With the rapid development of hardware and software techniques related to internet, skyline query has become one of the hot topics in the research field of database. Skyline query is a specific and relevant example of preference queries and has been recognized as a useful and practical way to make database systems more flexible in supporting user requirements. It provides an effective way to solve multi-criteria decision making problems. For instance, Stockholders want to buy a stock. There must be a criterion for them to select the stock they will buy. Generally the criterion is that the stock is cheap and has a great potential of making money, that is, it is needed to know how to select the quality stocks you want from a great number of stocks. Another example is that we plan to travel to shore to spend our vacation in the condition we will stay there spending as little as possible and playing well, which needs us to select a hotel with nice location and lower price. Skyline query is very helpful for solving these kinds of problems. It can provide the solutions for users to select by retrieving a series of data.

2. Related research work

Since the introduction of the skyline operator by Borzsonyi al. in 2001^[1], skyline query has been studied from the view of database, and several efficient algorithms have been proposed for the general skyline query. These algorithms take techniques such as divide-and-conquer, nearest neighbor search^[2], sorting^[3], and index structures to realize the general skyline queries. Some studies have also focused on the skyline query processing in a variety of problem settings such as data streams^[4] and data residing on mobile device^[5]. The skyline query algorithms are classified as two classes: query ones with indexes such as NN(Nearest neighbor) query algorithms ^[2], BBS(Branch and Bound Skyline) algorithms^{[6][7]}, DC-tree^{[8][9]} and query algorithms of using B-trees^[1] and ones without indexes. Generally the algorithms without indexes are implemented by scanning all data set at least one time, which results in their query efficiency low and high I/O cost, while the algorithms with indexes can achieve higher query efficiency and reduce I/O cost by reducing the amount of data set through setting pruning rules to exclude part of the data set impossible to be skyline points. For example, DC-tree algorithm^[8] first partitioned the data into four parts according to their coordinates by slipping window model with N tuples, then computed the skyline points on each part recursively, and finally combined all of these points together to form the final skyline, which is called DC-tree. In

the tree, every parent node recorded only the skyline of the part of data contained in the node. Therefore the final skyline was stored in the root node of the DC-tree. In this paper, we will discuss pruning rules and query algorithm for the skyline query under PR-tree index.

3. Related concepts and theorems

To illustrate the problem more clearly, the following definition and theorem are given first.

Definition 1. Given D, a point set of data in *d*-dimensional space. Suppose $p(p_1, p_2, \dots, p_d), q(q_1, q_2, \dots, q_d)$ be two points in D. *p* dominates *q* iff we have $p_i \leq q_i$ for $\forall i \ (1 \leq i \leq d)$ and there exists $j \ (1 \leq j \leq d)$ such that $p_j < q_j$ or called, *p* controls *q*.

Skyline query is to find a data set, users are interested in, any point in which is not dominated by any other point.

Theorem 1. In two-dimensional space, $p(p_1, p_2)$ dominates $q(q_1, q_2)$ if p is located in the third quadrant of the partitioned filed, and q in the first quadrant.

Proof. Suppose that each point on the boundary is infinitely near the boundary, then if $p(p_1, p_2)$ is in the third quadrant of the partitioned filed, and q in the first quadrant, it must be satisfied that $p_1 < q_1$ and $p_2 < q_2$ according to the condition in Theorem1, which results in the conclusion of Theorem1, that is, $p(p_1, p_2)$ dominates $q(q_1, q_2)$.

4. Skyline qury based on PR-quadtree

4.1PR-quadtree

PR-quadtree^[10] is a kind of domain quadtrees, It is a hierarchical structure based on the rule of decomposing a domain repeatedly. Actually it is a 2^k -tree, where k is the dimensionality of data space. Figure 1 shows a PR-quadtree in two-dimensional space.

The constructing procedure is simple. First to compute MBR(minimum bounding rectangle), then to separate the data space equally 2^k times until there is only a point in each quadrant. The four parts are counter-clockwisely defined the first quadrant, the second, the third and the fourth respectively.

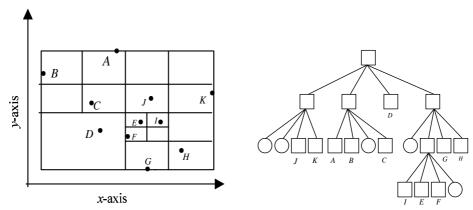


Fig. 1 A PR-quadtree in two dimensional space

PR-quadtree has the following properties:

(1) The structure is clear and easy to create.

(2) Data space is separated equally to make each quadrant have same size.

(3) Space usage is improved.

(4) Leaf nodes are not necessary on the same level so that the height of the tree is reduced. fined the first quadrant, the second, the third and the fourth respectively.

4.2 Skyline query based on PR-quadtree

The basic idea of searching algorithm is that some approximate skyline points are as initial skyline set to proceed the searching to prune the index tree for getting high pruning effectively.

Definition 2. Given a PR-quadtree with its head pointer *head*, if query is done each time by its second child node until a leaf node , then the leaf node is called the point p_1 of the tree.

Definition 3. Given a PR-quadtree with its head pointer *head*, if query is done each time by its third child node until a leaf node, then the leaf node is called the point p_2 of the tree.

Definition 4. Given a PR-quadtree with its head pointer *head*, if query is done each time by its fourth child node until a leaf node , then the leaf node is called the point p_3 of the tree.

In Figure 1, the point p_1 is B, the point p_2 is D, and the point p_3 is H. The initial skyline set is a nice approximation for the final skyline set.

The query algorithm is described as follows.

Algorithm PR-Skyline Query (*head*,S)

Input: the root node pointer *head*;

Output: the Skyline set S

Step1 S= Φ ;/*initialized*/

Step2 find the point p2;/*query p1 point of the tree according the definition 1*/

S←p2;

Step3 find the point p1 ;/*query p2 point of the tree according the definition2*/

If p1 is not dominated by p2 then

S←p2;

endif

Step4 find the point p3 ;/*query p3 point of the tree according the definition3*/

if p1 is not dominated by p2 then

S←p2;

endif

Step5 node \leftarrow *head*;

Step6 for i=1 to 3 do

if node*i* is a leaf node then

if node*i*.REC is not dominated by any point in S then

Delete the points in S dominated by node*i*.REC;

S←node*i*.REC; /*add node*i*.REC into Skyline set*/

else

if node*i*.REC is not nominated by any point in S then

node←node*i*;

goto step 5

Step7 return S;/*return Skyline S*/

5. Conclusion

In this paper, the PR-quadtree- based skyline search is studied. A new algorithm for finding the Skyline set of a data set indexed by a PR-quadtree is presented. The query efficiency of the algorithm is greatly improved through determining some approximate skyline points. Next better prunning rules will be designed to make the algorithm more effective for us to work on.

Acknowledgment

This paper is supported by the 2011 scientific and technological research project of the Education Department of Heilongjiang Province of China under Grant No.12511103.

- BORZSONYI, S., KOSSMANN, D., AND STOCKER, K. The skyline operator. In Proceedings of the International Conference on Data Engineering (ICDE'2001). 421–430.
- [2] KOSSMANN, D., RAMSAK, F., AND ROST, S. Shooting stars in the sky: An online algorithmfor skyline queries. In Proceedings of the International Conference on Very Large Databases(VLDB'2002). 275–286.
- [3] CHOMICKI, J., GODFREY, P., GRYZ, J., AND LIANG, D. Skyline with presorting. In Proceedings of the International Conference on Data Engineering (ICDE'2003). IEEE Computer Society, 717–816.
- [4] LIN, X., YUAN, Y., WANG, W., AND LU, H. Stabbing the sky: Efficient skyline computation over sliding windows. In Proceedings of the International Conference on Data Engineering (ICDE'2005).IEEE Computer Society, 502–513.
- [5] HUANG, Z., JENSEN, C. S., LU, H., ANDOOI, B.C. Skyline queries against mobile lightweight devices in MANETs. In Proceedings of the International Conference on Data Engineering (ICDE'2006).IEEE Computer Society.
- [6] PAPADIAS D,TAO Y,FU G,SEEGER B. An Optimal and Progressive Algorithm for Skyline Queries[C]. In Proceedings of the ACM SIMGOD International Conference on Management of Data,2003,467-478.
- [7] PAPADIAS D,TAO Y,FU G,SEEGER B. Progressive Skyline Computation in Database Systems[J].ACM Transactions on Database Systems,2005,30(1):41-82.
- [8] YANG J,QU B,LI C P,CHEN H. DC-Tree: An Algorithm for Skyline Query on Data Streams[M], In Advanced Data Mining and Applications,2008,644-651.
- [9] Wu Y X, Yang Q, Li C P, Chen H. DC-Tree: a kind of Skyline Query on Data Streams[J]. Computer Science, 2007,34(10),33-35.
- [10] Guo W, Guo J and Hu Z Y. Index Techniques of Spatial Database[M]. Shanghai Jiao Tong University Press, 2006, 100-103.

Research on reusable software process model based on Petri net

Guang-yi Tang^{1, a}, Deng-ju Yao^{1,b} and Li-jie Cui^{1,c}

¹School of Software, Harbin University of Science and Technology, Haerbin, China ^atanggy818@126.com, ^byaodengju529@163.com, ^candyclj1977@163.com

Keywords: Process Model; Reusable software Process; Petri Net; Value Petri Net

Abstract. Software process reuse can improve the quality of software products and save the cost of software development, in order to make it more convenient for software organization to build software process model rapidly and efficiently, a method was proposed to analyze the value model which is based on the Petri net, introduces the concept of time and the implementation of value, through a specific algorithm design to provide guidance and decision-making basis for assessing the reuse of software process.

Introduction

The quality of the software process has a crucial influence on the quality of software products, and the quality software process is fundamental to the success of software development. Software development process and software products have many similar characteristics, a complete software development, maintenance and evolution is composed of multiple software processes which are related to each stage of the related software. After long-term accumulation of experience, the industry software activity has gotten a large number of process templates or standard process, and forming a rich set of reusable software process assets, they usually get the tested process fragments from the actual process of software engineering projects, these reusable software process can be used to solve some typical problems that the practical software projects often encounter.

Reusing software components are similar to this, the process of software development and implementation can build suitable software process models for the target system efficiently through reusing the software process, then the product quality can be improved, the cost of software process modeling and analysis can be reduced at the same time. But in some large-scale software projects, software organizations are often confronted with problems that how to effectively select the appropriate reusable software process problems, so many software organizations need to assess, cut and combine varieties of software process reusing cases, we will obtain a complete software process model consists of a series of reusable software process finally, due to this point, we could improve software quality and reduce the cost of software implementation process .

Therefore, we proposed an analytical model of reusable software processes based on Petri, including the analysis of the process execution time and execution value in the model, so as to provide the decision-making basis and assessment guidance for reusing model.

Related research

With the research and practice on reusing software process more and more deeply, there has appeared a series of software reuse methodology and some results of the relevant researches.

CHEN pointed out the necessary basic characteristics and related concepts of reusing software process^[1], and also provided a conceptual framework for the research of software process reuse, such as multi-dimensional, particle size, abstraction mechanism, and correctness verification etc..

WU proposed "process pattern" approach, divided process model into three categories according to the abstraction levels and granularity of the software process reuse: the task process model, the stage process model and the overall process model, the overall process model constitutes the process model and the stage process model, while the stage process model contains one or more task process model and some other elements^[2].

Li Tong proposes a formal research method for software evolution and reuse of software process, and presents a formal software evolution process meta model EPMM, which can be used to support the definition and modeling of the evolution of software and software process^[3].

Silva J P summed up 20 kinds of common workflow pattern based on the characteristics and elements of workflow system, and classify them as: control flow, data, resources and exception handling workflow model and so on^[4]. The workflow model can be high-level abstracted, and described and studied through the use of workflow technology.

According to the software process maturity rating criteria, the U.S. Software Engineering Institute at Carnegie Mellon University developed a series of CMM and its' derivative models, this model can be used as a reference model to monitor and research on software development and maintenance process, intended to promote the software processes' standardization and normalization.

Software process reuse value model

When software organizations face many reusable software process models in a software project, there are multiple choices. In small scale software projects, you can easily select the appropriate reusable software process models, but in larger projects, because of the complexity among these reusable software processes and the various dependencies exist in the software process, making the composition of the entire software project's process model selection becomes more complicated. We can establish the value model according to the corresponding software process, which is as a preliminary basis for selecting a reusable software process^[5].

The assessment of the value about some reusable software process depends on software organization's subjective choice and judgment of its value. The value is that within a certain period of time, the difference between the expected benefits and pay when the software organization pull-in some software process:

$$v_t = m_t(e) - m_t(p) \tag{1}$$

Which v_t represents the value of a certain time period, and which $m_t(e)$ means that the expected return within a certain period of time, and $m_t(p)$ said he expected the transaction costs within a certain time. Any software project is time required; therefore, the time factor is a very important dimension in the assessment of the value. The time t is related to the sustainable time span during a software process's activity in some certain stage of the project life cycle.

How to evaluate $m_t(e)$ and $m_t(p)$ is related to the core capabilities that software organization's analysis and understanding, project resources, value evaluation and implementation ability about the software project.

To assess the value of a single software process cannot be taken as the ultimate criterion, software organizations need to select multiple similar software processed as candidates. According to the principle of rationality, V_t means the software organization decision, if the value V_t is greater, the more likely to choose the model of software organization, anyway, if $v_t \leq 0$, software organization will not select this software process. From formula (1), when $m_t(e)$ is stable, $m_t(p)$ will be the decisive factor for v_t , the influence of this time, the software process should be selected to meet the minimum principle of $m_t(p)$.

Value Petri net model

In order to value the global software process model which has pull-in some candidate software process. This paper extends the basic Petri nets, making each transition correspond to a value mapping function, so that we can get the Value-Petri nets. Benefits of doing so:

A. Basic Petri net can be utilized pretty well to model the enterprise business process, support the graphical representation, and analyze easily;

B. According to firing rules, basic Petri net's tokens could represent the control flow of software process very well;

C. Through value mapping function, so that each transition can quantitatively express the software process value^[6].

Definition 1 Value Petri net system is a six-tuple VPNS = (B, E, F, M, I, V), where:

(1) $B \cup E \neq \phi$ And $B \cap E = \phi$, and *B* called conditions set of the software process's execution, *E* called the transition set, that is software process set;

(2) $F \subseteq (B \times E) \cup (E \times B)$, which means the Cartesian product of the condition and transition;

(3) $M \subseteq 2^{B}$ is called Value-Petri net identification, which 2^{B} is called the power set of condition B;

(4) Transition $e \in E$ can be fired under the condition M is: $\exists b \in B$, meet $b \in e^*$, M(b) = 1 and $\forall b \in e^*$, with M(b) = 0;

(5) *I* indicates the time mapping function $i: I \to 0 \cup T^+$;

(6) V represents the value of the mapping function, see formula (1).

Definition 2 Value Petri net, assuming that VPNS=(B, E, F, M, I, V) is a Value Petri net system. Let $M_1 \subseteq M$ be an identity of Value Petri, VPN= (B, E, F, M_1, I, V) , then M_1 is called an initial identification of VPN, $d \in M_1$ called a token, VPN is called Value Petri Net.

As the definition of 1 and 2 can be seen, VPNS net system is a collection, VPN net is a collection of elements, between the two is a subject relationship.

Analysis of Value Petri net

Reachable analysis. Definition 3 the reachable of Value Petri net. in the Value Petri net :VPN= (B, E, F, M_1, I, V) , if there exists a VPN identification M_1, M_2, \dots, M_k , for: $1 \le j \le k$, and $\forall e_i \in E, b \in B$, that $M_j(b)[e_j > M_j$ was founded, called transition sequence $\delta = e_1, e_2, \dots, e_k$ under the identification, M_1 can be fired, and from identification M_k to M_1 is reachable, denoted as $M_1[\delta > M_k]$.

A necessary condition for determining reachable Value Petri net is, if $M_1[\delta > M_k]$, $\forall x$ so $M_k = M_1 + A^T X$, which A is an associated matrix of the model. It is difficult to directly judge that from M_1 to M_k is reachable, but it is simple to judge that from M_1 to M_k is unreachable.

Characteristics of the time and value. The time and value characteristics analysis of the software process implementation is derived by calculating the total time and the total value of the global software implementation process, and then the result will be regard as candidates of software process sequence.

Transition sequence $\delta = e_1$, e_2 , ..., e_k , where, $1 \le j \le k$, $\forall e_i \in E, b \in B$ make that $M_j(b)[e_j > M_j]$, and can be solved by reachable discrimination algorithms. Then, using algorithm 2 to get the comparative analysis of shortest time and the highest value when the entire software process model in different candidated software process implementation sequence, and to choose an appropriate software development process finally.

Algorithm 2 Analysis of the software process implementation's time and value

Step1: According to the reachable algorithm, seeking M_1 to M_k implement software process sequence { δ }:

```
Step2:

while \delta in \{ \delta \} do \{

while i \le n do \{

if(no-parallel relationship between the processes) then {

time_sum[num]+ = e[i]. time;
```

```
value_sum[num]+ = e[i].Value;
}else{ // Parallel relationship
max_parell_time = 0;
while(traverse all parallel processes) do{
    // Calculation of all parallel flow times and values
    if(e[i]. time> max_parell_time) then
        max_parell_time = e[i]. time;
    }
    time_sum[num]+ = max_parell_time;
    value_sum[num]+ = e[i].Value;
    }
    i ++;
}
num ++;
```

Step3: To get the time_sum and the value_sum from the software process sequence's implementation.

Taking the maximum time from the parallel executed software process and its value will be accumulated to obtain the shortest time and maximum values of each implementation sequence, as an alternative candidate for one of the bases of software process's selection.

Conclusion

Software process reuse is an important issue in the field of software process modeling, this article proposed an analysis method of the software reuse process's value model from the perspective of the value of the software reusing, at the first, we need to use this method to evaluate the candidate of the software process and to establish the software process reuse value-Petri net model, and then to analyze the executed time and value of the global software process, which can effectively offer the value assessment guidance and decision support for reusing the software process.

ACKNOWLEDGMENT

This work was supported by the Natural Science Foundation of Heilongjiang Province under grant number No.F201313.

- [1] CHEN Jian, LIAO Shou-yi, YANG Yan-li, et al. Decision-making method of computer generated forces based on fuzzy Petri-net[J].Application research of computers ,2013(31):96-102.
- [2] WU Yu-Chun, LI Shu-Yu. AADL model: Based on TPN[J].Computer technology and development,2014(2):67-72.
- [3] LI Tong. An approach to modeling software evolution processes [J]. Berlin : Springer-Verlag, 2008(14):2313-2316.
- [4] Silva J P, MdeMiguel, Briones JF, et al. Composing models with six different tools: a comparative study[J]. Model Transformation with ATL, 2009(11):103-109.
- [5] OASIS. Mapping of W3C Web service architecture work to SOA RMWork [J]. America: OASIS, 2005(9):1242-1245.
- [6] SUN Xing-ping, KANG Hong-wei, LIANG Zhi-hong, et al. An analysis approach for software process reuse value model[J]. Journal of Yunnan University,2011,33 (S2):192-195.

Research on Service Model Combination Method Based on Colored Petri Net

Guang-yi Tang^{1, a}, Deng-ju Yao^{1, b} and Li-jie Cui^{1,c} ¹School of Software, Harbin University of Science and Technology, Haerbin, China ^atanggy818@126.com, ^byaodengju529@163.com, ^candyclj1977@163.com

Keywords: Model Driven Architecture; Service Oriented Architecture; Service Model; Petri Net

Abstract. Model-driven architecture and service-oriented architecture are popular software development methods at the present, these two methods have their own advantages and disadvantages, the proposed SOA-based Model-driven Rapid Development Architecture by combining these two methods, Using colored Petri nets' tools to study service composition methods specifically, and described five basic logical structure of service composition through formal methods, then gave out the construction method of composite services, finally, verified the effectiveness and safety of the service composition method through the modeling.

Model-driven development framework

Methods of software development have experienced continuous changes. To some extent, alleviated the problem of the development process, but is not a fundamental solution to the demand for change, software migration, software reuse, interoperability and development efficiency and other issues. In this case, the model-driven development approach emerged as the times require. Proposed by the Object Management Group MDA (Model Driven Architecture) which is a software development framework and an object-oriented model of software development methods. Importantly, the model is no longer just a document. Model is more valuable than the code, the model will be precisely defined at the same time, so that the code could converse^[1]. Therefore, creating a model with reuse value is the key to the development of MDA.

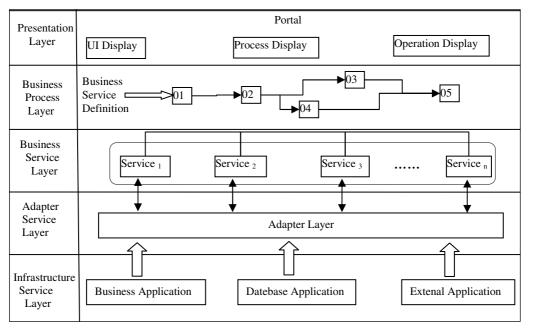
When we need to change a partial or the whole business, the MDA could be very fragile. We often need to modify most of the models, which influences the model's versatility and reusability. The SOA (Service Oriented Architecture) is a service-oriented thinking which is just to make up for this shortcoming of MDA. It makes the business model of MDA consist of the fine-grained basic service model. Thereby reducing the cost of modifying the model according to business changes, and improving the efficiency, reusability and maintainability of model development. This kind of situation requires a driven rapid development framework model based on SOA as shown in Figure 1.

SOA has many features such as platform-independent, loosely coupled, etc., so it could be released and adapted in an internet environment which is heterogeneous and open. While in a complex service, we need to have the right combination of services. So, how to properly use a combination of these services become the key to effective service^[2].

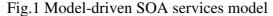
Service composition model based on Colored Petri Net

The basic elements of SOA architecture are the service, and service is the core of SOA implementation, SOA specifies a set of entities, which details how to provide and consume services. The system follows SOA concepts must have services; these services are interoperable, independent, modular, position clear, loosely coupled and can be found on the network. Services can be combined, which is an important feature of the service. It is determined by the following properties:

a. Service encapsulation. The function of encapsulating services into applications for business processes reusable components. It provides information or simply changes the business data from a valid, consistent state to another. Encapsulation hides complexity and API services remain unchanged so that the user will be free of the specific implementation of the changes^[3].



SOA-based Model driven Rapid Development Architecture



b. Service reuse. Service reusability design significantly reduces the cost. To achieve reusability, service only works in the context of a particular treatment process, independent of the underlying implementation and customer demand changes.

c. Service interoperability. Interoperability is not a new concept, in CORBA, DCOM, web-service the interoperability technology has been adopted. In SOA, to interoperate through established communication protocols between services^[4]. There are two types of synchronous and asynchronous communication mechanism. The SOA services interoperability features make itself more favorable to be reused in a number of occasions.

Thus, SOA services require a kind of asynchronous and parallel features, formal semantics and graphical representation so that it can be simplified and validation of the model. The Colored Petri Net through the use of colored Token way to make colored Petri net can completely describe the service model.

CPN basic concepts. Definition 1 *CPN* (Colored Petri Net) is a seven-tuple *CPN* = (W, P, T, F, E, C, G), where (P, T, F) is a network: W is the type of non-empty finite set, also known as non-empty finite set of colors. P is the set of finite-state; T is a limited set of changes of states; F is finite arc set $F \in (P \times T) \cup (T \times P)$; E is an arc function, $E: F \rightarrow Bool \exp ression$, represents an arc to mapping a Boolean expression, wherein, E represents the input to invoke a service, the output parameters; C is a color function, $C: P \rightarrow W$, C(p) represents the color type P is belong to W; G as a function of post, $G: T \rightarrow Bool \exp ression$, where, G represents the input conditions to be met outside except when calling a service.

Service Network Model. The SOA service model and colored Petri net for effective integration, construction of the service network model, and the service network model, defined as follows:

Definition 2 *SN* (Service Net) is a service network, SN = (W, P, T, F, E, C, G, In, out), wherein: (W, P, T, F, E, C, G) is a *CPN*; *In* is the input place of service where, $\forall x \in P \cup T : (x, In) \notin F$, which means that no previous set; *Out* is the output place of service, wherein, $\forall x \in P \cup T : (Out, x) \notin F$, which means that *Out* has no post set.

Definition 3 Atomic Service, that service can not be divided, simply call the function of itself to complete their missions, which is the basis of the composition of services, generally constituted by a basic service.

For atomic services S, the CPN model can be constructed SN = (W, P, T, F, E, C, G, In, out), where: $P = \{In, Out\}$; $T = \{service\}$; $F = \{< In, service >, < service, Out >\}$; $E = \{E(In, service), E(service, Out)\}; C = \{C(In), C(Out)\}; G$ by the semantics of the service may be.

Definition 4 *CS* (composite service), by calling the atomic service, completes services which are provided by itself. Two atomic services S_1, S_2 , wherein, $SN_1 = (W, P_1, T_1, F_1, E_1, P_1, C_1, G_1, In_1, Out_1)$, $SN_2 = (W, P_2, T_2, F_2, E_2, P_2, C_2, G_2, In_2, Out_2)$. Atomic services only have one basic structure of composite services, and comprise 4 basic structures:

A. sequence of service, two services perform in order, the operator "+", $CS = S_1 + S_2$.

B. parallel of service, parallel execution of two services, the operator " \oplus ", $CS = S_1 \oplus S_2$.

C. cyclic of service, repeat execution of a service, the operator "&", $CS = \& S_1$.

D. selecting of service, select an execution from two services, the operator " \odot ", $CS = S_1 \odot S_2$. The properties of the service net:

A. If each place of a transition has a token, then the transition shall be allowed. When a transition is enabled, a transition will occur, the token input library will be consumed, and generating a token for the output library at the same time. For basic service, as long as the library which contains a token starts, it must be able to lead into a transition, no matter if the service execution is successful, we will get the output finally.

B. The service which is obtained through the calculation step $\{+, \odot, \oplus, \&\}$, the sequence structure is an example which is shown in Figure 3, assuming two basic services S_1, S_2 , the A shows that if the initial identification is a non-death identity, then S_1 can be triggered.

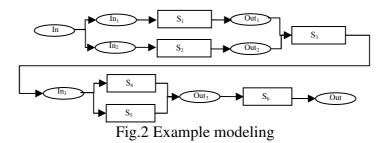
If the normal execution is completed, then generating and calling the initial conditions of service S_2 , and S_2 will be changed into the termination of the state after S_2 is triggered; If the service S_1 fails, then go directly to the termination of the state. Therefore, for the sequence structure, the conclusion is clearly established. For other structures may also prove that this conclusion can work.

C. The service which is got by $\{+, \odot, \oplus, \&\}$ of the complex multi-step operation that can be proved using mathematical induction. Using $\{+, \odot, \oplus, \&\}$ step operation for basic services, the conclusion is established. We assume that the conclusion will also work for the composite service after *n* steps, then the step through the n+1 complex arithmetic operations can be seen as one step operation through two composite services, by (B) shows that, for the step operation, the conclusion is established. Thus, for n+1 step operation resulting composite service conclusion will also work, so as for a multi-step complex computing, this conclusion is also established.

Examples of modeling

For example, in a simple case of insurance claims, insurance companies should first check the insurance time, and insurance type release expired is consistent, conduct reconnaissance review and make a decision whether to grant the claim, the claim will go to if given the claims process, otherwise to the clients Describe reasons not related to whether the claim should be the last copy archived. An activity can be viewed as a combination of these services, a total of 6 basic services, S_1 : Check the expiration Insurance release; S_2 : type of insurance is consistent; S_3 : survey and review and make decisions; S_4 : give and take the claims process claims; S_5 : not claim to explain the reasons for the client; S_6 : copy archive.

From the analysis, S_1 , S_2 is a parallel, and S_3 is the sequential relationship, S_4 , S_5 is the choice of relationship, and S_6 is the order relation, therefore, S can be expressed as $S = (S_1 \oplus S_2) + S_3 + S_4 \odot S_5 + S_6$. The service net is shown in figure 2.



The reachable graph is a simple and effective method, which applies in bounded Petri nets, due to the service combinations are bounded, so you can use the reachable graph to analyze. The reachable graph is in Figure 3.

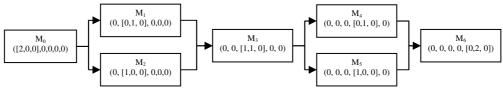


Fig.3 The reachable graph analysis

A. Identify the beginning and end with M_0 and M_6 , and they are connected, and not out of the M_6 , so the combination of the service can be terminated.

B. The composition in each state is bounded and therefore, the composition and the composition bounded service are safe.

C. From the beginning identity M_0 to the end identity M_4 , we can always find a sequence to make changes to reach the final state from the initial state, so there is no deadlock. From the above analysis, the combination of the service is correct and can terminate.

Conclusion

Combining the SOA and MDA is the main trend of the modern software development theories and methods. In order to achieve the best combination of them, and to provide the heterogeneous systems an ideal solution, the paper proposed framework on the basis of technology, defines five service combinational logical structure, described the features of services which are consist of the logical structure, and these properties are briefly proved. Finally, an example illustrates the structure proposed in this paper is correct.

ACKNOWLEDGMENT

This work was supported by the Natural Science Foundation of Heilongjiang Province under grant number No.F201313.

- XU Xiaofei, MA Chao, WANG Zhongjie. A value—oriented iterative service modeling process. VAN SINDERENM, et al. (Eds) : 2012 International IFIP Working Conference on Enterprise Interoperability (IWEI 2012), LNBIP 122, Harbin, China, September 6-7, 2012: 104-116.
- [2] WANG Hongda, ZHOU Liang. Research on Service Model Combination of Model-driven SOA Based on Colored Petri Nets [J]. Electronic Science and Technology, 2012(25):93-96.
- [3] Tan Wei, Fan Yushun, Zhou Mengchu. A Petri net-based method for compatibility analysis and composit ion of Web services in business process execution language [J]. IEEE Trans on Automation Science and Engineering, 2009, 6(1):94-106.
- [4] CHEN Jian, LIAO Shou-yi, YANG Yan-li, et al. Decision-making method of computer generated forces based on fuzzy Petri-net[J]. Application research of computers ,2013(31):96-102.

Web Pages Mining Based on Terms and Formal Concept Analysis

Bo Yu^{1,a}, Deng-ju Yao^{1,b} and Guang-yi Tang ^{1,c}

¹School of Software, Harbin University of Science and Technology, Harbin, China ^ahrbust_yubo1981@163.com, ^bydkvictory@163.com, ^ctanggy818@126.com

Keywords: knowledge extracting; Web page Mining; Web terms; Formal concept analysis; Galois Lattice

Abstract. In the face of immense Web pages of WWW, how to extract valuable knowledge from the Internet is a difficult problem. The main research work of this paper was to apply FCA (Formal concept analysis) and Web terms on the Web representing the relationship between Web pages and web terms. We deeply studied how to apply Galois to Web page mining, and used the Java language to design the Web pages mining system. The system uses the constructed Galois lattice to extract potential knowledge of WWW. The results prove that the use of Galois Lattices and Web terms for Web pages mining is feasible.

Introduction

According to the survey data of the 2013 year's statistic report of China network progress status, the number of web pages reached 122.7 billion in 2012, and the figure is still increasing rapidly [1]. Every Web page has many web terms or keywords used for intelligent information processing. Through the statistic data we can see that Web has developed into distributed information space.

As the Web page sets increase exponentially, we couldn't ignore the problem of information explosion, but knowledge is relatively deficient. At present, the search method is usually based on key terms matching search. The main problem of this method is information overloading. Users couldn't correctly and quickly gain the needed valuable information. Therefore we need to develop a new technology which is more advanced than the search engine technology. The new technology is Web page mining. Through Web page mining we can summarize, classify, cluster, and do an association analysis numbers of Web page sets.

The paper applied the core data structure of formal concept analysis—Galois Lattice and web terms to Web pages mining. Considering Web pages updating frequently, we used an incremental algorithm to construct the Galois Lattice. Therefore applying the Galois Lattice can extract diversified types of knowledge containing in the huge web pages in WWW, such as, implication rules, association rules, and classification rule. These knowledge could help users to find interesting Web pages, therefore it improves the performance of Web pages mining.

Moreover, considering the complexity of Web pages mining task, we constructed a model of Web pages mining which is a loose system consisting of multi-agent. In Web page mining, each agent independently finishes the corresponding concrete task. Each agent collaborate one another to find implicit, unknown, novel, usable, and finally apprehensible knowledge from numbers of non-structured Web page sets.

Galois Lattice Model

Professor Wille firstly proposed the theory of formal concept analysis for the discovery, sort and display of the concept [2]. In the formal concept analysis, the concept of extension is represented as belonging to the formal concept of a collection of all objects, while the content was represented as a common property of all of these objects collection. Galois lattice is its core data structure of the theory of FCA. Galois essentially reflects the relation between the objects and attributes, and the relationship of generalization and specialization between concepts. Formal concept analysis and Galois lattice model has been widely used in software engineering, data mining and other fields. Formal concept

analysis has been widely used in knowledge engineering, data mining [3], information searching [4], software engineering [5,6] and so on.

Definition 1. A formal context is a triad K = (P, T, R) which consists of two sets P, T and a relation R between P and T. The Galois Lattice of K is the set of all its concepts together with the hierarchical subconcept-superconcept-realation.

Each node of Galois Lattice represents a formal concept, which consists of two parts: the extension and the intension. The extension covers all objects belonging to this concept and the intension comprises all attributes valid for all those objects. Through Hasse diagram Galois Lattice can represent the relationship of generalization and specialization among concepts, reflecting the hierarchy of concepts and implementing visual data. So it is very suitable to process data mining from database. Hence, Galois Lattice is used as an effective tool for data mining and knowledge extracting.

Web Page Mining Model Based on Galois and Terms

A multi-agent model of Web pages mining based on Galois Lattice is shown in Fig. 1. The model encapsulates the process of Web pages mining using the technology of agent. Multi-agents collaborates one another to finish the task of Web pages mining. The technology of Multi-agent improves the flexibility and intelligence of the process model. In knowledge extracting Agent, applying the theory of Galois Lattice to process Web pages mining is the main difference compared with the former Web pages mining model. Fig. 1 shows the process of Web page mining model.

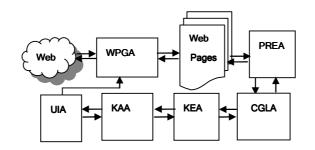


Fig. 1. A multi-agent model of Web pages mining based on Galois Lattice

WPGA. Firstly, clients submit query requests to WPGA (Web Pages Gathering Agent) through UIA (User Interface Agent). WPGA gathers Web page sets from Web.

PREA. In PREA (Preprocessing Agent), the main task of the PREA is gain web terms.

CGLA. In CGLA (Constructing Galois Lattice Agent), the relationship between non-structured Web pages and their terms is described by Galois Lattice.

KEA. In KEA (Knowledge Extracting Agent), applying the constructed Galois Lattice can effectively extract potential valuable knowledge from Web pages.

KAA. In KAA (Knowledge Appraising Agent), the quality of the extracted knowledge by KEA is appraised. If the appraising result of gaining knowledge doesn't reach a given threshold, the model returns the former agent to process the task of itself again through improving itself.

UIA. Lastly, UIA (Users Interface Agent) visualizes the knowledge gained by KAA to users. If users are not content with the mining knowledge, they can submit the query requests again.

Web Pages Mining Experiment

We used the tool-Concept Explorer programmed by Java to implement a Web pages mining experiment. Concept Explorer provides the following functionality: context editing, building Galois Lattices from context, and finding bases of implications. Concept Explorer realizes the functionality of CGLA and KEA.

Provided that WPGA found five Wet pages p1, p2, p3, p4, p5. Through PA we gained Web pages model, namely web term sets {Artificial intelligence, Data mining, Supervised learning}, {Artificial

intelligence, Data mining, Web mining}, {Artificial intelligence, Supervised learning, Rule reasoning}, {Artificial intelligence, Information integration, Semantic Web}, {Artificial intelligence, Data mining, Information integration, Text}. A context K = (P, T, R), P={p1, p2, p3, p4, p5}, T= {Artificial intelligence, Data mining, Supervised learning, Rule reasoning, Web mining, Information integration, Semantic Web, Text} can be easily represented by a cross table constructed by Concept Explorer, such as Fig. 2. A cross in row $p \in P$ and column $t \in T$ means that the object p has the attribute t.

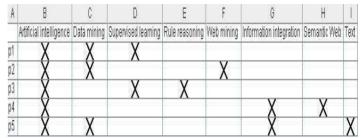


Fig. 2. A multi-agent model of Web pages mining based on Galois Lattice

We used the cross table for a context to construct Galois Lattice through Concept Explorer. Fig. 3 shows the constructed Galois Lattice, also called Hasse diagram or line diagram.

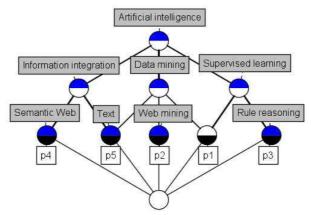


Fig. 3. The constructed Galois Lattice

Fig. 3 shows that the Galois Lattice constructed by Concept Explorer uses reduced labeling. So called reduced labeling is used in order to succinctly represent information about intents and extents of formal context. If label of attribute A is attached to some concept, that means, this attribute occurs in intents of all concepts, reachable by descending paths from this concept to zero concept(bottom element) of lattice. If label of object O is attached to some concept, this means, that object O lays in extents of all concepts, reachable by ascending paths in lattice graph from this concept to unit concept (top element) of lattice.

Formal Concepts. From the Galois lattice, we can see that each Galois grid node is a formal concept. Formal concept consists of two parts, denotation and connotation of the concept respectively. The extension of the formal concept represents all objects belonging to the concept, whereas the connotation of the concept is expressed as common properties belonging to all these objects. Therefore, Each concept in Galois lattice is the maximum common attributes of the collections of objects. Galois lattice structure constructing process is actually concept clustering process.

Implication sets. In the system, we can get implications from Galois lattice. The display format of association rule is as follows. Through Concept Explorer we can gain implications that are true in context as shown in Table 1.

Table.1. Implication sets got from the Galois lattice

(The format of the following implications is No <Number of objects> Premise ==> Conclusion. No simply means number of implication in list.

Number of objects shows, for how much objects implication holds.

Premise and conclusion are usually list of attribute names, that occur in premise (conclusion).)

No.	Association rules
1	<5> { } ==> Artificial intelligence
2	<1> Artificial intelligence Rule reasoning ==> Supervised learning
3	<1> Artificial intelligence Web mining ==> Data mining
4	<1> Artificial intelligence Semantic Web ==> Information integration
5	<1> Artificial intelligence Text ==> Data mining Information integration
6	<pre><0> Artificial intelligence Data mining Supervised learning Rule reasoning ==> Web</pre>
	mining Information integration Semantic Web Text
7	<pre><0> Artificial intelligence Data mining Supervised learning Web mining ==> Rule</pre>
	reasoning Information integration Semantic Web Text
8	<1> Artificial intelligence Data mining Information integration ==> Text

We explained some implications as follows.

Implication 1 suggests that all the Web pages have the term "artificial intelligence".

From implication 2, we can mine some knowledge that there are one Web page having the terms "Artificial intelligence" and "Web mining" must has the term "data mining".

Implication 4 implies some knowledge that there are one Web page containing the terms "Artificial intelligence" and "Semantic Web" must has the term "Information integration". Moreover, Implication 2, 3, 5, 8 imply the same knowledge.

From implication 6, we can mine some knowledge that there is no Web pages having the terms "Artificial intelligence", "Data mining", "Supervised learning", "Rule reasoning" also containing "Web mining", "Information integration", "Semantic Web", "Text".

Conclusions

In this paper, we used formal concept analysis—Galois and Web terms to Web pages mining. Web pages mining model based on Galois Lattice are proposed. Cooperation among agents can solve the complex tasks of Web pages mining. Experimental results show that the method proposed by this paper is feasible. We can effectively extract potential valuable knowledge from huge Web pages.

In summary, formal concept analysis in the application of Web mining is promising. Although studies in this paper achieved initial results, but there is much in-depth research works to do in future. The mapping of unstructured Web pages to structured Web term set is future research direction. Because of the huge number of Web pages and the corresponding formal context scale is very large. The dimension reduction of the formal context is also one of the future research directions.

Acknowledgement

The authors are grateful for the anonymous reviewers who made constructive comments. This work is Supported by the Natural Science Foundation of Heilongjiang Province (NO. F201313), the Harbin Technological Foundation for Innovative Talents (NO. 2012RFQXG089).

References

[1] Information on http://www.cnnic.net.cn.

- [2] B. Ganter and R. Wille: *Formal Concept Analysis* (Mathematical Foundations, Springer, Berlin 1999).
- [3] C. Carpineto and G. Romano: *Lecture Notes in Computer Science*, *Formal Concept Analysis: Foundations and Applications* (Springer Berlin Heidelberg, Berlin 2005).

- [4] J. M. Cigarran, J. Gonzalo, and A. Penas, and F. Verdejo: Lecture Notes in Computer Science, Galois Lattices, Second International Conference on Formal Concept Analysis, Sydney (2004), p. 74-87.
- [5] R. Godin, G. Mineau, and R. Missaoui: International Journal of Knowledge Engineering and Software Engineering Vol. 5 (1995), p. 119-142.
- [6] D. Corbett and A. L. Burrow: International Conference on Conceptual Graphs (ICCS'96). Sydney (1996), p. 56-60.
- [7] R. Godin, R. Missaoui, and H. Alaui: Computational Itelligence Vol. 11 (2001), p. 246-226.

The Research and Design of the Intelligence Application Platform in Public Security E-government

Yan Wang^{1, a}, Shaoyun Guan^{1, b}, Weihong Li¹ ¹Harbin University of Commerce , Harbin, China ^awangyan gumu@126.com, ^bgsyj91@163.com

Keywords: e-government; public security system; data process; the intelligence application platform

Abstract. The paper first expounds the reason that establish intelligence application platform in public security e-government. The data of cross-regional, cross-department, cross-police process through extraction, cleaning, conversion and loading and be shared. It introduces the procedure and methods of intelligence obtaining. Finally system architecture is listed one after another according of data layer, service layer, application layer, presentation layer and security mechanism.

Introduction

At present public security e-government has achieved better results, the principal business of various kinds of police can be in motion in its e-government system and means of information has been integrated into the actual work of the police.

E-government system is changing from a phase of basic construction and system construction into a phase of application-oriented construction. But with the deepening of application, some problems need to be solved. First, Basis data quality of existing information systems is not high and update untimely, so it restricts the actual effect. Second, the level of information sharing is low in crossregional, cross-department, cross-police, information resources integration and comprehensive development and utilization are lack. It is difficult to adapt to the increasingly heavy policing need in public security work. It is seriously hampered the sustainable development and expansion of modern police work space. Third, there are not established a unified intelligence acquisition and processing system, the utilization of intelligence is not enough. In the ordinary course of business of the police through the e-government system the means of analysis judged are fewer and low-tech, the range of application is small, the analyzing level is not high[1].

To solve the above problems, the resource processing platform of police intelligence should be established on the existing hardware and software. Meanwhile it can give full play to the overall advantages of the public security organs. The intelligence application platform of public security e-government can achieve dynamic control of key personnel and major case events early warning. Through the business data integration and mining, the intelligence application platform can improve the quality of intelligence analysis, and constantly adapt to real needs, it resolves that the work results will not be affected by police individual differences.

Data processing of the intelligence application platform

Data processing is an important cornerstone of the intelligence application platform, The data comes from police business systems, reported data collection, unstructured data (web information, electronic documents, images, audio and video etc) and social information data (air, rail, and taxation etc). These data must be extracted and purged, standardized and stored. Initial data should be extracted disposable in accordance with the Data Source Library standard. Incremental data extraction should be extracted by a different frequency[2]. It can ensure data fresh and accurate and to the source data of information systems can operate normally.

A. Data Extraction

The data from the various business units will be extracted and stored into the temporary database. These data mainly includes police comprehensive data, temporary residents, hotel accommodation staff, rental, criminal offenders, Internet cafe staff, drug addicts, etc.

B. Data Cleaning

Data cleaning is to find unreliable data which has been extracted from the business data. These unreliable data will be stored the database to check further. It would be cleaned if the data checked is inaccurate or erroneous. Because extraction data comes from internal network and external network, it is important to ensure in real reliable and effective etc factor.

C. Data Conversion

Data conversion is to transform the data which does not meet the standard data. The standard data is laws or rules of data for information processing and query to improve the efficiency of management and service in public security e-government. The main standard is << Guidelines for Open Directory of Government Public Information >> which is by published General Office of the State Council in January 2009[3]. It put forward the standardized reference views and become an instruction for data specification processing. It provides a solid theoretical foundation for the e-government query with different departments and regions.

D. Data Loading

Data loading is the integrated data stored into different database which is designed according to the rules stored. Data processing is shown in the Figure 1 below.

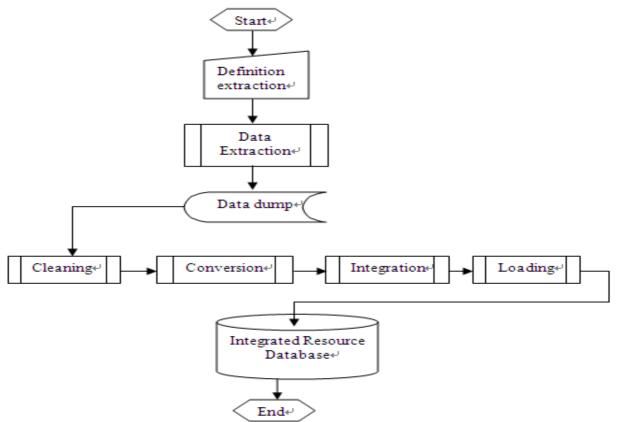


Figure 1 Data processing of the intelligence application platform

procedure and methods of Intelligence obtaining

Processes and methods of Intelligence obtaining is to analyze and judge through a large number of fragmented data and isolated information and link deeply to the persons, objects, incidents, the situation to find and obtain intelligence.

A. The Procedure of Intelligence obtaining

The processed Intelligence obtaining can be divided into three steps. The first step is to select the concern target and collect or grasp the relevant information as much as possible. The second step is to establish analysis model and pay close attention to its development and changes. The third step is to find abnormal situation and obtain intelligence.

B. The Methods of Intelligence obtaining

1) Relevance and Comparison. The important attribute characteristics people, things, the case (incident), the organization will be related and compared with the information resources in the various database by one to one, one to many, many to one or many-to-many. It would be satisfied with work needs of the fugitive arrest, risk warning, dynamic control etc.

2) *Frequency analysis.* The frequency of occurrence that the particular characteristics of target object is analyzed according to sorting and filtering multiplex. It would be satisfied with work needs of key personnel, management and control.

3) The depth of excavation. Through the establishment of appropriate working model investigation, the intrinsic link which is irrelevant ostensibly among the isolated, fragmented mass of information would be found. It can provide to the basis for the investigation.

4) Segmentation techniques. Unstructured text class information according to the important characteristics of their property is divided into the structured data. It would be satisfied with needs that the information of the same type of person crime or the same characteristic case can be discerned and classified automatic.

System architecture

The intelligence application platform is unified application system and establish centralized data center. By using a browser all users who based on their different levels and their different activities access the public security network intelligence platform to use different applications and data.

A. Data Layer

The data layer is a thematic database group which existing information resources of various business systems are centralized collection, integration, processing and building. It provides a solid data foundation for a variety of analytic applications judged. Data layer is not only the core but also complex in the intelligence application platform. Data is the basis of all the things of e-government system. The scientific data management enhances the function and quality of external services and improves the efficiency in internal organs besides reducing the service cost.

B. Service Layer

The service layer provides the common features, services and interfaces on the intelligence application which they are generally required to achieve by function development of various information applications. It is the important technical support linkage which builds the system and operates all kinds of intelligence application. Moreover it provides strongly public technical for sharing information and application linkage of different systems and different networks.

C. Application Layer

Application layer achieve analysis and judgment according to variety information to fulfill the information needs analysis. It bases on the data layer and the service layer is main functional parts. With the development of public security e-government, this layer can be continuously improved and expanded.

D. Presentation Layer

Presentation layer is the bridge which the user use the information resources and application functions. All the manifestations and functional operation of the intelligence application platform is shown most intuitively. It is the major man-machine interface.

The system architecture is shown in the Figure 2 below.

Conclusion

The intelligence application platform share data and eliminate "Information Island" in public security e-government. At present the task of grassroots policemen is heavy and cumbersome, The quality of handling the cases is different with the professional ability of different policemen. Now the work results of intelligence will not be affected by their individual differences. It should be achieved that functions of the public security department can be played with lower-cost and higher efficiency, the related clues and decisions base on reliable data and scientific means and methods, the public and policemen obtain convenient service and e-government development is sustained and in-depth.

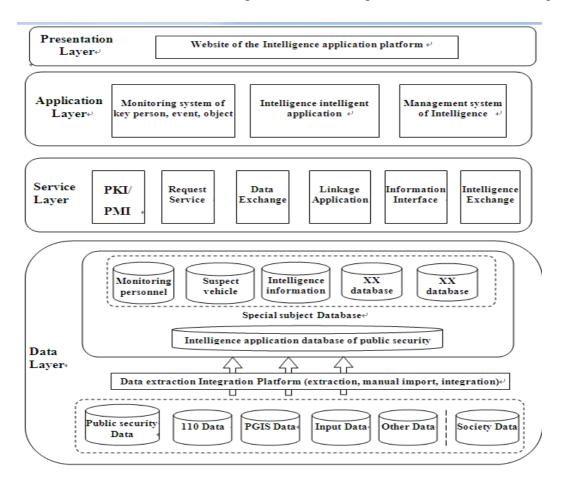


Figure 2 System architecture

Acknowledgements

This thesis is a stage achievement of the project of the Hei Longjiang Provence(The project code:2013B052).

- [1] Xieping Tang. Application Research of Computers. (in chinese) 7 2008
- [2] Shishou Li. Information Science. (in chinese)2009.3
- [3] Changsheng Wang, and Xiaoping Xu. Social Sciences Academic Press. (in chinese)pp6-8,76-77. 2010.

VEET: 3D Virtual Electrical Experimental Tool Supporting Multi-Modal User Interfaces and Platforms

Bowen Sun^{1,a}, Bin Shen^{2,b}, Wenwu Chen^{2,c}, Yanpeng Zhang¹, Jiaqi Lin¹ ¹Center of virtual simulation experiment, Harbin University of Science and Technology, Harbin, 150080, China

²College of Computer Science and Technology, Harbin University of Science and Technology, Harbin, 150080, China

^asunbw01@163.com, ^bshenbin_1989@126.com, ^cxiaowai0525@126.com

Keywords: Electrical Experiments, Virtual Reality, Augmented Reality, Cross-platform

Abstract. This paper introduces a practical and cross-platform virtual electrical experimental tool (VEET) based on an off the shelf game engine called Unity3D which is powerful and flexible to develop Virtual and Augmented Reality (VR/AR) applications. Taking the electrical experiments of technological university as examples, the well designed virtual experimental system has the characteristics of lifelike three dimensional (3D) experimental environments, AR interactive interface on mobile devices, intelligent detecting mechanism and cross-platform. We described VEET's flexible design and demonstrate its use in teaching where 120 students from three classes conducted electrical experiments with it. The experiments in VEET were presented on desktop, mobile and web browser using low cost common devices (personal computer, android handheld device, Chrome browser). Evaluating the main performance parameters, the well practicability was confirmed.

Introduction

These last decades, virtual reality technology has been widely used in the fields of military simulation, sports, medical and agriculture [1]. Many colleges and universities have developed their own virtual experimental system, such as the CircuitMaker of Wake Forest University and the iLab [2] of Massachusetts Institute of Technology. Nevertheless, most current virtual experimental systems are 2D interactive interfaces-based, which exist the shortcomings of abstract experimental results, single pattern of human-computer interaction and unintelligent in application; while the conventional 3D virtual experimental systems are also faced with problems, that is, high cost of software development, poor render effects and the dependency on a certain running platform. In order to solve the drawbacks above, this paper introduces a 3D virtual electrical experimental tool which is called VEET for short. VEET has four main characteristics; that is, considerably realistic experimental environments; automatic detecting and scoring mechanism; AR interactive interface on mobile devices, and cross-platform which is the most vital advantage.

The first part of this paper introduces the characteristics of the Unity3D game engine; the second part represents the key techniques and optimization included in detail; the performance evaluation of VEET is done in the third part, and the last part draws a conclusion of this paper.

Related Work

Unity3D. Unity3D is a game engine developed by Unity Technologies, and it has the powerful rendering engine fully integrated with a complete set of intuitive tools and provides developers with rapid workflows to create interactive and realistic VR/AR applications.

Unity's development environment runs on Microsoft Windows and Mac OS X, and the application built can be run on Windows, Mac, Xbox 360, PlayStation 3, Wii, iPad, iPhone, as well as android platform [3]. Besides, Unity contains powerful 3D physics engine developed by NVIDIA® PhysX®

Physics, which makes the environment looks lifelike. Unity3D can be used to rapidly prototype simulations to teach advanced electronic/electrical circuit theory [4].

Augmented Reality. The AR topic was first proposed by Sutherland in 1960. Then it became an emerging research topic when Milgram and Kishino published their paper and introduce about the concept of "Virtuality Continuum" [5]. AR technique allows computer generates virtual affine images in memory to exactly overlay physical objects in real time. AR supplements the real world with virtual objects generated by computers; achieving the effect that virtual world appears to coexist in the same space as the real world. With the rapid development of smart handheld devices, client users can experience AR easily.

Key Techniques of the VEET

Automatic detecting algorithm. A set of automatic error detection and evaluation mechanism is designed for the purpose of strengthening VEET's practicability and intellectuality. The final score depends on the correctness of apparatuses and wires connection. The realization of the detection module is used to detect the correctness of wires connection and apparatuses, which is shown in Fig. 1 (algorithm 1 is wires detection and algorithm 2 is for detecting apparatuses). The time complexity

of these algorithms both are O(n), which guarantees the good performance of VEET.

```
Algorithm 1
```

Algorithm 2

Input: w_s : right wires connection, w_u : user's wires connection	$\mathbf{Input}: a_{\mathbf{z}}: \mathbf{right} \mathbf{apparatuses}, a_{\mathbf{u}}: \mathbf{user's} \mathbf{apparatuses}$
Output : w _m : missing wires, w _w : wrong wires	$\mathbf{Output}: a_m: \text{ missing apparatuses}, a_w: \text{ wrong apparatuses}$
$1 \ w_s \leftarrow \text{initalize_std_answer} \ // \text{right wires connection initialization}$	n 1 $a_{\rm s} \leftarrow {\rm initalize_std_answer}$ //right apparatuses initiation
2 $w_{\it u} \leftarrow {\it user operation}$ //user's wires connection initialization	2 $\textit{a}_{\textit{u}} \leftarrow \textit{user} \textit{ operation //user's apparatuses initiation}$
3 $w_m, w_w \leftarrow \varnothing$ //detection results initialization	3 $a_m, a_w \leftarrow \varnothing$ //detection results initiation
4 for each $x_i \in w_s$ //wires connection detection	4 for each $z_i \in a_s$ //apparatuses detection
5 $if(x_i = y_i \in w_u)$	5 $if(z_i = r_i \in a_u)$
6 then remove y _i in w _u	6 then remover i in au
7 else w_m add x_i	7 else a_m add z_i
8 end for	8 end for
9 for each $y_i \in w_u$	9 if (a _u is not mull)
10 if (y _i == 1)	10 then for each $r_i \in a_u$
11 then w_w add y_i	11 $a_w \operatorname{add} r_i$
12 end for	12 end for
13 return	13 return

Fig. 1. Detection algorithms

The AR interaction module. To build the AR supporting interaction module, the Vuforia [6] technology is used. It uses the mobile device as a "magic lens" or looking glass into an augmented world where the reality and virtuality appear to co-exist.

Users can observe apparatuses in all directions while the position of the mobile device is changing, thus making the user experience more realistic, and achieving the effect of an AR interaction.Figure 7 is data flow diagram of the AR supporting interactive module in VEET, and the module can be divided into three parts as follows:

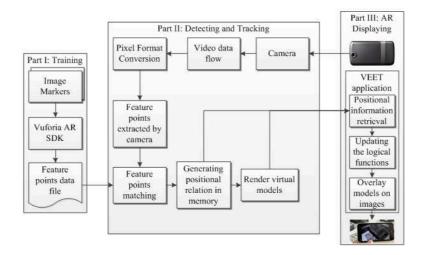


Fig. 2. Data flow diagram of the AR module

- i) Vuforia allows us to create colorful marker because it just extract the edge and contrast as a feature point, hence, developers can customize a variety of images as target resources. Before using the VEET, the information of feature points are trained and saved to a data file;
- ii) In the stage of running the VEET, Vuforia reads the information of feature points from the data file generated in part i, meanwhile, VEET will detect other feature points extracted from the RGB video data flow captured by the camera, and then match these two type feature points to build the positional relationship between the camera and the image target, thus preparing for displaying the virtual apparatuses in an AR way;
- iii) If the two type feature points match successfully in part ii, VEET will update the logical functions to build an object coordinate system (OCS) in the center of the image target according to the positional relationship calculated in part ii, then the apparatus models will be rendered in the OCS and displayed on the mobile device screen. Finally users can conduct and observe apparatuses in an AR supporting interaction.

Evaluation and Conclusions

Evaluation of VEET is made to confirm its practicability. The settings of the desktop and Web operating environment are shown as follows: Intel (R) Core (TM) i5-3470 k 3.4 GHz processor; 3.47 GB RAM; NVIDIA GeForce GTX 670 graphics card; 32-bit Windows 7 ultimate edition operating system. The settings of the mobile operating environment are shown as follows: 1.7 GHz Snapdragon 600 processor; 2 GB RAM; Adreno 320 graphics card; Android 4.1.0 operating system.

The performance results of VEET on desktop, Web and mobile devices are respectively shown in Fig. 3.



a) Car lamp circuit experiment

b) AR interaction on mobile device

Fig. 3. VEET runs on PC (a) and Web (b)

Table 1 discusses the main performance parameters obtained in the practice mode. The application performances fluently when the frames reach 30 fps (frame per second). The performance on desktop

and handheld device reaches to respectively 98 fps and 70 fps. Due to the optimization techniques given by Unity Technologies [7], the performance of VEET is improved significantly.

Experiments	Draw-Call	Vertex	Triangle	Performance Optimization
Car lamp circuit experiment	173	738.0k	728.8k	389.1%
Lighting circuit experiment	90	452.7k	507.3k	334.4%
Motor control experiment	96	463.3k	974.7k	303.9%

Table 1 The main performance parameters with optimization

Acknowledgements

This research is supported by the Heilongjiang Province Key Virtual Simulation Laboratory Foundation (40010-40), the educational teaching research project of Harbin University of Science and Technology (Z201300005) and the virtual simulation experimental center of Harbin University of Science and Technology.

- H. Chen, Q. Ma, D.H. Zhu: Research of Interactive Virtual Agriculture Simulation Platform Based on Unity3d, Journal of Agricultural Mechanization Research Vol. 3 (2012), p. 049 (in Chinese).
- [2] P. Orduna, J. Garcia-Zubia, D. Lopez-de-Ipina, et al, in: Sharing Laboratories across Different Remote Laboratory Systems, Advanced Learning Technologies (ICALT), International Conference on IEEE (2012), pp. 493-494.
- [3] J. Hu, X. Yu, in: A Pathfinding Algorithm in Real-time Strategy Game based on Unity3D, Audio, Language and Image Processing (ICALIP), International Conference on IEEE (2012), pp. 1159-1162.
- [4] M. Callaghan, M. Cullen: Game Based Learning for Teaching Electrical and Electronic Engineering Advanced in Computer Science and its Applications, Springer Berlin Heidelberg (2014): pp. 655-660.
- [5] M. Santoso, B.G. Lee, in: ARkanoid: Development of 3D Game and Handheld Augmented Reality, International Journal of Computational Engineering Research Vol. 2 (2012), pp. 1053-1059.
- [6] L. Csokmai, O. Moldovan, I. Tarca, et al: A Comprehensive Approach of Advanced Error Troubleshooting in Intelligent Manufacturing Systems, Applied Mechanics and Materials 404 (2013), pp. 631-634.
- [7] http://docs.unity3d.com/Documentation/Manual/OptimizeForIntegratedCards.html.

A Kind of Distributed Simulation Runtime Infrastructure Based on Grid

Ying Liu^{1,a}, Jianwang Hu¹ and Peizhang Cui¹ ¹Information Department, Mechanical Engineering College, China ^aly_oec@126.com

Keywords: Grid, RTI, Distribution Simulation, Infrastructure

Abstract. Although high level architecture (HLA) is the mainstream of application in distributed simulation technology, poor interoperability, deficit reuse of the codes of the simulation applications and inferior expansibility of the simulation system had became the research focus of simulation community at home and broad. And Grid is able to manage a large number of heterogeneous resources of geographically and organizationally distributed. So a kind of Grid-based distribution simulation runtime infrastructure (GSRI) was put forward. Here with WSRF specification, GT4 tools was used to encapsulate the pRTI interfaces. And given the performance analysis, it is shown that despite the latency created by the transmission through wide area network (WAN), the GSRI may support the large-scare distributed simulation applications. It has a profound theoretical significance and great value of the engineering.

Introduction

Traditionally, the primary aim of HLA is to build the large-scale simulation system and to implement the plug-and-play of the simulation applications. It can reach the quick combination and the re-configuration to guarantee the interoperability and the reuse for the different users' requirements or the diverse application targets. However, it is proved practically that the shortage of HLA used in distributed simulations may appear mainly as follows.

(1) Poor support for the interoperability in WAN. The communication mechanism of HLA/RTI software is developed based on TCP/UDP. The communication among the federate members is often obstructed by the firewalls.^[1]

(2) Deficit reuse of the codes of the simulation applications. There is a big coupling between the federate members and Local RTI Component (LRC) or between the LRC and RTI execution. It is difficult for the simulation resources to be operated or reused and with different granularities or levels among the different departments or organizations.^[2]

(3) Inferior expansibility of the simulation system. When the simulation system runs under the WAN with much more simulation nodes, it is hard to monitor its running states, detect its performance and control its managements.

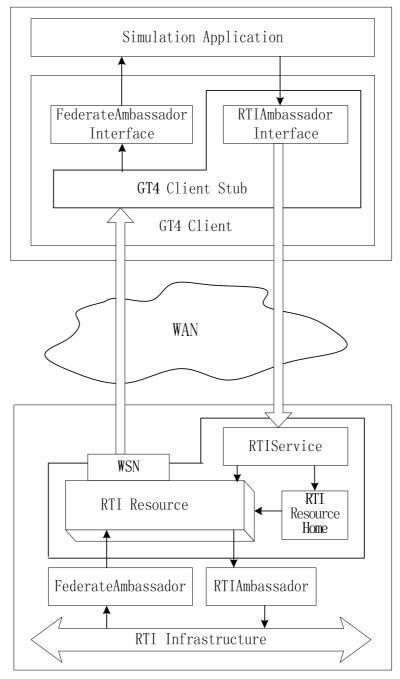
With the appearance of Grid, it provides a kind of new way to resolve the problems in the traditional distribution simulations. Here, a research on the HLA/RTI and Grid is made, in order to build a new kind of simulation runtime infrastructure.

Structure of Grid-Based Simulation Runtime Infrastructure

The RTI software, as the distributed simulation runtime infrastructure, runs at the mode of Client/Server. During the runtime course, the federation members with the related data and parameters ask the RTI for the services. And the RTI responses and reflects the requests from the federation members and reforms all other relative federates. The functions invoking between federates and RTI is defined by HLA interface specifications. It implements its functions via two external classes as RTIAmbassador and FederateAmbassador. The member functions of the RTIAmbassador class comprise all that RTI can provide and be called by the federate. And the member functions of the FederateAmbassador are pure virtual functions, which are invoked by RTI

and are realized in federation member applications, such as discovering the object instance, reflecting the attribute values and so on. ^[3]

The Grid-based simulation runtime infrastructure (GSRI) is that according to the HLA interface specifications, it uses Grid technique to encapsulate the six kind of services of HLA/RTI, such as federation management, declaration management, object management, ownership management and data distribution management, to implement the interconnection and interoperability among the simulation applications. As shown in Fig. 1, with the Client/Server mode, the GSRI keeps up the intrinsic characteristic of HLA/RTI. At client terminal, it implements the all the functions via two classes as RTIAmbassadorInterface and FederateAmbassadorInterface. The RTIAmbassadorInterface can transfer the invoking requests of RTI by federation members to the RTI server resource through GT4 client. And the FederateAmbassadorInterface can provide the callback interfaces for the simulation running at the server terminal.



Simulation Terminal





At the RTI server terminal, the RTI service resources are encapsulated by Web Services Resource Framework (WSRF). It is the RTI web services that can receive and analyze the information of the long-range invocation of HLA service. And the RTI resource home can research the instance of the service invocation, and maintain the service states by RTI Resource. The RTI resource can send data and invoke HLA services by calling the member functions of the RTIAmbassador provided by LRC. During the callback, the WSRF notification (WSN) mechanism is used, which can inform the long-range client by SOAP.^[4] Client can receive and analyze the callback information of the RTI resource instance and can callback the functions of the simulation applications by the FederateAmbassadorInterface.

In this infrastructure, the kernel is the RTI servitization. With the WSRF specification, the RTI factory/instance model is adopted at the server terminal. Here, four classes such as RTIResourceHome, RTIFactoryService, RTIService and RTIResource are built, shown as Fig. 2.

RTIFactoryService class: receive the requests from the user to create the RTI service resource, which return the reference by createResource() funciton.

RTIResourceHome class: create and manage the RTI service resource instance.

RTIService class: receive the operation request for RTI service resource instance, as well as search the service resource.

RTIResource class: realize the interfaces of the RTI kernel functions. It can be realized from two classes as hla.rti.RTIAmbassador and se.pitch.prti.FederateAmbassador_Impl, for the RTI software is programmed by Java language.

Consider the character of RTI, the design of the client terminal is shown as Fig. 3. With WSN specification, the topic-based publication/subscription model is used.

RTIResource: connect resource instance for client.

RTIInstance: call long-range service.

InfoListner: monitor service informing events.

RTIAmbassadorInterface: realize the invocations between the client and simulation application. FederateAmbassadorInterface: realize the callbacks between the client and simulation application.

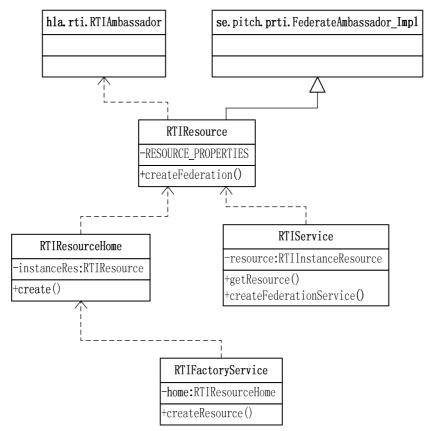


Fig. 2 Structure of RTI WS-Resource at the server

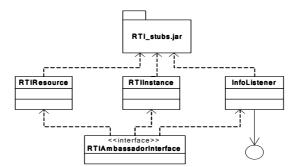


Fig. 3 Structure of RTI WS-Resource at the client

Simulation Procedure Analysis

Under the GSRI, the simulation procedure is shown as Fig.4.

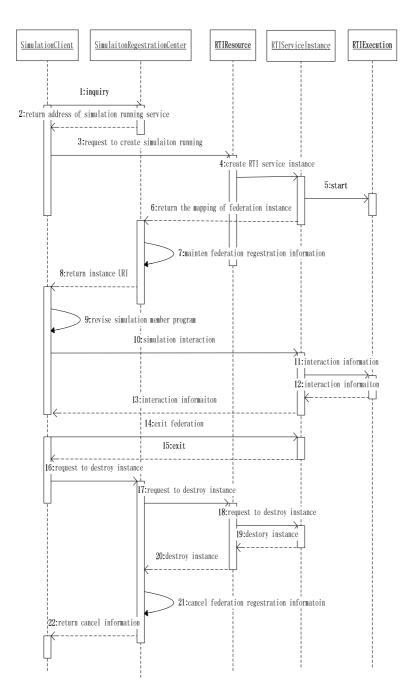


Fig. 4 Interaction process of GSRTI

Performance Analysis

With GSRI as the distributed simulation runtime infrastructure, the transfer time T' from one federate denoted by Sender_C, to the other federate denoted by Receiver_C through WAN is

$$T' = T(Sender_C \rightarrow WSRServer) + T(WSRF) + T(WSRServer \rightarrow RTI) + T(RTIExec)$$

$$+T(RTI \rightarrow WSRServer) + T(WSN) + T(WSRServer \rightarrow \text{Re ceiver}_C)$$
(1)

In Eq.1, $T(Sender_C \rightarrow WSRServer)$ denotes the time consumed by the data transferred from Sender_C to the RTI resource server. T(WSRF) denotes the average consumed time by the RTI processing operations such as analyzing and invoking etc. $T(WSRSever \rightarrow RTI)$ denotes the time consumed by the data transferred from the RTI resource server to the RTI execution. T(WSN)denotes the average consumed time by the RTI resource service callback operations. $T(RTI \rightarrow WSRServer)$ denotes the time consumed by the data transferred from the RTI execution to the RTI resource server. $T(WSRServer \rightarrow \text{Re}ceiver_C)$ denotes the time consumed by the data transferred from the RTI resource server to Receiver C.

Supposing that Sender_C and Receiver_C are deployed at peer to peer computers with the same hardware and software configuration in WAN, the average transfer time between the two federates denoted by T(WAN) is shown as Eq. 2.

$$T(WAN) \approx T(Sender _ C \rightarrow WSRServer) \approx T(WSRServer \rightarrow \text{Re ceiver } _ C)$$
 (2)

And assuming that the RTI resource server is deployed at the peer to peer computer in the LAN, Eq. 3 is got.

$$T(WSRServer \to RTI) \approx T(RTI \to WSRServer) \approx T(LAN)$$
 (3)

With Eq.1 to Eq. 3, Eq. 4 is got.

$$T' = 2T(WAN) + 2T(LAN) + T(WSRF) + T(RTIExec) + T(WSN)$$
(4)

Conclusions

In allusion to the limits of the HLA/RTI used in WAN, the GSRI, the Grid-based simulation runtime infrastructure is put forward. According to the character of the RTI interfaces such as invoking and callback operations, the GT4 tools are used to encapsulate pRTI function interfaces. With the analysis of the runtime performance of GSRI, it is shown that despite the latency created by the transmission through WAN, the GSRI may support the coarse-grained large-scare distributed simulation applications. It is a feasible solution for RTI applications in WAN.

Acknowledgment

Thanks to all those who helped me during the wring of this paper. I gratefully acknowledge the help of my supervisor, Mr. Zhu Yuanchang, who has offered me valuable suggestions in the academic studies. I also owe a special debt of gratitude to all the professors in my work department for their expert guidance. I should finally gratitude to my beloved families for their self-giving supports.

- [1] Katarzyna Rycerz, Marian Bubak, Maciej Malawski, et al. SIMULATION, 2005, 81(1):67~76.
- [2] Yong Xie, Yong Meng Teo, Wentong Cai. In:Proceedings of the Workshop on Principles of Advanced and Distributed Simulation (PADS'05), 2005, 135~143.
- [3] Pitch pRTI [EB/OL] http://www.pitch.se/products/pitch-prti/pitch-prti-overview.html (2006).
- [4] Bubak M., Malawski M., Zajac K.. Towards the Cross Grid Architecture. Berlin Heidelberg: Springer-Verlag, 2002. 75~82..

New Solution for Small File Storage of Hadoop Based on Prefetch Mechanism

Huixiang Zhou^{1, a}, Qiaoyan Wen^{1,b}

¹State Key Laboratory of Networking and Switching Technology, BUPT Beijing, China ^a zhouhuixiang168@163.com, ^bwqy@bupt.edu.cn

Keywords: cloud storage; Hadoop; HDFS; small file; Namenode; prefetch

Abstract. Hadoop performance a significant advantage in dealing with large files, but it is ineffective if we use Hadoop to handle a large number of small files, because the physical address of the Hadoop file is stored in a single Namenode. Suppose that the size of a small file is 100Byte, if there are such a large number of these small files, it may lead to greatly reduce the utilization of Namenode memory, and due to the large number of small files make the index directory increase, it also lower the rate of user accessing to files. To solve the problem described above, this paper propose a new solution for small file storage of Hadoop based on prefetch mechanism, experiment shows that this solution can effectively improve the memory utilization of Namenode and significantly improve the speed of user accessing.

Introduction

Cloud computing is now very popular that we often hear the term cloud computing in everyday life, but we still feel it some illusory feeling. Hadoop is an open source distributed computing for large data processing and analysis platform which is a development platform for cloud computing. In many large modern office business, the amount of data processed at TB level every day, and Hadoop[1] consists of HDFS (Hadoop distributed file system) and MapReduce programming model; HDFS consists of a name server and multiple node servers based data nodes. Large file stored in Hadoop by streaming data access pattern, and Hadoop platform with manager/worker model, data node and name node servers are deployed on ordinary PC.

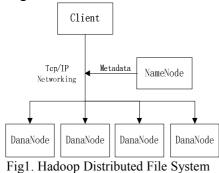
Although Hadoop performance a significant advantage in dealing with large files, but its efficiency is not ideal while we use Hadoop to handle a large number of small files, because the physical address of the Hadoop file is stored in a separate service node(the Namenode), and HDFS the server cluster of Namenode is a directory namespace manager in HDFS. Because of the HDFS Namenode is a single cluster, so all the metadata file system information [2] will occupy some memory space, assuming the size of a small file is 100Byte, if there is such a large number of small files store in Hadoop, it can greatly lead to reduce the utilization of memory for Namenode. There are large number of small files In practical applications, especially with the development of the network, resulting in a large number of dynamic and varied diversity of small file size is KB, so it is a very difficult problem for storage and process these large number of small files. In order to solve the problem of dealing with massive small files that Hadoop encountered as described above, we propose a new solution for small file storage of Hadoop based on prefetch mechanism.

Related research

Modern day cloud storage is based on highly virtualized infrastructure and has the same characteristics as cloud computing in terms of agility, scalability, elasticity andmulti-tenancy, and is available both off-premise and on-premise. It is believed to have been invented by Joseph Carl Robnett Licklider in the 1960s. However, Kurt Vonnegut refers to a cloud "that does all the heavy thinking for everybody" in his book "Sirens of Titan" published in 1959. Since the sixties, cloud computing has developed along a number of lines, with Web 2.0 being the most recent evolution. However, since the internet

only started to offer significant bandwidth in the nineties, cloud computing for the masses has been something of a late developer.

Apache Hadoop is an open-source software frame work that supports data-intensive distributed applications, licensed under the Apache v2 license. It supports the running of applications on large clusters of commodity hardware [3]. HDFS [4, 5] is a distributed, scalable, and portable file system written in Java for the Hadoop framework, each node in a Hadoop instance typically has a single Namenode, the situation is typical because each node does not require a Datanode to be present, each Datanode serves up blocks of data over the network using a block protocol specific to HDFS. The file system uses the TCP/IP layer for communication. The structure of Hadoop distributed file system as shown in Fig1.



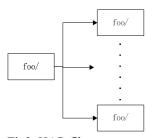


Fig2. HAR files structure

Clients use Remote procedure call (RPC) to communicate between each other. HDFS stores large files (an ideal file size is a multiple of 64 MB [6]), across multiple machines. It achieves reliability by replicating the data across multiple hosts, and hence does not require RAID storage on hosts.

With the default replication value, data is stored on three nodes: two on the same rack, and one on a different rack. Data nodes can talk to each other to rebalance data, to move copies around, and to keep the replication of data high. HDFS is not fully POSIXcompliant, because the requirements for a POSIX file system differ from the target goals for a Hadoop application. The tradeoff of not having a fully POSIX-compliant file system is increased performance for data throughput and support for non-POSIX operations such as Append, and Hadoop was designed to handle large file.

Solution for small file storage which Hadoop integrated

At present, Hadoop for the problem in dealing with small files massive that its encounted, there are two main methods: archive technologies [7] (HAR), sequence file technique (Sequence File) [8]. a) Hadoop Archives

Hadoop Archives (HAR files) file system is to provide a solution for small files, we can ease the burden due to the presence of a large number of small files stored to the Namenode. Hadoop Archives HAR file after the file is saved in HDFS block the merger, by creating a hierarchical file system to deal with relevant documents, can be generated by the Hadoop archive command. The structure of HAR files as shown in Fig2.

b) Sequence File

Sequence File is Hadoop API [9] which provides a binary file supported, multiple small files can be organized in a unified storage. The main idea is to use technology Sequence File file name as a keyword, the document as a value, a number of small files to be written to a single merged document to the sequence, can be used directly after the completion of the document. Its data structure is composed of a series of binary key / value composition, in this technique, the file name into the key, the file contents into the value, then a large number of small files can be merged into one big file.

Suppose there are 100,000 small 10KB file, you can write a program in accordance with the key / value structure of these small files stored in a container sequence file, create a sequence file map-reduce process can be used to complete the work index, it need to improve access for small files search algorithms are relatively free, nor restrict the number of users and files. But sequence file does not support random files in its internal storage access when we need to access files within it, and need to traverse the entire directory files, it causes the lower efficiency for file reading in Hadoop.

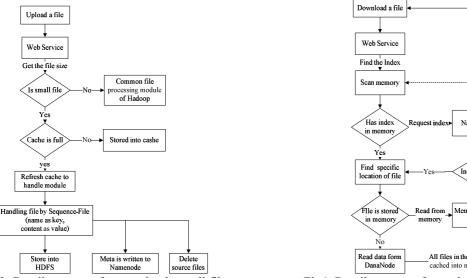
New solution based on prefetch mechanism

Prefetch of index file means that block of the file resides related index file is loaded into memory when a user accesses file, so users do not have access to these files and interact with Namenode; Prefetch data file refers to all file in the block is loaded into memory while a user accesses file first, so the speed will be significantly improved when there have user continue to access other files. Steps of usersto upload and download files as follows:

2. User uploads small file:

- 3. Determine whether the file is small file while user upload a file, if it is small file that can put it to the processing module of small file, otherwise, put it to the common file processing module of Hadoop.
- 4. Set a monitor and a buffer zone for processing of small file, then make the file name as key and the related file content as value by the Sequence File components when the file block size is larger than the total size of the buffer, and then write these small files to HDFS.
- 5. Delete files that have been processed, and write the relevant meta-information to the Namenode.

The detail process of user uploads small file as shown in figure 3. Firstly, user initiates a upload request to the web server, determine the size of the file after web server receives the request, if the size of this file is larger than the default block size of HDFS (usually 64M, can be set in the configuration file) that this file is considered to be a large file, then put it to the common file processing module of Hadoop, but if the size of this file is less than the default block size of HDFS that this file is considered to be a small file. Write this file to the buffer directly while the total site of data which written to the buffer is smaller than the threshold of buffer, otherwise, firstly write the data to buffer and then submit all the data of buffer to the Sequence File, finally, Sequence File store all small files which be processed into hadoop distribute file system, then delete the source files and write the metadata to Namenode.



Return Information of faile NameNode Index fined Memory of web server All files in the block cached into memory

Fig3. Detail process of user uploads small file.

Fig4. Detail process of user downloads small file.

6. User downloads small file:

- 7. Prefetch the index of all files which stored in the same block into the buffer while user access a file, so that user no longer interact with the Namenode when user access these files again.
- 8. Prefetch data means that prefetch all files which stored in the same block into the buffer while user access a file, as a result that the speed will be significantly improved while user continues to access other files.

The detail process of user uploads small file as shown in figure 4, firstly, the user initiates a request to a web server to read the file, then web servers determine whether information of the file index is cached in memory, read the index from memory directly if the index is cached in it, otherwise request file index from Namenode. If it did not find the file index from Namenode, then return error message that file request failed. Download the file according to the information of file index, if the index shows that file is in memory, then read the file directly from memory, otherwise read the file from the Datanode, and stored the other files which in same block into the memory of this Datanode, if the user continues to access the other files, the speed of file reading will be significantly improved.

To verify our solution we deployed one Namenode and five Datanode (configuration of these server hardware is the 4-core processor and 8GB memory), and the simulation results show that the average speed was 7.6M/s while user first visits a small file from Hadoop, and the average speed was 10.2M/s when a user visits a small file again, This shows that the file reading speed increased by 34%, so it can conclude that it effectively improve the speed of accessing small file by prefetching file index and all files which in same block into memory on Hadoop.

Conclusions

Hadoop be designed to handle large file, but if there are such a large number of small files be stored into Hadoop, it may lead to greatly reduced the utilization for Namenode memory decline in the rate of user access to files, we propose a new solution for small file storage of Hadoop based on prefetch mechanism, Prefetch of index file means that block of the file resides related index file is loaded into memory when a user accesses file, so users do not have access to these files and interact with Namenode; Prefetch data file refers to all file in the block is loaded into memory while a user accesses file first, so the speed will be significantly improved when there have user continue to access other files. The simulation results show that this solution improve the utilization for Hadoop system resource and greatly improve the speed of accessing small file. However, the security of the implementation has yet to be improved which is our next step to research.

Acknowledgment

This work is supported by NSFC (Grant Nos. 61300181, 61272057, 61202434, 61170270, 61100203, 61121061), the Fundamental Research Funds for the Central Universities (Grant No. 2012RC0612, 2011YB01).

References

- [1] White T. Hadoop: The Definitive Guide: The Definitive Guide[M]. O'Reilly Media, 2009.
- [2] http://Hadoop.apache.o-rg/common/docs/r0.20.2/Hadoop_archiv.
- [3] Borthakur D. The hadoop distributed file system: Architecture and design[J]. 2007.
- [4] Borthakur D. HDFS architecture guide[J]. Hadoop Apache Project. http://hadoop. apache. org/common/docs/current/hdfs_design. pdf, 2008.
- [5] Liu X, Han J, Zhong Y, et al. Implementing WebGIS on Hadoop: A case study of improving small file I/O performance on HDFS[C]//Cluster Computing and Workshops, 2009. CLUSTER'09. IEEE International Conference on. IEEE, 2009: 1-8.
- [6] Boulon J, Konwinski A, Qi R, et al. Chukwa, a large-scale monitoring system[C]// Proceedings of CCA. 2008, 8.
- [7] http://wiki.apache.org/Hadoop/SequenceFile.
- [8] White T. Hadoop: The Definitive Guide: The Definitive Guide[M]. O'Reilly Media, 2009.
- [9] Yang H, Dasdan A, Hsiao R L, et al. Map-reduce-merge: simplified relational data processing on large clusters[C]//Proceedings of the 2007 ACM SIGMOD international conference on Management of data. ACM, 2007: 1029-1040.

A Game Theoretic analysis of resource pricing and sharing in P2P networks

Qingfeng Zhang^{1, a}, Sheng Wang^{1, b}, Dan Liao^{1, c}

¹College of Communication and Information Engineering,

University of Electronic Science and Technology of China,

Chengdu, China,

^aqingfengzhang2010@126.com,^bwsh_keylab@uestc.edu.cn,^cliaodan@uestc.edu.cn

Keywords: P2P networks; Game theory; Incentive mechanism; the Cournot equilibrium sharing; Nash equilibrium sharing

Abstract—This paper proposed an incentive mechanism of resource pricing and sharing to achieve the maximum of profits, which based on game theory. Firstly, we proved the Cournot equilibrium sharing within different price and cost functions to achieve the maximum profits. Secondly, we analyze and solve the Cournot equilibrium sharing, the unit profit and the total profits. Finally, simulation show that the proposed model relationships among the number of providers, different of price and cost functions, the maximum profits parameter, the unit profit and the total profits.

Introduction

Peer-to-Peer (P2P) technologies have been wildly used in many fields such as: file-sharing, distributed storage and computing, person instant messaging and collaborative work between peers. It also has been one of the hot spots in study of business and academic.

Many literatures have been studied on how to allocate or sharing resources to the consumers, such as: price mechanisms [1]; credit mechanism [2];rank mechanisms [3]; game theory [4],[5]; Reciprocity and Barter mechanisms [6],[7]; reputation mechanism [8].

System model

In this paper, the peers are divided into the providers and the consumers. The providers sharing their resources to the consumers which must be incur sharing costs, so, the providers must be pricing their sharing resources to maximum profits.

Let the total number of the providers in p2p networks be n, which consists a set of player $\mathcal{N} = (1, 2, ..., n)$; Let x_i denote real resource sharing and ω_i denotes sharing capacity of provider i respectively, so that $0 \le x_i \le \omega_i$; let $\varphi(\mathcal{X})$ denote the unit price function depends on the total resources sharing $\mathcal{X} = \sum_{i=1}^n x_i$, which is also the demand of the consumer; let $c_i(x_i)$ denotes the cost function, which is related to the amount of the providers' resource sharing; Let $\mathcal{U}_i(x_1, x_2, ..., x_n)$ denote the payoff function of the provider $i(i \in \mathcal{N})$.

 $U_{i}(x_{1}, x_{2}, \dots, x_{n}) = x_{i}\varphi(\mathcal{X}) - c_{i}(x_{i}) = x_{i}\varphi(x_{1} + x_{2} + \dots + x_{n}) - c_{i}(x_{i})$

The resource sharing strategy set of provider i is $x_i = \{x_i \mid 0 \le x_i \le \omega_i\}$; so, the resource sharing set is consisting of bounded closed convex set for the providers.

If price function is a concave function and cost function is a convex function, the Cournot equilibrium sharing point must be exist for the providers.

Therefore, we assume that the price function is a concave function and the cost function is a convex function in the following.

A: price and cost functions are linear functions

Assume that the provider *i* unit cost is *c*, if there are no fixed cost of some resource, that means the provider unit marginal cost is a constant c > 0, the cost function is $c_i(x_i) = cx_i$; the price function is $\varphi(\chi) = a - \mathcal{E} \chi$, where a, \mathcal{E}, c are positive constants and a > c, let *a* denotes the maximum profits parameter, which depends on the providers sharing and demand of the consumer.

$$\begin{aligned} & \mathcal{U}_{i}(x_{1}, x_{2}, \dots x_{n}) = x_{i} \varphi(\chi) - c x_{i} = x_{i} \varphi(x_{1} + x_{2} + \cdots x_{n}) - c_{i}(x_{i}) = x_{i} (\varphi(\chi) - c) \\ & i = 1, 2, 3, \dots n \end{aligned}$$

the provider resources sharing and get the partial derivatives on resource sharing of the payoff function:

And

n

The equalization sharing is: $x_i^* = \frac{1}{n} \mathcal{X}^* = \frac{(a-c)}{(n+1)\delta}$, i = 1, 2, 3, ..., n(2)

And $x^* = (x_1^*, x_2^*, \dots, x_n^*)$ is the Cournot equilibrium sharing, where x_i^* is the equalization sharing.

The unit profit as:

$$\varphi(\mathcal{X}^*) - c = a - \vartheta \mathcal{X}^* - c = \frac{(a-c)}{(n+1)}$$

$$\mathcal{U}_i(x_1, x_2, \dots x_n) = x_i^* \frac{(a-c)}{(n+1)}$$
(3)
(4)

(4)

(6)

The payoff function is:
$$U_i(x_1, x_2, \dots x_n)$$

B: price function is non-linear function and cost function is linear function

Assume that the cost function of the provider *i* is $c_i(x_i) = cx_i$ and the price function is $\varphi(\chi) = a - \mathscr{b} \chi^{\alpha}, a, \vartheta, c, \alpha$ are constants and also a >c.

$$\begin{aligned} \mathcal{U}_{i}(x_{1}, x_{2}, \dots, x_{n}) &= x_{i} \varphi(x_{1} + x_{2} + \dots + x_{n}) - c_{i}(x_{i}) = x_{i} \varphi(\chi) - c x_{i} = x_{i} (\varphi(\chi) - c) \\ & i = 1, 2, 3, \dots n \\ (a - c - \vartheta \mathcal{X}^{\alpha}) - \vartheta \alpha(x_{1}^{\alpha} + x_{2}^{\alpha} + \dots + x_{n}^{\alpha}) = 0 \end{aligned}$$

Let $x_1^{\alpha} + x_2^{\alpha} + ... + x_n^{\alpha} = S$; Where the total resource sharing must be meet to the following equation: $\mathcal{X} = \sum_{i=1}^{n} x_i$

The total resource sharing of the Cournot equilibrium sharing is:

$$\mathcal{X}^* = \left(\frac{n(a-c)-b\alpha s}{nb}\right)^{\frac{1}{\alpha}}$$
(5)
$$x^*_i = \frac{1}{\alpha} \left(\frac{n(a-c)-b\alpha s}{c}\right)^{\frac{1}{\alpha}}, i = 1, 2, 3, \dots n$$
(6)

The equalization sharing is: The unit profit as:

$$\varphi(\mathcal{X}^*) - c = a - \delta \mathcal{X}^{*\alpha} - c = \frac{\alpha \delta S}{n}$$
(7)

The payoff function: $\mathcal{U}_i(x_1, x_2, \dots, x_n) = x_i^* (\varphi(\mathcal{X}^*) - c) = x_i^* \frac{\alpha \delta S}{n} = \left(\frac{n(a-c) - \delta \alpha S}{n\delta}\right)^{\frac{1}{\alpha}} \frac{\alpha \delta S}{n^2}$ (8) C: price function is linear function and cost function is non-linear function

Assume that the cost function is $c_i(x_i) = d + ex_i^{\beta}$, if there is no sharing, the cost is 0, that means $c_i(x_i) = c_i(0) = 0$, so, d=0, the provider's cost function becomes $c_i(x_i) = ex_i^{\beta}$; the price function is $\varphi(\chi) = a - \vartheta \chi$, where $a, \vartheta, \varepsilon, \beta$ are constants.

$$\begin{aligned} \mathcal{U}_{i}(x_{1}, x_{2}, \dots, x_{n}) &= x_{i}\varphi(x_{1} + x_{2} + \dots + x_{n}) - c_{i}(x_{i}) = x_{i}\varphi(\chi) - ex_{i}^{\beta}, i = 1, 2, 3, \dots n \\ \frac{\partial}{\partial x_{i}}\mathcal{U}_{i}(x_{1}, x_{2}, \dots, x_{n}) &= \varphi(\chi) + x_{i}\frac{\partial\varphi(\chi)}{\partial x_{i}} - e\beta x_{i}^{\beta-1} = 0 \implies a - \vartheta \mathcal{X} - \vartheta x_{i} - e\beta x_{i}^{\beta-1} = 0 \\ \text{And:} \qquad n(a - \vartheta \mathcal{X}) - \vartheta \mathcal{X} - e\beta (x_{1}^{\beta-1} + x_{2}^{\beta-1} + \dots + x_{n}^{\beta-1}) = 0 \\ \text{Let } x_{i}^{\beta-1} + x_{i}^{\beta-1} + \dots + x_{i}^{\beta-1} = T. \quad \text{Where the total measures sharing must be active.} \end{aligned}$$

Let $x_1^{p-1} + x_2^{p-1} + \dots + x_n^{p-1} = \mathcal{T}$, Where the total resource sharing must be satisfy the following equation: $\mathcal{X} = \sum_{i=1}^n x_i$

And the total resource sharing of the Cournot equilibrium sharing is:
$$\mathcal{X}^* = \frac{na - \epsilon\beta T}{(n+1)\delta}$$
 (9)
The equalization sharing is: $x_i^* = \frac{na - \epsilon\beta T}{r(n+1)\delta}$, $i = 1,2,3,...n$ (10)

he equalization sharing is:
$$x_i^* = \frac{n \cdot x_i^* \cdot p \cdot p}{n(n+1)\delta}$$
, $i = 1, 2, 3, ..., n$ (10)

The unit profit as:

$$a - \mathcal{C}\mathcal{X}^* - e = \frac{a - \varepsilon(n+1-\beta\mathcal{T})}{(n+1)} \tag{11}$$

The payoff function as:

$$\begin{aligned}
\mathcal{U}_{i}(x_{1}, x_{2}, \dots, x_{n}) &= x_{i}^{*} \varphi(\mathcal{X}^{*}) - \varepsilon x_{i}^{*\beta} = \frac{na - \varepsilon \beta T}{n(n+1) \delta} \left(a - \vartheta \frac{(na - \varepsilon \beta T)}{(n+1) \delta} \right) - \varepsilon \left(\frac{na - \varepsilon \beta T}{n(n+1) \delta} \right)^{\beta} &= \frac{na - \varepsilon \beta T}{n(n+1) \delta} \left(a - \frac{(na - \varepsilon \beta T)}{n(n+1) \delta} \right)^{\beta}
\end{aligned}$$
(12)

D: price and cost functions are non-linear functions

Setting the cost function is $c_i(x_i) = e x_i^{\beta}$ and the price function is $\varphi(\chi) = a - \delta \chi^{\alpha}$. Where $a, \delta, e, \alpha, \beta$ are constants.

 $\begin{aligned} \mathcal{U}_{i}(x_{1}, x_{2}, \dots, x_{n}) &= x_{i}\varphi(x_{1} + x_{2} + \dots + x_{n}) - c_{i}(x_{i}) = x_{i}\varphi(\chi) - \varepsilon x_{i}^{\beta} \quad i = 1, 2, 3, \dots n \\ \text{With assumes that:} \quad \frac{\partial}{\partial x_{i}}\mathcal{U}_{i}(x_{1}, x_{2}, \dots, x_{n}) = \varphi(\chi) + x_{i}\frac{\partial\varphi(\chi)}{\partial x_{i}} - \varepsilon\beta x_{i}^{\beta-1} \quad i = 1, 2, 3, \dots n \\ &\implies a - \vartheta \, \chi^{\alpha} - \vartheta \alpha x_{i}^{\alpha} - \varepsilon\beta x_{i}^{\beta-1} = 0 \\ n(a - \vartheta \chi^{\alpha}) - \vartheta \alpha (x_{1}^{\alpha} + x_{2}^{\alpha} + \dots + x_{n}^{\alpha}) - \varepsilon\beta (x_{1}^{\beta-1} + x_{2}^{\beta-1} + \dots + x_{n}^{\beta-1}) = 0 \\ \text{Let } x_{1}^{\alpha} + x_{2}^{\alpha} + \dots + x_{n}^{\alpha} = S; x_{1}^{\beta-1} + x_{2}^{\beta-1} + \dots + x_{n}^{\beta-1} = \mathcal{T}; \text{ where the total resource sharing must be satisfy the following equation: } \mathcal{X} = \sum_{i=1}^{n} x_{i}. \\ \implies \chi^{*\alpha} = \frac{na - \vartheta \alpha S - \varepsilon\beta \mathcal{T}}{n\vartheta} \end{aligned}$

The total resource sharing of the Cournot equilibrium sharing is: $\chi^* = \left(\frac{na - b\alpha S - e\beta T}{nb}\right)^{\frac{1}{\alpha}}$ (13)

The equalization sharing is:

$$x_{i}^{*} = \frac{1}{n} \left(\frac{na - b\alpha s - \epsilon \beta J}{nb} \right)^{\alpha}, i = 1, 2, 3, \dots n$$

$$(14)$$

$$a - h \Upsilon^{*\alpha} - e = \frac{b\alpha s + \epsilon \beta J}{nb} - e$$

$$(15)$$

The unit profit as:

$$a - \vartheta \mathcal{X}^{*\alpha} - e = \frac{\vartheta \alpha s + e\beta J}{n} - e \tag{15}$$

0

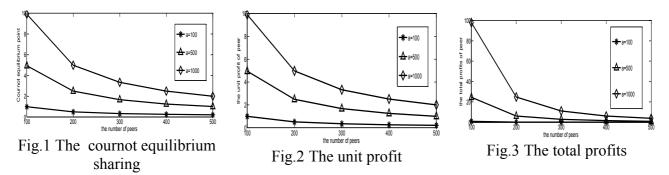
The payoff function as:

$$\mathcal{U}_{i}(x_{1}, x_{2}, \dots, x_{n}) = \frac{1}{n} \left(\frac{na - b\alpha\beta - \epsilon\beta\mathcal{T}}{nb}\right)^{\frac{1}{\alpha}} \left(a - b\frac{na - b\alpha\beta - \epsilon\beta\mathcal{T}}{nb}\right) - e\left(\frac{1}{n} \left(\frac{na - b\alpha\beta - \epsilon\beta\mathcal{T}}{nb}\right)^{\frac{1}{\alpha}}\right)^{p}$$
(16)

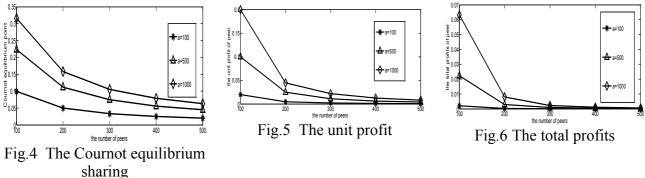
Simulation results

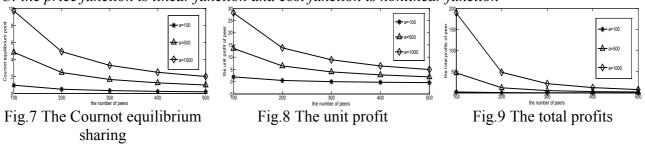
Assume that there are n providers (peers) sharing their resources to the consumer, the parameters of the price and cost functions as following: $\mathbf{e} = \mathbf{c} = \mathbf{e} = \mathbf{1}$; $\alpha = \beta = 2$; simulate and analyze the Cournot equilibrium sharing, unit profit and the total profits within the maximum profits. Within the maximum profits a=100,500,1000 respectively.

A: price and cost functions are linear functions



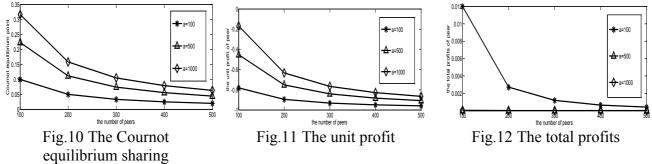
B: the price function is the nonlinear function and cost function is a linear function





C: *the price function is linear function and cost function is nonlinear function*

D: the price and cost functions are non-linear functions



Figures 1~12 show that: with the number of providers and the maximum profits increasing, the Cournot equilibrium sharing and the unit profit gradually decreasing but the speed is becoming slower and slower; with the maximum profits increasing, the Cournot equilibrium sharing and the unit profit is also increasing, but they are not increase with the same proportion. With the number of providers increasing, the speed is also becoming slower and slower.

References

- [1] Jaeok Park Mihaela vander Schaar "Pricing and Incentives in peer-to-peer Networks" IEEE Communications Society subject matter experts for publication in the IEEE INFOCOM proceedings (2010).
- [2] Josep Rius. Fernando Cores. Francesc Solsona, "A New Credit-Based Incentive Mechanism for P2P Scheduling with User Modeling" First International Conference on Advances in P2P Systems (2009).
- [3] Yong he Yan, Adel El-Atawy, Ehab Al-Shaer "Ranking-based Optimal Resource Allocation in peer-to-peer Networks" IEEE Communications Society subject matter experts for publication in the IEEE INFOCOM proceedings (2007).
- [4] C. Buragohain, D. Agrawal, and S. Suri, "A game theoretic framework for incentives in P2P systems" in Proc. 3rd Int. Conf. Peer-to-Peer Comput, (2003), pp. 48–56.
- [5] Jaeok Park and Mihaela vander Schaar, "A Game Theoretic Analysis of Incentives in Content Production and Sharing Over peer-to-peer Networks" IEEE Journal of Selected topics in signal processing, Vol. 4, no. 4, August (2010).
- [6] Chow-Sing Lin Yi-Chi Cheng, "A Barter-Based Incentive Mechanism for peer-to-peer Media Streaming" The 13th IEEE International Symposium on Consumer Electronics (ISCE2009).
- [7] Daniel Sadoc Menasch'e, Laurent Massouli'e, Don Towsley •Thomson Research, "Reciprocity and Barter in peer-to-peer Systems" IEEE Communications Society subject matter experts for publication in the IEEE INFOCOM proceedings (2010).
- [8] Lei Yang , ZhiGuang Qin, Hao Yang, Can Wang, Chao Sheng Feng. A reputation-Based Method for Controlling Free-ride in P2P Networks. 2010 IEEE.

Using Untiy 3D Game Development Platform to Develop Low Cost Online Real Estate Display System

Jiang-Rui^{1,a}

¹The Yellow River water conservancy vocational technical college of information engineering department ,Kaifeng ,he nan , China

^aidmt-4@126.com

Keywords: Virtual reality technology;3D model;Material and texture;Untiy 3D platform;Low cost online real estate display system

Abstract: The thermal situation in tackling the current real estate marketing cost is high, the display effect is poor, the purpose of effective communication problems such as less crowd, put forward using Untiy 3D game development platform to develop low cost online estate system method. Starting from the relevant concepts, mainly introduced how to make use of the existing 3D model technology, image processing technology, as well as Untiy 3D game development platform integration technology and so on the many kinds of virtual reality technology, complete the system, finally solve the relevant problems in real estate marketing.

Introduction

The current real estate continued high fever, the real estate developers have except than cost, quality, or geographic location, it is used when the marketing technique, spend a lot of effort, the huge advertising, elegant district propaganda animation or rendering sand table model. Which reduced proportion because of the large sand table should pass, therefore can only obtain the community have a bird's eye view of image, not by normal perspective feeling of architectural space, more can't get people walking in the true sense. At the same time, in after the model, the modified cost is very high, there is a big limitation. So developers spend vast sums of money, the introduction of the big 3D multimedia exhibition hall, its advantage is, of course, but its investment and effect than is questionable.

The first is the 3D multimedia exhibition hall are basic ring screen showroom design, because the cost problem exhibition hall area is finite, when opening may not be able to accommodate the influx of a large number of customers, resulting in customer waiting for the final produce anxiety, image marketing effect.Even at no cost to expand the exhibition hall area of acceptance of the client, relative to the on-site customer more and more people is through the telephone consultation and online consulting, to say the exhibition hall is good but in the face of these customers and how to implement the marketing effect directly into a can't solve the problem.So this article puts forward using Untiy 3D platform development low cost online real estate display system, through the powerful network function, and virtual reality technology to realize the complex virtual 3D digital network marketing and the checking experience.

1. Low cost online real estate display system

1.1 the virtual reality technology

VR (Virtual Reality, VR for short, is a high and new technology, at the beginning of this century is a hot spot in recent years, computer multimedia technology front.

Virtual reality is used computer simulations to create a 3d virtual world, to provide users simulation about senses such as vision, hearing, touch, let users as illustrates its general, timely, there is no limit to observe things in three dimensions.

1.2 Untiy 3d game development platform

Unity is a developed by Unity Technologies allow players to easily create such as 3d video game, architectural visualization, real-time 3d animation and other types of interactive content multi-platform integrated game development tool, is a comprehensive integration of the professional game engine. Unity is similar to the Director, the Blender game engine, Virtools or the Torque game Builder and other interactive pattern to make use of the software development environment as the primary way the editor running under the Windows and Mac OS X, can release the product to Windows, Mac, Wii, iPhone and Android platform, support for Mac and Windows web browsing.

1.3 low cost online real estate display system

Low-cost online housing system is the use of 3ds MAX 3d modeling, and use the Untiy 3d platform to realize integration, published as web browsing and mobile platforms support of virtual display system, and can give full play to the role of virtual reality technology in the real estate marketing.

For the inspection of the customer before the real estate is not built, there can be a personal and real experience is to decide whether to buy the image of a very important factors. And you can also show after the system from the virtual function to the real-time information query, the upgrading of advanced features such as content objects connected to control provides reserved interface, network era into thing truly league era provides intelligent building management system development platform provides a basis.

2. Low cost online estate system production

2.1 preparation

Because in the production of 3d model will be in Unity 3d digital platforms for clamping, at the same time created 3d digital city virtual system. So late Unity 3d digital platform for the production of 3d model from time to tome requirement, in order to improve the production efficiency of 3d model at the same time, also need to follow when making certain production specification.

Low cost online real estate display system often because according to the different requirements of customers is also different, so to provide customers with products that meet the requirements is the production staff of the mission, is also the key to improve the efficiency of production. Therefore it is necessary to establish good communication channels.

Low cost online real estate information display system is very large. The file type and quantity are many. Common file types of AutoCAD software. DWG files, 3ds Max. Max model file, Maps model, the map file. Tga, UV file to store 3ds Max software, and made with Photoshop. PSD files, map work. JPG: final model mapping files and transparent texture. PNG file. Therefore to establish a system for regular inspection sorting data, at the same time set up FTP server project folder, completes the data management.

2.2 3D modeling

Three-dimensional modeling phase is given according to the property of AutoCAD design drawings, topography of late to file, the building model, building facilities model files, as well as the model mapping file created. The details are as follows:

In 3ds Max software, need to change the background color from the default gray to black, this is in order to freeze the imported DWG figure, can still clearly see the graphics, facilitate tracing modeling.Secondly because building a very large area, not ordinary interior decoration, therefore the unit also needs the past mm, to meters.

Create die.it began from import processing good AutoCAD drawing, using 3ds Max capture tracing function, according to the imported AutoCAD drawing tracing in 3ds Max, tracing out into three-dimensional model, as shown in figure 1.

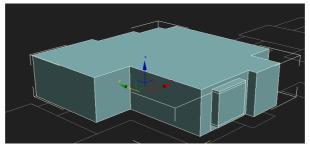


Fig.1 Tracing and extrusion

Repeat operation to complete building model, according to the actual situation of the building, copying out of each layer, forming a three-dimensional model of the whole building, as shown in figure 2.

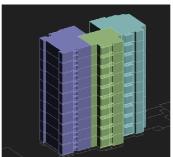


Fig. 2 In 3ds Max in the structure of the 3d model

3d model is created to late in the digital platforms, so in addition to meet customer needs, more need meet late synthesis.Specification requirements in accordance with the requirements of late synthesis and modeling and delete those can not see the face of the 3d model.

The production process and 3ds MAX normal map, divided the UV first, and then export the UV.But because the building is still in construction, it can be said that there is no physical for production map of real texture so, according to the design units to provide rendering made in Photoshop software.

Again into 3ds Max software, using UV coordinates positioning map.In 3ds Max at the same time the material editor window, select a sample of the ball material, in the column of "diffuse" map channel selection "bitmap", and put into the corresponding mapping file.Will make a good ball material samples on the material object is assigned to the object, in turn, will all the UV coordinates corresponding parts are finished, after collapse should be fixed in each corresponding surface, complete model effect as shown in 3.



Fig.3 Buildings each surface and the effect of the overall model

Building is from a family to a layer of floor, to multi-storey building, step by step, can complete the whole building, 3d modeling of the whole building effect of color mode such as 5.

The terrain and the supporting facilities for the community, such as street light, dustbin, pavilion, etc.), can also use this method to establish model.

2.3 Untiy 3d platform integration model

In 3ds Max software after finished all modeling, model needs to be saved to the specified folder (including map file).Need will become Untiy 3d model export can accept fang binxing format file, also in this folder for later use.

After entering the Untiv 3d software to create a new project file, the file is copied to the project and will be prepared "Assects" folder, and restart Untiv 3d into the project will be automatically added to the project.

Using Untiv 3d software to create the terrain, and according to the plan on CAD diagram of the complex put terrain model, building model, and other supporting model. As shown in figure 4.

In Until 3d software using tools such as brush, to make the ground hardening or lawn processing, at the same time using the resource bundle into trees, as shown in figure 4.



Fig.4 Building model object

In Untiv 3d software platform is very rich in resources, can make full use of its resources to achieve such as BOX is introduced into the sky and the first-person perspective or third person roaming control.

In order to the authenticity of roaming, generally USES the first perspective.First need to delete the scene in the Main Camera (Main Camera), and then add the First Person Controller (role with a first-person perspective, resource package), adjust the First Person Controller position to the right place in the scene, and set its height is about 1.73 to 2.1 (normal eye level).

In order to better roaming, can open the Standard of the area of the Project Assets under the Camera under the Scripts of Mouse Look script, the Quaternion originalRotation procedures section add a (as shown in figure 5) :

If (Input. GetAxis (" Fire2 ") = = 0) return;

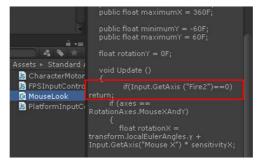


Fig.5 Modify the Untiy 3d first-person perspective roles in control

After debugging can click on the "File" menu of "Build Settings" command, the dialog box choose publishing environment, can be released into the WEB WEB browsing, more can make use

of mobile network and intelligent terminal, release said Android format, through the mobile phone to create low-cost online real estate display system.

Summary

Based on virtual reality technology is discussed here the practice method of low-cost online real estate display system and the main technical points, including preparation stage, the model establishment, platform integration and released several links, especially using Untiy 3d platform for integration, which was different from those using VRML programming, Untiy 3d platform embedded JAVA or c # programming, for subsequent platform upgrade information higher functions such as real-time query, something connected control upgrade provides a better interface reserve, has a higher practicability and better expansibility.

References

- [1] Magnesium, Wang Wenjian Bai Xuefei. Imperial university, shanxi building based on virtual reality technology recovery simulation, 201229 (Vol.11) :P.20-23,46-48
- [2] Jiang rui, Utilizing Vgs Techno -logy to Develop Cam -pus Net and to Set up Virtual Teaching En –ironment [C], 2009 China ningbo international computer science conference(2009)
- [3] Jiang rui, Using the plugin to realize 3D web technology [C], 2010 The third international modeling, calculation and simulation, optimization and application of academic exchange(2010)
- [4] Jiang rui, Using the QTVR technology to implement low cost 360° panorama of interior design display [C], 2011 The fourth international modeling, calculation and simulation, optimization and application of academic exchanges.(2011)

A Design of IT Enterprise Information Platform in Cloud Environment

Ling Wei^{1, a}, Weixi Zhang^{1,b}, Xinpeng Guo^{1,c}

¹Harbin University of Science and Technology Hei Longjiang Harbin , China ^aweiling@hrbust.edu.cn,^b394347018@qq.com, ^c393876641@qq.com

Keywords: Cloud computing, IT Alliance, Security, Information platform.

Abstract. This paper seeks to combine the advantages of cloud computing to design an IT enterprise alliance information platform based on cloud computing. In this study, we adopt B/S framework of tree cloud database to store IT enterprise alliance information for this platform, which is used for activity data collection and its subsequent analysis. Further, starting with the demand analysis of IT enterprise alliance information, we investigate the function of the information platform, including information release function, knowledge sharing function and online communication function and so on. At last, we propose and devise an effective IT enterprise alliance information platform utilizing the cloud resource to complete handling business problems between alliance enterprises effectively.

Introduction

Due to the application of computer technology in various industries in the society, the alliance between enterprises becomes the inevitable tendency. Alliances can provide information sharing, service sharing, resource sharing and security for each alliance member, which can improve the degree of correlation between enterprises. Also, the enterprise can get better utilization of resources and expand the market for further development. Because of foreign orders greatly reduced large foreign software and hardware business inroads into China. IT outsourcing market has suffered great influence. Therefore, IT market in China develops slowly, especially in small IT enterprises market. It is necessary to united IT industry, and establish IT alliance to resist foreign competition together. At present, IT industry penetration in vast rural areas, the township and midwest backward area is not high, which means that Chinese IT Market is huge and has further development space. The establishment of information service platform provides a foundation to realize industry alliance. According to certain rules and mechanisms, it promote the interaction between mass endpoint on the basis of mass information. On the platform, the relationship in enterprises can be set up and it become convenience to manage the intercompany transaction, technology sharing and improve the service efficiency.

The introduction for IT enterprise alliance information platform in cloud environment

Features of cloud computing. Basic principles of cloud computing is to use a collaborative work in distributed computer rather than to use the local computer or a remote server to deal with the problem of information storage^[1]. The data processing center collate internal and external information to realize internet effect by this mean. what makes the enterprise can be switched quickly to the resources needed for application and access the computer and storage system according to the demand^[2]. In the age of big data, cloud computing has good application prospect^[3]. It provides three main services: infrastructure as a service (IaaS), platform as a service (PaaS) and software as a service (SaaS). It has such features: information transparency, high utilization rate of resources, resource storage, distribution according to needs (namely buy namely distribution) etc.

Introduction of IT enterprise information platform under cloud environment. IT enterprise information platform under the environment of cloud is based on cloud computing. Through the use of large storage cloud and the characteristics of resource transparency, it adopt pay-on-demand to distributed compute and memory bandwidth resources. In the face of IT enterprise, alliance form

link enterprises together and use this platform to deal business processing, information resources sharing and so on. The biggest characteristic of IT enterprise information platform is targeted relatively strong. As it has screening function, it provides good protection for the rational use of this platform.

The database design of information platform in the cloud

Designing the IT enterprise information platform, the database adopt the B/S framework to finish it ^[4]. Correspondingly, the database is the traditional relational database type which provides data storage function, in which different users establish different tables. The function table associates by primary key and foreign key between the tables. These tables can set up cascade, cascade delete query functions, which brings users great convenience that it can easily query the required data for the item.

Taking advantage of the cloud to operate the platform, this platform finally adopt SaaS tree cloud database to store corresponding information, of what feature is mass storage and transparent transmission. Users don't have to worry about confidential information involved with enterprise and individual, because the platform is provided with a corresponding security measures. If the information leakage, the registrant will receive news via email or SMS way .That is, site managers will also take corresponding measures and strengthen the website security function.

The database based on cloud computing mainly includes the following operations: database design structure, database resource repository, multi tenant resource management and database table design. The reason of putting SaaS into the cloud computing use is because it provides service on demand and more and more applications exploited. Users can access via the internet cloud computing information platform to operation hardware, software and operating system. The platform with transparency and information services and information resources quantify trait, offers a good storage space and design environment. The users does not need to upgrade and maintain website personally, cloud computing will give the corresponding function, which refrains users delay business from maintenance.

IT alliance enterprises information service platform based on cloud computing need store a large number of enterprise information and personal information, so it must be very strict with storage. The corresponding data tables are stored in the database for different types and relationships between tables are associated with the primary key and foreign key .Database could update the dynamic information timely, making sure that it will not affect the user demand. IT enterprise information platform design the following database tables: news report (T_News), user, business scale (T_User), product promotion table (T_Products)etc.

Information platform function design

Information publishing function. It includes major information published by registered enterprise. Such as recruitment information, demand information cooperated enterprises, outsourcing information resources and information release.

Knowledge sharing function. This module mainly realizes technology and non technology information resources sharing, including transparent utilization. In this platform, users have the file information download or upload with certain integral condition permission. Through visits times, upload times, download times, users obtain more integrals.

Online exchange function. The platform adopts a popular means of communication, such as, exchange information online QQ, forum form of online communication. Registered users don't have to worry about some important information will leak. The paltform will do the security for your exchange of information and will not let the information exposure.

Recruitment function. Through this platform, enterprises add the required talent type, academic requirements and even more specific requirements in the corresponding module. The information

service platform will automatically classify and supply staff to choose. For example: we can set wages for several grades and supply of recruit selection.

Information feedback function. If the platform or some unscrupulous companies are not satisfied with, it can feedback to the administrator through the platform. The administrator will upgrade the platform, adjust substandard enterprises timely and correct information.

OLAP function. Through the platform of online services, it can provide the environment in which alliance enterprise could deal with process services. For example, it can open a separate space for business process through the cloud environment for enterprises

Function structure diagram is shown in Fig.1.

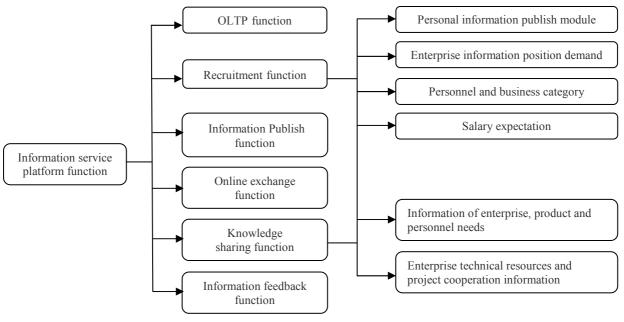


Fig.1 Information platform function structure

IT enterprise alliance information platform design in cloud environment

Cloud computing provids a "transparent" library, for which developers and users gain a great resource^[5]. Using the B/S framework, storage platform trade, browse, download and upload information through the clouds.

Using of cloud resources and multi user resource management functions, the resources such as CPU, memory, storage, process optimization are get optimized. Designers of platform code through the clouds. Considering the data storage security, it need allocate a separate unit of storage data table to make sure that the user information is stored in the cloud database. Using the characteristics of large storage, all the dynamic information storage site is very convenient.

Leased cloud computing development environment can guarantee program design and site services, database storage, the user good interface use, reduce the error probability of occurrence and reduce the error information.

Conclusion

The design of IT enterprise alliance information platform is based on cloud computing. In use of cloud storage in cloud environment, it can store user information, release enterprise information and other functions, which offers IT enterprise independently space to communicate with each other. Users can access this website using mobile information with good timeliness. With the big data developed rapidly, IT enterprise alliance information platform based on cloud computing will provide important the information and service support for the development of IT Alliance enterprise

Foundation item

- 1. The 2013 National Undergraduate Innovative Experiment Program (201319)
- 2. The national natural science fund project (71272191)

References

- [1] Yimei Kang, Jiang Hu, Guan Wang: Tree cloud database for SaaS cloud service model. 2011, 11 (20): 37-38.
- [2] Feng Li: Web-based application and development of Google cloud computing. 2011,1(20): 29-32.
- [3] Yaqiong Li, Ying Song, Yongbing Huang: A virtual cloud computing platform for memory optimization technology. 2011 (4): 684-693.
- [4] Feng Liao, Jingjing Cheng: Computing research and design scheme of database based on cloud computing cloud.2012, 3 (23): 45-48.
- [5] Guigang Zhang, Chao Li, Yong Zhang, Chunxiao Xing. Cloud storage model based on a study of massive information processing. 2012, 1(4): 32-36.

Algorithm for discovering community in multi-relational social network based on modified common neighbors similarity

Li-qing Qiu^{1,a}, Yong-quan Liang^{1,b}, Jian-jian Xu^{1,c}, Zhuo-yan Chen^{1,d}

¹ College of Information Science and Technology, Shandong University of Science and Technology, Qingdao Shandong 266590, China

^aliqingqiu2005@126.com, ^blyq@sdust.edu.cn, ^cSDKDCISE@163.com, ^dczy1012@yeah.net

Keywords: social network, multi-relational social network, community discovery, common neighbors similarity.

Abstract. The multi-relational social network is a new social network, which is proposed in recent years and more complex than single relational social network. Therefore, the existing community discovery algorithm is lack and their results are crude. The paper proposes a new algorithm for discovering community in multi-relational social network based on modified common neighbors similarity. The core idea is the more common neighbors are shared between two nodes, the more similar the nodes are. Finally, we test our generalized algorithm on an artificial sparse network in four dimensions.

1. Introduction

In modern society, social network plays an important role in a quickly changing world, and more and more people prefer to obtain information from social network. Therefore the analysis of social network has emerged as an area of great interest. Particularly the investigation of community structure is an important issue in the domains and disciplines. A community could be loosely described as a collection of nodes within a graph that are densely connected among them while being loosely connected to the rest of the graph [1, 2, 3].

Many works have been proposed to discover community [4, 5], which are on sound theoretical principles and have better performances identifying structures, and have become the state-of-the-art models. However, examining activities of users, we can observe different interaction networks between the same set of users. The existence of different types of interactions suggests heterogeneous interactions in social networks. In other words, social network has grown "up" instead of growing only in "width" [6]. Social network has become multi-relational, which is much more complex than traditional social networks. The existing community detection methods do not concern the multidimensionality of modern social network.

In this article we address community detection in multi-relational social network, which guided by common neighbors similarity [7] instead of just by the topology. Traditional methods for community detection based on topology are limited by ignoring the important element of "closeness" among the nodes. Community neighbors similarity is a similarity function based on attributes attached to nodes in social network.

The remainder of the paper is organized as follows: in Section 2 we discuss multi-relational social network and common neighbors similarity is introduced in Section 3. Next, we describe in Section 4 our generalization of community detection. In Section 5, we provide experimental studies. Finally in Section 6, we give the conclusion and future directions.

2. Multi-relational social network

Multi-relational social network has multiple types of interactions between the same set of nodes. Each dimension of the network represents one type of relations between nodes. A p-dimensional network is represented as:

$$A = \{A^{(1)}, A^{(2)}, \cdots, A^{(p)}\}$$
(1)

Where $A^{(p)}$ represents the interaction among nodes in the *i*-th dimension. With multiple types of interactions, the shared latent community structure can be complicated. It is necessary to integrate information from multiple dimensions to find out the shared community structure across multiple network dimensions.

Definition 1[6]: A multi-relational social network is defined as a tuple $\langle V, E, L \rangle$, where V is the set of nodes in the *l*-th dimension ($l \in L$); E is the set of edges in the *l*-th dimension ($l \in L$); L is the set of distinct dimensions.

A multi-relational social network may be represented by an undirected multi-dimensional graph. For instance, as in Figure 1, the example of three-dimensional social network is presented. A node can connect to his friends through three dimensions, in which each dimension represents one facet of diverse interaction. The set of nodes consists of $\{x, y, z, u, v, t\}$ so there are six nodes in the network that can be connected with each other in three dimensions d_1, d_2, d_3 . For example, in dimension d_1 there are five relationships between nodes: $\langle x, u, d_1 \rangle$, $\langle x, v, d_1 \rangle$, $\langle y, z, d_1 \rangle$, $\langle z, u, d_1 \rangle$ and $\langle v, t, d_1 \rangle$.

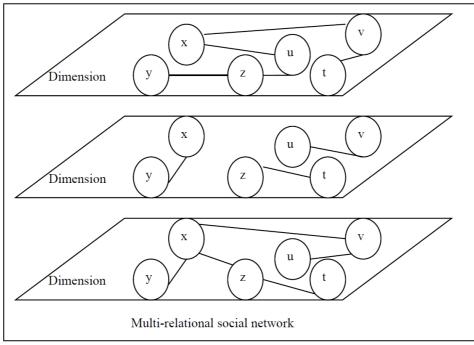


Figure1:A simple example of multi-relational social network. The nodes are connected with each other in three dimensions.

3. Modified common neighbors similarity

Common neighbors similarity is inspired by the set theory named the Jaccard Coefficient. To compute the similarity of two nodes i and j, the similarity function is the ratio between the number of neighbors two nodes share and the total number of nodes they are connected to.

Definition 2[7]: Common neighbors similarity is defined as:

$$Similarity(i, j) = \frac{|neighbors(i) \cap neighbors(j)|}{|neighbors(i) \cup neighbors(j)|}$$
(2)

Where neighbors(i) is the number of neighbors of node i, and neighbors(j) is the number of node j, respectively.

Common neighbors similarity incorporates attributes of individual nodes by considering the common neighbors. Instead of relying heavily on the topology of social network, the similarity can work effectively and efficiently. However, it is worth noting that common neighbors similarity is successfully utilized in traditional social network to detect community [6], what will results in when it is used in multi-relational social network? We define modified common neighbors similarity denoted as M – Similarity as follows:

$$M - Similarity(i, j) = \frac{\sum_{l=1}^{L} |neighbors(i,l) \cap neighbors(j,l)|}{\sum_{l=1}^{L} |neighbors(i,l) \cup neighbors(j,l)|}$$
(3)

Where *neighbors*(i,l) means the number of neighbors of node *i* in dimension l; *neighbors*(j,l) means the number of neighbors of node *j* in dimension *l*; and *l* is the number of dimensions of the network.

In other words we expand common neighbors similarity to multi-relational social network by computing cumulative sum.

4. Proposed algorithm

After introducing the definition of multi-relational social network and modified common neighbors similarity respectively, we give our generalization of community detection.

Suppose that in multi-relational social network, we have perfect knowledge of the connectivity of some set of nodes, we take advantage of agglomerative hierarchical clustering method. For every pair of i, j of nodes in the network, one calculates the value of M - Similarity(i, j) according to Equation (3), which measures how closely connected the nodes are. Starting from the set of all nodes and no edges, links are iteratively added between pairs of nodes in order to decreasing weight. In this way nodes are grouped into larger and larger communities, and the tree is built up to the root, which represents the whole network.

The algorithm is agglomerative indeed, which maximizes the M – *Similarity* value of nodes in a greed fashion. The algorithm infers local community structure by using the node-at-a-time discovery process which is directly analogous to the manner in which spider program harvests the hyperlink structure of the Internet.

5. Experimental results

To analyze the effect of the proposed algorithm in section 4, the paper constructed an artificial sparse network randomly. There are twelve nodes in the network that can be connected with each other in four dimensions as Figure 2.

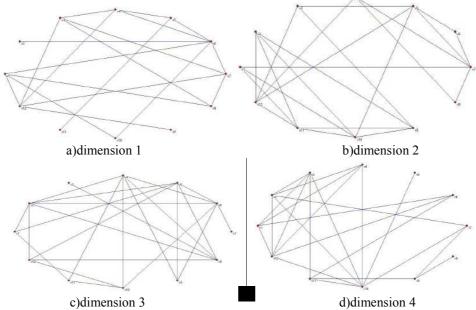
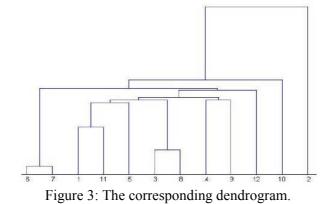


Figure 2: An artificial sparse network in four dimensions. There are twelve nodes in the network. Next, we illustrate the M – *Similarity* matrix according to Equation 3 as Table1.

	V1	V2	V3	V4	V5	V6	V7	V8	V9	V10	V11	V12
V1		0.4375	0.1200	0.2500	0.1905	0.1563	0.1250	0.1250	0.2500	0.3000	0.1765	0.1935
V2	0.4375		0.2000	0.2400	0.3478	0.0909	0.1200	0.1200	0.3529	0.4762	0.3684	0.2000
V3	0.1200	0.2000		0.2800	0.1739	0.1935	0.2083	0.0435	0.1429	0.2500	0.1875	0.2414
V4	0.2500	0.2400	0.2800		0.3077	0.2059	0.2800	0.1154	0.1111	0.2273	0.2000	0.2121
V5	0.1905	0.3478	0.1739	0.3077		0.1212	0.1667	0.1250	0.1765	0.1579	0.2105	0.1667
V6	0.1563	0.0909	0.1935	0.2059	0.1212		0.0313	0.2500	0.1500	0.2174	0.1667	0.2759
V7	0.1250	0.1200	0.2083	0.2800	0.1667	0.0313		0.1304	0.1250	0.2941	0.1875	0.1724
V8	0.1250	0.1200	0.0435	0.1154	0.1250	0.2500	0.1304		0.1429	0.1667	0.1429	0.2609
V9	0.2500	0.3529	0.1429	0.1111	0.1765	0.1500	0.1250	0.1429		0.3333	0.2143	0.1429
V10	0.3000	0.4762	0.2500	0.2273	0.1579	0.2174	0.2941	0.1667	0.3333		0.2500	0.2258
V11	0.1765	0.3684	0.1875	0.2000	0.2105	0.1667	0.1875	0.1429	0.2143	0.2500		0.1852
V12	0.1935	0.2000	0.2414	0.2121	0.1667	0.2759	0.1724	0.2609	0.1429	0.2258	0.1852	

Table 1: The M – Similarity matrix, B.

At last, we show the corresponding dendrogram of our algorithm as Figure 3. The dendrogram shows the community structure which is produced by the algorithm down to the level of single nodes.



6. Conclusions and Future work

In this paper, we present a novel algorithm to utilize community detection in multi-relational social network. The basic idea of the proposed algorithm is the more common neighbors are shared between two nodes, the more similar the nodes are. The algorithm can be used to detect communities in the multi-relational social network. As part of future work, we plan to extend our framework in two directions. Firstly, we will focus on complex examination of the proposed algorithm since there is not testing standards in multi-relational network. Secondly, we only considered the link information so far. In many applications, the content information is also very important. We are investigating how to incorporate content information into our algorithm.

Acknowledgement:

This paper is supported by: The Specialized Research Fund for the Doctoral Program of Higher Education (No.20133718110014), The Nature Science Foundation of Shandong Province (No.ZR2012FM003 and ZR2013FM023), and The National Science Foundation for Post-doctoral Scientists of China (No.2013M541938), and Shandong Province Postdoctoral special funds for innovative projects of China (No. 201302036).

References:

[1]Wasserman S, Faust K. Social Network Analysis. Cambridge University Press, Cambridge, 1994.

[2]Flake GW, Lawrence SR, Giles CL, Coetzee FM. Self-organization and identification of Web communities. IEEE Computer, 2002(35):66-71.

[3]Radicchi F, Castellano C, Cecconi F. Defining and identifying communities in networks. Proc. National Academy of Sciences of United States of America, 2004, 101(9): 2658-2663.

[4]Luxburg V. A tutorial on spectral clustering. Statistics and Computing, 2007, 17(4): 395-416.

[5]Newman M E J. Modularity and community structure in networks. Proc. National Academy of Sciences of United States of America, 2006, 103(23): 8577-8582.

[6]Brodka P, Filipowski T, Kazienkd P. An introduction to community detection in multi-layed social network. Information system, E-learning and knowledge management research, 2013:185-190.

[7]Karsten S, Nitesh V C. Community detection in a large real-world social network, Proceedings of the First International Workshop on Social Computing, Behavioral Modeling, and Prediction, Springer, 2008, 168~175.

WIFI network analysis and transplantation on android platform

Yao Wang^{1, a}, Huai-guo Dong^{1,b} and Guang-qi Wang^{1,c}

¹School of Software, Harbin University of Science and Technology, Haerbin, China ^awangyao1981@hrbust.edu.cn, ^bdonghuaguohrbust@163.com, ^cwangguangqi1992@163.com

Keywords: Embedded Technology; Android; WIFI network; Driver transplant

Abstract. Research the Android open source WIFI network technology. WIFI is verified by the transplantation of WIFI network to achieve process. Through in-depth analysis of android WIFI related the source code of classes, analyze the WIFI framework structure and design principle. Described in detail the initialization of WIFI module , enable , Scan the access point to achieve the whole process of configuration of IP Address

WIFI and Android System Introduction

The abbreviation of WIFI is Wireless Fidelity, specifically refers to IEEE802. 11 b wireless^[1]. standard.It makes the wireless users get network performance and availability of Ethernet level.And it can be seamlessly to a variety of LAN technology integration.It can form a maximize network to satisfy user needs^[2].

November 5, 2007, Google Inc. and the Open Handset Alliance led and developed based on Linux the free and open-source Android operating system, mainly used in mobile devices, such as smart phones and tablet PCs^[3]. Framework consists of 5 parts, its core is Linux2.6 kernel, collocation Libraries and Android Runtime, coordinate Application Framework, develop a variety of Application^[4].

WIFI frame analysis

The composition of WIFI frame. When systemServer of the Android system starts, it will create a ConnectivityServer object, it creates two instance of WifiService and WifiStateTracker in his constructor function, but WifiStateTracker starts WifiMonitor thread to get the underlying transaction. Monito clog listens and receives message sent by Wpa_supplicant .Here Wpa_supplicant is applicable to WEAP, WPA/WPA2 authenticated client. After receiving the message WifiMonitor, will send to WifiStateTracker. And a variety of network behavior broadcast through WifiStateTracker . If the application is registered broadcast, listeners can be processed according to broadcast content. The WifiService and WifiMonitor is the core module. WifiService responsible for starting or blockading wpa_supplicant, start or block WifiMonitor supervision threads and send the request to wpa_supplicant.

WifiManager major role:

A. Return, view, update, configure the network information list, you can modify some configuration parameters.

B. Judgment, activate WIFI network, connect or disconnect, check dynamic information of the network status.

C. Scan and connect to an access point of wireless network

D. Define the Intent behavior of changing WiFi state, and broadcast when the WIFI state is changed.

Android manage the WIFI module through WifiManager class, users can get a lot of information of the wifi module through the WifiManager class, for example the IP address, the MAC address, signal strength ,etc. It provides the interface for the remote wifi request operation. In order to the wifiservice can deal with these requests. Class wifistatetracker is responsible for monitoring the connection status

of wifi, it can be done by wifistatetracker when the state needs to be updated. In addition, it also handles some wireless network events, these handle requests of events originated from wifimonitor, it runs in a separate thread. Wifimonitor monitor the time request from the wpa-suppliant sever. But the requests of daemon thread come from wifinative. WifiStateTracker handle the event in the table below:

Table.1. Whistate Hackel handle the event						
WIFI-STATE-CHANGED-ACTION	Indicates that the network has been activated, banned, is starting. Is					
	prohibited and the unknown state					
SUPPLICANT- STATE- CHANGED-	Indicates a state information of AP connection has been changed, and					
ACTION	system status a new information.					
SUPPLICANT- CONNECTION- CHANGE-	Indicate connection has been established or disconnected with the					
ACTION	requester.					
SCAN- RESULTS- AVAILABLE- ACTION	Indicate AP scan has been completed and returned scan information.					
RSSI-CHANGED-ACTION	Indicate WIFI signal intensity has been changed					
NETWORK- STATE- CHANGED- ACTION	Indicate WIFI connection status has changed					
.NETWORK-IDS- CHANGED- ACTION	Indicate network ID number of Configuration of the network has					
	been changed.					

Initialization WIFI module, Start WIFI module, AP scanning and Configure AP parameters, WIFI connection and configure the IP address, android WIFI network connections require more than four stages.

WIFI module initialization. When an application needs to use wifi, Android system Wifi module must be initialized first, system open Systemsever and call init () to initialize. After the system is turned on service thread calls connectivityserver.getInstance () Gets an instance of a connectivityserver, the process will be carried out in connectivitythread thread. After obtaining an instance of connectivityserver, the system creates WifiStateTracker instance, WifiMonitor instance and WifiService instance, then added the wifiservice instance and the ConnectivityService instance after as a parameter to ServiceManager. WIFI module initialization process is Showing in Fig.1.

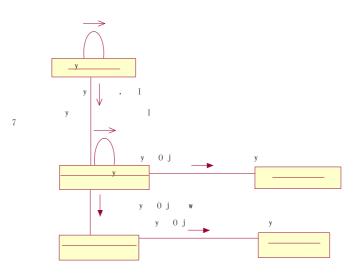


Fig.1. WIFI module initialization Collaboration Diagrams

1. **WIFI module start-up.** After the user opens a wifi module of the Android system management, system will call the function wifiEnable to handle wifi enabled through wirelessSetting, the change is monitored by the system, handled by the onPreferenceChange. WifiEnable calls the interface function of setwifiEnabled, this function is encapsulated in the class WifiManager. After that, WifiService will send the message of sendEnablemanager, the message will be returned to wifiservice after being processed, in the course of handling message, completed the wifi module enable. First, load the wifi driver and initialize wpa_supplicant. Then WifiStateTracker will create the WifiMonitor, to monitor the event sent from the bottom. When the WIFI module enabled, the broadcast mechanism will send a message. WifiEnabler has already registered to receive this broadcast, after receiving this message,

start scanning all access points within a certain range. WIFI module startup process is Showing in Figure Fig.2.

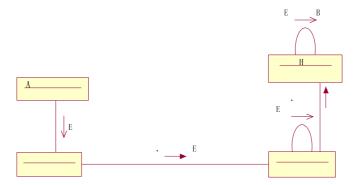


Fig.2. WIFI module startup Collaboration Diagrams

2. **AP scans and configuration parameters of AP.** In the process of scanning AP, the system will send a command that searching for the access point to the wpa-supplicant, wpa-supplicant will send an event notification to the outside world after handling this event. After receiving this event, wifi-wait-for-event function will call the handleEvent function to handle this event in the WifiMonitor and call the noifyscanResultsAvailable function notifing WifiStateTracker, the latter will send a broadcast SCAN-RESULTS-AVAILABLE-ACTION, WifiLayer which have registered to receive broadcast. It will call handleScanResultsAvailable function to handle related events and get access point scan information, the access point information is added to the list of GUI. In this process, onAccessPointSetChanged function of WifiSettings is called. Finally, the user can select the AP of WifiSettings list to open a dialog box where the user needs to fill in the access point parameters. WIFI access point scan process is Showing in Figure Fig.3.

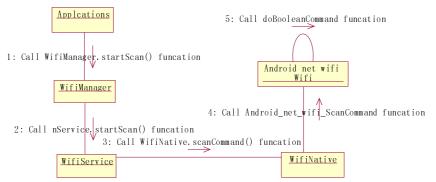


Fig.3. WIFI access point Collaboration Diagrams

3. WIFI connection and configure the IP address. After the user selects the corresponding encryption in the access point parameters dialog and input keys, through clicking the connect button to start connecting target access point. If the AP is not configured before the connection, there is no AP configuration information in the wpa-supplicant. WifiLayer will send the added commands to wpa-supplicant. After obtaining Id, WifiLayer sends commands to wpa-supplicant through the Id parameter again, saving the AP configuration information. After the WIFI module connected to AP, wpa-supplicant will send notifications of event to the outside, related events will be processed after the WifiMonitor receiving the notice. Then WifiStateTracker will be sent to themselves EVENT-NETWORK- STATE-CHANGED message initiates DHCP to obtain an IP address, when the DHCP to obtain an IP address, it will send a EVENT-INTERFACE- CONFIGURATION-SUCCEEDED message, Once the information is received by WifiLayer, it Will broadcast EVENT-NETWORK-STATE- CHANGED, and get complete information of IP addresses, registered recipient of this Intent in WifiLayer, and call the handle Network State Changed to process the message. IP address configuration end of Android System after calling the function succeed, system has a WIFI Internet function. WIFI module connection process is Showing in Fig.4.

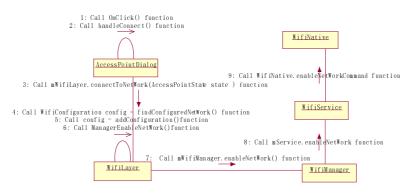


Fig.4. WIFI module connection Collaboration Diagrams

WIFI drive transplant and test

WIFI module drive transplant. Driver porting WIFI module selected is Marvell8686 SDIO WIFI, hardware platform is FS_S5PC100 development platform, based on Samsung's Cortex-A8 core. As follows is Simple transplant procedure:

A: Compile the kernel root path of make, create support for SD cards, And generate libertas.ko and libertas_sdio.ko drive module.

B: Configure the test environment, here is the use of open source software of wireless_tools_29.rar

C: WIFI module firmware sd8686.bin sd8686 helper.bin deposited to the designated location.

D: Compile android system, detect drive of SDIO, detect Wireless NIC. Detection wpa-supplicant function. AP access point connection.

E: Provide firmware to the drive, update BoardConfig.mk and enable wpa_supplicant.

F: Configuration wpa-supplicant.conf file, compile wpa-supplicant debugging information

G: Changing init.rc configuration path and permissions, associated wpa_supplicant and dhcpcd

H: Load SDIO driver and modify the source code of WifiStateTracker.

WIFI module test. After the completion of the drive transplant, restart Development Platform, WIFI module IP configuration and default gateway, use the wpa_supplicant-iwlan0 command to start wpa_supplicant, through returning the information of the list of information: wlan: connect to 00-1D-0F-90-43-00,you can determine that the connection has been successfully,use dhcp to get ip information, there is some information in the list of returned imformation, wlan0: leased 192.168.1.103 for 86400 seconds,at last, using the wireless and Internet options of Android system function in Wifi module management, AP search, connections and other functions. Confirm the development board has Wifi network with complete functions once again.

Conclusion

Through to the WIFI framework analysis and WIFI driver transplant, you can see the WIFI network is the most important function of Android smart mobile devices. Understand how it works can improve the performance of related applications, transplant the underlying drivers of WIFI. The android system transplantation is a very important link.

References

- [1] Chen Wen-zhou. Data Communications, 2008(02).
- [2] Wu Hong-ju, Shen Jian-hua. Microcontrollers & Embedded Systems, 2005(06)
- [3] Chen Jing, CHEN Ping-hua, LI Wen-liang. Modern Computer, 2009 (11).
- [4] Code Home. Android-An Open Handset Alliance Project [EB/OL].http: //code.google.com / android /what is android.html, 2008.

The Research of Information Monitoring System for Whole Producing Process Model

Zhang Min^{1, a}, Huang Weizhong^{1, b}, Li Hanxi^{1, c} ¹Hangzhou Cigarette Factory of China Tobacco Zhejiang Industrial Co., LTD ^azhangm@zjtobacco.com, ^bhuangwz@zjtobacco.com, ^clihx@zjtobacco.com

Keywords: Whole Producing Process; Information Monitoring System; Cigarette Production

Abstract: With the rapid development of science and technology, the popularization and application of new technology and administration of production safety level, the original monitoring and control system is showing more and more disadvantages, already can't satisfy the needs of safe production. In this paper, based on the current production process of the main business of Hangzhou cigarette factory manufacturing, it establishes corresponding cigarette production process model, the production information monitoring system overall design of the whole process, and the relevant software system structure and function design, in order to realize the reasonable production test of merge and quick positioning.

Introduction

With the rapid development of science and technology, the original monitoring and control system present more and more insufficiencies, can't satisfy the needs of safe production. Production monitoring system information construction is the requirement of work safety in production in the new period, and the need of strengthening safety supervision work, but also with the help of modern technology and equipment need to promote enterprise's safe production level [1]. Pays special attention to production safety monitoring system of information construction, which is beneficial to strengthen the enterprise's main body responsibility and government regulatory responsibility to implement, is conducive to enhancing regulatory efficiency and effectively promote the hidden governance, curb major workplace accidents [2]. In view of production safety in the process of cigarette production new technology application promotion and constantly improve the management level, in this paper, based on the current production process of the main business of Hangzhou cigarette factory manufacturing, establish corresponding cigarette production process model, has carried on the overall design, the production information monitoring system of the whole process and related software system structure and function design, in order to realize the reasonable production test of merge and quick positioning.

Whole producing process model analysis

Due to the rapid development of the manufacturing and the polytropy of market environment, reduce the production cost is no longer a manufacturing enterprises only focus on the improvement of the activity, how to shorten the production cycle, the rapid response to customer demand, become the target of the advanced manufacturing enterprises. In this paper, the main business of Hangzhou cigarette factory manufacturing production process, for example, on the hierarchical analysis, analysis of the necessity of production process optimization in the process of the enterprise production process optimization and how to plan, and the principle of planning. Through optimization, design a new production process, and the preliminary implementation [3]. Use in cigarette manufacturing, confirmed that the production process system has the high use value. It is shown in figure 1 below.

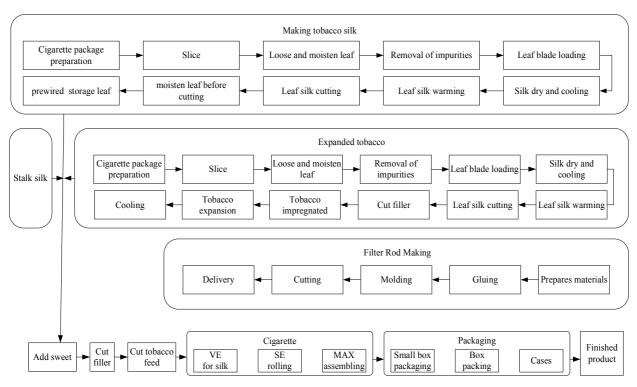


Figure 1. Whole producing process

Main production is divided into silk and wrap two link; Silk began from raw materials into the Hangzhou cigarette factory, Hangzhou cigarette factory according to the requirements of Hangzhou cigarette factory of raw materials, such as tobacco into slices of smoke from the raw material warehouse to factory overhead library, tobacco smoke from a piece of silk production line, the elevated began to enter respectively after slicing, loose embellish leaf, removing impurity, after feeding and shred, drying silk into leaf silk elevated library to use; For bulk yarn now new factory in the first phase of Hangzhou cigarette factory haven't built a production line, so bulky silk, silk and so on are consists of Hangzhou cigarette factory from other warehouse transferred to Hangzhou cigarette; The last part of the silk overhead in the library is to form by mixing and bulk silk, terrier silk and so on all kinds of brand of the finished product of tobacco into shreds elevated library.

Wrap link starts at material entrance, Hangzhou cigarette factory according to the volume of factories package material demand to arrange cigarette paper, wrapping paper and so on from the raw material warehouse to factory to enter so elevated library, filter stick the related accessories made of molding line filter rod to the cigarette machine, cigarette machine from into tobacco roll made from silk elevated library into packaging machines, in the packaging machine to pack into a box, bar, elevated box form of transportation to the finished product library, finally from the finished elevated library will smoke sent to Hangzhou cigarette factory of China tobacco Zhejiang industrial co., LTD's marketing warehouse.

The building of whole producing process model

Based on the current production process of Hangzhou cigarette factory manufacturing main business, all cigarette manufacturing process model can be envisaged as the interface of the service based on a data integration platform and exchange data to obtain the application process of interaction between the log and the status quo, in view of the key business application to extract the information infrastructure, application deployment information and historical status information, through the model association rules, the application of the single point of traditional associated combination for applications, processes, and the content of the three levels of data, eventually form application topology, panoramic view of the process, data flow rule [4]. Through visual display and fault pattern recognition and emergency disposal means, to ensure reasonable merge and quickly locate fault. Production all the process model is shown in figure 2.

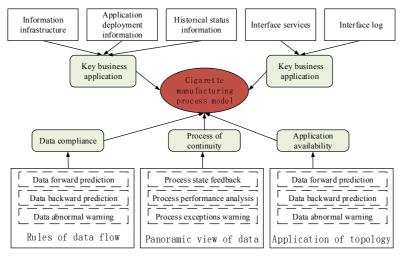


Figure 2. Whole producing process model

The design of information monitoring system for the whole producing process

The whole producing process of the main purpose of the information monitoring system is based on the production data of production process and machine status monitoring, real-time acquisition production workshop each working procedure and the machine of real-time production data and status, graphical analysis and summary on a plan of production, and the statistical analysis of the construction efficiency of the machine [5]. Producing monitoring system overall structure block diagram is shown in figure 3.

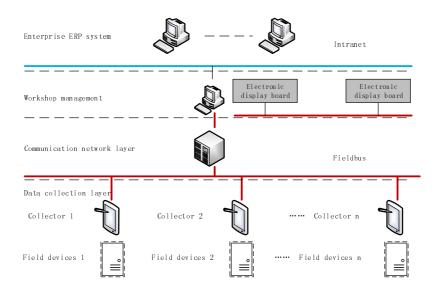


Figure 3.Information monitoring system for the whole producing process

The system is divided into three layers: management layer, field data collection, and communication network. Management layer through Intranet connected with enterprise ERP, in order to realize the seamless connection with ERP system, at the same time is responsible for equipment running status real-time monitoring and data processing, and can according to production requirements, generating various production reports. Production site electronic tablet adopts multiple screen display card or Ethernet extension. Field communication network layer is responsible for on-site data communication of the system, and implement equipment between nodes as well as the upper machine and lower machine data communication between the nodes. Mainly through on-site data collection layer installed on the equipment of field data acquisition unit to realize automatic monitoring of equipment, belonging to the bottom of the whole system.

The design of software system structure and function

Monitoring system of upper machine software through a network communication protocol and the lower machine, collect data of some equipment of information collected for unified management and preservation, and through the graphics, curve and text display, digital, convenient and staff understand the production status of the production, and reasonable production. Based on "one platform and two sub-systems ", the core idea of system building is divided into basic service platform, monitoring subsystem, and service management subsystem, as shown in figure 4.

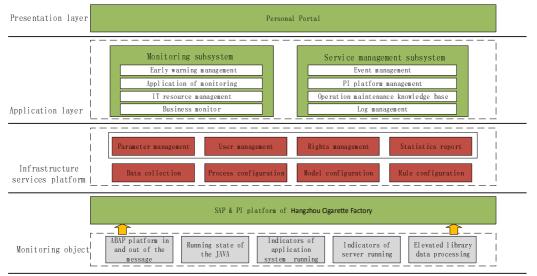


Figure 4. The software structure of information monitoring system

Infrastructure services platform. It is mainly responsible for data collection, process configuration, model configuration rules and configuration, etc. Monitoring subsystem. Monitoring subsystem includes the early warning management, application monitoring, surveillance IT resources and business production monitoring; Service management subsystem. Service management subsystem includes built-in event management, PI, platform management, operational knowledge base and log management.

This system has the high degree of flexibility, provides good extensible ability, realize customer flexible business requirements.

Conclusion

In this paper, combination with the practical situation of Hangzhou cigarette factory, the production information monitoring system is designed for the whole process, according to the ore to the technological process of cigarette production order, industrial network control layer from the spot for the enterprise to the management to achieve the comprehensive information integration, and provide the basis of an open architecture. This system for the enterprise safety production has brought great convenience, the cigarette automation system plays a more and more important role, having huge development potential and very broad prospects.

Reference:

- [1] W.H. Delone: Journal of management information systems, Vol. 19(2003) No.4, p. 9.
- [2] K. Peffers, T. Tuunanen, M.A. Rothenberger: Journal of management information systems, Vol. 24(2007) No.3, p. 45.
- [3] J.A. Jiang, C.L. Tseng: Computers and electronics in agriculture, Vol. 62(2008) No.2, p. 243.
- [4] C. Otto, A. Milenkovic, and C. Sanders: Journal of Mobile Multimedia, Vol. 1(2006) No.4, p. 307.
- [5] E. Cauza, U. Enserer, and B. Strasser: European journal of clinical investigation, Vol. 35(2005) No.12, p. 745.

Research of Intelligent Mobile Inspection System Based IT

Li Hanxi^{1, a}, Wang Yanping^{1, b}, Jin Zhenxun^{1, c}, Qian Jie^{1, d}

¹Hangzhou Cigarette Factory of China Tobacco Zhejiang Industrial Co., LTD

^alihx@zjtobacco.com, ^bwangyp@zjtobacco.com, ^cjinzx@zjtobacco.com, ^dqianj@zjtobacco.com

Keywords: RFID, Intelligent Inspection, Wireless Communications, Mobile

Abstract: With the development of wireless communication technology, mobile computing technology that all walks of life increasingly improve intelligence, the computer information technology are more and more been used in various fields. For Hangzhou cigarette factory, this paper is based on RFID technology, designs the wireless inspection service platform, and the system function is carried on the thorough analysis, so do the basis of dividing the corresponding subsystem and function modules, thus for the reasonable development, finally completing the design and planning of the whole system. Through wireless communication with the server for data interaction, it reduces the regional space and the limitation on the inspection work, improves the efficiency of the inspection work, and to ensure the quality of work.

Introduction

Wireless communication rapid development in recent years, more and more people live in their work, study and the use of wireless communication way for Internet browsing, data transmission, etc. Wireless communication is applied to intelligent inspection system can improve the download and upload the results of the task timely, avoids the limitations of the wired communication, shorten the checking work cycle [1-2].

During the period of "11th five-year plan", Hangzhou cigarette factory is to move to Zhuantang Town. Because the factory covers large area, widely distributed network point, and the information point is more, the link is relatively complex, the room cabinet is jump connection between the characteristics of all network wiring problem requires a lot of processing time, and most of the time it takes on the processing of query and browse non-critical work, greatly increased the fault processing time. In order to solve the problem of network equipment, the last kilometer, it need to develop a set of mobile inspection service platform, used to solve the network management software and network equipment itself cannot solve the problem.

Requirement Analysis of the System and inspection work process analysis

According to the demands of Hangzhou cigarette factory mobile inspection service platform including business consulting, architecture, analyst, system design, system development, system testing, implementation of personnel and the implementation of team, development and implementation of the system development and deployment of mobile inspection service platform and mobile inspection application. Specific requirements are as follows:

a) Provide data import function and configuration function, allow the network panel number to cabinet distribution frame port to the switch port location and cabinet equipment configuration management.

b) Support tablet through online or offline for route query and data maintenance, provide based on the business and all kinds of statistics and reporting data level, used for platform management and business decisions, implementation of multidimensional business data query function, allows users to corresponding marking equipment in a friendly way of interaction record and display the configuration changes of specific equipment and operational records;

c) Implement docking with the cisco network management system, provide the cisco network management system data associated with the system management, network equipment, data mapping by moving the inspection application can check the running status of the overall network equipment show core link-state, covering key equipment performance and analysis report, etc.;

d) Comprehensive combing Hangzhou cigarette factories network cabling infrastructure, organizing a cabinet and to encode jumper wire label, optimization of network configuration, optimizing operational processes;

e) Implement mobile inspection service platform of user management, mobile terminal management, rights management and log management;

f) Consider the follow-up with Hangzhou Cigarette Factory of China Tobacco Zhejiang Industrial Co., LTD's IT operations platform integration.

The intelligent inspection is a complete process, only step by step according to set good process can make the inspection work, achieve the desired purpose "inspection personnel arrived at the inspection site [3], through the hands of the RFID read-write device automatically obtain the location and the current time, and is compared with the original target positioning information in the database, to determine the inspection objects and the inspection location is correct, and the power equipment tags are read and write operations, to determine whether the power equipment has defects, and the defect information record to the handheld RFID to read and write in the Handheld RFID read-write device with the background database server to communicate, to read and write in the inspection data over a wireless network automatically imported into the database of background management system [4]. The background management software will be uploaded to inspection personnel data information classifying! Processing, generate the inspection records and equipment defect data" the whole flow chart shown in figure 1.

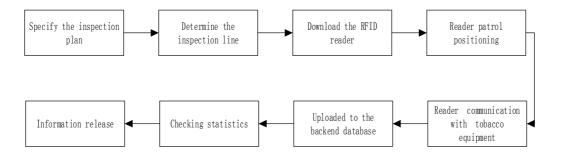


Figure 1. Inspection work process

The design of IT intelligent mobile inspection system software structure

IT intelligent mobile inspection system consists of data collection, data management (including data communications, query, report forms and protection, etc.) and Web query module, as shown in figure 2.

Data collection module. It is installed in the PDA, to collect on-site power equipment electronic tag read and equipment running status data. Inspection personnel according to task remind or equipment operation condition inspection operation, if found defective equipment, is to record and management of defects, and uploaded to the PC background management system [5].

Data management module. It installed on the PC background management system, including task management, defect management, inspection, inspection process tracking management, pending data management, short message management, basic data management, intelligent device management, rights management, system configuration, report generation and other functions, "it can receive the checking data collection, classification, storage, query, and generates related reports, and the equipment for statistical anomaly or into inspection management system defects generated in the equipment table.

Web query module. It is installed on the MIS (management information system) in the network Web application server, the MIS on any PC on the network can be a Web application server through the network to run the inspection data query, and on the basis of the need for statistics and generate related reports.

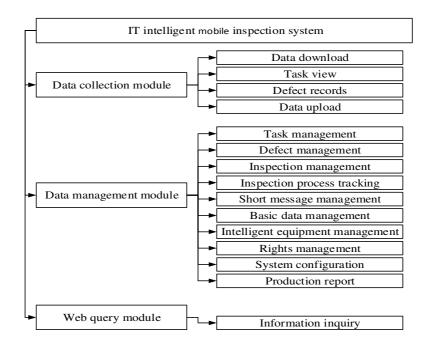


Figure 2. IT intelligent mobile inspection system software structure

The structure of the intelligent inspection system based on RFID

Based on RFID intelligent inspection system, which is geared to the needs of a certain area of the intelligent inspection system. The system uses the ID of front-end communication technology

implementation, using GSM, GPRS, CDMA, 3G technology to realize the back-end database system and communication of hand-held, speaking, reading and writing, and adopts the technology of the computer management and inspection operations and management of" intelligent inspection system, different from general computer system, it is a kind of data collection, information management and the integration of the application system of communication. So, should consider when the system demand analysis to the specific system itself, and to meet the requirements of each department. The network structure of IT intelligent mobile inspection system is shown in figure 3.

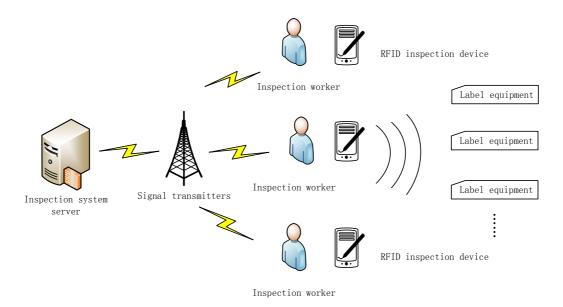


Figure 3. Structure of the intelligent inspection system based on RFID

We've learned from the above, the intelligent inspection system based on RFID network architecture by RFID terminals, mobile communication network, checking system server. RFID terminal mainly consists of the RFID electronic tag, RFID read-write device, the RFID electronic tag is installed on the need to carry on the inspection equipment, mainly by department according to the equipment system for deployment. Inspection handheld RFID read-write device, every once in a while manually or automatically sends a message to the back-end data server, report its location. Communication network is GSM, GPRS, CDMA, 3G wireless mobile communication network, such as through wireless communication network, the RFID terminal can system server and the background information, and the transmission of the data. Inspection system server belongs to the interior of the system network, it has two tasks: first, to be responsible for inspection of monitoring; Second, is responsible for accepting and dealing with RFID handheld devices transmit to data.

To safeguard Hangzhou cigarette factory, reliable, safe, continuous cigarette manufacturing as the total target, solving the existing network management system not covered, switches and between switches and host link management of each link node and endpoint, is to building a network management model in conformity with the present situation of Hangzhou cigarette factory; Combining with the currently existing cisco network management system, the whole network condition of Hangzhou cigarette factory provide auxiliary inspection mode of the knowledge base, to offer network data query quickly for the stable and healthy operation and positioning of the platform.

Conclusion

In today's rapid development of wireless communication technology, wireless network products increasingly are widely used in the field of data transmission. Wireless network communication technology and the Android platform for checking the client is introduced into the inspection business management system, is a very innovative idea. This paper studies the overall architecture based on RFID intelligent inspection system, design the overall structure, at present, this plan is in perfect stage, the need for the design and implementation of the system in detail, from the ease of use, safety, low cost, high efficiency, to the specific implementation of this system. Articles, of course, the proposed scheme need adjusted according to the various departments, and in this paper, the proposed security solution, although its security is relatively high, but its complexity is higher, needing further research.

Reference:

- [1] A.A.F. Nassiraei, and K. Ishii: Journal of Bionic Engineering, Vol. 4(2007) No.4, p. 217
- [2] A. Ahrary, M. Ishikawa M: Artificial Life and Robotics, Vol. 11(2007) No.1, p. 23
- [3] M. Khalid, E.L.Y. Lee, and R. Yusof: International Journal of Simulation System, Science and Technology, Vol. 9(2008) No.3, p. 9
- [4] M. Omid, A. Mahmoudi, and M.H. Omid: Expert Systems with Applications, Vol. 36(2009) No.9, p. 11528
- [5] J. Xu, N. Xi, and C. Zhang: Optics & Laser Technology, Vol. 43(2011) No.1, p. 1

Study on Self-configuration Model and Environment Awareness Algorithm for Mission-Critical Systems

Jian Wang^{1, a}, Guosheng Zhao^{2, b}*

¹ College of Computer Science and Technology, Harbin University of Science and Technology, Harbin, China

² College of Computer Science and Information Engineering, Harbin Normal University, Harbin, China

^awangjianlydia@163.com, ^b*zgswj@163.com

Keywords: mission-critical systems; self-configuration; environment awareness; context-modeling

Abstract. It is becoming more and more difficult to manage, maintain and keep the key services of mission-critical systems by manual because of hardware problems, software bug, misoperation and malicious attacks. In order to solve the above problems, a self-configuration model was proposed, and awareness algorithm was discussed. The heartbeat mechanism was utilized to realize internal environment awareness, and then the context-modeling technology was introduced to describe user activities and system resources formally, which can obtain the external environment awareness. The self-configuration model has interactivity among modules during operations, and able to improve the self-management ability of mission-critical systems effectively.

1. Introduction

With the advent of information age, various mission-critical systems have been widely used, and once the basic services interrupt, an enormous impact will be imposed on the national economy and people's living standards. Traditional security measures have improved system security, whereas kinds of invasions still occur. As a result, the ability of system to provide users with satisfied services after invasions must be taken into account.

Recently, the autonomic growth pattern for system security is studied. Among them, the more representative works are as follows: Jann proposed dynamic reconfiguration of autonomic computing based on the basic module construction ^[1]. Wllisnant oriented application software such as dynamic reconfiguration of manufacturing challenges, to explore and define system reconfiguration model to run, noting the need to get running static structure and dynamic behavior of the system. In the IBM project, APPavoo researched system configuration and self-recovery technologies ^[3], to ensure that the system to be able to insert or delete running certain software. In addition, researchers have also considered from different angles on autonomic computing systems for exploration, and research methods can be summed up as a subject in the configuration combining with M-Agent^[4], Grid Service^[5] and Web Service^[6]. Self-configuration technologies primarily intend for all kinds of application software, demand, while in this paper, the application of mission-critical systems, and a configuration management model based on domain knowledge in network environments and explores the perception of the core algorithms to improve service capabilities of the system in different internal and external environments.

2. Configuration model based on domain knowledge of the network environment

Overall description of the configuration management functionality is shown as in Fig.1, output of the environmental information reflects the state of network elements and the state of environments. Network segment consists of a number of different access technologies based on composition, each element, and using monitoring and perception. Among them, the monitoring process during a specific time period, each element needed for network fault conditions of traffic, mobility, used in configuration, and provides the QoS level. Network information system not only is used to update the

network key performance indicators, mine issues that may arise, but also provide services for the current situation in the region. This portion of the application indicates the terminal needs, preferences, levels of QoS and cost price restrictions. Implementation of the optimization process requires that information to determine the most suitable for the current environment information configuration. Policy information environment information processing guidelines and features specified in the output, the corresponding guidelines clearly every application allows QoS level through comprehensive consideration to all assigned QoS levels resulting from the application of user satisfaction, overhead costs and reconfiguration of various QoS level, find the best configuration to maximize the objective function. In a word, the optimization will process in considering the above environments, configuration and policy information, and output possible network configurations.

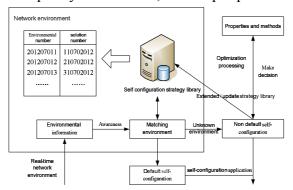


Fig.1 Configuration management model framework

As shown in Fig.1, a starting point for configuration management model is access to environmental information, including information about the status of the current network environment. Library contains a configuration policy has been addressed environmental information store after you perform the optimization of learning process of dealing with each environment configuration solution. Environment matching modules are designed to provide access to the network environment in real time to find the closest reference to the environment and the corresponding solutions. Self-configuration management model between the components running within the module as a whole has a certain interaction learning process through interactive access, and knowledge for the reconstruction of the system is able to adjust timely.

3. Environmental Sensing Algorithm

3.1 Internal environmental perception

Sensing for the internal environment within the environmental information and system behavior, is a system managed resource state of the detection, the internal state of the system that self-perception. A new heartbeat detection algorithm HB-SA, is used to change the internal state of the system dynamic process of perception. Furthermore, we intend in the present detection method using the PULL mode. If you only consider the case of two nodes, respectively, in the primary and secondary servers were set on two processes q and p, for each test condition. The failure threshold value as a measure for comparison with ρ to determine the state of the system. ρ is calculated as follows:

$$\rho = \begin{cases} 1 - \frac{\delta^2}{\left(t_{current} - sn_{current} \cdot \Delta t_i - u\right)^2 + \delta^2} & if\left(t_{current} - sn_{current} \cdot \Delta t\right) > u\\ 0 & else \end{cases}$$

The above formula, $t_{current}$ represents the query, the detection time of system operation; $sn_{current}$ represents the smallest serial number that there is no corresponding response message at current time; system detects the distribution of time D of the expectation and variance are represented by δ^2 and u respectively, both can be calculated by E(D) (D samples expectations) and V(D) (D variance). Based on the above consideration, we build the sliding window W_D , which is used to keep the system's detection time, the query time of the most recent response can receive, and the process for

calculating the expectation and variance of D to establish the sample. The entire algorithm is based on PULL mode, and the realization of the model is shown as Fig.2.

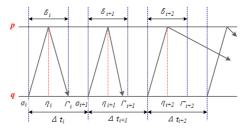


Fig.2 Model of HB-SA algrithm

In order to meet different application requirements for timely detection time requirements, the self-perception of heartbeat algorithm can be based on systems running at different times to dynamically change the heartbeat timeout. In the HB-SA algorithm, the system status can be calculated according to the recent history and current heartbeat time and the statistics value of heartbeat response time for history is referenced of the output for the algorithm. P is the failure threshold, its value can be user-specified parameters to calculate, meaning the quality of services for different user needs, and the specific testing process is shown as Fig.3.

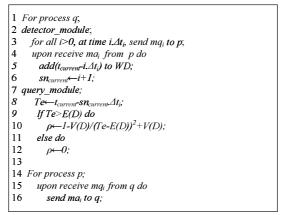


Fig.3 Detection process of system state

3.2 External environment awareness

External environment awareness facing the external environment information and system behavior, it is self-perception of external environment through real-time understanding the changes of system operating environment, system resource and distribution or other conditions. The context-modeling technology is introduced to describe user activities and system resources formally, and the context information can be described as the main entity information, divided by entity types as follows:

(1) The user entity. This entity may reflect the user's various properties such as knowledge experience, familiar with the system or the degree of mutual trust between users and system and so on. The user entity can be described as: *Entity1*:= (*UserID*, *Place*, *Time*, *Property*). In this formula, *UserID* represents the user identify; *Place* represents the location or places of the user use the system services; *Time* represents the user service time; *Property* represents the attribute set of the user.

(2) The spatial entity. This entity may reflect the system's resources, and spatial entity will consider resource information fully, co-ordinate arrangements for the use of system resources, then maximum provides ongoing and high quality resources for application system. The spatial entity can be described as: *Entity2*:= (*SpaceID*, *Place*, *Time*, *Resource*). In context information, these two entities are the most important, because the user and the space can describe the change of system resources, at the same time, other types of entities can also be identified by these two properties.

(3)Relation entity. When the user changes the service needs, the user entity may turn one spatial entity to another spatial entity. Relation entity is used to describe the roul between user entity and spatial entity, it appears when the user enters a space and play a role in spatial entity. The relation

entity can be described as: *Entity3*:=(*RelationID*, *Entity2*). In the conversion processing of relation entity, user's service needs could constitutes by a number of system subtasks. By performing these subtasks to complete the corresponding service, then the user entity will form a series of service chain in the spatial entity. The system activity to meet user requirements can be described as: *Activity*:= (*Entity1*, *Entity2*, *Resource, Servicechain, Entity3*).

The whole process of provided services for users may occur the state changes of the spatial entities resource. Using hidden Markov model (HMM) links the user system needs outside and changing state of spatial entity resource, achieving the perception for external environments of the system. The service status of the collection of user activity is represented by $S = \{s_1, s_2, ..., s_n\}$. Any user activity model is represented by λ , and $\lambda = (N, M, A, B, \pi)$. In this formula, N represents the number of states implicit, it's also the number of the system service used by user entity; M represents a state in either observation, based on the describe of resource attributes. If we use p to represent the resource properties of the relation entity's number, we can get M=P, it means the number of resources in relation entity $V = \{v_1, v_2, ..., v_M\}$; $A = \{a_{ij}\}, 1 \le i, j \le N$ represents the transition probability distribution of services state; $B = \{b_j(k)\}, b_j(k) = P[v_k|s_t = a_j], 1 \le j \le N, 1 \le k \le M$ represents the distribution of the resource state of the relation entity. The probability distribution is observed when the user is in service J, the initial distribution of any service is represented by $\pi = \{\pi_j\}, \pi_j = P[s_1 = a_j], 1 \le j \le N$ to represent.

4. Conclusions

This paper proposes a self-configuration model and environment awareness algorithm for mssion-critical systems. Interaction between modules is fully taken into account in the models when the components run, and the learning process is achieved through interaction, which is used to adjust knowledge database for system reconstruction in a timely manner. The proposed model and method can be deployed in existing mission-critical systems, so that the system is able to follow the desired state to run in a different environment, enhancing the capacity of the system services effectively.

Acknowledgment

This work is supported by the National Natural Science Foundation of China (61202458), the Specialized Research Fund for the Doctoral Program of Higher Education of China (20112303120007), the Foundation of Heilongjiang Educational Committee (12521146) and the Youth Foundation of Harbin University of Science and Technology (2011YF018).

References

- J.Jann, L.A.Browning and R.S.Burugula. Dynamic reconfiguration: basic building blocks for autonomic computing on IBM pseries servers. IBM system journal, 2003, 42: 29-37
- [2] K.Whisnant. Z.T.Kalbarczyk and R.K.Iyer. A system model for dynamically reconfigurable software. IBM system journal, 2003, 42: 45-59
- [3] J.Appavoo. Enabling autonomic behavior in systems software with hot swapping. IBM system journal, 2003, 42: 60-76
- [4] T.Gerald. A multi-agent systems approach to autonomic computing. Proceedings of the 3rd International Joint Conference on Autonomous Agents and Multi Agent Systems, 2004: 464-471
- [5] B.Youakim, M.Zakaria. Autonomic service-oriented grid to enhance e-learning experiences. Proceedings of the 3rd IEEE International Conference on Digital Ecosystems and Technologies, 2009: 649-654
- [6] P.Martin, W.Powley. The WSDM of autonomic computing: experiences in implementing autonomic web services. Proceedings of IDCE 2007 Workshops: International Workshop on Software Engineering for Adaptive and Self-Managing Systems, 2007

A Research and Exploration of Established Public Service Network Information Platform of University-enterprise Cooperation

Juan Wu^{1,a}

¹Shandong Women's University, Jinan, Shandong Province, China ^awujuan2001@163.com

Keywords: University-enterprise cooperation, public service Network, information platform, information model, win-win situation

Abstract. Practice teaching through the establishment of university-enterprise cooperation mechanism, the establishment of university-enterprise cooperation practice teaching operation mode, formulating university-enterprise cooperation practice teaching reform model, establishing higher education "university-enterprise cooperation, complement each other, "win-win" are to run the factors: professional practice teaching reform. So as to promote the development of colleges and universities, driving the development of enterprises to stimulate students' creativity, further developing the students' resilience. Building regional, public welfare, and participatory comprehensive embody characteristics of university-enterprise cooperation, joint institutions, trust each other, long-term cooperation, mutual benefit and mutual university-enterprise cooperation alliance of network organization operation pattern, is conducive to integrate scattered and disorderly flow of information in the market, reduce market transaction costs and risks of cooperation, realize the government, schools, industries and enterprises linkage, depth to promote university-enterprise cooperation, improve the public service level of regional cooperation between colleges.

Introduction

University-enterprise cooperation is important mode of our country's colleges and universities cultivate high-quality skilled personnel, also is a basic way to realize the goal of cultivating objectives of higher education. In this process, a variety of new scientific and effective training mode and implementation method continuously.

Continuous innovation of the sustainable development of the information industry and information network popularization has become a global economic and social development. Wide application, high penetration of information technology is expecting a new breakthrough. Information through the network platform construction, the school can get effective vocational guidance, employment information and employment help, improve the students' employ ability and entrepreneurship.

According to the Shandong province to promote the implementation of the modern vocational education system construction, practice bases needs to be established in the enterprise in Shandong province, the provincial companies play a good role practice training bases. Release information, Shandong province department of education in 2014 to establish a unity between public service network information platform, the unity of university-enterprise cooperation network information platform of public service in Shandong province, relying on the platform to develop human resources statistics, forecast, supply and demand information release, the implementation in the province in 2015.

In recent years, timely grasp the economic information, technical information and the future development tendency, helps the school actively adjust the training objectives and curriculum, reform the teaching contents, teaching methods and teaching management system, make the school education teaching activity is closely connected with the enterprise. Platform to make full use of modern technology, help between comprehensive cooperation and the parties.

(1) The small and medium-sized enterprises industry-university-institute cooperation consciousness weak information platform construction. As long as there is the requirements of the

enterprise can cooperate with universities, production-study-research cooperation has been developed from single original strength of strong enterprises "university-enterprise cooperation", "university city" cooperation for the development of nowadays, don't have the resources, channels of small and medium-sized enterprises are available through the university-enterprise cooperation network information platform construction of public service, development to find more opportunities for the enterprise.

Small and medium-sized enterprise development stage haven't reached to the degree of "production", but is a variety of forms of cooperation with colleges and universities, small and medium-sized enterprises can be active thinking through the information platform construction, actively explore cooperation way for their stage of development.

(2) Establish platform to improve the supervision and promote a long-term cooperation. In fact, production-study-research cooperation can bring huge benefits to the enterprise. Production cooperation can have such good results, thanks to" close "one word, between colleges and close to the construction of the platform. Production-study-research cooperation smoothly, based on the information platform to avoid the cooperation both sides does not have a fixed "place" and lead to cooperation time is not long. Building public service network, it provides the industry-university-institute cooperation docking platform, this is the center of a complete application, is the technology into production platform, in the traditional sense of production-study-research cooperation is difficult to achieve the goal of cooperation of both parties. The public service of network information platform, "supervision" of cooperation, played a real college scientific research advantage, and the achievement transformation ability of the enterprise.

Promoting long-term development of university-enterprise cooperation mode.

Shandong women's university has been the university-enterprise cooperation as the focus of the school, the school will continue to strengthen the contact and cooperation with the enterprise, in order to improve the comprehensive strength of the school and make unremitting efforts. Constructing university-enterprise cooperation network information platform of public service is to promote the measure of discipline development, in-depth cooperation between colleges and work in recent years, our research content is as follows:

First on the one hand, active contact enterprise, obtain employment recruitment information, provide suitable jobs for graduating students, mainly for enterprises in Shandong province and outside the province qualified graduates. On the basis of university-enterprise cooperation in running schools, to establish a stable conveying channel, to establish a public service platform construction of software and hardware environment actively. At the same time, we are actively contact member enterprise to join the network information platform, to understand the needs of different enterprises to employees, invite them to participate in our school, professional construction, and network information releases and feedbacks, lay the foundation for long-term cooperation.

Two aspects: information network service platform construction, development of comprehensive education, enterprise, electronic commerce, we establish an effective electronic commerce network for related products sales, and form effective working mechanism, relying on companies to establish business relations of cooperation, enterprises accept professional teachers to participate in the practice, urge students self-employment.

Factors. Through the above analysis, thus to establish the public service of network information platform with the practice of the practical significance and broad development space, to meet the needs of era, promote the comprehensive development of education, enterprise, business, promote social progress, the theoretical study and practical experience is worth popularization, this topic is based on this, advances, university-enterprise cooperation pattern of Shandong province and even the whole China to provide effective measures on the basis of, has a broad development prospects.

The construction mode.

Establishing university-enterprise cooperation network information platform of public service, we should take into account three aspects and joint into network, promote the information flow, convenient interaction, considering from the following three aspects: (1) from the perspective of

school should focus on the recruitment of students, teaching, management, employment, the cooperation between colleges and practice based on construction into consideration.(2) Enterprises should construction platform module from recruitment, enterprise communication, education, technology transfer, e-commerce information, etc. (3) from the perspective of students, employment unit should pay attention to practical training base of information and industry development. Schools, enterprises, students obtain tripartite win-win situation.

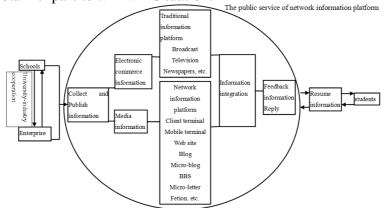


Fig. 1 University-enterprise cooperation network of public service information platform model

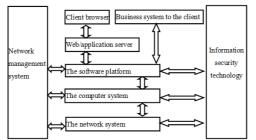


Fig. 2 Network platform management system model

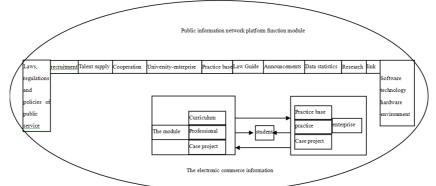
The public service of network information platform system is usually divided into network system, computer system, software platform of three parts. Among them, usually adopt C/S (Client/Server) or B/S (Browser/Server) to construct the application system software and hardware platform. Network systems, computer systems, software platform of the three levels on every level to a level provide necessary support and service.

Factors. By collecting university-enterprise cooperation at home and abroad successful experience, formed a women's college in Shandong "university-enterprise cooperation network information platform construction" typical case of the project, provide the reference for the similar government departments and institutions.

A lot of practice has proved that the public service of network information platform for schools to effectively integrate resources and enterprise production resources, expand the school space, strengthening personnel training of the resultant force, improve the education quality and managerial benefit.

The function modules.

Through the university-enterprise cooperation network information platform construction of public service, the enterprise supplies the demand information to the school, helps the school planning major setting, curriculum reform and teaching materials, designs the teaching process, at the same time the enterprise relates work process and philosophy thinking mode, information real-time transmission to the school, makes the enterprise of the scene teaching can promote the new technology, workplace atmosphere, enterprise culture and so on resources and the combination of classroom teaching content. Through the network platform of remote video teaching system, it gives full play to the quality of teaching and training resources efficiently.



The network information platform function module is as shown in figure(fig.3):

Fig. 3 University-enterprise cooperation network of public service information platform function module This topic in the process of the specific steps is as follows(fig.4):

Analysis of the situat	tion		
University-enterprise	e cooperation in shand	ong province analy	ysis of the present stage domestic and
public information s	ervice platform applicat	tion development, e	etc., of university-enterprise cooperation
and development of	small and medium ente	rprises in the main	positive factors and negative factors o
the construction of in	nformation, the proposed	l strategy is propose	ed.
Field investigation, inte	erview		
Determine questionnai	ire survey object, purp	ose and questionn	aire design, public information servi
platform for universi	ity-enterprise cooperati	on exhaustive sur	every the status of the application
information technology	y, data statistics results,	university-enterpris	se cooperation public information servi
platform application in	shandong province as a	case analysis of the	e specific role of these factors;
		\sim	
The system design			
			able for university-enterprise cooperation
public information serv	rice platform application	n development of in	iformation technology application system
framework and system	mode.		
The system design			
	a se statistical anotania	the design is suita	able for university-enterprise cooperation
According to the resul	it of statistical analysis,		
		n development of in	nformation technology application system

The specific ideas.1, establishing the organization, strengthen scientific management. For enhancing university-enterprise informatization is to promote, strengthen the work responsibility, to advance the informationization service platform construction.

2, strengthen training, improve ability. For many years, the department of digital media and the new visual collaboration, through "please come in", invited professor cities and counties in telecom experts to the scene teaching, seminar, respectively to business knowledge and application of network and information content such as computer basic knowledge training, improve the service ability. Also by way of "going out" graduate employment recruitment, use a variety of traditional media platform combined with the modern network information platform, strengthen the communication and propaganda, enhance exchanges and cooperation for schools and enterprises, providing students with powerful platform.

3, shareing resources. Actively we create a women's college in Shandong information integrated service platform, university-enterprise cooperation mobile virtual network, formed a new Internet site characteristic industry association. Informatization integrated service platform is the so-called "three vertical and a horizontal parallel", both inside and outside the site, "three vertical and" refers to the government, service, business, three total net and brings together various schools, enterprise information, "a horizontal" means a website platform carry all kinds of information, highlight the characteristics of industry and economy, show the characteristics of subjects, the web page layout is reasonable beautiful, rich in content. So-called mobile virtual network refers to the school for the unit, the related enterprise calls a virtual network, call each other all free. The so-called Internet refers to the distinctive characteristic industry and technology talent development association join the

Internet and so on, increase publicity of featured industries, to improve the quality of the talents training level.

Summary

The characteristics of our professional, has a leading level of the comprehensive experiment (training) center, has the high social recognition. Subject involved in the development of science and technology leading edge information technology equipment and services, such as the hardware configuration and software environment the demand is higher, with the brother institutions, cooperative enterprise of equipment and material resources to be shared.

University-enterprise cooperation network information platform construction of public service in Shandong province, advantage and characteristic analysis, questionnaire design, setting up a comprehensive information service platform of information technology application level evaluation system, based on the characteristics of university-enterprise cooperation network information platform of public service in Shandong province and the existing problems, put forward university-enterprise cooperation network information platform of public service in Shandong province proposed strategy of application of information technology, in order to construct public service network information platform in Shandong province the development of information technology and competitive advantage to provide the theory and method of instruction. Through the use of information technology, network information platform construction, reasonable design frame structure and support system, optimize the industrial structure, strengthen the interaction, the construction of informatization of national and international cooperation in running schools between colleges measures to promote theoretical experience, enhance the competitiveness of the education, economy, business.

Acknowledgements

This work was financially supported by "Analysis and Research on Shandong Information Industry Cluster Model", from Shandong province economic information commission, Project number:2012EI072.

"Research on the Application Of 3D Virtual Apparel Fitting of Interactive Platform in Electronic Commence", from youth key project in Shandong Women's University, Project number: ZD201101.

References

- [1] Shiwei Chi, Zhuo Chen, Tiejun Wu, in:Vocational Art Design Education of School-enterprise Cooperation Model. Proceedings of 2013 International Conference on Information, Business and Education Technology(ICIBET 2013)
- [2] Shoufang WANG, in: *On University-Enterprise Cooperation Innovation* (Proceedings of International Conference of China Communication and Information Technology (ICCCIT2010).
- [3] Huang, Hui-Hsin, in: *Data Mining Application of Marketing: A Bivariate Model of Customer Purchase Monetary and Interpurchase Time*[A]. Proceedings of 2012 International Conference on Smart Grid Systems(ICSGS 2012)[C]. 2012
- [4] Qiong Xu, Xiaoping Li, in: The Connotation of Informal Communication and its Application in Long Distance Vocational Education[A]. Proceedings of 2nd International Conference on Science and Social Research(ICSSR 2013)[C]. 2013
- [5] Bo Wang, in: Analysis Methods of RICH Core Element in Network Environment Based on Matrix Vector[A]. Proceedings of 2013 2nd International Conference on Management Science and Industrial Engineering(MSIE 2013)[C]. 2013
- [6] Juan Wu. Study on the Design of Virtual Apparel Fitting System and the Application of Motion Capture Technology in Electronic Commerce. Applied Mechanics and Materials Vols.519-520 (2014) 403-409.

The Performance Evaluation of Enterprise Informatization Research Based on Dynamic Balanced Scorecard

Ling Wei^{1, a}, Weixi Zhang^{1,b}, Wenzhi Xu^{1,c}

¹Harbin University of Science and Technology Hei Longjiang Harbin , China ^aweiling@hrbust.edu.cn, ^b 394347018@qq.com, ^c 358350782@qq.com

Keywords: Dynamic balanced scorecard; System dynamics; Enterprise informatization performance evaluation; VENSIM.

Abstract. The performance evaluation of enterprise informatization not only can accelerate the process of enterprise informatization, but also can avoid trapping in informatization investment. In view of the existing problems in the performance evaluation of enterprise informatization, the paper seeks to combine the use of the balanced scorecard and System dynamics as Dynamic Balanced Scorecard for performance evaluation. It aims to establish a model for the combination of these long- and short-term organisational activities as a framework for evaluating the enterprise informatization using Vensim software, of how core capabilities are managed to show how strategy impact on the enterprise operation. The study finds that, using the dynamic balanced scorecard method to the evaluation of enterprise informatization has good maneuverability and rationality.

Introduction

With the accelerating process of globalization, enterprise informationization has attract more concern. China's enterprises in the evaluation and management of ERP control system is far from perfect ^[1]. Recently, the study of ERP implementation performance appraisal mainly focuses on the following aspects. The American scholars Delone and Mclean presented 6 main indexes of evaluating IS success ^[2]. The ABCD testing table method presented by Oliver Wight gived each question an answer by "yes" or "no". But evaluation items are complicated in this method, which has a strong subjectivity and difficult operation. Zhu Zong-qian and Ji Hao built a mining model for ERP risk external evaluation information. However, the model is limited to the prediction of EPR implementation effect. Therefore, the establishment of evaluation index system of enterprise informatization performance has important theoretical and practical significance to the implementation of enterprise information and improving the information effect.

Dynamic Balanced Scorecard

The Balanced Scorecard is widely used in all walks of life around the world, according to the statistics of its worldwide use rate has reached 44% ^[3]. However, BSC pays much attention to the static performance measurement and neglects the dynamic monitoring of the measuring the execution result. Thus, it can't reflect the cause and effect feedback and nonlinear relationship, which also has time dilation. System dynamics theory was first put forward by Professor Jay W.Forrester. This theory can effectively explain the effects, which is brought by the factors that dynamically changed with time in political, economic and medicine ^[4]. Combining the system dynamics perspective and balance score card forms the dynamic balanced scorecard ideas. BSC makes up the lacks of insufficient dynamics and simple causality for BSC^[5]. It can gain the comparison of strategic performance improvement between different tactics by the computer simulation. And it also provides support for policymakers to choose the most reasonable strategy^[6].

The model of enterprise informatization Based on Dynamic Balanced Scorecard

In the design of key performance evaluation index system, BSC divides business performance into 4 dimensions: financial perspective, client perspective, procedure perspective, learning and growth perspective respectively. Though each level, can it form the enterprise informationization performance evaluation index system by choosing key performance indicators. Table 1 lists the key performance evaluation index of four dimensions. Based on the mentioned system causal loop diagrams above, combining the enterprise BSC key indicators and making the indictors quantitative, this paper establish system dynamics model by using Vensim software as shown in fig. 1.

view	index	working load influence on effect of training on employee satisfaction employee satisfaction
	The rate of cost reduction	<time> employee satisfaction</time>
financial perspective	profit	satisfaction change
	sales growth rate	the number of customers increase the number the decrease in the the decrease in the the decrease in the
Client perspective	customer satisfaction degree	of customers number of customers
	The number of customers	Advertising costs Customer satisfaction change
	service quality	<time></time>
procedure perspective	The quality of product	Profit The total business Service quality of Servic
	production capacity	income
learning and growth perspective	employee productivity	Sales revenue Financial investment
	employee performance	Fig. 1 Company information performance evaluation

Table1 Performance evaluation index of company

Fig. 1 Company information performance evaluation model

The empirical analysis

The A company is a paper company, registered in 1995. The A company established raw material management information system. Under the condition of double production quota, the staff cuts in half while the time is shortened 2/3. As a consequence, the efficiency improves nearly 30 than manual operation at the same time of improving the accuracy of quotation.

Simulation run and result analysis. This paper predicts its profits in the recent 10 years based on the implement condition that A company's enterprise information system automation rate is 0.6. The simulation result is shown in curve 1 of fig. 3. As it is seen the curve in curve 1 of fig. 2 that the executive condition of the current strategy is: the profit curve changes in a choppy in the next six years, rises slowly in the seventh year and the profit doesn't have a significant growth in ten years. At the same time, this paper makes prediction for the condition of employee satisfaction which is one of the most important factors that influence the profit. The simulation result is shown in curve 1 of fig. 2. We can see from the diagram that employee satisfaction index surges in the first year, while it has a sharp contrast in the second year, and employee satisfaction is tending towards stability from the third year.

This is because that the module of enterprise informatization increase with the enhancement of enterprise informatization rate in the short term, which improves the information processing capability and the degree of integration and provides more accurate and effective decision support for the company's managers. The company's efficient operation supplies convenience for

company's internal procedure. The shortening of delivery time increases the customer satisfaction, and then it comes to the peak value and keep a higher level. With the increase of customer satisfaction, the client retention increases. The increase of client retention brings more sales for the enterprise and the profit gradually improves. The improvement of profit brings more performance salary for the employee and the employee satisfaction begins to rise sharply.

However, as the client retention keeps increasing, on one hand the informationization degree of company's product service fails to keep up in time, the compatibility of material flow, capital flow and information flow begins to decrease; on the other hand, the workload of employee increases because the information systems automation rate doesn't improve, while the previous performance salary incentive has been unable to meet the psychological needs of employees, the service quality begins to decline. Thus employee satisfaction decreases and client retention reduces. These variables experience a period of delay rather than presenting ascendant trend all the time in the short term. Some factors accumulate in the beginning and present the trend of oscillation or declination in the following years. In the long term, the information strategy of the A company can't reach the company's performance target and is not conducive to the long-term development of the company. It should be improved.



Fig. 2 Employee performance trend graph

Fig. 3 Sales profit trend graph

Performance improvement Suggestions

The enterprise managers of A company need to adjust strategy to change the present situation according to the performance prediction and casual analysis above. They raise the enterprise information automation rate up to 0.8 and raise staff training times each month up to three. The results are shown in curve 2 in figure 2 and curve 2 in figure 3.

It can be seen from the prediction results, the profit curve ascends more quickly than it is in strategy 1 and keeps on a higher level on account of information automation rate raising to 0.8. After the period of oscillation, the profit has far surpassed the profit condition of strategy 2 and presents a rising trend. The employee satisfaction also has a integral improvement than it is in strategy 1. In that information automation rate raises to 0.8, the employee workload decreases and the employee satisfaction increases. The service quality improves accordingly, thereby the client number increases and the profit promotes. The operating speed of internal procedure promotes and

the decision-making efficiency and accuracy of enterprise senior leaders get promoted after the enterprise management information system improves effectively. This lays the foundation of client increasing. This also presents that the enterprise information results have the quality of time delay. The increasing of the number of training not only improves the quality of employees and service quality but also increases the training cost. So the enterprise profit doesn't increase much. But as the client increases, the effect is brought out gradually which gives security for the profit growth.

Conclusion

In view of the Balanced Scorecard time delay and dynamic problems, this paper introduce system dynamics theory to build a simulation model for dynamic balanced scorecard. The model is a valuable approach for the translation of longer-term purpose into strategic objectives and strategic themes. Using Vensim software, this model realized to simulate and emulate the enterprise informationization performance evaluation. Through the empirical analysis of the model, it intuitively reveals different effect of the enterprise informatization in different strategy. In order to avoid the subjective thinking defect management, it provides scientific and effective reference for the management to formulate modified strategy in practice.

Foundation item

1. The 2013 National Undergraduate Innovative Experiment Program (201319)

2. Heilongjiang Province Natural Science Fund Project(G201013)

References

- [1] Fengcai Tian: Exploration of accounting management method in the application of ERP transformation. Finance and accounting research, 2010(9).
- [2] Zachary Wong, Ph.D: A Proposed Revision to the DeLone and McLean's IS Success Model, 2010 International Conference on E-business, Management and Economics(ICEME2010), School of Business & Economics Sonoma State University Rohnert Park, California, USA, 2010, 12 (28).
- [3] Rigby, D: Management Tools and Techniques, A Survey, California Management Review, 2001, 43(2): 139–160.
- [4] Ting Lin Lee1, Shu-Chuan Yang: Using Balanced Scorecard and System Dynamics in Exploring the Performance of Taiwan's Pharmaceutical Industry, Master's Thesis, National University of Kaohsiung, 2011-06-20, 167.
- [5] Burkhardt, H. Decker, R. Preisach, Ch. Schmidt-Thieme: L.A Procedure to Estimate Relations in a Balanced Scorecard, 2008, Berlin, Springer Berlin Heidelberg.
- [6] Answerthink: Most Executives Are Unable to Take Balanced scorecards from Concept to Reality, According to The Hackett Group, October 22, 2004, retrieved on 09/04/06 from http://www.answerthink.com /04_news/01_press/pr_2004/pr_10222004_01.htmlOctober 22, 2004.

CHAPTER 3:

Computational Mathematics and Data Mining

On Normal Sequence in Abelian Group $C_n \oplus C_n$

Haiyan zhang^{1, a} and Xinsong Yang^{1, b}

¹Department of Mathematics, Harbin University of Science and Technology, Harbin 150080, P.R. China

^ayanhaizhang2222@sohu.com, ^byangxinsong2005@163.com

Key words: normal sequence; Davenport's constant; zero-sum

Abstract. Electronic information technology is based on expression, storage, transmission, and process of information. Information expression is usually generalized as information coding technology, one of whose heart theories is combinatorial number theory in algebra. In the process of storing, transmitting, and processing of electronic information technology, problems about encryption and safety need to use algebra theories of group, ring, and domain. It is thus clear that algebra is very important in electronic information theory. This paper makes use of abelian group basic theory of algebra, together with combination number theory, discusses construction problem of normal sequence in $C_n \oplus C_n$ of abelian group, and gives several sufficient conditions for a guess establishment of W.D.Gao.

Introduction

Let G be a finite abelian groups (written additively), and let D(G) denote the Davenport's constant of G, i.e. the smallest integer d such that every sequence of d elements (repetition allowed) in G contains a nonempty zero-sum subsequences. Let S be a sequence of elements in G with $|S| \ge D(G)[1]$. We say S is a normal sequence if S contains no zero-sum subsequence of length larger than |S| - D(G) + 1. For $n \in N$ let C_n denote the cyclic group with n elements. Let G be a finite abelian group (written additively), there are $n_1, \dots, n_r \in N$ such that $G = C_{n_1} \oplus \dots \oplus C_{n_r}$, where either $r = n_1 = 1$ or $1 < n_1 | \dots | n_r$, then r = r(G) is the rank of the group G and $n_r = \exp(G)$ its exponent. When $n_1 = \dots = n_r = n$, we write C_n^r instead of $C_n \oplus \dots \oplus C_n$ [2]. In this paper we study the group $G = C_n \oplus C_n$.

Let S be a sequence in G, we call S a zero-sum sequence if $\sigma(S) = 0$, a zero-sum free sequence if $0 \notin \sum(S)$. We call S a minimal zero-sum sequence if it is a zero-sum sequence and every proper subsequence is zero-sum free, and S a short zero-sum sequence if it is a zero-sum sequence with $1 \le |S| \le \exp(G)$ [3].

Let *S* be a sequence in *G* with $|S| \ge D(G)$ and *W* be the maximal (in length) zero-sum subsequence of *S*. Then, SW^{-1} is a zero-sum free sequence. Therefore $|SW^{-1}| \le D(G) - 1$ and $|W| \ge |S| - D(G) + 1$. If there is |W| = |S| - D(G) + 1, we call *S* a normal sequence. Clearly *S* is a normal sequence if and only if *S* contains no zero-sum subsequence of length larger than |S| - D(G) + 1[4]. A natural question is to ask what can be said about normal sequences. Then the following conjecture was given (see [5] [6] [7]):

Conjecture Let $G = C_{n_1} \oplus \cdots \oplus C_{n_r}$ be a finite abelian group with $1 < n_1 | \cdots | n_r$, and $k \le n_1 - 1$ a positive integer. Let *S* be a normal sequence in *G* of length |S| = k + D(G) - 1. Then

 $S = 0^k \prod_{i=1}^{D(G)-1} a_i$, with $\prod_{i=1}^{D(G)-1} a_i$ is a zero-sum free sequence.

In this paper we shall demonstrate that conjecture is true for some special cases.

Main Results

Theorem1. If conjecture is true for $C_n \oplus C_n$, then conjecture is true for $C_n \oplus C_{mn}$, where *m* is arbitrary positive integer.

Theorem 2. Conjecture is true for $C_n \oplus C_{mn}$ with $n \in \{2,4,5,3 \cdot 2^{\lambda}, 7 \cdot 2^{\lambda}\}$ and $\lambda \ge 0$, where *m* is an arbitrary positive integer.

Proofs of Theorem 1 and Theorem 2

Proof of theorem 1

Since $D(C_n \oplus C_{mn}) = n + nm - 1$, let $S = (a_1, a_2, \dots, a_{k+n+nm-2})$ be a normal sequence in $C_n \oplus C_{mn}$ of length |S| = k + nm - 2. It is sufficient to prove that S contains k zero elements. Without loss of generality we may assume that k = n - 1.

There is a natural homomorphism ϕ from $C_n \oplus C_{mn}$ onto $C_n \oplus C_n$, and $\ker(\phi) = C_m$. Under ϕ action, normal sequence Sbecomes $\phi(S) = (\phi(a_1), \phi(a_2), \dots, \phi(a_{2n+nm-3}))$, Where $\phi(S)$ be a sequence in $C_n \oplus C_n$. If m = 1, then $C_n \oplus C_{mn} = C_n \oplus C_n$, there is nothing to prove. We may assume that $m \ge 2$, and $|S| = |\phi(S)| = 2n + nm - 3 \ge 4n - 3$, while $s(C_n \oplus C_n) = 4n - 3$, by using lemma2.1[5] repeatedly, we can find some disjoint subsequence T_1, T_2, \dots, T_{m-1} of S with $|T_i| = n$, for every $i \in [1, m-1]$, such that every subsequence T_i satisfies $\sigma(\phi(T_i)) = 0$. Since $\sigma(\phi(T_i)) = \phi(\sigma(T_i)) = 0$, we have that $\sigma(T_i) \in C_m$, for every $i \in [1, m-1]$.

Let $A = (\sigma(T_1), \sigma(T_2), \dots, \sigma(T_{m-1}))$, we infer that A is a zero-sum free sequence in C_m . In fact, if A isn't a zero-sum free sequence, then there exists a nonempty subsequence A_0 of A, suppose $A_0 = (\sigma(T_{i_1}), \sigma(T_{i_2}), \dots, \sigma(T_{i_t})), 1 \le i_1 < i_2 < \dots < i_t \le m-1$, such that

$$\sigma(T_{i_1}) + \sigma(T_{i_2}) + \dots + \sigma(T_{i_n}) = 0,$$

That is

$$\sigma(T_{i_1} + T_{i_2} + \dots + T_{i_r}) = 0.$$

Therefore $T_{i_1}, T_{i_2}, \dots, T_{i_t}$ is a zero-sum subsequence of *S*, and $|T_{i_1}T_{i_2}\cdots T_{i_t}| \ge n$, a contradict to *S* being a normal sequence.

Let $B = S(T_1T_2 \cdots T_{m-1})^{-1}$, and |B| = 2n + mn - 3 - (m-1)n = 3n - 3, set $B = (b_1, b_2, \cdots, b_{3n-3})$, We have that $\phi(B) = (\phi(b_1), \phi(b_2), \cdots, \phi(b_{3n-3}))$ be a sequence in $C_n \oplus C_n$, since $D(C_n \oplus C_n) = 2n - 1$, $|\phi(B)| = 3n - 3 \ge 2n - 1$, we can find a subsequence T_m of B such that $\phi(T_m)$ be maximum zero-sum subsequence in the length of $\phi(B)$.

We derive $\sigma(T_m) \in C_m$ and $\phi(B)\phi(T_m)^{-1}$ is a zero-sum free subsequence of $\phi(B)$. In the following we want to prove that $|T_m| = n - 1$, we distinguish two cases.

Case 1 suppose $|T_m| < n-1$, then

$$|BT_m^{-1}| > 3n - 3 - n + 1 = 2n - 2, |BT_m^{-1}| \ge 2n - 1,$$

Therefore, there is a nonempty subsequence T_{m+1} of BT_m^{-1} , such that $\sigma(\phi(T_{m+1})) = 0$. So $\phi(T_{m+1})$ be a zero-sum subsequence of $\phi(B)\phi(T_m)^{-1}$, contradict to $\phi(B)\phi(T_m)^{-1}$ being a zero-sum free subsequence of $\phi(B)$.

Case 2 suppose
$$|T_m| > n-1$$
, we consider sequence $A\sigma(T_m)$. Since $A\sigma(T_m) = (\sigma(T_1), \sigma(T_2), \dots, \sigma(T_m))$

is a sequence in C_m with the length $|A\sigma(T_m)| = m$, A is a zero-sum free sequence, we can find a nonempty zero-sum subsequence of $A\sigma(T_m)$, which contains $\sigma(T_m)$, a contradict to S being a normal sequence again.

We have proved that $|T_m| = n - 1$, hence $|\phi(T_m)| = n - 1$, we infer that $\phi(B)$ is a normal sequence in $C_n \oplus C_n$. It follows from the hypothesis, we may set $\phi(B) = 0^{n-1}(c_1, c_2, \dots, c_{2n-2})$, so $\phi(T_m) = 0^{n-1}$. We want to prove that $T_m = 0^{n-1}$. Let $T_m = (d_1, d_2, \dots, d_{n-1})$, assume to the contrary that $d_i \neq 0$ for some $i \in [1, n-1]$. Since $\phi(d_i) = 0$, we get $d_i \in C_m$. Consider sequence Ad_i in C_m , similarity to in the front of proof, there is a zero-sum subsequence

 $(d_i, \sigma(T_{i_1}), \sigma(T_{i_2}), \dots, \sigma(T_{i_w}))$ $(1 \le i_1 < i_2 < \dots < i_w \le m-1)$ of Ad_i , which contains element d_i , such that $d_i + \sigma(T_{i_1}) + \sigma(T_{i_2}) + \dots + \sigma(T_{i_w}) = 0$. That is $\sigma(d_i + T_{i_1} + T_{i_2} + \dots + T_{i_w}) = 0$.

Sequence $d_i T_{i_1} T_{i_2} \cdots T_{i_w}$ be a zero-sum subsequence of *S*, contradict, hence $d_i = 0$. We have proved that $T_m = 0^{n-1}$. We complete the proof.

The proof of theorem 2 follows from theorem 1 and the following lemma. Lemma ([1], theorem 1.6) Conjecture is true for the following cases. (i) $G = C_n$, (ii) $G = C_n \oplus C_n$, with $n \in \{2,4,5,3 \cdot 2^{\lambda}, 7 \cdot 2^{\lambda}\}$ and $\lambda \ge 0$, (iii) $G = C_p^r$, with $p \in \{2,3,5,7\}$.

References

- [1] W.D.Gao, Addition theorems for finite abelian groups, J. Number Theory 53(1995)241-246.
- [2] W.D.Gao, A.Geroldinger Zero-sum problems in finite abelian groups: a survey, Expo. Math. 24(4)(2006)337-369.
- [3] W.D.Gao, A.Geroldinger, On zero-sum sequences in $Z/nZ \oplus Z/nZ$, INTEGERS: Electronic J. Combinatorial Number Theory 2003.
- [4] W.D.Gao, A.Geroldinger. On the order of elements in long minimal zero-sum sequences, Periodica Mathematica Hungarica44(2002)63-73.
- [5] W.D. Gao, J.J. Zhuang Sequence not containing long zero-sum subsequences, European Journal of Combinatorics 27(2006) 777-778.
- [6] P.Z. Yuan, Subsequence sums of a zero-sumfree sequence, European Journal of Combinatorics. 30 (2009)439–446.
- [7] G.J.Chang, S.H.Chen. on the number of subsequences with a given sum in a finite abelian group. Electronic J. Combinatorial Number Theory 18(2011)133-149.

The Application of Boosting Algorithm in Data Mining

Jinlong Du^{1, a}, Yan Qian^{2,b,*}

¹Heilongjiang University, Electronic Engineering College, Harbin, China ²Heilongjiang University, Physical Science and Technology College, Harbin, China ^a 375302394@qq.com, ^b 1075703409@qq.com

Keywords: machine learning methods; Boosting algorithm; Data Mining (DM)

Abstract. An algorithm which named Boosting algorithm occurred in the last ten years. It can raise the learning algorithm accuracy with multiple learning and obviously improve the efficiency of learning algorithm by adopting the principle of "comprehensive optimizing". In addition, it can effectively develop the "weak learning algorithm" with low efficiency into a "strong learning algorithm" with high efficiency. The boosting, a new learning method to integration machine, is based in learning theory and show its good qualities in many fields. The paper elaborates and summarizes the basic ideas of Boosting algorithm and applies it into Data Mining (DM). In recent years, the DM has been extensively adopted out of labs such as in commerce, technological research and engineering technology. In this background, the paper tries improving traditional DM algorithm to solve these problems in industrial application.

Introduction

Machine learning is an important branch of artificial intelligence, a kind if extensive technology and it is also the key and choke point of modern intelligence system ^[1]. And learning is the key of the system. It is difficult to think that a system without learning function is called as intelligent system. So what is learning in fact? There were many saying about learning before, and now the concept made by Simon is widely accepted, that is "It is learning if a system is able to perform a process of improving its performance." ^[2-4]

Machine learning algorithm are widely applied in many real situation, for example, how to forecast the weather in next week according to the data before and changing regulation in the weather forecast. Machine learning is as same as many new subjects, it is also is an interdisciplinary one and it learns from the achievement if math, artificial intelligence, probability statistics, neurobiology, cognition science, information theory, cybernetics, computational complexity theory and philosophy. Although the increasing crossing fields always accompanied with many problems, and it will also generate new world of research.

At present, the main research direction of machine learning includes Symbolic machine learning, statistical machine learning, integrated machine learning and enhanced machine learning. And ensemble learning is one of the features of the machine learning. It is the most important one of the four directions.

The overview of DM. DM is to extract rules, regulation and pattern from large amount of data. It also called as Knowledge Discover for Database (KDD). The DM has the broad sense and narrow sense. General DM is the same as KDD, and narrow DM is one of the steps of KDD ^[5]. KDD mainly includes the following steps: Data cleansing (eliminate noise and wrong data). Data integration (gather different data sources). Data selection (search and analysis related data in data base). Data transformation (transform data into the form which is suit for digging). Data mining (extract data pattern through various learning algorithm and intelligent algorithm). Pattern evaluation (estimate the getting model is meaningful or not through measures and judge mining). Knowledge representation

(elaborate the knowledge through digging to user by visual and knowledge representation technology).

DM function is the mode type found from DM. The task of DM can be generally divided into two types: description and forecast ^[6-7]. Descriptive mining tasks mainly describe the general characteristic of data in data base, and forecasting task infers on the base of existing data and to forecast.

The main function of DM includes the following points: concept description, association rules, classification, cluster and other specific functions.

To effectively extract information from large amount data in data base, the DM algorithm must be effective and elastic^[8]. If we combine the incremental algorithm with the renewal of data base, it is not necessary to study all of the data, but to gradually update the knowledge and strength the existing knowledge. Due to the wide application of relational data base and DW (data warehouse), the data base may contain complex data object, such as spatial data, time data or transaction data. Some cases about DM occurred in many fields such as business, finance, telecommunication, DNA analysis, scientific research and medical care and health, and most of the achievements can turned into particular use rapidly.

The summary of Boosting algorithm. Boosting is a way trying to raise the accuracy of learning algorithm^[9]. It stems from PAC (Probably Approximately Correct)learning model raised by Valiant. PAC is the theoretical base for statistical machine learning and integrated machine learning. Kearns and Valiant firstly raised the following question: In the PAC model raised by Valiant, whether a weak learning algorithm whose function is only a little better than randomly guessing can be developed into a strong algorithm with arbitrary precision.

The main thought of Boosting algorithm is to get a complex high-accuracy forecasting way through easy, not quite right, experience only primary prediction method. Boosting algorithm lays emphases on the cases which are easily to misunderstand, for example, when we recite English, we can remember some easy words in the first time, and we will pay attention on those difficult ones in the second time.

In recent years, Boosting algorithm has been applied in many fields. Such as text categorization, Image classification retrieval, NLU (natural language understanding) and voice recognition.

Compared with other algorithm, Boosting algorithm has many advantages such as the rapid speed, it can lead feature selection with classifying and it doesn't need other parameters except T iteration. In addition, Boosting doesn't need priori knowledge of weak classifier, and it can get a better strong classifier by weak classifier which is a little better than random, instead of trying to design an exact algorithm. At the same time, it also has theoretical base, it can reach any accuracy with enough data and weak classifiers.

In a word, Boosting algorithm is an algorithm which can integrate any weak classification algorithm in theory and it has theoretical base, and some experiments show that the algorithm can highly adapted to less sample and high dimensional data, compared with other algorithm, Boosting is more suitable and accurate. The raise and theoretical research of Boosting algorithm aim at classification problems, and the research on DM is less. So the paper is mainly study on the application of Boosting algorithm in DM.

Procedures and simulation. Here we choose Matlab software to simulate our algorithms. Matlab has very wide range of applications, including signal and image processing, communications, control system design, test and measurement, financial modeling and analysis, and computational biology, and many other applications. Additional kit (available separately dedicated MATLAB function sets) extends the Matlab environment to address these applications within the specific type of problem.

Therefore, we first call Matlab function library. By specifying the X-axis, Y-axis range, we simulate a set of Training Data. Make training data of two classes "red" and "blue" with 2 features for each sample (the position x and y). Above we talk about the AdaBoost algorithm as the representative algorithm of Boosting algorithm. Here we use AdaBoost algorithm to make a classifier and show the results of the training data classified with AdaBoost model. Then we show the error versus number of weak classifiers. Visually display the advantages of AdaBoost algorithm. At last we show the test data which classified with AdaBoost model in Figure 1. Finally we complete the simulation algorithm, and draw our conclusions.

Above all we can get the experimental results which showed in Fig. 1. In this figure we can easily find our AdaBoost algorithm can be used in Data Mining.

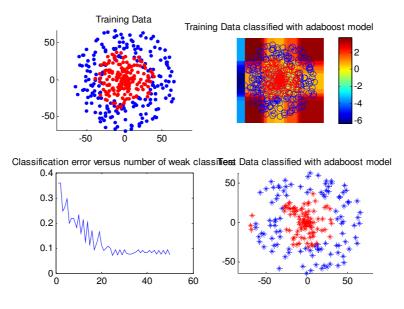


Fig. 1 The experimental results

Conclusions

At present, Boosting machine learning algorithm is relatively popular research direction. Meanwhile, Boosting algorithm is currently one of the best classification methods, gained more and more attention. It is an algorithm-independent machine learning techniques and does not depend on the particular classifier and specific learning algorithms and it can be used in combining with a variety of different learning algorithms. Boosting algorithm is widely used.

Of course, Boosting algorithm has some drawbacks: It is very dependent on the data and the weak learner, and very sensitive to noise on the data. It can not achieve arbitrarily high accuracy with the weak learner. This paper mainly studies the following elements: Summary and give a brief exposition to the Boosting overview the significance of data mining. And lead a more comprehensive analysis for data mining.

The Boosting algorithm is applied to data mining. Carry out using MATLAB software simulation data collection. And get the graphics of pattern recognition. The final experimental results show that Boosting is indeed a superior algorithm. It has played a very important role in data mining.

References

- H.A. Simon, "Why Should Machines Learn?" in Machine Learning: An Artificial Intelligence Approach, R.S. Miehalski, J.G. Carbonell, and T.M. Mitchell, Morgan Kaufmann Los Altos, 1983.
- [2] Dietterich.T.G Machine learning research: Four current directions[J].AI Magazine, 18(4): 97–136.1997.
- [3] Tom M. Mitchell: Machine Learning [J].McGraw Hill, 1997.
- [4] Thomas G Dietterich. In The Handbook of Brain Theory and Neural Networks, Second Edition[J],2002.
- [5] Michael Kearns, Leslie G. Valiant. Learning Boolean formulate or finite automata is as hard as factoring. Technical Report TR-14-88 Harvard University Aiken.
- [6] Friedman J, Hastie T, Tibshirani R. Additive logistic regression: a statistical view of boosting: [Technical Report],1998.
- [7] Schapire R.E.Singer Y. Boost Texer: A system for multiclass multi-table text categorization. Machine Learning, 1998.
- [8] Schapire R.E. Singer Y. Using output codes to boost multiclass learning problems. In machine learning: Proc. Of the fourteenth international conference[J]. 313-321,1997.
- [9] Dietterich T.G., An experimental comparison of three methods for constructing ensembles of decision trees: Bagging, boosting and randomization. AI Magazine[M],(18):97-136,1997.

Massive Data Analysis Based MapReduce Structure on Hadoop System

Xu Yiqiao^a Xi`an Jiaotong University, Shaanxi China ^acherry041032@gmail.com

Keywords: Hadoop System, MapReduce Module, K-Means Clustering Algorithms

Abstract. Massive Data analysis is becoming increasingly prominent in a variety of application fields ranging from scientific studies to business researches. In this paper, we demonstrate the necessity and possibility of using MapReduce [1] module on Hadoop System [2]. Furthermore, we conducted MapReduce module to implement Clustering Algorithms [3] on our Hadoop System [4] and improved the efficiency of the Clustering Algorithms sharply. We showed how to design parallel clustering algorithms based on Hadoop System. Experiments by different size of data demonstrate that our purposed clustering algorithms have good performance on speed-up, scale-up and size-up. So, it is suitable for big data mining and analysis.

Introduction

It is undeniable that the scale of data increasing rapidly and massive data mining can help both scientists and companies to get more useful information from a lot of data. Big data analysis is useful in many fields—analysis enable extracting business intelligence, enable processing data sets from scientific studies and simulations, enable web data mining and so on. Before the Hadoop was used, we have no method to deal with massive data. Analysis such big data demands a highly scalable solution to deal with the defects of both hardware and software, especially the limited capabilities of hardware. MapReduce, based on several commodity machines, is an efficient method to analysis massive data by parallel processing data. Hadoop is an implementation of MapReduce, primarily supported by Yahoo, and also in use at Facebook, Amazon, SETI@home project etc. In simple terms, Hadoop use several computers or servers together to analysis big data in a parallel way. Clustering Algorithms become more and more essential in many fields, but traditional method have a vital limitation on big data. Admittedly, traditional method for K-Means [6] Algorithms is a milestone in this field. However, when the data is large enough, the traditional method for Clustering Algorithms (e.g. The K-Means Algorithms) cannot make it efficiently. Obviously, we need to find another method to deal with this problem. The paper argues that we can handle massive data, such as one hundred million nodes which totally about 5GB size, because of MapReduce structure on Hadoop system. According to my results of experiment, it took about one hour to cluster one hundred million nodes by K-Means Clustering Algorithms.

Background of Hadoop

Hadoop is a system based on several computers as a computer cluster. It needs several slaves, one worked as a master and others worked as slaves. Hadoop consist of MapReduce module and the HDFS (Hadoop Distribute File System). HDFS has a high level of fault-tolerant and is designed for low-cost hardware. It also provides high level of throughput in order to visit data from applications. So HDFS is extremely suitable for massive data visiting and analysis. Because of advantages of Hadoop, it is used in many fields and many companies to deal with big data.

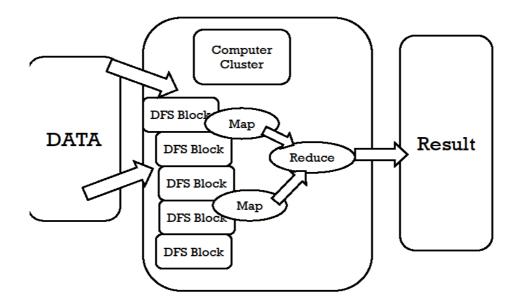


Fig1: The Structure of Hadoop

Picture Fig1 is the structure of hadoop system when it is working. It can be seen that, in Hadoop System, the input data are divided into several DFS Blocks(64MB per block by default). The map module get input data from these DFS Blocks and then they deal with these data with certain functions distributed. After that, the reduce module receive intermediate data from map modules. Finally, when reduce modules submit their data, these data is the final result. We can see that distributed methods is used in Hadoop System.

Clustering Algorithms

Clustering Algorithms is a useful algorithm in many fields (e.g. People distinguish customers by clustering algorithms and conclude their customs in order to make more profits). Researches of cluster have begun many years ago, people at that time realized that clustering algorithms will make a great contribution in future. So the studies of clustering algorithms become more and more popular. Clustering algorithms can be considered as the first step for data mining. It can also discover the deep information from the certain data bases and conclude every cluster characteristic.

There are several kinds of clustering algorithms, such as K-Means, K-Medoids, GMM(Gaussian Mixture Mode), clarans and so on. In this paper, we discuss K-Means for I implement K-Means by MapReduce model on Hadoop system.

Establish Hadoop System

To use the MapReduce module on Hadoop System, we must establish it on our own computers. We can not only use several computers as its nodes, but also use several virtual machines in one personal computer. During my research of Hadoop, I use the latter methods to build Hadoop System. In my VMware virtual machines, I made one master and two slaves which use CentOS6.0 as their operating systems. During establish Hadoop System, we need lots of extra knowledge. We need to know how to revise the configuration of iptables (firework in Linux) and how to build ssh for non-code connection between master node and slave nodes in order to avoid enter code when Hadoop System is worked. The procedure of establish Hadoop System is vital and difficult. I met large sums of challenges at that step and according to this, I wrote a documentation named 'Configure Hadoop System on Virtual Machines' to help other to make it easy and deal with almost all the problems they maybe come across.

To test the Hadoop System that I established in my virtual machines, I wrote several demos. All of them are written based on MapReduce module running on my Hadoop System.

- Wordcount Program : Deal with a data file to count how many words are there in
- Remove duplicate data Program : Delete duplicate data in one article
- Data sorting Program : Sort the data in the certain input file
- Tables association Program : Deal with several different tables

The succession of these programs guarantee that my Hadoop System is working well and it can provide a stable programming environment for me to implement K-Means clustering algorithms.

MapReduce Program for K-Means on Hadoop System

We can conclude from the principal of K-Means clustering algorithms that the major work is to cluster these points to their closest seed point. Obviously, the calculation of each point is the same procedure and it will be repeated again and again. Considered that, we can use the distribute MapReduce module, that using the same map function and reduce function to complicate the whole iteration until the result convergence. Here below are my steps for K-Means clustering algorithms:

- Write a C program to create a file which conclude about one hundred points as input data(totally size 7GB)
- Find k points as seed points randomly
- Store these seed points in HDFS as global variables
- Put these input data to MapReduce module

In my program, I divided the project into six sub-programs:

- K-Means.java
- KMapper.java
- KCombine.java
- KReduce.java
- NewCenter.java
- CenterInitial.java

K-Means is the main function and KMapper, KCombine, KReduce are map module, combine module, reduce module. CenterInitial is response for the first step that get these initial seed points. Meanwhile, NewCenter is due to get the next seed points during iteration. Following are the steps of the program.

- Running the Main function in KMeans.java
- Initialise seed points: CenterInitial centerInitial = new CenterInitial()
- Choose k seed points by random and save them into the file named center in HDFS
- Start-up job-tracker and go into map produce
- Running into KMapper.java and then running setup function to finish reading data of the initial seed points
- Data is operated from Mapper to Combine to Reducer and get new seed points
- Send these seed points to Main function and judge whether they meets the requirements
- Repeat these steps until new seed points meets the requirements
- Output the results

In my map module, get the data in the certain input file as <key, value> which is the MapReduce format by default. KMapper analysis the input data, calculate these data at first step and send it into combine module. Combine module is not necessary in a MapReduce program but it can improve the efficiency of the program rapidly. My combine handles the data that map submit into <key', value'> and then send them to the reduce module. In the reduce module, the data sent by combine module was finally get the new seed points and which points belong to which seed point until the result of the experiment iteration.

Analysis Result of Experiment

Picture Fig2 is a part of the experiment result. The first row is the seed point for each sub-cluster. And the other rows are the data which clustering to the seed points. On the other hand, the input file size is

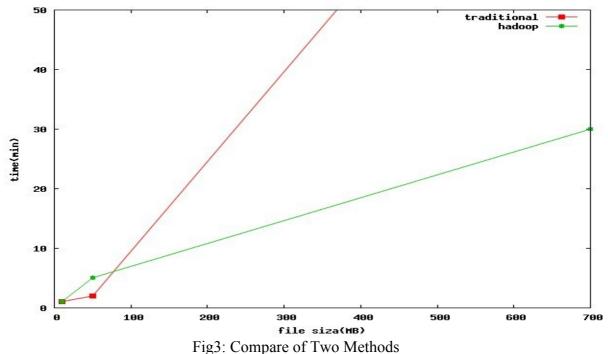
(17.67347,15.755102)	(20,22) (16,12)) (11,14) (1	2,14) (18,13)	(14,10) (18,8)
(18.011236,55.5618) (14	4,55) (16,49) (22	2,56) (24,58) (17,59) (25	,59) (25,55) (19
(18.57558,69.48837) (16	5,73) (22,64) (20	9,67) (17,64) (16,67) (22	,63) (22,65) (15
(18.889534,31.42442)	(24,29) (16,36)) (15,32) (1	3,35) (26,30)	(17,31) (17,24)
(20.995556,94.742226)	(24,97) (18,95)) (25,94) (2	8,97) (22,93)	(17,100) (18,10
(22.754387,43.497074)	(27,39) (22,46)) (23,43) (2	3,46) (20,39)	(22,46) (15,40)
(22.977478,82.445946)	(17,78) (16,87)) (25,79) (2	5,83) (22,81)	(17,79) (30,80
(25.5847,5.7814207) (28	3,4) (19,4) (24,9	9) (24,1) (2	9,1) (29,12)	(21,2) (30,7) (3
(28.335665,20.321678)	(24,16) (26,20)) (27,26) (3	4,17) (30,22)	(34,22) (25,23)
(30.208956,65.72139)	(36,64) (29,73)) (36,63) (2	8,65) (34,65)	(32,63) (28,68
(32.47208,51.847717)	(29,58) (34,54)) (35,59) (3	6,57) (33,44)	(33,57) (29,57
(33.904762,32.267857)	(40,28) (32,36)) (29,34) (3	8,35) (35,29)	(31,40) (32,30
(37.568626,93.56863)	(34,89) (32,91)) (44,99) (3	4,96) (32,87)	(37,91) (32,86
(38.045456,77.50455)	(34,72) (31,75)) (38,70) (3	3,77) (42,84)	(33,73) (31,76
(41.393204,6.461165)	(43,11) (45,2)	(37,3) (46,	7) (36,3) (38	,11) (40,7) (34
(41.60753,18.85484) (47	(48,15) (48,15) (43	1,23) (43,17) (48,14) (38	,13) (39,19) (4
(42.482956,40.573864)	(47,38) (49,36) (41,41) (5	1,38) (36,42)	(50,38) (41,34
(43.738937,61.584072)	(42,68) (38,60) (40,59) (4	6,61) (45,60)	(44,59) (38,62
/	100 001 10 001	1 1	-1 /1 /-	

about 700MB includes ten million points. My Hadoop System used about half an hour to get the certain result.

Fig2: Result of Experiment

I establish Hadoop System in my four virtual machines using VMware. The hardware configuration of my computer is: 6GB Memory, Intel Pentium p6200@2.13GHz CPU. The Hadoop version is 1.2.1 and the java version is 6. I test my Hadoop project by three data and their size are 10MB, 50MB, 700MB, 7GB. Then I input these data into the traditional K-Means algorithms program. According to the result of the experiment, we can arrival a conclusion that the program running by MapReduce Module is extremely more efficiency than the traditional method. When we use the traditional K-Means, it can only deal with 10MB input data. When the input data become 700MB size and 7GB size, the CPU occupancy reach to 99\%, so we can consider that the traditional algorithms cannot deal with big data clustering algorithms. The following picture is the result of the experiment when the input data was 700MB. And it takes about 20mins to finish the program.

So when the input data become big enough, the traditional K-Means algorithms is not suitable. We can conclude that the bigger the input data is, the more advantage that program running on Hadoop is shown.



265

In picture Fig3, we can clearly see that when the input file size is not big, cost time of traditional method for K-Means clustering algorithm is similar to the program running on Hadoop System based on MapReduce module. And as the input size become larger and larger, the capability of traditional method decreases sharply and we can consider is does not when the size of input file comes to 100MB. However, the Hadoop program is much better. Maybe it is still slow when the data is big enough, but obviously it is suitable for dealing with massive data.

Related Work

Google and Yahoo have made many of their projects based on MapReduce module running on Hadoop System. And there is another method to implement K-Means clustering algorithms on Hadoop System. One sub-project named Apache Mahout based on Hadoop. Mahout is encapsulated of three kinds of machine learning algorithms which including clustering algorithms. To deal with massive data by K-Means clustering algorithm, many researchers choose to use Mahout instead of the tradition Java program running on Hadoop System.

Conclusion

Analysis of massive data problem is becoming more and more important. It can be foreseen that in the future the huge data analysis can help people in many fields. In this paper, we discuss that the MapReuce program on Hadoop System can improve the efficiency of the program rapidly. And through implement the K-Means clustering algorithms on Hadoop System, apparently, we can conclude that the MapReduce module on Hadoop System can handle massive data with highly efficiency. In the future, the Hadoop System will develop well and will be used in more and more fields. I will implement more algorithms and deal with some certain real work on Hadoop System by MapReduce module and use Hadoop System to deal with large amount of small size files.

References

- J. Dean and S. Ghemawat, "MapReduce: Simplified data processing on large clusters," Google, Tech. Rep., 2005.
- [2] T. Write, Hadoop: The. Definitive. Guide, 2nd ed. TsingHua University, 2010.
- [3] D. Cutting, 2005, developed from the program of Apache Lucene.
- [4] "Welcome to Apache Hadoop," Apache, Tech. Rep., 2011, Information on http://hadoop.apache.org.
- [5] J. B. MacQueen, A Test for Suboptimal Actions in Markovian Decision Problems, 1967.

Modified Proportional 2-tuple and Its Application In Uncertainty Environment

Aiping Zhang^{1,a}, Tongjun Zhan^{2,b}

¹School of Mathematics, Hefei University of Technology, hefei, 230009 ,china
²School of Management, Hefei University of Technology, hefei, 230009 ,china
^a182828243@qq.com, ^b731032156@qq.com

Keywords: multiple attribute decision making; 2-tuple;modified proportional 2-tuple; aggregation operator; uncertain linguistic.

Abstract. A modified proportional 2-tuple was proposed to apply to the term sets in that the distance of the adjacent tems is not equal, and the comparison methods as well as the aggregation operators were proposed too. And the modified proportional 2-tuple fuzzy linguistic representation model is extended to uncertainty modified proportional 2-tuple fuzzy linguistic representation model, and the new comparison rule and aggregation operators were provided.

I. Introduction

About a decision making problem, the selection of the aggregation operator was very important. Scholars have proposed lots of aggregation operators according to different decision making problems. So far, there were three types of aggregation operator:(1)aggregation operators based on extension theory;(2)aggregation operators based on symbol model;(3)aggregation operators based on 2-tuple linguistic. In the above three types of aggregation operators, the first two kinds have some shortcomings, when we used the first two kinds of operations, after getting the final compositive aggregative value, we should use a approximate process to get the corresponding term in the term set to show the meaning of the aggregated value, therefore there would be some deviations, and the first two kinds of aggregation operators could not distinguish the fine differences by the final term. But the last kind of aggregation operator based on 2-tuple linguistic could overcome the shortcomings of the first two kinds by using a term of symbolic transformation.

Because of the advantage of the aggregation operators based on 2-tuple linguistic, scholars have done lots of research on it and put forward some operators[1-7], And the 2-tuple linguistic aggregation operators have been used in lots of research field[8-13].

But most of 2-tuple linguistic aggregation operators could only be used in the term set that the adjacent terms must have equal distance, so JinHsien Wang and Jongyun Hao provided the new version of 2-tuple fuzzy linguistic representation model to let the model could use in the situation of that the adjacent terms were not equal distances. But the new version of 2-tuple linguistic representation model has some problems, firstly the expression of symbolic proportion pair was not unique, secondly the operators of the new version of 2-tuple fuzzy linguistic representation model could not unify with the operators of 2-tuple linguistic representation model

So we proposed the modified proportional 2-tuple fuzzy linguistic representation model to solve the two disadvantages of the new version of 2-tuple linguistic representation model.

In order to do that, the paper is structured as follows: In Section II, we shall present a brief review of the 2-tuple fuzzy linguistic representation model and the new version of 2-tuple fuzzy linguistic representation model. In Section III, we present the concept of modified proportional 2-tuple fuzzy linguistic representation model and it's comparison rule and it's several aggregation operators. In Section IV, we extend the modified proportional 2-tuple fuzzy linguistic representation model to uncertainty environment. In Section V, a example is given to illustrate the steps of decision making problems. Finally, some concluding are made.

II. Preliminaries

Let $S = \{s_0, s_1, \dots, s_g\}$ is a term set, g is a odd number, s_i $(i = 1, 2, \dots, g)$ represent one of the linguistic values such as:good, very good, medium, etc. If g = 5, the term set can define as $S = \{s_0, s_1, s_2, s_3, s_4, s_5\}$, in that $s_0 = very \ poor$, $s_1 = poor$, $s_3 = medium$, $s_4 = good$, $s_5 = very \ good$.

In 2000, Herrera and Martínez proposed 2-tuple fuzzy linguistic representation model, the content is shown in definition1.

Definition 1[1]: Let $S = \{s_0, s_1, \dots, s_g\}$ is a linguistic term set, $\beta \in [0, g]$ is a value representing the result of a symbolic aggregation operation, then the 2-tuple that expresses the same information to β is obtained by the function:

$$\Delta: \quad [0 \quad g] \to S \times [-0.5, 0.5)$$

$$\Delta(\beta) = (s_i, \alpha), \text{ with } \begin{cases} s_i, i = round(\beta) \\ \alpha = \beta - i, \alpha \in [-0.5, 0.5) \end{cases}$$
(1)

Where $round(\cdot)$ is the usual round operation, s_i has the closest subscript to β , and α called symbolic translation.

The 2-tuple fuzzy linguistic model can only use in the term set of neighbor term's index must have equal distance, so in 2006 JinHsien Wang, Jongyun Hao proposed a new version of 2-tuple fuzzy linguistic representation model, we recall the concept of symbolic proportional pair in definition2. **Definition 2**[4]: Let $L = \{l_0, l_1, \dots, l_n\}$ be an ordinal term set, I = [0,1], and

 $IL \equiv I \times L = \{(\alpha, l_i) : \alpha \in [0,1], i = 0,1,...,n\}$, Given a pair (l_i, l_{i+1}) of two successive ordinal terms of L, any two elements $(\alpha, l_i), (\beta, l_{i+1})$ of IL is called a symbolic proportional pair, and α , β are called a pair of symbolic proportions, if $\alpha + \beta = 1$. A symbolic proportional pair $(\alpha, l_i), (\beta, l_{i+1})$ can be denoted as $(\alpha l_i, (1 - \alpha) l_{i+1})$, and the set of all of the symbolic proportional pair is denoted as \overline{L} .

$$\overline{L} = \{ (\alpha l_i, (1-\alpha) l_{i+1}) : \alpha \in [0,1], i = 0 \ 1, \dots, n-1 \} \begin{cases} l_i, i = round(\beta) \\ \alpha = \beta - i, \alpha \in [-0.5, 0.5] \end{cases}$$

Noticing that the term l_i (i=12,...,n-1) can denoted by symbolic proportional pairs $(0l_{i-1}, 1l_i)$ or $(1l_i, 0l_{i+1})$, the expression of it is not unique.

The definition of new version of 2-tuple fuzzy linguistic representation model is as definition3. **Definition 3**[4]:Let $L = \{l_0, l_1, \dots, l_n\}$ be a linguistic term set, $\beta \in [0, n]$ a value representing the result of a symbolic aggregation operation, then the proportional 2-tuple that expresses the equivalent information to β is obtained with the following function:

$$\Delta: \begin{bmatrix} 0 & n \end{bmatrix} \to L \times \begin{bmatrix} -0.5, 0.5 \end{bmatrix}$$

$$\Delta(\beta) = (l_i, \alpha), \text{ with}$$
(2)

Where *round*(·) is the usual round operation, l_i has the closest subscript to β , and α is the value of symbolic translation.

III. Modified proportional 2-tuple linguistic representation model and it's comparison rule

In definition2, we could see, when l_i (i=12,...,n-1) was translated into symbolic proportional pair, the expression of it was not unique. And in [4] the author defined aggregation operators based on canonical characteristic values, but the aggregation operators of 2-tuple model could not be used in the new version of 2-tuple model. Based on the above two disadvantages, we modified the definition3, given the modified proportional 2-tuple fuzzy linguistic representation model.

Let $\overline{S} = \{s_{\overline{1}}, s_{\overline{2}}, \dots, s_{\overline{n}}\}$ is the linguistic term set. In the term set \overline{S} , the distances between $s_{\overline{i}}$ and $s_{\overline{i+1}}$ is $\overline{i+1}-\overline{i}$, the distances of adjacent terms were different. $(s_{\overline{i}}, \alpha)$ is called modified proportional 2-tuple pair, $\widetilde{L} = \{(s_{\overline{i}}, \alpha) | \alpha \in [-0.5, 0.5) | i = 1, 2, \dots, n\}$ is called modified proportional 2-tuple pair term

set. The modified proportional 2-tuple fuzzy linguistic representation model was defined as definition4.

Definition 4: Let $\beta \in [\overline{1}, \overline{n}]$ is a aggregation value, if $\beta \in [\overline{i}, \overline{i+1})$, $(\overline{i} \in R, i \in Z)$, Let $\beta - \overline{i} = \alpha'(\overline{i+1} - \overline{i})$, then $\alpha' \in [0,1)$ is called proportional symbol translation, we can express the equivalent information to β by modified proportional 2-tuple pair by the function Δ :

$$\Delta: [\overline{1}, \overline{n}] \to S \times [-0.5, 0.5)$$

$$\Delta(\beta) = \begin{cases} (s_{\overline{i}}, \alpha'), \alpha' \in [0, 0.5) \\ (s_{\overline{i+1}}, \alpha'-1) & \alpha' \in [0.5, 1) \end{cases}$$
(3)

Remark: Let $\overline{S} = \{s_{\overline{1}}, s_{\overline{2}}, \dots, s_{\overline{n}}\}, s_{\overline{i}} (i = 1, 2, \dots, n)$ can be translated into the modified proportional 2-tuple pair $(s_{\overline{i}}, 0)$, the expression is unique.

 β can be represented by modified proportional 2-tuple pair $(s_{\bar{i}}, \alpha)$, also from the modified proportional 2-tuple pair $(s_{\bar{i}}, \alpha)$ we can get β by the inverse function of Δ .

Proposition 1: Let $\overline{S} = \{s_{\overline{1}}, s_{\overline{2}}, \dots, s_{\overline{n}}\}, (s_{\overline{i}}, \alpha)$ is a modified proportional 2-tuple pair, by the function Δ^{-1} , $(s_{\overline{i}}, \alpha)$ can return to aggregation value β . The definition of function Δ^{-1} is as follows:

$$\Delta^{-1} : S \times [-0.5, 0.5) \rightarrow [\overline{1}, \overline{n}]$$

$$\beta = \Delta^{-1} [(s_{\overline{i}}, \alpha)] = \begin{cases} \overline{i} + \alpha (\overline{i+1} - \overline{i}), \alpha \in [0, 0.5) \\ \overline{i+1} + \alpha (\overline{i+1} - \overline{i}) \end{cases} \quad \alpha \in [-0.5, 0)$$

$$(4)$$

In the decision problems, when we got the final integrated result of every objective, we should choose the best one from them, so there should need a comparison rule.

Comparison rule of modified proportional 2-tuple pairs:

Let there were two new proportional 2-tuple pairs: $(s_{\bar{i}}, \alpha), (s_{\bar{i}}, \delta), (s_{\bar{i}}, \delta)$

1) if
$$\overline{i} < \overline{j}$$
 then $(s_{\overline{i}}, \alpha) < (s_{\overline{j}}, \delta)$
2) if $\overline{i} = \overline{j}$ then if $\alpha < \delta$ then $(s_{\overline{i}}, \alpha) < (s_{\overline{j}}, \delta)$
if $\alpha = \delta$ then $(s_{\overline{i}}, \alpha) = (s_{\overline{j}}, \delta)$
if $\alpha > \delta$ then $(s_{\overline{i}}, \alpha) > (s_{\overline{j}}, \delta)$
3) if $\overline{i} > \overline{j}$ then $(s_{\overline{i}}, \alpha) > (s_{\overline{i}}, \delta)$

Aggregation operators of modified proportional 2-tuple linguistic representation model

In order to integrate every attribute's value to a synthesized result, we provided several aggregation operators based on the modified proportional 2-tuple linguistic representation model. Let $\overline{S} = \{s_1, \dots, s_n, s_n\}$ is the linguistic term set.

Definition 5: Let $x = \{(\gamma_1, \alpha_1), (\gamma_2, \alpha_2), \dots, (\gamma_n, \alpha_n)\}$ is a group of modified proportional 2-tuple

$$2MPLPA(x) = \Delta \left(\sum_{i=1}^{n} \frac{1}{n} \Delta^{-1}(\gamma_i, \alpha_i)\right) = \Delta \left(\frac{1}{n} \sum_{i=1}^{n} \beta_i\right)$$
(5)

We can see because of the application of α , the computation is without any loss of information.

In the real life, the attributes of a objective have difference importance degree, so when we aggregate the attributes' values, we should multiply the weight of every attribute's value.

Definition 6: Let $x = \{(\gamma_1, \alpha_1), (\gamma_2, \alpha_2), \dots, (\gamma_n, \alpha_n)\}$ is a group of modified proportional 2-tuple pairs, $w = (w_1, w_2, \dots, w_n)$ ($w_i > 0$, $i = 1, \dots, n$) is the corresponding weight vector of x, the modified proportional 2-tuple linguistic weighted average operator is defined as follows:

$$2MPLPWA(x) = \Delta \left(\frac{\sum_{i=1}^{n} \Delta^{-1}(\gamma_i, \alpha_i) \cdot w_i}{\sum_{i=1}^{n} w_i} \right)$$
(6)

Every weight of modified proportional 2-tuple linguistic weighted average operator was fixed with a special attribute. But in some circumstances, the weight was fixed with a special position, such as when getting the final score of a competitor, the weights of the highest score and the lowest score are zero, the weight was fixed with a position, in this situation, the modified proportional 2-tuple linguistic ordered weighted aggregation operator was needed. **Definition 7:** Let $x = \{(x, \alpha) \mid (x, \alpha)\}$ is a group of modified proportional 2-tuple

Definition 7: Let
$$x = \{(\gamma_1, \alpha_1), (\gamma_2, \alpha_2),, (\gamma_n, \alpha_n)\}$$
 is a group of modified proportional 2-tuple
pair, $w = (w_1, w_2, ..., w_n)$ ($0 \le w_i \le 1$, $i = 1, ..., n$) is the associated weight, $\sum_{i=1}^n w_i = 1$. Reorder
 $(\gamma_1, \alpha_{,1}), (\gamma_2, \alpha_2), ..., (\gamma_n, \alpha_n)$ from large to small, then get a new sequence
 $(\eta_1, \delta_1) (\eta_2, \delta_2), ..., (\eta_n, \delta_n)$, and $\Delta^{-1}(\eta_i, \delta_i) = \beta'_i (i = 1, 2, ..., n)$, define the modified proportional 2-tuple
linguistic ordered weighted aggregation operator as equation (7)

$$2MPLPOWA(x) = \Delta \left(\sum_{i=1}^{n} \Delta^{-1}(\eta_i, \delta_i) \cdot w_i \right) = \Delta \left(\sum_{i=1}^{n} \beta'_i \cdot w_i \right)$$
(7)

From the above three aggregation operators we could see the modified proportional 2-tuple linguistic aggregation operators were concordant with the aggregation operators based on 2-tuple linguistic representation model, and the other aggregation operators could also be used in the new proportional 2-tuple linguistic representation model.

IV.Modified proportional 2-tuple fuzzy linguistic model under uncertainty environment

Because of the complexity, uncertainty of the objective world and fuzziness of human thinking, the assessment terms gave by the experts usually were uncertainty linguistic terms like: [*medium*, good], etc. So we extended the modified proportional 2-tuple linguistic representation model to uncertainty environment to solve the uncertainty decision making problems.

Let $\overline{S} = \{s_{\overline{1}}, \dots, s_{\overline{i}}, \dots, s_{\overline{n}}\}$ is the linguistic term set, $[(s_{\overline{i}}, \alpha_{\overline{i}}), (s_{\overline{j}}, \alpha_{\overline{j}})]$ is called uncertainty modified proportional 2-tuple linguistic term pair, in that $(s_{\overline{i}}, \alpha_{\overline{i}})$ is the lower limit, $(s_{\overline{j}}, \alpha_{\overline{j}})$ is the upper limit, and the uncertainty modified proportional 2-tuple linguistic term set is $\widetilde{S} = \{(s_{\overline{i}}, \alpha_{\overline{i}}), (s_{\overline{j}}, \alpha_{\overline{j}})\} | s_{\overline{i}}, s_{\overline{j}} \in \overline{S}, \alpha_{\overline{i}}, \alpha_{\overline{j}} \in [-0.5, 0.5)\}$.

Definition 8: Let $[\beta^{-} \beta^{+}]$ is the integrated value, and $\beta^{-} \beta^{+} \in [\overline{1} \ \overline{n}]$, then we can transform $[\beta^{-} \beta^{+}]$ to an uncertainty modified proportional 2-tuple linguistic term pair by the function Δ : if $\Delta(\beta^{-}) = (s_{\overline{i}}, \alpha_{\overline{i}}), \Delta(\beta^{+}) = (s_{\overline{j}}, \alpha_{\overline{j}})$ $\Delta^{+} [\overline{1} \ \overline{n}] \times [\overline{1} \ \overline{n}] \rightarrow \overline{S} \times [-0.5, 0.5) \times \overline{S} \times [-0.5, 0.5)$

$$\begin{bmatrix} \overline{1}, \overline{n} \end{bmatrix} \times \begin{bmatrix} \overline{1}, \overline{n} \end{bmatrix} \rightarrow S \times \begin{bmatrix} -0.5, 0.5 \end{bmatrix} \times \overline{S} \times \begin{bmatrix} -0.5, 0.5 \end{bmatrix}$$
$$\Delta \left[\begin{bmatrix} \beta^-, \beta^+ \end{bmatrix} = \begin{bmatrix} \Delta \left(\beta^- \right) & \Delta \left(\beta^+ \right) \end{bmatrix} = \left[(s_{\overline{i}}, \alpha_{\overline{i}}), (s_{\overline{j}}, \alpha_{\overline{j}}) \right]$$
(8)

This model is called modified proportional 2-tuple fuzzy linguistic model under uncertainty environment.

Proposition 2: Let $\overline{S} = \{s_{\overline{1}}, \dots, s_{\overline{n}}\}, [(s_{\overline{i}}, \alpha_{\overline{i}}), (s_{\overline{j}}, \alpha_{\overline{j}})]$ is uncertainty modified proportional 2-tuple linguistic term pair, we can regain the aggregation value $[\beta^{-} \beta^{+}]$ by function Δ^{-1} : if $\Delta(\beta^{-}) = (s_{\overline{i}}, \alpha_{\overline{i}}), \Delta(\beta^{+}) = (s_{\overline{i}}, \alpha_{\overline{i}})$

$$\Delta^{-1}: \quad \overline{S} \times [-0.5, 0.5) \times \overline{S} \times [-0.5, 0.5) \to [\overline{1}, \overline{n}] \times [\overline{1}, \overline{n}]$$

$$\Delta^{-1} \left[(s_{\overline{i}}, \alpha_{\overline{i}}), (s_{\overline{j}}, \alpha_{\overline{j}}) \right] = \left[\Delta^{-1} (s_{\overline{i}}, \alpha_{\overline{i}}), \Delta^{-1} (s_{\overline{j}}, \alpha_{\overline{j}}) \right] = \left[\beta^{-}, \beta^{+} \right]$$
(9)

When we got the definition of uncertainty modified proportional 2-tuple linguistic term pairs, we wanted to utilize them to decision making problems, when the aggregation values were expressed as the form of uncertainty modified proportional 2-tuple linguistic term pair, we wanted to compare them to get the best one, so the comparison rule was needed.

Comparison rule of uncertainty modified proportional 2-tuple linguistic pairs:

Let $[(s_{\bar{i}}, \alpha_{\bar{i}}), (s_{\bar{j}}, \alpha_{\bar{j}})]$ and $[(s_{\bar{k}}, \alpha_{\bar{k}}), (s_{\bar{i}}, \alpha_{\bar{i}})]$ are two uncertainty modified proportional 2-tuple linguistic term pairs, define the comparison rule of them as follows:

If
$$\overline{i} < \overline{k}, \overline{j} < \overline{l}$$
 then $[(s_{\overline{i}}, \alpha_{\overline{i}}), (s_{\overline{j}}, \alpha_{\overline{j}})] < [(s_{\overline{k}}, \alpha_{\overline{k}}), (s_{\overline{i}}, \alpha_{\overline{i}})]$
If $\overline{i} = \overline{k}, \overline{j} = \overline{l}$ then
If $\alpha_{\overline{i}} = \alpha_{\overline{k}}, \alpha_{\overline{j}} = \alpha_{\overline{l}}$ then $[(s_{\overline{i}}, \alpha_{\overline{i}}), (s_{\overline{j}}, \alpha_{\overline{j}})] = [(s_{\overline{k}}, \alpha_{\overline{k}}), (s_{\overline{i}}, \alpha_{\overline{i}})]$
If $\alpha_{\overline{i}} = \alpha_{\overline{k}}, \alpha_{\overline{j}} < \alpha_{\overline{i}}$ then $[(s_{\overline{i}}, \alpha_{\overline{i}}), (s_{\overline{j}}, \alpha_{\overline{j}})] < [(s_{\overline{k}}, \alpha_{\overline{k}}), (s_{\overline{i}}, \alpha_{\overline{i}})]$
If $\alpha_{\overline{i}} < \alpha_{\overline{k}}, \alpha_{\overline{j}} = \alpha_{\overline{l}}$ then $[(s_{\overline{i}}, \alpha_{\overline{i}}), (s_{\overline{j}}, \alpha_{\overline{j}})] < [(s_{\overline{k}}, \alpha_{\overline{k}}), (s_{\overline{i}}, \alpha_{\overline{i}})]$
If $\alpha_{\overline{i}} < \alpha_{\overline{k}}, \alpha_{\overline{j}} < \alpha_{\overline{i}}$ then $[(s_{\overline{i}}, \alpha_{\overline{i}}), (s_{\overline{j}}, \alpha_{\overline{j}})] < [(s_{\overline{k}}, \alpha_{\overline{k}}), (s_{\overline{i}}, \alpha_{\overline{i}})]$
If $\alpha_{\overline{i}} < \alpha_{\overline{k}}, \alpha_{\overline{j}} > \alpha_{\overline{i}}$ then if $\frac{\overline{i} + \alpha_{\overline{i}} + \overline{j} + \alpha_{\overline{j}}}{2} < \frac{\overline{k} + \alpha_{\overline{k}} + \overline{l} + \alpha_{\overline{l}}}{2}$
then $[(s_{\overline{i}}, \alpha_{\overline{i}}), (s_{\overline{j}}, \alpha_{\overline{j}})] < [(s_{\overline{k}}, \alpha_{\overline{k}}), (s_{\overline{i}}, \alpha_{\overline{i}})]$
If $\overline{i} < \overline{k}, \overline{j} > \overline{l}$ then if $\frac{\overline{i} + \alpha_{\overline{i}} + \overline{j} + \alpha_{\overline{j}}}{2} < \frac{\overline{k} + \alpha_{\overline{k}} + \overline{l} + \alpha_{\overline{l}}}{2}$
then $[(s_{\overline{i}}, \alpha_{\overline{i}}), (s_{\overline{j}}, \alpha_{\overline{j}})] < [(s_{\overline{k}}, \alpha_{\overline{k}}), (s_{\overline{i}}, \alpha_{\overline{i}})]$

Aggregation operators of uncertainty modified proportional 2-tuple linguistic representation model

When the modified proportional 2-tuple linguistic representation model was used in uncertainty environment, there would be new aggregation operators. We putted forward several aggregation operators of uncertainty modified proportional 2-tuple linguistic representation model.

Definition 9: Let $x = \{[(\gamma_1, \alpha_1), (\eta_1, \lambda_1)], [(\gamma_2, \alpha_2), (\eta_2, \lambda_2)], \dots, [(\gamma_n, \alpha_n), (\eta_n, \lambda_n)]\}$ is a group of uncertainty modified proportional 2-tuple linguistic term pairs, the uncertainty modified proportional 2-tuple geometric mean of them is computed as equation(11)

$$2UMPLGA(x) = 2UMPLGA \{ [(\gamma_1, \alpha_1), (\eta_1, \lambda_1)], [(\gamma_2, \alpha_2), (\eta_2, \lambda_2)], \dots, [(\gamma_n, \alpha_n), (\eta_n, \lambda_n)] \}$$

= $[\Delta((\prod_{i=1}^n \beta_i^{-1})^{\frac{1}{n}}), \Delta((\prod_{i=1}^n \beta_i^{+1})^{\frac{1}{n}})]$ (11)

in that $\gamma_i, \eta_i \in \overline{S}, \alpha_i, \lambda_i \in [-0.5, 0.5), \Delta^{-1}(\gamma_i, \alpha_i) = \beta_i^-, \Delta^{-1}(\eta_i, \lambda_i) = \beta_i^+.$

In most cases, each attribute has different weights, so here needed the definition of the uncertainty modified proportional 2-tuple weighted geometric average operator.

Definition 10: Let $x = \{[(\gamma_1, \alpha_1), (\eta_1, \lambda_1)], [(\gamma_2, \alpha_2), (\eta_2, \lambda_2)], \dots, [(\gamma_n, \alpha_n), (\eta_n, \lambda_n)]\}$

 $(\gamma_i, \eta_i \in \overline{S}, \alpha_i, \lambda_i \in [-0.5, 0.5))$ is a group of uncertainty modified proportional 2-tuple linguistic term pairs, $w = (w_1, w_2, ..., w_n) (0 \le w_i \le 1, \sum_{i=1}^n w_i = 1)$, then define the uncertainty modified proportional

2-tuple weighted geometric average operator as follows: $2UMPLWGA(x) = 2UMPLWGA \{[(x, \alpha_1)(n, \lambda_2)][(x, \alpha_2)(n, \lambda_2)] = [(x, \alpha_2)(n, \lambda_2)]\}$

$$2UMPLWGA(x) = 2UMPLWGA\left\{ \left[(\gamma_{1}, \alpha_{1}), (\eta_{1}, \lambda_{1}) \right], \left[(\gamma_{2}, \alpha_{2}), (\eta_{2}, \lambda_{2}) \right], \dots, \left[(\gamma_{n}, \alpha_{n}), (\eta_{n}, \lambda_{n}) \right] \right\}$$

$$= \Delta \left[\prod_{i=1}^{n} (\beta_{i}^{-})^{w_{i}}, \prod_{i=1}^{n} (\beta_{i}^{+})^{w_{i}} \right]$$
(12)

In that $\Delta^{-1}(\gamma_i, \alpha_i) = \beta_i^-, \Delta^{-1}(\eta_i, \lambda_i) = \beta_i^+$.

The uncertainty modified proportional 2-tuple weighted geometric mean operator has added weight to every attribute, but in some cases, the weight was not corresponding to the attribute but corresponding to the position.so we putted forward the uncertainty modified proportional 2-tuple ordered weighted geometric average operator .

Definition 11: Let $x = \{[(\gamma_1, \alpha_1), (\eta_1, \lambda_1)], [(\gamma_2, \alpha_2), (\eta_2, \lambda_2)], \dots, [(\gamma_n, \alpha_n), (\eta_n, \lambda_n)]\}$

 $(\gamma_i, \eta_i \in \overline{S}, \alpha_i, \lambda_i \in [-0.5, 0.5))$ is a group of uncertainty modified proportional 2-tuple linguistic term pairs, $w = (w_1, w_2, \dots, w_n) (0 \le w_i \le 1, \sum_{i=1}^n w_i = 1)$, then the uncertainty modified proportional 2-tuple

ordered weighted geometric mean of x is defined as equation(13)

 $2UMPLOWGA(\mathbf{x}) = 2UMPLOWGA \{ \{ [(\gamma_1, \alpha_1), (\eta_1, \lambda_1)], [(\gamma_2, \alpha_2), (\eta_2, \lambda_2)], \dots, [(\gamma_n, \alpha_n), (\eta_n, \lambda_n)] \} \}$

$$=\Delta \left[\prod_{i=1}^{n} (\zeta_{i}^{-})^{w_{i}}, \prod_{i=1}^{n} (\zeta_{i}^{+})^{w_{i}}\right]$$
(13)

In that $\Delta^{-1}(\gamma_i, \alpha_i) = \beta_i^-, \Delta^{-1}(\eta_i, \lambda_i) = \beta_i^+$ and $[\zeta_j^-, \zeta_j^+]$ are the *jth* largest of $[\beta_i^-, \beta_i^+]$.

From the definition 11, we can easily get some property of the uncertainty modified proportional 2-tuple ordered weighted geometric average operator, such as: commutativity, idempotency, monotonicity, boundedness, etc.

If the integration process is to position and to attribute, need concept of hybrid weighted geometric average operator.

Definition 12: Let $x = \{[(\gamma_1, \alpha_1), (\eta_1, \lambda_1)], [(\gamma_2, \alpha_2), (\eta_2, \lambda_2)], \dots, [(\gamma_n, \alpha_n), (\eta_n, \lambda_n)]\}$

 $(\gamma_i, \eta_i \in \overline{S}, \alpha_i, \lambda_i \in [-0.5, 0.5])$ is a group of uncertainty modified proportional 2-tuple linguistic term

pairs, $w = (w_1, w_2, \dots, w_n)$ ($0 \le w_i \le 1$, $\sum_{i=1}^n w_i = 1$) is the weight corresponding to attribute,

 $\omega = (\omega_1, \omega_2, \dots, \omega_n)$ $(0 \le \omega_i \le 1, \sum_{i=1}^n \omega_i = 1)$ is the weight corresponding to position, the uncertainty

modified proportional 2-tuple hybrid geometric average operator is as equation(14)

 $2UMPLCWGA(x) = 2UMPLCWGA \left\{ \left[(\gamma_1, \alpha_1), (\eta_1, \lambda_1) \right], \left[(\gamma_2, \alpha_2), (\eta_2, \lambda_2) \right], \dots, \left[(\gamma_n, \alpha_n), (\eta_n, \lambda_n) \right] \right\}$

$$=\Delta \left[\prod_{i=1}^{n} (\psi_{i}^{-})^{w_{i}}, \prod_{i=1}^{n} (\psi_{i}^{+})^{w_{i}}\right]$$
(14)

In that $\Delta^{-1}(\gamma_i, \alpha_i) = \beta_i^-, \Delta^{-1}(\eta_i, \lambda_i) = \beta_i^+$ and $[\psi_i^-, \psi_i^+]$ is the *i*th largest of $[(\beta_i^-)^{n\omega_i}, (\beta_i^+)^{n\omega_i}]$, *n* is the balance factor.

V. Example

Set up a basketball team has five reserve players, to determine the order of play of the five reserve players, we need to sort the comprehensive performance of their. Let $x = \{x_1, x_2, x_3, x_4, x_5\}$ is the objective set, x_i represent the *ith* reserve player. $U = \{u_1, u_2, u_3, u_4\}$ is the attribute's set, u_1 skill, u_2 experience, u_3 psychological diathesis, u_4 injuries. There are three experts to review $D = \{d_1, d_2, d_3\}$, evaluation of the five reserve players represented by decision matrix $A_k = (a_{ij}^k)_{5\times4}, a_{ij}^k$ represents the evaluation of *kth* experts to the *ith* reserve players of *jth* attributes, and a_{ij}^k is the uncertainty modified proportional 2-tuple linguistic term pair. $v = \{0.33, 0.30, 0.25, 0.12\}$ is the weights of attribute, $\omega = (0.35, 0.32, 0.33)$ is the weights of experts. Let $\overline{S} = \{s_0, s_2, s_3, s_{1/2}, s_4, s_5, s_7\}$ is linguistic term set, in that s_0 : *extremely.poor*, s_2 : *very.poor*, s_3 : *poor*, $s_{1/2}$: *medium*, s_4 : *good*, s_5 : *very.good*, s_7 : *extremely.good*.

Step 1: Experts give the decision matrix.

$$A_{1} = (a_{ij}^{1})_{5\times4} = \begin{pmatrix} \left[(s_{3},0), (s_{72}^{-},0) \right] & \left[(s_{3},0), (s_{4},0) \right] & \left[(s_{4},0), (s_{5},0) \right] & \left[(s_{72}^{-},0), (s_{4},0) \right] \\ \left[(s_{2},0), (s_{3},0) \right] & \left[(s_{72}^{-},0), (s_{4},0) \right] & \left[(s_{3},0), (s_{4},0) \right] & \left[(s_{3},0), (s_{4},0) \right] \\ \left[(s_{2},0), (s_{3},0) \right] & \left[(s_{3},0), (s_{4},0) \right] & \left[(s_{3},0), (s_{4},0) \right] & \left[(s_{3},0), (s_{5},0) \right] \\ \left[(s_{0},0), (s_{2},0) \right] & \left[(s_{3},0), (s_{4},0) \right] & \left[(s_{3},0), (s_{72}^{-},0) \right] & \left[(s_{2},0), (s_{4},0) \right] \\ \left[(s_{2},0), (s_{3},0) \right] & \left[(s_{72}^{-},0), (s_{4},0) \right] & \left[(s_{2},0), (s_{4},0) \right] \\ \left[(s_{2},0), (s_{3},0) \right] & \left[(s_{72}^{-},0), (s_{4},0) \right] & \left[(s_{2},0), (s_{3},0) \right] & \left[(s_{72}^{-},0), (s_{4},0) \right] \\ \left[(s_{3},0), (s_{72}^{-},0) \right] & \left[(s_{72}^{-},0), (s_{4},0) \right] & \left[(s_{3},0), (s_{4},0) \right] & \left[(s_{72}^{-},0), (s_{4},0) \right] \\ \left[(s_{3},0), (s_{3},0) \right] & \left[(s_{3},0), (s_{4},0) \right] & \left[(s_{3},0), (s_{4},0) \right] & \left[(s_{72}^{-},0), (s_{4},0) \right] \\ \left[(s_{2},0), (s_{3},0) \right] & \left[(s_{2},0), (s_{3},0) \right] & \left[(s_{3},0), (s_{72}^{-},0) \right] & \left[(s_{72}^{-},0), (s_{4},0) \right] \\ \left[(s_{2},0), (s_{3},0) \right] & \left[(s_{3},0), (s_{72}^{-},0) \right] & \left[(s_{72}^{-},0), (s_{4},0) \right] \\ \left[(s_{2},0), (s_{3},0) \right] & \left[(s_{3},0), (s_{72}^{-},0) \right] & \left[(s_{72}^{-},0), (s_{4},0) \right] \\ \left[(s_{2},0), (s_{3},0) \right] & \left[(s_{3},0), (s_{72}^{-},0) \right] & \left[(s_{72}^{-},0), (s_{4},0) \right] \\ \left[(s_{2},0), (s_{3},0) \right] & \left[(s_{3},0), (s_{72}^{-},0) \right] & \left[(s_{72}^{-},0), (s_{4},0) \right] \\ \left[(s_{2},0), (s_{3},0) \right] & \left[(s_{3},0), (s_{72}^{-},0) \right] & \left[(s_{3},0), (s_{72}^{-},0) \right] \\ \left[(s_{3},0), (s_{4},0) \right] & \left[(s_{3},0), (s_{72}^{-},0) \right] & \left[(s_{3},0), (s_{72}^{-},0) \right] \\ \left[(s_{3},0), (s_{72}^{-},0) \right] & \left[(s_{72}^{-},0), (s_{4},0) \right] \\ \left[(s_{72}^{-},0), (s_{4},0) \right] & \left[(s_{72}^{-},0), (s_{4},0) \right] \\ \left[(s_{3},0), (s_{72}^{-},0) \right] & \left[(s_{72}^{-},0), (s_{4},0) \right] \\ \left[(s_{3},0), (s_{72}^{-},0) \right] & \left[(s_{72}^{-},0), (s_{4},0) \right] \\ \left[(s_{3},0), (s_{72}^{-},0) \right] & \left[(s_{72}^{-},0), (s_{4},0) \right] \\ \left[(s_{3},0$$

Step 2: Using the uncertainty modified proportional 2-tuple weighted geometric average operator (12) to integrated the attribute's values of each row, we can get x_i 's comprehensive decision value z_i^k that given by expert d_k .

$$\begin{aligned} z_1^1 &= \Delta \left[3^{0.33} \times 3^{0.30} \times 4^{0.25} \times \left(\frac{7}{2}\right)^{0.12}, \left(\frac{7}{2}\right)^{0.33} \times 4^{0.30} \times 5^{0.25} \times 4^{0.12} \right] &= \Delta [3.4, 4.1] = \left[\left(s_{7/2}, -0.2 \right), \left(s_{4}, 0.1 \right) \right] \\ z_2^1 &= \left[\left(s_2, 0.2 \right), \left(s_{7/2}, 0.2 \right) \right] \quad z_3^1 = \left[\left(s_3, -0.3 \right), \left(s_{7/2}, 0 \right) \right] \\ z_1^2 &= \left[\left(s_3, -0.1 \right), \left(s_4, -0.4 \right) \right] \quad z_2^2 = \left[\left(s_2, 0 \right), \left(s_{7/2}, -0.2 \right) \right] \\ z_3^2 &= \left[\left(s_3, 0.2 \right), \left(s_4, -0.4 \right) \right] \quad z_4^2 = \left[\left(s_3, -0.1 \right), \left(s_{7/2}, 0 \right) \right] \\ z_5^2 &= \left[\left(s_3, -0.3 \right), \left(s_{7/2}, 0 \right) \right] \quad z_1^3 = \left[\left(s_{7/2}, -0.2 \right), \left(s_4, 0.1 \right) \right] \\ z_4^3 &= \left[\left(s_3, -0.1 \right), \left(s_4, -0.4 \right) \right] \quad z_5^3 = \left[\left(s_{7/2}, -0.2 \right), \left(s_4, -0.4 \right) \right] \end{aligned}$$

Step 3: Integrated $z_i^k (k = 1,2,3)$ use of the uncertainty modified proportional 2-tuple linguistic hybrid geometric average operator (14), let w = (0.3, 0.4, 0.3), $\omega = (0.35, 0.32, 0.33)$.

$$z_{1} = \Delta \left\{ \left[\left(\Delta^{-1} \left(z_{1}^{1} \right) \right)^{3 \times \omega_{1}} \right]^{w_{1}} \times \left[\left(\Delta^{-1} \left(z_{1}^{2} \right) \right)^{3 \times \omega_{2}} \right]^{w_{2}} \times \left[\left(\Delta^{-1} \left(z_{1}^{3} \right) \right)^{3 \times \omega_{3}} \right]^{w_{3}} \right\} \right\}$$

$$= \Delta \left[(3.4)^{3 \times 0.35}, (4.1)^{3 \times 0.35} \right]^{0.3} \times \left[(2.9)^{3 \times 0.32}, (3.8)^{3 \times 0.32} \right]^{0.4} \times \left[(3.4)^{3 \times 0.33}, (4.1)^{3 \times 0.33} \right]^{0.3} \right\}$$

= $\Delta \left[3.6^{0.3} \times 2.8^{0.4} \times 3.4^{0.3}, 4.4^{0.3} \times 3.6^{0.4} \times 4.0^{0.3} \right]$
= $\Delta \left[3.2, 4.1 \right] = \left[(s_3, 0.4) (s_4, 0.1) \right]$
 $z_2 = \left[(s_2, -0.1) \left(s_{7/2}, 0.2 \right) \right] z_3 = \left[(s_3, -0.1) (s_4, -0.4) \right] z_4 = \left[(s_3, -0.3) \left(s_{7/2}, 0.2 \right) \right] z_5 = \left[(s_3, -0.5) \left(s_{7/2}, 0.2 \right) \right]$

Step 4: Ranking the five reserve players by z_i (*i* = 1,2,3,4,5), then we have

$$x_1 > x_3 > x_4 > x_5 > x_2$$

Step 5: The coach can arrange play order by their ranking.

VI. Conclusions

In this paper, we putted out the definition of modified proportional 2-tuple fuzzy linguistic representation model, this model improved the new version of fuzzy linguistic model.

• Made the expression of modified proportional 2-tuple fuzzy linguistic representation model only.

• Made the aggregation operators of modified proportional 2-tuple fuzzy linguistic representation model and 2-tuple fuzzy linguistic representation model unified.

• Extended the modified proportional 2-tuple fuzzy linguistic representation model in uncertainty environment, and got some aggregation operators.

VII. Acknowledgements

The author would like to thank the supporting by the fundamental research funds for the central universities.

Reference

[1] Francisco Herrera ,Luis Martínez,IEEE transactions on fuzzy systems.Vol 8,no. 6(2000), p.746-752.

[2] Shilin Zhang, Computers and Mathematics with Applications. Vol.62(2011),p.1916-1922.

[3] DuenYian Yeh, ChingHsue Cheng, Meilin Chi, Applied soft computing. Vol. 6 (2007), p. 1027 - 1034.

[4] JinHsien Wang, Jongyun Hao, IEEE transactions on fuzzy systems. Vol.14, no.3 (2006), p.435-445.

[5] Yejun Xu,Ling Huang,2008 ISECS International Colloquium on computing.Communication, control and management.(2008),p.73-77.

[6] Yejun Xu, Huimin Wang, Applied Soft Computing. Vol .11(2011), p.3988-3997.

[7] Wei Yang, Zhiping Chen, Expert Systems with Applications, Vol 39(2012), p.2662-2668.

[8] Francisco Herrera, Luis Martínez, IEEE transactions on systems, man, and cybernetics-part B:cybernetics.Vol.31, no. 2(2011), p.227-234.

[9] Yun Zhang, HongXu Ma, BaoHong Liu, Jian Liu, Soft compute , Vol. 16, (2012) p. 1439-1446.

[10] YanBing Ju , AiHua Wang, xiaoYu Liu, Expert systems with applications.Vol .39(2012), p.6972-6981.

[11] Wenpai Wang, Expert systems with applications. Vol .36(2009), p.3439-3447.

[12] Shih-yuan Wang, IEEE. Transactions on Fuzzy Systems. Vol .16, no. 1(2008 February), p.29-39.

[13] KueiHu Chang, TaChun Wen, Expert Systems with Applications.vol.37(2010), p.2362-2370.

Based on Non-redundant Electronic Scale Engineering Development Theory

Li Rui^{1,a}, and Li Peng¹

¹School of Electrical & Electronic Engineering, North China Electric Power University, Baoding, China

^a1130407682@qq.com

Keywords: electronic engineering design, non-redundant scale, combinatorial techniques, optimization, resolving ability, measurement

Abstract. This paper regards combinatorial techniques for electronic engineering design based on the mathematical apparatus of Non Redundant Scales theory (NRS theory).Combinatorial techniques is known to be of widespread applicability, and has been extremely effective when applied to the problem of finding the optimum ordered arrangement of structural elements in spatially or temporally distributed systems with non-uniform structure (e.g. line gages) with respect to resolving ability. These design techniques make it possible to configure electronic devices or systems with fever elements than at present, while maintaining on resolving ability and positioning precision. The NRS theory can be used to finding optimal design for wide classes of technological problems in measurement and radio electronic engineering based on combinatorial techniques.

1 Introduction

The remarkable property of the non-redundant ruler in comparison with usual ruler is nonuniform positioning of marks (0,1,4,6) so, that the each next in turn pair of the marks is within the distance from 0 to L=6 as follows:



Fig.1 Non-redundant ruler and usual ruler

Note, that set of distance values created from the nonredundant ruler (Fig.1) exhausts the natural numerical row 1,2,..., 6:

1 = 1 - 0, 2 = 6 - 4, 3 = 4 - 1, 4 = 4 - 0, 5 = 6 - 1, 6 = 6 - 0.

Underlying model is regarded for applications in minimum redundancy linear arrays [1] and numbered undirected graphs [2].

2 Sums on ordered-chain numbers

Let us calculate all Sn sums of the terms in the numerical n-stage chain sequence of distinct positive integers Kn= {k1,k2,, ..., ki, ..., kn}, where we require all terms in each sum to be consecutive elements of the sequence. Clearly the maximum such sum is the sum S max of all n elements:

$$S_{max} = k1 + k2 + ... + ki + ... + kn$$
 (1)

A sum of consecutive terms in the chain sequence can have any of the n terms as its starting point pj, and finishing point qj, and can be of any length (number of terms) from 1 to n. So, each of j numerical pair (pj,qj), pj,qj $\in \{1, 2, n\}$ corresponds to sum Sj = S (pj,qj), is equal:

$$S_{j} = S(p_{j}, q_{j}) = \sum_{i=p_{j}}^{q_{j}} k_{i}, p_{j} \le q_{j}$$
⁽²⁾

An ordered numerical pair (pj,qj) determines sum S (pj,qj) in the numerical n-stage chain sequence, and it is a numerical code of the sum. All sums of consecutive terms, calculated by (2), can be illustrated graphically by the Table 1.To see this, we observe that the maximum number of distinct sums is:

$$S'_{max} = 1 + 2 + ... + n = n(n+1)/2$$
 (3)

The ideal ordered -chain sequence is such numerical n-stage of distinct positive integers k1, k2, ... kn, , which exhausts the natural row of numbers wrote down into cells of Table 1.The sums of consecutive terms in ordered -chain sequence could be used for research of numerical sequences in order to speed up finding ideal or optimal solutions.

Pj	q_j				
	1	2		n-1	n
1	ki	$\sum_{i=1}^{2} ki$		$\sum_{i=1}^{n-1} ki$	$\sum_{i=1}^{n} ki$
2		k_2		$\sum_{i=2}^{n-1} ki$	$\sum_{i=2}^{n} ki$
			•••		
n-1				k_{n-1}	$\sum_{i=n-1}^{n} ki$
n					kn

3 Rapid test of programs

Evaluation of software quality is still a controversial issue. There has been an evolution of this concept and the definition depends also on the perspective (architecture, source code, processes or community). ISO/IEC 9126 [3] offers a standard with six quality characteristic divided into several subcharacteristics. This quality model has to be adapted to every program. Other models focus on the free software world, analyzing their typical aspects: Open Business Readiness Ration, QSoS [4] and QualOSS. However, applying those models to all the programs we have found is out of the scope of the present paper. We first have to pick up some of the software we have found. Thus, we have adopted a practical point of view and adopt the role of an electronic designer who wants to select a set of programs for further research. We have then specified five items in order to perform a rapid test.

3.1 Is there a stable version

A stable version would give confidence to software users. However, this question was not easy to answer. Traditionally release version 1.0 is the first one delivered to customers and considered stable. However, many free software projects follow the "release early, release often" rule, which means that the programs are available to the public well before they are considered stable. The Sourceforge repository includes information about the status of the software (alpha, beta or stable). But other downloadable programs have not this information. Therefore, this item was of limited use.

3.2 Can it be easily installed

If available, Windows versions usually pose no problem.For Linux users, probably the most interested in this kind of software, package management systems are the preferred way to install software because they solve all the dependencies. We have used the "aptitude" utility in the Kubuntu 8.01 distribution. If no package is available, we have tried to compile the program from the source code and tried to solve the problems that appeared.

3.3Is it likely to be maintained in the future

Any potential user should be interested in the project future and the probability that it will be debugged, improved, updated or extended. To answer this question, we paid attention to the frequency of new versions, the number of developers, the number of messages in mailing lists or the news that appeared in the corresponding sections.

3.4 Is the learnability good

This is probably one of the most important points to attract new users. We have looked for user's manuals, "getting started" guides, wikis or web pages, examples etc. They should at least allow the user to start working with the tool.

3.5 Can it work with a simple example

We tried simple examples in order to check that the program is not only installed, but that can run simple simulations, draw simple schematics, etc. This is similar to the idea of the "hello world" program that can be found in many introductory tutorials of programming languages.

The goal of this five item test is to determine whether or not it is worth evaluating the program in depth.

4 Ideal numerical rings

The idea of "perfect" numerical bundles provides development and design of other remarkable combinatorial constructions, such as Ring Bundles (IRBs). An n-stage ring sequence Kn= {k1, k2, ..., ki, ..., kn} of natural numbers for which the set of all Sn circular sums consists of the numbers from 1 to Sn= n(n-1) + 1, that is each number occurring exactly once is called an "Ideal Ring Bundle" (IRB).

Here is an example of a numerical ring sequence with n=4 and Sn=n(n-1)+1=13, namely {1, 3, 2, 7}, where k1=1, k2=3,k3=2, k4=7.Table of circular sums for the sequence is given below (Tabl.2).

Pj	q_{j}			
	1	2	3	4
1	1	4	6	13
2	13	3	5	12
3	10	13	2	9
4	8	11	13	7

TABLE 2. Table of circular sums for numerical ring sequence {1, 3, 2, 7}

Here is a graphical representation of one-dimensional IdealRing Bundle containing four (n=4) elements $\{1,3,2,7\}$. A number of consecutive elements in the IRB, is known, can be of a considerable length and the more length the more number of the IRB [5].

5 Design of electrical dividers based on the irbs

An one-dimensional Ideal Ring Bundle, which consists of n numbers, provides for obtain Sn = n(n-1)+1 circular sums. The property allows on reproduce the identical measuring range of numerical values. For example, IRB of five (n=5) elements {5,1,3,10,2} generates the set of circular sums from 1 to 21 exactly once, and accordingly provides improving of resolving ability of technical devices based on the underlying design technique. Here is scheme of electrical divider configured on the IRB.

We regard these design techniques will make it possible to configure devices with fewer elements that at present, while maintaining or improving on positioning precision and the other characteristics of the device.

6 Conclusion

The Non Redundant Scales (NRS)s theory relates to the optimum placement of structural elements in spatially or temporally distributed systems. The remarkable combinatorial properties of IRBs make these numerical models useful in applications to applied and scientific researches in measurements and radio electronic engineering, for improving such quality indices of measurements as positioning precision, resolving ability and low side lobe antenna design, using combinatorial optimization techniques based on the (NRS)s theory.

This theory discovers many opportunities to apply of the combinatorial techniques to electronic and system engineering, including contemporary micro- and nanotechnologies. The theory can be used to finding optimal design for wide classes of technological problems in ordered measures sets normative base with reduced level of informative redundant and electronic engineering.

References

- [1] Alan T. Moffet, IEEE Transaction on Antennas and Propagation, Vol. AP-16, No.2, pages 172-175; February,1963.
- [2] Gary S. Bloom and Solomon W. Golomb, Application of Numbered Undirected Graphs, Proceedings of the IEEE, Vol.65, No.4, 1977, pp.562-570.
- [3] International Standard ISO/IEC 9126-1, Software engineering-Product quality-Part1: Quality model.
- [4] J.C. Deprez, S. Alexandre, Comparing Assessment Methodologies for Free/Open Source Software: OpenBRR and QSOS, Lecture Notes in Computer Science, Vol. 5089, pp 189-203,2009.
- [5] Bandyrska O.V. (2000) Standardization of non redundant rows by method of optimum structural proportions. Manuscript. State University "Lvivska Politechnika", Ukraine.

L_p-type of Weighted Fuzzy Number Metrics Induced by Fuzzy Structured Element

Fei Zhao^{1,a}, Sizong Guo^{2,b}

¹ College of Science, Liaoning Technical University, Fu-xin, Liaoning, China
 ² College of Science, Liaoning Technical University, Fu-xin, Liaoning, China
 ^azhaofei19880220@126.com, ^bguosizong@163.com

Keywords: Fuzzy number; Fuzzy structured element; Weighted function; $E - L_p$ metric

Abstract. For the objective fact that elements with different membership degrees should have different contribution to the metric measure between fuzzy numbers, this paper presents Lp-type of fuzzy number metrics weighted by structured element. Firstly, we define a metric weighted by structured element d_p on the family (B[-1,1]) of all the same monotone and standard bounded functions on closed interval [-1,1], and discuss the completeness and separability of those metric spaces; Next, using the fuzzy functional induced by normal fuzzy structured element, we give out a method that the metric of the closed bounded fuzzy number space is induced by the metric on function space B[-1,1]. Furthermore, a fuzzy number metric d_{Np} weighted by structured element which is induced by d_{Np} is presented ,and analyze completeness and separability of the induced fuzzy number metric spaces; Lastly, the difference and relationship between d_{Np} and the metric defined by traditional method are shown.

1 Introduction

In practical problems, fuzzy numbers used to describe the uncertain number information. The distance of fuzzy numbers is the basic tools of ranking fuzzy numbers^[1,2], the measure in difference between fuzzy numbers^[3] and fuzzy analysis^[4-5], which is widely used in fuzzy decision making, fuzzy clustering, fuzzy programming, fuzzy areas of regression analysis^[6-9]. Therefore, many scholars do a lot of research work around the topic of fuzzy numbers and propose many different distance definitions of fuzzy numbers ^[10-15].

Diamond and Kloeden establish a consistent Hausdorff metric^[10] and L metric^[11] on the fuzzy number space. In the literature [12], they discuss in detail completeness, separability, convergence and other issues of consistent Hausdorff metric and L metric. Literature [13] starts from the actual background of fuzzy decision, considers the weight of the left and right sides of fuzzy membership function in the distance and proposes a δ_{q} distance. Liu Min et al ^[14] on the basis of their predecessors consider the role of cut set level and introduce level importance function to portray " Cut set level of impact on the research questions ".Establish two classes of broader fuzzy numbers measurement: UID metrics and LPID metrics. In defining these fuzzy numbers in the distance they all have the same way to definite, that is, introduce by the distance of the interval numbers composed of level sets. Reference [15] gives a method the distance function of same sequence monotone bound function space in [-1,1] induce the distance of fuzzy real space distance by using fuzzy structured element theory and the fuzzy number distance induced by Hausdorff distance and Hamming distance in function space. This method avoids the computational complexity brought by the promotion of the interval number distance. But it does not consider the effect of the level of cut set on fuzzy numbers distance.

This paper firstly definite a fuzzy structured element weighted distance on the same sequence standard bounded monotone function class B[-1,1], that is E - L metric and discuss completeness and separability of these functions metric space. Secondly, give a measurement method induced a

bounded closed fuzzy numbers by the metrics on B[-1,1] by using fuzzy functional derived by regular fuzzy structure element. Obtain a weighted measure of structure element of a class of fuzzy numbers and analyze the completeness and separability of this fuzzy number metric space. Proof the monotonic function of fuzzy number on B[-1,1] is existence and unique under given regular fuzzy structured element. Give the method to seek a monotonic function by the membership function of the fuzzy number. Discuss the contact and difference between the structure element weighted distance of this fuzzy numbers and traditional fuzzy number distance.

2 Preliminaries

In this paper *R* is real number set, I(R) is the whole of bounded closed interval in *R*, $\tilde{N}_C(R)$ is the whole of bounded closed fuzzy numbers in *R*, D[-1,1] means the set of all the same sequence bounded monotonic function (assumed to be single-increasing function)on [-1,1], $f(x_0+)$, $f(x_0-)$ means left limit and right limit of f(x) at the point $x = x_0$, the α -cut set of fuzzy set \tilde{u}

$$u_{\alpha} = \{x : \widetilde{u}(x) \ge \alpha\} (0 \le \alpha \le 1)$$
⁽¹⁾

for convenience, the paper noted $u_0 = \overline{\sup p\widetilde{u}}$.

Definition 2.1^[7] Let *E* be a fuzzy set on *R*, membership function is $E(x), x \in R$. If E(x) satisfies: 1) E(0) = 1; 2) E(x) is a monotonically increasing right continuous function in interval [-1,0), E(x) is a monotonically decreasing left continuous function in interval (0,1]; 3) When $-\infty < x < -1$ or $1 < x < \infty$, E(x) = 0. Then call the fuzzy set *E* is fuzzy structured element of *R*.

If fuzzy structured element *E* satisfies: (1) $\forall x \in (-1,1), E(x) > 0$; (2) E(x) is continuous and strictly monotonically increasing in [-1,0), E(x) is continuous and strictly monotonically decreasing in (0,1], *E* is called regular fuzzy structured element. If E(x) = E(-x), *E* is called symmetric fuzzy structured element. The following no special instructions, *E* means regular fuzzy structured element.

Theorem 2.1^[6] Let *E* be an arbitrary fuzzy structured element of *R*, membership function is E(x), Let f(x) is a monotonically bounded function in [-1,1], $\hat{f}(x)$ is extension set-valued functions of f(x), $\hat{f}(E)$ is bounded closed fuzzy number of *R*, and membership function of $\hat{f}(E)$ is $E(\hat{f}^{-1}(x))$, here $f^{-1}(x)$ is rotation symmetric functions of f(x) about variable *x* and *y* (If f(x) is continuous strictly monotonically, $f^{-1}(x)$ is inverse function of f(x)).

In the case of no confuse, note $\hat{f}(x)$ is f(x), $\hat{f}(E)$ is f(E).

Theorem 2.2^[6] For a given regular fuzzy structured element *E* and arbitrary finite fuzzy number \tilde{u} , there is always an monotone bounded function *f* in [-1,1], such that $\tilde{u} = f(E)$. Strictly speaking, if there is a set valued extension \hat{f} of *f*, such that $\tilde{u} = \hat{f}(E)$, saying fuzzy number \tilde{u} is generated by the fuzzy structured element.

Theorem 2.3^[5] If \tilde{u} is a bounded closed fuzzy number, $\alpha \in [0,1]$, let

$$\underline{u}(\alpha) = \inf\{x : x \in u_{\alpha}\}, \ \overline{u}(\alpha) = \sup\{x : x \in u_{\alpha}\}.$$
(2)

Then $\underline{u}(\alpha)$ and $\overline{u}(\alpha)$ are functions in [0,1] and satisfy:1) $u_{\alpha} = [\underline{u}(\alpha), \overline{u}(\alpha)]; 2) \underline{u}(\alpha)$ is monotonically increasing left continuous;3) $\overline{u}(\alpha)$ is monotonically decreasing left continuous;4) $\underline{u}(1) \le \overline{u}(1);$ 5) $u(\alpha)$ and $\overline{u}(\alpha)$ are right continuous at $\alpha = 0$.

Theorem 2.4^[14] Let $(X, d_X), (Y, d_Y)$ are two metric spaces, *F* is a one to one isometric mapping from (X, d_X) to (Y, d_Y) , *F* is a homeomorphism.

Definition 2.2^[11] Let $s:[0,1] \rightarrow [0,1]$, if the function $s(\alpha)$ is monotonically increasing and s(0) = 0, s(1) = 1, saying that $s(\alpha)$ is diminished function. If s also satisfies $\int_0^1 s(\alpha) d\alpha = 1$, saying that $s(\alpha)$ is regular diminished function.

For $\tilde{u}, \tilde{v} \in \tilde{N}_c(R)$, $s(\alpha)$ is diminished function, reference [11] consider the different levels of cut sets make different contribution to the distance of fuzzy numbers and give the following metrics:

$$\delta_{N2}(\tilde{u},\tilde{v}) = \left[\int_0^1 s(\alpha) [E(u_\alpha, v_\alpha)]^2 d\alpha\right]^{1/2},$$
(3)

 $E(u_{\alpha}, v_{\alpha})$ is the Euclid metric of u_{α}, v_{α} , that is

$$E(u_{\alpha}, v_{\alpha}) = [(\underline{u}(\alpha) - \underline{v}(\alpha))^{2} + (\overline{u}(\alpha) - \overline{v}(\alpha))^{2}]^{1/2}.$$
(4)

3 Lp-type structured element weighted metric on function space B[-1,1]

Definition 3.1 Let $f \in D[-11]$, for any discontinuity point $x \in (-1,1)$ of f, there is

$$f(x) = \frac{1}{2} [f(x+) + f(x-)],$$
(5)

and f is continuous on two endpoints in [-1,1], saying that f(x) is standard monotone bounded function in [-1,1]. B[-1,1] is the whole same sequence standard monotone bounded function in [-1,1] (This article assumes that are monotonically increasing function). Obviously, we have $B[-1,1] \subset D[-1,1]$.

Let $f \in D[-11]$, definite

$$\breve{f}(x) = \begin{cases} f(-1+), & x = -1 \\ [f(x-)+f(x+)]/2, & x \in (-1,1) \\ f(1-), & x = 1 \end{cases}$$
(6)

Obviously, $f \in B[-1,1]$, saying that f(x) is standard function of f(x). If f is standard monotone bounded function, we have f = f.

Definition 3.2 Let *E* be a regular fuzzy structure element of *R*. For $f,g \in B[-1,1]$, definite

$$d_{p}(f,g) = \left[\int_{-1}^{1} E(t) \left| f(t) - g(t) \right|^{p} dt \right]^{1/p}, f,g \in B[-1,1]$$
(7)

where $1 \le p < \infty$. Easy to verify d_p is metric of B[-1,1], saying that fuzzy structure element weighted L_p metric, is short for $E - L_p$ metric. Here B[-1,1] form metric space in the form of d_p noted $(B[-1,1], d_p, E)$.

Theorem 3.1 Let *E* be a regular fuzzy structure element, $K \in I(R)$ is nonempty, note that

$$B_{f}(K) = \{f: f \in B[-1,1], [f(-1), f(1)] \subseteq K\},$$
(8)

then $(B_f(K), d_p, E)$ is a complete metric space.

Proof : Let $\{f_n\}$ is a Cauchy sequence of complete metric space $(B_f(K), d_p, E)$, for any positive number $\varepsilon > 0$, there is a positive integer N, such that for any n, m > N, there is

$$d_{p}(f_{m},f_{n}) = \left[\int_{-1}^{1} E(t) |f_{m}(t) - f_{n}(t)|^{p} dx\right]^{1/p} < \varepsilon.$$
(9)

Given any positive number $\delta(0 < \delta < 1)$, from the definition of regular fuzzy structure element, there is a positive number $c(\delta)$, in $- +\delta - \delta$, we have $E(x) \ge c(\delta)$. Further we have

$$\varepsilon > \left[\int_{-1}^{1} E(t) \left| f_{m}(t) - f_{n}(t) \right|^{p} dx \right]^{1/p} \ge \left[\int_{-1+\delta}^{1-\delta} E(t) \left| f_{m}(t) - f_{n}(t) \right|^{p} dx \right]^{1/p}$$

$$\ge c^{1/p} \left(\delta \right) \left[\int_{-1+\delta}^{1-\delta} \left| f_{m}(t) - f_{n}(t) \right|^{p} dx \right]^{1/p},$$

$$(10)$$

that is

$$\left[\int_{-1+\delta}^{1-\delta} |f_m(t) - f_n(t)| \mathrm{d}x\right]^{1/p} \le \varepsilon / c^{1/p}(\delta) \,. \tag{11}$$

That means $\{f_n\}$ is a Cauchy sequence of $L_p[-1+\delta,1-\delta]$, $L_p[-1+\delta,1-\delta]$ is complete, so $\{f_n\}$ is convergent in $L_p[-1+\delta,1-\delta]$. Because of the arbitrary of δ , $\{f_n\}$ converges to (-1,1) about L_p metric, assume that h is a limit of sequence $\{f_n\}$.

Similar to the proof above-mentioned, we obtain h(x) is monotone and bounded in (-1,1), then h(-1+) and h(1-) exit, let

$$f(x) = \begin{cases} h(-1+), & x = -1 \\ [h(x+)+h(x-)]/2, & x \in (-1,1) \\ h(1-), & x = 1 \end{cases}$$
(12)

Easy to verify $f(x) \in B[-1,1]$ and it is a limit of Cauchy sequence $\{f_n\}$. f(x) and h(x) is different only at the discontinuity points in [-1,1], so

$$d_p(f_n, f) = d_p(f_n, g)$$
 (13)

Then f is a limit of $\{f_n\}$ in $(B_f(K), d_p, E)$, $\{f_n\}$ id convergent in $(B(M), d_p, E)$.

Example 3.1 $(B[-1,1], d_p, E)$ is not complete

$$f_{n+1}(x) = \begin{cases} f_n(x), & x \in [-1, 1 - 1/n^2] \\ n, & x \in (1 - 1/n^2, 1] \end{cases}, (n \ge 1)$$
(14)

where $f_1(x) = 0, x \in [-1,1]$.

Obviously $f_n(x)(n \ge 1)$ is bounded function, if $m \ge n$, we have

$$d_{p}(f_{m},f_{n}) < \left[\int_{-1}^{1} \left|f_{m}(t) - f_{n}(t)\right|^{p} dt\right]^{1/p} < \left[\frac{1}{(n+1)^{2}} + \frac{1}{(n+2)^{2}} + \dots + \frac{1}{m^{2}}\right]^{1/p} \\ < \left[\frac{1}{n} - \frac{1}{m}\right]^{1/p} < \frac{1}{n} \to 0 \ (m,n \to \infty)$$
(15)

So $\{f_n(x)\}$ is sequence of D[-1,1], its standard $\{\tilde{f}_n(x)\}$ is Cauchy sequence of B[-1,1], here the convergent function of $\{\tilde{f}_n(x)\}$ is a unbound function.

Theorem 3.2 Metric space $(B[-1,1], d_p, E)$ is separable.

Proof: $B[-1,1] \subset L_p[-1,1]$ and $L_p[-1,1]$ is separable, so B[-1,1] is separable about metric L_p . Assume $\{p_n\}$ is countable dense subset of $(B[-1,1],L_p)$, for any $f \in B[-1,1]$ and $\varepsilon > 0$, there is $p_{n_0} \in \{p_n\}$, such that

$$\left[\int_{-1}^{1} \left| f(t) - p_{n_0}(t) \right|^p \mathrm{d}t \right]^{1/p} < \varepsilon .$$
(16)

So

$$d_{p}(f, p_{n_{0}}) = \left[\int_{-1}^{1} E(t) \left| f(t) - p_{n_{0}}(t) \right|^{p} dt \right]^{1/p} < \left[\int_{-1}^{1} \left| f(t) - p_{n_{0}}(t) \right|^{p} dt \right]^{1/p} < \varepsilon,$$
(17)

Proof that $\{p_n\}$ is also a countable dense subset of B[-1,1] about metric d_p , then $(B[-1,1], d_p, E)$ is separable.

Deduction 3.1 Metric space $(B_f(K), d_p, E)$ is separable.

Proof: From theorem3.2, Metric space $(B[a,b],d_p,E)$ is separable, however $B_f(K) \subset B[-1,1]$, According to the property of separable this conclusion holds.

4 Fuzzy numbers metric induced by the fuzzy structured element

4.1 Fuzzy numbers space metric induced by the function space metric

From theorem2.1, for any given function $f \in D[-1,1]$ exist unique corresponding fuzzy number $\tilde{u}_f = f(E)$, fuzzy structured element determine a mapping from D[-1,1] to $\tilde{N}_c(R)$. From theorem2.2, if *E* is a regular fuzzy structured element, for any fuzzy number \tilde{u} , there is $f \in D[-1,1]$ such that $f(E) = \tilde{u}$. Monotone bounded functions only different at discontinuity point have the same set of values extension. f is not unique in D[-1,1], in order to meet the uniqueness of f, we limit f in B[-1,1].

Definition 4.1 Let E be a regular fuzzy structured element, consider mapping

$$H_E: B[-1,1] \to N_c(R), f \to H_E(f) = f(E) \in N_c(R)$$
(18)

Saying that H_E is fuzzy functional in B[-1,1] induced by fuzzy structured element E.

Definition 4.2 If d_B is metric of B[-1,1], $\tilde{u}, \tilde{v} \in \tilde{N}_c(R)$, definite

$$d_{NB}(\tilde{u},\tilde{v}) = d_B(H_E^{-1}(\tilde{u}), H_E^{-1}(\tilde{v})),$$
(19)

Where $H_E^{-1}(\tilde{u}), H_E^{-1}(\tilde{v})$ mean inverse image of \tilde{u} and \tilde{v} in the mapping $H_E \cdot d_{NB}$ is fuzzy number metric induced by fuzzy functional H_E via to $d_B \cdot \tilde{N}_c(R)$ becomes a metric space informed by d_{NB} and note $(\tilde{N}_c(R), d_{NB}, E)$.

For $\tilde{u}, \tilde{v} \in \tilde{N}_c(R)$, E is regular fuzzy structured element, there is $f, g \in B[-1,1]$, such that $\tilde{u} = f(E), \tilde{v} = g(E)$. B[-1,1] composed of the whole same sequence standard monotone function in [-1,1], that means H_E is a one to one mapping from B[-1,1] to $\tilde{N}_c(R)$. So $f = H_E^{-1}(\tilde{u}), g = H_E^{-1}(\tilde{v})$.

 $d_B(H_E^{-1}(\tilde{u}), H_E^{-1}(\tilde{v})) = d_B(f, g)$, then (19) can be written

$$d_{NB}(\tilde{u},\tilde{v}) = d_B(f,g).$$
⁽²⁰⁾

4.2 Fuzzy number metric d_{Np} induced by d_p

Reference [14] gives a common metric of function space (Hamming metric) induced metric on the space of fuzzy numbers. But the measure does not take into account differences of the contribution of the fuzzy number between different fuzzy number distance of the different levels under the cut set. That is the higher the cut set level, the greater the extent of the contribution from the cut set of objective. Therefore, in order to reflect this fact very well, the paper starts from the function weighted measure d_p , try to give a new class of fuzzy numbers measure.

Get d_p from metric d_B in B[-1,1], according to definition 4.2, d_{Np} is fuzzy number metric induced by d_p in mapping H_E . If $\tilde{u}, \tilde{v} \in \tilde{N}_c(R)$, we have

$$d_{Np}(\tilde{u},\tilde{v}) = d_{p}(H_{E}^{-1}(\tilde{u}), H_{E}^{-1}(\tilde{v})),$$
(21)

Let *E* be a regular fuzzy structured element, $\tilde{A} = f(E), \tilde{B} = g(E)$, where $f, g \in B[-1,1]$, then (21) can be written

$$d_{Np}(\tilde{u},\tilde{v}) = d_p(f,g).$$
⁽²²⁾

Saying that $(\tilde{N}_c(R), d_{Np}, E)$ is metric space induced by $(B[-1,1], d_p, E)$ in mapping H_E .

Easy to know, H_E is a one to one isometric mapping from B[-1,1] to $\tilde{N}_c(R)$. From theorem 2.4, H_E is a homeomorphism mapping.

Theorem 4.1 $(\tilde{N}_c(R), d_{N_p}, E)$ and $(B[-1,1], d_p, E)$ are homeomorphism.

According to the topological invariance, from theorem3.1, theorem 3.2 and inference 3.1, we have the following conclusions:

Theorem 4.2 Give the interval [a,b] in R,

$$\widetilde{N}_{c}[a,b] = \{ \widetilde{A} : \widetilde{A} \in \widetilde{N}_{c}(R), \sup p\widetilde{A} \subseteq [a,b] \}.$$
(23)

Then $(\tilde{N}_c[a,b], d_{N_p}, E)$ is complete metric space.

Theorem 4.3 $(\tilde{N}_c(R), d_{Np}, E)$ is not complete but separable.

5 Relations between d_{Np} and the traditional measure of fuzzy numbers

In consideration of the influence of degree of membership of the elements in the measure, the fuzzy number of measurements d_{Np} is more reasonable than traditional fuzzy measure. the greater the degree of membership, the higher the degree of contribution of the distance. The following reveals its links with traditional fuzzy numbers measure.

For $\tilde{u} \in \tilde{N}_c(R)$, E be a regular fuzzy structured element. Definite coresbonding functions

$$g_{\bar{u}}(x) = \begin{cases} \underline{u}(E(x)), -1 \le x \le 0\\ \overline{u}(E(x)), & 0 < x \le 1 \end{cases}.$$
(24)

From theorem 2.3, $g_{\tilde{u}}(x)$ is left continuous in [-1,0] and right continuous in [0,1], at the endpoints x = -1, 1 right continuous and left continuous. It is monotone decreasing in [-1,1], $g_{\tilde{u}} \in D[-1,1]$.

Lemma 5.1 Let *E* be a regular fuzzy structure element, fuzzy number $\tilde{u} \in \tilde{N}_c(R)$, $u_{\alpha} = [\underline{u}(\alpha), \overline{u}(\alpha)](\alpha \in [0,1])$, if $\tilde{u} = f(E), f \in B[-1,1]$, then $f(x) = \overline{g}_{\tilde{u}}(x), x \in [-1,1]$, where $\overline{g}_{\tilde{u}}$ represent regular function of $g_{\tilde{u}}$.

Proof: 1) Firstly, proof $\breve{g}_{\tilde{u}}(E) = \tilde{u}$. According decomposition theorem only need to proof for any $\alpha \in (0,1]$, there is $[\breve{g}_{\tilde{u}}(E)]_{\alpha} = u_{\alpha}$. Note that $E_{\alpha} = [e_{\alpha}^{-}, e_{\alpha}^{+}]$, according to the principle of expansion and $\breve{g}_{\tilde{u}}(x)$ is a monotone incising function, then

$$[\breve{g}_{\tilde{u}}(E)]_{\alpha} = \breve{g}_{\tilde{u}}(E_{\alpha}) = \breve{g}_{\tilde{u}}([e_{\alpha}^{-}, e_{\alpha}^{+}]) = [\breve{g}_{\tilde{u}}(e_{\alpha}^{-}), \breve{g}_{\tilde{u}}(e_{\alpha}^{+}+)].$$

$$(25)$$

 $\underline{u}(\alpha), \overline{u}(\alpha)$ is left continuous in (0,1], $\underline{u}(E(x))$ is left continuous in (-1,0], $\overline{u}(E(x))$ is right continuous in [0,1), so

$$[\breve{g}_{\tilde{u}}(e_{\alpha}^{-}),\breve{g}_{\tilde{u}}(e_{\alpha}^{+}+)] = [g_{\tilde{u}}(e_{\alpha}^{-}),g_{\tilde{u}}(e_{\alpha}^{+}+)] = \left[\underline{u}\left(E(e_{\alpha}^{-})\right),\overline{u}\left(E(e_{\alpha}^{+})\right)\right] = \left[\underline{u}(\alpha),\overline{u}(\alpha)\right] = u_{\alpha} .$$
(26)
We obtain $[\breve{\alpha},(E)] = u_{\alpha} \quad \breve{\alpha} \in E = \tilde{u}$

We obtain $[\breve{g}_{\tilde{u}}(E)]_{\alpha} = u_{\alpha}, \ \breve{g}_{\tilde{u}}(E) = \tilde{u}$.

2) Proof f is unique in B[-1,1]. Assume $f_1, f_2 \in B[-1,1]$ such that $\hat{f}_1(E) = \tilde{u}$, then $\hat{f}_1^{-1} = \hat{f}_2^{-1}$, $\hat{f}_1 = \hat{f}_2$, so $f_1 = f_2$, f is unique in B[-1,1]. So we have $f(x) = \bar{g}_u(x), x \in [-1,1]$. **Theorem 5.1** Let $\tilde{u}, \tilde{v} \in \tilde{N}_c(R)$, *E* is a regular fuzzy structured element, $f, g \in B[-1,1]$, such that $\tilde{u} = f(E), \tilde{v} = g(E)$. For $\forall \lambda \in (0,1], 1 \le p < \infty, u_\alpha = [\underline{u}(\alpha), \overline{u}(\alpha)], v_\alpha = [\underline{v}(\alpha), \overline{v}(\alpha)]$, then

$$d_{Np}(\tilde{u},\tilde{v}) = \left[\int_{-1}^{1} E(x) |f(x) - g(x)|^{p} dx\right]^{1/p}$$

$$= \left[\int_{0}^{1} \alpha |\underline{u}(\alpha) - \underline{v}(\alpha)|^{p} d\underline{E}(\alpha) - \int_{0}^{1} \alpha |\overline{u}(\alpha) - \overline{v}(\alpha)|^{p} d\overline{E}(\alpha)\right]^{1/p}$$
(27)

Proof: From lemma5.1, we get

$$d_{Np}(\tilde{u},\tilde{v}) = d_p(f,g) = d_p(\tilde{f}_{\tilde{u}},\tilde{g}_{\tilde{v}})$$
(28)

 $\breve{g}_{\tilde{u}} = g_{\tilde{u}}$ and $\breve{g}_{\tilde{v}} = g_{\tilde{v}}$ are founded almost everywhere in [-1,1], therefore $d_p(\breve{f}_{\tilde{u}},\breve{g}_{\tilde{v}}) = d_p(f_{\tilde{u}},g_{\tilde{v}})$. So

$$d_{Np}(\tilde{u},\tilde{v}) = d_{p}(f_{\tilde{u}},g_{\tilde{v}}) = \left[\int_{-1}^{1} E(x) \left|f_{\tilde{u}}(x) - g_{\tilde{v}}(x)\right|^{p} dx\right]^{1/p} \\ = \left[\int_{-1}^{0} E(x) \left|\underline{u}(E(x)) - \underline{v}(E(x))\right|^{p} dx + \int_{0}^{1} E(x) \left|\overline{u}(E(x)) - \overline{v}(E(x))\right|^{p} dx\right]^{1/p}$$
(29)

Let $l_E(x) = E(x), x \in [-1,0], r_E(x) = E(x), x \in [0,1]$. *E* is a regular fuzzy structured element, l_E is a monotone increasing one to one mapping from [-1,0] to $[0,1], r_E$ is a monotone decreasing one to one mapping from [0,1] to $[0,1], l_E^{-1}, r_E^{-1}$ exist and are all monotone one to one mapping, easy to know $\underline{E} = l_E^{-1}, \overline{E} = r_E^{-1}, \underline{E}, \overline{E}$ are differentiable almost everywhere in -, so we have

$$d_{Np}(\tilde{u},\tilde{v}) = \left[\int_{0}^{1} \alpha |\underline{u}(\alpha) - \underline{v}(\alpha)|^{p} dI_{E}^{-1}(\alpha) + \int_{0}^{0} \alpha |\overline{u}(\alpha) - \overline{v}(\alpha)|^{p} dr_{E}^{-1}(\alpha)\right]^{1/p}$$
$$= \left[\int_{0}^{1} \alpha |\underline{u}(\alpha) - \underline{v}(\alpha)|^{p} d\underline{E}(\alpha) - \int_{0}^{1} \alpha |\overline{u}(\alpha) - \overline{v}(\alpha)|^{p} d\overline{E}(\alpha)\right]^{1/p} .$$
(30)

Notice: In formulation (27), $\underline{E}(x)$, $\overline{E}(x)$ almost have derivatives $\underline{E}'(x)$, $\overline{E}'(x)$ everywhere in [0,1], then

$$d_{Np}(\tilde{u},\tilde{v}) = \left[\int_{0}^{1} \alpha \underline{E}'(\alpha) |\underline{u}(\alpha) - \underline{v}(\alpha)|^{p} - \alpha \overline{E}'(\alpha) |\overline{u}(\alpha) - \overline{v}(\alpha)|^{p} d\alpha\right]^{1/p}.$$
(31)

If *E* is symmetrical structure element, E = -E, $\underline{E}'(\alpha) = -\overline{E}'(\alpha)$, then

$$d_{Np}(\tilde{u},\tilde{v}) = \left[\int_{0}^{1} \alpha \underline{E}'(\alpha) \left[\left| \underline{u}(\alpha) - \underline{v}(\alpha) \right|^{p} + \left| \overline{u}(\alpha) - \overline{v}(\alpha) \right|^{p} \right] \mathrm{d}\alpha \right]^{1/p}.$$
(32)

Let p = 2, E be triangular structure element, that is $\underline{E}'(\alpha) = 1, \alpha \in [0,1]$, fuzzy number metric $\delta_{Np}(\tilde{u}, \tilde{v})$ (in the formulation (3)), let $s(\alpha) = \alpha$, δ_{Np} and d_{N2} are consistent.

6 Conclusions

In this paper, we define a class of function measure whose weight is regular fuzzy structured element in the same sequence standard monotone bounded functions in [-1,1] and get fuzzy numbers metric between $E - L_p$ and d_{Np} . Its theoretical significance is that such fuzzy numbers distance weighted by structured element considers the contribution of the metric membership of metric of fuzzy numbers distance. Due to the relationship between the fuzzy numbers metric and functions metric we can transform the research of characterization of fuzzy function space into the nature of function space .Open a way for the research of fuzzy numbers .

References

- [1] Ching-Hsue Cheng, A new approach for ranking fuzzy numbers by distance method[J], Fuzzy Sets and Systems, 1998, 95(3):307-317.
- [2] B. Asady, A. Zendehnam, Ranking fuzzy numbers by distance minimization[J], Applied Mathematical Modelling, 2007, 31(11):2589-2598.
- [3] Debashree Guha, Debjani Chakraborty, A new approach to fuzzy distance measure and similarity measure between two generalized fuzzy numbers[J], Applied Soft Computing, 2010, 10 (1): 90-99
- [4] Diamond P, Kloeden P. Metric space of fuzzy set: Theory and application[M].Singapore:World Scientific,1994.
- [5] Wu C X,Ma M,Fang J X.Structure theory of fuzzy analytics[M].Gui-yang:Gui-zhou Science and Technology Press,1994.(In Chinese)
- [6] Guo S Z. Principle of fuzzy mathematical analysis based on structured element[M]. Shen-yang: Northeastern University Press, 2004.(In Chinese)
- [7] Amelia Bilbao Terol, A new approach for multiobjective decision making based on fuzzy distance minimization, Mathematical and Computer Modelling, 2008, 47(9-10):808-826
- [8] Miin-Shen Yang, Cheng-Hsiu Ko, On a class of fuzzy c-numbers clustering procedures for fuzzy data[J], Fuzzy Sets and Systems, 1996, 84(1):49-60
- [9] Phil Diamond, Peter Kloeden, Characterization of compact subsets of fuzzy sets[J], Fuzzy Sets and Systems, 1989, 29(3):341-348.
- [10] Phil Diamond, Peter Kloeden, Metric spaces of fuzzy sets[J], Fuzzy Sets and Systems, 1990, 35(2):241-249.
- [11] Diamond P, Kloeden P. Metric spaces of fuzzy sets: Theory and application[M]. Singapore, London: World Scientific Publishing,1994.
- [12] William Voxman, Some remarks on distances between fuzzy numbers, Fuzzy Sets and Systems , 1998,100(1–3): 353-365
- [13] L Tran, L Duckstein. Comparison of fuzzy numbers using a fuzzy distance measure[J]. Fuzzy Sets and Systems,2002,130:331~341.
- [14] Liu M,Li F C,Wu D. Measure of the difference between fuzzy numbers based on its plane distance application in optimal scheduling problem[J]. China Science and E Keywords,2003,33(12):1138-1148. (In Chinese)
- [15] Guo S Z. Homeomorphic property between fuzzy number space and monotone function with same formal on [-1,1][J]. Advances in Natural Science, 2004, 14(11): 1318-1321.(In Chinese)

Advanced Materials Research Vol. 981 (2014) pp 287-291 © (2014) Trans Tech Publications, Switzerland doi:10.4028/www.scientific.net/AMR.981.287

An Improved Voice Activation Detection Method Based on Energy Acceleration Parameters and Support Vector Machine

Qian Liu^{1, 2,a}, Jinxiang Wang^{1,b}, Mingjiang Wang¹, Panpan Jiang²

¹Microelectronics Center, Harbin Institute of Technology, Harbin, P. R. China

²Department of Electronic Science and Technology, Harbin University of Science and Technology, Harbin, P. R. China

^aliuqian0428@126.com, ^bjxwang@hit.edu.cn

Keywords: voice activation detection, support vector machine, energy acceleration parameter.

Abstract. Voice activation detection is a very important part in speech related domain. The classic voice activation detection normally depends on feature parameters in time or frequency domain, or parameters from statistical model. An improved voice activation detection method based on energy acceleration parameters and support vector machine is proposed in this paper. The energy acceleration parameters are the voice activation detection parameters in ETSI Advanced front-end feature extraction algorithm. The training period of support vector machine is based on energy acceleration parameters and manually appended class labels of each frame. In the detection period, the detection result is derived from energy acceleration parameters and Lagrange parameters calculated from training period. The experimental result shows that the false alarm rate of proposed method is greatly decreased. It has been observed that the voice activation detection proposed is better than the voice activation detection in ETSI Advanced front-end feature extraction algorithm.

Introduction

Voice activation detection (VAD) is a very important part in speech processing. Its main task is to distinguish the speech segments and non-speech segments within a speech signal. It is widely used in the field of voice communicate systems[1], speech coding[2], automatic speech recognition[3], and some other speech related systems.

The classic voice activation detection is based on statistical model or some specified feature parameters. The statistical model is normally based on the complex Gaussian probability density functions (pdf's) assumption [4]. Its classification result is made upon the likelihood ratio over all frequency bands and a threshold value. On the other hand, the commonly used feature parameters are short-time energy, short-time average crossing zero rates, parameters of ITU-T G.729B[5], parameters of ETSI Advanced front-end feature extraction algorithm (AFE) [6], and some other feature parameters in time and frequency domain. Normally, those parameters are compared to a threshold to determine whether the current frame is a speech frame or a non-speech frame.

In recent years, a machine learning theory named support vector machine (SVM) is introduced to the voice activation detection domain. Q.-H. Jo[7] proposed a voice activity detector based on statistical model and support vector machine. Tomi Kinnunen[8] introduced a voice activity detector using MFCC features based on support vector machine. Enqing [9] applied support vector machine to voice activity detection based on the parameters of the ITU-T G.729B. No matter what parameters are chosen, the performances of each voice activation detection system based on support vector machine are better than the original one.

The voice activation detection algorithm in G.729B and ETSI AFE are both successive methods in commercial telecom system. The voice activation detection based on parameters of G729.B and support vector machine is already studied in [9], but the voice activation detection based on parameters of ETSI AFE and support vector machine still needs evaluation. In that case, a voice activation detector based on the parameters of ETSI AFE and support vector machine is proposed in

this paper. Its ROC curve shows that the performance of the detector proposed in this paper is also better than the original one.

VAD of AFE

ETSI AFE is a front-end standard to ensure the compatibility between the terminal and the remote recognizer. It is uesd to create Mel-Cepstrum parameters and their transmission which form part of a system for distributed speech recognition. Noise reduction is performed first in the feature extraction part. And then, waveform processing is applied to the de-noised signal and cepstral features are calculated. Voice activity detection is also implemented in the feature extraction period [6].

The voice activity detector depends on the energy acceleration parameters. It is a comparatively noise-robust characteristic of the speech. It includes three parameters: 1. energy values across the whole spectrum of each frame; 2. energy values over a sub-region of the spectrum of each frame. The sub-region of spectrum is the one which is likely considered to contain the fundamental pitch; 3. The "acceleration" of the variance of energy values within the lower half of the spectrum of each frame [6].

The voice activity detection in ETSI AFE has two stages: a detection stage and a decision stage. The frame-by-frame detection stage measures the three acceleration parameters first. And then, the three parameters should compare to an adaptive threshold respectively to get the three detection results. If the detection result is 1, it means current frame is a speech frame; if the detection result is 0, it means current frame is a non-speech frame. Those detection results will be the input of the decision stage. The decision stage gives the final classify result of current frame according to those detection results and a hangover facility. Firstly, those three detection results should be calculated by logic OR operation to get a roughly result. This means that if any of the three detection results is true, then the roughly result for the hangover facility is true. And then, the hangover facility will give the final decision algorithm. The purpose of hangover facility is smoothing the roughly results which are derived from energy acceleration parameters to get a stable and long interval between speeches.

The advantage of AFE VAD is that the entire speech frame can be recognized, but a drawback is also introduced by the hangover facility. Its drawback is that some non-speech frames also recognized as speech frames. The reason is that the hangover timer is count down from twenty-three at the most of the time in the decision stage. If the non-speech interval between two speech segmentations is smaller than 20ms, the VAD in AFE can not detect this interval at some certain circumstances.

Improved AFE

In order to improve the performance of AFE VAD program, the support vector machine was introduced to the VAD decision stage. Support vector machine is a pattern classifier based on statistics learning theory, which is first introduced by Vapnik. It has unique advantages in solving classification problems of small samples [13]. In recent years, support vector machine was introduced in voice activation detection, in that support vector machine has excellent performance in two-class classification.

If the non-speech frame is labeled as one class and the speech frame is labeled as the other class, then the voice activation detection can be regarded as a two-class classification. The feature parameters of support vector machine in this paper are the three energy acceleration parameters mentioned above. Label 1 means speech frame and label -1 means non-speech frame.

Assume a set of training data $\{(x_i, y_i)\}$ belongs to two classes: non-speech frame and speech frame. x_i represents the three energy acceleration parameters, the value of y_i denote the class of x_i . Fig 1 and Fig 2 give an example of support vector machine theory. Assume solid dot represents class A and hollow dot represents class B. In the VAD detection stage, the three energy acceleration parameters, as shown in Fig 1 by the solid dots and hollow dots, are mixed together, it is hard to separate them into two classes. But if the dots are implemented in a high dimensional feature space, as shown in Fig2, they can be separated easily. In that it becomes a linear separable case again.

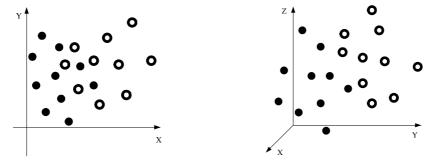


Fig 1: Non-linear separable case

Fig 2: Linear separable case

A kernel function can map the input vector into a high dimensional feature space, which can turn a nonlinear separable case into a linear separable case. The kernel function used in this paper is Radial Basis Function kernel, as presented in formula (1).

$$K(x, y) = \exp(-\frac{(x - y)^2}{2\sigma^2})$$
(1)

In the training period, its inputs are the three energy acceleration parameters and manually appended label of each frame, and its outputs are Lagrange multiplier and bias. The number of Lagrange multiplier is equal to the number of energy acceleration parameters. If the Lagrange multiplier is larger than 1e-5, then its corresponding energy acceleration parameter will be the support vector. For Radial Basis Function kernel, the bias normally is zero.

For the testing period, the classification result of current frame is derived by the formula (2):

$$f(x) = \operatorname{sgn}(\sum_{SV_s} \alpha_i y_i K(x_i, x) + b)$$
(2)

Where x_i is the i-th energy acceleration parameters in training; x is the energy acceleration parameters of current frame in testing, y_i is the i-th class label of the i-th training vector; α_i is the Lagrange multiplier, b is the bias, and K is the kernel function; f(x) is the predicted value, which equals to 1 or -1. If f(x) equals 1, it means the current frame is a speech frame; if f(x) equals -1, it means the current frame is a non-speech frame.

Experimental results

In order to evaluator the performance of the new VAD algorithm which is based on SVM and energy acceleration parameters, a segment of speech from standard speech library is used to generate the energy acceleration parameters. A 746s speech is randomly chosen from The DARPA TIMIT Acoustic-Phonetic Continuous Speech Corpus. 451s speech is chosen for training and 295s is for testing. Its sampling rate is 16 kHz, and save with 16bit.The proportion of non-speech frame is 44%, and the speech frame is 56%.

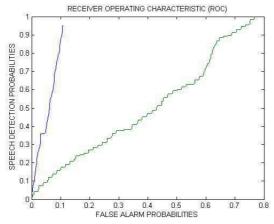
In the experiments, the analysis window size was 25 ms with 15 ms overlap. Each frame of the windowed signal was transformed to acceleration parameters according to ETSI AFE Standard. The labels for support vector machine are appended manually at very 10 ms through visual observation and listening.

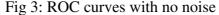
Table 1 shows the performance of the proposed VAD algorithm and ETSI AFE VAD by comparing them with their Pd, Pf and Pa. Pd is defined as the probabilities of voice detection and Pf as the probabilities of false alarm to evaluate the VAD performances. Pa is defined as the probabilities of correct detection of both speech and non-speech frames. Pd is calculated as the ratio of test sets when the hand-marked speech frame is correctly detected by the VAD algorithm. Similarly, Pf is the ratio of test sets when hand-marked speech regions are identified as noises. Pa is the ratio of test sets when hand-marked frame is correctly detected by the VAD algorithm.

	nce of VAD al	gorunns wun	no noise
	Pd	Pf	Pa
ESTI AFE VAD	100%	78.13%	55.47%
Proposed VAD	95.21%	10.81%	91.78%

Table 1: Performance of VAD algorithms with no noise

The results in Table 1 demonstrate that the AFE VAD algorithm has excellent performance in speech frame detection, but nearly 78% non-speech frames are identified as speech frames. The proposed VAD algorithm can greatly decrease the false alarm probability, and at the same time keep the high speech detection probability.

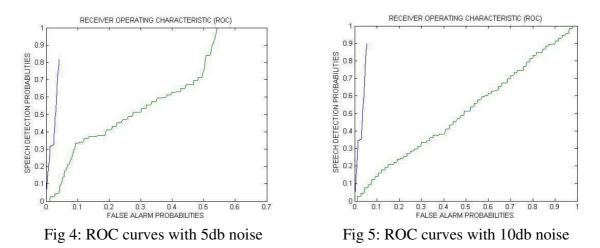




The receiver operating characteristics (ROC's)[10], which shows the trade-off characteristic between the speech detection and false-alarm probabilities (Pd and Pf), is also given to evaluate the performance of proposed method.

Fig 3 shows the ROC curves of the proposed SVM-based VAD with the ETSI AFE VAD methods. If the curve in ROC space is at the northwest of the other, then its performance is better than the other. Because in this case Pd is higher, Pf is lower, or both. According to this point, the proposed SVM-based VAD using the RBF kernel yielded higher performance than the AFE VAD method.

To evaluate the performance in noisy conditions, white noises are added to the clean speech data by 5 dB SNR and 10 dB SNR. Figure 4 and 5 gives the ROC curves at the different noise signal ration.



It has been observed that the performance of proposed VAD is better than the AFE VAD in noisy condition. The probabilities of voice detection are both decreased a little, but the probabilities of false alarm have different properties. It can conclude that the performance of proposed VAD is stable in noisy condition, but performance of AFE VAD is varied by the level of SNR.

Conclusions

If voice activation detection is seen as a two class classifier problem, then support vector machine, an excellent static classifier, can be introduced into the AFE voice activation detect stage. The proposed VAD algorithm uses acceleration parameters as the inputs of SVM. After getting some parameters by the training period, each frame can get a classified result according the relative parameters. The performance of proposed VAD and AFE VAD is compared by the speech database of TIMIT. By analysis the result of Pd, Pf, and Pa, and comparing their ROC curves, the proposed VAD algorithm has better performance than the AFE VAD algorithm.

References

- [1] Jamal Saeedi · Seyed Mohammad Ahadi · Karim Faez Robust voice activity detection directed by noise classification SIViP, April, (2013).
- [2] Beritelli, F., Casale, S., Ruggeri, G.: Performance evaluation and comparison of ITU-T/ETSI voice activity detectors. In: Proceedings ICASSP, (2001) ,pp. 1425–1428.
- [3] Srinivasant, K., Gersho, A.: Voice activity detection for cellular networks. In: Proceedings IEEE Speech Coding, Workshop, (1993), pp. 85–86.
- [4] SOHN J., KIM N.S., SUNG W.: A statistical model-based voice activity detection, IEEE Signal Process. Lett., 6, (1), (1999), pp. 1–3.
- [5] ITU-T Recommendation G729-Annex B, November, (1996)
- [6] Speech processing, transmission and quality aspects(STQ); Distributed speech recognition; Advanced front-end feature extraction algorithm; compression algorithms, ETSI ES 202, (2007)
- [7] Q.-H. Jo, J.-H. Chang J.W. Shin N.S. Kim. Statistical model-based voice activity detection using support vector machine, IET Signal Processing, Vol. 3, Iss. 3, (2009),pp. 205–210.
- [8] Tomi Kinnunen, Evgenia Chernenko, Marko Tuononen, Pasi Fränti, Haizhou Li, Voice Activity Detection Using MFCC Features and Support Vector Machine, International Conference on SPECOM, Vol. 2, (2007), pp. 556-561.
- [9] ENQING D., GUIZHONG L., YATONG Z., XIAODI Z.: Applying support vector machines to voice activity detection. Proc. Int. Conf. Signal Process., vol. 2, (2002),pp. 1124 1127.
- [10] Tom Fawcett.ROC Graphs: notes and practical considerations for researchers. HP laboratories, (2004)

CHAPTER 4:

Image Processing and Computer Vision

Athermalization Design of Wide Field Medium Wave Infrared Optical System

Lei Zhao^{1,a}, ZhaoHui Luan^{1,b} YanLing Xiong^{1,c} and LiJuan He^{1,d} ¹School of Applied Science, Harbin University of Science and Technology, China ^azhaoleiwm@163.com, ^blzhmj5@126.com, ^cxyling1964@163.com, ^dhlj6607@163.com

Keywords: athermalization, optical design, wide field, infrared optical system

Abstract. Based on the principle of passive optical athermalization, a wide field medium wave infrared optical system is designed for working at -40°C-60°C. A 320×240 focal plane array (FPA) detector as image plane is used in the system. The system has a field-of-view of $30^{\circ} \times 22.72^{\circ}$ and a relative aperture of f/2 at 3-5 µm with 100% cold shield efficiency. The modulation transfer function (MTF) of each field is greater than 0.6 at the Nyquist frequency and the maximum distortion is less than 3% at -40°C-60°C. The system can meet the demand of the excellent image quality. This work is valuable for athermalization design of wide field medium wave infrared optical system.

Introduction

In recent years, the infrared thermal imaging technology has been widely used in many fields, such as infrared guidance [1], infrared thermometry [2] and infrared monitoring [3]. For the high optical-thermal expansion coefficients of the infrared materials, the refractive index, radius of curvature and center thickness of the optical element will have the corresponding change when the infrared optical system works under the different temperatures. The change will cause image plane drift and affect the image quality [4]. In order to ensure the thermal stability of the infrared optical system, the athermalization design is necessary. The conventional ways of athermalization design include active electromechanical athermalization, passive mechanical athermalization and passive optical athermalization has the advantages of simple construction, small size, light weight and high reliability. Therefore it is widely used in the design of athermalization.

In this paper, a medium wave infrared optical system is designed based on the principle of passive optical athermalization. The system has the characteristics of a wide field-of-view of $30^{\circ} \times 22.72^{\circ}$, a large relative aperture of f/2 and wide working temperature at -40°C- 60°C. The results show that the optical system has an excellent image quality and easily applied to engineering.

Principle of Passive Optical Athermalization

Passive optical athermalization is a method using the different optical materials with different optical-thermal expansion coefficients to allocate the focal power, and make the image plane drift close to the length change of lens cone due to the hot-expansion and cold-contraction. Meanwhile, the optical system should have good achromatic performance [6].

The focal length formula of the optical system is:

$$\phi = \sum_{i=1}^{j} h_i \phi_i \tag{1}$$

Where h_i is the height of the first axial ray to each lens, ϕ_i is the focal power for each lens.

The achromatic relation can be written as:

$$\left(\frac{1}{h_1\phi}\right)^2 \sum_{i=1}^j h_i \frac{\phi_i}{\nu_i} = 0$$
⁽²⁾

Where v_i is the Abbe coefficient for each lens.

The condition of passive optical athermalization can indicate by the following formula:

$$\left(\frac{1}{h_1\phi}\right)^2 \sum_{i=1}^j h_i \chi_i \phi_i + \alpha L = 0$$
(3)

Where χ_i is the optical-thermal expansion coefficient for each lens, α is the linear expansion coefficient for lens cone material, L is the total length of optical system.

In the process of passive optical athermalization design, the above formula must be satisfied [7].

Design of Optical System

Performance Indicators. Based on the above theoretical analysis, a wide field medium wave infrared optical system is designed for working at -40°C-60°C. In order to make both cooled and uncooled infrared detectors apply to this optical system, the aperture stop is set in the rear position for realizing 100% cold stop efficiency. The specific indicators are summarized as follows:

(1)Wave band: $3 \sim 5 \mu m$

(2)Infrared detector: 320×240 , pixel size is 25 μ m

(3)Field-of-view: 30°×22.72°

(4)F-number: 2

(5)Working temperature: -40°C-60°C

(6)Lens cone material: Aluminum alloys, whose linear expansion coefficient is 23.6×10^{-6} /°C

Design Result. According to the above indicators, the optical system is optimized by using ZEMAX optical design software. The layout is shown in Fig. 1. It has five lenses and the fourth surface is aspheric surface. The materials of the lenses respectively are Silicon, Germanium, Silicon, Germanium and Silicon. The system has compact structure and the total length is 73.76 mm at 20°C. The system contains only an aspheric surface, thus the manufacturing difficulty and cost can be greatly reduced.

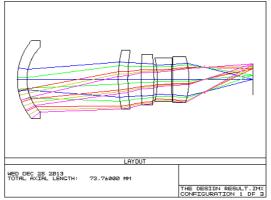
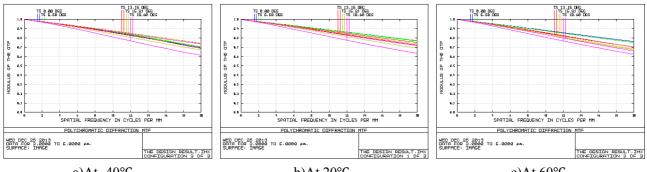


Fig. 1 Layout of optical system

Analysis of Athermalization Performance. The MTF is an important indicator for evaluating imaging quality of the optical system. Fig. 2 shows the MTF curves of optical system at -40°C, 20°C and 60°C. It can be seen that MTF of each field is greater than 0.6 at the Nyquist frequency (20lp/mm) in the whole range of temperature.





b)At 20°C

c)At 60°C

Fig. 2 MTF curves of optical system at different temperature Fig. 3 shows the spot diagrams of optical system at -40°C, 20°C and 60°C. It can be seen that the RMS radius of each field is less than the size of a pixel in the whole range of temperature.

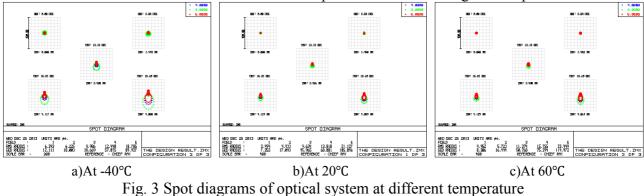


Fig. 4 shows the distortion of optical system at -40°C, 20°C and 60°C. It can be seen that maximum distortion is less than 3% in the whole range of temperature.

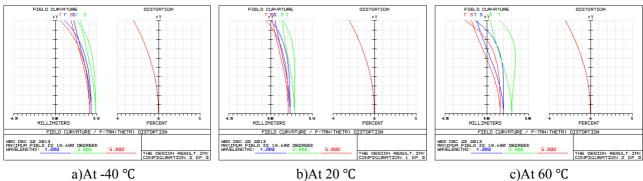


Fig. 4 Distortion of optical system at different temperature

According to the above analysis, the optical system can meet the demand of the excellent image quality at -40°C-60°C.

Conclusions

The theory and design method of athermalization are discussed in detail, and a wide field medium wave infrared optical system is designed based on the principle of passive optical athermalization. Through the analysis of imaging performance, the infrared optical system has a field-of-view of $30^{\circ} \times 22.72^{\circ}$, a relative aperture of f/2 and excellent image quality at -40°C-60°C. The optical system is simple and reliable, and easily applied to engineering.

References

- [1] Yaguang Geng and Mingqian Zhang: submitted to Infrared and Laser Engineering (2007) in Chinese
- [2] Jinqiu Xiao and Shumei Xu: submitted to Journal of Electronic Measurement and Instrument (2004) in Chinese
- [3] Yanlong Qi and Meng Duan: submitted to Infrared Technology (2009) in Chinese
- [4] Yan Li and Bao Zhang: submitted to Journal of Applied Optics (2013) in Chinese
- [5] Xingqiao Ai and Bo Liu: submitted to Proc. of SPIE (2010)
- [6] Yang Jiang and Qiang Sun: submitted to Acta Photonica Sinica (2013) in Chinese
- [7] Le Yang and Qiang Sun: submitted to Acta Photonica Sinica (2011) in Chinese

General Digital Image Processing Circuit and Its Applications

Yongjie Fan^{1,a}, Hua Chen^{1,b}

¹ School of science, Kunming University of Science and Technology, Kunming 650500, Yunnan,

China

^a fanyj1980@263.net, ^b93056460@qq.com

Keywords: FPGA, Image Processing, Thermal Imaging, Image Fusion, Video Stabilization

Abstract. In this paper, the design and architecture of general digital image processing circuit (GFDIPC) based on a Xilinx Virtex-5 FPGA processor is presented. The GFDIPC applications on thermal imaging, image fusion, real-time video stabilization and time-delay test for image processing system are described. The design of FPGA in each application follows the principle of functional modularity, pipeline processing and parallel computing, which brings FPGA high efficiency and high real-time performance.

Introduction

Nowadays, the embedded image processing system is developing with features such as the diversity of functions, the complexity of structures, system miniaturization, high real-time, low power consumption and high maintainability, etc. Meanwhile, FPGA, which features powerful functions, abundant resources, flexible designs and low development costs, become a suitable solution for image processing system. So, according to the requirements of the laboratory on image processing application, we have developed a general FPGA digital image processing circuits (called GFDIPC) based on a XC5VLX50T[1-5] processor and successfully applied it to thermal imaging, image fusion, video stabilization, and time-delay test for image processing system. Details of GFDIPC design and architecture are described in Section 2, followed by the introduction of its functional models and procedures in each application in Section 3 to Section 6. In Section 7, we conclude the paper by summarizing the main contributions.

The Design Principles and Architecture of GFDIPC

The design purpose of GFDIPC is to meet the needs for the image processing algorithms and video processing realization. Based on the requirements above, the complexity of related processing algorithms, system generalization, flexible use of resources, and expandability, our design principles of GFDIPC are as follows:

(1) Using massive FPGA as core processor.

(2) Associating FPGA with multiple types of mass storage memories, this will be convenient for future image data buffer and storage, and meet the requirements of mass storage of matrix parameters.

(3) The topological relation between core devices and peripheral devices is in a star shape, which makes core device can conveniently perform independent or joint operation on peripheral device.

(4) External interfaces combine the generalization and the standardization.

As Fig.1 shows, in the actual design, the whole circuit board applies XC5V LX50T FPGA as core processing device; the peripheral memories includes four $512K \times 18bit$ ZBT SRAM, one 4Gbit NAND flash, and one 128Mbit SDRAM; Video outputs include a VGA output and a PAL output; two RS422 busses are available; two external general purpose IO (GPIO) interfaces adopt two 60

pins connectors, and each connector contains 37-way user define IOs of TTL level and provides 12V, 3.3V power for the externals. The power supply of the GFDIPC is 12V, the power consumption is 4.8W in general, and the size is $12 \text{cm} \times 7 \text{cm}$.

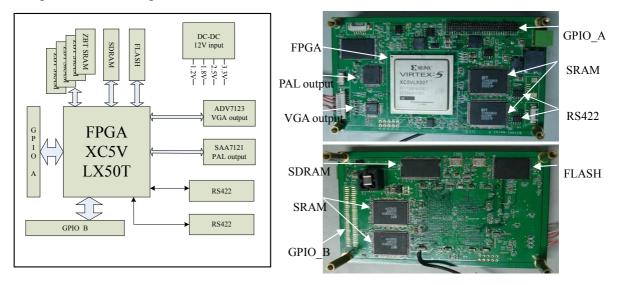


Fig.1 Structure diagram and top/bottom view of GFDIPC

GFDIPC for Medium Wave Thermal Imaging Application

An AD conversion circuit is designed to link detector (320x256 MWIR FPA) [6] with GFDIPC through GPIO interface. The AD circuit and GFDIPC form a double-layer structure. This AD circuit is used for providing IR detector power supply, bias voltage and necessary driving signals. It also converts four analog signals of IR detector into four digital signals which are then formed into one infrared digital video. The video is provided for and processed by GFDIPC.

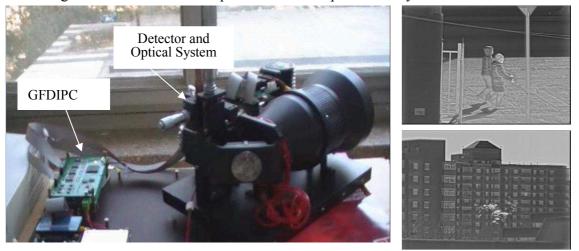


Fig.2 Working state of medium wave infrared imaging system

After receiving IR digital videos, GFDIPC runs fundamental processing module which contains non-uniformity correction, defect pixel compensation, dynamic compression, and buffering on the output videos. Non-uniformity correction includes calibration and one-point correction; defect pixel is replaced by the mean datum of normal pixels around it, and all the defect pixel locations are stored in a lookup table; dynamic compression reduce images dynamic from 14bit data to 8bit; at last the digital IR video is converted into PAL and VGA separately. All processing modules are mainly programmed in Verilog-HDL language, which are more practical and easily transplanted. The result of the test shows that the whole system works steadily, as shown in Fig.2.

GFDIPC for Image Fusion Application

The dual-channel image fusion system, which fuses a visible light video and an infrared video into a color video, provides natural color and retains rich information in both source videos for observers. Fusion algorithm mainly includes two parts, color fusion algorithm and color transfer algorithm, based on YUV space. Two-way video AD sampling circuit is adopted in GFDIPC application with a double-layer structure too. The optical match is used in the system also.

Two analog videos are transformed to CCIR656 digital video signal simultaneously by SAA7113. At first, the CCIR656 digital video will be buffered by ZBT SRAM after being sent into FPGA. Read from buffers, the data will be dealt by the image fusion algorithm and color transfer algorithm [7] in pipeline mode. The processing of the algorithm in each step on data stream shall only take a few pixel clocks. At the same time, the computing of parameters for next frame is simultaneous with the main processing course. All processing programs realized in FPGA are written in Verilog HDL Language. The time-delay of system is within 1ms.

Fig.3 shows the whole processing system is in a good working situation and performs the algorithm faithfully.

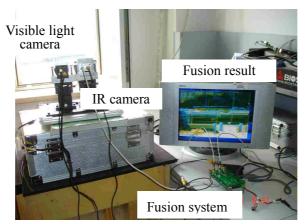


Fig.3 Working state of image fusion system

GFDIPC for Digital Video Stabilization Application

A real-time video stabilization system (RVSS) was implemented based on GFDIPC. The hardware is the same as image fusion application. The horizontal and vertical global interframe movements of video are estimated by enhanced integral projection matching approach [8]. The matching range is set to 1/3 view field. The global movements are low-pass filtered to high frequency components caused by platforms vibration and low frequency components representing the intentional motion. The unwanted movements are removed. The stabilization algorithm is mainly programmed in Verilog-HDL language, which is more practical and takes less chip resource. Microblaze in FPGA executes set-up and control functions. RVSS can meet the requirements of real time processing of PAL video. RVSS works steadily and the time delay is within 40ms. Working state of RVSS is shown in Fig.4.

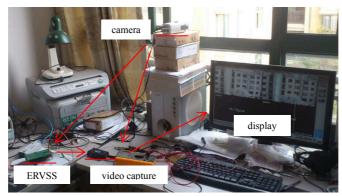


Fig.4 System in working state

GFDIPC for Image Processing System Time-delay Test Application

The time-delay always occurs during processing the video signal stream. And the time-delay of the system is a vital parameter in some strict environment with a high real-time requirement. So it is very practical for upper-level designers or users to obtain the precise time delay of image processing system. As Fig.5 shows, the application of GFDIPC on this field is to produce a test video which is convenient to be observed by oscilloscope. The image processing system to be tested, which is considered as a black box, processes the test video signals and outputs result video. The time delay between input and output video could be measured by oscilloscope.

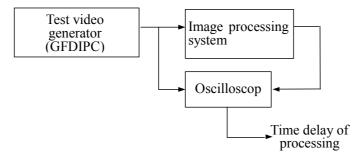


Fig.5 Principle of time-delay testing

Conclusions

GFDIPC mainly stays in experimental applications. But we still can see some features of FPGA, such as powerful functions, flexible designs, and high real-time, etc. It can be transformed to be a specialized mini processing system to meet the requirements of product level. For more complicated algorithm designs in the future, the system can be expanded through cascade connection to meet the needs of resources.

Acknowledgement

I would like to express my gratitude to all those who helped me during the researches and experiments, and also the writing of this paper. A special acknowledgement should be shown to Prof, Jin Weiqi of Beijing Institute of Technology for his useful instruction. Finally I wish to extend my thanks to the support of Yunnan Provincial Foundation Program (No. KKSY201207066).

Reference

[1] Virtex-5 FPGA User Guide. Information on http://china.xilinx.com

[2] Virtex-5 FPGA Data Sheet: DC and Switching Characteristics. Information on http://china.xilinx.com

[3] Virtex-5 FPGA Packaging and Pinout Specification. Information on http://china.xilinx.com

[4] Virtex-5 FPGA Configuration User Guide. Information on http://china.xilinx.com

[5] Xilinx ISE Design Suite 11 Software Manuals. Information on http://china.xilinx.com

[6] 320×256 MW IRCMOS Multimode Integrated Detector Dewar Cooler Assembly (IDDCA) with Microcooler Type K508 Technical Specification. Information on http://www.sofradir.com.

[7] SHI Shi-ming, WANG Ling-xue, JIN Wei-qi, et al, A Dual-band Color Imaging System for Visible and Thermal IR Images Based on Color Transfer in YUV Color Space, ACTA ARMAMENTARII, Vol 30, No 1, P 30-35 (2009)(In Chinese)

[8] Touraj Tajbakhsh, *Real-Time Global Motion Estimation for Video Stabilization*, Real-Time Image and Video Processing 2009, SPIE Vol. 7244: 72440B1-12. (2009)

Study Of Fiber Gyroscope Fiber Defects Image Enhancement Based On Bias-Normal And Fuzzy Processing

Lianjie Shan^{1,2}, Yingchun Liang¹, Wenqian Ge² ¹Harbin Institute of Technology, Heilongjiang Province, China ²Beijing Aerospace Times Optical-electronic Technology Co.,Ltd.,Beijing,China jenny_shan@126.com

Keywords: Fuzzy algorithm; minimum bias-normal distribution index; infrared image; defect

Abstract. Image contrast of fiber gyroscope fiber defects was low, at the same time object and background didn't discriminate easily. Fuzzy image enhancement processing was studied and part low gray level was set zero, which leads to original image information loss using the Pal fuzzy algorithm. Combine minimum bias-normal distribution index and modified fuzzy algorithm was put forward and spacing point is counted by minimum bias-normal distribution index and then automatically affirms sub region and nonlinearity transformation was used in inverse process. This algorithm can engender different enhancement effect in different image region, which enhance contrast ratio in object and background, outstanding defect character. The algorithm was used for fiber gyroscope fiber defect infrared image processing. Experiment results show that the algorithm is effectiveness.

Introduction

Fiber gyroscope is a new all solid state inertia instruments with characteristic of high reliable and long life, which is successful application in the field of astronavigation and weapons^[1]. Reliability and life require is becoming more and more height by kinds of application along with technology advanced and requirements enhancement^[2]. At the same time, there are many and complex manual operation steps of fiber gyroscope manufacturing process, which can cause some damages likely that leave quality hidden trouble for products properties.

Circular telegram status of fiber gyroscope light path is observed by infrared camera, when fiber gyroscope is working. There will be faint infrared light let out, when there is defect and damage on fiber. Fiber defect can be judge by image getting by infrared camera, but letting out infrared light is too faint, so image contrast is very low. Vein is hardly invisible for defect image edge fog. As the same time, the size of defect on fiber light path is too small, so this is small object in imaging. Exposure time of infrared camera is relative long in order to detect the faint infrared light, which cannot be avoid environment kinds of noise jamming even if in darkroom. Fiber detect infrared image should be enhancement before subsequent image process, which protruding characteristic of detect region and restraining background and strengthen signal. Those weaken disturb of kinds of noise and background.

Image enhancement can strengthen and restrain some image information by image processing method, which improve image visual effect and be easy to subsequent processing^[3]. There are vary domain and spatial domain two image enhancement methods, among them vary domain method using image information mapping to feature domain by vary technology such as frequency domain or wavelet and so on. Interested signal components were strengthen using the domain respective specific character, further inverse transform to spatial domain, so it can enhance image^[4]. Based on study of fuzzy enhancement method minimum bias-normal distribution index was used to definite the best threshold, fuzzy degree of membership function being computed by subarea and inverse transform being carry on, and the method was used to process fiber detect infrared image.

Image fuzzy enhancement

Fuzzy enhancement method. Fuzzy image enhancement is a method of combine fuzzy math theory and image enhancement theory, the basic thought is taking image vary from spatial domain to fuzzy domain using degree of membership and getting fuzzy characteristics flat, on which taking strength image processing, at last take it to spatial domain back and get enhancement image.

Based on fuzzy set concept the image with size of $M \times N$ and gray L can be denoted as a $M \times N$ fuzzy characteristics array^[4].

$$X = \begin{bmatrix} \mu_{11}/x_{11} & \mu_{12}/x_{12} & \cdots & \mu_{1N}/x_{1N} \\ \mu_{21}/x_{21} & \mu_{22}/x_{22} & \cdots & \mu_{2N}/x_{2N} \\ \vdots & \vdots & \vdots \\ \mu_{M1}/x_{M1} & \mu_{M2}/x_{M2} & \cdots & \mu_{MN}/x_{MN} \end{bmatrix}.$$
(1)

Where μ_{ij} denotes degree of membership function corresponding gray scale of gray x_{ij} with pixel (i, j). The degree of membership function in Pal method is^[5]:

$$\mu_{ij} = T(x_{ij}) = \left[1 + \frac{(L-1) - x_{ij}}{F_d}\right]^{-F_e}.$$
(2)

 F_e , F_d is index fuzzy factor and fraction fuzzy factor respectively.

Gray scale information of spatial domain is mapped to fuzzy domain by degree of membership function variety, and then the information was taken enhance processing in fuzzy domain. The form is as follows:

$$\mu'_{ij} = F_r(\mu_{ij}) = F_1(F_{r-1}(\mu_{ij})) \quad (r = 1, 2, ...).$$
(3)

$$F_{1}(\mu_{ij}) = \begin{cases} 2(\mu_{ij})^{2}, & 0 \le \mu_{ij} \le 0.5\\ 1 - 2(1 - \mu_{ij})^{2} & 0.5 < \mu_{ij} \le 1 \end{cases}$$
(4)

The operation result of equation (4) is: μ_{ij} was decreased when $\mu_{ij} \le 0.5$, μ_{ij} was increased when $\mu_{ij} > 0.5$. Enhancement operation is realized in fuzzy domain by these operation, then final μ'_{ij} is taken inverse transformation which change into pixel gray scale of spatial domain. It shown as $x'_{ij} = T^{-1}(\mu'_{ij})$, T^{-1} is inverse transformation of equation (2), where x'_{ij} is gray scale of enhanced image pixel (i, j).

Fuzzy enhancement analysis. Given $x_{ij} = X_c$, even if $T(X_c) = 0.5$, X_c is called transition point as shown in equation (3), as follows:

$$T(X_c) = \left[1 + \frac{(L-1) - X_c}{F_d}\right]^{-F_e} = 0.5.$$
(5)

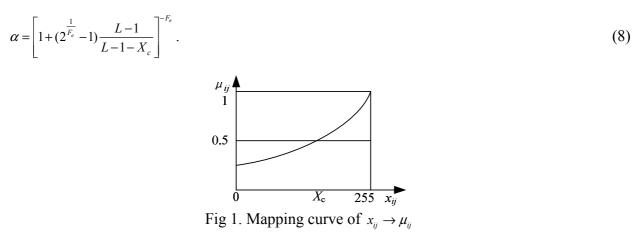
Therefore parameter F_d is shown as:

$$F_d = \frac{(L-1) - X_c}{2^{\frac{1}{F_c}} - 1} \,. \tag{6}$$

The equation(6) shows that F_d is decided jointly by X_c and F_e . It get $x_{ij} \rightarrow \mu_{ij}$ mapping curve after given X_c and F_e . As shown in Figure 1, where $F_e = 2$, when $x_{ij} = 0$ equation(4) get following result.

$$\mu_{ij} = \left[1 + (L-1)/F_d\right]^{-F_e} = \alpha .$$
(7)

Equation (6) is substituted into equation (7), it can get following result.



Where $\alpha > 0$ when $F_e = 2$, but it will appear $\mu'_{ij} < \alpha$ after fuzzy enhancement operator *T* operation, at present T^{-1} vary operation has no result. This situation was provide as $\mu'_{ij} = \alpha$ in the Pal algorithm, the result was some low gray scale been set zero in original image after enhanced image X', thus some gray information of original image. μ_{ij} was fixed 0.5 of iterated operation, which cannot satisfy with different image enhancement requirement because of be short of adjustability.

In order to overcome above fault, equation (2) ~equation (6) were modified using literature[6], expressions show as follows.

$$\mu_{ij} = T(x_{ij}) = \frac{x_{ij}}{L-1} \,. \tag{9}$$

$$\mu'_{ij} = F_r(\mu_{ij}) = F_1(F_{r-1}(\mu_{ij})) \quad (r = 1, 2, ...).$$
(10)

$$F_{1}(\mu_{ij}) = \begin{cases} \frac{\mu_{ij}^{2}}{\mu_{c}} & 0 \le \mu_{ij} \le \mu_{c} \\ 1 - \frac{(1 - \mu_{ij})^{2}}{(1 - \mu_{c})} & \mu_{c} < \mu_{ij} \le 1 \end{cases}$$
(11)

$$x'_{ij} = (L-1)\mu'_{ij} . (12)$$

Where $\mu_c = T(X_c) = X_c/L-1$ and μ_c uncertain equate to 0.5. The effect of enhancement operator F is: μ_{ij} decrease when $\mu_{ij} < \mu_c$ and then non-linear transformation result cause μ_{ij} close to 0 thus causing x_{ij} close to 0; μ_{ij} increase when $\mu_{ij} > \mu_c$ and then non-linear transformation result cause μ_{ij} close to 1 thus causing x_{ij} close to L-1; Image information of middle and low gray part do not lose by this method, but degree of membership function μ_{ij} denotes pixel (i, j) aiming at the max gray scale subordinate degree, the restrict cause to some part that should be enhanced do not be enhanced, at the same time the other part that should not be enhanced do be enhanced. Because of choosing X_c based on experience it is short of aimed at concrete image analysis. If defect region gray scale is less and close to X_c defect region will be enhanced appropriately, which easy to subsequent image processing.

Fiber defect infrared image enhancement processing

Minimum bias-normal distribution indexes the best threshold. In order to overcome defect of count μ_{ij} of equation (2), the method of threshold parameter define *t* based on minimum bias-normal distribution index is put out, which compute degree of membership function. Bias-normal distribution index that is tervalence core statistical moment of sample can measure degree of data distribution deviate to normal distribution. Fiber defect image main includes on defect region and background region, whether pixel gray scale defect and background region obey normal distribution. Bias-normal

distribution index of total image can denote degree of defect and background region gray level distribution deviate to normal distribution after segment^[7]. Image total bias-normal distribution index is minimum when object and background pixel gray level distribution are close to the origin image after segment. Contrarily statistical probability distributions of defect and background region have superior difference with original image; image total bias-normal distribution index is relatively more. Thus it can be seen, image bias-normal distribution index can be an estimate of image segment.

Image gray scale can be divided into defect and background by threshold *t*, we can think fiber defect is bright object on dark background, so the pixel gray scale that is little than *t* is defect region, greater than *t* is background. Normalization histogram of image is given as h(i), $(i = 0 \sim G)$, the of proportion pixel region and total pixel is $\theta(t)$.

$$\theta(t) = \sum_{i=0}^{t} h(i) .$$
(13)

Image total bias-normal distribution index K(t) is denoted as^[6]:

$$K(t) = |K_1(t)| + |K_2(t)|.$$
(14)

Where, $K_1(t)$, $K_2(t)$ denote bias-normal distribution index of defect and background region respectively, these are counted by equation (15).

$$K_{1}(t) = \frac{\sum_{i=0}^{L} [i - \mu_{1}(t)]^{3} h(i)}{[\sigma_{1}(t)]^{3} \theta(t)}$$

$$K_{2}(t) = \frac{\sum_{i=t+1}^{G} [i - \mu_{2}(t)]^{3} h(i)}{[\sigma_{2}(t)]^{3} (1 - \theta(t))}$$
(15)

Where, $\mu_1(t)$, $\mu_2(t)$ are gray mean value of defect and background region respective, these are counted by equation (16); $\sigma_1^2(t)$, $\sigma_2^2(t)$ are variance of defect and background region respective, these are counted by equation (17).

$$\mu_1(t) = \frac{\sum_{i=0}^{r} h(i)i}{\theta(t)}, \quad \mu_2(t) = 1 - \mu_1(t).$$
(16)

$$\sigma_1^2(t) = \frac{\sum_{i=0}^{t} [i - \mu_1(t)]^2 h(i)}{\theta(t)}, \quad \sigma_2^2(t) = \frac{\sum_{i=t+1}^{G} [i - \mu_2(t)]^2 h(i)}{(1 - \theta(t))}.$$
(17)

Modified fuzzy enhancement processing.

Choice of degree of membership function. Degree of membership function is the transform key of digital image to fuzzy spatial domain, which image gray value x_{ij} are mapping to corresponding characteristic value μ_{ij} of fuzzy characteristics plane. Information loss is few for low gray region using the method of define fuzzy matrix in low and high gray value respective, expression is as follows:

$$\mu_{ij} = T(x_{ij}) = \begin{cases} \frac{1}{2} \left(\frac{x_{ij}}{t}\right)^2 & x_{ij} \le t \\ 1 - \frac{1}{2} \left(\frac{x_{max} - x_{ij}}{x_{max} - t}\right)^2 & x_{ij} > t \end{cases}$$
(18)

Where x_{max} is the maximum gray value of image. *t* is the best threshold getting by bias-normal distribution index. Fiber image is divided into low gray and high region by the threshold, and then do mapping processing for two sub regions respective.

Choice of fuzzy enhancement operator. Fuzzy enhancement is completed in fuzzy characteristic plane. Gray contrast is enhanced in defect domain through fuzzy enhancement operator arithmetic. Thus the fuzzy enhancement operator needs a select principle. The gray value is increased for higher or lower than a certain gray value range, and the gray value is condensed for the pixels of the gray value range.

$$\mu_{ij}' = F(\mu_{ij}) = \begin{cases} 0 & \mu_{ij} < \mu_{\min} \\ \frac{\mu_{ij}^2}{\mu_t} & \mu_{\min} \le \mu_{ij} \le \mu_t \\ 1 - \frac{(1 - \mu_{ij})^2}{1 - \mu_t} & \mu_t < \mu_{ij} \le \mu_{\max} \\ 1 & \mu_{ij} > \mu_{\max} \end{cases}$$
(19)

Where μ_{\min} , μ_{\max} , μ_t are minimum, maximum and parting of defect and background corresponding degree of membership function respective in fiber defect image. It can be seen by equation (19), the range of $[\mu_t, \mu_{\max}]$ is amplified to $[\mu_t, 1]$ using fuzzy enhancement operator non-linear transformation, and enlargement μ_{ij} value, which be close to 1. At the same time, the range of $[\mu_{\min}, \mu_t]$ is amplified to $[0, \mu_t]$, and decrease μ_{ij} value, which be close to 0. At last, it can get spatial domain image by do inverse transform for enhanced fuzzy characteristics, expression is shown as follows:

$$X'_{ij} = \begin{cases} t\sqrt{2\mu'_{ij}} & X_{ij} \le t \\ x_{\max} - (x_{\max} - t)\sqrt{2(1 - \mu'_{ij})} & X_{ij} > t \end{cases}.$$
(20)

Experiment

The method of this paper was used for typical fiber defect infrared image processing, some common image enhancement method including gray scale transformation and histogram equalization was compared. The gray scale transformation method update pixel gray by point operation and expand image contrast and enhance characteristic. Histogram summarize all image gray scale content, at once modify all portion gray proportionate relationship by reform histogram, which it can get the aim of improving some object contrast.

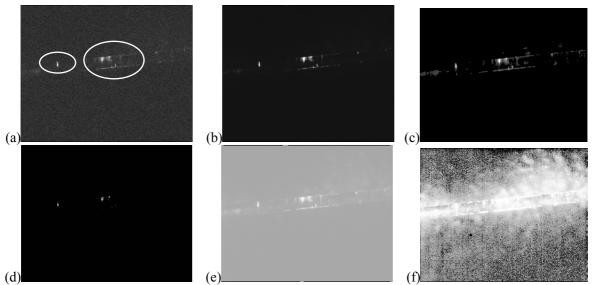


Fig 2. Processing result of fiber defect image enhancement: (a) Original image with defect, (b) The method of this paper, (c) linear transformation, (d) Exponential transform, (e) Log transformation, (f) Histogram equalization

As shown in Figure 2, these are the enhancement processing result of typical fiber defect image by different enhancement methods. Where (a) is infrared image including defect, (b) is processing result of this paper, (c) is processing result of gray scale linear transformation, (d) is processing result of exponential transform, (e) is processing result of log transformation, (f) is processing result of histogram equalization. We can conclude by the processing result that it can get different enhancement results by linear transformation choosing different transformation range; it needs repeated trials to get better enhancement result. Exponential transform make the defect image very dark, part defect detail couldn't be distinguished. Log transformation make total image gray scale height, the vast majority of defect region unable be distinguished. Histogram transform make the defect getting a certain extent enhancement, but histogram equalization couldn't take into account image content, which make part region too height or too dark, so the result is unsatisfactory. Comparatively speaking linear transformation, exponential transform, log transformation and histogram equalization transformation processing results couldn't satisfied enhancement request. The image enhancement results of sub region fuzzy algorithm based on bias-normal distribution index heighten contrast of image defect and background, which can strengthen image outlines information and these processing make defect characteristics enhance of image interest region. At the same it overcome fault of part gray information loss and degree of membership function amount of calculation big of the Pal method.

Conclusion

In order to overcome the question of part gray information loss when do image enhancement by fuzzy algorithm, the best segment threshold based on bias-normal distribution index was put forward, so then carry on part fuzzy processing. Experimental proof of the processing result of some common enhancement algorithm and the method that was used to fiber gyroscope infrared image enhancement processing that defect could be outstanding by the suggested method, and it not only could preferable restrain background and noise amplify but also do not reduce object details. Object outline was obvious outstanding and object brightness was raised; gray scale of background was reduced.

References

- [1] Wei Wang. Introduction of the interferometer fiber optic gyroscope technology. Beijing: China Aerospace Press, 2010. (in Chinese)
- [2] Baoping Wang, Huailiang Liu, Nanjing Li. Infrared and Laser Engineering, vol. 26, pp, 626-631, May 2007. (in Chinese)
- [3] Jerome M., Azeddine B. New interpretation and improvement of the nonlinear anisotropic diffusion for image enhancement. IEEE Transactions Pattern Analysis and Machine Intelligence, vol. 21, pp, 940-946, September 1999.
- [4] Wang B. P., Liu H. L., Li N. J. Journal Of XiDian University, vol. 32, pp, 307-313, February 2005. (in Chinese)
- [5] Pal S.K., King R. A. On edge detection of X-ray images using fuzzy sets. IEEE Transactions on Patt Anal and MachineIntell, vol. 5, pp, 69-77, January 1983.
- [6] Hui Wang, Jihong Zhang. Acta Electronica Sinica, vol, 28, pp, 145-147, January 2000. (in Chinese)
- [7] Guo Chen, Hongfu Zuo. PR&AI, vol, 15, pp, 465-472, April 2002. (in Chinese)

Adaptive Pixel Crosstalk Compensation for CMOS Image Sensor

Changrui Zhao¹, Xiaoming Chi², Zhenyu Wang¹, Wei Yan¹, Dong Li³

¹Peking University, No.5 Yiheyuan Road Haidian District ,Beijing
²Jing Meng Hi-Tech Mansion, Shangdi East Rd 5-2#, Haidian District ,Beijing
³No.28,Xianning West Road, Xi'an, Shanxi
^azhaocr@pku.edu.cn, ^bSimon.Chi@analog.com, ^czw@ss.pku.edu.cn,
^dyanwei@ss.pku.edu.cn, ^eIddyx123@126.com

Keywords: Pixel crosstalk compensation; Image frequency; Human visual system

Abstract. A new algorithm for removing pixel crosstalk in CMOS image sensors with Bayer color filter array was proposed. The algorithm can estimate low/high frequency image and provide adaptive threshold based on the human visual characteristics. By simulation experimentation on Macbeth color checker, resolution checker and real image, the experimental results revealed that this algorithm can remove the pixel crosstalk effectively.

Introduction

Crosstalk is a painful problem we faced in image processing. It decreases the dimensional resolution in an image sensor array, degrades entire sensitivity, and makes poor color separation, and brings additional noise in the image after color correction procedure. In general, the factors contributing to pixel crosstalk are usually as follows. Firstly, the spectral crosstalk is due to imperfect color filters passing through some amount of unwanted light of other colors. Secondly, the optical dimensional crosstalk is due to the neighboring pixels interfere with each other. The primary reason for this element is that the light comes at angles other than orthogonally passes through a filter and can partially be absorbed by the adjacent pixel rather than one below[1].Thirdly, the electrical crosstalk element of crosstalk results from photo-generated carriers having the possibility to move to neighboring charge accumulation sites, and it strongly depends on the pixel structure, collection area, and distribution of sensitivity inside a pixel.



Fig. 1 Image signal processing system

A typical image signal processing system with one-sensor CMOS imager, as shown in Fig.1, consists of three parts: optical part, analog part and digital part. The optical part consists of lens and color filter array (CFA) which are used to filter the incident light so that each sensor element is only exposed to one of the primary colors(Red, Green and Blue). The analog part is composed of an array of CMOS sensor elements, read-out circuits, amplifiers and ADC. The digital part will process the digital signal with sensor compensation, color interpolation and quality enhancement to produce the color image[2,3].

Conventionally, the spectral crosstalk, optical crosstalk, and electrical crosstalk can be reduced by micro-lens optimization, isolation layer inside the photo-diode and layout structure. Those techniques to optimize the characteristics of image pixel often accompanied with high cost. So the based algorithms are proposed to compensate the pixel crosstalk. We can use the local windows of Bayer format with algorithm to reduce the crosstalk after color interpolation to get high quality image[4], and the windows as shown in Fig.2.

This paper proposes an adaptive threshold to estimate low/high frequency image part based on human visual. This algorithm compensates the G component of raw data with the local windows of

Bayer format. This paper compares the different algorithms of compensation pixel crosstalk. A new algorithm is described for compensating the pixel crosstalk and experimental results are presented. The paper achieves a conclusion.

G ₁	R ₁	G ₂	R ₂	G3
B ₁	G4	B ₂	G ₅	B ₃
G ₆	R3	G ₇	R ₄	G ₈
B4	G9	B ₅	G ₁₀	B ₆
G ₁₁	R ₅	G ₁₂	R ₆	G ₁₃

G ₁	B ₁	G ₂	B ₂	G3
R ₁	G4	R ₂	G5	R ₃
G ₆	B ₃	G ₇	B4	G ₈
R ₄	G9	R ₅	G ₁₀	R ₆
G ₁₁	B ₅	G ₁₂	B ₆	G ₁₃

(a) The central pixel G_7 is Gr (b) The central pixel G_7 is GbFig.2 The 5×5 local windows of Bayer format image

Analysis of the existing algorithm

In this section we analyze and summarize the existing algorithm for reducing the crosstalk. All the color images can be acquired through the same color interpolation after the crosstalk compensation. Algorithm I proposes to remove the crosstalk using the following formula:

$$G_7^{new} = \frac{G_4 + G_5 + G_9 + G_{10}}{4} + \frac{(8+4) + [2(G_2 + G_6 + G_8 + G_{12}) + G_1 + G_3 + G_{11} + G_{13}]}{16}$$
(1)

Algorithm II suggests to remove the crosstalk using the following formula: For the Fig 2(a):

$$G_7^{new} = G_7 + (\overline{Gb} - \overline{Gr})/2 \tag{2}$$

$$Gb = (G_4 + G_5 + G_9 + G_{10})/4$$
(3)

$$Gr = (G_1 + G_2 + G_3 + G_7 + G_8 + G_9 + G_{11} + G_{12} + G_{13}) / 9$$
(4)

For the Fig 2(b):

$$G_7^{new} = G_7 + (\overline{Gr} - \overline{Gb}) / 2 \tag{5}$$

$$Gr = (G_4 + G_5 + G_9 + G_{10})/4$$
(6)

$$\overline{Gb} = (G_1 + G_2 + G_3 + G_7 + G_8 + G_9 + G_{11} + G_{12} + G_{13})/9$$
(7)

Algorithm III proposes an adaptive edge-preserving filter to remove the effect of crosstalk with the following formula:

$$G_7^{new} = G_7 + (d_2 - d_1)/2 \tag{8}$$

$$d_1 = (\beta_1 + \beta_2) / 2 \tag{9}$$

$$d_2 = (\beta_3 + \beta_4)/2 \tag{10}$$

$$\beta_{1} = SMF(G_{1} G_{3} G_{7} G_{11} G_{13})$$
(11)

$$\beta_2 = SMF(G_2 \ G_6 \ G_7 \ G_8 \ G_{12}) \tag{12}$$

$$\beta_3 = SMF(G_4 \ G_5 \ G_{10}) \tag{13}$$

$$\beta_4 = SMF(G_4 \ G_9 \ G_{10}) \tag{14}$$

Algorithm IV compensates the G component of raw data with the adjacent R or B components before interpolation. The detail for the figure 2(a) as following formula:

$$G_7^{new} - R = G - R \tag{15}$$

$$R = (R_3 + R_4)/2$$

$$\overline{G} = (G_1 + G_2 + G_3 + G_6 + G_7 + G_8 + G_{11} + G_{12} + G_{13})/9$$
(16)
(17)

$$R = (R_1 + R_2 + R_3 + R_4 + R_5 + R_6)/6$$
(18)

For the figure 2(b), we can take the same way to compensate the center pixel G.

Algorithm I and Algorithm II are easy to achieve. But the result is unsatisfactory after color interpolation because the color will be redder. Algorithm III is good at handling the high frequency image, while it works poor in processing the low frequency one. On the contrary, algorithm IV does well in handling the low frequency image, while it performs poor in processing the low frequency one.

The adaptive low/high frequency image processing (AL/HP)

Based on the change of the image gray degree, we can divide an image into high frequency part and low frequency part. The existing algorithm can only do well in processing one of the parts. The AL/HP algorithm are proposed to simultaneously estimate low/high frequency image and provide adaptive threshold based on the human visual characteristics for crosstalk reduction.

		G2					G2					G	2 ^{L3}		
	G ₄		G₅			G	d3 d2	G₅			G44			G₅L2	
G ₆		G7		G ₈	G ₆ -	d8	G	d1	-G ₈	G ₆		9			-G ^{L1}
	G9		G ₁₀			G ^{d7}	d6 d5	G ₁₀			G			G ₁₀	
		G ₁₂					G ₁₂					G	12		

(a) cell block diagram (b)compute gradient (c) compute direction Fig.3 Gradient and Direction compute block diagram

Firstly, we use Bayer format center pixel G7 and the eight nearest G pixels, that is $G_2G_4G_5G_6G_8G_9G_{10}G_{12}$, to acquire the gradient value and its direction, as shown is Fig.3(a). Then the parallel pixels' gray mean values in close regions are deployed to calculate threshold. Finally, the threshold are compared with human visual' sensitive formula. According to the compared results, we use corresponding algorithm to compensate crosstalk.

In Fig.3(b), d1, d2, d3, d4, d5, d6, d7, d8 are defined as the absolute grey subtraction value of G7 and close G pixels. That is $d1=|G_8-G_7|$, $d2=|G_5-G_7|$, $d3=|G_2-G_7|$, $d4=|G_4-G_7|$, $d5=|G_{10}-G_7|$, $d6=|G_{12}-G_7|$, $d7=|G_9-G_7|$, $d8=|G_6-G_7|$. Actually, we defined four directions. As shown in Fig.3(c), L1, L3, L2, L4 are respectively horizontal direction, vertically direction, and two diagonal directions.

To calculate the maximum threshold, firstly, we need to assure the maximum pixel grey gradient changing direction in the four directions. That is the maximum value of d1 + d8, d2 + d7, d3 + d6, d4 + d5 and we define its direction Lmax. Then observing the perpendicular direction of Lmax, and we calculate the threshold. For instance, if d4+d5 is the maximum value, Lmax=L3, and the threshold mdavg can be computed as following:

$$average = |G_4 + G_7 + G_{10}|/3 \ averge1 = |G_2 + G_5 + G_8|/3 \ average2 = |G_6 + G_9 + G_{12}|/3$$
(19)

$$davg1 = |average - average1| davg2 = |average - average2| mdavg = max(davg1, davg2)$$
(20)

If the threshold to judge the high/low frequency is fixed, the result of the gradient judgment will be incorrect. Consequently it's easy to produce false edge. The human visual system is insensitive to noise in the bright area, however, be sensitive to the noise of edge or structured region. Based on this characteristic, high/low frequency threshold can be changed through self-adaption algorithm as following formulas:

$$g(x) = -0.001738x^2 + 0.000072x + 15 \qquad 0 \le x \le 48$$
(21)

$$g(x) = -0.000491x^{2} + 0.125635x - 2.030474 \qquad 48 < x \le 206$$
(22)

$$g(x) = -0.009579x^2 + 4.885464x - 595.896710 \quad 206 < x \le 255$$
⁽²³⁾

Comparing the values of $|mdavg - g(G_7)|$ to decide which algorithm can be used for the Bayer format. Assuming $mdavg \leq g(x)$, taking the following formula to compensate the crosstalk.

$$G_{7}^{new} = ((G_{1} + G_{3} + G_{11} + G_{13}) + \sqrt{2} \times (G_{2} + G_{6} + G_{8} + G_{12}) + 2 \times (G_{4} + G_{5} + G_{9} + G_{10})) \times \frac{1}{8} \times \frac{1}{3 + \sqrt{2}} + \frac{1}{2}G_{7}$$
(24)

Otherwise, if mdavg > g(x), taking the following formula:

$$G_7^{mw} = G_7 + (d_2 - d_1)/2$$

$$d_7 = (B_1 + B_2)/2$$
(25)

$$d_{1} = (\beta_{1} + \beta_{2})/2$$

$$d_{2} = (\beta_{1} + \beta_{2})/2$$
(26)

$$a_{2} = (p_{3} + p_{4})/2$$

$$B = SMF(G, G, G, G, G_{4})$$
(27)

$$p_1 = SMF(G_1 \ G_3 \ G_7 \ G_{11} \ G_{13})$$

$$\beta = SMF(G_1 \ G_2 \ G_2 \ G_3 \ G_3)$$
(28)

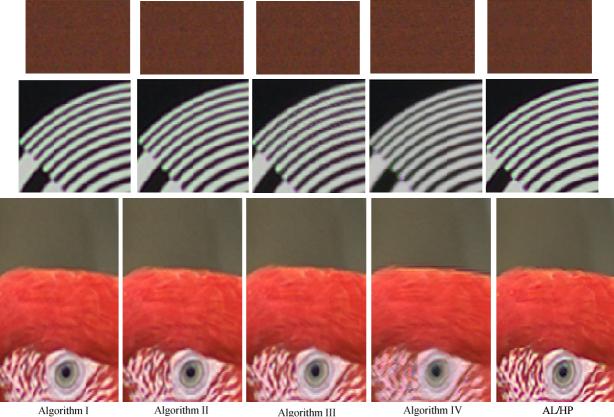
$$\rho_2 = SMF(G_2 G_6 G_7 G_8 G_{12})$$
(29)

$$\beta_3 = (G_4 + G_5 + G_{10})/3 \tag{30}$$

$$\beta_4 = (G_4 + G_9 + G_{10})/3 \tag{31}$$

Experimental Results

In this experiment, three figures are processed by a common color interpolation algorithm after handling by different algorithms. By comparing, the AL/HP algorithm has much better effect in high frequency image than other four algorithms, especially better than the algorithm III, as shown in Fig.4. Likewise, the result acquired by AL/HP algorithm in low frequency image also looks better, especially better than the algorithm IV.



Algorithm I

Algorithm II

AL/HP

Fig.4 Processed image with the same color interpolation

Conclusions

This paper comes up with a new algorithm for the purpose of eliminating the crosstalk. The result of AL/HP algorithm are compared with the other algorithms. It draws a conclusion that we can use a self-adaption threshold value judgment to divide the image into two parts, high frequency part and low frequency part, employing different ways to process the two parts respectively. By this method, we achieve the expected superior effect in handling images.

Acknowledgements

Industry-university-research cooperation of Jiangsu province 2013018.

References

- [1] Agranov G, Berezin V, Tsai R H. Crosstalk and microlens study in a color CMOS image sensor. Electron Devices, IEEE Transactions on, 2003, 50(1): 4-11.
- [2] Chiu S K, Lin C Y, Lu M L, et al. Adaptive edge-preserving filter for CMOS image sensor cross-talk compensation[C]//Digital Signal Processing Workshop, 12th-Signal Processing Education Workshop, 4th. IEEE, 2006: 580-584.
- [3] Li W, Ogunbona P, Shi Y, et al. CMOS sensor cross-talk compensation for digital cameras. Consumer Electronics, IEEE Transactions on, 2002, 48(2): 292-297.
- [4] Jian Z, Suying Y, Jiangtao X. Pixel cross-talk compensation for CMOS image sensors[C]//Intelligent Information Technology Application, 2009. IITA 2009. Third International Symposium on. IEEE, 2009, 2: 165-168.

A Clock Optimization Method in The Digital Zooming of The Image Signal Processing System

Dong Li^{1, a}, Xiaoli Wang^{1,b}, Simon Chi^{2,c}, Changrui Zhao^{3,d} and Bin Yang^{1,e}

¹Xi'an Jiaotong University, Xi'an, Shaanxi, China

²5-2 Shangdi East Road, Beijing, China

³Peking University, Beijing, China

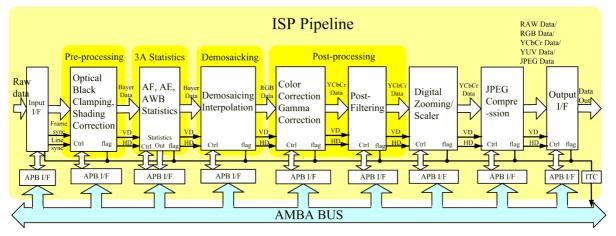
^alddyx123@126.com, ^bxlwang@mail.xjtu.edu.cn,^csimon.chi@analog.com, ^dsuccesszcr@qq.com, ^ekbby81@126.com

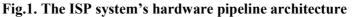
Keywords: ISP, digital zooming, clock optimization, FIFO

Abstract: We address the problem of producing an enlarged picture from a given digital image (zooming). We propose a method that tries to take into account the difficulty to apply the very fast clock in the digital zooming unit of an ISP system. The ISP system hardware is realized in the FPGA and the zooming algorithm is parabola interpolation architecture. This paper presents an optimization method by using a synchronization FIFO to greatly reduce the clock frequency of the digital zooming unit, and by this the power consumption is also decreased significantly.

Introduction

A camera image processing system that performs zooming and full color image reconstruction for single-sensor digital cameras is introduced. The ISP system in the camera processes the digital image data which come from the ADC unit. The ISP system's tasks mainly include: Shading Correction, Bad Pixel Correction, Demosaic Interpolation, Color Correction, Gamma Correction, Auto Exposure, Auto White Balance, Auto Focus, Post Processing, Digital Zooming, JPEG Compression, etc. The ISP system's hardware pipeline is shown in Fig. 1.





Compact and low-cost single-sensor solutions often lack optical zooming capabilities and thus depend on digital techniques. However, the computational power required for high-quality output using traditional techniques is generally too prohibitive to implement in such devices[1]. This paper focuses on the high-quality zooming result of the digital zooming unit. It realizes the Parabolic Farrow zooming algorithm in hardware and optimizes the clock.

Digital zooming

The essence of the digital zooming is that creating many new pixels according the surrounding pixels information, so it increases the pixels amount in the image, and the image looks larger than

before. The Fig.2 explains the digital zooming in brief, we call the region to be zoomed ROI (Region of Interest). Because the digital zooming zooms the ROI as large as the camera's screen, the location of the ROI can be calculated through the screen's area and enlargement factor[2]. Suppose screen's area is $W \times H$, both horizontal and vertical enlargement factor are M/N(usually M is greater

than N) and ROI is in the centre of the screen, thus the start of ROI is $\left(\frac{W}{2} \times \frac{M-N}{M}, \frac{H}{2} \times \frac{M-N}{M}\right)$,

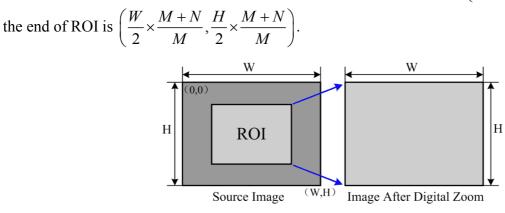
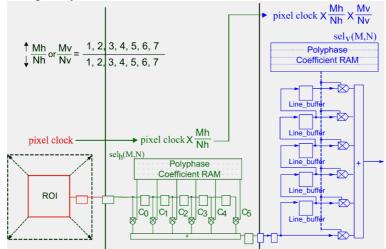


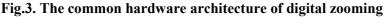
Fig.2. Digital zooming diagram

The zooming unit in this paper uses the parabola interpolation algorithm[3], and this unit with the others in the ISP system are realized in the FPGA.

The common hardware architecture of digital zooming

The Fig.3 displays the common hardware architecture of digital zooming that both horizontal and vertical magnify clock frequency.





Because this ISP is a real-time processing system, when the image data being transmitted arrive in the ROI, the horizontal filters begin to work. After finishing transfer of a row data of the ROI, the logic circuit completes the interpolation and increases the row image data. Thus the horizontal data amount become M/N times the ROI's, and the horizontal filters clock frequency equals to M/N times original pixels clock frequency. Every row data through horizontal interpolation are sent to a linebuffer. When the fifth row data are being sent, the data in former four linebuffers are used to do vertical interpolation process. So the vertical data amount also become M/N times the ROI's, and the vertical filters clock frequency equals to M/N times horizontal filters', therefore times original pixels clock frequency.

Provided that M/N equals to 3 and pixels clock frequency is 50MHz (which is relatively not high), so we need a 450MHz clock frequency in the zooming unit. It's hard to communicate with others low speed units, and the power consumption will be high.

The optimized hardware architecture of digital zooming

We notice that the pixels out of the ROI are redundant information, so we can desert them. If we can take full advantage of this idle time, a low speed clock will be used to do the interpolation process. In order to achieve, the synchronization FIFO can be employed. This paper inserts a FIFO only in the horizontal. This is a trade off so that fewer hardware resources will be used. As the Fig.4 shows:

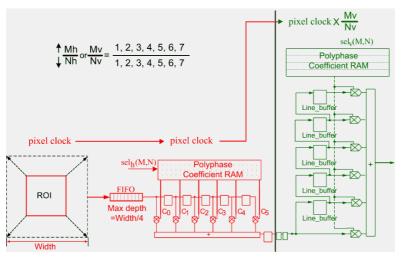


Fig.4. The optimized hardware architecture of digital zooming

The operating principle in Fig.4 is much similar to the one in Fig.3.The differences is that the horizontal filters clock frequency equals to 1 time original pixels clock frequency, and the vertical filters clock frequency equals to M/N times pixels clock. So the clock frequency in zooming unit is reduced greatly.

The optimal synchronization FIFO depth can be calculated. If the pixels clock frequency is , then its clock period is

$$T = \frac{1}{f}.$$
 (1)

Based on the analysis in the *Digital zooming* part of this paper, the horizontal pixels amount inside of the ROI is

$$P_{ROI} = W \cdot N/M \ . \tag{2}$$

The time spent to store these pixels to the FIFO is

$$T_{store} = P_{ROI} \cdot T$$
.

Because of the horizontal interpolation, the time spent to fetch one pixel from the FIFO is $t_{fetch} = T \cdot M/N.$ (4)

In the time of , the amount we can fetch from the FIFO is
$$P_{fetch} = \frac{T_{store}}{t_{fetch}} = W \cdot \left(\frac{N}{M}\right)^2.$$
(5)

For the FIFO can't overflow, its depth at least is

$$D = P_{ROI} - P_{fetch} = W \cdot \frac{N}{M} \cdot \left(1 - \frac{N}{M}\right) \le \frac{W}{4}.$$
 When $\frac{M}{N} = 1/2$, it's an equation. (6)

Therefore, when FIFO depth equals to a quarter of original image's width (or horizontal pixels amount) W, it won't overflow.

Conclusions

This paper comes up with a clock optimization method based on the hardware architecture of digital zooming. In the horizontal, a synchronization FIFO, with the depth equals to ¹/₄ linebuffer's width, is inserted to reduce the zooming unit clock frequency considerably. For example, this optimized

(3)

hardware architecture can enlarge the image to 9 times only using 3 times pixels clock frequency.Fig.5 shows the enlargement result by applying the ISP in the FPGA.

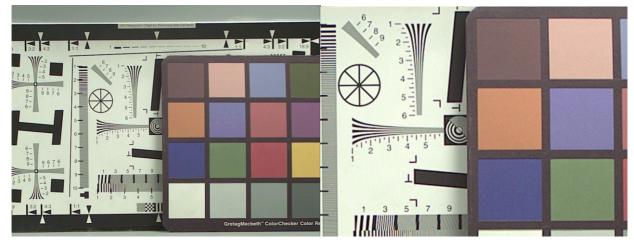


Fig.5. Zooming result

References

- Lukac, R.; Martin, K.; Platanoitis, K.N. : IEEE Transactions on Consumer Electronics. 2004, 50(1)
- [2] S. Battiato; G. Gallo; F. Stance: Image and Vision Computing. 2002, 20(11)
- [3] Kh. Rahsepar Fard: Applied Mathematical Sciences. 2013, 6(94)

A Novel Rapid Full-view Measuring Method by Coded Structured Light

Haibin Wu^{1, a}, Liang Tian¹, Beiyi Wang¹, Chao Liu¹, Yan Wang¹

and Zhenyu Wang¹

¹The higher educational key laboratory for Measuring & Control Technology and Instrumentations of Heilongjiang province, Harbin University of Science and Technology, Harbin, 150080, China

^awoo@hrbust.edu.cn

Keywords: coded structured light, registration target, orthogonal Gray code, color correction

Abstract. Point cloud registration is necessary to acquire full-view data in coded SL three-dimensional measurement, based on single-view measured data. Aiming at surface feature of metal parts or human body, matching point pair construction principle, and transition matrix optimization method are analyzed. First, auxiliary-stereo-target registration principle and device are presented to establish matching point pair, and least-squares ill solution and iterative misconvergence caused by coplanar matching points can be avoided. Second, ICP method is adopted for acquiring transition matrix, and then mismatch point pair rejection method based on orthogonal Gray code principle is designed to increase iterative convergence. Experimental results show, registration error is about 0.8mm, close to that of global camera method and higher than that of surface method. This method has no influence on measured surface, and simplifies measurement device.

Introduction

In coded SL measurement, to some large measured surface, restricted by camera field, single-view measurement range is not large enough, so we should measure the surface separately, and then merge measured local data into a global coordinate system, namely point cloud registration, which is the key of panoramic measurement [1, 2].

At present, high accurate registration methods [3-5] include: 1. precision machinery registration. Relationship between each coordinate system can be acquired from precision machinery directly, which reflects transition matrix between measurement device and measured surface. The method has high measurement accuracy while low measurement efficiency, because it is hard to accomplish 6-DOF registration only by rotation and translation along specific direction. 2. Electromagnetic tracking or laser tracking registration. Optical or electromagnetic location equipment is adopted to registration, so complexity of system and cost are increased greatly, and error component is introduced. 3. Matching point registration. There are two types named surface method and global camera method. The former pastes matching points on measured surface, and acquires transition matrix by tracking and matching them. It is not suitable for soft and damageable surface, and loses information under matching points; The latter pastes matching points on measurement device, whose orientation is captured by located global camera. Its disadvantage is the same as method 2.

Registration accuracy of these methods is about 0.x mm, that is comparative to accuracy of SL measurement device.

Aiming at characteristic of mental parts and human body, this paper plans to present a novel registration method with comprehensive advantages mentioned above, namely high efficiency, high accuracy, no introduced equipment and no influence to measured surface.

ICP method based on orthogonal Gray code

According to the matching-relation between several matching points, we can get the transformation matrix, then apply registration to all 3D data. The typical algorithm includes direct calculating algorithm, quaternion algorithm and iterative closest point algorithm. And the accuracy of iterative closest point algorithm [6] is the highest one.

In order to avoid the iteration into local extremum, the running speed of the ICP algorithm and global optimal convergence largely depend on the given initial transform estimate and the establishment of corresponding relation in the process of iteration. The method of establishing corresponding relationship mainly includes point-point, point to projection, and point to surface. The accuracy of point to surface algorithm is the highest in the three kinds of methods, but because it needs to compute the projection of point on the corresponding tangent plane, the running speed is slow.

Using the above mentioned methods to establish the corresponding points set will result in error corresponding points. This situation is especially obvious at the beginning of the iteration. The common method of removing error corresponding points mainly includes constraint method that based on the surface geometric feature, and constraint method that based on the rigid motion consistency. But such methods have many limitations and low running speed. So this paper presents the ICP method based on orthogonal Gray code. The steps are as follows:

1. Calculating the initial coordinate transformation relation R(0) and T(0) according to the matching point;

2. Calculating the data $\{m_i | i=1, 2, L, N_p\}$ under the perspective of P and the closest point under the perspective of Q. Judging $m_i(k)$ and $m_i'(k)$ are effective corresponding points according to the efficient point determination principles. Further, we can extract the set of corresponding points which from the overlap of perspective P and Q. These set are $\{m_i | i=1, 2, L, N_k\}$, $\{m_i'(k) | i=1, 2, L, N_k\}$, $N_k \le N_p$.

3. Removing the pairs of corresponding points according to orthogonal Gray code. If the orthogonal Gray codes of two corresponding point differ a stripe in horizontal or vertical direction (meet any direction), that means they belong to different stripe. Then we can ensure these corresponding points are wrong.

4. Solving the coordinate transformations R(k) and T(k) according to the two point sets $\{m_i | i=1, 2, L, N_k\}, \{m_i'(k) | i=1, 2, L, N_k\}$.

5. Calculating the objective function E(k) in equation (1).

$$E(k) = \sum_{i=1}^{Nk} \left\| m'_i(k) - \left[R(k)m_i + T(k) \right] \right\|^2$$
(1)

6. If $E(k-1)-E(k) \ge \varepsilon$, where ε is a given convergence precision, then k=k+1 and go to step 2. If $0 \le E(k-1)-E(k) < \varepsilon$, then recording R(k) and T(k), the program ends.

Auxiliary three-dimensional target method

Now, the methods to obtain corresponding points mainly include surface method and global camera method. This paper presents a method of auxiliary three-dimensional targets in order to overcome the lack of existing method of registration and devices. And it balances the influence of speed and precision of registration and the degree of complex, etc. This paper designs an auxiliary method of auxiliary three-dimensional targets. As is shown in figure 1(a), we design a normal hexahedron auxiliary target and set matching points on it. When we do registration, place the auxiliary three-dimensional targets near the measured surface and ensure the relative location of the two fixed. In this way, it's equivalent to set a matching point in the extension of the measured surface. Then the registration is finished. Three-dimensional target is different with planar targets, because it consists of six position-fixed and certain surfaces. When measuring panoramic scene, single perspective camera may takes any surface of the auxiliary three-dimensional targets. Color on six planes is different.

The characteristics of the method are as follows:

It solves the problem that can't set matching points. And it does not need additional auxiliary equipments.

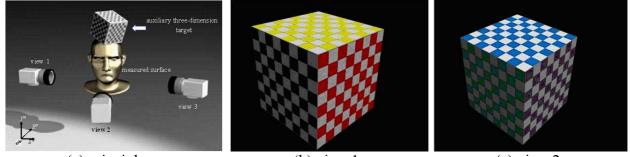
1. The matching points are not on the surface. In theory, the accuracy of registration is slightly lower than set matching points on surface. But we can adjust the initial relative position between surface and target, in order to make the matching points much closer to the surface. And the result by using the method to measure the distance between the matching points and surface can't be greater than by using the method of global camera. Therefore, the accuracy of registration can not be less than the result of global camera. However, it remains to be verified in lab.

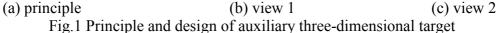
2. We design the auxiliary target that is set a matching point on every surface of the hexahedron. It can be shot from any perspective. That means we can achieve an image that contains the matching points in any angle when shooting. Even if adjacent measurement perspective image does not contain the same matching point on one surface, the we can also acquire registration, because we can solve the spatial relations of the point on different surface according to the different color surface.

3. We void the matching point that in the same plane which can lead to pathological least squares solution or no convergence of iterative operation.

4. The concrete technical scheme is as follows: the stereo registration block is metal material hexahedral. Each surface of the normal hexahedron is divided into eight lines, eight columns in grid. And there are only bright-and-dark grids. The color of each surface is different: 1-black, 2-red, 3-yellow, 4-green, 5-blue, 6-purple. 1-black corresponds to 4-green; 2-red corresponds to 5-blue; 3-yellow corresponds to 6-purple.

As be described in this paper, when using the three-dimensional registration block we should try to place it near the object. Face 3 or 4 should be placed as bottom. On any surface, all light or dark grids can be used as a matching point when doing registration, as is shown in figure 1(b), (c).





In this paper, cloud registration method based on auxiliary three-dimensional target point is to treat corner points on target as matching points and then combine with ICP algorithm.

Experiment

For the experimental data, we can evaluate the contact ratio which be effected by the degree of coincidence that from the result of the matching point coordinate transformation. Five specific points are set up as evaluation points on the measured surface, which can evaluate contact ratio accuracy according to their degree of coincidence in different view clouds of measurement points.

We have already known standard coordinate of any point in the simulation environment. By using measurement coordinates or standard coordinates of three index points to calculate the transform matrix, measurement errors will be evaluated respectively in two conditions when be included in contact ratio errors or be excluded from contact ratio errors.

The contact errors from five evaluation points are shown in table 1 and table 2.

According to the experimental results: 1. coincide accuracy of auxiliary 3D target method is slightly lower than surface method, that has proved the theoretical analysis; 2. coincide error is close to the measurement error but slightly greater than the measurement error in the simulation environment; 3. It illustrates coincide errors are mainly coming from measurement, concretely coming from image positioning errors of matching points. The factors of errors in the simulation environment are less. ICP displays obvious advantage, and even just using quaternion, coincide accuracy is almost the similar to ICP. The features of ICP is using the advantage of multi-point fitting, further averaging coincide accuracy.

Table	e 1 Contact e	rrors based or	measured po	oints (mm)	
	1	2	3	4	5
Surface method	0.034	0.033	0.033	0.038	0.035
Global camera method	0.035	0.033	0.035	0.039	0.037
Auxiliary 3D target method	0.033	0.033	0.035	0.037	0.036
Tabl	le 2 Contact e	errors based of	n standard po	ints (mm)	
	1	2	3	4	5
Surface method	0.016	0.015	0.018	0.018	0.011
Global camera method	0.019	0.017	0.022	0.019	0.016
Auxiliary 3D target method	0.017	0.016	0.019	0.019	0.016

There is no coincide error in the simulation environment by using multi-point fitting. Indeed, it will introduce other errors and lead to the decline of coincide accuracy. It is not agree with the physical truth. Registration error evaluated by method mentioned above in reality is about 0.8mm.

Conclusions

This paper presents auxiliary-stereo-target registration principle to establish matching point pair, and orthogonal Gray code based ICP method to reject mismatching point pair. Experimental results show, registration error is about 0.8mm, close to that of global camera method and slightly higher than that of surface method. The registration accuracy and target characteristic are suitable for mental part and human body, more over no auxiliary equipment added. The future work will focuses on modify target shape, so as to reduce distance between measured surface and target, and improve registration accuracy.

Acknowledgement

The article studies by the Education Department of Heilongjiang province science and technology research projects (12521069) funding.

References

- J. Pages, J. Salvi, R. Garcia. Overview of coded light projection techniques for automatic 3D profiling. IEEE International Conference on Robotics and Automation, Vol. 1 (2003), p. 133-138
- [2] Pribanić T, Mrvoš S, Salvi J: Image and Vision Computing, Vol. 28 (2010), p. 1255-1266
- [3] Xi Long, Yuexian Zhong: Journal of Tsinghua University, Vol. 42 (2002), p. 477-480 (in Chinese)
- [4] Guangjun Zhang, Junhua Sun, Zhenzhong Wei, Fuqiang Zhou: Chinese Journal of Scientific Instrument, Vol. 28 (2007), p. 441-445 (in Chinese)
- [5] Xinguo Wei, Tao Liu, Zhen Liu: Acta Optica Sinica, Vol. 33 (2013), p. 12-13 (in Chinese)
- [6] P. J. Besl, N. D. McKay. A Method for Registration of 3D Shapes. IEEE Trans.Pattern Analysis and Machine Intelligence, Vol. 14 (1992), p. 239-259

T 11 1 C

Design and Implementation of Unified DCT/IDCT Architecture Based on **FPGA**

Hai Huang^{1,a}, Jiaming Liu², Xuebin Lu^{1,b}, Bin Yu^{1,c}

¹ School of software Harbin University of Science and Technology, Harbin, China ² Department of Automation, Harbin University of Science and Technology, Harbin, China ^aic@hrbust.edu.cn, ^blxbsw@126.com, ^c277768267@gg.com

Keywords: DCT; IDCT; Unified architecture; Matrix decomposition; FPGA

Abstract. This paper proposes a unified architecture for computation of discrete cosine transform (DCT) and its inverse transform (IDCT). The matrix decomposition algorithm is used to deduce the proposed algorithm. Based on this algorithm, a unified DCT/IDCT architecture is developed. Then, this architecture is modeled in HDL, verified and implemented with FPGA. Experiment results show that the unified DCT/IDCT architecture has low hardware complexity and high calculation accuracy.

Introduction

In the aspect of reducing the correlation of image data, discrete cosine transformation (DCT) is most close to the performance of optimum orthogonal transformation Karhunen-Loev (K-L) transformation. Besides, DCT is easy to realize, so it is widely used in digital image processing and compression domain. There are many fast algorithms for DCT implementation, such as Loeffler algorithm [1], systolic based algorithms [2-4], CORDIC based algorithms [5-7]. Among these algorithms, Loeffler algorithm has fewer multiplications than other algorithms, only 11 multiplications and 29 additions are required. Systolic based algorithms have simple architecture and easy to pipeline. The CORDIC based fast algorithms have low computational complexity and power consumption, and are suitable for VLSI implementation. However, these algorithms all focus on reducing computational complexity, without considering the reconfigurability of the design, such as the unified architecture for computation of both DCT and its inverse transformation (IDCT). In this paper, a DCT/IDCT unified architecture is proposed using the matrix decomposition algorithm. This architecture is simulated in FPGA verification platform. Experiment results show that the proposed architecture has low hardware complexity and high calculation accuracy.

Algorithm description

The *N*-point 1-D DCT of a real data sequence C[k] is defined as:

$$C[k] = \alpha[k] \sum_{n=1}^{N} x[n] \cos\left[\frac{(2n-1)(k-1)\pi}{2N}\right], k = 1, \dots, N$$
(1)

where $\alpha[N] = 1/\sqrt{N}$, and for $\alpha[k] = \sqrt{2/N}$ k = NE

Equation
$$(1)$$
 can be expressed as matrix form as (2) .

$$\dot{Y}^{T} = \sqrt{\frac{1}{8} \cdot F \cdot R \cdot X^{T}}$$
⁽²⁾

Using the orthogonality property of the orthogonal transformation, IDCT can be expressed as (3).

$$X^{T} = \sqrt{\frac{1}{8}} \cdot R^{-1} \cdot F^{-1} \cdot \dot{Y}^{T}$$
(3)

where

$$\dot{Y} = \begin{bmatrix} Y(0) & Y(4) & Y(2) & Y(6) & Y(1) & Y(7) & Y(5) & Y(3) \end{bmatrix}$$
 (4)

			<i>R</i> =	$ \begin{array}{cccccccccccccccccccccccccccccccccccc$	$ \begin{array}{cccc} 1 & -1 \\ 1 & 1 \\ 1 & 1 \\ 1 & 1 \\ 1 & 1 \\ 1 & 1 \end{array} $	$ \begin{array}{cccccccccccccccccccccccccccccccccccc$	$ \begin{array}{cccc} 1 & -1 \\ 1 & 1 \\ 1 & -1 \\ 1 & -1 \\ 1 & -1 \\ 1 & -1 \\ \end{array} $		1	
		0	0	0	0	0	0	0	0	
0 0 0 0 0 0 0 0		0	0	0.92	0.38	0	0	0	0	
	F _	0	0	-0.38	0.92	-0.32	0.21	-0.07	0.51	
0 0 0.92 0.38 0 0 0 0	F=	0	0	0	0	0.91	0.18	-0.38	-0.07	
$\begin{array}{cccccccccccccccccccccccccccccccccccc$		0	0	0	0	-0.18	0.91	-0.07	-0.38	
$\begin{array}{cccccccccccccccccccccccccccccccccccc$		0	0	0	0	0.21	0.32	0.51	0.77	
$\begin{array}{cccccccccccccccccccccccccccccccccccc$		0	0	0	0	-0.32	0.21	-0.77	0.51	

The matrixes in (2) and (3) have same element with different dipositon, so uniform architecture can be used to compute both tranforms by reordering the data flow.

DCT/IDCT architecture implementation

Based on the proposed algorithm, a unified architecture of 1-D DCT/IDCT are presented in this section. According to row-column decomposition theory, 2-D DCT/ IDCT are achieved.

1-D DCT/IDCT architecture

For all elements of matrix R and R^{-1} are 1 and -1, the sign of inputs can be chosen firstly, and then making addition of these eight signed inputs with carry save adder (CSA) and carry lookahead adder (CLA). The fast adder array shows in Fig.1. For realizing matrix multiplication of F and F^{-1} , a multiplier array consist of four multipliers can be used. The fast multiplier array is depicted as Fig.2.

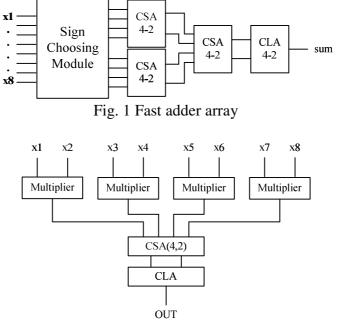


Fig. 2 Multiplier array

Using the above structures, the DCT/IDCT unified architecture is shown in Fig.3. In Fig.3, The operation of multiplying $\sqrt{1/8}$ can be realized by shifting and addition operation.

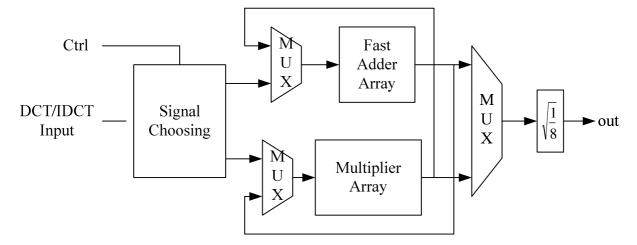


Fig. 3 1-D DCT/IDCT unified architecture

Two 1-D DCT/IDCT modules and one transposed memory is used to develop the 2-D DCT/IDCT using row-column decomposition theory.

FPGA implementation results and conclusions

The function verification is completed in Modelsim 6.5. Test vector are 8 by 8 matrixes of random datum. DCT and IDCT function simulation waveforms are shown in Fig 4 and Fig 5.

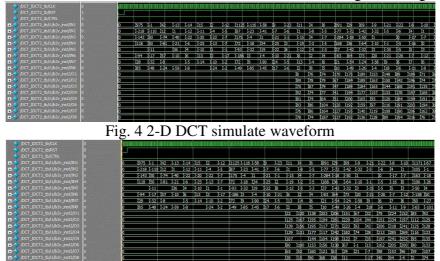


Fig. 5 2-D IDCT simulate waveform

Fig.4 and Fig.5 list the output results of the 2-D DCT and IDCT transformations respectively. The control signal CTRL is used to chose different transformations. Compared with the results from MATLAB, the simulation results have high calculation accuracy and satisfy the requirement of application. Then proposed architecture is implemented with FPGA. The comparisons between 1-D DCT and unified 1-D DCT/IDCT are shown in Table 1.

Table 1 Comparisons of 1-D DC1 and diffied 1-D DC1/IDC1						
	1-D DCT	Unified DCT/IDCT				
Used LE quantity/Available LE quantity	1626/50528	2375/50528				
Utilization	3.2%	4.7%				
	1D DOT					

Table 1 Comparisons of 1 D DCT and unified 1 D DCT/IDCT

The results show that the LE number used in 1D-DCT compared to the one in DCT/IDCT architecture only increase 46%. The number of the register unit doesn't increase.

To verify the practical usability of proposed architecture, the design is modeled in HDL, and implemented in FPGA verification platform. Four 128 by 128 pictures are ussed as test datum, the peak signal-to-noise ratio (PSNR) is used to measure the quality of reconstruction images. The comparison results and corresponding PSNR values are shown in Table 2.

Table 2 Origina	Table 2 Original and reconstruction images and their PSNR								
Picture name	Original Pic	Transformed Pic	PSNR						
Lena			43.0856						
Logo			42.4908						
Peppers			42.7838						
Mandrill	JU.	U	43.1614						

The comparison resulta show that all the values of PSNR are above 42. The proposed architecture has good reconstruction property and high calculation accuracy.

Summary

In this paper, a unified architecture which can be used to compute both DCT and IDCT is proposed. The proposed architecture achieve both DCT and IDCT by reording the data flows accroding to the different transforms. By resuing the uniform processing elements, the proposed architecture has low hardware complexity. The experimental results show that the unified structure only increases 46% of hardware resources compared to DCT. It also has high calculation accuracy.

Acknowledgment

This work was supported by Natural Science Foundation of Heilongjiang Province of China, (Grant No. F201314)

Reference

- [1] Loeffler C, Ligtenberg A. Acoustics Speech and Signal Processing 1989. Page(s): 988-991 vol.2
- [2] Sung Bum Pan and Rae-Hong Park, IEEE Trans. Circuits Syst. Video Tech., vol. 7, no. 2, pp. 413 - 419, Apr. 1997
- [3] L. W. Chang and M. C. Wu, IEEE Trans. Signal Processing, vol. 39, pp. 192 194, Jan. 1991.
- [4] M.H.Lee, IEEE Trans. Circuits Syst., vol. 37, pp. 1321 1323, Oct. 1990.
- [5] Sungwook Yu and Earl E. Swartzlander, IEEE Transaction on Signal Processing, vol. 50, No. 1, Jan 2002.
- [6] B. Das and S. Banerjee, IEE Proc.-Comput. Digit. Tech., vol. 149, No. 4, July 2002
- [7] C.-C. Sun, S.-J. Ruan, B. Heyne and J. Goetze, IET Circuits Devices Syst., vol. 1, No. 6, Dec. 2007

Diffusion-Substitution Mechanism for Color Image Encryption Based on Multiple Chaotic Systems

Tiejun Zhang^{1,a}, Ahmed A. Abd El-Latif^{2,b}, Mohamed Amin², Alaa Zaghloul²

¹School of Software, Harbin University of Science and Technology, Harbin, China.

²Department of Mathematics, Faculty of Science, Menoufia University, Shebin El-Koom 32511, Egypt.

^atiejun.zhang2006@gmail.com, ^bahmed rahiem@yahoo.com

Keyword: Image Encryption, Chaotic Systems, Diffusion, Substitution.

Abstract. In this paper, a new color image encryption mechanism based on multiple chaotic systems is proposed. In the proposal, two modules are achieved by mixing the features of horizontally and vertically adjacent pixels with the help of adopted multiple chaotic systems, respectively. Then, substitution/confusion is accomplished by generating an intermediate chaotic key stream image based on the adopted chaotic maps. Experimental results show that the proposed scheme is able to manage the trade-offs between the speed performance and security requirements.

1. Introduction

How to protect the secret information is an important issue in commercial or military application [1-5]. In this paper, we propose a new color image encryption scheme based on multiple chaotic systems. In the proposed scheme, two modules are achieved by mixing the features of horizontally and vertically adjacent pixels with the help of adopted multiple chaotic systems, respectively. Then, substitution/confusion is accomplished by generating an intermediate chaotic key stream image based on the adopted chaotic maps. Simulation results justify the feasibility of the proposed scheme in color image encryption purpose.

2. Description of the chaotic systems used in the proposal

In the proposed scheme, three chaotic systems are utilized to generate the encryption keys as follows [1, 2]:

(1) The Logistic – Tent system

$$x_{n+1} = \begin{cases} (r x_n (1-x_n) + (4-r) x_n/2) \mod 1 & x_i < 0.5 \\ (r x_n (1-x_n) + (4-r)(1-x_n)/2) \mod 1 & x_i \ge 0.5 \end{cases}$$
(1)

(2) The Logistic-Sine system

$$x_{n+1} = (r x_n (1 - x_n) + (4 - r) \sin(\pi x_n)/4) \mod 1$$
(2)
(3) The Tent-Sine system

$$x_{n+1} = \begin{cases} (r x_n (1-x_n) + (4-r) x_n/2) \mod 1 & x_i < 0.5 \\ (r x_n (1-x_n) + (4-r) (1-x_n)/2) \mod 1 & x_i \ge 0.5 \end{cases}$$
(3)

where $r \in [0,4]$.

3. Proposed scheme

3.1 Encryption scheme

The steps of the proposed encryption scheme is given by the following two steps

(1) Read the original color image as RGB color space $P = \{R_{m,n}, G_{m,n}, B_{m,n}\}$ where $1 \le m \le M$,

 $1 \le n \le N$, M, N are height and width of the plainimage in pixels.

- (2) Perform **Algorithm 1** to generate the diffusion keys using adapted chaotic maps with the correct values as the encryption process.
- (3) Apply Algorithm 2 to perform the horizontally diffusion step.
- (4) Apply **Algorithm 3** to perform the vertically diffusion step.
- (5) Perform Algorithm 4 to generate the confusion keys using adapted chaotic maps (CQ) with the correct values as the encryption process.
- (6) Perform Algorithm 5 by considering the cipherimage and *KCQ* keys as inputs.
- (7) Get the final cipherimage as unintelligible noise color.

Algorithm 1: Generation of the diffusion keys

Input: Initial values of the chaotic maps

Output: Diffusion key sequences

$$K^{\zeta} \in \{K^{R}, K^{G}, K^{B}\}$$
, $K^{R} = floor(S(1) \times 2^{26}) \mod 256$, $K^{G} = floor(S(2) \times 2^{26}) \mod 256$,
 $K^{B} = floor(S(3) \times 2^{26}) \mod 256$

where S(1), S(2) and S(3) are the key sequences generated by the three chaotic maps described before in Section 2.

Algorithm 2: Diffused horizontally image

Input: The original image S = {*RGB*}

Output: Diffused horizontally image DH = {*RGB*}

for i = 1 to M

for *j*=1 to *N*-1

for each
$$\zeta \in \{R, G, B\}$$
 and $K^{\zeta} \in \{K^R, K^G, K^B\}$ do
 $DH_{i,j+1}^{\zeta} = DH_{i,j}^{\zeta} \oplus S_{i,j+1}^{\zeta} \oplus K^{\zeta}$
if $(i < M)$
 $DH_{i+1,1}^{\zeta} = DH_{i,j+1}^{\zeta} \oplus S_{i+1,1}^{\zeta} \oplus K^{\zeta}$
end
ord

end

end end

COMMENT: ζ is one of the color symbols R, G, or B. All the operations in the above algorithm are linear.

Algorithm 3: Diffused vertically image

Input : Diffused horizontally image DH = {*RGB*} Output: Diffused vertically image DV = {*RGB*} for *j* = *N* down to 1 for *i*=*M* down to 2 foreach $\zeta \in \{R, G, B\}$ and $K^{\zeta} \in \{K^{R}, K^{G}, K^{B}\}$ do $DV_{i-1,j}^{R} = DH_{i-1,j}^{R} \oplus DV_{i,j}^{G} \oplus DV_{i,j}^{B} \oplus K^{\zeta}$, $DV_{i-1,j}^{G} = DH_{i-1,j}^{G} \oplus DV_{i,j}^{R} \oplus K^{\zeta}$, $DV_{i-1,j}^{B} = DH_{i-1,j}^{R} \oplus DV_{i,j}^{R} \oplus DV_{i,j}^{G} \oplus K^{\zeta}$

$$DV_{i-1,j}^{B} = DH_{i-1,j}^{B} \oplus DV_{i,j}^{R} \oplus DV_{i,j}^{G} \oplus K^{\zeta}$$

if (j>1)
$$DV_{M,j-1}^{R} = DH_{M,j-1}^{R} \oplus DV_{i-1,j}^{G} \oplus DV_{i-1,j}^{B} \oplus K^{\zeta},$$

$$DV_{M,j-1}^{G} = DH_{M,j-1}^{G} \oplus DV_{i-1,j}^{R} \oplus DV_{i-1,j}^{B} \oplus K^{\zeta}$$
$$DV_{M,j-1}^{B} = DH_{M,j-1}^{B} \oplus DV_{i-1,j}^{R} \oplus DV_{i-1,j}^{G} \oplus K^{\zeta}$$
end

end

end

end

COMMENT: ζ is one of the color symbols R, G, or B. All the operations in the above algorithm are linear.

Algorithm 4: Keys generation using adapted chaotic maps (CQ) **Input** : initial values for the chaotic maps

Output: Keys sequences image *KCQ*

for i = 1 to M

for j=1 to N

$$\begin{split} & KCQ_{i,j}^{R} = (floor(\xi_{1} * S_{i,j+1}(1) + \xi_{2})) \operatorname{mod} 256, KCQ_{i,j}^{G} = (floor(\xi_{1} * S_{i,j+1}(2) + \xi_{2})) \operatorname{mod} 256, \\ & KCQ_{i,j}^{B} = (floor(\xi_{1} * S_{i,j+1}(3) + \xi_{2})) \operatorname{mod} 256 \end{split}$$

end

end

Comment: ξ_1, ξ_2 are two large prime numbers

Algorithm 5: Confusion using adapted chaotic systems Input :Diffused vertically image DV = {RGB} Output: Cipherimage C for i = 1 to M for j=1 to N for each $\zeta \in \{R, G, B\}$ and $KCQ^{\zeta} \in \{KCQ^R, KCQ^G, KCQ^B\}$ do $C_{i,j}^{\zeta} = C_{i,j}^{\zeta} \oplus KCQ_{i,j}^{\zeta}$ end end

end

3.2 Decryption scheme

The decryption can be easily derive from the encryption routine by reverse the steps using the same encryption keys (i.e., reverse the confusion process (Algorithm 5), and reverse the vertically diffusion step (Algorithm 3), then reverse the horizontally diffusion step (Algorithm 2), respectively).

4. Experimental results

4.1 Visual test, sensitivity and entropy

Several images have been adopted in our experiments, USC-SIPI Image Database [5] and computer vision test images [6]. For convenience, the color "DOT" image is taken as an example for our discussion. The encrypted image is shown in Fig. 1 (b). However, with a tiny change in initial condition or control parameter, we cannot decrypt the cipherimage in Fig 1(b) as shown in Fig. 1(c). This illustrated that the proposed scheme is sensitive to tiny change in the keys. For the cipherimage of DOT, the corresponding entropy is grater than 7.99.

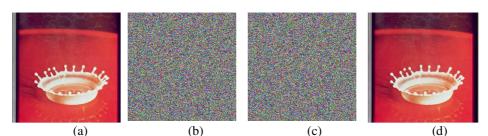


Fig. 1. (a) Original image (b) encrypted image with key 1 (c) decrypted image with wrong key (d) decrypted image correct key 1.

4.2 Performance speed

The proposed color image encryption only needs some simple operations, so, it takes less than 0.2 s to complete the encryption process for an image of 256×256 . The proposed encryption scheme is fast compared to other schemes such as in Ref. [3] and [4], which takes more than 0.5 s for the same image.

5. Conclusion

This paper has proposed an image encryption scheme based on multiple chaotic systems. In the proposed scheme, two diffusion modules are achieved by mixing the features of horizontally and vertically adjacent pixels. Then, substitution/confusion is accomplished by generating an intermediate chaotic key stream image with the help of chaotic systems. Results show that the proposed scheme has good performance.

Acknowledgment

This work was supported by the ministry of Higher Education and Scientific research (Egypt-Tunisia co-operation program 4-13-A1) and GZ11A302 of Heilongjiang Province, China.

References

- A. A. Abd El-Latif, L.Li, T. Zhang, X. Niu, Digital Image Encryption Scheme Based on Multiple Chaotic Systems. International Journal of Sensing and Imaging 13(2) (2012), pp 67-88.
- [2] Y. Zhou, L. Bao, C.L. Philip Chen "A new 1D chaotic system for image encryption", Signal Processing, Volume 97, April (2014), pp 172–182.
- [3] R.Rhouma, S.Meherzi, S.Belghith, OCML-based colour image encryption. Chaos, Solitons & Fractals (40) (2009), pp 309-318,
- [4] X. Huang, Image encryption algorithm using chaotic chebyshev generator. Nonlinear Dynamics Volume 67 (2012), Issue 4, pp 2411-2417.
- [5] Information on http://sipi.usc.edu/database/database.php.
- [6] Information on http://www.cs.cmu.edu/~cil/v-images.html.

Detecting Human Actions by 3D Deformable Parts Models

Ming Yang^{1, a}, Yong Yang^{2,b}

¹Jilin Technology College of Electronic Information,College of information technology, Jilin City, Jilin Province

²Jilin Technology College of Electronic Information, Jilin City, Jilin Province ^a66420890@gg.com, ^b1037903@gg.com

Keywords: Action Recognition; Deformable Parts; Latent SVM; 3D HOG

Abstract: In this paper, we introduce the high performance Deformable part models from object detection into human action recognition and localization and propose a unified method to detect action in video sequences. The Deformable part models have attracted intensive attention in the field of object detection. We generalize the approach from 2D still images to 3D spatiotemporal volumes. The human actions are described by 3D histograms of oriented gradients based features. Different poses are presented by mixture of models on different resolutions. The model autonomously selects the most discriminative 3D parts and learns their anchor positions related to the root. Empirical results on several video datasets prove the efficacy of our proposed method on both action recognition and localization.

Introduction

Last decade, action recognition in video sequence inspired many applications in various practical domains, such as video retrieve, human-machine interaction and video surveillance. The challenging problem continues to attract significant attention from different perspective. The vast majority of existing solutions still focus on bag-of-words description of video clips over space-time domain [1, 2]. Such sparse spatiotemporal representation of videos with conventional machine learning approaches provides an effective recognition to human actions. However, such methods cannot locate the occurrence of event accurately since they ignore the space relationship of features in the model. In this paper, we focus on the problem of action detection in video [3]. The advantage of direct action detection methods is that they can work without any video tracking method as pre-processing or any assumption of the space location of actions.

Deformable Part Models (DPM), which were proposed by Felzenszwalb *et al.* [4], achieved significant high performance in various practical object detection problems [5]. The models exploit the Latent Support Vector Machine (LSVM) algorithm to learn the object detection problem with latent variables in training set. Such latent variables provide the final models high capacity to tackle view change, serious occlusion and deformation in object detection problems. Wang *et al.* first introduced LSVM learning framework into human action recognition problem and proposed the Max-Margin Hidden Conditional Field (MMHCRF) model to deal with latent information in action event [6]. The method optimizes parts of actions on optical flow field as latent variables and converges to a local optimum by the Concave-Convex Procedure (CCCP). However, MMHCRF model relies on the reliable human location methods since it assumes the pedestrian appears in the center of images. To extend DPM into action detection field, Xie *et al.* proposed to detect pedestrians on every frame of video by DPM directly. The structural output of detection is then exploited to predict the human action in video. This method ignores the information over consecutive frames in videos, treating each frame as still image thus leads to mitigated performance.

In this paper, we extend the DPM to 3D framework, proposing to recognize and locate human actions in videos simultaneously. In this way, complicated action events from different perspectives in cluttered background can be learned without and object tracking as assumption. Furthermore, multiple actions from more than one person can also be detected and located simultaneously for

higher-level analysis and video understanding. The utilization of motion features over frames provides our method a better performance than other existing methods.

HOG3D Features

Our method is based on the HOG3D feature [7], which is a 3D video feature extended from 2D Histogram of Oriented Gradients (HOG) features. HOG3D is proposed by Klaser *et al.* for human action recognition at 2008. As 3D spatiotemporal volumetric expand of conventional HOG descriptor, the efficacy of HOG3D has been shown in. In our work, we use HOG3D features with small modifications as representation of video clips.

Each video clip is divided into a fixed number of non-overlapping cuboid cells. For each spatiotemporal cite in the video, we compute the gradients along x, y and t directions to represent the change over spatial image pixels and temporal optical flows. The (dx, dy, dt) gradient orientation vector is projected to a 20-dimensional vector distributed on a regular icosahedron. To smooth the histogram vector, we place a 3D Gaussian filter with different σ on different scales on the center of cell. The histogram is then normalized by L2 norm with rounding 4 cells as in standard HOG framework. Finally, we obtain the feature by concatenating the histograms of all cells. An interest point strategy with 3D Harris point detection as in traditional HOG3D [7] is not employed here. This is because we want to slide our models over different scales on videos, a dense spatiotemporal representation of video is necessary here.

HOG3D can help us to handle the variation of illumination and trivial deformation. During learning stage, we extract HOG3D on 5 different spatial scales for more efficient description of videos. During detection, 10 different scales are considered for a more accurate detection.

Deformable Part Models

Deformable Part Models (DPMs) [4] were proposed by Felzenswalb *et al.* The method has been proven to be quite effective in the field of object detection. Here we briefly review DPM and analyze how to extend the models from 2D to 3D action detection. Given a training set which consists of $\{(X_i, Y_i)\}_{1,...,N}$ as examples and labels, DPM method learns a mixture of deformable models to describe object from different point of views. However, in the case of action recognition, the change of views is not a serious challenge anymore. Here we still use mixture models to represent different poses of action cycles. Assume that the final DPM contains *M* components. Each component consists of one root p_0 and *n* parts $(p_1,...,p_n)$ to describe a pose. The features of root p_0 are extracted directly according to the supervision information from raw video data, while the latent parts $p_j = (x_j, y_j, t_j) \mid j \in \{1,...,n\}$ are utilized to measure spatiotemporal relative position between root and part. Here t_j represents the temporal displacement of action part caused by different frequency of actors. By using $c \in \{1,...,M\}$ as index of mixture components, all latent information can be collected in a latent variable $h = \{c, p_1, ..., p_n\}$.

To describe the global appearance and specific details of actions simultaneously, the root filter p_0 is sited as a bound box which includes the whole body of actor; whereas part filters $(p_1, ..., p_n)$ are sited on higher resolution layer of HOG3D feature pyramid to focus on local details. Root filter and part filters are combined by potential functions in a Conditional Random Field (CRF) as component $c = \{p_0, p_1, ..., p_n\}$. For each vertex $p_j \in c$, a unary potential is defined as result of filter F_j on HOG3D. For a pair of vertices $(p_0, p_j) | j \in \{1, ..., n\}$, we use the spatiotemporal displacement to penalize the part as pairwise potential (v_j, d_j) , where v_j is the 3D anchor point obtained by training and d_j is a 3D Gaussian kernel to measure the spatiotemporal displacement cost of current part. Finally, we can retain a more succinct annotation of the linear perceptron parameters of component c by putting everything together,

$$\beta_{c} = (F_{0}, F_{1}, \dots, F_{n}, d_{1}, \dots, d_{n}, b)$$
(1)

where *b* is the linear bias.

Implementation Details

In this paper, we learn our detection models under the standard CCCP framework, iteratively optimizing the hinge loss function with LSVM method. For class k of actions, following cost function of training set is considered:

$$\begin{split} \min_{\beta_k,\xi} \quad & \frac{1}{2} \|\beta_k\|^2 + C \sum_{i=1}^N \xi_i \\ s.t. \quad & \forall i : Y_i = k : \max_h \left\langle \beta_k, \Psi(X_i, Y_i, h) \right\rangle \ge 1 - \xi_i \\ & \forall i : Y_i \neq k : \max_h \left\langle \beta_k, \Psi(X_i, Y_i, h) \right\rangle \le -1 + \xi_i \\ & \forall i : \xi_i > 0, \end{split}$$

Where ξ is the soft margin, $\Psi(\cdot)$ is the final score of the *i*th example given all action features and latent information.

As initialization of models, we train different action models for different stages of actions without and latent variables separately. Based on learned root filters, we add latent variables into models step by step. First, we add mixture information into models, merging models from different stages together. Then we initialize part filters by choosing most salient parts from root filters with greedy methods, calculating corresponding locations on higher resolution features layers. All latent information from mixture models and part filters are considered together with LSVM method to get final detection models. During inference, we slide learned models on the HOG3D features, so that actions can be localized and recognized in spatiotemporal space of videos.

Experimental Results

We evaluate the performance of our method on 2 popular human action dataset: Weizmann and KTH. There are 10 classes of actions, bend, jack, jump, pjump, run, side, skip, wave1, wave2 and walk presented by 9 actors in Weizmann, while 6 classes, walk, jog, run, box, handwave and handclap from 16 actors in KTH. The ground truth data in Weizmann contains silhouettes of actors as bounding boxes of examples. This supervision information is exploited in training stage to provide positive examples as well as in inference stage as ground truth detection results. However, for KTH we utilized a background subtraction technique to collect the position information of actors. In our experiment, we randomly select 80% data for training and test the method on all data. A 5-fold method is considered for cross validation.

In the experiment, we model each class of actions with 3 mixture components consisting of 1 root and 10 parts. The experimental results are represented in Figure 1 by confusion matrices. One can see that our proposed approach performs better on Weizmann dataset than on KTH dataset. This observation agrees with the theoretical analysis since the intra-class variation of Weizmann is smaller than KTH, which contains severe scale and appearance change. From Figure 1(a), we can see that the confusion of the method mainly occurs between run and skip, as well as wave1 and wave2. On the other hand, as shown in Figure 1(b), the performance of our method on KTH is mainly mitigated on jog actions. Intuitively, we can observe the similarity between these confused actions from appearance directly, especially that jog actions look quite similar to run actions. We also compared the average performance of action recognition with other existing methods in Table 1. The comparison is organized on both Weizmann and KTH. One can see that our proposed method can meet the state-of-art in the literature.

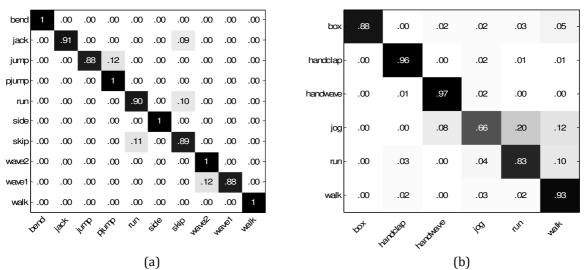


Figure 1: Confusion matrices of action recognition on (a) Weizmann dataset and (b) KTH dataset.

1	
1	0.925
0.988	0.917
0.996	N/A
0.728	0.815
0.946	0.8717
	0.728

Table 1: Comparison of average accuracies of various methods on videos.

Conclusion

By integrating DPMs into 3D spatiotemporal space on videos, we propose a unified action recognition and detection system in this paper. A direct extension of traditional object detection method has been preliminary proven to be a potential way for action detection in videos. We hope our research here can provide a complement to other 3D feature based action recognition system. More experiments will also be implemented in further work to validate our proposed method.

References

- [1] Laptev I.: On Space-time Interest Points, International Journal of Computer Vision, p. 107-123, (2005).
- [2] Lowe D.G.: Distinctive Image Features from Scale-invariant Keypoints, International Journal of Computer Vision, p. 91-110, (2004).
- [3] Yuelei X., Hong C., Zhe L., Luhong L., Xilin C. and Debin Z.: A Unified Framework for Locating and Recognizing Human Actions, CVPR, p. 25-32, (2011).
- [4] Felzenszwalb P.F., Girshick R.B., McAllester D. and Ramanan D.: Object Detection with Discriminatively Trained Part-based Models, IEEE Trans. on PAMI, p. 1627-1645, (2010).
- [5] M. Everingham, L. Van Gool, C. K. Williams, J. Winn, and A. Zisserman: The PASCAL Visual Object Classes Challenge 2007 (VOC2007) Results, http://www.pascalnetwork.org/challenges/VOC/voc2007.
- [6] Yang Wang, Mori G.: Hidden Part Models for Human Action Recognition: Probabilistic versus Max Margin, IEEE Trans. on PAMI, p. 1310-1323, (2011).
- [7] Klaser, Alexander, and Marcin Marszalek.: A spatio-temporal descriptor based on 3D-gradients, British Machine Vision Conference, p. 995-1004, (2008).

Video segmentation algorithm based on improved Kirsch edge operator and three-frame difference

Chunyu Chen^{1,a}, Mingyue Zhao^{1,b}

¹College of Information and Communication Engineering, Harbin Engineering University, Harbin, 150001, China

^aspringrain@hrbeu.edu.cn, ^bzhaomingyue@hrbeu.edu.cn

Keywords: Video segmentation; Three-frame difference; Kirsch edge detection; Moving target detection.

Abstract. For the most commonly used method of are susceptible to noise, it is difficult to extract a complete moving target . Aiming at this problem, we propose a video segmentation algorithm through the combination of an improved Kirsch edge operator and the three-frame difference. Firstly, we got a moving region through a differential by the three consecutive image frames, and then got the edge on the current frame using an improved Kirsch edge detection operator, Synthesis of the two test results, we got a more accurate moving object edges. Then using the edge connector algorithm to complete the connection of the fracture edge, and finally, got moving target mask image through regional filling, thereby dividing the complete moving target, thus dividing the complete moving target. Experimental results show that the algorithm has a certain robustness, and can accurately detect moving targets.

Introduction

With the development of society, people's safety consciousness gradually improve. Intelligent surveillance has gradually shifted from the field of professional military, scientific research into people's daily lives. In banks, airports, subways, residential and other safety requirements are very high occasions, we can see it plays a very important role. Moving object detection is the important and difficult point of the video analysis, moving target detection accuracy directly affect the subsequent research of moving target tracking and identification. Commonly used moving object detection algorithm can be divided into the following three categories: Inter - frame difference method[1], optical flow method[2], background difference method[3], and so on. Among them, frame difference method is with a good adaptability to dynamic environments, a small affected by the light change, a low computational complexity, and a simple implementation. But it can not detect a complete outline of the moving object, and the detected moving target is often accompanied by "holes" and "ghosting" phenomenon.

Kirsch proposed an edge detection operator based on direction in 1971[4]. This algorithm can maintain the details of the image edge and have a kind of ability of resisting noise to a certain degree and overcome the shortcoming of classic first order and second order edge detection operator are sensitive to noise.

This paper studies the respective target detection algorithm performance. Proposed a video segmentation algorithm with the combination of the Kirsch edge operator and three-frame difference. Combine this two algorithms, we get the edge of actual moving objects and it also can make up the deficiency of single algorithm, so we can get the complete and accurate moving object.

Moving target detection based on frame difference

Read three consecutive frames in the video sequence and convert them to gray images. They are f(x, y, t-1), f(x, y, t) and f(x, y, t+1) respectively, where, f(x, y, t) is the current frame at the moment. Usually the result of frame difference is frame difference operation between two adjacent frames.

$$D_{t,t-1}(x,y,t) = \begin{cases} 1 & if |f(x,y,t) - f(x,y,t-1)| > T \\ 0 & if |f(x,y,t) - f(x,y,t-1)| \le T \end{cases}$$
(1)

$$D_{t,t+1}(x,y,t) = \begin{cases} 1 & if \left| f(x,y,t) - f(x,y,t+1) \right| > T \\ 0 & if \left| f(x,y,t) - f(x,y,t+1) \right| \le T \end{cases}$$
(2)

Where, T is the threshold of the binary image. $D_{t,t-1}(x, y, t)$ is difference of the current frame f(x, y, t) and previous frame f(x, y, t-1). $D_{t,t+1}(x, y, t)$ is difference of the current frame f(x, y, t) and the later frame f(x, y, t+1). In the difference image, we consider it to be the foreground moving objects when the value of the point is '1' and we consider it to be the background when the value is '0'. So the moving target can be extracted from the video. Only according to the two-frame difference between images to detect moving targets exist many problems, just as shown in Fig.1(d) and Fig.1(e), because the difference between two adjacent frames is not completely moving target, the background covered by the moving target in the previous frame will appear in the next frame and be mistaken for foreground object.

In order to get better understanding and analysis of the movement we use three-frame difference instead of the two-frame difference to realize the moving target detection. it can be written as formula (3)

$$D_{3}(x, y, t) = D_{t,t-1}(x, y, t) \times D_{t,t+1}(x, y, t)$$
(3)

Fig.1 is a few pictures from a video that taken by myself, moving target edge $D_3(x, y, t)$ are obtained as shown in Fig.1(f). Making use of the three-frame difference method can detect the outline of moving object very quickly. It also can solve the problem of sheltering from each other and background reappearing problem, and the edge of the moving target is obtained accurately. It also can restrain the influence of light, shadow and noise in a certain extent.

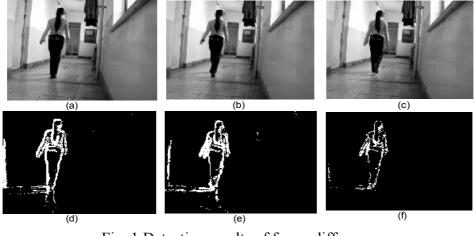


Fig. 1 Detection results of frame difference ((d),(e) use two-frame difference and (f) use three-frame difference)

Edge detection based on entropy-based blocks and adaptive Kirsch

Image entropy reflects how much information the image carry. A gray level image consists of discrete in space and limited gray levels of pixel. Assumed the image is quantified by Q bit, then the image has $M = 2^{Q}$ gray levels, if the gray level is $G_i = i(i = 0, 1, \dots, 2Q - 1)$, so the self- information and information entropy of the image is show as below respectively.

$$p(G_i) = \frac{n_i}{n_{total}}$$
(4)

$$I(G_i) = \log_2 \left[1/p(G_i) \right]$$
(5)

$$H = \sum_{i=0}^{2^{\mathcal{Q}}-1} p(G_i) I(G_i)$$
(6)

Among them, n_i is the frequency of pixel of gray level G_i in the whole image; n_{total} is the total number of pixels in the whole image. H is the information entropy.

Information entropy indicates the equalization of the gradient distribution and the continuity and integrity of the gray levels. The information entropy is high when the gray series is too many and balanced in distribution. Owing to the gray level in each part of the whole image is not even, there may be some parts have more details (large amounts of information), while some other parts are not (less the amount of information). When using Kirsch operator with the same threshold in the whole image, some details of the image may be ignored and may appear edge discontinuity, even the whole edge is undetected. Therefore we use the method of image blocks based on entropy[5]. The specific steps are as follows:

(1) The object $(2m \times 2n)$ is divided into 4 pieces in average, the size of each block is $m \times n$, if $\min(m, n) < \min size$, then go to (4), otherwise continue;

(2) Calculating information entropy of each block H_i , and get the maximum value H_{max} and the minimum value H_{min} ;

(3) Calculating $\Delta H = H_{\text{max}} - H_{\text{min}}$, if $\Delta H > th$, the segmentation is effective, and look at each block as a new processing object and turn to (1);

(4) To each processing object, we using adaptive Kirsch to detect edge. If there are some blocks that have not been detected by Kirsch, then look at these blocks as new processing objects and turn to (1), otherwise come to the end.

Minsize is the least value of the size of each block, it can represent the fine level of blocks.

The determined method of threshold is based on human visual characteristics. Human eyes sensitivity to gray value is not changed with the gray value varies linearly, according to the literatures, using the parabola[6] to calculate threshold is reasonable. So in the region [0, 48], [48, 206] and [206, 255] define a parabolic equation respectively. For all the gray images, the parabolic equation is applicable. The detection threshold M_t of each block is calculating as bellow:

$$M_{t} = \begin{cases} -0.001738x^{2} + 15 & (0 \le x \le 48) \\ -0.000491x^{2} + 0.125635x - 2.030474 & (48 < x \le 206) \\ -0.009579x^{2} + 4.885464x - 595.89671 & (206 < x \le 255) \end{cases}$$
(7)

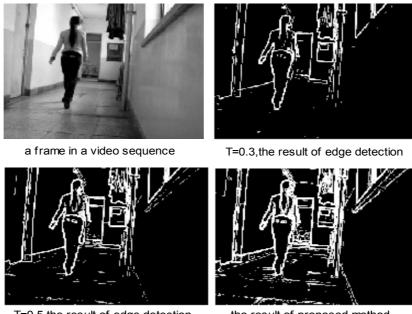
Where, x is the average pixel value in each block. The calculation formula can be written as formula(8):

$$x = \frac{1}{N} \sum_{i=1}^{N} G_i \tag{8}$$

Where, N is the number of pixels in the sub block, G_i is pixel value of each point.

In this paper, we compare the detection effect between traditional Kirsch to take different threshold and the proposed method in this paper. As shown in Fig.2, choose a frame in the video and use the traditional Kirsch to detect edge of the image. It can be seen that the detection effect of

different threshold has a very big difference. When T is small, the edge location precision is high, but continuity is poor, edge details of low intensity are missing. When T is large, the situation is just the opposite. The edge continuity is better when take the proposed method in this paper and not lose weak edge.



T=0.5,the result of edge detection

the result of proposed method

Fig. 2 Comparison of different Kirsch edge detection

Result and analysis of experiment

Assumed $D_3(x, y, t)$ is the motion region mask after three-frame difference, EI(x, y, t) is edge mask obtained by the improved Kirsch, then the final target edge M_{fe} can be written as formula (9). $M_{fe} = D_3(x, y, t) \times EI(x, y, t)$ (9)

But the edge discontinuity problem still exist, we need connect the edge of the moving target. We use adaptive mathematical morphology to connect the edge of image. Using adaptive elliptical structure element to carry on adaptive dilation to every endpoint. The size and direction of structure element can be adjusted according to the local characteristics of pixels, such as slope and curvature, and get closed edge of moving target after expansion defined as M(x, y, t). Finally, filling in the closed moving target boundary and get binary mask image of the moving target. If combined with the current frame f(x, y, t), the segmentation of moving targets will come true.

In order to verify the validity of the algorithm, we use this method on the ordinary PC machine (configuration is P42.6 GHz and memory is 1G) to process the image sequence. The format of the image sequence is JPG and the rate is 25 frames per second. Testing result is shown in Fig.3:

Fig.3(a)-(c) is three successive frames taken in image sequence; Fig.3(d) is result of three-frame difference; Fig.3(e) is the image edge obtained by improved Kirsch; Fig.3(f) is the final edge of the moving object after "and" operation; Fig.3(g) is filling in the moving object boundary and get binary mask image of the moving target; Fig.3(h) is realizing the segmentation of moving objects through combined (g) and current frame f(x, y, t). It can be seen from Fig.3(d) that the detected object is fuzzy through three-frame difference and the outline is not clear, furthermore, the detected edge of moving object have many noise and it will affect the accurate segmentation of the moving objects. However, the algorithm in this paper can accurately extract the boundaries of the moving object and solve the problem of traditional three-frame difference can not get a complete edge. To a certain extent solved the shortcoming of traditional three-frame difference is easy to produce "empty hole" and can extract the moving objects accurately.

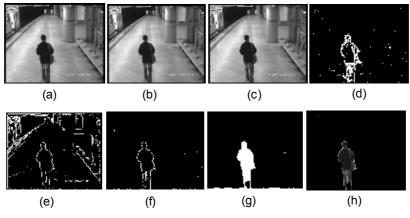


Fig.3 Detection results of proposed method

Conclusions

In this paper, we propose a video segmentation algorithm through the combination of an improved Kirsch edge operator and three-frame difference. This algorithm combines the advantages of the frame difference method is simple, fast and robustness. Making use of Kirsch operator to make up "ghosts" and "hole" phenomenon of three-frame difference. The threshold of Kirsch operator can not be set adaptively. Aiming at this problem, we proposed adaptive threshold setting method based on entropy of block. Experimental results show that this algorithm is able to respond to the changes of actual scenes quickly and realize moving object segmentation accurately and effectively.

Acknowledgements

This paper is funded by the International Exchange Program of Harbin Engineering University for Innovation-oriented Talents Cultivation, The project sponsored by National Natural Science Foundation of China (No. 61175126), The Doctoral Fund of Education Ministry (No. 20112304110009), International Science & Technology Cooperation Program of China (2014 DFR10240), National Natural Science Foundation of China (612111070), Harbin science and technology research projects (2013AE1BE003).

References

- [1] LIPTON A, FUJIYOSHI H, PATIL R. Proc IEEE Workshop on Application of Computer Vision. Princeton: NJ, 1998: 8-14
- [2] MEYER D, DENZ LE J, N IEMANN H. Proc IEEE International Conference on Image Processing. Santa Barbara, California, 1997: 78-81.
- [3] HARTAOHU I, HARWOOD D, DAVIS L. IEEE Trans Pattern Analysis and Ma2 chine Intelligence, 2000, 22(8): 809-830.
- [4] KIRSCH R A. Computers in Biomedical Research, 1971, 4(1): 315 328.
- [5] SONG Ying, CHEN Ke, LIN Jiang-li, ZOU Yuan-wen. In Chinese'.Computer Engineering,2010,36(14): 196-200
- [6] Kang Mu, Wang Baoshu, In Chinese'. J. Huazhong Univ . of Sci. & Tech. (Natural Science Edition), 2009, 37(4): 47-50

Denoise PET Images Based on a Combining Method of EMD and ICA

Qi WEI^{1,a}; Qi LIU^{1,b}

¹College of Electrical & Electronic Engineering, Harbin University of Science and Technology, Harbin China

^a weiqi@hrbust.edu.cn, ^b 6e7en@sina.com

Keywords: Positron Emission Tomography; Independent Component Analysis; Empirical Mode Decomposition

Abstract: The incidental component in addition to the measured target signals is considered as noise of Positron Emission Tomography (PET) images. A novel method to denoise the PET images based on Empirical Mode Decomposition (EMD) and Independent Component Analysis (ICA) associated with Sparse Code Shrinkage (SCS) technique is proposed in this paper. EMD is executed to decompose a PET image into a number of Intrinsic Mode Functions (IMFs), which are used to reconstruct a new PET image after chosen by means of an inverse EMD procedure. By applying ICA to the new PET image, an orthogonal dataset can be obtained and the signal-noise separation can be realized. Then a clearer PET image can be reconstructed by SCS. The simulation results indicate that the proposed method is effective to denoise PET images.

Introduction

Positron Emission Tomography (PET) is recognized as one of the most advanced large-scale medical diagnostic imaging equipments in the medical profession at present^[1]. In a sense, the process of the PET images denoising is the process to fight with various noises of the PET images. Different kinds of denoising algorithms have been proposed according to the features of actual images, the statistical characteristics of the noise and the distribution of the frequency spectrum, such as Median Filtering, Wavelet Filtering, Wiener Filtering and Independent Component Analysis (ICA)^[2]. ICA has a unique advantage that the need of the prior knowledge of images is very low. From the perspective of the ICA, the noise data and image data are generally independent to each other. ICA can remove the noise through obtaining the image components which are independent to the noise data using the high order statistics information of images^[3]. But at the same time of considering the statistic independence of the image and noise, there also is a negligence of the statistical correlation on the edge junction, which will result in the edge blur of the processed PET images. Empirical Mode Decomposition (EMD) is a time-frequency algorithm used to decompose a nonlinear and nonstationary signal into a number of Intrinsic Mode Functions(IMFs) of different frequencies adaptively^[4]. But sometimes there is an aliasing phenomenon between the noise and useful data in the IMFs. One new method combining EMD with ICA to denoise the PET images is presented in this paper, which integrates the advantages of the EMD and ICA to deal with the drawbacks reciprocally. The mode of obtaining IMFs according to different frequencies in EMD makes up the edge blur in ICA, and the statistical independence of ICA can avoid the aliasing phenomenon of EMD at a certain degree.

Empirical Mode Decomposition

The purpose of EMD is to decompose a signal to a set of IMFs meeting the rules of the Hilbert transform under the time scale^[5]. The decomposition purpose of EMD is to build a new set of IMFs after removing the ones with poor power from the original obtained dataset for the source signal reconstruction. But when there is an aliasing phenomenon between the noise and useful data in an

IMF sometimes, wiping off too many IMFs will remove the useful signal by mistake and can't reach a good denoising effect. Therefore, in order to achieve a better result, only the last residual component is removed in this paper. Then the new set of IMFs is used to reconstruct a new PET image after chosen by means of an inverse EMD procedure.

Independent Component Analysis

Assume n statistically independent source signals, which can be represented as $s(t)=[s_1(t), \dots, s_n(t)]^T$ in vector, pass through a m*n linear mixed matrix A, and get m observation signals $x(t)=[x_1(t), \dots, x_m(t)]^T$, which are with additive noise $n(t)=[n_1(t), \dots, n_m(t)]^T$, where T denotes the transpose of matrix. The hybrid mathematical model for ICA is defined as^[6]:

$$X = AS + n \tag{1}$$

The target of ICA is to find an unmixed matrix $W=A^{-1}$, which satisfies the model:

$$Y = WX = A^{-1}X = S \tag{2}$$

The purpose of unmixing is to make y_i independent to each other in the largest extent, so that it can solve the aliasing of the noise and useful information in a certain degree. In this way, the information of independent component in the PET image can be obtained. Furthermore the image can be reconstructed according to the independent information using Sparse Code Shrinkage (SCS).

Sparse Code Shrinkage based on ICA

Sparse Code Shrinkage (SCS) is same as ICA to extract features from the image data. Compared to other feature transforms, this process of the feature extraction is more dependent on statistical properties of the data^[7]. The idea of SCS algorithm is that the image after orthogonal ICA transform has a strong sparse feature, which can support to project the noise image onto the ICA signal's orthogonal basis for signal denoising and reconstruction of the target signal.

Assume that it's a typical sparse distribution and denote the variance matrix as $\sigma^2 I$ (I is unit matrix). If the unmixed matrix W is an orthogonal matrix and the noise variance of the estimation Y=WX of S after unmixing still is $\sigma^2 I$, then y_i is the sum of the variables to be estimated under super-gaussian distribution and Gaussian random variables. Then maximum likelihood estimation of the amount to be estimated has the form as ^[8]:

$$\widehat{s}_{i} = f(y_{i}) \operatorname{sng}(y_{i}) \max\left(0, |y_{i}| - \sqrt{2}\sigma^{2}\right)$$
(3)

Were f(yi) is a shrinkage function.

Use formula (3) to shrink every y_i obtained by unmixing, set the element of a smaller value as zero to eliminate the influence of noise in coding and retain the essence characteristic of image. The specific steps of SCS are as follows:

(1)Estimate the model and parameter of probability density of every obtained IC to get corresponding shrinkage function;

(2)Calculate the projection of the noised data $x(t)=(x_1(t), \dots, x_m(t))$ onto the independent basis:

$$Y = WX \tag{4}$$

(3)Apply SCS function to y_i to get corresponding estimation:

$$\hat{s}_i = g(y_i) \tag{5}$$

(4)Transform the estimated sparse codes to gain the data

 $x = W^T \hat{s}$

(6)

EMD-ICA Method

In this paper, based on the above algorithm principles, a method combining EMD and ICA is proposed to denoise the PET image by executing the following procedures:

(1)Decompose the noised PET image using EMD to a number of IMFs .

(2)Remove the residual IMF to make a new dataset, and then use it to reconstruct a new PET image by means of an inverse EMD procedure.

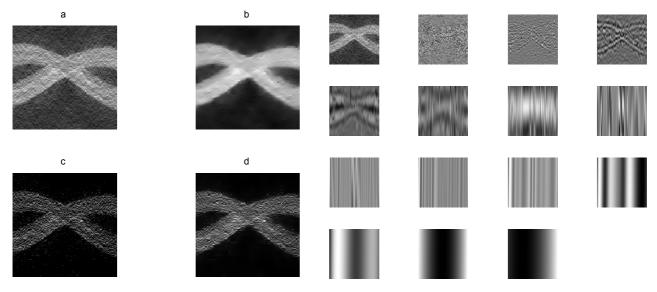
(3)Execute ICA on the new PET image to get a database of ICs.

(4)The noise components of ICA are forced to zero, and then the signal-noise separation can be realized.

(5)At last the clean signals are used to reconstruct a denoised PET image by SCS.

Experiment results

For simplicity, an 8 * 8 pixel image is intercepted from a 128 * 128 pixel PET image as an initial image for simulation using MATLAB simulation software in this paper.



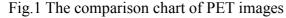


Fig.2 IMFs of the PET image after EMD

Fig.1 shows the comparison chart of PET images, where a is an initial PET image, b is the PET image after ICA denoising, c is the reconstructed PET image after removing the residual IMF by EMD, d is the denoised PET image after EMD-ICA. Fig.2 shows an initial PET image and a data set of IMFs after the EMD decomposition.

The comparison of the images in Fig.1, shows that the PET image after EMD-ICA proposed in this paper is clearer than images after ICA or EMD.

The value of Signal to Noise Ratio (SNR) represents the degree of noise suppression we have done and the image processing quality. So SNR is made as criterion to evaluate the denoising result in this paper, which is denoted as:

$$SNR = 10\log_{10}\left(\frac{S}{N}\right)$$
 dB

(7)

To calculate the SNR of an image, first count the local variance of all pixels of the image, make the maximum value of local variance as the signal variance (S in the above formula) and the minimum value as the noise variance (N in the above formula). Then calculate its value according to formula (7). The SNR values of denoising results of ICA, EMD and EMD-ICA algorithm are shown in Table 1.

Table 1 The SNR values of PET image denoised by ICA, EMD and EMD-ICA algorithm

Algorithm name	SNR value[dB]
ICA	39.7831
EMD	43.6727
EMD-ICA	59.7967

Table 1 show clearly, measured by SNR, EMD-ICA algorithm is better than ICA or EMD.

Conclusion

The simulation experiment and calculation results show that the EMD-ICA algorithm proposed in this paper has superiority on the PET image denoising, compared with ICA and EMD method. The algorithm is based on the respective advantages of EMD and ICA, and it can deal with the drawbacks reciprocally. The mode of obtaining IMFs according to different frequencies in EMD makes up the edge blur in ICA, and the statistical independence of ICA can avoid the aliasing phenomenon of EMD at a certain degree. The method also can be applied to other medical images, and further research works will consider more type images.

References

- [1] Beaulieu S, Rubin B, Djang D, et al. Positron Emission Tomography of Schwannomas: Emphasizing its Potential in Preoperative Planning. AJR, (2004),182(4):971-974.
- [2] Goerres G W, Burger C, Kamel E, et al. Respiration-induced Attenuation Artifact at PET/CT: Technical considerations. Radiology, (2003), 226(3):906-910.
- [3] Qiu-ping Xu, Qi Wei.Application of Independent Component Analysis on PET Image Denoising. Journal of Harbin University of Science and Technology, (2009), 14(6):61-65. In Chinese.
- [4] Huang N E, Shen Z, Long S R, The empirical mode decomposition and the Hilbert Spectrum for nonlinear and non-stationary time series analysis. Proc. R. Soc. Lond. A, (1998), 454: 903-995.
- [5] Fang Dai, Jianru Xue, Nanning Zheng. Combine EMD and ICA to Learn Image Bases. Congress on Image and Signal Processing. (2008).
- [6] XianHua Han, YenWei Chen, Keishi Kitamura. An ICA Based Noise Reduction for PET Reconstructed Images. Intelligent Information Hiding and Multimedia Signal Processing, (2007), 9: 113-116.
- [7] Hyvarinen A. Hoyer P O. Sparse code shrinkage for denoising. In Proc. IEEE Int. Joint Conf. on Neural Networks. (1998), 859-864.
- [8] Hyvarinen A. Noisy independent component analysis, maximum likelihood estimation, and competitive learning. IEEE International Conference on Neural Networks Conference Proceedings, (1998), vol.3:2282–2287.

An improved C-means clustering for image segmentation

Taifa Zhang^{1, 2, a}

¹School of Computer Science and Technology, Harbin Institute of Technology, Harbin 150001, China

²College of Science, Heilongjiang University of Science and Technology, Harbin 150022, China ^aztf991@163.com

Keywords: Image segmentation, Cluster analysis, C-means

Abstract. Image segmentation is an important part of the image process, and it is also the current hot and focus in image research. How to achieve better segmentation results are dominating targets of researchers. Currently, image segmentation based on clustering is the main research area. Firstly, this paper introduces the traditional C-means clustering algorithm and its characteristic has been analyzed. Then, the initial clustering center and the number are selected using the histogram. Finally, the image is converted from the RGB space to Lab space for clustering, and it has improved the accuracy and efficiency of image segmentation.

1 Introduction

In the study of image and its practical application, we are usually interested in the targets or the prospects in the image, which are generally specific areas with unique properties^[1-3]. In order to identify and analyze the target area, we must extract these areas for further use.

Since the 1960s, the research of image segmentation has a history of over fifty years. Scholars at home and abroad in the area of image segmentation have put forward many kinds of algorithms. But so far there is not an algorithm of image segmentation suitable for any cases. And the application ranges of the current algorithms are not identical. In addition, even for a specific application, how to choose the optimal segmentation algorithm is also a very difficult thing and it requires repeated demonstration and test.

2 Traditional C-means clustering

In general, clustering is to divide the sample set based on the principles of similarity between samples. According to the definition, each sample of the set must belong to one class and only belongs to the class. And the samples in the same class are similar, but the samples are not similar between different classes. Since clustering belongs to unsupervised classification method and statistical model of samples does not need prior knowledge, so membership degree of each sample to every class is not clear. Generally, the objective function is introduced for the evaluation division. Then the optimal solution is to search in the neighborhood of the division of change. If there is the optimal solution, the division will be modified until to achieve optimal results in the neighborhood of change^[4-5].

Image segmentation of clustering is put forward on the basis of some traditional methods, such as image segmentation based on threshold and areas. And it is also the focus of the current image segmentation technology research. C-means clustering, which is one of the most important clustering algorithms, is presented by McQueen in 1967. Each class is represented by the mean value of objects in the class. It is a traditional method to solve the problem of clustering. Its main advantages are quick and easy. But it may converge to the local minimum for different mean value and will produce different clustering results. In addition, since a small amount of noise data can have great impact on mean value, the criterion function is not suitable for the class in which size varies significantly. And it is particularly sensitive to the noise samples.

Euclidean distance is taken as similarity measure in C-means clustering algorithm and its criterion function of division evaluation is expressed as

$$J = \sum_{i=1}^{k} \sum_{x_i \in c_i} (dist(x_j, c_i))^2 = \sum_{i=1}^{k} \sum_{x_i \in c_i} (dist(x_j, \overline{x_i}))^2$$
(1)

where x_j is data sample of class c_i , $\overline{x_i}$ is the mean value of class c_i , and the distance between sample and class $dist(x_j, c_i)$ is represented by the average distance of the sample to the class $dist(x_j, \overline{x_i})$.

According to the formula (1), J is the error sum of all the class centers to the corresponding all samples in the class. The greater of the value J, the more dispersed of the class. Minimum of the square error sum is used to determine the optimal partition in C-means algorithm.

3 Improved C-means clustering

The key step is to select the initial cluster centers in C-means clustering algorithm. Usually, the center is chosen randomly from the sample set. The selection of the initial clustering center has great relevance to the clustering performance. The sample position is very important for the results of clustering. If the selection of C samples is not reasonable, it will increase the complexity of the operation and clustering results will not ideal. The clustering centers are selected based on histogram of image and the number of clustering centers is determined to improve effect of the clustering. The work has been done in the Lab color space to improve the accuracy and efficiency of image segmentation^[6].

3.1 The principle of improved C-means clustering

In traditional C-means clustering algorithm, we don't know the clustering centers and category number of the image. They are often randomly determined, so the clustering effect can not be controlled and the result is not very ideal. In the paper, the color image is firstly transformed into gray image, and then the histogram of the image is used to determine the number of categories. Lastly, it is revised according to the clustering effect. The number is added or subtracted 1 on the basis of the original number of categories generally. The values in the peaks of wave are always made as clustering centers, which will reduce the running time of programs and the number of experimental greatly.

C-means is a hard clustering algorithm and the data is clustered in the feature space. So clustering in different color space will cause the segmentation result different. Due to the strong affinity of three components in RGB color space, the paper chooses the uniform color space of CIE Lab. where L denotes the brightness of an image, a and b denote the color difference of an image respectively. The color differences in the Lab color space between the location of i and j pixel of an image can be represented as

$$\Delta C = \sqrt{(L_i - L_j)^2 + (a_i - a_j)^2 + (b_i - b_j)^2}$$
(2)

The bigger of the ΔC , the greater of color difference between two points. Therefore, Similarity index value function which describes similar degree of Lab uniform image pixels can be expressed as

$$J = \sum_{i=1}^{c} J_{i} = \sum_{i=1}^{c} \sum_{(L_{j}, a_{j}, b_{j}) \in K_{i}} \sqrt{(L_{j}, L_{i})^{2} + (a_{j}, a_{i})^{2} + (b_{j}, b_{i})^{2}}$$
(3)

where (L_j, a_j, b_j) is a three-dimensional coordinate of *j* th pixel in Lab uniform color space, and (L_i, a_i, b_i) is the coordinate of a clustering center in Lab space. Pixels *j* and the pixels *i* belongs to a same class when *J* in (3) tends to zero.

3.2 The steps of improved C-means clustering

According to the principle of the algorithm, the specific steps of improved C-means clustering are as follows.

Steps 1: the color image is read and then it is converted from RGB color space to Lab color space. Steps 2: the spatial information of b is extracted in Lab color space, and it is reshaped to a two-dimensional matrix M.

Steps 3: the data in matrix M are divided into k classes, and the clustering centers are obtained. The pixels in every different category are assigned the value of 1, 2,..., k automatically.

Step 4: the clustering results are rearranged to a matrix and then to generate the image.

3.3 Experiments and analysis

In the same configuration of computers experimental environment, the image segmentation are done using Matlab 7.0 as the programming language. Two color images, ships and island, are chosen randomly from database for the experiments. The results of C-means and improved C-means are shown in Fig.1 and Fig.2.



(a) input image



(b) C-means clustering (c) Fig.1 Segmentation results of ships



(c) improved C-means clustering



(a) input image



(b) C-means clustering (c) in Fig.2 Segmentation results of islands



(c) improved C-means clustering

It can be seen from the Fig.1 and Fig.2 that the image edges of improved results are sharper and clearer than the original C-means clustering and the cluster effects of every region are more obvious. The executing time in Table 1 show that C-means clustering takes more time than the improved C-means clustering. Experimental results prove that the improved C-means has improved accuracy and efficiency of the segmentation effectively. Segmentation effect is satisfactory and it is superior to the classic C-means clustering segmentation method and the effect.

Table 1 The exec	cuting time of the clus	stering
The methods of clustering	ships	islands
C-means clustering	2.31 s	3.70 s
Improved C-means clustering	1.70 s	1.90 s

4 Conclusions

Image segmentation is an important research topic in image processing. It decides the final result and the quality of the image analysis and image understanding. The algorithm of image segmentation based on C-means clustering is introduced and its shortcomings are analyzed in this paper. The paper puts forward that the cluster centers are obtained in the peaks of the histogram, and they are corrected for more reasonable results according to the image. At the same time, Conversion is done from RGB space to Lab space for the better results of image segmentation. It exist a lot of improvements in image segmentation based on the clustering and there will be more broad prospects and great achievement in the future research.

Acknowledgements

This work is funded by the Heilongjiang Natural Science Foundation, China (12531590) and Research Project in College of Science, USTH (201305).

References

- C.Carson, S.Belongie, H.Greenspan, etc. Blobworld: Image Segmentation using Expectation Maximization and Its Application to Image Querying[J]. IEEE TPAMI, Vol.24, No.8 (2002), pp. 26-38.
- [2] Taifa Zhang, Chaoyang Gao. Three-Dimensional Reconstruction of Teeth CT Images[J]. Lecture Notes in Electrical Engineering, Vol.163 (2014), pp. 247-254.
- [3] Zhong Wang, Guiquan Liu, Enhong Chen. A K-means Algorithm Based on Optimized Initial Center Points[J]. Pattern Recognition and Artificial Intelligence, Vol.22, No.2 (2009), pp. 299-304.
- [4] Lijun Zhang. Classification Study of Socio-economic Sustainable Development in Hebei Province based on K-means Clustering Analysis[J]. Journal of Hebei University of Engineering, Vol.23, No.6 (2010), pp.34-37.
- [5] Jian Zhang. Research of Image Segmentation by Clustering Analysis[D].Shandong University Master's Thesis (2011).
- [6] Yifeng Xu, Chunming Chen, Yunqing Xu. An Improved Clustering Algorithm for K-Means[J]. Computer Applications and Software, Vol. 25, No.3 (2008), pp. 275-277.

Coded-structured light system calibration using orthogonal phase shift coding combined with Zhang's method

Xiaoyang Yu¹, Xiaoliang Meng^{1,a}, Haibin Wu¹, Xiaoming Sun¹, Li Wang¹

¹The higher educational key laboratory for Measuring & Control Technology and Instrumentations of Heilongjiang province, Harbin University of Science and Technology, Harbin, 150080, China

^a1263886567@qq.com

Keywords: coded-structured light, imaging model, projector calibration, orthogonal phase shift

Abstract. In coded-structured light three dimensional system, system calibration plays a vital role for the measurement accuracy. The camera calibration method is very mature, but the study about projector calibration is less. Therefore, this paper proposes a projector calibration method with simple calibration process and high accuracy. This method combines the Zhang's plane model calibration method with orthogonal phase shift coding. In calibration process, this paper uses phase shift coding pattern to establish the relationship of projector image and camera corner point coordinates. According to the image coordinates in the projector's perspective, we program and calculate the projector's internal and external parameters matrix based on the Zhang's plane model calibration toolbox. The results show that the proposed method is simple and flexible, the maximum relative error of the calibration parameters is 0.03%, and it meets the requirements of system calibration in medical or industrial fields.

Introduction

Coded-structured light three dimensional system has the advantages of non-contact, high accuracy, high speed. Therefore, it has been widely used in the area of industrial inspection, machine vision, medicine, face recognition and so on. In coded-structured light system, projector calibration is one of the important parts of the system [1-3]. Currently the main research achievements of the projector calibration method are as follows:

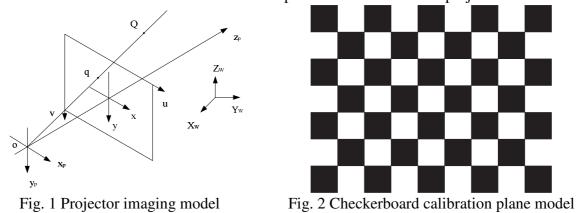
In 2008, Xiaolin Dai[4]put forward a projector calibration method based on phase matching technology. Although the accuracy of this calibration method is high, the algorithm is complex and the calibration process is slow. In 2009, Zhongwei Li[5] proposed a projector calibration method using the circular landmark point. This method used two different sets of coding image to establish the relationship of projector and camera, but error of the extracted center is big. In 2011, Dong Zhang[6] put forward a kind of projector calibration method base on color circular landmark pattern, this method used the common calibration checkerboard to project the color circular landmark pattern, according to the center coordinates of the color circular landmark pattern, it calculated the projector's parameters. But this method is complex and the accuracy is not very high. In 2013, Zhao Wang and Junhui Huang[7] proposed a kind of projector calibration method based on beam method, this method improves the calibration accuracy, but the calibration process is complex.

All in all, the study about projector calibration method is not very much, and there's a lot of faults and deficiencies to improve such as poor anti-interference ability, low calibration accuracy. Therefore, this paper will put forward a new projector calibration method which combines the Zhang's plane model calibration method and orthogonal phase shift coding.

Calibration principle

Projector imaging model. Because the projector can be regarded as a reverse camera, its imaging model can be regarded as a reverse camera pinhole model, the imaging model is shown in Fig. 1. A specific point in the space Q intersected with the point q of the imaging plane. In order to get the two dimensional coordinate of q, this paper proposed a method by projecting the orthogonal phase shift

coding pattern to the surface of the plane model, then calculated the two dimensional coordinate through the camera images, finally we can use the image coordinate (u, v) and the world coordinate (X_w, Y_w, Z_w) to calculate the internal and external parameters matrix of the projector.



Calibration procedure. This paper uses the checkerboard plane model to set up the relation between the projector images and camera images. In the calibration process, this paper used the phase shift pattern of horizontal and vertical direction to project the images. The main steps are as follows:

(1) Take a checkerboard plane model image using the camera, and project the horizontal and vertical phase shift images to the surface of the plane model, and use the camera to take these images, the calibration plane model images are shown in Fig. 2.

(2) Use the images taking from (1), use the calibration tool box to extract the corner sub-pixel coordinate of the checkerboard.

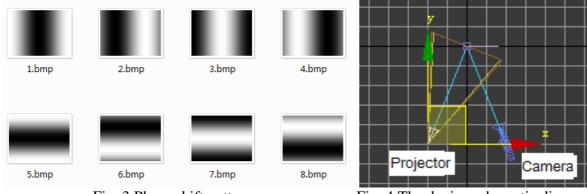


Fig. 3 Phase shift pattern

Fig. 4 The device schematic diagram

(3) Project the horizontal and vertical phase shift coding patterns which are shown in Fig. 3 to the surface of the checkerboard. After the phase-shift coding patterns are projected on the surface of the measured object, the phase shift coding patterns are formed on the measured object because of the adjustment of the surface of the measured object, the light intensity function can be denoted by the following equation:

$$I(x, y) = k \{ A(x, y) + B(x, y) \cos[\varphi(x, y) + \theta] \}$$

$$\tag{1}$$

Where I(x, y) is the light intensity of the point (x, y) which taken from camera; A(x, y) and B(x, y) are the light wave amplitude associated with the background; k is the wavelet coefficient; $\varphi(x, y)$ is the phase of the point (x, y), it is the function which is related to the object shape. We can calculate a phase value corresponding to each pixel, and the phase shift value is unique in one coding cycle.

The light intensity function of each step is given by:

$$I_{1}(x, y) = k \{ A(x, y) + B(x, y) \cos[\varphi(x, y)] \}$$
(2)

$$I(x, y) = k \{ A(x, y) + B(x, y) \cos[\varphi(x, y) + \pi/2] \}$$
(3)

$$I(x, y) = k \{ A(x, y) + B(x, y) \cos[\varphi(x, y) + \pi] \}$$
(4)

$$I(x, y) = k \{ A(x, y) + B(x, y) \cos[\varphi(x, y) + 3\pi/2] \}$$
(5)

Using the four step phase shift method to calculate the phase, then put it into the system mathematical model, we can obtain the three dimensional coordinates of the measured object. From (2) to (5), we can get the equation(6), the sine phase shift formula can be denoted by equation (7).

$$\tan \varphi = \frac{I_4(x, y) - I_2(x, y)}{I_1(x, y) - I_3(x, y)}$$
(6)

Where I_i (*i* = 1,2,3,4) is the light intensity value, $\varphi(x, y)$ is the phase value of the pixel (x, y).

$$\varphi(x, y) = \arctan \frac{I_4(x, y) - I_2(x, y)}{I_1(x, y) - I_3(x, y)}$$
(7)

This coding method can accomplish the point to point operation, it has the advantage of pixel level, therefore it has very high sampling density.

(4) Use the absolute phase values and the corner coordinate extracted in step (2) to calculate the image coordinate in the projector imaging plane.

(5) Repeat the above steps until we get at least three different perspective image coordinates of the projector to accomplish the internal parameters calibration of the projector, then choose another images to calculate the external parameters matrix of the projector.

Verification experiment

This paper uses the Autodesk 3ds Max 2010 software to verify the calibration experiment. The device schematic diagram can be shown in Fig. 4.

The parameters in the validation experiment are shown in Table 1.

	Device parameters		Coordina	ate rotation	Coordinate translation		
	$N^{p} \times M^{p}$	1024×768	$\boldsymbol{\omega}^p$	21.8°	t _x	0	
Projector	$oldsymbol{eta}_{ ext{l}}^{p}$	20°	$oldsymbol{arphi}^p$	-180°	ty	0	
	$oldsymbol{eta}_2^p$	15°	${oldsymbol{ ho}}^{\scriptscriptstyle p}$	90°	tz	538.516	

Table 1 The parameters of the projector

In the experiment, there's a distance between the camera and the calibration model plane, in order to ensure the camera can shoot all the corners of the calibration model plane, the checkerboard template should consider the range of the camera. In this paper, when we calculate the internal parameters, the size of the model plane is 210×270 . When we calculate the external parameters, the size of the model plane is 140×180 .

After calibration, the internal parameters matrix is

$$A = \begin{bmatrix} 1406.2463 & 0 & 0 \\ 0 & 1051.7779 & 0 \\ 0 & 0 & 1 \end{bmatrix}$$
(8)

The external parameters calibration results are

$$R_{p} = \begin{bmatrix} 0.000113 & 0.928820 & 0.370532 \\ 1 & -0.000094 & -0.000070 \\ -0.000030 & -0.370532 & -0.928820 \end{bmatrix}, T_{p} = \begin{bmatrix} 0.208793 \\ 0.275829 \\ 540.310406 \end{bmatrix}$$
(9)

The projector calibration results are shown in Table 2. Note that the projector in the simulation environment is off-axis projection.

	Table 2 The projector canoration parameters using the method of this paper								
System parameters	Calibration value	Real value	error	System parameters	Calibration value	Real value	Error		
<i>r</i> ₁₁	0.0001	0	0.0001	<i>r</i> ₃₂	0.3705	0.3714	0.0009		
r_{12}	0.9288	0.9285	0.0003	<i>r</i> ₃₃	-0.9288	-0.9285	0.0003		
<i>r</i> ₁₃	0.3705	0.3714	0.0009	t _x	0.2088	0	0.2088		
r_{21}	1	1	0	ty	0.2758	0	0.2758		
r_{22}	0	0	0	tz	540.3104	538.516	1.7944		
r_{23}	0	0	0	β_1	20.0077°	20°	0.0077		
<i>r</i> ₃₁	0	0	0	β_2	15.0031°	15°	0.0031		

Table 2 The projector calibration parameters using the method of this paper

In Table 2, the relative error between and calibration value and standard value is 0.03%, the error is very small, it can even be ignored, it verified the correctness of this kind of calibration method.

In the actual experiment, we use the orthogonal gray code coding method and this paper's method to measure the plane, the measurement error is shown in Table 3.

Table 5 The comparison of measurement data								
	Standard	Orthogonal	Gray code	Orthogonal phase shift coding				
	value/mm	Measured value/mm	error/mm	Measured value/mm	error/mm			
1	50	49.440	-0.560	49.950	-0.050			
2	50	50.116	0.116	50.006	0.006			
3	50	50.656	0.656	50.042	0.042			
4	50	49.106	-0.894	49.913	-0.087			
5	50	50.445	0.445	50.020	0.020			

Table 3 The comparison of measurement data

From the above table we can see that the accuracy of the orthogonal gray code coding method is significantly lower than the method of this paper.

Conclusions

In this paper, we combine the Zhang's plane model calibration method with the orthogonal phase shift coding, use the phase shift coding pattern to calculate the image coordinates on the imaging plane of the projector. The results show that the maximum relative error is 0.03%, some parameters error is small, it can even be ignored. This paper also uses the orthogonal Gray code to compare with the method of this paper, the results show that the accuracy of this paper's method is high.

References

- Xi Long, Yuexian Zhong. 3-D surface integration in structured light 3-D scanning. Journal of Tsinghua University, Vol. 42 (2002), p. 477-480
- [2] R. J. valkenburg, A. M. Melvor. Accurate 3d measurement using a structured light system. Image and Vision Computing, Vol. 16(1998), p. 99-110
- [3] Menudet J. F, Becker J. M, Fournel T, *et al.*. Plane-based camera self-calibration by metric rectification of images. Image and Vision Computing, Vol. 26(2008), p. 913-934
- [4] Xiaolin Dai, Yuexian Zhong, Chaolong Yuan, Yangbiao Ma. Research on projector calibration in one-camera 3-D measurement systems. Machinery Design & Manufacture, Vol.8 (2008) p. 194-196
- [5] Zhongwei Li, Yusheng Shi, Kai Zhong, Congjun Wang. Projector calibration algorithm for the structured light measurement technique. OPTA OPTICA SINICA, Vol.29 (2009), p. 3061-3065
- [6] Dong Zhang, Lixin Tang. A method of calibrating projector based on projecting color circular marks. Computer & Digital Engineering, Vol.39 (2011), p. 123-127
- [7] Zhao Wang, Junhui Huang, Jianmin Gao, Qi Xue. Calibration of the structured light measurement system with bundle adjustment. Journal of Mechanical Engineering, Vol.48 (2013) p. 32-40

Stereo Matching Algorithm Based on Pyramid Double Dynamic Programming

Wei Jizhou¹, Yu Shuchun^{1,a}, Dong Wenfei¹, Feng Chao¹, Xie Bing¹

¹The higher educational key laboratory for Measuring & Control Technology and Instrumentations of Heilongjiang Province, Harbin University of Science and Technology, 150080, China

^ayscls2013@163.com

Keywords: control points, dynamic programming, stereo matching algorithm, visual navigation

Abstract. A stereo matching algorithm was proposed based on pyramid algorithm and dynamic programming. High and low resolution images was computed by pyramid algorithm, and then candidate control points were stroke on low-resolution image, and final control points were stroke on the high-resolution images. Finally, final control points were used in directing stereo matching based on dynamic programming. Since the striking of candidate control points on low-resolution image, the time is greatly reduced. Experiments show that the proposed method has a high matching precision.

1 Introduction

Stereo vision technology is mobile robot visual navigation one of the key technologies in the field of ^[1]. Region-based stereo matching algorithm obtained parallax field that although sufficiently dense^[2], but the parallax figure have more miscellaneous points and poor quality. So both are not ideal. Ohta Y and Kanade T proposed stereo matching algorithm of dynamic programming^[3], after obtained the initial matching cost with the area matching method, using dynamic programming method to do global optimization, then the quality of the disparity map has been significantly improved, but the disparity map exists striped defects. Stephen S. Intille and Aaron F. Bobick introduced correction techniques of control point^[4], to further improve the quality of the disparity map greatly reduced stripe defects. But time of striking control point is longer, so that the whole time using matching algorithm increases, and affects the algorithm in real time.

In this paper, use visual navigation technology of mobile robot as background, firmly grasp the accuracy and real-time requirements of stereo matching algorithm, for the shortcomings of current algorithms, to improve stereo matching algorithm of dynamic programming for the control point correction, we propose a stereo matching algorithm based on double pyramid layer dynamic programming. In ensuring the matching accuracy of the algorithm of the premise, this algorithm can greatly improve real-time.

2 Stereo matching algorithm of dynamic programming based on the control point correction

2.1 Obtaining the parallax by dynamic programming algorithm

Dynamic programming algorithm is mathematical methods used to reduce the complexity of global optimization problem, it makes the overall optimize problem decomposed into stages to decided. Each stage show with variable k, the status of each stage is represented by x_k . Transition from one state to the next state called decision program, as represented by u_k with $V_{k,n}$, a criterion function to measure good or bad decision.

One of the most important features of a dynamic programming algorithm is with without markovin property that once when the state of a certain stage determines, after which the process of evolution is no longer affected by the previous decision and each state.

Another important feature of a dynamic programming algorithm is its separability of criterion function, namely:

$$V_{k,n} = \sum_{j=1}^{n} v_j(x_j, u_j) = v_k(x_k, u_k) + V_{k-1,n}$$
(3)

ln Formula (3) wherein $v_k(x_k, u_k)$ represents value of the criterion function at the k stage.

Essence of dynamic programming algorithm for global optimization is to find criterion function $V_{k,n}$ of the global optimum.

Make the dynamic programming algorithm specific to the stereo matching problem: k denotes the k pixel points; x_k represents the abscissa of the k pixel; u_k represents the parallax; $v_k(x_k, u_k)$ represents matching cost function.

Since the stereo matching algorithm based on dynamic programming consider the occlusion problem, so in $v_k(x_k, u_k)$ addition to the initial matching cost calculation includes (1), should also include blocking price. Namely:

$$v_k(x_k, u_k) = v_{data}(x_k, u_k) + v_{smooth}(x_k, u_k)$$
(4)

In Equation (4) $v_{data}(x_k, u_k)$ shows the initial matching cost calculated by the similarity measure; $v_{smooth}(x_k, u_k)$ indicates blocking cost function, in the blocked area, and its value will be significantly increased.

2.2 Stereo matching algorithm based on dynamic programming for control point correction

When dynamic programming algorithm obtaining parallax on parallax space images, planned path always tend to look for those points with a minimum matching costs. If you know in advance that some of the points as correct matching point and set the overall matching costs of these points to a smaller value, you can force the optimal path must go through the correct matching point, thereby reducing streaks flaws. These points are called control points. This stereo matching algorithm based on dynamic programming that artificial calculate and set the control points is stereo matching algorithm based on dynamic programming of control point correction.

Key to this approach is how to seek the correct control points. Obtaining control point to meet three basic rules [4]:

(1) control points must be parallax points could pass left and right consistency check

(2) matching cost of control points must be less than Block costs of dynamic programming

(3) the control point is not isolated

However, obtaining of the control point make the entire time-consuming of algorithms increased more than doubled, greatly affected the real-time of entire algorithm, how to reduce the time for obtaining the control points to become the key to improve the real-time nature of the algorithm.

3 Stereo matching algorithm based on double pyramid dynamic programming

3.1 pyramid algorithm for multi-resolution image

Pyramid algorithm is in multi-resolution analysis areas of wavelet theory, in image processing it is widely used.

To construct the image pyramid, first determine the number of stages of pyramid of k, progressively scaling level of r as required, the pixel values of low resolution images can directly using the corresponding pixel values of high resolution image, but also can obtained by averaging the lower pixels of an image. Generally r preferred to 2, then the number of pixels of the pyramid image at each level down to 1/4 of the original.

After obtain two low resolution images of left and right by using pyramid algorithm, we have to strike a candidate control point set on the low-resolution images, and then obtain the final control point set on the high-resolution images and use this control point set corrected stereo matching algorithm based on dynamic programming on the high-resolution image scores rate.

3.2 Obtaining a candidate set of control points on the low-resolution images

Accurate or not about obtaining control points, directly determines the correctness of the follow-up of dynamic programming, and its importance is obvious. Therefore obtaining control points must satisfy three basic rules in the literature [6]. The process to obtaining control point of this article is divided into two stages, in order to ensure its accuracy.

The first stage is to strike a candidate control point set GCPs first in the low-resolution images. This stage is divided into the following two steps:

(1) In the low resolution image using a conventional stereo matching algorithms for dynamic programming to conduct stereo matching, obtain parallax value for each point, and record the matching cost.

(2) Comparing the matching cost of each point with a predetermined threshold value α (generally selected blocking costs of stereo matching of dynamic programming on the high resolution images as the threshold value), the candidate control points less than α all incorporated into sets GCPs first. Otherwise, out of.

3.3 Strike a final control point set on the high-resolution images

The second stage is strike final control point set $GCPs_{last}$ on the high-resolution image This phase is divided into two steps:

(1) Calculate the initial matching cost on the high -resolution image of left and right images first, establish disparity space images.

(2) The matching costs of candidate control point recorded on low-resolution images, will be consideration with all the matching cost of corresponding columns of this point on the high-resolution image disparity space one by one . If its value is still minimal, then into the final control point set GCPs_{last}. Otherwise, out of.

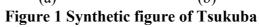
We have corrected the obtained disparity space images on high-resolution images with the final control point, then using dynamic programming method to do stereo matching. Because the major time-consuming work of this method to obtaining the control points conduct on low-resolution images, while greatly reducing time of algorithm.

4 Experiment and experimental results

In order to verify the correctness of the algorithm, using Tsukuba synthetic perspective view to conducted experiments. Tsukuba perspective view satisfy the principle of parallel stereo vision ranging and epipolar constraints, and no noise, it can be directly applied various stereo matching algorithm to it.

Left Tuskuba perspective view showing as 3(a), the width is 384, height is 288, the true disparity shown in in Figure 1(b).





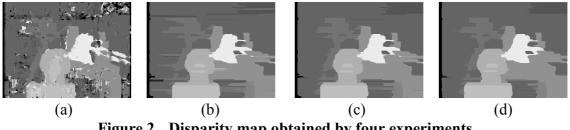


Figure 2 Disparity map obtained by four experiments

Through qualitatively comparison of the four experiments by figure 4, it can be seen, there are more false matching in the blocked area of disparity map outputted from experiments (a), therefore the parallax figure have more miscellaneous points; the quality of the parallax figure outputted from experiment (b) is much better, but there are streaks flaws; of the disparity map outputted from experiments (c) eliminates streaks defects significantly; the effect of experiments (d) and experimental (c) is almost the same.

In addition to qualitative comparison, we also quantitatively compare these four algorithms, as shown in Table 1.

Table 1 reflormance comparison of four groups experiments						
	Experiment (1)	Experiment (2)	Experiment (3)	Experiment (4)		
Matching rate	68.5%	85.4%	91.1%	91.0%		
Time	790ms	673ms	935ms	804ms		

Table 1 Performance comparison of four groups experiments

It can be seen by quantitatively comparison of Table 1, the matching rate of experiment (3), (4) is much higher than the experimental (1), (2), but the experiment (3) used too long time. The experiments (4) have high matching rate, low time consuming, it is the most ideal, which proves that the proposed stereo matching algorithm based on double pyramid dynamic programming is effective.

5 Conclusion

In this paper, conduct research for problem of excessive time-consuming of stereo matching algorithm based on control point dynamic programming, after accurately analysis of reasons for excessive time to use when obtaining control points, we propose a stereo matching algorithm of double pyramid dynamic programming.

This algorithm obtain high and low-resolution images by pyramid algorithms,, the first to strike candidate control point set on the low-resolution image, later obtaining the final control point set on the high-resolution images and use this control point set amended stereo matching of dynamic programming on the high resolution image, get good quality disparity map. Obtaining of candidate control point set is on the low-resolution image, but also greatly shorten the algorithm time. In order to ensure the matching accuracy of the premise, greatly improving the real-time of matching algorithm, laid the foundation for the completion of the subsequent mobile robot visual navigation task.

Acknowledgment

This study was supported by National University Students' Innovative Undertaking Training Program with name "Research on stereo vision 3D reconstruction method based on the works of snow sculpture(201310214023)" and Scientific and Technological Project of Education Department of Heilongjiang Province with grant number(12521083).

References

- Velianki Pratibha, Khambete Madhuri. International Journal of Computer Science Issues, 2011, 8(3): 483-486.
- [2] DeMaeztu Leonardo, Mattoccia Stefano, Villanueva, Arantxa, Cabeza Rafael.Proceeding of the IEEE International Conference on Computer Vision, 2011, 1708-1715.
- [3] Ohta Y and Kanade T. IEEE Trans on Pattern Analysis and Machine Intelligence, PAMI, 1985, vol. 7, no. 2, pp. 139-154.
- [4] Stephen S. Intille and Aaron F. Bobick. Disparity-space images and large occlusion stereo[A]. In: ECCV, 1994:179-186.

Accurate Calibration Method for a Computer Vision System

Wei Jizhou¹, Yu Shuchun^{1,a}, Wu Hongbing¹, Zhang Yawei¹, Feng Yongmeng¹

¹The higher educational key laboratory for Measuring & Control Technology and Instrumentations of Heilongjiang Province, Harbin University of Science and Technology, 150080, China

^ayscls2013@163.com

Keywords: Quantization noise; Quadrature error; Radial distortion; Tangential distortion

Abstract. A high-precision calibration method was proposed. This method is divided four steps: extracting calibration data, building model, calculating inside and outside parameters, and correcting camera distortion. Experimental results show that calibration is very accurate and the total error is not more than 0.06 pixels.

1 Introduction

Calibration process involves a computer vision system calibration block or calibration template production, calibration point coordinate data extraction, multiple stages of cameras inside and outside the parameters of the calculation and optimization^[1], calibration results by the calibration block machining precision calibration point data accuracy, precision factory camera, lens distortion, a variety of lighting conditions and other factors affecting contain a lot of errors. The calibration of the current domestic and foreign researchers working mostly focused on how to simplify the calibration algorithm^[2], calibration of the majority of the radial error to consider only the lens distortion ^[4], other errors are rarely mentioned or simply ignored^[4]. Such calibration results can often meet the low accuracy requirements of the occasion, the precision requirements of the job do not apply.

In this paper, a phased-precision calibration method was proposed. This method will work on computer vision system calibration clearly divided into calibration data extraction, calibration, model building, inside and outside the parameters of the calculation and optimization of the camera distortion correction four stages, with the progress of the calibration process, carried out by one of several major errors compensation or correction.

2 Phases precision calibration method

This paper proposes a phased, high-precision calibration method, the entire calibration process is divided into clear calibration data extraction, calibration, model building, inside and outside the parameters of the calculation and optimization of the camera distortion correction four stages. With the calibration work of several major errors get corrected one by one.

2.1Calibrationdata extraction

In order to reduce the overall cost of the calibration work, we used a two-dimensional calibration template. Template images generated by a computer, the background is black, a total of 256 white circular area on a black background. Each white circle with a radius of 5mm, two adjacent circle center distance of 15mm.Experiment,this template image pasted on a piece of aluminum carbide. This aluminum is lower than the overallprecision0.2mm, flatness of less than 0.03mm.

2.2Calibration model established

When the world coordinate sand image coordinate soft he calibration points extraction is complete, we need to create a visual model of the imaging system, will coordinate information linking the two, and then measured by the coordinate information obtained model unknown, it has been initial parameters of the visual system. Let an arbitrary point $W = [X, Y, Z]^T$ in the world coordinate point $m = [u, v]^T$ is projected on to the image plane, the projection of the geometric relationship between them can be expressed.

$$\begin{bmatrix} u & v & 1 \end{bmatrix}^T = P \begin{bmatrix} X & Y & Z & 1 \end{bmatrix}^T$$
(1)

Where in P is a perspective projection 3*4 matrix can be expressed as:

$$P = A[R \quad T] \tag{2}$$

2.3 Calculation and optimization of internal and external camera parameters

2.3.1 Camerasinside and outside the parameters of the calculation

Cameras in side and outside the parameters of this step is to calculate the optimization process behind the initial iteration provided. First, we use the front of the measured calibration data and calibration model, find the homography matrix H. And then closed solution algorithm derived using internal and external camera parameters.

2.3.2 Optimization of internal and external camera parameters

After the initial camera to get in side and outside the parameters, we use an iterative maximum likelihood be optimized.

The above method is used in two parts Zhang Zheng you calibration algorithm, due to limited space, not in this detail, see reference[4].

2.3.3 does not mind the error correction

Perspective projection, objects of arbitrary shape right mind would produce an error on the accuracy of the calibration data extraction, the impact is great.

In this paper, for example, between the time when a large plane and camera calibration template focal plane angle, calibration template image circle is not twisted heart error ellipse, we extract the center resulting in inaccurate. However, due to processing errors need to use this camera parameters, therefore, right to the heart of where errors can be corrected.

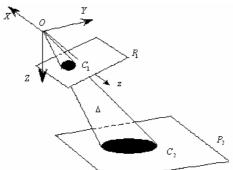


Figure 1 Asymmetric projection of a circle

Shown in Figure 3, the focus of the camera taken as the origin of the world coordinate system $\Omega_2(X, Y, Z) \in \Re^3$, Let P_2 Z axis orthogonal to the surface of the template P_2 on the circle C_2 to the origin O converging boundary projection, and form an helical cone Δ , Δ can be expressed as: $(X - \alpha Z)^2 + (Y - \beta Z)^2 = \delta^2 Z^2$ (3)

A formula in clination α , β respectively the X, Y direction, δ is a Δ sharpness.

 $\Omega_1(x, y, z) \in \Re^3$ in the camera coordinate system to the origin O, z axis orthogonal to the image plane P_1, x, y axis is parallel to the image u, v axes. Such transformation between the world coordinate system and the camera coordinate system Ω_1 below:

$$\begin{bmatrix} X \\ Y \\ Z \end{bmatrix} = \begin{bmatrix} a_{11} & a_{12} & a_{13} \\ a_{21} & a_{22} & a_{23} \\ a_{31} & a_{32} & a_{33} \end{bmatrix} \begin{bmatrix} x \\ y \\ z \end{bmatrix}$$
(4)

Where the vector $[a_{11}, a_{21}, a_{31}]^T$, $[a_{12}, a_{22}, a_{32}]^T$, $[a_{13}, a_{23}, a_{33}]^T$ is a set of orthonormal basis. You can now type(4) are translated to the camera coordinate system:

$$[(a_{11} - \alpha a_{31})x + (a_{12} - \alpha a_{32})y + (a_{13} - \alpha a_{33})z]^{2} + [(a_{21} - \beta a_{31})x + (a_{22} - \beta a_{32})y + (a_{23} - \beta a_{33})z]^{2} = \delta^{2}(a_{31}x + a_{32}y + a_{33}z)^{2}$$
(5)

Since the distance from the origin O to the plane P_1 is the focal length f, and the curve $C_1 \Delta P_1$ formed on the surface can be expressed as follows:

$$(n^{2} + k^{2} - r^{2})x^{2} + 2(kl + np - rs)xy + (l^{2} + p^{2} - s^{2})y^{2} + 2(km + nq - rt)x + 2(lm + pq - st) + m^{2} + q^{2} - t^{2} = 0$$
(6)

When $\delta = 0$, i.e., P_2 plane parallel to the plane P_1 , then all errors on the heart, the curve C_1 is a circle whose center $(\tilde{u}_0, \tilde{v}_0)$ is obtained by the formula:.

$$\widetilde{u}_0 = (lq - pm)/(kp - nl)$$

$$\widetilde{v}_0 = (mn - kq)/(kp - nl)$$
(7)

These results show that $(\tilde{u}_c - \tilde{u}_0, \tilde{v}_c - \tilde{v}_0)$ is not the heart errors. When we make the following image pixel type of correction, not the heart to correct the error.

$$u' = u - k_u (\widetilde{u}_c - \widetilde{u}_0)$$

$$v' = v - k_v (\widetilde{v}_c - \widetilde{v}_0)$$
(8)

After this method for all image coordinates calibration data error correction does not mind, you should re-optimize internal and external camera parameters.

2.4Distortion Correction

Lens distortion is the most important computer vision system error sources, in order to obtain high-precision calibration results, apart from the lens radial distortion correction, but also on the tangential distortion has been corrected.

(u',v') is the ideal coordinates of the image pixels, the pixel coordinates of the image (u,v) is measured with a radial and tangential distortion aberration, the relationship between the two is as follows:

$$u = k_{u} (k_{2}u'^{5} + 2k_{2}u'^{3}v'^{2} + k_{2}u'v'^{4} + k_{1}u'^{3} + k_{1}u'v'^{2} + 3p_{2}u'^{2} + 2p_{1}u'v' + p_{2}v'^{2} + u') + u_{0}$$

$$v = k_{v} (k_{2}u'^{4}v' + 2k_{2}u'^{2}v'^{3} + k_{2}v'^{5} + k_{1}u'^{2}v' + k_{1}v'^{3} + p_{1}u'^{2} + 2p_{2}u'v' + 3p_{1}v'^{2} + v') + v_{0}$$
(9)

Wherein k_1 , k_2 is a radial distortion coefficient, p_1 , p_2 is the tangential distortion coefficients.

3 Experiment and Analysis

We conducted experiments according to the method described above, the procedure is as follows:

(a) the template of Figure 1takentwice, rotated 90 degrees relative to the two cameras. The geometrical relationships between the calibration points 256 to strike the center of the world coordinates of the template because of high accuracy, the measurement error of the world coordinates negligible. Methods Figure 2 shows two images of the winning strike point image coordinates, which are up to sub-pixel accuracy, in addition to better quantify the impact of noise.

(b) the use of section 3.2 calibration model for obtaining initial parameters and optimize the camera. Since the model is scaled five full model parameters, the image factor and two-axis tilt factors are calculated, so that errors can be caused by both compensated.

(c) Using the method described in Section3.3.3ofthe heart does not fix the error, while optimizing the camera parameters again.

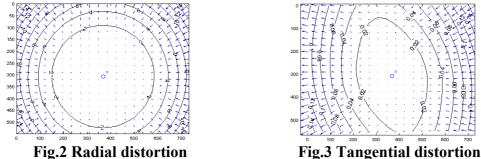
(d) using the method of 3.4, correcting lens distortion, while optimizing the camera parameters again. Through experiments we found:

(a) skew factor $\gamma = 0.00017$, which is equivalent to the image angle of 89.99045 degrees vertical and horizontal axes. This shows that the error caused γ small, for the general accuracy of the calibration may or slightly.

(b) the scaling factor $f_u / f_v = 1.0033$. This shows that the scaling factor is much larger than the tilt factor, if not the accuracy is very low, it is best not ignored.

(c) Does not mind the error caused by the error of the pixel coordinates within 0.02 pixel units, the general accuracy of the calibration mayor slightly.

(d) Effect of radial distortion and tangential distortion as shown below:



As can be seen from Figure 2, Figure 3, the greatest impact on the pixel coordinates of theradial distortion reaches 10 or more units of pixels, and tangential distortion, but the greatest impact on the unit pixel 0.14 pixel coordinates. Therefore, the general accuracy of the calibration, tangential distortion is negligible; radially distortion calibration process as the main error must be corrected.

Horizontal and vertical coordinates of the image can be seen that the total error after the calibration e_u , e_v are only 0.0578, 0.0407 units of pixels, a very accurate calibration.

5 Conclusion

Detailed analysis of the computer vision system calibration error in composition, and thus presents a high-precision calibration method. This method will work on computer vision system calibration clearly divided into four stages, with the progress of the calibration process, has the pixel quantization noise error, the image axis orthogonal error, does not mind the error, the lens radial distortion and tangential distortion error errors were corrected. The experimental results show that this method can be very accurate calibration results.

Acknowledgment

This study was supported by National University Students' Innovative Undertaking Training Program with name"Research on stereo vision 3D reconstruction method based on the works of snow sculpture(201310214023)"and Scientific and Technological Project of Education Department of Heilongjiang Province with grant number(12521083).

References

- [1] Sun Jin, Gu Hongbin. World Academy of Science Engineering and Technology, 2011, 60: 627-631.
- [2] Cai Shen, Zhao Zijian, Huang Longxiang. Liu Yuncai. Machine Vision and Applications, 2013, 24(3): 513-520.
- [3] Zhang, Z.Y. Proceedings of IEEE International Conference on Computer Vision, 1999, 1: 666~673.
- [4] Heikklia, Janne. IEEE Transaction on Pattern Analysis and Machine Intelligence, 2000, 22(10): 1066-1077.

A Image Retrival Method with Multi-Features Based on Dempster-Shafer Theory

Ji meng¹, Sun xiaoming^{1,a}, Chen xin¹, Qi lijun¹, Bao lei¹ and Huang lei¹

¹The higher Educational Key Laboratory for Measuring & Control Technology and Instrumentations of Heilongjiang Province, Harbin University of Science and Technology, Harbin 150080, China

^axiaoming_66881982@163.com

Keywords: image retrival, Multi-features fusion, multi-scale Gabor wavelet, Dempster-Shafer evidence theory

Abstract. Image content based retrieval is an important research area with application to digital libraries and multimedia databases. Its image characterization and similarity measure must closely follow perceptual characteristics. In this work, a new image retrieval method is proposed by combining color features and texture features based on Dempster-Shafer (D-S) theory. In this proposed method, Multi-color features included color histogram, color moment and color correlogram are used for color analysis, and gabor wavelet features is employed for texture analysis. Then these features are modeled as a mass function in evidence theory, and color and texture detection results are fused at decision-making level. The experimental results show that the proposed method takes advantage of the respective merits of color and texture features and texture detection results are fused at decision-making level. The experimental results show that the proposed method takes advantage of the respective merits of color and texture features and therefore improves retrieval accuracy and reduces recognition error rate.

Introduction

With the development of the internet, efficient image searching tools are required by users from various domains [1]. More and more people begin to research image retrieval algorithm. At present, There are two frameworks: text-based and content-based. Text-based method need text descriptors annotated manually, so this method is time-consuming, laborious; to address this, content-based image retrieval was introduced in the early 1980s[2-3].Content-based image retrieval means of retrieving and querying images by visual content, such as color, texture and shapes. Image retrieval include feature Extraction, feature fusion these two important steps. Though many sophisticated algorithms have been designed to describe color, shape, and texture features, there still have many limitations. The traditional content-based image retrieval method mainly use the single features of the images based on color, texture, shape features, or multi-features based on simple weighted[4]. In order to improve the retrieval accuracy, this paper proposes an image retrieval method with multi-feature based Dempster-Shafer theory.

Poposed algorithm for image retrieval based on Dempster-Shafer theory

1. Dempster-Shafer evidence theory

The combinational recognition of multi-sensor target is trying to combine imprecise and, incomplete information of target property in each sensor, to produce the more accurate and complete property estimates and judgment for property than single senor[5-7]. In D-S theory, a sample space is called a frame of discernment or the domain, which has a set of mutually exclusive and exhaustive elements, and is symbolized by $\Theta = \{\theta_1, \theta_2, ..., \theta_N\}$. In D-S theory, there are three important functions: the basic probability assignment function (BPA or m), the Belief function (Bel), and the Plausibility function (Pl).

The BPA on the frame of discernment Θ is a function m, which working space 2^{Θ} belongs to [0,1], and we called it the mass function. The value of the BPA for a given subset *A*, represented as

 $m(A), 0 \le m(A) \le 1$ and also meet this condition: $m(\emptyset) = 0, \sum_{A \subseteq \Theta} m(A) = 1$. The belief function Bel on the recognition framework Θ is defined as:

$$Bel(A) = \sum_{B \subseteq A} m(B), A \subseteq \Theta, B \subseteq \Theta, \text{ and } Bel(\emptyset) = 0, Bel(\Theta) = 1;$$
 (1)

The Plausibility function of the hypothetical set $^{A,A \in 2^{\Theta}}$, refers to extent of no objection A (or refute A). The Plausibility function on the recognition framework $^{\Theta}$ is defined as:

$$Pl(A) = \sum_{B \cap A \neq \emptyset} m(B), A \subseteq \Theta, B \subseteq \Theta$$
⁽²⁾

The Dempster combinational rule which is also known as the evidence combination formula, is defined as follows: for $\forall A \subseteq \Theta$, the Dempster's combinational rule of two mass functions m_1 , m_2 on the Θ is shown as:

$$m_1 \oplus m_2(A) = \frac{1}{1 - K} \sum_{B \cap C = A} m_1(B) \cdot m_2(C)$$
(3)

where $K = \sum_{B \cap C = \emptyset} m_1(B) \cdot m_2(C)$, the *K* refers to normalization factor and its value refers to degree of conflict between $m_1(B)$ and $m_2(C)$. The larger the *K*, the more conflicting the sources and the less sense their combination.

2. Model of data Fusion of color and texture features

The block diagram of image retrieval based on fusion of texture feature and color features is shown in Figure 1. According to D-S theory, we set the Frame of discernment is $\Theta = \{yes, no\}$ and the power set is $2^{\Theta} = \{\emptyset, \{yes\}, \{no\}\}$. Yes denotes that retrieval result is the retrieval image and no means retrieval result is wrong. For brief representation, let *Y* represents yes, *N* represents no; therefore, $\Theta = \{Y, N\}, 2^{\Theta} = \{\emptyset, \{Y\}, \{N\}\}$.

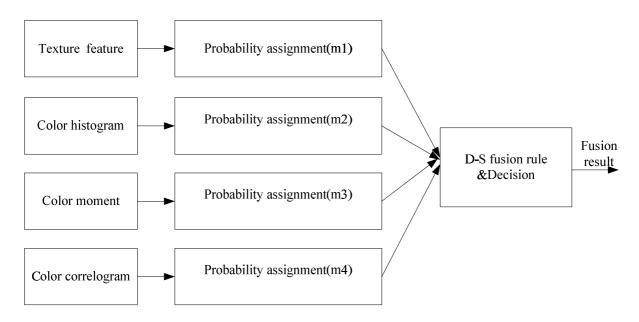


Fig. 1 The block diagram of image retrieval based on D-S theory

For the image color feature extraction, the single color feature cannot describe the color information comprehensively and accurately. For example, the most common feature color histogram, can describe the rough proportion of various colors in images, but it cannot describe the relative position of different colors. So in this paper, we use multi-color features about color histogram, color moments, and color correlation to express image color space position and color information more accurately. For the image texture feature extraction, this paper chooses the multi-scale Gabor wavelet transform which has good spatial locality and direction selectivity as texture features. The D-S combination rule of features is shown in Table 1. The value of the BPA m_i can be got from maximum Euclidean distance to measure the similarity between images. m(Y) and m(N) can be calculated from Eq.3. After D-S fusion, Retrieval results are sorted by m(Y)

Tał	ole 1 The D-S combi	nation ru	le of features
		Y	N
	Texture	$m_1(Y)$	$m_1(N)$
	Color histogram	$m_2(Y)$	$m_2(N)$
	Color moment	$m_3(Y)$	$m_3(N)$
	Color correlogram	$m_4(Y)$	$m_4(N)$
	After D-S fusion	m(Y)	m(N)

Experiment results and analysis

In order to verify the proposed method, we selected standard Corel image library to make experiments. Retrieval precision and recall were used as evaluation criteria for retrieval performance.

1. Select Africa image as query image, the number of images in library is 100. We just show a part of them, as shown in Fig.2. The precision was 90%, the recall rate was 18%.

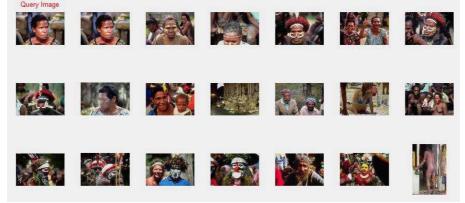


Fig. 2 The image retrieval result of africa based on D-S fusion

2. Select dinosaur image as query image, as shown in Fig.3. The precision was 95%, the recall rate was 19%.



Fig. 3 The image retrieval result of dinosaur based on D-S fusion

3. Select five categories of different type images, and compare the retrieval results between color feature, texture feature and fusion features. The comparison result is shown in Fig.4.

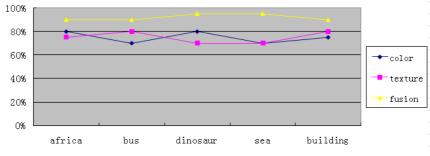


Fig. 4 Recall comparison based on color, texture and integrated multi feature

From the above experiments, we can see that the proposed method have high precision, and the retrieval algorithm accuracy is higher than the retrieval algorithm only based on the single feature.

Conclusion

In this paper, we introduce the Dempster-Shafer theory, and propose an image retrieval method with multi-features based on Dempster-Shafer theory; Then design the image retrieval system based on multi-featured fusion, The results show that the image retrieval algorithm with multi-featured fusion can effectively improve the accuracy of image retrieval, and meet the actual needs of content-based image retrieval. In future work, we will add shape features to the fusion detection method to improve the practicability of algorithm.

Aknowlegement

University Students' Innovation and Entrepreneurship Training Project of harbin university of science and technology(Design and implementation of content-based image retrieval system, number: 201310214040)

References

- [1] Ying Liu, Dengsheng Zhang, Guojun Lu, Wei-Ying Ma: A survey of content-based image retrieval with high-level semantics. Vol. 40 (2007), p. 262 282.
- [2] J. Eakins, M. Graham, Content-based image retrieval, Technical Report, University of Northumbria at Newcastle, 1999.
- [3] I.K. Sethi, I.L. Coman, Mining association rules between low-level image features and high-level concepts, Proceedings of the SPIE Data Mining and Knowledge Discovery, vol. III, 2001, pp. 279–290.
- [4] Ilea, Dana E., and Paul F. Whelan. Image segmentation based on the integration of colour-texture descriptors—A review[J].Pattern Recognition. 2011,44(10): 2479-2501.
- [5] van Lint, J. W. C. & Hoogendoorn, S. P. (2010), A Robust and Efficient Method for Fusing Heterogeneous Data from Traffic Sensors on Freeways, Computer-Aided Civil and Infrastructure Engineering, 25(8), 596-612.
- [6] Luo, R. C., Chang, C. C. & Lai, C. C. (2011), Multisensor Fusion and Integration: Theories, Applications, and Its Perspectives, Ieee Sensors Journal, 11(12), 3122-3138.
- [7] Treiber, M., Kesting, A. & Wilson, R. E. (2011), Reconstructing the Traffic State by Fusion of Heterogeneous Data, Computer-Aided Civil and Infrastructure Engineering, 26(6), 408-419.

The Projector Calibration Based on ZHANG's Self-calibration Method

Guang Yu^{1, a}, Boyang Yu^{2, b}, Shucai Yang^{1, c},Li Wen^{1, d},Wenfei Dong^{2, e} and Hui Wang^{2, f}

¹Engineering Training Center, Harbin University of Science and Technology, Harbin, China ²Measuring and Control Technology and Instrumentations, Harbin University of Science and Technology, Harbin, China

^a285294708@qq.com, ^b249578453@qq.com, ^c276936958@qq.com, ^d404241415@qq.com, ^e949333161@qq.com, ^f765724425@qq.com

Keywords: projector calibration, ZHANG's self-calibration, DMD, The internal and external parameters calibration

Abstract. Projector calibration can be seen as a special case of the camera calibration. It can establish the relationship of the three dimensional space coordinates for points and projector image coordinates for points DMD by using a projector to project coding pattern. In camera calibration, ZHANG's self-calibration was conducted in the maximum likelihood linear refinement. Operation process takes the lens distortion factors into account finding out the camera internal and external parameters finally. Using this algorithm to the projector calibration can solve the traditional linear calibration algorithm which is complex and poor robustness. Otherwise, it can improve the practicability of calibration method. This method can both calibrate the internal and external parameters of projector, which can solve the problem of independently inside or outside calibration.

Introduction

The projector calibration is a branch of camera calibration. The camera can establish the correspondence of CCD image coordinates for points and space standard coordinate for points. Because the calibration image template can not be captured by the projector, the correspondence between image coordinate for points and space standard coordinate for points must be established by the camera. The traditional linear calibration is algorithm and low calibration accuracy. This paper presents a new method for calibration of projector, which obtains the feature points by color coding pattern. Zhang's calibration method is introduced to establish the correspondence of three-dimensional feature coordinate for points and projector image coordinates for points DMD .It can calculate the intrinsic and extrinsic parameters of camera, using the comparing experimental to verify the accuracy of this method.

The System Modeling of Projector Calibration

This designed projector calibration system includes template, optical precision guide and supplemented a digital camera. Template move along the direction of projection of the projector on the specific optical guide, cameras take three pictures accordingly at least.

In the process of calibration of the projector, the projector can be seen as a reverse camera, learn from the establishment of camera calibration parameters, the projector parameter model can be expressed by Equation 1:

$$Z_{c}\begin{bmatrix} u\\v\\1\end{bmatrix} = \begin{bmatrix} f_{u} & \gamma & u_{0}\\0 & f_{v} & v_{0}\\0 & 0 & 1\end{bmatrix} \begin{bmatrix} R & t\\0^{T} & 1\end{bmatrix} \begin{bmatrix} X_{w}\\Y_{w}\\Z_{w}\\1\end{bmatrix} = K[R \quad T]M$$
(1)

The Intrinsic Parameters of Projector Calibration

The calibration template placed first at the space coordinates which is Z = 0 Can be obtained:

$$h_1^T A^{-T} A^{-1} h_2 = 0$$

$$h_1^T A^{-T} A^{-1} h_1 = h_2^T A^{-T} A^{-1} h_2$$
(2)

If there are n pieces of planar template image, by the formula (2) can be obtained linear equations:

$$Vb = 0 \tag{3}$$

Eventually it can solve the various internal parameters of the camera.

Coordinates Acquisition for Planar Feature Point of the Projectors

Acquisition process of feature point coordinates on the projector projection plane can be summarized as follows:

(1) At first, create an index table of color and location arrangement of color pseudo-random coded template based on window size.

(2) Extracting the adjacent six points on the image of the same size of the window ,then on the index table is sequentially scanned to get the same color combination, that is a successful match, then the matching coordinates of the six feature point in this window can be determined .

Intercept part of the projected image to illustrate, as shown in Figure 1.

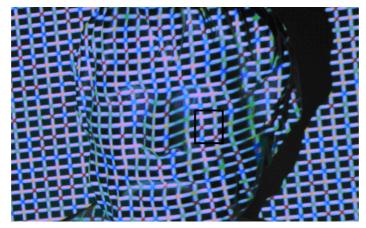


Fig.1 The work screenshot of detection window

The External Parameters of Projector Calibration

This article will solve the solutions of external parameters R and T of the projectors and that is the rotation matrix and the translation vector of the projector relative to the camera.

Wherein the parameters R can be represented by the three trigonometric functions of the Euler angles, α , β , γ respectively are the rotation angles around the projector of the axis X, and the axis Y and the axis Z (the camera optical axis), R can be expressed by the following equation:

$$R = \begin{bmatrix} \cos \gamma & -\sin \gamma & 0\\ \sin \gamma & \cos \gamma & 0\\ 0 & 0 & 1 \end{bmatrix} \begin{bmatrix} \cos \beta & 0 & -\sin \beta\\ 0 & 1 & 0\\ \sin \beta & 0 & \cos \beta \end{bmatrix} \begin{bmatrix} 1 & 0 & 0\\ 0 & \cos \alpha & -\sin \alpha\\ 0 & \sin \alpha & \cos \alpha \end{bmatrix}$$
(4)

Calibration Experiment and Data Analysis

The projector calibration image based on the color pseudo-random encoded is shown in figure 2:

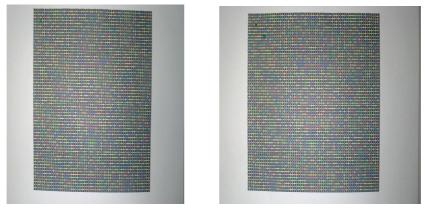


Fig.2 Pseudo-random color encoded calibration experiment image The intrinsic parameters result of projector calibration is shown in table 1: Table.1 The intrinsic parameters result of projector calibration

	-		
The measured parameters	Measured value	True value	Measurement error
k_1	0.0006	0.0007	0.0001
k_2	-3.9723	-3.9720	0.0003
f_x	1797.4	1796.8	0.60
f_y	1817.4	1816.9	0.50
u_0	515.0	513.7	1.3
v_0	254.7	253.3	1.4
S	-17.4	-17.1	0.30

The external parameters result of projector calibration is shown in table 2: Table 2 The external parameters result of projector calibration

Table.2 The external parameters result of projector canoration							
The measured parameters	Measured value	True value	Measu rement error	The measured parameters	Measured value	True value	Measure ment error
r_{11}^{p}	0.940	0.940	0.000	r_{32}^{p}	-0.000	0	0.000
r_{12}^{p}	0.000	0	0.000	r_{33}^{p}	0.940	0.940	0.000
r_{13}^{p}	0.326	0.326	0.000	$t_{\rm x}^{\ \rm p}$	-0.070	0	0.070
r_{21}^{p}	0.000	0	0.000	t_v^{p}	50.000	50.000	0.000
r_{22}^{p}	1.000	1	0.000	t_z^{p}	-617.233	-615.318	1.815
r_{23}^{p}	0.000	0	0.000	β_1^{p}	30.214°	30.284°	-0.070
r_{31}^{p}	-0.415	-0.415	0.000	β_2^{p}	17.590°	17.523°	-0.067

It can be seen from the above experimental results, the measurement error of intrinsic and external parameters is small based on the ZHANG's projector calibration method.

Summary

The projector calibration can be regarded as a special case of camera calibration. This paper carries on the projector calibration which is based on the principle of ZHANG's camera self-calibration.

This method is good stability, high accuracy, practical and easy to make the calibration template. The projector can be regarded as a reverse camera in the process of calibration, so ZHANG's self-calibration is applied to the projector calibration. This method is nonlinear solution based on maximum likelihood, which not only can improve the calibration precision, but also can increase the comprehensive calibration parameters. It can calculate the intrinsic and external parameters. At last, the results of experiments demonstrated that the system performances are good.

Acknowledgements

This paper is based on the innovation and entrepreneurship training program of Harbin University of Science and technology.

References

- [1] Zhang Song. High-resolution, real-time 3-D shape measurement[D]. Thesis for the Doctor's Degree in Engingeering. Stony Brook University, 2009: 101~108
- [2] Hirooka. Shinichiro, Nakano. Norihiko, Kazui. Masato. 3D camera calibration using Gray code patterns[C]. 2008 Digest of Technical Papers, International Conference on Consumer Electronics, The Mobile Consumer, 2010: 4587987
- [3] Wang Jian Hua.Shi Fanhuai.Zhang Jing A new calibration model of camera lens distortion 2010, (2):86-95.
- [4] Sirisantisamrid Kaset, Tirasesth Kitti, Matsuura Takenobu. Determine calibration parameters with satisfied constraints for coplanar camera calibration[C]. IEEE Region 10 Annual International Conference Proceedings, 2012: 4084939
- [5] Hartley R.self-calibration of stationary cameras. International Journal of Computer Vision,2005, 22(1):5-23.
- [6] Yu X Y, Ji R, Wu M Y, et al.. Simulation of 3D measurement system based on structured light calibration[C]. International Conference on Sensing, Computing and Automation, 2011, 13: 1481~1484

Sonar Image Segmentation using the Level Set Method without Reinitialization

Guangyu Liu^{1,a}, Yongjie Pang¹, Hongyu Bian², Enming Zhao³ ¹College of Shipbuilding Engineering, Harbin Engineering University, China ²College of Underwater Acoustics Engineering, Harbin Engineering University, China ³College of Science, Harbin Engineering University, China ^a2408468655@qq.com

Keywords: forward looking sonar image; level set; image segmentation; morphological operations

Abstract. To solve the problem that many image segmentation methods cannot be applied to forward looking sonar image accurately, an improved level set segmentation method was proposed in this paper. Firstly, the level set evolution without re-initialization was introduced. Secondly the different characteristics of forward looking sonar image from the optical image were analyzed, and we got the factors affecting segmentation. Then, to overcome these negative effects, this paper did preprocessing by morphological top-hat and bottom-hat transformation, and carried on level set method without re-initialization to construct an improved level set sonar image segmentation system. Finally, our method was compared with the traditional level set method in computer experiments. Simulation results show that it is more adapted to forward looking sonar image segmentation.

Introduction

Sonar image segmentation is the premise of late processing including target recognition, tracking, classification, and so on, it plays an important role in sonar image processing, so it is urgent and valuable for the research of sonar image segmentation. Today many scholars did the research of sonar image segmentation and have achieved some successful sonar image segmentation methods such as Markov random fields [1], neural networks [2], spectral clustering [3] and so on. In recent years, with the successful application of partial differential equation in image processing, image segmentation method based on level set [4] was put forward, and because it can be superior in solving curve topology structure transformation problems to the parameterization methods, it has become important research direction in mechanics, computer graphics, image processing and target tracking fields [5]. Level set application in image processing is mainly reflected in image segmentation. There have two kinds of image segmentation methods based on level set, one is the level set based on C-V model proposed by Chan and Vese [6], the other is level set without reinitialization proposed by Li [7]. The latter kind is an improved model by taking the local characteristics of the image into account. It amends the defects of the former essentially, and the computational complexity is greatly reduced.

This paper mainly studied the level set segmentation without re-initialization, which performance is prominent in optical image segmentation. But in sonar image segmentation, its application research is not enough yet. So we discussed the application of level set in sonar image segmentation and proposed an improved level set image segmentation method in this paper.

Level Set without Re-initialization

Active contour, also known as curve evolution, is a dynamic process of curve transformation over time. On the basis of active contour, level set partial differential equation evolution is relatively simple and easy to extend to higher dimensions. But it needs stopping evolution periodically and reinitialize the level set function to a signed distance function $\varphi(x)$. So some studies considered

for level set evolution method without re-initialization. In this paper, we use such method based on energy penalty term [8], and the energy function is defined as:

$$E(\varphi) = \mu P(\varphi) + E_m(\varphi) \tag{1}$$

Where μ is a constant. $P(\varphi)$ is the energy penalty term and $E_m(\varphi)$ is an energy driver of contour curve evolution. $P(\varphi)$ can be expressed in the level set evolution as:

$$\Delta \varphi - div(\frac{\nabla \varphi}{|\nabla \varphi|}) = div[(1 - \frac{1}{|\nabla \varphi|})\nabla \varphi]$$
⁽²⁾

where the $1-\frac{1}{|\nabla \varphi|}$ is a factor affecting the diffusion rate. It is easy to see the significance of the energy penalty term. When $|\nabla \varphi| > 1$, it is forward diffusion and the level set function becomes flat, and thus the gradient decreases. When $|\nabla \varphi| < 1$, it is reverse diffusion and the gradient increases. As we know that one important property of the signed distance function is $|\nabla \varphi| = 1$, so $P(\varphi)$ reduces the deterioration caused by breaking away from the signed distance function. It is equivalent to exert a counterforce to the level set function for maintaining a signed distance function appearance.

Sonar Image Segmentation Method Based on the Improved Level Set

Design Principle. Optical image usually have clear edges and sharp regional characteristics, while sonar image often have low resolution, incomplete and fuzzy boundary, existence of shadows and other features because of its imaging mechanism. So for a forward looking sonar image, the level set evolution without re-initialization is not very satisfactory sometimes. On the one hand, sonar image do not have precise, accurate, clear and obvious boundary feature as optical image, and the boundary of target objects often appear irregular, uncertain, leading to the non-feasibility of many optical image segmentation methods based on edge. On the other hand, noise and reverberation will bring inevitable difficulties to sonar image segmentation. And the existing segmentation methods will easily take interference part as the target object, leading to a segmentation mistake. Therefore, how to obtain a more accurate segmentation method is still a research focus in sonar image segmentation field.

The existing common interference removal methods are the preprocessing methods based on histogram equalization or gray threshold transform, but the result is unsatisfied, because some original image information may be broken at the same time [9]. So this paper do forward looking sonar image preprocessing by morphological operations in view of the application characteristics of enhancement and compensation for image [10]. And we use the level set method without re-initialization to segment forward looking sonar image because of the fuzzy or discontinuous boundaries. In this way, the segmentation result will be better.

Design Steps. Firstly, the morphological top-hat transformation is defined as:

$$I' = I - I \circ b = I - (I \odot b) \oplus b \tag{3}$$

Where *I*' is the output image and $I \circ b$ is the open operation of structure element b(i', j') to image I(i, j). The symbol ' \oplus ' and ' \odot ' are respectively expressed as the dilation and erosion operations. Open operation can remove details brighter than structural element, keep grey value and large bright area in the image basically unchanged, and get a uniform background estimate. Then the image with uniform background can be generated by subtracting the estimated background, and the interference effect can be eliminated.

Next, we take top-hat transformation and bottom-hat transformation together to do sonar image enhancement, and the bottom hat operation is defined as:

$$I' = I - (I \oplus b) = I - (I \oplus b) \ominus b \tag{4}$$

Close operation can remove the smaller dark details than structural element, keeping grey value and large dark area in the image basically unchanged.

After the implementation of the preprocessing based on morphological operations, the image interference has been removed and the edge has been enhanced. Then the level set evolution without re-initialization will be carried on:

$$\frac{\partial \varphi}{\partial t} = \mu [\Delta \varphi - div(\frac{\nabla \varphi}{|\nabla \varphi|})] + [\lambda g \delta(\varphi) + v \delta(\varphi) div(g \frac{\nabla \varphi}{|\nabla \varphi|})]$$
(5)

Where λ and ν are constants and g is the image edges index. Now the improved level set sonar image segmentation method will be finally obtained.

Experiments

In the following simulation experiments, we use two forward looking sonar images with different objects. The most obvious characteristic of these images can be seen easily in Fig.1. In the fish image, there is some interference and in the hand image, the target contour is not continuous. We carried on image segmentation by traditional level set method and our improved method to verify the effectiveness and feasibility we proposed. The experimental results of the two images are shown in Fig. 1(a) and Fig. 1(b) respectively.

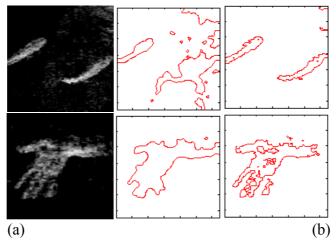


Fig. 1 The segmentation result comparison: (a) fish image; traditional level set method; our method (b) hand image; traditional level set method; our method

From Fig.1, it can be seen that the traditional method make interference to be exported out at the same time with fish, as one part of the foreground object. While the hand image can't be segmented clearly because of the bad image edge. Correspondingly, our method is obviously superior to the traditional level set segmentation method. The proposed level set method combining the morphological preprocessing has only segmented the target foreground without the interference part and its accuracy is improved significantly when the target edge is discontinuous. Therefore, compared with the traditional level set segmentation method, the proposed algorithm in this paper is more suitable for forward looking sonar image segmentation.

Conclusions

The current widely used level set segmentation method for optical image can't accurately segment forward looking sonar image. The biggest problem is the negative impact of interference and incomplete target region in the image. To solve this problem, this paper carried on morphological preprocessing to sonar image before segmentation and constructed a sonar image segmentation system based on the improved level set evolution without re-initialization method. The simulation experimental results demonstrate the feasibility and effectiveness of the proposed method.

Acknowledgments

The project is sponsored by Natural Science Foundation of China (No. 41376102 and No. 41306086). And the work in this paper was supported by the Natural Science Foundation of Heilongjiang province. Moreover, the authors would like to thank the anonymous reviewers who made constructive comments.

References

- S. Ning, S. Taebo, and H. Hernsoo. "Sonar image segmentation based on markov gauss-rayleigh mixture model," International Workshop on Geoscience and Remote Sensing, Shanghai, vol. 12, (2008), p. 704-709.
- [2] L. Zhuofu, S. Enfang, and L. Zhenpeng. "Sonar image segmentation using snake models based on cellular neural network," IEEE International Conference on Information Acquisition, vol. 6, (2005), p. 5.
- [3] C. Moustier, P. F. Lonsdale, and A. N. Shor. "Simultaneous operation of the seabeam multibeam echosounder and the seaMARC II bathymetric sidescan sonar system," IEEE Journal of Oceanic Engineering, vol. 15, no. 2, (1990), p. 84-94.
- [4] N. Li, M. Liu, and Y. Li. "Image segmentation algorithm using watershed transform and level set method," IEEE International Conferent on Acoustics, Speech and Signal Processing (ICASSP), Honolulu, (2007), p. 613-616.
- [5] S. Park, and S. Min. "Optimal topology design of magnetic devices using level-set method," IEEE Transactions on Magnetics. Vol. 45, no. 3, (2009), p. 1610-1613.
- [6] L. Vese, and T. Chan. "A multiphase level set framework for image segmentation using the mumford and shah model," International Journal of Computer Vision, vol. 50, no. 3, (2002), p. 271-293.
- [7] C. Li, C. Y. Kao, and J. Gore. "Implicit active contours driven by local binary fitting energy," IEEE Conference on Computer Vision and Pattern Recognition(CVPR), Minneapolis, (2007), p. 1-7.
- [8] C. Li, C. Xu, C. Gui. "Level set evolution without reinitialization: a new variational formulation," IEEE Conference on Computer Vision and Pattern Recognition, San Diego, vol. 1, (2005), p. 430-436.
- [9] S. Hong, Z. Chunhui, and S. Zhengyan. "Spectral Clustering for Sonar Image Segmentation using Morphological Wavelet and Gray Level Transformation," In 5th International Conference on Computer Science and Education, (2010), p. 1760-1764.
- [10] C. xiaofeng, P. baochang, Z. shenglin, Z. quanyou, and L. jian. "Estimate and eliminate background of image with top-hat transformation," Microcomputer Information, vol. 24, no. 3, (2008), p. 310-311.

Advanced Materials Research Vol. 981 (2014) pp 372-375 © (2014) Trans Tech Publications, Switzerland doi:10.4028/www.scientific.net/AMR.981.372

Cryptanalysis of Elementary Cellular Automata Based Image Encryption

Tiejun.Zhang^{1,a}, I. M.Manhrawy², A. A. Abdo³, A. A. Abd El-Latif^{3,b}, R. Rhouma⁴

¹School of Software, Harbin University of Science and Technology, Harbin, China
 ²Department of Basic Sciences, Modern Academy for Engineering and Technology, Egypt
 ³Department of Mathematics, Computer Science, Faculty of Science, Menoufia University, Egypt
 ⁴Ecole Nationale d'Ingénieurs de Tunis
 ^atiejun.zhang2006@gmail.com, ^bahmed_rahiem@yahoo.com

Keywords: Image encryption, cryptanalysis, elementary cellular automata.

Abstract. An image encryption based on elementary cellular automata was proposed in [Yu Xiao yang *et al.*, International Journal of Security and Its Applications Vol.7, No.5 (2013), pp.397-406.]. In this paper, we analyze the security weaknesses of their algorithm. Based on the given analysis, it is demonstrated that the scheme under study can be broken by various attacks (Chosen Plaintext and Chosen ciphertext attacks).

1. Introduction

Some researchers have pointed out that there exists tight relationship between cellular automata (CA) and cryptography [1- 4]. Many features of cellular automata, such as the periodicity, mixing and the sensitivity to initial conditions and parameters, can be connected with the "confusion" and " diffusion" property in cryptography. An elementary cellular automaton (ECA) is the simplest class of one-dimensional cellular automata, which is a linear array of cells with three neighborhood dependency, and state of each cell is 0 or 1. Based on ECA, an image encryption scheme based on elementary cellular automata (ECA) was proposed [5], where ECA is adopted to generate state attractors for image encryption process. In this paper, we found that the scheme is not secure against various attacks due to the insensitivity problems with respect to both the changes of plain-images and key streams generated by ECA.

2. Description of the scheme under study

The steps of image encryption scheme under study [5] can be described as follows:

Step 1: Select an elementary rule *R*, and specify a unity attractor *T* from *R* with length *k*. The unity attractor *T* satisfies *Eq.* {*state* (1), *state* (2) ..., *state* (*i*)..., *state* (*k*)} and $i \le k$ are the *k* states of such attractor *T*.

Step 2: Select an initial state *i* of the selected attractor *T*.

Step 3: Create randomly an $N \times N$ array T, where $N \times N$ is the original image size. T can be calculated from the Eq. 1.

$$T = \{t(x) \mid t(x) \in [1, k-1], 1 \le x \le seed \}$$

$$\forall x = (r, c), 1 \le r \le n, 1 \le c \le n$$
 (1)

where t(x) represents the number of encrypt time of the x^{th} group's gray value in QR code binary image. Similarly, k - t(x) represents the number of deciphering time. The size of 256*256 QR code binary images is used to do the simulation experiment, so N equals 256; k equals 8, and seed equals 8192.

Step 4: The encryption function of image pixel(x) is calculated by XORing pixel(x) with the successive states for t(x) times as Eq. 2 :

$$C(x) = pixel(x) \oplus state(i) \oplus \dots \oplus state(i+t(x))$$
(2)

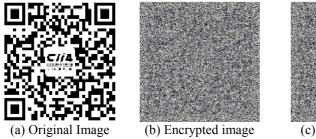
Step 5: The decryption function of image pixel(x) is calculated by XORing pixel(x) with the successive states for k-t(x) times as the following Eq.3:

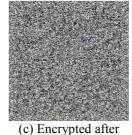
$$P(x) = C(x) \oplus state(i) \oplus \dots \oplus state(i+k-t(x))$$
(3)

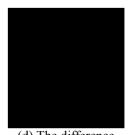
3. Security problems of the scheme under study

3.1 Insensitivity to the change of the plain-image

An image encryption procedure should be sensitive with respect to both the secret key and the plain-image [2]. A slight change in either the secret key or the plain-image should produce a completely different encrypted image. In Fig. 1, the difference between the two encrypted images Fig. 1 (b) and (c) is a black image Fig. 1 (d), which reveals the insensitivity with respect to the change of the plain image.







(c) Encrypted after changing one pixel in the original image.

(d) The difference between (b) and (c).

Figure 1: Simulations results of insensitivity to the change of the plain-image .

3. 2 Choosing-Plaintext Attack (CPA)

In this section, we describe how the secret matrix key K' of encryption algorithm can be extracted using a chosen- plaintext attack. The attack consists of two steps. First, K' is recovered. Then, the attacker uses K' to recover the plain-image P from the arbitrary encrypted image C.

Step1: Extracting the secret matrix T': The attacker chooses a zero plain-image P0 ($N \times N$ dimension) as an input to the encryption machinery. Using Eq.1 with the zero plain-image, the attacker can easily see that the encrypted image C_{rc} is exactly equal to the secret matrix key T' as:

$$\forall P_x : x(r,c) \mid r \in [1,n], c \in [1,n]$$
$$C_{rc} = 0 \oplus state(i) \oplus state(i+1) \oplus \dots \oplus state(i+t(r,c))$$
$$C_{rc} = state(i) \oplus state(i+1) \oplus \dots \oplus state(i+t(r,c))$$

As a result, the attacker obtains the secret matrix key $T'=C'_{rc}$ as the encrypted image for all zero plain-image P_0 .

Step2: Extracting the plain-image P: Once the attacker knows the secret matrix keystream T', he/she can use Eq.2 to correctly reveal the plain-image from an arbitrary encrypted image.

$$C' as \forall C_{n \times n} : r \in [1, n]$$
$$C' \in [1, n] \to P_{rc} = C \oplus T$$

Simulation results of breaking the cryptosystem in a scenario of CPA is given in Fig.2 which shows recovery of the image (QR Code Image) of size 256*256.

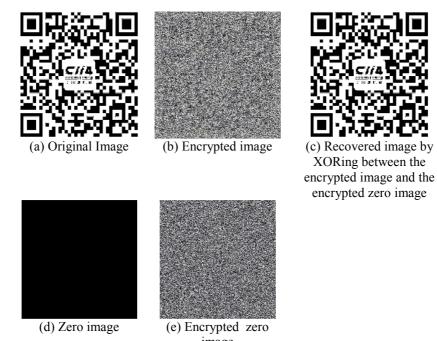


image Figure 2: Simulations results of choosing-ciphertext Attack (CPA).

3.3 Choosing-ciphertext Attack (CCA):

In this section, we describe how the secret matrix key K' of decryption algorithm can be extracted using a chosen ciphertext attack. The attack consists of two steps First, K' is recovered. Then, the attacker uses K' to recover the plain-image P from the arbitrary encrypted image C.

Step1: Extracting the secret matrix key *T*: The attacker chooses zero encrypted ciphertext image $C = \text{zeros}(N \times N)$ by using Eq. 3.

$$\forall P_{n\times n}: i \in [1, n], j \in [1, n] \rightarrow C'_{ii} = 0 \oplus K_{ii} = k_{ii}$$

As a result, the attacker obtains the secret matrix key T as the decrypted image for the all zero chosen ciphertext image C_0 .

Step 2: Extracting the plain-image *P*.

$$\forall P_{n \times n} : i \in [1, n], j \in [1, n] \rightarrow K_{ii} \oplus C_{ii} = P_{ii}$$

4. Conclusion

In this paper, we gave the security weakness of the recently proposed image encryption scheme based on ECA. Based on the given analysis, we demonstrated that the scheme under study can be broken by various cryptanalysis (choosing-plaintext and choosing-ciphertext attacks).

Acknowledgment:

This work was supported by the ministry of Higher Education and Scientific research (Egypt-Tunisia co-operation program 4-13-A1) and GZ11A302 of Heilongjiang Province, China.

References

- [1] J. Jun, Image Encryption Method Based on Elementary Cellular Automata, IEEE SoutheastCon'09, March 2009 Atlanta, (2009) 345-349.
- [2] J. Jun, An Image Encryption Method Based on Elementary Cellular Automata, optics and lasers in engineering 50 (2012), 1836-1843.
- [3] L. Huijun, Research and achievement of image encryption algorithm based on Chaos Cellular Automata, Master's degree thesis of Jiangxi University of Science and Technology, (2011), pp. 23-24.
- [4] X. Yonghong, Digital image encryption algorithms based on Cellular Automata , Master's degree thesis of Chongqing University, (2012), pp. 23-27.
- [5] Y.X. Yang, S. Yang, Y Yang, C. Hao and Y. Guan, An Encryption Method for QR Code Image Based on ECA, International Journal of Security and Its Applications Vol.7, No.5 (2013), pp.397-406.

Analysis of The Tongue Body Fat and Thin Based on The Neural Net

Kang ZHANG, Cheng-hua DING, Jian-qiang DU, Can-hua WANG^a, Shi JIN

Jiangxi University of Traditional Chinese Medicine, Nanchang 330004, China

^a21846498@qq.com

Keywords: Image segmentation, Plumpness and slenderness of tongue, curve fitting, neural net

Abstract. In this paper, first detect the edge of the tongue, to obtain the edge of tongue body coordinates. Then split the tongue using a variety of curve fitting function to analysis plumpness and slenderness of tongue, and compare the accuracy of different curve fitting. Finally, classify the fat tongue and thin tongue by using the neural network.

Introduction

Tongue inspection is the main content of four diagnostic methods for traditional Chinese medical science. The fat or thin of the tongue is the important research for the tongue inspection. The tongue is crimson and swollen, the reason is heart and spleen has hot. Usually cause by insufficiency of the spleen and deficiency of kidney. Comparing with the normal tongue in traditional Chinese medicine can determine the tongue body fat and thin. But due to the subjectivity of traditional Chinese medicine is strong, so normal tongue, fat tongue and thin tongue has no unified standard.

This thesis first to get the edge of the tongue body coordinates, analyze the edge of the tongue by using a quadratic function, Gaussian function, quartic function rounding odd items, quartic function and double-peak Gaussian function curve fitting. By analyzing the curve of the mouth size, analyze the tongue body fat. Finally, automatic classify the tongue body fat by using the neural network. In this paper, all image sources and artificial interpretation is provided by professor Ding Chenghua of JiangXi University of traditional Chinese medicine.

The analysis of tongue body fat and thin based on curve fitting

WEI Bao-Guo etc. has used four polynomials (give an odd number of times) for curve fitting of tongue image, determine the tongue body fat. But this method to determine tongue body fat relates to the equation parameter of symbols increases the recognition difficulty of tongue body fat. And because the abandoned an odd number of times, when the tongue body obvious asymmetry, curve fitting accuracy is reduced

This paper using a quadratic function $(y = ax^2 + bx + c)$, gaussian function $(g(x) = e^{-\frac{(x-a)^2}{2\sigma^2}} + b)$ and give an odd number of times of four function $(y = a1(x-a2)^4 + a3(x-a2)^2 + a4)$, containing an odd number of times a four functions $(y = a1(x-a2)^4 + a3(x-a4)^2 + a5)$, double-peak Gaussian function $(g(x) = e^{-\frac{(x-a1)^2}{2a2^2}} + e^{-\frac{(x-a3)^2}{2a4^2}} + a5)$ as a fitting function. Compare the accuracy of the tongue edge of curve fitting.

Use double-peak Gaussian function to simulate curve of tongue image, improve the asymmetry of tongue image curve fitting accuracy

1. The comparison of different function curve fitting

(1)the tongue body fat and thin analysis algorithm steps

[1]. First detect the edge of the tongue template, as shown in figure 1.get the edge image of tongue, as shown in figure 2. The tongue edge of the upper part to zero, to obtain the lower half part of the tongue edge image, as shown in figure 3.







Fig. 1 Tongue body template Fig. 2 The edge of tongue body Fig. 3 Lower edge of tongue body [2]. Get all nonzero pixel point row and column coordinates from figure3, and coordinates are normalized processing.

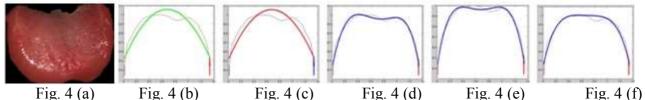


Fig. 4 (a) Fig. 4 (b) Fig. 4 (c) Fig. 4 (c)

[3] To curve fitting of figure3, as shown in figure4. Fig. 4 (a) is Original tongue image. Fig. 4 (b) is quadratic curve fitting. Fig. 4 (c) is gaussian curve fitting .Fig. 4 (d) is the double-peak gaussian curve fitting. Fig. 4 (e) is to give an odd number of times four function curve fitting. Fig. 4 (f) is containing an odd number of times four function curve fitting

(2)Comparison of five kinds of fitting accuracy

To determine the coefficients (R^2) , the residual sum of squares (RSS), the AIC criterion as indicators to evaluate the efficacy of the fitting of the model. Formula (2) and formula (3) numerical expression is smaller, the better fitting effect, the greater the numerical of formula (1), fitting the better the results.

$$R^{2} = \frac{\sum_{i=1}^{n} (F_{i} - \overline{F_{i}})^{2} - \sum_{i=1}^{n} (F_{i} - \hat{F_{i}})^{2}}{\sum_{i=1}^{n} (F_{i} - \overline{F_{i}})^{2}}$$
(1)

$$RSS = \sum_{i=1}^{n} (F_i - \hat{F}_i)^2$$
(2)

$$AIC = n\ln(RSS) + 2P \tag{3}$$

The F_i : the actual coordinates; F_i : model fitting values; F_i : the average F_i actual coordinates; n: the number of experimental data; P: the number of model parameters

By tongue images fitting data comparison, bimodal Gaussian function fitting accuracy rate is highest, quadratic curve fitting effect was slightly better than Gaussian function fitting.

2. The tongue body fat and thin analysis based on neural network

To imitate the human brain, neural network have strong fault tolerance, self-learning, self-organization function and inductive capacity. So this article uses the BP neural network to the tongue image classification.

Because the double-peak Gaussian function curve fitting of the highest accuracy, so the use of its equation parameters as input nodes of the neural network input data. In the expression,

 $g(x) = e^{-\frac{(x-a1)^2}{2a2^2}} + e^{-\frac{(x-a3)^2}{2a4^2}} + a^5$ has a total of five parameters, the a5 is completely independent and it determines the curve in the vertical direction displacement size. the tongue body fat depending on |a3-a1|, |a2| and |a4| three parameters, x1 = |a3-a1|, x2 = |a2|, x3 = |a4|.

Establish the BP neural network, the network input layer has three input nodes, the input data for the x1, x2, and x3, output layer has two outputs y1 and y2, when y2 y1 = 00, on behalf of fat tongue,

 $y_2 y_1 = 01$, on behalf of the thin tongue, $y_2 y_1 = 10$ representative not fat or thin. Network setup a hidden layer, the layer has 10 neurons. Network structure as shown in figure 5.

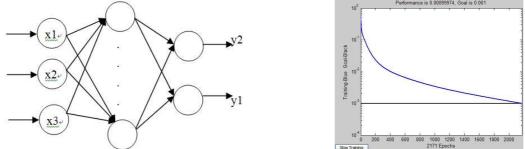


Fig. 5 The BP neural network Fig. 6 The training error curve of the netwok Three types of tongue body of each type of sample number is 6, the training set each type of 3 samples, test set each type of three samples.

The network is set to the mean square error, net. Trainparam. Goal = 1 e - 3, number of iterations for the net. Trainparam. Epochs = 10000.Mean square error (mse) iterative effect as shown in figure 6.

	1	2	3	4	5	6	7	8	9
1	0	0	0	0	0	0	1	1	1
2	0	0	0	1	1	1	0	0	0
				Fig 7	Ideal outpu	14 4			
	1	2	3	Fig. 7	Ideal outpu	it t 6	7	8	9

		CC-3CT-2 1970 (1970) (1970 (1970 (1970 (1970 (1970 (1970 (1970 (1970 (1970 (19				00010000000000			
2	0.04762	-0.024651	-0.030377	1.0289	1.0424	0.93169	0.0026676	-0.032752	0.03159
				Fig. 8	8 Output op)			

Through after the network training set, and then verified by testing network, t for the ideal output, as shown in figure7. The output is op by the network, as shown in figure8. Error = sum $((t - op)^2) = 0.018$

Conclusions

Bimodal Gaussian function to overcome the defects of the symmetric function. After curve fitting, through BP neural network, to classify the tongue image fat or thin accuracy rate is very high.

Acknowledgements

Department of Health of Jiangxi Province.(2013A085) Jiangxi University of Traditional Chinese Medicine.(2013ZR0075,07375104) The project of National Natural Science Fund.(81260527) Science and technology project of Jiangxi Province(2011ZBBG70050)

References

- [1] WEI Bao-Guo, SHEN Lan-Shun, Computer engineering, 2004.6:5~26.
- [2] Zhou yue, Yang jie, Shen li, JOURNAL OF BIOMEDICAL ENGINEERING, 2004, 21(6): 917-920
- [3] Hornik K, Stinchcombe M, White H. Neural Netwoks, 1990, 3(5):551-560
- [4] Prasanna Sahoo, Gurdial Arora. Pattern Recognition Letters, 2006, 27(6): 520-528
- [5] Wang LU, Cai Zi-Xing. Mini-Mico Syetems, 2005, 25(10): 1744-1777
- [6] Silvia Ferrari, Robert F Stengel. IEEE Trans on neural networks, 2005, 16(1):24-38

CHAPTER 5:

Communication and Signal Processing

The Beidou Satellite High-precision Timing Applied Research

Zhaopeng Hu^{1,2,a}, Yu Hua^{1,b}, Shifeng Li^{1,2,c}

¹National Time Service Centre, Chinese Academy of Sciences, Xi'an 710600, China ²Graduate University of Chinese Academy of Sciences, Beijing 100039, China ^ahujorpen@qq.com, ^bhy@ntsc.ac.cn, ^clishifeng@ntsc.ac.cn

Keywords: The Beidou(BD) satellite navigation & orientation system, high-precision timing transfer, Common-view

Abstract. The Beidou(BD) satellite navigation & orientation system is so important of national information infrastructure for our country. After research the BD system in the timing area, while analysed the advantage of the Beidou satellite timing technology compared with other conventional timing method, combined with high precision timing experiment and depending on the Common-view experimental results proved that the beidou statllite navigation & orientation system has high research value.

Introduction

"The BeiDou (BD) satellite navigation & orientation system" (shortened from "The Beidou system") is developed by China. It has been made into formal operation to the populace since April.2004, which works well and plays an important role in many realms, such as surveying and mapping, telecommunications, water conservancy, exploration and national security. The develop strategy of the system is planned by 3 steps. First, develop The BD satellite navigation positioning system. Second, develop The BD regional system. At last, complete the development of The BD system and realize global service in 2020. In The BD system, the fundamental of positioning is distance measurement; the fundamental of distance measurement is the measurement of electric wave delay; and the fundamental of the measurement of electric wave delay is the time standards. Therefore, time-frequency system should be developed when building position system.

BD System overview

1. BD Time System

The time base of The BD satellite navigation system is BD Time (BDT). The unit of BDT is The International System of Units (SI) of a second and without leap second. The start of BDT is January 1, 2006, 00:00:00 in coordinated universal time (UTC). Trace to the source, BDT is UTC, which is preserved by the National Time Service Center (NTSC), and the leap second information of BDT and UTC will be reported in navigation message. The deviation of BDT and UTC is in 100ns (module 1s). Because of the precision and stability, the BD system will play an important role in time service realm in future. Figure 1 is the comparison of BDT and others.

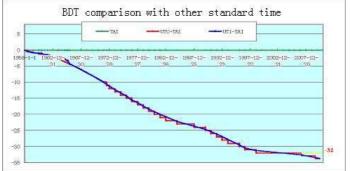


Figure 1: BDT comparison with other standard time

2. BD Coordinate System

The coordinate frame of BD satellite navigation system is China geodetic coordinate system 2000 (CGCS2000).

3. The major function and performance index of BD satellite navigation system regional service

Major function: orientation, velocity measurement, one way/both way time service, shout message communication;

Service region: China and surrounding area;

Orientation accuracy: better than 10 m;

Velocity measurement accuracy: better than 0.2 m/s;

Time service accuracy: 50 ns;

Short message communication: 120 Chinese characters/once.

4. BD system's three step

4.1 BD Dual-Satellite Positioning System

BD I Dual-Satellite Positioning System is a satellite navigation system which composed of two BD I satellite and a spare satellite. It's the primary stage of BD system. The unidirectional timing accuracy of BD Dual-Satellite System is 100ns, and the bidirectional timing accuracy is 20ns. Figure 2 is the schematic plot of BD Dual-Satellite System.

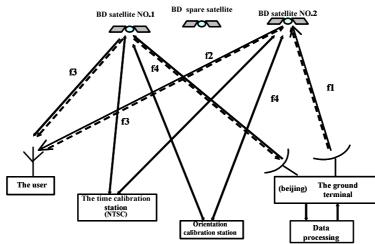


Figure 2: The schematic plot of BD Dual-Satellite System

4.2 BD Regional Navigation System

BD Regional Navigation System is a satellite navigation system which composed of 5 GEO, 5 BD regional navigation satellite and 5 IGSO. It's the medium term of BD system. After December 27th,2012. The BD Regional Navigation System has started to provide continuous navigation positioning and timing services for China and surrounding areas.

4.3 BD Global Position System

In 2009, China started the project "China Second General Satellite Navigation System" and plan to build the "China Second General Satellite Navigation System" with 32 satellites in 2020, which including 8 GEO satellites (including 4 IGSO satellites), 24 MEO satellites, 2 ground operational control station (a back-up control station) and several gauging stations. China Second General Satellite Navigation System and BD I,II Position System compose a great global position system, which is called BeiDou Global Positon System.

BD System Timing Experiment

To achieve high-accuracy time service, the timing experiment is very important. There are 3 frequency points (B1, B2, B3) in BD Satellite Navigation System. We can analyze the stability and accuracy of BD system time according the timing experiment, judge whether the system meets the requirement of high-accuracy time service or not according compare with other time references.

In December.2012, BD Regional Navigation System B1/B2 frequency point timing experiment has been accomplished in National Time Service Center, and the result showed that the timing accuracy of BD satellite is better than the primary level of GPS. The frequency point timing accuracy of B1/B2 frequency point are better than 20ns; The frequency point timing accuracy of B3 is better than 10ns. Figure 3 is the comparison of BD system time and cesium clock pulse per second 1PPS. Figure 4 is the comparison of the pulse per second of BD and the parsec of UTC (NTSC).

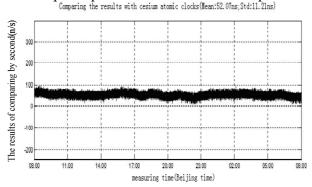


Figure 3: BD 1pps compared with the cesium atomic clock's

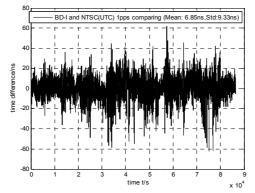


Figure 4: The comparison of the pulse per second of BD-1and the parsec of UTC (NTSC)

The Comparing and Transfer Method of BD High-accuracy Experiment

1. BD Common-view Theory

Common-view is a way to realize time synchronization. It needs 2 observers in different places observe the same sigh in the same satellite, same signal (eg: Beidou ,GPS,GLONASS signal and so on) and the same time.

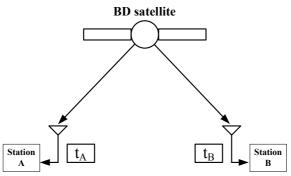


Figure 5: The satellite common-view theory

We know that this is a single receiving system from figure 5, and the local clocks work according to its own rate in each point of comparison. According to the compare requirement, the 1PPS signal for one second or other fixed rate clock pulse signals which are launched by satellite will be calculated.

\triangle TA BD=(TA– T BD)	(1)
Δ TB BD=(TB– T BD)	(2)

The time difference between the two stations is

$$(TA-TBD)-(TB-TBD)=TA-TB=\triangle TAB$$
(3)

If we get \triangle tAB (ti) at some point, after a time τ , namely we get \triangle tAB (ti+ τ) at ti+ τ , and the average relative frequency deviation in τ of the two clocks can be calculated by

$$\frac{f_A - f_B}{\tau} = \frac{\Delta t_{AB} (t_i) - \Delta t_{AB} (t_i + \tau)}{\tau}$$

(4)

2. BD I Common-view Experiment

To verify the performance of the BD common-view receiver and BD-I, we built a experimental platform in Xuancheng, Anhui Province and NTSC. The platform is composed of a variety of equipment and network, including BD-I, BD common-view receiver, computer, electronic counter, Internet, GPRS module, two UTC time systems of Xuancheng and NTSC and so on. Figure 5 shows the connect relationship. We can get a comparison of time common-view in two places according to the experiment. Figure 6 is the compare result.

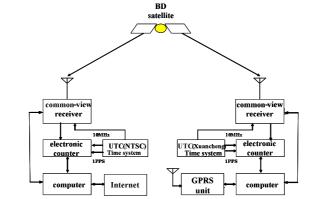


Figure 6: The connection diagram of BD-I common-veiw experiment

The experiment result of BD-I is based on simplified Julian day 54283 (00:00:00, July 2nd, 2007), a tendency of Xuancheng UTC time minus NTSC UTC time. According to the experiment, the minus of two UTC time is not more than 16ns. It shows the high-accuracy and the nice result of the experiment comparison.

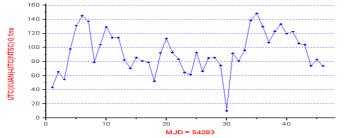


Figure 7: The compare result with the signal for 1pps of NTSC (UTC)

3. BD-II Common-view Experiment

The structure and theory of BD II common-view receiver is basically the same with BD I common-view receiver. The performance of BD II common-view receiver is not stable because it is newly verified. Therefore the compare result with the signal for 1pps of NTSC (UTC) is not expected, but it's illustrative. Figure 8 shows that the signal for one second produced by BD II does completely meet the requirement of time service and navigation. It lay a solid foundation for the study of time service and navigation for BD II.

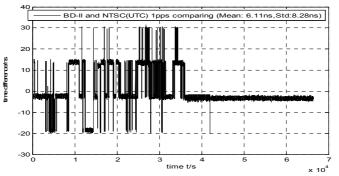


Figure 8: The comparison of the pulse per second of BD-II and the parsec of UTC (NTSC)

4. BD All-in-view Method

All-in-view is a way to common-view in multichannel satellite. It uses precise ephemeris, calculates the observe value from IGMAS time to global time, uses IGS TEC MAPS to calculate ionized stratum delay for single frequency receiver, reduces the affect of satellite position error, and was used in TAI multi channel global common-view comparison in Oct.2006.

The pattern of tracking every 16 minutes is still using after All-in-view was adopted. Since all the GNSS satellites can be observed by receiver and common reference epoch was set as 00:00:00, Oct 1st, 1997, release common-view every half year is not necessary any more.

All-in-view synchronization accuracy: 1~5ns.

5. BD Carrier Phase Method

The compare theory of BD carrier phase method is basically the same with common-view compare method. The difference is that common-view method adopted the information which transmitted by the satellite, used carrier phase and pseudo range to calculate the distance of the satellite and the earth, consequently improved the observe accuracy. Carrier phase method can reduce the influence of common-view synchronization which produced by ephemeredes, ionized stratum and troposphere.

The compare and transfer accuracy of carrier phase method can be 0.2ns theoretically, but because of the ambiguity of whole cycles, the order carrier phase method attained is nanosecond (1.8ns). The primary cause is that there are some problems in comparing stability.

Conclusion

We have been more and more demanding in time service accuracy because of the social development, such as grid transportation, high speed digital communication, financial network, network security, mobile communication, aerospace, military communication, scientometrics, satellite launching and monitoring, disaster relief, state security and so on. The requirements of these realms promoted the development of BD Satellite Navigation System and the technology of BD satellite time service. BD Satellite Navigation System is on a critical mission when facing difficulties by the other international GNSS time service systems. With the constantly improving of BD Satellite Navigation System, BD satellite time service technology surely will be the mainstay in the navigation time service realm.

Reference

- [1] Guohong Xu. Harbin Engineering University, 2007.in chinese
- [2] Li liu. Anhui University, 2010. in chinese
- [3] Zhiheng Jiang. in Journal of Astronautic Metrology and Measurement, pp 53-70, 2007. in chinese
- [4] Zhonghua Liu, Qigui Li. In National Time and Frequency Conference, 2009. in chinese
- [5] Feixue Wang, Xiaoyong Xu, Zhaowen Zhuang, China Association for Science and Technology, 2005. in chinese

A New Method of Time Domain Coherency for Radar Emitter Signal Sorting

Lirong Guo^{1, a}, Minghao He¹, Chunlai Yu¹ and Bingqie Wang¹ ¹ Air Force Early Warning Academy, Wuhan 430019, China ^aguolirongs@163.com

Keywords: coherent signal; time domain recognition; phase detecting; signal sorting

Abstract: Based on judging the change of pulse amplitude of phase detecting, a new method of time domain coherency for the radar emitter sorting is proposed in this paper. We analyzed the theory of the signal coherency recognition method. Then, the mathematic derivation process and specific recognition steps of the new method are detailedly given. But above all, the new method can be applied into the signal sorting of radar emitter. Simulation results also reveal that this new method can effectively sort the radar emitter signals under the low signal-to-noise ratio, and it is a huge help to solve the problem of " leakage-batch ". Results demonstrate that the new method has strong theoretical value.

Introduction

Existing reconnaissance equipments mainly make use of the conventional parameters in signal sorting^[1]. But, using intra-pulse characteristics as sorting characteristic parameters is formed as a common consensus in recent years^[2]. Compared with the conventional parameters, the intra-pulse characteristics can greatly improve the accuracy and stability of the result of radar signal sorting. While the increasingly complex signal environment gradually appeared, including the constantly emerging of the new complex system radar and the rapidly changing in the form of signal, which brought about much difficulty or error of extracting intra-pulse characteristics in such letter signals, and they also leaded to the low precision of signal sorting. In order to solve the above problems, we put our vision towards the time domain recognition that is, within a prescribed time and space, the coherent characteristics couldn't fluctuation with the change of frequency, modulation mode, emission waveforms, power and so on^[3]. It has the incomparable advantage over other characteristic parameters. Therefore, the research of using the coherent characteristics into radar signal sorting, for improving the ability of radar counter reconnaissance equipment in the signal sorting, has important application value.

This paper proposed a new method of radar emitter time domain coherent sorting. In this study, we carried out the phase processing of the pulse signal, according to the change of pulse amplitude of phase detecting output of phase discriminator, and identified the coherency of signal, then realized signal sorting. Now, the mathematical process of signal coherency time domain recognition is derived. We also make the recognition of coherent and un-coherent signals, extract the coherent characteristic parameter, give the specific sorting steps and analyze sorting simulation results. This provides theoretical foundation for adding new sorting characteristic parameters and studying the new signal sorting technology.

Mathematical model of the coherent pulse train signal

The coherent pulse signal originated from radar emitter goes through the band-pass filter of receiver and down-conversion, then they are translates to the intermediate frequency signal, which is sampled to signal:

$$s(n+K_{p}) = A_{p} \exp\left[2\pi f(n+K_{p})t_{s} + \varphi_{0}\right] + \upsilon(n+K_{p}) \xrightarrow{n=0,1,\dots,N-1}_{p=0,1,\dots,P-1}$$
(1)

Eq. 1, A_p is the amplitude of pulse p, φ_0 is the constant initial phase during the whole observation, f is the frequency of the signal, K_p is the initial sampling point of pulse p, t_s is the sampling interval, N is signal sampling points of each pulse, v is a complex white Gaussian noise.

Time domain recognition method of signal coherency

The coherent pulse signal originated from radar emitter has the continuity of pulse phase in pulses. If pulse i and j come from the same radar emitter pulse, pulse i and j are coherent, namely, the initial phase of pulse i and j are same. If pulse i and j come from different radar emitter pulse, pulse i and j are un-coherent, namely, the initial phase of pulse i and j are different^[4]. Based on the characteristics of coherent signal, this paper proposed a new method which is used to identify the coherent time domain recognition.

Phase discriminator use double balanced mixer features to reflect the phase relationship in signals. The time domain recognition method of signal coherency use the characteristic of phase discriminator, which is mainly consisted by the power divider, delay line, mixer and low pass filter. Principle of the method is shown in figure 1. Principle of the time domain recognition method^[5]: the pulse signal of reconnaissance receiver will be input into the phase discriminator power divider, then the signal is divided into two road, one directly into the mixer, the other one into the mixer after delay line (delay time is equal to a pulse repetition interval), then mix the two road signals and input to low pass filter, filtering the term of $2\pi ft$ and high frequency components. Finally output the phase detecting pulse amplitude.

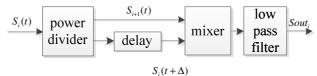


Fig. 1 Principle structure of the time domain recognition method Assume that the input pulse i is expressed as:

$$S_i(t) = A_0 \exp(2\pi f t + \varphi_i) + v(t)$$
(2)

Eq. 2, A_0 is the amplitude, f is the frequency, φ_i is the initial phase of pulse i, v(t) is the complex white Gaussian noise, its mean is 0 and variance is σ^2 .

Through the phase discriminator, the real component of $Sout_i(t)$ of pulse amplitude from phase discriminator is:

$$Sout_{i} = \frac{A_{0}^{2}}{2} \cos(\varphi_{i} - \varphi_{i+1} + \theta) + \upsilon'$$
(3)

Eq. 3, the noise term of v'(t) is the result of conjugate multiplication with noises and signals, its statistical properties is^[6]:

$$E[v'(n)] = 0 \quad E[v'(m)v'(n)] = 0 \quad E[v'(m)v'^*(n)] = 2A_0^2 \delta_{m,n} \sigma_v^2$$
(4)

According to the Eq. 4, the new noise item make the SNR reduced four times than the original signal (about 6 dB).

As to the coherent pulse train signal, the initial phase of all pulses are same^[7], satisfying the equation: $\varphi_i - \varphi_{i+1} = 0$. Therefore, the real component used time domain recognition method to output the pulse amplitude of phase detecting is:

$$Sout_i = \frac{A_0^2}{2}\cos(\theta) + \upsilon'$$
(5)

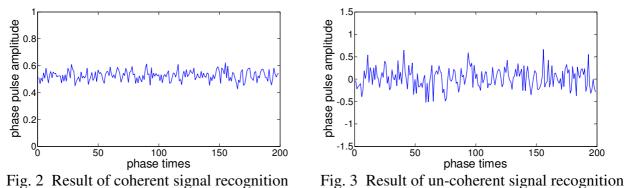
Eq. 5, the output phase detecting pulse amplitude is only related to A_0 , θ and v', A_0 and θ are fixed value, v' is the combination term of noises. Therefore, the outputting pulse amplitude of phase detecting are approximation of the same.

For the un-coherent pulse train signal, the initial phase of all pulses are different, which is the random quantity in $(-\pi,\pi)$, so $\varphi_i - \varphi_{i+1}$ is also the random quantity. Therefore, the real component used time domain recognition method to output the pulse amplitude of phase detecting is:

$$Sout_{i} = \frac{A_{0}^{2}}{2} \cos(\varphi_{i} - \varphi_{i+1} + \theta) + \upsilon'$$
(6)

Eq. 6, the outputting pulse amplitude of phase detecting is related to A_0 , θ and v', A_0 and θ are fixed value, v' is the combination term of noise, $\varphi_i - \varphi_{i+1}$ is the random quantity in $(-\pi, \pi)$. Therefore, the outputting pulse amplitude of phase detecting will randomly variate.

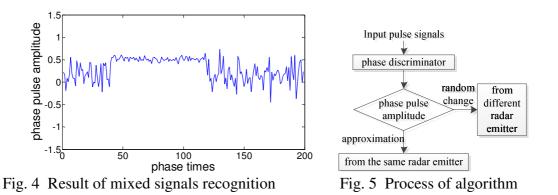
Set the experimental parameters: We take a string pulse signal, the pulse number is 200, not considering the influence of amplitude modulation function, the amplitude of pulse signal is $^{1/2}$, the sampling frequency is $f_s = 80$ MHz, the signal frequency is f = 30MHz, the pulse signal repetition interval is $^{PRI} = 50$ us, the width of pulse signal is $\tau = 2$ us, the additional phase caused by delay is $\theta = 2\pi f \cdot PRI$. For a string coherent signal, the each initial phase of signal is $\varphi = \pi/4$, For a un-coherent signal, the initial phase of signal is φ , which is the random quantity in $(-\pi, \pi)$. Under the condition of SNR 10 dB, we use the time domain recognition method of signal coherency to simulate, and the recognition results are shown in figure 2 and figure 3.



According to the figure 2, the pulse amplitude of coherent signal of phase detecting fluctuated from 0.4 to 0.6, but the change is very small. Because of the influence of noise term, the curve of pulse amplitude of phase detecting has small volatility. According to the figure 3, the pulse amplitude of un-coherent signal of phase detecting fluctuated randomly from -0.5 to 0.6. Therefore, we can get the conclusion from the simulation results, using time domain recognition method can effectively identify the signal coherent properties.

As to a string of mixed pulse signal, there are coherent and un-coherent signal, we also use the time domain recognition method to identify the coherency of mixed signals.

Set the experimental parameters: We take a string mixed pulse signal, which has 80 coherent signals and 120 un-coherent signals, not considering the influence of amplitude modulation function, the amplitude of pulse signal is $^{1/2}$, the sampling frequency is $f_s = 80 \text{MHz}$, the signal frequency is f = 30 MHz, the pulse signal repetition interval is $^{\text{PRI} = 50 \text{us}}$, the width of pulse signal is $\tau = 2 \text{us}$, the additional phase caused by delay is $\theta = 2\pi f \cdot \text{PRI}$. For a string signals, the each initial phase of coherent signal is $\varphi = \pi/3$, and the initial phase of un-coherent signal is φ , which is the random quantity in $(-\pi,\pi)$. Assumption the distribution of mixed signals is as follows: the first 40 pulses are un-coherent, the next 80 pulses are coherent, the last 80 pulses are un-coherent. Under the condition of SNR 10 dB, we use the time domain recognition method of signal coherency to simulate, and the recognition results are shown in figure 4.



According to the figure 4, phase discriminator output the first 40 pulse amplitudes of phase detecting which randomly changed in wide range, then the next 79 pulse amplitudes of phase detecting fluctuated in small scope, the last 80 pulse amplitudes of phase detecting also randomly change in wide range. The simulation result is consistent with the hypothesis. Therefore, the simulation results of the mixed signals further demonstrate that the time domain recognition method is feasible and valuable.

Characteristic parameters extraction and sorting simulation analysis

Selection of the characteristic parameters of signal sorting must satisfy the universality nature. It is obvious that the pulse amplitude of phase detecting will not change with the change of pulse parameters, so the change of pulse amplitude of phase detecting is consist with the universal applicability, the rule of the change of pulse amplitude of phase detecting can be used to distinguish the coherency of any two pulse signals. The conclusion can be come up with after a great deal of simulation experiments: The certain range of pulse amplitude of phase detecting can be used as the threshold to identify the coherency of signal. When the selected range of pulse amplitude of phase detecting is too small, easily producing " increasing-batch "; When the selected range of pulse amplitude of phase detecting is nection 3.3, the range of the pulse amplitude should change within 0.2, which can be considered as the threshold to identify the coherency of signal. And we can also use the threshold to distinguish whether any two pulses are coherent.

Based on the above comprehensive analysis and the pulse phase linearity, we can realize radar emitter signal sorting. The process of algorithm is as shown in figure 5, and concrete steps are as follows:

Step1: P pulse signals of reconnaissance receiver input phase discriminator, and get P-1 pulse amplitude of phase detecting values;

Step2: judge the change of the pulse amplitude values.

Step3: analyze the result of step2, if P-1 pulse amplitudes of phase detecting are approximation, the input pulse signals are coherent, which come from the same radar emitter; if P-1 pulse amplitudes of phase detecting randomly change, the input pulse signals are un-coherent, which come from different radar emitter.

Set the simulation experiment condition: A string pulse signal come from reconnaissance make the first sorting, but two pulses could not be distinguished whether they come from the same radar emitter. Assume that the two pulses belong to different radar radiation emitter. The two pulses have the same pulse parameters and the approximate modulation way, but the existing signal sorting method unable to judge whether the two pulses come from the same radar emitter, leading to "leakage-batch" problem of signal sorting.

The experimental parameters: We take a string pulse signal, not considering the influence of amplitude modulation function, the amplitude of pulse signal is $^{1/2}$, the sampling frequency is $f_s = 80 \text{MHz}$, the signal frequency is f = 30 MHz, the pulse signal repetition interval is PRI = 50 us, the

width of pulse signal is $\tau = 2us$, the additional phase caused by delay is $\theta = 2\pi f \cdot PRI$, the initial phase is the random quantity in $(-\pi,\pi)$. Select the range w of pulse amplitude of phase detecting to set the decision threshold, according to the determined threshold, and identify the coherency of signal. If the range of pulse amplitude of phase is less than w, adjacent pulses are coherent, and they come from same radar emitter; If the range of pulse amplitude of phase is more than w, adjacent pulses are un-coherent, and they come from different radar emitter. Count the number of falling into the determined threshold to calculate the radar emitter signal sorting accuracy. Under the different SNR, we independently make simulation experiment 100 times, and the simulation results are as shown in table 1 and figure 6.

According to table 1 and figure 6, based on the change of pulse amplitude of phase, we make the simulation experiment, and the increasing trend of sorting accuracy is the same with the SNR. When the SNR is equal or greater than 10 dB, the sorting accuracy is greater than 90%, while the existing sorting method under the condition of the simulation, the accuracy of signal sorting is almost zero. Therefore, the sorting method based on the change of pulse amplitude of phase can better solve the "leakage-batch " problem of signal sorting.

11.00	1401	. i bigilai	sorting accura	-			
different	SNR/dB						
threshold w	0	5	10	15	20	25	
0.16	74	80	90	96	99	100	
0.18	80	83	95	99	100	100	
0.20	85	90	100	100	100	100	
0.22	88	90	100	100	100	100	
0.24	95	97	100	100	101	100	

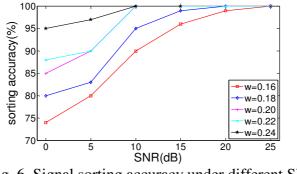


Fig. 6 Signal sorting accuracy under different SNR

Conclusion

In this paper, we study a kind of signal coherency time domain sorting method, the mathematical process of time domain recognition method of signal coherency is deduced, and the specific steps of the recognition are given, we also make simulation experiment and analysis with the coherent, un-coherent and mixed signals, extracting coherent characteristic parameter, then we apply it into radar emitter signal sorting. The research method can realize the signal sorting under the condition of low SNR, which provides theoretical basis for studying new method and technology of signal sorting in the future.

References

- [1] Qiang Guo. Research of Radar Signal Sorting Theory [M]. Beijing: Publishing House of Science. 2010.
- [2] Jun Han, Minghao He, Yuanqing Zhu, Jie Wang. Sorting Radar Signal Based on the Resemblance Coefficient of Bispectrum Two Dimensions Characteristic [J]. Chinese Journal of Radio Science. 2009, 24(5), 848-853.
- [3] Baochang Zhao. Method of Sorting Radar Emitter Signal Based on Coherency [D]. Wuhan: Air Force Radar Academy. 2010.
- [4] Peng Sun. Research on Mathematic Modeling and Extracting Technologies of Coherent Characteristics of Radar Emitter Signal [D]. Wuhan: Air Force Radar Academy. 2011.
- [5] Lin Zhou, Shaoquan Yang. Coherence Detection and Frequency Measurement for Recognizing Backscattered Signal of Pulse Doppler Radar [J]. Modern Radar. 2002,24(4), 27-30.
- [6] Chunlai Yu, Ronghui Zhan, Jianwei Wan. A Measurement Algorithm for Doppler Frequency Rate-of-change with BPSK Coherent Pulse Signal [J]. Journal of National University of Defense Technology. 2008,30(1), 53-56.
- [7] Yan Hu, Yu Liu. Coherent Pulse Train Identification Algorithm and Its Performance Analysis [J]. Journal of Data Acquistion & Processing. 2012(3), 314-319.

Design and Implementation of GPS L2C Signal Tracking Algorithm

Xuefen Zhu^a, Fei Shen^b, Yang Yang^c, Dongrui Yang^d, Xiyuan Chen^e

School of Instrument Science and Engineering, Southeast University, Nanjing, 210096, China

Key Laboratory of Micro-Inertial Instrument and Advanced Navigation Technology of Ministry of Education, Southeast University, Nanjing, 210096, China

^azhuxuefen@seu.edu.en, ^bsfseu0311@163.com, ^cyangyang33121@163.com ^dGanGeWans@163.com, ^echxiyuan@seu.edu.cn

Keywords: GPS L2C signal, tracking algorithm, code tracking, carrier tracking, signal-to-noise ratio

Abstract. The study of GPS L2C signal tracking algorithm aims to realize signal tracking in poor environment. The main topic includes L2C signal tracking principle and the performance of real signal tracking. The structure and applied background of the signal is stated in the introduction at first. The characteristic of time division multiplexing of CM code and CL code makes this tracking method utilize half of received energy inevitably. Then, as compositions of L2C signal tracking algorithm, the data demodulation, the code tracking and the carrier tracking module are showed their details in the paper, including the structure of the DLL tracking loop, the Costas carrier tracking loop and some necessary computational principles. Finally, compare happens on real excellent and poor signal-to-noise ratio environments by setting suitable parameters including the sampling frequency, the center frequency and the pseudo code rate to prove the effectiveness of tracking algorithm.

Introduction

Aiming to enhance applied range of GPS signal in weak signal environment, GPS offers new L2C signal for civil use because primary L1 signal is difficult to be captured in low signal-to-noise ratio environment. Firstly, the L2C signal has longer code and the integral time for tracking weaker signal. Secondly, it includes the moderate length (CM code) and the long code (CL code)^[1,2] which are based on time division multiplexing. According to the component of L2C signal, the CM code is for navigation data modulating and the CL code is for pilot frequency^[3] as an empty passageway. Meanwhile, the tracking is one of the most important algorithms when a receiver finishes the whole location solution process.

Most of existing tracking algorithms are based on GPS L1 signal. These tracking algorithms are inapplicable to the L2C signal because different particularities of them. Several papers such as the ref.[4,5] have put forward some tracking algorithms based on this new signal. But they don't include the real test or just make a simulation because of the rare numbers of eligible satellite. New test shows more than two satellites with GPS L2C signal can be tracked after the receiving front-end, and the algorithm in this paper is certifiable now.

So, the paper put forward a tracking method for GPS L2C signal. The principle involves the demodulation, the code tracking and the carrier tracking module. The DLL code tracking loop and the Costas carrier tracking loop are built to track code and carrier signal. Tracking result is included in the maximal in-phase signal finally. Then the perfect effectiveness of tracking is proved both in excellent and poor signal environment in this paper.

Principle of Tracking Algorithm

Summary of Principle. Though CM and CL code are both included in GPS L2C signal, the tracking process can be finished based on individual CM code because the former is for demodulation and the latter is for piloting frequency^[4]. However, CL code signal can obtain lower carrier-to-noise ratio than CM code signal. So, the paper puts forward a tracking algorithm which

uses the CM code to demodulate and the CL code to track. Firstly, the carrier in input signal is stripped by multiplying the local matched carrier. Secondly, the CM code is stripped by multiplying the local matched code. A simple representation of the frame of signal demodulation is shown in Fig. 1.

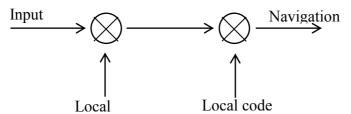


Fig. 1: Frame of signal demodulation for tracking

More accurate code phase and estimation of Doppler frequency are need after tracking. So, two interdependent tracking loops are designed in this implementation. One loop called carrier tracking loop is used to track Doppler frequency. The other called code tracking loop is to track CM code phase. According to the ref.[6,7], the former is designed as a phase lock loop (PLL) and the latter is designed as a delay lock loop (DLL).

Specification of Principle. The objective of tracking algorithm is to track GPS L2C signal whose system is still being built now. Several primeval satellites with L2C signal can be tracked yet, so the study of tracking is the pioneer and cogent. The integral time is limited inevitably due to 20ms' period of the CM code. At the same time, the demodulation and the tracking are individual by CM code and CL code because the receiver can't correlate CL code with local code directly. Process of tracking can be shown as next three steps.

Step 1. Data demodulation is involved in the CM code during 20ms integral time. According to the characteristic of GPS signal structure. After several down-conversions, the equation of L2 frequency band is shown in Eq.1.

$$y_{k} = A[D(t_{k})CM(t_{k} - t_{0}) + CL(t_{k} - t_{0})]cos[2\pi(f_{1} + f_{d})t_{k} + \emptyset_{0}] + v(t_{k}).$$
(1)

Where k means the No.k satellite; A is called the amplitude of received L2C signal; f_I is called the IF-FRE (IF-frequency); f_d means the Doppler frequency shift of input signal; ϕ_0 is called the initial carrier phase; CM(t) means CM code which is a rectangular pulse with 20ms period; CL(t) means CL code and its period is 1.5s; t_0 and t_k mean starting time and current time of L2C signal; D(t) is called navigation data value which is a rectangular pulse sequence with 20ms pulse width T; v(t) is called the noise.

Discrete digital signal can be expressed as follows after A/D sampling and narrow-band filtering.

$$y_{k}(n) = A[D(n)CM(n_{k} - n_{0}) + CL(n_{k} - n_{0})]cos[2\pi(f_{1} + f_{d})n_{k} + \emptyset_{0}] + v(n_{k}).$$
(2)

Then I (in-phase) and Q (quadrature phase) two baseband signals are separated from the digital intermediate frequency signal. Carrier is stripped by multiplying local accurate matched carrier. If local carrier has strict equality with signal carrier, the expression of signal can be

$$y_{k}(n) = -\frac{1}{2}A[D(n)CM(n_{k} - n_{0}) + CL(n_{k} - n_{0})]$$

$$y_{k}(n) = -\frac{1}{2}A[D(n)CM(n_{k} - n_{0}) + CL(n_{k} - n_{0})]$$

$$-\frac{1}{2}A[D(n)CM(n_{k} - n_{0}) + CL(n_{k} - n_{0})]cos[4\pi(f_{I} + f_{d})n_{k} + 2\emptyset_{0}].$$
(3)

The previous item of Eq.3 means product value and the second item means double intermediate frequency signal of carrier frequency. The second item will be filtered by low pass filter. The paper accumulates I, Q baseband signals of CM code and CL code during each integral time. Accumulated results of CM signal mainly are shown in Eq.4.

$$I_{CM}(\delta) = \sum_{k=mn}^{(m+1)n-1} y_k CM(t_k + \delta - t_s) \times \cos[(\omega_{L2} - \omega_d)t_k]$$
$$Q_{CM}(\delta) = \sum_{k=mn}^{(m+1)n-1} y_k CM(t_k + \delta - t_s) \times \sin[(\omega_{L2} - \omega_d)t_k].$$
(4)

Where n is called the sampling number each 20ms; m is called the reference number of navigation message during 20ms; The subscript CM means the CM code and the subscript CL means the CL code; I, Q means in-phase and quadrature phase of the number m coherent integrating range. The integral range begin with the number mn sampling point and the length of the range is n points; t_s means the difference of received code phase and local code phase; ω_{L2} is called frequency of L2C signal; $\omega_d t_k$ means carrier phase of receiver relative to IF signal. CL signal can also get similar accumulated results.

Step 2. The code tracking loop is used to track the change of CM code phase by matching local code phase. The loop is designed as a DLL which generates the instant, the advancing or the hysteretic code signal to match original signal. A block diagram representation of the frame of code tracking of CM code is shown in Fig. $2^{[6,7]}$.

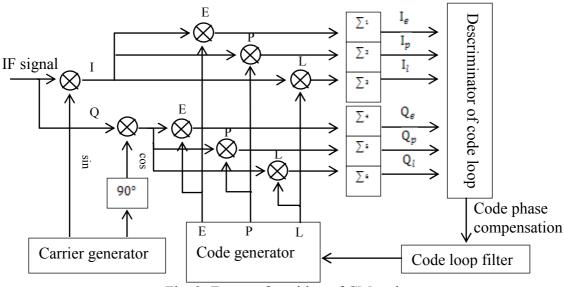


Fig. 2: Frame of tracking of CM code

Figure 2 shows the descriminator uses difference of advancing energy and hysteretic energy to compensate initial signal until the local code phase equals to the input code phase. The descriminator can get correct output through three branches of I_{CM} and Q_{CM} signal when the local code is different from the received code. The feedback called the discrimination factor is produced by descriminator to adjust code phase after the code loop filter. Calculation model of the discrimination factor is shown in Eq.5.

$$D = \frac{(I_{E}^{2} + Q_{E}^{2}) - (I_{L}^{2} + Q_{L}^{2})}{(I_{E}^{2} + Q_{E}^{2}) + (I_{L}^{2} + Q_{L}^{2})}.$$
(5)

Where D means the discrimination factor; I_E , Q_E mean advancing in-phase and quadrature phase signal; I_L , Q_L mean hysteretic in-phase and quadrature phase signal.

Step 3. The frequency tracking loop is built to track the carrier. When the phase-locked loop tracks CM carrier phase, the phase error estimation is extracted to control oscillator. According to the ref.[7,8], the Costas carrier tracking loop is used to adjust the phase inversion arose from the saltus of bit. A block diagram representation of the structure of the Costas carrier tracking loop is shown in Fig. 3.

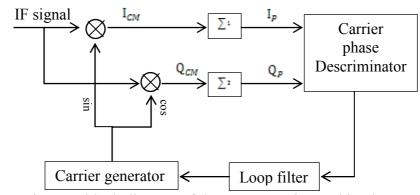


Fig. 3: A block diagram of the Costas carrier tracking loop

Figure 3 shows that the descriminator discerns the carrier phase error and outputs the error as feedback to adjust the local NCO. The I multiplier has in-phase signal with local carrier and the Q multiplier has 90[°] phase excursion with local carrier signal.

Only the CM signal is effective when finishing the carrier tracking, so the branch of CM signal is extracted as follows according to Eq.2.

 $y_{k}(n) = AD(n)CM(n_{k} - n_{0})cos[2\pi(f_{I} + f_{d})n_{k} + \emptyset_{0}].$ (6)

So, two aspects are involved in the calculation model. Firstly, CM code in IF signal is stripped by multiply Pseudo-Random Noise code. Then, the local CM carrier is added to the signal. The equation of the I_{CM} carrier can be shown as follows if the noise is negligible.

$$D(n)\cos[2\pi(f_{I} + f_{d})n_{k} + \emptyset_{0}] \times \cos[2\pi(f_{I} + f_{d})n_{k} + \emptyset_{0} + \theta]$$

= $\frac{1}{2}D(n)\cos(2\pi f_{e}n_{k} + \emptyset_{0} + \theta) + \frac{1}{2}D(n)\cos(2\pi f_{e}n_{k} + 2\pi f_{I}n_{k} + \emptyset_{0} + \theta).$ (7)

Where subscripts c, l and e mean the input carrier signal, the local carrier signal and the error signal. The equation $f_e = f_l - f_c$ is called the difference of local carrier and input carrier; θ means phase difference of them. The similar equation of the Q_{CM} carrier can be shown in Eq.8.

$$D(n)\cos[2\pi(f_{I} + f_{d})n_{k} + \emptyset_{0}] \times \sin[2\pi(f_{I} + f_{d})n_{k} + \emptyset_{0} + \theta] = \frac{1}{2}D(n)\sin(2\pi f_{e}n_{k} + \emptyset_{0} + \theta) + \frac{1}{2}D(n)\sin(2\pi f_{e}n_{k} + 2\pi f_{I}n_{k} + \emptyset_{0} + \theta).$$
(8)

Integration and accumulation operations are used to these two signals and then the paper gets I_p and Q_p values which are shown in Eq.9 after filtering the $2f_I$ frequency signal.

$$I_{p} = \sum_{n=0}^{N-1} \frac{1}{2} D(n) \cos(2\pi f_{e}n + \phi_{0} + \theta)$$

$$Q_{p} = \sum_{n=0}^{N-1} \frac{1}{2} D(n) \sin(2\pi f_{e}n + \phi_{0} + \theta).$$
(9)

Where N means the sampling number during the sampling period; The I_{CM} signal and the Q_{CM} signal constitute a compound signal whose phase can be expressed as phase difference of local carrier and input signal. The phase difference of the descriminator can be

$$\theta = tan^{-1} \left(\frac{Q_p}{I_p}\right). \tag{10}$$

Equation 10 shows when the I signal has maximum, the output error is smallest. Meanwhile, the Q signal gets minimum. So, the frequency error and the phase error are ignorable when the carrier tracking loop keeps stable. At this time, the I signal includes navigation message information and the process of tracking is finished.

Verification of Experiment for Signal Tracking

Experiments are designed to prove the effectiveness of the GPS L2C signal tracking theory. Receiver tracks 2 to 4 satellites with this new signal. Sampling time ranges from 30s to 90s. When receiving the signal, the sampling frequency and center frequency are set as 10MHz and 2.5MHz. And the pseudo code rate is set as 1.023MHz. When tracking the signal, the tracking data time is set as 20ms each time and the tracking time is initialized as 12 times.

Result shows that the carrier-to-noise ratio of environment changes with the time. When the GPS signal data time is 1.2s, excellent and poor carrier-to-noise ratios of the No.5 satellite in different environments are shown in Fig. 4.

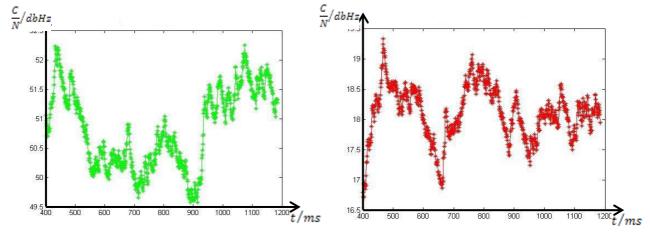


Fig. 4: The excellent and poor carrier-to-noise ratios of the No.5 satellite

From Fig. 4, the real carrier-to-noise ratio of satellite changes with time which breakthroughs traditional simulations whose carrier-to-noise ratio is artificial or constant. The left picture of Fig. 4 shows the excellent carrier-to-noise ratio which means the receiving front-end stays in an open space. And the right one shows a poor carrier-to-noise ratio environment. The acquisition of L2C signal has been finished based on FFT both in independent environments before tracking.

When tracking, two captured IF signals above are input to the tracking loop. Pictures of instant pertinent peak which are shown in Fig. 5 express the changing process of signal tracking.

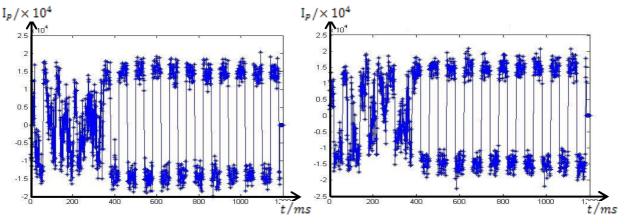


Fig. 5: The instant pertinent peaks of excellent and poor environments

Figure 5 shows the adjustment of tracking loop happens before 400ms and it tends to be stable after 400ms both in excellent and poor environments. The input code and carrier phase equals to local code and carrier phase when it is 400ms in both pictures.

Meanwhile, the instant pertinent peak value is approximate regardless of which environment the receiver in when stable. So, the tracking of real GPS L2C signal realizes perfectly. And the performance of tracking in poor environment proves that L2C signal is more suitable in weak signal than traditional L1 signal due to the longer integral time. Final tracking quality based on the new method being put forward by the paper is full and satisfactory.

Conclusions

After a deep study of GPS L2C tracking, several conclusions can be obtained. Tracking method based on GPS L2C signal includes the signal demodulation, the code tracking and the carrier tracking module. Purpose of signal demodulation is to get baseband signals from the digital IF signal. The code tracking loop and the carrier tracking loop aim to match the code phase, the carrier phase with local code phase and carrier phase. The final result of tracking is involved in the maximal in-phase value. The effectiveness of tracking L2C signal is proved in poor carrier-to-noise ratio environment.

The GPS signal tracking method is found to be quite satisfactory. Tracking realizes in poor environment, meanwhile small computation complexity and fast operating rate are applied in this method. Although a preliminary try, it offers foundation for the application of GPS L2C signal in the new field.

Acknowledgments

The project is supported by National Natural Science Foundation of China (41104015). We would like to thank NSFC for the funding help.

References

- [1] Xuefen Zhu, Xiyuan Chen: Journal of Chinese Inertial Technology. 18(04) (2010), p.434-438
- [2] Xuefen Zhu, Xiyuan Chen, Jianfeng Chen: Journal of Southeast University. 28(03) (2012), p.305-309
- [3] Tran M and Hegarty C: Receiver algorithms for the new civil GPS signals. ION NTM 2002, SanDiego, California, USA (2002), p.778
- [4] Muthuraman K, Shanmugam S K and Lachapelle G: Evaluation of Data/Pilot tracking algorithms for GPS L2C signals using software receiver. ION GNSS 2007, Fort Worth, TX, USA (2007), p. 2499-2509
- [5] Gernot C, Keefe O K, and lapchapelle G: Combined L1/L2C tracking scheme for weak signal environments. ION GNSS 2008, Savannah, GA, USA (2008), p.1758.
- [6] Kai Borre, Dennis M Akos, Nicolaj Bertelsen, et al: A Softwave-Defined GPS and Galileo Receiver-A Single-Frequency Approch (Birkhauser, 2007).
- [7] Zhe Liu: Research and Realization of High-Sensitivity GPS Software Receiver Algorithm Based on DSP. Dissertation for the Academic Degree of Master of Engineering (2010)
- [8] Yaobo Shang, Yin Guo: Space Electronic Technology.2009(04) (2009), p.35-38 (In Chinese)

Design and Implementation of Digital Communication Platform Based on FPGA/DSP

Shengguo Zhou^{1,a}, Wenjing Shang^{1,b}, Nan WANG^{2,c}, Rublev Victor^{3,d}

¹Harbin Engineering University, China, Heilongjiang, Harbin, 150001

²The 719th Research Institute of China Shipbuilding Industry Corporation, China, Hubei, Wuhan, 430064

³School of Engineering of Far Eastern Federal University, Russia, Vladivostok, 690950

^azhoushengguo@hrbeu.edu.cn, ^bshangwenjing@hrbeu.edu.cn, ^cKingsout@163.com,^dLavr@mail.ru

Keywords: Digital Communications; DSP; FPGA; QPSK; Software Radio.

Abstract. A method to design and implement digital communication platform was in introduced in this paper. The platform based on software radio method can change modulation method conveniently without the change of hardware system because it used FPGA and DSP to do modulation and signal process. The QPSK modulation and demodulation was implemented in the platform to test this platform.

Introduction

With the rapid development of the communication technology, the digital communication is playing a more and more important role in communication system with the advantages of high dependability, flexibility and easy saving. It is hard for the traditional communication system based on hardware to follow the rapid upgrade and update of the digital communication. So the method of software radio comes¹. The transform from analog to digital must be as close to the antenna as it can so that most work such as modulation in communication system can be processed by DSP and FPGA which has powerful digital processing ability and high flexibility. This digital communication platform was designed to meet the rapid development of the communication technology and enhance the system flexibility. QPSK is widely used in many fields because of its strong anti-interference ability and high bandwidth efficiency². The QPSK modulation and demodulation was implemented in the platform to verify the practicality of the platform³.

Hardware system design

This platform was design based on the method of software radio which gave as much work as it can to the software⁴. The "DSP +FPGA+ peripheral" method was used in the hardware design. Fig. 1 shows the hardware system block diagram.

The system was composed in baseband communicate module, signal send and receive module and signal process module. The baseband communicate module was design to transmit message between platform and host computer; the function of signal send and receive module was sending and receiving modulated signal; the signal process module was the core of this system and it was used to do the modulation and channel coding.

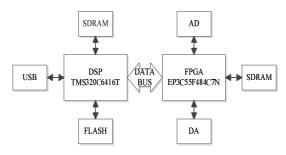


Fig. 1 Hardware system diagram

Baseband communicate module. The core chip of this module was the CY7C6801 of CYPRESS. It was connected to DSP in this platform so that the host computer can communicate with the DSP easily. During the communication, the initiative was controlled by host computer, so host computer can access DSP's memory directly. The communication between them was supported by HPI (Host Port Interface) of DSP. In modulation system, the baseband message which was going to be sent was transmitted from host computer to DSP, and the result of demodulation was transmitted from DSP to host computer.

Signal process module. This module which was the core of the platform used DSP and FPGA to process signal. The DSP which can be in-circuit debug was TM320C6416 of TI, and memory chips such as FLASH were connected to it; the EP3C55F484C7N was Altera FPGA, and it was connected with DAC and ADC. The communication between DSP and FPGA was a problem in this system. The FPGA was treated as a memory of DSP so that DSP could access FPGA with EMIF (External Memory Interface).

Signal send and receive module. The module was designed to transmit modulated signal between receiver and transmitter. The DAC in transmitter was the 12-bits TLV5639 from TI, and the receiver used ADC12040 which was the 12-biTS ADC of TI to receive modulated signal. Both of the transmitter and receiver had ADC and DAC to make sure that both of them can be duplex.

Implementation of QPSK

QPSK was implemented on the platform to verify the platform's reliability and validity. Two platforms connected by coaxial were used to be transmitter and receiver.

QPSK transmitter. The function of transmitter was receiving message from host computer, signal processing and sending modulated signal to receiver. Just like Fig. 2 shows.

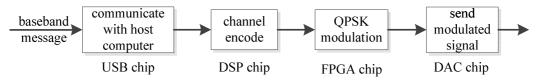
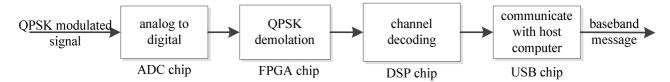


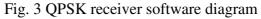
Fig. 2 QPSK transmitter software diagram

The baseband message was transmitted to platform by USB. Before it was received by FPGA throw EMIF, DSP acted as a Hamming encoder. After QPSK modulation, modulated signal was sent out by the DAC. The QPSK was generated in quadrature modulation method, and the corresponding phase is shown in Table 1.

Table 1 QPSK phase with I and Q							
Ι	Q	phase	Ι	Q	phase		
0	0	0	1	1	π		
0	1	π/2	1	0	3π/2		

QPSK receiver. The receiver's function was demodulating high frequency modulated signal to baseband signal and sending it to the host computer. Fig. 3 is the software diagram of QPSK receiver.





After the QPSK modulated signal was transformed from analog digital by ADC, demodulation, frame synchronous and bit synchronous were done by FPGA. Before the baseband message was send to the host computer by USB, DSP decoded the channel code message. The key of QPSK demodulation was carrier synchronization and the Costas loop was used in this design by FPGA. It used differential encoder to avoid the phase ambiguity.

System Test

Hardware test, waveform test and message transmit test were done to verify the practicality of this platform.

Hardware test. The object of hardware test was DSP's external memory SDRAM and FLASH. It used the TI's CCS3.3 to test the read and write of them. SDRAM was tested at first. The 128M bit SDRAM HY57V283220 was connected to the CE3 of DSP's EMIF so that DSP can read and write it throw EMIF. The test data was written to the memory at first and the CCS was used to verify whether it was written rightly or not. Just like the Fig4 shows, data in address 0x80000000(the first address of CE3) is "this is sdram test, hello sdram". The SDRAM was tested successfully.

0x8000000	t	h	i	s		i	s
0x80000007	-	s	d	r	а	m	-
0x800000E	t	e	s	t		h	е
0x80000015	1	1	0	-	s	d	r
0x8000001C	a	m	1	-		-	-

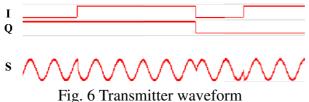
Fig. 4 SDRAM read and write test

SST39VF800 was an 8 Mbit FLASH used as the code and data memory of DSP in this platform. It was connected to the CE1. It should be erased before written which was complex than SDRAM and the operation of read was same with SDRAM. The test result of FLASH was showed in Fig5. We can see that in the address 0x64000000(the first address of CE1) data was "hello flash test!".

0x64000000	h	e	1	1	0		
0x64000006	f	1	а	s	h	-	
0x6400000C	t	e	s	t	1	-	
	•	~					

Fig. 5 FLASH read and write test

Software test. The aim of this test was to verify whether the QPSK modulation was successfully or not. Transmitter was tested at first. According to the Table1, the change of I and Q was correspond to the change of carrier phase. Fig6 shows the waveform of transmitter.



In Fig. 6, signal I and Q represented I and Q channel baseband signal while signal S was the QPSK modulated signal. When I and Q changed from "00" to "10", the phase of QPSK changed from 0 to $3\pi/2$; the phase of QPSK changed from $\pi/2$ to π when I and Q changed from "01" to "11".

The receiver was designed to demodulate QPSK modulated signal to baseband message and send it to the host computer. Fig. 7 shows the waveform of receiver.

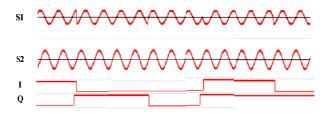


Fig. 7 Receiver waveform signal

The carrier synchronous, which was implemented by Costas Loop, was the most important part of receiver. From Fig7 we can see that S1 was the QPSK modulated signal and S2 was the local carrier generated by Costa Loop. S1 and S2 had the same frequency and phase. Signal I and Q were the demodulation result. Signal I and Q changed from "00" to "10" when the phase of S1 changed from $\pi/2$ to π . So the receiver demodulated the QPSK modulated signal successfully.

System test. Test message was send continuous from the host computer on transmitter and the BER (bit error rate) can be calculated by count error bit in the receiver message on the receiver host computer. The BER can be less than 10^{-5} when SNR was 12dB.

Conclusions

A digital communication platform based on FPGA and DSP was introduced in this paper. Every part of it can work stability after many tests. This platform has strong versatility and high flexibility and common modulation and signal process can be successfully implemented on it.

Acknowledgments

This paper is funded by the International Exchange Program of Harbin Engineering University for Innovation-oriented Talents Cultivation, International Science & Technology Cooperation Program of China (2014 DFR10240), National Natural Science Foundation of China (612111070), the Fundamental Research Funds for the Central Universities (China) [HEUCFD1304], China Postdoctoral Science Foundation (2013T60346), Harbin science and technology research projects (2013AE1BE003), Heilongjiang province natural science foundation projects (F201344).

References

- [1] Li Weidong, Yao yan. Software Radio: Technology & Implementation. China Institute of Communications(CIC), The Chinese Institute of Electronics(CIE),(1998).
- [2] Bernard Sklar. Digital Communications Fundamentals and Applications. Beijing Publishing House of Electronics Industry, (2002), p.128.
- [3] Wenmiao Song, Qiongqiong Yao . Design and Implement of QPSK Modem Based on FPGA. Chengdu: IACSIT, (2010).
- [4] Ziye Long, Chenxi Wang, Derong Cai, Xiaoli Li, Jing Zhu. Design and Realization of IF Digital Demodulator based on Software Radio. Chinese Institute of Electronics (CIE), (2009).

The Research of Multi-points Sources Signal Power Synthesis Technology

Liu Qi-bo^{1,2,a},Zeng Fang-ling^{1,2},and Chen Qiu-ju¹ ¹Electronic Engineering Institute, Hefei 230037,China ²AnHui Province Key Laboratory of Electronic Restriction, Hefei 230037, China ^aliuqibo90@sina.com

Keywords: multi-points sources power synthesis, random space disposal, cross beam, spatial power combination

Abstract: This article introduces the basic principle and theory model of the crossbeam space power synthesis, and presents the result of system simulation and analysis. The author has adopted random sparse disposal and compounded the multi-points sources of transmitted power in space, through controlling the accurate orientation of the beam, reaching the aim of enhancing power. Meantime, arbitrary distributed array has been adopted to make the system more practical.

Introduction

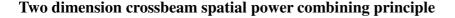
Currently, in the field of multi-source power, spatial power combining is mainly synthesized by conventional compact line array in the main direction, which forms a fan-shaped target area with target direction as the center. There are few researches concerning sparsely distributed multi-source, which enhanced power by interference effects in the intersection area.

Professor Zhang Jiayan and Shu Ting, from National Defense University, studied the dual cross beam synthesis of dual sparse array. Through the analysis results, the shorter the wavelength of the two cross-beams of work cause the intersection point of the region to interfere with long point more dense; The larger angle of two beams cause interfere long points is more dense. They have not given further analysis and discussion when the increase in the number of point sources.

The article is based on the antenna array on sparsely distributed, by using the control beam pointing, it is to conduct multi-source research in the area of the intersection of interference effects, analytical power superimposed situation.

Due to the sparse array of cross beams in the intersection region of space power combining reticular distribution in the intersection area to achieve the purpose of superimposed signal power, consider the target point as a reference point, the point source to calculate the reference point of the signal propagation delay and be compensated in the signal transmission, so that each point source signal at the target point with the overlay, in order to achieve power combining intersection region.

In the synthesis of the basic principles and theoretical models on the basis of multi-source cross-beam space power, the simulation analysis of the number of sites, station distribution affect the shape of the intersection area power synthesis.



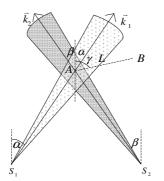


Figure 1 Binary sparse array of cross beam synthetic

Recalling the first binary sparse array of cross beam power combiner, shown in Figure 1. Let constitute a binary sparse matrix, A is the target, the target points, respectively, and the direction of the wave vector, respectively antennas and antenna tilt angle of the main direction. Assuming both are linearly polarized beam, the same polarization. A region known to be a point of intersection, such as phase two beams interfere with long-wave point, point B is located in the plane and another, etc. A nearby phase interference with long points, which means that the vertical line segment AB the angle between the direction of the point A and the adjacent angle γ relative to other points of the point B as the distance L

$$L = \left| \frac{\lambda}{\cos(\gamma - \alpha) - \cos(\gamma + \beta)} \right|$$

 $_{\textcircled{D}}\gamma = 0^{\circ}$, and assume that $0^{\circ} < \alpha, \beta < 90^{\circ}$, then $L = \left|\frac{\lambda}{\cos \alpha - \cos \beta}\right|$, so, the smaller λ the samller L

is, the bigger $\cos \alpha - \cos \beta$ the smaller L is.

$$_{\odot}\gamma = 90^{\circ}$$
, $L = \left|\frac{\lambda}{\sin \alpha + \sin \beta}\right|$, so, the smaller λ the smaller L is, the bigger $\sin \alpha + \sin \beta$ the

smaller L is; in particular, when α , β are small angles , we have $L \approx \frac{\lambda}{|\alpha + \beta|}$, then λ the

smaller L is, the more that two beams intersect angle increases, then L is smaller.

From the above preliminary analysis, the two cross beams work shorter the wavelength, the length of the intersection point of the region to interfere with the more dense; greater the angle of the two beams intersect and interfere with long points more dense.

Further, analysis of multi-source can also be cross-beam synthesis of space, the field distribution within the region should also be the intersection of reticular distribution. But the increase in the number of point sources, it is difficult to form a multi-point sources are in the peak phase long point, difficult to give exact calculations with a long point, multi-point source beam to explore the area at the intersection of power only through the electromagnetic field theory of superposition synthesis, the strength and the power that is superimposed on a certain point defined as the effective interference.

Therefore, multi-point source cross beam spatial power combining, at the intersection region of space interference effects can also be achieved through the power of the overlay, the same is the case with the binary at the same wavelength as the phase-point intensive long, the beam should be increased cross angle.)

Multi-dimension cross beam spatial power combining principle

More power synthesis the basic principle of point source cross area

Consider a point source greater than or equal three sparse distributed array, shown in Figure 2, set the coordinates of a point source of electromagnetic radiation in each intersection point region

P(x, y, z), each point $A_i(x_i, y_i, z_i)$, $i = 1, 2, \dots, n, n \ge 3$, First, calculate the signal strength in the synthesis of field points.

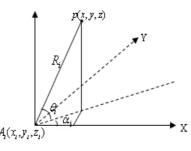


Figure 2 Signal source and P point geometry structure diagram

© Assuming the signal emitted by the first point sources resulting in a strong field point is $\vec{E}_i = \frac{\Delta_c}{R_i} e^{-jkR_i + j\varphi_i}$, among, $\Delta_c = \sqrt{30PG}$ Point source depending on antenna gain and transmit

power, in the theoretical analysis which are not considered as a constant; $k = \frac{2\pi}{\lambda}$; R_i is the distance b- etween two points, θ_i is the angle between the i-th point source and point of connection with the P plane xoy, Q_i is the angle between the i-th point source and point of connection on P xoy the plane and the x-axis; φ_i phase of the signal (To compensate for the differences with the source to the specified reference point wave path difference delay planned).Point A and point P in space stations relationship shown in Figure 2), the distance between two points is $R_i = \sqrt{(x_i - x)^2 + (y_i - y)^2 + (z_i - z)^2}$.

⁽²⁾Axis direction vector decomposition and synthesis of components of the field strength according to the spatial relationship between the superimposed, assume n stations), let each station antenna directivity function) W (j) ,j=0,...,N-1,the original projecting phrase is φ_i , then we can obtain the magnitude of the resultant field strength $|\vec{E}_x|$, $|\vec{E}_y|$ and $|\vec{E}_z|$ of directions of axis x,y,z.The intensity of the resultant field strength in each direction vector component superimposed on the total synthesis of P-point field), then: $|\vec{E}| = \sqrt{|\vec{E}_x|^2 + |\vec{E}_y|^2 + |\vec{E}_z|^2}$

$$\vec{E}_{x}\Big|^{2} = \left(\sum_{i=0}^{N-1} \frac{\Delta_{c}}{R_{i}} w(i) \cos \theta_{i} \cos \alpha_{i} \cos \phi_{i}\right)^{2} + \left(\sum_{i=0}^{N-1} \frac{\Delta_{c}}{R_{i}} w(i) \cos \theta_{i} \cos \alpha_{i} \sin \phi_{i}\right)^{2}$$
(1)

The same can be $\left|\vec{E}_{y}\right|^{2}$ and $\left|\vec{E}_{z}\right|^{2}$, then

$$\vec{E}\Big|^{2} = \left|\vec{E}_{x}\right|^{2} + \left|\vec{E}_{y}\right|^{2} + \left|\vec{E}_{z}\right|^{2}$$

$$= \Delta_{c}^{2} \left(\sum_{i=0}^{N-1} \frac{w(i)^{2}}{R_{i}^{2}} + 2\sum_{i=0}^{i=N-2} \sum_{j=i+1}^{j=N-1} \frac{w(i)w(j)}{R_{i}R_{j}}\right)$$

$$\cos(\phi_{i} - \phi_{j})[\cos\theta_{i}\cos\theta_{j}\cos(\alpha_{i} - \alpha_{j}) + \sin\theta_{i}\sin\theta_{i}])$$
(2)

In the above formula reflects the synthesis of P point field strength of the signal frequency, phase, and point source and specify the relative orientation of the reference point, the relationship between the locations.

To reach the intersection region superimposed signal power purposes, and binary array similar to consider the direction of the main lobe of each point source at the target point, the target point roughly in the center of each intersection point source region by calculating each point source to the target point propagation delay, the delay compensation equivalent to the data source each point on the initial phase of the transmitted signal, then the target points, each point source signal with superimposed and adjacent to the target point, the formation of electromagnetic interference area.

Establish cross-regional interference effects within the mathematical model

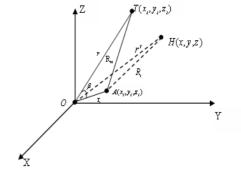


Figure 3 Point sources and interference point of spatial locations

Spatial location map point source and point of interference

Let T be the target point. The same frequency of the signal emitted by each point source, delay compensation by making a strong field at the T-point phase stack. In Figure 3, any one of the selected station as the origin O, in order to calculate for each point source of the delay.) r, r' respectively, is the distance from the origin point to Point T and H, R_{it} is the distance from point i to Point T, R_i is the distance from point i to Point H, i is among the interval $0 \sim N-1$, N is Number of point sources. To ensure that the target point T to achieve power with superimposed, Let $\varphi_i = \frac{2\pi R_{it}}{\lambda} - \varphi_0$, After each station to reach the target point of the phase offset can be considered by the wave path 0 or a fixed value φ_0 , we get the resultant field strength at the point T

$$\vec{E}_t = \sum_{i=0}^{N-1} \frac{\Delta_c e^{-J\varphi_0}}{R_{it}}$$

Therefore, By delay compensation, so that each point source emits a signal to reach the T-point field strength in phase, that is, too:

$$\left|\vec{E}_{t}\right|^{2} = \Delta_{c}^{2} \left[\sum_{i=0}^{N-1} \frac{1}{R_{it}}\right]^{2}$$

Let H be the intersection point of the region to another, H-point total for the direction of the electric field strength component of the vector field strength superposition, Let

$$\phi_i = -\frac{2\pi R_i}{\lambda} + \varphi_i,$$

therefore:

$$\vec{E}_{h}|^{2} = \left|\vec{E}_{hx}\right|^{2} + \left|\vec{E}_{hy}\right|^{2} + \left|\vec{E}_{hz}\right|^{2}$$

$$= \Delta_{c}^{2} \left(\sum_{i=0}^{N-1} \frac{w(i)^{2}}{R_{i}^{2}} + 2\sum_{i=0}^{i=N-2} \sum_{j=i+1}^{j=N-1} \frac{w(i)w(j)}{R_{i}R_{j}}\right)$$

$$\cos(\phi_{i} - \phi_{j})[\cos\theta_{i}\cos\theta_{j}$$

$$\cos(\alpha_{i} - \alpha_{i}) + \sin\theta_{i}\sin\theta_{i}]) \qquad (3)$$

Due to interference and electromagnetic wave propagation effects, when the H point is at a different location within the intersection area, combined power value is different in the case of multiple sources, is difficult to figure out the situation as a binary distribution with a long point, so the definition of effective the concept power point. According to the power point and the relationship between T H point, will meet

$$\frac{\left|\bar{E}_{h}\right|^{2}}{\left|\bar{E}_{t}\right|^{2}} \ge \eta_{0}$$

H-point ,which satisfy the formula , is valid power point, the value η_0 determined according to the actual needs. The points satisfying the above inequality is referred to the half power point, thus constituting a multi-point calibration out of the active power source cross-point area. Here to study the distribution of effective power points through simulation.

Multi-source cross beam power combining simulation analysis

Simulation conditions: Let multi-point source aligned with the direction of the main lobe of the antenna reference point, the next picture shows the antenna pattern, 3dB angle range of about- 1.5° - 1.5° .

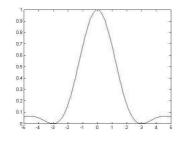
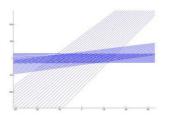


Figure 4 The antenna directivity diagram

Simulation 1: 3-point source as an example to discuss the relationship between the site and the intersection of the regional distribution of the half-power point distribution

Let the target point of origin, three-dimensional coordinates of the array is taken as) (5200,0), (4213.2,3554.6), (903,5032.4),Unit: m;signal frequency f=300MHz,interference zone sampling interval: $\Delta x = \Delta y = 0.3m$ (The following figure is a horizontal coordinate of x, y coordinates of the longitudinal)





(a) 3 dimensional array -1 schematic intersection region(Unit: m)

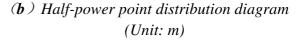
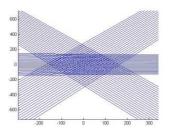
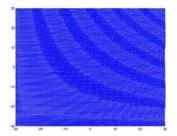


Figure 5 3 dimensional array -1 and half-power point distribution diagram (Unit: m) Increasing the distance between stations, three-dimensional coordinates of the array is taken as (5200,0), (2750,4789.1), (-2600,4425.4) and set the signal frequency f = 1000MHz, interference zone sampling interval: (bottom transverse x coordinates, the vertical y-coordinate), the simulation results are:





(a) 3 dimensional array -2 schematic
 (b) Half-power point distribution diagram
 intersection region(Unit: m)
 Figure 6 3 dimensional array -2 and half-power point distribution diagram (Unit: m)

So we can conclude, multi-point power source and binary matrix synthesis is similar to the effective interference showing regular distribution points, the greater the cross point of view, the more concentrated the intersection area, the more concentrated and effective interference points, increasing signal frequency, phase and more intensive long point.

Further increase in the number of point sources, the concept is more complex with long points, in addition to the target point, it is difficult to find other points, each point source radiating the signal reaches the same point are superimposed, then the need to further explore the power efficient synthesis of the meaning of this content will be the follow-up study.

Conclusions

The above describes the multi-area power source intersection principle model synthesis and simulation analysis, based on the spatial relationship of the point source and the target point, the vector field strength of the signal decomposition and synthetic overlay, get the radiation cross-regional power combining principle model and effective power point mathematical models. In the multi-source signal interference effects were achieved through the power Preliminary synthesis of multi-source signal power combiner further research to applications with meaning.

Reference

- [1] Zhang Jiayan,Shu Ting, Yuan Chengwei. A preliminary study of high power microwave synthesis of spatial power. Laser and Particle Beams.
- [2] Jiang Zhihao, Cai Derong, Wang Zhi. Synthesis efficiency of spatial power combining technology. Radio communications technology.
- [3] Song Kaijun. Synthesis technique based on microwave and millimeter wave waveguide power space. PhD thesis. University of Electronic Science and Technology.(2007)
- [4] Zhao Rong, Hou Deting, Guo Jie, Chen Yong, High Power Microwave Synthesis Methods spatial power, Newspaper of Information Engineering University.
- [5] Qi Yaping, Zhu Linfang. Shortwave stations spatial power combining multiple communications jamming technology research. Electronic confrontation. Vol3.
- [6] Tan Xianyu. Technical status and development of high-power microwave weapons new concept. Aviation Ordnance.
- [7] Zhang Yubing, Zhang Hao, Liao Guisheng, Arbitrary decentralized jammer array machine spatial power combining technology. Xi'an University of Electronic Science and Technology.

A Flat Fiber Raman Amplifier by Optimizing a Single-Wavelength Laser Diode

Yu Ma¹, Yanchao Li¹, Chunyu Liu¹, Jiuru Yang^{1,a}

¹Key lab of Electronics Engineering, College of Heilongjiang Province, Heilongjiang University, P.R. China

^ayangjr@hlju.edu.cn

Keywords: Fiber Raman amplifier, gain-flatness, optimization, simulation

Abstract. Gain-flatness is one of the crucial parameters for the application of fiber Raman amplifier (FRA). To obtain the ideal gain-flatness within the wide spectrum, the devices should be optimized in a FRA system. In this article, rather than a complicated design reported in the traditional schemes, we adopt a single-wavelength laser diode to flatten the gain spectrum of FRA through optimize its pumping power and wavelength simply. The numerical results by simulation show that the gain-flatness of the designed FRA system is controlled within ± 1 dB in the range of 1500 nm ~1560 nm by a laser diode with 1435 nm and 250 mW.

Introduction

Due to wide gain bandwidth, fiber Raman amplifier (FRA) is one of the key devices in the design of dense wavelength division multiplexing (DWDM) system [1]. Currently, with the increasing demand of rate and bandwidth in transmission, the gain-flatness of FRA has received much attention by many researchers [2-4]. Generally speaking, the gain-flatness of FRA is critical dependent on three key factors: pumping wavelength, pumping power and the length of gain fiber. Koch got less than 1.27dB un-flatness within 70 nm of FRA by means of a long period fiber grating [5]. Dai adopted a chirp fiber grating to obtain the \pm 0.6 dB gain-flatness within 50 nm. But, the shortcoming is fiber grating is unstable [6]. Comparatively, multi-wavelength pumping (the number is usual larger than 3) is regarded as another efficient method to flatten the gain spectrum and some high flatted recodes have been reported [7]. Nevertheless, it is hard to achieve the matched wavelength interval and pumping power among such multi-pumping sources. Consequently, the gain-flatness is challenged and still one of the hot topics in the study of FRA. In this article, we simplify the complexity of the FRA system and flatten the gain-spectrum through a single-wavelength laser diode. And our work concentrates on optimizing the wavelength and power of the laser diode as unique pumping source. To evaluate the performance of this method, necessary analysis and simulation is conducted. In the following sections, the makeup of the designed FRA system is first demonstrated. Then, we study the features of wavelength and power on the gain-flatness of FRA. Thirdly, the length of gain fiber is should be determined with the optimized laser diode, and the ideal numerical results are obtained.

Experimental Model

As shown in Fig. 1, an experimental model of fiber Raman amplifier is made from five parts: (1) signal lights, (2) pumping source, (3) gain fiber, (4) filter and isolator, (5) analyzer. In the first part, several laser diodes as transmitters denoted by Tx *i* (*i*=1, 2, ..., *n*) emit signal lights. Here, we set n=6. Then six wavelengths in the band near 1550 nm are chosen, which is from 1510 nm to 1560 nm, and the interval is the same and equal to 10 nm. On account of low gain efficiency of FRA, the input power of signals is designed as -3 dBm.

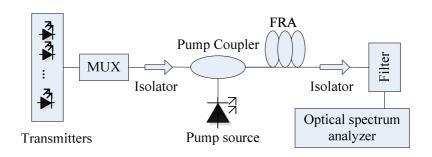


Fig.1 Experimental model of FRA

Next, we choose a single-wavelength laser diode as pumping source, whose center wavelength (λ) is at 1415 nm and pumping power (denoted by P_{pump}) is about 200 mW. Specially, a backward pumping is adopted in the following studies. In the third part, the gain fiber is a 25-kilometer-length single mode fiber (SMF), and the value of NA is 0.22. The isolator and filter can alleviate the effects of forward and backward amplified spontaneous emission (ASE) noise. In such model, the signal lights go through wavelength coupler and are amplified in SMF by pumping source. Finally, the output signals will be received by an optical spectrum analyzer denoted by OSA. Obviously, the pumping source and gain fiber (i.e. SMF) are the two key factors to optimize the gain-flatness of output spectrum of FRA.

Simulation and Optimization

First, we define the fluctuation of gain spectrum is

$$\Delta G = G_{max} - G_{min} \tag{1}$$

where G_{max} and G_{min} are the maximum and minimum of gain power, respectively. The average gain-flatness is defined as

$$G_{ave} = \frac{1}{n} \sum_{i=1}^{n} G_i \tag{2}$$

where G_i is gain power of the i_{th} signal light, and the maximum of i is equal to six. Furthermore, the signal noise ratio is presented by

$$SNR = \frac{G_{ave}}{P_{ASE}}$$
(3)

where P_{ASE} is defined as the average power of noise. Based on the above three parameters, we then evaluate the performance of the FRA system in gain-flatness by varying the wavelength and power of pumping source.

a. Vary wavelength of pump source

Initially, the fiber length (denoted by *L*) is unchanged and designed at 25 kilometer. The pump power is as well as constant and equal to 300 mW. We then choose three pumping wavelengths (1415 nm, 1435 nm and 1455 nm) and study the features of FRA in gain-flatness by simulation. As shown in Fig. 2, in the output spectrum of FRA, the maximum and minimum of gain are 2 dB and -7.5 dB, respectively. So the value of ΔG is 9.5dB when λ =1415nm. It is obvious that the gain-flatness is not ideal in this case. Similarly, we observe the situations of gain-flatness when λ =1435nm and λ =1455nm. Compare with the case of 1415 nm, we find the gain-flatness of output spectrum is improved with the increase of pump wavelength. Especially, in the case of λ =1435nm, the value of ΔG is only 2.5dB. At the same time, we notice that the lowest noise, -67dB, is also obtained at λ =1435nm, and the corresponding value of SNR is about 70 dB. So the ideal pump wavelength for gain-flatness should be equal to 1435 nm in this FRA system.

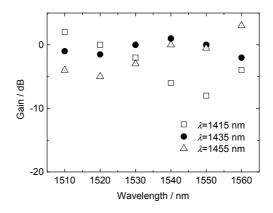


Fig. 2 Gain-flatness by varying pump wavelength

b. Vary power of pump source

In this part, we fix the length gain fiber (25 kilometer) and pump wavelength (1435 nm), and we observe the gain-flatness of output spectrum of FRA by vary the power of pump source, and the result is shown in Fig. 3. Compare to that of Fig. 1, it is clear that the improvement of gain-flatness of FRA at λ =1435 nm. From the obtained numerical results, we see the maximum of gain is about 0 dB, the minimum of gain is -4.5 dB, and the average fluctuation of gain spectrum is about ±2 dB. Furthermore, compare the three group values, a better gain-flatness occurs at P_{pump} =250mW, in which ΔG is less than ±1 dB. Similarly, the value of noise power in the case is under the line of -70dBm, and SNR reaches 69 dB.

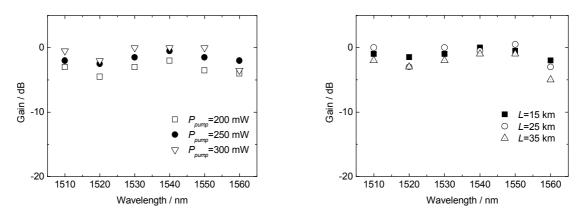


Fig. 3 Gain-flatness by varying pump power

Fig. 4 Gain-flatness by varying fiber length

Here, we should notice that the above results are gained in the situation L=25km. In fact, the fiber length has an effect on the gain-flatness of FRA too. In other words, L=25km maybe not an ideal parameter for the optimized single-wavelength laser diode. Therefore, we take another study on the various fiber lengths by simulation. According to the results in Fig. 4, when $\lambda=1435$ nm and $P_{pump}=250$ mW, the optimal gain-flatness is observed at L=15km. It is due to the facts that both spontaneous scattering signal and noise energy will become bigger with the increase of fiber length. This also leads the SNR becomes lower.

Summary

In this article, we design an experimental model of FRA based a backward-pump single-wavelength laser diode. By simulation and analysis, the wavelength and power of the single-wavelength are determined for getting the optimal gain-flatness of FRA. We also get the ideal fiber length with high gain-flatness and SNR.

Acknowledgement

This work is supported by National Natural Science Foundation of China (61302075, 61205071, 61177079), Science Foundation of Heilongjiang Province of China (F201009), China Postdoctoral Science Foundation funded project (2012M520779).

References

- Zhi Tong, Huai Wei, Shuisheng Jian. Optimal Design of Distributed Raman Amplifiers Employed in Long Haul Optical Transmission System [J]. Acta Physica Sinica, Vol. 55(2006), p. 1873-1882
- [2] Lei Wen, Wei Chen, Liyan Zhang, et al. Ranman Scattering Characteristics of Tellurite Glass used as Broadband Raman Amplifier [J]. Acta Photonica Sinica, Vol. 37 (2008), p. 178-180
- [3] Masuda H. Review of Wide-Band Hybrid Amplifiers [J]. IEEE/OSA OFC, Vol. 1(2000), p. 2-4
- [4] Ting Zhang, Xiupu Zhang, Guodong Zhang. Distributed Fiber Raman Amplifiers with Incoherent Pumping [J]. IEEE Photon. Technol. Lett., Vol. 17(2005), p. 1175- 1177
- [5] Koch F, Lewis S, Chernikov S V, et al. Broadband Gain Flattened Raman Amplifier to Extend operation in The Third Telecommunication Window [J]. IEEE/OSA OFC, Vol. 4(2000), p. 103 -105
- [6] Bizhi Dai, Zaixuan Zhang, Dan Geng, et al, The Development for Dispersion Compensating Fiber Raman amplifier of S-band Flat Optimizing[R]. The 5th national photonics conference (in Chinese), 2004.
- [7] Jianhua Chang, Tingting Wang, Zaihong Tao, et al, The Optimization Design of Multi-Wavelength Broadband Raman Amplifier [J]. Chinese Journal of Computational Physics (in Chinese), Vol. 24 (2007): 227-233.

Simulation of FBG Wavelength Signal Demodulation Based on Sideband Filter

Naikui Ren, Yanling Xiong^a, Mingze Wu, Hao Xu, Zhenyu Ma and Jiyun Zou College of Applied Science, Harbin University of Science and Technology, Harbin, 150080, China ^axyling1964@163.com

Keywords: Wavelength demodulation, FBG, Sideband filter, Matlab software

Abstract. The wavelength of Fiber Bragg grating (FBG) sensor signal demodulation simulation system based on the quasi-linear relationship between the transmission side band of optical filters and wavelength was established by the simulation software of MABTLAB. The simple system only consists of broadband source, sideband optical filters, couplers, a FBG, data acquisition and processing system. The relationship between the information of FBG central wavelength and the transmitted light intensity of sideband filter were obtained when the alternating and gradually varying signal applied to the FBG sensors, respectively. The FBG wavelength demodulation can be achieved by sideband filtering, and results are consistent with the theory.

Introduction

Fiber Bragg grating as a new sensing element, has the advantage of fiber optic sensors and has some unique advantages of quasi-distributed, wavelength encoding and absolute measurements. In recent years, various studies about the characteristics of FBG strain, temperature and other physical sensor have been made. Meanwhile, people develop various fiber Bragg grating wavelength demodulation schemes, such as tunable filter scheme[1], fourier transform[2], tunable light source method [3]and unbalanced Mach-Zehnder interferometer demodulation[4]. The demodulating methods require expensive equipment and don't have the temperature compensating functions. The FBG demodulation scheme based on two long-period fiber grating edge filtering proposed by Professor Zhu Zhu[5] and FBG demodulation scheme based on Coarse Wavelength Division Multiplexer (CWDM) edge filtering raised by Professor Zhang Jian[6] are very interesting and worth further investigation.

In some practical engineering applications, the requirements for demodulating systems are simple structure, low cost and not very high resolution. Based on those demands, the sideband filter, widely used in optical fiber communication. This paper use it for the demodulation of the FBG wavelength signal. The main idea is to convert the center wavelength shift of FBG to the changes of light intensity, and establish the relationship of function between the wavelength and the output light intensity using the selective of band edge to wavelength. Wavelength information was obtained by measuring the output light intensity. This method is suitable for both dynamic and static measurements, and it has a good linear output in a small wavelength range about 5 nm. In addition, there is a system with the advantages of quick response, simple structure and low cost. Therefore, the research about FBG wavelength demodulation based on sideband filtering technology is significant.

Optical fiber sensing and demodulation principle

Fiber grating is a core Bragg grating, which can be prepared from optical fiber by UV irradiation. The narrow spectrum which satisfies the Bragg condition in incident broadband light can be reflected more than 90% through FBG. The effective refractive index and the period of FBG determine The center wavelength of the narrow band reflection spectra. The central wavelength can shift because the strain and/or temperature variation change the refractive index and period of FBG. Therefore, the external physical information can be obtained by the center wavelength reflection spectrum of the FBG, which can be detected by the spectrometer or other equipment. The formula about temperature and strain sensing is

 $\Delta\lambda_{\rm B}/\lambda_{\rm B} = (\alpha + \zeta)\Delta T + (1 - P_{\rm e})\varepsilon = f(\Delta T, \varepsilon).$ (1)

where, α , β , P_{ϵ} are the thermal expansion coefficient, thermo-optic coefficient and the effective elasto-optical coefficient of the fiber material, respectively.

The center wavelength of common optical sideband filter transmission spectrum is about 1550 nm. The variation of the transmittance is about 40 dB within a few nanometers wavelength range. The region, with the largest transmittance variation, can be regarded as approximate linear region. The relationship between the intensity and wavelength about the output light can be expressed as correlation of the linear sidebands transmittance and FBG Gaussian reflection spectra, as shown in Figure 1. When the central wavelength of FBG reflection spectrum changed with outside the physical quantity, the relationship between the intensity and reflected wavelength can be obtained by the FBG through transformation of the sideband:

 $\Delta I = C \Delta \lambda_B = K R_0 (\pi/a)^{\frac{1}{2}} f(\Delta T, \varepsilon).$

(2)

And the relationship between the output light intensity and change measured outside can be seen be approximate to a quasi-linear relationship.

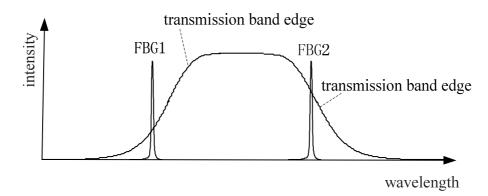


Fig. 1 Transmission spectra of Sideband filter and FBG reflection spectrum

This paper establishes the experimental system as the optical path shown in Figure 2. The broadband light, emitted by a broadband light source, enters the FBG through the coupling; the corresponding center wavelength of the light is reflected back along the same way, the remaining wavelengths of light transmitted. The reflected light enters sideband filter through the coupler. Since sideband transmittance indexes are different at different wavelengths, the output signal change can be achieved through data acquisition and processing system.

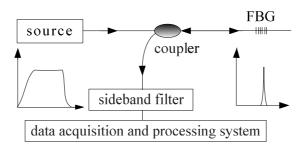


Fig. 2 The diagram of the sideband demodulation experimental system

Simulation Analysis

In simulation, the data of FBG reflection spectrum is used which the FBG center wavelength is 1548.1nm and the bandwidth of 3dB is 0.2nm. The center wavelength of the sideband filter is1550nm and the wavelength interval of sideband is from 1544nm to1552.5nm. The data, used to

simulate sideband of filter, is actually achieved by spectrometer to ensure that the results are reliable. The results of FBG signal demodulation based on sideband filtering, Obtained by MATLAB simulation software, shown in fig.3. Where, A1 and B1 are the diagram of the sideband filter transmission spectrum and FBG reflection spectrum, which the alternating and gradually varying signal applied to the FBG sensors, respectively. Sideband is selected which the relationship between transmittance and wavelength is approximately linear. FBG1 is a FBG reflection spectrum which there are no signal applied to FBG sensors, locate in the center position of the sideband spectrum. FBG2 is a FBG reflection spectrum which FBG center wavelength drifted by applying signal to FBG sensor. A2 and B2 are alternating and gradually varying signal which applied to the FBG sensor from outside, respectively. A3 and B3 represent the transmission spectrum of FBG2 through sideband modulation, which the applied signal are the alternating and gradually varying signal, respectively. A4 and B4 represent corresponding optical signal intensity, respectively.

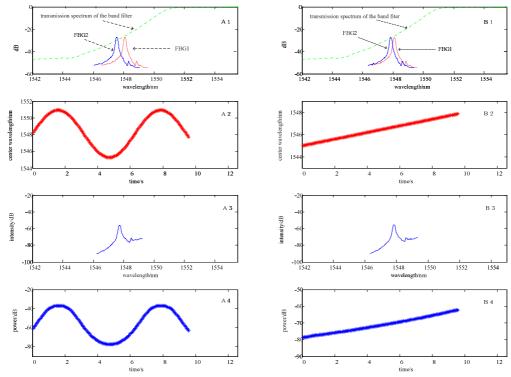


Fig. 3 The result of sideband demodulation simulation

It can be seen from A2, when the alternating signal is applied to FBG which the center wavelength is 1548.1nm, the FBG center wavelength varies periodically with time. The corresponding time of FBG sensor can be found by the information of wavelength. The detailed information about transmission spectrum when light through sideband and corresponding wavelength can be found from A3. A4 is the transmitted optical intensity of the FBG reflection spectrum through the sideband modulation. As can be seen from A2 and A4, FBG sensor output signal and the input signal have the same period, phase, and the amplitude is corresponding, the input signals can be detected by the rule of the output signal. Can be seen from B2 and B4, when the gradually varying signal is applied to FBG sensor, the output signal and the input signal has a quasi-linear relationship. Therefore, based on the MABTLAB simulation software, the FBG wavelength demodulation can be realized by using linear side band filter. The simulation match with the theoretical formula (2).

Summary

This paper presents an edge filter demodulation about FBG reflection wavelength signal. The Matlab simulation software was used to do simulation study on the alternating and gradually varying signal applied to the FBG. The FBG central wavelength is 1548.1 nm. The linear range of the sideband filter ranges from 1544 nm to 1552.5 nm, and the achieved linear demodulation region is about 8.5nm. As a result of all-fiber design, the speed of demodulation system can be up to several kHz.

Acknowledgements

This work was financially supported by the National Undergraduate Training Programs for Innovation and Entrepreneurship (201310214019).

References

- [1] Davis M A and Kersey A D: Electron. Lett Vol. 31 (1995), p. 822-825
- [2] Ohn M M, Huang S Y and Measures R M et al: Electron. Lett Vol. 33 (1997), p. 1242-1243
- [3] Brady G, Kalli K and Webb D J et al: Opt. Lett Vol. 20 (1995), p. 1340-1342
- [4] kersey A D, Ribeiro A B L and Morey W W: Opt. Lett Vol. 18 (1993), p. 972-974
- [5] Zhu zhu, dakai liang and hongbing sun: Chinese Journal of Lasers Vol. 40 (2013), p. 110-116 (In Chinese)
- [6] Jian zhang, hong zhao and yanling xiong: Chinese Journal of Scientific Instrument Vol. 27 (2006), P. 1464-1467 (In Chinense)

Research on the Method of CPM Signal Phase Smoothing Based on Different Power Sine Function

Wenjing Shang^{1,a}, Shengguo Zhou^{1,b}, Nan Wang^{2,c}, Rublev Victor^{3,d}

¹ College of information and communication engineering, harbin engineering university, harbin , 150001, China

²The 719th Research Institute of China Shipbuilding Industry Corporation, Wuhan, 430064, China

³School of Engineering of Far Eastern Federal University, Vladivostok, 690950, Russia

^ashangwenjing@hrbeu.edu.cn, ^bzhoushengguo@hrbeu.edu.cn,^cKingsout@163.com,^dLavr@mail.ru

Keywords: CPM signal; phase smoothing ; sine function; power spectrum

Abstract. Continuous phase modulation(CPM) signal has the advantages of high bandwidth efficiency, continuous phase, faster decay speed of power spectrum, constant envelope and so on, which is widely used in communication systems. The degree of the phase smoothing is one of main factors that affect the decay speed of CPM signal power spectrum. One method of smoothing CPM signal phase based on different power sine function as the frequency modulation function is proposed. We draw the phase trajectory of baseband signal and the normalized power spectrum by using the MATLAB software. The spectrum characteristics of the signal generated have great improvement compared with MSK signal, which reach the desired goal.

Introduction

Phase modulation signal has constant envelope and attractive spectral properties, which is widely used in communication systems¹, such as QPSK and BPSK signal in the application of satellite communication system and deep space communication system, GMSK signal in the application of mobile communication system², and so on. Phase modulation signal is divided into the continuous phase modulation signal and the discontinuous phase modulation signal. When the discontinuous phase modulation signal is transmitted over the band-limited channel, more severe signal waveform distortion and intersymbol interference are produced. It increases the certain difficulty for the demodulation process, reduces the reliability of the system. For continuous phase modulation signal spectrum characteristics has large improvement than discontinuous phase modulation signal spectrum characteristics, so it has faster decay speed of power spectrum, less out-of-band radiation energy, and more efficient utilization with limited spectrum resources. It has important practical significance for spectrum resources becoming increasingly tense today. In other words, the variation of modulation signal phase trajectory has great influence to its power spectrum. So we can study it to further improve the utilization efficiency of CPM signal frequency band, and reduce its energy radiation interference outside the band.

This paper introduces a new method to smooth phase by utilizing different power sine function as the frequency modulation function for traditional continuous phase modulation system.

Continuous phase modulation

For CPM systems, the transmitted signal^{3,4} is

$$S(t) = \sqrt{\frac{2E}{T}} COS\left(2\pi f_{c}t + 2\pi h \int_{0}^{t} \sum_{i=1}^{N-1} d_{r}^{(i)}g(t-iT)dt + \varphi_{0}\right) \qquad 0 \le t \le (N-1)T \qquad (1)$$

Where $d_r^{(i)}=\pm 1, 3, \ldots, \pm (M-1)$ —is a N symbols sequence of uncorrelated *M*-ary data symbols, *E* is the symbol energy, *T* is the symbol time, f_c is the carrier frequency, *h* is the modulation index, frequency modulation function g(t) is chosen to change the trajectory of smoothing phase, φ_0 is an arbitrary constant phase shift which can be set to zero. When different pulse functions g(t) are chosen, changing the base number a and modulation index h, a variety of CPM signals can be produced. We can select the appropriate pulse signal g(t) satisfies the trajectory of the phase modulated signal continuous conditions.

Different power sine function implementation phase smoothing

Different power sine functions have higher derivative continuous, that is to say, the signal is smooth. The following we will discuss how to use this feature to achieve the purpose of smoothing CPM signal phase. The phase variation of CPM signal is smoother, and its spectral density, especially the out-of-band spectrum decay will be faster⁵.

We have analyzed different power sine function as frequency modulation function, the phase variation value in a symbol interval *T* is $\pi/2$ and modulation index is 1/2. When we select the power sine function n = 2, the frequency modulation function can be expressed as follows

$$g_{1}(t) = \begin{cases} K \sin^{2}\left(\frac{\pi t}{T}\right) & 0 \le t \le T \\ 0 & t < 0, t > T \end{cases}$$
(2)

where K is an assumed constant coefficient.

From $\int_0^T g(t) dt = 1/2$, the assumed constant coefficient K can be obtained is 1/T, so the expression and Fig. 1 below provide the function of frequency modulation and waveform.

$$g_1(t) = \begin{cases} \frac{1}{T} \sin^2\left(\frac{\pi t}{T}\right) & 0 \le t \le T \\ 0 & t < 0, t > T \end{cases}$$
(3)

According to the relationship between phase transformation function and frequency modulation function, the formula of the transformation track of phase in a symbol interval can be expressed as follows.Fig.2 shows its waveform; Fig. 3 shows the phase variation when provided binary random sequence as 0110111010. It is observed that the phase trajectory is smoothing, not only keep continuous, but also higher derivative of the inflection point of symbol period keeps continuous.

$$\psi_{1}(t) = 2\pi h \int_{0}^{t} g(t) dt = \begin{cases} -\frac{\sin \frac{2\pi t}{T}}{4} + \frac{\pi t}{2T} & 0 \le t \le T \\ \frac{1}{2}\pi & t > T \end{cases}$$
(4)

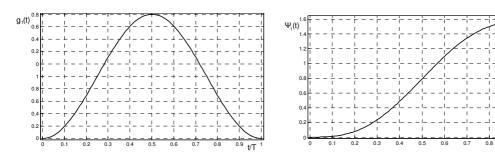
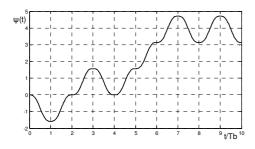


Fig.1 The wave form of frequency modulation function g (t)



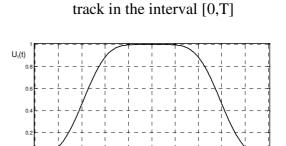


Fig. 2 The waveform of phase modulation

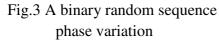


Fig.4 The base-band symbol signal of in-phase channel and orthogonal channel

The CPM signals can be generated by quadrature modulation. In this way, the single base-band symbol of in-phase channel and orthogonal channel can be expressed as follows. Fig.4 shows its waveform:

$$U_{1}(t,d) = \begin{cases} U(t,+1) = \cos\left(-\frac{1}{4\pi}\sin\frac{2\pi t}{T} + \frac{t}{2T}\right) & |t| \le T \\ U(t,+1) = 0 & |t| > T \\ U(t,-1) = -U(t,+1) & (5) \end{cases}$$

Comparisons are made with same method as above, we can respectively obtain the frequency modulation function and phase variation with the power value n=3,4, the expression of the base-band symbol signal of in-phase channel and orthogonal channel.

n=3:

$$g_{2}(t) = \begin{cases} \frac{3\pi}{8T} \sin^{3}\left(\frac{\pi t}{T}\right) & 0 \le t \le T \\ 0 & t < 0, t > T \end{cases}$$
(6)

$$\psi_{2}(t) = \begin{cases} \frac{\pi}{8} \cos^{3} \frac{\pi t}{T} - \frac{3\pi}{8} \cos \frac{\pi t}{T} + \frac{\pi t}{T} & 0 \le t \le T \\ \frac{1}{2} \pi & t > T \end{cases}$$
(7)

$$U_{2}(t,d) = \begin{cases} U(t,+1) = \cos\left(\frac{\pi}{8}\cos^{3}\frac{\pi t}{T} - \frac{3\pi}{8}\cos\frac{\pi t}{T} + \frac{\pi t}{T}\right) & |t| \le T \\ U(t,+1) = 0 & |t| > T \\ U(t,-1) = -U(t,+1) & (8) \end{cases}$$

n=4:

$$g_{3}(t) = \begin{cases} \frac{4}{3T} \sin^{4}\left(\frac{\pi t}{T}\right) & 0 \le t \le T \\ 0 & t < 0, t > T \end{cases}$$
(9)

$$\psi_{3}(t) = \begin{cases} \frac{1}{24} \sin \frac{4\pi t}{T} - \frac{1}{3} \sin \frac{2\pi t}{T} + \frac{\pi t}{2T} & 0 \le t \le T \\ \frac{1}{2}\pi & t > T \end{cases}$$
(10)

$$U_{3}(t,d) = \begin{cases} U(t,+1) = \cos\left(\frac{1}{24}\sin\frac{4\pi t}{T} - \frac{1}{3}\sin\frac{2\pi t}{T} + \frac{\pi t}{2T}\right) & |t| \le T \\ U(t,+1) = 0 & |t| > T \\ U(t,-1) = -U(t,+1) & (11) \end{cases}$$

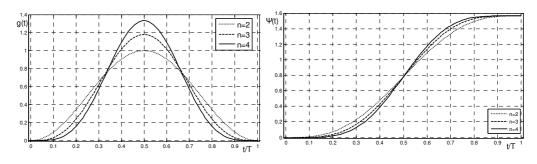


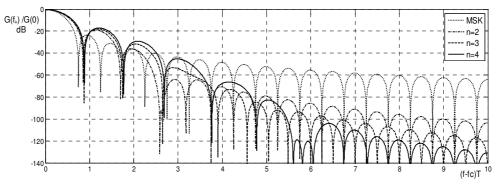
Fig.5 Frequency modulation function contrast figure

Fig.6 Phase trajectory contrast figure

Analysis of the spectrum spreading

The simulation of quadrature modulation and coherent demodulation process are completed by the software Matlab. The normalized power spectral density curve are calculated and compared with traditional normalized MSK signal power spectrum in Fig. 7. In Fig. 7, G(f) is the power spectrum of the signal generated, G(0) is the value of G(f) when f=0, which take half shaft with a positive frequency curve. Also shown in the figure, when $G(f_+)/G(0)$ =-60dB, the frequency band width of the MSK is about 8fT , After 8fT the MSK signal $G(f_+)/G(0)$ always stay at approximately -60 dB. When the sine function U(t) which value of power n=2 is used as symbol function in quadrature modulation, the frequency bandwidth is 2.8fT, decreased by 2.9 times than the MSK.

When introducing the value of power n = 3, n = 4 sine functions, the normalized power spectrum of CPM signals after their implementation phase smoothing has faster decay speed than the normalized power spectrum of the MSK signal, which explains that the power of out-band signals is



smaller. That's to say the signals of adjacent channel can be obstructed smaller. When the value of power n is greater the decay speed will be faster with more obvious superiority.

Fig.7 Normalized power spectral density curve

Summary

This paper proposes a new way of using different power sine function as frequency modulation function to realize phase smoothing of continuous phase modulation signals, and frequency modulation functions and phase modulation functions of CPM signals are provided. It is clear the phase of obtained signals is more smoothing from the track of phase variation and the normalized power spectral density curve. Not only the inflection point of symbol interval, but also higher derivative of the inflection point keeps continuous. The signal is obviously superior to the characteristic of the frequency spectrum of MSK signal. The simulation results proved the feasibility of this method

Acknowledgment

This paper is funded by the International Exchange Program of Harbin Engineering University for Innovation-oriented Talents Cultivation, International Science & Technology Cooperation Program of China (2014 DFR10240), National Natural Science Foundation of China (612111070), the Fundamental Research Funds for the Central Universities (China) [HEUCFD1304], China Postdoctoral Science Foundation (2013T60346), Harbin science and technology research projects (2013AE1BE003), Heilongjiang province natural science foundation projects (F201344).

References

- [1] He Wei,Du Shuanyi,Yu Jie. Continuous phase modulation and capture technology research[J] Electronics Technology, 2008,21(3): 38-42.
- [2] Linz A, Hendrickson A. Efficient implementation of an I-Q GMSK modulator [J]. Circuits and Systems H: Analog and Digital Signal Processing, IEEE Transactions on,1996,43(1):14-23.
- [3] Zhou Li, Lu Li.Continuous-phase modulation signals and their phase trajectories [J].Journal of Nanchang Institute of Aeronautical Technology. 2002.12. Vol. 16, No. 4:13-17.
- [4] J.B. Anderson, T.Aulin, C.-E. Sundberg. Digital phase modulation[M]. Plenum press, N.Y.,1992.
- [5] He Wei, Du Shuanyi, Yu Jie. Research into the Technology of Modulation and Acquisition for CPM[J]. Electronic Science and Technology. 2008. 21 (3):38-42.

Corrected Differential Evolution Particle Filter for Nonlinear Filtering

Chaozhu Zhang, Lin Li^a

College of Information and Communication EngineeringHarbin Engineering University ^alilin0214@yeah.net

Keywords: Nonlinear filtering, Particle filter, Corrected differential evolution, Resampling optimization.

Abstract. Particle filter is the most successful nonlinear filter for nonlinear filtering. However its resampling process has the critical problem existing is the particle impoverishment problem. In this letter, we propose a new corrected differential evolution particle filter for solving this problem. In this algorithm, the particles sampling from the importance distribution are regarded as the initial population of the Corrected Differential Evolution (CDE) algorithm, and the corresponding weights as the fitness functions. The optimal particles are obtained by the process of the CDE algorithm. Experiment results indicate that the proposed method relieves the particle degeneracy and impoverishment and improves the estimation precision.

Introduction

Nonlinear filtering is a very active topic in signal processing and control theory. There is a vast literature on this subject; see [1-3] for excellent references among others. Although the equations of the optimal nonlinear filter have been developed since the middle of the 1960s, the involved integrals are intractable. Hence, many suboptimal nonlinear filters have been proposed. Now the more popular solution method is using Monte Carlo methods, which the typical representative is the particle filter (PF), which goes back to the 1950s, but it was not used in practical applications until 1993 when Gorden proposed the sequential importance resampling (SIR) algorithm [4]. The PF has been used successfully in many domains; however, its performance depends heavily on the choice of the importance distribution function and the resampling algorithms. To improve the performance of the PF, choosing a good proposal distribution, and / or modifying the resampling scheme are often adopted [5-8].

In this paper a new method which uses the corrected differential evolution (CDE) as resampling schemes for the PF is proposed, which regard the resampling process as an optimization problem. We refer to it as improved differential evolution particle filter (CDEPF).

Problem Statement

Many nonlinear filtering problems can be written in the form of the dynamic state space (DSS) model as follows:

$$x_k = f(x_{k-1}, u_{k-1})$$
 (System equation) (1)

 $z_k = h(x_k, v_k)$ (Observation equation) (2)

where x_k and z_k are the state variable and observation at time k, respectively. k is the time index. $f(\cdot)$ and $h(\cdot)$ are some known functions, system noise u_{k-1} and v_k are random variable at time of given distributions. u_{k-1} and v_k are independent of past and current states. The objective of filtering is to recursively estimate the posterior density $p(x_k | z_{1:k})$ of the state x_k based on all available measurements $z_{1:k} = \{z_1, z_2 \cdots, z_k\}$. The PF utilizes some random particles with associated weights to approximate the true posterior density function. But the resampling process of PF leads to loss of diversity among the particles.

Proposed method

Differential evolution algorithm (DE) is proposed by Price and Storn [9], is a population-based stochastic algorithm for global optimization. However, it has insurmountable shortcomings, such as the slower convergence rate in latter periods, even failing to local extremes. Then a corrected differential evolution algorithm is proposed by [10]. The new algorithm records the difference vector, which is employed in mutating each individual by differential evolution algorithm. Each mutated individual was regarded as the center of a neighborhood, the corresponding difference vector as radius, and then the search of the mining type will be executed. This is called the correction step, which enhances the convergence capability of the DE in latter periods and improves the robustness of the DE algorithm. Detailed steps are presented accordingly in the sequel.

Step 1: Creating initial population.

The first step of CDE is to create the initial population samples (the number of generations is g = 0) in *n* dimension space as follows:

$$x_{ij}(0) = x_{ij}^{L} + rand_{ij}(0,1)(x_{ij}^{U} - x_{ij}^{L})$$
(3)

where i = 1, 2, ..., NP; j = 1, 2, ..., n, NP is the population size. x_{ij}^U and x_{ij}^L denote the upper and lower limits of the *j* th variable in the population respectively.

Step 2: Mutation operation

The function of mutation in CDE is to maintain the diversity of population. A typical CDE mutation samples formulation is:

$$h_{ij}(g) = x_{ij}(g) + F \cdot (x_{r1j}(g) - x_{r2j}(g))$$
(4)

where g represents the g th generation, $h_{ij}(g)$ are the mutated vector samples. $r1 \neq r2 \neq i$, and r1, r2 are randomly selected integers within NP, $r1, r2 \in \{1, 2, ..., NP\}$. F is scaling factor.

Step 3: Crossover operation

The basic crossover process is a discrete recombination, which employs a crossover constant $CR \in [0,1]$ to determine if the newly generated individual samples are to be recombined. The expression of the crossover process is given in Eq. 4:

$$v_{ij}(g) = \begin{cases} h_{ij}(g) & rand(0,1) \le CR \\ x_{ij}(g) & rand(0,1) > CR \end{cases}$$
(5)

where $v_{ij}(g)$ are the trial vector samples.

Step 4: Selection operation

Following the crossover is the selection step. In this step, $v_{ij}(g)$ and $x_{ij}(g)$ which has a higher value of objective function will survive into the next generation, that is

$$x_{ij}(g) = \begin{cases} v_{ij}(g) & f(v_{ij}(g)) \ge f(x_{ij}(g)) \\ x_{ij}(g) & otherwise \end{cases}$$
(6)

Step5: Correction operation

First, we calculate the corrected vector $x'_{ij}(g) = x_{ij}(g) + rand(0,1)$. Then correction selection step will be executed, that is

$$x_{ij}(g) = \begin{cases} x'_{ij}(g) & f(x'_{ij}(g)) \ge f(x_{ij}(g)) \\ x_{ij}(g) & otherwise \end{cases}$$
(7)

When the new population is propagated, the step 2 to step 5 are repeated until the optimum is found or a prespecified maximum G of the number of generations is reached.

In the presented algorithm, the resampling scheme of the particle filter uses the corrected differential evolution. A single iteration of the proposed particle filters based on CDE resampling algorithm is given as follows:

In the first step, we obtain the initial sampling particles by sampling the prior probability, $x_0^i \sim p(x_0), i = 1, ..., N$.

In the second step, the corresponding weights w_k^i of the updated particles can be calculated by $q(x_k^i | x_{0:k-1}^i, z_{0:k})$, and normalized by equation (6).

In the third step, we use the CDE algorithm to obtain optimal particles.

The last step, the estimated state is calculated by $x_k = \sum_{i=1}^{N} \overline{x}_k^i \overline{w}_k^i$.

Simulation Results

To demonstrate the performance of the proposed filter, we consider the following state-space model, which is also used in [8]:

$$x_{k+1} = 1 + \sin(w\pi k) + \phi_1 x_k + v_k$$
(8)

$$z_{k} = \begin{cases} \phi_{2}x_{k}^{2} + n_{k} & k \leq 30\\ \phi_{3}x_{k} - 2 + n_{k} & k > 30 \end{cases}$$
(9)

where v_k is a Gamma(3,2) random variable modeling the process noise, and w = 4e-2 and $\phi_1 = \phi_3 = 0.5$, $\phi_2 = 0.2$ are scalar parameters. The observation noise n_k is drawn from a Gaussian distribution N(0,0.00001). The different filters were used to estimate the state sequence x_k for k = 1, 2, ..., T, the total observation time is T = 50. In the proposed filters, F = 0.9, Cr = 0.6 and the maximum number of generations is G = 20. To measure the performance of the algorithms, we introduce the root mean squared error (*RMSE*) and its mean \overline{RMSE} , the root mean squared error for M simulations with observation time RMSE'.

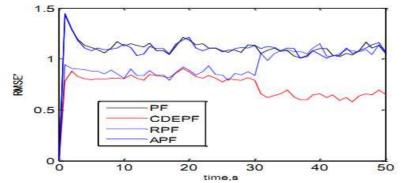


Figure 1. RMSE' of PF, APF, RPF with observation time for 500 MC simulations, where N=10

Algorithm	Mean (RMSE)	Variance (RMSE)
PF	1.1147	0.0218
CDEPF	0.5873	0.0122
APF	1.1055	0.0228
RPF	0.9594	0.0172

Table 1: Mean and variance of RMSE of PF, APF, RPF for 200 MC simulations with N=10

The estimation root mean squared error (RMSE) with observation time for different filters is shown in Fig. 1. Table 1 summarizes the performance of the five filters. The table shows the means and variances of the state estimates. From Fig. 1 and Table 1, it is clearly that the estimation accuracy of the proposed algorithm (CDEPF) is much higher than other filters.

Conclusions

In this paper, a new particle filter algorithm was developed for solving the nonlinear problem of the radar target tracking. The corrected differential evolution (CDE) is used as the resampling scheme and is the major new contribution of this paper. The proposed resampling algorithm reduces effectively the particle degeneracy and impoverishment problem, and improves state estimation accuracy. In addition, the convergence performance of the corrected differential evolution is better than the differential evolution by utilized the corrected search.

Acknowledgment

This work is supported by the National Natural Science Foundation of China (Grant No. 61172159) and the Fundamental Research Funds for the Central Universities (HEUCFT1101).

References

- [1] Doucet. A., Gordon. N.: Sequential Monte Carlo Methods in Practice, Springer Verlag, New York, (2001).
- [2] J. Liang and X. Y. Peng: Electron. Lett, Vol.44 (2008), p. 553-555.
- [3] J. Liang and X. Y. Peng: Electron. Lett, Vol. 44 (2008), p. 1275-1277.
- [4] Gordon. N., Salmond, D. and Smith, A.: IEEE Proc. F, Vol. 140 (1993), p. 107-113.
- [5] Pitt. M.: Journal of the American Statistical Association, Vol 94 (1999), p. 590-559.
- [6] Musso. C., Oudjane. N. and Legland. F.: Springer-Verlag, p. 247-271, (2001).
- [7] De Freitas. J.F.G., Niranjan. M. and Gee. A.H.: Neural Comput, Vol. 12 (2000), p. 955-993.
- [8] Merwe. R., Doucet. A., Freitas. N. and Wan. E.: The Unscented Particle Filter, Technical report CUED/F-INFENG/TR 380, Cambridge University Engineering Department, p. 1-40, (2000).
- [9] S. Rahnamayan: IEEE Trans.on Evolutionary Computation, Vol 12 (2008), p. 64-78.
- [10] Zhong.B Hu: Journal of Wuhan University of Technology (In Chinese), Vol. 29 (2007), p.125-129.

Implementation of FFT Algorithm Based on IP Core

Cheng Ma^{1,a}, Ze Long He^{1,b}

¹School of Electrical and information Engineering, Heilongjiang Institute of Technology, Harbin 150050, China

^amch_28@126.com, ^bhrbhzl@126.com

Keywords: FFT, FPGA, IP

Abstract—In this paper, we propose a new way to implement the FFT Algorithm, which based on FPGA. At first we introduce the theory of FFT algorithm and its applications. Then the features of FFT IP core based on Altera FPGA is discussed. We elaborate the usage method of the customizable Altera FFT MegaCore function. A logic state machine is designed to create some command signals of this FFT IP core. Finally we use simulation tools Signal-Tap in quartus II inviroment to simulate and debug our FFT control module's function. The result shows that this new control method of FFT IP core is feasible.

1. Introduction

FFT(Fast Fourier Transform) is an algorithm for increasing the speed of the computer calculation of the DFT(Discrete Fourier Transform).FFT is widely used in many application fields because it is much faster than DFT. FFT computes the DFT and produces exactly the same result as evaluating the DFT definition directly. FFT can be implemented by CPU ,DSP ,ASIC(Application Specific Integrated Circuit) or FPGA. ASIC is an integrated circuit customized for a particular use, rather than intended for general-purpose use. ASIC is not flexible than other method. FFT algorithm can be computed by CPU or by DSP easily, but they have the lower speed than ASIC or FPGA. Using FPGA to implement FFT algorithm is both faster and more flexible.

2. FFT IP Core based on Altera FPGA

The FFT MegaCore function is a high performance, highly-parameterizable Fast Fourier transform processor. The FFT MegaCore function implements a complex FFT or inverse FFT for high-performance applications. It implements fixed transform size architecture and variable streaming architecture.

The fixed transform architecture FFT implements a radix-2 or radix 4 decimation-in-frequency fixed-transform size algorithm for transform lengths of 2^m where $6 \le m \le 16$. This fixed transform architecture accepts as an input a two's complement format complex data vector of length N, where N is the desired transform length in natural order, the function outputs the transform-domain complex vector in natural order. An accumulated block exponent is output to indicate any data scaling that has occurred during the transform to maintain precision and maximize the internal signal-to-noise ratio. Transform direction is specifiable on a per-block basis via an input port.

The variable streaming architecture FFT implements two different types of architecture. The variable streaming FFT variations implement either a radix- 2^2 single delay feedback architecture, using a fixed-point representation, or a mixed radix-4/2 architecture, using a single precision

floating point representation. After you select your architecture type, you can configure your FFT variation during runtime to perform the FFT algorithm for transform lengths of 2^m where $3 \le m \le 18$.

3. Create a FFT MegaCore

A FFT MegaCore function should be created before we start to use it. We can use MegaWizard Plug-In Manager tools in quartus II to instantiate manually in our design. In this flow, a FFT MegaCore function is customized by the MegaWizard Plug-In Manager, and auto integrated into the quartus II design.

The point of customizing this FFT MegaCore is to parameterize some key parameters for the FFT MegaCore. These important parameters are transform length, data precision and twiddle precision. Transform length can be set 128 points, 256 points, 512 points and so on. More points need more logic resource of FPGA, for example more logic elements and more memory elements. Of course the results are more precise. The twiddle factor precision must be less than or equal to data precision. There are four data flow structures can be selected, they are streaming, variable streaming, buffered burst and burst structures. The streaming structures needs more resources than burst structures. There are three kinds of data flow order for this FFT MegaCore's input port and output port. They are natural order DC centered and bit reverse order. How to choose these parameters depend on your applications and your FPGA's resource.

4. FFT MegaCore's Interface Signals

There are seventeen kinds of signals for the FFT MegaCore. The following is the descriptions of some major signals. clk is the clock signal that clocks all internal FFT engine components; reset_n is active low asynchronous reset signal; sink_eop is to indicate the end of the incoming FFT frame; sink_error is to indicate an error has occurred in an upstream module; sink_imag is imaginary input data, which represents a signed number of data precision bits; sink_ready is the signal asserted by the FFT engine when it can accept data; Sink_real is real input data, which represents a signed number of data precision bits; sink_ready is the signal asserted by the FFT engine when it can accept data; Sink_real is real input data, which represents a signed number of data precision bits; sink_sop is to indicate the start of the incoming FFT frame; Sink_valid is the signal asserted when data on the data bus is valid; Source_eop is the signal marks the end of the outgoing FFT frame; source_imag is imaginary output data; source_real is real output data; source_sop is the signal marks the start of the outgoing FFT frame. source_valid is the signal asserted by the FFT when there is valid data to output.

In order to make the FFT MegaCore work regularly, we must feed the input interface appropriate sequence signals. Next section we discuss the detail way which create these signals.

5. Generation of input signals for FFT MegaCore

A reset signal should be asserted at first. Following the deassertion of the system reset, the data source asserts sink_valid to indicate to the FFT function that valid data is available for input. A successful data transfer occurs when both the sink_valid and the sink_ready are asserted. When the data transfer is complete, sink_sop is deasserted and the data samples are loaded in natural order. Figure 1 shows the input flow control flow chart.

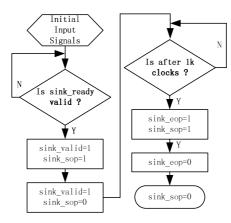


Figure 1 Input flow control

6. Take results from output signals of FFT MegaCore

After the FFT MegaCore accepts valid input signals, this FFT MegaCore will output corresponding conversion results from the source_real and source_imag ports. When the FFT has completed the transform of the input block, it asserts source_valid and outputs the complex transform domain data block. The FFT function asserts the source_sop to indicate the first output sample. The order of the output data depends on the output order that you select when it is customized. We must take the results at appropriate time. Figure 2 shows the flow of getting results.

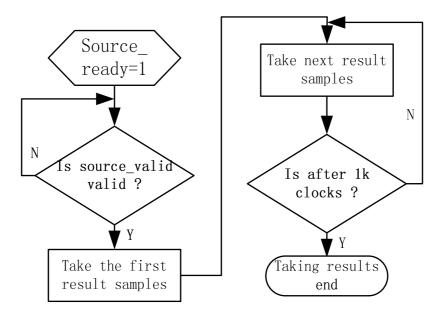


Figure 2 Take results flow

6. Simulation analysis and conclusion

Finally, we simulate and verify the way how to control FFT MegaCore in quartus II. The program was written by verilog HDL, and create corresponding block design file. Figure 3 shows the entire design block file. In figure 3, the left part inst9 is FFT MegaCore created by the MegaWizard Plug-In Manager in quartus II, which is 1024 points FFT IP Core; the right part inst7 is our major design-FFT MegaCore control block, which is designed by verilog HDL. This design is based on quartus II and Altera's FPGA EP3C40F484.

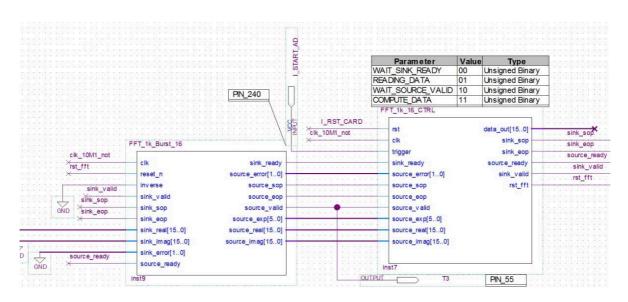


Figure 3 Design block in quartus II

Type	Alias	Name	-2048	-1024	0	1024
5		16_CTRL:inst current_state.COMPUTE_DATA				
5		FFT_1k_16_CTRL:inst source_real				
5		FFT_1k_16_CTRL:inst source_valid				
5		FFT_1k_16_CTRL:inst source_sop				
0		FFT_1k_16_CTRL:inst source_eop				
0 C		FFT_1k_16_CTRL:inst sink_ready				
00		FFT_1k_16_CTRL:instjsink_sop				
0°		FFT_1k_16_CTRL:instjsink_eop				
0 J		FFT_1k_16_CTRL:inst sink_valid				
0		16_CTRL:inst current_state.READING_DATA				
0		CTRL:inst current_state.WAIT_SINK_READY				
ů^		TRL:inst current_state.WAIT_SOURCE_VALID				
R		FFT_1k_16_CTRL:inst[rst_start_counter				
3		FFT_1k_16_CTRL:inst source_error	-			
5		FFT_1k_16_CTRL:inst source_ready				

Figure 4 Simulation waveform of input flow control

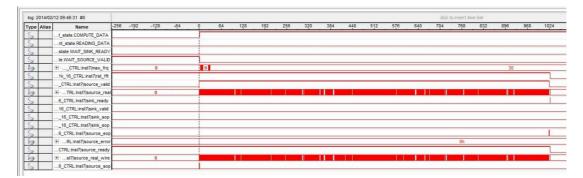


Figure 5 Simulation waveform of output flow

The signalTap II tool is employed in quartus II, the correct results are obtained by the hardware simulation based on signalTap II. Figure 4 shows the simulation waveform of input flow control, and figure 5 shows simulation waveform of output flow. The input and output waveform shows us that we control the FFT IPCore successfully, and get the right results we want.

References

- [1] Marcus Bednara. Automatic Synthesis of FPGA Processor Arrays from Loop Algorithms. The Journal of Supercomputing,2003,26(2)
- [2] P Mal. The Circuit Designs of an SRAM Based Look-Up Table For High Performance FPGA Architecture. PROCEEDINGS OF THE IEEE MIDWEST SYMPOSIUM ON CIRCUITS AND SYSTEMS,2002
- [3] S -S Chin. Rapidly Configurable Coarse-Grained FPGA Architecture for Digital Filtering Applications. PROCEEDINGS OF THE IEEE MIDWEST SYMPOSIUM ON CIRCUITS AND SYSTEMS,2002
- [4] Zhi Guo. Automatic generation of VHDL from C for code acceleration on reconfigurable devices. University of California, Riverside,2006
- [5] Vinoo Natt Srinivasan. Partitioning for FPGA-based reconfigurable computers. University of Cincinnati,1999
- [6] Huang Motao. On the evaluation of deflections of the vertical using FFT technique. Geo-spatial Information Science,2001,4(1)
- [7] Essam Ghanem. Discussion on some FFT problems to determine the geoid. Geo-spatial Information Science,2000,3(2)

Design of Router Supporting Multiply Routing Algorithm For NoC

Zhanpeng Jiang^{1, a}, Rui xu^{1,b}, Changchun Dong^{1,c}, Linhai Cui^{1,d}

¹Department of Integrated circuits design and integrated systems, Harbin University of Science and Technology, Harbin, Heilongjiang, China

^ajzpp@vip.qq.con, ^bruirui@163.com, ^cdcc@163.com, ^dcuilinhai@126.com

Keywords: NoC. Router. Multiply routing algorithm

Abstract. Network on Chip(NoC), a new proposed solution to solve global communication problem in complex System on Chip (SoC) design, has absorbed more and more researchers to do research in this area. Due to some distinct characteristics, NoC is different from both traditional off-chip network and traditional on-chip bus, and is facing with the huge design challenge. NoC router design is one of the most important issues in NoC system. The paper present a high-performance, low-latency two-stage pipelined router architecture suitable for NoC designs and providing a solution to irregular 2Dmesh topology for NoC. The key features of the proposed Mix Router are its suitability for 2Dmesh NoC topology and its capability of suorting both full-adaptive routing and deterministic routing algorithm.

Introduction

In SoC base on NoC, the entire system can be seen as a micro-network composed with IP cores, where each IP core is abstracted as a network node, and the cores will be connected by the micro-network. The nodes of router are connected to IP via a local network interface, and adjacent routers are connected by connecting link.

An example of NoC is shown in Fig. 1, who works as follows: the packet of data from the source IP sent into the input channels of routers through the link, then will be sent forward to output channel by crossbar of the router, and then sent to the next router via a link or sent to the local IP core connected with the router, in which the crossbar will decide which channel the data will be exported by caching data packets and arbitration of router.

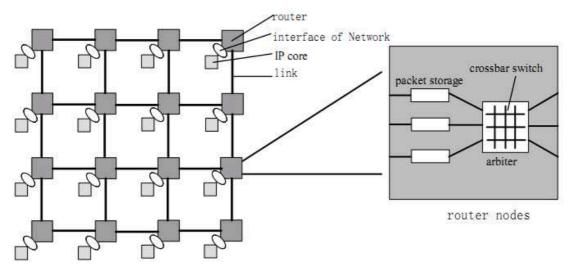


Fig. 1 Prototype of the Network Architecture Based on NoC

Architecture of network on chip specify the topology and structure of micro-network. Scalable NoC consists of three basic components: a router (or switch fabric), a network interface and links. How organize these is determined by the network topology. The task of router is to take the data packets injected to their destination via the data path statically or dynamic determined, specifically, the router will sent the data packet from an input port to one or more output ports.

Design of The router for NoC

Router is one of the basic elements of the network on-chip, which is responsible for routing the packets from a network node to another in the network, and because that data transmissions with long-distance in the network are completed by the router, so it directly affects the performance of the entire network. So far, researchers have made a lot of significant exploration for the NoC router design, and there are many attempts about pipeline design of the router, but practice shows that two levels or three levels pipeline is more appropriate due to the peculiarities of router on chip. The design combines the characteristics of the router, choices the two levels pipeline. The structure of pipeline is shown in Fig. 2, taking account that the distance between routers on chip is long, and delay will be longer, registers will be insert into both sides of the routers, which is not be included in the depth of the pipeline.

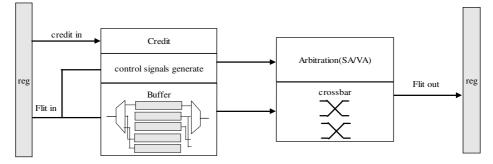
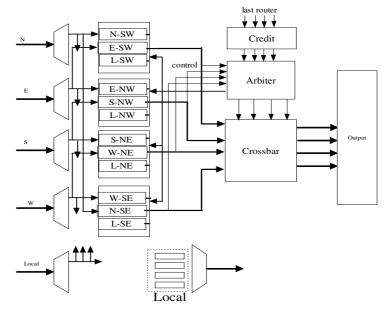
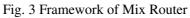


Fig. 2 Pipeline Diagram of Router

According to the depth of pipeline and the function of the router, the overall structure of the router will be got, as shown in fig. 3, the router includes five modules: input module, quadrant module, arbitration module, crossbar and output module. Since the router using the quadrant structure and there are four quadrants, each with two input ports and two output ports, local packets may be injected into any virtual channel of the four quadrants, so twelve virtual channels are needed. Data packets will be sent to the right virtual channel by judging ID of the virtual channel and control signals, then completed the scheduling of packets.





The network on chip is similar to the plane coordinate system, there are four quadrants, as shown in Figure. 4, Mix Router has three virtual channels in each quadrant, packets will be fixed in the

exclusive one of the quadrant, and then transmitted one router by one router until that it reaches the destination node and then sent from local to IP, and the transmission is completed.

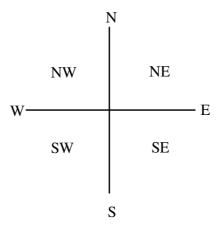


Fig. 4 Framework of Quadrant

Results and analysis of the verification

In order to analyze the performance of the mix routing, it will be compared with deterministic routing and adaptive routing by adaptive distribution, take account that irregular routers adopt the program which combines routing tables and determinate routing algorithms, only the regular deterministic router with topology of 2Dmesh.

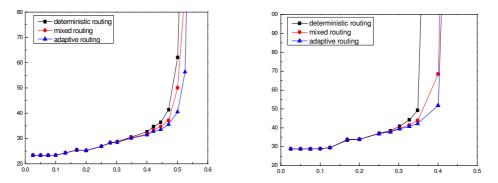


Fig. 5 Average Network Latency Compare Graphs between Locality and Uniform

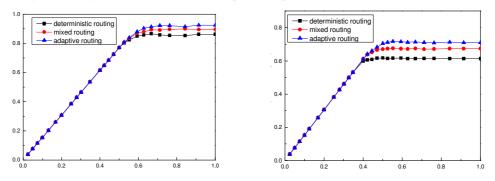


Fig. 6 Network Throughput Compare Graphs between Locality and Uniform

Assuming that the length of packets, the depth of FIFO are all the same, the results under different distribution is shown in Fig. 5, the abscissa is the average rate of injection, and the ordinate is the average latency, we can see that whatever locality or uniform under which the latency of network of mix routing is between deterministic routing and adaptive routing, and the average latency of mix routing under locality is more smaller than the one under uniform.

And the comparison of network throughput is shown in Fig. 6, the abscissa is the average rate of injection, and the ordinate is the throughput, we can see that the throughput of mixing routing is between deterministic routing and adaptive routing, and the throughput of mix routing under locality is bigger than the one under uniform, and the result will be more evident with the throughput being higher.

Summary

The paper develop the framework implementation mechanism of a router for network on chip, and than design the router which have a low latency and supports both adaptive and deterministic algorithm, and the results show that the performance of regular mix router is better than non-regular router, including throughput and the average latency.

References

- [1] ITRS, International Technology Roadmap for Semiconductors, Update 2008
- [2] S. Bourduas, Z. Zilic. Latency Reduction of Global Traffic in Wormhole-Routed Meshes Using Hierarchical Rings for Global Routing. Application-specific Systems, Architectures and Processors, ASAP. IEEE International Conference, 2007:302~307
- [3] D. Park, R. Das, C. Nicopoulos. Design of a Dynamic Priority-Based Fast Path Architecture for On-Chip Interconnects. 15th IEEE Symposium on High-Performance Interconnects. 2007, Stanford, CA, USA:15-20
- [4] ARM. AMBA AXI Protocol Specification. 2003,6
- [5] Israel Cidon, Swaminathan, S., Tessier, R. NoC-Network or Chip, Proceedings of the First International Symposium on Networks-On-Chip (NOCS'07), 2007, Princeton, New Jersey, USA:269-272
- [6] Zeferino, C.A., Susin, AA. SoCIN: A Parametric and Scalable Network-On-Chip. 16th Symposium on Integrated Circuits and Systems Design (SBCCI'03), Sep. 2003, Sao Paulo, Brazil:169~174
- [7] Rui Xu, Zhanpeng Jiang.Design of a 6502-compatibable microprocessor. Applied Mechanics and Materials Vols.380-384(2013) pp 3279-3282

Research on Signal Aliasing in Long Baseline Positioning System

Jun Cao^{1,a}, Dajun Sun^{*1,b}, Dianlun Zhang^{1,c}

¹Science and Technology on Underwater Acoustic Laboratory , College of Underwater Acoustic Engineering, Harbin Engineering University, Harbin 150001, China

^acaojun1105@sina.cn, ^bsundajun@hrbeu.edu.cn, ^czhangdianlun@hrbeu.edu.cn

Keywords: Long baseline, Signal aliasing, Overlap degree, Overlap energy, Positioning accuracy

Abstract. In the long baseline positioning system, underwater vehicle use transponder reply signals for positioning and navigation, reply signals aliasing is the main reason of inaccurate detection and instability detection. This paper aimed at the problem and research on signal aliasing in long baseline positioning system, theoretical and simulation results show that: Both overlap degree and overlap energy have a certain distribution. The size of signal aliasing area associated with signal overlap degree. The number of signal aliasing is different in different aliasing area. Signal aliasing will affect signal detection, and reduce the long baseline positioning accuracy.

Introduction

Underwater acoustic positioning system is an essential means of Marine scientific research, Marine resources exploration, Marine resources development and deep space station construction and other projects, it can provide positioning, navigation and communications support for underwater important carrier such as ROV and AUV[1,2], these commercial and civil projects demand for increasingly high positioning accuracy. Long baseline positioning system can not only achieve high-precision positioning independent of the depth, but also can achieve high positioning accuracy in the larger context. However, the positioning accuracy is affected by many factors, delay estimation error is one of the important factors affecting the accuracy of positioning systems. Delay estimation error comes from the offset between turn around time and synchronization clock, environment, circuit noise, reverberation and multi path [3,4].

In the long baseline positioning system, the time and energy of reply signals received by underwater vehicle is different. In some specific location reply signals will aliasing in together, when a reply signal is detected, the other reply signal will be considered as interfering signal. The overlap degree of interfering signal, the overlap energy of interfering signal and the number of signals aliasing will affect the accuracy of delay estimation.

Overlap degree analysis

The time of the transponder reply signals received by the underwater vehicle is different, so the Overlap degree of received signals is different. Time multiplied by the speed of sound to give the distance, we can analysis the overlap degree of received reply signals by the distance between the underwater vehicle and the transponders.

Suppose there are two transponders T_1 and T_2 , $|T_1T_2| = 2c(c > 0)$. The midpoint of line T_1T_2 is set as the origin, establish a Cartesian coordinate system where the straight line T_1T_2 for the x axis ,then $T_1(-c,0)$, $T_2(c,0)$, set the position of the underwater vehicle as Fixed point P(x, y).

Through
$$|PT_1| - |PT_2| = 2a$$
, we get $\sqrt{(x+c)^2 + y^2} - \sqrt{(x-c)^2 + y^2} = \pm 2a$ (1)

$$(\sqrt{(x+c)^2 + y^2})^2 = (\pm 2a + \sqrt{(x-c)^2 + y^2})^2$$
(2)

$$(c^{2} - a^{2})x^{2} - a^{2}y^{2} = a^{2}(c^{2} - a^{2})$$
(3)

Firstly, if a = 0, the equation is transformed into x = 0, trajectory is the y axis, the vertical line of line T_1T_2 . This means, the minimum of absolute value of the difference between the received signal delay is 0, distribution is the vertical line of connection line of the two transponder.

Secondly, if |2a| = 2c, the equation is transformed into y = 0, where $x \le -a$ or $x \ge a$. This means, the maximum of absolute value of the difference between the received signal delay is 2c/speed of sound, distribution is the ray which the transponder position as vertex.

Finally, if 0 < |2a| < 2c, set $b^2 = c^2 - a^2$, Both sides divided by a^2b^2 , the equation is transformed into $x^2/a^2 - y^2/b^2 = 1$, expressed as hyperbola with $(\pm c, 0)$ as focus, $(\pm a, 0)$ as vertex. This means, when the absolute value of the difference between the received signal delay is some fixed value, distribution is hyperbola.

The overlap degree of the received signal is shown in Fig.1. The figure meets the analytical results.

The partial enlarged figure of overlap degree is shown in Fig.2. When the absolute value of the difference between the received signal delay is reduced, distance between two vertices of the hyperbola decreases, Distribution get close to The midpoint of the two transponders. When the absolute value of the difference between the received signal delay is less than a certain value, this area is the aliasing region.

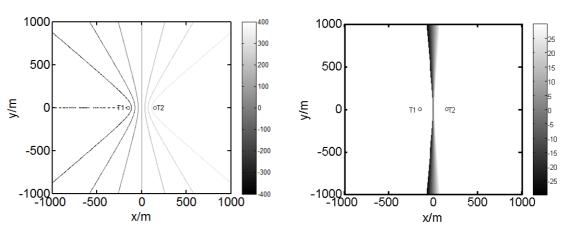
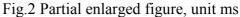


Fig.1 Overlap degree of signal, unit ms



Overlap energy analysis

The energy of the transponder reply signals received by the underwater vehicle is different, the sound level of the received signal is $RL_i = SL_i - TL_i = SL_i - 20\log_{10}(PT_i)$ [5], the transponder Model is same, so the transmit source level is same. The difference of received signal level is $RL_1 - RL_2 = 20\log_{10}(PT_2) - 20\log_{10}(PT_1) = 20\log_{10}(PT_2/PT_1)$. We can analysis the difference of received signal level by the distance between the underwater vehicle and the transponders.

Through
$$|PT_1|/|PT_2| = \lambda$$
, we get $\sqrt{(x+c)^2 + y^2} = \lambda \sqrt{(x-c)^2 + y^2}$ (4)

$$(1-\lambda^2)x^2 + (1-\lambda^2)y^2 + 2c(1+\lambda^2)x + (1-\lambda^2)c^2 = 0$$
(5)

Firstly, if $\lambda = 1$, the equation is transformed into x = 0, trajectory is the y axis, the vertical line of line T_1T_2 . This means, when the difference of received signal level is 0, distribution is the vertical line of connection line of the two transponders.

Secondly, if $0 < \lambda < 1$, the equation is transformed into $(x + \frac{1 + \lambda^2}{1 - \lambda^2}c)^2 + y^2 = (\frac{2\lambda c}{1 - \lambda^2})^2$, expressed

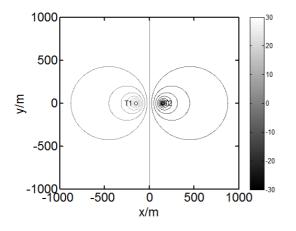
as a circle, with $\left(-\frac{1+\lambda^2}{1-\lambda^2}c,0\right)$ as center, $r = \frac{2\lambda c}{1-\lambda^2}$ as radius, located in the left y-axis. This means, when the difference of received signal level is greater than 0, distribution is a circle, when the difference of received signal level is increased, the center get close to T_1 , and the radius decreases.

Finally, if $\lambda > 1$, the equation is transformed into $(x + \frac{1 + \lambda^2}{1 - \lambda^2}c)^2 + y^2 = (\frac{2\lambda c}{1 - \lambda^2})^2$, expressed as a

circle, with $(\frac{1+\lambda^2}{\lambda^2-1}c,0)$ as center, $r = \frac{2\lambda c}{\lambda^2-1}$ as radius, located in the right y-axis. This means, when the difference of received signal level is less than 0, distribution is a circle, when the difference of received signal level is decreased, the center get close to T_2 , and the radius decreases. If the distance ratio is λ and $1/\lambda$ ($\lambda \neq 1$), the two circles symmetry about the vertical line of line T_1T_2 [6].

The difference of received signal level is shown in Fig.3. The figure meets the analytical results.

The partial enlarged figure of signal level is shown in Fig.4. When the absolute value of the difference between the received signal level is reduced, the center get away from the transponder and the radius increases. In aliasing area, the difference of received signal level is small.



1000 500 // 0 T1 0 oT2 -0.2 -500 -0.6 -0.8 -1000 -1000 -500 0 500 1000 x/m

Fig.3 Difference of signal level ,unit dB

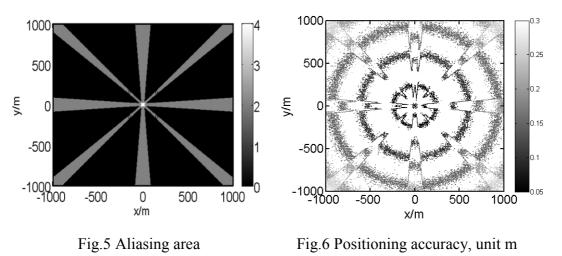
Fig.4 Partial enlarged figure, unit dB

Positioning Simulation and Analysis

Simulation conditions: the position of the four transponders are $T_1(-L/2, -L/2, h)$, $T_2(L/2, -L/2, h)$, $T_3(L/2, L/2, h)$, $T_4(-L/2, L/2, h)$, the baseline length L = 300m, the depth of transponder h = 50m, the working depth of Underwater vehicle is 50m. When the absolute value of the difference between the received signal delay is less than signal length, the signal is considered aliasing.

In long baseline positioning, distribution of the received signal aliasing is shown in Fig.5. Color bar represents the number of signal aliasing. It can be seen from the figure: First, in the central region of the transponder array, there will be three or four reply signal aliasing. Second, in the "+" region, the underwater vehicle will receive the signal from the closer two transponders and the signal aliasing together, then the farther two transponders. Third, in the "x" region, the underwater vehicle will receive the signal from the transponder Symmetry about the fixed point P and the signal aliasing together. Fourth, in the other region, the signal will not aliasing together.

The long baseline positioning simulation result is shown in Fig.6. It can be seen from the figure, in the aliasing region, the positioning accuracy has declined. The center of the array was originally precision area, signal aliasing causes positioning accuracy decreases.



Conclusion

In the long baseline positioning systems, reply signals aliasing may cause detection bias and detection instability. The paper research on this problem, and get the following conclusions: First, The distribution of the overlap degree is hyperbola, it determines the size of the aliasing area. Second, the distribution of signal level difference is circle. In aliasing area, the difference of received signal level is small. Third, in long baseline positioning, the number of signal aliasing is different in different regions. Fourth, in long baseline positioning, signal aliasing will affect signal detection, and reduce the positioning accuracy.

References

- [1] Junying Hui, Xueli Sheng. Underwater acoustic channel [M]. Beijing: National Defense Industry Press, 1992:1-29
- [2] Tan Tian. Underwater positioning and navigation [M]. Beijing: National Defense Industry Press, 2007:1 -5
- [3] Tan Tian, Guozhi Liu, Dajun Sun. Sonar technology [M]. Harbin: Harbin Engineering University Press, 2000:247-256
- [4] Guoqing Gao, Xiangbin Ye, Chunjie Qiao, Shen Zhao. Underwater acoustic positioning system theory and error analysis [J]. Sichuan Ordnance Technology: Automation Technology, 2010, 31 (6) :95-97
- [5] Bosheng Liu, Jiayu Lei. Water acoustics [M]. Harbin: Harbin Engineering University Press, 1993:68-72
- [6] Defan Xia. The trajectory of the distance ratio of the set value of the two fixed points [J]. Mathematics Teaching, 2009, 10:26-27

A Novel Algorithm for Multiuser Resource Allocation of OFDM

Zhongnan Zhao^{1, a}, Jian Wang^{1, b} and Hongwei Guo^{2, c}

¹ College of Computer Science and Technology, Harbin University of Science and Technology, Harbin, China

² Department of Mathematics, Heilongjiang Institute of Technology, Harbin, China ^apiconet@163.com, ^bwangjianlydia@163.com, ^cx11windows@126.com

Keywords: OFDM; downlink; subcarriers; swarm intelligence

Abstract. Orthogonal Frequency Division Multiplexing is considered as the key technology of the fourth generation of mobile communication technology. In this paper, an idea is proposed which solves the issue of multiuser resource allocation for OFDM based on swarm intelligence theory, and terminal bandwidth limitation is set as constraints addition as well. Theoretically, swarm intelligence algorithm could allocate resources more efficient and simulation results show that the proposed method is able to achieve better performance and higher system data rate than other similar algorithms under the same condition.

1. Introduction

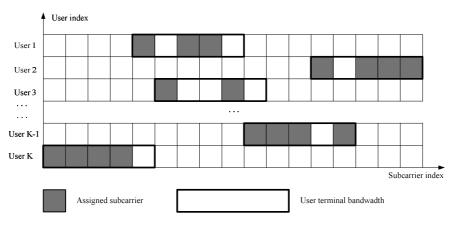
With the rapid growth of needs for multiple businesses in high-speed mobile status, the next generation of mobile communication system requires higher data transfer rate and higher spectrum efficiency. OFDM is a high-speed transmission technology in wireless environment. The Wireless resource management technology mainly focuses on improving spectrum efficiency in the OFDM system, and the dynamic sub-carrier allocation method is used. By allocating the subcarriers reasonably, the error bit rate and the needed transmission power may be reduced, and the bandwidth utilization will be increased, as well as the capacity of system or the data transfer rate. As a result, it is significant that we do some researches of resource allocation for a multi-user communication system.

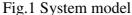
In the single-user OFDM system, the water-filling algorithm^[1] can achieve the optimal allocation of subcarrier and power in order to obtain the maximization of system capacity. While oriented the problem of resource allocation in the multi-user OFDM system, the existing researches are based on rate adaptation and remaining adaptation at home and abroad. J.Jang achieved the maximum of total capacity through assigning each sub-carrier to the user on which the channel gain is maximum^[2]. W.Rhee proposed a minimum capacity maximization algorithm^[3], which provided resource fairness for users and ensured that all users had the approximately equal rate. Both Linear and Root-finding algorithms^[4] achieved the total capacity was allocated proportionally among users. The WSA algorithms proposed in literature [5,6] could achieve the larger system capacity. From the view of methodology, at present, the theories used to resolve the problem of resources allocation are listed as follows: Genetic Algorithm, Game Theory, Graph Theory and so on. But unfortunately, the above algorithms have not considered the bandwidth limitation. While in the practice multi-user OFDM system, it's quite likely that many user terminals are not able to operate over the entire spectrum, so the user bandwidth limitation has to be considered. Literature[7] has addressed terminal bandwidth limitation in resource allocation for OFDM systems, but which is based on the exhausted search principle, is prohibitively computational expensive. To solve the problem, a novel multiuser resource allocation strategy based on swarm intelligence algorithm with user bandwidth limitation is proposed, which is a heuristic search algorithm to obtain its performance.

2. Modeling Background

Due to the channel status of OFDM is always changing, and different subcarrier has different transport ability. In OFDM, typically resources are assigned in the form of time-frequency block, that

is, the combinations of subcarrier and user channel, which can make the whole resources accessed by every user, and make the resources allocation more flexible as well. In this paper, user bandwidth limitation is adopted as constraints, so the system model of OFDM is shown as Fig.1.





We assume that there are K users in downlink of OFDM system, the whole bandwidth is divided into L subcarriers, and assuming every channel is fade flat individually. At the same time, the base station can transport signals to multiuser with whole bandwidth, whereas every single user can only receive N(0 < N < L) continuous subcarriers. Simultaneously, the base station may get information of L subcarriers which will be assigned to K users.

According to the Fig.1, formulas of this system model are shown as below.

$$\max_{\{P_{k,l},\rho_{k,l}\}} \sum_{k=1}^{K} \sum_{l=1}^{L} \rho_{k,l} \log_2 \left(1 + \frac{P_{k,l}h_{k,l}}{N_0} \right)$$
(1)

$$\sum_{k=1}^{K} \sum_{l=1}^{L} P_{k,l} = P \tag{2}$$

 $\rho_{k,l} = 1 \text{ or } 0, \text{ for all } l \in \{1, ..., L\} \text{ and } k \in \{1, ..., K\}$

and
$$\sum_{k=1}^{K} \rho_{k,l} = 1$$
, for all $l \in \{1, ..., L\}$ (3)

$$\max\left\{ \arg_{l} \left(\rho_{k,l} = 1 \right) \right\} - \min\left\{ \arg_{l} \left(\rho_{k,l} = 1 \right) \right\} < N,$$
(4)

for all
$$k \in \{1, ..., K\}$$

Formula (1) is subject to formula (2). Among them *P* represents the whole power of per transmission; $P_{k,l}$ represents the power assigned to the K_{th} user who owns subcarrier l_{th} ; N_o represents the noise power over every subcarrier; And $\frac{\arg}{l}(g(x))$ represents the x value(s) satisfying g(x). As the constraints, formula (2) represents the amount of all the power of every subcarrier total up to *P*, the formula (3) shows that one subcarrier can be allocated to one user only, the formula (4) denotes that the limitation of user bandwidth for transaction, which is the constraints worth to study, different from the constraints above, few articles mentioned before.

3. Resources Allocation Algorithm based on Swarm Intelligence

3.1 Limitations

Classical algorithm water-filling can allocate resources to the subcarrier. The better status of subcarrier the more resource assigned. It works without bandwidth limitation, but if under the condition of downlink bandwidth limitation it is different. Just because the distance of two different subcarriers which assigned most resource beyond the bandwidth limitation, so new way is needed.

3.2 Artificial Fish School Algorithm

As one of the algorithms of swarm intelligence, Artificial Fish School Algorithm (AFSA) is adopted in the paper to prove the idea. Status of AF can be defined as a vector with *K* dimensions: $X=(x_1, x_2, ..., x_L)^T$, $x_i(i=1,2, ..., L)$ is a dimension of the vector. Food concentration in certain status is expressed as: Y=f(X), where f(X) is called fitness function or objective function, and distance between AF is expressed as formula (5).

$$d_{i,j} = \|X_i - X_j\| = \sqrt{(x_{i1} - x_{j1})^2 + (x_{i2} - x_{j2})^2 + \dots + (x_{iL} - x_{jL})^2}$$
(5)

Shown as Fig.2, where *Visual* is perception range of every artificial fish, *step* means maximum distance that fish move in every step, δ represents factor of crowded degree, *try_number* represents times of random search in searching food.

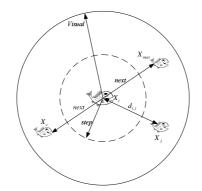


Fig.2 Visual and step of AFSA

There are three behaviors in AFSA, such as Searching Food, Congregation and Following Behavior. Through behavior selection the optimal can be achieve. For more details see Literature [8]. **3.3 Algorithm description**

This part, the resources allocation algorithm based on AFSA is proposed. According to food concentration, not only user will be assigned to the subcarrier which has maximum gain, but also the sum of the power of N subcarriers is max. The details are shown as formula (1), formula (2) and formula (3). Due to the bandwidth of user terminal in the OFDM system is limited in reality, in the paper, the boundary of data rate for user is set within less than N subcarriers, shown as formula (4).

The concrete process is shown as below:

Step1. Initializing AFSA.

Step2. Selecting subcarriers and user channel.

Step3. Searching for the user channel which has the max gain.

Step4. Searching for max power of user channel.

Step5. Update bulletin board.

Step6. Assign the resource ,and judge if the process over, if "no" then back to step2, or to step7 Step7. The end.

4. Simulations

This part, Monte Carlo simulation will be used to validate the performance of algorithm proposed. The data rate without user bandwidth limitation is offered which can serve as the upper bound for the data rate with user bandwidth limitation, and algorithm SPSS^[9] is chosen as the reference to be compared with. The amount of all subcarriers is *L*, assuming *L*=256, noise power is N_o , and the *S/N* (signal to noise ratio) of the link is 3db. The parameters of AFSA are below: number of AF is 10, *Step is 1, Try_number is 3, Visual is 1, \delta* is 0.11, address sequence length is *L*.

Assuming each subcarrier is independent Rayleigh faded. The number of user is K, and the value of K is 10. Subcarriers of user Bandwidth are range from 32 to 128, and the user can take up a portion of the system bandwidth only, shown as Fig.3. Comparing with the SPSS algorithm, with the user's bandwidth increases, the proposed algorithm makes the rate of system increase higher.

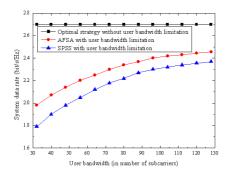


Fig.3 The impact on system data rate with user bandwidth

5. Conclusions

In this paper, an adaptive algorithm based on AFSA is proposed to solve the resource allocation problem for OFDM. In simulation, through comparing with SPSS algorithm the proposed algorithm can make the system achieve high performance. In future work, we will combine dynamical self-adjustment with AFSA technology to improve the resources allocation efficiency.

Acknowledgment

This work is supported by the Specialized Research Fund for the Doctoral Program of Higher Education of China (20112303120007) and the Youth Foundation of Harbin University of Science and Technology (2011YF018).

References

- [1] T.M.Cover and J.Thomas. Elements of Information Theory, 1991
- [2] J.Jang and K.B.Lee. Transmit power adaptation for multi-user OFDM systems. IEEE Journal Selected Areas on Communication, 2003, 21(20): 171-178
- [3] W.Rhee and J.M.Cioffi. Increase in capacity of multi-user OFDM system using dynamic subchannel allocation. Proceedings of the IEEE International Vehicular Technology Conference, 2000: 1085-1089
- [4] I.C.Wong, Z.Shen and B.L.Evans. A low complexity algorithm for proportional resource allocation in OFDMA systems. Proceedings of the IEEE International Workshop on Signal Processing Systems, 2004: 2056-2060
- [5] J.W.Zhang, J.X.Chi and X.R.Xv. Worst suv-carrier avoiding water-filling sub-carrier allocation scheme for OFDM-based CRN. Journal of Electronics, 2012, 3(29): 204-21
- [6] T.T.Liu, C.Y.Yang and L.L.Yang. A low-complexity sub-carrier power allocation scheme for frequency division multiple access systems. IEEE Transactions on Wireless Communications, 2010, 9(5): 1571-1576
- [7] Y.Li, N.Lu, M.G.Peng and W.B.Wang. Multiuser Resource Allocation for OFDM Downlink with Terminal Bandwidth Limitation. Proceedings of the IEEE Wireless Communications and Networking Conference, 2010: 1-5
- [8] X.L.Li. A New Intelligent Optimization Method-Artificial Fish School Algorithm. Ph.D.Dissertation, 2003
- [9] Y.Li, N.Lu. Multiuser Resource Allocation for OFDM Downlink with Terminal Bandwidth Limitation. Proceedings of the 2010 IEEE Wireless Communications and Networking Conference, 2010: 1-5

A modified DFE-MMSE equalization algorithm

Yu Xia^{1,a}, Fang Ye^{2,b}, Yibing LI^{3,c}, Ling Wang^{4,d}

^{1,2,3,4}Department of Information and Communication Engineering, Harbin Engineering University, Harbin, China

^axiayu@hrbeu.edu.cn, ^byefang@hrbeu.edu.cn, ^cliyibing@hrbeu.edu.cn, ^dlingwang@hrbeu.edu.cn

Keywords: Turbo equalization; DFE-MMSE; Correction factor; Bit error rate

Abstract. In wireless communication, inter symbol interference (ISI) and signal distortion are often caused by the frequency deviation and time offset of wireless channel. To eliminate or reduce ISI, people proposed the channel equalization technology. However, traditional decision feedback equalization algorithm based on MMSE criterion equalizer (DFE-MMSE) often introduces the error diffusion which degrades the performance of the equalizer in iterative system. In this paper, we propose an improved DFE-MMSE algorithm to reduce the error diffusion and improve the performance of iterative equalization, with a correction factor λ . Simulation results show that our algorithm achieves better bit error rate, which makes it competent in more practical cases.

Introduction

In wireless communication, the mutual interference brought from the effect of frequency offset and time offset in wireless channel, often results in the distortion of the signal. For a better performance of communication system, people proposed the channel equalization technology to eliminate or reduce the ISI [1, 2]. Originally, the equalizer and decoder work respectively on their functions. But with the presence and the development of turbo coding technology, these two procedures are combined as the turbo equalization technology [3] due to its unique coding and decoding structures.

Frequently-used turbo equalization algorithms including [4, 5, 6]: the linear equalization algorithm based on MMSE criterion (LE-MMSE), the DFE-MMSE algorithm and the MAP equalization algorithm. The equalization algorithm based on MMSE criterion is relatively simple and easy to implement, but with a suboptimal performance. MAP equalization algorithm, which increases exponentially with the channel length, will make it unpractical in application. So people often utilize the equalizer based on the MMSE criterion for its simplicity and practicality. As a compromised method between noise inhibition and eliminating ISI, LE-MMSE can remarkably suppress the noise, but it also brings additional ISI. It's well known that DFE-MMSE outperforms the linear equalizer in a non-iterative system because it can judge the current result by the previous decoding result, but it still can't avoid the error diffusion phenomenon in an iterative system, which will reduce the equalizer's performance. In this latter, we propose a solution with a corrective factor λ to handle the error diffusion phenomenon involved in the decision feedback equalization (DFE) algorithm. Simulation results show the improved performance of the iterative equalization.

The remainder of this paper is structured as follows. Section II introduces the system model of turbo equalization; in Section III, the traditional DFE algorithm and the improved equalization algorithm are proposed; Section IV presents a comparison of the BER performance between different equalization algorithms; Conclusions are presented in Section V.

System Model

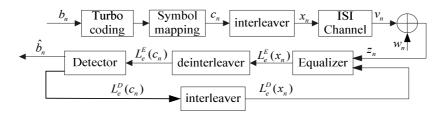


Fig.1 Turbo equalization system model

Fig.1illustrates the turbo equalization system, whose operation mechanism is described in [7]. The input binary data b_n is encoded by turbo encoder and mapped into c_n , then interleaved by random interleaver and transmitted through ISI channel. In receiver, the equalizer's output——the extrinsic information $L_e^E(x_n)$ is deinterleavered and then be used as the prior information $L_a^D(c_n)$ of the decoder according to the channel output. Based on the soft information generated from the equalizer, the decoder outputs its extrinsic information $L_e^D(c_n)$ which is interleavered and used as the equalizer's prior information $L_a^E(x_n)$ in the next. Circularly, the equalizer generates more accurate extrinsic information utilizes the prior information for the next iteration. After certain times of iterative calculations, the bit error rate will be significantly reduced with the soft information transmitted between the decoder and the equalizer being increasingly precise.

The relationship of soft information transmitted between the decoder and the equalizer is given by:

$$L_{a}^{E}(x_{n}) = \Pi(L_{e}^{D}(c_{n})) \quad L_{a}^{D}(c_{n}) = \Pi^{-1}(L_{e}^{E}(x_{n}))$$
(1)

Where Π denotes interleaver, Π^{-1} denotes deinterleaver.

Channel Equalization Algorithm

Decision Feedback Equalization Algorithm Based on MMSE Criterion. The system model of the decision feedback equalization algorithm based on MMSE criterion is shown in Fig.2. The equalizer consists of one forward filter and one backward filter, whose length are N and N_b , with

time-varying parameters respectively denoted as $c_{n,k}$ and $c_{n,k}^{b}$, where $k = -N_1, -N_1 + 1, \dots, N_2$,

 $N = N_1 + N_2 + 1$. (N_1 is the length of the non-causal filter, N_2 is the length of the causal filter.)

The impulse response of the channel filter is given by,

$$h(n) = \sum_{k=-M_1}^{M_2} h_k \delta(n-k)$$
⁽²⁾

Where n is the index of the discrete time and the length M ($M = M_1 + M_2 + 1$).

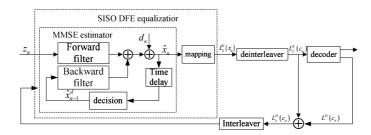


Fig.2 DFE-MMSE turbo equalization system model

We set the filter parameters as: $N_2 = M_1, N_b = M - 1, N_1 = N - M_1 - 1$. We assume that \mathbf{X}_n is the transmitted code word, \mathbf{W}_n is the noise sample, \mathbf{Z}_n is the received code word. The filter parameters $(\mathbf{C}_n, \mathbf{C}_n^b, d_n)$ are computed based on MMSE criterion in order to gain the minimum $E\{|x-\hat{x}_n|^2\}$. After formula derivation, it can be defined as:

$$\mathbf{C}_{n} = \left(\boldsymbol{\sigma}_{w}^{2}\mathbf{I}_{N} + \mathbf{H}\mathbf{V}_{n}\mathbf{H}^{H} + \left|\overline{\mathbf{x}}_{n}\right|^{2}\mathbf{s}\mathbf{s}^{H}\right)^{-1}\mathbf{s}$$
(3)

$$\hat{x}_n = \mathbf{C}_n^H \left(\mathbf{Z}_n - \mathbf{H} \overline{\mathbf{X}}_n + \overline{x}_n \mathbf{s} \right)$$
(4)

In which, **H** is a channel convolution matrix of $N \times (N + M + 1)$, \mathbf{I}_N is an identity matrix of $N \times N$, while the superscripts $(\cdot)^H$ stands for the Hermitian transpose operation. So the equalizer output extrinsic information is described as:

$$L_e^E(x_n) = \frac{2\hat{x}_n}{1 - \mathbf{s}^H \mathbf{c}_n}$$
(5)

The variables \overline{x}_n , v_n , \overline{X}_n , V_n , s in Eq.3 - 5 can be obtained through Eq. 6 shown below

$$\overline{x}_{n} = E(x_{n}) = \tanh(L_{a}^{E}(x_{n})/2)$$

$$v_{n} = \operatorname{cov}(x_{n}, x_{n}) = 1 - |\overline{x}_{n}|^{2}$$

$$\overline{X}_{n} = \left[\overline{x}_{n+N-1}, \dots, \overline{x}_{n}, \hat{x}_{n-1}^{d}, \dots, \hat{x}_{n-M+1}^{d}\right]^{T}$$

$$V_{n} = \operatorname{diag}\left[v_{n+N-1}, \dots, v_{n}, 0_{1 \times (M-1)}\right]^{T}$$

$$\mathbf{s} = \mathbf{H}[0_{1 \times (N_{1}+M_{1})} \ 1 \ 0_{1 \times (N_{2}+M_{2})}]^{T}$$
(6)

Where decided estimates \hat{x}_n^d are obtained by an appropriate Decision function.

Proposed new channel equalization algorithm. Turbo equalization is a technology combined with turbo principle and equalization. As the iteration deepens, the information transferred between equalizer and decoder will be increasingly convergent for a more accurate judgment. In non-iterative system, the reason why DFE-MMSE outperforms LE-MMSE is that it can fully use the past time's decision to reduce ISI. Nevertheless, in the process of iteration, this feature in iterative system would decrease its performance as the errors in the current judgment could affect the judgment of the following iterations, which leads to the error diffusion. Finally, the figure of soft information transmitted between decoder and equalizer will be larger than the real one [8]. This paper introduces a correction factor λ , whose figure is less than one, to modify the soft information transmitted between the equalizer can be redefined as:

$$L_a^E(x_n) = \lambda \Pi(L_e^D(c_n))$$

$$L_a^D(c_n) = \lambda \Pi^{-1}(L_e^E(x_n))$$
(7)

With the deepening of the iteration, the error diffusion will get worse. And the information is deviated from the real value further. So we adapt the improved the correction factor λ which will decrease with the number of iteration increased. The value of λ_i is given by:

$$\lambda_l = \lambda_1 - \frac{l-1}{2L}, \ 1 \le l \le L \tag{8}$$

Where *L* is the sum of iterations, λ_l is the correction factor of the *l* th iterative, λ_l is the correction factor of the first iterative. What's more, the figure of λ_l should be smaller as the frequency deviation and time offset of wireless channel getting worse, usually we choose as: $0.5 < \lambda_l < 1$. In this paper, we set $\lambda_l = 0.9$ considering our adaptation of Proakis B channel model. Then the Eq. 7 can be modified as:

$$L_{al}^{E}(x_{n}) = \lambda_{l}\Pi(L_{el}^{D}(c_{n}))$$

$$L_{al}^{D}(c_{n}) = \lambda_{l}\Pi^{-1}(L_{el}^{E}(x_{n}))$$
(9)

Where $L_{el}^{D}(c_{n})$, $L_{al}^{D}(c_{n})$ are the decoder extrinsic information and prior information of the *l*th iterative. And $L_{ek}^{E}(x_{n})$, $L_{ak}^{E}(x_{n})$ are the equalizer extrinsic information and prior information of the *l*th iterative

Performance Analyses and Simulation

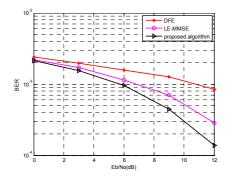
In this paper, we make simulation about the performance of the turbo equalization in the Proakis B channel (the length is 3) with $h[n]=0.408\delta[n+1]+0.815\delta[n]+0.408\delta[n-1]$. The parameters of the forward

and back filter are set as: $N_1 = 7, N_2 = 7(N=15) N_f = 15, N_b = 2$. During the simulation, a rate R=1/2

recursive systematic convolution code is used. Five times of iterations between equalizer and decoder are performed. In the case of low SNR, where the noise power is stronger, the error diffusion phenomena caused by decision feedback equalizer is more obvious, in which case the improved algorithm will have a better performance. So we choose to simulate the algorithm under low SNR.

Fig.3 shows the contrast of LE-MMSE and DFE-MMSE algorithm with the fixed correction factor λ =0.7. Results show that the BER performance of the improved DFE algorithm is superior to the LE-MMSE and traditional DFE. Because of the error diffusion generated in the process of iteration, the performance of traditional DFE is worse than the linear equalizer. Meanwhile, the improved algorithm with adding correcting factor overcomes the defect and obtains performance of turbo equalizer when the correcting factor takes different values is compared. Fig.4 shows that the improved DFE - MMSE algorithm can obtain better performance when the correcting factor is set to 0.7. Finally, Fig.5 shows the comparison results between the fixed correction factor and adaptive correction factor, where the fixed factor is 0.7 and the adaptive value λ_1 starts at 0.9, then

decreases gradually along with the number of iteration increased. It shows that the better performance belongs to the adaptive correction factor.



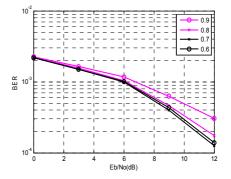


Fig.3 Different equalizers comparison

Fig.4 Correcting factor takes different values

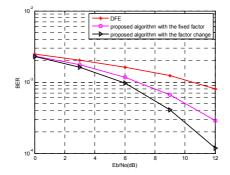


Fig.5 The fixed correction factor and adaptive correction factor

Conclusions

A modified decision feedback turbo equalizer based on MMSE principle was presented in this letter. Both the theoretical analysis and simulation results show that the error diffusion can be effectively eliminated with the improved DFE algorithm, and we got significantly improved performance in the whole decoding procedure. The simulation results also confirmed a better performance of the improved algorithm proposed in this paper.

Acknowledgment

This paper is funded by the International Exchange Program of Harbin Engineering University for innovation-oriented Talents Cultivation, the Fundamental Research Funds for the Central Universities of China under Grant HEUCF130807 and Heilongjiang Province Natural Science Foundation for the Youth under Grant QC2012C070.

Reference

- [1] Stefan Parkvall,in: *The Fundamentals of 4G Mobile CommunicationTechnology: LTE and LTE-Advance*, edited by Erik Dahlman/Post Telecom Press Publising, Beijing(2012),in press.
- [2] Suo Shiqian,in: *3GPP Long Term Evolution: Principle and System Design*, edited by Shen Jia /Post Telecom Press Publising, Beijing(2008),in press.
- [3] Michael Tüchler and Andrew C: IEEE Transactions on Information Theory publication information. Vol,57, NO. 2,(2011),p.920
- [4] Lei Xia,in: *Turbo Equalization Techniques in Wireless Communication Systems*, edited by Li Qiang/ National Defense Industry Press Publising, Beijing(2010),in press.
- [5] Xu Ke. *Research on Key Technologies of Turbo Decoding and Turbo Equalization*. Hunan: National Defense Industry Press(2011).
- [6] Gui Xin. *Research of Data Processing Technology in LTE-FDD E-NodeB Uplink Physical Layer.* Harbin: Harbin Engineering University(2012).
- [7] Wang Weiliang. *Research on turbo code and turbo equalization*.Beijing: Beijing University of Posts and Telecommunications(2006).
- [8] Guo Jian: Telecommunications Science. NO. 6,(2011),p.74, In Chinese.

Power Allocation Algorithm Based on QoS Strategy in Power-line Communication

Ke Zhou^{1,a} , Ying Deng^{1,b} ,Wei He^{1,c} and Xia Zhang^{1,d}

¹Electrical Engineering College of Guizhou University, GuiYang ,Guizhou ,550025, P.R.China ^a462665185@qq.com , ^bspears_yuhua@sina.cn, ^c512407654@qq.com, ^d1191893483@qq.com

Keywords: QoS Strategy, Power-line channel, OFDM, Maximum channel capacity

Abstract. In order to maximize low power-line channel capacity within the limited transmission bandwidth, a new transmitting power allocation algorithm based on the quality of service (QoS) strategy is proposed in this paper.Orthogonal frequency-division multiplexing (OFDM) is considered to support remarkable capacity of power-line channel. In order to derive the closed form expression of the maximum channel capacity in an OFDM power communication system, the relationship between channel capacity, signal to noise ratio (SNR) and modulation scheme is analyzed.Furthermore, some influence factors of power-line channel capacity, such as branches number, branches length and end-load impendence are analyzed in this paper. Simulation result shows that the mainly factors that affect the channel capacity of low power-line are branch number and load impendence; the performance of proposed algorithm is superior to the existed water-filling algorithms at the same SNR.

Introduction

The use of the power line to transmit data and voice has attracted much attention and has become a mature subject of research in the recent years. However, due to the considerable differences between power line network and conventional communication mediums in topologies and physical properties, the implementation of such a system is not an easy task[1-3]. For example, the power line channel characterized by frequency selective phenomena, presence of echoes, impulsive and colored noise with the superposition of narrow-band interference. All of the negative features push to consider communication techniques that can effectively face such an hostile environment.

Orthogonal frequency-division multiplexing (OFDM) is a real candidate for overcoming the negative features of power lines. OFDM is a special case of multi-carrier transmission, where a single data stream is transmitted over a number of independent sub-channel, to implement flexible resources management strategies in order to cope with channel impairments, to provide fine granularity in multimedia services by supporting variable data rates, and to achieve remarkable capacity [4-6].

Studies regarding channel capacity of low power line network at home and abroad is to use Lagrange multiplication coefficient method to calculate its maximum value. The classical water filling has been carried out by [7] to analyze the maximum transmission rate and capacity of power line channel. However, the transmission band proposed in [7] is relatively narrow compared to the popular bandwidth 1~30MHz. Specific factors that influence channel capacity have been proposed in [8], but the distribution of power in each sub-channel has not been restricted, thus causing the uneven distribution of power. Bound water injection proposed in [9] and [10] ensures a reasonable power distribution of each sub-channel and acquires a bigger capacity. However, the residual power has not been allocated to the optimal sub-channel which leads to the waste of power. Quality of Service (QoS) is a security mechanism of communication industry used to measure the speed and reliability of data transmission and commonly represented by throughput, transmission delay and bit error rate (BER). An improved water filling algorithm based on specific QoS is proposed in [10] to quantify the power allocated to each sub-channel and guarantee a certain QoS level. However, the allocated power in each sub-channel and guarantee a certain QoS level. However, the allocated power in each sub-channel and guarantee acertain QoS level. However, the allocated power in each sub-channel and guarantee acertain QoS level. However, the allocated power in each sub-channel and guarantee acertain QoS level. However, the allocated power in each sub-channel and guarantee acertain QoS level. However, the allocated power in each sub-channel and guarantee acertain QoS level. However, the allocated power in each sub-channel and guarantee acertain QoS level. However, the allocated power in each sub-channel and of 1~30MHz.

In order to compensate what aforementioned shortages in these papers, a bound water injection algorithm and QoS strategy are combined to design a new transmitting power allocation algorithm in this paper.

The rest of this paper is organized as follows: in section 2, a channel model of a PLC system is presented. In section 3, the channel capacity of a PLC system based on OFDM is introduced and the relationship between channel capacity, signal to noise ratio (SNR) and modulation scheme is analyzed. Moreover, in this part, a new power allocation algorithm based on bound water injection algorithm and QoS strategy is proposed. Section 4 presents simulation results which correspond to the capacity analysis.

Low Power-line Channel Model

The channel provided by power line has a transfer function that is both time and frequency variant. This means power-line channel is a harsh thoroughfare for sending high frequencies. According to [11],the structure model of low power-line communication system can be described in Fig. 1.

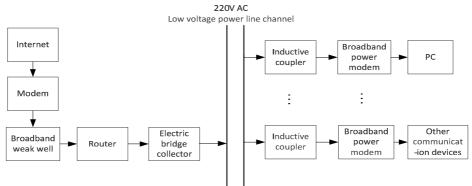


Fig. 1: Structure model of low power-line communication system

In Fig. 1,220V AC line is the so called low-voltage power line communication channel.For the sake of analyzing the main factors influencing the channel capacity for low power line, it is necessary to build an appropriate channel model.Recently,power line channel model constructed by researchers are mainly divided into two kinds:multipath transmission type and network topology type.Due to the huge number of parameters remained to be acquired from experimental test, network topology type is not easy to control and revise.In addition, the topology structure of branch terminal loads for low power line is considerable complex.However,Multipath transmission model is characterized by high frequency carrier signal transmitting in multipath power line to study the transmission performance of signals.It can reflect the physical propagation process of signals directly.Investigation into the behavior of power line channel has led to power line channel being treated as a multipath channel [12].

Power line multipath channel model is proposed by M.K., its frequency response is given by Eq.1.

$$H(f) = \sum_{i=1}^{N} g_i e^{-(a_0 + a_1 f^k)d_i} \cdot e^{-j2\pi f \tau_i}$$
(1)

Eq.1 takes the time variant and frequency variant behavior of the power line channel into account . g_i represents the gain of each path at i^{th} path, exponent of second term in Eq.1 represents the attenuation of H(f) with respect to frequency and the exponent of third term in Eq.1 represents the delay (phase changes) in the received multipath at i^{th} path. N represents the number of multipath in fading channel or the number of branch in a power line channel, it can control accuracy of the model dramatically. a_0 , a_1 , k and g_i represent the attenuation coefficient, which all can be measured by actual experiments. Usually k is set to be 0.5~1. d_i means the length of channel branch, and the delay of branch is $\tau_i = \frac{d_i}{\sqrt{\varepsilon_r}}$.

Channel Capacity

The channel capacity of an ideal, band limited, additive white Gaussian noise channel is given by Eq.2 which is termed as Sharon's theory. In Eq.2, C is the capacity in bits per second, B is the channel bandwidth, S is the average transmitted power and N is the average noise power.

$$C = B \cdot \log_2\left(1 + \frac{S}{N}\right) \tag{2}$$

In an OFDM system, the available channel bandwidth *B* is exactly divided into several narrow band channels. These channels can be either allocated to different users or modulation scheme. For such a case, Eq.2 can be given by:

$$C = \int_{f_1}^{f_2} \log_2 \left[1 + \frac{S(f)}{N(f)}\right] df$$
(3)

In Eq.3, $S(f) = |H(f)|^2 \times P(f)$, where S(f), H(f), N(f) and P(f) represents received signal power spectrum, channel transfer function, noise power spectrum and input signal power spectrum respectively. In order to facilitate analysis, background noise is considered only in this paper, where the probability density function of N(f) is a gaussian or normally distributed.

From Eq.3, to achieve the best performance, the power allocated to each sub-channel should be optimized according to the channel and noise frequency responses.

Power Allocation Algorithm. The power distribution mechanism among sub-channels depends on the optimization criterion. In this paper we consider the criterion which maximizes the system capacity and require some QoS constrains to deduce a power allocation and modulation scheme.

In practice, a modulation scheme such as M-PSK (Phase Shift Keying), M-QAM (Quadrature Amplitude Modulation) is often adopted at each sub-channel. The modulation stages of these modulation are the power of 2 (such as 2, 4, 6, 8) and not continuous. Once the modulation scheme at each sub-channel is made certain, the transmitted bit q_{MQAM} on each sub-channel is also decided. In a power line communication system, the M-QAM modulation scheme is adopted dominantly.

Let Eq.4 denote the error function.

$$erf(x) = \frac{2}{\sqrt{\pi}} \int_0^x e^{-\eta^2} d\eta$$
 (4)

Then the error rate of a M-QAM modulation scheme can be given by Eq.5 from [13].

$$P_{eMQAM} = 1 - erf^2 \sqrt{\frac{3}{2} \cdot \frac{1}{2^q - 1} \cdot \frac{P}{N}}$$

$$\tag{5}$$

Where, q is the transmitting bit and $q = \log_2 M$.

Define $x = \zeta(y)$ as the inverse function of y = erf(x). According to Eq.5, Eq.6 can be deduced easily.

$$q_{MQAM} = \log_2(1 + \frac{3}{2}\zeta^{-2}(\sqrt{1 - P_{eMQAM}}) \cdot \frac{P}{N})$$
(6)

From Eq.5 and Eq.6, in order to maximize the channel capacity, for a set of parallel sub-channels when the bandwidth is fixed, requires maximization of the achievable q_{MQAM} of each sub-channels under a given total input power constrains and a target probability of error.

Now, the allocated power of each sub-channel which will maximize the channel capacity using the following process (choose the sub-channel j as an example) is determined.

Step 1 Let the available power line channel bandwidth *B* be divided into *M* narrowband flat fading sub-channel whose space is Δf , the capacity of sub-channel can be given by Eq.7.

$$C_{j} = \Delta f \log_{2} (1 + \frac{P_{j} |H_{j}|^{2}}{N_{j}})$$
(7)

where P_j is the allocated power to the j_{th} sub-channel, H_j is the frequency response of the j_{th} sub-channel and N_j is the noise power of the j_{th} sub-channel.

The total capacity of these discrete channels can be expressed as

$$C_{\Sigma} = \sum_{j=1}^{M} C_j = \sum_{j=1}^{M} \Delta f \log_2 \left(1 + \frac{P_j |H_j|^2}{N_j}\right)$$
(8)

In Eq.8, $P_j > 0$, $\sum_{j=1}^{M} P_j \le P_{in}$, where P_{in} is the total input power allocated to the power line channel.

Step 2 Let M_j , S_j , P_{ej} represent the modulation order, SNR and BER respectively, they meet the relationship given by Eq.5. Moreover,

$$S_{j} = \frac{P_{j} |H_{j}|^{2}}{N_{j}}$$
(9)

Step 3 Let the threshold of BER in a power line communication system be $\Phi = 10^{-6}$ which meets the QoS need $P_{e_i} \le \Phi$.

Step 4 The optimal power allocation in each sub-channel can be achieved by using Lagrange multiplier method under the total transmit power constraint. We introduce a new variable λ called Lagrange multiplier and study the Lagrange function defined by Eq.10.

$$C = \sum_{j=1}^{M} \Delta f \log_2 \left(1 + \frac{P_j |H_j|^2}{N_j}\right) - \lambda \left(\sum_{j=1}^{M} P_j - P_{in}\right)$$
(10)

Step 5 Differentiating with respect to P_i and let $\partial C / \partial P_i = 0$ produce

$$P_{j} = \frac{\Delta f}{\lambda \ln 2} - \frac{N_{j}}{|H_{j}|^{2}}$$
(11)

 P_j is the maximized power allocated to each sub-channel. In a power line communication system, the maximized power in sub-channel will led to EMI (Electromagnetic Interference), which will impair the performance of communication system. In order to suppress the EMI, the power allocated to sub-channel should be limited.

Step 6 Let $\psi_j > 0$ represent the limited power allocated to any sub-channel. To meet the need of the specific QoS, the maximum available M_{Φ_j} , S_{Φ_j} , P_{Φ_j} can be deduced according to Eq.5 and Eq.9.

Step 7 When the allocated power $P_j > \psi_j$, let $\Delta p_j = P_j - \psi_j$ and make $P_{\Phi_j} = \psi_j$; when $0 < P_j \le \psi_j$, let $P_{\Phi_j} = P_j$; when $P_j < 0$, make $P_{\Phi_j} = 0$ and shut down the corresponding sub-channel.

Step 8 Add the remaining power Δp_j to the next one, let $P_{\Phi(j+1)} = P_{\Phi(j+1)} + \Delta p_j$, repeat step 5 and 6 until the total power allocated to all sub-channels where the allocated power should meet $0 < P_{\Phi_i} \le \psi_i$.

Step 9 Subject to a total transmit power constraint of $\sum_{j=1}^{M} P_{\Phi_j} \leq P_{in}$, adjust ψ_j iteratively and

calculate P_{Φ_j} until $\sum_{j=1}^{M} P_{\Phi_j}$ is closing to P_{in} limitless. Tacking the current P_{Φ_j} into Eq.11 generates

$$\lambda = \frac{\Delta f \left| H_{j} \right|^{2}}{\left(S_{\Phi j} + 1 \right) N_{j} \ln 2}$$
(12)

Step 10 Taking Eq.12 into Eq.10. Thereby, the maximum channel capacity C_{max} can be computed as

$$C_{\max} = \sum_{j=1}^{M} \Delta f \log_2(1 + \frac{P_{\Phi_j} |H_j|^2}{N_j}) + \frac{\Delta f |H_j|^2}{(S_{\Phi_j} + 1)N_j \ln 2} (P_{in} - \sum_{j=1}^{M} P_{\Phi_j})$$
(13)

In Eq.13, $P_{\Phi j}$ and $S_{\Phi j}$ can be produced in step 9. The noise power N_j of any sub-channel is considered constant approximately. Consequently, the vital factor that affects C_{\max} is H_j . However, H(f) is commonly affected by channel branch number M, branch length d_i and the attenuation caused by terminal loads connected to those branches. Therefore, in experimental simulation, the channel capacity is mainly analyzed from these three aspects: branch number, branch length and terminal loads.

Algorithm Simulation and Analysis

Monte Carlo is utilized to simulate the new power allocation algorithm proposed in this paper. As we know, the channel capacity for low voltage power-line is mainly affected by branch number, branch length and terminal loads. Here, each case is investigated.

A. Channel with pure resistive load. Set branch length is 5 meter, branch numbers are 4, 6, 12, 15 respectively and then simulate the proposed algorithm, the result is shown in Fig. 2.

Fig. 2 shows that when branch number increases, the channel capacity decreases. with the increasing of SNR, the performance difference among each case is widening. When SNR=40dB, compared to channel capacity for 4 branches, channel capacity for 6 branches decreases about 100Mbps. When branch number increases form 4 to 15, channel capacity decreases about 300Mbps. That results shows the increasing branch number of power line channel will led to the reflection points encountered by the transmitting signal increase, which aggravate the multi-path effect in the power line channel. So, the channel capacity decreases sharply.

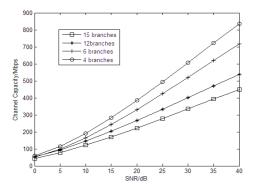


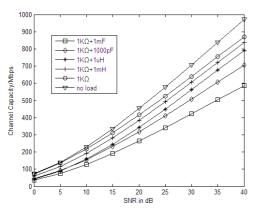
Fig. 2: Relationship between branch number and channel capacity

Fig. 3: Relationship between branch length and channel capacity

B. Channel with pure resistive load, Set branch number is 12, branch lengths are 5 meters, 10 meters and 20 meters respectively. The result simulated is shown in Fig. 3.

Fig. 3 shows that the channel capacity is nonlinear increasing along with the increasing SNR. When SNR=40dB, the channel capacity can reach 540Mbps. Though with the increasing branch length, the capacity decreases slightly. This is because the branch length d_i of low voltage power-line indoor is short commonly,when d_i increases from 5 meters to 20 meters, the value of H(f) changes slightly still and so the corresponded channel capacity changes little. It just so happens that the experimental phenomenon corresponds the result discussed in [7].

C. Channel with 12 branches, the length of which is 5 meters. Set the terminal loads are pure resistive load, inductive load, capacitive load and none load conditions respectively. The simulation result is shown in Fig. 4.



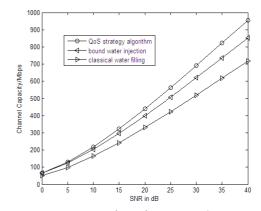


Fig. 4: Relationship between branch end-impendence and channel capacity

Fig. 5: Contrast of performance between each algorithm

Fig. 4 shows that when there is no load connected to the branch terminal, channel capacity can reach its top. When SNR=40dB, channel capacity reaches 1000Mbps nearly. However, when connecting terminal loads to the branch, the capacity for low power line channel will drop, especially for capacitive load. The terminal loads connected to the branches attenuate the signal power, which increase the transmitting loss and decrease the SNR, resulting the performance of system degraded.

In experimental simulation, the existed classical water filling and bound water injection are elicited to make a comparison with the proposed algorithm. The corresponding result is shown in Fig. 5. It shows that the channel capacity of the proposed algorithm is higher than the classical water filling and bound water injection method. As the QoS is considered and the total power is limited, those methods (classical water filling and bound water injection method) can not allocated the power completely, so the channel capacity is lower compared to the method proposed in this paper. Furthermore, the difference among those algorithms will grow bigger when SNR increases. The capacity proposed in this paper can reach 960Mbps which is 1.4 times of the classical water filling and 1.1 times of bound water injection method respectively when SNR=40dB.

Conclusions

In this paper, a novel power allocation algorithm for low voltage power-line communication is proposed and some affect factors to channel capacity in low power line communication are also investigated. From the simulation results, we know that in order to improve the channel capacity for low power line, it is better to shorten the distance among PLC devices and select power-line with fewer branches and none load as communication link. If necessary, an optimizational device should be utilized to change the load characteristic in indoor LAN topology structure to improve the impedance value of terminal loads and transform capacitive load into resistive load as far as possible to reduce the interference of terminal load on carrier signals. Furthermore, in order to evaluate the performance of proposed algorithm, the classical water filling and bound water injection method are also involved in to make a comparison at the same experimental condition. Test results indicate that the novel power allocation algorithm can provide higher channel capacity to the users, for example, when SNR=40dB, channel capacity can surpass 900Mbps, which can meet the demand of high speed data communication system.

Acknowledgements

This work is supported by Guizhou Provincial Natural Science Foundation (2013)2125 and Guizhou Provincial Department of Education Foundation (2009)0028.

References

- R.Hashmat, P.Pagani, T.Chonavel and A.Zeddam: A Time-Domain Model of Background Noise for In-Home MIMO PLC Networks. IEEE Transactions on Power Delivery, Vol.27 (2012) No.4, p.2082-2089.
- [2] W.Cai, J.Le, C.Jin, et al:Overview of the channel modeling methods of power line carrier communication. Power System Protection and Control, Vol.40 (2012) No.10,p.149-154.
- [3] H.L.Liu, B.H.Zhang, L.N.Tan:Research On The Channel Capacity In A Low Voltage Network Channel. Automation of Electric Power Systems, Vol.28 (2004) No.4, p.40-44.
- [4] G.Athanasios,Lazaropoulos and P. G. Cottis:Capacity of Overhead Medium Voltage Power Line Communication Channels. IEEE TRANSACTIONS ON POWER DELIVERY, Vol.25 (2010) No.2,p.723-733.
- [5] P. Amirshahi, S. M. Navidpour, and M. Kavehrad:Performance analysis of uncoded and coded OFDM broadband transmission over low voltage power-line channels with impulsive noise. IEEE Trans. Power Del., Vol.21 (2006) No.4,p.1927-1934.
- [6] Y. H. Ma, P. L. So, and E. Gunawan: Performance analysis of OFDM systems for broadband power line communications under impulsive noise and multi-path effects.IEEE Trans. Power Del., Vol.20 (2005) No.2,p.674–682.
- [7] H.T.Liu, B.H.Zhang, L.N.Tan: Research On The Channel Capacity In A Low Voltage Network Channel. Automation of Electric Power Systems, Vol.28 (2004) No.4,p.40-44.
- [8] W.L.Luo, X/K.Ke, M.Ma: Study of channel capacity for low voltage power-line based on monte carlo simulation. Chinese Journal of Radio Science, Vol.24 (2009) No.4, p.691-696.
- [9] J.Jiho,K.B.Lee and Y.H.Lee:*IEEE GLOBECOM'2003* (San Francisco,USA Proc.Dec 2003)Vol.2,p.858-862.
- [10] H.B.Xu, H.Tian,Y.J.Gao and P.Zhang: Wireless Communications and Networking Conference 2008 (Las Vega, USA, April 2008) Vol.1, p. 1838-1843.
- [11] X.Geng,Y.H.Li:Analysis for channel characteristics and research for channel model of low voltage power line communication.Power System Communication,Vol.4 (2004),p.19-21.
- [12] J.Anatory, N.Theethayi, R.Thottappillil: Channel Characterization for Indoor Power-Line Networks. IEEE Transaction on power delivery, Vol.24 (2009) No.4, p.1883-188.
- [13] J.G.Proakis: Dagital Communications. 4th ed. (New York, USA, Nov 2001)Vol.1,p.191-203.

A Novel DFT-Based Channel Estimation for LTE-A Uplink

Ling Wang^{1,a}, Fang Ye^{1,b}, Yibing Li^{1,c} and Yu Xia^{1,d}

¹Department of Information and Communication Engineering, Harbin Engineering University, Harbin, China

^alingwang@hrbeu.edu.cn, ^byefang@hrbeu.edu.cn, ^cliyibing@hrbeu.edu.cn, ^dxiayu@hrbeu.edu.cn

Keywords: LTE-A; channel estimation; noise power estimation; DFT

Abstract. Conventional DFT-based channel estimations suppress the noise by a cut-off filter in time domain. However, the potentially suffer significant performance loss due to the energy leakage. In this paper, based on the detailed analysis of the channel impulse response (CIR) leakage in the LTE-A uplink system, a novel discrete Fourier transform (DFT)-based channel estimation algorithm is proposed. This algorithm estimates the average noise power in frequency domain to get a noise threshold, which is then used in time domain to eliminate the noise by DFT and reduce the spectrum leakage. The simulation results show that the proposed algorithm can effectively improve the BER performance, and has a moderate complexity compared to existing DFT based algorithms.

Introduction

One of the key elements of LTE-A is the use of orthogonal frequency division multiple (OFDM), which is suitable for carrying high data rates and resilient to interference. Unfortunately OFDM has a high peak to average ratio, it is unacceptable for the mobile where power is a particular problem. As a result, LTE-A uses a modulation scheme known as single carrier frequency division multiplex(SC-FDMA) for uplink transmission, which combines the low peak to average ratio offered by single-carrier systems with the multipath interference resilience and flexible subcarrier frequency allocation that OFDM provides[1].

To improve system performance, there are many key technologies need to be solved or improved in LTE-A system, where channel estimation is one of them since the propagation path between transmitters and receivers is complicated due to path loss and multipath fading[2]. A class of block oriented channel estimators for OFDM have been proposed based on the least square (LS) algorithm, liner minimum mean squared error (LMMSE) algorithm and discrete Fourier transform (DFT) algorithm[3]. The LS channel estimation algorithm, neglecting the existence of noise, has a low complexity with an obvious error. The LMMSE channel estimation algorithm has good performance of the system, but it requires the channel prior acknowledge and the noise variance and has high computational complexity. The DFT-based channel estimation algorithm has a tradeoff between performance and complexity, which is more suitable for practical implementation in the LTE system[4]. The DFT-based channel estimation takes the N noisy frequency-domain observations and transforms them to the time domain by an inverse discrete Fourier transform (IDFT), and transforms the result back to the frequency domain by a DFT. At present, ideas of mature research achievements in this field are similar with different points lying in the processing of channel impulse response (CIR). In [5], the samples beyond the length of channel maximum delay spread are taken as noise in order to obtain the average noise power, with twice the average noise power as a decision condition. In [6], it clears the CIR beyond the length of channel maximum delay spread and takes the CIR average power of the length of delay spread as the decision threshold. The length of the CIR is unknown when it comes to the actual system, so the

algorithms mentioned in [5] [6] both have the shortcoming of erroneously deleting useful CIR samples when removing the noise. This leads to spectrum leakage. In [7], it takes the whole CIR into account and proposes a sinc-null based noise power estimation method with a dynamic noise removal technique. Furthermore it takes times noise power as the threshold in time domain to filter noise. Thus the choice of proportional coefficient directly affects the performance of the system. The algorithm proposed in [7] applies to the transmit resource blocks in small amounts. When the number of transmission resource blocks is close to the allowed maximum, the calculation of noise power approximates the average of estimated channel energy. This leads to a large threshold in higher SNR and results in performance degradation.

In current algorithms, however, the noise power is estimated in time domain, they didn't take good use of all the values of estimated channel. In this paper, we propose a novel DFT-based channel estimation algorithm for the actual LTE-A system. Firstly we estimate the CIR through LS algorithm then use the results in frequency domain to estimate the noise average power as the threshold to be compared with the whole time domain channel energy, thereby reduce the energy leakage and improve BER performance of the system.

This paper is organized as follows. In section II, the LTE-A uplink system model is given. Section III introduces the traditional channel estimation algorithm and the improved channel estimation algorithm. Section IV presents a comparison between the different estimation algorithms performance in BER and MSE with multipath Rayleigh fading channel. Finally, we conclude this study in Section V.

System Model

Consider an LTE-A uplink system illustrated in Fig.1, we suppose that the effective subcarrier number is N, the subcarrier mapping points is $M \,.\, X_n$ is the transmitted data through bit level processing, then through a series of symbol processing containing the serial-to-parallel conversion, N-point DFT, inserting the pilot sequences, then the subcarrier mapping, adding CP (cyclic prefix). It is assumed that the length of CP is longer than the maximum channel delay. The symbol after above processing is sent by the antenna after the up-conversion, through the channel and is processed by the corresponding inverse process at the receiver. In this paper, we consider the slowly varying multipath Rayleigh fading channel which impulse response is constant within a symbol.

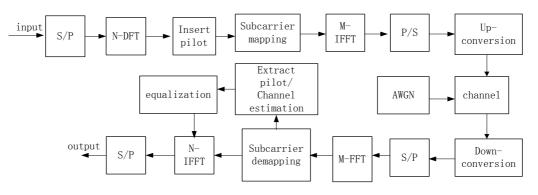


Fig.1 LTE-A uplink system model

The time domain received signal at the eNodeB after CP removal in a symbol interval can be expressed as

$$y_n = x_n \otimes h_n + w_n, n = 0, 1, \dots, M - 1.$$
(1)

Where \otimes denotes cyclic convolution operation, h(n) = [h(1), h(2)], is channel impulse response,

L is the channel length; w_n is the Gaussian white noise with zero mean and variance σ^2 .

Then the frequency domain received signal of the pilot sequence at subcarrier k is given by

$$Y_{p_k} = X_{p_k} H_{p_k} + W_{p_k} k = 0, 1, ..., M - 1$$
 (2)

Where the pilot sequences is the ZC sequence with low PARR and good cross-correlation characteristic.

Channel Estimation Algorithm

Conventional DFT-based channel estimation. By LS estimator, the initiate channel frequency response on each pilot subcarrier can be obtained

$$\hat{H}p_{k} = \frac{Yp_{k}}{Xp_{k}} + \frac{Wp_{k}}{Xp_{k}}$$

$$= Hp_{k} + Xp_{k}^{-1}Wp_{k}, k = 0, 1, ..., N - 1$$
(3)

The channel impulse response can be gotten by IDFT.

$$\hat{h}p_k = IDFT(\hat{H}p_k), k = 0, 1, ..., N - 1.$$
 (4)

Because the CP length is larger than the length of the CIR, so the channel impulse response can be further written as:

$$\hat{h}p_{k} = \begin{cases} \hat{h}p_{k}, k = 0, 1, ..., CP - 1 \\ 0, other - else \end{cases}$$
(5)

Using DFT, thus we can get the whole channel impulse response in frequency domain.

$$\hat{H}p_{DFTk} = DFT(\hat{h}p_k), k = 0, 1, ..., N-1.$$
 (6)

Proposed new channel estimation. The conventional algorithm removes noise interference by a hard cut-off window, however, it decreases some useful energy of channel impulse response at the same time and causes the problem of energy leakage. At the same time, it keeps the noise in the length of CP. There are some methods to estimate the noise power in time domain as a threshold such as paper [7], which is estimated by taking the average of the samples in the vicinity of the sinc nulls. However all these methods don't take good use of all the values of estimated channel to obtain the noise power estimation. To solve above problems, the improved algorithm utilizes the whole frequency domain LS estimation results for noise power estimation. Then according to the

.....

(**-**)

results of the estimated noise power, we make it as a new threshold compare with time domain channel impulse response energy in order to further suppress the noise.

The detailed algorithm is described as follows.

Firstly, the channel frequency response $\hat{H}_{p}(k)$ is estimated by LS estimator according to the Eq. 3.

Secondly, the noise average power is estimated according to the channel frequency response. Take the subcarrier $\hat{H}p_k$, $\hat{H}p_{k+1}$, $\hat{H}p_{k+2}$ in the $\hat{H}p$:

$$\hat{H}p_k = Hp_k + Xp_k^{-1}Wp_k \,. \tag{7}$$

$$\hat{H}_{p_{k+1}} = H_{p_{k+1}} + X_{p_{k+1}}^{-1} W_{p_{k+1}}.$$
(8)

$$\hat{H}p_{k+2} = Hp_{k+2} + Xp_{k+2}^{-1}Wp_{k+2}.$$
(9)

For the slowly varying multipath Rayleigh fading channel, the channel state keeps constant on two adjacent subcarriers, therefore the noise is obtained by:

$$Wk' = 2Xp_{k+1}^{-1}Wp_{k+1} - Xp_{k}^{-1}Wp_{k-2} + 2^{-1}Wp_{k+2} \cdot$$

$$= 2\hat{H}p_{k+1} - \hat{H}p_{k-2} + \hat{H}p_{k+2}$$
(10)

Then the noise threshold can be estimated by

$$\hat{\sigma}^2 = \frac{1}{(N-2)} \sum_{k=1}^{N-2} |W_k|^2 \quad .$$
⁽¹¹⁾

Where $\hat{\sigma}^2$ is the threshold.

In the end, compare the threshold with the $\hat{h}p_k$ in time domain calculated by Eq. 4.

$$\hat{h}p_{k} = \begin{cases} \hat{h}p_{k} , if(abs(hp_{k}) \ge \hat{\sigma}^{2}) \\ 0 , other-else \end{cases}.$$
(12)

Transform the $\hat{h}_{n}(k)$ into frequency domain, and get the final estimation results.

After obtaining the CIR of pilot, the whole channel estimation can be obtained by interpolation.

Performance Analyses and Simulation

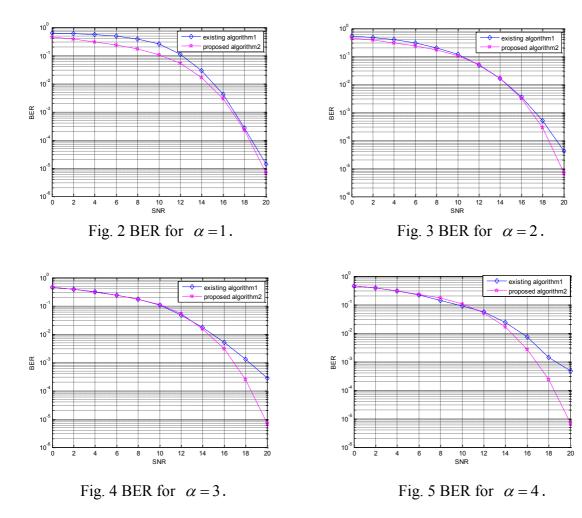
In this section, we compare the performance of proposed algorithm and another DFT-based algorithm proposed in [7]. The simulation parameters are shown in table 1.

Name	Parameters	Numerical value
Bandwidth	W	5[MHz]
Sample frequency	Fs	7[MHz]
Number of IFFT	М	512
Number of RBs	nRB	10
Number of effective subcarriers	Ν	120
СР	Normal CP	0: 160 <i>Ts</i>
		1-6:144 <i>Ts</i>
Modulation mode	16QAM	
Channel model	EPA	

Table 1 Simulation parameters

In the literature [7] the noise power is estimated by taking the average of the samples in the vicinity of the sinc nulls and multiplied by a scaling factor α as the noise margin.

Fig. 2,3,4,5 are the BER performance curve contrast for the algorithm 1 proposed adopting different scaling factor in [7] and the algorithm 2 of this paper. Here we adopt $\alpha = 1$, $\alpha = 2$, $\alpha = 3$, $\alpha = 4$ in [7]. From these figures, find that the BER performances of the proposed algorithm are better than the algorithm in [7] no matter what α is. Especially, when $\alpha = 3$, $\alpha = 4$, the performances of the algorithm in [7] are obviously worse than the proposed algorithm in high SNR, which is caused by the loss of the useful information due to the threshold selection.



Conclusions

In this paper, a novel DFT-based channel estimation for LTE-A uplink system has been proposed, which estimates the noise average power as a threshold using the LS estimate results, then derive the threshold to determine significant channel taps and to remove the noise in time domain. The simulation results show that the proposed algorithm can significantly get a good performance compared with the present schemes.

Acknowledgment

This paper is funded by the International Exchange Program of Harbin Engineering University for innovation-oriented Talents Cultivation, the Fundamental Research Funds for the Central Universities of China under Grant HEUCF130807 and Heilongjiang Province Natural Science Foundation for the Youth under Grant QC2012C070.

Reference

- [1] Erik Dahlman, Stefan Parkvall, Johan Skold, in: *The Fundamentals of 4G Mobile Communication Technology: LTE and LTE-Advance*, translated by Du Jiu-hui, Liao Qing-yu, Beijing:Post Telecom Press (2012).
- [2] Yuan Qiang. *Research on LTE-A Uplink Pilot Design and Channel Estimation Algorithm*. Xi'an Electronic and Engineering University (2011).
- [3] Li Xiaowen, Song Haibei, Xiao Lei: Application Research of Computers, Sep (2011), p. 3467-3473, In Chinese.
- [4] Lu Xin, Cai Tie, Xu Jun: Computer Engineering, Vol. 36-11 (2010), p. 11-13, In Chinese.
- [5] Y.Kang,K.Kim,H.Park.IET Commun, Vol. 1-2 (2007), p. 197-202
- [6] Xie Bo, Li Yi-bing, Ye Fang: Applied Technical Science, Vol. 39-6 (2012), p. 49-52, In Chinese.
- [7] Meilong Jiang, Guosen Yue, Prasad, N. Rangarajan. Vehicular Technology Conference (VTC Spring) (2012).
- [8] Huang, G., Nix, A., Armour. Vehicular Technology Conference Fall (VTC 2010-Fall), (2010).
- [9] Gui Xin. Reasearch of Data Processing Technology in LTE-FDD E-NodeB Uplink Physical Layer ,Harbin Engineering University (2012).

Based on the Jerk system phase space division of the study of the method

Jie Yi¹, Limin An¹, Duohui Li², Jiayu Tian¹, Xuehang Wang³, Chunxia Liu^{1,a} ¹Heilongjiang University. College of Physics Science and Technology. 150080 Heilongjiang Harbin; ²Harbin Engineering University. College of Science. 150001 Heilongjiang Harbin; ³Heilongjiang Province sanitary supervision institute. 150000 Heilongjiang Harbin

^aliuchunxia@hlju.edu.cn

Keywords: Jerk model; Track control; Delay feedback control; Phase space differentiate area

Abstract. Existing vortices volumes of chaotic signal control and create just increase the limitations of system complexity, and put forward the phase space vortex roll signal control alone method. The first use of Simulink Jerk system established the visualization model, Jerk system to delay feedback control, get the phase space of track not at the intersection of vortices roll chaotic attractor, then puts forward two methods-tracking method and the balance point estimate method is to make sure that each vortex roll attractor parameter range of chaos, realized the phase space of vortices volume control signal path, finally, to phase space area division, given the division standard and regional boundary, mathematical model of that work for more into the study of the method of chaotic modulation system to provide a idea and may.

Introduction

In the nonlinear equations arising in various types and is suitable for secure communication of chaotic and hyper chaotic signal, It is a hot topic in the research of physics and Information Science in recent years, Using multi-scroll characteristics of multi-scroll attractors and more complex dynamic behavior, In the chaotic secure communication can be used more widely.

The existing method to generate and control of multi-scroll chaotic signal, can only produce a certain amount of Scroll chaotic signal, But can't reach to scroll chaotic signals are independent control, Thus generating multi-scroll chaotic signal has only increased the system security, has not been resolved spectrum of effective utilization of resources and information transmission speed problem, is still confined to study under laboratory conditions. Multi-scroll chaotic attractor can be controlled based on phase space trajectory, wide signal bandwidth, realize independent control of multi-scroll chaotic attractors in phase space, the digital information can be chaotic attractors with different phase space based on one corresponding relation, achieve efficient use of multiple communication and spectral information, speed information the transmission speed, provides the speed and bandwidth guarantee for the application of chaotic communication.

1 The mathematical model of Jerk system

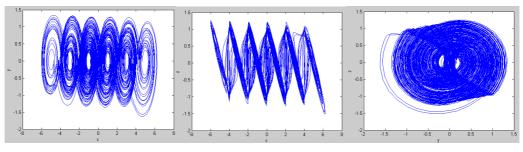
1.1 One-dimensional multi-scroll Jerk system

Study the following Jerk system:

$$\begin{cases} \dot{x} = y \\ \dot{y} = z \\ \dot{z} = -x - y - az + f(x) \end{cases}$$
(1)

Where f(x) = sgn(x) + sgn(x+2) + sgn(x-2) + sgn(x+4) + sgn(x-4), when a=0.6, System can

generate six-scroll chaotic attractors, Using Simulink simulation software, Jerk visual modeling chaotic systems, 6 scroll resulting phase diagram as shown in Fig.1.



(a) Phase of the XY (b) Phase of the YZ © Phase of the XZ Fig.1 The phase diagram of 6-scroll

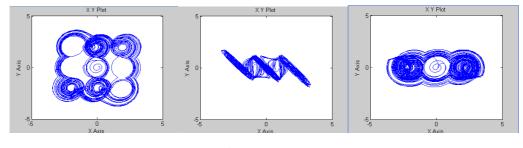
1.2 Two-dimensional multi-scroll Jerk System

The recursive equation (1) to two-dimensional case, Jerk system equation is:

$$\begin{cases} \dot{x} = y - f(y) \\ \dot{y} = z \\ \dot{z} = -x - y - az + f(x) + f(y) \end{cases}$$
(2)

Among f(x) = sgn(x) + sgn(x+2) + sgn(x-2) f(y) = sgn(y) + sgn(y+2) + sgn(y-2)

Then the 3 \times 3 two-dimensional multi-scroll chaotic attractors, the phase diagram as shown in Fig.2.



(a) Phase of the XY (b) Phase of the YZ \bigcirc Phase of the XZ Fig.2 The phase diagram of 3×3 -scroll

2 Delayed feedback control

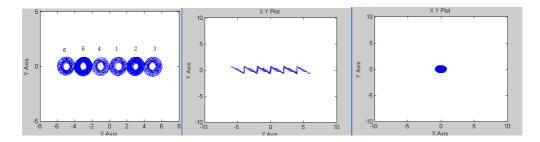
Fig.1 and Fig.2 can be seen in the XY phase space trajectories spiral cross between entanglement phase trajectory in order to get a clear chaotic attractors of chaos and a delayed feedback control. By using delay feedback method of 6 scroll chaotic Jerk stability control. By using the nonlinear characteristics of the system itself, to control the system variables, in the control of the Jerk system,

need to type (1) of the third equations of the right to add a control input u(t) = k[z(t-T) - z(t)],

Thus obtaining a controlled chaotic system such as:.

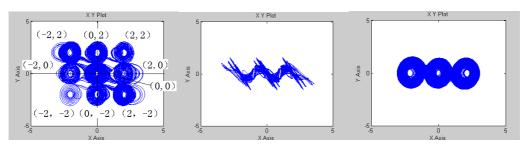
$$\begin{cases} \dot{x} = y \\ \dot{y} = z \\ \dot{z} = -x - y - az + f(x) + u(t) \end{cases}$$
(3)

The gain is set to 0.5, the delay time in the range [2.4s, 2.8s], Can get the orbit is clear, well-defined circular attractor. The delay time of 2.5s as an example, there is an obvious variable interval distribution of X, y and Z variables have periodic variation. The phase diagram as shown in Fig.3, the XY phase diagram on the boundary between the chaotic attractor trajectories is clear, have their own regional, disjoint.



(a) Phase of the XY (b) Phase of the YZ © Phase of the XZ Fig.3 The delay feedback control phase diagram of 6-scroll(delay time of 2.5 s)

The delay feedback control phase diagram of 3×3 -scroll(delay time of 2.6 s), The phase diagram as shown in Fig.4, the XY phase diagram on the boundary between the chaotic attractor trajectories is clear, have their own regional, disjoint.



(a) Phase of the XY (b) Phase of the YZ \bigcirc Phase of the XZ Fig.4 The delay feedback control phase diagram of 3×3 -scroll(delay time of 2.6 s)

3 Chaotic attractor trajectory control

The delayed feedback control of the system, the boundary between the chaotic attractor trajectories obtained obviously, further study on this basis, analyze each attractor trajectories corresponding to the formation of interval parameters, through setting different initial value, can be run in different position of the chaotic attractor. The initial value is set to [0.1,0.1,0.1], you can get 6 scroll chaotic attractors, track boundaries between the 6 scroll obviously, but slow down the speed of scroll, scroll respectively to 6 number, as shown in Fig.4 (a) shows, can be found, the attractor trajectories through a complex process to form (the sampling time of 0.1 seconds. The running time of 5000 seconds):one \rightarrow two \rightarrow three \rightarrow two \rightarrow one \rightarrow four \rightarrow one \rightarrow two \rightarrow three \rightarrow two \rightarrow one \rightarrow four \rightarrow one \rightarrow two \rightarrow three \rightarrow two \rightarrow one \rightarrow two \rightarrow three \rightarrow two \rightarrow one \rightarrow four \rightarrow one \rightarrow two \rightarrow three \rightarrow two \rightarrow one \rightarrow two \rightarrow three \rightarrow two \rightarrow three \rightarrow two \rightarrow one \rightarrow four \rightarrow one \rightarrow two \rightarrow three \rightarrow two \rightarrow one \rightarrow four \rightarrow one \rightarrow two \rightarrow three \rightarrow two \rightarrow three \rightarrow two \rightarrow three \rightarrow two \rightarrow three \rightarrow two \rightarrow three three three three \rightarrow two \rightarrow three three \rightarrow two \rightarrow three three

For each scroll around the equilibrium point of formation, to determine the parameters according to the equilibrium point scroll position, show in the Tab. 1.

Chaotic attractor	Parameter area	Time
		(S)
1	[1,0.1,0.1]~[-0.1126,-0.1487,0.03761]	95
2	[3,0.1,0.1]~[1.877, -0.1487,0.03761]	95
3	[5,0.1,0.1]~[3.877, -0.1487,0.03761]	95
4	[-1,0.1,0.1]~[-2.113, -0.1487,0.03761]	95
5	[-3,0.1,0.1]~[-4.113, -0.1487,0.03761]	95
6	[-5,0.1,0.1]~ $[-3.880, 0.1563, -0.04390]$	91

Tab.1 The method is used to determine a balance estimated 6-scroll track corresponding dimension parameter

Equilibrium point estimate method scroll formed a regular, run-time is relatively long, but the determination of the initial value, there is a certain degree of difficulty, and each one corresponding control parameters scroll less.

In the chaotic attractor trajectory control parameter determination process based on their own needs, you can choose the appropriate method.

According to the number of 3×3 scroll signal scroll equilibrium point coordinates, as shown in Figure 6 (a), is the use of equilibrium point estimation scroll parameter method are shown in Tab.2.

Tab.2 The method is used to determine a balance estimated 3×3-scroll track corresponding dimension parameter

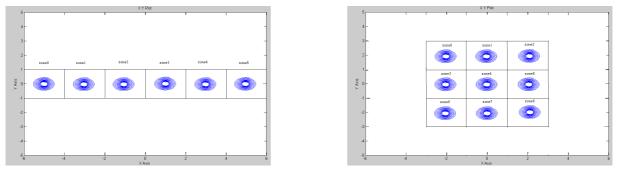
Chaotic attractor	Parameter area	Time(S)
[0,0]	[0.1, 0.1, 0.1]~[0.1669, -1.011, -0.3921]	56.6
[2,-2]	$[0, -2, 0] \sim [1.689, -1.033, 0.6699]$	111.2
[-2,2]	$[0, 2, 0] \sim$ [-1.511, 1.201, -1.004]	111
[0,2]	$[2, 2, 0] \sim [0.7378, 1.841, -1.445]$	110.5
[0,-2]	[-2, -2, 0] ~[-0.3067, -0.9271, 0.4824]	111.3
[-2,0]	$[-2.1, 0, 0] \sim [-2.345, 0.938, 0.733]$	96.5
[2,0]	[2.1, 0, 0] ~[2.345, -0.938, -0.733]	96.5
[2,2]	[2, 0, 2] ~[2.404, 1.126, -0.8435]	47.5
[-2,-2]	[-2, 0, -2] ~[-2.404, -1.126, 0.8435]	47.5

4 Phase space region partition

Literature [8] first proposed the use of the domain splitter for Duffing oscillator phase trajectory patterns were detected, thereby detecting weak signals.

Phase trajectory shape discrimination and weak signal detection rule is: If the Duffing oscillator phase trajectory repeated many times across the boundary of the rectangular region segmentation, indicating Duffing oscillator phase trajectory for the chaotic state, then there is the driving force of phase with the internal weak sinusoidal signal to the chaotic system; if Duffing oscillator phase trajectory does not cross the boundary of the domain segmentation, indicating that the phase trajectories into a large-scale periodic state, indicating that there is an internal driving force in phase with a weak signal joined chaotic system.

The equilibrium point or balanced near the values into the system, the running time is set to 90 seconds to obtain a signal corresponding scroll, scroll one-dimensional phase space distribution 6, the space is divided into six regions, shown in Fig.5, so get six phase space disjoint chaotic attractor. Two-dimensional 3 * 3 scroll phase space distribution as shown in Fig.6, the space is divided into 9 areas. From Fig.5 and Fig.6 visible, multi-scroll signals has the respective region in phase space, the regional boundary obviously.



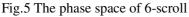


Fig.6 The phase space of 3×3 -scroll

Phase space division of the region is mainly developed areas by the two-dimensional phase space and complete the zoning rules, given the boundaries of each sub-region corresponds to the expression. Regional division first determines the region of space each scroll, each region of the range of variables can be determined, in any region of phase space *zone_i* as an example, the corresponding to the left, right, upper, lower boundary respectively $x_i^l, x_i^r, y_i^b, y_i^u$, if a Jerk oscillator in the region, then the corresponding variable ^x, ^y must satisfy the following relationship:

$$\begin{cases} x_{u}^{l} < x < x_{i}^{r} \\ y_{i_{b}}^{b} < y < y_{u_{i}}^{u} \end{cases}$$
(4)

By formula (4) shows that, at the moment t, Jerk oscillator phase track appears in the region, the chaotic signal x corresponding is greater than the region of the left circle and less than the right margin, chaotic signal Y is greater than the zone boundary and smaller than the upper boundary value.

Field will be divided into the idea of using M-ary chaotic modulation, the phase space area to be divided, different ary phase space corresponding to the information of different chaotic attractors, establish a mapping table substitution ary using chaotic sequence information into channel, namely to achieve a M-ary information chaotic modulation, increasing the system's privacy and information transfer rate. If the trajectory of chaotic signals appear in the area, can be determined through a mapping table information corresponding to the M-ary, M-ary information chaos demodulation.

5 Conclusion

Delayed feedback control of the Jerk model, can get the track boundaries clear, clear multiple chaotic attractor, estimation and tracking method in different phase space regions of chaotic attractor disjoint using the balance point, obvious boundary between each sub area, which provides the convenience for detection chaos model for M-ary chaotic communication, research work is carried out based on the model of M-ary chaotic secure communication based on the next step.

ACKNOWLEDGMENT

The authors would like to thank the Science and Technology Projects of Heilongjiang Provincial Education Department. (Number: 12511430)

References

- [1] YU S M, LIN Q H, QIU S S. Multi-level Digital Chaos Shift Keying Based on Multi-scroll Chaotic Systems[J]. Journal of Image and Graphics, 2004, 9(12):1473-1479
- [2] Yalcin M E, Suykens J A K, Vandewalle J. Families of scroll grid attractors [J].Int J Bifurcation and Chaos, 2002, 12(1):23-41.
- [3] HUANG R S, HUANG H. Chaos and its applications (second edition) [M]. Hubei: wuhan university press ,2005:41-76
- [4] LIU M H, LUO W, WU D L. Circuit implementation of Jerk system[J]. Microcomputer Information, 2007, 23(7-2):301-302
- [5] Liu C X, Yi J, Xi X C, et al. Research on the multi-scroll chaos generation based on Jerk model, Procedia Engineering, 2012(29):957-961.
- [6] Liu C X, Yi J, Wei H, et al. Reserch on Jerk visual model simulation and control based on Simulink, Proceedings of ICCTA2011, Beijing, China, 14-16 october 2011:1005-1008
- [7] SHAO Y B, Communication system modeling and simulation example is analyzed based on Matlab/Simulink[M]. Beijing: Tsinghua university press, 2008:20-47.
- [8] Fu Y Q, Wu D M, Zhang L, Li X Y. A circular zone Partition method for identifying duffing oscillator state transition and its application to BPSK signal demodulation [J]. SCIENCE CHINA Information Sciences, January, 2011, 54(3):1~9.
- [9] ZHAN F. The Research of Chaos M-ary Modulation and Demodulation Method Based on Chaotic Oscillator[D]. Harbin engineering university master's degree thesis , 2011:34~47.

Design of an ultra-wideband four arms sinuous antenna

Wei Wang ^{1,a}, Xuetian Wang ^{1,b}, Ying Li ^{2,c} and Song Song^{3,d}

¹School of Information and Electronics, Beijing Institute of Technology, Beijing 100081, China

²Beijing Institute of Ratio Metrology & Measurement, Beijing 100854, China

³The Academy of Equipment, PLA. Beijing 101416, China

^awangwei_hhuc@126.com, ^bwangxuetian@bit.edu.cn, ^cly880530@126.com, ^dsoongs2008@yahoo.cn

Keywords: Sinuous antenna; Ultra-wideband, Conical form

Abstract. Due to the advantages of ultra-wideband, single caliber, symmetric pattern, full polarization, the sinuous antennas have gradually displaced the traditional spiral antennas in the Missile guider, reflector feed, wideband direction finding system. Based on the traditional planar sinuous antennas, this paper designed a novel 2-22 GHz 3D sinuous antenna in the conical form. Results show that the designed antenna showed high performance within 2-22 GHZ frequency band.

Introduction

In 1980s, Duhamel Raymond first proposed the concept of sinuous antenna. Sinuous antenna, which is formed according to Similarity principle, it is a kind of frequency independent antenna. Compared to the traditional ultra-wideband helical antenna, sinuous antenna can provide more flexibly in the polarization conversion, can achieve double polarization and dual circular polarization technology. Sinuous antenna has gradually replaced helical antenna in many applications such as the microwave guider and the feed of reflector antennas in recent years. With the rapid development domestic and abroad, sinuous antenna will hold broad application prospects in the relevant fields ^[1-2].

However, the traditional plane sinuous antenna belongs to bidirectional radiating structure. In order to achieve unidirectional radiation, commonly a metallic back cavity structures loaded with absorbing material is added to one side of the antenna, which will eliminates the radiation energy of the antenna in this side ^[3]. Based on the design methods of plane sinusoidal antenna, the paper improved the structure of antenna from a plane type to a three-dimensional type, designed a new four-arm sinuous based on cone structure. This method avoids the use of metallic back cavity, and the electromagnetic energy is fully used, the structure of the antenna is effectively simplified, and the gain of the antenna is at the same time improved. The antenna has the advantages of ultra-wideband, fully polarization, single caliber, stable input impedance and pattern of rotational symmetry, etc. Due to the design tools, processing technology and other factors at present, there are few studies in domestic and abroad.

Basic principle and structure of four arms sinuous antenna

The structure of sinuous antenna belongs to the log-periodic or quasi log-periodic structure with frequency independence, and the basic sinuous antenna is simply determined by the angle α and scale factor τ . The curve is constituted by a series of line segments unit, the segment p is defined as:

$$\phi = (-1)^{p} \alpha_{p} \sin\left(\frac{180 \ln\left(r/R_{p}\right)}{\ln \tau_{p}}\right)$$
(1)

Among it, r and φ represent the polar coordinates of unit curve, the radius R_p is determined by the following relation.

$$R_p = \tau_{P-1} R_{P-1} \tag{2}$$

The basic sinuous curve centered at the origin, rotated clockwise and counterclockwise respectively in an angle δ , we will get another two curves. The area is enclosed by the two curves and constitutes an arm of the sinuous antenna. Rotating the arm from the origin for 90 °, 180 ° and 270 °respectively, then we will get the 4 arms sinuous antenna, as is shown in Figure 1.

The antenna pattern beam width is relevant to the value of α_p and δ , Experimental studies show that, for the given δ =22.5, if the α_p =45, the typical values of the E-plane and H-plane 3dB beam width of the antenna are all about 75°. The beam width of the log-periodic sinuous antenna in the entire band is almost unchanged. While for the quasi log-periodic antenna, it changes appropriately with the frequency variation and these changes relates to the change of α_p . According to this feature, we can control the antenna beam width purposely, which cannot be done by the general planar spiral antenna ^[4]. Generally when the $\alpha_p + \delta < 70$, the impedance of 4 arms sinuous antenna is stable in the entire frequency band.

Conical four arms sinuous antenna is formed by projecting plane sinusoidal to the surface of a cone. The advantages of the new structure antenna are that the gain and the front and back ratio of radiation pattern are improved. Given the front to back ratio of radiation pattern and gain of the antenna, the paper set the angle of cone as 45 degrees.

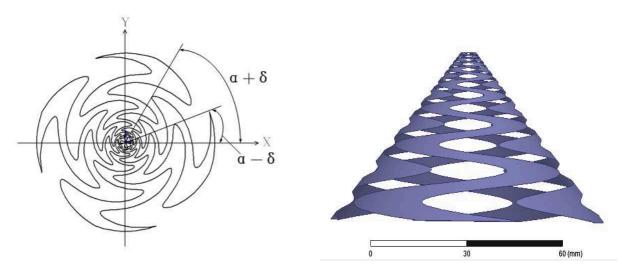


Fig.1 Basic structure of the antenna

Fig.2 Antenna model in HFSS

In this paper, we generally use the self-complementary log-periodic form, where $\alpha = 45$, $\delta = 180/2N = 22.5$, N = 4 which represent the number of arms. The basic shape of the antenna is shown as flowing. The arms of the antenna look like a zigzag transmission line fluctuating back and forth. Only the area where the length of the arm is closer to $\lambda/2$ or odd times of $\lambda/2$ is the radiation zone, while the area where the length of the arm is less than $\lambda/2$ is the transmission zone. At the working time, the antenna will motivate the traveling waves. When the current reaches at the radiation zone, the energy will radiate outside in the form of electromagnetic waves, and then the current reaches the decay zone. For any frequency point in the frequency band, there are transmission zone, radiation zone and decay zone in the antenna arm. The phase difference between the two symmetrical arms should be 180° when the two arms is fed. The electric field will be combined in the perpendicular direction of the arm axis, so the maximum of the electric field is in the normal direction of antenna ^[5].

Simulation results and analysis

Based on the design analysis above, in this paper, it designed a 2-22GHz 4 arms conical sinuous antenna. Figure 2 shows the model of Antenna radiation element in the Electromagnetic simulation software Ansoft HFSS.

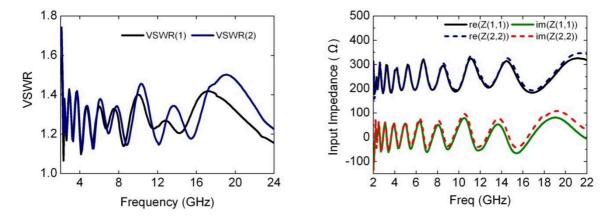


Fig.3 Results of VSWR and impedance value of the designed antenna

Figure 3 shows the curve of VSWR from the simulation, and we can see the VSWR performs well across the 2-22GHz frequency band. Also, it can be seen in Figure 3 that the impedance characteristics of the antenna designed are relatively stable, so it has a good frequency-independent property.

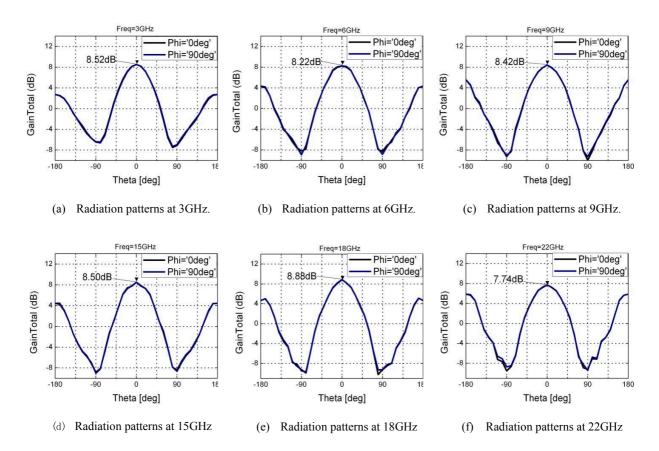


Fig.4 Radiation patterns of the designed antenna in 3, 6, 9, 15, 18, 22GHz

Freq (GHz)	3	6	9	15	18	22
Gain (dB)	8.52	8.22	8.42	8.50	8.88	7.74
3dB beam width(°)	65.2	65.3	62.5	64.1	57	65.4

Table 1. Value of the antenna gain and 3dB beam width

As can be seen from the Figure 4, the antenna designed has reached a relatively high Directivity within the whole frequency band. The antenna gain in each frequency point is almost bigger than 8 dB (except the 22 GHz point), as shown in Table 1. In addition, the directional pattern in E plane and H plane is almost completely overlapped.

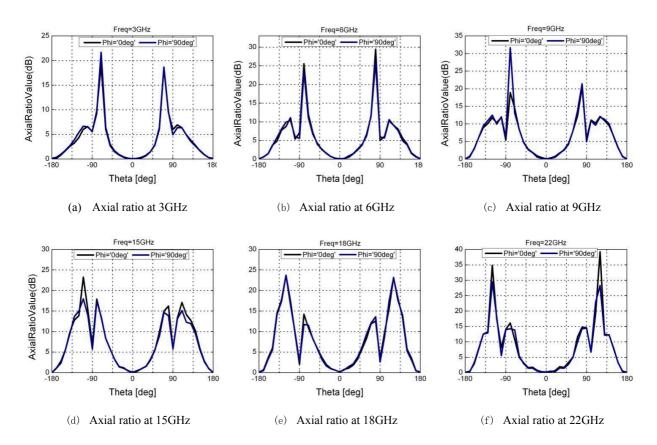


Fig.5 Axial ratio of the designed antenna in 3, 6, 9, 15, 18, 22GHz

It can be seen in Figure 5, within the range of plus or minus 50° , the axial ratio of the designed conical four arms sinuous antenna, has met the design requirements successfully in each frequency point.

Conclusion

In this paper, we designed an ultra-wideband conical four arms sinuous antenna. As can be seen in the simulation results, the designed novel antenna shows an excellent performance in regard to the Ultra-wideband characteristics and the frequency –independent characteristics. At the same time, the directional pattern in E plane and H plane is of rotational symmetry. The performance results have met the design requirements and process operation needs. This new designed conical four arms sinuous antenna has broad application prospects in the missile seekers, reflector feed antennas, and the wideband direction test systems in the future.

References

- [1] Song Li-zhong, Qiao Xiao-lin, Ye Zhun. Design and experiments of the conical sinuous antenna fed by microstrip Balun [J]. CHINESE JOURNAL OF RADIO SCIENCE. 2012, 06: 1204-1212.
- [2] Yuan Jing. Design of a novel UWB antenna [J]. Fire Control Radar Technology. 2009. 38(2): 72-75
- [3] Chen Zhen-hua. Niu Zhen-yi. Cao Qun-sheng. A planar sinuous antenna and the miniature Balun[J]. Aero Weaponry. 2009(5):44-45.
- [4] jiang Fan-jie. The Design of four-arm sinuous antenna [J]. Modern Radar. 2006. 28(2): 64-67.
- [5] Chen yu-lin, Fang Shan-xi. Design of a novel wideband dual-circular polarization antenna [J]. Fire Control Radar Technology, 2010, 39 (1): 83-86.
- [6] Cloete, J.H.; Sickel, T. The planar dual-polarized cavity backed sinuous antenna-a design summary[C]. Antennas and Propagation in Wireless Communications (APWC), 2012 IEEE-APS Topical Conference on1169-1172
- [7] Gawande, R. and R. Bradley, Towards an Ultra Wideband

Low Noise Active Sinuous Feed for Next Generation Radio Telescopes [J]. Antennas and Propagation, IEEE Transactions, 2011. 59(6): p. 1945-1953.

- [8] Song, L., G. Cong and H. Hong. Simulation and analysis of a hemispherical conformal sinuous antenna with four arms[C]. Ultra-Wideband (ICUWB), 2010 IEEE International Conference. 2010. Nanjing.
- [9] Cloete, J.H. and T. Sickel. The planar dual-polarized cavity backed sinuous antenna a design summary[C]. Antennas and Propagation in Wireless Communications (APWC), 2012 IEEE-APS Topical Conference. 2012. Cape Town.
- [10]Manna, A., P. Baldonero and F. Trotta. Novel UWB low-profile sinuous slot antenna[C]. Antennas and Propagation (EUCAP), Proceedings of the 5th European Conference. 2011. Rome.
- [11]Edwards, J. and G. Rebeiz. Dual-polarized sinuous antennas on silicon dielectric lenses[C]. Antennas and Propagation Society International Symposium (APSURSI), 2010 IEEE. 2010. Toronto, ON.
- [12]Olsson, R., P.S. Kildal and S. Weinreb, The eleven antenna: a compact low-profile decade bandwidth dual polarized feed for reflector antennas [J]. Antennas and Propagation, IEEE Transactions, 2006. 54(2): p. 368-375.

The Wireless Sensor Networks Based on Adjacent Strong Edge Chromatic Number

Zongjian Sun^{1,a}, Jing Chen^{2,b}

¹College of Sciences, Hebei University of Science and Technology, Shijiazhuang 050018, China

²College of Polytechnic, Hebei University of Science and Technology, Shijiazhuang 050018, China

^a zongjiansun@126.com, ^bchenjing198458@126.com

Keywords: Wireless sensor network; Link similarity; Optimization; Adjacent strong edge chromatic number; Join graph

Abstract. The adjacent strong edge chromatic number of graphs can be applied to the optimization design of wireless sensor network to make the network design more reasonable. An algorithm, based on the basic principle of page sorting technology, is designed to search for the adjacent strong edge coloring of certain join graphs. Therefore, the adjacent strong edge chromatic number of a join graph is obtained, and it can avoid the repetition of wireless sensor network.

Introduction

In recent years, with the rapid development of wireless communication, integrated circuit, sensor and MEMS technology, the mass production of micro wireless sensor with low cost, low power, multi-function becomes possible. These micro sensors have the functions of wireless communication, data acquisition and processing, cooperative and so on. As wireless sensor network is composed of numerous wireless sensor nodes, wireless sensor networks can be defined as following. Wireless sensor network is composed of a set of wireless sensor network in the wireless self-organized, and its purpose is to perceive the object regional cooperative sensing, collecting and processing information of the covered, and then send to the observer.

Node in the communication network distance is limited, generally in the range of tens to hundreds of meters, so nodes can only communicate with its neighbors. If you want to communicate its radio range outside of the nodes, the routing through intermediate nodes needed. In order to avoid the adjacent frequency interference, frequency sends to adjacent nodes cannot same. The application of the principle corresponds to the adjacent strong edge coloring theory in graph theory.

The adjacent strong edge number plays an important theoretical and practical significance. It is a main question of graph theory, the basic problem of which is to determine the chromatic number of different types of graphs.

In 1990, the vertex-distinguishing proper edge colorings and vertex-distinguishing general edge colorings had been widely considered in [1-3] and [4-8], respectively. The appropriate chromatic numbers are called the vertex-distinguishing proper edge chromatic number (or strong chromatic number, or observables) and point-distinguishing chromatic index, respectively. After that, adjacent strong edge coloring is proposed as a new concept in [9].

In this article, an algorithm is designed to search for the k-adjacent strong edge coloring of certain join graphs and the adjacent strong edge chromatic number of a wireless sensor network is given. Then the wireless sensor network which is designed in this article can be realized.

Basic definitions

Definition 1([10]) *G* is said to be a *join* graph if *G* is the complete union of two graphs $G_1 = (V_1, E_1)$ and $G_2 = (V_2, E_2)$. In other words, $V = V_1 \cup V_2$ and $E = E_1 \cup E_2 \cup \{uv : u \in V_1, v \in V_2\}$. If *G* is the join graph of G_1 and G_2 , we shall write $G = G_1 \vee G_2$.

Definition 2([10]) For graph G, an k-edge coloring f is an assignment of colors $1, 2, \dots, k$ to the edges of G. f is called k-proper edge coloring if no two adjacent edges have the same color.

Definition 3([9]) For a graph G(V, E), if a proper k – edge coloring f is satisfied with $C(u) \neq C(v)$ for $uv \in E(G)$, where $C(u) = \{f(uv) | uv \in E(G)\}$, then f is called the k – *adjacent strong edge coloring* of G(V, E), abbreviated k – *ASEC*; and $\chi'_{as}(G) = \min\{k | k - ASEC \text{ of } G\}$ is called the *adjacent strong edge chromatic number* of G.

Basic lemmas

We have Lemma 1 by definition 3.

Lemma 1([11]) If *G* is a graph which has two adjacent maximum degree vertices, then $\chi'_{as}(G) \ge \Delta(G) + 1$, where $\Delta(G)$ is the maximum degree of graph *G*.

Lemma 2([9]) For the complete bipartite graph $K_{nn}(1 \le m \le n)$, we have

 $\chi'_{as}(K_{m,n}) = \begin{cases} n, & m < n \\ n+2, & m = n \ge 2 \end{cases}$.

The algorithm of searching for adjacent strong edge coloring

As $\Delta(C_3 \lor K_{m,n}) = m+n+2$ and the maximum degree vertices is adjacent, we got $\chi'_{as}(C_3 \lor K_{m,n}) \ge m+n+3$ by Lemma 1. Based on the basic principle of page sorting technology, an algorithm ([12]) is designed to search for the adjacent strong edge coloring rule of $C_3 \lor K_{m,n}$ when *m* and *n* is smaller. Steps are followed:

1) Input m, n;

2) Select m+n+2 numbers $a_1, a_2, \dots, a_{m+n+2}$ among $1, 2, \dots, m+n+3$;

3) Give a one-to-one correspondence between $w_i u_i, w_i v_j$, $w_1 w_2, i = 1, 2, \dots, m, j = 1, 2, \dots, n$ and a_i $(i = 1, 2, \dots, m + n + 2)$;

4) Select m+n+1 numbers $a_1, a_2, \dots, a_{m+n+1}$ among $1, 2, \dots, m+n+3$;

5) Give a one-to-one correspondence between w_2u_i, w_2v_j , $w_2w_3, i = 1, 2, \dots, m, j = 1, 2, \dots, n$ and a_i $(i = 1, 2, \dots, m + n + 2)$;

If $C(w_1) = C(w_2)$, then, turn 4), else, turn 6);

6) Select m+n numbers a_1, a_2, \dots, a_{m+n} among 1, 2, $\dots, m+n+3$;

7) Give a one-to-one correspondence f between w_3u_i , w_3v_j ($i = 1, 2, \dots, m; j = 1, 2, \dots, n$) and a_i ($i = 1, 2, \dots, m + n$);

If $C(w_1) = C(w_2)$, then, turn 8), else turn 7);

8) Give a one-to-one correspondence f between $u_i v_j$ $(i = 1, 2, \dots, m; j = 1, 2, \dots, n)$ and $\{1, 2, \dots, m + n + 3\}$,

If $f(u_i x) = f(u_i y)$ $(x, y \in \{w_1, w_2, w_3, v_1, v_2, \dots, v_n\}$ and $x \neq y; i = 1, 2, \dots, m;$, or $f(v_i x) = f(v_i y)$ $(x, y \in \{w_1, w_2, w_3, u_1, u_2, \dots, u_m\}$ and $x \neq y; i = 1, 2, \dots, n;$,

Then, turn 9), else turn 8);

9) Found a method of (m+n+3) – adjacent strong edge coloring, output all the colorings,

Then, turn 2) to search for a next correspondence, in order to found other (m+n+3) – adjacent strong edge coloring method, else turn 3).

When *m* and *n* are smaller, an (m+n+3)-adjacent strong edge coloring of $C_3 \lor K_{m,n}$ is obtained according to the above algorithm. By analyzing the coloring method, an (m+n+3)-adjacent strong edge coloring of $C_3 \lor K_{m,n}$ is also obtained, followed by the adjacent strong edge chromatic number.

Main results

Theorem 1 For join graph $C_3 \vee K_{m,n}$, we have

 $\chi'_{as}(C_3 \vee K_{mn}) = m + n + 3$, when m < n - 2.

Proof Since $\Delta(C_3 \lor K_{m,n}) = m + n + 2$, and $C_3 \lor K_{m,n}$ has two vertices of maximum degree which are adjacent, we have $\chi'_{as}(C_3 \lor K_{m,n}) \ge m + n + 3$ by Lemma 1. In order to prove $\chi'_{as}(C_3 \lor K_{m,n}) = m + n + 3$, we need to give an (m + n + 3) – adjacent strong edge coloring of $C_3 \lor K_{m,n}$.

Supposing the independent sets of two parts of $K_{m,n}$ are $\{u_1, u_2, \dots, u_m\}$ and $\{v_1, v_2, \dots, v_n\}$, $C_3 = w_1 w_2 w_3 w_1$, $S = \{1, 2, \dots, m+n+3\}$ and $n = n \pmod{n}$.

When m < n-2, the question is discussed as follows:

Step 1 We now give an edge coloring of $K_{m,n}$ as follows:

 $f(u_i v_j) = \begin{cases} n+i+j-1, i = 1, 2, \cdots, m; j = 1, 2, 3\\ (i+j-1) \mod n, i = 1, 2, \cdots, m; j = 4, 5, \cdots, n \end{cases};$

Step 2 We now give a coloring of $f(w_i u_j) = i + j - 1, i = 1, 2, 3; j = 1, 2, \dots, m$; $f(w_i v_j) = m + i + j - 1, i = 1, 2, 3; j = 1, 2, \dots, n$.

Step 3 We now give a edge coloring of C_3 as follows: $f(w_1w_2) = m+n+2$; $f(w_2w_3) = 1$; $f(w_3w_1) = m+n+3$.

Obviously, f is an (m+n+3)-proper edge coloring of $C_3 \vee K_{m,n}$.

And $C(u_i) = \{1, 2, \dots, n, n+i, n+i+1, n+i+2\}, i = 1, 2, \dots, m; C(v_i) = \{n+i, n+i+1, \dots, n+m+i-1, m+i, m+i+1, m+i+2\}, i = 1, 2, 3; C(v_i) = \{i, (i+1) \mod n, (i+2) \mod n, \dots, (i+m-1) \mod n, m+i, m+i+1, m+i+2\}, i = 4, 5, C(w_1) = \{1, 2, \dots, m+n, m+n+2, m+n+3\} = S - \{m+n+1\}; C(w_2) = \{1, 2, \dots, m+n+1, m+n+2\} = S - \{m+n+3\}; C(w_3) = \{1, 3, 4, \dots, m+n+2, m+n+3\} = S - \{2\};$

It is easy to see that f is the (m+n+3)-adjacent strong edge coloring of $C_3 \vee K_{m,n}$. Combining above, we have that $\chi'_{\infty}(C_3 \vee K_{m,n}) = m+n+3$ when m < n-2. The proof of this theorem is completed.

Conclusions

Consider the wireless sensor network of a graph, which is the join graph of C_3 and $K_{m,n}$. Based on page sorting algorithm, we modified the algorithm in [12], and changed one part of the union graph in [12] from C_2 to C_3 . According to the method, an adjacent strong edge coloring of $C_3 \vee K_{m,n}$ is obtained, and then the adjacent strong edge chromatic number of it is confirmed by definition 1.

In practice, $w_1, w_2, w_3, u_1, u_2, \dots, u_m, v_1, v_2, \dots, v_n$ in join graph $C_3 \vee K_{m,n}$ represent different nodes, and w_1w_2 , w_2w_3 , w_3w_1 , w_ku_i , w_kv_j ($k = 1, 2, 3, i = 1, 2, \dots, m, j = 1, 2, \dots, n$) represent the frequency between two nodes. There is a wireless sensor network between w_1 and w_2 , and the m + n + 2 different nodes from w_i (i = 1, 2) to others are put in set A_i (i = 1, 2). Our purpose is giving minimum frequency to make $A_1 \neq A_2$ and so on. The

number of minimum frequency is the adjacent strong edge chromatic number of join graph $C_3 \vee K_{mn}$ from above discussion. In this way, the wireless sensor network is realized.

Acknowledgements

This paper is supported by the Natural Science Foundation of Hebei University of Science and Technology (XL201260) and the Natural Science Foundation of Department of Education of Hebei Province (Z2012047).

References

- [1] Burris A. C. and R. H. Schelp.Vertex-distinguishing proper edge-colorings, *Journal of graph theory*, Vol. 6, No. 2(1997), p. 73-82.
- [2] Zhang Z. F., Li J. W., Chen X. E., Cheng H., and B. Yao. D(β)-vertex-distinguishing proper edge-coloring of graphs, *Acta mathematica sinica*, Vol. 9, No. 3(2006), p. 703-708.
- [3] Bazgan C., Harkat Benhamdine A., and H. Li.On the vertex-distinguishing proper edge-colorings of graphs, *Journal of combine theory ser B*, Vol. 75, No. 2(1999), p. 288-301.
- [4] Hornakm, Stakr. The fifth jump of the point-distinguishing chromatic index of $K_{n,n}$, *Arsbin*, Vol. 42(1996), p. 233-242.
- [5] Hornakm, Sotakr.Localization of jumps of the point- dstinguishing chromatic index of $K_{n,n}$, *Discuss. Math. graph theory*, Vol. 17, No. 2(1997), p. 243-251.
- [6] Hornakm, Zagagliasn.On the point-distinguishing romatic index of complete bipartite graph, *Ars Combin.*, Vol. 80(2006), p, 75-85.
- [7] Zagagliasn.On the point-distinguishing chromatic index of $K_{n,n}$, Ars Combin., Vol. 25, B, p, 93-104, 1998.
- [8] Zagagliasn.On the value of the point-distinguishing chromatic index of $K_{n,n}$, Ars Combin,Vol. 29(1990), p. 235-244.
- [9] Zhang Z. F., Liu L. Z. and J. F. Wang.Adjacent strong edge coloring of graphs, *Applied mathematics letters*, No.5(2002), p. 23-626.
- [10] Bondy J. A. and U. S. R. Murty. Graph theory with application, *The Macmillan Press*, New York, 1976.
- [11] Tian S. L., Li J. W. and Z. F. Zhang.On the adjacent strong edge chromatic number of $C_m \lor K_n$, *Journal of Shandong university*, Vol. 40, No. 1(2005),p.7-10.
- [12] Sun Z. J., Li Z. C., Luo H. P. and J.D. He, "Gracefullness of up-down ladder graphers L_{3m+n+1} ", Application research of computers, Vol. 24, No. 12(2007), p. 132-133.

The Effects of RB Usage on Single User Rate in TD-LTE

Ting Li^{1, a}

¹Fuzhou Strait Vocational College, Fuzhou, China

^aspidersmile@tom.com

Keywords: TD-LTE; Resource Block; User Rate

Abstract. Resource Block (RB) allocation effects network coverage and throughput. The impact principles are analyzed in theory. Exist TD-LTE network data is collected, organized and analyzed. The results show that the effects of RB allocation on user rate in downlink is greater than uplink and uplink RB usage is more stable.

Introduction

Time-Division Long-Term Evolution (TD-LTE), also referred to as Long-Term Evolution Time-Division Duplex (LTE TDD), [1] is a 4G mobile-telecommunications technology and standard co-developed, since late 2007. China has been holding large-scale network construction using LTE TDD technology in a bid to move the country to faster 4G networks after 4G licensing on December 8, 2013. The hot topics in construction, operation and maintenance of the TD-LTE network are focus on capacity, rate, quality, coverage and cost. Generally the network's performance is affected by comprehensive factors, including the site selections of eNodeB (eNB), antenna erected, wireless environment, disturbance from other networks, parameter configuration, etc..

In this paper, the effects of RB allocation on the system's capacity are paid attention to. The organization of this paper is as follows. In section II, RB is introduced in simple words. Section III analysis what the RB allocation will affect and why. In section IV, exist TD-LTE network data is used to prove the reslut in section III. Finally, conclusions are presented in section V.

Definition of Resource Block

In the time domain, different time intervals within LTE are expressed as multiples of a basic time unit $T_s=1/30720000$. The radio frame has a length of 10 ms ($T_{frame}=307200 T_s$). In the frequency domain, the number of sub-carriers N ranges from 128 to 2048, depending on channel bandwidth with 512 and 1024 for 5 and 10 MHz, respectively, being most commonly used in practice [2]. In a microcell, the coherence bandwidth of the signal is in the order of 1 MHz. Within the LTE carrier bandwidth of up to 20 MHz there are some sub-carriers that are faded and other are not faded. Transmission is done using those frequencies that are not faded. The transmission can be scheduled by RB which is discussed separately in downlink RB and uplink RB.

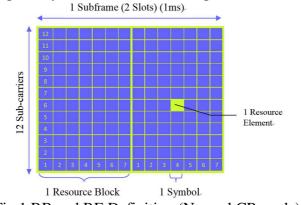


Fig.1 RB and RE Definition (Normal CP mode)

Downlink RB is divided into physical resource block (PRB) and virtual resource block (VRB). PRB is used to describe the actual situation of physical resources' allocation. A PRB consists of 7 / 6 OFDM symbols (in short CP / long CP mode) and 12 consecutive sub-carriers, or 180 kHz, for the duration of one slot (0.5 ms). In the other words, a PRB consists of 7 (or 6) ×12 resource elements (REs), which is defined as 1 OFDM symbol by 1 sub-carrier. Fig.1 is RB and RE definition under normal CP mode. VRB includes Localized VRB (LVRB) and Distributed VRB (DVRB). The former assigns several continuous sub-carriers to one user, and the latter disperses the sub-carriers distributed to one user into the whole system's frequency bandwidth.

Uplink RB can also be divided into LRB and DRB. The standard only accepts LRB because it is difficult to estimate the channel and use the frequency scheduling if DRB is used. Obviously, when we use LRB, the rate of UE becomes higher with the increased of the occupancy of the bandwidth.

Effects of RB Allocation

In TD-LTE system, the number of RB distributed to user impacts on coverage and user data rate.

Effects on coverage. The system's coverage is mainly determined by the power. The user will get higher data rate as more RBs are distributed, thus the noise of receiver will increase with the wider bandwidth the user occupies. In general, downlink RB allocation's effect on coverage is smaller than uplink.

Downlink equivalent transmit power of eNB aimed at single user is getting larger with the increasing of the number of RB the user occupies for the reason that the power is distributed for very RB on the whole system bandwidth equally. Downlink coverage is lager at the same time. Conversely downlink coverage will shrink by more receive noise caused by wider bandwidth which can offer more RB. Colligating both, downlink coverage's variation is not so obviously. Uplink coverage is seriously affected by RB usage because user's biggest emissive power is limited so that uplink power can't increase. [3]

Effects on user data rate. The way to calculate the peak data rate is as follows. First assume a TD-LTE system with exact channel bandwidth and MIMO mode. Calculate the number of resource elements (RE) in a subframe (a subframe is 1 msec, maintains 2 RB, and equals to 212×7 RE). Then calculate the data rate after choosing the modulation method. At last we have to subtract the overhead related to control signaling such as PDCCH and PBCH channels, reference and synchronization signals, and coding.

For example, we assume a 2×20 MHz LTE system with 4×4 MIMO configuration and 64QAM code rate 1. Downlink data rate = 4 x 6 bps/Hz x 20 MHz x (1-14.29%) x (1-10%) x (1-6.66%) x (1-10%) = 298 Mbps. 14.29% is Pilot overhead of 4 Tx antennas, 10% is downlink bandwidth efficiency, 6.66% is CP overhead in normal CP mode, and 10% is common channel overhead adequate to serve 1 UE/subframe.[4]

The calculation of uplink data rate is similar to downlink, except there is no MIMO and have to consider random access overhead instead of downlink bandwidth efficiency. Uplink data rate is 82Mbps in the system indicated above.

It is obverse that user data rate is depend on how many RB distributed to the user in a sense. But is it correct that the user data rate is proportional to the number of RB the user occupies?

Example

Throughput or network throughput, the average rate of successful message delivery over a communication channel, reflects the system capacity directly. According to the analysis in section III, we find that the number of RB allocated to a user plays an important role to the maximum rate that the user can reach. So RB allocation is one influencing factor of the TD-LTE capacity.

29 uniform distributed sites in different sectors are taken. The sites near the eNB and those on the edge of the cell are both included. Table 1 shows the data of the test.

On the basis of the data in the table 1, we get 3 relationship diagrams: downlink throughput and downlink PRB usage (shown in Fig.2), the maximum number of online users and downlink PRB

usage (shown in Fig.3), uplink throughput and uplink PRB usage (shown in Fig.4) and comparison of uplink RB usage and downlink RB usage (shown in Fig.5).

Site Name	RSRP	SINR	DL throughput	UL throughput	DL PRB Usage	UL PRB Usage	Maximum number of Online Users
2234_C	-96	12	11.4	3.5	39.283	72.313	19
3874_C	-87	6.5	12.4	5.2	7.963	43.925	7
3019_A	-96	0.5	3.19	2.83	49.418	51.74	14
3942_A	-65	27	13.1	3.1	86.938	56.902	42
3853_A	-102	2	1.87	2.1	81.856	50.521	21
2226_B	-105	-2.25	1.08	1.1	68.09	74.852	28
10315_A	-84	3.75	5.1	3.48	57.575	42.308	7
2134_C	-105	4.25	3.09	1	13.255	41.135	6
2134_B	-102	8	5.9	2.66	17.295	43.863	6
2385_A	-96	-0.5	3.33	1.6	29.785	49.902	18
3543_B	-87	11.75	23.1	5.5	1.533	37.99	9
10316_C	-87	14	16.6	5.4	1.581	38.424	6
3062_A	-77	24	26.6	5.5	11.426	50.841	18
eNB_2093_0	-91	15.5	4.49	2.27	81.556	65.58	29
3079_A	-84	15	24	5.3	1.618	42.033	7
eNB_3781_b	-84	16.5	1.56	1.52	96.306	48.332	73
3028_C	-101	4.5	5.84	1.5	17.106	50.679	16
3017_B	-94	6	3.3	2.5	61.336	51.335	41
3731_A	-110	1	5.2	0.62	3.048	36.086	7
3167_C	-101	17	0.59	0.31	93.076	43.969	123
3967_A	-96	18.75	7.01	2.32	83.38	46.673	57
3074_A	-88	11.5	4.62	2.8	63.105	58.083	23
3116_A	-95	8.5	4.9	2.1	54.705	56.828	28
3955_C	-86	11	7.9	3.21	63.101	58.868	16
2515_B	-88	16	2.4	0.72	94.576	53.548	32
3242_B	-95	3.5	2.82	4.85	85.79	41.911	47
3519_C	-96	7.25	3.2	3.4	40.61	52.318	19
10320_C	-103	7.25	9.9	0.95	10.89	52.788	15
2015_B	-105	7	5.8	2.3	6.635	36.632	7

Table 1 Data from exist TD-LTE network

According to these Figures, the effects of RB usage, in the other words RB allocation, on the throughput are evident. On the whole, the number of online users in a cell is tune with RB usage. Or we will say more users requests more RB usage. When downlink, the throughput is proportional to SINR and reverse RB usage (100 – RB usage) if the network congestion is not serious. This means downlink throughput will increase with the increase of SINR while decrease with the increase of downlink PRB usage. But the situation is different in testing 2515_B and 3942_A. Although both of the sites' SINR is good enough, their throughput is very low. The reason for this is that their rate of RB occupation is too high to be assigned to sufficient RB resources.

In the terms of uplink, the fluctuation of RB usage, from 36% to 74%, is not as obvious as downlink, in which the RB usage is from 1.5% to 96%. The reason uplink RB usage is generally high but not lead to the network congestion is that there are at least 16 RB is distributed to PUSCH and others to PRACH etc. in uplink channel. Thus even though there is no user, uplink PRB usage is around 20%. And this can also prove it is easier to congestion in downlink channel than in uplink.

When the network doesn't congest, uplink RB usage is universally higher than downlink RB usage. While when downlink congestion happens, uplink RB usage is not always higher. Fig.5 is the comparison of DL PRB usage and UL PRB usage. Network congestion accords in Cell 2515 B, and its UL PRB usage is lower than DL PRB usage.

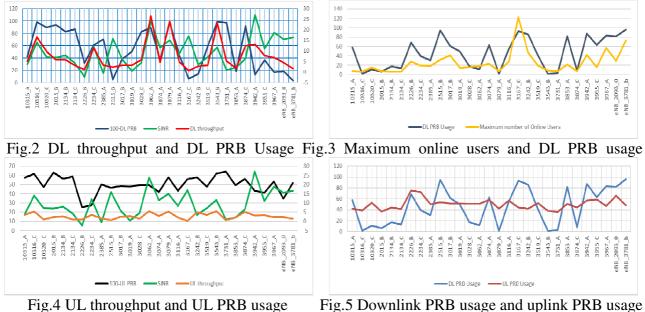


Fig.5 Downlink PRB usage and uplink PRB usage

Conclusions

RB is the basic unit of resource scheduling in LTE. Enough RB allocation brings high throughput. Throughput is proportional to channel quality if there are sufficient RB resources. The better signal quality brings higher modulation and golay codes, and leads to double throughput at the end. In general, RB allocation is one of the key factors affect quality of TD-LTE networks. Reasonable RB allocative decisions can enhance network quality especially in coverage and throughput.

Acknowledgements

This work is supported by Educational & Scientific Research Program for Middle-aged and Young Core Instructor in Fujian Province, China named "Study of TD-LTE network scheme and Analysis of Performance Optimization" (No.JA13445)

References

- [1] Information on http://www.cio.com
- [2] LTE in a Netshell: The Physical Layer. Telesystem Innovations Inc. (2010), p. 4-7
- [3] Morita, Nobukiyo, Hamabe: Uplink power control method for LTE femtocells based on resource usage aggregation. Personal Indoor and Mobile Radio Communications (PIMRC), (2012), p. 442-447
- [4] Dongzhe Cui: LTE peak rates analysis. Wireless and Optical Communications Conference, 2009. WOCC 2009. 18th Annual (2009), p. 1-3
- [5] 3GPP TS 36.521-1, "Evolved Universal Terrestrial Radio Access (E-UTRA); User Equipment (UE) conformance specification; Radio transmission and reception; Part 1: Conformance Testing ". V9.2.0 (2010-09).
- [6] 3GPP TS 36.213, "Physical layer procedures (Release 10)," V10.1.0 (2011-03)
- [7] Stefania Sesia, Issam Toufik, and Matthew Baker in: LTE The UMTS Long Term Evolution 2nd Edition, Wiley; 2 (2011-07)

Effects of Energy Harvesting Rate on Lifetime and Throughput Capacity in Wireless Sensor Networks

Yang Zeng^{1,a}, Xuedan Zhang^{1,b} and Yuhan Dong^{1,c} ¹Department of Electronic Engineering, Tsinghua University,China ^azy1014@126.com, ^bxuedanzhang@gmail.com, ^cyuhandong@gmail.com

Keywords: WSN; Throughput Capacity; Lifetime; Energy Harvesting Rate.

Abstract. Energy-harvesting Wireless sensor networks have gained more and more attention in recent years. For traditional battery-powered WSNs, the effect of transmission power on the throughput capacity and the lifetime have been well studied. The throughput capacity of WSNs is defined usually as the largest common throughput that can be provided to each source-sink pair nodes. Researches showed that high transmission power increases the throughput capacity of WSNs However, the high transmission power leads to a high energy consumption, thus the tradeoffs between the capacity and the lifetime under different transmission power have been analyzed.

Introduction

Energy-harvesting Wireless sensor networks have gained more and more attention in recent years. For traditional battery-powered WSNs, the effect of transmission power on the throughput capacity and the lifetime have been well studied. The throughput capacity of WSNs is defined usually as the largest common throughput that can be provided to each source-sink pair nodes. Researches showed that high transmission power increases the throughput capacity of WSNs [1]. However, the high transmission power leads to a high energy consumption, thus the tradeoffs between the capacity and the lifetime under different transmission power have been analyzed [2].

This paper addresses the effect of the ambient energy supplement on the lifetime and the throughput capacity in WSNs. Focusing on the case of fixed transmit power, we analyze the relationships between the lifetime, the throughput and the energy-harvesting rate.

Our research can provide useful guidance for the design of WSNs with renewable energy sources. For example, network designers can utilize our results to calculate the solar panel size which determines the energy-harvesting rate to meet the throughput and lifetime demands.

Model

Network Model.

We consider a finite WSN with 10 nodes deployed randomly in an area of $100 \times 100m^2$. The sink node is selected randomly among the 10 nodes.

Energy Model.

We adopt the energy model provided by Heinzelman in [3]. E_{elec} is the energy/bit consumed by the transmitter's electronics which is a distance-independent term. E_{amp} is the energy/bit consumed by the radio amplifier which is a distance-dependent term, and $E_{tx,ij}$ is the required transmit energy for node *i* to transmit one bit to node *j*. Let d_{ij} be the distance between node *i* and node *j* and β be the path loss exponent ($2 \le \beta \le 4$). Hence, the energy required to transmit one bit from node *i* to node *j* over distance d_{ij} is:

$$E_{tx,ij} = E_{elec} + E_{amp} * d_{ij}^{\beta} \tag{1}$$

In this paper, we assume that all sensor nodes have the same amount of initial energy and the same energy-harvesting rate while the sink node has infinite energy so it never runs out its energy.

Communication Model

As mentioned by Gupta and Kumar in [4], there are two types of communication models: Protocol Model and Physical Model. In this paper, we only consider the Protocol Model. Let node X_i transmit to node X_i . Then this transmission can be successfully received by node X_i if

$$|X_k - X_i| \ge (1 + \Delta) |X_i - X_i|$$

for every other node X_k which transmits simultaneously over the same channel. Δ is set to be 1 in this paper.

An independent set ψ indicates that links in set ψ can operate concurrently without conflicts. Considering a scheduling-based MAC protocol such as TDMA, the network can only transmit packets across designated links that belong to a single independent set in each time slot. Packets routed across a multi-hop path are buffered at relay nodes when awaiting transmission. **Problem Formulation**

E _{tx,ij}	The required transmit energy for node i to transmit one bit to node j
E_{rx}	The required receive energy to receive one bit
E_r	The energy harvesting rate
E_0	Initial Battery Energy
P_i	Power consumption of Node <i>i</i>
T_{req}	The required lifetime of the WSN
5	A set of links
$\lambda_{_f}$	Throughput of Flow <i>f</i>
α_{ς}	Time Fraction for which ς is active
ζ	Collection of all Independent Sets
ζ_{l}	Collection of all Independent Sets containing <i>l</i>
R_{f}	Set of all routes of flow
\pmb{R}_{f}^{l}	Set of all routes of flow f which pass through l
x _{ij}	The number of bits transmitted from node i to node j per second

In this section, we provide a linear programming (LP) formulation for the analysis of the throughput capacity with energy-harvesting rate. The variables and parameters that are used in our LP model are summarized in Table 1.

The LP formulation for the analysis of the throughput capacity:

 λ_f Subject to: (3) - (8)

$$sum_{r \in R_f} \phi_f^r = 1 \tag{3}$$

$$sum_{\varsigma\in\zeta}\alpha_{\varsigma} \le 1 \tag{4}$$

$$x_{ij} = \lambda_f \sum_{r \in R_f^{(i,j)}} \phi_f'$$
(5)

$$x_{ij} \le \sum_{\varsigma \in \zeta_{(i,j)}} \alpha_{\varsigma}$$

$$P \le \frac{E_0}{1 + E}$$
(6)

$$P_i \leq \frac{1}{T_{req}} + E_r \tag{7}$$

$$P_{i} = \sum_{j=1, j \neq i} E_{tx, ij} x_{ij} + E_{rx} \sum_{j=1, j \neq i} x_{ji}$$
(8)

(2)

Constraint (3) is the flow conservation constraint. It suggests that at the source node, the flow out of the source balances the flow injected to the source through different routing.

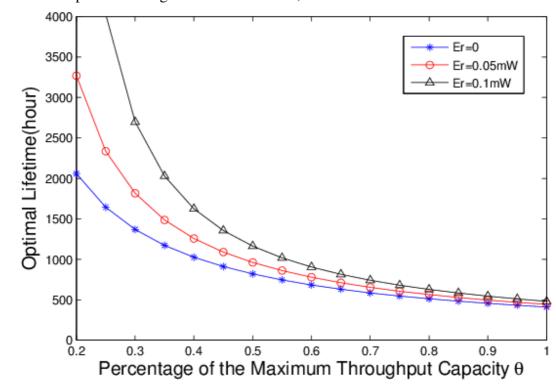
Constraint (4) must be met for any feasible scheduling. To achieve the throughput capacity, $sum_{c\in \zeta} \alpha_c$ should be 1 if there is no lifetime requirement. Otherwise, $sum_{c\in \zeta} \alpha_c$ may be less than 1.

Constraint (5) and (6) is the link capacity bound. It means that the amount of flow going through a link is bounded from above by the link capacity (represented by the product of the link data-rate (unity) and the scheduled time).

Constraint (7) ensure that at each node the energy consumed cannot be larger than the sum of the battery capacity and the the renewable energy received during its required lifetime.

Constraint (8) is the energy consumption model.

Results



We solve the LP problem using ILOG CPLEX 12.2, and the results are as follows:

Fig.1. Optimal Lifetime vs. Throughput Requirement for Fixed Energy Harvesting Rate

Fig.1 presents the tradeoffs between the throughput and the lifetime under different energy-harvesting rates. Energy supplement can prolong the lifetime to maintain the maximum throughput capacity. It is obvious that the energy harvesting enhances the network lifetime a lot under low throughput requirement.

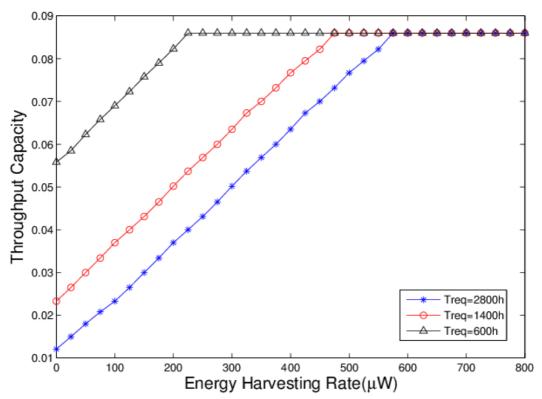


Fig. 2. Throughput Capacity vs. Energy Harvesting Rate for Fixed Lifetime Requirement

In Fig.2, we find that with a fixed lifetime requirement, the throughput capacity increases linearly with the energy-harvesting rate before reaching the schedule limit. High lifetime requirement decreases the throughput capacity and results in more energy supplement to achieve the maximum throughput capacity.

Conclusion

In this paper, we present a LP formation to analyze the relationships between the lifetime, the throughput and the energy-harvesting rate. The numerical results have shown how energy-harvesting improves the throughput capacity and the lifetime. Our researches provide useful guidance for the design of WSNs with renewable energy supplement. Specially, We find that with a fixed lifetime requirement, the throughput capacity increases linearly with the energy-harvesting rate before reaching the schedule limit, and the lifetime requirement has nothing to do with the slope, in which the throughput capacity changes along with energy-harvesting rate.

References

- Behzad, Arash and Rubin, Izhak, "High transmission power increases the capacity of ad hoc wireless networks," IEEE Transactions on Wireless Communications, vol. 5, no. 1, pp. 156–165, 2006
- [2] J.Luo, A.Iyer, and C.Rosenberg, "Throughput-lifetime trade-offs in multihop wireless networks under an SINR-based interference model," IEEE Transactions on Mobile Computing, vol. 10, no. 3, pp. 419–433, 2011.
- [3] W. B. Heinzelman, "Application-specific protocol architectures for wireless networks," Ph.D. dissertation, Massachusetts Institute of Technology, 2000.
- [4] P.Gupta and P.R.Kumar, "The capacity of wireless networks," IEEE Transactions on Information Theory, vol. 46, no. 2, pp. 388–404, 2000.

Modified Fast Directional Multilevel Algorithm for Analysis of Scattering of Microstrip Patch

Chen Hua^{1,2, a}, Fan Yong jie^{1,2,b}

¹Kunming University of Science and Technology, Kunming, 650500, China ²Key Laboratory of Unconventional Metallurgy, Ministry of Education,Kunming University of Science and Technology, Kunming 650093, China ^a93056460@qq.com, ^b47883027@qq.com

Keywords: Modified fast directional multilevel algorithm, microstrip antenna array, radiation.

Abstract. In this paper, the modified fast directional multilevel algorithm (FDMA) is presented for analyzing microstrip patch. The FDMA has been successfully applied to analyze scattering in free space and then it was extended to solve mircrostrip problems. The quad-tree structure is used in this method, which is the same as that in fast multipole method. In our method, the finest level group size can be set smaller than 0.2λ without suffering from subwavelength breakdown. The resulting algorithm has the memory requirement and the CPU time per iteration proportional to O (NLogN), where N refers to the number of unknowns. Numerical results of microstrip structures are presented to show the efficiency of this method.

Introduction

The method of moments (MoM) [1] is often used in the analysis of microstrip structures, such as mircrostrip antennas, microwave integrated circuits. However, for large-scaled complex microstrip structures, it is impractical to solve resultant matrix equation because it has a memory requirement of O (N^2) and computational complexity is proportional to O (N^3) . Many iterative methods are developed for making the operation count reduce to $O(N^2)$. Then many fast algorithms combined with the discrete complex image method (DCIM) [2-3]occured to speed up the matrix-vector product operation. The popular fast algorithms such as the adaptive integral method (AIM) [4], are based on FFT technique which can't reduce the iteration number of the Krylov subspace iterative solvers, which is largely depends on the spectral properties of the integral operator or the matrices of discrete linear systems. the Though the popular method fast multipole method (FMM) [5-7] is successfully applied to the microstrip problems, the procession is always difficult because of its dependence on the Green's function. At the beginning, FMM is tried to combine with DCIM to solve the static and two-dimensional problems [5]. Unfortunately, it will be lack of accuracy when the frequency is high. Though FMM is employed in [6] for full wave analysis, the implementation is very complicated because the surface-wave poles are extracted in DCIM. The FMM also has been applied to thin layer structures as the thin stratified medium fast multipole algorithm [7] which is adaptive to thin-stratified media.

The fast directional multilevel algorithm is originally applied in the analysis of scattering problem of free space [8-9]. The method is kernel independent and the Green's function is expanded by low rank representation which is demonstrated efficient in [9]. Recently, the fast directional multilevel algorithm is successfully applied for analysis of multilayer microstrip problems[10]. In this paper, fast directional multilevel algorithm are applied to the analysis of microstrip antenna array for radiation problems. Similar to the FMM, a quad-tree structure is used. The FDMA is applied to accelerate the evaluation of the far interaction. By the use of the multilevel algorithm, the complexity is reduced to O (NLogN). Numerical results for microstrip antennas are presented to demonstrate the efficiency and accuracy of this method.

FORMULATIONS AND FDMA

Consider a microstrip structure as is shown in Fig.1. The MPIE can be written as

$$j\omega\mu_0\hat{n} \times \left[\mathbf{A}(\mathbf{r}) + \frac{1}{k_0^2} \nabla \Phi(\mathbf{r}) \right] = \hat{n} \times \left[\mathbf{E}^i(\mathbf{r}) + \mathbf{E}^r(\mathbf{r}) \right]$$
(1)

where

$$\mathbf{A}(\mathbf{r}) = \iint_{S} G_{a}(\mathbf{r}, \mathbf{r}') \cdot \mathbf{J}(\mathbf{r}') ds'$$
⁽²⁾

$$\Phi(\mathbf{r}) = \iint_{S} G_{q}(\mathbf{r}, \mathbf{r}') \nabla \cdot \mathbf{J}(\mathbf{r}') ds'$$
⁽³⁾

The spatial domain Green's function can be obtained by applying DCIM and using Sommerfeld identity,

$$G_a = \frac{e^{-jkr}}{r} + \sum_{k=1}^{M_1^a} a_{1k}^a \frac{e^{-jkr_{1k}^a}}{r_{1k}^a} + \sum_{k=1}^{M_2^a} a_{2k}^a \frac{e^{-jkr_{2k}^a}}{r_{2k}^a}$$
(4)

$$G_{q} = \left(1 + \frac{1 - \varepsilon_{r}}{1 + \varepsilon_{r}}\right) \frac{e^{-jkr}}{r} + \sum_{k=1}^{M_{1}^{q}} a_{1k}^{q} \frac{e^{-jkr_{1k}^{q}}}{r_{1k}^{q}} + \sum_{k=1}^{M_{2}^{q}} a_{2k}^{q} \frac{e^{-jkr_{2k}^{q}}}{r_{2k}^{q}}$$
(5)

Galerkin's method is applied which results in a matrix equation

$$ZI = V$$
(6)

Using the fast directional multilevel algorithm, the matrix-vector product ZI can be written as:

$$\mathbf{Z}\mathbf{I} = \mathbf{Z}_{N}\mathbf{I} + \mathbf{Z}_{F}\mathbf{I}$$
(7)

Here \mathbf{Z}_N is the near part of \mathbf{Z} and is computed directly. \mathbf{Z}_F is the far part of \mathbf{Z} and the computation of \mathbf{Z}_F is accelerated by FDMA. Those elements in \mathbf{Z}_F are not explicitly computed and stored.

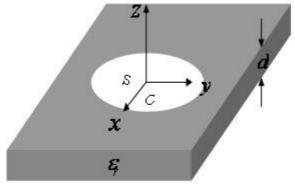


Fig. 1 The geometry of microstrip

The implemention of FDMA can refer to [10].

NUMERICAL RESULTS

In this section, a number of numerical examples are presented to demonstrate the efficiency of the FDMA for solving linear systems arising from the discretization of MPIE for analyzing microstrip structures. In the implementation of the FDMA, the restarted version of GMRES algorithm is used as the iterative method. All experiments are performed on a Core-2 6300 with 1.86 GHz CPU and 1.96GB RAM in single precision. The iteration process is terminated when the normalized backward error is reduced by 10^{-4} for all examples.

8×8 antenna array

The second example concerns the radiation from microstrip corporate fed planar arrays. The geometry of an $^{8\times8}$ antenna array is depicted in Fig.2(a), where $\mathcal{E}_r = 2.2$ and the substrate thickness is d = 1.59mm. The width of rectangular patch is W = 10.08mm with L = 11.79mm. The fed line is of the width $d_1 = 1.3mm$, $d_2 = 3.93mm$ with the length $L_1 = 12.32mm$, $L_2 = 18.48mm$. The interval between patches are $D_1 = 23.58mm$ and $D_2 = 22.40mm$, respectively. The frequency is 9.42 GHz. Four levels FDMA is used here, in which the lower two levels are non-directional while the top two levels are directional with eight directions for the top level and four directions for the lower level. The E-plane and H-plane radiation pattern which are observed at $\phi = 90^{\circ}$ are shown in Fig.2 (b). The result agree well with these obtained by Wang and Ling in [11]. \mathbf{E}_{θ} is due to the θ -polarized electric current element and \mathbf{E}_{ϕ} is due to the ϕ -polarized electric current element.

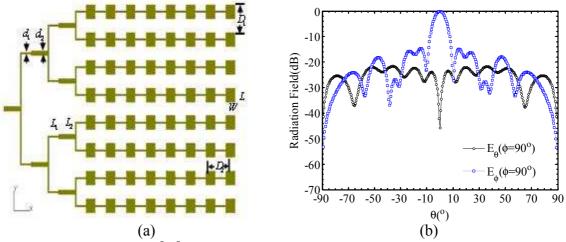


Fig. 2 (a) The geometry of $^{8\times8}$ microstrip corporate-fed planar array (b) The E-plane and the H-plane radiation patterns of the planar array are computed by four levels FDMA

The complexity analysis of FDMA

In this part, the complexity of this algorithm is computed. The CPU time per iteration and the memory requirement versus the number of unknowns are plotted in Fig.3. The geometries we concerned are microstrip patch antennas. It is can be seen that the CPU time per iteration and the memory requirement are all scaled as O (NLogN). According to the plots, the memory requirement is 41.158 MB and the CPU time per iteration is 3.375 s even for the microstrip patch antenna array involves 8192 triangle facets with 11264 unknowns. For the conventional MoM, the memory requirement is over 600 MB and the CPU time per iteration is 15.8 s for an antenna array which involves 6569 facets with 8668 unknowns [7].

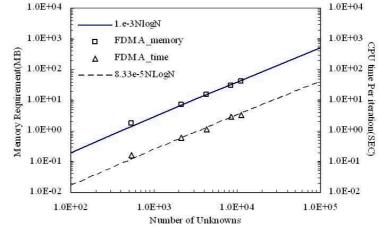


Fig. 3 Complexity of FDMA for memory requirement and CPU time per iteration

CONCLUSION

In this paper, the fast directional multilevel algorithm is applied for analyzing radiation from large finite arrays of microstrip antennas. With the aid of DCIM, the MPIE is discretized in the spatial domain. The new method is easily implemented because it is kernel independent. The complexity of the algorithm is scaled as O(NLogN). The efficiency and accuracy of this method is demonstrated by numerical results.

ACKNOWLEDGEMENTS

The author would like to thank Doctor Jiang Zhaoneng. for providing useful discussions and Prof. R.S.Chen for his useful instruction. Thank the support of the International S&T Cooperation Program of China (No. 2012DFA70570), the Yunnan Provincial International Cooperative Program (No. 2011IA004), Yunnan Provincial Foundation Program (No. 2013FZ016), the National Technology Research and Development Program of China(No. 2013AA064003), NSFC(No. 51304097).

References

- S. M. Rao, D. R. Wilton, and A. W. Glisson, "Electromagnetic scattering by surfaces of arbitrary shape," IEEE Trans. Antennas Propag., vol.30, no.3, pp.409-418, 1982.
- [2] D. G. Fang, J. J. Yang, and G. Y. Delisle, "Discrete image theory for horizontal electric dipoles in a multilayered medium," *Proc. IEEE*, *pt.H*, vol. 135, pp. 297-303, Oct. 1988.
- [3] Y. L. Chow, J. J. Yang, D. G. Fang, and G. E. Howard, "A closed-form spatial Green's function for the thick microstrip substrate," *IEEE Trans. Microwave Theory Tech.*, vol. 39, pp. 588-592, Mar. 1991
- [4] F. Ling, C. F. Wang, and J. M. Jin, "An efficient algorithm for analyzing large-scale microstrip structures using adaptive integral method combined with discrete complex image method," in *IEEE APS Int. Symp. Dig.*, vol. 3, 1998, pp. 1778-1781.
- [5] L. Gurel and M. I. Aksun, "Electromagnetic scattering solution of conducting strips in layered media using the fast multipole method," *IEEE Microwave Guided Wave Lett.*, vol. 6, pp. 277-279, Aug. 1996
- [6] P. A. Macdonald and T. Itoh, "Fast simulation of microstrip structures using the fast multipole method," Int. J. Numer. Modeling: Electron.Networks, Devices, Fields, vol. 9, pp. 345-357, 1996.
- [7] F. Ling, J. M. Song and J. M. Jin, "Multilevel fast multipole algorithm for analysis of large-scale microstrip structures," IEEE Microwave Guided Wave Lett., vol. 9, pp. 508-510, Dec. 1999.
- [8] B. Engquist, L. X. Ying, "Fast directional multilevel algorithms for oscillatory kernels," SIAM Journal on Scientific Computing, vol. 29, No. 4, pp. 1710-1737, 2007
- [9] H. Chen, K. W. Leung and Edward K.N. Yung, "Fast directional multilevel algorithms for analyzing wave scattering", IEEE Trans. Antennas Propag., vol. 59, no. 7, July, pp.962-974, 2011
- [10] H. Chen, "Efficient Analysis of Multilayer Microstrip Problems by Modified Fast Directional Multilevel Algorithm," has been accepted by Applied Computational Electromagnetics Society (ACES) Journal.
- [11] F. Ling, C. F. Wang, and J. M. Jin, "A fast full-wave analysis of scattering and radiation from large finite arrays of microstrip antennas," IEEE Trans. Antennas Propag., vol.46, no.10, pp.1467-1474, 1998.

The Analysis on Research Progress of the Typical Hybrid Routing Protocol in Ad Hoc Networks

Jing WU^{1,2,a}, Guo-Zhao HOU^{3,b}, Zhen-Guo CHEN^{1,c}, Li-Qin TIAN^{1,2,d}

¹College of Computer, North China Institute of Science and Technology, Yanjiao Hebei 101601, China

²College of Computer, Qinghai Normal University, Xining Qinghai 810008, China

³Department of Basic, Army Aviation Institution of PLA, Beijing 101123, China

^a99061632@163.com, ^bwonderh@yeah.net, ^czhenguo_chen@126.com, ^dtianliqin@ncist.edu.cn

Keywords: Ad hoc networks, Hybrid routing protocol, ZRP

Abstract. The research progress of the typical hybrid routing protocol (ZRP, Zone Routing Protocol) in ad hoc networks is analyzed, which includes the analysis on ZRP and the analysis on ZRP related research. This work can provide a reference of basic theory research of ZRP for experts and scholars. And it will get ready for the further research work in the future.

Introduction

Ad hoc network is a multi-hop and acentric network, which is temporarily composed of a series of mobile nodes with wireless transceivers. It can provide a communication supporting environment with no network infrastructure^[1]. In the network, each node has the function of host and router at the same time. The function of host refers to that the node can run some applications. The function of router refers to that the node can run the corresponding routing protocol in order to get some work done such as route discovery, route maintenance and packet forwarding^[2].

At present, ad hoc networks have become a hot research for experts and scholars at home and abroad. And flat routing protocol is one of the main research contents in ad hoc networks. According to the different route discovery schemes, flat routing protocols are divided into the following three kinds: proactive routing protocols, on-demand routing protocols and hybrid routing protocols. A hybrid routing protocol combines a proactive routing protocol and an on-demand routing protocol, which has a more extensive scope of application. In this paper, the research progress of the typical hybrid routing protocol (ZRP, Zone Routing Protocol) is analyzed, which includes the analysis on ZRP and the analysis on ZRP related research.

The Analysis on ZRP

Since application scenarios and network modes of ad hoc networks are in a wide range, it is very difficult to design a general routing protocol for all application scenarios. Many existing routing protocols are designed for network scenarios with a particular type, in which the protocol performances are the best. ZRP adopts a hybrid routing technology. It designs the framework for routing protocols, which combines basic routing protocols together to apply to all ad hoc networks^[3].

Based on a multi-range technology, the framework of a hybrid routing protocol (Zone Routing Framework) is proposed in ZRP. The proactive routing protocol is adopted in the intra-zone to maintain the routing information constantly. The on-demand routing protocol is adopted in the inter-zone to choose a route on demand. The size of a zone can be adjusted to adapt to the local or temporary network changes and to get the best network performance ^[3].

In this paper, we will use the example shown in Fig. 1 to illustrate the route discovery process of ZRP. The concrete description is as follows.

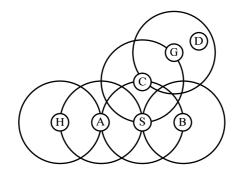


Fig.1 The route discovery process of ZRP

The source node *S* will send a packet to the destination node *D*. If *S* discovers that *D* is not in its routing zone, it sends a routing request to the boundary nodes such as *A*, *B*, *C* in its routing zone. If each boundary node discovers that *D* is not in its routing zone, it also forwards the routing query packet. When *C* sends the routing query packet to *G*, *G* discovers that *D* is in its routing zone. *G* returns a reply, which shows that the path from *S* to *D* is *S*-*C*-*G*-*D*^[3].

The Analysis on ZRP Related Research

In recent years, many experts and scholars carried out further researches on ZRP. The research contents include the improvement and application researches on ZRP.

The improvement researches on ZRP are described as follows. ZRP is improved on load balancing in literature [4]. On the basis of ZRP, a more flexible IZR is proposed in literature [5]. A ZRP-based secure and reliable route discovery scheme is proposed in literature [6], which improves route security by authentication mechanism. By taking the minimum total overheads, a configuration method of an optimal radius for ZRP is studied in literature [7]. The optimization strategy of cache mechanism for ZRP is researched in literature [8]. In literature [9], a velocity-based adaptive zone routing protocol is proposed, a node adjusts the size of its zone radius according to its velocity. In literature [10], a ZRP-based routing protocol (EZRP) is proposed, which reduces network load and improves network performance by reducing the number of useless control packets. In literature [11], an adaptive zone routing protocol (AZRP) is proposed, in which a node adjusts the size of its zone radius according to the ratio of routing overheads to total overheads produced itself. In literature [12], an effective zone routing protocol based on consideration of power consumption is proposed. In literature [13], a zone routing protocol with timer based caching technique is proposed. In literature [14], a secure zone routing protocol (SZRP) is proposed. Based on ZRP, SZRP introduces digital signal and integration method of symmetric and asymmetric key encryption technology, which has achieved some security goals such as information integrity, data confidentiality and end-to-end authentication for IP layer. In literature [15], a location aided ZRP (L-ZRP) in MANET is proposed. In literature [16], a routing protocol (T-ZRP) is proposed, which improves ZRP on power by referring to an energy saving algorithm based on judgment factor. In literature [17], the research and simulation on a new routing protocol (ZRP-DV), which is based on node density and node speed, is proposed. ZRP-DV makes node density and node speed as the main reference factors for dynamic radius adjustment.

The application researches on ZRP are described as follows. In literature [18], ZRP is applied to blue-tooth scatter networks. In literature [19], ZRP is applied to multicast routing. In literature [20], ZRP is applied to heterogeneous network scenarios. In literature [21], ZRP is applied to virtual backbone networks. In literature [22, 23], ZRP is applied to multi-path routing.

Conclusions

The research progress of the typical hybrid routing protocol (ZRP) in ad hoc networks is analyzed, which includes the analysis on ZRP and the analysis on ZRP related research. This work can provide

a reference of basic theory research of ZRP for experts and scholars. And it will get ready for the further research work in the future.

Acknowledgements

This work was financially supported by the Fundamental Research Funds for the Central Universities(3142014087,3142013098,2011B026),Natural Science Foundation of Qinghai Province of China (2012-Z-935Q, 2012-N-525), Key Prevention and Control Technology of Major Safety Accidents in Production(2013).

References

- [1] Z. Xiangquan. Practical tutorial of wireless ad hoc network technology. Tsinghua university press, 2004. (In Chinese)
- [2] W. Fangwei, Z. Yunkai, D. Zhenguo, et al. Research development of topology control strategies for wireless ad hoc networks. Computer Science, 2007, 34(10): 70. (In Chinese)
- [3] Y. Hongyi. Wireless mobile self-organized network. Posts and Telecom Press, 2005. (In Chinese)
- [4] T. Thongpook. Load balancing of adaptive zone routing in ad hoc networks. 2004 IEEE Region 10 Conference, 2004: 672-675.
- [5] P. Samar, M.R. Pearlman, Z.J. Haas. Independent zone routing: an adaptive hybrid routing framework for ad hoc wireless networks. IEEE/ACM Transactions on Networking, 2004, 12(4): 595-608.
- [6] K.J. Kim, T.M. Chang. A ZRP-based reliable route discovery scheme in ad-hoc networks. Proceedings of the International Conference on Security and Management, 2004: 325-331.
- [7] Z. Changlin, Z. Weidong, Y. Kuiwu. Zone routing protocol analysis and optimal radius configuration for wireless ad hoc networks. Radio Engineering, 2005, 35(1): 25-26, 49. (In Chinese)
- [8] W. Zhuolin. The catch scheme improvement of the mobile ad hoc network protocol-ZRP. The Master's Degree Thesis from Zhejiang University of Technology, 2005. (In Chinese)
- [9] J.Y. Zhou, Y.L. Cheng, J.L. Lu. Velocity based adaptive zone routing protocol. International Symposium on Intelligent Signal Processing and Communication Systems, 2007: 337-340.
- [10] A. Koyama, J. Arai, L. Barolli, et al. EZRP: an enhanced zone-based routing protocol for ad-hoc networks: research articles. Concurrency and Computation: Practice & Experience, 2007, 19(8): 1157-1170.
- [11]D. Qi. Research on an adaptive algorithm of zone routing protocol for ad hoc networks. The Master's Degree Thesis from Nanjing University of Science and Technology, 2007. (In Chinese)
- [12]Z. Hui. Research on an effective zone routing protocol based on consideration of power consumption. The Master's Degree Thesis from Xidian University, 2008. (In Chinese)
- [13] M. Tote, V. Gulhane. Timer based caching technique for zone routing protocol. The International Conference and Workshop on Emerging Trends in Technology, 2010: 1008.
- [14] N. K. Pani. A secure zone-based routing protocol for mobile ad hoc networks. A Thesis Report Submitted in Partial Fulfillment of the Requirements for the Degree of Master of Technology in Computer Science (Information Security), 2009.

- [15] S. Ronghua, L. Qifeng. Location-aided ZRP in MANET. Journal of Hunan University, 2009, 36 (8): 38-42. (In Chinese)
- [16] X. Xingfu, Z. Andong, Y. Lugang, et al. Applying energy-saving algorithm based on determine factor to ZRP protocol. Computer and Digital Engineering, 2010, 38(4): 33-35. (In Chinese)
- [17]H. Xiaoling. Ad hoc network routing protocol ZRP research and simulation. Computer knowledge and technology, 2010, 6(9): 2115-2118. (In Chinese)
- [18] R. Kapoor, M. Gerla. A zone routing protocol for bluetooth scatternet. 2003 IEEE Wireless Communications and Networking, 2003: 1459-1464.
- [19]X.F. Zhang, L.K. Jacob. Multicast zone routing protocol in mobile ad hoc wireless networks. Proceedings of 28th Annual IEEE International Conference on Local Computer Networks, 2003: 150-159.
- [20] X.F. Zhang, L.K. Jacob. Adapting zone routing protocol for heterogeneous scenarios in ad hoc networks. Proceedings of 2003 International Conference on Parallel Processing, 2003: 341-348.
- [21]J.L. Xu, H.Y. Wang. Zone routing with backbone for tactical network. 4th International Conference on Wireless Communications, Networking and Mobile Computing, 2008: 1-4.
- [22] Y. Ge, G.J. Wang, W.J. Jia, et al. Node-disjoint multipath routing with zoning method in MANETs. 10th IEEE International Conference on High Performance Computing and Communications, 2008: 456-462.
- [23]Z. Wu, Y. Sun, J.K. Wu, et al. Robust multi-path zone routing protocol for video transport over reconfigurable wireless networks. Journal of Signal Processing Systems, 2008, 51(2): 183-194.

Mobile Prediction Idea based Clustering Algorithm and Related Mathematical Quantitative Description

Jing WU^{1,2,a}, Tie-Jun SHAO^{1,b}, Zhen-Guo CHEN^{1,c}, De-Sheng CAO^{1,d}

¹College of Computer, North China Institute of Science and Technology, Yanjiao Hebei 101601, China

²College of Computer, Qinghai Normal University, Xining Qinghai 810008, China ^a99061632@163.com, ^b834564106@qq.com, ^czhenguo_chen@126.com, ^dcds@ncist.edu.cn

Keywords: Clustering algorithm, Mobile prediction, Stability

Abstract. Mobile prediction idea refers to predicting link expiration time with relative velocity and relative position between different nodes. In ad hoc networks, mobile prediction idea is adopted in MSWCA, and cluster stability is measured by link expiration time. MSWCA only considers on intra-cluster stability, and neglects inter-cluster stability. Aiming at the above problem, MPICA (Mobile Prediction Idea based Clustering Algorithm) was proposed. Firstly, involved concepts were given with mathematical quantitative description. Secondly, the realization process of MPICA was described. Lastly, the complexity of MPICA was analyzed. MPICA considers intra-cluster and inter-cluster stability at the same time, which is in favor of improving cluster stability and reducing cluster maintenance overheads.

Introduction

In ad hoc networks, MSWCA is an improved algorithm for combination degree based clustering algorithm WCA^[1,2]. The basic idea is described as follows. We consider on some factors such as load balancing, power energy and stability, and the total weight value is obtained by using a weighted combination of various factors. The node with the maximum weight value is chosen as a cluster head, and then clustering is conducted. Here, cluster stability is measured with link expiration time. The link expiration time is computed with a mobile prediction method ^[3,4], and obtained by comprehensively considering on motion velocity and motion position ^[5]. The computation method for a total weight value W_i of node *i* is shown in Eq.1.

$$W_i = -w_1 (C_i - K)^2 + w_2 P_i + w_3 T_i$$
(1)

Among them, w_j (j = 1,2,3) is the corresponding weight value of each factor, which can be set with an initial value in advance and can be dynamically adjusted. C_i is the number of neighbor nodes of node *i*. *K* is the ideal number of neighbor nodes. If $C_i = K$, this factor takes the minimum value, otherwise it increases in parabola way. The smaller the value of this factor is, the more beneficial to reduce the loads of a cluster head, reduce the energy consumption of a cluster head and extend the life cycle of a cluster. P_i is the battery power of a node. The greater the value of this factor is, the more beneficial to extend the lifespan of a cluster head. T_i is the cumulative sum of link expiration times between the node and all of its neighbor nodes. The link expiration time adopts mobile prediction method, and it is computed with relative position and relative velocity between different nodes, which measures the maintaining time after a node becomes a cluster head. The greater the value of this factor is, the smaller the possibility for the neighbors of a node moving out of its coverage is, the longer the maintaining time after a node becomes a cluster head is, the higher the stability is^[5].

Cluster stability includes intra-cluster and inter-cluster stability. They will make important influence on clustering performance. So they should be paid attention at the same time. MSWCA only

considers on intra-cluster stability with a cumulative sum of link expiration times between a cluster head and all of its neighbors, and neglects to consider on inter-cluster stability. Aiming at the above problem, MPICA (Mobile Prediction Idea based Clustering Algorithm) is proposed in this paper. MPICA considers intra-cluster and inter-cluster stability at the same time, which is in favor of improving cluster stability and reducing clustering maintenance overheads.

Related Mathematical Quantitative Description

Here, some concepts involved in MPICA are given with mathematical quantitative description.

Definition 1 (Virtual Cluster): Before clustering, each node constructs a virtual cluster in which the cluster head is itself and the cluster members are all of its neighbor nodes.

Definition 2 (Total Connectivity): Refers to the total number of all connections in intra-cluster or inter-cluster. In this paper, we research on *VIATC* (Virtual IntrAcluster Total Connectivity) and *VIETC* (Virtual IntErcluster Total Connectivity), which are taken as properties for the creator *i* of a virtual cluster. The calculation methods are shown separately in Eq.2 and Eq.3.

$$VIATC(i) = |N(i)|.$$
⁽²⁾

$$VIETC(i) = \sum_{j \in N(i)} |N(j) - N(i) - \{i\}|.$$
(3)

Among them, N(i) and N(j) are neighbor sets of *i* and *j* respectively. |N(i)| and $|N(j) - N(i) - \{i\}|$ are the number of set elements.

Definition 3 (Link Expiration Time): LET (Link Expiration Time) is proposed from a mobile prediction idea. It predicts maintaining time of the connection between any two nodes according to the effective transmission distance, position and velocity of each node. The calculation method is shown in Eq.4.

$$LET(i,j) = \left(-(ab+cd) + \sqrt{(a^2+c^2)r^2 - (ad-bc)^2} \right) / \left(a^2+c^2\right)$$
(4)

Among them, $a = v_i \cos \theta_i - v_j \cos \theta_j$, $b = x_i - x_j$, $c = v_i \sin \theta_i - v_j \sin \theta_j$, $d = y_i - y_j$, r is the effective transmission distance of i and j, (x_i, y_i) and (x_j, y_j) are coordinates of i and j respectively. v_i and v_j are average velocities of i and j respectively, θ_i and θ_j ($0 \le \theta_i, \theta_j \le 2\pi$) are average velocity directions of i and j respectively^[6]. If $v_i = v_j$ and $\theta_i = \theta_j$, which means that i and j are in the same direction, then $LET(i, j) \rightarrow \infty$. The two nodes can always keep connecting. If LET(i, j) < 0, the two nodes can not connect. If LET(i, j) > 0, the two nodes can connect. The larger LET(i, j) is, the longer the connection between the two nodes can maintain for ^[6].

Definition 4 (Total LET): Refers to a sum of expiration times of all connections in intra-cluster and inter-cluster. In this paper, we research on *VIATLET* (Virtual IntrAcluster Total LET) and *VIETLET* (Virtual IntErcluster Total LET), which are taken as properties for the creator *i* of a virtual cluster. The calculation methods are shown separately in Eq.5 and Eq.6.

$$VIATLET(i) = \sum_{j \in N(i)} LET(i, j).$$
(5)

$$VIETLET(i) = \sum_{j \in N(i)} \sum_{k \in \{N(j) - N(i) - \{i\}\}} LETHash(j,k).$$
(6)

Among them, LET(i, j) is link expiration time between *i* and its neighbor node *j*. *LETHash* is a hash table that saves link expiration times. *LETHash*(*j*,*k*) is a key value corresponding to the key name *k*, which is link expiration time between *j* and *j*'s neighbor node *k*.

Definition 5 (Average LET): Refers to an average value of all link expiration times, which is the ratio of total LET and total connectivity. In this paper, we research on *VIAALET* (Virtual IntrAcluster Average LET) and *VIEALET* (Virtual IntErcluster Average LET), which are taken as properties for the creator *i* of a virtual cluster. The calculation methods are shown separately in Eq.7 and Eq.8.

$$VIAALET(i) = VIATLET(i)/VIATC(i).$$
⁽⁷⁾

$$VIEALET(i) = VIETLET(i)/VIETC(i).$$
(8)

Definition 6 (Property Superiority Degree): Refers to the superiority degree of a property of a node in the same properties of the node and all of its neighbors, which is a comparative value between a property value of a node and average value of the same properties of the node and all of its neighbors. In this paper, we research on three property superiorities including $SD_{VIAALET}$ (VIAALET Superiority Degree), $SD_{VIEALET}$ (VIEALET Superiority Degree) and SD_{VIATC} (VIATC Superiority Degree), which are taken as properties for the creator *i* of a virtual cluster. The calculation methods are shown separately in Eq.9, Eq.10 and Eq.11.

$$SD_{VIAALET}(i) = VIAALET(i) / \left(\sum_{j \in N(i) \cup \{i\}} VIAALET(j) / |N(i) \cup \{i\}| \right).$$
(9)

$$SD_{VIEALET}(i) = VIEALET(i) / \left(\sum_{j \in N(i) \cup \{i\}} VIEALET(j) / |N(i) \cup \{i\}| \right).$$
(10)

$$SD_{VIATC}(i) = VIATC(i) / \left(\sum_{j \in N(i) \cup \{i\}} VIATC(j) / |N(i) \cup \{i\}| \right).$$

$$(11)$$

Definition 7 (Total Superiority Degree): Refers to the total superiority degree of a node in a set consisting of the node and all of its neighbors. It's comprehensively formed by some property superiority degrees. Based on a clustering scheme of combination degree, the weight value of each property superiority degree is set according to important degree in a particular scenario. The weight values are comprehensively controlled. In this paper, we research on *TSD* (Total Superiority Degree), which is comprehensively formed by three property superiority degree including *SD*_{VIAALET}, *SD*_{VIEALET} and *SD*_{VIATC}. *TSD* is taken as a comprehensive property for the creator *i* of a virtual cluster. The calculation method is shown in Eq. 12. Among them, $0 \le w \le 1$ and $\sum_{i=1}^{3} w_{i} = 1$

calculation method is shown in Eq.12. Among them, $0 \le w_i \le 1$ and $\sum_{i=1}^{3} w_i = 1$.

$$TSD(i) = w_1 SD_{VIAALET}(i) + w_2 SD_{VIEALET}(i) + w_3 SD_{VIATC}(i).$$
⁽¹²⁾

Realization Process of MPICA

Initializing Process. In initializing process, the main goal is to complete the *TSD* calculation and provide the basis for clustering. *TSD* calculation needs to exchange three rounds of control packets between each node and its neighbors. Finally, each node and its neighbors exchange one round of control packets to get the *TSD* information of its neighbors.

Clustering Process. In clustering process, clustering is conducted by electing each cluster head on the basis of maximum *TSD*. If a node and its neighbors have the maximum *TSD* at the same time, the node with the minimum node *id* is chosen as a cluster head.

Complexity of MPICA

The communication complexity of MPICA is analyzed as follows.

(1) During the initializing process, each node sends four messages to all of its neighbor nodes including three messages sent during *TSD* is computed and one message sent during *TSD* is exchanged. Assuming that there are N nodes in the network, they send a total of 4N messages during the initializing process. (2) During the clustering process, each cluster head sends a Cluster message to all of its neighbor nodes, each cluster member sends p Join messages on average to all of its neighbor nodes. Assuming that there are x cluster heads in the network, and there are N - x cluster members. They send a total of $x + (N - x) \bullet p messages during the clustering process.(3) During the initializing process and clustering process, all the nodes send a total of$ *Total* $<math>< 4N + p \bullet N$, that is *Total* $< (4 + p) \bullet N$, messages. In conclusion, the communication complexity of MPICA is O(N).

Conclusions

Mobile prediction idea refers to predicting link expiration time with relative velocity and relative position between different nodes. In ad hoc networks, mobile prediction idea is adopted in MSWCA, and cluster stability is measured by link expiration time. MSWCA only considers on intra-cluster stability, and neglects inter-cluster stability. Aiming at the above problem, MPICA is proposed. Firstly, involved concepts are given with mathematical quantitative description. Secondly, the realization process of MPICA is described. Lastly, the complexity of MPICA is analyzed. MPICA considers intra-cluster stability at the same time, which is in favor of improving cluster stability and reducing cluster maintenance overheads.

Acknowledgements

This work was financially supported by the Fundamental Research Funds for the Central Universities(3142014087,3142013098,2011B026),Natural Science Foundation of Qinghai Province of China (2012-Z-935Q, 2012-N-525), Key Prevention and Control Technology of Major Safety Accidents in Production(2013).

- [1] M. Chatterjee, S. K. Das, D. Turgut. An on-demand weighted clustering algorithm (WCA) for ad hoc networks. Proceedings of IEEE Globecom'00, 2000: 1697–1701.
- [2] M. Chatterjee, S.K. Das, D. Turgut. WCA: a weighted clustering algorithm for mobile ad hoc networks. Cluster Computing, 2002, 5(2): 139-204.
- [3] W. Su, S.J. Lee, M. Gerla. Mobility prediction in wireless networks. Proceedings of 21st Century Military Communications Conference, 2000: 491-495.
- [4] R. Chellappa, A. Jennings, N. Shenoy. A comparative study of mobility prediction in fixed wireless networks and mobile ad hoc networks. IEEE International Conference on Communications, 2003: 891-895.
- [5] H. Weihong, L. Renfa, P. Xianwu. Clustering algorithms for wireless self-organized networks based on mobile holding time. Micro-computer Information, 2007, 23(9): 95-96,119. (In Chinese)
- [6] J. Yi, S. Haoshan. An adaptive clustering algorithm based on mobility prediction in ad hoc networks. Computer Science, 2007, 34(3): 28-29. (In Chinese)

CHAPTER 6:

Mechatronics, Control and Automation

Design of Coal Mine Main-fan Automatic Monitoring System Based on ZigBee

Hongquan Zhang^{1,a}, Zihong Zhang^{1,b}

¹College of Electronics and Information Engineering, Heilongjiang University of Science and Technology, Harbin, Heilongjiang Province, China

^adaqingzhq@163.com, ^bzzhzlcgc@163.com

Keywords: coal mine main-fan, wireless sensor network, automatic monitoring, CC2430

Abstract. The existing wired monitoring systems for coal mine main-fan has some shortcomings such as complex working environment, bad flexibility and low reliability and so on. This paper developed a main-fan automatic monitoring system based on wireless sensor network with ZigBee technology, including monitoring host, sensor node, coordinator node and several data acquisition sensor. In order to meet requirements of coal mine environment monitoring signals, CC2430 is chosen as master control chip. The system achieved functions of automatic monitoring of coal mine main-fan supported by ZigBee technology, which is stable, low power consumption, and has practical value and bright development prospect.

Introduction

Mine ventilation system is the key equipment in coal production, shoulder the important task of the discharge of harmful gas, transportation of fresh air to the mine, and keep the safety of coal mine [1]. Main-fan is usually in the long-term continuous operation of the state, if the ventilation system is out of the question, the underground staffs' lives and safety and the economy of the country can suffer a huge loss. Now there are many mature coal mine ventilator monitoring systems, but the traditional monitoring systems mostly use the way of cable network, suffer coal mine site clutter, poor environment, and the equipment is easily damaged as a result of frequent disassembly. These problems can easily lead to the reliability of data transmission and real-time difference; it is difficult to achieve effective transmission and early warning monitoring data. Wireless sensor network technology is becoming more sophisticated, and provides a new approach for automatic monitoring of coal mine main-fan.

ZigBee Wireless Sensor Network

Wireless sensor network is a wireless communication technology for various electronic devices within a short distance, low data transmission rate [2]. Sensor nodes are distributed throughout each part of wireless sensor network, not only to be responsible for monitoring data acquisition, and have dual functions as routing node, in addition to collect local information, simply processing and memory, but also to store and manage the data coming from other nodes. The monitoring data can be processed by one or more nodes when the sensor nodes transport hop by hop, through the coordination of some sensor nodes, multi hop routing to the coordinator node. The coordinator node is used to connect the wireless sensor network and external network, the whole area of the data to the monitoring host computer for centralized processing analysis, at the same time to issue instructions to the wireless sensor network.

Traditional wired monitoring system is mainly composed of sensors, station, master station, monitoring host, transfer medium usually use cable [3,4]. In view of coal mine complex work environment, low reliability of traditional wired monitoring system, the cable between monitoring station and sensors are replaced by ZigBee wireless network.

General design of the monitoring system

The system consists of the monitoring host, a ZigBee coordinator node, multiple sensor nodes and wind speed sensor, pressure sensor, vibration sensor, the temperature sensor and methane sensor, the general structure is shown in Fig. 1. The monitoring host and coordinator nodes are connected by serial interface, the coordinator and each sensor node form a ZigBee star network. The coordinator is responsible for receiving data from each sensor node, and the data are sent to the monitoring host computer through the serial port for real-time display.

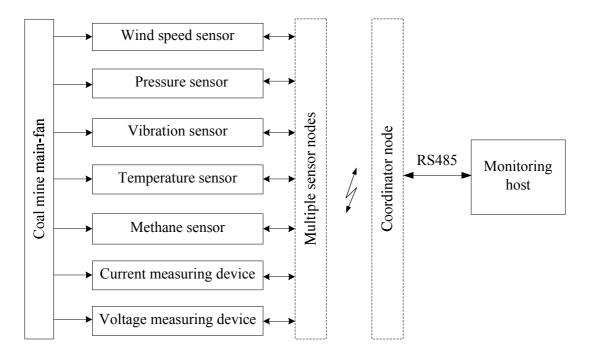


Fig. 1 Diagram of the monitoring system

Design of system network nodes hardware

The design of wireless sensor network node needs to consider the chip cost, the difficulty of system development. Choosing the right chip and development environment can help to reduce development costs and shorten the development cycle. The CC2430 use an industry-standard enhanced 8051 MCU. Therefore, this system uses CC2430 as the main control chip.

Sensor node design. Hardware block diagram of wireless sensor nodes is shown in Fig. 2, the system consists of CC2430 main control chip, data acquisition module, antenna interface module, key control module and power conversion module.

The CC2430 combines the excellent performance of the leading CC2420 RF transceiver with an industry-standard enhanced 8051 MCU, 32/64/128KB flash memory, 8KB RAM and many other powerful features [5]. Combined with the industry leading ZigBee protocol stack from Texas Instruments, the CC2430 provides the market's most competitive ZigBee solution. The CC2430 is highly suited for systems where ultra low power consumption is required. This is ensured by various operating modes. Short transition times between operating modes further ensure low power consumption.

Data acquisition module mainly consists of various sensors, because the CC2430 chip holds analog digital conversion function, without the need for external analog to digital conversion design, and can connect with multiple sensors as the terminal data acquisition equipment._But the choice of sensors needs to consider the actual working conditions, such as power, precision, interference and

so. Pressure sensor using industrial grade B0300 micro pressure transmitter, generally used for the measurement of differential pressure, pressure, negative pressure, has the advantages of long service life, being affected by small dynamic pressure, allowing to be installed outdoors and other excellent characteristics. Vibration sensor using HS-421 acceleration sensor, the output is proportional to the velocity and acceleration of the exchange. Use PT100 as temperature sensor, the sensor with platinum resistance as temperature sensing element, which is characterized by sensitive reaction, high measurement accuracy, stable performance. Power conversion module uses the DC/DC power module BSD-24D15, power conversion chip LM2576, amplifier on using LM324 chip. Key module realizes communication control and reset functions with coordination nodes.

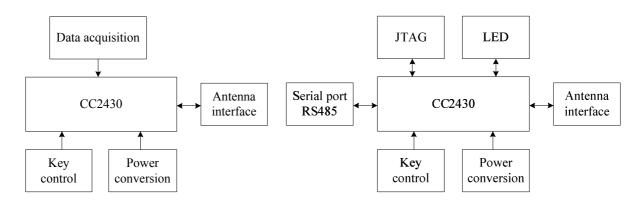


Fig. 2 Sensor node diagram

Fig. 3 Coordination node diagram

Coordination node design. The coordinator node connecting the sensor network and external cable network, realizes the communication protocol conversion between the two systems, delivers a monitoring task of the server at the same time, and sends the collected data to the external cable network. As sensor nodes, the coordinator node uses CC2430 as the core, the hardware circuit consists of CC2430 main control chip, antenna interface module, power conversion module, a key control module, serial port module, JTAG debugging interface module and LED indicating module, as shown in Fig. 3.

Design of system software

The sensor node is responsible for collecting parameters of monitoring area, the collected data are processed, and sent to the coordinator node by the antenna interface module. When the coordinator node data request command, data collection and transmission are carried out. If not, it will be into a sleep mode to reduce energy consumption. The sensor node software design process is shown in Fig. 4.

The coordinator node is the central node of wireless sensor network, which is responsible for creating the network, the allocation of network address, reading the information from terminal node and routing node, and sending the information to the monitoring host. The coordinator node software design process is shown in Fig. 5.

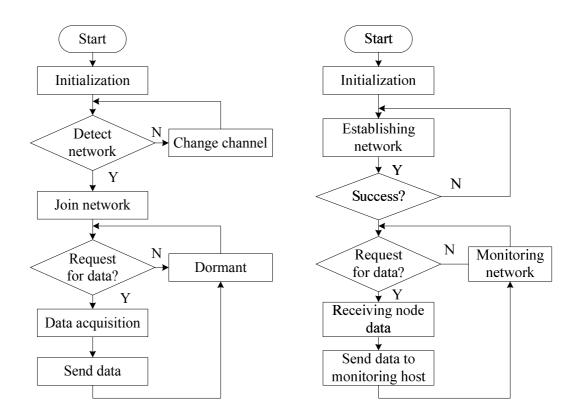


Fig. 4 Software flow chart of sensor node

Fig. 5 Software flow chart of coordinator node

Summary

This paper presents an automatic monitoring system based on ZigBee technology in coal mine main-fan, which has simple network, small overhead, self-organizing ability, and is very suitable for coal mine special environment. To guarantee the safe and reliable operation of man-fan, reliable scientific basis for management and repair equipment are provided. The application of ZigBee technology will enable the monitoring system of coal mine main-fan automation to be more networked and intelligent.

- [1] Xin Yan, Peng Dai, Zi-yan Wan: Research and Application of Monitoring System of Mine Ventilation Fan, Coal Mine Machinery. Vol. 34, No.04 (2013), p237-239 (in Chinese)
- [2] Akyildiz I F, Weilian S, Sankarasubramaniam Y, et al: A survey on sensor networks, IEEE Communications Magazine, Vol.40(2002), p102-114
- [3] Xuequan Chen, Zhigang Sun, Li Xiao: Design of ZigBee based wireless sensor node in underground coal mine, Modern Electronics Technique, Vol. 36,No. 24(2003), p118-121 (in Chinese)
- [4] Lei Ma, Yan Zhao: Application of ZigBee Technology in Coal Mine Monitoring System, Industrial Control Computer. Vol. 26, No.10 (2013), p41-42 (in Chinese)
- [5] Information on http://www.ti.com/product/cc2430

Chaotic Decision Model in the Collaborative Decision of Command and Control System

Xiao Yujie^{1, a}, Zhang Dingxiong^{2, b} and Shi Zhangsong^{1, c}

¹ Naval University of Engineering, Wuhan, 430033, China

² Naval Equipment and technology Institute, Beijing 100072, China

^axiaoyujie19870502@163.com, ^b285400807@qq.com,^cshizhangsong@163.com

Keywords: Cooperative Combat, Mathematical Model, Objective Optimization, Task Model.

Abstract. In order to explore the method of collaborative decision of command and control, first of all, the relationship between chaotic decision and collaborative decision is compared, the complexity and chaos of the system of collaborative decision is discussed from the theoretical level, on this basis, chaos characteristics of decision system is described by Li - York theorem.

Introduction

System decision refers to using systems engineering approach to analyze decision-making factors, analyze and evaluate a number of possible schemes, compare advantages and disadvantages of various schemes, and choose the best solution in order to achieve system goals. Decision-making process of the system is shown in Figure1 .Command and control system itself is a complex system. The performance of the complexity can be shown in its uncertainty and complexity of environments, multi-level characteristic of decision-making systems, multi-unit, multi-function and multi-target, nonlinear, uncertainty, non-deterministic non-equilibrium and chaos of predicted and control system, the interaction between various factors and the complexity of environment in the process of self-organization^[1].Chaos theory and coordination theory are important self-organization methods. Complex system is chaotic and synergistic unity of opposites. The complexity and chaos of decision-making system is the basis and premise of the collaborative command and control system studies. This paper compares the relationship between chaos and individual decision-making, group decision-making, collaborative decision-making and points out that the decision-making method of chaotic of multi-units can be applied in collaborative decision-making process to dynamically make cooperative schemes.

Chaos Decisions

In 1963, the American meteorologist Lorentz combined their practice observation, comprehends by analogy and made famous Chaos Theory. Military theorist Clausewitz describes it: three-quarters of the war is seemed to hidden in the mist, which is always a sea of chaos.

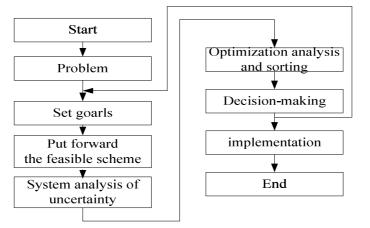


Figure 1 The decision process of system

Information era, "Bounded rationality" decision model proposed by Herbert Simon will have even more extraordinary value. There is a famous parable about the ants in Simon's study: An ant on the beach crawls to nest, it only knows the general direction of the nest, but the specific route cannot be expected, so it leaves a tortuous trajectory. This illustrates the complexity of coast and limited vision of ants.

Simon likened ants to decision makers, believes that makers' cognitive ability is limited. In a complex environment, makers cannot make the best decisions, and only make the most satisfiable decisions. Simon's "bounded rationality" decision model is a chaotic decision-making^[2].

Relationship between Decision-making and collaborative Chaos Decision

Literature [3] describes the relation and distinction of collaborative decision-making and individual decision-making, group decision-making. Chaos decision-making can be understood as directed against the complexity of the problems and limitations of decision-making subject's cognitive combat units, and seek a satisfactory solution for dynamic decision-making. Table 1 shows the comparison of four decision-making.

	1			0		
name	constitute	relationship	cooperative conditions	the form of solution	results	
individual decision-making	one unit	non	non	optimal , satisfied, or no inferior	dynamic	
group decision-making	multi-units	parallel relationship	rule	optimal or satisfied	static	
chaotic decision-making	one unit or multi-units	non or hierarchical relationship	non or mechanism rule	satisfied	dynamic	
collaborative decision-making	multi-units	hierarchical relationship	non or mechanism rule	optimal or non inferior	dynamic	

Table 1 Comparison of four decision-making methods

Chaotic mathematics description of collaborative decision systems

Suppose the scheme given by make decision system for time *i* is F_i , and time *i*+1 is F_{i+1} . Scheme F_{i+1} has both hereditary and variability, which is relative to scheme F_i . Hereditary and variability can be described by integrated control parameters $r \cdot F_{i+1}$ and F_i exist the following relationship^[4]:

$$F_{i+1} = f(r, F_i) \tag{1}$$

Dynamic optimizing process of the decision scheme is limited by internal and external constraints. Assuming the best scheme can be represented by F_{best} , the space of optimization is $F_{best} - F_i$. So the formula (1) can be rewritten as following:

$$F_{i+1} = r \cdot F_i \left(F_{best} - F_i \right) \tag{2}$$

Then,

$$\frac{F_{i+1}}{F_{best}} = rF_i \left(1 - \frac{F_i}{F_{best}}\right)$$
(3)

$$\frac{F_{i+1}}{F_{best}} = rF_{best} \frac{F_i}{F_{best}} \left(1 - \frac{F_i}{F_{best}}\right)$$
(4)

Assuming
$$\omega_i = \frac{F_i}{F_{best}}$$
, so $\omega_{i+1} = rF_{best}\omega_i(1-\omega_i)$ (5)

$$\boldsymbol{\omega}_{i+2} = rF_{best}\boldsymbol{\omega}_{i+1}(1-\boldsymbol{\omega}_{i+1}) = rF_{best}\left[rF_{best}\boldsymbol{\omega}_i(1-\boldsymbol{\omega}_i)\right]\left[1-rF_{best}\boldsymbol{\omega}_i(1-\boldsymbol{\omega}_i)\right]$$
(6)

 ω_i is called by the degree of optimal realization of scheme, which can reflect the distance degree from scheme F_i to F_{best} , in which $\omega_i \in [0,1]$.

Theorem 1(Li - York theorem)^[5-10]: Assuming that f(x) is a continuous function $x \in [0,1]$, and the following inequality can be stratified, f(x) is chaotic in interval [0,1].

$$f^{3}(x) \le x < f(x) < f^{2}(x) \text{ or } f^{3}(x) \ge x > f(x) > f^{2}(x)$$
 (7)

In the above formula $f^3(x) = f(f^2(x)), f^2(x) = f(f(x)).$

According to this theorem, we can know that formula (6) meets the condition of formula (7).

So dynamic optimizing process of collaborative decision-making meets the theorem of Li - York Theorem, which can prove the decision-making system is chaotic. System dynamic behavior is constrained by the environment; on the other hand, it mainly depends on the interaction of nonlinear factors.

Summary

In this paper, first of all, the relationship between chaotic decision-making and collaborative decision-making are compared, the complexity and chaos of the system of collaborative decision are discussed from the theoretical level, on this basis, chaos characteristics of decision system is described by Li - York theorem. From then on, we can use the methods of chaos theory to analysis and research the collaborative decision of command and control system.

- [1] Aseem K. N., Herbert K.. A macro-institutional perspective on supply chain environment complexity. International Journal of Production Economics, Vol.2, pp.283-295, 2008.
- [2] Zhang X. C.. Decision across the chaos. The PLA Daily, Beijing, July 2013.
- [3] Bu X. J. Modeling and Analysis Military Organization Cooperation. Beijing: Defense industry press, 2009.
- [4] Zhang H., Zhang T.N., Shen J.H.. Research on Characteristics of Chaos in Enterprise Strategic System and Chaos Management. International Conference on Management Science and Engineering, pp.393-399, September 2008.
- [5] Zhang H.. Optimization of collaborative mechanism of enterprise strategy. Economic Science Press, Beijing, 2010.
- [6] Frantisek P. K., Tadashi K. T., Stanislav C. P.. Explanation of appearance and characteristics of intermittency chaos of the impact oscillator. Chaos, Solitons and Fractals, Vol.5, pp. 1251-1259, 2004.

- [7] Tracey E. R. Z. Laura K. Cricis Management in the Wake of Hurricane Katrina .Professional Psychology Research and Practice, Vol. 2, pp.77-85,2008.
- [8] Wang D.L., Song X. F.. Study on the Complexity of Enterprise Strategy and a Strategic Design Model . Science & Technology Review, Vol. 9,pp.65-69,2007.
- [9] Mark M. C.. A discrete time car following model and the bi-parameter logistic map. Communications in Nonlinear Science and Numerical Simulation, Vol.1, pp.233-243,2009.
- [10] Marcelo A.. Effects of randomness on chaos and order of coupled logistic maps. Physics Letters A, Vol. 5, pp. 389-395,2007.

Effectiveness Evaluation Model for Collaborative Command and control System

Xiao Yujie^{1, a}, Qiu Zhiming^{2, b} and Shi Zhangsong^{1, c}

¹Naval University of Engineering, Wuhan, 430033, China

²System Divisions, Naval Equipment Institute, Beijing 100161, China

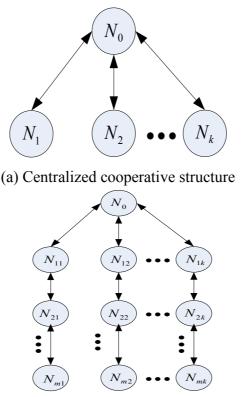
^axiaoyujie19870502@163.com,^bqiuzhiming280@sohu.com,^cshizhangsong@163.com

Keywords: Effectiveness Evaluation, Collaborative Command and Control System, Information Entropy, Structure Entropy.

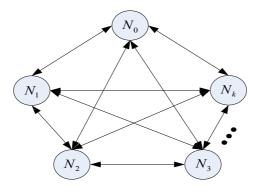
Abstract. Based on the theory of information and structure entropy, this paper analyses the influence of collaborative command and control system on information flow. Two concepts, time-effect and equality of information flow, are introduced, and the time-effect quality model is established, which can be used for evaluating the order degree of collaborative command and control system. Centralized, recursive and network cooperative structure and its time and space complexity respectively discussed. Study has shown that the recursive cooperative structure under the control of the command center is a relatively good structure.

Introduction

All the command and control system contain information processing, control procedure is the process of access to information, delivery, transform, application. So whether the information structure of the combat organization has enough information channel or not is its prerequisites. If it can meet the corresponding information structure condition, command and control system are called to be able to communicate ^[1-2]. At present, there are 3 main types of the tactical command and control structure, as shown in figure 1.



(b) Recursive cooperative structure



(c) Network cooperative structure Figure 1 3 types of the tactical command and control structure

Effectiveness Evaluation Model Based on Information and Structure Entropy

System time-effect and information entropy

System time-effect can represent the degree of uncertainty of the flow of information during the transfer process between element and element in the system. And information entropy can represent the degree of uncertainty of system time-effect during the transfer process between element and element in the system. So in this paper, the degree of time-effect can be instead of calculating the degree of information entropy. References [3-4] have given the detailed calculation of information entropy, so its method of calculation has been not written up due to the limited space.

System equality and structure entropy

System equality can represent the degree of accuracy of the flow of information between element and element in the system. And structure entropy can represent the degree of uncertainty of information equality. So in this paper, the degree of system equality can be instead of calculating the degree of s entropy. References [5-6] have given the detailed calculation of structure entropy, so its method of calculation has been not written up due to the limited space.

Simulation Analysis

It can be got the relationship between complexity and different collaborative structure, which is as

shown in Table 1. It can be also got the information order degree R_1 , structure order degree R_2 and

its related parameters based on the method of calculating the theory of information entropy and structure entropy, which is as shown in Table 2. The simulation result is as shown in Table 3,

When m = 2, k = 5.

It can be saw that the recursive cooperative structure under the control of the command center is a relatively good structure, which is very suitable for collaborative Command and control System, according to analysis the Table 1, Table 2 and Table 3.

complexity collaborative structure	information order degree	structure order degree	
centralized structure	<i>k</i> (<i>k</i> +1)	<i>k</i> +1	
recursive structure	mk(mk+1)	mk+1	
network structure	k^2	<i>k</i> + 1	

Table 1 The relationship between complexity and different collaborative structure

Table 2 The information, structure order degree and its related parameters

type		centralized		network
		cooperative	recursive cooperative structure	cooperative
entropy	ropy structure			structure
information order degree	R_1	$1 - \frac{1}{k} - \frac{(k-1)\ln k^2}{k\ln 2k^2}$	$\frac{mk}{A_1}\left(\frac{m(m+1)}{2}-\frac{\ln(2^2\cdot 3^3\cdot m^m)}{\ln A_1}\right)$	$1 - \frac{\ln(k+1)}{\ln k(k+1)}$
	$\frac{dR_1}{dk}$	>0	-	$\frac{dR_1}{dk} > 0$
	$\lim_{k\to\infty}R_1$	0	-	$\frac{1}{2}$
structure order degree	<i>R</i> ₂	$\frac{1}{2} - \frac{\ln 2}{2 \ln 2k}$	$1 - \frac{\ln 2m}{2m\ln 2mk} - \frac{(m-1)\ln mk}{m\ln 2mk} - \frac{1}{2m}$	$1 - \frac{\ln(k+1)}{\ln k(k+1)}$
	$\frac{dR_2}{dk}$	<0	$\frac{\partial R_2}{\partial m} < 0 , \frac{\partial R_2}{\partial k} < 0$	$\frac{dR_2}{dk} > 0$
	$\lim_{k\to\infty} R_2$	$\frac{1}{2}$	$\lim_{k \to \infty} R_2 = \frac{1}{2m},$ $\lim_{m \to \infty} R_2 = 0, \lim_{\substack{m \to \infty \\ k \to \infty}} R_2 = 0$	0

complexity collaborative structure	information order degree	structure order degree
centralized structure	0.1417	0.3495
recursive structure	0.1802	0.2500
Network structure	0.4732	0.4732

Table 3 The relationship between complexity and different collaborative structure

Summary

It is very important for collaborative Command and control System to research the method of Effectiveness Evaluation. Based on the theory of information and structure entropy, this paper analyses the influence of collaboration system on information flow. Two concepts, time-effect and equality of information flow, are introduced, and the time-effect quality model is established, which can be used for evaluating the order degree of collaborative command and control system. Centralized, recursive and network cooperative structure and its time and space complexity respectively discussed. Study has shown that the recursive cooperative structure under the control of the command center is a relatively good structure.

- [1] Bu X. J. Modeling and Analysis Military Organization Cooperation. Beijing: Defense industry press, 2009.
- [2] Zhou F. Liu Z. Wu L. Intelligent Command and Control System. Beijing: Defense industry press, 2013.
- [3] Zhang Z. G., Huang W. W., Yu M. Evaluation Analysis of Top Structure of Command System based on Entropy Theory. Fire Control & Command Control, vol. 6, pp. 73-75, 2010.
- [4] Ji P. W., Zhang X. G. Research on description and evaluation of command operational system of troops based on entropy theory. Inner Mongolia University 2012.
- [5] Tan, C.Q., Wang K.. Effectiveness Evaluation Model for Command Network System of Digitized Forces. Fire Control & Command Control, Vol. 6, pp. 65-69,2003.
- [6] Cao J., Bai J. L.. Evaluation of C4ISR system based on structure entropy. ELECTRONICS OPTICS & CONTROL, Vol. 2, pp. 85-88, 2007.

Design The PCI Bus Servo Control Card Based On The PCI9052

Wenlan Guo^{1, a}, Haijiao Xing^{1,b} and Xiaonan Dong^{1,c}

¹College of Computer Science and Technology, Harbin University of Science and Technology, Harbin, 150080, China

^aguowenlan@sohu.com, ^b417048772@qq.com, ^cfengyunxiaohan@163.com

Keywords: PCI bus, PCI9052, Servo control card, Linux

Abstract. This article designs a servo control card based on PCI9052 for the motor control of large CNC cutting machine. The design contains the hardware design of circuit and the software design of drive. The hardware design used PCI9052 to realize the communication of the host and the PCI bus, and realized the internal logic control of data communication on hardware circuit of CPLD by Verilog HDL language. Devised the hardware system principle and PCB diagram, producted circuit board by Altium Designer 6.9, and and finally debugged successly. The software driver design analyzed the relationship between Linux kernel and the device driver, proposed the servo control card design process according to the structure of Linux device driver, completed the identification and communication to servo control card by Industrial PC. The analog, switch and pulse transmission integrated on the same circuit board is different from previous, and it obtained a stable application in a number of CNC equipments.

Introduction

This article describes the overall design concept of the PCI bus servo control card hardware structure, and analyzes the function of each module and the implementation method of the hardware part, finally, proposes servo control card drivers for the Linux operating system design process according to Linux device driver structure, completes the identification and communication of industrial PC Linux system servo control card.

The Overall Design Concept of Servo Control Card Hardware System

According to the feature of servo motor and servo drives [1,2], the servo motor drive operation usually requires a certain voltage range of the analog signal, or a certain frequency range of pulse signal, and the switch signals used to control the sending and feedback of other digital information. The hardware functions of the servo control card of this design use simulated instructions control and pulse control. As the whole hardware structure is shown in Fig. 1. It contains bus interface module, logic control module, all kinds of data input and output module.

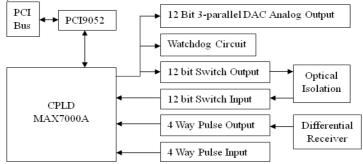


Fig.1. Overall hardware architecture of PCI bus servo control card

Bus Interface Module

PCI9052 provides a seamless connection with PCI bus, and it connected to the PCI bus side just reference data about the pin definition in the manual. In addition, in this PCI bus side power supply part has added four 100 uf electrolytic capacitor for filtering the 5V power supply on the bus.

Because PCI9052 is working under high frequency, the power frequency, relays, etc. are easily affect the stability of pallets because of the interference formed through the power line. This design use decoupling capacitors for the power input filter to make the device work in a stable working voltage. This design configure a decoupling capacitor size 0.1uF for each pin of the 10 pairs of power and ground pins on chip PCI9052.

The TEST pin which is the manufacturer used for testing on PCI9052 cannot be vacated, it needs to link to ground with a 10K resistor. In addition, the pin LHOLD need link to ground with 1K resistor, and the pin BTERM# need pull with 10K resistors.

The important configuration information of PCI9052 is stored in the serial EEPROM, these configurations is one of the most critical part of this design because of they are directly related to the properly work of the board. This design use 93LC46B chip of Mircochip Technology Company.

When the PCI bus master device want to read and write the serial EEPROM, it will set the register enable bit to 1, and operate the control register to generate a clock for the serial EEPROM at the same time [3,4], then give the corresponding code of instructions by pin EEDI. Then if there is 0 as the output from the pin EEDO, it means we can do read and write operations by the EEPROM. When you want to end this operation, only set the enable bit of register to 0.

EEPROM configure the PCI configuration register and local configuration register, EEPROM will not read and write if you use PLXMON online programmer, so the success rate is very low. We use programmer to program, and select the in line DIP package EEPROM.

According to the functions PCI9052 needs to achieve, designers must define their own base address of PCI bus devices, the CS signal, descriptor and scope of address space, and write the contents of the configuration register by analyzing the PCI9052 chip manual. PCI9052 and local bus interface use 16-bit multiplexed bus mode in this design, it can be setted with the configuration information of EEPROM.

The CPLD Logic Control Module

The CPLD device includes three kinds of structure[5]: the programmable interconnect line; the programmable I/O unit; and the programmable logic macro unit. The CPLD device on the servo control card of this design uses EPM1270 of MAX II series of the Altera to make the PCB board, which package is a 144 pin TQFP.

This design uses EDA integrated software development tools Quartus II which is independent developed by the Altera company. In this environment, the device that downloaded can be selected. The selected device is CPLD chip name and its model of Altera. This system uses 8 bit address / data multiplexing approach to read and writ in the main module of communication.

Periphery Control Module

The motion controller control the servo motor will use two kinds of control methods generally: (1)Control method of analog signal

Motion control system will send the analog voltage signal servo between +10V and -10V to the servo driver as the control signal, then it receive one feedback signal offered by the detection device from linear grating or the same position of motor encoder.

(2)Control method of digital pulse signal

The motion controller provide a pulse control signal with "pulse / direction" type for servo drive.

This servo control card contains these two kinds of instruction mode. Analog signal control motion refers to the analog voltage signal of +10V~-10V is sent to the servo driver as instruction, servo driver will receive the position feedback information of the position detecting element from

the motor encoder at the same time. Debug the child module of analog output in Verilog program, control the read and write timing of the controller chip, control analog output data changes, through the debugging of PC applications test, then, use the multimeter to measure the voltage of analog output port, make sure its value changes between +10V and-10V. The experiment proved, the analog output is correct by the modified Verilog program. So, the correctness and accuracy of the hardware circuit is verified.Hardware circuit receives the pulse signal from outside, the receiving circuit is shown in Fig. 2.

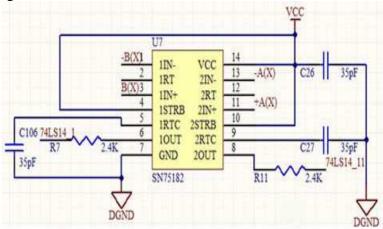


Fig.2. Part of pulse input circuit

Hardware circuit sends out the pulse signal from the host, the transmitting circuit is shown in Fig. 3.

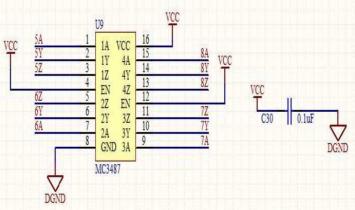


Fig.3. Part of pulse output circuit

Digital pulse control mode refers to send pulse command signal to the servo drive. At this time, servo drive mode is under position control mode, and its position loop is completed by the servo driver. Adjust the pulse input/output Verilog sub module program, modificate the hardware counter program, then applicate the test program by debugging the PC. Control the changes of pulse input/output data, use the oscilloscope to measure the frequency and amplitude changes of the pulse quantity. The experiment proved, the Verilog program can achieve the correct input and output of pulse quantity by modifying. If the pulse input / output hardware circuit is correct can verify by this.

Drive development of servo control card under Linux

The design of the software driver analysis the relationship between Linux kernel and device driver program, then propose the driver program the design flow of servo control card under the Linux operating system according the Linux driver structure. Finally, this design comeplete the identification and communication of the industrial PC Linux system to the servo control card.

The driver program development under Linux operating system is completely different with the Windows operating system just the same as the kernel structure of Linux operating system and the Windows operating system[6]. Therefore, before the PCI bus servo control card driver program development based on the Linux operating system, it must be comparative understanding about the

device driver of Linux system. Linux device driver program is a necessary software layer between the actual devices and application programs, and the interaction between computer and the hardware device is in the charge of this software layer, at the same time, it also will be responsible for a universal interface, which can link the equipment to the Linux file system, so that the application can visit the hardware equipment as the manner of controling the ordinary files. The most characteristic of Linux device driver development is the device can be processed as a document.

Unlike ordinary application, the device driver of Linux system is not start by main function running, it loads and uninstalls the driver program by the fixed entrance function and exit function. Module programming subroutine is including these two main functions. The first one is called when the module loading to the kernel, its primary function is to provide new functionality to the kernel registration module; the new function refers to the new software abstraction features or the complete driver program of device; this function The function is to register each new feature by using its kernel function. The other one is called when the module uninstalling, this function offer all kinds of features for the cancellation module in the kernel, and it will call the kernel function corresponding with itself to log off.

In this design, all function index of the servo control card is checked, after debugging the program, the servo control card start running on the industrial control PC. Then test and improve this card, introduce the driver development of servo control card under Linux system simply, and completed the debugging and applicating of servo control card.

Conclusion

This paper design a PCI bus servo control card by PCI9052, and introduce the process of this development under Linux system. This design completed the debugging and applicating of servo control card, it proved, this card can stabily run on the industrial control PC.

- [1] Wang Tong. The selection principles of servo motor in the field of mechanical and electrical [J]. The application of science and technology, 2001, 28(1): 6-8.
- [2] Qin Shaojun, Fu Minshi, Wu Hongqi. The choice research of spindle motor [J]. Combination machine tools and automatic processing technology, 2006,6: 24-25.
- [3] Meng Haoran, Yin Yumei, Yang Xiaoxia. The design method of general servo control card based on PCI bus [J]. Electronic measurement techniques, 2011.9.
- [4] Xu Guanghui. The embedded development and application based on FPGA [M]. Beijing: Electronic industry press, 2006.9.
- [5] Xu Xin. Embedded system design based on FPGA [M]. Beijing: Mechanical industry press, 2012.9.
- [6] Han Bingdong, Song Kefei, Yu Tao, etc. VPDM driver design of PCI data acquisition card [J]. Journal of Northeast Normal University (Natural Science Edition), 2005.1: 36-40.

Study of Nonlinear Observer for Dynamic Friction Compensation of High-Accuracy Servo-System

Wang Lizhi^a

School of Mechanical and Electrical Engineering, Ningbo Dahongying University, Ningbo, 315175, China

^a1045600085@qq.com

Key words: Non-linear observer, dynamic compensation, servo-system friction

Abstract: In this paper, a nonlinear observer is designed for a servo system with non-linear dynamic friction. With this kind of observer, the dynamic friction can be estimated and then be compensated using the input and output data on-line. A recursive formula of the nonlinear observer is derived by using the block pulse function which can be easily implemented on-line with microcomputers. The designed non-linear observer is applied to high accuracy servo system running at very low speed and prove to be effective and satisfactory.

Introduction

Servo motors are the most commonly used rotary actuators that allow for precise control of angular position or rotor speed. Fig. 1 is a block diagram commonly used in control systems. From the above diagram, we can see that besides the effective input signal, a disturbance signal is also applied to the system as load torque. Normally, the load torque is mainly the friction torque. So when the system is running at very low speed, that is to say, the running speed exceeds a certain marginal value(The minimum stable speed), fluctuation may take place, which will affect the working order of the system, hence deteriorate the working quality. A computation friction model of all the parts in the system is need to be established in order to analyze the friction vibration. Frictional forces depends on a number of factors, on which, up to now, no final conclusion has yet been reached. In addition to that these factors may vary greatly to the working environment and correlate to the running velocity and acceleration .The normal method dealing with this is piecewise linearization[1], but from time to time, it shows unsatisfactory. In this paper, $M_{f}(n)=M_{s}-k.n$ is used as the model to approximate the fiction nonlinear curve at extreme low velocity, M_s here is the static friction and can be obtained in experimental measurement. k is a time-varying coefficient or simply a constant which will be estimated online with nonlinear observer. Therefore, the friction can be gained and friction torque can be entirely compensated.

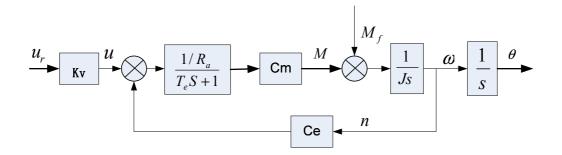


Figure 1 Block Diagram of a of a Servo System

Deduction of the Non-liner Observer

To simplify the computation, T_e is ignored, then

$$\Omega(s) = \frac{n(s)}{\mu(s)} = \frac{1/c_e}{T_m s + 1}$$
(1)

Where $T_m = \frac{JR_a}{c_e c_m}$ is the electro mechanic time constant.

Convert the numeric value of M_f to its equivalent disturbance voltage representation u_f , from Fig 1.

$$\frac{\frac{u_f(s).c_m/R_a}{(1+T_e s)}}{\Delta(s)} = \frac{M_f(s)}{\Delta(s)}, \text{ where } \Delta(s) \text{ is the closed-loop characteristic polynomial. i.e.}$$

$$M_f = \frac{u_f(s).c_m/R_a}{(1+T_e s)} \tag{2}$$

As T_e is usually a very small factor and can be ignored, $u_f = R_a/C_m$. M_f is deduced .The simplified Equivalent diagram is showed in Fig.2.

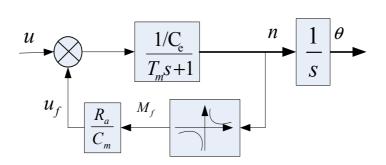


Figure 2. Simplified Equivalent Model of the Servo System

From above it can be seen that if u_f can be estimated, the friction effects can be compensated by a compensator. After that controller of the system can be designed according to the corresponding control theory.

$$\frac{u(s) - u_f(s)}{c_e} = T_m n(s) + n(s) , \quad \text{i.e.} \qquad \frac{u - u_f}{c_e} = n + T_m n$$

$$n + \frac{1}{T_m} n = \frac{(u - u_f)}{c_e T_m} , \text{Let } b_0 = \frac{1}{T_m c_e}, a_0 = \frac{1}{T_m} \quad \text{then}$$

$$(u - u_f) b_0 = n + a_0 n \qquad (3)$$

State Equations and the Existence of the Non-liner Observer

Let $n=x_1$,add a new slow time-varying variable k'= x_2 , hence $x_2=0$, the overall set of equations are determined as below:

$$\begin{aligned} x_1 &= -a_0 x_1 + b_0 (u - u_s + x_1 x_2) \\ x_2 &= 0 \end{aligned}$$
(4)

Here $u_s = \frac{M_s / R_a}{K_v c_m}$ is the voltage corresponding to the static friction M_s .

The output equation is $y = x_1$. For a non-linear system :

$$\begin{cases} x = f(x,t) \\ y = h(x,t) \end{cases}$$
Its observable condition is $rank \begin{bmatrix} (\frac{\partial h}{\partial x})^T \\ N(\frac{\partial h}{\partial x})^T \\ \vdots \\ N^{n-1}(\frac{\partial h}{\partial x})^T \end{bmatrix} = n$
(5)

Where $N(\frac{\partial h}{\partial x})^T = \frac{\partial}{\partial t}(\frac{\partial h}{\partial x})^T + f^T \{\frac{\partial}{\partial x}(\frac{\partial h}{\partial x})^T\} + (\frac{\partial h}{\partial x})^T \frac{\partial f}{\partial x}.$

Substitute all the parameters in Eq.2 according to the system values, then:

$$\left(\frac{\partial y}{\partial x}\right)^{T} = \begin{bmatrix} \frac{\partial y}{\partial x_{1}} \\ \frac{\partial y}{\partial x_{2}} \end{bmatrix}^{T} = \begin{bmatrix} 1 \\ 0 \end{bmatrix}^{T} = \begin{bmatrix} 1 & 0 \end{bmatrix}$$

$$f^{T} \left\{\frac{\partial}{\partial x}\left(\frac{\partial y}{\partial x}\right)\right\}^{T} = \begin{bmatrix} 0 & 0 \end{bmatrix} , \quad \text{Hence}$$

$$\frac{\partial f}{\partial x} = \begin{bmatrix} -a_{0} + b_{0}x_{2} & b_{0}x_{1} \\ 0 & 0 \end{bmatrix}$$

$$\left(\frac{\partial y}{\partial x}\right)^{T} \cdot \frac{\partial f}{\partial x} = \begin{pmatrix} 1 & 0 \end{pmatrix} \begin{pmatrix} -a_{0} + b_{0}x_{1} & b_{0}x_{1} \\ 0 & 0 \end{pmatrix} = \begin{pmatrix} -a_{0} + b_{0}x_{2} & b_{0}x_{1} \end{pmatrix}, \text{therefore}$$

$$N\left(\frac{\partial y}{\partial x}\right) = \begin{pmatrix} -a_{0} + b_{0}x_{2} & b_{0}x_{1} \end{pmatrix}$$

$$rank \begin{pmatrix} 1 & 0 \\ -a_0 + b_1 x_2 & b_0 x_1 \end{pmatrix} = 2$$

Hence the nonlinear observer existence is proved.

Design of the Observer and Compensation Strategies

To design the state observer, let $y_1 = x_1 + a_0 x_1 - b_0 (u - u_s) = b_0 x_1 x_2$

The original system model changes to $\begin{cases} x_2 = 0\\ y_1 = x_1 + a_0 x_1 - b_0 (u - u_s) = b_0 x_1 x_2 \end{cases}$

Suppose the observer's math model is $\gamma = G(y_1 - b_0 x_1 \gamma) = Gy_1 - Gb_0 x_1 \gamma$

Where γ is x_2 , namely the observation value of the k ,and G is the gain of the observer. Let $Gb_0x_1 = S_*$, The desired pole therefore is $-S_*$. Here the state is gain-related, what is one of the characteristics of the nonlinear observers. From all above, the nonlinear observer is established as the following form:

$$\gamma = -s_*\gamma + \frac{s_*}{b_0 x_1} y_1$$

= $-s_*\gamma + \frac{s_*}{b_0 x_1} [x_1 + a_0 x_1 - b_0 (u - u_s)]$
= $-s_*\gamma + c$

Apparently, after the value of γ is observed, the friction can be compensated.

$$b_0 = \frac{1}{c_e T_m}$$
, $a_0 = \frac{1}{T_m}$

 a_0 and b_0 can be calculated beforehand. x_1 is the rotation speed, u_s can be measured.

$$x_1(i) = \frac{\theta(i) - \theta(i-1)}{T_s} \tag{6}$$

Where T_s is the sampling period . $x_1 = \frac{x_1(i) - x_1(i-1)}{T_s}$, S_* is determined by the observer

convergence speed. Hence the parameter C can be calculated online.

From Flower Transform, $s = \frac{1}{T_s}(1-z^{-1})$, we get the below form:

$$\gamma(i) = \frac{\gamma(i-1) + c(i)T_s}{1 + T_s S_*} \tag{7}$$

$$c(i) = \frac{S_*}{b_0 n(i)} \left\{ \frac{n(i) - n(i-1)}{T_s} + a_0 n(i) - b_0 [u(i) - u(i-1)] \right\}$$
(8)

$$n(i) = \frac{\theta(i) - \theta(i-1)}{T_s}$$
(9)

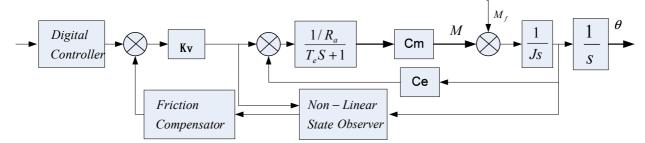


Figure 3 Block Diagram of the Friction Compensation Strategy

Conclusion

This kind of nonlinear observer for a servo system with nonlinear dynamic friction is very simple to design and easy to be put into realization. With this kind of observer, the dynamic friction can be estimated and then be compensated using the input and output data on-line. The recursive formula of the nonlinear observer is derived by using the block pulse function which can be easily implemented on-line with microcomputers. The designed nonlinear observer is applied to high accuracy servo system running at very low speed and prove to be effective and satisfactory. This compensation scheme can be applied to other similar systems.

- Lee J-I, van der AA M, Verschuren C, Zijp F, van der Mark M (2005), Development of an air gap servo system for high data transferrate near field optical recording. JJAP 44(5B):3423–3426
- [2] Lee KT, Hong SN, Kim JE, Kim CK, Seo JK, Ko ES, Choi IH, Min,BH (2007) Dynamic tilt control of SIL with 4-axis actuator in NFR System, ODS

Solar Tracking Device Based on Electronic Compass and Accelerometer

Zhongran Zhang^{1,a}, Yuan Ma¹, Bo Jiao^{1,b*} and Tongliang Liu¹ ¹Rongcheng College, Harbin University of Science and Technology, Rongcheng 264300, China ^aranshao317@126.com, ^{b*}jiaobo@hrbust.edu.cn

Keywords: Solar tracking, Embedded system, Electronic compass, Accelerometer

Abstract. A solar tracking device was designed in this paper. First, In order to determine the initial direction of the mechanism and the east, HMC5883L was used for measuring the magnetic field of earth. Then, the mechanism began to operate according to the solar position which was confirmed though the astronomical calculation. Finally, the azimuth and the elevation angle of solar were measured and corrected by HMC5883L and MPU6050 respectively. HMC5883L was calibrated by the ellipse fitting, which was obtained though the least square method. The horizontal error of HMC5883L was compensated. The experimental study was performed. And the results show that the solar tracking device has the characteristics of stable operation, high flexibility and low requirement of installation precision.

Introduction

The energy crisis and environmental protection have become a serious task. It turns to be common issues for all the nations that improving the structure of energy usage and reducing the use of fossil fuels. Solar technology has become an important approach to save energy and protect environment. Moreover, the energy receiving rate can be increased by 37.7% [1, 2] though the solar tracking device. Important achievements on the solar tracking methods have been made. For example, some designed solar orientation tracker through the photoelectric sensor [3]. Some calculated the elevation and azimuth angle of solar by solving initial phase of alternating current, caused by rotation of the PV battery. Some used the combination of light-sensitive tracking and time tracking to determine solar orientation. Others utilized the characteristics of memory metals to achieve passive solar tracking, which is based on temperature change caused by sunshine [4]. However, there are still some limitations in above methods. The measurement range of photoelectric sensor is narrow. It is hard to ensure the consistency of performance of optical components due to instability. Besides, it also needs added power to work. Time tracking based on the astronomical calculation has poor flexibility and bad adaptability. Current measurement tracking is susceptible to the effect of shade. The characteristics of memory metal are difficult to control, and it is also hard to produce. A novel solar tracking device was designed in this paper. It is based on the astronomical calculation of solar orientation. And the gravitational field and magnetic field of earth are calculated using electronic compass and accelerometer to determine the position of the device to achieve a closed-loop control.

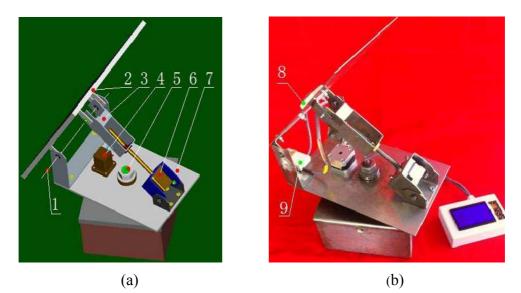
Design scheme

The system is designed and manufactured, as shown in Fig.1. It has two degrees of freedom. The worktable of azimuth axis is perpendicular to the ground plane, and the pitch axis is perpendicular to the azimuth axis. It is mainly composed of mechanical part, electronic compass, accelerometer, micro controller, stepper motor and driver. When the system works, the azimuth axis and the pitch axis rotates respectively to track the azimuth and the elevation angle of solar.

Control system design

The MCU controller is the core in this system. The azimuth of the solar panel is calculated, according to the data of accelerometer installed on the solar panel through the IIC bus. The azimuth of the solar panel is determined, according to the data of HMC5883L installed on the worktable. The solar panel

is made perpendicular to the sunlight, by comparing the difference between the current sloar location and the solar panel.



Pitch axis; 2. Solar panel; 3. Ejector pin; 4. Azimuth motor; 5. Azimuth axis;
 6. Push rod motor; 7.Worktable; 8. MPU6050; 9. HMC5883L
 Fig.1 Picture of system structure (a) 3D model; (b) experimental setup

STC12C5A60S2 MCU is adopted as the controller. MPU6050 six axis motion sensor and HMC5883L electronic compass are used in the system. The accurate time is obtained by DS1302 though calculating the elevation and azimuth angle of solar. The two-phase four wire 42 stepper motor and driver are utilized, according to the mechanical structure and load condition. 12864 LCD and serial industrial touch screen are taken as the human-computer interaction module.

When the system starts, it is in alignment mode. And the sun elevation and azimuth angle are determined, through the calculation of local time, longitude and latitude [5]. Solar elevation angle h (°) is as shown in Eq.1, as well as solar azimuth A (°) in Eq.2. The positive is used for the conditions before 12 at noon, while the negative is for those after 12 at noon. The sysem will not work when the sun goes down.

$$h = \arcsin\left(\sin\phi \cdot \sin\delta + \cos\phi \cdot \cos\delta \cdot \cos t\right). \tag{1}$$

$$A = \pm \arccos\left(\frac{\sin h \cdot \sin \phi - \sin \delta}{\cos h \cdot \cos \phi}\right).$$
(2)

in which, ϕ -- local latitude, (°); δ -- solar declination angle, (°); t-- solar hour angle, (°).

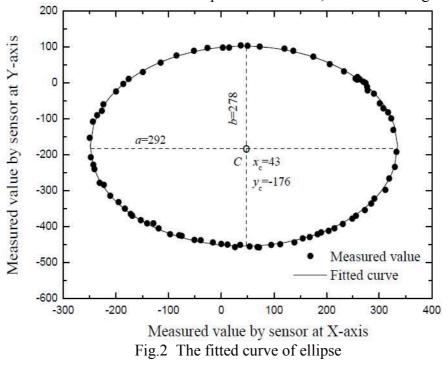
The elevation and azimuth of solar panel are detected by MPU6050 and HMC5883L, respectively. The difference between the actual and theoretical value is compared, and then the angle difference is converted to pulse output to control stepper motor driver.

Calibration of electronic component

The elevation angle can be determined by accelerometer, which can measure the acceleration. The direction of the magnetic north pole is determined by electronic compass, which can calculate the magnetic field of the earth. However, the magnetic field of the earth is only 0.5G in general. The detected result is easily affected by other magnetic fields. Therefore, the revision is necessary.

When the electronic compass rotates a circle (360°) , the output of the two horizontal vectors of the magnetic field is round ideally. When it is affected, the measured value of the magnetic field

vector is the sum of the earth and the interfering magnetic field. The center of curve determined by the electronic compass shifts. The output of electronic compass is transformed into an ellipse due to the magnetic deviation. Therefore, the calibration of magnetic deviation is transformed into the ellipse fitting. The least squares estimation method is used [6]. When the worktable rotates a circle, about 100 magnetic field vectors of the electronic compass are obtained, as shown in Fig. 2.



The coordinate of the center of ellipse (x_c, y_c), the semi major axis *a* and semi minor axis *b* can be obtained. The revised magnetic-field vectors, $[X_m, Y_m]^T$, are calculated by Eq. 3, though the magnetic-field vectors, $[x_m, y_m]^T$, acquired by the electronic compass.

$$X_{\rm m} = x_{\rm m} - x_{\rm c}, \quad Y_{\rm m} = \frac{a \times (y_{\rm m} - y_{\rm c})}{b}.$$
 (3)

The angle of the worktable is affected by its own movement. Therefore, the compensation of the electronic compass cannot be neglected. The pitch and roll angle of the worktable are measured by the accelerometer. The magnetic-field component is acquired by three axis magnetoresistive sensor. Based on the above results, the intensity of earth magnetic field H_X , H_Y can be determined [7]. There is a difference, β , between the north magnetic pole and the geographic north pole. And the value varies at different place. Finally, the compensated azimuth is calculated by Eq. 4.

$$\alpha = \arctan\left(\frac{H_{\rm Y}}{H_{\rm X}}\right) + \beta. \tag{4}$$

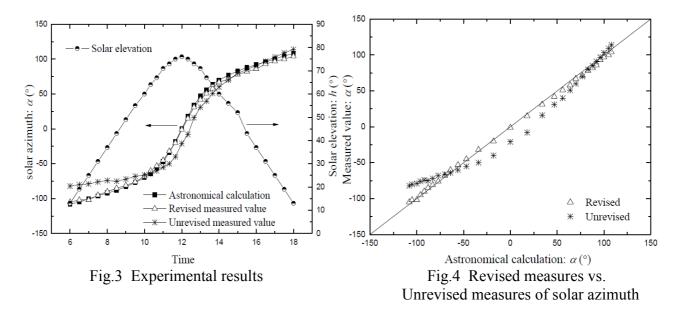
Experimental results

The system was tested at Rongcheng College of Harbin University of Science and Technology, in June 22, 2013, which is located at longitude and latitude of 122°30′ and 37°9′. Theoretical and practical values of azimuth and elevation angle were recorded, as shown in Fig. 3. As the direction of gravitational acceleration can be accurately measured, the elevation angle of the solar panel is not modified. It can be found that the angular deviation is larger than calculated value in the morning and evening, and smaller at noon when the sensor is not revised. The revised and unrevised measures of solar azimuth are compared with the astronomical calculations in Fig. 4. When the data calibration

and angle compensation have been made, the angles of the mechanism and the astronomical calculations are basically coincident. The existing error of the revised measures, which is mainly in the range of $1^{\circ} \sim 3^{\circ}$, is mainly due to the volatile performance of electronic components. In order to further improve the accuracy of system tracking, the core controller and sensor with high performance should be adopted.

Conclusions

In this paper, a solar tracking device is designed. The solar orbit is calculated according to the local time, latitude and longitude. Then, the magnetic and gravity fields of earth are measured and calculated respectively, by electronic compass and accelerometer. The closed-loop control is realized. It has the feature of control accuracy, strong adaptability, easy to implement and adjustment, and so on. The error of the system is $1^{\circ} - 3^{\circ}$. It can be used for different mechanical structures through simple adjustment.



Acknowledgements

This work was supported by Science and Technology Research Project (12521126) from the Education Department of Heilongjiang Province, China.

- [1] Y. Tsur and A. Zemei: Solar Energy, Vol. 68 (2000) No.5, pp.379-392.
- [2] R. Eke and A. Senturk: Solar Energy, Vol. 86 (2012) No.9, pp.2665-2672.
- [3] S Abdallaha and S Nijmehb: Energy Conversion and Management, Vol. 45(2004) No.11-12, pp. 1931-1939.
- [4] W.W. Shi and C. Liu: Renewable Energy Resources, Vol. 31(2013) No. 1, pp. 9-12. (In Chinese)
- [5] H.Z. Wang: In partial fulfillment of the requirements for the degree of Master of Engineering (MS., Dalian Maritime University, China 2012), pp.20-40. (In Chinese)
- [6] H.W. Sun, J.C. Fang and Y. Li: Optics and Precision Engineering, Vol.17 (2009) No. 12, pp.3035-3039. (In Chinese)
- [7] T.T. Shao: Chinese Journal of Sensors and Actuators, Vol.20 (2007) No.6, pp.137-139. (In Chinese)

The Analysis of the Phase Noise of the Closed-loop Driver Circuit in Micromechanical Gyroscope Based on the Phase-locked Principle

Wang Guanshi^{1, a}, Liu Xiaowei^{1, b} ¹Harbin Institute of Technology,Harbin, China ^aOhno1999@126.com, ^blxw@hit.edu.cn

Keywords: micromechanical gyroscope; phase noise; closed-loop.

Abstract. Compared with the closed-loop drive circuit in micromechanical gyroscope of AGC principle, the closed-loop driver circuit based on the phase-locked principle can overcome its shortcomings which cannot control the frequency characteristics of the output signal, reducing the frequency deviation and the frequency jitter of the output signal, and shortening the settling time of the closed-loop drive system. In this paper, the noise of the closed-loop phase drive circuit based on phase-locked principle is analyzed and deduced its phase noise expressions.

Introduction

The role of micro-mechanical gyro driver circuit is to generate an electrostatic driving force to drive the quality of the sensor structure blocks along the driving direction with a fixed frequency and amplitude stability^[1-3]. Drive circuit should make the drive frequency of the driving force of an electrostatic MEMS gyroscope the same as the consistent natural frequency. In this case, the vibration amplitude of the vibration displacement of the sense direction and velocity direction of the driving direction are the largest, and the drive circuit does not require a closed loop circuit are able to meet the phase shift of the self-excited oscillation conditions^[4,5]. Further, since the vibration velocity is proportional to the mass at the sense derection subjected to the Coriolis force, in order to ensure the amplitude of the Coriolis force is constant to improve the accuracy of the sensor system, the vibration velocity amplitude of the driving mass in the driving direction must be a constant value, whereby the amplitude of the drive signal should remain constant^[6,7]. Closed-loop stability and frequency of the drive signal match can be amplitude by the driving circuit, and when the natural frequency of the drive mode of the gyroscope changes due to the external environment, the closed loop circuit can automatic drive track the frequency, therefore the closed-loop drive mode become a preferred driving mode of the high-performance micromechanical gyroscope^[8,9].

In this paper, the phase noise of the closed-loop drive circuit based on the phase-locked principle is analyzed. The closed-loop drive circuit based on the phase-lock principle is analyzed in the second part, its phase noise expressions is derived in the third part.

The principle of the closed-loop drive circuit based on the phase lock theory

Fig.1 shows the principle of a closed-loop drive circuit based on the phase lock theory.

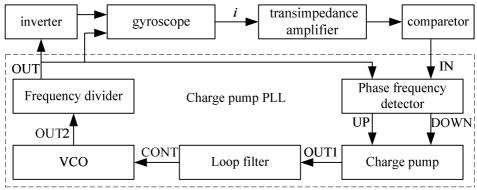
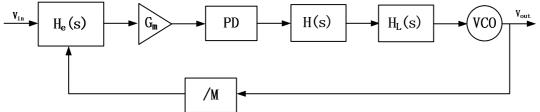


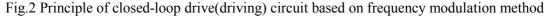
Fig.1 Principle of closed-loop driving circuit based on phase locked theory

In this figure, sense current of the driving direction flows over the transimpedance amplifier switch into a voltage signal, this voltage is a sinusoidal signal, converts by conversion to the square wave signal IN with the same frequency and phase. The portion of dotted line is the charge pump PLL, PFD which detects the frequency difference and the phase difference between the input signal IN and the feedback loop signal OUT, and generates a corresponding voltage signals UP, DOWN to control the charge pump working condition. Charge pump converts the signal UP, DOWN into outputs voltage OUT1, after a low -pass filter, OUT1 output a DC level CONT as the control voltage of the controlled oscillator, the output signal OUT2 is high, so it is added to the frequency divider to reduce the resonance frequency in the same order of magnitude. Divider output OUT is a square wave signal, as an AC drive voltage of the micromechanical gyroscope, which has been inverted to a square wave signal as the AC drive voltage of another micromechanical gyroscope. In addition, OUT also serves as a feedback signal input of the PDF. When the PLL is locked, CONT is a constant voltage, the phase and frequency of the input signal IN and feedback loop signal OUT have the same value, and the micromechanical gyroscope is in the resonant state.

Phase noise analysis of the drive circuit based on the phase lock theory

Analysis of the phase noise characteristics of the drive circuit in Figure 1, a block diagram of the frequency can be derived as a transfer function:





Where He(s) is a mechanical meter, Gm is the gain of the transimpedance amplifier, PD is the phase detector, H(s) is the charge pump, HL(s) is a filter, VCO is voltage-controlled oscillator, /M is the sub-frequency.

The resonant loop at the driving direction corresponds to a band-pass filter, the signal frequency is equal to the resonant frequency of the ambient noise is amplified, and the other signal are filtered, we can first table the resonance loop as a filter before the steady state study.

Assuming the mass at the x direction effected by the environmental noise $k_w w(t)$, the kinetic equation at the x direction can be expressed as:

$$M_d \frac{d^2 x}{dt^2} + \lambda_d \frac{dx}{dt} + K_d \cdot x = k_w w(t)$$
⁽¹⁾

Where, M_d is the quantity of the drive mass; λ_d is the damper coefficient of the drive mass at x direction; K_d is the elastic coefficient of the drive mass at x direction; x is the displacement of the drive mass at x direction. Let $\omega_d = \sqrt{\frac{K_d}{M_d}}$, which is the natural frequency of the drive mode

; $\xi_d = \frac{\lambda_d}{2M_d\omega_d}$, which is the damper ratio of the drive mode; $Q_d = \frac{1}{2\xi_d} = \frac{M_d\omega_d}{\lambda_d}$, which is the character coefficient of the drive mode.

$$\frac{d^2x}{dt^2} + 2\xi_d \omega_d \frac{dx}{dt} + \omega_d^2 x = k_w w(t)$$
⁽²⁾

While, $i = 2N_2 V_p \varepsilon_o \frac{z}{v} \frac{dx}{dt}$

So,
$$\frac{dx}{dt} = \frac{y}{2N_2 V_p \varepsilon_{oz}} i$$
, make $\frac{y}{2N_2 V_p \varepsilon_{oz}} = A$, then $\frac{dx}{dt} = Ai$

Because
$$\frac{d^2x}{dt^2} + 2\xi_d \omega_d \frac{dx}{dt} + \omega_d^2 x = k_w w(t)$$

We can get that $A\frac{di}{dt} + 2\xi_d \omega_d A i + \omega_d^2 A \int i dt = k_w w(t)$

Phase is the integral of the frequency, at phase domain:

$$ii + 2\xi_d \omega_d A \int idt + \omega_d^2 A \int \int idt = k_w \int w(t)dt$$
(3)

then
$$A \frac{d^2 i}{dt^2} + 2\xi_d \omega_d A \frac{di}{dt} + \omega_d^2 A i = k_w \frac{dw}{dt}$$

By the laplace transform:

$$As^{2}I_{\Phi}(s) + 2\xi_{d}\omega_{d}AsI_{\Phi}(s) + \omega_{d}^{2}AI_{\Phi}(s) = k_{w}sW_{\Phi}(s)$$
(4)

$$\frac{I_{\Phi}(s)}{W_{\Phi}(s)} = \frac{k_w s}{As^2 + 2\xi_d \omega_d As + \omega_d^2 A}$$
(5)

The phase difference of the ideal output and the input of the phase detector output signal is proportional at the phase field, the phase detection model can be modeled as a gain constant Kp module. As the loop is slower, phase and charge pump modules together can be modeled as a continuous-time integrator, and add a zero to improve the stability of the loop:

$$K_p H(s) = \frac{I}{2\pi C_p} \frac{\tau_1 s + 1}{s}$$
(6)

Where I is the charging current of the charge pump, Cp is the charge pump capacitors. τ_1 id the time constant at zero point.

The model of the low-pass filter in resonant loop can be represented by the formula:

$$H_{L}(s) = \frac{as+1}{bs^{2} + cs + 1}$$
(7)

VCO can be modeled as an ideal integrator model, so:

$$H_{VCO}(s) = \frac{K_{\nu}}{s} \tag{8}$$

So:

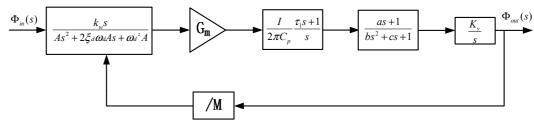


Fig.3 Schematic of integrator

In the figure $\Phi_{in}(s)$ represents as an input phase error, $\Phi_{out}(s)$ is output phase error.

$$\frac{\Phi_{out}(s)}{\Phi_{in}(s)} = \frac{M \frac{k_w s}{As^2 + 2\xi_d \omega_d As + \omega_d^2 A} G_m \frac{I}{2\pi C_p} \frac{\tau_1 s + 1}{s} \frac{as + 1}{bs^2 + cs + 1} \frac{K_v}{s}}{M + \frac{k_w s}{As^2 + 2\xi_d \omega_d As + \omega_d^2 A} G_m \frac{I}{2\pi C_p} \frac{\tau_1 s + 1}{s} \frac{as + 1}{bs^2 + cs + 1} \frac{K_v}{s}}{\frac{bs^2 + cs + 1}{s} \frac{as + 1}{s}}$$

$$= \frac{M G_m I k_w K_v (\tau_1 s + 1) (as + 1)}{2\pi C_p M (As^2 + 2\xi_d \omega_d As + \omega_d^2 A) s (bs^2 + cs + 1) + G_m I k_w K_v (\tau_1 s + 1) (as + 1)}$$
(9)

When s->0, $\frac{\Phi_{out}(s)}{\Phi_{in}(s)} \rightarrow M$

It means that the phase of the input signal increases at M times.

When the input is
$$\omega_{in}$$
, $\Phi_{in}(s) = \frac{\omega_{in}}{s^2}$, the steady-state phase error is:

$$\phi_{error} = \lim_{s \to 0} s \Phi_e(s) = \lim_{s \to 0} s \frac{\omega_{in}}{s^2} \frac{\Phi_{in}(s) - \Phi_{out}(s) / M}{\Phi_{in}(s)}$$

$$= \lim_{s \to 0} \frac{\omega_{in}}{s} \frac{2\pi C_p M (As^2 + 2\xi_d \omega_d As + \omega_d^2 A) s (bs^2 + cs + 1)}{2\pi C_p M (As^2 + 2\xi_d \omega_d As + \omega_d^2 A) s (bs^2 + cs + 1) + G_m I k_w K_v(\tau_1 s + 1) (as + 1)}$$

$$= \frac{2\pi C_p M \omega_d^2 A \omega_{in}}{G_m I k_w K_v}$$
(10)

The phase error of the steady state is proportional to the input frequency and in the steady state $\omega_{in} \approx \omega_d$, then: $\phi_{error} \approx \frac{2\pi C_p M \omega_d^3 A}{G_m l k_w K_v}$, which is proportional to the cube of the resonant frequency of the gyroscope, when the resonance frequency is higher the phase errors at steady-state is lager.

Conclusion

In this paper, phase noise of the self-excited driving circuit of the micromechanical gyroscope based on the lock-in principle is analyzed, the steady-state phase error $\phi_{error} \approx \frac{2\pi C_p M \omega_d^3 A}{G_m l k_w K_v}$ is given, which is proportional to cube of the gyro-resonant frequency, when the resonant frequency is higher, the phase error at steady-state is larger.

- C. Acar, A. M. Shkel. An Approach for Increasing Drive-Mode Bandwidth of MEMS Vibratory Gyroscopes. Journal of Micro Electro Mechanical Systems. 2005,14(3): 520~528
- [2] D. Tsai, W. Fang. Design and Simulation of a Dual-Axis Sensing Decoupled Vibratory Wheel Gyroscope. Sensors and Actuators, A: Physical. 2006,126(1):33-40
- [3] B. Xiong, L. Che, Y. Wang. A Novel Bulk Micromachined Gyroscope with Slots Structure Working at Atmosphere. Sensors and Actuators, A: Physical. 2003, 107: 137~145
- [4] K. Tanaka, Y. Mochida, M. Sugimoto, K. Moriya, T. Hasegawa, K. Atsuchi, K. Ohwada. A Micromachined Vibrating Gyroscope. Sensors and Actuators, A: Physical. 1995,50(1-2):111-115
- [5] Y. S. Oh, B. L. Lee, S. S. Baek, H. S. Kim, J. G. Kim, S. G. Kang, and C. M. Song. A Tunable Vibratory Microgyroscope. Sensors and Actuators, A: Physical. 1998,64(1):51-56
- [6] J. S. Yang. A Piezoelectric Gyroscope Based on Extensional Vibrations of Rods. International Journal of Applied Electromegnetics. 2003,17(4):289~300
- [7] X. Wu, W. Chen, X. Zhao. Structure Design of Levitating Coil in Micro-machined Gyroscope with an Electro-magnetic Levitated Rotor. Journal of Shanghai Jiaotong University. 2005,23(1):125~128
- [8] W. A. Clark, R. T. Howe, R. Horowitz. Surface Micromachined Z-axis Vibratory Rate Gyroscope. Tech. Dig. Solid-state Sensors and Actuators Workshop. Los Angeles, United States, 1996:283-287
- [9] S. E. Alper, I. E. Ocak, T. Akin. Ultra-Thick and High-Aspect-Ratio Nickel Microgyroscope Using EFAB TM Multi-Layer Additive Electroforming. MEMS, Istanbul, Turkey, 2006:670-673.

Development and Research of Open CNC System Based on Motion Controller

ZHANG Hang-wei^{1,a}, Chen Chan-juan^{1,b}

¹College of Mechatronic Engineering, Shaanxi University of Science & Technology, Xi'an, Shaanxi 710021, P.R. China

^azhanghangwei@sust.edu.cn, ^bchencj@sust.edu.cn

Keywords: Open Numerical Control System, Master-Slave Control System, User Interface, Data Pretreatment.

Abstract. A lab platform of Open Numerical Control System was designed to develop NC system based on PC and Motion Controller, a Master-Slave control system. The user interface application software was developed by C++ Builder and WINDOWS. It realized explanation and testing for bug function, data pretreatment function, NC code translation, NC simulation and execution, as well as motion controller function.

Introduction

Traditional NC systems were closed and incapable of extensions with high reliability. They cannot meet the requirements of users in some specialty environments. The hardware of CNC system had low versatility. Furthermore, the software of CNC system had poor transferability with high requirements to the user and machine provider[1-2]. A special open NC system was constructed with GT Series Multi-axis Motion Controller by Shenzhen Googol Technology Co. Ltd. [3]. The GT motion controller is served as a standard independent component which can obviously shorten development cycles of new products. The users can invent their own products easily and convenience.

DSP (Data Signal Processor) is served as a motion control processor in GT Motion Controller. PC (Personal Computer) is served as an information processing platform. Motion Controller is plugged in PC, namely "PC + Motion Controller"[4]. This system takes advantages of PC and Motion Controller. Information processing capability with an open style on PC is integrated with motion trace control ability on Motion Controller. This system has high information processing capability, high opening degree, more accurate motion trace control, and more versatile. Open NC system based on "PC + Motion Controller" is the trend of NC technology because this system realizes high integration between flexibility of PC and high operating rate of DSP.

Hardware of a lab platform in Open NC System

Hardware of the lab platform is constituted of a Motion Controller and its interface board, a PC, stepping motors, motor divers, home switches, limit switch and power sources[5]. More details are in the following. The Motion Controller is GT-400-SV-PCI motion controller made by Shenzhen Googol Technology Co. Ltd.. A PC or an industrial PC must be with PCI Slot. The voltage range of a DC power source is from +12v to +24v which is used for the interface board.

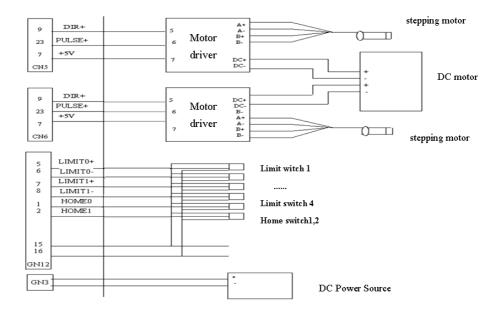


Fig. 1 Wiring Diagram of Hardware

Main Forms in Application Software on the lab platform of Open NC System

This Open NC System based on PC is one of master-slave control systems. The slave control system is the control system based on GT-400-SV-PCI motion controller. It is in charge of input/output of switch values and analog parameters, interpolation and self-correction. It also receives manufacturing instructions from PC. At the same time, the feedback signal about machine status can be transferred. The master control system is an industrial PC which is in charge of scheduling, interaction, parameter setting, dynamic simulation, state display and interpretation of parts' NC program. Furthermore, the master control system sends commands to Motion Controller by PCI bus. It realizes distributed management in the whole NC system.

Implementation of application software is based on Form which is one basic element in C++Builder programming. According to the functions of NC system, Forms can be divided into five categories.

Translation Form. The function of translation form is that NC program should be transformed into electric signals which can be received by PC. The main procedures of NC translation are syntax debugging and NC interpretation.

Syntax debugging is executed NC blocks one by one. Some kinds of malfunctions can be detected such as mistakes on case-sensitive, illegal characters, mismatch of parameters' numbers, over range of parameters, program format error and reuse of modal NC codes from the same group, etc.. The interpretation of part program is also executed NC blocks one by one. Firstly, all the letters and data of part program are separated. Then, according to categories of the letters, data can be stored in different storage units. Through attributes of base classes and derived classes in C++Builder, the coordinate parameters can be called up easily. These parameters include coordinates, displacements, velocities, accelerations and other auxiliary information. It improves the effective of part programs' execution and enhances extendibility of this application program.

Execute Form. Data can be exchanged between PC and Motion Controller by the execute form. To call up the functions of Dynamic Link Library in Motion Controller, Execute function on PC should be implemented. Uniformity of function interface are enhanced because of using some static and dynamic characteristics of C++ language such as function overloading, virtual functions, the abstract base classes, dynamic binding and polymorphism. In different situation, one Execute function can be called up to implement different NC codes such as rapid traverse, line positioning, circular interpolation clockwise and anticlockwise.

DataPreProcess Form. In parameters transfer of function, the parameters should meet the requirements of functions' definition. This is the role of DataPreProcess. There are different data process methods in G90 (Absolute Coordinate Positioning) and G91 (Incremental Positioning). The same situation is also in preprocess of cutter length or radius compensate, conversion between the metric system and English system, and the other matching.

Drawing2D Form. It is in charge of dynamic simulation of NC program. Uniformity of function interface are enhanced because of using some static and dynamic characteristics of C++ language, the same as Execute Form. The classification of classes is seen in Figure 2. Drawing2D function can be called up to fulfill the simulation of rapid traverse(G00), line positioning(G01), circular interpolation clockwise(G02) and anticlockwise(G03).

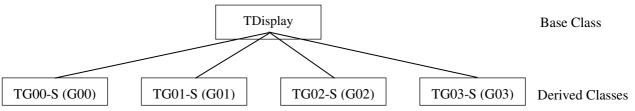


Fig. 2 Application of Base Class and Derived Classes in Drawing2D Function

DisplayThread Form. It is designed for realize coordinate display, 2D dynamic simulation display and NC program execution or interpretation simultaneously. Positioning coordinates of each axis can be displayed when NC program is executed in Motion Controller by utilizing this form. At the same time, machining curve can be displayed dynamically when NC program is interpreted in PC by utilizing this form.

Functions of the Application Program on the Lab Platform of Open NC System

The forms illustrated before are the main fulfill styles in the application software but they are not the total. Therefore, it is necessary to talk about functions of this system.

The functions of this system can be divided into two parts, management and motion control systems[6]. Look at Figure 3. The application software realizes NC program management function such as read, print, save, save as, font setting, code query, find and replace, testing for bug and data pretreatment. It also completes single axis motion control such as Jog, Rapid Traverse and Handle modes. In execution function, NC codes can be executed in single block, block skip and continuous mode. To improve reliability, dynamic simulation can be done on PC screen in 2D drawing pattern. Moreover, to get a friendly man-machine interface, necessary information such as NC program executed, motion parameters, axis positions, conditions of on/off variables, system status can be displayed on the screen. At the same time, some basic parameters can be query in parameters query mode to make interface more friendly. The application software has also malfunction diagnose, alarm massage release and help function.

Summary

A lab platform of Open Numerical Control System was designed. It realized explanation and testing for bug function, data pretreatment function, NC code translation, NC simulation and execution, as well as motion controller function. It increases the expandability of NC system and user-oriented.

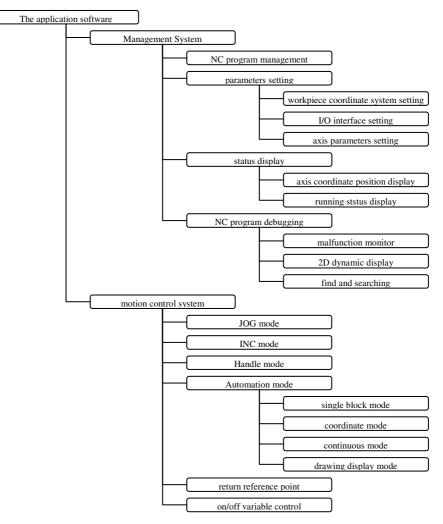


Fig. 3 Architecture of the application software

Acknowledgement

Thanks for the Foundation of Natural Science Projects by Shaanxi Educational Department (Project's No., 2013JK1020). Thanks for the State Scholarship Fund (No., 201308615015).

References

[1] C.H. Zhao, X.S. Qin, H. Tang. Mechanical Science and Technology. Vol. 24 (2005), p. 1109-1112

[2] H. Zhang. Machine Tool Electronic Apparatus. Vol. 2 (2005), p. 20-21

[3] Shenzhen Googol Technology Co. Ltd.. GT Series Motion Controller Programming Manual (in publish)

[4] H. Zhang, F.P. Li. Machinery Design and Manufacture. Vol. 6 (2008), p. 171-172

[5] D.W. Wu. Modular Machine Tool & Automatic Manufacturing Technology. Vol. 12 (2006), p. 51-57

[6] H.H. Design and Research of Open NC System on Windows. University of Electronic Science and Technology.(Master Degree Paper)

Application of the K-means Immune Particle Swarm Optimization Algorithm in the Steam Generator Water Level Control

Guimin Sheng^a, Yucui Xue, Boyang Zhang School of Electrical Engineering, Suihua University, Suihua, China ^aoxsgm@163.com

Keywords: SG(Steam Generator), Water Level Control, KIPSO(K-means Immune Particle Swarm Optimization), PID controller.

Abstract. The Stability of SG water level plays an important role in the safety of nuclear power plants, but tuned the parameter of water level PID controller is hard. Proposed a novel algorithm, KIPSO, which tuning PID controller parameters. Determine the cluster centre through K-means value cluster algorithm, and take the cluster territory as the characteristic value of vaccine set, enhance the vaccine multiplicity. Updated vaccine extraction by self-adaptive method, improved the convergence and adaptability. Analyzed the algorithm robustness in detail, and gave the rule which the immunity selection parameter. The simulation results shows: compares with the PID controller whose parameters are tuned by ZN method, KIPSO have a smaller overshoot, a better stability, and a shorter adjustment time. The simulation results show that the proposed method is effective for tuning PID parameters.

Introduction

The SG water level system is highly nonlinear, time-varying characteristics^[1]. The system exist serious "contraction" and "expansion" phenomenon on the transient, startup and low power operation condition, and the phenomenon results in false level signals. So it is difficult to tune the parameters of PID controller. As a result, the system is difficult to take into account the best dynamic and static characteristics at the same time.

Particle swarm optimization algorithm is a stochastic global optimization algorithm based on swarm intelligence. According to the disadvantages of classical PSO algorithm^[2, 3], such as easy to fall into local optimum and dimension disasters, etc, proposed a new algorithm, KIPSO by literature [4] is for PID controller tuning. And simulating test is proceeded by mat lab.

KIPSO Algorithm

Vaccine extraction. The position and velocity updates for each particle can be formulated as:

$$v_{id}^{k+1} = wv_{id}^{k} + c_1 \times rand() \times (p_{id} - x_{id}^{k}) + c_2 \times rand() \times (p_{gd} - x_{id}^{k})$$
(1)
$$x_{id}^{k+1} = x_{id}^{k} + v_{id}^{k+1}$$
(2)

Where i=1,2,...,m, *m* is the number of particles in the swarm, and v_{id}^k is d-dimensional velocity component of particle *i* in the *k*th iterations, and p_{id} is d-dimensional best position of particle, p_{gd} is the best position of global value, and *w* is the inertia weight, c_1 and c_2 are positive constants, *rand*() is random in the range[0,1].

Vaccine extraction process of particles swarm *X* is as follows:

1. After several iterations, extracting all the fine individual group from the population.

2. Using the K-means value cluster algorithm to determine the highest average cluster center of fitness value and the biggest neighborhood.

3. Note the gene position, cluster center and the biggest neighborhood of the best average fitness cluster field as the characteristic of the fine individual.

Vaccine Inoculation. 1. An individual, each gene position vaccination probability in the position region is,

$$P_{c} = 1 - \frac{f(x_{i})}{\sum_{i=1}^{N} f(x_{i})}$$
(3)

where $f(x_i)$ is the *i*th individual fitness value, determine vaccination probability in terms of fitness value. The larger the fitness value is, the less the vaccination probability becomes.

2. Perform the immunity examination for the accepted vaccine individual, if the affinity of antibody and the antigen is inferior to the father generation, and then the individual will be substituted by corresponding individual in father generation

Immune Selection. The probability choice formula as follows:

$$P(x_{i}) = \alpha \frac{\sum_{j=1}^{N} \left| f(x_{i}) - f(x_{j}) \right|}{\sum_{i=1}^{N} \sum_{j=1}^{N} \left| f(x_{i}) - f(x_{j}) \right|} + \beta \frac{e^{\frac{f(x_{i})}{T_{k}}}}{\sum_{i=1}^{N} e^{\frac{f(x_{i})}{T_{k}}}}, i = 1, 2, \cdots, N$$
(4)

where α , β are adjustable parameter between 0 and 1, $f(x_i)$ is the x_i the particle fitness value. As we can see the eq.4, if the probability which will be selected is high, and the individual that the density and the fitness value are high.

KIPSO Algorithm Description

In PSO, particles communicate information through eq.1 and eq.2. Here all the particles joined the vaccine extraction and vaccination, immunity choice operations of immunity algorithm. The algorithm operating procedure is as follows:

Step1.Determine the particle swarm algorithm parameter. Particle (antibody) swarm number N, positive constants c_1 , c_2 , vaccine extraction interval generation L.

Step2. Produce the new particle (antibody). Obtain the new particle through eq.1 and eq.2, and the linear decreasing weight law evolution, compute the fitness value, and take the current global optimal fitness value particle as the memory particle in the memory storehouse.

Step3. Judgment if procedures end. If satisfied the termination condition, stop running and to output the result, if did not satisfy the termination condition, inspect the iteration number of times. The immunity operation is performed each process of L iteration, otherwise, turn to Step3.

Step4. Vaccine extraction. Using the K-means cluster algorithm, obtains the individual vaccine characteristic value.

Step5. Vaccine inoculation. Extract individual randomly in the population according to certain proportion $N_r = N * r$, r (0 < r < 1), and obtain the new community, which the individual each gene position is inoculated with probability P_c .

Step6. Choose the Particle(antibody) based on the density and the fitness value, calculate N particles the choice probability through eq.(4), and choose Q particles according to the probability to form the particle swarm E_k .

Step7. Update the particle(antibody) swarm. The worst fitness value in particle swarm E_k is replaced by the memory particle in the memory storehouse, if $N \neq Q$, then produces *N*-*Q* particle stochastically, and form a new generation particle swarm, then turn to Step3.

Experiment Analysis

Analyze and simulate use the simplified mathematical model of the SG water level which is proposed by E.Irving^[5]. Tune PID controllers of Feed water, and the SG water level is controlled on this basis. The structure of control system is shown in Fig.1, Usually the parameters of SG level model change when adding perturbation. This situation is analyzed and simulated as follows: Water level is set 0mm, and then stability controls the water levels in the set value. Add perturbation of steam flow at 300s, then the response of water level is simulated when steam flow step signal change.

1. Simulation of steam flow positive step signal change: at first the water level is stabilized at the level set value 0mm on the condition of 50% loading. The steam flow is increased from 660kg/s to 815kg/s at 300s. As shown in Fig 2, the PID controller whose parameters are tuned by KIPSO reduces overshoot, and its convergence speed raise, its stability enhancements.

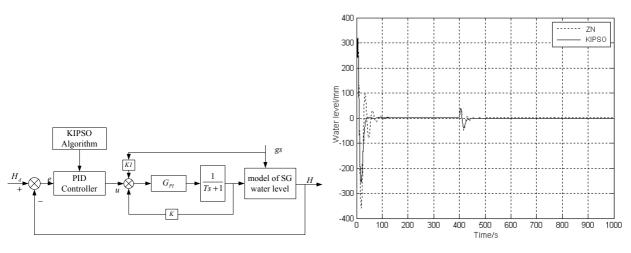
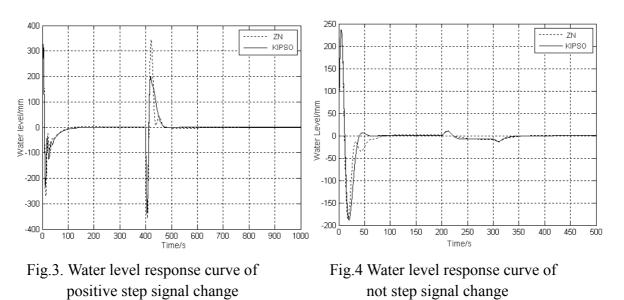


Fig.1 The structure of control system

Fig.2. Water level response curve of positive step signal change

2. Simulation of steam flow positive step signal change: at first the water level is stabilized at the level set value 0mm on the condition of 70% loading. The steam flow is decreased from 970kg/s to 180.8kg/s at 300s. As shown in Fig 3, the PID controller whose parameters are tuned by KIPSO reduces overshoot, and its convergence speed raise, its stability enhancements.



3. The situation which simulated and analysis above is on the condition of a wide range of steam flow step signal disturbance. However, in the actual operation of the power station the power is not step signal change in general. So this condition is used: at first the water level is stabilized at the level set value 0mm on the condition of 30% loading, then the loading increase gradually to 50% between 200s and 300s. As shown in Fig.4, the Water level changes reduced significantly at the time of loading variation. The performance of KIPSO is better than ZN method.

Conclusions

1. According to the simplified mathematical model of the steam generator water level, used a novel algorithm, KIPSO, which overcome PSO algorithm in falling into the local extremum easily problems tuning parameters of the water level controller, and simulate the response of water level when the condition varies.

2. Determine the cluster centre through K- average value cluster algorithm, and take the cluster territory with the highest average fitness value and the biggest neighborhood as the characteristic value of vaccine set, each time select one of the vaccine inoculation randomly, enhance the vaccine multiplicity.

3. In the immunity selecting operation, had considered the influence that the individual fitness value and the individual the density selection probability, maintains the antibody multiplicity, prevents the community degeneration.

4. Analyzed the algorithm robustness in detail, and gave the rule which the immunity selection parameter.

5. The simulation results shows: comparing with the PID controller whose parameters are tuned by ZN method, that is tuned by KIPSO have smaller overshoot, better stability, shorter adjustment time. The results of simulation prove the effectiveness of KIPSO algorithm in tuning PID parameters.

Acknowledgement

The authors would like to thank the Science and Technology project of Suihua University (K1201002).

References

- [1] Jizhou Zhu. The operation of PWR Nuclear Power Plant .M. Beijing: atomic energy press, 2000, 12: p.138-139."In chinese"
- [2] Senthil Arumugam, M; Ramana Murthy, G; Rao, M.V, C; Loo,C.K. A novel effective particle swarm optimization like algorithm via extrapolation technique ,J. 2007 International Conference on Intelligent and Advanced Systems, 2007, p.516-521.
- [3] CLERC M, KENNEDY J. The particle swarm-explosion stability and convergence in a multidimensional complex space J. IEEE Transaction on Evolutionary Computation, 2002, 6(1): p.58-73.
- [4] Man chuntao, shengguimin, zhangtao. Adaptive Vaccine Extraction Immune Particle Swarm Optimization Algorithm, J.2009 2nd International Gonference on Biomedical Engineering and Inform-atics.2009. p.1626-1629
- [5] E.Irving. Toward Efficient Full Aromatic Operation of the PWR Steam Generator With Water Level Adaptive Control, C. Proc 2nd Int Conf Boiler Dynamics and Control in Nuclear Power Stations2. Bournemouth, 1979: p.309-329P

The Application of Medical Robotics in the MRI-Guided Invention

Wenlan Guo^{1, a}, Zhijia Wang^{1, b}, Yun Zhang^{2, c}

¹College of Computer Science and Technology, Harbin University of Science and Technology, Harbin, 150080, China

²Department of Electrical and Computer Engineering, University of Texas at Austin, 78741, US

^aguowenlan@sohu.com, ^bhuangjin0706@126.com, ^c zhangyun@utexas.edu

Keywords: robot, the medical robotics, MRI

Abstract. This proposal focuses on the interventional MRI technology and the MRI compatible robots which are used to overcome some limitation of the MRI. In the introduction part, the development and the limitation of the current MRI interventions are introduced and a possible solution, MRI compatible robotic assistance, is proposed. In the design part, the specification of the MRI robot is discussed, including the MRI compatible material, the motor and encoder, the control unit and the combination of haptic sensor. Finally, the possible future application of the MRI compatible interventional robots is introduced.

Introduction

Magnetic Resonance Imaging has long been known as an excellent tool for the non-invasive diagnosis due to its perfect soft tissue contrast and no harmful radiation compared with CT and X-ray imaging. Thanks to the combination of novel fast imaging technology allowing immediate follow-up on the MRI image and excellent problems location, MRI is now becoming an imaging tool for guiding various interventional procedures. Nowadays, various inventions and biopsy procedures on different organs including the brain, breast, liver, prostate and the heart are being investigated. The studies on the vascular and spine interventions which is very challenging have also made great progress. However, there are some technique problems which greatly limit the development and application of the MRI-Guided interventions.

The use of a medical robot guided by the MRI has many advantages beyond remote controllable, which would have the potential to eliminate the restrictions and expand the application of MRI interventions. The robotic assistant will also minimize the potential for human errors and mis-registration associated with the current procedure. What is more, unlike human beings, the robots are digital devices that may communicate directly with the MR digital images. The automatically controlled robot could therefore give a more accurate performance of detection and execution. It would not only augment the physician's manipulation, but also establish a digital platform for integrating medical information. Currently, the design and construction of such a robot is still technically very challenging. Firstly, the material of all the parts of the robot, including the dynamic system, the power system and the sensor system, must be MRI-compatible with satisfied mechanical strength. Another constraint is the space limitation of some special application. Furthermore, the traditional surgery depends not only on the MRI images and the visualization, but also the sense of touch of the medical staff. Therefore, the diverse bio-sensor system including the haptic feedback capacities should be further developed. In this proposal, I will give the design method and further possible application of the medical robot guided by MRI.

History Review and Current Achievement

Previously research on MRI compatible robots has been quantitatively limited, yet a company has already introduced a commercial MG-IGT robot. The earliest work is a robotic surgical assistant constructed for open MRI representing five piezoelectrically actuated degrees of freedom. The manipulator is located at the top of the imager between vertical coils of MRI, and presents two arms that extend to the imaging area to provide a guide for manual instrument manipulation[1].Work

continued the development of a one arm needle support[2] and improved accuracy results[3]. The University of Tokyo has built an MRI-compatible needle insertion manipulator. The system was designed for neurosurgical applications[4]. A research group for the University of Calgary has reported their on-going work for the development of an MRI neurosurgical assistant with bilateral arms[5]. The most evolved work started at the Institute for Medical Engineering and Biophysics. Several versions of a robotic system for breast lesion biopsy and therapy under MR guidance were developed[6]. This group also introduces the first commercial MRI-compatible robot MG-IGT system. The system includes a 5 DOF robot to position a needle guide for manual needle insertion, and has very elegant and compact way of fitting with the MRI bore based on an outstanding kinematic design[7].Recently, the research at the Johns Hopkins University has developed a fully-actuated, electricity-free, non-magnetic and dielectric robot for image guided access of prostate gland, named MrBot. This achievement was through the invention of a new type of pneumatic motor which provides easily controllable, precise and safe pneumatic actuation[8]. Currently, many research institutions all over the world focus on the design of MRI-compatible robotic assistant for various medical application. However, most designs could not be widely used for clinical purples and need further clinical test.

Design Method

(1) The Material of the MRI-compatible Robots.

For MRI compatibility, all components of the robot should be constructed of nonmagnetic and dielectric materials, such as Polyetherimide, Nylon, Delrin, high-alumina ceramic, glass, sapphire, and silicon rubber which have already been tested for MRI compatibility. Other properties of the material, including the mechanical strength and the stability should also be considered and tested accounting for their function in the robot.

(2) Motor and Encoder.

The motor and encoder are the important parts of the whole robot system. The traditional electromagnetic motor could not be applied in the MRI environment. The hydraulics is decoupled from the electro-magnetism and is MRI-compatible, but it is dismissed for its risk of leakage that would compromise sterility and its complicated configuration. Pneumatic actuation is considered as an optimal choice, but always be dismissed for the reliability concern and the difficulty for the design of fail-safe implementation. Currently, a modified pneumatic actuation named PenuStep which is the first pneumatic step motor is designed combining easy controllable motion, fail-safe operation and full MRI compatibility. This motor has already been applied in the robot for prostate intervention. Another optimal choice is the ultrasonic motor which applied the inverse effect of the piezoelectric ceramics and the ultrasonic vibration changing the tiny transformation of the material to rotor and slider through the amplification of the mechanical resonant and friction coupling. The ultrasonic motor will thus never generate any electrical field or magnetic field. Together with advantages of a satisfactory weight, fast response and easy controllable motion, it could be widely applied as the motor of the MRI-compatible robots.

The motor should include a custom fiber optic quadrature encoder for closed-loop control. The feedback signal from the motor is transported to the electric equipment outside the shielding room for further data processing and imaging through optic fiber.

Design of Sensor System

Controlling robotic interventions could not only depend on the MR images, other types of sensors including haptic sensors which could refine the information provided by the MRI should also be combined. This complicated sensor system reproduces the multiplicity of sensing source used by the human beings and allows the MRI-compatible robots to give more accurate performance in the procedure of detection and operation. As MRI-based vision modeling remains highly sensitive to objects surface characteristics, haptic sensors can be advantageously integrated to complement the 3D models. Following this direction, the addition of a haptic component to MRI-compatible robot

appears as a straight forwardimprovement that can help in identifying the small objects and estimating their characteristics including the their shapes and texture that are critical to achieve haptic control of fine robot manipulation.

The proposed medical robotic haptic sensing system consists of a custom-designed instrumented passive-compliant wrist which is inserted between the tactile array sensor and the end-effecter and a tactile array sensor. The compliant wrist included in the proposed haptic sensor system allows the tactile sensor to accommodate the constraints of local geometry of the explored objects surface and, thus increase the amount of information acquired. The wrist consists of two rigid planar plates, one being passively mounted on springs. This provides the wrist with three relative degrees of freedom. Four linear displacement transducers allow one to measure the distance between the two plates of the wrist's plates. Referring to the base of the robot, position sensors placed in the robot's joints along with the coordinators provided by the instrumented wrist determine the kinesthetic information about the tactile sensor position an orientation.

The tactile sensor performs the cutaneous component of sensing that provides the contact geometric profile of the touched object. This information being combined with that of the wrist allows a complete construction of the 3D-shape of the surface located within the tactile sensor probe.

All the data collected from the tactile array sensors and the wrist is sent out of the MRI shielding area through optic fibers.

Design of Control Unit

In this proposal, the ultrasonic motor is applied as the driver of the robot. DSP controller could be used as the key element in the design of the control system. According to the feedback signal of the photoelectric encoder and the tracks

setting given by the surgery planning system which is manipulated by the medical staff based on the MR images and the response from the haptic sensors, the DSP controller sends control signals to the driver of the ultrasonic motor. The driver receives the control signal from the DSP controller and the vibrating feedback signals of the piezoelectric ceramic inside the ultrasonic motor and gives out frequency modulated ultrasonic sinusoid signals to the piezoelectric ceramic on the stator of the motor.

The control system of the MRI-compatible interventional robot is demonstrated in the figure 1. The current location collected from the MR images and the optical positioning system is compared with the location of the target. The velocity value is obtained through the PI adjust ring based on the deviation of the position. The given velocity value is then compared with feedback velocity from the photoelectric encoder of the ultrasonic motor and the obtained deviation value is applied as the input signal of the General Predictive Controller (GPC). The General Predictive Controller will finally give out the effective control signal to the ultrasonic motor.

The Future Application of MRI-Compatible Robot in MRI Inventio

The development of the MRI-compatible robot will definitely improve the surgery procedure of current MRI interventions and expand the application area of the MRI interventions. Use of a robotic assistance will minimize the potential for human errors associated with current procedures and will better address the practical issues of operating in MR bore. The robotic system may also serve as a validation tool for researchers whose work requires precise targeting anatomical regions identified by MR imaging for treatment such as drug delivery or tissue biopsy.

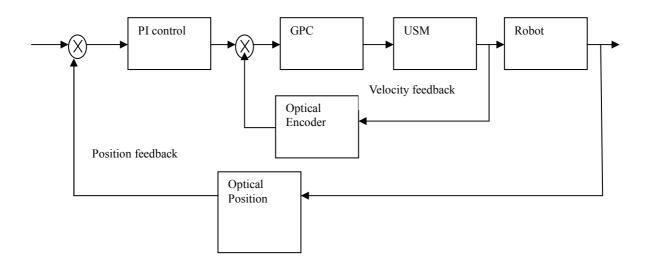


Fig.1 The configuration of the control system

References

- [1] Chinzei K, Miller K. Towards MRI guided surgical manipulator, Med Sci Monit. 2001,7: pp.153–163.
- [2] Koseki Y, Koyachi N, Arai T, Chinzei K .Remote actuation mechanism for MR-compatible manipulator using leverage and parallelogram - workspace analysis, workspace control and stiffness evaluation, Robotics and Automation, 2003,1: pp.652–657.
- [3] Koseki Y, Kikinis R, Jolesz FA, Chinzei K. Precise evaluation of positioning repeatability of MR-compatible manipulator inside MRI, Medical Image Computing and Computer- Assisted Intervention, 2004,3217: pp.192–199.
- [4] Masamune K, Kobayashi E, Masutani Y. Development of an MRI-compatible needle insertion manipulator for stereotactic neurosurgery,J Image Guid Surg, 1995,1: pp.242–248.
- [5] Louw DF, Fielding T, McBeth PB. "Surgical robotics: a review and neurosurgical prototype development," Neurosurgery, 2004,54:pp.525-536.
- [6] Kaiser WA, Fischer H, Vagner J, Selig M, Robotic system for biopsy and therapy of breast lesions in a high-field wholebody magnetic resonance tomography unit, Invest Radiol, 2000,35, pp.513—519.
- [7] Hata N, Jinzaki M, Kacher D, Cormak R. MR imagingguided prostate biopsy with surgical navigation software: device validation and feasibility, Radiology. 2001,220: pp.263–268.
- [8] Dan Stolanovici ,Danny Song.MRI Stealth'' robot for prostate intervention, Minimally Invasive Therapy, 2007,16: pp.241–248.

Key Technology Research Based on the Smart Home BSNs

Wang chunying ^{1, a}, Zhang Jun ^{2,b}

¹ School of Software, Harbin University of Science and Technology, Harbin, Heilongjing, China ² HeiLongJiang Office Of China Banking Regulatory Commission, Harbin, China ^aspring_hrbust@163.com, ^bzhangjun_y@cbrc.gov.cn

Keywords: Smart home; BSNs; Home wireless network; Intelligent control; Behavior recognition

Abstract. In recent years, Mobile computing and intelligent household hot topic, more and more get the attention of people. The current smart home systems for self-help to collect information about the indoor environment, at the same time can also interact with the user, but the system when the user needs to send control commands always spend time learning about the current state of household environment, manual control will become a kind of bondage. So this paper using a user activity recognition system based on smart phone, its main function is based on the current user on sensor information to obtain the user's current activity, the current environment control command. Combining the system and smart home system, family equipment according to the user's activities independently adjust to cooperate with users, users are more focused on the main transaction processing. This paper will be focused on energy saving problem, smart home system based on smart phone user activity recognition and the coordination between them.

Introduction

Smart Home is based on people's living environment, using advanced computer technology, network communication technology, wireless sensor and embedded technology will be the family Home appliance system, security system, and other organic combination, realize the environmental data real-time acquisition, analysis, processing and communication, and then make unified management control, thus providing a Smart, safe, comfortable, energy-saving residential environment. Compared with the smart home, smart home not only with all of its functions, but also the original relatively independent of the connecting link between devices and subsystems, the mutual exchange of information between functions, at the same time time guarantee within the family and household unobstructed information exchange.

At present, the smart home system control is mainly the user control command according to the will of the individual input, the system of the occurrence of any activities need to be involved in, increase the user's workload, reduce the intelligent degree of the system. In this paper, activity recognition is introduced to avoid these two problems, between people and household system has always been using your mobile device to connect through the network, transmission of information between each other. Activity recognition is mainly in the various activities section of the human body sensor node deployment can provide the most effective information, such as the direction of acceleration sensor, sensor, etc., when people after action, attached to the body of the sensor node will receive the current data uploaded to the server, the server will receive the characteristic value of the original data are extracted, and then through the classifier of the activities and the user's activity sequences, and then according to the activity sequence analysis of the user's intention, thus the user intent again into a smart home system control command, the whole system is attached to the user and does not require users to participate in the whole automation system at home.

Previous studies is the use of a centralized way to identify the user activity, all the sensor data are uploaded to the host for unified processing analysis. Spectral graph partitioning and transition label method is used to identify major tradition mode[1]; Put forward the distributed activities of using only part of the node classification recognition model[2,3], Host after synchronous processing using the decision tree classification, the model USES 9 sensor node can identify 25 in activity, recognition

accuracy reaches 93.3%; Joined the feedback module, makes the general activity recognition system gradually into a targeted[4]; For event handling in stages, events and activities, using the markov model to identify some of the more complex activities, reduced the demand for training data set[5]; Using the activity recognition system based on hidden markov model and low latency gesture recognition[6], Kit can be used as a teaching and research.

The Key Technology and Solution

(1) in the smart home system of each sensor node energy effective problem solving

- ① According to node function, communication distance, etc., choose the sensor nodes.
- ② According to the type of sensor, reasonable set the frequency of the data.

③ Reasonable deployment of each sensor node, starting from the overall system, reduce the power consumption of the system as a whole.

(2) each node in the smart home system based on BSNs communication network structure design Family environment node deployment as shown in Fig. 1, the blue triangle coordinator, said green triangle according to the router, the Yellow River delta said sensor nodes, the controller node. Coordinator at the core of the network, network management and data distribution, covering 50% of the router. Router as access nodes communicate with sensors, covers each relatively independent space; Always controller through a router connected to the network, as the intelligent data processing, the control unit is responsible for the control of whole room; Sensor as a data provider, is responsible for collecting the information such as indoor temperature, light, humidity; Controller for the room appliances, facilities of various control unit is responsible for the corresponding control command. Body sensors on the composition of an independent state-controlled bharat sanchar nigam, carried by the user's smartphone communications in state-controlled bharat sanchar nigam and household system, is responsible for receiving a household system feedback, at the same time will control commands sent to the home system.

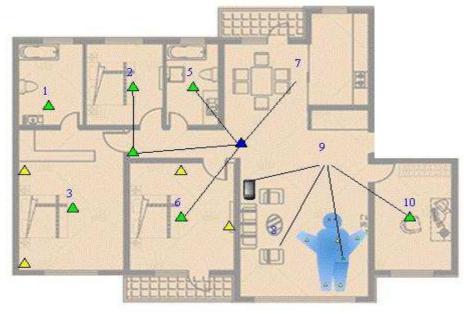


Fig. 1. BSNs based intelligent home environment node deployment diagram (3) real-time algorithm of the single user activity recognition on a mobile device

Activity recognition need access to the user of information, the data provided by sensor nodes, so the selection and deployment of sensor type is an important factors affecting user activity recognition accuracy. User activities including static and dynamic activities, static activities show users over a period of time to maintain a fixed posture, sensor data to maintain the basic stability; Dynamic activities according to the user is in the midst of the activity state body, the change of the sensor data is bigger. Activity recognition first determines the user activity is a dynamic or static activities, depending on the activity recognition using appropriate and efficient algorithm.Smartphones receives

the sensor nodes to upload the activities of the characteristic value of information, standard variance, analysis of characteristic value when the upload for this value is more than a set limit, argues that user is currently for the dynamic action, otherwise to static action.

If for dynamic activities, the introduction of concept, it is the basic unit of the composition activity. Activities, before define all active slices as much as possible in the first place, then according to the activity is used to identify the activities. Sensor nodes of the body after uploading data to the original data segmentation, the eigenvalues of the segmentation fragments regarded as a piece of characteristic value of ID3 algorithm to classify active slices. ID3 algorithm based on decision tree to classify information, introducing the concept of entropy in information theory, using the statistical features of information gain decided to the order of attribute classification, information gain is larger that the information on the classification of the most useful. Activity classification a classification properties of five, respectively, mean value, standard variance, correlation data, amplitude and extremum, ID3 algorithm from the statistics for each attribute information gain, then according to the size of the information gain the best selected attributes sorting order. Known set of size R, training set S, S information entropy is:

$$H(S) = \sum_{I} - p(I) \log_2 p(I) \tag{1}$$

Attribute of information gain is:

$$G(S,A) = H(S) - \sum_{v} \left(|S_{v}| / |S| \right) \times H(S_{v})$$

$$\tag{2}$$

There is | Sv | property A v value S the number of subsets. Said a known after attribute reduction of entropy, the greater the information gain illustrate this property to provide the more information for classification, classified more effective.

Determine a user's activity after, use the epsilon - the NFA state machine in a steady stream of activity state transition analysis, until finally the produce activity. Due to the low limbs activity is rich, and less activity of the waist, can directly determine can get the waist activities, limbs using a state machine, onset of state machine types, generate results for each of the activities of the limbs. As shown in Fig. 2.

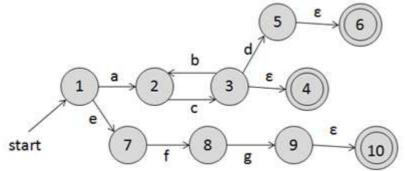


Fig. 2. Identify activities epsilon - the NFA

(4) the user activity recognition algorithm to identify new user activity

In the process of this topic, the single user activity recognition using the concept of active slices, which is the basis of all activities, after defined the basic will not change. When meet new activities, only to the activities of the upper increase new identification process of the sequence, the last name of the user define an activity for the results and the corresponding control command.

Use the epsilon - the NFA state machine to determine a condition met the current activity cannot make jump, also can't enter the end state, argues that activity recognition system has met the new user activity. Starting from the transfer of the current state of the node failure, read one tablet each time, first create a new state, and then add the transfer function between two states, add after successful determine a termination condition, then optimize the new state nodes, eliminate duplicate nodes. After the local new activities, smart phones and collect the current local activities for a period of time the rest of your body to upload, agreed to prompt the user for the current activity title after processing, and to control the equipment.

(5) the group activity recognition, various mobile devices data aggregation and scalability of the system

This topic only used in household environment in the group activity recognition, the rest of the scene using single user activity recognition. Initialization system, to set an area in the home environment, when the user is located in the region within the group using situation, because the family members of the collective activity has practical significance for smart home system control, when a user is beyond the area user activity and its relevance only impact on its current location, and the impact on household scenario is limited to sensor to identify the special action.

(6) system, the data security problem in the process of communication

When users need to remote to interact with household system need to transmit data through the network, and the data in the network transmission process there are a variety of potentially unsafe factors, so requires increased security mechanism in the process of interaction, the moment to ensure data security and integrity, avoiding the smart home system is invaded, personal privacy was leaked.

Summary

Of this paper is given for the smart home system based on ZigBee wireless communication technology, fully considering the possible energy consumption problems, then puts forward the corresponding solution, can effectively improve the network lifetime and reduce the amount of data transmission, as human energy saving consciousness and the improvement of system performance requirements, energy-saving household system will certainly has a large consumer market.

This paper in the use of mobile real-time identification of user activity, and the external environment, in turn, regulated, simplify the way people interact with the outside world, the platform can be applied to other places, such as offices, schools and hospitals. A simple action can make the external environment according to the user's intention to adjust, without too much action. In addition, with the system application scope and scene gradually expand, it is entirely possible that in the future will be all independent scenes of form a complete intelligent space, the objective of the research results will play a potential in the development of intelligent space.

References

- Raza Ali, Louis Atallah, Benny Lo, Guang-Zhong Yang: Transitional Activity Recognition with Manifold Embedding. Body Sensor Networks. (2009)
- [2] Liang Wang, Tao Gu. Real-time Activity Recognition in Wireless Body Sensor Networks: From Simple Gestures to Complex Activities. IEEE International Conference on Embedded and Real-Time Computing Systems and Applications. (2010)
- [3] Hassan Ghasemzadeh, Roozbeh Jafari. Physical Movement Monitoring Using Body Sensor Networks: A Phonological Approach to Construct Spatial Decision Trees. IEEE Transactions on Industrial Informatics. (2011)
- [4] Z.Q. Ding. I.M. Chen. Intergration of sensing and feedback components for human motion replication. International Conference on Body Sensor Networks. (2010)
- [5] Min Xu, Satish Iyengar. A two-stage real-time activity monitoring system. International Conference on Body Sensor Networks. (2011)
- [6] Daniel roggen, Marc Bachlin. An educational and research kit for activity and context recognition form on-body sensors. International Conference on Body Sensor Networks. (2011)

Database Design of NC Cutting Tool Matching and Management System

Xiulin Sui^{1,a}, Di Wang^{2,b}, Xinyang Liu^{3,c} and Yan Teng^{4,d}

¹College of Mechanical and Power Engineering, Harbin University of Science and Technology, Harbin Heilongjiang150080, China

^asuixiulin@sina.com; ^b448932122@qq.com; ^c393994192@qq.com; ^d996309937@qq.com

Keywords: NC cutting tool; Matching and management system; Database

Abstract.In order to improve efficiency of the cutting tool in the practical production process and mend the phenomenon of disjunction between previous NC cutting tool matching and cutting tool management, integrate matching with management of cutting tool and regard Access as the backstage database and apply VC++6.0 software to develop database management systems of cutting tool matching and management. The production process of cutting tool efficient matching and the management process of cutting tool information is studied, according to the application requirements of system, then the function target of the system realization is established, the overall structure model of the system is constructed and the function and operation procedure of each functional module is designed.

Introduction

With the development of mechanical technology, more and more companies introduce machining centers, NC lathes, milling machines and other NC machining equipments in modern machining, so that the NC cutting tool is widely used in the production of first line to instead of the traditional NC cutting tool becomes a major role in NC machining [1]. The quality and performance of the actual machining NC cutting tool have a directly impact on processing efficiency, dimensional accuracy and surface roughness of the workpiece and other related indicators [2]. According to statistics: 16% of the plan stopping is caused by of lack of cutting tool, 30% to 60% of the cutting tool inventory is out of control, machine operators spend 60% of the time in finding and matching the cutting tool [3,4].Therefore, the performance, optimizing selection and management of the cutter plays an important role in enterprises efficiencies such as production quality, production cost, production efficiency and so on. This paper based on Access database as the background, used VC++ 6.0 software development for database management system of tool selection and management.

System Requirements Analysis

Cutting tool matching and management are complex task which works separately, one is depending on the basis of NC technology personnel working experience and another is depending on the relevant records of the operator carried out based. Currently, with the increasing of cutting tool types and quantity while the limited condition of machining workshop, borrowing cutting tool from each other between different equipments and product parts has brought great difficulties about cutting tool management, also laid a great risk to the production efficiency and product quality[5]. Cutting tool matching and cutting tool data efficiency management play important roles in increasing machining efficiency and reducing machining costs in the manufacturing process of product. With the increasing of the number of NC equipments and new product categories, selection and management of cutting tool cannot meet the needs of the modern production just depend on the work experience of technical staff and the workshop site search. Through employed of advanced cutting tool matching and management, the scientific use of cutting tool are urgent required in modern production.

Overall design of the system architecture

Management process analysis. In this paper, the development of cutter tool matching and management system combine the cutting tool matching and cutting tool information management, tracking and managing the whole process during the storage of new cutter tool and the final scrapped of ancient cutter tool. For this reason, the system needs to generate an unique cutting tool code during new cutter tool are put in storage which record the basic information, stock information, life information, parameter information and so on; considering various factors, optional personnel matching the cutter tool in accordance with the principle of matching, including the existed matching principle, CAPP, production plan and a series of cutting parameters obtained through physical simulation and so on. At the same time, the cutting tool administrator according to the requirements to edit the information of cutting tool storage, also according to the storage information and product plan to proceed the application of purchase, and make an scrapped operation of life end cutter tool. To fulfill the requirements of cutting tool management, the system could apply specific methods for statistical accounting on the cutting tool storage along with the ability of producing related report. Meanwhile the operator should track and record the inputs, output, storage, lifetime and other related information on the cutting tool. In order to meet the requirement of system maintenance, system administrators are provided with the functions of adding users, changing users, using log management, system maintenance and so on.

Function modules.According to the overall system design, this system is designed into five sub-modules: user management, cutting tool matching, cutting tool search, cutting tool management and help module, as shown in Fig.1. Wherein each module features include:

(1)User management module: used to fulfill user registration, addition, modify.

(2)Cutting tool matching module: used to fulfill cutting tool matching, assembly, testing.

(3)Cutting tool management module: used to fulfill cutting tool addition, deletion, maintain and refresh.

(4)Cutting tool search module: used to achieve the desired cutting tool according to different needs.

(5)Help module: for system maintenance, use and management.

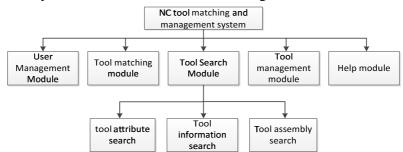


Fig.1 System functional block diagram

System Operation Process Analysis.Making an analysis for the requirement of cutting tool matching and management, the system flow chart can be shown as follow. Firstly, the user enters an user name and password for the user login screen when the user has the correct name and password for input, then enter into the corresponding main interface; If the user name does not exist or the password is incorrect, then user needs re-enter. For different user base, there are different user interface and different modules should be used. Such as system information administrator can enter into basic information repository; cutting tool matching personnel and cutting tool assembled inspectors can enter into tool matching information database; inventory managers can enter into inventory MIB and so on. Specific processes are shown in Fig.2.

Design of Database

User requirements reflected in various information input, save, modify, and query. This requires that the database structure can fully meet the various input and output information. Data, data structures and data flow processing is the basis for the design of the database. Analysis the business processes of cutting tool matching and management system, design data term and data structure as below shown.

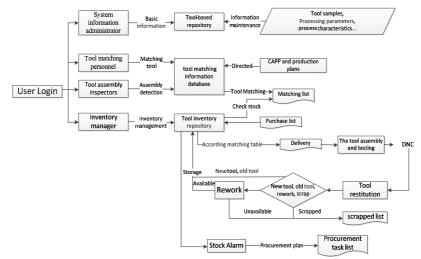


Fig.2 System process analysis

User Lists : User ID, user name, and password. Cutting tool and process information database table features : cutting tool name, cutting tool number, cutting tool properties, cutting tool quantity, manufacturer, cutting tool life, production date. Cutting tool matching database: properties number, cutting tool number, cutting tool name, cutting tool parameters, cutting tool properties matching components. Cutting tool storage information: cutting tool purchase, cutting tool out of storage, cutting tool repair, cutting tool inspection, cutting tool scrapped, inventory alarm, cutting tool matching and so on. Supporting Components Table : parts number, parts name, parts properties, specifications, notes .

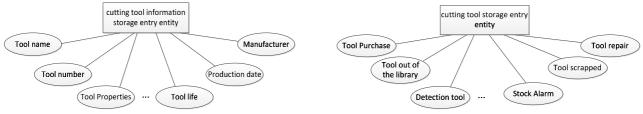


Fig.3 Tool information into the entity

Fig.4 Cutting tool information storage entry entity

Design of Database Concept. After obtaining data terms and data structures, all kinds part that can meet user requirement and their relationship can be designed, which make the basis for logical design structures, this including various specific information, through internal function to form data flow. Fig.3 shows input entity ER diagram for cutting tool information, Fig.4 shows input entity E-R diagram for cutting tool storage.

🔲 The t	The tool information input sheet							Components supporting table						
/II	D • The tool •			Number of • Tool				ID ·	÷ I	Comnonent -	Tool numb	- Commonent	· Specifica ·	Remark •
	1		e:material:45		15	2013/2/23		12					-	itomat ii
	2		e:Tool diamet e:Tool diamet		8	2013/5/4 2011/6/18			1	1	CFW2080050	0 Straight s	h XX Steel	
	4		e:Iool diamet e:material:45		10	2011/6/18 2012/7/19			2	2	CLMG100040	0 Straight s	h XX Steel	
	5		e:Ordinary cu		20	2011/2/13			3	3	CLZG100020	0 Straight s	h XX Steel	
	6		e:Ordinary cu		23				d			0 Curved bar		
	7		1 Ordinary to		5	2010/6/9 2011/6/21			т					
	8		l High-speed t Ordinary to		10	2011/6/21 2013/6/23			5	5	CLZT080020	0 Straight s	h YY Steel	
	10		t Ordinary to			2013/8/23			6	6	CMZG080020	0 Straight s	h ZZ Steel	
	11	Threading	t Tool diamet	11	10	2012/5/31			7	7	CW7T050020	0 Straight s	h 77 Steel	
	12	Threading	t NC tool	7	10	2012/7/12			1			-		
	13	Threading	t NC tool	21	9	2012/9/21			8	8	XPMG050010	0 Curved bar	XX Steel	

Fig.5 Tool information into tables

Fig.6 Components supporting table

Design of database logical structure.Logical structure of database is defined as using above database structure design translate into Access database system which support data model.the information of cutting tool storage is shown in Fig.5, supporting parts table is shown in Fig.6, cutting tool properties table is shown in Fig.7, cutting tool out and storage table are shown in Fig.8.

	Tool prop	erties table				Access table								
_						/ ID -	Access ta'r	Access on -	Access st -	Access tool -	Access tool nam •	Access to •	Access am •	Date 🔻
\angle	ID	 Tool attr 	Tool numb 🔹	Tool name 🔹	Tool Prop 🔹	1	11	Enter	¥	XMZG080020021	udrical facing mil	D factory	5	
	1	1	CLZG0800100	Threading tool	NC lathe	2	12	Enter	S	CLZG100040022	Threading tool	S factory	10	2013/5/4
	T	1		0		3	13	Out	D	CYMG080020023	rical shank hole	A factory	5	2011/6/18
	2	2	XMZG1000200	Facing mill	NC milling	4	14	Out	F	XIZG040010024	Piece cutter	B factory	4	
	2	2	XPMG0800200	Disc mill	NC milling	5	15	Enter	G	XIMT080020025	Piece cutter	C factory	5	2011/2/13
	0	0			-	6	16	Out	H	CLZG120040026	Threading tool	D factory	12	2010/5/6
	4	4	XMMT0600100	Facing mill	NC milling	7	17	Out	J	XPZG100020027	Disc cutter	V factory	14	2010/6/9
	5	5	CLZG1000400	Threading tool	NC lathe	8	18	Enter	K	XING080010028	Piece cutter	B factory	12	
	J	J	CLIGIOUO400	IIII Cauling (001	NCIALLE	9	19	Out	L	CLZG100040029	Threading tool	C factory	23	2013/6/23
	6	6	CYZG0800200	lindrical shank To	NC lathe	10	20	Out	G	CLMG120040030	Threading tool	D factory	5	2011/3/14

Fig.7 Tool attribute table

Fig.8 Access table

As above four graphs shown, cutting tool information storage table through "cutting tool number" and cutting tool properties table and "cutting tool number" of matching components table, which establish relation with "out and storage number", then internal relation of cutting tool database graph can be get, as shown in Fig.9.

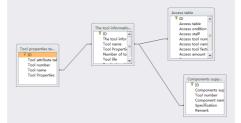


Fig.9 Showing the relationship between the internal database

Conclusions

This paper studies the product process of cutting tool quick matching and cutting tool information management proceed, construct overall structure model of the system, design features and operating procedures of each functional module. As background of the Access database, applying VC++6.0 software develop database management system for cutting tool matching and management. The system has cutting tool selection and management two important function, it can finish the cutting tool rapid matching in the manufacturing process and the effective management of the whole life of the cutting tool.

Acknowledgments

This research was sponsored by Excellent Academic Leaders Project of Harbin science and technology innovation talents of special fund (2013RFXXJ064).

References

- [1] Yao Liu. Research CNC tool is automatically selected CAD systems[D]. Shenyang: Shenyang University,2009:15-20.
- [2] Xincheng Wang. High-speed machining technology and tool selection[J]. Technology Vision, 2013,12 (7): 55.
- [3] Yang Liu, Wang ChengYong, Song Yuexian. Tool management system research and application[J]. Mold Manufacturing Technology,2007:64-67.
- [4] Pengwei Ren. Full life-cycle management tool systems research and development [D]. Qingdao, Qingdao Technological University,2012,12:13-16.
- [5] Xiaojun Lin, Gao Chun and so on. Tool management system database technology [J]. Aeronautical Manufacturing Technology, 2013,12 (7),70-73.

Exponentially Stable Sampled-data Control for Uncertain Systems

Liying Fan^{1,a}

¹Department of Mathematics, Harbin University of Science and Technology, Harbin, 150040, China ^afan living@163.com

Keywords: Uncertainty, Time-varying delay, Sampled-data control, Input delay

Abstract. In this paper, the problem of the exponentially stable sampled-data control was investigated for a class of uncertain systems. Based on the input delay approach, the system was modeled as a continuous-time system with the delayed control input. Attention was focused on the design of a state feedback sampled-data controller which guarantees the exponential stability of the closed-loop system for all admissible parametric uncertainties. Using linear matrix inequality(LMI) approach, sufficient conditions are obtained. Simulation example was given to demonstrate the effectiveness and correctness of the proposed method.

Introduction

In recent years, sampled-data control theory has attracted extensive attentions in control system literatures, two approaches often have been presented for the sampled-data control problem. The first one is the lifting technique^[1], where the sampled-data system is transformed into an equivalent discrete system with finite dimensional state space. The second one is jump method. More recently, input delay approach is presented to solve the problem of sampled-data H_{∞} control^[2], in which the sampled-data system was modeled as a continuous-time one with an input delay. Parameter uncertainties often exist in real systems due to modeling inaccuracies or changes in the environment and is frequently a cause of instability and performance degradation. Therefore, it is important to study the stability of systems in the presence of uncertainty. However, there have been few results in the literature of an investigation for the robust exponential stability of the sampled-data systems, it is still open and remains challenging.

Motivated by the above analysis, in this paper, we focus our interest on the exponentially stable problems of a class of systems with norm bounded time-varying parametric uncertainties. By using input delay approach, sufficient conditions are proposed, which guarantee the system is internally exponentially stable. Numerical example shows that these results are feasible and effective.

Problem Statement and Preliminarie

Consider the following uncertain system:

$$\begin{cases} \dot{\boldsymbol{x}}(t) = (\boldsymbol{A} + \Delta \boldsymbol{A}(t)) \boldsymbol{x}(t) + (\boldsymbol{B} + \Delta \boldsymbol{B}(t)) \boldsymbol{u}(t) \\ \boldsymbol{z}(t) = \boldsymbol{C} \boldsymbol{x}(t) + \boldsymbol{D} \boldsymbol{u}(t) \end{cases}$$
(1)

where $\mathbf{x}(t) \in \mathbb{R}^n$, $u(t) \in \mathbb{R}^{n_u}$ and $\mathbf{z}(t) \in \mathbb{R}^{n_z}$ denote the state, control input and controlled output vector, respectively. *A*, *B*, *C* and *D* are known real constant matrices with appropriate dimension, $\Delta A(t)$ and $\Delta B(t)$ are time-varying parametric uncertainties in the form of

$$\begin{bmatrix} \Delta \mathbf{A}(t) & \Delta \mathbf{B}(t) \end{bmatrix} = \mathbf{MF}(t) \begin{bmatrix} \mathbf{N}_1 & \mathbf{N}_2 \end{bmatrix}$$

where M, N_1 and N_2 are known real constant matrices. The uncertain time-varying matrix F(t) satisfies: $F^{T}(t)F(t) \le I \quad \forall t$

It is assumed that all the elements of F(t) are Lebesgue measurable. For state-feedback sampled-data control with zero-order hold, the controller takes the following form:

$$u(t) = u_d(t_k) = Kx(t_k), \quad t_k \le t < t_{k+1}, \quad k = 0, 1, 2, \cdots.$$

where t_k is the sampling instant and u_d is a discrete-time control signal. Assume that $\mathbf{I} \quad t_{k+1} - t_k \leq h, \quad \forall k \geq 0$.

We represent the digital control law as a delayed control as follows:

$$u(t) = u_d(t_k) = u_d(t - \tau(t)), \quad \tau(t) = t - t_k, \quad t_k \le t < t_{k+1}$$
(2)

Main Results

Theorem 3.1. Given $\alpha > 0$, let there exist $n \times n$ -matrices P > 0, U > 0 and P_2 , P_3 such that the LMIs (3), (4) are feasible. Then system (1) is exponentially stable with the decay rate α . If LMIs (3), (4) are feasible for $\alpha = 0$, then (1) is exponentially stable with a small enough decay.

$$\boldsymbol{\Psi}_{s0} = \begin{vmatrix} \boldsymbol{H}_{1} & \boldsymbol{H}_{2} & \boldsymbol{0} & \boldsymbol{P}_{2}^{\mathrm{T}}\boldsymbol{M} & (\boldsymbol{N}_{1} + \boldsymbol{N}_{2}\boldsymbol{K})^{\mathrm{T}} & \boldsymbol{0} & \boldsymbol{0} & \boldsymbol{0} & \boldsymbol{0} \\ * & \boldsymbol{H}_{3} & \boldsymbol{0} & \boldsymbol{P}_{3}^{\mathrm{T}}\boldsymbol{M} & \boldsymbol{0} & \boldsymbol{0} & \boldsymbol{0} & \boldsymbol{0} & \boldsymbol{0} \\ * & * & \boldsymbol{0} & \boldsymbol{0} & \boldsymbol{0} & \boldsymbol{0} & \boldsymbol{K}^{\mathrm{T}}\boldsymbol{N}_{2}^{\mathrm{T}} & \boldsymbol{0} & \boldsymbol{K}^{\mathrm{T}}\boldsymbol{N}_{2}^{\mathrm{T}} \\ * & * & * & -\boldsymbol{\varepsilon}_{1}\boldsymbol{I} & \boldsymbol{0} & \boldsymbol{0} & \boldsymbol{0} & \boldsymbol{0} \\ * & * & * & * & -\boldsymbol{\varepsilon}_{1}^{-1}\boldsymbol{I} & \boldsymbol{0} & \boldsymbol{0} & \boldsymbol{0} & \boldsymbol{0} \\ * & * & * & * & * & -\boldsymbol{\varepsilon}_{2}\boldsymbol{I} & \boldsymbol{0} & \boldsymbol{0} & \boldsymbol{0} \\ * & * & * & * & * & * & -\boldsymbol{\varepsilon}_{2}^{-1}\boldsymbol{I} & \boldsymbol{0} & \boldsymbol{0} \\ * & * & * & * & * & * & * & -\boldsymbol{\varepsilon}_{3}\boldsymbol{I} & \boldsymbol{0} \\ * & * & * & * & * & * & * & * & -\boldsymbol{\varepsilon}_{3}\boldsymbol{I} & \boldsymbol{0} \end{vmatrix} \right] < 0$$
(3)

$$\boldsymbol{\Psi}_{s1} =$$

$ig _{m{H}_1}$	\boldsymbol{H}_2	$-h\boldsymbol{P}_2^{\mathrm{T}}\boldsymbol{B}\boldsymbol{K}$	$\boldsymbol{P}_2^{\mathrm{T}}\boldsymbol{M}$	$(N_1 + N_2 K)^{\mathrm{T}}$	$-h\boldsymbol{P}_{2}^{\mathrm{T}}\boldsymbol{M}$	0	0	0	
*		$-h\boldsymbol{P}_{3}^{\mathrm{T}}\boldsymbol{B}\boldsymbol{K}$		0	0	0	$-hP_3^{\mathrm{T}}P_3^{\mathrm{T}}MM$	0	
*	*	$-hUe^{-2\alpha h}$	0	0	0	$\boldsymbol{K}^{\mathrm{T}}\boldsymbol{N}_{2}^{\mathrm{T}}$	0	$\boldsymbol{K}^{\mathrm{T}}\boldsymbol{N}_{2}^{\mathrm{T}}$	-
*	*	*	$-\varepsilon_1 I$	0	0	0	0	0	
*	*	*	*	$-\varepsilon_1^{-1}I$	0	0	0	0	< 0(4)
*	*	*	*	*	$-\varepsilon_2 I$	0	0	0	
*	*	*	*	*	*	$-\varepsilon_2^{-1}I$	0	0	
*	*	*	*	*	*	*	$-arepsilon_{3}I$	0	
*	*	*	*	*	*	*	*	$-\varepsilon_3^{-1}\boldsymbol{I}$	

$$\dot{\overline{V}}(t) + 2\alpha \overline{V}(t) \leq 2\dot{\mathbf{x}}^{\mathrm{T}}(t) \mathbf{P} \mathbf{x}(t) + 2\alpha \dot{\mathbf{x}}^{\mathrm{T}}(t) \mathbf{P} \mathbf{x}(t) - e^{-2\alpha h} \int_{t-\tau(t)}^{t} \dot{\mathbf{x}}^{\mathrm{T}}(s) \mathbf{U} \dot{\mathbf{x}}(s) \mathrm{d}s + (h-\tau(t)) \dot{\mathbf{x}}^{\mathrm{T}}(t) \mathbf{U} \dot{\mathbf{x}}(t)$$
(6)

Denoting $\mathbf{v}_1 = \frac{1}{\tau(t)} \int_{t-\tau(t)}^{t} \dot{\mathbf{x}}(s) ds$. We use the Jensen's inequality

$$\int_{t-\tau(t)}^{t} \dot{\mathbf{x}}^{\mathrm{T}}(s) \boldsymbol{U} \dot{\mathbf{x}}(s) \mathrm{d}s \ge \tau(t) \boldsymbol{v}_{1}^{\mathrm{T}} \boldsymbol{U} \boldsymbol{v}_{1}$$

$$\tag{7}$$

and descriptor method(Fridman,2001). Setting $\boldsymbol{\eta}_1(t) = col\{\boldsymbol{x}(t), \dot{\boldsymbol{x}}(t), \boldsymbol{v}_1\}$, we obtain that:

$$\overline{V}(t) + 2\alpha \overline{V}(t) \le \boldsymbol{\eta}_{1}^{\mathrm{T}}(t) \boldsymbol{\Psi}_{s} \boldsymbol{\eta}_{1} < 0$$
(8)

if the following matrix inequality is feasible:

$$\boldsymbol{\Psi}_{s} = \begin{bmatrix} \boldsymbol{\Phi}_{1s} & \boldsymbol{\Phi}_{2s} & -\tau(t) \boldsymbol{P}_{2}^{\mathrm{T}} (\boldsymbol{B} + \Delta \boldsymbol{B}) \\ * & \boldsymbol{\Phi}_{3s} & -\tau(t) \boldsymbol{P}_{3}^{\mathrm{T}} (\boldsymbol{B} + \Delta \boldsymbol{B}) \\ * & * & -\tau(t) \boldsymbol{U} e^{-2\alpha h} \end{bmatrix} < 0$$

$$\tag{9}$$

where

$$\boldsymbol{\Phi}_{1s} = \boldsymbol{P}_{2}^{\mathrm{T}} \left(\boldsymbol{A} + \Delta \boldsymbol{A} + \boldsymbol{B}\boldsymbol{K} + \Delta \boldsymbol{B}\boldsymbol{K} \right) + \left(\boldsymbol{A} + \Delta \boldsymbol{A} + \boldsymbol{B}\boldsymbol{K} + \Delta \boldsymbol{B}\boldsymbol{K} \right)^{\mathrm{T}} \boldsymbol{P}_{2} + 2\alpha \boldsymbol{P}$$

$$\boldsymbol{\Phi}_{2s} = \boldsymbol{P} - \boldsymbol{P}_{2}^{\mathrm{T}} + \left(\boldsymbol{A} + \Delta \boldsymbol{A} + \boldsymbol{B}\boldsymbol{K} + \Delta \boldsymbol{B}\boldsymbol{K} \right)^{\mathrm{T}} \boldsymbol{P}_{3}, \quad \boldsymbol{\Phi}_{3s} = -\boldsymbol{P}_{3} - \boldsymbol{P}_{3}^{\mathrm{T}} + \left(\boldsymbol{h} - \tau(t) \right) \boldsymbol{U}$$

From Schur complement, we get that:

$$\boldsymbol{\Psi}_{s} = \begin{bmatrix} \boldsymbol{H}_{1} & \boldsymbol{H}_{2} & -\tau(t)\boldsymbol{P}_{2}^{\mathrm{T}}\boldsymbol{B}\boldsymbol{K} & \boldsymbol{P}_{2}^{\mathrm{T}}\boldsymbol{M} & (\boldsymbol{N}_{1} + \boldsymbol{N}_{2}\boldsymbol{K})^{\mathrm{T}} & -\tau(t)\boldsymbol{P}_{2}^{\mathrm{T}}\boldsymbol{M} & \boldsymbol{0} & \boldsymbol{0} & \boldsymbol{0} & \boldsymbol{0} \\ * & \boldsymbol{H}_{3} & -\tau(t)\boldsymbol{P}_{3}^{\mathrm{T}}\boldsymbol{B}\boldsymbol{K} & \boldsymbol{P}_{3}^{\mathrm{T}}\boldsymbol{M} & \boldsymbol{0} & \boldsymbol{0} & \boldsymbol{0} & -\tau(t)\boldsymbol{P}_{3}^{\mathrm{T}}\boldsymbol{M} \\ * & * & -\tau(t)\boldsymbol{U}\boldsymbol{e}^{-2\alpha\hbar} & \boldsymbol{0} & \boldsymbol{0} & \boldsymbol{0} & \boldsymbol{K}^{\mathrm{T}}\boldsymbol{N}_{2}^{\mathrm{T}} & \boldsymbol{0} & \boldsymbol{K}^{\mathrm{T}}\boldsymbol{N}_{2}^{\mathrm{T}} \\ * & * & * & -\varepsilon_{1}\boldsymbol{I} & \boldsymbol{0} & \boldsymbol{0} & \boldsymbol{0} & \boldsymbol{0} & \boldsymbol{0} \\ * & * & * & * & -\varepsilon_{1}^{-1}\boldsymbol{I} & \boldsymbol{0} & \boldsymbol{0} & \boldsymbol{0} & \boldsymbol{0} \\ * & * & * & * & * & * & -\varepsilon_{2}^{-1}\boldsymbol{I} & \boldsymbol{0} & \boldsymbol{0} & \boldsymbol{0} \\ * & * & * & * & * & * & * & -\varepsilon_{2}^{-1}\boldsymbol{I} & \boldsymbol{0} & \boldsymbol{0} \\ * & * & * & * & * & * & * & * & -\varepsilon_{3}\boldsymbol{I} & \boldsymbol{0} \\ * & * & * & * & * & * & * & * & * & -\varepsilon_{3}^{-1}\boldsymbol{I} \end{bmatrix}$$
 (10)

The inequality (10) for $\tau(t) \to 0$ and $\tau(t) \to h$ leads to the LMIs (3) and (4). Denote by $\eta_0 = col\{\mathbf{x}(t), \dot{\mathbf{x}}(t)\}$, then (3) and (4) imply (8)

Theorem 3.2. Given $\alpha > 0$, let there exist $n \times n$ – matrices P > 0, U > 0, X, X_1 , P_2 , P_3 , T and Y_1 , Y_2 such that the LMIs (11), (12), and (13) are feasible. Then system (1) is exponentially stable with the decay rate α .

$$\boldsymbol{\Xi}(h) = \begin{bmatrix} \boldsymbol{P} + h \frac{\boldsymbol{X} + \boldsymbol{X}^{\mathrm{T}}}{2} & h\boldsymbol{X}_{1} - h\boldsymbol{X} \\ * & -h\boldsymbol{X}_{1} - h\boldsymbol{X}_{1}^{\mathrm{T}} + h \frac{\boldsymbol{X} + \boldsymbol{X}^{\mathrm{T}}}{2} \end{bmatrix} > 0$$
(11)

$$\boldsymbol{\Phi}_{0}(h) = \begin{bmatrix} \boldsymbol{\Psi}_{11} - (1 - 2\alpha h) \frac{\boldsymbol{X} + \boldsymbol{X}^{\mathrm{T}}}{2} & \boldsymbol{\Psi}_{12} + h \frac{\boldsymbol{X} + \boldsymbol{X}^{\mathrm{T}}}{2} & \boldsymbol{\Psi}_{13} + (1 - 2\alpha h) (\boldsymbol{X} - \boldsymbol{X}_{1}) & \boldsymbol{P}_{2}^{\mathrm{T}} \boldsymbol{M} & \boldsymbol{N}_{1}^{\mathrm{T}} \\ & \ast & \boldsymbol{\Psi}_{22} + h \boldsymbol{U} \\ & \ast & \boldsymbol{\Psi}_{22} + h \boldsymbol{U} \\ & \ast & \ast & \boldsymbol{\Psi}_{33} - (1 - 2\alpha h) \frac{\boldsymbol{X} + \boldsymbol{X}^{\mathrm{T}} - 2\boldsymbol{X}_{1} - 2\boldsymbol{X}_{1}^{\mathrm{T}}}{2} & \boldsymbol{\theta} & \boldsymbol{K}^{\mathrm{T}} \boldsymbol{N}_{2}^{\mathrm{T}} \\ & \ast & \ast & & \ast & -\varepsilon \boldsymbol{I} & \boldsymbol{\theta} \\ & \ast & \ast & & \ast & & -\varepsilon \boldsymbol{I} & \boldsymbol{\theta} \end{bmatrix}$$

$$\boldsymbol{\Psi}_{1}(h) = \begin{vmatrix} \boldsymbol{\Psi}_{11} - \frac{\boldsymbol{X} + \boldsymbol{X}^{\mathrm{T}}}{2} & \boldsymbol{\Psi}_{12} & \boldsymbol{\Psi}_{13} + (\boldsymbol{X} - \boldsymbol{X}_{1}) & h\boldsymbol{Y}_{1}^{\mathrm{T}} & \boldsymbol{P}_{2}^{\mathrm{T}}\boldsymbol{M} & \boldsymbol{N}_{1}^{\mathrm{T}} \\ & * & \boldsymbol{\Psi}_{22} & \boldsymbol{\Psi}_{23} & h\boldsymbol{Y}_{2}^{\mathrm{T}} & \boldsymbol{P}_{3}^{\mathrm{T}}\boldsymbol{M} & \boldsymbol{\theta} \\ & * & * & \boldsymbol{\Psi}_{33} - \frac{\boldsymbol{X} + \boldsymbol{X}^{\mathrm{T}} - 2\boldsymbol{X}_{1} - 2\boldsymbol{X}_{1}^{\mathrm{T}}}{2} & h\boldsymbol{T}^{\mathrm{T}} & \boldsymbol{\theta} & \boldsymbol{K}^{\mathrm{T}}\boldsymbol{N}_{2}^{\mathrm{T}} \\ & * & * & * & -h\boldsymbol{U}\boldsymbol{e}^{-2\alpha h} & \boldsymbol{\theta} & \boldsymbol{\theta} \\ & * & * & * & * & -\boldsymbol{\varepsilon}\boldsymbol{I} & \boldsymbol{\theta} \\ & * & * & * & * & -\boldsymbol{\varepsilon}^{-1}\boldsymbol{I} \end{vmatrix} < 0$$
(13)

Numerical example

Consider the uncertain system (1), and the matrices are given by

$$A = \begin{bmatrix} 0 & 1.1 \\ 0 & -0.1 \end{bmatrix}, \quad B = \begin{bmatrix} 0 \\ 0.1 \end{bmatrix}, \quad M = \begin{bmatrix} 0.1 \\ -0.1 \end{bmatrix}, \quad x(0) = \begin{bmatrix} 0.1 \\ 0.1 \end{bmatrix}, \quad N_1 = \begin{bmatrix} 0.2 & -0.8 \end{bmatrix}, \quad N_2 = 0.1, \quad \tau(t) = 1$$

By using LMI Control Toolbox to solve (12), (13) and (14), we get $\mathbf{K} = \begin{bmatrix} -3.6716 & -12.0980 \end{bmatrix}$ Choosing h = 1.3, and applying LMIs(12), (13), we find that the system (1) is exponentially stable with the decay rate $\alpha = 0.4$, shown in Fig. 1.

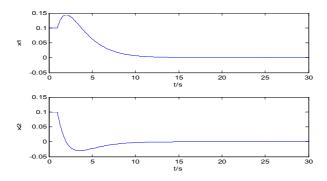


Fig. 1 State response curve

Conclusions

The problem of sampled-data control of uncertain system under uncertain samplings with a given upper bound on the sampling intervals has been investigated via a delay system approach. By using an input delay approach, the close-loop system has been transformed to a delay system. The stabilization controllers have been formulated in the form of linear matrix inequalities.

Acknowledgment

This work is partially supported by science and technology studies foundation of Heilongjiang educational committee of 2014.

References

- [1] Huijin Gao, Junli Wu, Peng Shi. Automatica, 45(7):1729-1736, 2009.
- [2] K. Liu, V. Suplin, and E. Fridman. Proc. of the 19th international Symposium on mathematical Theory of Networks and Systems. Budapest, hungary, July 2010
- [3] H.Gao, T.Chen, and J. Lam. IEEE Transactions on Automatic Control ,53(3):655-667, 2008.
- [4] Jiang, X., Han, Q. L., Liu, S., & Xue, A. IEEE Transactions on Automatic Control, 2008,53(4):1025-1032
- [5] E. Fridman. Automatica, 2010, 46(2): 421~427
- [6] Naghshtabriza, P., Hespanha, J., & Teel, A. Systems&Control Letters, 2008,5(57):378-385
- [7] Fan Liying, engWu Junf. J. Cent. South Univ. Technol. 2011, 18(6): 2056-2060
- [8] Liying Fan, Junfeng Wu, Jixiang Li, Shigang Wang. The 6th International Forum Strategic Technology. Harbin, China, August 22-24, 2011, 2: 1045-104

Simulation Research on Fuzzy Control of Main Steam Temperature in Power Series

Tian Siqing^{1,a}, Wei Qiang^{1,b}, Mu Xiao feng^{1,c}

¹China Jia Musi city of Heilongjiang Province, Jiamusi University ^atian_siqing@126.com, ^bm15164510939@163.com, ^cmxf0311@126.com

Key words: super-heater; Temperature control; Cascade fuzzy; The simulation

Abstract: due to the characteristics of large delay, nonlinear super-heater, time-varying, multivariate and self balance ability .It is difficult to establish accurate mathematical model, this paper uses the cascade fuzzy control, realize the effective control of the main steam temperature. Simulation results show that, the temperature cascade fuzzy control has fast dynamic response, good steady-state performance and robustness.

0 Introduction

The main steam temperature is an important indicator of the quality of boiler operation, it has a great influence on safety and economy of the power plant. The control of main steam temperature cascade control system usually uses the style of PID, but since PID fixed parameters has been unable to meet the industrial process more complicated, especially the serious nonlinear process and uncertain systems. Those year, the use of fuzzy control technique to control the main steam temperature has been achieved certain results. But the traditional fuzzy control effect on the hysteresis control object is not ideal. So we make the design of fuzzy controller, and can well solve the problem ^[1].

1 main steam temperature control system

The main steam temperature control system plays an important role in the safe and economic operation of the control system in thermal power plant. The automatic control of the main steam temperature is the task of maintaining steam temperature of super-heater outlet protection within the allowable range, the main steam temperature is too high or too low will affect safety and economy of the plant ^[2]. The main steam temperature control system is shown in Figure 1, the spray desuperheating change super-heater entrance and outlet temperature of super-heater temperature change, divided into the inert area and the pilot area. The main steam temperature is an important indicator of the quality of the operation of the boiler.

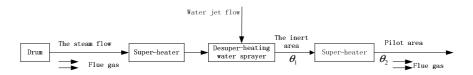


Fig. 1 Schematic diagram of the main steam temperature control system

But the main steam temperature of power plant have large delay, nonlinear, strong interference, so it is very difficult to realize. In recent years, the development of intelligent control, has aroused great concern. By the people as a control system controller is an intelligent control system of a typical, including senior intellectual activity of human. Fuzzy control to a certain extent, imitating human control, including control of the experience and knowledge of people, he does not need accurate model of the object, so it is an intelligent control method. The fuzzy control method can be used for simple systems, can also be used for complex systems. In this paper, the design of the cascade fuzzy control system to realize the control of the main steam temperature, the system has excellent control quality and strong adaptive ability.

2 Design of fuzzy controller for the main steam temperature

The design of the fuzzy controller we set 2 input, the temperature changes were e and deviation rate were ec, one output of fuzzy controller is set that u. The fuzzy controller using fuzzy language variable has three. They are E (temperature), EC (changes in temperature deviation rate) and U (valve). The fuzzy controller structure shown in Figure 2.



Figure 2 Structure of fuzzy controller block diagram

Fuzzy temperature e, the temperature deviation change rate ec and output u variables set the integer domain is [-2,2], it can be divided into 5 gear, namely: e, ec, $u \in \{-2, -1, 0, 1, 2\}$.

The control objective knowledge base contains a main steam temperature cascade fuzzy control system requirements. It is usually by the database and fuzzy control part two rules.

2.1 make fuzzy database

First, discuss the main steam temperature cascade fuzzy control system design process, database related content.

In main steam temperature cascade fuzzy control system design process, the variables using the three grade classification, positive, negative description method in two directions and the zero state. {PB, PM, ZE, NM, NB}5 state to describe.

In main steam temperature cascade fuzzy control system design process, fuzzy e temperature, temperature change rate of EC and u output variables set the integer domain is [-2,2], fuzzy subset set temperature, temperature change rate of e EC and u output variables corresponding respectively E, EC, U, among them. E={NB, ZE, PB}, physical meaning are expressed as temperature {below the standard temperature, no, higher than the standard temperature}; EC={NB, ZE, PB}, the rate of physical meaning are representation of the temperature change of {temperature decreased with increasing, constant, the temperature rise increases}; U={NB, NM, ZE, PM, PB}, physical meaning are said to spray cooling valve {closed, slightly close, do not move, slightly open, open}.

Linguistic variables on fuzzy subset domain can be described by the membership function, membership function can be determined by the experience of the operator or by the fuzzy statistical method. Among them, for the domain {-2, often using -1,0, +1, +2}, NB, values in the 5 linguistic variables, the definition of NM, ZE, PM, fuzzy subset of PB, with the maximum degree of membership "1 elements" people used to take into:

$$\mu_{NB}(x) = 1 \to x = -2; \quad \mu_{NM}(x) = 1 \to x = -1; \quad \mu_{ZE}(x) = 1 \to x = 0; \quad \mu_{PM}(x) = 1 \to x = +1;$$

$$\mu_{DR}(x) = 1 \to x = +2$$

This paper uses the isosceles triangular membership functions to represent the fuzzy numbers, fuzzy numbers and the conclusion part control the condition parts of the rules of the E, EC and u membership function are shown in Figure 3 and figure 4.

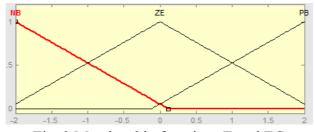


Fig. 3 Membership functions E and EC

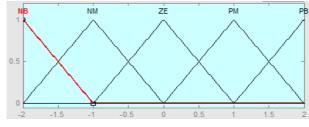


Fig. 4 Membership functions u

2.2 fuzzy control rules

According to the change of thermal power plant expert knowledge and operator "control of the superheated steam temperature rate, prevent overshoot" the experience has 8 rules for fuzzy control:

- (1) if e=NB then u=NM
- (2) if e=NB and ec=NB then u=NB
- (3) if e=NB and ec=PB then u=PM
- (4) if e=ZE then u=ZE
- (5) if e=ZE and ec=NB then u=NM
- (6) if e=ZE and ec=PB then u=PM
- (7) if e=PB and ec=NB then u=PM
- (8) if e=PB and ec=PB then u=PB

In practical application, there are three defuzzification methods commonly used. The maximum membership degree method, the maximum membership degree average method and the "center of gravity" (COA). Center of gravity method is also called the centroid method or the center of area method, is the most commonly used method, this method has the minimum mean square error.

Mathematical expressions of center of gravity method is $\int_{y}^{y} \mu_{o}(y) y dy / \int_{y}^{y} \mu_{o}(y) dy$. In this paper, the

fuzzy reasoning method is the Max-Min-COA method of [3], the solution of fuzzy median method.

3 main steam temperature cascade fuzzy control system simulation

According to the characteristics of the controlled object of the super-heater, the cascade control and fuzzy control technology, main steam temperature cascade fuzzy control system, this system should be able to improve the main steam temperature control system in dynamic performance. In the main steam temperature fuzzy controller to Deputy regulator e temperature and temperature change rate EC two variables as input, with the spray valve opening u for output. The construction of the two inputs, one output membership function editor [4], as shown in figure 5.

FIS Editor: Untitled12	3		
File Edit View			
° °	Untitle (mam		u
FIS Name: Untitle	d123	FIS Type:	mamdani
And method	min	Current Variable	
Or method	max 🔹	Name	•
Implication	min 💌	Type Range	input [-2 2]
Aggregation	max 💌		
Defuzzification	centroid 🗾	Help	Close
Renamed FIS to "Untitled123"			

Fuzzy controller Figure 5 superheated steam temperature control system in the MF editor By the fuzzy rules have been proposed, the FIS fuzzy rule editor as shown in Figure 6.



Figure 6 FIS fuzzy rule editor

The cascade fuzzy control system, the secondary regulator for the fuzzy controller structure, so main steam a cascade fuzzy control system, as shown in figure 7. The main steam cascade fuzzy control system simulation structure, as shown in figure 8.

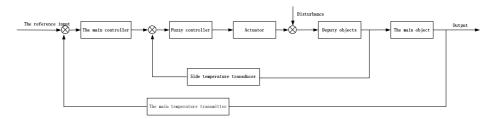
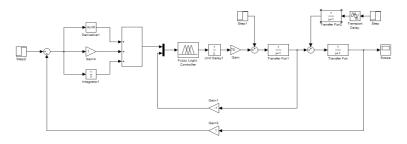


Figure 7 The main steam cascade fuzzy control system block diagram



Simulation Figure 8 main steam cascade fuzzy control system

The stable operation condition, the area before the transfer function of controlled object $\frac{1}{s+1}$; Object transfer function $\frac{1}{s+1}$; The steam flow disturbance2m³/h; The flue gas turbulent transfer

function $\frac{e^{-15s}}{s+1}$; The parameters were set as the main controller: P=1, T1=1, P=1 deputy controller. In addition, the characteristics of the valve is 1, slope efficiency is 1 temperature transmitter, actuator

magnification is 70. In order to make the whole cascade without static deviation of fuzzy control system, in addition to the main controller using PID control law, also adding a magnification ratio of 1. In t=10, to join the amplitude of steam flow order 2 step disturbance and amplitude for flue gas flow order 2 step disturbance, the simulation of $^{[5]}$ main steam temperature cascade fuzzy control system and output the results as shown in figure 9.

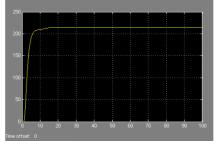


Fig. 9 Steam, smoke and steam flow disturbance in main steam temperature cascade fuzzy control system simulation curve

Figure 9: simulation results show that the main steam temperature cascade fuzzy control system, steam, smoke is in Super-heater steam flow disturbance and other major disturbance, no dynamic deviation, transition curve is better than the previous main steam temperature cascade control system, can maintain the non periodic better and the static error free exponential curve, process control quality is better than the main steam temperature cascade control system^[6].

4 Conclusion

According to the control requirements of the superheater has the characteristics of superheated steam temperature and thermal power plant large delay, nonlinear, multi variable, put forward the main steam temperature cascade fuzzy control strategy, its main purpose is to make the cascade control and fuzzy control of complementary advantages. The simulation results show that, in the flue gas, steam disturbances, system has a better tracking performance, and can overcome the disturbance in a relatively short period of time, to resume normal work [7], control over the quality of the main steam temperature cascade control system, is conducive to the safety, economic operation of thermal power plants, with the prospect of application of ^[7] wide.

Acknowledgment

This work is supported by the scientific research project of Education Department of Heilongjiang Province (12511556).

Reference

- [1] Liu Shutang, Han Chongzhao. Adapctive inverse control [M]. Xi'an: Xi'an Jiao Tong University press, 2009,9
- [2] Yang Yanzhi, Mai edge. Application of fuzzy control in thermal power steam temperature control system [J]. Guangxi electric power, 2004.27 (5)
- [3] Wang Guoyu, Han Pu. Fuzzy adaptive predictive function control [J]. proceedings of the CSEE China main steam temperature system, 2003,10
- [4] Wang Dongfeng, Han Pu et al. Application of [J]. to simplify the DMC-PID cascade control and in the steam temperature system in electric power science and engineering, 2003,4
- [5] Ruan Gang. New strategies for dynamic simulation of [J]. central China electric power boiler superheated steam temperature control, 2004,17 (5)
- [6] Yang Xiaofei. Artificial pattern recognition of variable cycle controller and its application [J]. Zhengzhou Industrial University Based on 2001,4
- [7] Tao Wenwei. The single neuron controller and its application [J]. automation and instrumencts in superheated steam temcperature control, 2000,2

Impact Velocity Analysis of Capacitive RF-MEMS Switch

Rui Wu¹, Mingxin Song^{1,a}

¹ College of Applied Science, Harbin University of Science and Technology, Harbin 150080, China

^asongmingxin@126.com

Keywords: RF-MEMS Switch; Impact Velocity

Abstract. Impact velocity is an important performance parameter for capacitive RF-MEMS switch. This paper establishes a differential equation, in order to analyse the influencing factors of impact velocity. The simulation results show that impact velocity can reach 1.5m/s when bias voltage equals to 0.7V, frequency equals to 3×10^5 Hz, voltage type adopts rectangular wave.

Introduction

With the development of current communication technology, traditional switch can not meet the increasing requirements. At the same time RF-MEMS switch come into people's eye. RF-MEMS switch has the advantages of low inserting loss, high isolation, which is correspondent with the development of future radio frequency system[1]. It will be notable enhance the RF system performances and will be widely applied in outer space exploration and military defense[2]. At present, RF-MEMS switch commercialization is hindered by the problem that mainly refer to the fast impact velocity [3]. This paper is researched based on the momentum theorem to study the switch impact velocity and influence factor. Fig.1 shows that the model of RF-MEMS switch.

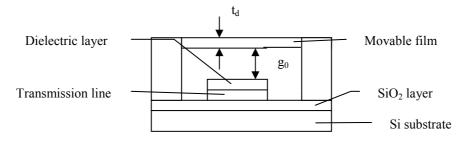


Fig.1 Model of RF-MEMS switch

Establishing the Impact Velocity Model of Movable Film

When switch works, the top electrode pulls down. There has static friction between movable film and Si_3N_4 dielectric film[4], so reduce the impact velocity of movable film can reduce static friction force, in order to improve lifetime of RF-MEMS switch. Switch is regarded as single degree of freedom damping system. Driving voltage is shown in Eq1 and elasticity is shown in Eq2. We can know that A is area, g_0 is thickness of air layer, t_d is thickness of Si_3N_4 dielectric film, σ is residual stress, v is Poisson ratio, w and L are the wide and length of movable film.

$$V_{\rm T} = V \left(g = \frac{2}{3} g_0 \right) = \sqrt{\frac{8K}{27\varepsilon_0 A} g_0^3}$$
(1)

$$K=32Ew\left(\frac{t_{d}}{L}\right)^{3}+8\sigma(1-\nu)w\left(\frac{t_{d}}{L}\right)$$
(2)

$$W_{e} = \frac{1}{2} C V_{T}^{2} = \frac{1}{2} \frac{\varepsilon_{0} A V^{2}}{g}$$
(3)

$$\sum_{i=0}^{n} F_i t = m \frac{\partial z}{\partial t}$$
(4)

$$\frac{\partial z}{\partial t} = \frac{1}{m} \int_0^{t_j} \left(\frac{\partial W_e}{\partial z} - kz - \xi \frac{\partial z}{\partial t} \right) dt \tag{5}$$

Based on electrostatic energy equation (as Eq.3 shown), combining momentum theorem as Eq.4 shown, the impact velocity equation is established as Eq.5 shown. In the equation, W_e is the electrostatic energy of the swith, the initial condition is as Eq.6 and Eq.7 shown.

Initial displacement:
$$Z/_{t=0} = 0$$
 (6)

Initial velocity:
$$(\partial z / \partial t) /_{t=0} = 0$$
 (7)

This paper solve the impact velocity equation through MATLAB software, and then simulate the influencing factors such as bias voltage, frequency and voltage type. In the process of calculation, ignore the effect of gas viscosity because of it so little.

Impact Velocity Simulation

(1) The influence of bias voltage

Fig.2 is the relationship between bias voltage and the impact velocity. It can be seen that as the bias voltage increases, the impact velocity increases. When the bias voltage is small, impact velocity changes quickly. When the bias voltage is greater than 0.55V, impact velocity changes small, but they are both linearly in two positions of the curve. The smaller the impact velocity, the smaller the loss of the switch, so the bias voltage needs to be as small as possible. But small bias voltage could lead to opening time longer, which reduce switch sensitivity. Therefore, when bias voltage equals to 0.7V, impact velocity is 1.5m/s, which satisfy low bias voltage and opening time requirement.

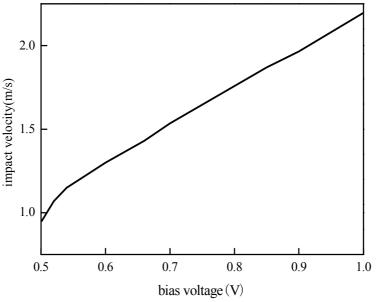


Fig.2 The relationship between bias voltage and the impact velocity

(2) The influence of different types of bias voltage

It is adopted that beam material is Al, beam length and width, beam thickness and dielectric layer thickness equal to $300\mu m$, $30\mu m$, $0.8\mu m$ and $0.2\mu m$ respectively. Bias voltage between beam and dielectric layer is 0.7V. Using matlab software select pulse wave, square wave and sine wave, in order to simulate the effects of bias voltage on the impact velocity. We can know from figure 3 that when square wave voltage is applied between beam and dielectric layer, impact velocity is 5.5m/s. While

sine wave voltage coule made impact velocity 2m/s. When pluse wave voltage is applied between beam and dielectric layer, impact velocity is only 1.2m/s. It can be inferred that pulse wave voltage can significantly reduce impact velocity of movable film, and then improve the life of RF-MEMS switch.

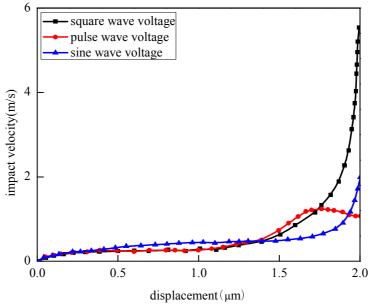


Fig.3 The relationship between impact velocity and displacement with different types of bias voltage

(3) The influence of different frequency pulse voltage

Using matlab software select 0.25MHz, 0.3MHz, 0.5MHz and 1MHz pulse wave voltage respectively to study the effect of frequency on the impact velocity, and the simulation results is shown in Fig.4. It can be seen that when pulse wave frequency is 0.25MHz, impact velocity is 2.5m/s. When pulse wave frequency is 0.3MHz, 0.5MHz, 1MHz, impact velocity is 1.5m/s, 1m/s and 0.8m/s respectively. So increasing pulse wave frequency can ruduce the film impact velocity, which can increase the life of switch. But at the same time, frequency increasing will lead drive voltage increasing. High frequency pulse wave can not meet the requirement of low drive voltage, so this paper adopt the pulse wave frequency equals to 0.3MHz.

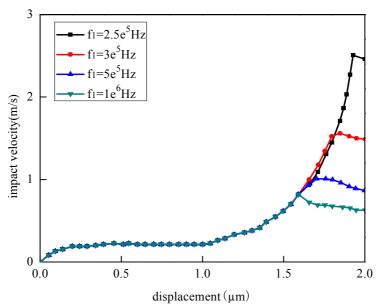


Fig.4 The relationship between impact velocity and displacement with different frequency pulse wave voltage

Summary

Capacitive RF-MEMS switch has a good prospect, but its' commercialization is hindered by impact velocity and reliability problem. This paper study the effect of different bias voltage on the switch, which show that when bias voltage equals to 0.7V, voltage type adopts pulse wave voltage, frequency is 0.3MHz, the switch impact velocity is only 1.5m/s.

Acknowledgement

This work is supported by Science and Technology Research Project of Education Department of Heilongjiang Province (Grant No. 12511076).

References

[1] Song Mingxin, Wu Rui: Research on the dynamic response of capacitive RF-MEMS switch[C]. Chemical and Mechanical Engineering. Vol. 791, p. 1909-1912. (2013)

[2] Lixin Qu: Research and development of MEMS switch technology[J].Modern Electronic Technique. Vol. 1, p. 147-149. (2008)

[3] Allen,M.S., Massad, J.E.: Input and design optimization under uncertainty to minimize the impact velocity of an electrostatically actuated MEMS switch[J]. Journal of Vibration and Acoustics, Transactions of the ASME. Vol. 130.(2008)

[4] Liu, Z.W.: RF MEMS switch and its applications[C]. China Semiconductor Technology International Conference. Vol. 44, p. 1361-1366. (2012)

Microwave Performance Simulation of RF-MEMS Switch

Rui Wu^{1, a}, Mingxin Song^{1,b},

¹Dept. Electronics and Science Institute of Applied Science and Technology Harbin University of Science and Technology Harbin, China

^awuruiguaiguai19@163.com ^bsongmingxin@126.com

Keywords: RF-MEMS Switch; Microwave Performance.

Abstract. This paper presents the calculation model of capacitive RF-MEMS switch for the isolation and insertion loss, and then adopts CST software to simulate microwave performances. The simulation results show that return loss can reach -21.5dB and isolation can reach -0.26dB when the distance between contacting metal and dielectric layer adopts $2\mu m$, $6 \times 10^3 \mu m^2$ of contacting area and 20µm of groove depth.

Introduction

RF MEMS switch have a great advantage than conventional microwave solid state switches in many aspects, such as isolation, insertion loss, power consumption and linerity, so it shows great potential in the field of microwave application[1]. Since RF MEMS switch is reported, the industry has developed many different structures. In Ka-band, capacitive RF MEMS switch have shown a good performance in either insolation or insertion loss[2]. However, at low frequency, lower isolation limits capacitive RF MEMS switch application in X-band. To overcome the above shortcomings, J.B.Muldavin proposed a method, which adds a high-impedance transmission line between the switch beam and ground plane, so series inductance of the transmission line make LC resonance frequency reaching the X-band, thus obtain isolation higher than -20dB in X-band[3]. This paper presents a substrate groove method between CPW transmission line and coplanar waveguide ground plane of capacitive RF MEMS switch, improving isolation and applying to the X-band. This design does not change circuit structure and improve switch performance, which provides a reference for designing RF MEMS high performence circuit based on CPW structure. Fig.1 shows that the model of capacitive RF MEMS switch.

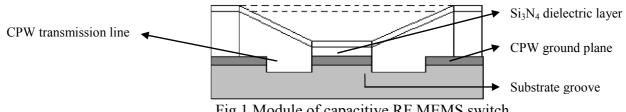


Fig.1 Module of capacitive RF MEMS switch

Equivalent Circuit Model

RF MEMS switches always have small size, so in X-band, using lumped parameter model to characterize electromagnetic properties of the switch[4]. When drive voltage is not applied, movable film is not bending, so the switch is turned off. When drive voltage is applied, movable film moves down and contact with the dielectric layer, so the switch is in the "on" state. The corresponding lumped parameter model of switch structure is shown in Fig. 2.

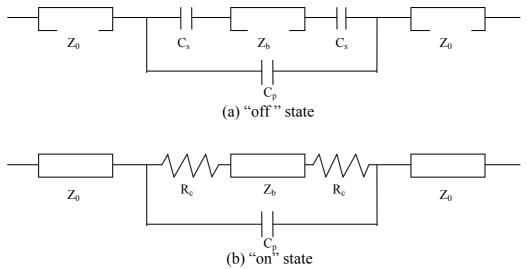


Fig.2 Lumped parameter model of RF MEMS switch

In Fig.2, Z_0 is the characteristic impedance of the transmission line and it is influenced by groove depth, Z_b is the characteristic impedance of the contacting metal, C_s is the series capacitance between transmission line and contacting metal, C_p is air capacitance on "off" state, R_c is contacting resistance between contacting metal and transmission line on "on" state.

When the switch is on "off" state, the totle capacitance expression is shown in Eq.1.

$$C_{off} = \frac{C_s \cdot C_p}{C_s + C_p} \tag{1}$$

 C_s is mainly affected by the dielectric layer thickness (t) and contacting area (A). C_p is affected by the distance between contacting metal and dielectric layer (g) when is on "off" state. But the impact of dielectric layer thickness is smaller than the distance between contacting metal and dielectric layer. Isolation can be shown as Eq.2, so g and A is main influencing factors of isolation.

$$|S_{21}|^{2} = 4\omega^{2}Z_{0}^{2} \frac{\binom{C_{off}}{2}^{2}}{\left(1 + \frac{l}{2Z_{b}C_{off}V_{p}}\right)^{2}}$$
(2)

In Eq.2 the contacting metal is equivalent to high impedance transmission line which length is *l*;

 ω is the angular velocity of the wave and V_p is the phase velocity of the transmission line.

When the switch is on "on" state, the totle resistance expression R_s is shown in Eq.3. It can influence insertion loss and return loss of the switch.

$$R_s = 2R_c + 2R_{s1} + R_1 \tag{3}$$

In this case, the corresponding return loss S_{11} can be expressed as Eq.4. Because switching loss can be expressed as Eq.5 and Eq.6, according to Eq.4, Eq.5, Eq.6, the insertion loss S_{21} is obtained as Eq.7.

$$|S_{11}|^2 = \left(\frac{R_s}{2Z_0}\right)^2$$
(4)

$$IL = 1 - \left|S_{11}\right|^2 - \left|S_{21}\right|^2 \tag{5}$$

$$IL = \frac{R_s}{Z_0} \tag{6}$$

$$\left|S_{21}\right|^{2} = 1 - \frac{R_{s}^{2} + 4R_{s}Z_{0}}{4Z_{0}^{2}}$$
⁽⁷⁾

Therefore when designing structural parameters of switch, microwave performance requirements should be considered.

Microwave performance simulation

For capacitive RF MEMS switch has a good microwave performance in X-band, this paper using CST software simulate influencing factors of S_{11} and S_{21} , including the distance between contacting metal and dielectric layer, contacting area and groove depth.

(1) The influnce of the distance between contacting metal and dielectric layer

It can be seen from Fig. 3 that when $g=2\mu m$, returen loss can reach -21.5dB. As the distance increases, the return loss reduced, but the isolation increases (as Fig.4 shown). At the same time, a big distance can cause a big driven voltage which need additional power supply circuit. So how to make a compromise between them is important that not only improve microwave performance but also meet low driven voltage requirement. Usually we adopt $g=2\mu m$ which is common used in experiment.

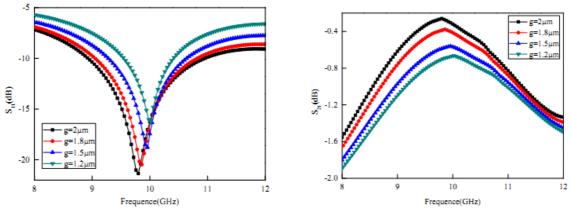


Fig.3 The relationship between S₁₁ and frenquence in different distance

Fig.4 The relationship between S_{21} and frequence in different distance

(2) The influnce of the contacting area

Fig.5 and Fig.6 is the curve of \tilde{S}_{11} , S_{21} and frequence under different contacting area. It can be seen that the smaller contacting area, the better the microwave performance. But small contacting area will lead the difficulty of process increasing. Above all, the contacting area adopts $6 \times 10^3 \mu m^2$.

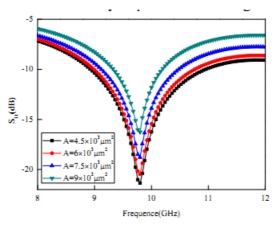


Fig.5 The relationship between S_{11} and frequence in different contacting area

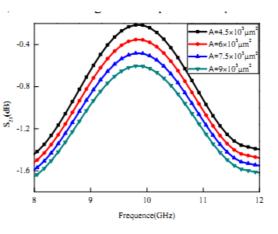


Fig.6 The relationship between S_{21} and frequence in different contacting area

(3) The influnce of groove depth

Simulation results are shown in Fig.7 and Fig.8. From the figure, it can be seen that groove depth make a big influence on micowave performance. When groove depth is $20\mu m$, the S₁₁ parameter reaches to a minimum value which is -21.5dB. At the same time, the isolation reaches to -0.26dB. But the increasing groove depth may be restricted by processing. So the $20\mu m$ is usually selected as groove depth.

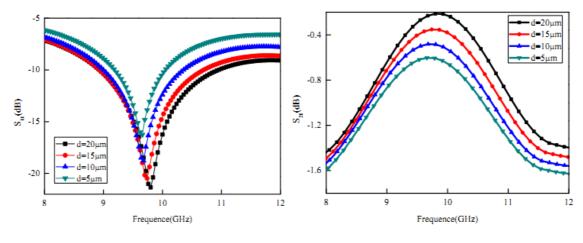


Fig.7 The relationship between S_{11} and frequence in different groove depth

Fig.8 The relationship between S_{21} and frequence in different groove depth

Summary

At low frequency, lower isolation limits capacitive RF MEMS switch application in X-band. This paper presents a substrate groove method between CPW transmission line and coplanar waveguide ground plane and adopts CST software to simulate microwave performances. The simulation results show that when the distance between contacting metal and dielectric layer adopts $2\mu m$, contacting area equals to $6 \times 10^3 \mu m^2$ and groove depth is $20\mu m$, return loss can reach -21.5dB and isolation can reach -0.26dB.

Acknowledgement

This work is supported by Science and Technology Research Project of Education Department of Heilongjiang Province (Grant No. 12511076). The authors also thank Guoxu Zheng for his technical instruction support.

References

- [1] Ling Jin: RF MEMS technology status[J], Microwave Journal. Vol.21, p.58-65. (2011)
- [2] Zhongliang Deng, Xingjie Cao: Design and Simulation of K Band RF MEMS Tunable Combline Filter[C], Advanced Materials Research. Vol.875, p.2219-2223. (2013)
- [3] Muldavin Jeremay B, Radiation Lab: High-isolation CPW MEMS shunt switches[J]. Microwave Theory and Techniques. Vol. 48, p.1045-1052. (2000).
- [4] Rebeiz G.M, Michigan Univ.: RF MEMS switches and switch circuits. Microwave Magzine. Vol.2, p.59-71.(2001)

CHAPTER 7:

Methods, Devices and Systems for Measurement and Monitoring

The Design of Wind Control LED Display System Applied on Ice lantern

Lan Lan^a, YiJiang Cao, Jiamu Cao

Department of Electronic Science and Technology, College of Applied Science, Ministry of Education Harbin University of Science and Technology, Heilongjiang Harbin 150080, China

^alanlan_goodluck@163.com

Keywords: wind control; LED display; MCU control; ice lantern

Abstract. This paper presents a LED display system triggered by the natural wind which can be used for ice lantern, the system includes a signal detection unit, control unit and LED display unit. When the system detects a natural wind signal , the center control module will make a signal processing for the signal, LED display module set the display mode according to the results of processing options, the display modes include the following, the LED lamps sequentially turned on in accordance with wind direction, or make the pattern presetting on the LED array move with the natural wind direction , when the natural wind signal is very weak, system will control LED array display static pattern. A stable system model is realized in accordance with the design requirements, after testing, system performance is stable, reached the set requirements.

Introduction

Ice Lantern is one of a traditional art in the northeast of China in winter. In recent years, it becomes bigger in scale and many different forms come out. People prefer new designs and interesting works. Now, it is stirring to create a production to mix together wind and light! Fluorescent lamp is routinely used to make traditional Ice Lantern. It contains a mass of ballasts, hard to setup and has a low reliability [1]. LED costs less energy, works in a stable condition and has little light pollution [2]. Now, it has been widely used in many fields. Accordingly, the paper use LED instead of traditional light source, realizes a LED display system triggered by natural wind.

System Architecture

System consists of three major components, they are signal collection module, control center module and LED display module, when the information collection module collecting information, pass it on to the control center module, the control center module select LED display mode, the overall architecture shown in Fig.1.

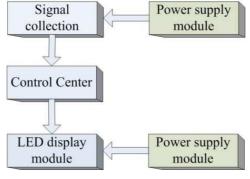


Fig. 1 The system architecture

The center control module includes an information processing unit and a MCU control unit, LED display module comprises a drive unit and a display unit. Information collection module make the strength of natural wind into a corresponding voltage signal, the information processing unit determine the direction or the size of the wind by comparing the voltage difference between two points. When the MCU receives the processing results, it will be able to accurately control the LED display module to display the dynamic images with wind changing, so when watching the Ice lantern,

people's feeling of the wind direction is basically consistent of the LED changing direction, creating a beautiful and magic atmosphere.

Hardware Design

System hardware includes the following modules: information collection module, information processing module. Among the several module, LED display module's power is larger, set power supply module individually, other modules use the same power supply module.

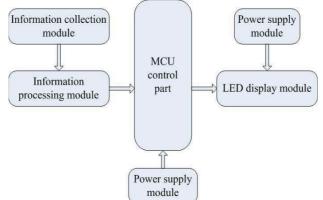


Fig. 2 Diagram block of the system hardware module

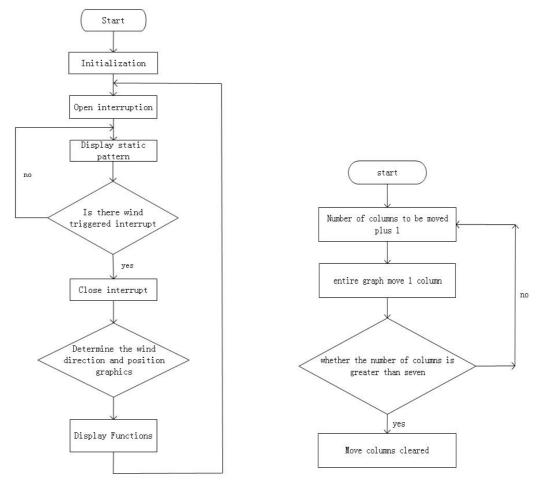
Information collection module. Information collection module consists of a sensor and an amplifier circuit, the sensor selects electronic microphone [3], which are put in the four directions of the LED display model. Electronic microphone has the Characteristics of small size, wide frequency range, negligible distortion and low cost. Microphone consisting of a metal coated with an electronic film and a metal electrode with a plurality of apertures above it [4], and there is air between the two metal electrodes, both sides of the metal layer as an electrode to form a plate capacitor. A lot of free charge distributed on the electronic film, when the natural wind blows, it will produce some vibration, this vibration causes a displacement of the electronic film, and changes the distance between the plates of the capacitor. So the capacity of the capacitor would be changed. Since the number of charges on the electronic film remains constant, According to the formula: Q =CU, Therefore, when C changes inevitably lead to changes in the voltage U across the capacitor, we got the output voltage signal, the detection of natural wind signal is converted into a voltage signal detected. The output voltage signal is relatively weak, so it needs to go through the amplifier circuit. Four directions were got four voltage signals.

Information processing module. The role of information processing module is make the judgment and conversion to the collected natural wind signal and turn it into a digital signal recognized by MCU. When the natural wind reaches a certain size it will be perceived by people. After repeated tests to find the critical value and its corresponding output voltage value, We call this voltage value of the reference voltage, the collected voltage signal and the reference voltage signal are connected to the inverting input terminal and the positive input terminal of the comparator, if the collected voltage signal is greater than the reference voltage signal, comparator output is 0, on the contrary, comparator output is 1. Four directions connected in the same method. Thus, if a certain direction output of the comparator is 0 and that means the direction of wind. After the microcontroller determining wind direction, LED display module can control the direction of the light off, create a wind effect.

LED display module. The model consist of 4 pieces LED panel, north south east and west directions. Each panel includes 8*8 LED lights. As different types of Ice Lantern want to be displayed with the wind, we should setup LED lights and sensors according to the actual conditions. We use transistor to drive LED and use single chip to drive transistor through control latch. Thus we can control the light and shade of LED. We use the method of scan program to control LED's pattern and pattern shift.

Software Design

Monitor program of the control center. The program design adopts the modular design method, the flow diagram of the program shown in figure 5, when opening the power supply of the system, firstly initialize the system and steady it, including the address pointer setting and so on, open the system interrupt, then shows static graphics each column, after the determine whether there is a wind, if not, static graphics display does not change, otherwise, trigger interrupt, after entering interrupt, shut down interrupt, later on determine the direction of the wind, after that, call the corresponding function display, so that the LED display panel displays the corresponding content, then return from interrupt.



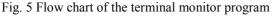


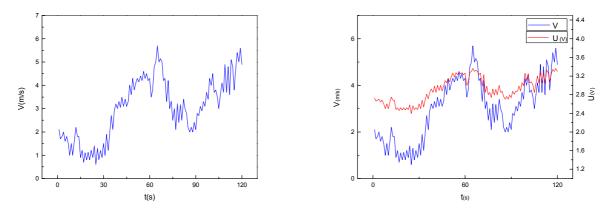
Fig. 6 LED display Flowchart

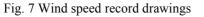
LED display module program design. The program of LED display module in total is divided into four subsystems, which varied from different direction. From the east side to the west is the subprogram 1, and from west to east is subroutine 2, and from south to north is subroutine 3, and from north to south is subroutine 4. We use subroutine 1 as an example, and the program flow chart is shown in figure 6. The initial value of mobile number of columns is 0. The number of columns will always plus 1 after the circulation when it enters into the program. The effect that we can see is pattern movement westward from one column to another. When the mobile column number is greater than or equal to 7, it will jump out of the loop, and mobile number of columns will be 0. The display is over.

System Testing

The system module was established through building each hardware module and writing the software program according to the design requirements. Making a test outdoor, collecting wind speed data by digital anemometer. At the same time, collecting the output voltage of the information collection circuit, so as to the information processing module, making a collection of the output voltage in

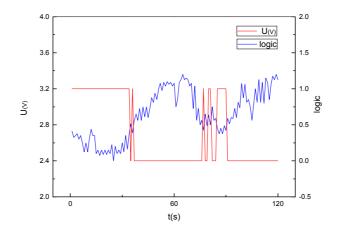
comparator for real-time, these three types of data are synchronized. In 120 seconds, the collected speed recording shown in Figure 7.







The BoFu wind scale shows that when the wind speed is $0.0 \sim 0.2$ m/s, the smoke will be in the vertical upwards direction. When the wind speed is $0.3 \sim 1.5$ m/s, the smoke will show the direction of the wind[5]. When the wind speed is $1.6 \sim 3.3$ m/s, people will feel the existence of the wind. By using digital anemometer for the actual detection, we can know when the wind speed is greater than 2.4m/s, we will perceive the wind in case of sensitivity. In the amplification part of information acquisition circuit, magnification won't be changed any more once have been set up. When we record the wind speed above, the record of corresponding voltage value is shown in figure 8.





In Figure 8, the wind speed 2.4m / s corresponding to the output voltage is 2.8V, in the information processing circuit, the reference voltage is set to 2.8V, connected to the comparator's positive input terminal, the output voltage of the information acquisition circuit connected to inverting input terminal of the comparator, when recording of the two data, the output of information processing circuit record shown in Figure 9, is the digital signal could be identified by MCU, reached the design requirements. MCU interrupt source's trigger is falling edge trigger, when a falling edge is detected, MCU interrupt is triggered, execute the interrupt service routine. After testing, the direction of LED display and the real wind direction are the basically same.

Conclusion

The paper presents a LED display system triggered by the natural wind. According the testing results, the system can be sensitive to wind accurately when the wind speed is over than2.4m/s, moreover, it can identify the direction of the wind as the pre-set programming. The electric signal of the system is stable, so as to the patterns of the LED display module, and it can be changed with the direction of the

wind rapidly. All functions reached design requirement. The system power consumption is $1w\sim1.8w$. The system has wide extensibility. It could be used in Ice Lantern and can also apply to city lightening. It makes the beneficial exploration for science and technology combined with traditional art and culture.

References

- [1] Giorgio Spiazzi, Simone Buso,: Applied Power Electronics Conference and Exposition, 2004.APEC '04. Nineteenth Annual IEEE , Vol.pp 1495 1500, 2004
- [2] Dongmei Li, Sch. of Mech. & Electron.: Electronic Packaging Technology & High Density Packaging, 2009. ICEPT-HDP '09. International Conference, pp 393 – 397, 10-13 Aug. 2009
- [3] Sessler, G.M., West, J.E.: Broadcast and Television Receivers, IEEE Transactions on ,Vol 10, pp73 – 76, May 1964
- [4] Hsieh, W.H., Tseng-Yang Hsu, Yu-Chong Tai.:Solid State Sensors and Actuators, 1997. TRANSDUCERS '97 Chicago., 1997 International Conference on ,Vol 1, pp 425 – 428, 16-19 Jun 1997
- [5] Espinoza, C.E.M., Villanueva, J.M.M., Catunda Cavalcanti, S.Y.: Instrumentation and Measurement Technology Conference (I2MTC), 2010 IEEE, pp 624 – 628, 3-6 May 2010

Design of The Pulse Wave Digital Filters Based on MATLAB

Helin ZHANG^{1,a}, Guolong ZHANG^{1,b}, Kang ZHANG^{*1,c}

¹ School of computer, Jiangxi University of Traditional Chinese Medicine, Nanchang 330006, China ^alin_he99@163.com,^b65168700@qq.com,^c305224190@qq.com

Keyword: digital filter, MATLAB, processing, pulse wave

Abstract: Quality of human pulse waveform graph determine the results of the disease analysis and affect disease diagnosis accuracy, Through the MATLAB software design of a digital filter is used to filter the pulse signals, Optimizing the pulse waveform graph. And the simulation test of digital filter, results showed that filter completed the pulse wave denoising.

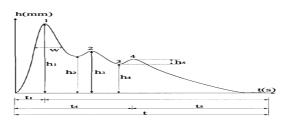
Introduction

Pulse signal contains a large number of human physiological and pathological information, the signal quality directly affects the pulse signal analysis result is true or not, so the signal analysis before the filter denoising is very important. However, in the process of pulse signal detection of actual body due to noise, jitter interference caused by hardware filtering is very difficult, we have the necessity to carry on the software digital filtering.

Pulse graph theory and pulse waveform characteristics

As we all know, the heart of every beat of a cycle, pressure and volume of human arteries and blood flow in the state will change, reflected the pulse of the pulse is these changes in arterial. And these changes can be perceived by fingers or pulse sensor. For example, the traditional pulse diagnosis is through the doctor's fingers to be perceived by subjects pulse frequency, depth and strength of a series of changes, so as to acquire the information of pulse.

Pulse curve (Figure 1) consists of multiple wave, mainly by the ascending and descending branches. Descending from the dicrotic front wave (also known as tidal wave), the descending isthmus and dicrotic wave (also called the dicrotic wave). Changes in each sub wave represents the physiological and pathological significance of specific.



1).main wave; 2). Dicrotic front wave; 3). The descending isthmus; 4). Dicrotic wave Fig 1 Schematic diagram of pulse graph structure

The pulse signal of human body has a low frequency and weak characteristic signal. And pulse signal recording and from living, many factors affecting the with the examinee mental, nerve and fluctuation. Detection and analysis of its objective is difficult.

From the time point of view, the pulse waveform is a typical non stationary quasi periodic signals. Its frequency is mainly distributed in $0.5 \sim 25$ Hz, $0 \sim 5$ in the surface voltage about mV.

Pulse signal noise analysis and design of digital filter

Noise analysis of pulse signals

The pulse signal of human body is the low frequency signal, its frequency are mainly concentrated in the range of $0.1 \sim 50$ Hz, the actual application, and generally the pulse signal frequency between $0.2 \sim 45$ Hz can better meet the requirements of detection and diagnosis. In the acquisition process of pulse signal, vulnerable to outside interference, the noise is the main noise; frequency interference, baseline drift and human respiratory movement caused by high frequency interference, baseline drift removal which is very important in the pretreatment of pulse signal, it directly affects the parameters of the signal waveform calculation.

As shown in Figure 2, is the result of pulse wave of frequency distribution of data in MATLAB software by performing the Fu Live transform on the pulse wave are obtained.

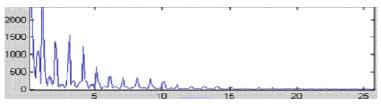


Fig2 Analysis of FFT frequency pulse signal

The above knowable, the hardware simulation circuit unit filter, pulse signal frequency is mainly concentrated in the range of $0.5 \sim 25$ Hz, especially 25Hz the following more concentrated. Therefore, in the design of the digital filter with a cut-off frequency of the frequency range from 0.5 to 25Hz.

Design of digital filter

In this paper, MATLAB, a FIR digital filter is designed by using the window function method, By comparing the performance of window function, Use Kaiser window design this filter, We can change according to the free parameter to set the corresponding parameters

Using MATLAB programming, first need a can produce ideal low-pass filter impulse response sequence of function. In the process of implementation, in order to avoid being zero except the sampling sequence m, need to add a decimal. At the same time, the need for a function to the system frequency response function of the system are given, various technical indicators and the other for a function of the input (such as the stop band attenuation, the pass band frequency, stopband frequency) to determine the various parameters of the Kaiser window function. The implementation of this function can be based on the experience formula design given above, but note that, because of the window function is symmetric about the midpoint of the window function, so the calculated length (i.e., the filter length) should be odd.

The function realization, in order to satisfy the two requirement, should first calculate the passband ripple value with fluctuation and resistance, and then to the smaller of the two into the calculated minimum stopband attenuation, and then calculate the stopband attenuation value. When we calculate the filter length M, should first determine whether it is even, if it is, you need to add 1 to meet the requirements of the odd length.

The free parameters of specific Kaiser window is 3.4, the filter length M=61, order number 20, pass band cutoff frequency 0.5~25Hz, We provide the MATLAB function Kaiser (M, beta) to generate the above parameters.

FIR digital filter is part of the MATLAB source code is as follows:

fs=200; // Set the sampling frequency f=[0.5,25] wn=2*f/fs; w1=kaiser(61,3.4); b1=fir1(60,wn,w1); signal2=filter(b1,1,data); freqz(b1);

Simulation test

At the end of the FIR filter design of the simulation test by MATLAB, the results as shown in figure 3 and figure 4:

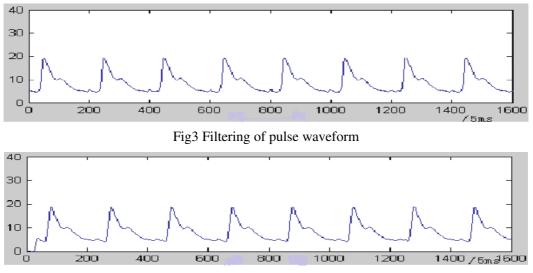


Fig4 Waveform pulse filter

The results showed that, the FIR filter is better to retain the pulse waveform characteristic wave, the signal of peaks and troughs in the disturbance and sharp (i.e. noise sign) has strong filtering effect. The filtering effect of the pulse wave digital filter design is excellent.

Conclusions

In the corresponding digital filter design for pulse signal should give full consideration to the characteristics of pulse signal, FIR filter based on MATLAB design, simulation results show that the pulse wave signal noise processing effect is obvious, and achieved the desired effect. If the joint for pulse signal processing hardware filter circuit with continued it will get a better effect.

Acknowledgements

This work was financially supported by the project:: Jiangxi University of traditional Chinese medicine and natural science research project (project number: JZJSJ-2012-09)

References

[1] Xue nianxi [M].Application of MATLAB in digital signal processing. Beijing: Publishing House of Tsinghua University(In Chinese), 2003,10-75

[2] Huang Dawei. Digital filter [M]. Beijing: China Railway Publishing house(In Chinese).1991

[3] Lou Shuntian, Li Bohan. Based on the window function of system analysis and design of signal processing [M]. Xi'an: Xi'an Electronic and Science University press(In Chinese).2000

[4] H Brandenstein, R Unbehauen. Weighted least-squares approxi- mation of FIR by HR digital filters[J]. IEEE. Tram on Signal Processing, 2001,49(3): 558 - 568.

Measuring the Submarine's Induced Magnetic Field by Geomagnetic simulation method

ZHANG Zhao-yang^{1,a}, YI Jun^{1,b}

¹Navy Equipment Technology Institute, Shanghai, China ^azzy810514@163.com, ^byijunb@online.com

Keywords: induced magnetic field, magnetic field measurement, geomagnetic simulation, submarine, degaussing

Abstract: The induced magnetic field is an important parameter in submarine degaussing, the measurement of which by course-changing method now wastes much time and force. By analysing the producing and measuring theory of the induced field, a method for measuring the submarine's induced magnetic field by geomagnetic simulation was founded. The geomagnetic field can be changed by galvanizing the geomagnetic simulation loops, and the submarine's induced field can be calculated according to the change of the submarine's field before and after galvanizing, which can achieve the goal of fast measuring the submarine's induced field. The experiment of the mockup showed that the method is feasible, and the submarine's induced field can be measured fast and accurately. In the actual measuring of submarine's induced magnetic field and degaussing work, the method has important application value.

Introduction

The induced magnetic field is an important component of the submarine's magnetic field, which is an important parameter for dealing with permanent magnetism and adjusting degaussing system and changes with change of location and the course^[1]. At present, the study on the induced magnetic field mainly focus on numerical calculation work. The usual methods include finite element method^[2,3], integral equation method^[4-6], equivalent source method^[7], as well as the burgeoning magnetic moment method (MMM)^[8], and so on. But the numerical calculation can't replace the actual measurement. First, the accuracy of the calculation result for certain submarine can't be ensured; Second, the accuracy of the numerical calculation result need to be validated by actual measurement. The actual measurement of the submarine's induced magnetic field is generally achieved by course-changing method and two-location method. For the course-changing method, as the submarine has big and special shape and the entrance and the sea-route are very strait, the process of course-changing for a submarine often consumes much time and force. In addition, after course-changing, the anchored location changes oftentimes, which resulted that the relative measurement location changes and big error can be introduced. The submarine's vertical induced magnetic field can be measured by two-location method in theory, but as the magnetic state of the submarine after sailing for long range can't be ensured invariable, so it is unfeasible in practice and accuracy.

According to the above problem, we started the research from analysing the measuring theory of the induced magnetic field, and a method for measuring the submarine's induced magnetic field by geomagnetic simulation was founded. Without change of course and location, by galvanizing the geomagnetic simulation loops, the local geomagnetic field can be changed, based on which the induced magnetic field can be calculated according to the changes of the submarine's magnetic field before and after galvanizing. As a result, the method can avoid wasting of time and power in course changing and location changing, which will obviously shorten the degaussing time and enhance the degaussing efficiency, and it has importance sense for improving the submarine's magnetic defence ability.

Method

With the effect of the geomagnetic field, the magnetization process of the submarine is an instantaneous linear magnetization response, which has two characters. The first is that the induced field derived from magnetization is synchronous with the geomagnetic field, and the second is that the magnitude of the induced field is proportional to the magnitude of the geomagnetic field. The relation of the induced field and the geomagnetic field is as follows:

$$\begin{cases}
B_{ix} = K_x \cdot T_{Dx} \\
B_{iy} = K_y \cdot T_{Dy} \\
B_{iz} = K_z \cdot T_V
\end{cases}$$
(1)

where B_{ix} is the lengthways component of the induced magnetic field, B_{iy} is the transverse component, and B_{iz} is the vertical component. K_x, K_y and K_z represent the lengthways induced susceptibility, the transverse induced susceptibility and the vertical induced susceptibility respectively. T_{Dx} is the lengthways component of the geomagnetic field effecting on the submarine, T_{Dy} is the transverse component, and T_y is the vertical component.

Whether the course-changing method or the two-location method, the entitative theory is all that the measurement of the induced field is achieved by changing the external magnetic field effecting on the submarine. So we can assume one such method: without changing course, simulating to change the local geomagnetic field and achieving the measuring goal. Using the geomagnetic simulation loops to measure the field is an optional method. By laying lengthways simulation loops (X loops), transverse simulation loops (Y loops) and vertical simulation loops (Z loops) to change the local geomagnetic field, measuring the 3 components of the induced magnetic field can be achieved.

According to the above analysis, without magnetic disturbance and current, the submarine's magnetic field excitated by the x component of geomagnetic field T_{Dx1} is written as B_{x1} . When galvanizing X loops, the x component of the geomagnetic field becomes T_{Dx2} , and simultaneously the submarine's magnetic field becomes B_{x2} . And $B_{x2} - B_{x1}$ is the induced magnetic field corresponding to the geomagnetic changing $T_{Dx2} - T_{Dx1}$, so we can get the submarine's induced magnetic field B_{ix} derived from T_{Dx} as follows:

$$B_{ix} = T_{Dx} \frac{B_{x2} - B_{x1}}{T_{Dx2} - T_{Dx1}}$$
(2)

With the same theory, we can get the transverse induced field B_{iy} derived from T_{Dy} :

$$B_{iy} = T_{Dy} \frac{B_{y2} - B_{y1}}{T_{Dy2} - T_{Dy1}}$$
(3)

And also the vertical induced field can be written as:

$$B_{iz} = T_V \frac{B_{z2} - B_{z1}}{T_{V2} - T_{V1}} \tag{4}$$

Where the physical explanations of the variables in equation (3) and (4) are similar with equation (2).

According to equation(2) to equation (4), without course changing, the measurement of the induced field can be achieved by geomagnetic simulation. At present, to carry out the geomagnetic simulation, two methods can be considered. The first is to lay the geomagnetic simulation loops according to the optimization of loops' design; the second is to take the compensation loops in the existent degaussing station as the geomagnetic simulation loops.

Optimization Design of the Geomagnetic Simulation Loops

According to the theory of the method on single course, to measure the field accurately, the change of the exterior magnetic field effecting on the submarine should be uniform, so good uniform degree for the field of the geomagnetic simulation loops in definite area is necessary, and the optimization design of the simulation loops is needed. In the article, the uniform degree is defined by $J_i = B_i/B_0$, where B_0 represents the field in the center, and B_i represents the field at random point.

The design of the geomagnetic simulation loops should be carried out according to the following steps. First, determine the size of the uniform area according to the actual demands, and set reasonable uniform degree index; Second, choose loop shape according to the actual engineering environment and applying demands, and set the parameters of the simulation loops; Third, found the multi-objective optimization model based on the uniform degree error and the cable length; Finally, solve the model by multi-objective optimization method (such as the optimization method based on the relations of Pareto domination algorithm)^[9], and the parameters of the loops can be gotten, based on which the design scheme can be obtained. The detailed flow chart is displayed in Fig. 1.

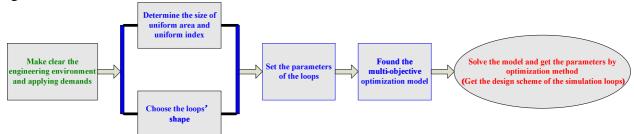
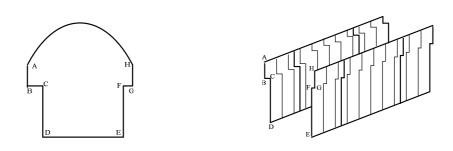


Fig. 1 The flow chart of the optimization design of the geomagnetic simulation loops

Following the above steps, we can get the geomagnetic simulation loops satisfying the design demands, but there is no such simulation loops in practice at present. In fact, as the compensation loops in degaussing stations have geomagnetic compensating effect, we can take the compensation loops as simulation loops, by which the aim to change the geomagnetic field can be achieved. In this way, we carried out the mockup experiment using the geomagnetic compensation loops as in some degaussing station.

Measuring Experiment

In the measuring experiment, the main process is described as follows: take the induced magnetic field measured by course-changing method as the standard field, and compare it with the field measured by geomagnetic simulation method on single course, from which the feasibility of the method based on geomagnetic simulation can be tested. As only the lengthways induced field *Zix* and the transverse induced field *Ziy* can be measured in the degaussing station, we only did the comparing work for *Zix* and *Ziy* in the experiment (If the method for *Zix* and *Ziy* is feasible, also for the vertical induced field *Ziz*). In the experiment, the distributings of the lengthways compensation loops and the transverse compensation loops (scale models) are shown in Fig. 2, from which we can see that the lengthways loops are shown by single loop (In fact, the lengthways loops are superposed loop by loop in lengthways direction with some space between), and the transverse loops are distributed by multi-section and divided into two parts (left and right).



(1) Lengthways compensation loops (2) Transverse compensation loops Fig. 2 The sketch map of the geomagnetic compensation loops

Choose a representative submarine mockup as the experiment object. The length of the mockup is 5.48m, and the width is 0.48m. Below the mockup, there are 3 lines of magnetometers, including 12 magnetometers below the port and the starboard respectively, and 24 magnetometers below the keel, as illustrated in Fig. 3, in which the measuring length is longer than the length of the submarine.

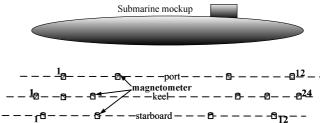


Fig.3 The sketch map of magnetic measurement for the submarine

A. Measuring Process

The measuring process mainly includes the following steps.

Step 1: Carry out the preparing work before the submarine mockup's entering the loops model. Including checking the lines, the measuring system and the power supply, as well as measuring the field of the geomagnetic simulation loops.

Step 2: Measure the magnetic induced field by course-changing method, which will be considered as the standard induced field. In this step, the invariance of the relative measuring location must be kept, which is the most important.

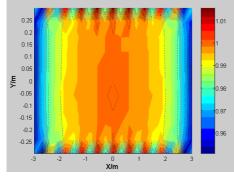
Step 3: Galvanize the simulation loops and the geomagnetic field will be changed, and measure the total field of the submarine and the loops.

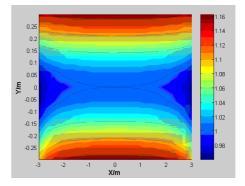
Step 4: Cut off the power supply, and measure the field of the submarine.

Step 5: Calculate the induced field of the submarine, and compare it with the standard field.

B. Result

For simulation loops model, give a certain current to X loop and Y loop respectively, and calculate the uniform degree of the magnetic field generated by the two loops. The calculation result is shown as illustrated in Fig. 4.

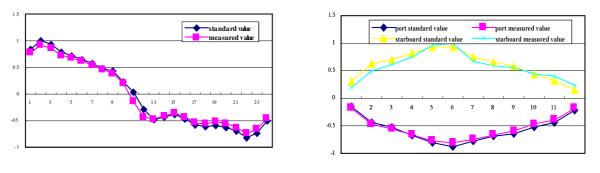




(1)The uniform degree of X loop (2)The uniform degree of Y loop Fig. 4 The uniform degree distributing of X and Y loops

From Fig. 4, we can know that the area in the figure includes the submarine's area, and the uniform degree error of X loop is not beyond 5%, the error of Y loop is not beyond 15%. More closer near the center, more better the uniform degree is; and more closer near the edge, more worse the uniform degree is. As a whole, for the most area of the submarine, the field of the geomagnetic simulation loops is uniform, which can satisfy the demand for the change of the geomagnetic field.

According to the measuring process above, we measured Zix and Ziy by the method based on geomagnetic simulation, and compared it with the standard value, which is shown in Fig. 5. The result in Fig. 5(1) showed the value for Zix under the keel, and the result in Fig. 5(2) for Ziy under the port and the starboard. By calculation, the relative rms (root mean square error) for the measured value of Zix under the keel is 6.3%, and the relative rms for Ziy under the port and starboard is 4.7% and 8.5% respectively. The mockup experiment showed that the method based on geomagnetic simulation is feasible, and the value of the induced magnetic field measured by course-changing method can be replaced by the value measured by the single course method to be applied in the degaussing work.



(1) The result for *Zix* (2) The result for *Ziy* Fig. 5 The result for the submarine mockup experiment

Conclusion

By analysing the producing and measuring theory of the induced magnetic field, we studied on the measuring method based on geomagnetic simulation. By changing the geomagnetic field via galvanizing the simulation loops, the accurate measuring of the submarine's induced magnetic field can be achieved on single course. The submarine mockup experiment validated that measuring Zix and Ziy on single course is feasible, and we can conclude that measuring Ziz by the method by geomagnetic simulation method is also feasible. With the character of saving time and power, the method can be applied to the degaussing station equiping with geomagnetic compensation loops, which can help to measuring the submarine's magnetic field rapidly and improving degaussing efficiency.

References

- [1] ZHANG Lian-kui. Analysis of the naval vessel's magnetic field-degaussing with temporary loops [M]. Wuhan: navy university of engineering, 1991. (In Chinese)
- [2] Brunotte X, Meunier G, Bongiraud J. Ship magnetization modeling by the finite element method [J]. IEEE Trans. Magn., 1993, 29(2):1970-1976.
- [3] Gordon J C Aird. Modelling the induced magnetic signature of naval vessels [D]. U.K., Glasgow: Department of Physics and Astronomy University of Glasgow, 2000.
- [4] Chadebec O. Modelisation du champ magnetique induit par des toles, Identification de L'aimantation [D]. Grenoble: institut national polytechnique de Grenoble, 2001.

- [5] Vuillermet Y, Chadebec O, Coulomb J L, et al. Scalar potential formulation and inverse problem applied to thin magnetic sheets [J]. IEEE Trans. Magn., 2008, 44(6): 1054-1057.
- [6] T.-S. Nguyen, J.-M. Guichon, O. Chadebec, et al. Ships magnetic anomaly computation with integral equation and fast multipole method [J]. IEEE Trans. Magn., 2011, 47(5): 1414-1417.
- [7] Kazimierz J., Pawel Z., Miroslw W. Multidipoles model of ship's magnetic field[J]. International Journal of Applied Electromagnetics and Mechanics, 2012, 39: 183-188.
- [8] Guo C B, Liu D M. Prediction of magnetic signatures of ship's induced vertical magnetization[J]. IEEE, 2012.
- [9] Coello C A, Cortes N C. Solving multiobjective optimization problems using an artificial immune system [J]. Genetic programming and Evolvable Machines, 2005, 6(2): 163-190.

Design of Induced Power Supply System for On-line Monitoring Device of Power Cable

Xinlao Wei^{1,a}, Bo Zhu^{1,b}, Bing Pang¹, Tong Liu², Song Wang², Ruihai Li²

¹ Harbin University of Science and Technology, China

² Electric Power Research Institute, China Southern Power Grid, China

^aweixinlao@163.com, ^bzhubo1219@163.com

Keywords: Power supply system, Rogowski coils, Super capacitor, Energy storage

Abstract. The paper described a sort of power supply system featured as a hybrid of Rogowski coil, super capacitor and Li-battery. The proposed power supply obtains energy from the magnetic field induced by installing a Rocowski coil on the cable. The design of the power supply system is introduced in the paper. The results of test show that the power supply system can provide a stable $\pm 12V$, $\pm 5V$ voltage to the on-line monitoring devices.

Introduction

A stable power supply is one of the critical components for the on-line monitoring system, which ensure the system nramal operation. Usually the monitoring system should be installed close to the power cable, the cpable operate environment where has no conventional power sources. Due to the fact that monitoring system should be continuously work outdoors, the stable power supply need to work for a long time without maintenance. Therefore, how to provide a stable electrical power for the monitoring system is a challenging problem to resolve.

At present powering the monitoring system by solar energy is a popular used method[1], but the solar panel power supply is influenced by the weather, and it need to clean the solar panel when covered by snow , dust and ice. The laser energy has been applied in the electronic current transformers and active optical current transformer, but the method is not fit for outdoor operation and has a high cost[2]. The super capacitors can work in a wider temperature from -40° C to 70° C than conventional batteries. The advantage of it is vital for the on-line monitoring devices in the hot or cold area. Meanwhile, the super capacitors have the lower rate of leakage current and stable performance. The shortcut of it is that the storing energy density is lower than batteries. So the power system using super capacitors and Li-batteries may play a better performance [3]. Another method is to obtain power energy from current-carrying conductors by using a specially designed Rogowski coil which is install on the conductor. It can obtain the energy from the primary side to secondary side. The similar approacher have been presented in ref [4,5], but systematic research has not been performed yet. It is necessary to promote the power supply base on Rogowski coil into practice.

In the present paper we provide a power supply system for on-line monitoring system which is consist of Rogowski coils, super capacitors and Li-battery. The power system can continue to supply constant power.

The Basic Principle of Current Transformer Inductive Power

The basic principle of current transformer is the use of Faraday's law of electromagnetic induction by using current transformer which can induce AC voltage from the high voltage power cable, then after rectifying, filtering, voltage reduction. Finally, it can output stable DC voltage for on-line monitoring devices. The current transformer is consist of the primary winding, secondary winding and magnetic core. According to the knowledge of the electromagnetic theory [6], the current flows cross the cable core will generate magnetic field which can be transformed into electricity. The schematic diagram of power supply is shown in Fig. 1.

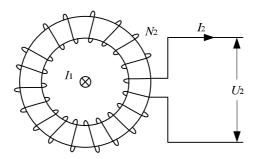


Fig.1 Schematic diagram of power supply

According to the motor theory, the secondary voltage valid value is as follow:

$$U_2 \approx E_2 = 4.44 f N_2 \Phi_m \tag{1}$$

Where E_2 is magnetic induction electromotive force; f is the power frequency; N_2 is the secondary side winding turns; Φ_m is magnetic flux amplitude which is given by:

$$\Phi_m = \lambda B_m S \tag{2}$$

In Eq.2 λ is laminated coefficient; $B_{\rm m}$ is the saturation magnetic induction; S is the cross-section area of the core.

The relation of magnetic induction peak and magnetic field strength peak is given by:

$$B_m = \mu_0 \mu_r H_m \tag{3}$$

Where μ_0 responses the vacuum permeability; μ_r responses the relative permeability of magnetic core; H_m is the peak of the magnetic field strength.

According to the Ampere's circuital law:

$$H_m l = \sqrt{2} N_1 I_1 \tag{4}$$

Where *l* is the average length of magnetic path; I_1 is the exciting current; N_1 is the primary winding turns, which takes 1.

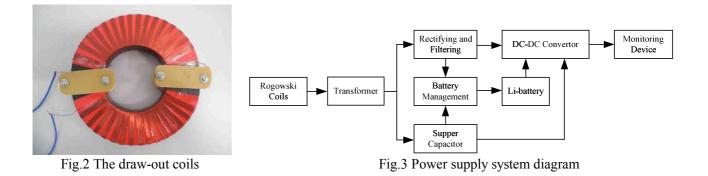
The secondary side winding turns is obtained:

$$N_2 = \frac{U_2 l}{4.44\sqrt{2\lambda\mu_0\mu_r}fN_1SI_1}$$
(5)

The Choices of Magnetic Core Materials and Winding Turns

In order to ensure reliable power supply when the transmission line has heavy load or small load, the choices of the iron core should be with a small starting volatge. From Eq.1 to Eq.4, we know that the method to reduce the starting current is to improve the initial permeability of magnetic core, and the iron core should have high energy transfer efficiency. The effective method to improve the efficiency of energy transfer is reducing excitation and choosing high permeability material. We choose the cold silicon sheet, the core model is steel-1008.

Determining the winding turns of coil is a complex process with theoretical and experimental verification. According to the result of test, we determine that the winding turn of the cores are 350 turns. The actual picture of the assemble draw-out coil is shown in Fig. 2. In oredr to maximize use of existing resource of the power cable, we put Rogowski coils on the cable.



Design of Power System

The power supply consists of draw-out coil, surge protection, step-down module rectifying and filtering circuit, solar batteries, super capacitor group, Li-batteries and DC-DC converter, etc. The diagram of power design is shown in Fig. 3. The power apparatus get electricity from the high voltage cable by the draw-out coil, then through the step-down module, rectifying and filtering circuit and DC-DC converter produces $\pm 12V$, $\pm 5V$ voltage for on-line monitoring devices.

For the monitoring system, it needs a stable $\pm 12V$, $\pm 5V$ voltage and about 1A current supply. The circuit is to convert the fluctuant voltage into a stable and reliable constant source. The super capacitor and Li-batteries should be pre-charged respectively before the power system began to work, the reason is that the transient change may cause the over-current in the charging circuit.

During the charging phase, the voltage induced by Rogowski coils is used to charge super capacitor and management Li-battery. The super capacitor can remain a higher voltage than Li-battery, so it would charge the Li-battery and itself be charged by Rogowski coils at the same time. The charging energy is limited by the Rogowski coils, although the charging voltage is higher than capacitor, the voltage across the super capacitor would not rise rapidly. Therefore, the super capacitor can provide monitoring system constant voltage.

If the load current is decrease which lead to the power system cannot supply enough power to monitoring system, the super capacitor would continue to supply the monitoring system and charge the Li-battery. When the voltage of supper capacitor decrease lower than the Li-battery, the Li-battery will supply power till energy come. The super capacitor in power system is connected in parallel, and a current-limiting circuit should be arranged between Li-battery and capacitor to prevent the battery from damage.

Before the power system began to work, the super capacitor and Li-batteries must be pre-charged respectively which can prevent over-current caused by the transient change in the charging circuit.

In the power system, we take BQ24008PWP as the battery management, the Li-battery charge circuit is shown in Fig. 4.

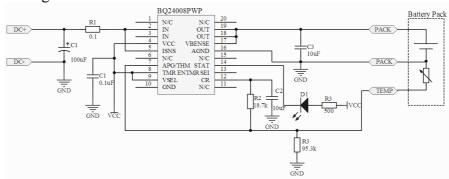


Fig.4 The Li-Battery charge circuit

The Experimental Results

The test circuit is consisted of voltage regulator, transformer, power cable, Rogowski coil, power supply system, current sensor and oscilloscope. We do short-circuit for the power cable, and obtain

the induced voltage from current-carrying of power cable by using Rogowski coil, and test the current flow across the cable by using current sensor (A621) made in Tektronix Company. The output voltage of power supply system and the value of the short- circuit current can be obtained by the oscilloscope. The test circuit is shown in Fig. 5.

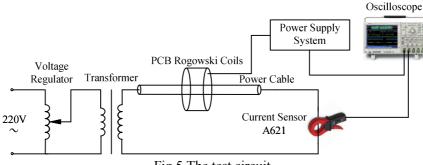


Fig.5 The test circuit

The test resluts are shown that power supply system can provide a stable $\pm 12V$, $\pm 5V$ voltage when the short-circuit current reaches to 400A. If the short-circuit current is lower than 400A, the super capacitor power system $\pm 12V$, $\pm 5V$ voltage.

Conclusions

In the present paper, we study the issue about the power for on-line monitoring device of cable insulation. The results show that power system using Rogowski coil to induce energy, and using super capacitor, Li-battery can continue to supply constant power.

Acknowledgment

The work is supported by the National Basic Research Program of China (2012CB723308), The Major Program of China Southern Power Grid and The Major Project of Graduate Innovation Fund in Heilongjiang Province of China (YJSCX2012-078HLJ).

References

- H. Matsuo, K. Kobayashi, Y. Sekine: IEEE Transactions on Industrial Electronics, Vol.53 (2006), No.1, p. 281.
- [2] Y. Neyatani, N. Hosogane, M.Matsukawa, H. Ninomiya, H. Horiike, S. KTsuji: 14th IEEE/NPSS Symposium on Fusion Engineering, Vol.2 (1991), p. 1183.
- [3] P.P. Barker: IEEE Power Engineering Society Summer Meeting, Vol.1 (2002), p. 316.
- [4] E. F. Donaldson, J. R. Gibson, G. R. Jones, N. A. Pilling, B. Taylor: IEEE Proceedings of Generation, Transmission and Distribution, Vol. 147 (2000), No. 5, p. 304.
- [5] N. A. Pilling, R. Holmes, G. R. Jones: IEEE Proceedings of Generation, Transmission and Distribution, Vol. 140 (1993), No. 5, p. 351.
- [6] G.Y. Qiu: Circuit. (Trans Higher Education Publications, Beijing 1999).

Research on PCB Rogowski Current Transformer Based on AD7742

Xinlao Wei^{1,a}, Bo Zhu^{1,b}, Bing Pang¹, Tong Liu², Song Wang², Ruihai Li²

¹ Harbin University of Science and Technology, China

² Electric Power Research Institute, China Southern Power Grid, China ^aweixinlao@163.com, ^bzhubo1219@163.com

Keywords: Current transformer, Digital integrator, Rogowski coils, AD7742, VFC

Abstract. Rogowski coils is a kind of special structure hollow coils, it has good linearity, no iron core, no magnetic saturation phenomenon and wide measuring range, which has been used to measure all kinds of various changes current. The current transformer consist of PCB Rogowski coil and digital integrator has been designed, includes the structure of PCB Rogowski coils and the principle digital integrator based on AD7742. The test of PCB current transformer show that it has high accuracy and PCB coils has good linearity. It can meet the requirement of current measurement.

Introduction

In recent years, Printed Circuit Board (PCB) technology brings a new method to design and fabricate Rogowski coils. The design of PCB Rogowski coils is using software to finish it, such as PROTEL software. The wire is printing on the printed circuit board instead of the coil wire. According to the theoretical design, every turns of coils placed suitable on the PCB board. Using digital control processing technology not only ensure every turns of coils on the PCB board space position same and shape accuracy, but also ensure the parameter and geometric dimensions of the actual produce coil consistency with the theoretical design. The PCB coils have been proved to have high accuracy, stability, sensitivity, and better temperature stability over traditional handmade Rogowski [1,2]. More information about PCB Rogowski coils can be found in reference [3] and in reference [4].

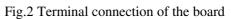
The analog integrator has non-ideal factors, such as the actual devices are not ideal, zero-drift of operation amplifier or other analog devices, loss of capacity, etc, all these factors will affect the results. Compared with analog integrator, digital integrator has its outstanding advantages. Such as, it has good consistency becase of the calibration and amplitude is decided by the calibration, the AD converter and other cicuit of digital integrator are relatively simple which making it less influenced by zero-dift, and the structure is flexible and easy to adjust [5]. In the present paper, we choose AD7742 as the digital integrator. The PCB coils and the whole current transformer are tested. Experiment shownd that it can be used to measure current accuracy.

The Structural Design of PCB Rogowski Coils

Fig.1 A basic coil of the board

The new type of field assemble PCB Rogowski coils is consists of basic unit coil of the board, mechanical terminal connection of the board, and electromechanical terminal connection of the board.





The basic unit coil is based on the basic principle of Rogowski coils, which is consist of a rectangular multilayer printed circuit board, and with electromechanical terminal connection at the

ends of the basic unit coil. The shape of the basic coil of the board is shown in Fig. 1. Each layer of the PCB board is printed planar coils, which is made of 18 rectangular turns in series. The different layers of the planar coils is used via on the PCB board to connect together in series and form a basic unit coil of the board. Therefore, the basic unit coil of the board is consist of 108 rectangular turns in series when the number of PCB layers is 6.

The shape of two kinds of terminal connection is shown in Fig. 2. Terminal connection of the board have two main functions: one is mechanical terminal connection which function is connect multiple basic unit coils, fix together and make it become a whole, like Fig. 2(a); another is electromechanical terminal connection which function is connect multiple basic unit coils together at terminal end on electrical, like Fig. 2(b). The difference between two kinds of connection is mechanical terminal connection has via, pad, and without connecting with lines. PCB Rogowski coils is consist of two macrocell coils assemble in the paper. Each macrocell coil assemble with mechanical terminal connection of the board, electromechanical terminal connection of the board, electromechanical terminal connection of the board. The number of the basic unit coil of the board is decided by the number of holes on the terminal connection of the board. The completely macrocell coils assemble PCB Rogowski coils is shown in Fig. 3. The PCB coils can be assembled by using the terminal connection board put two macrocell coils together to realize mechanical and electromechanical connection.



Fig.3 The macrocell coils assemble completely

The Option of Digital Integrator

The voltage to frequency converter has become quite popular due to their low cost and application versatility in variety of electronic control and measurement. It is an oscillator whose frequency is linearly proportional to control voltage. We take AD7742 as digital integrator which is new generation of CMOS synchronous voltage to frequency converter (VFC) that uses a charge-balance conversion technique. It has four buffered inputs that may be configured as two fully-differential inputs or three pseudo-differential inputs. The AD7742 is a multichannel version, the input voltage signal is applied to a proprietary programmable gain front-end based around an analog modulator that converts the input voltage into an output pulse train, and it contains an on-chip +2.5V bandgap reference and operate from a signal +5V supply. It can be used for any which has linear between input and output voltage frequency converter to integrate signal. The voltage to frequency is given by

$$\int_{t_{1}}^{t_{m}} u(t) dt = \Delta t \sum_{k=1}^{m-1} u_{k}$$
(1)

Where Δt is time quantum, from t_1 to t_m ; u_k is the voltage at a certain moment. According to principle of VFC [6], the frequency f_k can be obtained by measuring the voltage u_k .

$$f_{k} = f_{\min} + \frac{f_{\max} - f_{\min}}{u_{\max} - u_{\min}} \left(u_{k} - u_{\min} \right) = 0.25f + 0.2f \frac{u_{k}}{u_{ref}}$$
(2)

Where $u_{\min}=-u_{ref}$, $u_{\max}=u_{ref}$, $f_{\min}=0.05f$, $f_{\max}=0.45f$. u_{ref} , is reference voltage, f is system frequency.

Then Eq.2 times Δt , it is obtained

$$\Delta t f_k = \Delta t 0.25 f + \Delta t 0.2 f \frac{u_k}{u_{ref}}$$
(3)

Eq.3 can be written as

$$u_k \Delta t = \frac{\Delta t f_k - 0.25 f \Delta t}{0.2 f} u_{ref} \tag{4}$$

Inserting Eq.4 into Eq.1, it yields the following results

$$\int_{t_1}^{t_m} u(t) dt = 5u_{ref} \left(T_0 \sum_{k=1}^{m-1} N_k - 0.25(t_m - t_1) \right)$$
(5)

Where T_0 is clock period, N_k is the number of AD7740 output pulse in Δt .

$$\sum_{k=1}^{m-1} N_k = N_{\Sigma} \tag{6}$$

Where N_{Σ} is the number of output pulse in $[t_1, t_m]$.

$$\int_{t_1}^{t_m} u(t) dt = 5u_{ref} \left(T_0 N_{\Sigma} - 0.25 T_0 N_t \right) = 5u_{ref} T_0 \left(N_{\Sigma} - 0.25 N_t \right)$$
(7)

The Eq.7 is given a simple way for signal to realize integral transform by using AD7742. It only need to count the number of output pulse and the number of clock after 1/4 frequency divider, then make count subtract. The integrator principle is shown in Fig. 4.

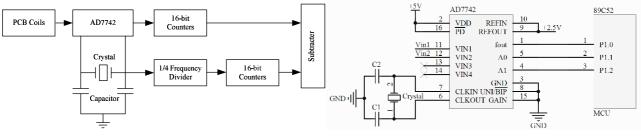


Fig. 4 Integrator principle diagram

Fig.5 The connection diagram

The connection digram for AD7742 is shown in Fig. 5. The analog inputs are configured as fully differential, bipolar inputs with a gain of 1. A quartz crystal provides the master clock source for it, and it is necessary to connect C1 and C2 capacitors on the crystal to ensure that it does not oscillate at overtones of its fundamental operating freuency.

The Experimental of Current Transformer

First, PCB Rogowski coils of current sensors were test as follow. The test was used current sensor (A621) made in Tektronix Company to test the current circuit, and used PCB Rogowski coils of current sensors which designed in the paper to test the current circuit at the same time, the measuring range is 20~200A. The output signal of the Tektronix current sensor and the output signal of the PCB coils were input digital oscilloscope (DPO4104B) made in Tektronix to measurement. The test circuit is shown in Fig. 6.

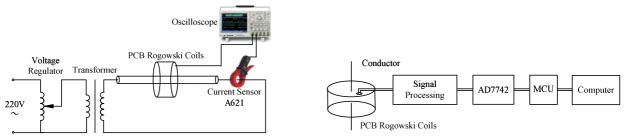


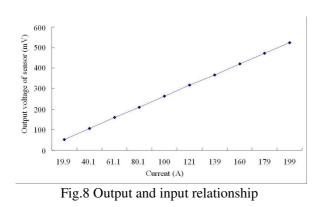
Fig.6 The test circuit

Fig.7 Diagram of current transformer

Second, we test the current transformer which consist of PCB coil and digital integrator. The digram of current transformer is shown in Fig. 7. We use Micro Controller Unit (MCU) based on the struture of MCS-51 to count the number output pulse.

Experimental Results

The results are shown in Figure 8, we can find that input current and output voltage of PCB coils has good linearity. And the Table 1 is shown that the deviation between actual measurement and theoretical calculation PCB coil is very small, the average deviation is 0.13%.



No.	Current (A)	Test Current (A)	Error (%)
1.	20	19.95	-0.25
2.	40	40.08	0.20
3.	60	60.11	0.18
4.	80	80.13	0.16
5.	100	100.15	0.15
6.	120	119.85	-0.13
7.	140	140.14	0.1
8.	160	159.84	-0.1
9.	180	179.83	-0.09
10.	200	199.86	-0.07

Table.1 The test results

Conclusions

A current transformer is designed in the paper, we take PCB coil as the current sensor and take AD7742 as the digital ingegrator. The structure of PCB Rogowski coils has been introduced, through test we find that the PCB coils has good linearity. And test the current transformer, the results show that the current transformer has high accuracy.

Acknowledgment

The work is supported by the National Basic Research Program of China (2012CB723308), The Major Program of China Southern Power Grid and The Major Project of Graduate Innovation Fund in Heilongjiang Province of China (YJSCX2012-078HLJ).

References

- N. Karrer, P. Hofer-Noser: Proceedings of IEEE 31st Annual Power Electronics Specialists Conference, Vol 3 (2000), p. 1296.
- [2] C.Y. Wang, Y.P. Chen, G. Zhang, Z.D. Zhou: Proceedings of IEEE International Conference on Mechatronics and Automation, 2007, p. 3801.
- [3] Y. Neyatani, N.Hosogane, M. Matsukawa, H. Ninomiya, H. Horiike, S. Tsuji: Proceedings of 1991 IEEE/NPSS Symposium on Fusion Engineering, Vol. 2 (1991), p. 1183.

- [4] L.Kojovic: Computer Applications in Power. IEEE, Vol.15 (2002), No.3, p. 50.
- [5] K. W. Zhang, N. Wang, X. Y. Duan, J. Y. Zou, Z. Y. Huang: Proceedings of the CSEE, Vol. 24 (2004), No.12, p. 104.
- [6] M. Stork: Internatonal Conference on Electronics, Circuits and Systems, Vol.2 (2002), p. 631.

Research on Small-capacity Capacitor Type Sensor Detection Method

Weitong Hu^{1, a}, Yuxuan Zhang^{2,b}, Yan Sun^{1,c}, Wangsheng Liu^{1,d},

Lizhong Zhang^{1,e}

¹ Aviation University of Air Force, Changchun City, Jilin Province, China 130022

² Jilin University, Changchun City, Jilin Province, China 130012

^aweitonghu@126.com, ^bcsoft@hotmail.com, ^c475758819@qq.com, ^dWangsheng@163.com, ^elizhongWangsheng@163.com

Keywords: Small capacitor testing, Capacitance measurement method with reference and comparison, Analog Switches, Multivibrator

Abstract. In the field of industrial measurement, capacitive sensors are widely used. In many types of capacitive sensors, the output capacitance value range of many sensors is very small, generally between 10pF to 1000pF, but accuracy is usually required to be more than one thousandth. The conventional method of detecting capacitance value is generally the capacitor charge and discharge. By charging and discharging time statistics and calculations, capacitance values are deduced finally. The inherent disadvantages of this method are: (1) Temperature drift of the measurement circuit is large. (2) The spatial magnetic field under special circumstances impact on measurement circuit. (3) Long-term stability of the device will deteriorate. In this paper, a "capacitance measurement method with reference and comparison" is summed up through a lot of measurement experiments of humidity capacitance, that method can eliminate three kinds of defects in the capacitor charging and discharging process.

Introduction

"Capacitance measurement method with reference and comparison" is based on a traditional capacitor charge and discharge measurement method. The difference from the conventional method is to add the reference comparison circuit. After adding this circuit, the reference capacitance can be stabilized by eliminating the "the environment temperature, circuit boards, and other unstable factors" to the measurement value of the sensor capacitance errors caused . The entire circuit is divided into two parts, hardware and software: 1 The hardware part includes measuring circuit, reference capacitor and capacitance sensor to be measured. 2 The software part includes CF transformation formula processing software, reference and comparison measurement software and capacitance characteristics curve fitting software.

Hardware

The hardware includes a measuring circuit, a reference capacitor and a capacitance sensor to be measured. The Measuring circuit includes "Analog Switches" and "Multivibrator". The Reference capacitor comprises two capacitors of C1 and C2, C1 is the upper limiting capacitance (meaning that the maximum capacitance value of the sensor to be measured is always less than or equal to this capacitance value), C2 is the lower limit capacitance (measuring that minimal capacitance of of the sensor to be measured is always greater than or equal to this capacitance value) . The two capacitors have a lot of the actual measurement needs special requirements in industrial applications in harsh environments and even special occasions , requiring temperatures from -55 °C to +125 °C when the volume changes of 0 ± 30 PPM, capacitance and dielectric loss requires the most stable in drift 5 PPM, recommend the use of rubidium , samarium and other rare oxides of NPO capacitor. CX means measured capacitance sensor. In order to adapt requirements of precision measurement, the link between "C1, C2, CX" and "Analog Switches" may be short as possible.Distributed

capacitance of the circuit board must be small, if forced to need wires to connect, the link must be covered under tight shield, the shield is required connected to the system ground of the power supply finally.

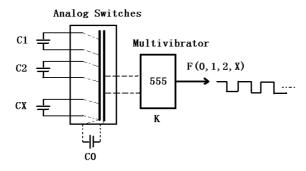
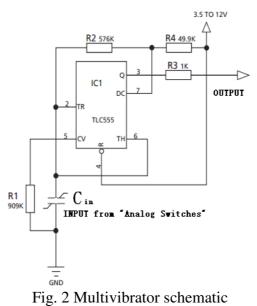


Fig. 1 Hardware system block diagram

The internal resistance of the analog input channels must be small (must be less than 0.1 ohm, otherwise it will affect the following "Multivibrator" input parameters). Between analog channels the same capacitance is distributed. If the capacitance values of channels are not equal, the entire circuit will lose effectiveness. In fact, the channel is equal to the capacitance between the easily achieved as long as the same piece of silicon crystal made by "Analog Switches" very consistent properties due to the PN junction capacitance value of the difference of its analog channels is very small, can be neglected [1].

"Multivibrator" uses classic 555 chip, Cin means output of "Analog Switches ",ultimately Fout is outputed to the count input or input frequency meter of microcontroller chip. The circuit components are almost no special requirements, in which resistor precision and circuit boards wiring accuracy can be carried out according to the method of production of circuit boards generally. The only requirement is to try not to use switching power supply. If switching power supply is forced to used, an LDO regulator device must be placed at the power input, to reduce power supply ripple coefficient effect on the measuremen stability[2].



Software

Softwaresection contains: CF transformation formula processing software, reference and comparison measurement software and capacitance characteristics curve fitting software. the core method of CF calculated conversion processing software is CF transformation formula

$$FX = 1/(C0 + CX)K \tag{1}$$

Where FX is represents the frequency output, CX is measured capacitance, C0 is the parasitic capacitance of analog switches for each channel, K is "Multivibrator", together determined by R1, R2, R3 and R4, that value at different ambient temperatures has a great change, and its algorithm is very complicated.But not to care about this factor, even without calculating this factor, we can eliminate K value by reference and comparison measurement software.

Reference and comparison measurement software is derived as follows:

(1) First were to establish CF transfer equations containing C1, C2, CX parameters.

$$F1 = 1/(C0 + C1)K$$
 (2)

$$F2 = 1/(C0 + C2)K$$
 (3)

$$FX = 1/(C0 + CX)K \tag{4}$$

(2) Coefficient K can be derived from the above three equations ((1) (2) (3)).

$$K = (F2 - F1)/F1F2(C1 - C2)$$
(5)

Where F1, F2, C1, C2 are known values.

(3) The capacitance value of an analog switch for each channel (C0) can be calculated by three equations ((1) (2) (3)).

$$C0 = F1F2(C1-C2)/FX(F2-F1)-C1$$

(4) The CX value can be calculated by substituting K and C0 into FX = 1 / ((C0 + CX) K).

$$CX = F1F2(F2 - FX)(C1 - C2)/F2FX(F2 - F1) + C2$$

CX is the sensor capacitance, which don't contain the capacitance coefficient K, and is not affected by the sensor capacitance value C0, but the capacitance value of the sensor need have corresponding relationship with output value of the real one. Then we need to use capacitance characteristics curve fitting software.

Relational formula between the capacitor and humidity is obtained generally by multiple equation curve fitting method, as follows :

$$Y = AX^{3} + BX^{3} + CX^{2} + DX + E_{0}$$

(Where A, B, C, D, E values are recursively guessed by capacitance characteristic curve-fitting software on the based of a large number of sensor experimental data).

The company's common HUMIREL humidity sensor HS1101 capacitive humidity corresponding formula is as follows :

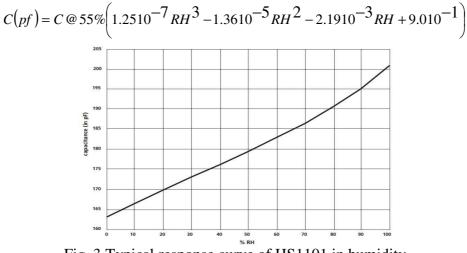
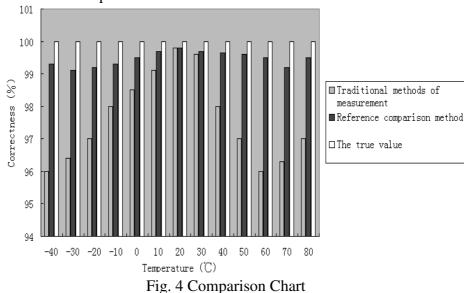


Fig. 3 Typical response curve of HS1101 in humidity

In order to verify the accuracy of capacitance measurement method with reference and comparison, we conducted a one-year experiment in the environment test chamber instrument meteorological environment Changchun Institute with comparing two methods ("capacitance measurement method with reference and comparison "" direct measurement ") to measure the

capacitance at the same time and with the same environment. The result shows that" capacitance measurement method with reference and comparison "is better than" direct measurement".

The chart below shows the comparison results between "Sensor true value", the measurement value by "capacitance measurement method with reference and comparison" and the one by " direct measurement" at different temperatures.



Summary

As can be seen, the measurement value by "capacitance measurement method with reference and comparison" is closer to "Sensor true value".

References

[1] T. Scientist, Title of the paper, in Proceedings of the Conference on 'Smart Sensors and Systems: Technology and Applications (SSS&TA' 2003)', Paris, France, 16-19 March 2003, pp. 123-127.

[2] Sensors Web Portal (http://www.sensorsportal.com).

The Measurement of DC Electric Field for Transformer Oil System Based on the Kerr Electro-optic Effect

Tao Shen^{1,2,a}, Chao Hu^{2,b}, Mingxin Song^{1,2,c}, Xinlao Wei^{1,d}, Qianru Yang^{2,e} ¹College of Electrical and Electronic Engineering, Harbin University of Science and Technology, Harbin, China

²College of Applied Sciences, Harbin University of Science and Technology, Harbin, China

^ataoshenchina@163.com, ^bhuchaokobe123@163.com, ^csongmingxin@126.com, ^dweixinlao@163.com, ^eyangwenlong1983@163.com

Key words: DC electric field; Kerr electro-optic effect; transformer oil; CCD measurement system

Abstract: This study presents a effective approach for the measurement of electric field in liquid dielectric with small Kerr constant based on the principle of Kerr electro-optic effect. In the paper, the distribution of electric field in transformer oil is measured of different electrode materials below 30KV. According to experiments it can be concluded that the intensity of light corresponds with the electric field between the two parallel-plane electrodes in test cell in a certain range of the voltage applied. The conclusion reveals that the distribution and variation tendency of the electric field between the two electrodes can be drawn by the analysis of the light intensity.

Introduction

Transformer is the core equipment DC electric transmission project ,the rationality of the insulation design is very important to the electric power system security and reliable operation[1]. The electric field distribution of transformer oil is usually associated with many factors because of the space charge effect under DC voltage so that the distribution of DC electric field has some uncertainty[2, 3]. The formation and movement of the space charge and the relationship with the electrode material and other external conditions is not clear in physics, reciprocal causation self consistent characteristics between electric charge and electric field lead the mathematical treatment is especially difficult. So,It is of important significance to measure the electric field in transformer oil by the experimental method. In this paper, which based on the principle of Kerr electro-optic effect, we set a new measuring system with CCD photoelectric receiving device, and measured the electric field distribution in transformer oil. The conclusion provides a new way for the measurement of electric field and space charge distribution of liquid medium with small Kerr constant.

The measuring principle

Kerr electro-optic effect the production ofdouble refraction in certain transparent substances by the application of a strong electric field, is given by[4]:

$$\Delta n = n_{\mu} - n_{\perp} = B\lambda E^2 \tag{1}$$

Where n // is the refractive index of perpendicular electric fields, $n \perp$ is the refractive index of perpendicular electric fields, B is the Kerr constant, E is the strength of the electric field ,and λ is the wavelength of the light.

Put the two polarizers orthogonally, and the light intensity through the polarizer is:

$$I = I_{m} \sin n^{2} (\frac{\phi}{2}) = I_{m} \sin n^{2} (\frac{\pi B L}{E^{2}})$$
(2)

where I_m is the maximum light intensity, ϕ is the phase difference caused by Kerr electro-optic

effect, L is the length of the Kerr electrode ,E is the strength of the electric field caused by electro-optic effect.

By (2) shows that, the corresponding relationship between electric field and electric field intensity, which can reflect the size by measuring light intensity.

The establishment of a measurementsystem

The electro-optic measurement system based on the effect of Kerr as shown in Fig. 1, it can be used to measure liquid medium of transformer oil Kerr constant small. The system consists of DC high voltage power supply system for the Kerr effect, optical system, CCD light receiving part three device system, completed in the vibration isolation platform darkroom environment.

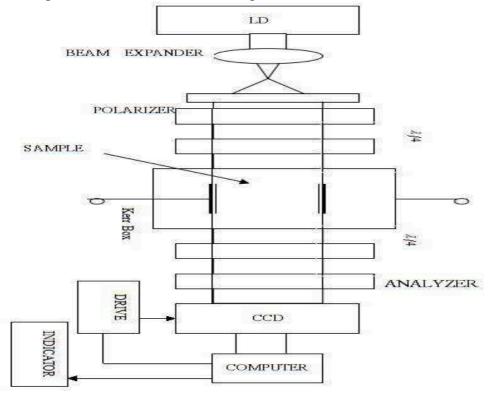
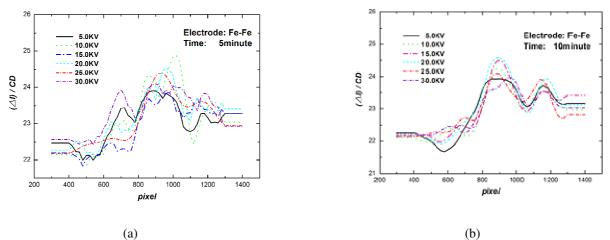


Fig.1 Schematic diagram of measuring equipment

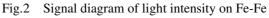
Experimental results and analysis

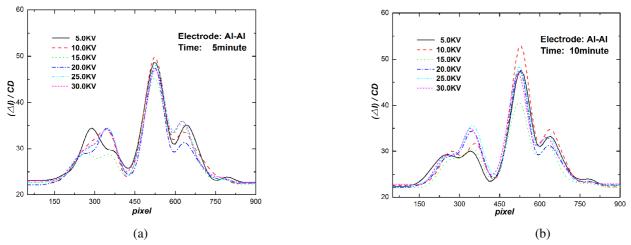
Experiments were conducted with iron - iron, aluminum – aluminum and copper - iron as electrodes respectively. The electrode space is 5mm. The intensity curve is measured between the two electrodes Kerr cell and mathematically smoothed curve as shown in Fig. 2, 3 and 4. From the graph, we can see the light intensity distribution is basically unchanged when the voltage is applied from 5KV to 30KV and the light intensity distribution is substantially unchanged when the pressing time was in 5 minutes and 10 minutes. It indicates that the electric field in the transformer oil is not distorted and

there is no space charge formed between the electrodes. By comparing the different electrode materials, we find that the light intensity distribution is most unobvious by the Fe-Fe electrode, the light intensity distribution is obvious by the Al-Al electrode and the light intensity distribution is most obvious by Al-Fe.

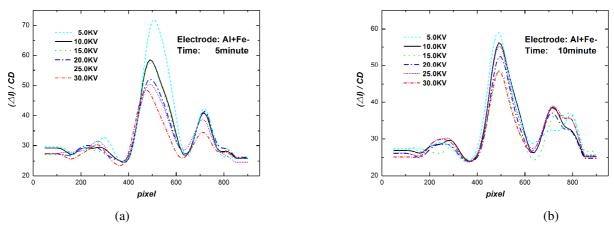


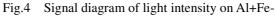






Signal diagram of light intensity on Al-Al Fig.3





Conclusion

The results show that the measurement of the electric field distribution of transformer oil Kerr constant small, through the electro-optic measuring system based on Kerr effect. The charge distortion is different in the range of 30KV. Light gray value reflects the change of charge. But in the range of 30KV and the applied voltage is not directly proportional relationship. The results and discussions we have presented could be referenced by some applications of DC electric field in the future.

Acknowledgements

The authors acknowledge financial support from Natural Science Foundation of Heilongjiang (E201303), the Education Department of Heilongjiang (12531134) and National Undergraduate Training Programs for Innovation and Entrepreneurship of China (201310214010).

References

[1] Yanbing Zhang, Jin Zheng, Dehua Wang: High Voltage Engineering, Vol.36-1 (2010), p. 255.

- [2] Kaicheng Wen and Ruizhen Wang: TRANSFORMER, Vol.34-11 (1997), p. 10.
- [3] Kaicheng Wen and Ruizhen Wang: TRANSFORMER, Vol.34-12 (1997), p. 28.

[4] Xiaowei Ma and Zongren Peng: High Voltage Engineering, Vol.30-1 (2004), p. 19.

Research on a liquid color detecting device

Zhen Zhou^{1, 2, a}, Dixing Li^{1, 2, b}, Yong Qin^{1, 2}, Lifeng Liu^{1, 2}

¹School of Measurement and Communication Engineering, Harbin University of Science and Technology, HeiLongJiang Harbin 150080, China

²The Higher Educational Key Laboratory on Measuring & Control Technology and Instrumentations of Heilongjiang Province, HeiLongJiang Harbin 150080, China

^azhzh49@126.com, ^bldxchn@163.com

Keywords: liquid, color, detecting device

Abstract. At present, the error rate of color detecting device is generally between 1%-5%, and mainly for the solids. To improve the detection accuracy further, and adapt liquid color detection, this research uses a new method to build light paths, and combines the United States TAOS's TCS3200 color sensor and STM32 microcontroller. A new type of liquid color detecting device is designed, system structure and testing process of the device are also given. This device has more than 10-bit A/D conversion accuracy, 0.5% or less error rate, and less than 30% of the price of similar products. It has broad promotion and application prospects, and can be widely used in chemistry, biology, grain and other fields.

Introduction

Traditional identification of color mainly depended on the naked eyes according to the different individual's ability to distinguish colors and human limitations, this method gives only an estimate. With advances in technology, a variety of products develop into automation and intelligence. Distinguishing the color is no longer simply by eyes, but mainly by color identification devices, which have the advantages of high precision, good reliability, and can display color information by digitals intuitively. Such as color detector (mainly colorimeters) and so on. American Applied Color Systems, British Instrumental Color Systems and Switzerland Datacolor are the three main color control equipment companies in the world [1]. Their products are widely used in color recognition, color correction, print recognition, robot control and other fields [2].

The color detecting equipment above is mainly used to detect the color of solid substances. Liquid color detection is very important in chemistry, biology, grain, oil and other fields. However, researches are relatively few in this area. Zhiwei Duan [3] achieved the detection of oil products. Xi Chen [4] improved the detection accuracy. In this study, the conventional color detecting devices are improved. The results show the error rate of this device is less than 0.5%, and the price is about 30% of other similar products. So it has broad promotion and application prospects.

Hardware selection

Light source. Now there is a wide range of artificial lights, the spectral distributions of light sources also have different frequencies [5]. To unite color measurement and color evaluation criteria, CIE recommends several standard light sources, including standard illuminants A, B, C, D55, D65, D75 and so on. Thus, evaluation and measurement of color can be lighted in CIE illuminant-viewing conditions, and have a uniform standard [6,7]. White LED has the advantages of low heat and high brightness, and the color temperature is about 6500K, exactly in line with the standard D65 light source, so white LED is used as a light source.

Color sensor. The United States TAOS (Texas Advanced Optoelectronic Solutions)'s new color sensor TCS3200 is selected. It combines configurable silicon photodiodes and a current to frequency converter on a single monolithic CMOS integrated circuit. The output is a square wave with frequency directly proportional to light intensity. Fig. 1 shows the structure of TCS3200.

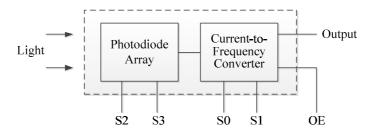


Fig. 1 The structure of TCS3200

In TCS3200, the light to frequency converter reads an 8 x 8 array of photodiodes. Sixteen photodiodes have blue filters, it is the same for green and red filters, and the others are clear with no filters. The four types (colors) of photodiodes are interdigitated to minimize the effect of non-uniformity of incident irradiance [8]. All photodiodes of the same color are connected in parallel. Pins S0 and S1 are used to select output frequency scaling. Pins S2 and S3 are used to select which group of photodiodes (red, green, blue and clear) are active. Table 1 is the specific function of pins S0 to S3.

Table 1 Logic function of each pin

				-	
S 0	S 1	Output frequency scaling (fo)	S2	S 3	Photodiode type
L	L	Power down	L	L	Red
L	Н	2%	L	Н	Blue
Н	L	20%	Н	L	Clear (no filter)
Н	Н	100%	Н	Н	Green

Main controller. STM32F100 series microcontrollers have proven to be ones of the most cost-effective chips. The STM32F100 value line family incorporates the high-performance ARM 32-bit RISC core operating at a 24 MHz frequency, high-speed embedded memories, and an extensive range of enhanced peripherals and I/Os connected to two APB buses. All devices offer standard communication interfaces, and include six general-purpose 16-bit timers and an advanced-control PWM timer.

STM32F100C8T6B is selected in this series. It has an excellent real-time performance, superior efficacy, highly Integrates and low-power characteristics, fully corresponds the needs of this device, but also provides a good platform for the subsequent development of technology. Fig. 2 shows the overall architecture of the system.

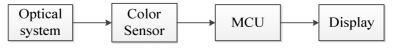


Fig. 2 The overall architecture of the system

Display module. The display module is mainly selected in two ways: LED display and LCD. Features of digital LED are bright and clear in the daytime. The disadvantage is only to display numbers and special characters. The LCD is not with the character limit, or not to display clearly in

bright light. Compared to the digital display, it has lower power consumption. Taking into account the detecting devices are mainly used indoors and light changes little, so this method of liquid crystal display is selected. As the amount of information is not displayed, universal LCD1602 exactly corresponds our requirements.

Optical structures

On the optical path of the structure, there are three main solutions.

Solution I: The 45/0 standard is selected in "Standard illuminants and illuminating-viewing conditions". Liquid sample is irradiated with 45° oblique, and the color sensor receives light in the normal direction [5]. Currently, this method is used in the vast majority of color detectors shown in Fig. 3.

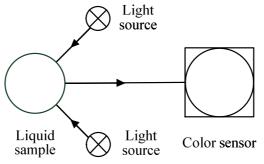


Fig. 3 Solution I schematic diagram

Solution II: The 0/0 standard is selected in "Standard illuminants and illuminating-viewing conditions". Light source, liquid sample and color sensor are placed in a straight line [5]. Principle of optical transmission is selected to detect the color of the liquid sample shown in Fig. 4.

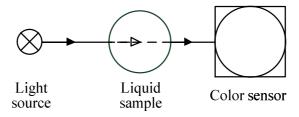


Fig. 4 Solution II schematic diagram

Solution III: The 45/0 standard is selected in "Standard illuminants and illuminating-viewing conditions". To obtain a more uniform white light in the normal direction, white balance board is irradiated with 45° oblique. Following 0/0 standard, this light beam irradiates liquid sample, the color sensor is placed to receive color information on the other side of the liquid sample. It is shown in Fig. 5.

Based on these solutions, even though solution I is the most widely used method, considering the influence of the reflection of the inner and surface of container and the liquid's nature of the colloid, it is easy to produce uneven brightness. It is shown in Fig. 6(a). Moreover, this method is applicable to solid color detection, not to apply to liquid. Solution II is a standard lighting method, due to a single source, it is easy to have an impact on the accuracy of the color sensor and shown in Fig. 6(b). In solution III, it combines the advantages of these two programs, and has an effort to avoid the negative impact. So it is an ideal solution to build the optical path and shown in Fig. 6(c).

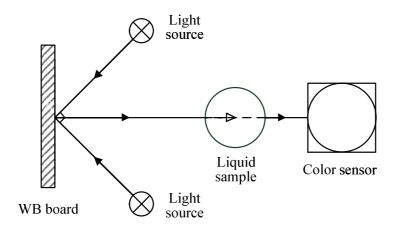


Fig. 5 Solution III schematic diagram

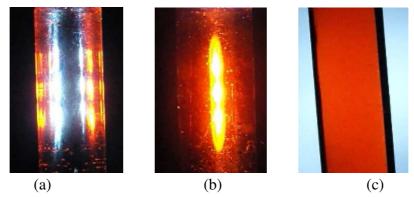


Fig. 6 Comparative effects of three types of lighting solutions

As the color sensor is extremely sensitive to light, the relevant optical inspection needs to be carried out in a matt darkroom, and to avoid light pollution caused by some non-optical components. Based on the two points above, all the components of the instrument are placed in a sealed box. And the light-absorbing material is uniformly coated on the surface of the non-optical element, in order to minimize the impact caused by light pollution in color detection.

Software design

Software design is divided into White balance calibration and color detection section. When white balance calibration, it automatically detects the light information reflected from the white balance board, calculates and stores the scale factor of white balance. When color detection, system can select R, G, B modules in the color sensor, reading and processing data. It combines scaling factor of white balance, calculates color information of the liquid sample, and passes data to LCD. System main flow chart is shown in Fig. 7.

Testing and application

This device provides high A/D converted accuracy since TCS3200 color sensor has more than 10-bit precision. The response frequency is between 2 Hz to 500 kHz, and STM32 processor has equally high precision. Theoretically, the error rate is 0.5% or less. Furthermore, the introduction of the balance calibration function makes sensor system improve its adaptability. Standard colorimetric cards were used to test the entire device [9]. After performing the white balance calibration, 8 different color colorimetric cards are placed in front of the white balance board. Measured results are shown in Table 2.

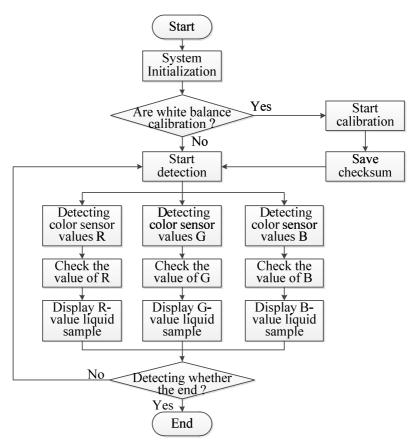


Fig. 7 System main flow chart

Standard values			Measured values		
R	G	В	R	G	В
255	255	255	242	248	245
255	0	0	251	1	3
230	40	30	225	42	33
180	130	170	178	131	167
180	20	90	183	24	96
130	150	200	136	148	211
40	160	210	38	154	201
20	230	100	26	238	109

Table 2 Standard values a	nd measured values
---------------------------	--------------------

The obtained data is processed by using Matlab software for three-dimensional graphics, shown in Fig. 8. Two curves are very close, in theory, human eyes can not distinguish these two colors. Slight deviation is caused by the color sensor itself, and also by a long storage time and stored properly on colorimetric cards. How to improve precision further more needs more in-depth study.

Liquid color detecting device has wide application in the future. For example, in the determination of grain's fatty acids, it needs to detect the color change of the solution. In chemical and biological detection, it can help us determine the color of acid-base indicator, bacterial content of the liquid and so on. This device has only cost 30% of the similar products, and market potential is huge.

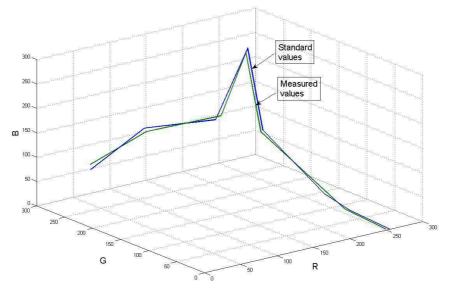


Fig. 8 The curve of stander values and measured values

Conclusions

This research designs a new liquid color detecting device, using the latest TCS3200 color sensor and STM32 microcontroller, combining with the improved optical system. The research results show the device has high accuracy, in theory, the error rate is less than 0.5%. It fully suffices the needs of the relevant liquid color detection, and only cost 30% of other similar products. So it has broad promotion and application prospects.

References

- [1] Weijia Sun. Research on Color Image Detection System[D]. Harbin University of Science and Technology, (2010).
- [2] Juan Liu. Color Measurement Methods[J]. Printing Quality & Standardization, (2008).
- [3] Zhiwei Duan, Bingkun Gao, Jinbo Song. Design of oil color detection system based on RGB color sensor[J]. Control and Instruments in Chemical Industry, (2013).
- [4] Xi Chen, Xuechen Zhao. Design and Implementation of the Color Detection System[J]. Process Automation Instrumentation, (2011).
- [5] A. Borbely, A. Samson, J. Schanda. The Concept of Correlated Color Temperature Revisited [J]. Color Research & Application, (2001).
- [6] GB3979-2008. Methods for the measurement of object color[S]. China National Standard, (2008).
- [7] GB3978-1994. Standard illuminants and illuminating-viewing conditions[S]. China National Standard, (1994).
- [8] TCS3200 Programmable color light-to-frequency converter[DB/OL]. [2010]. http://www.taosinc. com/Downloads.aspx.
- [9] Zhen Zhou, Weijia Sun, Yong Qin. Research on precise color Detector system based on TCS230[J/OL]. [2009]. http://www.paper.edu.cn.

Coal Mine Safety Monitoring System Based on ZigBee

Xin Liu^{1, a}, Hongquan Zhang^{1,b} and Zihong Zhang^{1,c}

¹College of Electrical and Information Engineering, Heilongjiang University of Science and Technology, Harbin, China

^aliu_xin1128@163.com, ^bdaqingzhq@163.com, ^czzhzlcgc@163.com

Keywords: ZigBee, KGS-20, methane concentration

Abstract. A methane monitoring system, consisting of methane sensor nodes and controllers with ZigBee networks between them, has been investigated for coal mine safety. The nodes were in comparatively flexible position. While not working, the nodes were put into hibernation so as to low consumption. While working, the sensor KGS-20 detected methane and sent voltage to CC2430 to carry on A/D conversion. After data processing by CC2430, the node would alarm and display and transmit data to its controller. The controller transmitted data to monitoring station by CAN bus. In experiment a sensor node was put in methane with eight different concentrations and the results were shown in LCD. The results show that all errors are all less than 0.05% and its average error is 0.023%. The errors are accordance with the rules for error range in coal mine.

Introduction

Coal plays an important role in industry production as a kind of energy and is vital to national economy and holds its safety. The accidents caused by exceeding mine gas standards lead to heavy casualties and great financial loss in mining production process [1]. Wired connections in coal mine safety monitoring system made it applied in main tunnels in China. In working face with high methane concentration the wired connections in safety monitoring system can not easily changed with tunnels and give rise to dead monitoring zone because of large equipment location changes during the mining. Besides, the wire connection monitoring system has disadvantages of cabling complexity, labour intensity, high application and maintenance cost [2]. It can contribute to the improvement in the field of gas monitoring to apply the wireless sensor network to mine gas monitoring system combined with cable one to build a coal mine safety monitoring system[3].

A coal mine safety monitoring system with low-power consumption is studied based on ZigBee technology combined with wireless sensor networks, which can meet the requirements of complicated surroundings in coal mine and monitoring tasks.

Design of Safety Monitoring System

The ZigBee is a very low-cost, very low-power consumption, two-way, wireless communications standard based on IEEE802.15.4[4]. The framework of mine gas monitoring system is shown in Fig.1. The system is composed of wireless methane sensor nodes and wireless controllers. The nodes which are laid on monitoring points monitor methane concentration and transmitter data to wireless controllers through ZigBee networks. Without wired connections between sensor nodes and wireless controllers, nodes can ease over. Wireless controllers transmitter data to monitoring station through CAN bus. Warning signal will be given when methane concentrations exceed 1%.

Hardware Design

The wireless methane sensor nodes are important part of the monitoring system, which are composed of gas detecting module, ZigBee wireless communication module, alarm and display module and power module, as shown in Fig.2. The modules perform different functions.

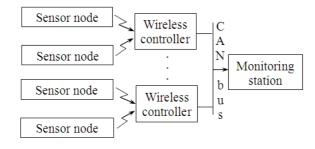


Fig.1 Framework of mine gas monitoring system

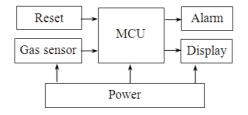


Fig.2 Wireless methane sensor node design

Gas Detecting Module Design. KGS-20 is a kind of Semiconductor device used to detect combustible gas. Its essential characteristic is extremely high sensitivity and low-power consumption. Its response and recovery time are less than 20s and 30s separately. Then its power consumption in static and alarm state is 150 [mW] and 300[mW] separately[5]. It has many advantages of small volume and simple circuit. The standard operating condition of KGS-20 is shown in table 1 and its drive circuit is shown in Fig.3. The load resistance R_L changes with sensitive resistance R_S and R_S can be known by voltage across load resistance R_L . When working, methane sensor can change physical quantity of gas concentration to voltage and transmit it to CC2430 P0.0 pin. CC2430 will carry on A/D conversion.

ruble i Standard operating conditions of ROS 20[0]							
Symbol	Parameter	Specification	Conditions				
V _H	Heater voltage	$0.9\pm0.05[V]$	DC				
R _L	Load resistance	$\geq 200[\Omega]$					
R _H	Heater resistance	2.8±0.2[Ω]	at room temperature				
I _H	Heater current	130[mA]	$I_{\rm H} = V_{\rm H} / R_{\rm H}$				
P _H	Heater power consumption	120[mW]	$P_{\rm H} = V_{\rm H}^2 / R_{\rm H}$				

Table 1 Standard operating conditions of KGS-20[6]

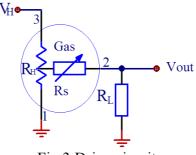


Fig.3 Drive circuit

Control and Communication Module Design. The CC2430 is a true System-on-Chip (SoC) solution specifically tailored for IEEE 802.15.4 and ZigBee applications. It enables ZigBee nodes to be built with very low total material costs. The CC2430 combines the excellent performance of the leading CC2420 RF transceiver with an industry-standard enhanced 8051 MCU, 32/64/128 KB

flash memory, 8 KB RAM and many other powerful features. The CC2430 is highly suited for systems where ultra low power consumption is required. This is ensured by various operating modes. Short transition times between operating modes further ensure low power consumption[7]. The peripheral circuit is simple. CC2430 received data from nodes and sent to controller by RF.

Power Module Design. Considering the movement of sensor nodes the power supply used two 5# 1.5V battery, which could be replaced periodically.

SOFTWARE DESIGN

Methane Sensor Node Design. Methane sensor node software design will perform these functions such as joining in ZigBee network, data collection, alarming and data transmission and software flow chart is shown in Fig.4. First, system initialization is carried on; Secondly, methane sensor nodes connect to ZigBee network and are put into hibernation. After awaken, the sensors conduct to collect methane concentration. Then the system will alarm when the concentration exceeds a particular number and exceeding signal will be transmitted to wireless controllers_o

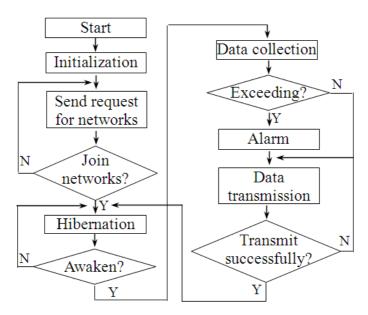


Fig.4 Software flow chart of node

Wireless Controller Design. The software flow chart of wireless controllers is shown in Fig.5. A wireless controller can mainly complete two functions. It can receive commands from monitoring station and transmit them to sensors. Also, it can receive methane concentration data and exceeding signal and transmit them to monitoring station.

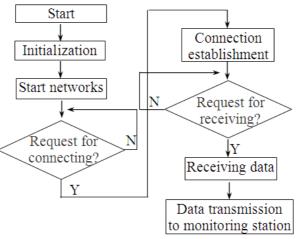


Fig.5 Software flow chart of wireless controllers

Results and Discussion

The methane alarm concentration in coal mine is 1%. The experiment was carried out for gas sensor node in methane surrounding with different concentrations. The test time is 3 minutes and the results are shown in Table 2. The errors are all less than 0.05% and its average error is 0.023%, which is in accordance with the rules for error range in coal mine.

Sample concentration[%]	0.0	0.4	0.8	1.0	1.2	1.5	1.8	2.0
Test time[min]	3	3	3	3	3	3	3	3
Experimental data[%]	0.00	0.38	0.81	1.03	1.22	1.54	1.83	2.04
Error[%]	0.00	0.02	0.01	0.03	0.02	0.04	0.03	0.04

Conclusions

A methane detecting system based on ZigBee, containing the sensor nodes and controllers, was investigated for its suitability to detect methane in coal mine. The shift ability of sensor nodes as well as low-power consumption is attractive facts for mass application. The system used KGS-20 and CC2430 to sense methane and transmit data separately. CC2430 served as connection between sensor nodes and controllers. The results of detecting methane demonstrate good performance.

Acknowledgements

This work is supported by China national coal association and I would like to express my heartfelt gratitude to my colleagues.

References

- [1] CHEN Yan-xiu: Journal of Guizhou Normal University (Natural Sciences) Vol.30 No. 2(2012), p110-120(In Chinese)
- [2] XU Zhen—feng, YIN Jing-jing: SCIENCE & TECHNOLOGY INFORMATION Vol.29(2012), p 31-32
- [3] Kiumi Akingbehin, Akinsola Akingbehin: Alternatives for Short Range Low Power wireless communications, IEEE Computer Society ,Washington Vol. 94(2005), p 94-95
- [4] Srinivasa A. H, G. Varaprasad: Design and development of a sensor model for coal mines. ACM SIGBED Review - Special Issue on the Work -in -Progress(WIP) Session at the 2009 IEEE Real-Time Systems Symposium[C], Vol. 7(2010), p6-11
- [5] SONG Zhi-yue: Software Vol. 32(2011), p46-48(In Chinese)
- [6] Information on http:// wenku.baidu.com/link?url =En8NoKKiQLs6Y _H0xPGQDabvRWHJKJ wtrvnL- YWo XYkq3FSc-9odpFZQa5Pny0nBWEqiKWlPaZqynkuR_8vkikw9hDLdQCbPy JMHfkVUxkG
- [7] Ding E J, Wang M Y, Wen J C et al: 2009WRI World Congress on Computer Science and Information Engineering. Los Angeles: CSIE, 2009: 452 ~ 455.

The Design of Wireless Video Monitoring System Based on FPGA

Yajie Yue^{1, a}, Xiaojing Zhang^{1,b} and Chenming Sha^{1,c} ¹School of Software,Harbin University of Science and Technology,Harbin,China ^ajielu1981@aliyun.com, ^bxzj81@163.com, ^cshachm@163.com

Keywords: Wireless Video, FPGA, Monitor System, VGA .

Abstract. The wireless video monitoring system contains the video acquisition device,video transmission device,video storage device and VGA display device. In this paper,we use video acquisition device to collect video signals in real-time. The analog video signal is transmitted by using wireless technology. The video signal is converted to a digital signal by using the dedicated A/D chip. At the same time, the YCrCb signals will be converted into RGB signals by the format converting module. Then, the digital RGB signals are converted to analog RGB signals through the D/A, and they are finally displayed on the VGA monitor in real-time. The design mainly uses the wireless transmission technology to transmit analog video signals and uses ADV7181 to decode. The controlling system of FPGA deals with the decoded digital signals which will be transmitted to the D/A and the data finally will display in real time.

Introduction

With the development of science and technology,our security consciousness enhance unceasingly and the demand for video monitor equipment continues to grow. Accompanied by the development of wireless technology, we have entered an wireless era and wireless technology will be more convenient for us. The conventional video monitoring system are wired and bulky. When installing it, we need to rewire. The ease of monitoring system will be reduced. For households, because wireless video monitoring system is easy to install and move, it increases the residents' autonomy of adjustable initiative. In order to develop a high-speed, convenient and secure wireless video monitoring system , the paper uses FPGA to design the wireless video monitoring system. FPGA has the high integration level, high processing capability of video signal, flexible structure, easy modular design, high efficiency of the algorithm , short development cycle , low cost, easy to maintain and upgrade and so on[1]. That is why FPGA is used to design the wireless video monitoring system.

We use the 2.4G wireless transmission to transmit video data. The way it works is a full-duplex transmission mode. It has an more absolute advantage than 27MHz wireless technology in the anti-interference performance. The advantage decides its strong anti-interference and maximum transmission distance of up to 10 meters. The 2.4G wireless technology also has theoretical data transmission rate of 2M and Bluetooth has theoretical data transmission rate of 1M .Compared to Bluetooth, the transmission rate is doubled. So it increases the reliable protection for the application layer. Among the three kinds of common wireless transmission technology, 2.4G wireless transmission rate, strongest anti-interference, largest transmission distance and lowest power consumption[2].

The General Design of the Wireless Video Monitoring System

The whole wireless video monitoring system uses CCD analog camera to collect video signals which are transmitted by wireless transmitter. And wireless receiver receives the analog video signals. After using ADV7181 to decode, the received analog signals are passed to the FPGA controlling module. Using the I2C module of FPGA, ADV7181 chip is configured. The video analog signals are decoded into a digital signals. Then using the decoding module and the color space conversion module of FPGA, the video data are converted into digital RGB signals. By VGA controlling module, ADV7123 encodes digital video signals. The horizontal synchronizing signal, vertical sync

signal and RGB color signals are displayed in VGA display terminal. Thus the wireless monitoring function is attained. The system block diagram is shown in Fig. 1.

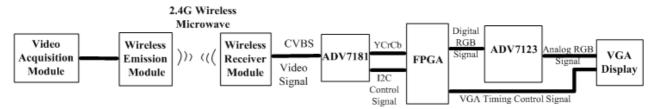


Fig. 1 The system block diagram of the wireless monitoring system

The Video Coding Principle and Wireless Transmission System

As one part of the video monitoring system, the camera module is the "eyes" of the whole system. We use the CCD sensor as the image acquisition sensor. CCD is a semiconductor device and it can convert the optical image into a digital signal. On the CCD there are many small photosensitive matter called pixels[3]. The more pixels CCD contains , the higher screen resolution is. The role of CCD is like the film, but it converts image pixels into digital signals. On the CCD there are many neatly arranged capacitors which can sense light and convert image into digital signals. By an external control circuit, each small capacitor can transfer its charge to adjacent capacitor. The original video signals obtained by the camera is an analog RGB signal. After the gamma correction, the nonlinear signals are compensated. Then R'G'B'signal is obtained. By the matrix transformation, the video luminance signal Y with the higher bandwidth is obtained, Y = 0.299R' + 0.587 G' + 0.114 B'.Atthe same time, two chrominance signals with low bandwidth are obtained. They are R'-Y ' and B'-Y'.Two chrominance signals with low bandwidth respectively pass the low-pass filter, the two new signals are added after quadrature modulation with the color subcarrier. Finally, the added signal is new chrominance signal. Then the analog video signals turn into a luminance signal and a chrominance signal.Adding up the luminance signal, chrominance signal, composite synchronizing signal and the color synchronizing signal, we obtain the composite video signal (CVBS signal).

The Controlling System of FPGA

FPGA has two main functions.One is to make appropriate treatment for input data.Thus it can cooperate the work of peripheral chips and devices.Another is to appropriately configure for peripheral chips.The block diagram of control system is shown in Fig.2.FPGA control module mainly consists of two sub-modules, namely I2C_AV_Config and TV_TO_VGA. I2C_AV_Config module is used to configure the ADV7181 of TV decoder. TV_TO_VGA module includes itu_r656_decoder, dual-port line buffer, HSYNC × 2, YCbCr2RGB and VGA_Timing_Generator and so on. After the configuration data is downloaded to the FPGA, FPGA configures register parameters

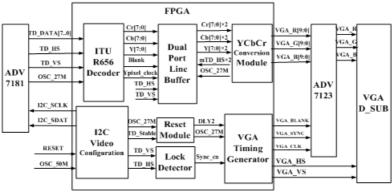


Fig.2 The block diagram of FPGA control system

of television decoder by I2C_AVConfig module. Via I2C communication protocol I2C_AVConfig communicates with the television decoders.

I2C configuring Module. The AIN6 of the chip is chosen as composite video signal input of CVBS, and it controls the behavior of ADV7181 through the reading / writing registers of I2C bus. ADV7181 can output YCrCb 4:2: 2 video data of 16-bit or 8-bit which can compatible with CCIR656 standard. The data contain VS signal, HS signal, Blanking signal and so on. Because of the powerful function of the device, its internal 240 registers must be configured reasonably. So we design the I2C_Controller module and I2C_AV_config module to meet project needs. Each register configuration of I2C_AV_config requires following steps: The mSetup_ST signal shows which step is done at current. When mI2C_GO = 1, it indicates starting I2C transmission. When mI2C_END = 1, it indicates ending I2C transmission. When mI2C_ACK = 0, it means that the response signal is active. Once the reset signal is valid, it indicates that the configuration registers into the first step. At the moment, the 8-bit slave unit address and 8-bit register address connect to 8-bit data and 24-bit transmission data are formed. Then I2C transmission is started and the second step begins. Thereafter if the end of transmission(mI2C_END = 1) is detected, the response signal mI2C_ACK is judged. If the response signal is valid, the next step begins. Otherwise it returns to mSetup_ST = 0 and retransmits data .

ITU_R656_DECODER Module.As a result of the PAL camera, the effective resolution of its video screen is 720 * 576 .By judging SAV signal, the vedio decoding file judges the following data whether or not is valid.If it is, the synchronizing signal oDVAL and valid data Y, Cb, Cr are further separated. At the output port, the data of 640 * 480 are displayed. So the input PAL video signals are accordingly cropped. Using a divider the video is cropped. It mainly crops each line video data from 720 pixels to 640 pixels. When designing, first the serial to parallel module should be constructed, so that the effective signal is separated from the serial signal. And each group of signals are processed separately .Utilizing QuartusII Megafunction Wizard tool, a LPM_DIVIDE core is created to crop redundant pixels.

Sdram_Control_4Port Module.Sdram_Control_4Port module completes the function of the dual-port line buffer. The buffer comes from the YCrCb signal of ITU_R656_DECODER module.Using the model of one writing port and two readout ports 1 in and 2 out ,the video data is cached in the Sdram_Control_4Port module of SDRAM.It processes interlaced data which ITU_R656_DECODER output .It completes the conversion from the interlaced data to line data. The cut video resolution is 640 * 576. While writing data into SDRAM,640*576 pixels all are written. Because the odd data is ahead and the even data is behind,data of the first 640 * 288 rows are the odd field data and data of the last 640 * 288 rows are even field data. When reading the video data, using ping-pong operation to read the odd and even field data and consist of a complete picture.

VGA Controlling Module. Timing control module of VGA is the key part of the display controller. At a certain frequency, it produces an accurate timing relationship and reads memory data of ROM. The design uses a $800 \times 600 \times 75$ Hz mode. Based timing standards, each row contains 1056 points including 800 points for the effective display area and 256 points for the blanking area. The low-level width of horizontal sync pulse is 80 pixels.Similarly there are 625 lines per field including 600 effective lines and the low-level width vertical sync pulse is 3 lines.VGA timing contains horizontal timing and vertical timing.Included timing parameters of the two timing is the horizontal /vertical sync pulse, the width from the end of horizontal /vertical sync pulse to the start of the effective display area of image data, the width of effective image display area, the width from the end of the effective display area of image data to the start of horizontal /vertical sync pulse.

Simulation Results of Wireless Monitoring System

I2C_Controller uses 33 clock cycles of I2C to process each 24-bit data. The first clock cycle is used to initialize the controller, the second to third cycles are used to start transmission, from 4 to 30 cycles data are transmitted and the last three cycles is used to stop transmission. Among the program, SD_counter are counted for transmission, and controlled data transmission. Fig.3 is the simulation waveform of I2C controller.Fig.4 is the simulation waveform of VGA controller.

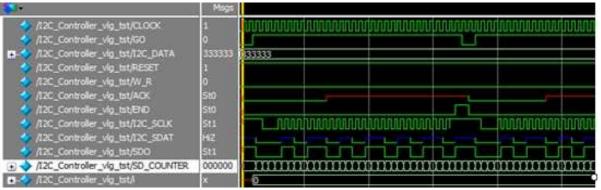


Fig.3 Simulation waveform of I2C controller.

In Fig.3,when GO=1,SD_COUNTER signal begins counting.When SD_COUNTER=1,I2C controller starts working.When 2<SD_COUNTER<11, the host address is assigned to the SDO. When 11<SD_COUNTER<20, the slave address is assigned to the SDO.When 20<SD_COUNTER <29, the data is assigned to SDO and when SD_COUNTER = 30,it stops sending data.

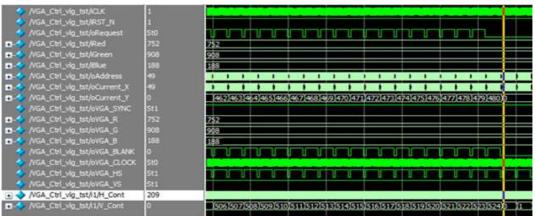


Fig.4 Simulation waveform of VGA controller.

The oVGA_R,oVGA_G and oVGA_B are extended to 10 bits based on iRED, iGREEN, iBLUE.From Fig.5,the timing of the filed blanking, line blanking, filed sync signal and the line sync signalcan been clearly seen.

Conclusions

The wireless monitoring system based on FPGA uses the camera to collect analog video signals and uses wireless transmission technology to transmit them to VGA display terminal in real time. Thus the effect of wireless monitoring is achieved. As the controlling core, FPGA controls the A/D module, D/A module and VGA and processes transmitted signals. The design provides a new method for wireless monitoring system and successfully achieves the appropriate results.

Acknowledgements

Heilongjiang province, students' innovation and entrepreneurship training program: Design of Wireless Monitoring System and FPGA Implementation

References

- [1] Wang Jianping: Wireless Network Technology (Tsinghua University Publications, China 2013).
- [2] Lun Cuifen, Ma Jiwei and Fan Hua:Computer Design and Applications .Vol. 4(2010), p. 496
- [3] Du Bo,Zhang Xin and Cai ChangQing:Computer Application and System Modeling. Vol. 6(2010), p. 408

Hydrogel coated long period grating sensor for high relative humidity measurement

Xiujuan Yu^a, Jintao Zhang^b, Xuefeng Chen^c and Shengchun Liu^d Optical Fiber Research Institute, Heilongjiang University, Harbin, 150080, China ^ayuxiujuan@tsinghua.org.cn, ^bzhang890070@163.com, ^cicebergice@sohu.com, ^dshengchunliu@163.com

Keywords: long period grating, hydrogel, humidity sensor, high relative humidity.

Abstract. A very sensitive hydrogel coated long period grating (LPG) humidity sensor is developed and experimentally investigated for high relative humidity monitoring. A thin-film of PINPAM hydrogel is deposited onto the cladding of LPG by using dip-coating technique. The transmission spectrum of the coated LPG is studied at different humidity levels. For humidity levels greater than 95%, the resonant dip depth suffers a sharp linear increase with a span of 10.26 dB and the resonant wavelength suffers a redshift of 8.6nm. The proposed hydrogel coated LPG humidity sensor shows a high sensitivity of 2.86dB/%RH at high relative humidity region.

1. Introduction

Humidity measurement is very important in many applications, such as, industry process control, medical facilities, goods preservation, weather forecasting, air conditioning in construction, and agricultural measurements. So the relative humidity(RH) sensors are of great significance and have extensive development prospect, especially the devices for measuring high RH in the range of 90~100%RH. Optical fiber based humidity sensors have many advantages, such as electromagnetic immunity, high integration, multi-sensor integration, and remote and stable sensing, so they have attracted numerous attentions and been studied extensively. The main technique used by current optical fiber base humidity sensors are as follows: evanescent wave [1-3], plastic optical fibers [4], fiber Bragg grating [5], long period grating (LPG) [6-7], photonic crystal fiber [8]. In this paper, we present a hydrogel coated LPG humidity sensor for monitoring high relative humidity. The dip-coating method is used to coat a sensitive hydrogel thin-film onto the cladding of LPG. The spectral characteristics of the coated LPG, including the resonant wavelength and the minimum transmission, are studied at different relative humidity levels.

2. Theory

For a general LPG, the phase matching condition between the core mode and the ν th forward-propagating cladding mode is achieved at resonant wavelengths is given by Equ.(1),which is dependent on the product of the difference between the effective indices of the core and cladding modes with the period of the modulation.

$$\lambda_{\nu} = \left[n_{eff,co}(\lambda_{\nu}) - n_{eff,cl}^{\nu}(\lambda_{\nu}) \right] \Lambda \tag{1}$$

where Λ is the grating period, $n_{eff,co}(\lambda_{\nu})$ is the effective refractive index of the propagating core mode and $n_{eff,cl}(\lambda_{\nu})$ is the effective index of the ν th cladding mode at wavelength λ_{ν} . The effective refractive indices of the cladding modes are strongly dependent on the refractive index of the surrounding environment, and as such the resonant wavelength is sensitive to changes to it.

The depth of the attenuation band centred at a resonant wavelength is mainly influenced by two factors: the grating length and the cross-coupling coefficient between the core mode and the cladding mode that couples at the resonance wavelength, it can be expressed approximately as followed:

$$T_{\nu} = 1 - \sin^2 \left(\kappa_{cl}^{\nu} L \right) \tag{2}$$

where *L* is the length of the LPG and κ_{cl}^{ν} is the cross coupling coefficient from the core mode to the vth cladding mode which is dependent on the overlap integral of the core and cladding mode and the photo-induced refractive index modulation.

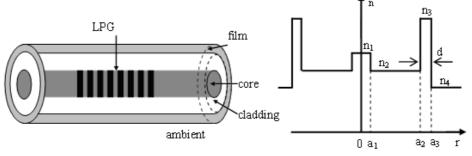


Fig 1. Schematic diagram of the four-layer waveguide structure

For a film-coated LPG, it can be regarded as a four-layer step-index waveguide structure which is shown in Fig.1. The mode eigen-value equation can be determined by applying the four-layer model boundary conditions to Maxwell's equations. The theoretical calculation about the LPG thin-film sensors in Ref.[9] shows that the the parameters (thickness and refractive index) of the film will directly related to the refractive index of cladding mode, which will causes the spectral characteristics. When the coated LPG sensor experiences differnt humidty levels, the thickness and the refractive index of the hydrogel film will change, leading to the shift of the resonant wavelength and the change of the transmission minimum. By monitoring these changes, the humidity levels will be obtained.

3. Experimental results and discussions

In our experiment, the LPG was fabricated by use of a high-frequency pulsed CO₂ laser exposure on a single mode fiber with a period of 400µm and a period number of 50. Humidity-sensitive poly (N-isopropylacrylamide)(PNIPAM) hydrogel was prepared by UV-initialed photopolymerization and deposited on the LPG using the dip-coating thehnique. Fig.2 shows the transmission spectra of the LPG before and after coating, respectively. The solid and dashed lines represent the transmission spectra of the uncoated and coated LPG, respectively. For the bare LPG, the resonant wavelength and dip depth are 1553.90nm and -26.22dB respectively. It is obvious that the resonant wavelength experiences a blue-shift of 5.6nm and the depth of resonant dip decrease 19.9dB for the LPG after coating. This is due to the addition of hydrogel coating which results in the increase of the effective index of cladding mode.

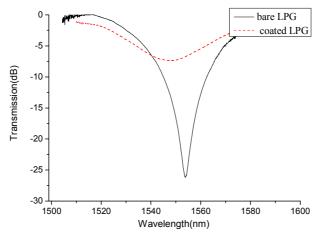
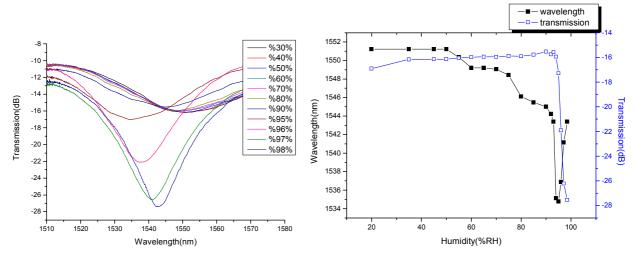


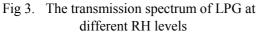
Fig 2. The transmission spectrum of a LPG before and after coating

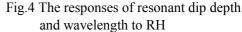
To carry out the humidity tests, the hydrogel coated LPG was placed into a in a programmable temperature & humidity chamber (TYH-1P Gaoyu technical Co., Ltd.) where both temperature and humidity can be controlled exactly. For the chamber, the temperature and humidity resolutions are 0.01°C and 0.1%RH, respectively. For humidity test, one end of the LPG was connected to a broad-band light source while the other end was connected to an optical spectrum analyzer (OSA) AGILENT 86140B with a wavelength resolution of 0.06 nm and a level resolution of 0.01dB.

To investigate the performance and response of the hydrogel coated LPG RH sensor, we increased the humidity from 20%RH to 98%RH which in the measurement range of the chamber. For each measurement, the humidity was left to stabilize for 30 minutes before recording. The temperature of the chamber was held constant at 25°C during the test with a fluctuation of ± 0.1 °C.

The transmission spectrum of the coated LPG at different RH levels is shown in Fig.3, the resonant wavelength and dip depth is very sensitive to the change of humidity for RH values above 90%. Fig.4 gives the values of the resonant dip depth and wavelength at different humidity level. For humidity levels less than 50%RH, the wavelength is barely affected by the humidity and generally kept stable. This behavior may be due to the intrinsic material properties of the coated film since there is little or no water absorbed by the material when the humidity is below 50%RH. For humidity levels range from 50%~95%RH, the resonant wavelength suffers step decrease and shifts to shorter wavelengths. Especially for RH levels range from 90%~95%, the resonant wavelength suffers a sharp decrease of 10.2nm. For humidity levels above 95%RH, the resonant wavelength shifts back to longer wavelength direction and the LPG experiences a redshift of 8.6 nm up to 98%RH. The linear fit is shown in Fig.5. The sensitivity is 2.57nm/%RH and the correlation coefficient the linear fit is 0.957.







During the process of humidity levels increase, the resonant dip depth also changes. For RH values less than 95%RH, the resonant dip depth decreases slightly. For the humidity levels ranging from 95%RH to 98%RH, the hydrogel coated LPG undergoes a significant linear increase in the resonant dip depth with a span of 10.26dB, exhibiting a sensitivity of 2.86dB/%RH. The correlation coefficient of the linear fitting curve is -0.96. The linear fitting line is shown in Fig.6. The hydrogel coated LPG show high sensitivity in high humidity region. Therefore, it has potential to apply in high humidity level.

Considering the 0.06nm wavelength resolution of the OSA in the experiment, a 0.02%RH resolution could be obtained in the range from 95%RH to 98%RH for the resonant wavelength monitoring. Considering the 0.01dB resolution of the OSA, a 0.004%RH resolution is feasible. As it is known that LPG is highly sensitive to small changes in the index of refraction, as small as $\Delta n \sim 6 \times 10^{-5}$, the resolution of the coated LPG RH sensor is limited instead by the calibration systems such as the OSA used in the experiments.

It is noteworthy that the resonant wavelength responses to humidity obviously turn out different behaviors with a turning point around 95% for different RH ranges. This is related to the hydrogel film properties. As the hydrogel structure absorbs the water, it attempts to swell in volume, which causes an increase in thickness of the hydrogel film. The increase on the film's thickness will cause a decrease of resonant wavelength. So the blueshift of wavelength for humidiry ranges from 50%RH to 95%RH is due to the hydrogel structure swelling. It is should remember that the average refractive index of the water-hydrogel composite will decrease as more water is absorbed by the hydrogel. This leads an increase of resonant wavelength. So the redshift of wavelength for humidity level greater than 95% is due to the reduction of the refractive index becoming the dominant effect.

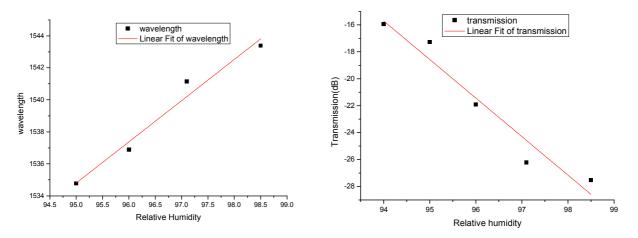


Fig 5. The responses of resonant wavelength to RH

Fig.6 The responses of resonant dip depth to RH

4. Conclusions

In summary, a very sensitive hydrogel coated LPG humidity sensor was developed and experimentally investigated for high humidity sensing. For humidity level above 95%, sensitivities of 2.57nm /%RH and 2.86dB/%RH can be achieved as the resonant wavelength and dip depth are used as sensing parameter, respectively. The sensing mechanisms are analyzed. For humidity level less than 95%RH, the hydrogel structure swelling is the dominant effect to induce a blueshift of the resonant wavelength. For humidity level greater than 95%RH, the reduction of the refractive index of the hydrogel becomes the dominant effect to cause a redshift of the resonant wavelength.

Acknowledgements

This work was supported by the Youth Foundation of Heilongjiang University through Grant No. QL201205.

References

- [1] L. Xu, J. C. Fanguy, K. Soni, and S. Tao: Opt. Lett.29, 1191–1193 (2004).
- [2] J. M. Corres, F. J. Arregui, and I. R. Matias: IEEE J. Lightwave Technol. 24, 4329–4336 (2006).
- [3] I. R. Matias, F. J. Arregui, J. M. Corres, and J. Bravo: IEEE Sens. J. 7, 89–95 (2007).
- [4] S. Muto, O. Suzuki, T. Amano, and M. Morisawa :Meas.Sci. Technol. 14, 746–750 (2003).
- [5] P. Kronenbery, P. K. Rastogi, P. Giaccari, and H. G. Limberger: Opt. Lett. 27, 1385–1387 (2002).
- [6] N. D. Rees, S. W. James, R. P. Tatam, and G. J. Ashwell: Opt. Lett. 27, 686–688 (2002).
- [7] L. Wang, M. Zhang, D. Tu, X. Mao, and Y. Liao: Meas. Sci. Technol. 18, 3131–3134 (2007).
- [8] S.J. Zheng, Y, N Zhu, S. Krishnaswamy: Sensors and Actuators B: Chemical, 176, pp.264-274 (2013).
- [9] X. J. Yu, M. Zhang, L.W. Wang, M. Lei, Y.B. Liao: Acta Optica Sinica, 29(10), 2665~2672(2009).

A New Sensor for the Electrical Equipment Leakage Current

Wei Xinlao^{1,a}, Zheng Wenlei^{1,b}

¹ College of Electrical and Electronic Engineering, Harbin University of Science and Technology, Harbin, Heilongjiang Province, China

^aweixinlao@163.com, ^bbarceniho@126.com

Keywords: faint current measurement, non-contact detection, Rogowski coil, microcrystalline alloy, single-turn cored clamp-type.

Abstract: To achieve the accurate and non-contact detection of the electrical equipment leakage current at the millampere level, this paper presents a new single-turn cored clamp-type sensor named the Microcrystalline-alloy Rogowski coil. The creative construction technique of the new sensor remedies the disadvantage of the Rogowski coil with the structure of microcrystalline alloy core. The experimental test of the prototype was carried out to show the superior performance and the excellent practical value in the application of the faint current measurement.

Introduction

The accurate measurement of the leakage current, which is a major method of the electrical equipment insulation detection, plays an important role in ensuring the safe and stable operation of power grid. The leakage current of the normally running equipment is commonly at the ma level and measured by the detection instrument emplaced at the cut of the ground wire. However, these traditional measurement methods are not suitable unless the grid allows the detection instrument to disconnect the ground wire. Moreover, the single-turn cored clamp current transformer is able to achieve the measurement without disconnecting the ground wire in practical application, but it is difficult to meet the requirements of the accuracy ^[1].

In order to resolve the contradiction among the above factors and achieve the accurate measurement of the leakage current at the ma level, a new current sensor which is based on the Rogowski coil and the microcrystalline alloy core structure is designed in this paper.

The basic principle of the Rogowski coil is that the electromotive force induced by the magnetic field, which is generated by the detected current, is proportional to the differential signal of the detected current flowing through the central conductor. Since invented at the beginning of the twentieth century, a lot of studies have been generally carried out in the application of current detection. With the advantages, such as, the large measurement range, the wide frequency band, the perfect linear characteristic, the simple structure and the low cost, the Rogowski coil has a superior performance in the accurate measurement of the large current ^[2-5].

However, the output voltage of the Rogowski coil is too faint to achieve the accurate and stable measurement when the detected current is the leakage current at the ma level. As the key of the new sensor, the structure of the microcrystalline alloy core is combined with the Rogowski coil in this paper. Both the magnetic field and the induction electromotive force are greatly enhanced because the permeability of the microcrystalline alloy is extremely higher than the air ^[6]. The new current sensor, which is named the Microcrystalline-alloy Rogowski coil by the author, is able to measure the faint leakage current of the electrical equipment accurately.

The basic principle of the Microcrystalline-alloy Rogowski coil

As shown in Figure 1, the parameters of the Microcrystalline-alloy Rogowski coil are given, such as the inner radius, the outer radius, the section height and the permeability of magnetic material. Among them, μ_0 is the permeability of vacuum, and μ_r is the relative permeability of the microcrystalline alloy.

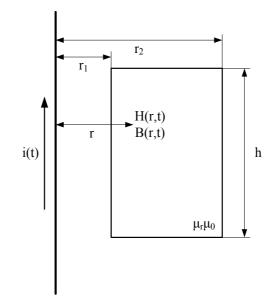


Fig.1 The Microcrystalline-alloy Rogowski coil of rectangular section

According to the Ampere's law, the magnetic field is generated when the current flowing through the central conductor, and the relationship between them is

$$i(t) = \oint_{l} H(t) \cdot dl = 2\pi r \cdot H(t)$$
⁽¹⁾

Both the magnetic field intensity and the magnetic induction intensity at a distance of r away from the central conductor are

$$H(r,t) = \frac{i(t)}{2\pi r},\tag{2}$$

$$B(r,t) = \mu \cdot H(r,t) = \frac{\mu_r \mu_0}{2\pi r} i(t)$$
(3)

The magnetic flux passing through the section of the coil is

$$\phi(t) = \int_{S} B(t) \cdot dS = \int_{r_1}^{r_2} B(r, t) \cdot h dr = \frac{\mu_r \mu_0 h}{2\pi} \ln \frac{r_2}{r_1} \cdot i(t)$$
(4)

Therefore, when the number of turns is n, the induction electromotive force of the coil is

$$e(t) = -n\frac{d\phi(t)}{dt} = -\frac{n\mu_{r}\mu_{0}h}{2\pi}\ln\frac{r_{2}}{r_{1}} \cdot \frac{di(t)}{dt},$$
(5)

and the output voltage of the coil is

$$u(t) = -e(t) = \frac{n\mu_r \mu_0 h}{2\pi} \ln \frac{r_2}{r_1} \cdot \frac{di(t)}{dt}$$
(6)

According to the equation, the output voltage of the Microcrystalline-alloy Rogowski coil is proportional to the differential signal of the detected current flowing through the central conductor, and the detected current signal is obtained by the integral computation and amplitude adjustment of the output voltage signal.

The design of the Microcrystalline-alloy Rogowski coil

As shown in Figure 2, the new sensor designed in this paper consists of two parts: the Rogowski coil and the microcrystalline alloy core.

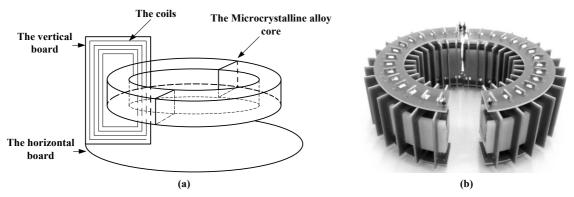


Fig.2 The prototype of the Microcrystalline-alloy Rogowski coil

The Rogowski coil is made up with two kinds of printed circuit boards, the vertical boards and the horizontal boards. Twenty turns of coils are printed on a vertical board, and thirty vertical boards are all fixed and connected on the horizontal board.

The microcrystalline alloy core is designed by the author and customized by a domestic manufacturer. In order to achieve the non-contact detection and the single-turn cored clamp type, the core is processed by the curing technology and cut in half at the central axis. The factory parameters are given in the Table 1.

rable.1 The factory parameters of the interfet ystamle alloy core						
Parameter	The inner radius	The outer radius	The section height	The relative		
	/mm	/mm	/mm	permeability		
Value	50	65	20	2000		

Table.1 The factory parameters of the microcrystalline alloy core

The prototype test of the Microcrystalline-alloy Rogowski coil

In order to test the performance of the Microcrystalline-alloy Rogowski coil prototype, as shown in Figure 3, the test circuit consists of the regulator T_1 , the transformer T_2 , the precision sampling resistor R_0 and the coil prototype.

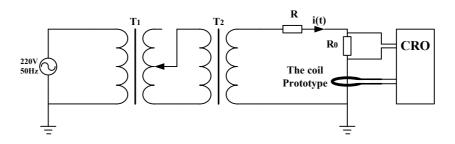


Fig.3 The test circuit of the Microcrystalline-alloy Rogowski coil prototype

The sample signal of the precision resistor and the output signal of the coil prototype are monitored by the oscilloscope at the same time. The detected current in the test circuit is changed every 0.5ma in the range of 0 to 10 ma with the appropriate adjustment of the regulator, meanwhile the amplitude and waveform of two signals are recorded and displayed by the oscilloscope. With the analysis and process of the Origin, the relationship between the detected current and the output voltage is obtained.

The Figure 4 shows that the output voltage signal of the Microcrystalline-alloy Rogowski coil prototype has the perfect performance of the linear characteristic and the phase position, and proves that the new sensor designed in this paper is able to achieve the non-contact detection of electrical equipment leakage current at the ma level accurately.

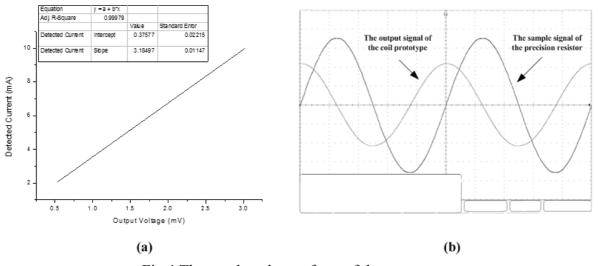


Fig.4 The graph and waveform of the prototype test

Summary

A new single-turn cored clamp-type sensor is presented to achieve the accurate measurement of the millampere leakage current in this paper. The prototype test proves, with the structure of microcrystalline alloy core, the Microcrystalline-alloy Rogowski coil is able to have a superior performance in the application of the faint current measurement where the normal Rogowski coil has never been. The creative construction technique of the new sensor has excellent engineering significance and practical value for the accurate and non-contact detection of the electrical equipment leakage current.

Acknowledgements

The project was supported by National Natural Science Foundation of China (51277046) and Specialized Research Fund for the Doctoral Program of Higher Education (20122303110007).

References

[1] Li Peiyan, Zhao Xuezeng, Dai Lizhou. Study on passive zero flux current transformer with single-turn cored structure, Transducer and Microsystem Technologies (2006).

[2] Karel Draxler, Renata Styblikova, Jan Hlavacek. Calibration of Rogowski Coils With an Integrator at High Currents, IEEE Transactions on Instrumentation and Measurement (2011).

[3] Ibrahim A. Metwally. Coaxial-Cable Wound Rogowski Coils for Measuring Large-Magnitude Short-Duration Current Pulses, IEEE Transactions on Instrumentation and Measurement (2013).

[4] Chen Qing, Li Hongbin, Zhang Mingming. Design and Characteristics of Two Rogowski Coils Based on Printed Circuit Board, IEEE Transactions on Instrumentation and Measurement (2006).

[5] Ehsan Abdi-Jalebi, Richard McMahon. High-Performance Low-Cost Rogowski Transducers and Accompanying Circuitry, IEEE Transactions on Instrumentation and Measurement (2003).

[6] Wang Hongxia, Liu Zongbin, You Pei, etc. Application of Nanocrystalline Alloy in Cores of Measuring Current Transformer, Transformer (1999).

Evanescent Field Absorption Sensor Based on Special U Shaped Optical Fiber

Chunlan Liu^a, Enming Zhao^{b,*}, Entao Li^c, Ai Zhou^d and Xinghua Yang^e

Key Laboratory of In-Fiber Integrated Optics, Ministry of Education, College of Science, Harbin Engineering University, Harbin 150001, China

^alclliuchunlan@163.com, ^bZhaoenming@hrbeu.edu.cn, ^clientao@hrbeu.edu.cn, ^dzhouai@hrbeu.edu.cn, ^eyangxh@hrbeu.edu.cn

Keywords: Evanescent field, Absorption sensor, U shaped, Special Optical Fiber

Abstract: In this article, an evanescent field absorption sensor based on special U shaped optical fiber is proposed. This optical fiber has a hollow structure and an inner core in the cave. The methylene blue is absorbed into the optical fiber and the absorbance is tested. Results show that the value of the absorption will reflect the concentration of the concentration of methylene blue in optical fiber.

Introduction

Design of new sensors has a great significance for science and technology innovation and technological progress in the field of sensing and development of novel structure. Excellent functionality sensor has been the pursuing goal of researchers and entrepreneurs. Currently, general optical fiber structure changes have occurred, people introduced a variety of microstructures in optical fibers by their extraordinary imagination. Microstructured optical fiber (MOF) is a kind of novel waveguide. Compared with the normal optical fibers, MOF has unique optical properties because of the introduction of the microstructures, such as wide single-mode transmission, highly nonlinear, large mode area, controllable dispersion, etc. Microstructured optical fiber sensors have been widely used in the measurement of pressure, temperature, fluid concentration various physical quantities due to the advantages of low cost, small size, flexibility, high temperature resistance, corrosion resistance, etc. In these techniques, researchers have produced a variety of optical fiber sensor structure, such as D-shape^[1], U-shape^[2] and polished^[3] optical fibers.

In the past few years, evanescent field absorption sensor have received considerable attention due to their widespread applications in continuous monitoring of concentrations of reactants in chemical processes and in the study of the absorption spectra of liquids and pastes.^[4-17]

In this article, we described a detailed experimental study of the optical fiber evanescent wave absorption sensor based on the U-shaped sensing region.^[18-20] The U shaped optical fiber is made by bending the optical fiber with suspended core.

Experimental apparatus and principle

The optical field distribution of the optical fiber is different from the normal optical fiber. When the optical fiber was bent, there is a part of light will propagate in the evanescent field at the part of U shaped region. The core diameters of the optical fiber with inner core is about 30 μ m, the inner and outer diameters of the optical fiber are 180 μ m and 300 μ m, respectively. Fig. 1 shows the optical field distribution of the optical fiber with suspended core.

Computed Transverse Mode Profile (m=0,neff=1.459911)

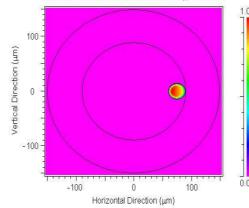


Fig. 1 The optical field distribution of the optical fiber with suspended core

Fig. 2 shows the experimental apparatus of the evanescent field absorption sensor based on U shaped optical fiber with inner core. In the experimental setup, a broadband light source with the wavelength of 400-2000 nm is used. The corresponding absorption spectrum was acquired by optical spectrum analyzer (OSA). The process of the U-shaped optical fiber sensor fabrication can be separated into three steps. Firstly, a 50 cm long of the optical fiber with inner core was cut and the two ends of the fiber were polished for avoiding the scattering light of the environmental disturbance. Then, a 10 cm long cladding of the fiber was removed from the middle of the optical fiber with inner core. At last, the fiber was bent by a flame carefully and slowly. Thus evanescent field absorption sensor based on U shaped optical fiber with suspended core was manufactured completely.

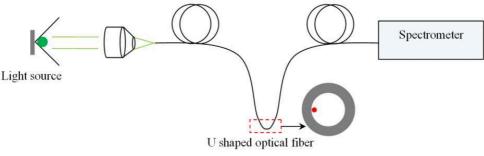


Fig. 2 Sketch of the U-shaped optical fiber sensor

Results and discussion Conclusion

To study the sensitivity of the evanescent field absorption sensor in detail, experimental investigations have been carried out with methylene blue solutions in the optical fiber. Firstly, 0.2 g of methylene blue was dissolved in the water and diluted before using. Secondly, the solutions were absorbed into the optical fiber and the optical fiber was set in the optical path. Thirdly, the absorption were tested. Fig. 3(a) shows the absorption spectrum of the sensor using 1.2 mmol/L methylene blue solution. From the spectrum, we can observe the peak is at 650 nm. When the liquid concentration was varied from 0.2 to 1.7 mmol/L, the absorbance peak shows a increasing.

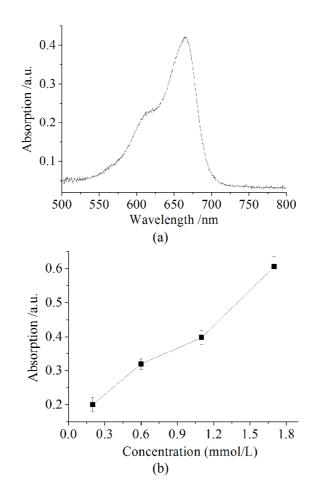


Fig. 3 Response of the U shaped optical fiber absorption sensor (a) Absorption spectra of methylene blue (b) The value of absorption at different concentrations.

The absorbance peak as a function of liquid concentration change was shown in Fig. 3(b). The absorbance peak has a nearly linear relationship with the liquid concentration change. Moreover, It can be seen that the evanescent field absorption sensor based on U shaped optical fiber with inner core has a good sensitivity, which is useful to the practical applications.

Conclusion

In this paper, we demonstrate and fabricate an evanescent field absorption sensor based on U shaped optical fiber with inner core. The light leak of evanescent field at the part of U shaped region caused by bending of the optical fiber introduces a high sensitivity to the concentration change. The absorbance peak has a nearly linear relationship with the liquid concentration change. Therefore, this sensor has great potential in many different applications such as microanalysis.

Acknowledgements

This work is supported by the National Natural Science Foundation of China (NSFC, 61007053, 61205027, 61377085, 61177081, 61227013), the 111 project (B13015) to the Harbin Engineering University, and Fundamental Research Funds for the Central Universities.

References

[1] F.T. Wang: Opt. Commun. Vol. 253 (2005), p.283

- [2] S.K. Khijwania, K.L. Srinivasan, J.P. Singh: Opt Eng Vol. 44 (2005)
- [3] J.L. Cruz: Sensors Actuators Vol. 73 (2001), p.95

- [4] P.H. PAUL and G. KYCHAKOFF: Appl. Phys. Left. Vol. 51 (1987), p.12
- [5] S. SIMHONY, A. KATZIR and E.M. KOSOWER: Anal. Chem. Vol. 60 (1988)
- [6] C.A. VILLARRUEL, D.D. DOMINGUEZ and A. DANDRIDGE: Proc. SPIE Vol. 798 (1987), p.225
- [7] S. SIMHONY, I. SCHNITZER, A. KATZIR and E.M. KOSOWER: J. AppL. Phys. Vol. 64 (1988)
- [8] I. SCHNITZER, A. KATZIR, U. SCHIESSL, W.J. RIEDEL and M. TACKE: J. Appl. Phys. Vol. 66 (1989)
- [9] V. RUDDY: Fiber Integrated Opt. Vol. 9 (1990), p.142.
- [10] V. RUDDY, B.D. MACCRAITH and J.A. MURPHY: J. Appl. Phys. Vol. 67 (1990)
- [11] L.C. SHRIVER-LAKE, G.P. ANDERSON, J.P. GOLDEN and F.S. LIGLER: Anal. Lett. Vol. 25 (1992)
- [12] S.R LOWRY, T.E. MAY and A. BORNSTEIN: Appl. Spectrosc. Vol. 47(1993), p.30
- [13] B.D. GUPTA, A. SHARMA and C.D. SINGH: Int. J. Optoelectron. Vol. 8(1993), p.409
- [14] B.D. GUPTA and C.D. SINGH: Appl. Opt. Vol. 33 (1994)
- [15] B.D. GUPTA, C.D. SINGH and A. SHARMA: Opt. Engng. Vol. 33(1994)
- [16] B.D. GUPTA and C.D. SINGH: Fiber Integrated Opt. Vol. 13 (1994), p.433
- [17] B.D. GUPTA, A.K. TOMAR and A. SHARMA: Opt. Quantum Electron. Vol. 27 (1995), p.747
- [18] T. TAKEO and H. HATTORI: Jpn. J. AppL Phys. Vol. 21 (1982)
- [19] T. TAKEO and H. HATrORI: Proc. SPIE Vol. 1544 (1991), p.282
- [20] T. TAKEO and H. HATTORI: Appt. Opt. Vol. 31 (1992), p.44

A Measuring Method of Liquid Food Conductivity Based on Pulse Response Measurement Method

WEI Xin-lao^{1,a}, LI Yu-long^{1,b}

¹College of Electrical & Electronic Engineering, Harbin University of Science and Technology, Harbin, 150040, China

^aweixinlao@163.com, ^bliyulong8117560@126.com

Keywords: Liquid food; Conductivity measuring; Pulse response method

Abstract. The food conductivity is one of impact factors on pulsed electric field sterilization. Abnormal breakdown of high conductivity liquid is also one of the bottlenecks in pulsed electric field sterilization technology. The conductivity of liquid food should be accurate calculated for searching the mechanism of abnormal breakdown deeply. An accurate measuring method of conductivity of liquid food is proposed based on pulse response method. Conductivity can be calculated by data recorded from oscilloscope with electrical pulse treating on the conductance cell. This method can decrease the impact of stray capacitance and polarization phenomenon on measured results.

Introduction

Liquid conductivity is one of the basic physical parameters which are significant index to judge the water quality and solution concentration. The conductivity measurement technology is widely used in the area of chemical engineering, biology, medical science and environmental protection.Research shows that liquid conductivity has great influence on pulse electric field sterilization. The disinfection rate decreases as the conductivity of liquid increases [1]. The abnormal breakdown in the treatment chamber is easy to happen during the dealing progress. Abnormal discharge produces high temperature arc which produce unknown materials. The liquid breakdown mechanism is ambiguous. So, it is vital to analyze the influence of conductivity on breakdown voltage in order to solve the abnormal breakdown. Pulse response measurement method is proposed to measuring the food conductivity.

Principle of pulse response method

There are four main measuring methods including electrode conductivity measurement method, electromagnetic conductivity measurement method, phase sensitive detection measurement method, pulse method. During these and dynamic methods, electromagnetic conductivity measurement method avoids the problem of electrode polarization and corroding by strong acid and alkali.However, this method can only measure the high conductivity liquid, the measurement range is narrow, and the equipment is large and expensive. Phase sensitive detection measurement method neglects the influence of double electrode layer, so this method brings error in principle [2]. Dynamic pulse method needs to change the pulse width and amplitude, so this method cannot measure fast [3]. Electrode conductivity measurement method has the advantage of simple construction, low cost and wide measuring range which is suitable for most liquid.

There are two problems in the conductivity measurement. First, double layer charge will form at the contact surface between electrode and solution which can be treated as the stray capacitance series with liquid resistance when measured with AC. So AC measurement brings the error [4]. Second, electrode polarization phenomenon including chemical polarization and concentration polarization

will occur in the conductivity measurement under DC voltage which bringing the error [5]. So pulse response measurement method is proposed to be used in order to avoid the problems because of its short processing time. The coaxial treatment chamber used in the pulse electric field sterilization is chose to be the conductance cell. The coaxial treatment chamber is equivalent to the circuit with resistance and capacitance in parallel. The pulse response method is shown in Figure 1. U_0 is the amplitude of the square wave source. R_0 is the non-inductive resistance. R_x and C_x is the equivalent parameter.

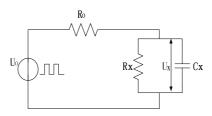


Fig. 1 The pulse-response method diagram

The source output square waveform is shown in Figure2. The measured waveform is shown in Figure3.

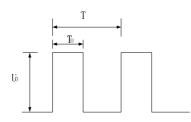


Fig. 2 Wave of square wave source

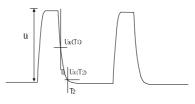


Fig. 3 Wave of voltage acted on the liquid

The voltage on the conductance cell under the pulse voltage based on the time-domain analysis is as follows:

$$U_{1} = \frac{R_{x}}{R_{0} + R_{x}} U_{0} \left(1 - e^{-\frac{T_{0}}{\tau}} \right)$$
(1)

When $T_0 >> \tau$,

$$U_1 = \frac{R_x}{R_0 + R_x} U_0 \tag{2}$$

 $T_0 \gg \tau$ is the basic premise which needs to check before calculation. The R_0 is in series with the liquid equivalent resistance during the high level of pulse voltage. The equivalent resistance can be calculated by U_1 , U_0 and R_0 .

$$R_{\rm x} = \frac{U_1 R_0}{U_0 - U_1} \tag{3}$$

As
$$G = \frac{1}{R} = \frac{1}{\rho} \cdot \frac{l}{A} = \sigma \cdot \frac{l}{A} = \frac{\sigma}{K}$$
, (4)

$$\sigma = KG \tag{5}$$

Where σ is liquid conductivity(μ S/cm), *K* is conductance cell constant (cm⁻¹), *G* is conductance. When the square wave voltage is 0, the voltage U_x on the conductance cell decreases from U_1 to 0. The equivalent resistance of conductivity cell internal discharges by equivalent capacitance. The voltage $U_x(T_1)$ and $U_x(T_2)$ of two time points T_1 and T_2 took in the falling edge are as follows:

$$U_{x}(T_{1}) = U_{1}e^{-\frac{T_{1}}{\tau}}$$
(6)

$$U_{x}(T_{2}) = U_{1}e^{\frac{T_{2}}{\tau}}$$
(7)

According to the value of T_1 and T_2 , τ can be obtained by dividing the two equations

$$\tau = \frac{T_2 - T_1}{\ln(U_x(T_1)/U_x(T_2))}$$
(8)

Measuring Circuit

The main circuit is composed of rectifier bridge, filter capacitor, non-inductive resistance and MOSFET. The pulse voltage is generated by controlling the MOSFET on and off. The equivalent capcitance charges when the switch is on. The conductance cell progress internal discharges when the switch is off. The main circuit is shown in Figure 4.

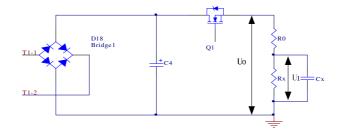


Fig. 4 The main measuring circuit

The measured results and analysis

The $0.001 \text{mol} \times \text{L}^{-1}$ KCL conductivity calibration solution is selected to demarcate the conductance cell constant. The conductivity of solution is $143.3 \mu \text{S} \cdot \text{cm}^{-1}$. The resistance of the solution measured by pulse response method is 21.87Ω . So the conductance cell constant can be calculated as follows:

$$K = \sigma \cdot \mathbf{R} = 143.3 \times 10^{-6} \,\text{s/cm} \times 21.87 \,\Omega = 0.3133971 \times 10^{-2} \,\text{cm}^{-1} \tag{9}$$

The conductance cell filled with tap water is applied by pulse voltage, and the pulse width T_0 is 8.87 μ S, pulse voltage amplitude U_0 is 143.6 V. Both the waveform applied on conductance cell and the pulse voltage waveform can be got from the Tektronix oscilloscope. The waveform is shown in Figure 5.

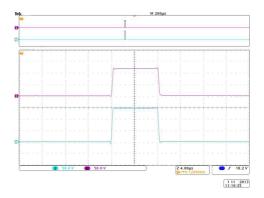


Fig. 5 Measured waveform of tap water

 τ can be calculated as follows:

$$\tau = \frac{T_2 - T_1}{\ln \left(\frac{U_x(T_1)}{U_x(T_2)} \right)} = \frac{0.2 \times 10^{-5}}{\log \left(105.125/10.6094 \right)} = 0.872 \mu S$$
(10)

The calculation results shows that $T_0 >> \tau$, this method meet the calculation premise. The equivalent resistance and conductivity can be calculated as follows:

$$R_x = \frac{U_0 \cdot R_0}{U_1 - U_0} = \frac{119.625 \times 6.1}{146.742 - 119.625} = 27.09\Omega$$
(11)

$$\sigma = K / R = 0.2229 \times 10^{-2} / 27.09 = 82.28 \,\mu \text{s/cm}$$
(12)

The conductivity of tap water is 82.28µS/cm.

Conclusion

The pulse response measurement method can measure liquid conductivity. There are no stray capacitance, chemical polarization and concentration polarization during the measuring progress.
 This method is suitable for most liquid without corrosive liquid as acid and alkali. The method needn't to change the electrode constant.

Acknowledgements

The authors acknowledge financial support from National Natural Science Foundation of China (Grant 51277046) and Specialized Research Fund for the Doctoral Program of Higher Education (20122303110007)

References

[1]Patrick C.Wouters, AD P. BOS, Joerg Ueckert. Applied and Environmental Microbiology, 2001, 67(7): 3092-3101.

[2]LIN Bo. Tangshan: Hebei University of Technology, 2006: 9-10

[3]LIU Kai-pei,CAO Shun-an,LI jun-e. Thermal power generation. 1992(2).51-53

[4]LAN Jing-hui. dalian: Dalian University of Technology, 2002: 13-15

[5]ZHANG Xiao-wei. Tangshan: Hebei University of Technology, 2006: 14-15

Piezoelectric Resonant Temperature Sensor

Yu Yao^{1, a}, Xu Jun^{1,b}, Ma Jing^{1,c} and Chen HaiYan^{1,d} ¹Harbin University of Science and Technology, Harbin, Heilongjiang, CHINA ^ahljlgxj@126.com, ^blixin68@hrbust.edu.cn, ^chljlgxj@tom.com

Keywords: Piezoelectric, Resonant, Thermal sensing, Temperature sensor.

Abstract. This paper describes a piezoelectric resonant tuning fork designed for temperature sensor. The sensor is based on a directly detection and analyses of relationship between frequency shift and temperature change. The main working components of quartz tuning fork temperature sensor are quartz tuning fork resonator (QTFR) and driving circuit, according to the piezoelectric effect principle of quartz crystal, researching on correlative incentive mode, selecting cut type and setting electrodes reasonably, and applying finite element method and Matlab to simulate and analyze the vibration mode as well as temperature and frequency characteristic. The experimental result indicates that the sensitivity of this sensor can reach 70ppm/°C in the temperature range from -30 to 100°C, it guarantees that precision is 0.05°C, the resolution is 0.02°C, and the response time is 4S.

Introduction

With the development of quartz crystal's processing technology and microcomputer, quartz tuning-fork temperature sensor has faster development. Quartz tuning-fork temperature sensor is a new digital temperature sensor, it has high stability, high precision, high resolution and it can resist electromagnetic interference.

Quartz tuning-fork temperature sensor's main advantages can be described as follows: High sensitivity, good long-term stability, it has good anti-aging performance, high accuracy, quartz crystal temperature sensor outputs frequency signals, it has high resolution and low frequency, strong anti-inter-ference ability, insensitive to pressure, sensor outputs frequency signals corresponding to temperature, anti-noise ability is powerful, and digital signal processing is very easy, the volume is small, the oscillation circuit's power consumption is very small, the response speed is fast, and the linearity is very good.

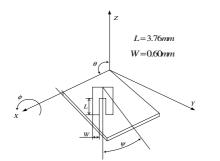
Quartz crystal temperature sensor can be not only applied in high precision temperature measurement system(such as measurement of gas flow temperature's change in aeronautics and astronautics, measurement of deep well bottom and underground's temperature change in petroleum exploitation), systems that temperature change is slow or minimal, but also be suitable for the areas that the environment is bad and the requiring temperature measure bound is wide(such as marine meteorology temperature measuring system, polar environmenttemperature measuring system, ultra low temperaturemeasurement and control system as well as nuclear energy control system and so on, whose temperature testing systems have strong electromagnetic field environment.

Design principle and method

To design quartz tuning-fork temperature sensor, not only piezoelectric quartz crystal sensor's requirements to quartz crystal's single vibration mode and piezoelectric activity should be satisfied, but also quartz crystal's frequency- temperature characteristic should be considered specially on this basis. To adapt to the domestic existing processing technology and level of quartz crystal, decrease the processing cost of sensor, $\theta=116^{\circ}$, $\phi=-10^{\circ}$ is selected as ZYtw w(θ/ϕ) quartz crystal temperature sensor's double rotation angle cutting type. Thus, quartz crystal temperature sensor's new cutting type is obtained as shown in Fig.1.

The Quartz tuning fork temperature sensors are tuning -fork quartz crystals using new cut and vibrating in flexural mode, they are designed so that their frequency is both extremely sensitive to temperature and highly linear. This high sensibility offers the ability to detect fine changes in

temperature and this frequency-based technique has the advantage of being immune to amplitude noise in measurement system in comparison with thermocouple and resistance temperature detector based temperature sensing techniques.



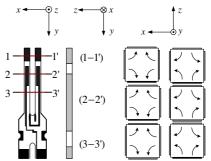


Fig. 1. Thermal cut Orientation of QTFR

Fig. 2. Electrodes setting of QTFR

Only reasonable electrode setting can make two-end quartz crystal tuning-fork generating bending vibration opposite to width direction phase. It can be concluded, to make quartz tuningfork generating width bending vibration, we must set two electric fields along width direction, they are in same size, opposite direction. Motivate double end tuning tuning-fork quartz resonator's double tuning-forks by piezoelectric effect, and then make it generating bending vibration with contrary phase. When adopt circumferential fusion segmentation method to arrange electrodes, section is at quartz crystal's wave knot. For the crystal whose length is two ends fixed, its fundamental frequency has two wave knots, where the stress T=0, they are separately located in a distance for 0.2241 and 0.7761 to one end. Therefore, positive and negative electrodes is separated at wave knot. To avoid consuming vibration energy, decreasing the value of resonator, increasing dynamic resistance value, and influencing frequency-temperature characteristic, the electrode leader should be welded at the nodes as shown in Fig. 2.

According to researchers' theories for many years, quartz crystal's frequency is changing with the change of temperature. Quartz temperature sensor's working mechanism utilizes the characteristic of changing with temperature to measure temperature. In the temperature range of 200~200°C, quartz crystal's frequency-temperature characteristic can be represented as three-order polynomial:

$$f = f_0 [1 + \alpha (T - T_0) + \beta (T - T_0)^2 + \gamma (T - T_0)^3]$$
(1)

Where T_0 is reference temperature, T is temperature to be measured, f is frequency that is corresponding to temperature to be measured, f_0 is natural frequency of certain reference temperature, α is first order frequency-temperature coefficient, β is second order frequency-temperature coefficient, γ is third order frequency-temperature coefficient.

Flexural mode tuning-fork temperature sensor's sensitivity is very high, up to 70ppm/°C. Its dynamic resistance value is reasonable, and it can meet both working in wide temperature range and low power consumption' s requirements. Its requirement to fabrication process error is not harsh. Therefore, we decide to select flexural mode. Flexural mode tuning-fork temperature sensor's natural frequency f is shown as follow:

$$f = \frac{\lambda^2}{4\pi\sqrt{3\rho S'_{22}}} \cdot \frac{W}{L^2} \cdot \frac{1}{\sqrt{1 + \frac{\lambda^2 N}{12} (\frac{W}{L})^2 (1 + \frac{S_{44}}{K' S''_{44}})}}$$
(2)

Where, λ is the solution that satisfies equation $1 + \cos \lambda \cosh \lambda = 0$, $N = \frac{2tgh\lambda \cdot tg\lambda + \lambda tgh\lambda + tg\lambda}{\lambda(tgh\lambda - tg\lambda)}$, ρ is the

density of crystal material; S_{ij} (*i*, *j*=1,2,3,4) is the elastic compliance cofficient, *K'* is the constant that is determined by the shape of tuning-fork cross section, *W* is the width of tuning-fork arm, *L* is the length of tuning-fork arm.

The influence of shear deformation and moment of inertia can be seen from piezoelectric quartz crystal cantilever beam's natural vibration frequency equation, it will decrease the quartz crystal cantilever beam's bending vibration natural vibration frequency. And with the increase of piezoelectric quartz crystal cantilever beam natural vibration frequency order, the influence will be larger; in addition, with the increase of cantilever beam's width length ration *W/L*, the influence will increase.

Quartz tuning-fork temperature sensor is made of quartz crystal, electrode, stent and shell and so on. Quartz tuning-fork temperature sensor is usually placed in a seal shell, so that quartz crystal's surface deposition solid particles, water vapor and other harmful substance can be avoided. Seal shell can improve sensor's reliability and prevent the aging of quartz crystal. sensor's connection between base and tuning-fork electrode adopts hot pressure welding method, finally use cold pressure welding to seal quartz vibrator in a miniature metal tube-shell. Quartz crystal temperature sensor's structure is shown in Fig.3.

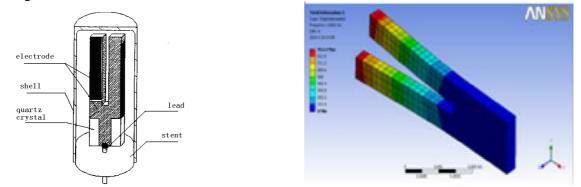


Fig.3. Structure of quartz crystal temperature sensor Fig.4 FEM analysis of the tuning-fork

The tuning fork resonator is made of a quartz single crystal ZYtw-cut plate. In actual design of tuning fork crystals, however, other important design parameters must also be considered such as geometry of tuning fork blanks and electrodes and other manufacturing requirements. The three-dimensional model of the quartz tuning fork is established by using commercially available FEM software as shown in Fig. 4. The dependence of the individual crystal parameter sensitivity on various design parameters can be comprehensively analyzed by FEM and detailed information on geometry of tuning fork blanks and electrodes.

Experimental Results

The physical quantity tested by sensor basically has two forms, one is steady(static or quasi-static)form, this kind of signal will not change with time(of change rather slowly), the other is dynamic(periodic variation or transient)form, this kind of signal changes with time changing. Owing to input physical quantity state's difference, input and output characteristics expressed by sensors are different, existing so-called static and dynamic characteristic. Owing to different sensor has different parameters, their static characteristics and dynamic characteristics have different features, their influences on testing results are different. Fig. 5. and Fig. 6. are separately quartz tuning fork temperature sensor's static frequency-temperature characteristic and error analysis.

Dynamic characteristic is one of the most important characteristics. Dynamic characteristic is the response characteristic when the sensor's input changes with time change. We always hope the relationship of sensor's output changing with time changing can reappear the relationship of sensor's input changing. But in fact, except proportional characteristic component, output signals won't be fully consistent with input signals. Dynamic characteristic includes dynamic error and response speed, so that it can be used to describe sensor's performance when added outer variable input signals.

Dynamic characteristic includes dynamic error and response speed, so that it can be used to describe sensor's performance when added outer variable input signals. Step response method is adopt to conduct dynamic characteristic test of tuning fork quartz temperature sensor, the result is shown in Fig. 7. The response time of the proposed micro quartz tuning-fork temperature is determined to be 5 s in the relative temperature range from 0 °C to 100 °C.

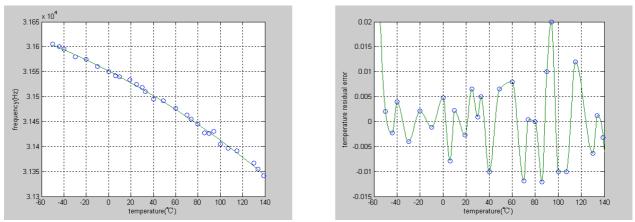


Fig.5 Frequency-temperature characteristic of sensor Fig.6 Temperature residual error analysis

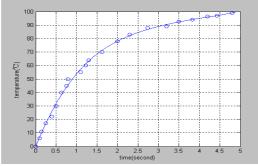


Fig.7 Dynamic characteristics of quartz temperature sensor

Summary

A new miniature heat-sensitive quartz tuning-fork temperature sensor base on resonance is presented in this paper. In the design of quartz tuning fork temperature sensor, selecting the cut type of quartz tuning fork according to the each anisotropic nature of quartz tuning fork, so that there is a linear relationship between quartz tuning fork frequency and temperature, quartz tuning fork produces bending vibration along width direction and be opposite to phase direction through reasonable electrode setting. we evaluate the sensor through the established quartz tuning fork temperature sensor test system. The largest deviation of the sensor does not exceed ± 0.05 °C in a temperature interval from -30 °C to 100 °C, which is close to the theoretically calculated value.

Acknowledgments

This work was supported by the Natural Science Foundation of Heilongjiang Province (Project Grant No. F201136, No. F201308) and the Education Department of Heilongjiang Province Science and Technology Research Project (Project Grant No. 11551074).

References

- [1] S Tadigadapa and Mateti, Piezoelectric MEMS Sensors: State-of-the-art and Perspectives, Meas. Sci. Technolol., 20 (2009) 1-30.
- [2] J. M. Friedt and E. Carry, Introduction to the Quartz Tuning Fork, Am. J. Phys. 75(2007) 415-422.
- [3] N. Wakatsukil, Y. Kagawa, K. Suzuki2 and M. Haba, Temperaturefrequency Characteristics Simulation of Piezoelectric Resonators and Their Equivalent Circuits Based on Three-dimensional Finite Element Modelling, International journal of numerical modelling, 16(2003) 479-492.

Research on the On-line Measuring Method of Transformer Shortcircuit Reactance

Yunbing Wei^{1,a}, Dong Zhang^{1,b}

¹Institute of Electrical and Information Engineering, Zhengzhou University of Light Industry, Zhengzhou 450002

^aee_dmegc@263.net, ^bzhangdonghnay@163.com

Keywords: Power transformer; short-circuit reactance; on-line measurement; channel error

Abstract: The short-circuit reactance is an important parameter to characterize the transformer ability to resist the attack of short-circuit current in the design the operation process. In this paper, the on-line measuring method for short-circuit reactance based on electrical parameters' characteristics was presented, and the feasibility to carry out on-line monitoring for the transformer operation condition was also analyzed. Besides, the principle of two on-line measuring methods based on respectively exciting current compensation and elimination technique was researched, and the calculation equations were deduced. The comparison between the on-line results measured from moving mold experiment and those from off-line short-circuit experiment showed that these two methods were accurate and valid.

1.Introduction

Power transformer is one of the most important electrical equipment in the power system, which runs the state is extremely important for the reliability of the power system. Winding is one of the most important parts of the transformer. It is prone to irreversible deformation under the action of mechanical force or electrical power due to the impact of a short circuit, the manufacturing process or improper handling during transport impact, this gives the safe operation of the transformer leave serious problems even can cause severe damage to the transformer. So ,it has a very important significance for normal operation of the power system to carry out winding transformer on-line monitoring of work conditions.

The traditional transformer fault detection are mostly off-line testing. Field test environment is complex, many confounding factors, detection and testing takes a very long period, high hardware costs and testing costs, the impact of human factors are also great. Therefore it is the most prominent problem that how to achieve an accurate real-time on-line monitoring in transformer fault detection techniques.

Short-circuit reactance is an important performance parameters of the transformer, and it is reactance transformer internal equivalent impedance when the load impedance zero and load current rating. As the short-circuit reactance a is related to winding geometry and relative position, so it is possible to reflect the change in the internal structure of the transformer windings. When a transformer winding deformation occurs, the short-circuit reactance values will change. If the operation of the transformer by the impact of short-circuit current, in order to check whether the winding deformation, we can comparison before and after the short-circuit of the reactance to judge it. During the operation of the transformer, it can certain extent reflect whether the normal state of the transformer if the short-circuit reactance line measurement compare short-circuit reactance value under normal circumstances.

2.Short-circuit reactance line measuring principle

It is a very simple way that former vice-side differential voltage mode divided by primary current mode to calculation of short-circuit reactance this algorithm is simple but it ignores the impact of the transformer magnetizing current , that is considered to convert the primary current to the

primary side and the secondary side of the current is equal which will bring the error to the results and this is not allowed on the transformer condition monitoring.

In this paper, single-phase two-winding transformer for the study, the equivalent circuit is shown in Fig. 1:

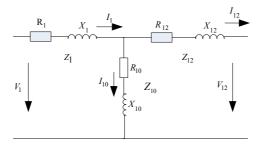


Fig.1. Equivalent circuit

In the Fig. 1, $Z_1 R_1 X_1$ respectively a side impedance, resistance, reactance; $Z_{12} R_{12} X_{12}$ respectively secondary side impedance, resistance, reactance value of the primary side imputed; $Z_{10} R_{10} X_{10}$ respectively magnetizing impedance, resistance, reactance; V_1 is a side input voltage; V_{12} is the two side of the terminal voltage at a side of the imputed values; I_1 is a side input current; V_{12} is the two side of the end of the current in the primary side of the imputed values; I_{10} is excitation current.

Short-circuit reactance X_{sh} can be expressed as: $X_{sh} = X_1 + X_{12}$

Based on excitation current compensation short-circuit reactance line measurement method From the graph:

$$V_1 - V_{12} = I_1 Z_1 + I_{12} Z_{12} = Z_1 I_1 + Z_{12} (I_1 - I_{10}) = (Z_1 + Z_{12}) I_1 - Z_{12} I_{10}$$
(1)

Short-circuit reactance can't be measured directly by direct measurement of $DV(DV = V_1 - V_{12})$ and I_1 and divide, because of the finally excitation current presence.

I, Within the specified voltage range no exceed the rated voltage, excitation current I_{10} and a secondary side voltage V_1 to the side, there:

$$I_{10} = C_{10}V_1 \quad (C_{10} \text{ is real constant}) \tag{2}$$

II, When the transformer load test, considered the a secondary side voltage and magnetic current the phase difference of 90 degrees, that:

$$I_{10}^{(0)} = V_1^{(0)} / j\omega L_M = V_1^{(0)} / jX_M \quad (\text{load state})$$
(3)

Among, X_M is the magnetizing reactance of the transformer, $I_{10}^{(0)} V_1^{(0)}$ respectively current and voltage measurements next of the transformer in load state.

III, The magnitude and phase of the excitation current concerned only with a secondary side voltage, and the load changes can't change the magnitude and phase of the excitation current, so we can get the exciting current by transformer load test when the transformer load.

IV, Ignore short-circuit impedance reactance component, and the equivalent reactance of a side and the equivalent reactance secondary side to the primary side approximately equal, that:

$$Z_1 = Z_{12} = jX_1 = jX_{12} = jX_{sh} / 2$$
(4)

After the above assumptions, formula (1) can be changed:

$$V_1 - V_{12} \approx j(X_1 + X_{12})I_1 - jX_{12}(V_1 / jX_M)$$
(5)

After finishing can be drawn:

$$V_{1}(1 + \frac{X_{sh}}{2X_{M}}) - V_{12} \approx j X_{sh} I_{1}$$
(6)

Thus available short circuit reactance calculated as:

$$X_{sh} \approx \frac{V_{1}(1 + \frac{X_{sh}}{2X_{M}}) - V_{12}}{jI_{1}}$$
(7)

Among, magnetizing reactance can be calculated by experimental data load:

$$X_{M} = \left| \frac{V_{1}^{(0)}}{I_{10}^{(0)}} \right| \tag{8}$$

The value of X'_{sh} can get by into the short-circuit reactance measurement in short circuit test. The short-circuit reactance final calculation formula:

$$X_{sh} \approx \left| \frac{V_1 (1 + \frac{X_{sh}^{'} I_{10}^{(0)}}{2V_1^{(0)}}) - V_{12}}{jI_1} \right|$$
(9)

3.Experimental verification

3.1, The experimental verification of the short-circuit reactance line measurement method

In this paper, a simulation test inorder to verify the correctness of the transformer short circuit reactance line measurement method. The test transformer is three single-phase transformer bank and the way link is $y_n/d11$. Single-phase transformer winding structure is shown in Fig. 2:

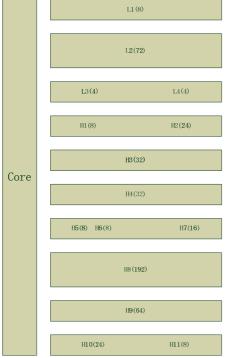


Fig.2. The winding structure of single-phase transformer

Core structure for the back and high and low voltage windings are arranged from top to bottom and the winding for continuous. High and low voltage windings are having a plurality of taps. According to the experiment, the voltage winding needs to be divided into L1-L4 of four subwindings and the high voltage winding needs to be divided into H1-H11 of 11 sub-windings. To change of the internal structure of winding by changing the wiring to tap, thus change the shortcircuit reactance. In this experiment the low-voltage winding from the L2, L3 consisting of 76 turns and the high voltage winding from the H2, H3, H5, H6, H7, H9, H10 consisting of 176 turns. The rated voltage of single-phase transformer is 95 V/220 V and the rated capacity is 2KVA.The sampling rate of 100 points per cycle. The parameter identification is choosed two cycles of data. The current of the transformer in load is 1.1%, and the load loss is 0.9%, and the short-circuit test results are shown in Table 1.

	Phase A	Phase B	Phase C
Short-circuit reactanceX/ Ω	1.055	1.050	1.053

For the connection transformer of the above were calculated using the short-circuit reactance line measure methods described herein under different load conditions and calculation error of the measurement results are the basis of short-circuit test. The calculation results based on the excitation current compensation law are shown in Table 2.

Table 2. The calculation results of excitation based on current compensation method

Project		Load	Load factor		
	100%	90%	60%	30%	
Phase A/ Ω	1.0548	1.0556	1.0564	1.0551	
Error/%	-0.10	-0.02	-0.08	-0.09	
Phase B/ Ω	1.0462	1.0447	1.0425	1.0358	
Error/%	-0.26	-0.38	-0.61	-1.24	
Phase C/ Ω	1.0536	1.0511	1.0507	1.0512	
Error/%	-0.02	-0.26	-0.30	-0.25	

Optional load impedance type (LR), which is based on reactor and resistor load conditions, is calculated in other different load, This line measurement method based on load changes that calculated for each time needs two kinds of load conditions and the calculation results are shown in Table 3.

Project	Load factor				
110,000	100%			30%	
Phase A/ Ω	1.0602	1.0571	1.0572	1.0568	
Error/%	0.30	0.02	0.02	-0.01	
Phase B/Ω	1.0516	1.0501	1.0455	1.0456	
Error/%	0.26	0.10	-0.33	-0.31	
Phase C/ Ω	1.0584	1.0571	1.0533	1.0495	
Error/%	0.42	0.29	-0.08	-0.42	

Table 3. The calculated results of online measurement based on the change of load

3.2, Error analysis

This approach has its own error for it made some assumptions to simplify the model of the transformer before pushing the formula. Short-circuit reactance of the reference value got by transformer short-circuit test measurements itself has errors, because the calculation of the reference value does not consider the impact of excitation current another reason for a large number of negative error is that the values by got by the way that primary voltage divided by secondary current in the primary side of the imputed value is too large than the actual value of the short-circuit reactance. Further, the phase compensation act was used during the data processing procedure but this compensation runs in the assumption that each point on the same set of data capture card is the same as the acquisition interval and the actual situation is not necessarily the case grabber so it may bring the error. when calculating the short-circuit reactance based on load changes for the subtract two are from the same channel acquisition card collection and the channel errors cancel each other out in making the difference so this method affected by the acquisition cartoon channel errors will be reduced.

4.Conclusion

In this paper, the transformer short circuit reactance line measurement based on the method of excitation current compensation was proposed and took into account considering the channel capture card error and the experimental simulation results show that:

(1) The results obtained by this method, most of the data in the error of 0.5% or less, it shows that the correctness of this transformer short circuit reactance calculation method. It also shows that the assumption prior to derive short-circuit reactance formulas is the basic established.

(2) At the same time tap connection the short-circuit reactance line measurement basically unchanged as the load changes, This shows that the value of the short-circuit reactance only has relationship with the geometry and the mutual position of the transformer winding and it does not change with the load changes.

References

- [1] Bengtsson. Status and Trends in Transformer Monitoring[J].IEEE Transaction On Power Delivery, 1996, 11(3): 1348-1379.
- [2] E.Arri, A.Carta, F. Mocci, M. Tosi. Diagnosis of the stateof power transformer windings via on- line measurement ofstray reactance[J]. IEEE Trans. On Instrum Meas. SpecialIssue, 1993, 42(2): 312- 378.
- [3] Gangyuan Zeng. Effective method of measurement to determine the short-circuit reactance is winding deformation [J] transformer, 1998, 35 (8). In Chinese.
- [4] Peng Li.Based on the amount of electrical characteristics and prospects of transformer winding deformation monitoring technology status [J]. Electric Power Automation Equipment, 2006.In Chinese.
- [5] Dake Xu.Research transformer winding deformation monitoring [J] High Voltage Engineering, 2001, 27 (4): 21 23.In Chinese.

Analysis of Data Mining Method for Near Infrared Spectral Data of Dairy Products Based Orthogonality

Lijie Wang^{1,2,a}, Zhen Zhou^{1,2}, Yong Qin^{1,2}, Jinying Yin^{1,2}, Jianying Guo^{1,2}, Wenning Dong^{1,2} and Dan Wang^{1,2}

¹College of measure-control technology and communication engineering, Harbin university of science and technology, China

²The higher educational key laboratory on measuring & control technology and instrumentations of Heilongjiang province, China

^awlj@hrbust.edu.cn

Keywords: spectrum analysis, data mining, orthogonality, time domain, frequency domain.

Abstract. There are advantages such as real time, quick, multi-constituents simultaneous measurement, green and no pollution, and so on, of using near infrared spectral method to detect concentration information of dairy products constituents. From time domain and frequency domain, near infrared spectral data mining methods based on orthogonality were separately researched to realize noise filtering and useful information extracting. For milk spectrum, methods in the time domain including Orthogonal Signal Correction and Direct Orthogonalization, Wavelet Transform de-noising method in the frequency domain, were separately explored and used in spectral preprocessing, PLS method was used to build calibration model, and processing effect of different data mining methods to make data mining for milk spectrum, the complex interfering signal and noise information uncorrelated with the measured constituents can be can reduced effectively, and the correlated information with the measured constituents is reserved in maximal limitation, prediction capability of calibration model is improved, furthermore, the Orthogonal Signal Correction method is better than the Direct Orthogonalization method, moreover, in the frequency domain, wavelet de-noising is better than the orthogonality methods within the time domain.

Introduction

For the past few years, it has been one of the most concerned about livelihood issues of good or bad of dairy products' quality. In the ingredients table for dairy products such as milk, contents of protein, fat and solid, and so on, are all needed to be labeled. During sales or storage process, internal quality of the dairy products is also changed along with time unavoidably. So it has been became an important question within domain of the dairy inspection that how to effectively control the dairy products' quality during collection, production and processing, and sale.

There are not simple, fast, real-time detecting methods and equipment except the standard chemical analysis methods in current detection means for the dairy products' quality. Near Infrared (NIR) spectral analysis is a kind of quantitative analytic technology rapidly developed in recent years, there are advantages such as fast analytical speed, plenty spectral information, no any pretreatment to the measured sample, multi-constituents simultaneous measurement, and so on, of using near infrared spectral method to detect concentration information of dairy products constituents. Besides liquid, gas, solid samples, some type of samples such as powder, paste, suspended classes are all could be detected [1], therefore, there are advantages highlighted of using NIR spectral analysis method to test concentration of dairy products constituent. Recently, the research communities participated in development in the fields at home and abroad are being appeared constantly.

At present, one of the bottlenecks of the NIR spectral analysis technology is spectral information effectively parsing problem, in nature, it is data mining problems of valid concentration information of the sample. The reason of bottleneck above are derived from the multiple absorption or frequency absorption of the hydrogen groups in the near infrared spectral region, the absorption intensity is

weak, Overlap is serious, background is complex, and signal-to-noise ratio is lower. So to realize effectively resolution spectrum, there are two necessary factors, spectrum acquisition apparatus with higher stability and resolution, and stable samples spectrum and spectral data mining methods suitable the measured sample. From time domain and frequency domain, near infrared spectral data mining methods based on orthogonality are separately researched in the following to realize noise filtering and useful information extracting for NIR spectrum of dairy products.

Analysis in Time Domain

Routine Methods in Time Domain. Routine methods [2] such as Smoothing, Derivation, Multiple Scattering Corrections (MSC), Standard Normal Variable transformation (SNV) are all belong to the NIR spectral pretreatment methods of the time domain. Usually processed and analyzed object is the spectrogram itself, influence of the concentration matrix is not being considered during the processing. So during the pretreatment, some useful information to build calibration model is most likely lost, noise could be cancelled not completely, moreover, robustness of the built model would be affected. Noise above is mainly caused by the factors such as stray light, chemical composition fluctuation, thermal noise of resistance, environmental temperature, and so on. In nature, the above factors are irrelevant or approximately irrelevant with spectrum data information of the measured constituent, therefore, pretreatment can be implemented to NIR infrared spectrum of the dairy products making use of orthogonality between these target information and non-target information in theory.

Data Mining Methods in Time Domain Based on Orthogonality. In research, preprocessing based on orthogonality is carried out to near infrared spectrum data in time domain. The processing is not only in view of the spectrogram itself, meanwhile considering the influence of the measured constituent concentration. Basic thought of the data mining methods in time domain based on orthogonality is that before the quantitative calibration model is built, spectral data matrix is orthogonally processed to reference concentration matrix of the measured constituent, non-target information no relation to the concentration information is filtered. Next, multivariate calibration model is built, so robust of the model is improved and prediction ability of the model is raised.

Net signal is only corresponding with spectral signal of the measured constituent, and is orthogonal to space constructed with all other interfering signals [3]. Thus, the orthogonal feature can be taken advantage of to eliminate interference in theory.

Orthogonal Signal Correction of S.Wold (S.Wold-OSC) and other OSC methods derived by it such as Fearn-OSC, Feal-OSC, Piece-wise OSC, and so on, are a class of typical spectral data mining methods based on orthogonal projection [4], in the following, operation mechanism of this class methods will be deeply analyzed.

Firstly, original spectrum data matrix is made centered to concentration matrix, purpose of doing so is to make all data is distributed on both sides of zero. Centralized data can reflect the degree of spectral information change, and simplify behind regression algorithm and make it stable.

Next, Setting original spectrum data matrix is X, concentration data matrix is Y, PCA is made to matrix X, first principal component scores is selected to be initial value of orthogonal score vector, so larger system change information contained in the spectral data matrix is included in the first principal component scores.

$$X = TP^{T}$$
(1)

This process above is essentially orthogonal decomposition, a set of non-orthogonal vectors x_1 , x_2 ..., are linearly transformed into a set of pair wise orthogonal vectors t_1 , t_2 ...

$$t_1 = x_1 t_2 = x_2 - p_{21} t_1 : t_i = x_i - p_{i1} t_1 \cdots - p_{ii-1} t_{i-1}$$
(2)

In order to make

$$(t_1^T t_2) = (t_i^T t_1) = \dots = (t_i^T t_{i-1}) = 0$$
(3)

Take

$$P_{ij} = (X_i^{T} t_j) / (t_j^{T} t_j) \qquad (j = 1, 2, \cdots, i - 1, i = 1, 2, \cdots, n)$$
(4)

According to Eq. 1, first hidden variable t_1 is variable whose correlation coefficient with Y is maximum in X, t_1 is only correlated with x_1 , and is not correlated with other variables. Second variable t_2 is only correlated with the first two variables in matrix X, the No.i variable t_i is also correlated with the first *i* variables in matrix X, and is not correlated with other variables, and the like.

 t_1 is in the first, t_2 is the second, variables in the back is little correlated with *Y*, noise components contained in these variables are more, usually existence of these variables could result in higher *PRESS* value of calibration model, in further spectral resolution, *PRESS* criterion can be used to excavate these variables information and get rid of them.

 t_1 is made orthogonalization to Y, next, this part of the corresponding orthogonal information is removed. one after another, the first principal component scores is changed into the second principal component scores, the third principal component scores, and so on, recycling to the last loop, until cycling through all the principal component number.

From the angle of the abstract, the spectral data mining method based on orthogonal projection is examined. Aim of its processing is to get rid of parts uncorrelated with Y from X. From the angle of the mathematical sense, as long as the removed parts is orthogonal to Y, information contained in the parts must be uncorrelated with Y but all kinds of noise mixed in the NIR background spectrum, the parts above uncorrelated with Y may be orthogonal to Y actually. Only a projection on the orthogonal direction of Y is removed by OSC, it appeared to a false correlation of residual parts of noise with predicted values of the model. In the circumstances above, stability of the model is bound to be affected, the prediction model is easy to generate over fitting. This failing weakness also explains why the strictest orthogonal algorithm, Direct Orthogonalization[5] (DO), cannot be achieved obviously superior performance than other OSC methods.

Analysis in Frequency Domain

Wavelet Transform (WT) [6] is a new de-noising method that be raced to research and explore by related scholars in NIR spectrum analysis domain recently. From the time domain to the frequency domain, Various frequency of mixed signal contained in near infrared spectral information can be decomposed into a series of different frequency block signals according to different distinguish scale. By extracting wavelet coefficients of signal and removing wavelet coefficients of noise, interference is eliminated and new interference is not introduced.

Suppose there is the following observation signal

$$f(t) = s(t) + n(t)$$

In Eq. 5, f(t) is observation signal, s(t) is Original signal, n(t) is noise signals.

WT is linear, so wavelet transform of signals mixed with noise f(t) is equal to the sum of wavelet transform of the signal s(t) and wavelet transform of the noise n(t). There is resolution of the non-uniform distribution of WT, high frequency resolution and low time resolution are adopted at the low frequency, low frequency resolution and high time resolution are adopted at the high frequency, so WT is more suitable for the analysis of singular signal. According to relationship between the local singularity of function and the gradual decay of maximum value of the function wavelet transform modulus, characteristics of s(t) and n(t) under the wavelet transform can be obtained. General signal increases with the increase of decomposition scale, maximum modulus, consistency and variance of wavelet coefficients of general noise will be smaller with the increase of decomposition scale. Therefore, signal-noise ratio can be decomposed by WT by using the opposite characteristics of the wavelet transform of the signal and noise.

Near infrared spectrum of the dairy products is of multi-scale, data distribution of useful information and interference information under different scales is not the same, so multi-scale wavelet transform is adopted. According to Eq. 3, the wavelet transform is made for near infrared original spectrum of samples f_0 (c_0). Important information of the signal is contained in the corresponding wavelet coefficients after transformation, whose amplitude is larger, but the number is less. Distribution of corresponding wavelet coefficients of the noise is agreed, the number is more,

(5)

and amplitude is smaller. Adopting low-pass filter H and high-pass filter G to make WT, detail signal and approximate signal are obtained after threshold quantization under a series scales.

$$c^{i+1} = Hc^{i}, d^{i+1} = Gc^{i}$$
(6)

In Eq. 6, c is detail coefficient, d is approximate coefficient, $i = 1, 2, \dots, n-1$.

Reconstructing and conversing

 $f_{1} = G^{T} d^{1}, f_{2} = H^{T} G^{T} d^{2}, \cdots, f_{n} = {}_{1} H^{T} H^{T} H^{T} G^{T} d^{n}, f_{n+1} = {}_{1} H^{T} H^{T} H^{T} C^{n}$ (7)

In Eq. 7, $f_1, f_2, ..., f_n$ are the detail signal after reconstruction under different scales, f_{n+1} is the approximate signal reconstruction after n times decomposition.

Frame information of the original signal is reflected by the approximation signal after reconstruction, and local subtle information is reflected by the detail signal. The dimension detail of the detail signal and approximate signal are same with the original signal, spectrum after de-noising can be obtained by rearrange the detail signal and approximate signal.

$$f_0 = \sum_{i=1}^{n+1} f_i$$
(8)

Acquisition and Analysis of Milk Spectrum

NIR spectrum of milk samples are acquired by the AOTF NIR SPECTROMETER. Way of spectral acquisition is scattering. Data scanning range is 5800-10000 cm⁻¹, resolution is 5 cm⁻¹, scanning times is 5. Experimental samples are provided by a milk center, concentration values of reference are measured by MilkoScan FT120, constant temperature of the samples is 40 °C in the experiment, wavelength variables in the process is 98. 86 calibrating set samples and 27 predicted set samples are selected in spectral analysis, the following several ways are adopted in the process.

The first is that calibration model is built using PLS method without preprocessing. The second is that PLS model is built after DO preprocessing (DO-PLS). The third is that PLS model is built after OSC preprocessing (OSC-PLS). The fourth is that PLS model is built after WT of Multi-scales preprocessing (WT-PLS). The fifth is that PLS model is built after Savitzky-Golay smoothing preprocessing (S-G-PLS). The last is that PLS model is built after MSC preprocessing (MSC-PLS).

During the WT analysis, two kinds of wavelet basis function of sym and db series are separately used to make discrete wavelet transform to original spectrum. Through comparison of correlation coefficients under different decomposition scale of the two classes wavelet above, the biggest is taken priory, corresponding wavelet basis function and decomposition layer number are also the best. In the research, db orthogonal wavelet is determined to be wavelet base function, according to calculation, the scale of the wavelet decomposition is 4.

Prediction results of fat concentration in milk samples corresponding different spectral analytical methods are listed in Table 1.

Analysis methods	Orthogonal principal component number	Optimal number of principal components	Correlation coefficient	Prediction deviation of cross validation %	Actual prediction deviation %
PLS	0	6	0.942	0.383	0.280
DO-PLS	3	3	0.953	0.363	0.283
OSC-PLS	3	2	0.959	0.345	0.230
WT-PLS	-	3	0.977	0.301	0.231
S-G-PLS	-	6	0.942	0.351	0.326
MSC-PLS	-	4	0.946	0.367	0.380

Table 1 Prediction results of PLS models of different spectral analysis methods

From theory analysis and data processing results in Table 1, it is shown that

Firstly, relative to no processing, Savitzky-Golay smoothing preprocessing and MSC preprocessing can purify spectra to a certain extent.

Secondly, relative to the conventional near infrared spectral preprocessing methods such as Savitzky-Golay smoothing and MSC, orthogonal method including DO and OSC in the time domain are feasible in NIR spectral data mining. Modeling after orthogonal pretreatment, correlation coefficient between the predicted values and the reference value is improved, prediction deviation is reduced, and number of principal components used in modeling is also reduced. Analyzing from processing means, in OSC preprocessing, PCA is made to original spectral matrix X in the first stage of the pretreatment, score vector of the first principal component is immediately taken orthogonal processing to concentration matrix, then orderly iterated, and noise information eliminated in turn. From operation mechanism, OSC can be effectively guaranteed that the filter out the spectral information has nothing to do with concentration matrix Y as much as possible. Judging from the overall effect of filtering, OSC is better than DO.

Lastly, in the frequency domain, affection of the multi-scales wavelet de-noising is in general better than orthogonal methods in the time domain, this is the results of the following processing and operation during WT, on the one hand, baseline correction is realized through setting zero to wavelet coefficients in the low frequency within the wavelet domain for spectral signal, on the other hand, noise is removed through threshold processing to wavelet coefficient in the higher frequency. In Table 1, practical prediction deviation of the WT-PLS is slightly higher than the OSC-PLS, it is because of the wavelet transform only dealing with spectral data itself, and ignoring the influence of concentration of information.

Conclusions

Using orthogonality to make near infrared spectrum data mining, by means of removing interference information from the original spectral information of milk, the number of principal components of calibration model is reduced, uncertainty of spectral data is brought down, so it is feasible of the data mining method for near infrared spectral data of dairy products based orthogonality whether in theory or in practice.

In the time domain, OSC and DO are all belong to the software filtering methods based on orthogonal projection, but concrete ways and order are different. For concentration of fat in milk spectrum, OSC is better than DO, and the two methods above are superior to smoothing and MSC.

In the frequency domain, Wavelet de-noising is overall better than time-domain orthogonal method. As a kind of spectral data mining method, Baseline correction and noise filtered can be done

simultaneously by means of using WT, the characteristic of its flexible filtering is incomparable of other methods of time domain. But within the real number field, there is no strictly compact,

symmetry, and orthogonal unbalance uni-wavelet function; this is also one of the reasons of actual prediction deviation of the WT-PLS higher than orthogonal methods of the time domain. In further study, de-noising study using multi-wavelet transform will be discussed.

Acknowledgements

This work was financially supported by the the Scientific Research Fund of Heilongjiang Provincial Education Department (12521122).

References

- H.Y. Wu, Y. Liu, Y.M. Zuo: Academic Periodical of Farm Products Processing, No.3 (2010), p.76 In Chinese
- [2] W.Z. Lu, H.F. Yuan, X.L. Chu: Near Infrared Spectrum apparatus (Chemical Industry Press, China 2010). In Chinese
- [3] R. Liu, L.N. Lv, W.L. Chen, K.X. Xu: Spectroscopy and Spectral Analysis, Vol.24 (2004), p.1042 In Chinese

- [4] S. Wold, H. Antti, F. Lindgren, J. Ohman: Chemometrics and Intelligent Laboratory Systems, Vol. 44 (1998), p. 175
- [5] Claus A. Andersson: Chemometrics and Intelligent Laboratory Systems, No.47 (1999), p.51
- [6] X.J. Chen: ANALYTICA CHIMICA ACTA, Vol. 634 (2009), p.166

The Equal Precision Measurement Data Processing System Based on Virtual Instrument

Lingfei Zhang^{1,a}, Shengyu Wang^{1,b}

¹Institute of physics and Electronic Information Engineering of Qinghai Nationalities University,

Qinghai, Xining, China, 810007

^aZhanglingfei99@163.com, ^bwshengyu93@163.com

Keywords: Equal precision measurement, Data processing, Error analysis, G language, VI

Abstract: During quantitative analysis on measured object by using equal precision measurement method, there remains certain difference between the measuring result and truth value due to the impact on measuring method, measuring tools and measuring environment. In order to reduce measurement error, we usually make continuous equal precision measurements on the measured object repeatedly. Then we get the final result by theoretical calculations, error analysis and dispose on measurement data. The data processing shows complicated and error-prone .But now we take computer as a carrier, then combining with virtual instrument technology to accomplish the data-processing system. It can cover the manual computation shortage and can take humanization disposal on measurement data. Moreover, the results can show with multi-mode intuitively.

I Introductions

During the equal precision measurement data-processing, the calculations procedure is relatively complex, and it is likely to bring more measuring errors due to artificial calculation errors. Thus the most advisable approach is via computer's efficient function of data-processing. At present, on account of various computer data processing systems, it can use various language programs to finish system design, take VB or VC for an example. For these programs, most are text language, which need to memorize abundant key words and write many program source codes. Meanwhile, the workload is heavy and the development cycle is long. LabVIEW is a graphical development environment which is also transformative. It has a built-in function of signal acquisition, measurement analysis and data display. Using graphical programming language (G language), the interface is intuitively clear. It basically doesn't write code, but take flow chart to replace it. In this way, it can greatly improve the efficiency, and the developed data-processing system functions can be added or removed randomly. The man-machine interface can make humanized design.Using G language to complete the system design makes it simple and convenient.

II Classification And Treatment of Measurement Errors

The measuring errors may have its root in measurement instruments, environmental impact, method, theory and so on. According to their natures, it can be divided into the system error, random error and negligence error. In the measurement results, measured value deviates significantly from the truth values and forms the negligence error (parasitic error). All the measurements containing parasitic error can be regarded as the worst value and should firstly be removed in data processing, for the random errors, we can use statistical averaging method to reduce its influence on the measurement work, we should take measures to reduce its influence. Because it is not easy to be found, so we should pay more attention to the system error, as far as its characteristics is concerned, it can be divided into constant, linear, periodic and complex changes. System error in the measuring process is complex, but can determine the system error existence and to take effective measures to reduce the error.

In order to obtain reasonable measuring results, we must analyze and dispose the measured data. According to the equal precision measurement results processing steps as follows: (1) Calculate the arithmetic average of n times measurements.(2)Figure out n times residual error.(3)Find the standard deviation estimate value by using the Bessel formula.(4) Judging the measurements whether it contains errors, then eliminate bad value. (5) Repeat (1) ~ (4) steps for the rest data until the bad values are removed completely.(6)Judging whether it contains error variable system error.(7)Find the standard deviation estimate value of the arithmetic mean value.(8)Compute the uncertainty of the arithmetic mean value.(9)Give the final measurement results expression.

III The Front Panel Design And The System Software Flowcharts

The front panel is a human-computer interface, so the design is an important content ,graphical language use flow chart to complete the design, compared to traditional text language more to reflect its development advantages, it consists of numeric input, Boolean, array, string display and waveform chart controls.

The system program execution in accordance with the sequence structure to achieve the confidence probability selection, data input, data processing, data display and save as shown in Fig.1.

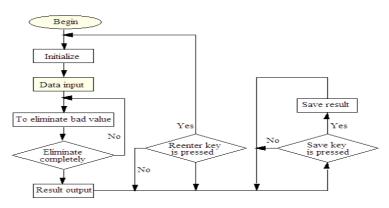


Fig.1 System software flowcharts

IV The Structure of The System And Data-processing

The LabVIEW environment provides the user a lot of node functions and the reference of function nodes makes the program development simple and flexible. In order to reflect the characteristics of the development process of program module, firstly, create a project according to the data processing steps of the precision measurement as it is mentioned in the part I, we regard each step of the data processing as a Sub VI. Therefore, the whole system contains several modules such as confidence probability ,data input, data processing and data processing results show and preservation. Data processing part includes the arithmetic average Sub VI, residual error Sub VI, Bessel formula Sub VI, systematic errors and periodic linear system error criterion Sub VI, eliminate bad value Sub VI and data display and storage Sub VI. Each Sub VI forms a single icon, it also can be thought of as an independent node function. It can make the structure of flow process diagram more clearly, the procedure calling is more convenient and fully embodies the advantages of G language.

(1) Selection of Confidence Probability : The error eliminating in the system should have a certain basis. Without identifying the cause of the case, we should firstly determine whether suspicious measurement data contain gross errors. The basic idea for this is to give a confidence

probability, and determine the corresponding confidence interval. For those that is beyond the error confidence interval can be considered a gross error, the system confidence probability has two kinds, one is of %95 and another is %99 ,which are realized by two button dialog function.

(2) Data Input: In the system, data input is completed by a figure input control. The data input portion put every input figure in a one-dimensional array. When it comes to a large amount of data, such input form will be more convenient than direct input in the array control. The program uses a "while" loop structure and an event structure. Once the confirm button pressed, then the figure in the input control will be added to the array .It will not enter the data processing program unless the start button pressed.

(3) Data Processing (1) Arithmetic Average VI

$$\overline{x} = \frac{1}{n} \sum_{i=1}^{n} x_i \,. \tag{1}$$

According to the Eq.1, the arithmetic average VI used the array sum and array size function. 2 *Residual Error VI*

$$u_i = x_i - \overline{x} \,. \tag{2}$$

The residual error VI uses for loop structure to process the data based on Eq.2. (3) Bessel Formula VI

$$\hat{\sigma} = \sqrt{\frac{1}{n-1} \sum_{i=1}^{n} u_i^2} .$$
(3)

The Bessel formula VI program based on Eq.3 that as shown in Fig.2.

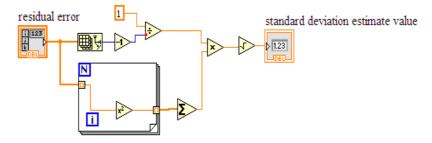


Fig.2 Bessel formula VI program

(4) System Error Criterion VI

System error criterion VI is used to judge whether the system has an error or not. The program includes two criterion, Marley Kopf criterion and the Abbe-Helmert criterion. The Marley Kopf criterion is used to detect whether there is linear system error. Methods are based on Eq.4.

$$\Delta = \begin{cases} \sum_{i=1}^{\frac{n}{2}} u_i - \sum_{i=\frac{n}{2}+1}^{n} u_i & \text{n is an even number} \\ \sum_{i=1}^{\frac{n-1}{2}} u_i - \sum_{i=\frac{n+3}{2}}^{n} u_i & \text{n is an odd number} \end{cases}$$
(4)

If the absolute value of Δ is greater than the maximum value of ui (luimaxl), then there is a linear system error.

The Abbe-Helmert criterion is used to detect whether there is periodic system error. If the Eq.5 was established, then there exists a periodic system error. System error criterion sub VI is shown in Fig.3.

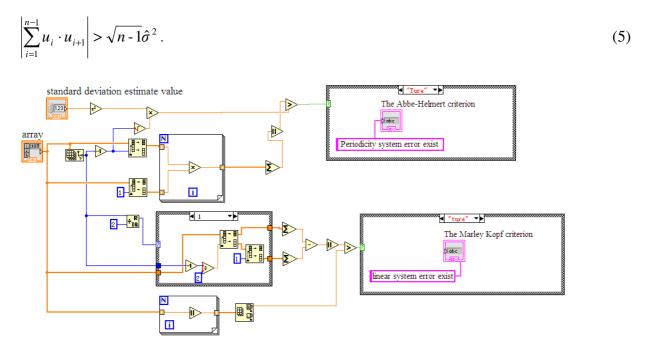


Fig.3 The system error criterion VI program

(5) To Eliminate Bad Value VI

The system eliminates bad value VI accomplished by Grubbs test method. excluding bad values on the basis of Eq.6. G is Grubbs coefficient, detected by Grubbs coefficient G table.

$$|u_i| > G\sigma \ . \tag{6}$$

Eliminate bad value program is based on Eq.6 to obtain a Boolean array, then put the Boolean data into eliminate bad value VI, find the index of true Boolean elements in the Boolean array, then delete the worst value according to the index of the original data , loop execution of this process, until the last processing array have the same treatment results with this time.

According to the above every data processing sub module together constitute the total program of the system block diagram is shown in Fig.4.

(4) Display and Preservation of Data- processing Results

Data processing results in the string VI and are displayed in the form of string and waveform charts .The String displays the original data number, many useful data, arithmetic average, standard deviation estimated value, the arithmetic average uncertainty, the Marley Kopf criterion, the Abbe-Helmert criterion result and measuring result, waveform charts show the tendency of residual error. The final result will be saved in the form of text files, which are convenient for calling and printing. For example, in physics teaching, with equal precision measurement, we measured a set of data of a steel ball's diameter, processed through the system the conclusion as shown in Fig.5, the system processing results and artificial calculation results agreed very well, and with high accuracy, speed, description the system has stronger practicability.

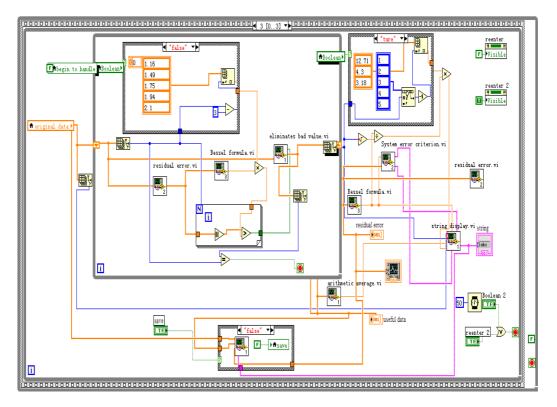


Fig.4 Block diagram of virtual measurement data processing system

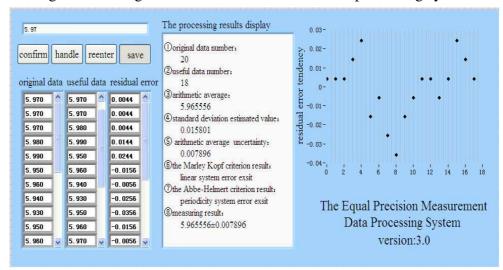


Fig.5 Measurement data processing results display

V Conclusions

The system is developed with LabVIEW software, the graphical programming language is driven by data flow, which efficiently make the relevant procedure or the system developed much higher than other languages such as (1)The system function that developed with G language has strong expansibility, and the operation is simple.(2)The user can increase functions on the system foundation according to their actual needs, he also can design more personalized user interface.(3)The system error diagram can also be displayed in 3D.This system can be applied to engineering measurement or teaching domain.

References

- [1] Zhanjiang Lin.Electronic Measurement Technology (Second Edition) (In Chinese) [M].Beijing:Publishing House of Electronics Industry,2007
- [2] Chengyong Xiao.LabVIEW2010 Basic Tutorial (In Chinese) [M]. Beijing:China Railway Publishing House, 2012
- [4] Gang Liu. LabVIEW8.20 Chinese version programming and application (In Chinese) [M]. Beijing: Publishing House of Electronics Industry,2008
- [5] Zhen Fan, Zhenshan Yu.*Improvement of direct equal precision measurement column data processing method (In Chinese)* [J].measurement technology,1990,9:33~35
- [6] Peizhen Fan. *Random error analysis and data of equal precision measurement process* (In *Chinese*) [J]. measurement technology, 2002,1:9~12
- [7] [6] Wangui Liang. Automatic test system of error analysis and processing based on Virtual instrument (In Chinese) [J]. Railway communication signal,2007,4:9~10

A Synchronous Sampling System of On-line Monitoring for Long-distance Cable Insulation Based on DSP and GPS

Xinlao Wei^{1,a}, Bo Zhu^{1,b}, Bing Pang¹, Tong Liu², Song Wang², Ruihai Li²

¹ Harbin University of Science and Technology, China

² Electric Power Research Institute, China Southern Power Grid, China

^aweixinlao@163.com, ^bzhubo1219@163.com

Keywords: Monitoring system, DSP, ADS8364, GPS, Cable insulation

Abstract. The induced voltage of the long-distance power cable will reach high value, so the metallic sheath of cable should be cross-linked to reduce the induced voltage. It is safe and economic enough but bring out problem of monitoring the situation of insulation. In order to solve the problem, a new method is provied and a monitoring system based on Digital Siganl Processor and Global Positioning System are designed. The composition of system has been introduced, includes the hardware and software design. The results show that the monitoring system can reflect the situation of cable insulation, and the mothod is proved to be validity and feasibility.

Introduction

With the wide application of Cross Linked Polyethylene (XLPE) cable in electric power system which has easy technical process, reliable electric characteristics, larger transmission and convenient installation, etc, the on-line monitoring of XLPE cable insulation becomes more and more important. At present there are many on-line monitoring methods of cable insulation, such as DC component method, DC superposition method, dielectric loss factor method, partial discharge method, the low frequency superposition method and the AC superposition method, etc. In recent years a large numbers of cable which length is more than 1000 meters appears in 110~220kV power system [1]. For the long distance power cable, it is known that the induced voltage on the metallic sheath is proportional to the length of the cable. When XLPE cable is longer enough or the current flows cross cable core is large, the induced voltage will reach a high value to do harm to cable insulation. Therefore, metallic sheath should be cross-linked when the length of the cable is more than 1000 meters [2,3]. The entire cable is divided into several segments which are connected both ends of the metallic sheath to the ground, and then each segments are subdivided into three short sections, the metallic sheath of the each section is crossover connection by coaxial cable. After two consecutive crossover on the metallic sheath in each segment, the induced voltage between each section of the three-phase have been canceled by the phase relationship of the induced voltage between metallic sheath of three-phase cable, which greatly reducing the total induced voltage on metallic sheath [4,5]. It is economic and safe enough but brings out problem of monitoring the situation of insulation. The reason is that the current which flows cross the main insulation of each segment of the cable is hard to be got by direct measurement [6]. A new monitoring method has put forward in the paper, and we develop the high speed and accuracy measurement system for long-distance power cable. We use a digital signal processor (DSP) as the high-speed processor and a global positioning system (GPS) signal for synchronized measurement. The dielectric loss factor $(\tan \delta)$ of cable insulation has been calculated to judge the condition of cable insulation.

The Monitoring Method of Cable Insulation

First, it need to install current transformer (CT) on both ends of three-phase cables respectively, and the current is measured synchronously by using GPS module. The current difference of two terminals is equal to leakage current which flows through cable insulation. Then install voltage transformer on

one end of each cables to measure the operating voltage. Through calculated the phase angle difference between leakage current and operating voltage, and complementary angle can be calculated, which is named dielectric loss angle, then dielectric loss factor can be calculated. The tan δ is used to reflect the integrity defects of the cable insulation, which is the main criterion for capacitive equipment insulation in electric power system. Therefore tan δ is used to assess the condition of cable insulation in the paper.

The System of Hardware Design

The on-line monitoring system consists of signal processing circuit, digital-to-analog converter ADS8364, digital signal process chip TMS320F2812, GPS module, GPRS module and its peripheral circuit. The system schematic is shown in Fig. 1. Signal after the data acquisition channels into 16-bit A/D converter ADS8364 is converted into digital signal, then the converted digital signal via the bus into DSP, and calculate insulation parameters by DSP data processing and computing. These parameters are sent through by GPRS module to the computer.

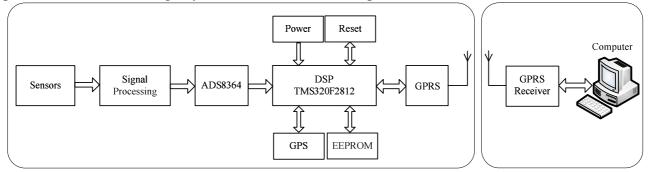
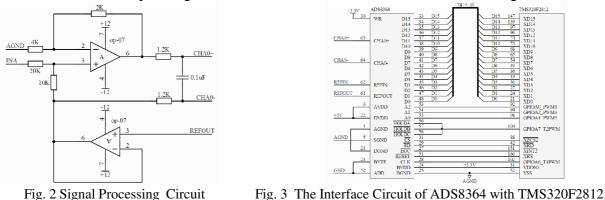


Fig.1 Block diagram of the monitoring system

The Option of DSP. The hardware design of system takes the TMS320F2812 of TI Company as core which is 32bit DSP processor, Harvard structure, takes on high static CMOS performance, low power design. The instruction cycle is 6.67ns on 150MHz main frequency which increases the signal process speed distinctly. It has the ability of digital signal processing, embedded control and incident management, especially suitable for mass data processing of measurement situations, such as intelligent instrumentation, on-line monitoring system and industrial automation, etc.

Signal Processing. Signal acquisition and conversion channel circuit by the voltage and current transformer and its auxiliary circuit. By using a simple OP-07 amplifier circuit featuring four, high-precision external resistors, the ADS8364 can be configured to accept bipolar inputs. In the paper, we choose ± 2.5 V input ranges could be interfaced to ADS8364 is shown in Fig. 2.



The Option of A/D Conversion. In the on-line monitoring system, we choose an analog-to-digital conversion chip ADS8364 of TI Company as the system sampling device, which is six channel analog input and 16 bit parallel output of A/D conversion. Six channel analog input is divided into three groups(A, B and C), each input has signal to keep all channels of simultaneous sampling and conversion functions, it is very suitable for multi-channel acquisition system needs. Therefore, it is

especially suitable for on-line monitoring system. The interface circuit of ADS8364 with TMS320F2812 is shown in Fig. 3.

The Option of GPS and GPRS Module. In the on-line monitoring system, we choose the Resolution-T GPS of Trimble Company as the receiver. It is a 12-channel, parallel-tracking, all-in-view, embeddable GPS. The receiver outputs a 1 Pulse-per-second (PPS) timing signal accurate to within 15ns of GPS, and it is designed for 3.3V DC prime power. The TXDA and RXDA pin of GPS connect to SCITXDA and SCIRXDA pin of TMS320F2812 respectively which realize the GPS module and DSP communication. PPS pin connect to the GPIOE0 pin which provide pulses per second signal to system.

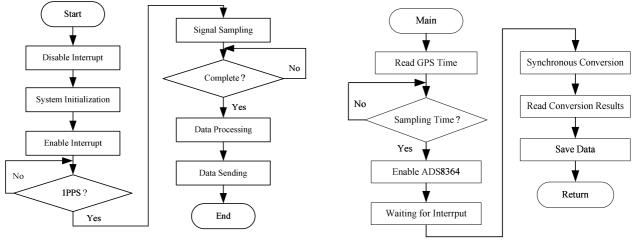
The option of GPRS module, we choose the ADR-D2910 of ADAER Company as GPRS module. It can transmit data through wireless network by a standard serial port RS232 or RS485 to realize data transmission. In the present paper we use RS232 serial port which is connected to DSP, and the monitoring data is transferred to memory in the host PC through the GPRS module.

Other Circuits. Besides above basic modules, there are some auxiliary circuit, includes communication, keyboard, power supply, etc, which are integral parts of a system. Keyboard is connected with the I/O ports of DSP to finish the corresponding operation of the system through typing related information in the DSP internal, finally transmit the output data to display, and achieve the man-machine communication, which can facilitate better operation and analysis cable insulation parameters.

The System of Hardware Design

An excellent device requires equipping corresponding software, although software is designed on hardware, but favorable software design is also an important factor that evaluates a system or device. The system uses C programming language in CCS environment, which has integrated visualization code editing interface to write C language directly, has the data graphic display tools to render time/frequency domain waveform and has basic debugging tools to support multiple DSP debugging, etc. The software design of system includes main program and sampling interrupt program, etc.

The main program will finish all the hardware initialization and process the monitoring data. The main program flow chart is shown in Fig. 4.



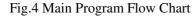


Fig.5 Synchronous Sampling Flow Chart

In the synchronous sample interrupt subroutines, 1PPS triggered signal make program access sampling. The GPS receives a 1PPS from the GPS satellites synchronizing to the universal time coordinate with high accuracy. It can obtain the absolute time inforamtion from all over the world. The synchronous sampling is realized by using the GPS clock, ADS8364 will be started when GPS time arrival the sampling time. And when receives the interrupt from DSP, both side ADS8364 is starting synchronous conversion. The synchronous sampling flow chart is shown in Fig. 5.

Experimental Results

In order to verify the method of on-line monitoring system correctness and effectiveness, using the signal generator to provide known signal to the on-line monitoring system. The experimental results are shown in Table 1.

$\delta\left(^{\circ} ight)$			$tan\delta(\%)$	Actual value (%)	
Measurement times		1	5	10	
А	0	0.01	0.00	0.00	0.000
В	0	0.00	0.01	0.00	0.000
С	0	0.00	0.00	0.01	0.000
А	0.0069	0.0121	0.0119	0.0120	0.0120
В	0.0068	0.0120	0.0121	0.0121	0.0119
С	0.0068	0.0119	0.0119	0.0119	0.0119

Table.1 Results of the tes	Table.1	Results	of the	test
----------------------------	---------	---------	--------	------

Comparing the actual measurement and theoretical calculation of $\tan \delta$ value, it can be seen the measurement system has high accuracy, verify the on-line monitoring system effectiveness and correctness. We find that the monitoring system can be used to monitor the any situation of cable insulation whether the matallic sheath of cable cross-linked or not.

Conclusions

In the present paper we propose a synchronous sampling system on-line monitoring synchronous sampling system for long distance cable insulation. In the system DSP is used as high-speed processor and GPS is used for synchronized measurement. The results show that the system adapts the request of on-line monitoring situation of insulation of long-distance power cable and has a high industrial use value.

Acknowledgment

The work is supported by the National Basic Research Program of China (2012CB723308), The Major Program of China Southern Power Grid and The Major Project of Graduate Innovation Fund in Heilongjiang Province of China (YJSCX2012-078HLJ). Thanks for all the researchers in Harbin University of Science and Technology.

References

- [1] M. A.Dakka, A. Bulinski, S. S. Bamji: IEEE Electrical Insulation, Vol.27 (2011), No.4, p. 34.
- [2] U. S. Gudmundsdottir, B. Gustavsen, C. L. Bak, W. Wiechowski: IEEE Transactions on Power System, Vol.27 (2011), No.3, p. 1403.
- [3] F. De Leon, M. L. Marquez-Asensio, G. Alvarez-Cordero: IEEE Transactions on Power System, Vol.26 (2011), No.3, p. 2060.
- [4] H. Y. Luo, Z.G. Guan, X.Y. Yi: High Voltage Engineering, Vol.31 (2005), No.11, p. 63. (in Chinese)
- [5] L.R. Chen, R. Xia, J.H. Luo: International Conference on Electricity Distribution, 2010, pp. 1-6.
- [6] C.W. Long, Y. H. Gao, J.H. Luo: International Conference on Electricity Distribution, 2010, pp. 1-6.

Design of Wireless Sensor Network for Fire Detection

Ning Du^{1, a}, Zhilong Liu^{1, b}, Huaiguo Dong^{1, c}

¹School of Software, Harbin University of Science and Technology, Harbin 150040, China ^aduning6677@126.com, ^bliuzhilong0627@gmail.com, ^cdhg0086@163.com

Keywords: Fire Detection; ZigBee; Routing; XBee

Abstract. The prevention and detection of fire have been hotly researched in worldwide. In this paper, an elaborate method of wireless sensor network for building fire safety is proposed. ZigBee technology is adopted in the wireless sensor system to help saving the energy cost and reducing energy consumption. In the routing selection, we choose MESH topology in wireless sensor networks in order to enlarge the monitoring scope. Each end module consists of a microcontroller on Arduino Due board and an Xbee Pro S2 wireless communication module based on the Zigbee standards. Sensors are used for detection which makes it possible to detect fire before inflammation.

Introduction

Nowadays, according to large amount of flammable materials used in buildings, more and more requirements are put forward on building fire detection system[1]. Comparing to the wired systems, wireless systems will offer opportunities for fire fighters to work out fire fighting strategies before arrival at the fire scene.

This paper explores the use of wireless sensor network technology in building fire detection system. During the recent years, the paradigm of Wireless Sensor Networks (WSN) has been adopted to tackle this problem[2]. Cheap and tiny wireless sensor devices which operate in a cooperative and autonomous manner deployed over a territory may detect hazardous gases and monitor wild fires [3]. There are two main strategies used by sensor nodes to detect a wild fire. The strategy is based mostly on temperature, relative humidity sensors and CO sensors [4].

This paper applies the ZigBee technology into fire detection system in order to solve the existing one's shortage, such as higher false alarm, wire difficulty and maintenance difficulties. ZigBee is an open global standard built on the IEEE 802.15.4 MAC/PHY. ZigBee defines a network layer above the 802.15.4 layers to support advanced mesh routing capabilities[5]. As a new short-range wireless communication technology, ZigBee is widely used in industrial control, telemedicine, wireless office, building automation and smart home, etc.

Implementation of XBee ZigBee Network

ZigBee network establishment

ZigBee is summarized into three types:star topology, peer-to peer topology and cluster tree topology. In the peer-to peer topology, the communication is established between devices and a single central controller, called the PAN(Personal Area Network) coordinator. The PAN coordinator may be mains powered, while the devices are most likely battery-powered. A peer-to peer network can be ad-hoc, self-organizing and self-healing. Applications such as industrial control and monitoring, wireless sensor networks, asset and inventory tracking would benefit from such a topology. It also allows multiple hops to route messages from any device to any other device in the network. It can provide reliability by multipath routing. In this paper, we established the network according to the mesh topology. The proposed system adopts XBee Pro S2 which is as communication module, so the architecture of the system is by using experience of the available solution for reference. The whole structure of the system is shown in Fig.1, once the coordinator (FFD, Full Function Device) is activated for the first time, it establishes its own network and becomes the PAN coordinator. Then it initializes the hardware, stack and application variables, choosing an

unused PAN identifier, and waiting for connection message form router or end device (RFD, Reduced Function Device). Once the router discovers a valid network, it sends an association request to the device that sent a valid beacon requesting a join on the ZigBee network. The device allowing the join then sends an association response frame that either allows or denies the join. Similar to routers, end devices must also discover and join a valid ZigBee network before they can participate in a network. After an end device has joined a network, it can communicate with other devices on the network. Since end devices are intended to be battery powered and therefore support low power (sleep) modes, end devices cannot allow other devices to join, nor can they route data packets.

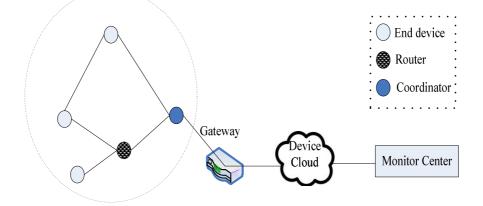


Fig.1. Structure of fire detection system.

Routing selection

ZigBee employs mesh routing to establish a route between the source device and the destination. Mesh routing allows data packets to traverse multiple nodes (hops) in a network to route data from a source to a destination. Routers and coordinators can participate in establishing routes between source and destination devices using a process called route discovery. The Route discovery process is based on the AODV (Ad-hoc On-demand Distance Vector routing) protocol, as shown in Fig.2.

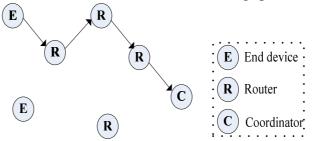


Fig.2. AODV routing algorithm sample transmission

Routing under the AODV protocol is accomplished using tables in each node that store the next hop (intermediary node between source and destination nodes) for a destination node. If a next hop is not known, route discovery must take place in order to find a path. Since only a limited number of routes can be stored on a Router, route discovery will take place more often on a large network with communication between many different nodes. When a source node must discover a route to a destination node, it sends a broadcast route request command. The route request command contains the source network address, the destination network address and a path cost field (a metric for measuring route quality). As the route request command is propagated through the network, each node that re-broadcasts the message updates the path cost field and creates a temporary entry in its route discovery table.

Design of End Module

Sensors of fire monitor

Sensor nodes are the basic unit and the basic platform of wireless sensor networks. Three factors compose the basis of a building fire: the fire source, environmental elements and combustible

material. A building fire usually occurs as the result of their combined effects. Firstly, the moisture content of the combustible material plays an important role in fires, which means the probability of fires depends on the moisture content. Therefore, the moisture content of combustible materials is a major point of assessment and predicts whether a fire will take place. Secondly, the early fire is in the smoldering stage, there would be a lot of smoke particles and harmful gases such as CO gas in the combustion and the temperature.

Structure of the fire detection node

ZigBee Wireless detection node is composed of the data transceiver unit, data processing unit, data sensor unit and battery-powered unit. Data acquisition unit is primarily through sensors to detect CO gas concentration, temperature, humidity of the region. Data processing unit controls the node to process the detection data. Data transceiver unit completes the interaction with the router and coordinator. Energy power unit is responsible for the energy of the node. The structure of the end node is shown in Fig.3.

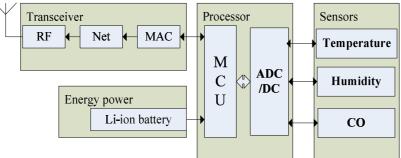


Fig.3. Architecture of end node

The end node utilizes temperature/humidity sensors and CO dioxide sensor. These sensors can measure the key parameters which indicate fire occurrence and the possibility of fire spreading. The task of the attached sensors is to sense the environment and to measure the appropriate parameters of interest. The application running in the MCU includes algorithms which use the measured values. Those algorithms define whether it is a dangerous situation or not according to some previously determined parameters' thresholds. A part of the code which runs on the Arduino and indicates an alarm situation is presented in Fig. 4.

If humidity < 55% &&
If Temperature > 40 ℃
If CO >200 ppm
then
Alarm("Alarm!!")
Broucast(humity,temperature,C
O,sensor address)

Fig.4. Code running on Arduino

Sleep mode of end node

ZigBee has an inherent advantage for these modes of operation due to its short attach time and/or its ability to remain in the sleep mode for long periods. In wireless sensor network, sleep mode is applied in the end node which can help saving energy. XBee end devices support two different sleep modes: pin sleep and cyclic sleep. We adopt cyclic sleep in our application, XBee end devices poll their parent every 100ms while they are awake to retrieve buffered data. When a poll request has been sent, the end device enables the receiver until an acknowledgment is received from the parent. It generally takes less than 10ms from the time the poll request is sent until the acknowledgment is received. The acknowledgment indicates if the parent has buffered data for the end device child or not. If the acknowledgment indicates the parent has pending data, the end device will leave the receiver to receive the data. Otherwise, the end device will turn off the receiver and enter idle mode (until the next poll request is sent) to reduce current consumption (and improve battery life).

The exact scheme is configuring a device to sleep for 20 seconds, but set SN such that the On/Sleep line will remain deasserted for up to 1 minute.

Hardware design of the fire detection node

Efforts are being made to develop multi-function detection node for simultaneously detecting fire and monitoring indoor air quality. Multi-function detection node that combines inputs from several different chemicals or physical processes would be expected to reduce the rate of false alarms and increase the speed of detection of real problems. The implement of the fire detection system is shown in Fig. 5. We use Arduino USB Board which uses the chip ATMEGA328 as a processor, controlled by the computer via USB port. Arduino composed of Analog I/O and Digital I/O which can interface with the other devices such as I2C, SPI, digital and analog. In our prototype system, we choose TMP37 as temperature sensor, DTH11 as humidity sensor and SEN-09403 as CO sensor. All the sensors we choose are suitable for Arduino.

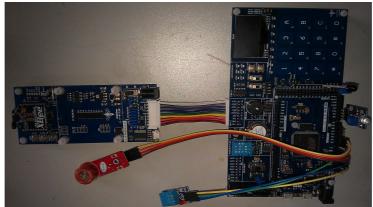


Fig.5. Hardware design of end device

Conclusions

This paper adopts new international intelligent building technologies to improve fire safety. Firstly, we give the architecture of the whole system. Secondly, we explicitly elaborate the method of building wireless sensors network. In the routing algorithm selection, mesh topology is used in the routing topology to expand the transmission scope. Suitable sensors and wireless sensors will not only reduce expenditure on sensors, but also reduce false alarms, speed response times and reduce fire-related losses. Lastly, we introduce the low cost scheme and the hardware design of the fire detection end device. The integration of fire detection and alarm systems with other building systems should also increase fire safety in the building.

References

[1] Z Liu, J Makar, AK Kim. Development of fire detection systems in the intelligent building. 12th. International Conference on Automatic Fire Detection. Gaithersburg, MD, 2001: 561-573.

[2] C.Y. Chong, S. P. Kumar, "Sensor networks: Evolution, opportunities, and challenges" Proceedings of the IEEE, vol.91, no. 8, August 2003: 1247-1256.

[3] T. Antoine-Santoni, J. F. Santucci, E. De Gentili, B. Costa."Wildfire impact on deterministic deployment of a wireless sensor network by a discrete event simulation," 14th IEEE Mediterranean Electrotechnical Conference:, 5-7 May, Ajaccio, France, 2008.

[4] Z. Chaczko, F. Ahmad, "Wireless sensor network based system for fire endangered areas," 3rd International Conference on Information Technology and Applications, vol. 2, Australia, July, 2005: 203-207.

[5] ZigBee Standards Organization. (2006). ZigBee specification.

CHAPTER 8:

Power Engineering and Power Supply

Study on Low Frequency Oscillation of Wind Power System Based on HHT

XIE Hongling^{1, a}, YUE Ting^{1,b}

¹North China Electric Power University, Baoding, China. ^ahdlyq@163.com,^b616090807@qq.com.

Keywords: HHT; wind power system; low frequency oscillation; detection

Abstract. For the output of wind power system has the characteristics of randomness, volatility and intermittence, the voltage of wind power system low frequency oscillation is one of the most common fluctuations in the system. For the problem of low frequency oscillation, the limitations of the detection methods such as the Lyapunov linearization method, the Prony method, wavelet transform method are summed up, and a new detecting method named Hilbert-huang Transform(HHT) is put forward in this paper, which can detect the oscillation accurately and timely. To solve the problem of end effect in the process of empirical mode decomposition(EMD), B-spline empirical mode decomposition based on support vector machine is applied in dealing with the end issue. an extension of the original signal is applied. Then, calculating the average curve of the signal by B-spline interpolation method. Finally getting the intrinsic mode function(IMF) by empirical mode decomposition(EMD). The practicality of the method is verified by Matlab simulation.

Introduction

It is essential to develop other forms of energy for the problem of a gradually reduce of primary energy reserves. Renewable and clean wind gradually cause concern at home and abroad in the related field. Our country has massive land, abundant wind power, if we make full use of this energy, not only can we create economic benefits, but we can also effectively relieve the energy, and we also can provide long-term effective energy supply[1].

Wind power is vulnerable to natural climate. The output of wind power system has the characteristics of randomness, volatility and intermittence. Low frequency oscillation is one of the most common form of voltage fluctuation. It has serious impact on the power quality of wind power system, causes great harm to the sensitive loads. Severe low frequency oscillation can even leads to out-of-step and parallel off. and seriously restricts the large-scale development of wind power.

At the present, there are several common methods for low frequency oscillation detection in wind power system, such as Lyapunov linearization method, the Prony method, wavelet transform method. To some extent, these methods can complete the detection of low frequency oscillation, but any kind of method is not perfect.

To detect the real-time instantaneous amplitude and frequency of low frequency oscillation effectively and to offer amount of compensation measures to improve power reliability and power quality. This paper puts forward the BS-EMD method based on support vector machine HHT method to test the low-frequency oscillation. The simulation results prove the practicability of this method.

Method Introduction

HHT Introduction. HHT is a new developed method for signal analysis. This method consists the EMD and Hilbert transformation[2]. Through the EMD decomposition, signal can be decomposed into a series of IMF. The IMF is a signal which is approximate to single frequency components, which means at all times, there is only one signal frequency component. For each intrinsic mode function on Hilbert transform, we can get the instantaneous spectrum of each IMF.

The Principle of BS-EMD[3]. Empirical mode decomposition is a limited time filtering to get nonlinear and non-stationary signals called IMF which has the following two properties: ① The number of the points which past the extreme point and zero point is the same or differ at most one. ②At any point of the function, the mean value of the envelopes defined by the local extreme should be zero[4].

[a,b] is a finite interval. $\Delta a = u_0 < u_1 \dots u_{N-1} < u_N = b$. The b spline node values is u_i . The k times b-spline basis function is:

$$B_{i,k} = \frac{u - u_i}{u_{i+k-1} - u} B_{i,k-1}(u) + \frac{u_{i+k} - u}{u_{i+k} - u_{i+1}} B_{i+1,k-1}(u)$$
(1)

$$B_{i,1}(u) = \begin{cases} 1, (u_i \le u \le u_{i+1}) \\ 0, (others) \end{cases}$$

In the condition of the denominator in Eq.1 is 0, it will be defined by 0. The i times local support of the B spline function is

$$B_{i,k}(u) = \begin{cases} \ge 0, (u_i \le u \le u_{i+k+1}) \\ 0, (others) \end{cases}$$
(2)

The average of the signal m (t) calculated by b-spline is as follows:

$$m(t) = \sum_{j \in z} \omega_j B_{i,k}(t)$$
(3)

Among them: ω_j as the control points of b-spline, can be obtained by the moving average of the extreme. Moving average calculation formula for three times is as follows:

$$\omega_j = \frac{1}{4} \left[x \left(\mu_{j+1} \right) + 2x(\mu_{j+2}) \right] + x(\mu_{j+2}) \tag{4}$$

 μ_i is the extreme value point of the signal.

The process of the BS-EMD is: it is assumed that the original signal x (t) is infinitely. The difference function is: x(t) - m = h

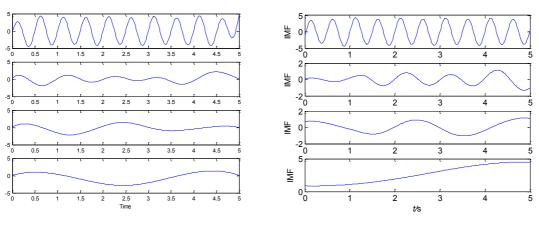
Take h as the new x(t) and repeat the above process, we can get c_i as IMFs .Stop until r is monotonic or |r| is very small. The result of the decomposition is as follows:

$$\mathbf{x}(\mathbf{t}) = \sum_{i=1}^{n} \mathbf{c}_i(\mathbf{t}) + \mathbf{r} \tag{5}$$

Examples of BS-EMD based on support vector machine

Using the original HHT and BS-EMD HHT method to analyze the signal

 $x = \sin(2\pi t) + 4\sin(4\pi t) + \sin(\pi t) + t$







In Fig.1, Each IMF has serious distortion. They have the endpoint effect and interior pollution. In Fig.2, The IMFs by the BS-EMD HHT are accurate. It proved that the method is better than the original method in applying to the signal analysis.

In reality, because of the wind power system voltage is affected by the natural environment, volatility is relatively complex, this paper will have the simulation analysis for wind power system low-frequency oscillation. Assume that the low frequency oscillation signals is as follows

 $x = 1.5e^{-0.2t}\cos(2\pi \times 1.5t) + 1.48e^{-0.7t}\cos(2\pi \times 0.5t)$

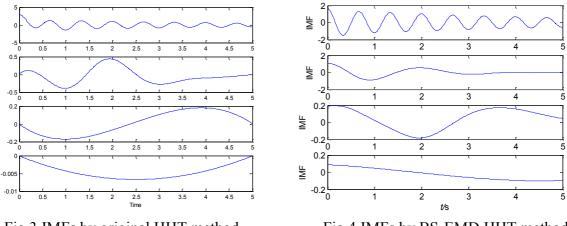
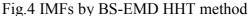


Fig.3 IMFs by original HHT method



With the BS-EMD, we can get the amplitude and frequency of IMF1 timely in Fig. 5. It helps us to analysis the signal by those information. There is a contrast of the calculated parameter and the desired value in Tab.1. The calculated parameters are close to the desired value. The method is feasible and accurate[5].

(6)

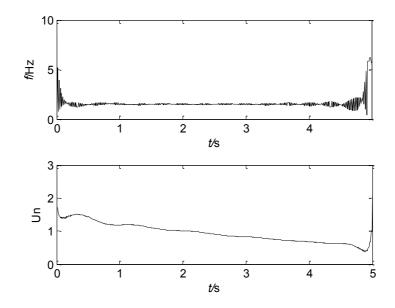


Fig.5 IMF1 amplitude, frequency

IMF	Calculated parameters				
	initial amplitude	Attenuation factor			
	[MW]	[Hz]			
IMF1	1.58	1.70	-0.22		
IMF2	1.53 0.56 -0.73				
IMF	Desired value				
	initial amplitude	F	Attenuation factor		
	[MW]	[Hz]			
IMF1	1.5	1.5	-0.2		
IMF2	1.48	0.5	-0.7		

Tab.1 Comparison of perfect parameters and parameters extracted by HHT

Summary

This paper applies HHT to the real-time and accurate detection of low frequency oscillation for wind power system. In order to solve the endpoint effect of EMD decomposition, we use BS-EMD based on support vector machine to manage endpoint effect. Matlab example simulation results show that the HHT can detect the situation of low frequency oscillation in wind power system effectively and in real time, can accurately judge the transient oscillation frequency and amplitude. Export wind power system is influenced by the natural environment, so the export is fluctuating. Practical problems are more complex than the research of low frequency oscillation in this paper and it is more difficult to detect oscillation. In order to strengthen the control of the wind power system.

References

- [1] Zhang Yuan, Gao Guodong, in: China Electric Power Press(2002).
- [2] . Li Yuntian, Zhao Yan, Li Nan. Analysis of Low Frequency Oscillation us Using HHT Method, volume 26 of Proceedings of the CSEE(2005).
- [3] Chen Qiuhui, Huang N E, Riemenschneider S, et al. A B-spline approach for empirical mode decomposition. Volume(24) of Advances in Computational Mathematics(2006).
- [4] Yi Jianbo, Huang Qi, Ding Lijie, analysis and improvement of the accuracy of the HHT method. Volume(29) of Power System and Clean Energy(2013).
- [5] Li Yuntian, Xie Jiaan, Zhang Fangyan, Li Xiaochen. The Application of The Low Frequency Oscillation Modal Parameters Extraction by HHT. Volume(27) of Proceedings of the CSEE(2007)).

CHP Microgrid Optimized Operation Based on Bacterial Foraging Optimization Algorithm

LI Rui^{1,a}, LI Peng¹

¹State Key Laboratory of Alternate Electrical Power System with Renewable Energy Sources (North China Electric Power University), Baoding 071003, Hebei Province, China

^a1130407682@qq.com

Keyword: micro grid, ptimal operation, CHP, bacterial foraging optimization

Abstract: CHP system with Energy saving, environmental protection, economic and other characteristics, have good prospects for the development and application value. This paper directe a micro grid system consisted by photovoltaic cells, wind turbines, fuel cells, microturbines, auxiliary boilers, thermal energy storage systems and batteries and heat load and electrical load. Considering various distributed power generation costs, environmental costs and micro-grid equipment maintenance costs, To meet the constraints of micro-grid operation, optimization of the different micro-grid distributed power and energy storage system power output, make the system's total operating costs are minimized. This paper analyzes the economic and environmental of micro-grid optimal operation characteristics, given a model of CHP micro-grid. For the cost of power generation and emissions of different weights, using bacterial foraging optimization(BFO) algorithm, through a numerical example verified the Correctness and effectiveness of mathematical model and optimization algorithm.

1. Introduction

Because of rising energy prices, an upcoming shortage of fossil fuels, environmental issues, power quality and power supply reliability problems, small-scale distributed generation has been rapid development[1]. Distributed generation of high efficiency, close to the load demand side, so that the energy generated by the nearest vicinity of use, thereby reducing transportation and transmission and distribution losses in.It contain renewable energy technologies (wind Turbine, photovoltaic,.biomass power generation,etc.) and non-renewable technologies (diesel generator, fuel cell and microturbine).Distributed generators for power distribution system is a challenge because it requires changing the operating strategy and distribution network design.

Although the impact of distributed generation may appear beneficial (environmental benefits, reduce distribution losses, power reliability, reduce new investments for the grid, more stable system, easy to expand based on ready-made products, etc.), however, individual applications of distributed generators may lead to an increase loss in the distribution system[2].Microgrid concept involves distributed generators, which provide electrical power to the users, and in some cases, the heating can also be microgrid sometimes through the PCC connected to the main power grid[3,4].Microgrid also includes some storage devices, such as batteries, flywheel energy storage, these devices to compensate for fuel cells, micro-turbine the disadvantage of slow response time to meet the load demand.Optimization of micro-grid operation must be considered to minimize costs, especially fuel consumption and environmental costs, the use of distributed combined heat and power(CHP) has become a strong competitor for the traditional centralized power plants. Ref. [5] shows the general efficiency of the microturbine 25%~35%, while the micro gas turbine combined heat and power efficiency up to 80%. CHP micro-grid is a complex energy system, there are various energy balance. Meet the electrical load demand in the premise, how to develop the systems based on micro-source configuration for next period of time to run programs(the DG power allocation in each period). To enable the system to obtain best value for money, is an important element of the microgrid for the study of economy operation[6]. So far, the domestic research has

only limited in the level electric power micro-grid[7], for CHP aspects involving less, but in foreign countries, this aspect of research is already underway.Ref.[8] studied by the microturbine, waste heat boiler and absorption chiller into CCHP system, establish a simple linear model of the system, and the system is running strategy for optimization.Ref.[9] in order to minimize the cost objectives, establish a CHP microgrid, the optimal allocation of various types of micro-source model, and using particle swarm optimization PSO algorithm to solve it.

In this paper, establish a microgrid system with renewable energy, and equipped with a CHP system and the auxiliary heating boilers, CHP system to achieve efficient use of energy, from the two aspect of operating costs and pollution emissions to detail analysis microgrid's role of the economic and environmental, and use bacterial foraging algorithm to solve numerical example shows that CHP microgrid system can indeed improve fuel efficiency and reduce emissions, has great economic and environmental benefits.

2 BFO algorithm

For the characteristics of CHP microgrid system economic and environment optimized, in this paper ,bacterial foraging optimization algorithm is a new bionic algorithm was adopted[10].Bacterial foraging algorithm wos proposed by K. M. Passino in 2002, accroding to the behavior of E.coli bacteria swallowe food in the human gut. This algorithm have some advantage of parallel search, easy to escape from local minima, etc. Become a new hot spot of biological heuristic calculation algorithm research.

This paper based on a simplify structure of CHP microgrid system ,has been built on the micro-economic model to simplify network analysis,can be sinplified analysis,due to the receach is microgrid daily load distribution,so this paper will defined the objective function containing operating costs and emission cost objective function,taking into account the power balance constraints,DG unit output maximum and minimum constraints,emission constraints.Using Matlab language tools to write the suitable optimization algorithm for the model and simulation calculations.

Bacterial foraging optimization algorithm by simulating the behavior of E.coli chemotaxis medicine, that are based on chemotaxis, eproduction and eispersal of these three operators iterative to optimize. The algorithm does not involve the influence of the group of bacteria and interactions mechanisms, mainly used to solve optimization problems locally[11].

1 Chemotactic

In the process of chemotactic, bacterial motion pattern includes forward and flip.Forward is defined as when the bacteria complete a flip, if the fitness is worth to improve, will continue to move in this direction, until it can no longer improve fitness, or has reached a predetermined threshold number of forward step.Flip is defined the unit step of the bacteria moves.The process of chemokine can be expressed as follows:

$$\theta^{i}(j+1,k,l) = \theta^{i}(j,k,l) + C(i) \frac{\Delta(i)}{\sqrt{\Delta^{T}(i)\Delta(i)}}$$
(1)

where $\theta^i(j,k,l)$ is the position of ith bacterium, jth chemotactic, kth reproductive, and lth elimination and dispersal step, C(i) is the moving length vector of ith bacterium, $\Delta(i)$ is unit direction vector, $\Delta \in (-1,1)$.

2 Reproduction

When a bacterium found food, it will try send singal give its near bacterial groups. This action helps other bacterial groups found nutrients more rapid. In the bacterial groups, signals between cells can be expressed as the following function:

$$J_{cc}(\theta, P(j,k,l)) = \sum_{i=1}^{S} J_{cc}^{i}(\theta, \theta^{i}(j,k,l))$$

= $\sum_{l=1}^{S} [-d_{attract} \exp(-W_{attract} \sum_{m=1}^{p} (\theta_{m} - \theta_{m}^{i})^{2})] + \sum_{l=1}^{S} [-h_{repelent} \exp(-W_{attract} \sum_{m=1}^{p} (\theta_{m} - \theta_{m}^{i})^{2})]$ (2)

where $Jcc(\theta, P(j,k,l))$ is added to the actural objective function with the time varying function. S is the total number of bacteria, P is the number of optimization variables, $d_{attract}$, $w_{attract}$, $h_{repelent}$ and $w_{repelent}$ are different coefficients.

After *Nc* chemotactic steps, a reproduction step is taken, *Nc* is the maximum step in the chemotactic process. In the reproduction step, half of healthy bacteria (with a higher value of the objective function) to survive, each of survival bacteria split into two identical bacteria, and then placed in the same location. Therefore, the total number of bacteria remain unchanged.

3 Elimination and Dispersal

Due to the consumption of nutrients or some other reasons, the number of living bacterium may gradually or suddenly changed, this may cause some bacteria were killed, move to another location within the area. To simulate this phenomenon, each of the bacteria are chosen to eliminate and diffusion with the probability is P_{ed} .

This paper put bacterial foraging algorithm applied to the microgrid optimal operation, and made the following improvements:

1)In the classical bacterial foraging algorithm, can eliminate and prevent the spread of beacteria, avoid falling into local optimum. But for the searched in a large constraint problem, it is difficult to find the global optimum. To overcome this problem, use the strategy of update bacterial location after each chemotactic step. With this improvement strategy, the bacteria have a better direction of movement, and improve the accuracy of local and global optimum.

Assume θ^{k_1} , θ^{k_2} and θ^{k_3} are the positions of three beactiria, k1, k2 and k3 are random integer between 0 and S, and $k_1 \neq k_2 \neq k_3$. The location of mutant bacteria can be determined as follows:

$$\theta_{mul}(j,k,l) = \theta^{k1}(j,k,l) + F \times (\theta^{k2}(j,k,l) - \theta^{k3}(j,k,l))$$

$$(3)$$

F is the mutation factor, it genetally between 0.1 and 1.Let $\theta_{new}^i = [\theta_{new1}^i, \theta_{new2}^i, \theta_{new3}^i]$ is the position vector of the bacteria, the new location of its elements is calculated as follows:

$$\theta_{new1}^{i} = \begin{cases} \theta^{i} & Cr_{1} > rand \\ \theta_{mut} & else \end{cases}, \quad \theta_{new2}^{i} = \begin{cases} \theta^{i} & Cr_{2} > rand \\ \theta_{best} & else \end{cases}, \quad \theta_{new3}^{i} = \begin{cases} \theta_{best} & Cr_{3} > rand \\ \theta_{mut} & else \end{cases}$$
(4)

Where θ_{best} is the location of bacteria when objective function get the minimum value. caculate the value of θ_{new1}^i , θ_{new2}^i and θ_{new3}^i , obtained the value of the objective function, if this value less than $J(\theta^i)$, their location will be replaced by θ^i .

2)Units moving step of bacterium is an important parameter for the speed of convergent and accuracy of global best optima. If the step size selected too large, the global best optima accuracy will be reduced, and if the selection is too small, then the convergence rate will be reduced. In Ref. [12], proposed a non-linear decreasing dynamic function to enhance the accuracy and search capabilities of the best optima. We use a dynamic function which is shown as follow:

$$C(i, j+1) = \left(\frac{C(i, j) - C(Nc)}{Nc + C(Nc)}\right)(Nc - j)$$
(5)

where j is chemotactic step, Nc is a predetermined parameter.

3 Simulation and results

In this paper, a CHP microgrid system was used as a caculate example based on a particular area, this system consist of PV,WT,ME,FC,CHP system and electrical and thermal storage devices, and through intelligent energy management system (IEMS) to manage the microgrid devices within the system. Various DG parameters within the system are shown in table 1.

_	Table1 DG parameters						
	ID	Туре	Min power (kW)	Min power (kW)	Start-up/shut-down cost (yuan/kW)		
_	1	MT	6	30	0.90		
	2	FC	3	30	1.16		
	3	PV	0	25	0		
	4	WT	0	15	0		
	5	ESS	-30	30	0		

set the weigheing coefficients of operating costs is 0.95 and weigheing coefficients of pollution emission cost is 0.05, at this time, the operating cost is much larger than the emissions cost, adjust DG output plan, obtained the minimum value of the total cost by through optimization calculation. Each types of DG 24 hour output are shown in figure 1. At this time, operating cost J_1 = 1165.89 yuan, emissions cost J_2 =110.45 yuan, at this case, although the lowest operating costs, but higher emissions, emissions of each types of pollutants within a day are :CO₂ is 1165.68kg, NO_X is 0.2925kg, SO₂ is 0.2683kg.

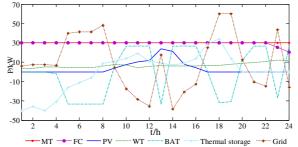


Figure1 Key consideration operating costs of the DG output

4 Conclusion

In this paper,under the premise of meet the load demand and distributed power output restrictions, taking into account the cost of electricity generation and pollutant emissions, proposed CHP microgrid model. For the cost of power generation and emissions of different weights, using bacterial foraging algorithm for optimal scheduling.

5 Acknowledgment

This work is supported by National Natural Science Foundation of China(50977029), and Natural Science Foundation of Hebei Province (E2013502074).

Reference

- [1] Molderink A, Bakker V, Bosman MGC, Hurink JL, Smit GJM. Innovative Smart Grid Technologies (ISGT); 2010. p. 1e8.
- [2] Gomez San Román T, Rivier Abad J. IEEE Trans Power Syst 2006;21(2):533-40.
- [3] Lasseter RH, Akhil A, Marnay C, Stephens J, Dagle J, Guttomson G, Meliopoulous A, Yinger R, Eto. The CERTS microgrid concept white paper for transmission reliability program, office of power technologies, US Department of energy;2002.
- [4] Lasseter RH. MicroGrids. Proc PES Winter Meet 2002;1:305-8.
- [5] Hawkes A D, Leach M A. Applied energy, 2009, 86(7): 1253-1265.
- [6] Wang Rui, Gu Wei, Wu Zhi. Automation of Electric Power System, 2011, 35(8): 22-27.
- [7] Ding Ming, Zhang Yingyuan, Mao Meiqin, et al. Automation of Electric Power System, 2009,33 (24): 78-82.
- [8] Li Jingzhao. Mode of domestic 300MW thermal power unit. Journal of North China Electric Power University (Hebei), 2005.
- [9] Lu Tai, Wang. JOURNAL OF SHENYANG INSTITUTE OF ENGINEERING (NATURAL SCIENCE) ,2008,04:306-309.

[10]Dong H;Ajith A;Jae H. Journal of Information Science, 2007,(18).

- [11] Liu Xiaolong, Zhao Kuiling. Journal of Computer Applications , 2012, 32 (3): 634-637.
 [12] Farhat I A, El-Hawary M E. IET generation, transmission & distribution, 2010, 4(9): 989-999.

Community Based of CHP Microgrid Optimal Operation

LI Rui^{1,a}, LI Peng¹

¹State Key Laboratory of Alternate Electrical Power System with Renewable Energy Sources (North China Electric Power University), Baoding 071003, Hebei Province, China

^a1130407682@qq.com

Keywords: CHP microgrid;optimization;load management;bacterial foraging optimization algorithm; Photovoltaic

Abstract: This paper presents a community-based CHP microgrid model for optimal operation. The model introduces a microgrid controller and consumption parameters, and that the existing restrictions, the optimization of microgrid operation.bacterial foraging optimization(BFO) algorithm was used to develop microgrid problems. Test results show the effectiveness of the model micro-grid operation.

1. Introduction

The need for more flexible power systems, changing regulatory and economic situation, energy conservation and environmental impact powered microgrid (MG) development, is expected to play an increasing role in the electric power system in the near future [1]. One of the important applications of MG units, is the use of small, modular residential or commercial units on-site service. MG units can choose to make them all the time at the lowest cost to meet customer load demands.

Demand response applications considering intertemporal load characteristics were proposed in [2]. A real-time demand response model was presented in [3]. The experimental results of applying peak pricing to residential customers were analyzed in [4]. The role of communication infrastructure to support demand response was described in [5]. Load control strategies for air conditioning/heating were investigated in [6]. An automatic framework for residential energy consumption scheduling representing a trade-off between minimizing the payment and the elapsed time for operating an appliance was proposed in [7]. These approaches would find the optimal load schedule of a single demand response-enabled customer which is based on time-dependent electricity prices. In this paper, the optimal operation of a community-based microgrid, including several residential customers, is explored. Microgrid could lower the cost of energy delivery, improve load-point reliability, enhance power quality for its customers, reduce power plant emissions, reduce investment costs on power transmission, and reduce the vulnerability of large-scale power systems.

In this paper, we rigorously study the MG components in terms of accuracy and efficiency of having a system model based on the costs of fuel, operation and maintenance, as well as the emission costs. The system model clearly has the potential to explain the costs in detail. However, developing the overall system model gives a possibility to study minimizing of the total cost of the system. Thus, it is important that the problem of minimization the cost as well as serving the load of the MG be investigated.

The second objective of this paper deals with solving the optimization problem which uses several scenarios to explore the benefits of having optimal management of the MG. The exploration is based on the minimization of running costs and is extended to cover a load demand scenario in the MG. It will be shown that by using a good system model, the optimization problem can be solved accurately and efficiently.

Our optimization method incorporates an explicit cost minimization criterion which is applied to the MG architecture. The formulation in this study to seeks the most economical generation to satisfy the load demand and constraints. The problem is decomposed into several stages, starting with building the system model which is an important stage to understand the problem. The next stage is the development of a new algorithm . The algorithm consists of determining at each iteration the optimal use of the resources available considering wind speed, temperature, and irradiation which are inputs to the model. If the produced power from the wind turbine and the photovoltaic is less than the load demand then the algorithm proceeds to the next stage here the other alternative are used according to the load amount and the cost of the resource.

2 Optimization problem

The goal we proposed of energy management are under the economy and environmental standards to provide electricity and thermal load. In this study, assumed that all of the electricity load demand supplied by DG, thermal energy generated is proportional to the CHP units electrical energy emitted. If the generated heat exceeds the thermal load demand, the excess heat will be deposited into thermal energy storage system, if it is below the thermal load demand, through the auxiliary boiler to compensate the energy needed. The micro-grid system's total cost objective function is as follows:

$$\min \quad F = \alpha J_1 + \beta J_2 \tag{1}$$

Where F is the total cost; J_1 and J_2 are operating costs and emissions costs of microgrid system, respectively; α and β are the weigheing coefficients of operating costs and of pollution emission cost, respectively. Different values of α and β means operating costs and of pollution emission cost considered are different, so optimal results will be different.

2.1 Operating cost minimization

Microgrid operating costs, including DG and auxiliary boiler fuel cost, maintenance cost, and start-up/shut-down costs, the cost of exchanging electrical power with the utility grid, the cost of supply natural gas for the auxiliary boiler. This objective function can be written as:

$$J_{1} = Min \sum_{t=1}^{T} \{\sum_{i=1}^{N_{g}} [u_{i}(t)P_{gi}(t)(B_{gi} + K_{OM_{1}}) + S_{gi}|U_{i}(t) - U_{i}(t-1)| + \sum_{j=1}^{N_{Es}} [u_{j}(t)P_{Sj}(t)B_{Sj}] + P_{Grid}(t)B_{Grid}(t) + (C_{gas} + K_{OM.bl})G_{bl}(t)\}$$
(2)

Where Ng is the total number of generators; N_{Es} is the total number of batteries; B_{gi} and B_{Sj} are the total electricity /heat generating cost of ith DG and jth of storage device; $P_{gi}(t)$ is power output of the ith DG unit; $P_{sj}(t)$ is charge/discharge power of the jth storage device; $U_i(t)$ is switching state of each unit at hout t; S_{gi} is the start-up/shut-down costs of ith DG unit; B_{Grid} is the price of purchase clectricity energy from utility grid; is the price of natural gas in $\frac{1}{M^3}$. K_{OMi} and $K_{OM,bl}$ are the cost of maintenance conefficients of ith DG unit and auxiliary boiler; $P_{grid}(t)$ is the power of purchase (sale) electricity between microgrid and utility grid, could be calculated as follows:

$$P_{Grid}(t) = P_L(t) - \left[\sum_{i=1}^{N_g} P_{gi}(t) + \sum_{j=1}^{N_{Es}} P_{Sj}(t)\right]$$
(3)

It must be mentioned that, when its value larger than zero,microgrid purchase electricity energy from utility grid; when its value less than zero,microgrid sale electricity energy of utility. **2.2 Pollutants emission minimization**

The objective function is about atmospheric pollutants, such as NO_x , SO_2 , and CO_2 . About pollutant emissions mathematical formula shown as follows:

$$J_{2} = Min \sum_{t=1}^{T} \left[\left(\sum_{i=1}^{T_{E}} \delta_{j} \left(\sum_{j=1}^{N} EF_{ij} P_{gi}(t) \right) + P_{bl}(t) EF_{bl} \right) \right]$$
(4)

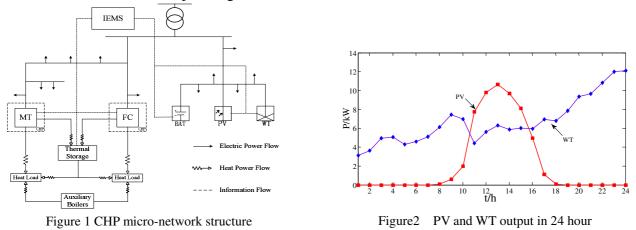
Where EF_{ij} is emission factor of emission type j pollutant emissions from the ith DG unit; T_E is the type of pollutant emissions (NOx, SO2 and CO2); δ_j is emission cost of type j pollutant emission; N is the total number of pollutant generators(MT,FC); E_{bl} is emission factors for auxiliary boilers.

3 Simulation and results

3.1 Microgrid structure and parameters

In this paper,a CHP microgrid system was used as a caculate example based on a particular area,this system consist of PV,WT,ME,FC,CHP system and electrical and thermal storage devices, and through intelligent energy management system (IEMS) to manage the microgrid devices within the system, the structure are shown in figure 1.the MT and the FC are considered as CHP systems, generating according to the thermal load demand.Microgrid connection with utility grid, can supply the electrical energy for the microgrid at the necessary time,make full use of the different of peak and valley electricity price,adjustments the plan of sale/ purchase electricity energy,in order to obtain greater economic benefits.The price of natural gas is 2.5 yuan/m3,the time period studied in 1 day, unit interval of 1 hour. PV and WT are intermittent energy sources,its output can not controllable, the predicted of PV and WT output at different times are shown in figure 2.

A lot of different types of load in the demand side in the microgrid system, including thermal load and electrical load, the energy intelligent management system (IEMS) under different load values at each time, to make the best optimal generation scheme.



3.2 Optimization Results

adjust DG output plan, obtained the minimum value of the total cost by through optimization calculation.Each types of DG 24 hour output are shown in figure 3.At this time,operating cost J1= 1203.87yuan,emissions cost J2=101.97yuan,at this case,although the lowest operating costs,but higher emissions, emissions of each types of pollutants within a day are:CO2 is 1078.68kg,NOX is 0.2633kg,SO2 is 0.2414kg.We can be seen from the figure,when the electricity price is lower than generation costs,can increase the purchase of electricity from the utility grid,to meet the electrical load and the battery charging within the system,reduce the output of the DG,to save fuel costs and reduce emissions.When the electricity price is higher than generation costs,the DG will be in the maximum output,meet the electrical load,and sale electricity energy to the grid,this action will not only be able to achieve greater benefit, but also to ease the pressure of peak load.

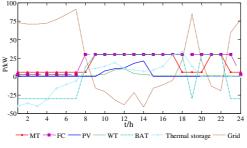


Figure 3 Final optimization results

4 Conclusion

In this paper,under the premise of meet the load demand and distributed power output restrictions, taking into account the cost of electricity generation and pollutant emissions, proposed CHP microgrid model. For the cost of power generation and emissions of different weights, using bacterial foraging algorithm for optimal scheduling.

5 Ackonwledge

First and foremost, I would like to show my deepest gratitude to my supervisor, Dr. Li Peng, a respectable, responsible and resourceful scholar, who has provided me with valuable guidance in every stage of the writing of this thesis. Without his enlightening instruction, impressive kindness and patience, I could not have completed my thesis. His keen and vigorous academic observation enlightens me not only in this thesis but also in my future study.

This paper is based on the fund program :National Natural Science Foundation of China(50977029); Natural Science Foundation of Hebei Province (E2013502074).

Reference

- [1] Hernandez-Aramburo, C. A., and Green, T. C., and Mugniot, N., IEEE Transactions On Industry Applications, Vol. 41, Issue. 3, May/June. 2005, p. 673-681.
- [2] A. Khodaei, M. Shahidehpour and S. Bahramirad, IEEE Trans. Smart Grid, to be published.
- [3] A. J. Conejo, J. M. Morales and L. Baringo, IEEE Trans. Smart Grid, vol. 1, no. 3, pp. 236-242, Dec. 2010.
- [4] F.Wolak, Residential customer response to real-time pricing: The Anaheim critical peak pricing experiment, Center for the Study of Energy Markets, Working Paper 151, May 2006.
- [5] M. Ann-Piette, G. Ghatikar, S. Kiliccote, D. Watson, E. Koch, and D.Hennage, J. Comput.Inf. Sci. Eng., vol. 9, pp. 1 – 9, Jun. 2009.
- [6] S. Tiptipakorn and W. J. Lee, North Amer. Power Symp., Las Cruces, NM, Oct. 2007.
- [7] A. H. Mohsenian-Rad and A. Leon-Garcia, IEEE Trans. Smart Grid, vol. 1, no. 2, pp. 120-133, Sep.2010.
- [8] Bhuvaneswari R, Edrington C S, Cartes D A, et al. North American Power Symposium (NAPS), 2009. IEEE, 2009: 1-6.

Power Supply Efficiency Analysis and Techno-economic Evaluation of IGCC Projects

XIE Chuansheng^{1, a}, ZHAO Chenchen^{1, b}, ZHONG Pengyuan^{1, c}, ZHOU Chengying^{1, d}

¹North China Electric Power University, 2nd Beinong road, Changping disctrict, Beijing, China ^axiecs@sohu.com, ^byiyizhaochen@163.com, ^czpy0401@163.com, ^d120671552@qq.com

Keywords: integrated gasification combined cycle; power supply efficiency; techno-economic evaluation

Abstract. Integrated gasification combined cycle (IGCC) is an efficient, low-pollution clean coal power generation technology and efficient use of IGCC technology is helpful to realize clean conversion and comprehensive utilization of coal resources in China. This paper analyzed the factors that influence the power supply efficiency of IGCC power plants, determined assessment model for power supply efficiency of IGCC power plants. Then based on IGCC power plant construction specific data including power supply efficiency, combining the general technical and economic evaluation of the project, the technical and economic evaluation step of IGCC plant was determined. The economic evaluation of IGCC power plant was carried out as well as sensitivity analysis in terms of static total investment, utilization hours and standard coal tax price. The results showed that introduced IGCC of 40 megawatt had higher tariff and utilization hours had maximum impact on tariff.

Introduction

With emerging of increasingly serious environmental pollution, use of new technology to change the status quo of energy consumption and taking lower carbon development path have become important strategy in China. Integrated gasification combined cycle technology has high power generation efficiency and better environmental performance ^[1]. In the current technical level, the net efficiency of IGCC power generation is up to 43% to 45% and pollutants emission is only 1/10 of conventional coal-fired power plants. What's more, the desulfurization efficiency is up to 99%, with sulfur dioxide emission level at around 25mg/Nm3 which is far below the emission standard 1200 mg/Nm3. Therefore, IGCC power plants attract more and more attention at home and abroad ^[2-4]. However, IGCC plants require significant investments in engineering design and development costs, which limits its rapid development. So it is important to study practical techno-economic assessment methods of IGCC power plants.

At present, domestic and foreign experts have carried out some related research on technical and economic characteristics of IGCC power plants. For example, literature [5] simulated IGCC power plant based on dry pulverized coal gasification technology using process simulation software Aspen Plus; literature [6] analyzed economic performance of IGCC plants by economic performance computing software developed by the U.S. Department of Energy; literature [7-8] did efficiency and economy evaluation of IGCC power plant CO₂ capture technology. Power supply efficiency analysis and techno-economic evaluation of IGCC projects under the status quo of technological development and grid development is basis for feasibility evaluation of IGCC power plant construction. Therefore, techno-economic evaluation of IGCC projects is necessary.

Based on IGCC power supply efficiency impact factors analysis and estimation formula, according to general power plant construction in China and level of foreign technology, parameters of IGCC projects were set. Then economic evaluation and sensitivity analysis of 40 megawatt IGCC plants were carried out, which showed feasibility of IGCC power plants and construction issues needing attention.

IGCC plant power supply efficiency

A. Factors affecting IGCC power supply efficiency

Integrated gasification combined cycle (IGCC) power generation technology is based on advanced power systems combining gasification and combined cycle and it is composed of two parts, namely, coal gasification and purification parts and gas-steam combined cycle power generation parts. IGCC power plant process has full use of gas, less pollution characteristics^[9].

Technical feasibility and economy of IGCC power plants have great relationship with the power supply efficiency because gasification, combustion turbines and other technical parameters determine the power supply efficiency values and the latter has a relationship with investments, costs and earnings. Therefore, efficiency study helps its technical and economic evaluation. In this paper, technical parameters and corresponding power supply efficiency of typical IGCC power plants are summarized. Fuel, gasifier, gas turbine and power supply efficiency of six IGCC plants are shown in Table 1.

	Netherlands	Spain	USA	USA	Italy	Japan
IGCC plants	Nuon Buggenum	Elcogas Puertollano	Wabash River	Tampa	ISAB	Negishi
fuels	coal	coal, petroleum coke	coal	coal	asphalt	bitumen
ASU	100%	100%	0	0	0	0
single gas turbine output [MW]	159	222	192	192	166.6	270
net output [MW]	253	300	265	253	521	342
LHV	43.2%	45%	38.3%(HHV)	36.7%	<40%	36%

Table 1 Comparison between gas turbine and efficiency of IGCC

In general, the key factors affecting power supply efficiency of IGCC power plants mainly include following four categories.

- Gasifier type. Under normal circumstances, cold gas efficiency of gasifier for dry pulverized coal gasification is higher than that of coal water slurry gasification because the latter cannot spend a lot of energy in evaporating water in the coal water slurry gasification.
- Fuel quality. The species of Coal and fuel quality will affect gasification efficiency of gasifier. Higher quality coal has higher gasification efficiency, while low-quality coal in high content of ash and moisture will evaporate water vapor and melt ash when coal gasification.
- Partial integral rate of air separation unit (ASU). The more the share of air ASU inlet provided by gas turbine compressor, the higher the power supply efficiency of IGCC because without inefficient separate compressor, the power supply efficiency will be greatly reduced.
- Gas-steam combined cycle. The main power equipment of IGCC is gas turbine whose output is 60%~70% of total output, so power supply efficiency of IGCC depends largely on the efficiency of gas turbine. The key parameters are initial temperature T3 and pressure ratio. The higher these two parameters, the greater the output of the gas turbine. Accordingly, power supply efficiency of IGCC will reach higher level.

B. IGCC power supply efficiency evaluation

Based on above analysis of factors affecting power supply efficiency of IGCC power plants, combining general thermal power supply efficiency calculation methods, this paper considers power supply efficiency of IGCC power plants can be approximated by Eq. 1:

$\eta_{IGCC} = \eta_B \times \eta_{CCSG} \times (1-\eta_e)$.

(1)

Where, η_{IGCC} is power supply efficiency of IGCC power plants; η_B is energy conversion efficiency of coal gasification system (including gasification, gas cooler and ash desulfurization unit, etc.), and the value is approximately equal to thermal efficiency of coal gasification systems; η_e is IGCC power consumption rate.

The value of η_B relates to the type of gasifier, coal supply conditions, gas desulfurization ash methods, and so on. The η_B value of dry coal gasification system is more than that of coal slurry feed gasifier.

For IGCC plants, power generation efficiency shall be calculated based on energy input involved gas turbines act, and the value is slightly higher than power supply efficiency of conventional natural gas combustion combined-cycle. Combined cycle power generation efficiency can be formulated as Eq. 2:

$$\eta_{\text{CCSG}} \approx (1.05 \sim 1.08) \times \eta_{\text{CCSG}}^{\text{net}}$$
(2)

Combined cycle power generation efficiency η_{IGCC} has relationship with gas turbine models, waste heat boiler types and steam turbine unit configurations. For a gas turbine supporting a waste heat boiler and steam turbine group, η_{IGCC} is a function of the gas turbine model and provided by gas turbine manufacturers. Table 2 shows correspondence between gas turbine combined cycle efficiency and gas turbine models.

Table 2 Gas turbine combined cycle efficiency table						
gas turbine models	GE S109E	GE S109FA	GE 109H	V94.2	V94.3A	
combined cycle power ISO[MW]	193.2	390.8	520	235	383	
combined cycle efficiency η_{ccsg}^{net} [%]	52	56.7	60	52	58	

In terms of IGCC plants using completely separate low-pressure air separation and gas turbine without nitrogen reinjection, power consumption rate η_e can be controlled at 11% ~ 13%. For IGCC plants using completely separate high-pressure air separation and gas turbine with nitrogen reinjection, power consumption rate η_e is about 20%. For IGCC plants using partial holistic air separation system and gas turbine with nitrogen reinjection, if 50% of air that these IGCC plants need is extracted from gas turbine compressor, η_e is about 12%~13%.

IGCC project proposal and techno-economic evaluation steps

A. IGCC project proposal parametric analysis

The program will introduce two 2000 t / d Shell gasifier and 1 GE 9F gas turbine, and the rest equipments are domestic procurement. Specifically, combined cycle uses a gas turbine supporting a waste heat boiler and steam turbine group. The whole plant net output is 40 megawatt, power supply efficiency for 42%, and power consumption rate for 13%. As for emissions, the carbon content of standard coal is 74%, the sulfur content for 3%, and the entire system desulfurization rate for 99.8 %.

For economic parameters, Planning Institute estimated the hospital of $6208 \sim 7751$ Yuan / kWh for IGCC plants in 2006 IGCC Seminar, so this paper sets the unit cost of 8000 Yuan / kWh. Utilization hour is 5,000 hours and total construction period is 36 months. Sources of funding are 20% of the registered capital and 80% of the loan. Loan period is 15-year (including construction period). Using the straight-line depreciation method, depreciation period is 15-year and residual rate is set at 5%. What's more, fixed capital formation is 95%.

B. IGCC project techno-economic evaluation steps

Technical differences between different technical solutions for IGCC power plants embody in the efficiency of power generation, power consumption rate, the total static investment, availability and environmental emissions and other technical and economic parameters. Technical and economic evaluation key steps include determination of the project plan, estimation of cost-effectiveness, financing plan, the financial economic evaluation and uncertainty analysis ^[10]. Evaluation method process is shown in Fig. 1.

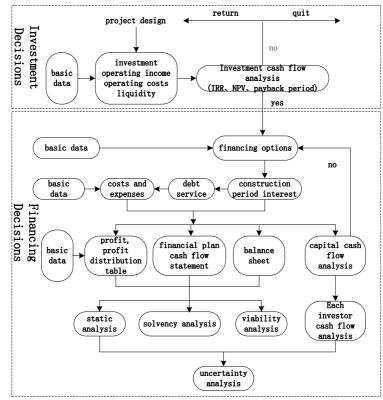


Fig. 1 IGCC project economic evaluation flowchart

IGCC project techno-economic evaluation results and analysis

A. Economic evaluation results

Tariff is set in accordance with plant sales revenue meeting the total cost of power generation, sales taxes and surcharges, income tax, corporate statutory fund, Community Chest and loan repayment and it should also meet investors registered capital for 8% of internal rate of return determined conditions. It was determined that at this stage, for IGCC plant of 40 megawatt level, tax tariff in operating period was 438.75 Yuan / MWh, IGCC project life cycle cost of power generation, asset-liability ratio and cumulative net cash flow are shown in Fig. 2, Fig. 3 and Fig. 4, respectively.

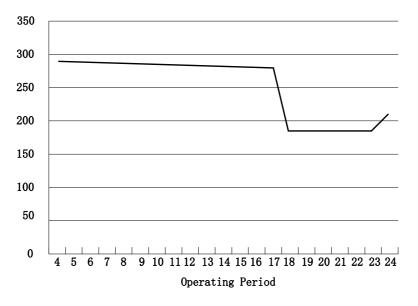


Fig. 2. Generation costs in operating period of 40 megawatt IGCC project

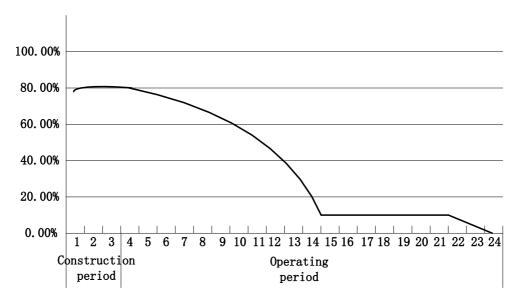


Fig. 3. Asset-liability ratios in operating period of 40 megawatt IGCC project

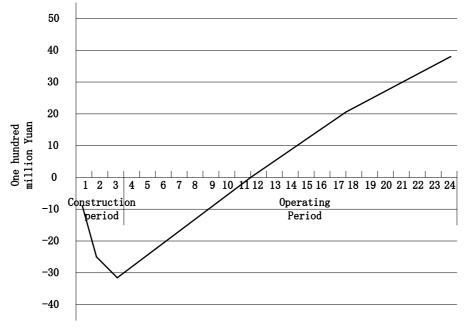


Fig. 4. Full investment cumulative net cash flow of 40 megawatt IGCC project *B. Sensitivity analysis*

This paper made static total investment, utilization hours of coal prices and tax standard coal price in the range of \pm 30% change respectively. The results show that, changes in magnitude of investment margin rate, net profit margin of capital and investment tax rate are smaller, while IRRs of full investment and own funds are both greater than benchmark yield 7%. These results illustrate strong anti-risk ability of 40 megawatt IGCC plant. Impacts of static total investment, utilization hours and tax standard coal price on tax tariff are shown in Table 3.

investment	tax tariff	utilization	tax tariff	standard	tax tariff
[Yuan / kW)]	[Yuan/MWh]	hours	[Yuan/MWh]	coal price	[Yuan/MWh]
		[hour]		[Yuan / t]	
6400	384.93	3500	552.83	100	317.07
7200	411.84	4000	505.44	200	352.17
8000	438.75	5000	438.75	450	438.75
8800	465.66	6500	376.36	600	490.23
9600	491.4	7000	361.53		

The corresponding intervals of three factors in $\pm 30\%$ change magnitude are as follows: Unit costs are 5600 ~ 10,400 Yuan / kW, standard coal prices are 315 ~ 585 Yuan / ton and utilization hours are 3500~6500 hours. The results show that utilization hour has maximum effect on tariff, followed by the total investment, and finally the standard coal price.

Comparing the results of this IGCC project and techno-economic evaluation results of a 2×60 megawatt of supercritical power plant in China^[11], the results show that tariff of the former is higher than that of the latter and the difference is about 111 Yuan / MWh. Therefore, the construction of IGCC power plants should consider that the site should be selected at a higher price affordability region and should be given higher tariff or preferential policies to encourage the development of this clean and efficient coal gasification power generation technology.

Conclusions

In this paper, the power supply efficiency of IGCC plants was analyzed and technical and economic evaluation of IGCC projects was carried out. The main conclusions are as follows:

- Evaluation results have relationship with technical and economic parameters, and these parameters depend largely on technological level and economic development current situation in China.
- Studies on power supply efficiency and techno-economic evaluation of IGCC projects help policy makers and technical personnel to understand economy of IGCC projects and issues that need attention, which will help promote the development of IGCC.

Refferences

- [1] H. Liu, W. Ni, Z. Li, and L. Ma, Energy Policy, vol. 36, no. 1, pp. 1-11, 2008
- [2] Rezvani, S., Huang, Y., McIlveen-Wright, D., Hewitt, N., and Mondol, J. D., Fuel, vol. 88, no. 12, pp. 2463-2472, 2009
- [3] Huang, Y., Rezvani, S., McIlveen-Wright, D., Minchener, A., and Hewitt, N., Fuel Processing Technology, vol. 89, no. 9, pp. 916-925, 2008
- [4] Shinada O, Yamada A, and Koyama Y., Energy Conversion and Management, vol. 43, no. 9, pp. 1221-1233, 2003
- [5] J. Meng, J. Xiong, and H. B. Zhao, Journal of Engineering Thermo physics, vol. 34, no. 1, pp. 40-44, 2013
- [6] H. Zhang, H. T. Zheng, Z. Li, and W. D. Ni, Gas Turbine Technology, vol. 16, no. 3, pp. 6-12, 2003
- [7] Chen C., and Rubin E. S., Energy Policy, vol. 37, no. 3, pp. 915-924, 2009
- [8] Descamps C, Bouallou C, and Kanniche M, Energy, vol. 33, no.6, pp. 874-881, 2008
- [9] Pérez-Fortes, M., Bojarski, A. D., Velo, E., Nougués, J. M., and Puigjaner, L., Energy, vol. 34, no.10, pp. 1721-1732, 2009
- [10] Kaldellis J K, Vlachou D S, and Korbakis G, Energy Policy, vol. 33, no.15, pp. 1969-1985, 2005
- [11] Zhaofeng, X., Hetland, J., Kvamsdal, H. M., Zheng, L., and Lianbo, L., Energy Procedia, vol. 4, pp. 1933-1940, 2009

Study on Relationships between High-frequency High-voltage Pulse Breakdown Voltage of Air-Gaps and Pulse Delay Time

Lili Li^{1, a}, Yulong Wang^{1, a} and Hongda Yang^{1, a}

¹Harbin University of Science and Technology, College of RongCheng, China ^aFly712@126.com

Keywords: High-frequency and High-voltage Pulse Voltage, Breakdown Voltage, Pulse Delay Time, Pulse Coefficient.

Abstract. In the paper, power frequency and high-frequency high-voltage pulse breakdown voltage of air-gaps were measured by circuits of spark gap switches respectively, and then output waveforms were obtained by sampling circuits, finally a large number of data in experiments were recorded and were drawn into curves. It can be seen from curves: firstly, relationships between pulse breakdown voltage of air-gaps and pulse delay time or between pulse breakdown voltage of air-gaps and pulse delay time or between pulse breakdown voltage of air-gaps and pulse delay time or between electrodes are different, secondly, relationships between pulse breakdown voltage and air-gap distances are analyzed under 100kHz pulse voltage when electrodes are spherical electrodes.

Introduction

In the early days, the high-voltage pulse technology is mainly used in national defense and scientific research, such as military radar, nuclear weapons simulation source, particle beam weapon and high-energy physics research, etc [1,2]. Until the 1990s, it begins to turn into civil fields, for instance flash photography, environmental science, irradiation industry, and the like [3,4]. In the last ten years, it is applied more and more widely and enters into the rapid development, such as electrostatic precipitation, high voltage pulse sterilization, and high voltage pulse uninterruptible power supply and so on. In fact, the high-voltage pulse technology obtains the peak power through condensing the pulse energy on time axis in essence, which's biggest feature is extreme high instantaneous peak power (several hundred kW to MW, even GW and TW) and smaller mean power (a few hundred kW).

In high-voltage pulse equipments, switches' properties limit the most important characteristics of the output pulse, such as delay time, repetition frequency, voltage amplitude, and so on [5]. So limitingdevices usually adopt those switches, for instance thyratron, ignitron, spark gap switch, liquid switch, solid switch, magnetic switch and so on. In the paper, gas spark switches are used to ensure pulse characteristics.

The high-voltage pulse technology is applied more and more widely, it is because that there is some scientific significance, for example influencing factors of pulse voltage amplitude, shape, frequency, effective breakdown time and breakdown process when high-frequency voltage is applied to air-gaps between the two electrodes and so on. In the paper, breakdown processes are studied in experiments and relationships between voltage amplitude and breakdown time in high-voltage pulse voltage are analyzed in detail.

Types and Parameters of Pulse Voltage

There are two kinds of high-frequency and high-voltage pulse waveform, which are index pulse and quasi square wave pulse (or square wave pulse) respectively, and their waveforms are shown in Fig. 1.

In breakdown experiments, it was found that pulse breakdown voltage had been higher than dc or ac breakdown voltage when voltages were applied to break down the air-gaps especially in non-uniform electric field. It can be seen that the amplitude of pulse voltage becomes U_m if normal breakdown voltage is U_o when the air-gap is broken down, and breakdown time delay τ is which is the

time between U_o and breakdown voltage, in addition to the ratio coefficient β ($\beta=U_m/U_o$) which is pulse coefficients [6,7]. Obviously, pulse coefficient is not constant and maybe change with pulse voltage waveforms, electrode shapes and distances between electrodes.

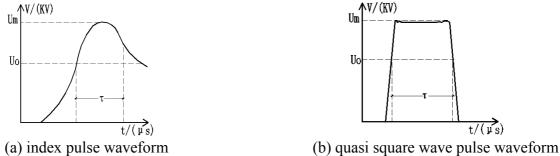


Fig. 1 High-frequency high-voltage pulse waveforms

Parameters Measurements of Breakdown Voltage in Air-Gaps under High-frequency and High-voltage Pulse Voltage

High-frequency and High-voltage Pulse Voltage Generator. It is shown in Fig. 2 that the typical circuit of spark gap switches to produce high-frequency and high-voltage pulse voltage. In Fig.2, the step-up transformer B_1 can raise voltage to thousands of volts. As transformer's secondary voltage rises, the voltage charges to capacitor C_1 through primary coil L_1 of transformer B_2 , and then the voltage U_{ab} on the air-gap G_1 increases with the increase of the voltage on C_1 . When U_{ab} reaches to the igniting voltage of G_1 , the air-gap G_1 breaks down immediately. It can be seen that the attenuation oscillatory discharge pulse is produced by R-L-C discharge circuit which is made up of C_1 , L_1 and G_1 .

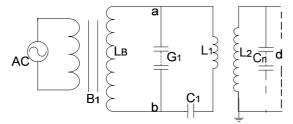


Fig. 2 The typical circuit of spark gap switches

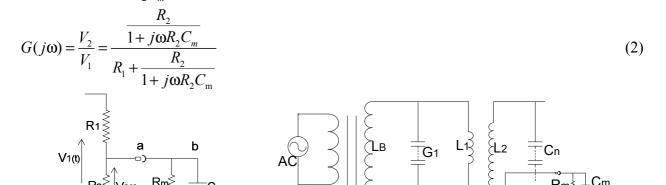
The amplitude of oscillation process becomes zero after over 20 cycles, and its duration time (a wave train) is $10^{-4} \sim 10^{-5}$ s [8]. When oscillation process sustains a wave train, the current in the circuit becomes zero, and then G₁ is switching out after that secondary voltage generated by the B₁ charges to C₁ again. The air-gap is broken down in G₁ again when the voltage of G₁ arrives at the igniting voltage, and then a high-frequency oscillation wave train is generated. In general, G₁ can be broken down two or three times in each half cycle, and the process is always maintained. The amplitude of oscillation wave train is close to amplitude of igniting voltage, which is about kilovolt level, and then it is raised by tubular transformer B₂, finally there is high-voltage and high-frequency pulse voltage at the voltage level of thousands of volts at the ends of d.

In the article, the capacity of transformer B_1 is 35kVA. The capacitor C_1 is obtained by multiple high-voltage capacitors in series or in parallel which's dielectric strength is 9kV, and the air-gap G_1 is made up of several air-gaps which every air-gap distance is 2mm. adjustable inductance L_1 can adjust the oscillation frequency of the circuit, and the role of current-limiting resistance is to protect the transformer, and C_n is the discharge capacitance, finally the ends of d can output high-frequency and high-voltage pulse voltage. In the circuit of spark gap switches, breakdown voltages are measured at G_1 applied power frequency pulse voltage and at C_n applied high-frequency pulse voltage respectively.

Circuits Measuring Pulse Voltage Parameters. It is shown in Fig. 3 that the circuit of resistor divider ignoring stray capacitance to ground, and U_{ab} in the Fig. 2 was measured by the resistor divider.

In Fig. 3, R_1 and R_2 are connected in series to divide voltage which's relationship is that R_1 is greater than R_2 , and R_2 is low resistance and parallels with impedance of the measuring equipment, so that the voltage ratio is affected. The measuring signal is transmitted from resistor divider to oscilloscope through the terminal matching coaxial cable when high-frequency pulse voltage is applied. The input impedance of oscilloscope is usually expressed as the impedance which is a megohm resistor R_m and a capacitor C_m about 10~50pF in parallel, and capacitor of coaxial cable is generally in the range of 20~100pF/m. The voltage ratio is shown in eq. 1, and the transfer function gotten by the plural form is shown in eq. 2. The output voltage $V_2(t)$ can be calculated through system theory.

$$a = \frac{V_1}{V_2} = \frac{R_1 + \frac{R_2}{1 + j\omega R_2 C_m}}{\frac{R_2}{1 + j\omega R_2 C_m}}$$
(1)



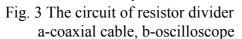
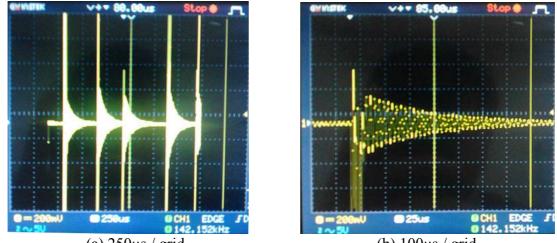


Fig. 4 Circuit measuring discharge current measured a-coaxial cable, b-oscilloscope

It is shown in Fig. 4 that the output current is measured by high-frequency power resistance R in the discharge output place and the output signal through R is transmitted to oscilloscope through the terminal matching coaxial cable.

High-frequency and High-voltage Output Current Waveforms. According to circuits in the Fig. 3 and Fig. 4, high-frequency and high-voltage pulse discharge waveforms of C_n are shown in the Fig. 5.



(a) 250µs / grid

(b) 100µs / grid

Fig. 5 High-frequency and high-voltage pulse discharge waveforms of C_n

Waveforms of Fig. 5 are discharge waveforms of C_n which's frequency was 140kHz, and properties of high-frequency pulse voltage can be seen from Fig. 5. It is seen from Fig. 5 that electromagnetic interference increases with the increase of frequency from 50kHz to 1MHz which

decreases the stability of the measured data. It is found that the high-frequency and high-voltage breakdown voltage of air-gaps stabilizes relatively from 50kHz to 150kHz in experiments.

Relationships between Breakdown Voltage of Air-Gaps and Pulse Delay Time or Pulse Frequency

When dc, power frequency or audio frequency voltage is applied on air-gap, the breakdown voltage is the same. In these cases, the breakdown voltage is always determined by voltage amplitude. If pulse voltage or high-frequency voltage is applied on air-gap, there are vastly different, in other words, when the pulse voltage is applied on air-gap, the breakdown voltage is closely related to pulse time delay τ , and when the high-frequency voltage is applied on air-gap, the breakdown voltage is closely related to pulse time delay τ , and when the high-frequency voltage is applied on air-gap, the breakdown voltage is closely related with frequency.

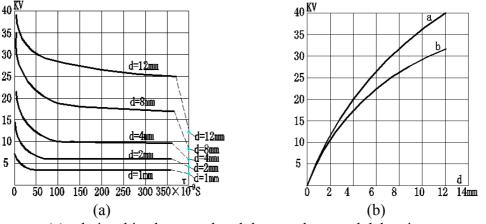
Relationships between Breakdown Voltage of Air-Gaps and Pulse Delay Time. The delay time coefficient stands for breakdown time under certain conditions. The higher the voltage, the faster the dissociation process. So it is predicted that the time delay τ is small when U_m is greater than U_o, in other words, the time delay τ should be large when pulse coefficient is small.

According to pique formula, the relationship between pulse coefficients β and delay time τ is shown in eq. 3 and α is a coefficient determined by electrodes and waveforms in eq. 3.

$$\beta = 1 + \frac{\alpha}{\sqrt{\tau}} \tag{3}$$

The pulse coefficient in power frequency pulse voltage was discussed. If the electric field was uniform electric field and every air-gap distance was 2mm, the breakdown voltage of air-gap was 8.4kV when the power frequency voltage was applied. But when the pulse voltage was applied, τ was 2×10^{-8} s, α was 2.678×10^{-5} (experience value), the breakdown voltage of air-gap was 10kV, and the pulse coefficient β was 1.19. In the Fig. 6(a), it is shown that the relationship between breakdown voltage and delay time τ when electrodes are needle electrodes and the air-gap distance is not large. The points on the right side are obtained by applying an applied voltage (dc voltage or ac voltage) for a long time, and pulse coefficient is $2 \sim 2.2$ when τ is 10^{-7} s, meanwhile pulse coefficient is up to 3 when τ was 10^{-8} s. For example, when the distance between needles is 12mm, τ was a few microseconds, pulse coefficient reaches to 2. Finally they are seen from results as follows:

- 1. When τ is $10^{-5} \sim 10^{-6}$ s, diameter of the spherical electrodes is 62.5mm and spark gap distance is 150mm, the pulse coefficient is 1.1.
- 2. Pulse coefficient may be associated with not only distances between the electrodes but also polarities of the needle electrode in the needle-plate electrode system. When the needle electrode is electronegative, the pulse coefficient is very large.
- 3. Air-gaps break down in a non-uniform electric field, and the pulse coefficient is very large.



(a) relationships between breakdown voltage and delay time(b) relationships between breakdown voltage and distanceFig.6 Relationships of breakdown voltage and delay time or distance

Relationships between Breakdown Voltage and Frequency. In this paper, power frequency breakdown experiments of air-gaps were done in G_1 and high-frequency breakdown experiments of air-gaps were done in C_n during 50kHz~1MHz in the circuit of spark gap switches. Breakdown voltage curves are shown as Fig. 6(b) using different electrodes in the condition of high-frequency voltage and power frequency voltage respectively, which curve a is measured under power frequency voltage, and curve b is measured under 100kHz voltage. It is found that 100kHz voltage is lower than power frequency voltage (about 20%).

Conclusions

The pulse breakdown voltage of air-gaps is higher than dc or power frequency breakdown voltage and pulse coefficient β expresses the relationship between power frequency breakdown voltage and high voltage pulse breakdown voltage, which is that β is large when delay time τ is small and that the high voltage pulse breakdown voltage is larger than the power frequency breakdown voltage.

- 1. There are relationships between pulse delay time τ and pulse breakdown voltage for different air-gap distances: the smaller the pulse delay time τ , the greater pulse coefficient β for the same air-gap, that is to say, pulse breakdown voltage is β times as much as power frequency breakdown voltage;
- 2. When pulse delay τ is different, pulse coefficient β is different for the different electrodes, of which pulse coefficient β is smaller for spherical electrode, and pulse coefficient β is larger for needle electrode;
- 3. The high-frequency pulse breakdown voltage is far less than the power frequency breakdown voltage in air-gaps. It can be known from experiments that 100kHz voltage is lower than power frequency voltage about 20%, and the relationship between breakdown voltage and frequency is analyzed in detail in the later experiments.

References

- [1] Manyin Hu, Yi Zhao and Zhong Liu, in: Dust Removal Technology, edited by Chemical Industry Publisher, Beijing (2006). In Chinese
- [2] Hong Li: submitted to Electric Drive (2001). In Chinese
- [3] Zhang Q H, Barbosacanovas G V and Swanson B G: submitted to Journal of Food Engineering (1995).
- [4] Li Xing, Hairong Bao: submitted to Agricultural Engineering Technology (2008). In Chinese
- [5] Mingzhong Gu: submitted to Electrical Measurement and Instrumentation (1982). In Chinese
- [6] Zhilyaev A P, Langdon T G and San Martin M F: submitted to Progress in Materials Science (2008).
- [7] Wei Wang, Youping Tu, in: high voltage Technology, edited by Mechanical Industry Press, Beijing (2011). In Chinese
- [8] A dolf J. Schwab, in: High-voltage Measurement Techniques, edited by Electric Power Industry Press, Beijing (1982). In Chinese

The Control Technology of the Z-source Three-phase Four-leg Inverter based on Computer Simulation

Ming Su^{1,a}, Xueyan Ma¹, Yan Sun¹ ¹Institute of Liren College of Yanshan University, Qinhuangdao, Hebei, China ^aeagle_pro@163.com

Keywords: Z-source inverter, three-phase four-leg inverter, unbalanced load, imbalanced voltage

Abstract:Z-source inverter can boost the voltage of the DC-side, allow the two switches of the same leg conducting at the same time and it has some other advantages. The zero-sequence current flows through the fourth leg of the three-phase four-leg inverter so the three-phase four-leg inverter can work with unbalanced load. This paper presents a Z-source three-phase four-leg inverter which combines a Z-source network with three-phase four-leg inverter. The circuit uses simple SPWM modulation technique and the fourth leg uses fully compensated control method. The inverter can maintain a symmetrical output voltage when the proposed scheme under the unbalanced load.

Introduction

Z-source inverter with Buck-Boost characteristic can boost the low DC power to a specified high voltage, and the two switches of the same leg can conduct at the same time. Then there is no longer necessary to add the dead zone, thereby Z-source inverter can reduce the harmonic content because of the dead zone setting, and improve the quality of the power conversion. The traditional three-phase inverter can not provide pathways for the zero sequence current which is generated by unbalanced load, It is only suitable for balanced load. Three-phase four-leg inverter increases a leg on the basis of the traditional three-leg inverter structure. And this leg constitutes midline and then eliminates the need of the midpoint transformer when the load is unbalanced, reduces the volume and weight of the system. Dq0 rotating coordinate variables are mutually orthogonal, there is no coupling, they can be individually controlled, but the disadvantage of this method is the large amount calculation of the coordinate transformation and coordinate inverse transformation. The paper separates the fourth leg from the other control coupled leg. The fourth leg is individually controlled. Based on the advantages of the Z-source network and three-phase four-leg inverter, this paper presents Z source three-phase four-leg inverter, and it can improve the voltage pressure, under the unbalanced load it is able to maintain a good symmetrical output voltage.

1. Analysis of the main circuit

1.1. The main circuit

The main circuit is shown in Figure 1. Z-source impedance network is provided by the diode D, capacitor C1, C2 and inductors L1, L2. In the design of the Z impedance network, the capacitance value of C1, C2 is equal and the inductance value of L1, L2 is equal. And the formula is C1 = C2 = C, L1 = L2 = L.

The fourth leg of the three-phase four- leg inverter is added to the traditional three-phase three arms. The fourth leg consists of switching tube Q7, Q8. The midpoint of the leg connects the inductor Ln to the load neutral point. The main function of the inductance Ln is to filter the switching ripple of the neutral current. Z-source network and three-phase four-leg inverter are combined to form a Z -source three-phase four-leg inverter. The DC voltage Udc boost by the Z-source network then changes into alternating current through the four-leg inverter then the alternating current powers the unbalanced load through the LC filter.

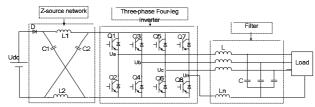


Figure 1 The main circuit topology of Z-source three-phase four-leg inverter

1.2. Working principle of Z-source inverter

Z-source inverter has two working conditions which are the active state and the shoot-through state. The inverter can be equivalent to a controlled current source iin.

Figure 2 (a) shows the active working state of the Z-source inverter's equivalent circuit diagram. When the switching state is one of the active state or the traditional zero vector, the input of the diode D is conducting, the power source and the inductors L1, L2 simultaneously power the load, capacitor Cl and C2 are charging status.

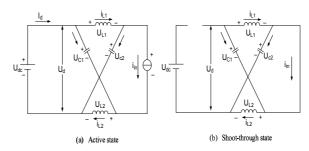


Figure 2 The status of the Z-source inverter

Figure 2 (a) can be obtained:

$$u_{dc} = u_{C_1} + u_{L_2} = u_{C_2} + u_{L_1}$$

$$u_{in} = u_{C_1} - u_{L_2} = u_{C_2} - u_{L_1} = u_{C_2} - u_{L_2}$$
(1)

Calculate the above two formulas, we can obtain:

$$u_{in} = 2u_C - u_{dc} \tag{2}$$

Where uin is the DC side input voltage.

Figure 2 (b) shows the shoot-through working state of the Z-source inverter's equivalent circuit diagram. Diode D is cutoff. Inductor and capacitor exchange energy. Capacitance charges inductance .We can obtain from figure 2 (b):

$$u_{C_1} = u_{C_2} = u_C = u_{L_1} = u_{L_2} = u_L \tag{3}$$

$$u_{\rm in} = 0 \tag{4}$$

The inductor L1 (L2) should satisfy the volt-second characteristic within a switching period Ts (the average storage energy of a switching cycle is zero). During a switching cycle, anti-shoot-through state works time is T1, shoot- through state works time is T0, and T1 + T0 = Ts, d0 is the straight-through duty cycle. Then we can obtain:

$$(u_{dc} - u_C)T_1 + u_C T_0 = 0 (5)$$

$$u_{C} = \frac{T_{1}}{T_{1} - T_{0}} u_{dc} = \frac{1 - d_{0}}{1 - 2d_{0}} u_{dc}$$
(6)

$$u_{in} = \frac{1}{1 - 2d_0} u_{dc} \tag{7}$$

It can be seen that when T0 varies within the range of 0-0.5T, Uin / Udc is theoretical from 1 to infinity.

1.3. The simple boost SPWM modulation method

The basic idea of the Z source three-phase inverter SPWM modulation is as follows. When Z-source inverter works in traditional zero vector state and shoot-through zero vector state, the three-phase load is short-circuited. Replace the part time of the traditional zero vector time with the shoot-through

zero vector time, keep the effective vector works time the same, then can increase the output voltage value of the Z-source inverter. The modulation principle is shown in Figure 3.

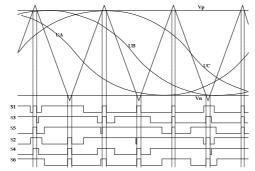


Figure 3 Simple boost SPWM modulation technology schematic.

In figure 3, Vp is equal to or greater than the peak value of the three-phase reference voltage, and Vn is equal to or smaller than the carrier negative peak voltage. They are used to control the the straight duty cycle. When the carrier amplitude is higher than Vp or lower than Vn, the inverter operates in the shoot-through zero state, when the carrier amplitude is between Vp and Vn, the inverter is in the traditional SPWM modulation state.

Can be obtained, D0 will be reduced when the modulation factor M increases. The maximum value of D0 of is (1-M), when M is 1, D0 is 0. The output phase voltage amplitude of inverter is:

$$u_{\rm a, b, c} = M \times \frac{u_{\rm in}}{2} = MB \times \frac{u_{\rm dc}}{2} = G \times \frac{u_{\rm dc}}{2} \tag{8}$$

$$B = \frac{1}{1 - 2d_0} = \frac{1}{2M - 1} \tag{9}$$

$$G = M * B = \frac{M}{2M - 1} \tag{10}$$

Uin is the DC side of the inverter input voltage. B is the boosting factor. M is the modulation factor of the inverter. G is a gain factor.

By the formula (9) and formula (10), knowing that the an arbitrary size's AC output voltage can be obtained by controlling the d0 and M,. It expands the conversion range of the entire system, and is applicable to more applications.

1.4. The fourth leg control principle

Figure 4 is a circuit diagram of the three-phase four-leg inverter.

$$\mathbf{a} + \mathbf{i}\mathbf{b} + \mathbf{i}\mathbf{c} = \mathbf{0} \tag{11}$$

when three-phase three- leg inverter with three-phase linear balanced load. uan, ubn, ucn are determined by ua, ub, uc.

$$\dot{\mathbf{i}}_a + \dot{\mathbf{i}}_b + \dot{\mathbf{i}}_c \neq 0 \tag{12}$$

when the three-phase four-leg inverter with unbalanced load, uan, ubn, ucn are jointly decided by ua, ub, uc and un.

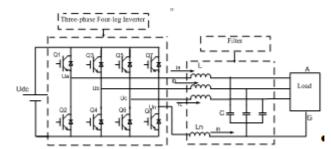


Figure 4 Three-phase four-leg inverter structure diagram

Assumptions:

$$\begin{cases} u_a = m_a \sin(\omega t - \theta) \\ u_b = m_b \sin(\omega t - \theta - 2\pi/3) \\ u_c = m_c \sin(\omega t - \theta - 4\pi/3) \end{cases}$$
(13)

 $L_n = L$, by the formula (11) can be obtained

$$u_a + u_b + u_c = Ldi_n/dt + (u_{AG} + u_{BG} + u_{CG}) + 3(u_n + Ldi_n/dt)$$
(14)

If $u_a + u_b + u_c = 0$, then

$$Ldi_{n}/dt + (u_{AG} + u_{BG} + u_{CG}) + 3(u_{n} + Ldi_{n}/dt) = 0$$
(15)

If the fourth leg's un is designed to be

$$u_{\rm n} = -4/3 * L di_n / dt \tag{16}$$

Then

$$u_{AG} + u_{BG} + u_{CG} = 0 \tag{17}$$

Output voltage is balanced.

In the actual control, k ($u_{AG} + u_{BG} + u_{CG}$) items is add to adjust the three-phase asymmetry.

2. Three-phase output voltage control

2.1. Mathematical model of the three-phase four-leg inverter under the three-phase rotating coordinate system (d, q, 0)

Differential equations of the three-phase four-leg according to figure 4 can be listed as follows:

$$L\frac{\mathrm{d}}{\mathrm{d}t}\begin{vmatrix} I_{a} \\ I_{b} \\ I_{c} \end{vmatrix} = L_{n}\frac{\mathrm{d}}{\mathrm{d}t}\begin{vmatrix} I_{n} \\ I_{n} \\ I_{n} \end{vmatrix} + \frac{U_{\mathrm{in}}}{2}\begin{vmatrix} d_{a} \\ d_{b} \\ d_{c} \end{vmatrix} - \begin{vmatrix} U_{AG} \\ U_{BG} \\ U_{CG} \end{vmatrix}$$
(18)

$$C \frac{d}{dt} \begin{bmatrix} U_{AG} \\ U_{BG} \\ U_{CG} \end{bmatrix} = \begin{bmatrix} I_a \\ I_b \\ I_c \end{bmatrix} - \begin{bmatrix} I_{oa} \\ I_{ob} \\ I_{oc} \end{bmatrix}$$
(19)

Among them da, db, dc are three-phase phase voltage duty cycles, Ia, Ib, Ic are output phase current of the inverter. Ioa, Iob and Ioc are three-phase load current. In is the neutral inductor current. Uin is the DC side input voltage of the inverter.

Stationary coordinate system (a, b, c) changes to the rotating coordinate system (d, q, 0) coordinates. The transformation matrix is as follows.

$$T_{abc/dq0} = \frac{2}{3} \begin{vmatrix} \sin \omega t & \sin(\omega t - \frac{2\pi}{3}) & \sin(\omega t + \frac{2\pi}{3}) \\ \cos \omega t & \cos(\omega t - \frac{2\pi}{3}) & \cos(\omega t + \frac{2\pi}{3}) \\ 1/2 & 1/2 & 1/2 \end{vmatrix}$$
(20)

The correspondence relationship between the abc coordinate physical quantity with dq0 coordinate physical quantity is as follows.

$$\begin{bmatrix} U_{d} \ U_{q} \ U_{0} \end{bmatrix}^{T} = T_{abc/dq0} \begin{bmatrix} U_{AG} \ U_{BG} \ U_{CG} \end{bmatrix}^{T}$$

$$\begin{bmatrix} I_{d} \ I_{q} \ I_{0} \end{bmatrix}^{T} = T_{abc/dq0} \begin{bmatrix} I_{a} \ I_{b} \ I_{c} \end{bmatrix}^{T}$$

$$\begin{bmatrix} I_{od} \ I_{oq} \ I_{o0} \end{bmatrix}^{T} = T_{abc/dq0} \begin{bmatrix} I_{oa} \ I_{ob} \ I_{oc} \end{bmatrix}^{T}$$

$$\begin{bmatrix} d_{d} \ d_{q} \ d_{0} \end{bmatrix}^{T} = T_{abc/dq0} \begin{bmatrix} d_{a} \ d_{b} \ d_{c} \end{bmatrix}^{T}$$
(21)

Consolidate the formula (18) (19) (20) (21) can be obtained.

$$\frac{d}{dt}\begin{bmatrix} I_d\\I_q\\I_0\end{bmatrix} = \frac{U_{dc}}{2}M\begin{bmatrix} d_d\\d_q\\d_0\end{bmatrix} - M\begin{bmatrix} U_d\\U_q\\U_0\end{bmatrix} - \boldsymbol{\omega}\begin{bmatrix} -I_q\\I_d\\0\end{bmatrix}$$
(22)

$$C \frac{\mathrm{d}}{\mathrm{d}t} \begin{bmatrix} U_{d} \\ U_{q} \\ U_{0} \end{bmatrix} = C \omega \begin{bmatrix} U_{q} \\ -U_{d} \\ 0 \end{bmatrix} + \begin{bmatrix} I_{d} \\ I_{q} \\ I_{0} \end{bmatrix} - \begin{bmatrix} I_{Ld} \\ I_{Lq} \\ I_{L0} \end{bmatrix}$$
(23)

(24)

Where the matrix M is

 $M = \begin{bmatrix} \frac{1}{L} & 0 & 0 \\ 0 & \frac{1}{L} & 0 \\ 0 & 0 & \frac{1}{3L_n + L} \end{bmatrix}$ From the formula (22) and (23) we can obtain the coupling between the dq axis, 0 axis is independent.Feedforward compensation is used to release the coupling between the dq axis,after decoupling, After decoupling, d-axis, q-axis, 0 axis are the three single-input single-output independent control system.

Under the dq0 rotated coordinate system, inductor current loop is the inner loop, the capacitor voltage loop is the outer loop. The controlled schematic diagram is shown in figure(5) as below:

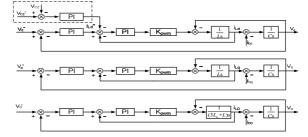


Figure 5 Dq0 axis control schematic structure diagram

2.2. Z-source network capacitor voltage control design idea

Here is the controlled method of Z-source network capacitor voltage. The Z-source network capacitor voltage control block diagram is shown in Figure 5. In the design of the capacitor voltage out loop, the current inner loop is regarded as a gain link in the out loop path. Ignoring the inverter bridge own loss under the condition of unity power factor, the active power of the inverter AC side is equal to the active power of the inverter circuit DC side, then we can obtain the formula (25).

$$u_{in}i_{in} = \frac{3}{2}u_{a}i_{a} = \frac{3}{2}u_{d}i_{d} + \frac{3}{2}u_{q}i_{q}$$
(25)

In order to simplify the design of the controlled system, q axis vector voltage was regarded as the 0 vector voltage in the two-phase synchronous rotating coordinate system (d, q). so formula (25) is converted into formula (26).

$$u_{in}i_{in} = \frac{3}{2}u_{a}i_{a} = \frac{3}{2}u_{d}i_{d}$$
(26)

There are formulas(27), (28) of the Z-source network as follows.

$$u_{in} = 2u_c - u_{dc} = \frac{1}{1 - 2d_0} u_{dc}$$
(27)

$$i_{in} = i_{ZL} - i_C \tag{28}$$

According to formula (27) and formula (28), formula (29) can be obtained. Where uin is the DC side of the inverter input voltage, iin is the DC side of the inverter input current, udc is the power supply of the system. iZL is the current in the inductor Z-source network.

$$i_{c} = i_{ZL} - i_{in} = i_{ZL} - \frac{3}{2} \frac{u_{d} i_{d}}{u_{in}} = i_{ZL} - \frac{3}{2} \frac{u_{d} i_{d} (1 - 2d_{0})}{u_{dc}}$$
(29)

So capacitor current ic of the voltage loop can be controlled by controlling the load AC current id and thus control the capacitor voltage.

3. The simulation results

Table 1 System simulation parameters				
Three-phase output phase voltage:	$110\sqrt{2}/50$ Hz			
Input voltage of the DC side:	330V			
Three-phase filter inductor:	1mH			
Midline inductance:	1mH			
Filter capacitor:	25µF			
Z-source network inductance:	2mH			
Z-source network capacitor:	3300µF			

The next two cases were analyzed: (1) the Z source three-phase three-leg with unbalanced load (two-phase no-load, one phase with a load of 50 ohms) (2) Z-source three-phase four-leg with unbalanced load(two-phase no-load, one phase with a load of 50 ohms).

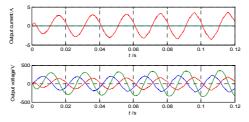


Figure.6 Three-phase three-leg simulation waveforms with unbalanced load From Figure 6, we can see the output waveforms quality is poor and the load voltage is unbalanced when Z-source three-phase three-leg inverter circuit is with unbalanced load.

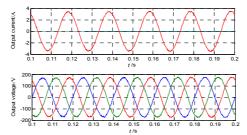


Figure.7 Three-phase four-leg with unbalanced load simulation

From Figure 7, we can see the waveforms in the Z-source three-phase four-leg inverter system with the same load have been greatly better. The degree of imbalance of output voltage is small. But the amplitude does not have a very good stability in expectation, there is a growing trend, so the control mode needs to improve.

4. Conclusion

This paper presents a Z-source three-phase four-leg inverter which combines a Z-source network with three-phase four-leg inverter. The circuit uses simple SPWM modulation technique. The three-phase four-leg use PI control in synchronous rotating coordinate system, the fourth leg use independent methods to control. The simulation results demonstrate the Z-source three-phase four-leg inverter can output three-phase sine wave voltage under unbalanced load conditions.

References

- [1] F. Peng, X. Fang, B. Gu, et al. Trans. China Electrotech Soc, Vol. 19(2004), p.47
- [2] M S.Shen, J.Wang , F Z.Peng , et al. IEEE Industry Applications Society Annual Meeting, 2004: 142-1.
- [3] E. Wit and J. McClure, "Statistics for Microarrays: Design, Analysis, and Inference," 5th Edition, John Wiley & Sons Ltd., Chichester, 2004.

- [4] X. Ding, Q.Zhao, B. Cui, et al. Fuzzy PID controller for DC-link boost voltage in Z-source inverter. Proceedings of the CSEE, 2008, 28(24): 31-38.
- [5] P.Chiang , Vilathgamuwa, D.M, Gajanayake, C.J, .Lim, T.Chen . Transient Modeling and Analysis of Pulse-Width Modulated Z-Source Inverter. EEEE Transaction on Power Electronics, 2009, 22(2):498-507.
- [6] B.Li, G.Zhao, et al. Study on three-phase photovoltaic grid-connected inverter system based on compositive control. Power System Protection and Control, 2010, 38(21): 44-47.
- [7] L.Jun, C.Green, C. Feng. Increasing Voltage Utilization inSplit-Link, Four-Wire Inverters[J].IEEE Trans. on Power Electronics.2009,6(24):1562-1569.
- [8] Loh P. C.VilathgamuwaD.M., Gajanayake C.J. WongL.T., Ang C. P. Z-Source Current—Type Inverters: Digital Modulation and Logic Implementation. IEEE_Transactions on Power Electronics, 2007 22(1):169-177.

Power System Probabilistic Production Simulation Including Efficiency Power Plant

Chuansheng Xie^{1,a}, Pengyuan Zhong^{*1,b}, Chenchen Zhao^{1,c}, Chengying Zhou^{1,d}

¹North China Electric Power University, 2nd Beinong road, Changping disctrict, Beijing, China ^axiecs@sohu.com, ^bzpy0401@163.com, ^cyiyizhaochen@163.com, ^d120671552@qq.com

Keywords: efficiency power plant; probabilistic production simulation; equivalent energy function

Abstract: As a measure of demand-side management, efficiency power plant (EPP) can save energy and bring economic and environmental benefits to the power system, although the widely used EPP technology may have negative effect on both power system stability and operation costs. The concept of EPP and its related characteristics such as capacity, output curve, and cost were introduced, and a probabilistic production simulation model based on the equivalent energy function (EEF) method was established to analysis the impact and benefits of EPP. With a numerical example, a result is found that EPP can not only improve the reliability and load rate of power system, thus reducing the social costs of power outage, but also reduce the total production and operating costs of power system.

Introduction

With the rapid growth of China's economy in recent years, the power shortage and environmental pollution became the critical problems that most cities were forced to face. As an important means to ease the power shortage, demand side management (DSM) is introduced by taking a variety of administrative, economic, technical and guiding methods. Efficiency power plant (EPP) is applied and promoted as one of the most available measures of DSM in China especially in recent years, which can help to reduce the impact of power shortage, and protect the electricity demand of terminal users.

EPP and other energy-efficient projects have been successfully implemented in more than 30 countries and regions such as the United States, Canada, France and so on, and achieved remarkable results in reducing power construction investments and energy consumption, improving economy and reliability of grid operation, and improving environmental quality. Recently, EPP construction in China is also gradually expanded, which makes it necessary to analysis the impact of EPP on power scheduling and system stability. Therefore, it should be introduced of EPP production during power system simulation.

Probabilistic production simulation is an algorithm that calculates the power generation, production cost and system reliability with the production of power plants being optimized, and the random of generators failures and load stochastic being considered. It has been widely used in power plant planning, reliability assessment and other aspects[1]. Currently, the probabilistic production simulation algorithm mainly includes the piecewise linear approximation method[2], sub-block method[3], the sequence algorithms [4], semi-invariant method[5,6], equivalent energy function method [7] and so on.

In this paper, the concepts and characteristics of EPP are introduced and a probabilistic production simulation model of power system with EPP is established using the equivalent energy function method. Finally, an empirical case is used to analysis the economic and social benefits of EPP.

Efficiency power plant

Efficiency Power Plant (EPP) is a virtual power plant, which makes use of a great deal measures of saving power energy and efficiency items to get more power energy to meet need of power energy users and reduce the power supply of power plant. The construction of EPP can promote the energy conservation and environmental governance, help the government to achieve low-carbon development and green development, and improve the competitiveness of the power enterprises by reducing their costs.

A. Capacity of EPP

The capacity of EPP can be divided into theoretical capacity and clipping capacity. The theoretical capacity C_l is the savings capacity under the implementation of EPP projects, which is calculated by the minus of conventional power equipment and energy-saving equipment with the same efficacy. The clipping capacity C_x is the capacity savings of peak load with EPP. The relationship of clipping capacity and theoretical capacity is as formula 1, where α is the coincidence factor of energy-saving equipments, valuing between 0 and 1.

$$C_x = \alpha C_l \tag{1}$$

B. Output curve of EPP

The EPP's power curve is the difference between the aggregated load curves of replaced power equipment and that of energy-saving equipment consisting of EPP. Generally, the EPP output curve is calculated as formula 2:

$$P(t) = \alpha_t (\mathbf{P}_c - \mathbf{P}_j) = \alpha_t \mathbf{P}_c - \alpha_t \mathbf{P}_j = \mathbf{P}_c(t) - \mathbf{P}_j(t)$$
(2)

Where α_t represents the coincidence factor of EPP energy-saving equipments at the load point t; P_c is the total power of conventional equipments replaced by saving equipments; P_j is the total power of the EPP saving equipments; $P_c(t)$ is the aggregated load curve of the conventional equipment; $P_j(t)$ is the aggregated load curve of the EPP energy-saving equipment.

As to the EPPs whose energy-saving equipments have the same alternative coefficients, the output curve can be calculated as formula 3:

$$P(t) = \alpha_t (P_c - P_j) = \alpha_t (\lambda - 1) P_j$$
(3)

Where K represents the alternative coefficient of energy-saving equipment, and $K = P_c/P_j$.

Given the load curve of energy-saving equipment, then the EPP output curve can be calculated as formula 4:

$$P(t) = P_c(t) - P_j(t) = (\lambda - 1)P_j(t)$$
(4)

C. Cost of EPP

The investment cost of EPP is calculated by the difference between energy-saving equipment and conventional equipment. From the perspective of government or the power companies, only a percentage of the difference subsiding to enterprises can promote the construction of EPP, which can make the investment costs being lower. Running costs are the difference between energy-saving equipment and conventional equipment in maintenance and labor costs.

Equivalent energy function

The equivalent energy function (EEF) method is presented for power system probabilistic modeling. The method performs convolution and deconvolution by using electric energy directly so that the probabilistic modeling is considerably simplified. The EEF method is not only more efficient than any other available method in this domain, but is also more flexible in treating assigned energy units. An approximate deconvolution algorithm and a loss-of-load-probability (LOLP) formula are also given which enable probabilistic modeling to be performed even faster.

The system load curve F(x) during the study period T is shown as figure 1, in which P_{Lmax} represents the maximum load in the system, and (x_c, t_c) means the duration time t_c during which the system load is higher than x_c . The discrete equivalent energy function is defined as formula 5:

$$\begin{cases} E(k) = T \int_{x}^{x + \Delta x} F(x) dx \\ k = \langle x / \Delta x \rangle + 1 \end{cases}$$
(5)

Where E(*k*) is the load power corresponding to the load curve of $x - x + \Delta x$; $\langle x/\Delta x \rangle$ is the integer not greater than $x/\Delta x$.

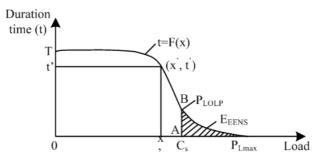


Figure 1. Load duration curve

Considering the decommissioning factors of turbines, a correction factor of random power outages needs to be used to correct the equivalent energy function. With the original load curve $F_{(0)}(x)$ and its equivalent energy function $E_{(0)}(x)$, the equivalent load curve $F_{(i-1)}(x)$ is defined after the running arrangements of the generator *i*-1, with its equivalent energy function of $E_{(i-1)}(x)$. Then, as to the generator *i* being arranged to run, given its installed capacity C_i and forced outage rate q_i , its equivalent energy function can be defined by formula 6:

$$\begin{cases} E_{(i)}(\mathbf{k}) = p_i E_{(i-1)}(\mathbf{k}) + q_i E_{(i-1)}(\mathbf{k} - \mathbf{m}_i) \\ p_i = 1 - q_i; \quad \mathbf{m}_i = C_i / \Delta x \end{cases}$$
(6)

And the generation of generator *i* should be calculated based on the equivalent power function of $E_{(i-1)}(k)$, as formula 7, where $k_{i-1}=x_{i-1}/\Delta x$, and $k_i=(x_{i-1}+C_i)\Delta x$:

$$E_{C_i} = p_i \sum_{k=k_{i-1}+1}^{k_i} E_{(i-1)}(k)$$
(7)

With all of the generators running in arrangement, the probabilistic production simulation process is completed, and thus the total running cost and reliability index of this system needs to be calculated. Assuming that the generator number of this system is *n* with its total capacity being C_s , its equivalent energy function is defined as $E_{(n)}(k)$, and the index of expected-energy-not-supplied E_{EENS} and loss-of-load-probability P_{LOLP} are calculated as formula 8, 9:

$$E_{EENS} = \sum_{k>k_n} E_{(n)}(\mathbf{k})$$
(8)

$$P_{\text{LOLP}} \approx \frac{E_{(n)}(\mathbf{k}_{n}) + E_{(n)}(\mathbf{k}_{n}+1)}{2T\Delta x}$$
(9)

EPP systems probabilistic production simulation model

- A. Simplifying assumptions
 - The forced outage probability of EPP is not considered. During the simulation processing, the outage of EPP will not cause a shortage of electricity supply because of the decreased load correspondingly. Therefore, the EPP forced outage probability is generally not considered during the simulation.
 - Operating cost is assumed to be zero, which is calculated by the difference of maintenance and labor costs between energy-saving equipment and routine equipment.
 - Irreversible assumptions. Since the essence of EPP is to use energy-efficient equipment to replace conventional equipment, its investment must be irreversible, which means that once operational, the EPP units can not quit.

B. Simulation process

The process of EPP systems probabilistic production simulation based on the EEF method is shown in Figure 2.

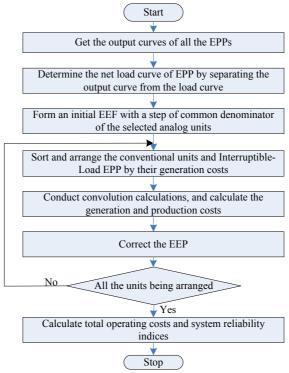


Figure 2. Flow chart of power system probabilistic production simulation including EPP

Case study

Three types of EPPs are chosen in this paper, namely high-efficiency industrial motors operating continuously, office regenerative systems and interruptible loads. As to the office regenerative systems, their theoretical capacity varies during the peak hours (08:00-21:00) and low hours (the remaining hours). The interruptible load can be considered as conventional power plants, with the implementation cost of 150 \$/ (MW h). The coincidence factor and capacity of three types of EPP are set in Table 1 and Table 2 respectively.

Table 1 Setting coincidence factor of EPP									
	СС	oincidence fa	actor	_	c	oincidence factor			
Hour	Industrial	office	Interruptible	Hour	Industrial	office	Interruptible		
	motors	system	loads		motors	system	loads		
0	1	0.2	0.8	12	1	0.5	0.5		
1	1	0.1	0.8	13	1	0.4	0.4		
2	1	0.1	0.8	14	1	0.4	0.4		
3	1	0.2	0.8	15	1	0.5	0.5		
4	1	0.3	0.8	16	1	0.6	0.6		
5	1	0.4	0. 7	17	1	0.7	0. 7		
6	1	0.4	0. 7	18	1	0.7	0. 7		
7	1	0.5	0. 7	19	1	0.6	0.6		
8	1	0.6	0.6	20	1	0.4	0.4		
9	1	0.6	0.6	21	1	0.3	0.3		
10	1	0.6	0.6	22	1	0.3	0. 7		
11	1	0.5	0.5	23	1	0.2	0.8		
			Table 2 Setting	capacity	of EPP				
Number	r Load ty	Load type Project				Theoretical capacity			
1	Continu	Continuous load industrial mo		otors		80			
2	Randon	ndom load High-efficien		nt applia	appliances 100				
3	Variable	e load	office system	ns		100 (peak hour)			
			-		-120 (low hour)				
4	Variable	e load	interruptible	loads		40			

 Table 1
 Setting coincidence factor of EPP

The 18-unit system is used as conventional units, with installed capacity of 3 420 MW, and the parameters and load sequence of them are set in Table 3. Load data is chosen from the literature [8], in which the load curve used IEEE RT S load with the annual maximum load of 2 850 MW, and the simulation duration were 49th week to 52ed week in the winter with a total of 672 h. Probabilistic production simulations are conducted before and after the implementation of EPP project, and the results are shown in Table 4.

Table 5 Generators data of 16-unit system								
Num	Fuel type	Capacity	Quantity	Force outage (FOI	rate Fue	l costs ⁄IWh)	Opera fixed (\$/kV	
1	Nuclear	400	2	0.12	2	6.0	5.0	0.30
2	Coal	350	6	0.08	8 1	1.4	4.5	5 0.70
3	Oil	100	4	0.04	4 2	23.0	8.5	5 0.80
4	Gas	20	6	0.10	0 4	3.5	0.3	3 5.00
Table 4 Simulation result								
Scene	E _{EENS} (MWh)	P _{LOLI} (%)			Total fixed cost (\$)	varial	otal ole cost (\$)	Total operation and maintenance costs (\$)
1	2622.580	05 2.015	4 13,53	8,210	1,298,923	791	,154	15,628,287
2	1520.169	0.672	4 12,51	3,005	1,298,923	762	,040	14,573,968

Table 3 Generators data of 18-unit system

From Table 4 we can get that, the expected-energy-not-supplied value EEENS is decreased from 2,623MWh to 1,520MWh with the implement of EPP project (reducing by 42%); the loss-of-load-probability PLOLP is reduced from 2.0154% to 0.6724%, which means that the system reliability has been significantly improved. Meanwhile, the overall operation and maintenance costs of the power system are also declined remarkably.

Conclusion

In this paper, the concept of EPP is introduced, with its difference from conventional units being analyzed. Then, with analysis of the impact of EPP on power system, a EPP system probabilistic production simulation model is established using the equivalent power function method. Finally, a numerical analysis of the power system including EPP is conducted based on the probabilistic production simulation, which results illustrate that the reliability of the system including EPP can be significantly improved, while the total production and operating costs can be decreased significantly. The improvement of system reliability means that EPP can delay the construction of conventional power plants with the system reliability being ensured, and reduce the social costs of power shortage by the reduction of expected-energy-not-supplied value. The decreased total costs give us confidence of substantial economic benefits by the appropriate implementation of EPP project. In additional, the environment can also be improved after the implementation of EPP project, because of the saved power in supply side. Furthermore, the EPP projects also improve the loading rate of power system and help to optimize the grid load characteristics.

Acknowledgment

The authors greatly appreciate the invaluable comments of the two anonymous referees. Professors and researchers from North China Electric Power University are also acknowledged.

Refferences

- [1] M. Lin, A. Breipol, F. Lee. Comparisons of probabilistic production cost simulation methods, IEEE Trans, 1989, 4 (4): 1326–1333..
- [2] R. R. Booth. Power system simulation model based on probability analysis. IEEE Trans on Power Systems, 1972, 91(1): 62-69.
- [3] K. F. Schenk, R. B. Misra, S. Vassos, et al. A new method for the evaluating of expected energy generation and loss of probability. IEEE Trans on Power Systems, 1984, 103(2) : 294-303.
- [4] L. R. Noyes. Two-area probabilistic production costing by the method of bi-variant cumulants. IEEE Trans, 1983, 102 (2): 433–443.
- [5] N. S. Rau, P. Toy, K. F. Schenk. Expected energy production cost s by the method of moment s. IEEE Trans on Power Apparatus and Systems , 1980, 99(5) : 1908-1917.
- [6] J. P. Stremel, R. T. Jenkins, R. A. Babb, et al. Production costing using the cumulant method of representing the equivalent load curve. IEEE T ran s on Power Apparatus and Systems, 1980, 99(5): 1947-1956.
- [7] E. Kaplani, S. Kaplanis. A stochastic simulation model for reliable PV system sizing providing for solar radiation fluctuations. Apple Energy, 2012, 97(9): 70-81.
- [8] The Reliability Test System Task Force of the Application of Probability Methods Subcommittee. IEEE reliability test system. IEEE Trans on Power Apparatus and Systems, 1979, 98(4): 2047-2054

Advanced Materials Research Vol. 981 (2014) pp 701-705 © (2014) Trans Tech Publications, Switzerland doi:10.4028/www.scientific.net/AMR.981.701

Study on Fault Diagnosis Method for Nuclear Power Plant Based on Fuzzy Rough Sets and Decision Tree

Yu Mu^{1,a}, Guimin Sheng², Hong Xia³, Punan Sun¹, Yan Qian¹

¹College of Physics Science and Technology Heilongjiang University, Harbin, China

²School of Electrical Engineering, Suihua University, Suihua, China

³Nuclear Safety and Simulation Technique National Defense Key Subject Laboratory; Harbin Engineering University; Harbin, China

^amuyufffff@126.com

Keywords: Nuclear Power Plants; Fault Diagnosis; Fuzzy Rough Set; Decision Tree

Abstract. The technology of real-time fault diagnosis for nuclear power plants(NPP) has great significance to improve the safety and economy of reactor. Nuclear power plants are complex system, which collect and monitor the vast parameters. A parameter reduction method based on fuzzy rough sets was proposed. According to the characteristics the parameters were fuzzed, and they were reducted using the algorithm of forward greedy search. The decision tree was applied to learn from training samples which were the typical faults of nuclear power plant, i.e., loss of coolant accident (LOCA), feed water pipe rupture, steam generator tube rupture (SGTR), main steam pipe rupture, and diagnose by using the acquired knowledge. The result shows that this method can diagnose the faults of the NPP rapidly and accurately.

Introduction

Nuclear power plants are complex system, which collect and monitor the vast parameters^[1]. So it is very hard to diagnosis the fault of NPP. Rough set theory is a mathematical tool which studies fuzzy and uncertainty problem. Rough set theory reduct parameters on the condition of maintaining classification ability. Classical rough set theory can only deal with discrete variables. Although the neighborhood rough set can handle continuous variables. But a neighborhood value is share by all of the parameters. The fact is ignored which different parameters have various features. Fuzzy rough set is used to reduct the parameters. The parameters are fuzzed by different membership function before computing the dependency degree. So the prior knowledge can be made full use to process parameters, and the effect of parameter reduction is improved.

Fundamentals on Fuzzy Rough Sets

A structural data used for classification learning can be written as an information system, denoted by $IS = \langle U, A \rangle$, where U is a nonempty and finite set of samples $\{x_1, x_2, ..., x_n\}$, called a universe, A is a set of attributes (also called features, inputs or variables) $\{a_1, a_2, ..., a_m\}$ to characterize the samples. To be more specific, $IS = \langle U, A \rangle$ is also called a decision table if $A = C \bigcup D$, where C is the set of condition attributes and D is the decision attribute^[2].

A set of fuzzy input and output attributes $\{P_1, P_2, \dots, P_p\}$ and *d* are given to describe the objects $U = \{x_1, x_2, \dots, x_n\}$. Each attribute is limited to a small set of fuzzy linguistic terms $A(P_i) = \{F_{ik} | k = 1, 2, \dots, C_i\}$. Each object $x_i \in U$ is classified by a set of classes $A(Q) = \{F_i | i = 1, \dots, C_Q\}$, where *Q* is a decision attribute and F_i can be a fuzzy set or a crisp set. One can generate a family of fuzzy information granules with *P*, where the fuzzy partition is defined as $U/P = \{F_{ik} | i = 1, \dots, p; k = 1, \dots$

1, ..., C_i }. Given arbitrary fuzzy set A in U, $u_A(x) : U \to [0,1] \forall x \in U$ and $F_{ik} \in U/P$, one

define a tuple $\langle u_{\underline{A}}, u_{\overline{A}} \rangle$, where lower and upper approximation membership functions are defined as

$$u_{\underline{A}}(F_{ik}) = \inf_{x \in U} \max\{1 - u_{F_{ik}}(x), u_{A}(x)\}$$
(1)

$$u_{\overline{A}}(F_{ik}) = \sup_{x \in U} \min \{ u_{F_{ik}}(x), u_A(x) \}$$
(2)

The positive region of a fuzzy set F_l is the maximal membership degree with which a unique class can be classified by fuzzy set F_{ik} , written as

$$u_{POS}(F_{ik}) = \sup_{F_l \in \mathcal{A}(Q)} \left\{ u_{\underline{F_l}}(F_{ik}) \right\}$$
(3)

The membership of $x \in U$ to the fuzzy positive region is given by

$$u_{POS}(x) = \sup_{F_{ik} \in A(P_i)} \min\{u_{F_{ik}}(x), u_{POS}(F_{ik})\}$$
(4)

With the definition of fuzzy positive regions, one can compute the dependence function as

$$\gamma_P(Q) = \frac{\sum_{x \in U} u_{POS}(x)}{|U|} \tag{5}$$

Where $|\bullet|$ is the cardinality of a set. Dependency function reflects B's power to approximate D.

 $0 \le \gamma \le 1$. We say D completely depends on B if $\gamma = 1$. It means that the decision can be precisely

described by the elemental information granules generated by attributes B. This function measures the significance of categorical attributes relative to the decision. In practice, the attributes may be numerical or fuzzy. Correspondingly, the relation and partition induced by these attributes are fuzzy. In this case, we are involved in approximating a fuzzy or crisp set with a family of fuzzy information granules.

Reduction Algorithm

As mentioned above, the dependency function reflects the approximating power of a condition attribute set. It can be used to measure the significance of a subset of attributes. The aim of attribute selection is to search a subset of attributes such that the classification problem has the maximal consistency in the selected feature spaces. In this section, we construct some measures for attribute evaluation, and then present greedy feature selection algorithms.

Given fuzzy decision system, $\langle U, A \cup D, N \rangle$, $B \subseteq A$ one can define the significance of *a* in

B as

$$Sig(a, B, D) = \gamma_{B \cup a}(D) - \gamma_B(D) \quad \forall a \in A - B$$
(6)

We say attribute *a* is superfluous in *B* with respect to *D* if Sig(a,B,D) = 0; otherwise, *a* is indispensable in *B*.

The objective of rough set based attribute reduction is to find a subset of attributes which has the same discriminating power as the original data and has not any redundant attribute. Although there usually are multiple reducts for a given decision table, in the most of applications, it is enough to find one of them. With the proposed measures, a forward greedy search algorithm for attribute reduction can be formulated as follows^[4].

1. reduct set $red \rightarrow \Phi$;// red is the pool to contain the selected attributes

- 2: For each $a_i \in C red$
- 3: Compute $\gamma_{red}(D)$
- 4: Compute Sig (a_i, B, D)
- 5: end
- 6: select the attribute a_k satisfying $SIG(a_k, red, D) = \max(SIG(a_i, red, D))$

7: If $SIG(a_k, red, D) > \varepsilon$, // ε is a little positive real number use to control the convergence

- 8: $red \cup a_k \rightarrow red$
- 9: go to step2
- 10: else
- 11: return red
- 12: end if

There are four key steps in a feature selection algorithm: subset generation, subset evaluation, stopping criterion and result validation. In the algorithm, we begin with an empty set red of attribute, and we add one feature which makes the increment of dependency maximal into the set red in each round. This is the strategy of subset generation. We embed the subset evaluation in this strategy by maximizing the increment of dependency. The algorithm does not stop until the dependency increase less than e by adding any new feature into the attribute subset red.

Simulation Analysis

The typical faults of NPP which are chosen for analysis are as follows: loss of coolant accident (LOCA), feed water pipe rupture, steam generator tube rupture (SGTR), main steam pipe rupture. The sample set is as table 1. There are 48 characteristic parameters of NPP, such as water level of pressurizer, flow, pressure and temperature of main steam etc.

Table1. Information of Sample Set				
Class	Fault Type	Number		
Label	Fault Type	of Sample		
1	Normal	100		
2	LOCA (Cold Leg)	42		
3	LOCA(Hot Leg)	43		
4	SGTR	253		
5	Main Steam Pipe Rupture	67		
6	Feed Water Pipe Rupture	91		

At First the parameters are fuzzed by membership functions as shown in Fig.1. C_2 is the parameters for normal operation. C1 and C3 are low and high parameters. m_1,m_2,m_3,m_4 are the threshold values which are chosen according to various features of the parameters.

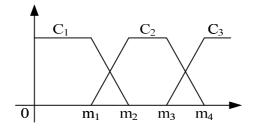


Fig.1 Membership functions

Secondly, the dependency function is computed by fuzzy rough set, the dependency function of each parameter as shown in fig.2. And the parameters is reduced by algorithm1.

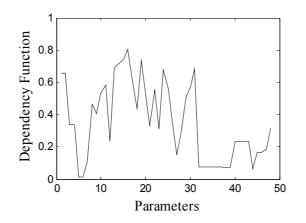


Fig.2 Dependency Function

There are 6 parameters in the reduction set. They are temperature of containment increase, radiation dose of secondary loops, flow of main steam, flow of feed water, pressure of SG, flow of cold leg coolant. Then the fault diagnosis model is built by decision tree C4.5 algorithm. And the model is tested by 10-fold cross-validation.

Table2 Fault Diagnosis Results				
	Before	After		
	Reduction	Reduction		
training time/s	0.31	0.02		
accuracy (total)/%	98.0	97.3		
accuracy (class1) /%	100	100		
accuracy (class2) /%	95.2	90.5		
accuracy (class3) /%	93.0	93.0		
accuracy (class4) /%	99.2	99.2		
accuracy (class5) /%	94.0	95.5		
accuracy (class6) /%	98.9	95.6		

The simulation results is shown in table2. The results show that there is little difference in the classification accuracy of diagnostic. And the training time is reduced an order of magnitude. So reduction can greatly improve the efficiency of the diagnostic model without affecting the diagnostic accuracy. Comparing with the results of literature [1], the classification accuracy of reduction set improves a little. For in the neighborhood rough set, a neighborhood value is share by all of the parameters. The fact is ignored which different parameters have various features. And in fuzzy rough set, the parameters are fuzzed by different membership function. So the prior knowledge can be made full use to process parameters, and the effect of parameter reduction is improved.

Conclusions

The fault samples are collected from the NPP simulator of QINSHAN NPP Unit 1. And the parameters are fuzzed by different membership function according to various features of the parameters, and then the importance of them is evaluated by fuzzy rough set. A forward greedy search algorithm is proposed for attribute reduction. So the fault sample set is reduced by the algorithm. At last, the fault diagnosis model is built by decision tree C4.5 algorithm. And the model is tested by 10-fold cross-validation. The results show that reduction can greatly improve the efficiency of the diagnostic model without affecting the diagnostic accuracy. The fuzzy rough set have a good performance in the parameter reduction.

Acknowledgment

The authors would like to thank the Science and Technology Projects of Heilongjiang Provincial Education Department, Natural Science Foundation of China (12531514).

References

- [1] Mu Yu, Xia Hong, Liu Yongkuo. Study on Fault Diagnosis Method for Nuclear Power Plant Based on Decision Tree and Neighborhood Rough Sets. Atomic Energy Science and Technology, 2011, 45(1): p. 44-47.
- [2] Qinghua Hu, Zongxia Xie, Daren Yu. Hybrid attribute reduction based on a novel fuzzy-rough model and information granulation. Pattern Recognition 40 (2007): p. 3509–3521.
- [3] Yin Yong, Sun Ruying. Knowledge Acquisition Approach Based on Fuzzy-rough Set. Journal of Chongqing University(Natural Science Edition). 2006 29(5):p. 108-111.
- [4] Qinghua Hu, Daren Yu, Jinfu Liu, Congxin Wu. Neighborhood rough set based heterogeneous feature subset selection. Information Sciences. 178 (2008): p. 3577-3594.

CHAPTER 9:

Engineering of Weapons Systems

Research on Temporal Fire Distribution of Shipboard-gun Neutralization Firing Anti-shore

Deqing Liang^{1, a}, Xuwen Sun^{1, b}, Huichuan Wang¹, Dehu Wang¹, Feng Tian ¹ ¹Dalian Naval Academy, Dalian 116018, China ^aliandqin@tom.com, ^b13591796389@126.com

Keywords: shipboard-gun, oppressive fire, time domain, fire distribution

Abstract: In order to satisfy the need of automatic decision-making while shipboard-gun oppressive fire to the shore, This paper research the problem of shipboard-gun temporal fire distribution .This paper put forward the elements of oppressive fire distribution and solve out the calculation of every oppressive fire distribution elements(such as quick-firing's quantity, surveillance firing's quantity, every quick-firing's ammunition wastage, every surveillance firing's ammunition wastage and firing occasion). It could provide technical support for the realization of automatic decision-making while shipboard-gun suppression firing anti-shore.

1. Introduction

This work is supported by the Science Research Foundation of Dalian Naval Academy. Fire distribution study belongs to a kind of resource allocation, stressing distributing "the right thing" to "the right place" at the "right time". At the same time, what must be given more attention to is that resource distributing happens not only in the event of resource allocation behavior, but also in space domain and time domain. Aiming at firing distribution in time domain when suppressive firing. That is to cope with how to distributing the fire resource allocated to specific fire task when operating.

2. Overview for neutralization fire

Neutralization Fire means the shooting used for make the target invalid ^[1]. The tactical purpose is to suppress the targets which are attacking us and thus to achieve our tactical purpose. The suppressing fire is usually used for suppressing large area targets, and also used for strongly protected fire point. Suppression of shooting is more used to suppress the shore with larger area target, also to suppress protection strong weapon emplacements. Due to the suppression of shooting is difficult to completely destroy the enemy fire effectively, After the stop fire, enemy fire may be restored, So when pressing shooting for a long time, need not regularly used incoming radiation and monitoring, make the enemy difficult to master our law of fire application.

A mass of war information shows that, different suppression degree has different damage, and there is a relationship between the suppression degree and the damage degree, which is as the following tab1. Thus, when certain suppression tasks are given, the ammunition consumption is determined. For the different type of targets, the damage degree can be characterized by the mathematical expression of the damage probability.

Table 1 <u>Relation between suppression degree and damage</u> degree ^[2]

8	$\overline{\mathbf{U}}$
Damage degree (%)	
10~15	
20~30	
35~45	
	10~15 20~30

3. Elements of suppressing fire temporal distribution

The task of the firing distribution activity is the distribution for the firing resources in time domain. There are many detailed tasks in the suppression fire distributing such as the frequency and the ammunition consumption of the urgent firing and monitoring firing, and also the firing occasions. So, the elements of suppression firing temporal distribution are that: frequency of urgent firing, frequency of monitoring firing, ammunition of each urgent firing, ammunition of each monitoring firing, and occasions of each firing^[3].

4. Process for the construction of the elements of temporal firing distribution

Considering the target state, degree of suppression performing on the effects of the parameters mentioned above, corresponding elements generating process is designed as follows: first, determine the urgent firing pressing time T; second, determining the firing frequency C_{jx} based on the determining principle, suppressing degree, and suppressing time of urgent firing; third, determining the monitoring pressing time C_{js} ; fourth, determining urgent firing frequency C_{jx} based on the determining principle, suppressing degree, and suppressing time of urgent firing; fifth, computing the ammunition consumption n_{jx} of urgent firing on the basis of determining principle, suppression frequency and the computed consumption N; fifth, determining monitoring firing ammunition consumption n_{js} , based on the determining principle, suppressing degree, and suppressing degree, and suppressing degree, and suppressing firing monitoring firing ammunition consumption n_{js} , based on the determining principle, suppressing degree, and suppressing degree, and suppressing degree, and suppressing firing monitoring firing ammunition consumption n_{js} , based on the determining principle, suppressing degree, and suppressing time; at last, according to the setting principle of urgent firing and monitoring firing occasion, generating firing occasions at random in certain scope.

5. Model of temporal fire distribution factors for urgent firing

5.1 The firing frequency C_{jx} of urgent firing

5.1.1 Theoretical model

According to the principle that the firing frequency of urgent firing is less than i A to B (A < B, and A, B are constants), considering the restrictive relation between fire density and firing frequency under the condition of fixed ammunition consumption, the firing frequency of urgent firing nasty fixed ammunition consumption the restrict relationship, the number of incoming radiation C_{jx} is determined as follows:

When general suppression or temporary suppression firing, the ammunition consumption needed is less, the first aim is to restrict the troops and fire power of enemies, so, which needed is not many times of urgent firing but high density firing in urgent firing. When special suppression firing, firing density is high because of the large amount of given ammunition, furthermore, many times urgent firing is in favor of continuously suppressing and killing enemies, so there should be many times urgent firing in special suppression.

So, the mathematical model of urgent firing frequency C_{jx} is:

$$C_{jx} = \begin{cases} AT & general \text{ sup pression firing or temporary sup pression firing} \\ BT & \text{sup pres sin } g \deg rece is special \text{ sup pression} \\ 2T + 1 & 0.5h \le T < 1h \\ 1 & T < 0.5h \end{cases}$$
(1)

When the result of Eq.1 is decimal, truncating is needed to get rid of the decimal place number. 5.1.2 The solving algorithm

(1) According to suppression degree, judging the frequency c_{jx} per hour in suppression time;

	A	temporaty sup pression	
$c_{jx} =$	{ A	general sup pression	(2)
	B	special sup pression	

(2) Computing the origin value of urgent firing frequency C_{jx} suppression time T (min);

$$C_{jx} = c_{jx} \cdot T / 60 \tag{3}$$

(3) If the value of C_{jx} is decimal, truncating it to integer number.

(4) During the truncating, when C_{jx} is smaller than 1, the value of C_{jx} is 1, this is because in the suppression firing, there must be at least 1 times urgent firing. So:

$$C_{jx} = C_{jx} + 1, \quad C_{jx} = 0$$
 (4)

(5) If C_{ix} is smaller than 2, but is larger than 1, the value added 1 to the integer part of itself.

$$C_{jx} = C_{jx} + 1, \quad C_{jx} = 1$$
 (5)

(6) If the value of C_{ix} is larger than 2, just reserve the integral part of the value.

5.2 Determine ammunition consumption *n*_{ix} of each urgent firing.

5.2.1 Theoretical model

According the principle that C percent of the given ammunition completing firing task is used for urgent firing, and the ammunition consumption of first urgent firing is D times of other urgent firing (C and D are all constant), ammunition consumption of each urgent firing n_{jx} is determined by the following formulation:

$$n_{sj} = CN \{ 100S \cdot [1 + (C_{jx} - 1)/D] \}$$
(6)

$$n_{jx} = \begin{cases} n_{sj} \cdot S & \text{first urgent firing} \\ \frac{n_{sj}}{D} \cdot S & \text{every urgent firing of others} \\ N & \text{when there is only 1 urgent firing} \end{cases}$$
(7)

 n_{sj} is the average ammunition consumption per acreage of firing area; *S* is the acreage of the target. 5.2.2 The solving algorithm

The consumption of each urgent firing n_{ix} can be determined as follows:

(1) Calling urgent firing frequency C_{ix} and the ammunition consumption computing result N;

(2) Determining the frequency of urgent firing;

(3) If the frequency of urgent firing is 1, then, the ammunition consumption n_{jx} of this urgent firing is N, because monitoring firing is not needed, in that case, the return value is n_{ix} ;

(4) If the frequency of urgent firing is not 1, then the ammunition consumption N_{sj} of the first urgent is computed by the following formulation:

$$N_{si} = C \cdot N / (100 \cdot (1 + C_{ix} - 1/D))$$
(8)

(5) The ammunition consumption of each urgent firing of the rest firing is $N_{s,i}/2$;

(6) The ammunition consumption of each of the rest urgent firing is n_{jx} .

5.3 The launching occasion of each urgent firing

5.3.1 Theoretical model

If the firing in the queue is "i", its launching occasion is T_i min after beginning suppression, then, the T_i can be generated by the following formula:

$$T_{i} = \begin{cases} 0 & i = 1 \\ \sum_{n=1}^{i-1} \frac{60T}{C_{jx} - 1} \sin A_{n} & i > 1 \end{cases}, \quad i = 1, 2, \cdots, C_{jx}$$
(9)

In the formula, *T* is the suppression time, which is measured by hour.

In order to avoid the case that launching shooting occasions between urgent firing and monitoring firing is too short, the A_n should alter in the scope of $(\pi/3, \pi/2)$.

5.3.2 The solving algorithm

The steps of the algorithm of all urgent firing occasions generated are as follows:

(1) Call C_{ix} , enter the suppressing time T and the sequence number i of urgent firing.

(2) As to the first urgent firing launching occasion, that is, if i = 1, the result is 0, that is, when beginning suppression, launching first urgent firing.

(3) When the launching occasion computed is not the first occasion, that is, $i \neq 1$, set the circle figure variable b = 1 (the maximized value of b is i);

(4) if b is equals to i, output random value, otherwise, output T_i sequenced in i:

$$A_n = \frac{60 + 30rand()/65536}{360 \cdot 2\pi} \tag{10}$$

(5) Compute and record the launching occasion T_b of the urgent firing sequenced b:

$$T_{b} = T_{b-1} + 60T/(C_{jx} - 1) \cdot sinA_{n}$$
(11)

(6) After adding 1 to b, switch to the 4th step.

6. Conclusions

In this article the factors in the temporal suppression firing distribution is established, which include urgent firing frequency, monitoring frequency, ammunition consumption of every urgent firing, and their launching occasions. In order to satisfy the automated decision of shipboard gun weapons when firing anti-shore, mathematical model is established, and the algorithm of the above factors is solved by the new generating model and generating process, furthermore, the generated model is not only useful, but also easy and quick to compute, and thus provide strong technical support to the automation of the decision-making of the shipboard gun weapons when firing anti-shore.

References

- [1] Military Training and Branch Department of Headquarters of the General Stuff. American Joint Publications1-02, Department of Defense Dictionary of Military and Associated Terms, as amended trough 7 May 2002, [M],2002:642.
- [2] Chen Yun-men. Principles for evaluating firing efficiency. Liberation Press, Beijing China, 1984: 388.
- [3] Guan Qing-yun, Li Xue-qi. Memoir of "Nerver Center"2009 "Chinese command and control" High-Level Forum, 2009.10:203.

Operational Capability of Ship-to-air Missile Weapon System

Lu Yonghong^{1,a}, Dou Jihua^{1,b}, Yang Xingbao^{1,c} and Zhu Chuanwei^{1,d} ¹667#, Jiefang Road, Zhongshan District, Dalian City, China

^alyh222@163.com, ^bedjhs@163.com, ^cyxfsf@126.com, ^dzhuchswe@163.com

Keywords: Ship-to-air missile, Weapon system, Operational capability, Evaluation

Abstract. As operational capability of the weapon system can be varied with each fire, it proposes operational capability evaluation method for the weapon system, afterwards it proposes operational capability evaluation method for the weapon fire taking the impact indicators such as single target detection probability of shipborne early-warning radar into account.

Introduction

All manuscripts must be in English. Please keep a second copy of your manuscript in your office (just in case anything gets lost in the mail). When receiving the manuscript, we assume that the corresponding authors grant us the copyright to use the manuscript for the book or journal in question. Should authors use tables or figures from other Publications, they must ask the corresponding publishers to grant them the right to publish this material in their paper.

Operational capability evaluation of ship-to-air missile weapon system is an important elementary work for the combat employment of the weapon system. Zhao C.G.¹ proposes the exponential method for the operational capability evaluation, Jia C.² proposes the queuing method. These methods can not assess the operational capability evaluation indicators in an operational environment. Although Ma L.T.³ proposes fuzzy comprehensive method in an operational environment, this method can not take the impact indicators of the operational capability such as single target detection probability of shipborne early-warning radar, control probability of shipborne combat command system, single target acquisition probability of tracking radar, single target damage probability into account, and still needs to assess the operational capability evaluation indicators of the weapon system.

Therefore, the next step in the operational capability evaluation method for ship-to-air missile weapon system is to take the above impact indicators into account, which can assess the operational capability evaluation indicators of single ship-to-air missile weapon system onboard single surface ship in an operational environment.

Operational capability evaluation method for the weapon system

Once ship-to-air missile weapon system is in total failure or done with the designated air defense mission, the operational phase of the weapon system which includes N_s times of weapon fires is over, $N_s \ge 1$.

Usually the operational capability of the weapon system can be varied with each fire, it should firstly construct the operational capability evaluation model of the weapon fire, which can obtain the operational capability evaluation indicators of the weapon fire such as single target damage probability, multi-target damage probability, expected target damage. Through the addition operation of the above evaluation indicators, it can obtain the operational capability evaluation indicators of the weapon system such as single target damage probability, multi-target damage probability, expected target damage probability, multi-target damage probability, multi-target damage probability, expected target damage probability, multi-target damage probability, multi-target damage probability, expected target damage probability, expected target damage probability, expected target da

Operational capability evaluation method for the weapon fire

In the process of the weapon fire, there are more than one target to fire at. It should firstly construct the capability evaluation model of firing at single target to assess single target damage probability, and then construct the capability evaluation model of the weapon fire.

Capability evaluation model of firing at single target

Usually shipborne early-warning radar delivers target information to shipborne combat command system after it detected targets. Afterwards shipborne combat command system is in the control process of track processing, Identification Friend or Foe (IFF), threat estimation and so on. In the end, shipborne combat command system offers target designation to ship-to-air missile weapon system under its operator's control. We denote single target damage probability by C_{db} , it can be calculated by

$$C_{db} = P_r P_c P_b P_s \tag{1}$$

where P_r is single target detection probability of shipborne early-warning radar⁴, P_c is target acquisition probability of the weapon system's tracking radar, P_b is control probability of shipborne combat command system, P_s is single target damage probability.

The reliability of single man-machine system is the multiplication of machine reliability and operator's reliability⁵. P_c can be calculated by

$$P_{c} = R_{sht} R_{shtry} P_{sb}$$
⁽²⁾

where R_{zht} is the operational reliability of shipborne combat command system which can be assessed by using fuzzy comprehensive evaluation method⁶, R_{zhtry} is operator's reliability which can be assessed by using expert evaluation method, P_{sb} is the probability of IFF⁷.

 P_b can be calculated by⁸

$$P_b = \zeta_{bq} P_a$$
 (3)
where ζ_b is the influence coefficient of marine meteorological environment P is the target

where ζ_{bq} is the influence coefficient of marine meteorological environment, P_{α} is the target acquisition probability of single-scan of the tracking radar antenna.

Usually the main influence factors of P_{α} is signal-to-interference ratio (C/I) of tracking radar receiver. C/I can be calculated by

$$C/I = \frac{G_s}{G_z + \sum G_{jy} + \sum G_{jw}}$$
(4)

where G_s is target echo signal power of the receiver⁹, G_z is instantaneous noise power of the receiver¹⁰, G_{jy} , G_{jw} are active and passive jamming signal power of the receiver respectively¹¹, Σ is addition operator.

As reference 8 proposes the method for assessing P_{α} according to target designate accuracy and target fluctuation characteristics. If C/I is in normal distribution, it can assess P_{α} by using C/I instead of signal-to-noise ratio (S/N) in reference 8.

 P_s can be calculated by N_{dm}

$$P_{s} = 1 - \prod_{i=1}^{mn} (1 - P_{si})$$
(5)

where N_{dm} is ship-to-air missile number fired at single target in the process of the weapon fire, P_{si} is single target damage probability for No.i missile which can be calculated by

$$P_{si} = R_{sfi} P_{sti} \tag{6}$$

where R_{sfi} is the flight reliability of No.i missile which is affected by missile check-out reliability, missile fire reliability, missile guidance reliability and missile hit reliability. As triangular fuzzy number¹² can be used to assess missile flight reliability, we denote triangular fuzzy number of ship-to-air missile flight reliability by P_f , it can be calculated by

$$p_{f} = \min\{p_{f}, p_{f}, p_{f$$

where a_f is the left point of p_f , m_f is the middle point of p_f , b_f is the right point of p_f , p_{ff} , p_{fs} , p_{fs} , p_{fx} , p_{fm} are the triangular fuzzy numbers of missile check-out reliability, missile fire reliability, missile guidance reliability and missile hit reliability respectively. Then R_{sfi} can be determined by P_f :

$$\mathbf{R}_{\mathrm{sfi}} = {}^{m_f} \tag{8}$$

where P_{sti} is single target damage probability of No.i missile in normal flight which can be calculated by

 $P_{sti}=\zeta_{stqi}\zeta_{stji}P_{stli}$ (9) where ζ_{stqi} is influence coefficient of marine meteorological environment, ζ_{stjc} is influence coefficient of target's anti-missile maneuver, P_{stli} is single target damage probability of No.i missile under electromagnetic interference. Reference 13 provides the method for assessing P_{stli} under the conditions of direct damage and fragment damage.

Capability evaluation model of the weapon fire

We denote the target number in the process of the weapon fire by N_d , K targets damage probability can be defined by

$$P(x=K) = a_K \tag{10}$$

$$\prod_{I=1}^{N_d} [(1-P_I) + P_I z] = \sum_{K=0}^{N_d} a_K z^K, P_I \text{ is No.I target}$$

where a_K is the coefficient of z^K for the equation $\prod_{I=1}^{L} \prod_{I=1}^{L} \prod_{I=1}$

We denote the expected target damage of the weapon fire by E, it can be calculated by

$$E = \sum_{I=1}^{N_d} P_I \tag{11}$$

Summary

Usually the operational phase of ship-to-air missile weapon system includes multiple fires. As the operational capability of the weapon system can be varied with each fire, it proposes the operational capability evaluation method for the weapon system, afterwards it proposes the operational capability evaluation method for the weapon fire taking the factors including single target detection probability of shipborne early-warning radar, control probability of shipborne combat command system, single target acquisition probability of tracking radar, single target damage probability into account. In the end, it can obtain the operational capability evaluation indicators of the weapon system, which can assess the operational capability of single ship-to-air missile weapon system onboard single surface ship in an operational environment, and provide an operational capability evaluation method for other weapon system.

The development of the proposed method has been an ongoing project, the next step in the research is to implement the proposed method in surface ship air defense operations and exercises.

References

- [1] C.G. Zhao, et al. Journal of Projectiles, Rockets, Missiles and Guidance, Vol.21, 31(2001).
- [2] C. Jia, Journal of Modern Defence Technology, Vol.33, 22(2005).
- [3] L.T. Ma, W.C. Han, Journal of Modern Defence Technology, Vol.32, 11(2004).
- [4] L.X. Chen, Effectiveness Evaluation of Network Air Defense Missile Systems, *National Defence Industrial Press*, China (2007).
- [5] P.G. Xu, Tactical Missile Technology, 7(1993).
- [6] J.F. Zhang, Applications of Fuzzy Mathematics. *Geological Publishing House*, China(1998).
- [7] C.F. Huang, *Telecommunication Engineering*, 1 (2000).

- [8] D.K. Barton, Radar System Analysis and Modeling, Artech House Publishers (2004).
- [9] R.L. Liang, *Shipboard Electronic Countermeasure*, Vol.26, 34 (2003).
- [10] Y. Jiang, S.H. Huang, Journal of Yangtze University, Natural Science Edition, Vol.1, 17(2004).
- [11] Y.B. Liu, et al. Systems Engineering-theory & Practice, 142 (2008).
- [12]L.B. Yang, Y.Y. Gao, Fuzzy Mathematics Theory and Application, *South China University of Technology Press*, China(1993).
- [13]G.Y. Wang, L.D. Wang, Radar Electronic Warfare System Mathematical Simulation and Evaluation, *National Defence Industrial Press*, China (2004).

The Research of Conventional Weapons Proving Ground Information System Construction

Zhang Xiao-ying^{1,a} Lu kun^{1,b} Wang Huai-jun^{1,c} Ma Hai-hui^{2,d}

¹Baicheng Weapon Test Centre, Baicheng, 137001, China

²PLA,No. 63961 Troop, Beijing 100012, China

^axiaoerl@163.com, ^blukun9898@sohu.com, ^cwanghj72@sina.com, ^d568238167@qq.com

Keywords: High level architecuture(HLA);Information, Conventional Weapons Proving ground, Federation member

Abstract. In order to meet our military weapons of information-based development, reform methods and models of proving ground test, improve function test of the technology and tactics and combat efficacy evaluation of weapons, this article proposed ideas and methods of conventional weapons proving ground transformation based on HLA. This article based on the basic concepts, methods and principles of HLA, introduced to the HLA simulation architecture in information proving ground building. This page analyzed and designed the information system of proving ground. On this foundation, system structure of the system was built, and the realization method of federation members' classification and the design of FOM / SOM and members' interface were introduced.

Introduction

Modern war is the confrontation of system-to-system. It covers all-system, all-direction and multiarms of the services containing the Army, the Navy and the Air Force. It must set off innovation of shooting range test method and model, demand that our army shooting range should adapt to information weaponry, provide information war environment near actual combat, finish the technology and tactics function test and combat efficacy evaluation of information war weaponry. It is inevitable of building the information proving ground to accomplish the test task with high quality and efficiency.

Information proving ground that based on digital information network covering the entire area of the proving ground and relied on highly visual test command connecting various proving grounds and each trachea of the trial with computer-based digital communication subsystems and the information system platform, realizing the data identification, collection, transmission, processing, sharing and use of the information.

The main feature of information proving ground includes digitization, automation, networking and visualization, precision.

Digitization that is the base of automation and networking uses of various means of communication, high-capacity broadband, high-speed multi-link information channel to achieve test information timely, accurate, long-distance transmission and switching. The automation is that the information of test equipment automates collection, collation, dissemination, processing and decision-making. The visualization is that network monitoring that consists of sensors links to the command center for Visualization, control, automatic management of the entire trial. The network is that various devices united an organic whole in spreading throughout, constituted a test environment for information equipment and real-time transmitted. The real-time is an important prerequisite that results is scientific, reasonable and accurate. Precise command and safeguard, which relies on C⁴IRS system, with the decision support system, timely and accurately analysis processing information, fine and accurately plans for a variety of test resources, makes accurate security schemes, provides reasonable and effective test method, timely and accurately commands and controls for the experiment, reduces risk and loss during the experiment, makes a scientific and reasonable identification for weapon system based on evaluation system.

A Brief Introduction to HLA

HLA is a common high-level architecture in areas of the modeling and simulation, issued by the U.S. Department of Defense. It provides a standard architecture for interconnection, interoperability and reusability among different simulation applications^[1].

HLA consists of three parts:

- Rules;
- Object Model Template (OMT);
- Run-Time Infrastructure (RTI).

Rules define a number of principles that should be consistent with federation and federal members. RTI is an HLA software of the simulation host, and equal to a distributed operating system. The simulation applications communicate with the local RTI to notice RTI what data to be issued or required. Then RTI communicate with other simulation applications in order to achieve an exchange of information between the entities.

RTI offers six kinds of service:

- Federal management, which coordinates activities within the federal scope throughout the life of federal operation.
- Announce management, which provides services to the federal members for stating the object state and interaction information that they want to create and receive, and carrying out object-based classes or interactive classes of data filtering.
- Object Management, which provides services to create or delete objects, of object-data transmission and data exchanging.
- Ownership management, which provides services to convert the ownership of object attribute among the federal members.
- Time management. which control and coordinate to advance local-clock management types of federal members (such as the DIS simulation system, the real-time simulation system, the time step simulation system, the simulation system, Event-driven simulation system and the optimistic mechanism simulation system) on the federal timeline , and provides services to meet the different data transmission (such as the reliable transmission and the best-effect transmission) requirements for all federal members.
- Data distribution management, which provides the dynamic-interest-description, information members want to be able to send and receive, for federal members, in order to achieve value-based data filtering.

Overview of HLA-based Information Conventional Weapons Proving Ground

a) Functions and Role of Information proving ground^[2]

The technical and tactical performance of weapons and equipment is inspected and identified, and its operational effectiveness is evaluated. The digital weapon testing, scientific decision-making, timely and efficient testing, data sharing, quick and easy information inquiring, command decision-making assisting, function of Analyses evaluation and automatically generates test program are realized, making use of modeling and simulation technology. The information proving ground is built. The online training carries out. Training and exercising information warfare commander meets future information warfare. It establishes a scientific and reasonable testing program for greatly improving the efficiency of testing command.

b) The Main Features of the Information proving ground

It is the main features of the information proving ground that systems such as the battlefield environment simulation system, the battlefield threat simulation system, the electromagnetic environmental monitoring system, the target feature measurement and positioning system, the command and control system, and so on, can achieve information exchange in the control network. The proving ground, uses HLA specifications to build test networks, connects the various subsystems throughout everywhere into an organic whole, constitutes the test environment for the information weaponry, and builds a virtual proving ground.

c) Test Equipment Configuration of Proving Ground

- ground and air tracking systems;
- theodolite;
- data collection and transmission system;
- communication system;
- telemetry system;
- speed measuring system;
- electronic display device;
- geodetic system;
- GPS measurement and control system;
- environment simulation system.

d) Compositions of the Information Proving Ground

(a)Network communication layer: Test network of proving ground which divides into wired and wireless network achieves scheduling system resources, dividing sub-networking of task, making a plan of system working and equipment scheduling, configuring strategy of data distribution and IP addresses, managing public resources that includes IP addresses, port, node identification of information, avoiding configuration conflicts.

(b)The basic resource layer consists of a basic database and a model base management system, with the resource server as a carrier. It does not only provide storage, query, retrieve, extract, backup, recovery, but also complete the inspection, who, statistics, analysis, sorting, processing and so on, for all types of address registration resources. And it ensures the independence, integrity, modifiability, scalability, and security confidentiality of simulation resources.

(c)The simulation support layer has a complete simulation support tools and platforms including model testing, operation, demonstration and evaluation. It easily extracts the simulation resources of weapons and carries out design, development, integration, operation, demonstration, evaluation of simulation test. It is the important information bridge between simulation resources and simulation applications.

(d)The Management control system is the system control center and the management center. It is composed of a whole using all kinds of simulation resources and nodes. It achieves integration of analysis of weapon system and function of simulation system. It achieves integration and automation of Management control.

e) The Architecture of the HLA-based Digital Proving Ground

The HLA-based system block diagram is shown in Figure 2. It includes the HLA-based architecture simulation system, the simulation environment generation system, the model database, the simulation and testing system, the performance evaluation system, the command and control system, the test and exercise trend monitor system, the equipment testing platform and so on. All of them complement each other, and constitute a organic whole^[3].

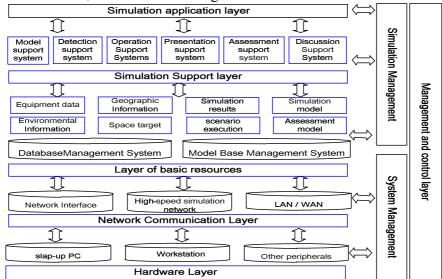


Figure 1 The HLA-based information proving ground's structure

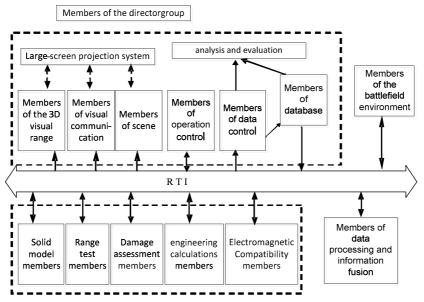


Figure 2 The HLA-based system block diagram

The Design ideals of the HLA-based information conventional weapon Proving Ground

a) The construction principle of information proving ground

The construction of proving ground should rely on existing equipment and networks, and highlight the top-level design. It haves a comprehensive test capability, and is complement and each other authentication along with test site. It adheres to the "practical, reliable, advanced, economy" principles, adopts the sophisticated and advanced technology. It uses design of modularization, standardization and network, emphasizes practicality, openness and scalability.

b) The design of information proving ground

(a)It uses the existing network system, establishing all-round and three-dimensional visual network which is consists of monitoring equipment and sensors, linking to the test field area of command and control center, so that the whole test are visualized and controlled, and achieves transmission and switching of multimedia test information that is time, accurate, and long-distance.

(b)It is C⁴IRS system as the core, with a help of decision support system, relying on the existing analysis and evaluation system, accurately and timely collecting various test data, improving capabilities which a variety of facilities and equipment analyses and information makes decision, fast processing, analyzing, evaluating the obtained information. It timely and accurately controls during the test implementation, reduces the risks and losses to a minimum, so that the command is more precise and accurate.

(c)To establish high-quality accurately electronic proving ground, through aerial photography, geodesy, it establishes GIS geographic information system of proving ground, and creates a virtual electronic proving ground in using electronic maps. It selects the point of impact areas and clearance information by the decision-making system which uses the data of electronic proving ground.

(d)Using in line with HLA / RTI software MAK RTI to establish all the federal members, and reforming the existing simulation systems in adopting RTI interface, it was joined in the federal member FOM/SOM model and expressed in OMT templates.

(e)It creates three-dimensional model with cultigens creator, generates the format that 3D Max can identify by 3D Exploration conversion tool changing, and establishes three-dimensional simulation system by visual simulation tool named Vega. Some simulation tools software development model can directly compiles and generates executable file by common programming languages (such as c, c++, C#, etc) so that the file can be run independently of the simulation environment. The model code can be modified so that it can be able to complete the required functionality HLA standard.

The Design and Implementation of the HLA-based Information Proving Ground

a) Upbuilding Federal Members

The existing ten items of HLA rules respectively regulate federation and federal members, the specific structures of which are shown in Figure 3.

(a) Members group of the director side.

Members of simulation manager group: According to the simulation users' requirements, manage, control and surveil the simulation; modify the performance parameters of the weapon system; control the content of the presentation.

Members of evaluation group: Evaluation team will take the treatment process according to the index system, the output of the simulation application system, which is the number or percentage of every weapons and equipment of every operational unit of the other power (the red power or the blue power) damaged by one power's every weapon of every basic operational unit.

Collection members of the data device: The data collection tool (DCT) collectes memberinteraction data defined by FOM, and archives it in a database; The members themselves recorde the internal private data.

Members of the three-dimensional visual display: To be used in the process of simulation; Using MultiGen Creator and Vega to exploit and design.

(b)The red power and the blue power include three categories of member srespectively.

Real class members: Members of weapons, members of electronic supporting, members of the battlefield threat simulation, members of the electronic countermeasure. Members of weapons comprise armored assault weapons, suppression weapons, air defense weapons, long-range strike weapons, airborne weapons, cruise missiles, ship-borne weapons and small arms.

Virtual members: Members accessed to the simulator (physical) node.

Structural members: Members with HLA standard from the software implementation.

(c)Environmental member groups: The meteorological environment members, the electromagnetic environment members and the geography environment members.

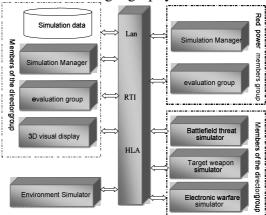


Figure3 The structure of HLA-based digital proving ground's member

b) Federal / Simulation Object Model (FOM / SOM) Design

HLA object model is mainly used to describe the various members of the federation (SOM) and the federal members with the mutual information exchange characteristics (FOM)^[4]. OM is divided into three levels: The bottom layer is the object; the middle layer is the federal member; the top layer is the federation. Its description consists of OMT and OMT extension. OMT is composed of the object class structure table, the object interactive table, the properties / parameters table and the FOM / SOM dictionary. OMT extension is composed of the component structure table, the relationship table and the object model metadata. The data exchanges among members by means of the "Object Properties" and the interactive "public" and "order" service provided by RTI: In the federal operation process, the statement releases the object class attribute or interaction class members continue to

provide updates of property values or interaction, and the ordering data members themselves receive data and localize it to be used.

The design and implementation of the digital proving ground is based on the object model development tool KD-OMDT, which includes the model identification table, the object structure table, the attribute table, the interaction table, the parameter table, the enumerative type data table, the complex type data table, the routing space table and the model dictionary table. Users fill in the table of the model information. And it can automatically generates *. fed and *. omt files with the V1.3 standard.

c) HLA federate interface design and implementation

RTI software mainly consists of RtiExec, FedExec and libRTI, and they run in a separate workstation. Process RtiExec manages the creation and withdrawal of the federation, and instructs members to enter the right federal execution. FedExec manages the federal members's joining and leaving, each running federation corresponds to a FedExec process. LibRTI is a C + + library providing a range of services of the HLA interface specification definition for the member-developers. Members communicate with RtiExec, FedExec and the others, by libRTI calling the HLA-service.

The interfaces with RTI of federal members include Creating and joining federation, initializing RTI data, the announcement / order relationship requesting time promoting, updating and reflecting the object's attribute value, sending and receiving interactive, exiting and revocation of federal, etc. Specific procedures are as follows:

Start run.

Initialize member data.

Create RTIAmbassdor object rtiAmb.

Create FederateAmbassador object fedAmd.

Initialize simulation objects.

Call RTIamb.createFederationExecution to create federation.

Joined the federation-executive.

Call RTIamb.joinFederationExecution to join the federation.

If an exception occurs when adding, it will exit the program.

Obtain the object class and its attribute, the interactive class and its parameter's handle value, defined by Fed files.

Call rtiAmb.getObjectClassHandle to get the handle value of the object class.

Call rtiAmb.getAttributeHandle get the handle value of the object class' attribute.

Call rtiAmb.getInteractionClassHandle to get the handle value of the interaction class.

Call rtiAmb.getParameterHandle to get the handle value of the interaction class' parameters

Announce the ordering relationship.

Call RTI :: AttributeHandleSetFactory :: to create a handle set for each object.

Call rtiAmb.subscribeObjectClassAttribute to order an object set.

Call rtiAmb.publishObjectClass to publish an object class.

Order and publish an interactive class by calling rtiAmb.subscribeInteractionClass and rtiAmb.publishInteractionClass.

Announce the time promoting policy (default is neither Regulationg nor non-Constrained)

Call rtiAmb.enableTimeConstrained to announce the time promoting as Constrained.

Call rtiAmb.enableTimeRegulationg to announce the time promoting as Regulationg

If it is necessary to create a new object, call rtiAmb.registerObjectInstance to register and record the returned value of the instance handle.

Update the object instance attribute value and send interaction.

Uupdate attribute values.

Call RTI :: AttributeSetFactory :: create. Creat RTI :: AttributeHandleValuePairSet. Call rtiAmb.updateAttributeValues to update the instance attribute value. Send interaction Call RTI :: ParameterSetFactory :: create. Create RTI :: ParameterHandleValuePairSet. Call rtiAmb.sendInteraction to send interactive. If the simulation is finished, jump to 8). Call rtiAmb.timeAdvanceRequest to request the time promoting. RTI call rtiAmb.tick processing events until the allowed time promoting, jump to 8). End the program execution Call RTIamb.resignFederationExecution to secede federation. Call RTIamb.destroyFederationExecution to withdraw federation.

Conclusion

As a new generation of the distributed simulation architecture, HLA provides an effective method and means for weaponry research and improving it's performance, in the application of a proving ground test simulation system. It has the reconfigurability, interoperability, and spatial-temporal consistency, which can enhance the combat simulation fidelity, improve the system stability and efficiency and meet the requirement of complex systems for the flexibility and scalability. HLA becomes the future development direction of the distributed simulation technology.

References

- [1] Qiu Xiao-gang, Huang Kedi. Computer Simulation, 1998 (1).
- [2] Su Ying, KANG Fengju, YAN Jintun, et al. Journal of System Simulation, 2004 (12).
- [3] Liang Yangang, Tang Guojin, Yong Enmi. Journal of National University of Defense Technology, 2004, (5).
- [4] Zhou Yan, Dai Jianwei. HLA Simulation Program Design[M]. Publishing House of Electronics Industry, Beijing, 2002

Research on Armored Mechanized Forces' Equipment Support Simulation Training System

Zhang Xiao-ying^{1,a}, Lu kun^{1,b}, Wang Huai-jun^{1,c}, Ma Hai-hui^{2,d}

¹ Baicheng Weapon Test Centre, Baicheng, 137001, China

² PLA,No. 63961 Troop, Beijing 100012, China

^axiaoerl@163.com, ^blukun9898@sohu.com, ^cwanghj72@sina.com,^d568238167@qq.com

Keywords: Armored Mechanized Forces; High level architecture(HLA);equipment support; training

Abstract: Armored mechanized forces' equipment support simulation training system is the use of HLA technology combines emulator, computer generated forces and other devices as a whole which form a virtual battlefield environment in time and space coupling by network. This paper simulation training, introduces the construction of project, establishes the System architecture, and designs the idea which is used in distributed equipment support simulation training system based on the concepts, methods and principles of HLA.

Introduction

Equipment support is an important part of the combat effectiveness of armored mechanized forces. As an important part of military training, equipment support training is the basic way to improve the armored mechanized forces' ability of equipment support. he technology of HLA, armored mechanized forces' equipment support simulation training system which is an effective means to improve the equipment support efficient of simulation. Through the network it makes the emulators scattered around, computer-generated forces, and other equipment as a whole, which forms a battlefield environment time and space, coupled to each other virtual.

Armored Mechanized Forces' Equipment Support Simulation Training System Analysis

Theoretical knowledge of equipment support learning and assessment evaluation functions, battlefield environment production, browsing, analysis functions, equipment support icon plotting function, plan making and text editing functions. Icon plotting based on the electronic map and the military standard library, all kinds of plan documents to draw, edit and realize the automatic conversion of plan and icon.

Building the equipment damage database and armor equipment maintenance expert-base functions ,equipment support force allocation, deployment and the program of managing customization functions. The functions of customizing equipment support force allocation, deployment and the program of managing, which lay a data base for assessment of the way to support.

Equipment support command training function. This function can train the equipment support commander of the formations and brainwave disposal capacity. This function is designing of command and control model to meet the demand of the future digital forces.

Equipment security agencies at all levels of networking tasks according to their own. Equipment support institutions at various levels training with networking according to their own task function. According to the number of tasks and participating in the training, you can choose the specific equipment support institutions to organize networking training in this function.

System Structure of Simulation System Based On HLA

a) Overview of HLA

In 1996, the U.S. Department of Defense released a common technical framework for modeling and simulation, which composed by the CMMS (Conceptual in only a Model of Mission Space CMMS),

modeling and simulation of high-level system structure (High Level Architecture, HLA for short), and a series of data standards in three parts. The core of HLA ideology is interoperability and reuse. its remarkable characteristics is to provide a universal and relatively independent support service program to separate the achievement, the management of simulation running and the bottom communication transport ,through the operation support environment (Run Time Infrastructure, RTI). The three separations are concealed their respective implementation details, so that each part can be developed relatively independently, and makes full use of advanced technology in their respective fields. It can provide more mass, integrated environment which makes the structural simulation, virtual simulation, and live simulation together to realize all kinds of simulation system of mutual operation, the dynamic management, point-to-multipoint communications, reuse of systems and components and to establish the different level of object model.

HLA consists of three parts^[1]: Rules gives the rules that the simulation must follow to join into the HLA system. The aim is to ensure the simulation applications can be interoperated when simulation is running. Interface specification of RTI (Run-time Infrastructure),its function is similar to distributed operating system for a particular purpose, which provides members with a variety of services which is needed to run.RTI provided federal management, declaration management, object management, ownership management, time management and data distribution management, six categories of services. Through the application interface layer and the network interface layer, it can separate simulation applications, the bottom support and the RTI function modules. Object Model Template defines a standardized description of the simulation objects, the format and content of information that simulation objects exchange, to ensure the reusability of modeling and simulation components.

b) System Structure of System

Armored mechanized forces equipment support training simulation platform, whose research object is equipment support training of division and regiment two level equipment departments^[2]. The main contents includes three subsystems: equipment support theoretical knowledge, equipment support business and skills training, equipment support simulation training. The ultimate goal is to achieve the full training from soldiers to the head, the full training from start to the end of battle, the full training from the unit to the organ system-wide in networking of training. As shown in figure 1 below.

Simulation Training System Design of Armored Mechanized Forces Equipment Support^[3,6]

a) Equipment Support Theoretical Knowledge Base Subsystem

Producing equipment support theoretical learning courseware by Flash, multimedia and other technology, including job responsibilities of various equipment support, business processes, operational demonstrations, various types of equipment support action decomposed demonstration, and equipment support the database.

b) Equipment support business and skills training subsystems

Equipment support business and skills training subsystem can be divided into business training and skills training, the two subsystems. As shown in figure 2 below.

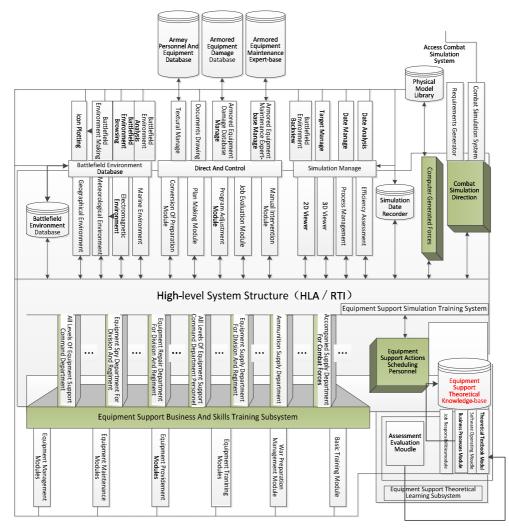


Figure 1 System structure of armored mechanized forces equipment support simulation training system

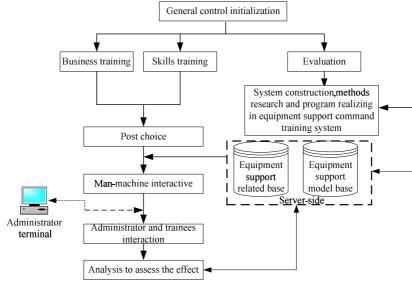


Figure 2 System Structure of Equipment Support Business and Skills Training Subsystem The subsystems use the equipment support network resources base and the physical model library base, to realize role-based equipment support business and skills training to meet the requirements of equipment departments and support team mastering post business and skills.

Equipment support business training subsystem includes equipment management module, equipment repair module, equipment supply module, equipment training module, war preparation

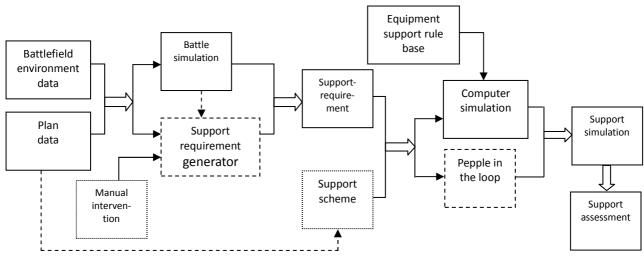
management module according with the idea of " management, repair, supply, training, preparation ". By the way, the basic skills training of the military tactical staff and the equipment assistants attribute to the basic training module. Equipment support business and skills training subsystems as the six business training to basic content, including a variety of data support (database) and the corresponding data management module, constitutes an equipment support business training network ,which is based on the role-based. It can simulate to complete equipment department and the unit's operation and meets the equipment department and the element's business training needs.

The subsystem of equipment support skills training can be set for the seven parts, equipment support command skills training module, battlefield equipment support reconnaissance training module, equipment with rescue skills training module, equipment repair skills training module, equipment supply and training module, ammunition supply module, accompanying supply for combat units training module in accordance with the ideas of the battlefield specialization. It can be self-contained to train, can also be added to the HLA network for networking training as a federal member.

c) Equipment Support Simulation Training System

Equipment Support Simulation Training System, including eight large systems, battlefield environment subsystem, adjusting control subsystem, simulation management subsystem, battle background inference subsystem, computer generated forces subsystem, people in the loop equipment support skills training subsystem, equipment support actions scheduling subsystem, the HLA network subsystem., realizes the main function of the simulation training of forces' equipment support department.

As shown in Figure 3 below.





(a)Battlefield Environment Subsystem

Battlefield environment subsystem's main function is processing and integrating the data of the battlefield environment of exercise training ground, analyzing terrain features, observing the exercise venues and exercise process, in any point, at any angle, any distance n. Its main purpose is to provide real-time, field and a full range of battlefield browsing for the military tactical staff, but also analyzing the battlefield data to provide more detailed quantitative information of the exercise area for exercise designing and adjusting controlling. On the other hand, it can generate a database of the battlefield environment, and provide data base to support operations simulation.

As the HLA federal members, the geographical environment, the meteorological environment, the electromagnetic environment, the marine environment, accessed high-level system structure, provide real-time battlefield environmental data for simulation training equipment support.

And other auxiliary functions include icon plotting, battlefield making, battlefield browsing, battlefield analysis and so on.

(b) Adjusting Control Subsystem

The adjusting control subsystem includes the structure conversion module, the plan making module, the demand generation module, the program adjustment module, the job evaluation module, the manual intervention module, the equipment damage database, the equipment maintenance expert database, etc. It can provide data support and guide control for support action simulation to run smoothly

The structure conversion module's main functions include structure conversion, units and elements conversion ,equipment conversion data maintenance and other. It can complete the training of conversion process that units from peacetime structure to war time structure.

The plan making module is used to draw equipment support tactical background and actions added plan, realizing plan documents and data generated. This module can edit and generate military plan in manual semi-automatic way (extracted template and the bottom data from the database), using the method of the guide. The process is simple. The subsystem also has various equipment documents templates, and can write by itself.

The program adjustment module includes support requirements generation module, the deployment module, the force allocation module. Its main purpose is to provide basis data for support action simulation.

(c) Simulation Management Subsystem

It includes the 2D, 3D viewers module, the process management module, the efficiency assessment module and the data recording, management, analysis, playback module.

Using of modern evaluation theory, the efficiency assessment module establishes a rational, scientific, and effective evaluation index system, performs assessment to equipment support actions based on the equipment support scheme, results of a comprehensive and each individual assessment. As basis for the various security programs, the module determines the advantages and disadvantages of the various security programs, and then determines a more reasonable support scheme to provide support for equipment support command decisions. The function includes the capacity assessment, program evaluation, and comprehensive evaluation, and other.

(d) Battle Background Inference Subsystem

The battle background inference subsystem sets two main battle background inference way, one is simple battle process simulation, using equipment support requirements generator to generate support needs. The other is accessing battle simulation system.

(e) Computer Generated Forces Subsystem

The subsystem includes the equipment support autonomous behavior modeling and simulation, autonomous behavior modeling and simulation of the blue forces, as well as other peripheral modeling and simulation.

(f) People In The Loop Equipment Support Skills Training Subsystem

According to the classification of the equipment support departments, the main training objects include all levels of equipment support command departments, equipment spy department for division and regiment equipment rescue department for division and regiment, equipment repair department for division and regiment, equipment supply department for division and regiment, ammunition supply department for division and regiment for combat element

Equipment support command department includes the support command group of division and regiment. This group was mainly targeted at training equipment support command, that is the focus of training.

(g) Equipment Support Actions Scheduling Subsystem

The subsystem includes the various types of equipment support resource scheduling, battlefield event trigger, path planning, and other content.

D. Conclusion

As a new generation of distributed simulation system structure in the armored mechanized forces equipment support simulation training ,HLA provides effective ways and means in training to improve the teaching of theory and skills for armed forces to develop equipment development, support and management tasks coach activities of for the realization of integrated joint operations, thereby improving the overall comprehensive quality of officers and soldiers and effectively enhance the forces' ability of combat and support.

References:

- [1] Qiu Xiao-gang,Huang Ke-di HLA object model's concept,description and establishment. Computer simulation.1998 (1)
- [2] Gan Bin,Hao Jia-xin Lu Ming-yun. Design and Implementation of HLA-based Air Defense Simulation Framework. Journal of System Simulation .2009(01)
- [3] Wang Yi-zeng, Zhang Ji-long, Liu Zhi-qin. C~2 Model of Ground-to-Air Missile System with HLA-Based Simulation. Computer simulation. 2004(12)
- [4] He Jia-zhao, He Quan-ming, Guan Zheng-xi. Development of Missile Launching Training Simulation SystemBased on HLA. Journal of System Simulation . 2006(12)
- [5] Xu Sheng-liang,Li Ren-song. Research of the key technologies of naval aviation operation command train system. Ship Science and Technology.2009(5)
- [6] Li Xiang-yang, Huang Xian-xiang, Long yong, Zhang Zhi-li, Development of Surface-to-Surface Missile Operation Training Simulation System Based on HLA. Journal of System Simulation . 2008(21)

Detection Performance Analysis of Space-based Radar to Near Space Hypersonic Target

Song XIAO^{1,a}, Xiansi TAN^{1,b}, Hong WANG^{1,b} and Zhifang ZUO^{1,b} ¹No.2 Department, Air Force Early Warning Academy, Wuhan 430019, China ^atracyoioi@163.com, ^bwang572g@sina.com

Keywords: space-based radar; near space; hypersonic; detection; performance

Abstract. Aimed at the problem that it is hard to detect near space hypersonic target for conventional radar because of its high flight speed, flight height, and flight distance and so on, the detection performance of space-based radar to near space hypersonic target was analyzed. The characteristics of near space hypersonic target and the advantages of space-based radar was introducted, and then, the detection performances of space-based radar to near space hypersonic target from detection range, searching and tracking mode were studied. It has certain guiding significance for space-based radar development and perfection of near space detection system.

Introduction

The near space hypersonic target (NSHT) has the characteristics of high altitude, hypersonic, high mobility, low radar cross section (RCS) and so on, the problems are very prominent that the existing radar is difficult to find it in time and can not track stabling [1,2]. With the rapid development of near space target, the goal of early warning detection becomes more and more urgent, so the study of near space hypersonic vehicle detecting and tracking technology can lay the technical foundation for the improvement of the existing radar and the development of new detection equipment, and provide theoretical support for the construction of the target [3,4] of early warning detection system. Space based radar (SBR) is a satellite, space shuttle and space station as the platform of space rendezvous radar, synthetic aperture radar [5]. It can find the global scope, location and identification of ground targets, missile, strategic bombers, satellite, space debris, near space target and nuclear explosion and so on [6].

1 Near space hypersonic target characteristics

The electromagnetic scattering characteristics: the degree and frequency of plasma, electron collision frequency and radar frequency on the effect of plasma on the target RCS, when the radar frequency and plasma frequency are equal, plasma is the target echo attenuation effect; the plasma frequency and the electron collision frequency are mainly affected by the target altitude and speed, increases with the increasing of speed, and decreases with the height increasing; when the target speed is less than 8Ma, the scattering characteristics affected by the plasma is very small that can be neglected.

Infrared characteristics: there are mainly 3 kinds of strong source of infrared radiation in general: a) the engine nozzle and thermal components; b) the engine plume; c) heat radiation induced by aerodynamic heating.

The peak wavelength of radiation target decreases with the increasing of temperature, when the target temperature at 500~5 000K range, the peak wavelength of radiation is between $0.580 \sim 5.796\mu m$, covering the visible light ($0.38 \sim 0.78\mu m$), near infrared ($0.78 \sim 3\mu m$) and mid infrared ($3 \sim 6\mu m$) three regions.

Motion characteristics [7,8]: a) High flight speed. NSHT flight speed is between $5 \sim 16$ Ma, America NASA was successfully completed in 2004 X-43A flight experiment, speed can reach 9.8Ma; HTV-1 in the simulated flight Maher numbers 10 and 14, successfully carried out 30 times of hypersonic flight wind tunnel experiment. Visible, such goals in a short period of time to the global

target for rapid precision strike, the reaction time for defense system put forward higher requirements [7]. b) High flight height. NSHT flies at $20 \sim 100$ km high, higher than the traditional air combat, the goal of survival ability is enhanced, therefore, for the traditional air defense system operational distance put forward higher requirements. c) Strong motor ability. In cruise flight, NSHT general use cruise cycle way jumping maneuver, overcomes the ballistic vehicle susceptible to detection and interception defect, difficult to measure the flight data, flight trajectory is not easy to determine, therefore, are facing great difficulties for the detection and interception.

2 Advantages of space-based radar detecting the near space target

Space-based radar is capable of all-weather, to work in all weather, global coverage is not influenced by geographical, political, strategic, has many advantages of large observation range, anti stealth ability, detection of multiple functions, strong survival ability, especially in the missile and near space target defense, as long as the space-based radar did some modification, it can supply the geostationary infrared satellites, ballistic missiles and near space target fired warning function, mainly in the following areas:

a) The effect of SBR is not affected by clouds, it can provide a longer warning time. The missile cannot be determined under the clouds of the launching missiles by the traditional infrared sensor. SBR can detect the target before the target through the atmosphere which can save valuable time tens of seconds to intercept system, contribute to the successful implementation of interception, especially booster climb interceptors and midcourse interceptors.

b) SBR in tracking the incoming missile is more effective than infrared sensor. The incoming missile in the engine shut down after the "cool", especially the near space hypersonic target, the periodic hopping, ramjet cycle working scramjet, give continuous infrared detection difficult.

c) SAR SBR imaging can be flexible conversion, can be used for positioning, transmitting device for near space target surveillance and tracking of mobile system; SBR has the air moving target indication (AMTI) tracking ability, can monitor a plurality of a known location, at the same time the launch of providing a single transmit information.

d) SBR can provide near continuous reconnaissance capability, a 12 satellites constellation coverage on the surface of the average of about 5 min gap; while the 24 satellite constellation can be shortened to $1\sim2$ min gap.

3. Performance analysis of space-based radar

SBR itself does not improve weapon accuracy, but it can act as a cue and target source, guide other sensor on the possible target areas in order to observation, and guide the air plane to the expected target track nearby to capture and target. SBR and earth geometry is shown in Fig.1.

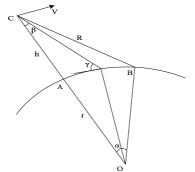


Fig.1 Geometric of SBR and earth

In Fig.1, C is satellite point; B ground points; H satellite altitude, respectively; β is the radar beam relative to the satellite velocity vector in the azimuth direction and downwards angle, α is the geocentric angle, r is the earth's average radius, γ is beam grazing angle. Rail height is given, grazing angle is a parameter satellite geometry relations between the most important.

a) Detection distance

The space-based radar detection range formula is:

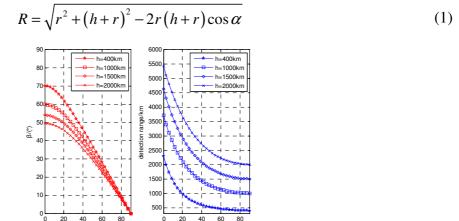


Fig.2 Relationship between grazing angle and downwards angle, detection range

As can be seen from Fig.2, with the increase of grazing angle, angle and detection distance decrease, the grazing angle unchanged, under the angle decreases with the SBR platform height, detection distance increases with the increasing of SBR platform height.

b) Constellation coverage capability

Space-based radar on the ground area covered by the beam maximum, minimum grazing angle and satellite height restrictions, and the geometric relationship between the available, covering area of space based radar:

$$S_e = 2\pi r^2 (\cos\phi_{\rm max} - \cos\phi_{\rm min}) \tag{2}$$

In the formula, ϕ_{min} , ϕ_{max} are respectively the largest and smallest grazing angle corresponding to the geocentric angle, grazing angle range is generally $3^{\circ} \sim 80^{\circ}$. Geocentric angle and detection area are shown in Fig.3.

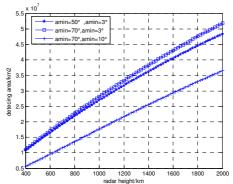


Fig.3 Relationship between geometric and detection area

When the target speed is smaller, less impact on the probability of detection, when the speed reaches hypersonic, detection probability will no longer increase with the accumulation time. When the accumulation time is less, because of the distance around is smaller, find probability increases with the increasing of the accumulation time. With the accumulation of time increases, more and more large range walks, detection probability reaches its maximum, but becomes smaller. The target with greater speed, can achieve the detection probability is small, the probability that the peak sooner. From the figure, when the speed is 5Ma, while the maximum probability of detection can reach more than 0.6, but the accumulation time requirement is above 60ms. By the above analysis, the traditional coherent accumulation limits, pulse accumulation time of up to 45ms. That is to say the target velocity is 5Ma; the maximum probability of detection can reach 0.55.

When the target acceleration is small and less impact on the probability of detection, with the increase of the acceleration, radar target detection probability is no longer strictly increases with the accumulation time, after reaching the maximum value, acceleration decreases.

c) The average power and antenna aperture

Radar range equation using signal to noise ratio (SNR) is:

$$S_{NR} = \frac{P_a \sigma A^2 t_o}{4\pi R^4 \lambda^2 L k T_s}$$
(3)

In the formula, S_{NR} is the signal to noise ratio, P_a emission average power, A antenna effective receiving area, t_o beam dwell time, σ radar cross section of target, R detection distance, T_s is the equivalent noise temperature; L system loss; λ radar operating center wavelength; k Pohl Seidman constant.

Searching model:

When the radar is in the search mode, 3dB beam area:

$$S_{3dB} = \frac{R^2 \lambda^2}{A} \tag{4}$$

Spatial search speed (namely the area coverage for ACR), dwell time:

$$t_o = \frac{S_{3dB}}{V} \tag{5}$$

Relations are derived for P_a and V:

$$P_a A = \frac{4\pi S_{NR} k T_s L R^2 \nu}{\sigma} \tag{6}$$

In the formula, $kT_s = 4 \times 10^{-21}$ W/Hz, $\gamma = 7^\circ$, $S_{NR} = 10 dB$ assuming that the receiver noise figure of $F_n = 5 dB$, the loss of system L = 7 dB.

Tracking model:

From the analysis of the characteristics of target, it can be seen that the near space hypersonic target has a strong mobility. The motor ability, maneuver and maneuver can bring the following effects to stabilization tracking:

a) Conventional tracking model is difficult to describe the changeable target maneuvering form

From the analyzing of target characteristics analysis and conventional maneuvering target tracking model, we can see that because of the variable near space hypersonic maneuvering forms, the traditional single model can not effectively describe the target maneuver, traditional multiple model will only a plurality of motor behavior, single model also can not accurately describe the target, so, the targeted model must be designed for the description of near space hypersonic target.

b) The target motion state converts faster than the conversion rate of traditional interacting multiple model.

Set the tracking number is N_T , the update interval is T_U , dwell time for a single target is:

$$t_o = \frac{T_U}{N_T} \tag{7}$$

$$P_a A^2 = \frac{4\pi S_{NR} k T_s L R^4 \lambda^2 N_T}{\sigma T_U}$$
(8)

In the formula, $kT_s = 4 \times 10^{-21}$ W/Hz, $\gamma = 10^\circ$, $S_{NR} = 15 dB$, assuming that the receiver noise figure of $F_n = 5 dB$, the loss of system L = 7 dB. The power aperture and square power aperture product search mode and tracking mode of the product is shown in Fig.4.

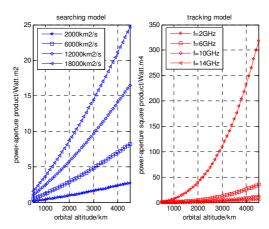


Fig.4 Power aperture product for searching model and tracking model

4 Conclusions

In recent years, near space hypersonic vehicle's political, economic and military value attracted worldwide attention and it becomes a research hotspot. Space-based radar with its special platform height and detection angle, to near space hypersonic target tracking monitoring, especially the early launch detection function of SBR can save valuable time of a few seconds for the defense system which contributes to the successful implementation of interception, it will become an important development direction of aerospace defense future.

References

- [1] Woolf, Amy F. Conventional prompt global strike and long-range ballistic missiles: background and issues. USA: Library of Congress Washington DC Congressional Research Service (2011).
- [2] Dodiyal A K, Garg P. Reducing RF Blackout During Re-entry of the Reusable Launch Vehicle. (IEEE Publications, Big Sky 2009).
- [3] Huber P. Hypersonic Shock-Heated Flow Parameters for Velocities to 46,000 Feet per Second and Altitudes to 323,000 Feet. Washington: National Aeronautics and Space Administration (1963).
- [4] Robinson, Jeffrey S. An overview of NASA's integrated design and engineering analysis (IDEA) environment. USA: American Institute of Aeronautics and Astronautics (2011).
- [5] Steven A.L, Thomas W. M. Overview of the Innovative Space-Based Radar Antenna Technology Program. Journal of Spacecraft and Rockets, Vol. 48 (2011), p. 135.
- [6] Steyskal, H, Schindler, J K. Distributed Arrays and Signal Processing for the TechSat21 Space-Based Radar. Air Force Research Lab (2009).
- [7] Voland R T, Huebner L D, Mcclinton C R. X-43A Hypersonic Vehicle Technology Development. Acta Astronautica, Vol. 59 (2006), p. 181.
- [8] Graham C, Johnson H, Alba C, et al. Analysis of modal growth on the leeward centerplane of the X-51 vehicle.USA: University of Minnesota (2009).

Cooperative Path Planning of Jammer Formation in Penetration Attack

Jianjun Ou^{1, 2, a}, An Zhang ^{1, b}, Zhongqi Chen^{2, c}

¹School of Electronics and Information, Northwestern Polytechnical Universityy, Xi'an 710072, P. R. China

²Engineering College of Aeronautics and Astronautics, Air Force Engineering University, Xi'an 710038, P. R. China

^aou_jian_jun@163.com, ^bzhangan@nwpu.edu.cn, ^cchenqi0321@163.com

Keywords: Cooperative penetration attack, cooperative jamming, jamming troop, penetration attack, path planning

Abstract. The study of cooperative fighting between jammer and fighter aircraft is helpful to improve the ability of penetration attack. Firstly, the conception of path point threat assessment is given, based on the jamming troop model. Secondly, the jammer free fly region conception, relative theorem and the resolving strategy are given, and as a result, the dynamic searching space can be got. Thirdly, by improving Sparse A* Search(SAS) algorithm and applying it in cooperative path planning of jammer formation, the realizing process is designed. At last, simulation is made. The results show that the strategy can quickly get the best cooperative path of jammer formation whatever fighter aircraft's penetration attack task.

I. Introduction

In modern complex battlefield environment, the survival of fighter aircraft is confronted with severe challenges. Confronting with interference, anti-radiation missile, low altitude invasion and stealth target, the enemy's counteraction ability in ground threat has been effectively improved through the network technology^[1]. Modern aircraft, even if has a good stealth performance, is hard to realize safe penetration^{[2]-[4]}. In order to improve the survival capability and attack power, fighter aircraft often need to resort to jammer to effectively suppress the enemy's threat nets. Collaborative operation is research focus of the current domestic and foreign electronic warfare, and has made great achievements. In Ref. [5], the authors gave the definition of jamming distribution, and pointed out that the purpose of the collaborative is to effectively attack, however, this research was limited to linear form and fan-shaped distribution of jammer. Literature [6] focused on the formation of self-defense interference. Through the airspace superposition method, the formation synergy airspace of electronic jamming was simplified into interference airspace of single jammer, and through the integer programming method, the electronic jamming power collaborative allocation model in air combat was established. In Ref. [7] & [8], the authors established the model of radar detection space influenced by electronic interference. This research showed that the collaborative oppressive jamming can effectively compress threat space and expand the optimal assault path search space, if the position of jammer was given. Unfortunately, these researches have few considered the degree of impact interference effect for target maneuvering and these authors generally limited jammer on a little position. These obviously contrary to actual combat situations. In Ref. [1] & [9], the authors considered the influence of target maneuvering, but jammer was limited to a specific circular area, and not to interfere with the research of optimal collaborative trajectory. The purposes of these researches about optimal trajectory of the jammer synergy are: 1) In order to effectively save limited interference resources, controling the jammer to occupy a suitable location to implement interference according to the position of the assault warplanes. 2) Through continuous adjusting the position of the jammer, guaranteeing the safety of the jammer.

Based on existing researches, in this paper, on the basis of the demand modeling of jamming troop and analysis on the interference effect, we research on the path optimization strategy of the formation of jammer against any specific assaults, and the simulation result is given.

II. Calculation Model of Jamming Troop

A. Suppression zone model based on the jamming support

By radar electronic interference principle, we know [10]-[12], assuming that the minimum suppress coefficient for the radar is K and a single jammer implement interference, its maximum detection distance is calculated as

$$R_{\max} = \sqrt[4]{\frac{P_t G_t^2 \sigma \lambda^2}{(4\pi)^3 F_n k T_0 B_n L K + \frac{P_j G_j(\varphi) G_t(\theta) \gamma_j B_r 4\pi L}{R_j^2 L_j B_j} K}}$$
(1)

According to the signal superposition principle, if a radar bears the interference of a number of jammers, its maximum detection range can be expressed as

$$R_{\text{max}} = \frac{P_{t}G_{t}^{2}\sigma\lambda^{2}}{(4\pi)^{3}F_{n}KkT_{0}B_{n}LK + \sum_{i=1}^{m}\frac{P_{ji}G_{ji}(\varphi_{i})G_{t}(\theta_{i})\gamma_{ji}B_{r}4\pi L}{R_{ji}^{2}L_{ji}B_{ji}}K}$$
(2)

where P_t and P_j are the transmitting power of radar and jammer respectively. G_t and G_j are the transmitting gain of radar and jammer respectively. σ represents the target RCS. λ is the radar wavelength. R_t is the range between radar and target R_j is the range between radar and jammer, γ_j is called a polarization loss of the jammer. F_n and k are the noise coefficient and Boltzmann constant respectively. T_o is operating temperature. B_n, B_r and B_j represent the signal bandwidth of noise, radar and jammer respectively. L and L_j are the comprehensive loss factor of radar and jammer respectively. $G_j(\varphi)$ is the antenna gain of jammer with respect to radar direction. $G_t(\theta)$ is the antenna gain of radar with respect to jammer direction. P_{ji} , R_{ji} , L_{ji} , B_{ji} , γ_i and $G_{ji}(\varphi_i)$ are parameters of the *i*th jammer and they indicate the transmitting power, distance far from enemy radar, comprehensive loss factor, signal bandwidth, polarization loss and the antenna gain of jammer with respect to radar form enemy radar.

In the paper, we think that the radar shares the same antenna in transmitting and receiving, and assume that the jamming principle is "one-for-one" or "many-for-one", so radar direction angle φ is zero.

B. Jamming troop calculation model

1) Definition of evaluation index about track point threat

About evaluation index of track point threat, many factors should be considered, such as the detect ability to target, the dynamic characteristics of target RCS, and the impact of the terrain shelter, and so on. And second, the calculating strategy of the assault height should be combined. At last, based on the investigation of threat information of a track point about the specific track, it should be determined that the number of threats which can detect the point. 2) Model of evaluation index about track point threat

The cooperative jamming situation is depicted in Fig.1. For the current track point Pc, evaluation index E_c is given by

$$E_{c} = \sum_{i=1}^{N_{th}} x_{ci}$$
(3)

with

$$x_{ci} = \begin{cases} 1 & d_{ci} \cos(\theta_{ci}) \le \min(R_i \sin(\theta_{Ri}), R_i') \\ 0 & d_{ci} \cos(\theta_{ci}) > \min(R_i \sin(\theta_{Ri}), R_i') \end{cases}$$
(4)

where xci is the evaluation of the current track point concerning the ith radar threat. dci is the range between the current track point and the ith threat. Nth represents number of threat sources in battlefield. R_i is the detection distance with a current track height hci, considering the impact of the terrain shelter. R_i , θ_{Ri} , θ_{ci} be expressed in Fig.1.

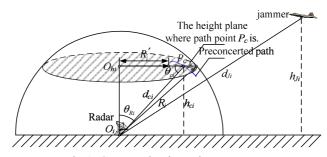


Fig.1. Cooperative jamming geometry

Since we have assumed that the jamming principle is "one-for-one" or "many-for-one", we always think that the evaluation index be the smallest jamming troop needed by the current track point threat.

III. Calculation Model of Jammer Free Fly Region

A. Analysis on the jamming effect

In order o explain the influence to jamming effect owing to the position of the jammer relative to the radar, the radar mainlobe's direction and the jammer's interference radiating way, we combined with the suppressive jamming principle mentioned in section 2.1 and the performance parameters of jammer and radar in Ref. [8], and we can calculate and obtain the following results.

In Fig.2, we showed jamming effect's change relations with the distance far from enemy radar and the angle between the jamming orientation and the radar mainlobe's direction.

As shown in Fig.2, the jamming effect become weak with the distance increasing. More than a certain distance, the jamming would have no effect. Along with the jamming orientation far from the radar mainlobe's direction, the jamming effect quickly decays. If the angle exceeds 90°, the jamming would have no significant effect. The last view was illustrated by the relation curves between the jamming effect and deviation angle in Fig.3.

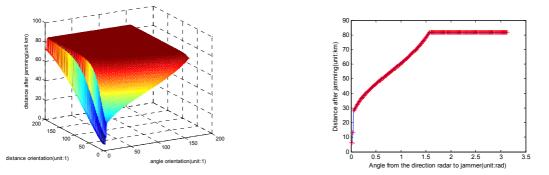


Fig.2. Relation of the detection range to distance and angle Fig.3. Relation of the detection range to deviation angle

B. Definition of jammer free fly region

Free fly region of a jammer: For a certain threat **R** of the radar, regardless of the impact of terrain shelter, a jammer **J** in the plane surface of height h_J will be employed to impose blanket jamming to the threat **R** to ensure that the point *P* in the plane surface of height *h* not to be detected. Under the circumstance of the point *P* in the plane of height *h* not to be detected, the region within the plane surface of height h_J where the jammer **J** locates, but outside the detecting scope of threat **R** is defined as the free fly region of the jammer **J** relative to *P* in the plane surface h_J concerning radar **R**, simply named as the free fly region of a jammer or the free fly region.

Free fly region of a jammer is affected by many kinds of factors, such as jammer's height, track point position, radar threat and jammer's performance. Free fly region of a jammer would be any position outside of the detection range when the track point is sheltered by terrain.

It should be noted that free fly region of a jammer relative to a track point be a similar conical area, and the connection from threat source to track point share the similar tapered region.

We should mention, if a jammer can't ensure that the track point not to be detected, and assume that the jammer is located in the point of intersection place of radar detection boundary and extension cord from a threat-radar to a track point, free fly region concerning it will not exist.

As long as the jammer that imposes blanket interference to threat-radar locates in free fly region, it can guarantee the safety of the jammer and the track point. For multiple track points in the same threat range, just need to make sure that the jammer is located in the intersection of free fly region of each jammer relative to these track points, you can ensure that each track point is safe at the same time.

C. Connectivity judgment of jammer free fly region

Connectivity of free fly region relative to track point is to guarantee that the path search space of a jammer are continuous, It is also a necessary conditions for optimal track of a jammer.

If the sum of half angle of free fly region relative to two track points concerning a radar is greater than the geometry angle of the two points relative to the radar, two free fly regions would be connected.

It is noteworthy that the terrain influence was not considered in these conclusions above. If consider terrain influence, especially the impact of terrain shelter, the free fly region will be expanded to threat direction until the blind area.

For any jammer and threat-radar, from the above, it is known that the jamming boundary of $0^{\circ} \sim$ 90° relative to threat source can be calculated within the scope of a certain distance. At last, based on the jamming boundary data, we can make a database, named as effects library of blanket jamming.

IV. Generation Strategy of Cooperative Jamming Optimalpath

This paper still uses algorithm idea of the sparse A * search (SAS) In Ref. [13]. The algorithm has been improved and can be applied to solving the problem.

A. Estimation of collaborative step-size

We can get a dynamic blanket jamming safety area by using cooperative jamming, but must meet the following two requirements:

1) Free fly regions of two adjacency track points in the desired path should be connected.

2) When we are choosing the collaborative step-size, we should guarantee that every extended node is always in the free fly region relative to the corresponding track point, so that the jammer can get up with the assault aircraft.

Assume that the sampling step length in the desired path is S and the average speed the assault aircraft is \overline{V} , then

$$t_l = S/\overline{V} \tag{5}$$

At the same time, if the jammer's speed range is $V_j \in [V_{jmin}, V_{jmax}]$, then single step's length of the jammer collaborative planning should meet:

$$S_{j} = V_{j} \cdot t_{l} \in \left[V_{jmin} t_{l}, V_{jmax} t_{l} \right]$$
(6)

To meet the requirement 1), step length S can't be too big. In order to combine (6) and conditions 2) to determine S_i , we can adopt dynamic regulation to adjust jammer's collaborative step-size.

B. Jammer track cost model

In determining path search space for jammer, we think that the jammer is always not only in the same flying height, but also outside the detecting scope of threat-radar. At the same time the jammer will also be restricted the minimum non-stop flight distance, the maximum turn angle and total flying range, etc. Therefore, we can give the single dimensional track cost model. For these reasons, we can give the single dimensional track cost model:

$$\begin{array}{ll} \min & cost = \sum_{j=1}^{i} S_{i} \quad i = 1, 2, \cdots \\ st & S_{i} \geq L_{min} \&\& \psi_{Pmax} + \psi_{Qmax} > \angle POQ \&\& S_{i} \in \left[V_{jmin}t_{i}, V_{jmax}t_{i}\right] \\ & \varphi \leq \varphi_{max} \\ & \sum_{j=1}^{i} S_{i} \leq S_{max} \end{array}$$

$$(7)$$

where, S_j is length of the ith section path. The first constraint condition is to meet the limits of jammer's minimum non-stop flight distance, connectivity of free fly region and jammer's collaborative step-size. The second constraint condition refers to meet the limit of the maximum turn angle φ_{max} . S_{max} represents jammer's maximum fuel flying range.

C. Realization for collaborative optimal path

In this paper, we obtain collaborative optimal path for jammer through the algorithm named as improved sparse A* search (ISAS).

1) Characteristics analysis on collaborative path planning for jammer

What makes ISAS different from SAS in Ref. [13] is the following respects:

(1) Jammer cooperative fighting is to ensure that fighter aircraft is always in a safe area. Jammer's path must adapt to the intended track of the fighter aircraft, so starting point and end point of the collaborative path planning for jammer are uncertain.

(2)Collaborative path planning for the jammer need not evade threats because it is always outside the detecting scope of threat.

(3) In order to collaborate fighter aircraft to implement assault, path search space for jammer relative to each track point of the fighter aircraft is a similar tapered dynamic changing region. It's search step-size has the characteristic of the dynamic change.

2) Cost function ISAS algorithm

In ISAS algorithm, cost function g(n) about current node n quote formula (7). A difficulty is how to determine the heuristic function h(n) because we must first choose a right point as target. On the basis of the information above, it is known that last point on the intended track in the detecting scope of threat should have a certain free fly region for jammer, and the termination condition of the algorithm is that the jammer gets into the region. Therefore, we can choose any one point as an end. The linear distance fome current node n to the end point can be used as function h(n).

3) Realization process of jammer collaborative optimal path based on the ISAS

Based on the characteristics of the problem, the realization flow chart of jammer collaborative optimal path be shown in Fig. 4.

In order to get the free fly region of jammer relative to any path point by means of a look-up table, we must make standard blanket jamming effects library. In Fig. 4, R_0 is the detecting range within the plane surface of height h. If consider terrain shading effects, R_0 may be a very small value. R_{max} depends on the operational requirement and jamming capability.

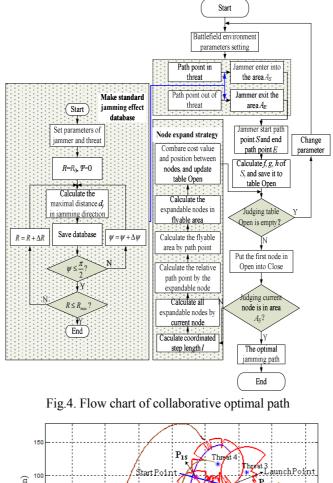
The information about each node contains position, index, father node index, track cost and the flight speed, etc. In order to extend jammer track node and realize cooperative combat of jammer and assault aircraft, we must identify path point of the assault aircraft relative to the desired track first. Then, we calculate the free fly region of the correlative jammer and take it as the search space of the jammer relative to the current node.

V. Simulation

In order to verify the above model and algorithm, we set the battlefield environment which coordinates of threat 1, threat 2, threat 3, threat 4 are (68.58 km, 39.26 km), (39.44 km, 68.50 km), (111.93 km, 104.41 km) and (68.58 km, 117.08 km) respectively. The parameters of threat-radar are P_t =100kW, G_t =14, B_r =1MHz, L=12, B_n =0.2 kHz, F_n =2.5, K=5, T_0 =340 K, λ =0.1 m, H=50 m. The parameters about jammer have P_j =30 kW, G_j =4, B_j =2 MHz, L_j =20 and the jammer's maximum turn angle is 50°, the shortest straight flight distance is 5km, the biggest route length is 1.2 times the

straight distance from starting point to target point, the flying height h_J is 3 km, the speed $v_J \in$ is the 200 m/s to 300 m/s. The average speed of the fighter aircraft is 240 m/s. The maximum number of nodes is 200 in OPEN list and M = 7, S = 0.

The penetration attack task is depicted in Fig.5. The route height h of fighter aircraft is 2km, and the detection range of threat-radars impacted by the terrain shelter is described in Fig. 5. Combinined (3) with (4), we know that at least two jammers should be used to cooperative jamming from both sides separately. Through calculating the jamming effect, we can further identify that the only two jammers may finish the collaborative jamming task. Assumed that the first jammer implements jamming from the right, and the second from the left.



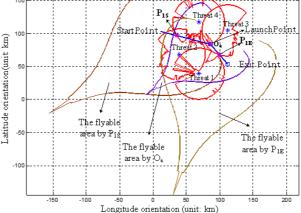


Fig.5. Free fly region of a jammer relative to track point

1) Production of standard jamming effect

We may choose a jammer and a threat-radar to carry on the jamming effect calculation since every jammer have the same parameters and every radar-threat is also same. The paper choose threat 1 and jammer 1. When $\Delta R=0.15$ km, $\Delta \Psi=0.01$ rad, $R_0=2$ km, $R_{max}=250$ km, the results is shown in Fig. 6. In Fig.6, transverse direction represents angle, and longitudinal direction represents distance from threat source in the height direction. Obviously, the threat range follows the law of Fig.3 in the blanket jamming.

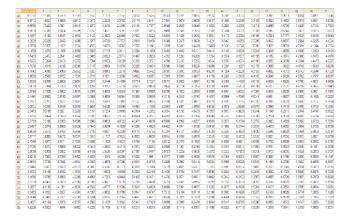
2) The free fly region of a jammer relative to track point in the threat environment

Using the blanket jamming effects library, the free fly region of a jammer relative to any track points concerning threat-radars can be calculated fast. The calculation results of the entering threat starting point P_{1S} , the release point O_r and the quiting threat point P_{1E} about the jammer are shown specifically in Fig.6.

The Fig.6 shows that the free fly region of the jammer is a similar tapered region. P_{1S} and P_{1E} is located in the detecting edge of the threat source, so the corresponding free fly region is large, but the region relative to the release point O_r located in the detection range is small. The corresponding path point is safe as long as the jammer is flying in the free fly region. The distance from the track point to the threat source is a main influence factor on the size of the free fly region.

3) Jammer collaborative optimal path

Let's take the optimal trajectory of jammer 1 for example. According to the corresponding jammer free fly region of the PJS and PJE in Fig.5, using ISAS algorithm and combined the calculating process shown in Fig.4, the decision makers can determine the planning starting point coordinates (16.3km, 50km) and end point coordinates (66.7km, 9.4km), and can also quickly get the collaborative optimal path of the jammer as shown in Fig.7.



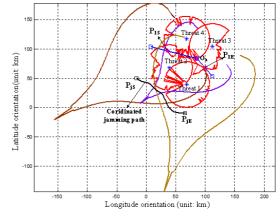


Fig.6. Part datum of the blanket jamming effects library

Fig.7. Jammer collaborative optimal path

The planning of the collaborative optimal path is in the same height for a jammer, so the search space can be restricted in the horizontal plane, and do not limit the enter direction. At the same time, the threat processing and the calculation about the free fly region has been previously saved threat database and the blanket jamming effects library. When each node is expanded, only to find the corresponding track points, the flying area corresponding to the points outside the threat range can be quickly identified by look-up table method and then completed the final track search. The route search time need only 2s. Fig.8 shows the jammer cooperative trajectory similared to the track trends of the fighter aircraft, and always outside the detecting scope of threat. In order to guarantee the jammering effect, the jammer collaborative optimal path should be close to the threat when the distance tends to decrease from the path point of fighter aircraft to it.

VI. Conclusion

It is very important to study the strategy of electronic warfare in penetration attack, particularly for promoting the survivability of a fighter aircraft and the ability to cooperate and fulfill its tasks. This paper discussed the jammer movement's influence on the jamming effect, and established the calculation model of jamming troop. The definition and related conclusions about the free fly region of a jammer were put forward, and all these provide an important theoretical basis for dynamic generating cooperative search space of a jammer. Finally, the ISAS algorithm was applied to

generation of the jammer collaborative optimal path, and the optimal path against any assault task can be quickly got.

The result of this paper broke the tradition of restrict jammer's path. It had an important meaning in improving the fighter aircraft's viability and effectively using jamming resource.

References

- [1] Shen X J, Wang G Y, Wang L D, et al. Effect Evaluation for Electronic Jamming Aircraft against Netted Surveillance Radars [J]. Journal of System Simulation 2008, 20(4): 997-1000.
- [2] Frank W Moore. Radar cross-section reduction via route planning and intelligent control [J]. IEEE Transactions on Control Systems Technology, 2002, 10(5):696-700.
- [3] K. Misovec, T. Inanc. Low-Observable nonlinear trajectory generation for unmanned air vehicles [J]. IEEE Conference on Decision and Control, 2003, 12: 3103-3110.
- [4] Tamer Inanc, Kathy Misovec, Richard M. Murray. Nonlinear trajectory generation for unmanned air vehicles with multiple radars [J]. IEEE Conference on Decision and Control, 2004, 12: 3817-3822.
- [5] Xing M L, Xiao J P. Research on Cooperative Jamming in Complex Electromagnetic Environment [J]. Journal of Telemetry, Tracking and Command, 2010, 31(4):30-35.
- [6] Li B, Gao X G. Algorithm of power allocation for cooperative electronic jamming in air combat of formation [J]. Journal of Systems Engineering and Electronics, 2008, 30(7): 1298-1300.
- [7] Rao D H, Huang G M, Chen Q. Route Planning of Low-Altitude Penetration with Cooperation of Electronic Jamming [J]. Electronic Optics &Control, 2010,17(5): 18-21.
- [8] Shi H S, Li D, Zhao Z G. The Simulation and Research of Electronics Jamming Influence on Radar Net Detection Space and Flight Path Planning of Aircraft[C]. International conference on radar. Shanghai: IEEE press, 2006:1-5.
- [9] Li Y Z, Wu D J, Hou H Q, et al. Simulation Analysis on Track Program That 3-plane Jamming and Suppressing The Netted Radar[J]. Shipboard Electronic Countermeasure. 2008, 31(1): 39-42.
- [10] Mingyan Li, Lordanis Koutsopoulos, Radha poovendran. Optimal jamming attack strategies and network defense policies in wireless sensor networks [J]. IEEE Transactions on Mobile Computing, 2010, 9(8):1119-1133.
- [11] Christina Popper, Mario Strasser. Anti-jamming broadcast communication using uncoordinated spread spectrum techniques [J]. IEEE Journal on Selected Areas in Communications, 2010, 28(5): 703-715.
- [12] S.M.Andraws. Optimal C4ISR networks in the presence of enemy jamming[R]. Naval Postgraduate School: NTIS, 2010.
- [13] Szczerba R J. Robust algorithm for real-time route planning [J]. IEEE Transactions on Aerospace and Electronic Systems, 2000, 36(3):869-878.

Study on A New Algorithm for Tracking Ballistic Missile in Free Flight

Phase

Chen Chuxin^{1,a} and Zhou Deyun¹

¹School of Electronics and information, Northwest Ploytechnical University, Xian, Shaanxi Province,

China

^accxdst@126.com

Keywords: Kalman filtering, algorithm, statistics, simulation, Doppler frequency, ballistic missile

Abstract. This paper presents an application of a new adaptive filtering algorithm based on a standard earth ellipsoid model in tracking ballistic missile in free flight phase. The traditional Extended Kalman Filtering algorithm (EKF) has defect in two aspects: 1) observation values applied in observation equation mainly include azimuth, pitch angle and radial distance (or radial velocity), without Doppler frequency; 2) Jacobi matrix of the system needs to be calculated, and high nonlinearization could result in degradation of calculation precision. In this paper, an algorithm used for tracking ballistic missile in free flight phase which is based on UKF observation equation with Doppler frequency is presented. The algorithm has been applied in hybrid coordinate system of the standard earth ellipsoid model (the earth is assumed as an ellipsoid planet). It has higher tracking precision compared with EKF algorithm. Monte Carlo simulation conducted to model ballistic missile in free flight phase by using MATLAB software justified the efficacy and the reasonableness of the new algorithm.

Introduction

Free flight phase of ballistic missile (BM) refers to the flight phase of a ballistic missile flies from end of booster phase until it reentries atmosphere, the free flight phase approximately accounts for over 80%~90% of the entire ballistic missile flight phase. The free flight trajectory is part of the ellipse trajectory. The ballistic missile movement in free flight phase is more predictable compared with booster phase and reentry phase. [1]

The technology used for tracking ballistic missile in free flight phase is comparatively matured as study on it can be traced back to 1960s. However, the target motion state equation used in sensor coordinate system is dependent and it is heavily coupled to equation processing in hybrid coordinate system [2], which has resulted in complicated algorithm structure, furthermore, the foregoing equation cannot be directly applied to track information e.g. flight angle and Doppler frequency. Whereas radar can not only directly measure approaching velocity of an air vehicle, but it is MTI performance (Moving Target Indicate) [3] through detection of Doppler frequency, i.e., air vehicle's echoes are separated from its clutters before clutters are eliminated. Actually, in most cases, a target's state equation and its observation data are nonlinearly correlated to the target's motion parameters (i.e., target measurement equation is nonlinear). The traditional approach used to deal with this problem is to convert a nonlinear filtering problem into a similar linear filtering problem, and one of the most commonly used linearization method is Taylor series expansion, the resulted filtering is called EKF filtering [4]. However, UKF algorithm needs neither calculation of Jacobi matrix of the system nor requirement on the system's nonlinearity, moreover, the similar calculation complexity could result in higher calculation precision.

Therefore, for the above mentioned problem, this paper presents a filtering model for an algorithm used for tracking ballistic missile in free flight phase setting up based on UKF observation equation with Doppler frequency. The filtering model is established in standard earth

ellipsoid model. After Doppler frequency is used in observation equation in hybrid coordinate system, adaptive filtering is conducted by using UKF algorithm, so that this new algorithm can result in higher filtering precision than traditional EKF algorithm.

A new adaptive filtering algorithm based on standard earth ellipsoid model I Missile kinetic model with ECI coordinate system

ECI coordinate system is located in an inertial space, which is immobile compared to a "stationary" star. Its origin is at the center of the earth ellipsoid model, and axis in equatorial plane points to mean equinox, and axis is perpendicular to equatorial plane and coincides with the earth's spin axis, pointing to the Arctic pole. The direction of the axis is the direction of right-handed Cartesian coordinate system.

In ECI coordinate system, are used to represent position vector and velocity vector respectively, and then, nonlinear state equation of state vectorof ballistic missile flying in free flight phase is as follows:

$$\mathbf{X} = \begin{bmatrix} \dot{\mathbf{R}} \\ \dot{\mathbf{V}} \end{bmatrix} = \mathbf{f} \begin{pmatrix} \begin{bmatrix} \mathbf{R} \\ \mathbf{V} \end{bmatrix} \end{pmatrix} \triangleq \begin{bmatrix} \mathbf{V} \\ \mathbf{a}_{\text{Gravity}}(\mathbf{R}) \end{bmatrix}$$
(1)

Sphere earth model is replaced by ellipsoidal earth model in order to obtain more accurate gravity acceleration model. Considering ellipsoidal shape of the earth, second-order harmonic coefficient is applied to earth gravity model to obtain more precise gravity model [5]

$$a_{\text{Gravity}}(R) = -\frac{\mu}{r^2} \left\{ \mu_r + 1.5 J_2 \left(\frac{R_e}{r} \right)^2 \left[\left(1 - 5 \left(\mu_r^T \cdot \mu_z \right)^2 \mu_r + 2 \left(\mu_r^T \cdot \mu_z \right) \mu_z \right) \right] \right\}$$
(2)

where, $J_2 (= 0.108627989 \times 10^{-2})$ is the earth's second-order harmonic coefficient;

 $R_e(= 6378137m)$ is the earth's equator radius; $\mu_z (= \begin{bmatrix} 0 & 0 & 1 \end{bmatrix}^T)$ is unit vector in ECI coordinate

system along $O_{e}Z_{I}$ direction.

For most of ballistic missile tracking, this model is widely accepted as the one with adequate precision but with high nonlinearity. Corresponding kinetic model of ballistic missile in free flight phase [6] is as follows:

$$\begin{bmatrix} \ddot{\mathbf{X}}_{e} \\ \ddot{\mathbf{Y}}_{e} \\ \ddot{\mathbf{Z}}_{e} \end{bmatrix} = -\frac{\mu}{r^{s}} \begin{bmatrix} \mathbf{X}_{e} + \frac{\mathbf{C}_{e}}{r^{2}} \left[1 - 5 \left(\frac{\mathbf{Z}_{e}}{r} \right)^{2} \right] \mathbf{X}_{e} \\ \mathbf{Y}_{e} + \frac{\mathbf{C}_{e}}{r^{2}} \left[1 - 5 \left(\frac{\mathbf{Z}_{e}}{r} \right)^{2} \right] \mathbf{Y}_{e} \\ \mathbf{Z}_{e} + \frac{\mathbf{C}_{e}}{r^{2}} \left[3 - 5 \left(\frac{\mathbf{Z}_{e}}{r} \right)^{2} \right] \mathbf{Z}_{e} \end{bmatrix}$$
(3)

where, $C_e = \frac{3}{2}J_2R_e^2$

II Radar station reference coordinate system

EC (Earth-centered) coordinate system $O_e - X_f Y_f Z_f$ is a relatively stationary coordinate system compared with the Earth, its origin is at the center of the Earth O_e , axis $O_e X_f$ in equatorial plane points to the meridian, where Royal Greenwich Observatory is located, axis $O_e Z_f$ is perpendicular to equatorial plane and points to the Arctic Pole. $O_e - X_f Y_f Z_f$ make up of right-handed Cartesian coordinate system.

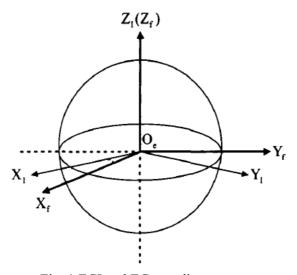


Fig. 1 ECI and EC coordinate systems

For convenience of discussion, it is usually assumed that at the two coordinate systems are overlapping at the reference moment (i.e. the moment when a missile is launched or the moment when radar has detected target). After time interval t from the reference moment, included angle of $O_e X_I$ and $O_e X_f$ is $\omega \cdot t$, in which, $\omega = 7.2921151467 \times 10^{-5} \text{ rad/s}$ (th e earth's rotation angular velocity). The relation of the two coordinate systems refers to Fig. 1. Obviously, the transformation matrix relation of the two coordinate systems is as follows:

$$\begin{bmatrix} x_{f} \\ y_{f} \\ z_{f} \end{bmatrix} = \begin{bmatrix} \cos(\omega \cdot t) & \sin(\omega \cdot t) & 0 \\ -\sin(\omega \cdot t) & \cos(\omega \cdot t) & 0 \\ 0 & 0 & 1 \end{bmatrix} \begin{bmatrix} x_{I} \\ y_{I} \\ z_{I} \end{bmatrix}$$
(4)

Radar station reference coordinate system (RRC) $O_r - X_r Y_r Z_r$ used in ballistic missile tracking is a widely applied non-inertial coordinate system. Its coordinate origin is at the center of radar, O, $O_r X_r$ and $O_r Y_r$ are tangent lines of the reference earth ellipsoid, pointing to the east and the north respectively, and axis $O_r Z_r$ is perpendicular to the local horizontal plane to upward, so, this coordinate system is usually known as ENU, coordinate system. Relation of ENU and EC coordinate systems refers to Fig. 2.

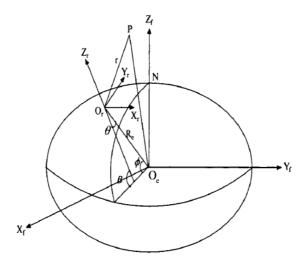


Fig. 2 ENU and EC coordinate system

The included angle of geodetic meridian plane (where radar station O_r is located) and prime meridian plane, i.e., geographical longitude, is defined as ^L; the included angel of the normal (from O_r to ellipsoidal earth) and equatorial plane, known as geodetic latitude, is defined as ^B; the distance from O_r to normal of earth ellipsoid, known as geodetic height, is defined as ^H.

When the earth model is assumed to be standard ellipsoid, coordinates of radar station center O_r in EC coordinate system are as follows:

$$\begin{cases} X_{re} = (N + H)cosBcosL \\ Y_{re} = (N + H)cosBsinL \\ Z_{re} = [N(1 - e^2) + H]sinB \end{cases}$$
(5)

where, $N = a_x / \sqrt{1 - e^2 \sin^2 B}$; a_x is semi-major axis of reference ellipsoid; **b** is short radius of

ellipsoid; e is compression of the earth, e = $\sqrt{1 - b^2/a_x^2}$

The relation of conversion of EC coordinate system into radar station ENU coordinate system is as follows (conversion of two rectangular coordinate systems):

$$\begin{bmatrix} x_{r} \\ y_{r} \\ z_{r} \end{bmatrix} = C_{EC}^{ENU} \left(\begin{bmatrix} x_{e} \\ y_{e} \\ z_{e} \end{bmatrix} - \begin{bmatrix} x_{re} \\ y_{re} \\ z_{re} \end{bmatrix} \right) = C_{EC}^{ENU} \begin{bmatrix} x_{e} \\ y_{e} \\ z_{e} \end{bmatrix} - \begin{bmatrix} 0 \\ e^{2}NsinBcosB \\ N + H - e^{2}Nsin^{2}B \end{bmatrix}$$
(6)

where, C_{EC}^{ENU} is transformation matrix.

$$C_{\text{EC}}^{\text{ENU}} = \begin{bmatrix} -\sin(L) & \cos(L) & 0\\ -\cos(L)\sin(B) & -\sin(L)\sin(B) & \cos(B)\\ \cos(L)\cos(B) & \sin(L)\cos(B) & \sin(B) \end{bmatrix}$$
(7)

where, $\begin{bmatrix} x_{re} & y_{re} & z_{re} \end{bmatrix}^T$ is location of radar station in EC coordinate system.

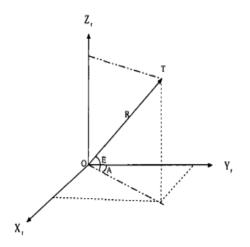


Fig. 3 Radar station ENU coordinates and spherical coordinates

Radar station spherical coordinates are (R, A, E), of which, R is distance from target to radar, A is azimuth, i.e., included angle between projection of line linking target and radar on plane OXZ and axis X. Radar station ENU coordinates and spherical coordinates refer to figure 3. Its function relation is as follows:

$$R = \begin{bmatrix} R \\ A \\ E \end{bmatrix} = \begin{bmatrix} \sqrt{x_r^2 + y_r^2 + z_r^2} \\ \arctan\left(\frac{x_r}{y_r}\right) \\ \arctan\left(\frac{z_r}{\sqrt{x_r^2 + y_r^2}}\right) \end{bmatrix}$$
(8)

III State equation of ballistic missile in free flight phase in hybrid coordinate system

In general, hybrid coordinate system and spherical coordinate system are used for tracking missile in free flight phase, and the precision of tracking ballistic missile in free flight phase is higher in hybrid coordinate system then in spherical coordinate system [7]. Therefore, this paper presents tracking ballistic missile in free flight phase by using hybrid coordinate system.

Hybrid coordinate system is used to establish state equation of ballistic missile in ENU coordinate system and to establish observation equation of ballistic missile in spherical coordinate system. To deduce targeted motion acceleration is critical for establishment of state equation in tracking ballistic missile in free flight phase.

Position vector and velocity vector of EC inertial coordinate system are defined as $\mathbf{r}_{e} = [\mathbf{x}_{e} \ \mathbf{y}_{e} \ \mathbf{z}_{e}]^{T}$ and $\dot{\mathbf{r}}_{e} = [\dot{\mathbf{x}}_{e} \ \dot{\mathbf{y}}_{e} \ \dot{\mathbf{z}}_{e}]^{T}$ respectively, position vector and velocity vector of radar $\mathbf{r}_r = [\mathbf{x}_r \ \mathbf{y}_r \ \mathbf{z}_r]^{\mathrm{T}}$ and as **ENU** defined station coordinate system are $\dot{\mathbf{r}}_{\mathbf{r}} = [\dot{\mathbf{x}}_{\mathbf{r}} \ \dot{\mathbf{y}}_{\mathbf{r}} \ \dot{\mathbf{z}}_{\mathbf{r}}]^{\mathrm{T}}_{\mathrm{respectively.}}$ It is assumed that the earth model is a standard ellipsoid model, the earth's rotation angular velocity $\omega = \begin{bmatrix} \omega_x & \omega_y & \omega_z \end{bmatrix}^T = \begin{bmatrix} 0 & \omega \cos B & \omega \sin B \end{bmatrix}^T$, radar station geodetic longitude is L, geodetic latitude is B, elevation is L, and assuming EC inertial coordinate system and EC coordinate system are overlapping at reference moment, then, according to Eq. 4 and Eq. 7, at moment t (reference moment is zero), transformation matrix between ECI coordinate system to radar station ENU coordinate system is as follows:

$$C_{e}^{r}(t) = \begin{bmatrix} -\sin(L + \omega t) & \cos(L + \omega t) & 0\\ -\cos(L + \omega t)\sin(B) & -\sin(L + \omega t)\sin(B) & \cos(B)\\ \cos(L + \omega t)\cos(B) & \sin(L + \omega t)\cos(B) & \sin(B) \end{bmatrix}$$
(9)

Then, transformation matrix from ENU to ECI is C_r^e , $C_r^e(t) = [C_e^r(t)]^T$.

Hence, relation of vector transformed from ECI coordinate system to radar station ENU coordinate system is as follows:

$$\mathbf{r}_{\mathbf{r}} = \mathbf{C}_{\mathbf{e}}^{\mathbf{r}}(\mathbf{t}) \cdot \mathbf{r}_{\mathbf{e}} - \mathbf{p} \tag{10}$$

where, P is vector of distance from the earth center to radar station $(\mathbf{p} = [\mathbf{p}_x \ \mathbf{p}_y \ \mathbf{p}_z]^T = [0 \ \mathbf{e}^2 \text{NsinBcosB} \ \text{N} + \text{H} - \mathbf{e}^2 \text{Nsin}^2 \text{B}]^T)$

Correspondingly, transform position vector in ENU coordinate system into position vector in ECI coordinate system from:

$$\mathbf{r}_{\mathbf{e}} = \mathbf{C}_{\mathbf{r}}^{\mathbf{e}}(\mathbf{t})(\mathbf{r}_{\mathbf{r}} + \mathbf{p}) \tag{11}$$

Taking the derivative of Eq. 11, so,

$$\dot{\mathbf{r}}_{\mathbf{e}} = \mathbf{C}_{\mathbf{r}}^{\mathbf{e}}(\mathbf{t}) \cdot \dot{\mathbf{r}}_{\mathbf{r}} + \dot{\mathbf{C}}_{\mathbf{r}}^{\mathbf{e}}(\mathbf{t})(\mathbf{r}_{\mathbf{r}} + \mathbf{p}) \tag{12}$$

$$\dot{C}_{e}^{r}(t) = \omega \begin{bmatrix} -\cos(L+\omega t) & -\sin(L+\omega t) & 0\\ \sin(L+\omega t)\sin(B) & -\cos(L+\omega t)\sin(B) & 0\\ -\sin(L+\omega t)\cos(B) & \cos(L+\omega t)\cos(B) & 0 \end{bmatrix}$$
(13)

$$\ddot{C}_{e}^{r}(t) = \omega^{2} \begin{bmatrix} \sin(L+\omega t) & -\cos(L+\omega t) & 0\\ \cos(L+\omega t)\sin(B) & \sin(L+\omega t)\sin(B) & 0\\ -\cos(L+\omega t)\cos(B) & -\sin(L+\omega t)\cos(B) & 0 \end{bmatrix}$$
(14)

Taking the derivative of Eq. 10, relation of transformation of velocity vector in ECI coordinate system to velocity vector in ENU coordinate system is obtained as follows:

$$\dot{\mathbf{r}}_{\mathbf{r}} = \dot{\mathbf{C}}_{\mathbf{e}}^{\mathbf{r}}(\mathbf{t}) \cdot \mathbf{r}_{\mathbf{e}} + \mathbf{C}_{\mathbf{e}}^{\mathbf{r}}(\mathbf{t}) \cdot \dot{\mathbf{r}}_{\mathbf{e}}$$
(15)

Taking the derivative of Eq. 15, relation of transformation of acceleration vector in ECI coordinate system to acceleration vector in ENU coordinate system is obtained as follows:

$$\ddot{\mathbf{r}}_{\mathbf{r}} = \ddot{\mathbf{C}}_{\mathbf{e}}^{\mathbf{r}}(\mathbf{t}) \cdot \mathbf{r}_{\mathbf{e}} + 2\dot{\mathbf{C}}_{\mathbf{e}}^{\mathbf{r}}(\mathbf{t}) \cdot \dot{\mathbf{r}}_{\mathbf{e}} + \mathbf{C}_{\mathbf{e}}^{\mathbf{r}}(\mathbf{t}) \cdot \ddot{\mathbf{r}}_{\mathbf{e}}$$
(16)

then,

$$\ddot{\mathbf{r}}_{e} = -\frac{\mu}{r^{2}} \left\{ \mu_{r} + 1.5 J_{2} \left(\frac{R_{e}}{r} \right)^{2} \{ [1 - 5(\mu_{r}^{T} \cdot \mu_{z})^{2}] \mu_{r} + 2(\mu_{r}^{T} \cdot \mu_{z}) \mu_{z} \} \right\}$$
(17)

It is deduced that:

$$\ddot{\mathbf{r}}_{\mathbf{r}} = -\mu \frac{\mathbf{r}_{\mathbf{r}} + \mathbf{p}}{\|\mathbf{r}_{\mathbf{r}} + \mathbf{p}\|^{3}} - \omega^{2} \cdot \Phi_{2}(\mathbf{r}_{\mathbf{r}} + \mathbf{p}) - 2\omega \cdot \Phi_{1} \cdot \dot{\mathbf{r}}_{\mathbf{r}}$$
(18)

$$\omega^2 \Phi_2 = C_e^r(t) \cdot \ddot{C}_r^e(t) = \omega^2 \cdot \begin{bmatrix} -1 & 0 & 0 \\ 0 & -\sin^2 B & \sin B \cos B \\ 0 & \sin B \cos B & -\cos^2 B \end{bmatrix}$$

where,

$$\omega \Phi_1 = C_e^r(t) \cdot \dot{C}_r^e(t) = \omega \cdot \begin{bmatrix} 0 & -\sin B & \cos B \\ \sin B & 0 & 0 \\ -\cos B & 0 & 0 \end{bmatrix}$$

To simplify Eq. 18, and subscript r is omitted, then, acceleration of ballistic missile of free flight phase in ENU coordinate system is as follows:

$$\begin{bmatrix} \ddot{x} \\ \ddot{y} \\ \ddot{y} \\ \ddot{z} \end{bmatrix} = -\frac{\mu}{r^{5}} \begin{bmatrix} \left(1 + \frac{C_{e}}{r^{2}} \left(1 - 5\left(\frac{z + p_{z}}{r}\right)^{2}\right)(x + p_{x})\right) \\ \left(1 + \frac{C_{e}}{r^{2}} \left(1 - 5\left(\frac{z + p_{z}}{r}\right)^{2}\right)(y + p_{y})\right) \\ \left(1 + \frac{C_{e}}{r^{2}} \left(3 - 5\left(\frac{z + p_{z}}{r}\right)^{2}\right)(z + p_{z})\right) \end{bmatrix} - 2\Omega \begin{bmatrix} \dot{x} + p_{x} \\ \dot{y} + p_{y} \\ \dot{z} + p_{z} \end{bmatrix} \\ \left(1 + \frac{C_{e}}{r^{2}} \left(3 - 5\left(\frac{z + p_{z}}{r}\right)^{2}\right)(z + p_{z})\right) \end{bmatrix} - 2\Omega \begin{bmatrix} \dot{x} + p_{x} \\ \dot{y} + p_{y} \\ \dot{z} + p_{z} \end{bmatrix}$$
(19)

$$r = \sqrt{(x + p_{x})^{2} + (y + p_{y})^{2} + (z + p_{z})^{2}, \Omega} = \begin{bmatrix} 0 & -\omega_{z} & \omega_{y} \\ \omega_{z} & 0 & -\omega_{x} \\ -\omega_{y} & \omega_{x} & 0 \end{bmatrix}$$

where,

Based on the above result, state variable is defined as X, $\mathbf{X} = [\mathbf{x} \ \mathbf{y} \ \mathbf{z} \ \dot{\mathbf{x}} \ \dot{\mathbf{y}} \ \dot{\mathbf{z}}]^{\mathsf{T}}$, then, state equation of missile in radar station ENU coordinate system is as follows:

$$\frac{\mathrm{dX}}{\mathrm{dt}} = \mathbf{f}(\mathbf{X}) = [\dot{\mathbf{x}} \ \dot{\mathbf{y}} \ \dot{\mathbf{z}} \ \ddot{\mathbf{x}} \ \ddot{\mathbf{y}} \ \ddot{\mathbf{z}}]^{\mathrm{T}}$$

$$= \begin{bmatrix} \dot{x} \\ \dot{y} \\ \dot{z} \\ \begin{pmatrix} \frac{\mu}{r_0^3} + 1 \end{pmatrix} x + 2\dot{y}\sin B - 2\dot{z}\cos B \\ \begin{pmatrix} \frac{\mu}{r_0^3} + \sin^2 B \end{pmatrix} y - (z + R_{eh})\sin B\cos B - 2\dot{x}\sin B \\ -y\sin B\cos B + \begin{pmatrix} \frac{\mu}{r_0^3} + \cos^2 B \end{pmatrix} (z + R_{eh}) + 2\dot{x}\cos B \end{bmatrix}$$
(20)

To discretize Eq. 20, then,

$$X_{k+1|k} = X_{k|k} + f(X_{k|k}, t_k) \Delta t + \frac{1}{2} F(X_{k|k}) f(X_{k|k}, t_k) \Delta t^2$$
(21)

where, Δt is sampling interval to be determined by tracking data rate, $F(X_{k|k})$ is Jacobi matrix of

f(X(k|k), k) relative to $X_{k|k}$.

$$F(X_{k|k}) = \frac{df}{dx}\Big|_{X=X_{k|k}} = \begin{bmatrix} 0_{3\times3} & I_{3\times3} \\ \frac{\partial \ddot{r}}{\partial r} & -2\omega\Phi_1 \end{bmatrix}_{X_{k|k}}$$
(22)

where,
$$\frac{\partial \ddot{r}}{\partial r} = \begin{bmatrix} a_{11} & a_{12} & a_{13} \\ a_{21} & a_{22} & a_{23} \\ a_{31} & a_{32} & a_{33} \end{bmatrix}$$

Elements in matrix are expressed as follows: $a_{11} = -\mu \frac{1}{r^5} + 3\mu \frac{x^2}{r^5} + \omega^2 , \quad a_{12} = 3\mu \frac{xy}{r^5} ,$

$$a_{13} = 3\mu \frac{x(z+R_{eh})}{r^5}, a_{21} = a_{12}, a_{22} = -\mu \frac{1}{r^5} + 3\mu \frac{y^2}{r^5} + \omega^2 \sin^2 B, a_{23} = 3\mu \frac{y(z+R_{eh})}{r^5} - \omega^2 \sin B \cos B,$$

$$a_{31} = a_{13}$$
, $a_{32} = a_{23}$, $a_{33} = -\mu \frac{1}{r^s} + 3\mu \frac{(z+R_{eh})^2}{r^5} + \omega^2 \cos^2 B$

Since state vector is described in ENU coordinate system and observation shall be based on radar station spherical coordinates, so observation equation is nonlinear.

$$Z_{k} = h(X_{k}) + n_{k} = \begin{bmatrix} \left(x_{k}^{2} + y_{k}^{2} + z_{k}^{2}\right)^{\frac{1}{2}} \\ \tan^{-1}\left(\frac{x_{k}}{y_{k}}\right) \\ \tan^{-1}\left(\frac{z_{k}}{\sqrt{x_{k}^{2} + y_{k}^{2}}}\right) \end{bmatrix} + \begin{bmatrix} n_{k}^{R} \\ n_{k}^{A} \\ n_{k}^{E} \end{bmatrix}$$
(23)

Noise measurement parameters in the above equation n_k^R, n_k^A, n_k^E are considered to be independent and subject to Zero-mean Gaussian distribution, their covariances are $\sigma_R^2, \sigma_A^2, \sigma_E^2$ respectively, therefore, noise measurement covariance matrix can be defined as:

$$R_{k} = \begin{bmatrix} \sigma_{R}^{2} & 0 & 0\\ 0 & \sigma_{A}^{2} & 0\\ 0 & 0 & \sigma_{E}^{2} \end{bmatrix}$$
(24)

To solve Jacobi matrix for $h(X(k|k), k), H(X_{k|k})$

$$H(X_{k|k}) = \frac{dh}{dX}\Big|_{X=X_{k+1|k}} = \begin{bmatrix} \frac{x}{r} & \frac{y}{r} & \frac{z}{r} & 0 & 0 & 0\\ \frac{y}{r^{2}+y^{2}} & \frac{-x}{r^{2}+y^{2}} & 0 & 0 & 0 & 0\\ \frac{xz}{r^{2}\sqrt{x^{2}+y^{2}}} & \frac{-yz}{r^{2}\sqrt{x^{2}+y^{2}}} & \frac{\sqrt{x^{2}+y^{2}}}{r^{2}} & 0 & 0 & 0 \end{bmatrix}_{X=X_{k+1|k}}$$
(25)

Nonlinear functions $f(\cdot)$, $h(\cdot)$ and expression of its Jacobi matrix F, H are determined, i.e., EKF and UKF filtering technology can be used for tracking ballistic missile of free flight phase in hybrid coordinate system.

IV A new algorithm for tracking ballistic missile in free flight phase

Doppler frequency \mathbf{f}_{d} is expressed as:

$$f_{d} = \frac{2f_{0}}{c}\dot{R} = \frac{2f_{0}}{c}(\dot{x}cosAcosE + \dot{y}sinAcosE + \dot{z}sinE) = \frac{2f_{0}}{c}\frac{\dot{x}x + \dot{y}y + \dot{z}z}{\sqrt{x^{2} + y^{2} + z^{2}}}$$
(26)

where, C is speed of light, $C = 2.99792458 \times 10^8$, f_0 is carrier frequency. Then, in coordinate system, system observation is as follows:

$$Z_{k} = \begin{bmatrix} R \\ A \\ E \\ f_{d} \end{bmatrix} = h(X_{k}) + n_{k} = \begin{vmatrix} \sqrt{x_{k}^{2} + y_{k}^{2} + z_{k}^{2}} \\ \tan^{-1}\left(\frac{x_{k}}{y_{k}}\right) \\ \tan^{-1}\left(\frac{z_{k}}{\sqrt{x_{k}^{2} + y_{k}^{2}}}\right) \\ \frac{2f_{0}}{\sqrt{x_{k}^{2} + y_{k}^{2} + z_{k}^{2}}} \end{vmatrix} + \begin{bmatrix} n_{k}^{R} \\ n_{k}^{A} \\ n_{k}^{E} \\ n_{k}^{f_{d}} \end{bmatrix}$$
(27)

Noise measurement parameters in the above equation n_k^R , n_k^A , n_k^E , $n_k^{r_d}$ are considered to be

 σ_R^2 , σ_A^2 , σ_E^2 , $\sigma_{f_d}^2$

independent and subject to Zero-mean Gaussian distribution, their covariances are respectively, therefore, noise measurement covariance matrix can be defined as:

$$R_{k} = \begin{bmatrix} \sigma_{R}^{2} & 0 & 0 & 0 \\ 0 & \sigma_{A}^{2} & 0 & 0 \\ 0 & 0 & \sigma_{E}^{2} & 0 \\ 0 & 0 & 0 & \sigma_{f_{d}}^{2} \end{bmatrix}$$
(28)

Finally, based on UKF filtering concept, a new filtering algorithm with observation equation using Doppler frequency in hybrid coordinate system is put forward, the specific steps are as follows:

Step1. Initialization of nonlinear system

$$\mathbf{X}_{0|0} = \mathbf{E}(\mathbf{x}_0) \tag{29}$$

$$P_0 = E([x_0 - \bar{x}_0][x_0 - \bar{x}_0]^T)$$
(30)

Step2. Calculation sigma points

$$\mathbf{X}_{\mathbf{k}} = \left[\widehat{\mathbf{X}}_{\mathbf{k}|\mathbf{k}}, \widehat{\mathbf{X}}_{\mathbf{k}|\mathbf{k}} + \gamma \sqrt{\mathbf{P}_{\mathbf{k}|\mathbf{k}}}, \widehat{\mathbf{X}}_{\mathbf{k}|\mathbf{k}} - \gamma \sqrt{\mathbf{P}_{\mathbf{k}|\mathbf{k}}} \right]$$
(31)

where, $\gamma = \sqrt{L + \lambda}$, L is dimension of state vector x, $\lambda = \alpha^2 (L + k) - L$. Constant α determines

density of sigma points distributing surrounding \bar{x} , which is usually small, $10^{-4} < \alpha < 1$; k is proportionality factor, it is usually set as zero when state is evaluated, and set as 3-L when factor is evaluated.

Step3. One-step prediction of Sigma points and covariance matrix

$$\tilde{X}_{k+1|k} = f(X_k)$$
 (Calculated according to Eq. 20) (32)

$$X_{k+1|k} = \sum_{j=0}^{2L} W_{j}^{(m)} \breve{X}_{j,k+1|k}$$
(33)

where,

$$\widetilde{P}_{k+1|k} = \sum_{j=0}^{2L} W_{j}^{(c)} (\widetilde{X}_{j,k+1|k} - \widehat{X}_{k+1|k}) (\widetilde{X}_{j,k+1|k} - \widehat{X}_{k+1|k})^{T}$$
(34)

where, $W_{j}^{(c)} = \begin{cases} \frac{\lambda}{L+\lambda} + 1 - \alpha^{2} + \beta, & j = 0\\ \frac{1}{2(L+\lambda)} & j = 1, \dots, 2L \end{cases}, \quad \beta \text{ is used to combine factors } \chi \text{ prior distribution} \end{cases}$

information; for Gaussian distribution, $\beta = 2$ is optimal.

 $W_{j}^{(m)} = \begin{cases} \frac{\lambda}{L+\lambda}, & j = 0\\ \frac{1}{2(L+\lambda)}, & j = 1, \cdots, 2L \end{cases}$

$$\mathbf{P}_{\mathbf{k}+1|\mathbf{k}} = \tilde{\mathbf{P}}_{\mathbf{k}+1|\mathbf{k}} + \mathbf{Q}_{\mathbf{k}} \tag{35}$$

Step4. One-step prediction of Sigma points and observed quantity

$$X_{k+1|k} = \left[\widehat{X}_{k+1|k}, \widehat{X}_{k+1|k} + \gamma \sqrt{P_{k+1|k}}, \widehat{X}_{k+1|k} - \gamma \sqrt{P_{k+1|k}} \right]$$
(36)

$$Z_{k+1|k} = h(X_{k+1|k})$$
(Calculated according to Eq. 27) (37)

$$\hat{Z}_{k+1|k} = \sum_{j=0}^{2L} W_j^{(m)} Z_{j,k+1|k}$$
(38)

Step5.Calculation of Kalman gain matrix and updating state quantity and covariance matrix

$$\widetilde{P}_{\widetilde{Z}_{k+1}\widetilde{Z}_{k+1}} = \sum_{j=0}^{2L} W_{j}^{(c)} (Z_{j,k+1|k} - \widehat{Z}_{k+1|k}) (Z_{j,k+1|k} - \widehat{Z}_{k+1|k})^{T}$$
(39)

$$P_{\tilde{Z}_{k+1}\tilde{Z}_{k+1}} = \tilde{P}_{\tilde{Z}_{k+1}\tilde{Z}_{k+1}} + R_{k+1}$$

$$\tag{40}$$

$$P_{X_{k+1}Z_{k+1}} = \sum_{j=0}^{2L} W_{j}^{(c)} (X_{j,k+1|k} - \widehat{X}_{k+1|k}) (Z_{j,k+1|k} - \widehat{Z}_{k+1|k})^{T}$$
(41)

Simulation contrastive analysis

Assuming component of target initial position is $[x_0, y_0, z_0]^T = [35,8,8]^T$ (Unit: km), initial

velocity component is $[\dot{\mathbf{x}}(\mathbf{k}), \dot{\mathbf{y}}(\mathbf{k}), \dot{\mathbf{z}}(\mathbf{k})]^{\mathrm{T}} = \left[0.3 \cos{\frac{\pi}{6}}, 0, 0.3 \sin{\frac{\pi}{6}}\right]^{\mathrm{T}}$ (Unit: km/s), system state vectors

are unrelated, sampling time is 1s; assuming Q₀ is null matrix, radar sensor's variance of azimuth,

 $R_{0} = \text{diag}(\sigma_{\theta}^{2}, \sigma_{\varphi}^{2}, \sigma_{j}^{2}) = \text{diag}(1.5\text{mad}, 1.5\text{mad}, 10^{-4}\text{Hz})$ evaluation index is root mean square error (RMSE) [9].

Simulation filtering results obtained by using new algorithm and EKF algorithm refer to Fig. 4.

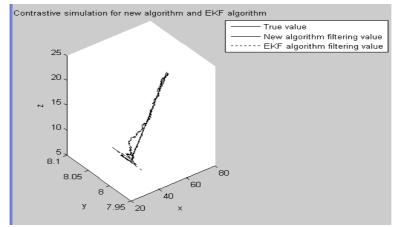
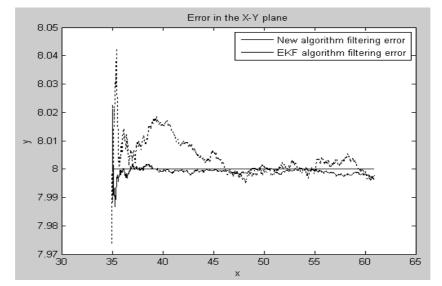


Fig. 4. Tracking results by using new algorithm and EKF algorithm



Errors of new algorithm and EKF algorithm on X-Y plane are as shown on Fig. 5.

Fig. 5 Comparison of errors of new algorithm and EKF algorithm on X-Y plane

It can be clearly observed on Fig. 4. and Fig. 5 that the new algorithm has higher precision and compared with the traditional algorithm has higher accuracy and higher convergence than traditional algorithm, which has justified the reasonableness and efficacy of the new algorithm.

REFERENCES

- [1] Zhang Yi, Yang Hui, and Li Junli, Ballistic Missile Ballistics, Changsha: National University of Defense Technology Press, 1999, p.173-199.
- [2] G. P. Cardillo, A. V. Mrstik, and T. Plambeck, "A Track Filter for Reentry Objects with Uncertain Drag", IEEE Trans. AES, 1999, 35(2): p.395-409.
- [3] W. S. George and Wu Hanping, An Introduction to Airborne Radar, Beijing: Electronic Industry Press, 2005.
- [4] P. J. Costa, "Adaptive Model Architecture and Extended Kalman-Bucy Filters", IEEE Trans, Aerospace and Electronic Systems, 1994, 30(2): p.525-533.
- [5] Jia Peiran, Chen Kejun, and Heli, Long-Range Rocket Ballistics, Changsha: National University of Defense Technology Press, 1993.
- [6] X. R. Li and V. P. Jilkov, A Survey of Maneuvering Target Tracking-Part II: Ballistic Target Models. In Proc. 2001, SPIE Conf. on Signal and Data Processing of Small Targets, vol. 4473, San Diego, CA, USA, 2001.
- [7] Zhao Yanli, "Study on ballistic missile radar tracking and recognition", Changsha: National University of Defense Technology, engineering Ph.D dissertation, 2007.
- [8] Chen Chuxin, Zhou Deyun, and Wang Lingxiao, "Unscented kalman filter with Doppler frequency", Application Research of Computers, 2011, 28(4): p.1530-1532.
- [9] X. R. Li, Z. L. Zhao. Evaluation of Estimation Algorithms Part I: Incomprehensive Measures of Performance. IEEE Trans. Aerospace and Electronic Systems, 2006, 42(4): p.1340-1358.

Conceptual Model of Information Naval Gun Weapon System Using Weapon System Engineering Method

Xuwen Sun^{1, a}, Feng Tian¹, Deqing Liang¹, Hongyan Shan¹, Xinjie Zhang¹

¹Dalian Naval Academy, Dalian 116018, China

^a13591796389@126.com

Keywords: systematic method, systematic demonstration, naval gun weapon system, conception model; conception system

Abstract: Lining along systematic method, aiming at systematic, whole, accuracy description and definition of the conceptual system, following the steps of synthesis—analysis—synthesis, this article establishes the conception model of information naval gun weapon system. First, the task objectives is analyzed, and the task profile is determined, then, based on decomposing of function, the structure of information naval gun weapon system is analyzed, finally, the conception of the system is gained, which builds foundation for further demonstrating of information naval gun weapon system.

Introduction

This work is supported by the Science Research Foundation of Dalian Naval Academy.

Systematic method is a scientific methodology which is a breakthrough against traditional thinking mode of analysis—synthesis—analysis, and it begins and aims at synthesis, uses analysis and synthesis form beginning to end, considers the object as a whole, moving, living, interactive organism, so, it is a complementary and modification for the traditional thinking mode in studying complicated system.

Weapon system is a familiar complicated system which is studied usually using systematic method in weapon system engineering, especially in the demonstrating of a new type of weapon equipment. To develop any new weapon equipment, the first thing is to get a clear understanding of it, and form a series conceptions which can definitely, qualitatively describe the new weapon equipment system. While at this stage, "Information naval gun weapon system (INGWS for short)" is brought forward in order to adapt the new mode of naval war under information conditions in future, so, the research on conception model of information naval gun weapon system is necessary and meaningful.

Conceptual model is description of a system, an entity, a phenomenon in mathematics, physics and logic ^[1]. Conceptual model is quantitative description for exterior and interior characters of a system using language, symbols, or drawings ^[2]. In another word, conception model is quantitative description of certain factors such as the target, the principle, the constituents and the restrictions of a system.

The establishing of concept model is a process in which the information naval gun weapon system is known and studied, and the understanding of it is deepened from sensible to rational. It is helpful for wholly and accurately defining the new weapon system. Conception modeling is the beginning of all new type of weapon systems, so, it is indispensable for the information naval gun weapon system that, the conception model is studied.

According to the thinking mode of systematic method of synthesis—analysis—synthesis, the conception of ISNGWS is developed as follows: first, task objectives are summarized, then, task profile is analyzed, and functions supporting the tasks are decomposed, finally conception model is established, and it is described as fig 1.



Figure. 1. Researching steps according to systematic method

Synthesis: Task objectives of INGWS

The development of equipment is guided by military requests. The development of any weapon equipment is derives from the request of future war and certain operational application ^[3]. The principle demonstrating task in the stage of the generating of a new weapon equipment is confirming the objectives of it task, as is called "task objectives" for short. Task objectives of a new type of weapon equipment is series of system conceptions generated after analyzing and studying according to the current similar weapon equipment.

The task objectives of INGWS are descriptions objectives and criterions or supposing effects of in certain operational application. According to the request of future naval war, the task objectives of INGWS are defined as that: as an effect combat resource, performing effective combat of anti-shore, and-sea, anti-air and special combat in information condition, meanwhile, it is a training equipment of high effect-to-cost, and it also can be maintained easily.

According to the task objectives, and the traditional operational application of naval gun, the chart of its task objects described in dendrite morphology is gained as Fig 2.

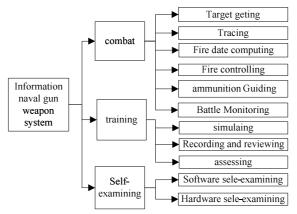


Figure.2 Task objects in dendrite morphology

Analysis: Task profile of INGWS

Task profile of INGWS is descriptions in time sequence of all the events and environments during given operational application tasks of a weapon system, and it is also concrete explanation combining the function of the system and the request of the system ^[4]. In face, the concrete explanation of performance capability is description for the system in achieving given task objectives.

So that, the task profile of INGWS can be determined by data flowing, in another word, the task profile of INGWS can be determined according to the information from beginning to end.

It is known to all that, to accomplish any task, 3 stages must be covered: first, information receiving (including target information and control information), then, decision-making (including automatically and manually), finally, weapon application. Under the information conditions, the INGWS will be a node of the net of ship-born combat systems, and the target information is transferred from the main data bus. Thus, according to the flow of data, the task profile of the system in combat is finally gained as Fig 3, omitting the training and self-checking function.

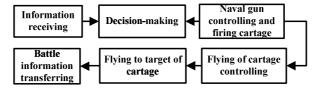


Figure. 3 Flow chart of task profile of INGWS

Reference data and request of task profile for INGWS is analyzed and listed as in Tab 1.

Num	Operational application	Content of major task	Time request	scope	Task request	Remark
1	Data receiving and feedback	Communicating continuously	Almost live	Whole ship	Live	Perception of battle is accomplished by sensors of all ship-born combat system
	Decision-making	Threat evaluating and fire distributing	Allowed retardation	DICING	Accurate	More detailed decision-making after upper system of combat system composed of all ship-born weapons
2	Feedback	Transfer data of decision-making data to data bus	Almost live	INGWS		
	Controlling and firing	Projectile firing and controlling	Allowed retardation	INGWS	instantaneous and accurate	When using information ammunition, guiding and controlling must be considered
3	Feedback	Data of decision-making to data bus Data of reaction of naval gun to data bus	Almost live			
		Battle information	Allowed retardation	Whole ship		Mainly gained by television detecting ammunition in video frequency covering the battle
4	Target killing battle monitoring and controlling	Monitoring killing effect, modifying next firing	From beginning	to end	Accurate and full-scale	Result of monitoring can be transferred to data bus, after amalgamation with original data gained by sensors, new situation of battle is formed, the information flow in closed loop

Table 1 Reference data and request of task profile

ANALYSIS: FUNCTIONS DECOMPOSED FROM TASKS OF INGWS

The tasks of a system is gained after synthesizing for functions of a certain actual system, while as for a uncertain system , it is on the contrary that it is supposed to analyze functional request and composing according to given task from the point of analysis. Thus, based on the analysis above, the functions of INGWS can be decomposed from top to bottom.

According to the data flow of a typical combat process, the functions of INGWS can be determined. As for the combat function, the system receives data, traces targets, computes firing data, controls the direction of naval gun, launches projectile, monitors and controls the movements of the projectile; except that it should have simulating function, assessing, recording, hardware self-checking and software self-checking functions. Fig 4 shows all the above functions.

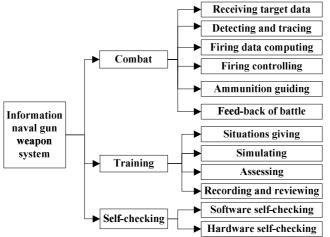


Figure.4 Functions composing tasks of INGWS

Synthesis: Conception model of INGWS

(1)Definition of conception system for INGWS

A valid and useful conception model must has the characters as uniqueness, accuracy and specification.

According to all of the foregoing analysis, the definition of INGWS can be defined as: The INGWS is a new type weapon system which is composed of such sub system as gun weapon system using information ammunition, command and control system, fire control system, devices for network communication, it can execute operation functions such as accurate attack, effective

damaging, live monitoring and controlling the battle environment, also, it has the training function and can be maintained easily.

(2)Description of the conception system as following: ①The INGWS is an organism integer. ② There are relationships among factors composing the system. ③It is for special task profile and certain task objectives and factors composing the system is determined and required by tasks giving by task profile. ④When performed for operational application, it behaviors in dynamic states, which changes under different task profile. ⑤The system has adapting capability to environment.

(3)Composing of conception system: According to the description of conception system, integrating with the decomposing, instantiating the functions to corresponding devices, then, the devices composing the system is gained, as is shown in Fig 5.

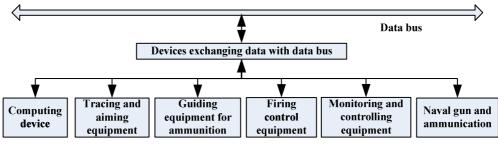


Figure.5 Physical structure of INGWS

Conclusions

By means of the systematic method that is synthesis—analysis—synthesis, after analyzing of task objectives, determination of task profile, decomposing of functions supporting the task profile, gaining the composing of devices, defining the conception system, the research of conception model of INGWS is developed. The conception model builds the foundation for further demonstrating of INGWS in structure analysis, performance target analysis, etc.

References

- [1] WANG Xing-ren. Development and application of modeling and simulating [J]. Science &Technology Review 2007, 25(2), pp. 22-27.
- [2] DAI Feng. Modern systematic engineering—thoughts, processes and methods in large scale decision-making[M]. Zhengzhou: Henan People's Press. 1988, pp. 25.
- [3] SONG Gui-bao, SHEN Ru-song, ZHOU Wen-song, etc. Weapon system engineering [M]. Beijing: National Defense Industry Press. 2009.2.
- [4] LI Ming, LIU Peng, etc. Theory and practice of an integrated and systematic demonstration method for development of weapon and equipment [M]. Beijing: National Defense Industry Press. 2004.4, pp. 265, 282.

Advanced Materials Research Vol. 981 (2014) pp 758-761 © (2014) Trans Tech Publications, Switzerland doi:10.4028/www.scientific.net/AMR.981.758

Research on the Simulation of Naval Gun Exterior Trajectory Differential Equations in Real-Time Solution

Feng Tian^{1, a}, Xuwen Sun¹, Xu Zhang¹, Hongyan Shan¹, Lijun Wang¹,

¹Dalian Naval Academy, Dalian 116018, China

atf0411cmc@163.com

Keywords: exterior trajectory differential equations; simulation; forth-order Runge-Kutta algorithm

Abstract: Giving the concept of the aero ballistics, the equations of mass trajectory of pill in the rectangular coordinate system under standard conditions and the equations of mass trajectory of pill considering the influence of wind are introduced in this paper. Forth-order Runge-Kutta algorithm is used for the equations to simulate, the experiment analysis has been discussed in the last. The result shows that such method of simulation has more accuracy in direction and distance.

Introduction

Trajectory differential equations is one of core of exterior trajectory theory, which is used in the fire control ballistic model when chase guns shoot at the seashore. Because of the complicate elements which have effect on projectile flight, if we correct all, it is not only miscellaneous and time-consuming, but also unnecessary in fact. Therefore, when we study on the actual trajectory of projectiles, firstly we will use the theoretical trajectory model in ideal conditions to analyze and calculate. Then we will consider about some common factors that may have influence on it, such as the crosswind, range wind, sway as the naval craft moves, and so on. And we also should do some essential correction of parameter and variable in the theoretical trajectory model to meet needs in practical situation ^[1].

The motion equations of projectile in rectangular coordinate system

Under the condition of supposing that there are only gravity and air obstructing projectiles, the vector equation of projectiles center of mass motion is $dv/dt=a_x+g$. Then we can get the motion equations of projectile in rectangular coordinate system fixed with the Earth and we can deal with the gas weight function and resistance function with curve fitting and experimental formula.

According to the theory of exterior ballistics ^[2], we have the motion equations of projectile in rectangular coordinate system in which t is the argument,

$$\begin{cases} du/dt = -cH_{\tau}(y)G(v_{\tau})u\\ d\omega/dt = -cH_{\tau}(y)G(v_{\tau})w - g\\ dy/dt = \omega\\ dx/dt = v\\ v_{\tau} = \sqrt{v^2 + \omega^2}\sqrt{\tau_{0n}/\tau} \end{cases}$$
(1)

(1) The rule of τ in the equation distributing as the variation of the height is,

$$\tau = \begin{cases} \tau_0 - G_1 y & (y \le 9300m) \\ A + B(y - 9300) + C(y - 9300)^2 & (9300m < y < 12000m) \\ 221.5K & (12000m < y < 30000m) \end{cases}$$
(2)

Among it, $\tau_{0n} = 288.9$ K, G1=6.328×10⁻³, A=230.0°, B=-6.328×10⁻³, C=1.172×10⁻⁶.

(2) Gas weight function $H_{\tau}(y)$ in the equation is a one-variable function that often changes as $H_{\tau}(y) = H(y) \sqrt{\tau/\tau_{0n}} = \pi(y) \sqrt{\tau_{0n}/\tau}$. This paper will adopt this formula. There is experimental formula for H(y) as follows, and when $y \le 10000m$, it is precise enough,

H(y)=exp(-1.059×10-3y) or H(y)=(20000-y)/ (20000+y). Or we can use the formula of $\pi(y)$ directly,

$$\pi(y) = \exp\left[\left(-g/G_1\right)\int_0^y dy/\tau\right]$$

(3) Resistance function adopts the experimental formula as $G(v_{\tau}) = F(v_{\tau})/v_{\tau}$, In the formula, $F(v_{\tau})$ is,

$$\begin{array}{ll} 0.00007454v_{\tau}^{2} & (v_{\tau} < 250 \, m/s) \\ 629.61 - 6.0255v_{\tau} + 1.8756 \times 10^{-2} v_{\tau}^{2} \\ -1.8613 \times 10^{-5} v_{\tau}^{3} & (250 \, m/s \le v_{\tau} \le 400 \, m/s) \\ 6.394 \times 10^{-8} v_{\tau}^{3} - 6.325 \times 10^{-5} v_{\tau}^{2} \\ +0.1548v_{\tau} - 26.63 & (400 \, m/s \le v_{\tau} \le 1400 \, m/s) \\ 0.00012315v_{\tau}^{2} & (v_{\tau} > 1400 \, m/s) \end{array}$$

$$(3)$$

(4) The relation between the speed of projectile, v and v_{τ} is

$$v_{\tau} = v_{\sqrt{\tau/\tau_{0n}}} \tag{4}$$

In the computer, to solve center of mass motion rule of projectile substantially is to solve the starter problem in system of differential equations. After considering the requirements of the precise and real-time of the aim in the chase gun's shooting movement, we often adopt the forth-order Runge-Kutta [2] algorithm to do the numerical solution. This method has very good precise, and it can change the step in the calculation. The most important thing of the algorithm is the choice of the iteration step. If the step reduces, the precision will be higher. But accordingly the time of calculation will be longer, and the accumulated error will be bigger, otherwise the precision will be lower. If the step increases, it will lead to the iteration divergence. Therefore, the key point of this algorithm is to choose proper iteration step and set cycle index to prevent that iteration divergence enters infinite loops.

Analysis of trajectory simulation in rectangular coordinate system

As an example of some type of chase gun with large diameter, we can set up the simulation model of the motion equations of projectile in rectangular coordinate system. From the classical theory of exterior ballistic, we can get that when the initial velocity, angle of fire, and the ballistic coefficient are fixed, there will be only one ballistic curve. Ballistic coefficient consists of elastic coefficient, the elastic core diameter, and the projectile mass. Among them, ballistic coefficient, $c=id^2/m\times10^3$, $i=C_{x0}(M)/C_{x0n}(M)$, *i* goes along the whole trajectory because the axis angle changes endlessly. But as to the fire control computation, we can use an average that doesn't change in some place to replace the ballistic coefficient. When in the process of trajectory simulation, we can use the Matlab 7.1 software to programming. The ballistic coefficient is the same with the firing table calibration coefficient, and we can set, $v_0=950m/s$, c=0.4685, direction 150°, and begin to simulate from time zero. Fig 1(*a*) is the trajectory simulation panel. Fig 1(*b*) the projectile trajectory. Table 1(*a*) is the comparison between the firing-table in the firing distance and calculate distance when the angle of fire is from 5° to 26.8° of the carronade. Table 1(*b*) gives the comparison between the flight time and the solution time of flight in the firing table.

From Table1 (*a*), we can calculate the arithmetic average deviation of the error between the calculate distance and the scheduled launch range from formula (5). After calculation, the distance arithmetic mean deviation is 33.8m. From Table1 (*b*), we can get that the arithmetic average deviation of the error between the resolving time and the scheduled time can be calculated with formula (5), among which the arithmetic average deviation is nearly 0 that can be ignored.

$\overline{d} = \sum_{1}^{n} d_i $	×(1/n)					(5)
Direction 150 Wind direction 0 Radial velocity 302.3278	Angle of firing 12 Wind speed 0 Vertical velocity -134.7605 Cal	Step 0.02 Target bearing 150 Transverse velocit 0	Radial distance Height Lateral separation Time y The apex height Actual velocity	16125.50 -1.8169 0 31.28 1220.2637 331.0022	$1500 \rightarrow 0$ $500 \rightarrow 0$ $500 \rightarrow 0$ $500 \rightarrow 0$ $0 \rightarrow 0$ $0 \rightarrow 0$ $0 \rightarrow 0$ $0 \rightarrow 0$ $100 \rightarrow 0$ 1	
	Fig.1 ((a) Traje	ctory simula	ation pane	1 Fig.1 (b) Projectile trajectory	

Fig.1 (a) Trajectory simulation panel

Table.1 (a) Comparison between the firing table in the firing distance and calculate distance

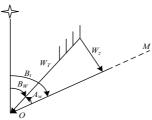
Angle of fire	5°	12°	15°	21.5°	24.5°	26.8°
Firing Table(<i>m</i>)	9877	16095	17924	21216	22497	23411
Calculating(m)	9915	16155	17947	21198	22473	23371
Error(<i>m</i>)	-38	-60	-23	18	24	40

Table1.(b) Comparison between the flight time and the solution time of flight in the firing table

Angle of fire	5°	12°	15°	21.5°	24.5°	26.8°
Firing Table(s)	14.8	31.2	37.3	49.4	54.8	58.9
Calculating(s)	14.82	31.2	37.36	49.50	54.84	58.88
Error(s)	-0.02	0	-0.06	-0.1	-0.04	0.02

Considering the motion equations under the influence of wind

When the wind blows, it has effect on the speed of projectiles relative to the air, and then it also influences the landing position of projectiles. Generally speaking, wind direction and shooting direction is inconsistent. We can divided the wind vector into two components which are range wind W_x and crosswind W_z . Supposing that the real wind direction is B_W , the real wind speed is W_T , the intersection angle between the shooting direction and the wind direction is A_W , and the target bearing is B_t . See Fig 2,



(6)

Fig.2 Influence of wind direction and shooting direction

$$\begin{cases} W_x = W_T \cos A_W = -W_T \cos(B_t - B_w) \\ W_z = W_T \sin A_W = W_T \sin(B_t - B_w) \end{cases}$$

Therefore we can get the motion equations while considering the influence of wind to the projectile as long as we use relative velocities to replace the velocity vector or its components of the items of air resistance in the basic problem of equations,

$$\begin{cases} du/dt = -cH_{\tau}(y)G(v_{r\tau})(u-W_{x}) \\ d\omega/dt = -cH_{\tau}(y)G(v_{r\tau})w-g \\ d\dot{z}/dt = -cH_{\tau}(y)G(v_{r\tau})(\dot{z}-W_{z}) \\ dy/dt = \omega \\ dx/dt = u \\ v_{r\tau} = \sqrt{(u-W_{x})^{2} + \omega^{2} + (\dot{z}-W_{z})^{2}}\sqrt{\tau_{0n}/\tau} \end{cases}$$

$$(7)$$

When the initial condition is t=0, then there are $u = v_0 \cos\theta_0$; $\omega = v_0 \sin\theta_0$; x = y = z = 0, $\dot{z} = 0$. In the practical use, we only need to substitute the real initial velocity, ballistic coefficient, temperature, air pressure, cross wind and range wind into formula (7).

Analysis of trajectory simulation considering the wing effect

The choice of ballistic coefficient is similar with the motion equations of projectile in rectangular coordinate system. Set $v_0=950m/s$, c=0.4685, direction 150°, step 0.02s, crosswind 10m/s (wind direction 240°), and range wind 10m/s (wind direction 150°). And they start to simulate from time zero. Fig.3 are the data show of the trajectory simulation panel and the projectile trajectory with crosswind 10m/s, angle of firing 15°. In the firing table, the range correction of the range wind that changes 10m/s is the fore-and-aft distance between placement and the central trajectory when the range wind changes 10m/s. And the sum of the distance correction value and the gun range is the actual range of the schedule. Table 2 is the comparison between the scheduled launch range and the calculation of the firing distance when wind range is 10m/s and firing angle is from 5° to 26.8°.



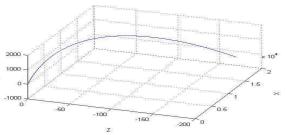


Fig.3 (*a*) Data show of the trajectory simulation panel Fig.3 (b) with crosswind 10m/s, angle of firing 15° with

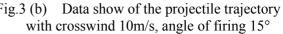


 Table.2
 Comparison between the scheduled launch range and the calculation of the firing distance when the range wind is 10m/s

1 1 6 6		100	1.50	01.50	0 4 50	2 (00
Angle of fire	5°	12°	15°	21.5°	24.5°	26.8°
Firing Table(<i>m</i>)	9941	16289	18171	21518	22899	23850
Calculating (<i>m</i>)	9976	16319	18198	21557	22881	23812
Error(<i>m</i>)	-35	-30	-27	-39	18	38

From Table2, the arithmetic average deviation of the errors between the scheduled launch range and the calculation of the firing distance can be got with formula (5) when the range wind is 10m/s, and the angle of firing is from 5° to 26.8°. After calculation, the distance arithmetic mean deviation is 31.1m.

Conclusions

This paper has given us the exterior ballistic differential equations considering the wind effect under the standard and non-standard conditions, which are based on MATLAB 7.1 software adopting Forth-order Runge-Kutta algorithm to simulate. And then we compare and analyze the simulation result and the firing table data, which proves that while we use this Model calculation of ballistic, there is high precision both in direction and distance. What's more, the arithmetical mean error of the calculating value and the tabular data error is far smaller than the impact dispersion error probability. The time of flight of the projectile and the scheduled time is almost the same. There is rather big practical meaning to design the simulation panel to show the projectile flight parameter. As the model is pretty good at real-time, commonality, and precision, other types of chase guns also can use this method to stimulate the trajectory.

References

- [1] Wang Xuli. Chinese Journal of Electron, 2007, 12, p.2297.
- [2] Pu Fa. Exterior Ballistcs[M].Beijing: National Defence industry Press, 1989.
- [3] Zhao Junming. Journal of Projectiles, Rockets, Missiles and Guidance, 2006, 27, 1, p.147-151.
- [4] Ma Linbin. Journal of North University of China., 2006, 27, 5, p.412-415.

CHAPTER 10:

Mechanical Engineering

Analysis and design on coal mining machinery system

Huawen Zhou^{1, a}

¹ Changchun University of Science and Technology, Changchun,Jilin, 130022, China ^azhw@cust.edu.cn

Keywords: mining machinery; equipment selection; mechanical design

Abstract. The rational design of coal mining machinery improves the efficiency of coal production and reduces the production cost. Basing on specific mining examples, a set of mining machinery system was obtained by technologically analyzing the calculation of production efficiency, as well as the selection of mining machinery, supporting device, and conveyor etc.

Introduction

The electromechanical integration technology in coal mechanical design and technology can achieve the high efficiency, economy, and safety of mining machinery mainly. The original parameters designed and selected in this study include the working face length :150 m; coal seam Pitch: 30° ; average coal seam thickness:3.5m; roof stability :moderate stable; A=230N/mm; f=3.5.

The design of the electromechanical integration technology on fully mechanized coal face

Selection of shearer

The selection condition of shearer. Considering the technological characteristics of shearer, coal seam can be divided into three classes mainly according to the basic coal seam pitch. The first class is the gently inclined coal seam, with an inclination angle of $0-25^{\circ}$; the second class is the inclined coal seam, with a basic angle range of $25-45^{\circ}$; the third class is the sharply inclined coal seam, with a basic angle range of $45-90^{\circ}$. The coal seams with inclination angle less than 12° are most favorable for the machinery mining. In this condition, the anti-slipping property of machinery mining is generally not taken into consideration.

Once the coal mining working condition turns dry, the friction coefficient of between metals reduced to 0.3 below. Moreover, in case of the inclination angle exceeding 12° , the shearer moving by guide rail and the floor-based shear supported and guided by conveyor should be equipped with anti-slipping devices.

Once the coal mining working condition turns moist, the friction coefficient of between metals reduces definitely. Moreover, in case of the inclination angle exceeding 8°, the shearer should be equipped with suitable anti-slipping devices

Chainless haulage shearer is applicable to the working face with inclination angle of 40-50 $^{\circ}$ due to its reliable brake device and high traction effort. However, in the condition of inclination angle exceeding 40 $^{\circ}$, this kind of shearer should be installed with face conveyor to guide the coal flow sliding along the safe direction required in practice.

The suitable hardness of coal rocks .

Soft coal: $f \le 1.5, A < 180N / mm$

Moderately hard coal: $f = 1.5 \sim 3.0, A = 180 \sim 240 N / mm$

Hard coal: $f \ge 3.0, A = 240 \sim 360 N / mm$

The coal mining process is inevitably involved with the use of plough which is very effective for the mining of soft coal. Rotary plough is suitable for the moderately hard coal, while the mining of completely hard coal calls for the high-power plough.

Suitable mining height

a. 0.55-0.9m, the plate-based shearer is preferable;

b. 0.8-1.2m, the shearer moving by guide rail is used;

c. 1.1-1.9m ,We usually adopt single drum shearer;

d. 1.2-2.5m, For general mining working face, single or double drum shearer can be used.

The actual coal mining condition suggests that the coal seam is moderately hard with hardness of 4 ,and shows an inclination angle of 30° . Therefore, the high-power double-drum shear is required.

Calculation of productivity

Theoretical productivity:

$$Qt = 60HBv_p \rho = 60 \times 3.5 \times 0.63 \times 5.98 \times 1.3 = 1028.5t/h$$
(1)

Where, H is the average mining height of working, in unit of m; B is the effective width of the drum, in unit of m; v_p is the possible maximum traction velocity on the given working face, in unit of m/min; ρ is the solid density of coal and valued by 1.3-1.4t/m3. Technological productivity:

Technological productivity:

$$Q = Q_t K_1 = 0.7 \times 1028.5 = 920t / h \tag{2}$$

Real productivity:

$$Q_m = QK_2 = 920 \times 0.65 = 598t/h \tag{3}$$

The diameter and the section width of the drum. When coal seam thickness is controlled in certain range, it is better to use double-drum shear to mine the coal. Generally, mining activities were operated on the upper and lower parts of the shearer to more effectively complete the whole circular process. Using formula, this process is expressed as $D \ge H \cdot 1/2 = 1.75m$. However, the drum of the shear is also systematized. Therefore, it is needed to comprehensively consider the drum width. Generally, the drum width of the shear with moderate thickness is controlled in a range of 0.6-0.63 m.

Traction velocity. In common, the traction velocity is less than 10 m/min.

To sum up, the MG300/700-WDK shearer was used.

Product type applied is MG300/700-WDK; mining height ranges from $1.8 \sim 3.7$ m; suitable inclination angle is less or equal to 35° ; total installed power is $300 \times 2 + 40 \times 2 + 20kW$; the machine is 1426 mm in height with arm length of 2267 mm; the swinging center distance of arm is 6800 mm; minimum undercover volume is 380 mm; drum diameter is 0.63m; drum rotation speed is 38.3r/min,33.6r/min,29.4r/min; cutting depth is set to 630 mm; speed control mode: electric traction; traction force is 520/388 kN; traction mode used is pin-track chainless mode; the voltage is 3300 V; With supporting main cable type of $MCP3 \times 50 + 1 \times 25 + 4 \times 6$; supporting conveyor used is SGZ764/400; with 47 t approximately.

The selection of supporting device

Type selection principle. The supporting device selected adapts to the basic strength and the basic pressure. Meanwhile, in the structural selection of the support device, the storage condition of coal seam etc. should also be taken into consideration.

Basis for type selection .

a. Coal seam thickness

The thickness and height of coal seam is closely correlated with the working stability of the support device. Once the coal seam thickness exceeds 4 m, supporting device is needed to resist horizontal trust to provide the shielding stand support.

b. Inclination angle of coal seam

The inclination angle of coal seam is closely related to the stability of the support. Commonly, the supports with skipping and falling-resistance are used.

c. Floor condition

d. Gas emission quantity

In case of overlarge gas emission quantity, it is needed to ensure the adequate ventilation on the ventilated position of the support.

e. Tectonic structure

f. Equipment cost

Determination of the fire monomer pillar of hydraulic support .

a. Support strength and working resistance Support strength:

$$q = kH\rho g = 8 \times 3.5 \times 2.5 \times 103 \times 10 - 6 = 0.7MPa$$
(4)

Working resistance:

$$Fz = qA \tag{5}$$

b. Setting load

Setting load shows large influences on the supporting ability and basic cost of support. In case of overlarge setting load, the support is capable of quickly reaching to the resistance needed in the mining process to reduce the falling velocity of floor and stabilize the roof. Generally, setting load is $0.6 \sim 0.8$ times of the working resistance. $F_1 = 0.8 \times 3880 = 3104 kN$.

c. Working resistance

The ratio of the effective working resistance and the working resistance of support is called as supporting efficiency η of support. Considering the supporting efficiency, the total working resistance P needed by each pillar is expressed as $P = Q/\eta$.

d. Advancing force and pushing force of support

The advancing force is related to the support structure, support quality, coal seam thickness, and floor property etc.. According to the type selection principle and calculation, the () hydraulic support was selected.

The bearing process of support.

a. Setting phase. In the rising process of the support, it should be ensured that the support is contacted with top beam and roof constantly. Subsequently, the support is raised by the fluid pressure under the pillar to the position where the pressure is bearable for the pump station.

b. Resistance increase phase. After the setting phase, the operation valve is moved to the middle timely. Meanwhile, the hydraulic one-way valve is closed in time. The fluid pressure in the pillar constantly increases with the descending of roof. In this condition, the support force of support continuously increases and presents a kind of blocking phenomenon by load increasing.

c. Constant resistance phase. When the fluid pressure in the pillar constantly increases to the basic pressure set in the safe valve, the safe valve is started and the data in the pillar was compressed downwardly. Meanwhile, the basic pressure of the liquid in the pillar continuously reduces. When the basic pressure reduces to the basic numerical value set in the safe valve, the safe valve is automatically closed for protection.

To sum up, the ZY4800/26/50 hydraulic support is preferable. The basic condition of this support is indicated as follows: working resistance: 4800 kN; height: 2600-5000 mm; strength: 0.78-0.8 MPa; floor specific pressure: 17-2.2 MPa; pushing force: 360 kN; advancing force: 633 kN. The support is a kind of large mining shielding hydraulic support. The front-axle beam of the hinge carries a secondary face guard in purpose of timely support and wall caving prevention. The whole base is equipped with a trail mechanism that bears anti-falling and skipping devices.

The type selection of scraper conveyer

The matching principle of scraper conveyer with shearer and hydraulic support.

a. Consistent forms and structures

b. The conveying ability should satisfy the basic requirements.

c. The chute length should satisfy the basic requirement and be matched with the distance and structure of relative devices that can move the jack.

The type selection of the scraper conveyer. Basing on the principles above, the SGZ-830/630 scraper conveyer is selected. The technological parameters of this conveyer are indicated as follows: Conveying amount: 1200 t/h; length: 200 m; installed power: 2x315 kW; scraper chain speed: 1.31 m/s; scraper chain: double stranded chain, 34x126-C round-link chain; central slot: cast welding sealing type; shearer traction mode: gear- pin-track type; chain tensioner: brake-disc tight-chain telescopic tail.

Considering the large inclination angle of the coal seam, corresponding anti-skipping device should be installed in necessary conditions.

Summary

The electromechanical integration in the technology and design coal machinery covers all aspects of coal machinery. This study merely analyzed part of the aspects. By introducing a large amount of advanced design ideas and perfect technological process into the coal machinery manufacturing, China's coal industry can be effectively promoted to develop toward a better direction under the guidance of modern technology.

References

- [1] Jianyun Hong,Bingwen Li,Jianwu Wang.The Application of LCC Technology inHyperstatic Hydraulic support. Mechanic Automation and Control Engineering (MACE) . 2011
- [2] M.Gurel Senyur.Auger mining of thin seams at Zongguldak colliery/Turkey. Journal of Mines,Metal & Fuels . 2003
- [3] K.Matsui,A.Yabuki,H.Shimada.A Practical Trial to Increase the Coal Recovery in Highwall Auger Mining in Australia. International Symposium on Mine Planning and Equipment Selection . 2003
- [4] Yu Bo.Numerical Simulation of Continous Miner Rock CuttingProcess. . 2005
- [5] I. A. Basher, M. Hajmeer. Artificial Neural Networks: Fundamentals, Computing, Design and Application. Journal of Microbiological Methods . 2000
- [6] Wu Hong-ci.Neural networks in mining Industry. .1996
- [7] Fu G,et al.Study on Dust-Control water Injection in Fully-Mechanized Top-Coal Caving Longwall Faces. Journal of China University of Mining and. Technology . 1997

Energy Efficiency Analysis of Piston Type Air Compressor

Zheng Sulu^{1, a}, Mao Yunyan¹, Wang Xiangping¹, Zheng Zhiyun¹, He Shenxi¹, Huang Zengyang^{1,b} and Wang Dongdong^{1,c}

¹Quzhou quality and technical supervision and Inspection Center, the city of quzhou,China ^aqztj_zsl@163.com, ^bhzy2031@163.com, ^cicecpioneer@126.com

Keywords: Piston type air compressor ,Analysis of Energy efficiency ,Specific power

Abstract. In the paper, the relationship of the energy efficiency and its impact factor such as intake valve lift, exhaust valve lift, clearance volume and rotational speed has been researched and the optimal conditions of the air compressor running was found . By adjusting the parameters of intake valve lift, exhaust valve lift, clearance volume and rotational speed, the total energy of a W-1.6/5 compressor could be reduced by 10.9%.

Introduction

Energy and energy consumption have become one of the key problems in the world, most of the countries have put their energy and the amount of energy consumption generated by the sustained operation of the national economy as an important indicator of the quality of economic operation. China is an energy-poor country and is also a big country of energy consumption, per unit of GDP is required to reduce energy consumption by 16% during the "Twelfth Five-Year" period, the task of saving energy has a long way to go[1].

Air compressor is the basic industry of the national economy, which has a close connection with the defense, chemical, pharmaceutical, food, petroleum, construction, transportation and mining. According to the industry statistics, annual power consumption of the air compressors operating accounts for 7% of the total power consumption of the national economy. Its power consumption growth synchronized with China's GDP growth , obviously it is a large energy industry[2,3]. Therefore, the scientific research on energy saving of air compressor will produce a very large social and economic benefits , which has a very important practical significance for the national economy

Research ideas

Research on energy saving of compressor from two aspects:

The one, from the design and manufacturing level, it will improve the compressor performance parameters by scientific and rational design; through the advanced manufacturing equipment and higher manufacturing standards to meet the design requirements and improve the quality of the air compressor;

The other one, based on the level of operating and running, proper processional and operational parameters were calculated through the experiment; by improving the operator's skill level so as to arrange the above parameters properly, Only by doing which can improve the energy saving effect of the compressor.

In this Paper, take the typical piston air compressor W-1.6/5 as the research target, using the compressor inspection system, starting by experimental study as a entry point, test for detection of variable conditions on parameters were carried out; according to the analysis of test data, best optimization regional of variable condition test was chosen.

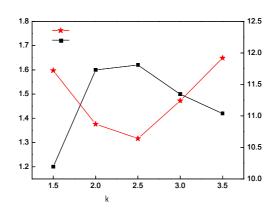
Experimental research

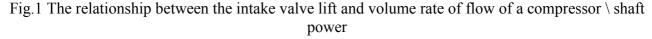
By adjusting the intake valve lift, exhaust valve lift, clearance volume and rotational speed of w-1.6/5 compressor, whose relationship with volume rate of flow and shaft power were carried out and whose regular pattern were found. Specific test data as follows:

The relationship of intake valve lift and energy efficiency. The test data of intake valve lift, volume rate of flow and the shaft power is shown in Table 1 and Figure 1. We can see that ,for suction valve, when the spring force is too large and the suction valve is closed early, it will lead to lack inspiration. When the spring force is too small ,it will lead to a delayed close of valve, the gas inside the cylinder back to the suction chamber. Throuch the test analysis , for the Valve plate of cantilever valve produced by 20 or T10 ,when having a thickness between 3.0mm ~3.5mm and a end maximum stroke between 2.0mm~2.5mm , its comprehensive performance is best.

No.	intake valve lift/mm	Volume rate of flow of a compressor / m ³ /min	Shaft powers / kW
1	1.5	1.20	11.72
2	2.0	1.60	10.87
3	2.5	1.62	10.64
4	3.0	1.50	11.24
5	3.5	1.42	11.92

Table 1 The test data of intake valve lift \ volume rate of flow \ shaft power





The relationship of exhaust valve lift and energy efficiency. The test data of Exhaust valve lift, volume rate of flow and the shaft power is shown in Table 2 and Figure 2. We can see that ,for the exhaust valve, if there's too much spring force which will cause the exhaust valve' early close, while by the end of the exhausting, the gas pressure of cylinder compression chamber increased, and not all the compressed gas was exhausted, which will lead to increased gas pressure in the clearance volume, depressedvolume rate of flow of compressor and increased energy cost; while the spring force is too small, may lead to exhaust valve' late close, which will cause the fact that the compressor stay in open during the oxygen inhalation status, at this time the compressor is kind of in a vacuum state, which lead to depressed volume rate of flow and increased energy cost and temperature.

Throuch the test analysis, for the Valve plate of cantilever valve produced by 20 or T10 ,, it'll work in its best condition with its thickness between 4.5 mm ~ 5.0 mm and end miximum stroke between 3.5 mm ~ 4.0 mm.

No.	Exhaust valve lift/mm	Volume rate of flow of a compressor / m ³ /min	Shaft powers /kW
1	1.5	1.000	11.96
2	2.0	1.35	11.82
3	2.5	1.44	11.50
4	3.0	1.57	11.04
5	3.5	1.64	10.87
6	4.0	1.68	10.62
7	4.5	1.51	11.26

Table 2 The test data of Exhaust valve lift \ volume rate of flow \ shaft power

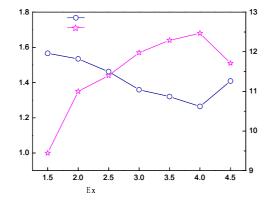


Fig.2 The relationship between the exhaust valve lift and volume rate of flow of a compressor \ shaft power

The relationship of Clearance volume and energy efficiency. Test data of clearance volume, volume rate of flow and shaft power is shown in Table 3 and Figure 3. We can see that , for determining the size of the clearance volume , When the clearance volume is too large the compressed air can not be effectively discharged, if the volume rate of flow of the air compressor decreases, a serious waste of energy efficiency will loss. Clearance volume is so small that it will cause top cylinder accident prone. According to test results, when the piston compressor is at its maximum stroke position, the piston head and the suction valve plate spacing should be $1.0 \sim 1.2$ mm

Table 3 The test data of clearance volume/ Volume rate of flow/ Shaft powers

No.	Clearance volume / m ³	Volume rate of flow of a compressor / m ³ /min	Shaft powers / kW
1	0.2	1.610	11.50
2	0.4	1.620	11.42
3	0.6	1.630	11.32
4	0.8	1.650	11.18
5	1.0	1.660	10.93
6	1.2	1.656	10.76
7	1.4	1.652	11.04
8	1.6	1.634	11.38

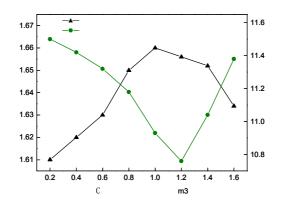


Fig.3 The relationship between the clearance volume and volume rate of flow of a compressor \ shaft power

The relationship of rotational speed and energy efficiency.the test data of rotational speed, volume rate of flow and the shaft power is shown in Table 4 and Figure 4. We can see that ,for W-1.6/5 air compressor, when the exhaust pressure is constant , under normal circumstances the higher the rotational speed, the biggerthe exhaust volume, but the more Energy consumption , the less the ratio of energy consumption and exhaust volume (Specific power). Throuch the test analysis, the optimum rotational speed should be at $1000 \sim 1100 \text{ r} / \text{min}$, witch is an ideal state.

No.	Rotational speed / r/min	Volume rate of flow of a compressor / m^3/min	Shaft powers / kW
1	500	1.23	13.53
2	600	1.40	10.87
3	700	1.53	13.33
4	800	1.57	12.87
5	900	1.61	12.86
6	1000	1.63	12.57
7	1100	1.62	12.15
8	1200	1.56	13.65

Table 4 The test data of clearance volume/ Volume rate of flow/ Shaft powers

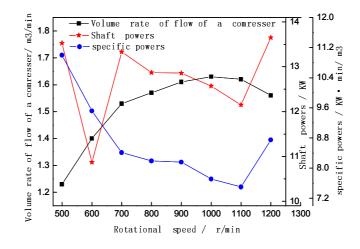


Fig.4 The relationship between the rotational speed and volume rate of flow of a compressor \ shaft power\specific power

Summary

In summary, by adjusting the suction valve lift, exhaust valve lift, clearance volume and rotational speed of piston compressor reasonablely could decrease the energy consumption of air compressor. When the intake valve lift is at 2.5 ~2.5 mm, the exhaust valve lift is at 3.5 ~4.0 mm, the clearance volume isat $1.0 \sim 1.2$ mm, the rotational speed at 1000 ~ 1100 r / min , the total energy consumton of a W-1.6/5 compressor could be decreased by 10.9%.

References

[1] Youzeng Yuan. Disscussion of Energy-saving and Consumption Reducing in Compressed Air System. Cotton Textile Technology.2008.10 (In Chinese)

[2] LiLi.The. way to improve energy efficiency of industrial compressed air system.energy technology and management.2007(3):87-88. (In Chinese)

[3] Qingfeng Wang, Anguo Li.energy conservation ways of reciprocating congpresser.energy conservation technology,2005,23(6):562-563. (In Chinese)

The Optical Design of Achromatic Phase Matching System Based on ZEMAX

Liuyang Zhang^a, Yujiang Liu^b, Jinzhe Huang^{c*}

Department of Optoelectric Information Science and Engineering, Harbin University of Science and Technology, West campus, P.O.Box 130, Harbin 150080, China

^ajohnien@163.com, ^bliuyj@163.com, ^chjinjer@126.com

Keywords: achromatic phase matching, second harmonic generation, ultrashort pulses, optical design, ZEMAX.

Abstract. The system of achromatic phase matching (APM) based on grating pairs is designed by the commercial optical design software ZEMAX. Firstly, we theoretically calculate the theoretical incident angular where each frequency components exactly reaches the phase-matching in nonlinear crystals. Subsequently, the model of APM system is built and optimized in ZEMAX. The results are well in accordance with the theoretical ones. In addition, the effects of grating frequency and aberration produced by the focus lens on APM scheme are analyzed.

Introduction

With the fast development of femtosecond pulse generation, second harmonic generation (SHG) has attracted a great deal of attention [1-5]. However a finite phase matching-bandwidth places limitations in frequency doubling of ultrashort pulses [6-9]. Because of wide spectral range of ultrashort pulses, the phase matching condition cannot by fulfilled simultaneously for all spectra components. In order to overcome this difficulty, extremely short crystals are employed which drastically lowers the efficiency. To increase the phasing-bandwidth and no lower the efficiency, a scheme called APM is proposed [10-12]. APM is a dispersive arrangement where the different spectral components of a pulse are spectrally dispersed so that each component falls on the crystal under the proper phase-matching angle. This is equal to canceling the group velocity mismatch. The method allows efficient frequency doubling of pulses as short as several femtoseconds with crystals of a few millimeters in length. However, a good APM places greater demands on the parameters of the experimental configure, e.g. the distance between gratings, the focus length of the lens, the period of the gratings, etc. It is complex to calculate these parameters by general geometry methods. In this work, we employ ZEMAX to design APM system based on gratings. We not only obtain the parameters of the optical configure, but also consider the effects of the aberration introduced by lens.

APM scheme

The APM scheme is shown in Fig. 1 which contains a pair of gratings and a focus lens. The grating pairs introduce spatial chirp which distribute different frequency components into different spatial position and all the frequency components have the same propagated direction. These parallel rays are focused by consequent lens which make different frequency components strike onto nonlinear crystals in different directions. If parameters of the scheme are appropriate, each component exactly reaches phase-matching in nonlinear crystals. So parameters of the optical system should be chosen carefully.

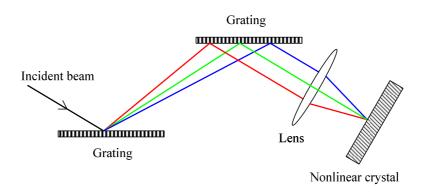


Fig. 1 The APM scheme.

In this work, a 10 fs optical oscillator is employed with central wavelength 0.8 μ m. Then the frequency spectra have a width of 140 nm. We choose BBO as the frequency doubling media and consider type I phase-matching case.

Theoretical incident angles for different components striking onto BBO

The dispersive formula of BBO is from Ref. [13]:

$$n_o^2(\lambda) = 2.7359 + \frac{0.01878}{\lambda^2 - 0.01822} - 0.01354\lambda^2,$$

$$n_e^2(\lambda) = 2.3753 + \frac{0.01224}{\lambda^2 - 0.01667} - 0.01516\lambda^2,$$
(1)

where n_o, n_e represent the ordinary refractive index and extraordinary refractive index, respectively. According to Eq. (1), the phase-matching angles for different frequency components are

$$\theta(\lambda) = \arccos\left(\frac{n_o(\lambda/2)\sqrt{n_o^2(\lambda) - n_e^2(\lambda/2)}}{n_o(\lambda)\sqrt{n_o^2(\lambda/2) - n_e^2(\lambda/2)}}\right).$$
(2)

We choose the central wavelength as the reference ray which exactly reaches phase-matching as the incident ray is perpendicular to the incident surface of BBO. Then a certain frequency component which exactly satisfies phase-matching condition must travel in a specific direction. The angle between the specific direction and the normal of the crystal surface can be named the theoretical incident angle. The theoretical angles for different frequency components can be express as

$$\phi(\lambda) = \arcsin\{n_o(\lambda)\sin[\theta(\lambda) - \theta(\lambda_0)]\},\tag{3}$$

where λ_0 is the central wavelength of the first harmonic pulses.

Table 1 The theoretical and the practical incident angle for different wavelength

Wavelength [µm]	0.73	0.74	0.76	0.78	0.80	0.82	0.84	0.86	0.87
$\phi(\lambda)$ [×10 ⁻² rad]	8.56	7.19	4.61	2.22	0	-2.06	-3.98	-5.77	-6.62
practical incident angle [×10 ⁻² rad]	7.63	6.53	4.35	2.17	0	-2.16	-4.31	-6.45	-7.52

The model and the optimization in ZEMAX

Considering the experimental conditions, we choose the entrance pupil as 2mm, and the wavelengths traced in ZEMAX are the same as those listed in Table 1. The tilt of gratings and the angle of rays striking onto the grating are realized by adding coordinate break surfaces. Nonlinear crystals can not be simulated in ZEMAX or it is not necessary to simulate nonlinear crystals in order to get the parameters of APM. Here we instead nonlinear crystal by a planer surface, since we

only care the angles in which different frequency components strike onto nonlinear crystals, but not the birefringence and frequency doubling properties of the nonlinear crystals.

Merit function is not default one. Operands in merit function mainly contain two classes. One is the control of the angles for different frequency components onto the image plane (i.e. nonlinear crystal) by the operand REAB. REAB gives real ray y-direction cosine of the ray after refraction from a surface. Another is the operand REAR which controls the position of the ray striking the optical elements for the central wavelength and guarantees the ray inside the elements during the optimization process.

The variables used in optimization may be the grating frequency, the length between grating pair and the angle of rays striking onto the first grating. The three parameters affect the spatial chirp. We chose the focus length of the lens and the grating frequency as 50 mm and $1\mu m^{-1}$, respectively. The parameters of the optical system after optimization are shown in Table 2. The practical incident angle is shown in Table 1. Holding the focus length of the lens and changing the grating frequency, we obtain the lengths of gating pair and the values of the merit function which is shown in Table 3.

	Surface: type	Thickness[mm]	glass	Tilt about <i>x</i> [degree]
OBJ	standard	infinity	-	-
STO	standard	10.0	-	-
2	coordinate break	0	-	-60
3	diffraction grating	-107.5	mirror	-
4	coordinate break	0	-	0
5	diffraction grating	5.0	mirror	-
6	coordinate break	0	-	60
7	paraxial	50.0	_	-
IMA	standard	-	-	-

Table 2 The parameters of APM system

Table 3	Variation	of length	between	gating	pair with	grating	frequency.

grating frequency [µm ⁻¹]	0.2	0.4	0.6	0.8	1.0	1.2	1.4	1.6	1.8
length between gating pair [mm]	193.6	159.4	141.8	125.2	107.5	88.7	69.2	49.7	30.7
merit function $[\times 10^{-3}]$	4.8	4.6	4.8	5.2	5.9	6.8	8.1	10.0	14

A grating with a bigger frequency will produce a larger dispersion. As is shown in Table 3, the length between grating pair decreases with grating frequency. The reduction of optical system size can be realized by employing a grating with big frequency. However, this will produce a bigger deviation from the theoretical incident angle and decrease the efficiency. So a trade-off must be made between the size of optical system and the accuracy of APM.

In the above design, the focus lens is an ideal one. Since the focus length is small, the lens maybe produces a considerable aberration. Next we will employ a real lens instead of the ideal one. For grating frequency 1 μ m⁻¹ and focus length 50 mm case, the merit function is from 5.9×10⁻³ down to 5.2×10⁻³. It is obviously that the aberration produced by focus lens partly compensates the deviation from the theoretical incident angle.

Conclusions

The APM system is designed by ZEMAX. The results show that grating frequency and the length between grating pair will severely affect the performance of the APM system. A grating with bigger frequency produces major dispersion lead to considerable deviation from the theoretical incident

angles. However, a little frequency grating will prolong the length of APM which may be reduced by a telescope system. Simultaneously, the APM system can benefit from the aberration originating from the focus lens.

Acknowledgment

The authors thank the Education Department of Heilongjiang province in China for the fund under Grant No. 12511113.

References

- [1] S. G. Rodrigo, H. Harutyunyan, and L. Novotny: Phys. Rev. Lett., Vol. 110 (2013), p. 177405.
- [2] J. Dai, J. H. Zeng, and S. Lan : Opt. Express, Vol. 21 (2013), p. 10025.
- [3] H. Shen, N. Nguyen, and D. Gachet: Opt. Express, Vol. 21 (2013), p. 12318.
- [4] Y. Chong, C. Yang, and X. Li: J. Opt. Soc. Kor., Vol. 17 (2013), p. 491.
- [5] P. Zeil, A. Zukauskas, and S. Tjornhammar: Opt. Express, Vol. 21 (2013), p. 30453.
- [6] N. Fujioka, S. Ashihara, amd H. Ono: Opt. Lett., Vol. 31 (2006), p. 2780.
- [7] S. Ashihara, T. Shimura, and K. Kuroda: J. Opt. Soc. Am. B, Vol. 20 (2003), p.853.
- [8] A. V. Smith, D. J. Armstrong, and W. J. Alford: J. Opt. Soc. Am. B, Vol. 15 (1998), p. 122.
- [9] J. J. Huang, Y. Q. Chang, T. Shen, and Y. Q. Yang: Opt. Comm., Vol. 281, (2008), p. 5244.
- [10] P. Baum, S. Lochbrunner, and E. Riedle: Opt. Lett., Vol. 29 (2004), p.1686.
- [11] A. M. Schober, M. Charbonneau-Lefort, and M. M. Fejer: J. Opt. Soc. Am. B, Vol. 22 (2005), p.1669
- [12] J. J. Huang, L. Y. Zhang, W. C. Zhang, J. Opt. Soc. Am. B, Vol 30 (2013), p. 431
- [13] V. G. Dmitriev, G. G. Gurzadyan: Handbook of Nonlinear Optical Crystals (Springer, 2003)

Mechanical Design of End Support in Coal Mine

Huawen Zhou^{1, a}

¹Changchun University of Science and Technology, Changchun, Jilin, 130022, China ^azhou_huawen@126.com

Keywords: coal mining equipment, end support, mechanical design

Abstract. End support on coal face is an important equipment of improving the work efficiency and the safety of coal mine production. Based on the work environment and the requirements for end support, the research analyzed the mechanical design of end support, such as its structure and composition. Moreover, several features which need to be paid attention to in the design of end support were proposed as well.

Introduction

In coal mine production, the upper and lower ends of coal face refer to two areas (upper roadway and lower part of slope to coal face; lower roadway and upper part of slope to coal face) with length of 10 cm along coal face. The roadway of upper and lower sections directly connects to the ends of coal face. In addition, the arrangement of machine tail and die of regional scraper conveyor is directly influenced by the disturbance stress of coal face and roadway. Meanwhile, due to frequent manual operation and variety of electromechanical devices, accidents are likely to b occurred in the roadway of upper and lower sections. The production safety and efficiency of stopping coal face is greatly influenced by the design of end support on coal face. Therefore, studying the design of end support on coal face is of great significance in the improvement of the safety and efficiency of coal mine production.

The end support on coal face and its defects

First, with the gradual propulsion of coal face, the prop drawing and supporting require to be carried out continuously, thus resulting in frequently happening accidents, low work efficiency and great work intensity. This influences the production efficiency and safety on coal face. Second, the surrounding rock is unstable on the advance support part which is influenced by disturbance to some extent as well. As a result, this part is difficult to be supported and presents lots of hidden dangers, as well as large deformation and pressure. Third, when the surrounding rock of roof and floor is fragile and mild and there is large pressure on coal face, the support bears great pressure as well and the upper end shrinks apparently. Meanwhile, it leads to large difficulty in the management and the transportation of staff and materials. It is not safe in this situation. Fourth, the end support is not fit with the hydraulic support method applied on coal face. In this situation, it does not adapt to present production mode which is rapidly impelled and highly mechanized with high efficiency and yield, therefore greatly restricting the improvement of unit yield of coal production.

The design requirements and functions of end support

The main functions of end support. End support is designed to protect the intersection of coal face and the roof of roadway. And then it provides a preferable work environment for workers, improves the production efficiency, and ensures the work intensity reduction of workers in the space. The flexibly movable end support offers power to move forward to transfer machine and the machine tail and die of scraper conveyor and then contributes to the regular work on coal face. End support helps to connect the transfer machine and the scraper conveyor closer at the end part, thus ensuring the regular operation of transportation equipment. Regarding the fully mechanized coal face with large dip, the coal face and end support closely adjoins each other, therefore decreasing the occurrence of toppling over of support on coal face. End support ensures the recycle of shed legs and capple in the propulsion of coal face. Since the ends of fully mechanized coal face are places where the shearer feed turns over, end support is effective in providing good work conditions for the self-incision of shearers.

The design of end support. First, since end support requires to ensure the antedisplacement of crusher and transfer machine, as well as that of itself and the die of scraper conveyor, there is high requirements on its pull support and tractive forces. Second, the ends with large areas are located on the edge of fully mechanized coal face. Therefore, end support requires presenting large roof cutting ability if not applying gob-side entry retaining. Third, the end parts of fully mechanized coal face are places where the shearer feed turns over. In order to improve the production efficiency and relieve work intensity of workers, the end support requires being favourable to the self-incision of shearers. Fourth, since fully mechanized coal face is usually applied as return airway, the ventilation section of end support needs to be built, so that ensures the production safety on coal face. Fifth, fully mechanized coal face is workers' access roadway and presents large staff flow. But accidents frequently happen at this part. So, end support needs to be designed more reliable and solid to protect workers. Sixth, end support is designed to ensure the regular propulsion of fully mechanized coal face and the use of sully mechanized supporting facilities as well.

The designed structure of end support

The structure mode of end support. The design of end support is based on the structure mode of cantilever support. Generally, end support mainly consists of three parts, several intermediate supports, tail support, and initial support. as shown in Fig.1.

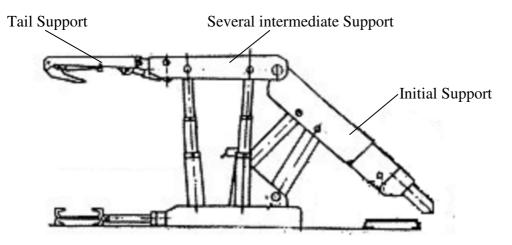


Fig.1 The structure mode of end support

According to the requirements for end support on coal face and the crushing situation of end support, various design data of intermediate supports were determined. All intermediate supports consist of side turning over beam, end beam, turning over beam, monomer pillar, and support top beam etc... Initial support includes the following primary parts, such as beam hydraulic cylinder of the ends, joist, slide way, turning over beam hydraulic cylinder, turning over beam, monomer pillar, and support top beam etc... And the adjacent supports are connected using advancing support hydraulic cylinder. Tail support includes joist, slide way and tail support top beam etc...

The designed structure of end support. The movable secondary beam is installed on end beam to achieve the effect of connecting roof support. In order to reach the beam support effect, the spherical pillar socket is designed at the bottom of the end beam. And spherical pillars are fixed between supports, so that it is convenient to support the carriage die. When the connecting roof support is not

applied, the secondary beam can be removed. The bases of valve group lifting plates can be arranged at top beam and installed symmetrically at both sides of roadway. The angle of bottom hold valve group lifting plates can be adjusted properly as required, so that the supports can be used in coal face with dips. The valve group lifting plates can be used uprightly. In the 30 min before using, roadway is wide enough for the arrangement of supports which are close to the lower working. Since the narrowest section of roadway is merely 1.8 m in width, when support is applied at the area full of coal with inverted roof, the roadway needs to be broadened in advance or adjusted using slabbing or straightening etc.. Since turning over beam needs large activity space when the roadway roof dip changes, and due to the lack of the equipment of increasing space, the turning over beam can not be limited. Regarding coal mine workers, they can avoid colliding with the support pillars when they pay more attention to them in the mechanical operation.

Focuses in the design of end support

The novel design of end support mainly presents the following features. First, the end support is easy to be dismounted and transported, all of which can be accomplished on coal face in situ. Second, by applying the box-type massive structure to top beam, the area of roof protection exceeds 95%. This is effective for the closed-off management of the roof, and even if the roof crushes, the risk of roof leakage will not occur. Third, since the joist system integrated the coal face supports, the safety and stability of support are greatly improved and the occurrence rate of twisting and collapsing support on coal face decreases. Moreover, the potential risks of collapsing and slanting of cantilever support are realized. The coal face support and end support are arranged crossly in the angle of 90°, and can move forward crosswise. For this reason, it is called cross end support.

Conclusions

Mechanical design is an important part in the work content of coal mine production enterprises and plays a fundamental role in coal mine production. It ensures the regular and safe production of these enterprises. At present stage, the mechanical management in coal mine production requires to do well in the management and design of coal mine production equipment step by step using the economic lever, based on foundation work, centered on the decrease of coal mine production accidents, and aimed at improving production efficiency. Improving the reasonability of mechanical design in coal mine production is the only approach to ensure the improvement of coal mine production efficiency and safety and the production of more and more social and economic benefits to the coal mine production enterprises.

The upper and lower end supports on coal face are designed to improve the safety of the end export on coal face, thus ensuring the machinery presents enough supporting intensity. In order to guarantee the enough activity space for equipment operation and maintenance personnel and the fast and normal operation of machine tail and die, large support spans are set generally. In this way, it is effective in improving operating rate and decreasing the service time of ends simultaneously. Therefore, the reasonable design of the technology and features of end support on coal face is effective in realizing the improvement of coal mine production, the economic benefit of coal mine production enterprises, the yield, and the safety.

References

- [1] INDRARATNA B,OLIVEIRA D A F,BROWN E T,et al. *Effect of soil-infilled joints on the stability of rockwedges formed in a tunnel roof.* International Journalof Rock Mechanics&Mining Sciences . 2010
- [2] Zhang Daobing, Luo Yixin, Zhu Chuanqu, *Reliability analysis on bolt support structure of coal roadway under the influence of mining*. Engineering Sciences. 2008
- [3] FRALDI M,GUARRACINO F.*Evaluation of impending collapse in circular*. Tunnelling and Underground Space Tech-nology . 2011
- [4] Qian Qihu. Establishing Underground Expressways and ULS in Extra Large Cities—a New Approach to The Traffic Problems. Science and Technology Review . 2004.
- [5] Whittaker.B.N,Woodron.G.G M etc.*Design Loads for Gateside pack and SupportSystem*. Mining Engineering . 1997.
- [6] Chao-yu Hao,Ji-ren Wang,Cun-bao Deng,Qing-sheng Wan. *Numerical simulation and actual research on safety and suitable position of roadway driving along next goaf.* Journal of Coal Science and Engineering (China). 2010.
- [7] Yang X L,Huang F.Collapse mechanism of shallow tunnel based on nonlinear Hoek-Brown failure criterion. Tunnelling and Underground Space Technology . 2011
- [8] LU Yan,LIU Changyou. *Similarity simulation of bolt support in a coal roadway in a tectonic stress field*. Mining Science and Technology. 2010.

System Precision of Thermal Insulating Door in Environmental Laboratory

Huawen Zhou^{1, a}

¹ Changchun University of Science and Technology, Changchun, Jilin, 130022, China ^azhw@cust.edu.cn

Keywords: thermal insulating door, system precision, installation error

Abstract. Thermal insulating door is a critical component of environmental laboratory. By analyzing the structure, manufacturing and installing precision of thermal insulating door, the installation error of guide, and the selection of elements applied in electric control system of thermal insulating door etc, the research proposed the method of ensuring the system precision of thermal insulating door.

Introduction

Environmental laboratory is the place in which performance indexes of equipment are tested under various conditions. By carrying out tests in the laboratory according to specified requirements, the performance of equipment can be comprehensively evaluated. Meanwhile, by analyzing the parameters measured in the laboratory, valid data can be provided for the design and manufacture of equipment. Thus, environmental laboratory plays an important role in the improvement of manufacture and machining quality of equipment.

Thermal insulating door, as a key component of environmental laboratory, plays its role in thermal insulating and sealing. The door is opened in tests, and with the movements of equipment, the door requires to slide within a certain scope arbitrarily. That's why the sealing quality of thermal insulating door determines the quality of equipment tests carried out at various specified temperatures in environmental laboratory.

The system precision of thermal insulating door in environmental laboratory can be divided into the thermal insulation precision and the motion precision.

The thermal insulation precision

The thermal insulation precision depends on the structure of the door, the manufacturing and assembling precision of the mechanical system of the door, the material of the door, and the air curtain. The door applies ladder structure. And the wall is trimmed with its side shape be consistent with the shape of the door, so that they can touch each other tightly. In statics state (without test), the thermal insulation of the door is realized by the door itself, the sealing rubber on side faces of the doors, and the sealing strips between the bottom of the doors and the wall. In tests, the corresponding door is opened. In this situation, the air curtain separates the air in and out the laboratory, and the thermal insulating precision of the laboratory lies on the velocity and quantity of the airflow ejected from the linear tuyere of the air curtain and the nozzle direction. The structure parameter of the air curtain, the nozzle size of the linear tuyere, and the airflow velocity and quantity etc are determined according to the technical requirements for sealing the wall of the opened door. At the same time, according to the features of air pressure in and out the laboratory, when pressure difference presents in and out, the thermal insulation inside can be realized by adjusting the nozzle angel, thus meeting the requirements of thermal insulation, that is the temperature varies within $\pm 10^{\circ}$.

The manufacturing and assembling precision

The manufacturing and assembling precision of thermal insulating door system refers to the following aspects, including the manufacturing and assembling precision of the door itself and the screw-nut pairs and support bearing etc of moving door, as well as the quality of air cylinder. The assembling precision of thermal insulating door requires to be at the magnitude of millimeter, which is easy to be achieved in machining. Based on this magnitude, the above parts need to be manufactured strictly according to the design requirements, so that they are precise enough.

The air cylinder which offers power for moving doors is of high quality. And the assembling precision of the screw-nut pairs is at the magnitude of micron dimension, which can be achieved in machining. In order to ensure the precision of the relative positions of different thermal insulating doors, several guides and supports are installed on the unified foundation part which is fixed on the wall.

Regarding linear rolling guide pair, due to lots steel balls it bearing, it can balance the error. In addition, owing to the elastic deformation of the guide, the error on the installation surface decreases. And the multi-slider homogenizes the error as well. As a result, the motion error of the moving parts fixed on the guide can decreases to $1/2 \sim 1/5$ of that on the installation surface. Therefore, in generally, the installation surface is merely machined by finish planning and milling, instead of ground finish. (If the guide requires to be high precise after installation, the installation surface needs to be high precise as well.)

The analysis of installation error of the guide

The installation error influences the frictional resistance and the service life of the guide pair. Large installation error leads to the increase of dynamic friction and reduce of service life of the guide pair and the thermal precision of thermal insulating door. Generally, when the installation error is within the acceptable range, the guide pair presents little and stable frictional force and long service life.

Analysis of the error of installation reference and main motion direction of the guide. The guide is a purchased component, and its manufacturing error depends on its manufacturer. Meanwhile, there is error in its installation process as well. The research analyzed the error of installation reference and main motion direction of the guide.

In the following discussion, X denotes the directional line, X_0 represents the installation reference line of the guide, X_C is the main motion direction line, L indicates the theoretical length of the installation reference line, and ΔX_0 represents the radial error of the installation reference line.

Situation 1: $X//X_C//X_0$. It is an ideal state, as shown in Fig. 1 (a). In this situation,

 $\triangle X_0=0$,

It is an error free state.

Situation 2: $X//X_c$, while X_0 is not parallel with X. It can be considered that the installation reference line rotates around the axis Z for an angle of α , as displayed in Fig. 2. Under this condition,

 $\triangle X_0$ =Ltan α

The calculation above indicates that the radial displacement error caused by the misalignment of the directional line, the installation reference of the guide, and the main motion direction, is as follows:

 $\triangle X_0$ =Ltan α

It is observed that the radial displacement error $\triangle X_0$ is small enough to meet the requirements of precision.

(1)

(2)

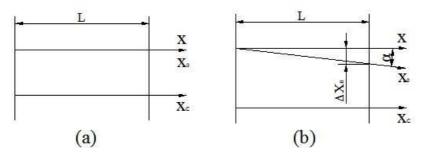


Fig.1 The error of installation reference and main motion direction of the guide

The error of installation reference of the guide and the guide. In the following discussion, X denotes the directional line, X₀ represents the axis of the guide, X_C is the installation reference line of the guide, L indicates the theoretical length of the guide, $\triangle X_0$ represents the radial error of the guide, and $\triangle X_c$ is the radial error of the installation reference line of the guide.

Situation 1: $X/X_C/X_0$, which is an ideal state, as shown in Fig. 2 (a). In this situation,

$$\triangle X_0 = \triangle X_C = 0 \tag{3}$$

It is an error free state.

Situation 2: $X//X_c$, while X_0 is not parallel with X. It can be considered that the guide rotates around the axis Z for an angle of α , as displayed in Fig. 2 (b). Under this condition,

$$\Delta X_0 = L \tan \alpha$$

$$\Delta X_C = 0$$
(4)
(5)

$$\Delta X_{\rm C}=0 \tag{5}$$

Situation 3: Xc is not parallel with X, while $X_0//X$. It can be regarded as the guide reference turns around the axis Z_C for an angle of α_c , as stated in Fig. 2 (c). In this situation,

$$\Delta X_{C} = 0$$

$$\Delta X_{C} = L \tan \alpha_{c}$$
(6)
(7)

$$\Delta X_{C} = Ltan\alpha_{c}$$

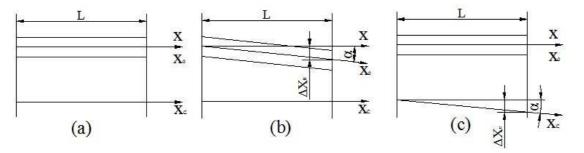


Fig.2 The error of installation reference of the guide and the guide

Situation 4: X is not parallel with X_C, and the same for X₀ and X. It presents same result no matter α is in the same direction with α_c or not.

$$\triangle X_0 = L \tan \alpha \tag{8}$$

(9) $\triangle X_{C}$ =Ltan α_{c}

The calculation above indicates that the misalignment of the directional line, the guide, and the installation reference in installation causes the radial error $\triangle X_i$, which is displayed as follows:

 $\triangle X_i = \triangle X_{0i} + \triangle X_{ci} = (\tan \alpha + \tan \alpha_c)L$

The radial displacement error $\triangle X_i$ is small enough to meet the requirements of the precision.

Precision of Motion

The motion precision of thermal insulating door mainly depends on the following aspects, including the precision of the relative positions of the door blocks, the manufacturing precision of electric elements applied in the process of block movements, the control precision of electric control system,

and the synchronous precision of the gunbarrel lifting and falling with the opening and moving speed of the door blocks.

The precision of relative positions of thermal insulating door blocks lies on the manufacturing and assembling precision of the foundation part fixed on the wall.

Electric elements of high quality are purchased to ensure the manufacturing precision. The piston motion velocity of the air cylinder depends on its airflow quantity and pressure inside. The coordinated actions of the uplift and fall of the gunbarrel and the orderly open and close of the door blocks is guaranteed by the precision of electric control system. While the precision of this system is controlled by the Programmable Logic Controller (PLC), and the C200HG-CPU43 PLC from Japanese OMRON company is applied. This type of PLC employs a compact modular structure and its maximum I/O point number is 480. It presents the long-distance I/O system as well. It is a PLC with modular structure and high quality and property, which ensures the motion precision in the open, close, and movement of thermal insulating door.

Conclusions

Based on the above analysis, the authors concluded that by controlling the manufacturing and assembling precision of thermal insulating door in a reasonable range, selecting proper material and structure for thermal insulating door, and applying PLC of high quality in electric control system, the system precision of thermal insulating door in environmental laboratory can be guaranteed.

References

- [1] Chen.J: *The reliability of the mechanical and structural system*. Xian university of electronic science and technology press, 1995
- [2] He.S, Wang.S: *Analysis and design of Structural reliability*. National Defence Industry Press, 1993
- [3] An.W: *Design of Structural system reliability and optimization based on reliability*. National Defence Industry Press, 1997.
- [4] Huang.S, Liu.J, Automatic door system for urban rail vehicles. Technology for Electric locomotive, 2001.
- [5] Robert Filer, George Leinonen, *Programmable Controllers Using Allen-Bradley SLC500 and Control-Logix*. ISBN: 0-13-025603-X. 2002
- [6] Nanette et al. Bauer Verification of PLC Programs Given as Sequential Function Charts Computer Science, ISSN: 0302-9743 November, 2004
- [7] Jin Hyun Kim, Su-Young Lee, Young Ah Ahn, et al. *Development of RTOS for PLC Using Formal Methods*. ISBN:3-540-23610-4 2004

Advanced Materials Research Vol. 981 (2014) pp 786-789 © (2014) Trans Tech Publications, Switzerland doi:10.4028/www.scientific.net/AMR.981.786

Study on Feature Extraction of Ship Radiated Noise Based on Cepstrum and Anti-noise Property

Shuai Zhan^{1,a}

¹Army 92419, Xincheng 125100, Liaoning Province, China ^azhanshuai364@sina.com

Keywords: Cepstrum, Feature extraction, Anti-noise Property

Abstract. Line spectrum is one kind of important feature information of the ship radiated noise, which provides a strong basis for the ship detection and identification. Due to the complexity of marine environment and the special nature of underwater acoustic channel, it is difficult to obtain ship radiated noise' signals from the complex background noise. Under this situation, this paper proposed the cepstrum as the extraction method of obtaining feature information of the ship radiated noise, and the robust to noise performance was analyzed and compared. The analysis' result shows that the method is simple, which is able to accurately extract feature line spectrum and shows good robust to noise.

Introduction

Passive sonar receive the ship radiated noise as the main information source for target recognition, the Ship Noise Recognition is Significant for ship covert operations underwater, but also The current hot issues of international research in the field of underwater acoustic. Propeller noise is one of the main components of the ship radiated noise. When the water flows through the propeller, it can Produce a single frequency component called "singing tone" in the propellers, It is a line spectral noise components, and its frequency components is stable, Mainly under -1KHz, Performance as line spectrum consisting of Fundamental frequency and harmonic On the spectrum. Cepstrum is used to analyze the cycle components of the spectrum. Therefore, use Cepstrum extract harmonic component has a prominent role. This paper presents a theoretical model and the principle of the cepstrum as the extraction method of obtaining line spectrum, and analysis the anti-noise Property[1,2].

Ship radiated noise characterization

Propeller noise is radiated from the rotating propeller, Including propeller cavitation noise and vibration generated by the propeller blades. Cavitation noise has continuous spectrum. The typical spectrum is shown in Fig.1[3]. In the high frequency band, the spectrum level declined by the slope of decline -6dB/oct with the increasing of frequency. In the low frequency band, the spectrum level increased with the increasing of frequency. Therefore, the spectrum Lines form a peak, this peak is usually in the 100 - 1000Hz octave, and change with the speed and depth. Propeller noise spectrum is the "leaf rate" spectrum related with the number of blades and propeller speed directly. It Satisfies the following formula: $f_m = m * n * s$. Where, n is the number of propeller blades. s is the propeller speed, the unit is turn/s. f_m is the corresponding frequency, the unit is Hz. This "singing tone" performance as the line spectrum superimposed on the continuous spectrum, it is the main component of Submarine low frequency (1 - 100Hz) Noise[4]. Fig.1 shows this pattern.

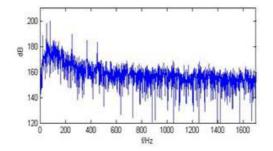


Fig.1 Simulation of ship noise power spectrum

Theory model and principle of cepstrum

Assuming a steady sequence x[n], c[n] is the inverse Fourier transform of the Logarithm amplitude spectrum of x[n].

 $c(n) = f^{-1}[ln | X(e^{jw}) |]$ (1)

Obviously, the inverse Fourier transform of the Logarithm amplitude spectrum does not return the signal to the time domain, but into a new domain, this new field is called "inverted spectral domain". With c[n] represents "inverted spectrum", Referred as "cepstrum"[5].

The principle of using cepstrum extract ship noise: Assuming the signal r(t) consists of periodic component p(t) and non-periodic component q(t), r(t) = p(t) + q(t). Usually ship noise is periodic component p(t), which meets the "Dirichlet conditions": In a cycle, if there is discontinuity point exists, the number of the discontinuous point should be finite. The number of maxima and minima should be finite. Signal is absolutely integrable.

Thus, the periodic signal p (t) may be expanded to Fourier series:

component $p_c(f)$. frequency domain signal Fourier series expansion:

$$p(t) = \sum_{n=1}^{\infty} c_n \cos(2\pi n f_1 + \emptyset_n)$$

It can be seen from the formula (2), Periodic signal p(t) can be decomposed into a plurality of sine and cosine components, The frequency of these sine and cosine components are integer multiples of the fundamental frequency f_1 . We call the components of f_1 as fundamental, Then components of $2f_1$, $3f_1$, $4f_1$ are called second harmonic, third harmonic and fourth harmonic, etc. In the spectrum,

line spectrum appears at the fundamental frequency and its harmonics frequency,

Therefore, the spectrum of signal p(t) is expressed as:

$$p(f) = \sum_{n=1}^{\infty} d_n \,\delta(f - nf_1)$$

(3)After the signal transmitting through the channel, the number of harmonics occurs is uncertain. If the harmonic frequency components of the signal is more and more continuous, Then the pulse of the spectrum p(f) on fundamental frequency and harmonics frequency may be considered appears periodicity based on the fundamental frequency f_1 . Thus on the spectrum, there have been periodic

$$p_{c}(f) = \sum_{n=1}^{\infty} e_{n} \cos(\frac{2\pi n}{f_{1}} + \varphi_{n})$$

$$\tag{4}$$

The frequency of sine and cosine components decomposed by spectrum signal $p_c(f)$ must be an integer multiple of the fundamental frequency $1/f_1$, then $1/f_1$ is the fundamental frequency of Spectrum Signal, harmonics of $1/f_2$, $1/f_3$ is the second harmonic frequency spectrum and third harmonic frequency.

Application of cepstrum extraction the fundamental frequency of line spectrum of the ship radiated noise, Has the following characteristics: pulse appears in inverted frequency of $1/f_1$, $1/f_2$, $1/f_3$, $1/f_4$.only the fundamental frequency $1/f_1$ Relatively obvious in the cepstrum, Harmonic

(2)

frequency components are very weak or even submerged in the background noise. The reason is that the original signal has a non-periodic component, periodicity of frequency domain signal is attenuated. Secondly, the Harmonic number of the spectrum signal is uncertain. Thus, the harmonic components of spectrum is often ignored, the fundamental frequency of spectrum, the reciprocal of the fundamental frequency, its Amplitude is Relatively obvious in the cepstrum, which can be extracted as useful features of the signal.

Simulation Analysis

Simulation conditions: simulation signal is a superposition of the fundamental frequency is 35.65Hz, Sine family composed by Harmonic and Gaussian noise. Sample frequency $F_s = 10^4$ Hz.Calculate in MATLAB, use cepstrum extract the ship noise, compare with the traditional method of power spectrum, verify the anti-noise performance of the method used in this paper [6].

The fundamental frequency has little effect on the simulation, so we randomly select the fixed fundamental frequency. The power spectrum and cepstrum are shown in Fig.2, Fig.3 and Fig.4.

Simulated signal was separated into three groups. The first group: the fundamental frequency is 35.65Hz, the harmonics are Second harmonic, third harmonic, the fifth harmonic, the sixth harmonic, the seventh harmonic, SNR is 20dB. The second group: Missing fundamental frequency, the harmonics are second harmonic, third harmonic, fourth harmonic, the fifth harmonic, the sixth harmonic, the seventh harmonic, SNR is 10dB. The third group: the fundamental frequency is 35.65Hz, the harmonics are Second harmonic, third harmonic, the fifth harmonic, the sixth harmonic, the seventh harmonic, SNR is 10dB. The third group: the fundamental frequency is 35.65Hz, the harmonics are Second harmonic, third harmonic, the fifth harmonic, the sixth harmonic, the seventh harmonic, SNR is 0dB.

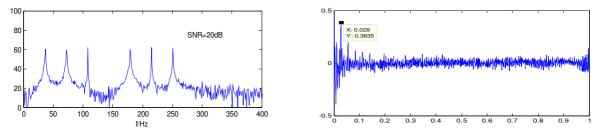


Fig.2 Power spectrum and cepstrum of the first group

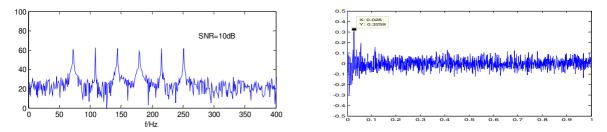


Fig.3 Power spectrum and cepstrum of the second group

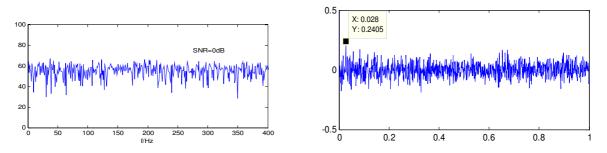


Fig.4 Power spectrum and cepstrum of the third group

As seen from Fig.2, Fig.3 and Fig.4, in the case of worsening SNR, traditional power spectrum can't clearly identify the characteristic information of Line spectrum, cepstrum can still Appear significant peaks Periodically, the Pour frequency where the peak appear is about 1/35.65Hz and its multiples [7]. Thus the fundamental frequency was extracted by cepstrum successfully. In summary, In the case of harmonic partial deletion and poor signal to noise ratio, use cepstrum extract fundamental frequency of radiated noise still has a good estimation results.

Conclusion

This paper studies the feature extraction of ship noise with cepstrum. Because of the complexity of signals in the sea, it is difficult to fully extract the complex signal using the traditional method of power spectrum, so this paper proposed the cepstrum as the extraction method of obtaining the ship radiated noise. In this paper, the original signal is Simulation of ship noise, the extraction methods of cepstrum were validated, and compared with the traditional method of power spectrum. We get the following conclusions: Cepstrum can extract the fundamental frequency component of the harmonic signal, and has better estimation results than traditional power spectrum in low SNR. The cepstrum shows good robust to noise in the exaction of ship radiated noise.

References

- [1] Xuanmin Du, Yahao Jiang. Research on ship radiated noise simulation technology [J]. Acoustics 1999 (01)
- [2] Guoqing Wu, Jing Li, Yaoming Chen, Yi Yuan, Yue Chen. Ship noise identification (I)--Overall framework, line spectral analysis and extraction [J]. Acoustics Journal (Chinese Edition) 1998 (05)
- [3] DuchunTao. research on ship noise rhythm (I)--Mathematical model and power spectral density [J] Journal of Acoustics 1983 (02)
- [4] Bosheng Liu, Jiayu Lei. Water acoustics [M]. Harbin Shipbuilding Engineering Institute Press, 1993
- [5] Xiaoliang Liu, Ligang Chen, Yong Shi, Bingcheng Yuan. A estimate method of underwater target radiated noise line spectrum [J]. Ship Science and Technology 2007 (06)
- [6] Stephen C Wales, Richard M Heitmeyer. An Ensemble Sourcespectra Model for Merchant Ship-radiated Noise. The Journal of The Acoustical Society of America . 2002
- [7] T W Frison, et al. Nonlinear analysis of environmental distortions of continuous wave signals in the ocean [J]. J Acoust Soc Am, 1996, 99(1): 139-146.

CHAPTER 11:

Material Science and Technologies of Processing

Digital Henon Sequences Generation and Its Analysis

Bingbing Song^{1, a}, Jing Pan^{1, b}, Qun Ding^{1, c,} *

¹Electronic Engineering College, Heilongjiang University, Harbin, China ^asongbingbing1988@163.com, ^bpan_hlju@163.com, ^{c,*}(corresponding author): qunding@aliyun.com

Keywords: Henon map; DSP Builder; statistical characteristics; pseudo-randomness

Abstract. In this paper, the typical two-dimensional Henon map is studied. Firstly, the model of Henon map is proposed based on DSP Builder platform in Simulink library, so it can generate digital output sequence of Henon map. Then, its statistical properties are analyzed for such output sequences, including balance test, run test and autocorrelation test. Finally, the numerical results show that such digital Henon sequences have good pseudo-randomness.

Introduction

Recently, the research of chaotic system has been one of the hot-point studies, for its basic features can be used in cryptology, such as ergodicity, initial value sensitivity, etc., therefore, generating digital chaotic sequences for message encryption becomes a new way in cryptography. Nowadays, researchers have proposed a variety of chaotic maps, such as Logistic map, Tent map and Lorenz map. With the development of information technology and computer networks, information security is of great importance. Therefore, the information security techniques have attracted more and more attentions with the developing of internet, such as text encryption, image encryption, video encryption, etc. [1]. Since discrete chaotic systems have nonlinear dynamic behaviors, digital sequences generated by chaotic systems are pseudo-random and sensitive to initial conditions. These excellent features make chaotic systems widely applied to encryption systems [2]. Many scholars have analyzed a lot of chaotic maps. However, most of their studies are based on real-value chaotic system with theoretical simulations, and in this paper, the typical two-dimensional Henon map from another point of view will be studied.

Firstly, the model of Henon map has been built by the DSP Builder modules in Simulink library based on its equation. Secondly, the output sequences of such model are analyzed by pseudo-random tests, including balance test, run test and autocorrelation test. Finally, it comes to a conclusion that these digital sequences generated by Henon map model have good pseudo-randomness characteristics, corresponding to the experimental results.

Digital Sequences Generation of Henon Map.

Henon Map. As it's known to all, Henon map is defined as follows [3]:

$$\begin{cases} x_{n+1} = 1 - ax_n^2 + y_n \\ y_{n+1} = bx_n \end{cases}$$
(1)

where *a* and *b* are parameters, *n* is the nth iteration, x_n and y_n are the nth states. Henon map is the simplest two-dimensional map. Henon system becomes chaotic when the parameters *a* and *b* are in some range [4]. Fig. 1 presents the bifurcation diagram of Henon map for b = 0.3 and $a \in [0,1.4]$ [5].

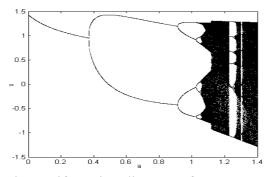


Fig. 1 Bifurcation diagram of Henon map

From Fig. 1 we can find that as the parameter a increases, the system gradually becomes chaotic. Thus, parameter values can be chosen according to the bifurcation diagram [6].

Digital Henon Sequences Generation Model. According to Eq. 1, this paper proposes a digital Henon sequences generation model by using DSP Builder modules in Simulink library.

This model consists of initial value module, data selector module, delay unit module, multiplication module, addition operation module, fixed-point to floating-point conversion module and quantization module. All the structures diagram of this digital Henon sequences generation model is shown in Fig. 2.

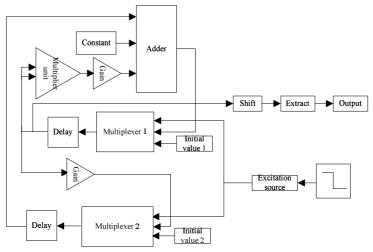


Fig. 2 Structures diagram of Henon map

In Fig. 2, initial value 1 module is the initial value of x, and initial value 2 module is the initial value of y. The implementation of the whole process consists of some steps: firstly, when the excitation source is high, the two initial values will enter the multiplexer 1 module and the multiplexer 2 module respectively, otherwise, the whole iteration starts, including delay, multiplier, gain, and adder; eventually, after shift and extraction, the binary output sequences of x are obtained from the output module.

Pseudo-random Test of Output Sequences.

0-1 binary sequences can be obtained after quantizing the real-value sequences, then the following tests are based on pseudo-random tests for binary sequences in order to obtain its statistical characteristics. Pseudo-random tests contain three basic tests. They are balance test, run test and autocorrelation test. Moreover, the experimental tests are shown below in details.

Balance Test. Actually, balance test is used to test whether the number of 0 and 1 in the binary sequence is approximately equal or not.

Unbalance formula is defined as follows [7]:

$$E(N) = \frac{|Q_1 - Q_0|}{N}\%$$
 (2)

where Q_1 is the number of 1, Q_0 is the number of 0, and N is the length of the sequence. According to Eq. 2, balance test results of digital Henon sequences are shown in Table 1. Table 1 Balance test of Henon map

Length N	10000	20000	30000	40000	60000	80000
Number of Q_0	5029	10145	15233	20212	30263	40369
Number of Q_1	4971	9855	14767	19788	29737	39631
Degree of unbalance	0.0058	0.0145	0.0155	0.0106	0.0088	0.0092

From the experimental results, we find that the number of 0 and the number of 1 are approximately equal. So it can be concluded that the digital Henon sequence can satisfy the balance test requirement.

Run Test. Run test is usually used to determine if the number of run 1 or run 0 satisfies the requirements of the pseudo-randomness of digital sequences. The number of k-length run is about $1/2^k$ of the whole run in the same sequences. The run test results of digital Henon sequences are shown in Table 2.

N-length Run	1	2	3	4
Sequence length 30000	7436	3779	1832	922
Proportion of the total run	0.4977	0.2530	0.1226	0.0617
Sequence length 50000	12546	6289	3055	1535
Proportion of the total run	0.5012	0.2513	0.1221	0.0613
Sequence length 80000	19979	10084	4956	2438
Proportion of the total run	0.4495	0.2521	0.1239	0.0609
Sequence length 100000	24942	12540	6197	3096
Proportion of the total run	0.4996	0.2511	0.1241	0.0620

Table 2 Run test of Henon map

From the results, 1-length run nearly satisfies the theoretical value 1/2, 2-length run nearly satisfies the theoretical value $1/2^2$, 3-length run nearly satisfies the theoretical value $1/2^3$, 4-length run nearly satisfies the theoretical value $1/2^4$. So it can be concluded that the digital Henon sequence can satisfy the run test requirement.

Autocorrelation Test. The purpose of autocorrelation test is used to detect the correlation between sequences at a certain time and that at another time. The autocorrelation coefficient is defined as follows:

$$R(m) = \frac{1}{N} \sum_{i=1}^{N-m} x(i) \cdot x(i+m)$$
(3)

where N is the length of the sequence, and m is the value of the step length. The autocorrelation result of digital Henon sequences is shown in Fig. 3.

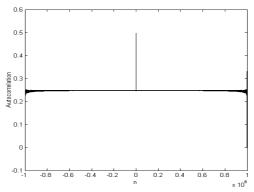


Fig. 3 Autocorrelation result of Henon map

As Fig. 3 shows, the sharp peak is at 0, and at other time the correlation is small. That is to say, the period of the sequence is great. Since the length of the sequence is 10^6 , the period is at least 10^6 . Thus, the digital Henon sequence is similar to pseudo-random sequence.

Conclusions

In this paper, the model of generating digital Henon sequences is proposed based on DSP Builder platform. And after getting the digital sequences, it performs three pseudo-random tests to study their characteristics, including balance test, run test and autocorrelation test. Then, through the experiments, this digital Henon sequence generation model can generate good performance pseudo-random sequences. Therefore, from the results we can draw a conclusion that digital Henon sequences can be used in cryptology in future.

Acknowledgements

This paper is supported by Innovated Team Project of 'Modern Sensing Technology' in colleges and universities of Heilongjiang Province (No. 2012TD007) and Institutions of Higher Learning by the Specialized Research Fund for the Doctoral Degree (No.20132301110004).

- [1] Fan Zheng, Xiaojian Tian, Jingyi Song, Xueyan Li. Journal of China Universities of Posts and Telecommunications, 2008, 15(3): 64-68.
- [2] Xuefeng Zhang, Jiulun Fan. Tsinghua Science and Technology, 2007, 12(S1): 156-161.
- [3] Zhengwei Shen, Weiwei Liao, Yanan Shen. Blind Watermarking Algorithm Based on Henon Chaos System and Lifting Scheme Wavelet. Proceeding of the 2009 International Conference on Wavelet Analysis and Pattern Recognition, 2009.
- [4] Zhengwei Shen, Fucheng Liao. Adapitive Watermark Algorithm Based on Fast Curvelet Transform. Wavelet Analysis and Pattern Recognition, 2008. p. 276-282.
- [5] J.S. Armand Eyebe Fouda, J. Yves Effa, Martin Kom, Maaruf Ali. Applied Soft Computing, 2013. p. 4731-4737.
- [6] Lijun Luo, Yinshan Li, Tong Li, Qingtian Dong. Computer Simulation, 2005, 22(12): 285-288. "In Chinese"
- [7] Yinhui Yu, Weidong Liu. Journal of Chongqing University of Posts and Telecommunications (Natural Science), 2004, 16(3): 61-64. "In Chinese"

Fluorescence from the Compound System of PVK molecules and SiO₂ Nanoparticles with different sizes

Limin An¹, Yanfang Duan¹, Hong Liu², Jie Yi¹, Chunxia Liu¹, Xiaoguang Li¹, Lizhi He¹, Lingsong Zhou¹, Puyu Wang¹, Wenyu An^{1, a}

¹College of Electronic Engineering and Physics, Heilongjiang University, Harbin, 150080, China

²Department of Foundation, Harbin Finance University, Harbin, 150030, China

^aanwenyu@hlju.edu.cn

Keywords: photoluminescence, NPs, energy transfer

Abstract. SiO₂ nanoparticles (NPs) are synthesized in ethanol solution and mixed with polyvinyl carbazole (PVK). The sizes of SiO₂ NPs are 40nm and 60nm. PVK/SiO₂ NPs compound systems with different sizes and with different ratios of mass fraction are obtained. Photoluminescence spectra are employed to research the optical properties of PVK molecules and PVK/SiO₂ NPs compound system. In compound system, the process of interface energy transfer between PVK and SiO₂ NPs are observed. The mainly energy transfer form is nonradiative resonance transfer.

Introduction

Polyvinyl carbazole (PVK) is a hole transmission mode conducting polymer, its electron affinity is 1.5eV, it is usually used for transport layer in electroluminescent devices and as a research hotspot in fundamental research and in the field of optoelectronics applications [1-3]. The filling modification of polymer has a long history of the study, the research of photoluminescence, electroluminescence and the change of current-illumination characteristic of PVK got a lot of publicity to use PVK mixed with high fluorescence efficiency material, with rare earth luminescence complexes, with C_{60}/C_{70} system [4].

The nanoparticles (NPs) composite is a kind of composite that the dispersed phase dimension at least has one dimensional less than 100 nanometer. NPs have quantum size effect, large specific, strong interfacial interaction and unique physicochemical property [5, 6]. It shows many novel characters of polymer/NPs composites and can make many kinds of composites, such as thermal resistance, magnetism, light absorption, chemical activity, and biological activity. It has extensive application prospect and practical value in chemical engineering, medicine, chemistry, material synthesis and so on, the research of polymer/NPs composites is the current hot spot [7]. In polymer/NPs compound system, when polymer or NPs excited to excited state by light, it can produce energy transfer and charge transfer because of the difference of electron affinity and the energy band matching. Charge transfer changes the photoconduction of compound system. The fluorescence intensity of polymer extinct and the life of excited state become shorter because of energy transfer [8-10].

We use sol-gel method got SiO_2 NPs with two kinds of grain sizes, mixed them with PVK respectively, and got PVK/SiO₂ NPs compound system, then study fluorescence effect and interfacial effect of the system.

Experimental Section

Absolute ethyl alcohol (analytically pure) 50ml, ammonium hydroxide (analytically pure) 1.7ml, deionized water 1ml, TEOS (analytically pure) 1ml into reaction bulb in proper order are heated when water bath achieved 40° C in SiO₂ NPs synthesis [11]. TEOS (analytically pure) 1ml is mixed for 3 hours. Then the solution in the bottle becomes milk white which is SiO₂ NPs. We observed the grain size of SiO₂ NPs is 60nm by transmission electron microscope, and they are homogeneous distribution. All other things being equal, to change the dosage of ammonium hydroxide to 2ml, and then we can get SiO₂ NPs have 40nm grain size.

Dissolve PVK powder in chloroform, mix some SiO₂ NPs solution with PVK solution, and stir it. Then we can obtain PVK/SiO₂ NPs compound systems with four kinds of the mass percent of PVK (5%, 20%, 40%, and 60%). Use natural evaporation method to form a uniform on Si substrate.

Results and Discussions

PVK molecule consists of a hybrid five-ring, two conjugate of benzene rings and a long polyethylene chain. After stimulated emission, π electrons in conjugate of benzene rings transfer from bonding orbital to antibonding orbital, release energy and emit visible fluorescence through radiative relaxation ($\pi^* \rightarrow \pi$ transition).

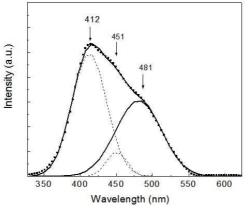


Fig. 1. PL spectrum of PVK film fitted with multi-peaks of Gaussian. PL spectrum measured in the experiment (dot), fitted curve (solid), three fitted separated PL spectra (dash).

We were fitting the spectrum of PVK thin film under 325nm pump light. According to the peak shape and luminous mechanism, we use Gaussian Fitting divided them into three peak, as Fig. 1 shows. The discontinuous dots are the measured curve, and the continuous full line is the fitted curve, they are match exactly. We can see the PVK luminescence is located in 350 ~ 550nm range, highest luminous peak at 412nm belongs to free excitonic luminescence. The unconspicuous weak acromion at 451nm is bound exciton luminescence. The luminescence located in 495nm is defect state luminescence [12].

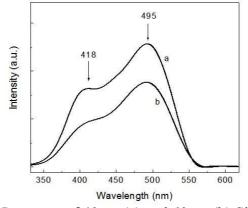


Fig. 2. PL spectra of 40nm (a) and 60nm (b) SiO₂ NPs

Fig. 2 is the photoluminescence spectrum of SiO_2 NPs with different sizes (40nm (a), 60nm (b)) under 325nm laser. We can see: it has two obvious luminous peaks located in 418nm and 495nm. SiO_2 is an insulation material, its band gap is wide, and its luminescence can only come from flaw, but not come from band gap, so its half width is very wide. The luminous locations of SiO_2 with grain sizes 40nm and 60nm is the same, but the light intensity of 40nm SiO_2 is stronger than the light intensity of 60nm SiO_2 . Because the smaller the grain size of the NPs, the more flaws the surface has, the light from surface defects get stronger. Compared the photoluminescence spectra of PVK thin film and SiO_2 NPs, the luminous peaks are all very wide, and overlapped each other, but

the strength distributions of them are not the same. In Fig. 1, the light intensity of PVK is stronger at 412nm of high-energy side than the light intensity at 481nm of low-energy side; but in Fig. 2, the light intensity of SiO_2 is stronger at 495nm of low -energy side than the light intensity at 418nm of high-energy side.

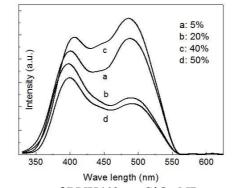


Fig. 3. PL spectra of PVK/60nm SiO₂ NPs complex films

Fig. 3 is the photoluminescence spectra the thin film of 60nm SiO_2 NPs mixed with PVK respectively, a, b, c, d are the luminescence spectra when the mass fraction of PVK is 5%, 20%, 40% and 60% respectively. Based on the above analysis, the luminescence around 400nm is mainly comes from band gap luminescence of PVK, and the luminescence around 500nm is mainly comes from the surface state luminescence of SiO₂ NPs. We use the ratio of the integrated intensity of the luminous peak at 400nm to the integrated intensity of the luminous peak at 500nm to compare luminosities of different grain sizes and different dosage concentration. We can see clearly from the Tab that for PVK/60nm SiO₂ nano particle composite membrane, when the mass fraction of PVK is 5%, the ratio of integrated intensity is 0.71, with the increase of PVK, the mass fraction is up to 20%, the ratio is up to 1.01, however, when the mass fraction of PVK is 40%, the ratio dropped to 0.67, when the mass fraction of PVK is 60%, the ratio is up to 0.90, it's still less than 1.01 of the mass fraction of PVK is 20% [11]. It shows that it exist energy from PVK to SiO₂ in PVK/ SiO₂ compound system, and when the mass fraction of PVK is 40% (for 60nm SiO₂ nano particle), the ratio of luminous peak is minimum, that is, the efficiency of energy transfer between PVK and SiO₂ is maximum at the moment. The reason may be that the mass fraction of PVK in this ratio can modify the surface of SiO₂ NPs better, and the distribution of SiO₂ NPs in PVK is uniform [12]. The grain sizes of SiO₂ NPs are different, so the mass fractions of PVK are different when the efficiency of energy transfer up to maximum, this is because the nano particle has large superficial area, many surface defects, large energy transfer probability when its grain size is small, so in order to get the same effect, the mass fraction of small grain size NPs should be less, that is, the mass fraction of PVK should be more.

The absorption range of SiO₂ NPs is very wide and overlapped with the emission spectrum of PVK. It provides a requirement for the energy transfer from PVK to SiO₂ NPs. Energy transfer has many kinds of forms, such as collision transition probability, reabsorption process, resonance transfer, form molecular complex and so on. We suppose the mainly form in PVK/SiO₂ is nonradiative resonance transfer. Because it accord with three conditions of resonance transfer: 1. the distances between molecules are 5-10nm. 2. the fluorescence spectra of donor is overlapped with the absorption spectrum of receptor. 3. the donor must be fluorescent. It shows that it has strong interaction between the surface of SiO₂ NPs and PVK molecules; it's a good mode to study the interfacial effect between organic nanometer system and inorganic nanometer system.

Conclusions

The effective energy transfer process exists between PVK and SiO_2 NPs. To compare the photoluminescence spectra of PVK mixed with SiO_2 NPs of different grain sizes and different mass fractions to find the best mass fraction of PVK for energy transfer, the reason may be that the mass fraction of PVK in this ratio can modify the surface of SiO_2 NPs better, and the distribution of SiO_2

NPs in PVK is uniform. The research shows that the PVK/SiO_2 NPs compound system has strong interfacial effect; it's a good mode to study the interfacial effect between polymer and inorganic nanometer system.

Acknowledgments

This paper is sponsored by Postdoctoral Science Foundation of China (2013M541420), Natural Science Foundation of China (21173063) and Heilongjiang University Foundation (201107), Natural Science Foundation of Heilongjiang Province (A201105), Key Laboratory of Functional Inorganic Material Chemistry (Heilongjiang University), Ministry of Education (2013), the 12th Five-Year Plan for the Education Science of Heilongjiang Province (GBD1211048), Higher Education and Teaching Reform Project of Heilongjiang Province of China (JG2012010500), the High Level Innovation Teams of Heilongjiang University under Grant (HD-028), the Second "Three Education" Research Project of Heilongjiang University (SK1216) and the Degrees and Graduate Education Reform Project of Heilongjiang University (JGXM_YJS_2012025).

- [1] Y. Wang. Nature, VOL 356 (1992), p. 585
- [2] N. Cui, X.T. Han, X.L Chen. Advanced Materials Research, VOL 712-715 (2013), p. 246
- [3] M. Kocher, T.K. Däubler, E. Harth. Appl. Phys. Lett., VOL 72 (1998), p. 650
- [4] D.L. Tao, B.G. Huang, Y.Z. Xu. Spectroscopy and Spectral Analysis, VOL 21 (2001), p. 740 (in Chinese)
- [5] L.M. An, X.T. Han, X.L. Chen. Applied Mechanics and Materials, VOL 268-270 (2013), p. 551
- [6] J. Yi, X.T. Han, X.L. Chen, C.X. Liu, W.Y. An, X. Dong, M.L. Liu, L.M. An, Y.M. Luo. Thin Solid Films, VOL 521 (2012), p. 112
- [7] B.O. Dabbousi, M.G. Bawendi. Appl. Phys. Lett., VOL 66 (1995), p. 1316
- [8] J. Qian, F.K. Shan, D.M. Huang. Chin. J. Light Scattering, VOL 9 (1997), p. 24 (in Chinese)
- [9] L.M. An, Y.Q. Yang, W.H. Su, J. Yi, C.X. Liu, K.F. Chao, Q.H. Zeng. J. Nanosci. Nanotech., VOL 128 (2010), p. 2099
- [10] L.M. An, K.F. Chao, Q.H. Zeng, X.T. Han, Z. Yuan, F. Xie, X. Fu, W.Y. An. J. Nanosci. Nanotech., VOL 13 (2013), p. 1368
- [11] L.M. An, G.Y. Shan, X. Wang. Chin. J. Luminescence, VOL 23 (2002), p. 590 (in Chinese)
- [12] M.Yan, L.J. Rothberg, E.W. Kwock. Phys. Rev. Lett., VOL 75 (1995), p. 1992

Charge Transfer and Energy Transfer between CdSe Semiconductor Nano Crystals and Polyaniline Molecule

Wulei Zhou¹, Tuo Cai¹, Jian Xiao¹, Xueting Han², Jianbo Liu², Liang Xu², Jianguang Chi², Shaohong Gao², Xiping Cai², Limin An^{1, 2, *}

¹Department of Physics and Electronic Science, Qiannan Normal College for Nationalities, Duyun, Guizhou 558000, China

²College of Physics Science and Technology, Heilongjiang University, Harbin, 150080, China

*anlimin@hlju.edu.cn (corresponding author)

Keywords: semiconductor nano crystals (NCs), CdSe, Polyaniline (PAni), fluorescence life, charge transfer, energy transfer

Abstract. CdSe semiconductor nano crystals (NCs) and Polyaniline (PAni) are mixed uniformly to prepare CdSe NCs/PAni complex. PAni can quench the fluorescent signal of CdSe NCs. The fluorescent intensity of CdSe NCs/PAni complex is related to the size of CdSe NCs and concentration of PAni. Ultraviolet visual (UV-Vis) absorption spectra and fluorescence spectra are employed to analysis the quenching phenomenon. The mechanism of fluorescence quench is dependent on two factors: on one hand, the FÖrster resonance energy transfer conducts from CdSe to PAni; on the other hand, PAni can intercept the electron charge of CdSe and lead to the interruption of radiative recombination.

Introduction

Conductive polymer has not only the electronic and optical properties of metal and inorganic semiconductor, but also the mechanical property and manufacturability of organic polymer. In addition, it is excellent redox active material. Polyaniline (PAni) is a polymer composite material, commonly known as the conductive plastics. PAni has become one of the most promising conductive polymers because of its simple preparation (The batch productions can be conducted through the chemical oxidation polymerization), low cost and good stability [1, 2]. Semiconductor nano crystals (NCs) whose radii are smaller than the bulk exciton Bohr radius constitute a class of materials intermediate between molecular and bulk forms of matter. Consequently semiconductor NCs exhibit efficient optical and electronical property, whose energy or color can be controlled easily by adjusting their sizes [3-5]. We can make PAni copolymerization with the other functional materials and get variety of composite materials which can be used in the aerospace, microelectronics, automotive, communication, biomedicine, textile and many other fields [6, 7].

In 1994, V. I. Colvin combined CdSe NCs with Poly-Phenylene Vinylene (PPV) and manufactured double-deck electroluminescent device for the first time [8, 9]. There are several problems in the research on the electroluminescent devices which are fabricated through the mixture of the conductive polymers and NCs. The charge carrier transport mechanism has not been explained between polymer layer and NCs layers. The luminous efficiency and the service life still need to improve. Due to the limitation of the resolution of transmission electron microscope, the structure of organic molecules can not be observed, so the research on the interface between NCs and organic molecular can be conducted only through some indirect methods. In this paper, we mixed two advanced functional materials to synthesize CdSe NCs/PAni complex. One of the materials is the CdSe semiconductor NCs, which has good performance on luminous. The other one is PAni which has broad prospect of application. The physical mechanism of fluorescent signals quenches from CdSe NCs caused by PAni are also discussed with the method of spectroscopy analysis.

Experiment

CdSe NCs were prepared according to the previous method [10]. A stock cadmium stearate solution was prepared by heating a mixture of 0.228g of stearic acid, 0.0256 g of cadmium oxide and ODE in a 50 ml three-neck flask to 200 °C under stirring and continuously flowing of nitrogen until a clear, solution was obtained. After this solution was cooled to room temperature, HDA and TOPO were added into the flask with the molar ratio of 4:1.20. Under nitrogen flow, the mixture was reheated to 280°C. At this temperature, a selenium solution (prepared by dissolving 0.158 g Se powder into the TOP and ODE mixture under ultrasonic conditions) was guickly injected. The temperature was reduced to 240 °C within several minutes for core growth. After the reaction was completed, the reaction flask was removed from the heating mantle and allowed to cool to 40 °C. The reaction mixture was extracted by the hexane/methanol system to purify the NCs from side products and un-reacted precursors. Then, the hexane system was extracted. The acetone was added to precipitate the NCs. The NCs precipitate was collected by centrifugation and re-dissolved in hexane or chloroform. By systematically changing the nuclei temperature and growth time, it was possible to finely tune the size of the CdSe NCs from 2.1nm to 5.6nm. The CdSe NCs and PAni were mixed and stirred thirty minutes in hexane on magnetic stirring apparatus. Then, the CdSe NCs/PAni complex is synthesized.

Results and discussion

We respectively mixed different amount of PAni with the different sizes of CdSe NCs, and stirred well by the magnetic stirring apparatus, then get the CdSe NCs/PAni complex. The key problem of the directly mixed methods is how to disperse NCs homogeneously under the premise of keeping the fluorescence. Usually, the mixes of different materials cause serious phase separation and lead to gather, destroy the original performance. But, in this experiment we find that the dispersion between NCs and PAni is homogeneous. We suggest that the separate regulation of NCs in PAni is similar to the separation behavior of blending polymer or embedded polymer. The flexible polymer chains of PAni just match the HDA on the surface of CdSe NCs, so it is not easy to separate.

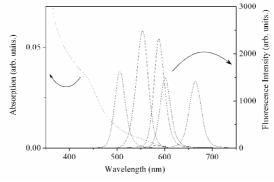


Fig. 1 Absorption spectrum of PAni (dash) and fluorescence spectra of different size CdSe NCs (s olid) in CHCl₃

The main chain of PAni contains alternate benzene ring and the nitrogen atoms, so PAni is a special kind of conductive polymer, e.g. p-semiconductor. Its ultraviolet visible (UV-Vis) absorption spectrum is shown in figure 1. The first exciton absorption peaks is 450 nm, and there is absorption in the areas of less than 600 nm. In the experiment the fluorescence excitation wavelength is 480 nm, so CdSe NCs is only excited and PAni not. The fluorescence spectra of different size CdSe NCs and absorption spectrum of PAni are shown together in figure 1. The fluorescence emission peak from 506 to 662 nm covers the whole visible area. It can be seen clearly that all the CdSe NCs' emission spectrum expect the peak in 662 nm overlap with the PAni' absorption spectrum. This accords with the basic rules of fluorescence resonance energy transfer (FÖrster resonance energy, FRET) that donor's emission spectrum overlap receptor's absorption spectra, in other words, energy transfer can happen between PAni and CdSe NCs. When the

distance between the donor and the receptor is less than FÖrster radius, fluorescence energy transfers from the donor to the receptor, which leads to the decrease of the donor's fluorescence emission intensity and the excited state lifetime, and the increase of the receptor's fluorescence enhancement.

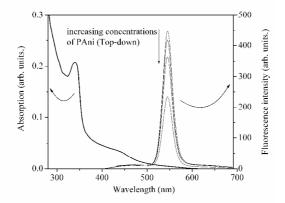


Fig. 2 Absorption and fluorescent spectra of CdSe NCs/PAni complex with different concentration of PAni

In order to further define the interaction between the PAni and CdSe NCs, we discuss the influence of the concentration of PAni on the CdSe NCs emission. As shown in figure 2, with the variation of PAni concentration the PAni absorption spectroscopy and the shape of CdSe NCs fluorescence spectra have not significant change, but the fluorescence intensity of CdSe NCs reduce nonlinearly with the increasing of the PAni concentration. CdSe NCs in figure 2 whose fluorescence emission peak is 553 nm. The same quench phenomenon is also observed in other CdSe NCs/PAni complex although the extent of the quench is different.

The fluorescence intensity of CdSe NCs reduces sharply after adding PAni. The possible physical mechanisms of fluorescence quench are listed: (1) forming new radiation center or non-radiation center. The probability can be excluded because CdSe NCs fluorescence emission peak position is not changed almost, and new fluorescence peak does not appear after adding PAni. (2) Excitation competition leads to the decrease of excitation density. This mechanism can also be excluded because the excitation wavelength is 480 nm, and it can only stimulate CdSe NCs fluorescence, can't stimulate PAni. (3) Energy transfer. The donor (CdSe NCs) in the excitation state transfer energy to the receptor (PAni) and it go back to ground state. The energy transfer mechanism of fluorescence quench is possible. (4) Charge transfer. That is excited state charge transfers between CdSe NCs and PAni leading to the interruption of radiative recombination. This mechanism also can't be ruled out.

According to the different energy transfer environment of donor and receptor, the kinds of energy transfer mechanism have: radiation mechanism, the resonance mechanism and exchange electronic mechanism. The energy transfer of radiation mechanism can not change the lifetime of the donor because the energy transfer of radiation mechanism is only the follow-up process of radiation transition. When there is only energy transfer of the radiation mechanism, the lifetime of the donor is just determined by the rate of molecular deactivation process. In the experiment the lifetime of the composite system of CdSe NCs and PAni changes. So we can eliminate the radiation mechanism. The rate index of energy transfer for electronic exchange mechanism decreases with the increase of the distance between donor and receptor (R). When R is larger than 0.1nm, the rate of energy transfer caused by electronic exchange mechanism can be omitted compared to other inactivation process. But the distance between CdSe NCs and PAni is far over 0.1 nm. So the main energy transfer mechanism is the resonance mechanism on the composite system of CdSe NCs and PAni.

The transfer efficiency of energy transfer Φ_{ET} is connected to the overlapping degree of the donor emission spectrum, the distance between the donor and the receptor, the relative orientation of transition dipole moment, and so on. The definitions of the following:

$$\Phi_{\rm ET} = 1 - \frac{A(\lambda_{\rm D})}{A_{\rm D}(\lambda_{\rm D})} \frac{I_{\rm D}(\lambda_{\rm D})}{I_{\rm D}^0(\lambda_{\rm D})}$$
(1)

 $A_{\rm D}(\lambda_{\rm D})$ is absorbance without receptor, $A(\lambda_{\rm D})$ is absorbance with receptor, $I_{\rm D}^{0}(\lambda_{\rm D})$ is the fluorescent integral strength of quantum dot without receptor, $I_{\rm D}(\lambda_{\rm D})$ is the fluorescent integral strength of CdSe NCs with receptor. $\lambda_{\rm D}$ is excitation wavelength.

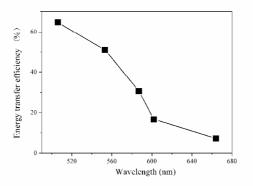


Fig. 3 Energy transfer efficiency of CdSe NCs/PAni with different NCs size

Fig. 3 shows the relationship of resonance energy transfer efficiency between different size CdSe NCs and PAni in the same PAni concentrations. In fig. 3 the fluorescence emission peak position of CdSe NCs is horizontal ordinate, the energy transfer efficiency of CdSe NCs/PAni polymer is vertical coordinate. The energy transfer efficiency is calculated according to formula (2). In a certain PAni concentration, energy transfer efficiency decreases with the increase of the NCs size. The reason is that fluorescence emission wavelength increases with the increase of the NCs size, and the overlap between PAni absorption spectroscopy and the CdSe NCs emission spectrum decreases.

It must be pointed out that the fluorescence spectrum for the red NCs with the peak at 662 nm and absorption spectrum of PAni doesn't overlap totally (figure 1). So it doesn't meet the resonance energy transfer conditions. But the fluorescence intensity of NCs declines still about 7% (fig. 3). The main reason of fluorescence quench is resonance energy transfer mechanism, but there is also other mechanism.

$$CdSe + h\nu \to CdSe(h^{+} + e^{-}) \to CdSe + h\nu'$$
⁽²⁾

$$CdSe(h^+) + PAni \rightarrow CdSe + PAni^+$$
 (3)

After CdSe NCs are excited, the electrons in valence band absorb photon energy to enter conduction band. At the same time the holes emerge in the valence band. After a quick vibration relaxation, the electrons in conduction band release phonons and reverse back to the bottom of conduction band, then radiative recombination of electrons and holes emits hv', as shown in formula (2). After the addition of PAni, the holes in the valence band may be transferred because PAni is a kind of good p-type conducting polymer, as shown in formula (3). Then the radiative recombination process is interrupted. So the fluorescence quenches effect of PAni on CdSe NCs contains the resonance energy transfer mechanism and the charge transfer mechanism.

Conclusions

We mixed CdSe NCs and PAni to synthesize the complex and analyzed the interaction between CdSe NCs and PAni through the spectrum analysis. PAni can quench the fluorescent signal of CdSe NCs. The fluorescent intensity of CdSe NCs/PAni complex is related to the size of CdSe NCs and concentration of PAni. There are two reasons for this kind of fluorescence quench mechanism. On the one hand, the energy transfer exists from CdSe NCs to PAni. On the other hand, PAni can intercept the charge carrier of CdSe NCs and interrupt the radiative recombination process.

Acknowledgments

This paper is sponsored by the Foundation of Scientific Innovative Research Team of Education Department of Guizhou Province (201329), the Provincial Experimental Teaching Demonstration Center of Guizhou Province (201310), Natural Science Foundation of Education Department of Guizhou Province (QJK07092), Postdoctoral Science Foundation of China (2013M541420), Natural Science Foundation of China (21173063) and Heilongjiang University Foundation (201107), Natural Science Foundation of Heilongjiang Province (A201105), Key Laboratory of Functional Inorganic Material Chemistry (Heilongjiang University), Ministry of Education (2013), the 12th Five-Year Plan for the Education Science of Heilongjiang Province (GBD1211048), Higher Education and Teaching Reform Project of Heilongjiang Province of China (JG2012010500), the High Level Innovation Teams of Heilongjiang University under Grant (HD-028), the Second "Three Education" Research Project of Heilongjiang University (SK1216) and the Reform Project Degrees and Graduate Education of Heilongjiang University (JGXM YJS 2012025).

- [1] C. Kim, A. Facchetti, T.J. Marks. Science, VOL 318 (2007), p. 76
- [2] N. Cui, X.T. Han, X.L Chen. Advanced Materials Research, VOL 712-715 (2013), p. 246
- [3] L.M. An, X.T. Han, X.L. Chen. Applied Mechanics and Materials, VOL 268-270 (2013), p. 551
- [4] Z.A. Peng, X. Peng. J. Am. Chem. Soc., VOL 123 (2001), p. 183
- [5] L.M. An, Y.Q. Yang, W.H. Su, J. Yi, C.X. Liu, K.F. Chao, Q.H. Zeng. J. Nanosci. Nanotech., VOL 128 (2010), p. 2099
- [6] J. Yi, X.T. Han, X.L. Chen, C.X. Liu, W.Y. An, X. Dong, M.L. Liu, L.M. An, Y.M. Luo. Thin Solid Films, VOL 521 (2012), p. 112
- [7] L.M. An, K.F. Chao, Q.H. Zeng, X.T. Han, Z. Yuan, F. Xie, X. Fu, W.Y. An. J. Nanosci. Nanotech., VOL 13 (2013), p. 1368
- [8] V.L. Colvin, M.C. Schlamp, A.P. Alivisatos. Nature, VOL 370 (1994), p. 354
- [9] H. Goto, K. Akagi. Macromolecules, VOL 35 (2002), p. 2545
- [10] L. Qu, X. Peng. J. Am. Chem. Soc., VOL 124 (2002), p. 15119

Synthesis of CdS-Capped CdSe Nanocrystals without any Poisonous Materials

Wulei Zhou¹, Tuo Cai¹, Yun Chen¹, Xuanlin Chen², Yuqiu Qu², Xingbin Huang², Wenjiang Dai², Dehang Xiao², Changbin Yu², Hong Wei¹, Limin An^{1, 2, *}

¹Department of Physics and Electronic Science, Qiannan Normal College for Nationalities, Duyun, Guizhou 558000, China

²College of Physics Science and Technology, Heilongjiang University, Harbin, 150080, China

*anlimin@hlju.edu.cn (corresponding author)

Keywords: Nanocrystals (NCs), CdSe, aqueous solution, CdSe/CdS

Abstract. CdS-capped CdSe nanocrystals (NCs) which show high luminescence quantum yield are synthesized without any Poisonous Materials in aqueous solution. The synthesis in an aqueous medium without any poisonous materials is attached importance to. The absorption spectroscopy and photoluminescence spectroscopy are employed to analyze the NCs. It takes 78s that the intensity decreases to the half for bare CdSe NCs, but 442s for CdSe/CdS core/shell NCs. The photo stability of CdSe NCs under 325nm laser irradiation is enhanced greatly after CdS overcoating.

Introduction

Semiconductor nanocrystals (NCs) whose radii are smaller than the bulk exciton Bohr radius constitute a class of materials intermediate between molecular and bulk forms of matter. The synthesis of CdSe NCs has become well established [1]. In the framework of the colloidal chemistry approach, high quality NCs of different II-VI materials can now be obtained. The two existent general strategies of NCs preparations are an organometallic synthesis based on the high-temperature thermolysis of the precursors [2] or on a dehalosilylation reaction and the synthesis in an aqueous medium using polyphosphates or thiols as stabilizing agents [3].

The organometallic methods developed initially for the preparation of CdSe NCs involved the use of highly pyrophoric organometallic substrates such as dialkyk cadmium. More recently, safer reagents were proposed, such as cadmium oxide and cadmium acetate. Thus, a simple oil synthetic route for the preparation of the high quality CdSe NCs without the use of any organometallic precursors is realized [4]. This synthesis route is carried out widely now. But there are still TOP and TOPO which involve poisonous organic P in the oil solution [5]. So, the synthesis in an aqueous medium without any poisonous materials is attached importance to. The simplicity and high reproducibility are notable among the advantages of the aqueous synthesis. Colloidal CdSe NCs with size distribution about 10% can be prepared without the hot-injection technique which is necessary for the synthesis of NCs in TOPO-TOP mixture. As a result, the aqueous synthesis of thiol-capped NCs can be carried out equally effectively on a vast scale, whereas the scaling up of the organometallic synthesis is difficult due to its poor reproducibility [6].

In this article we report on an aqueous synthesis, the structures, and optical properties of highly luminescent and stable CdSe/CdS NCs.

Experimental Section

For a typical synthesis [7], 1.97 g (4.7 mmol) of $Cd(ClO_4)_2 \cdot 6H_2O$ is dissolved in 250 mL of water, and 11.2 mmol of thioglycolic acid are added under stirring, followed by adjusting the pH to 11.2 by dropwise addition of 1 M solution of NaOH. The solution remains turbid firstly and turns very clear when the pH is over 9.0. The solution is placed in a three-necked flask and deaerated by N₂ bubbling for 30min. Under stirring, NaHSe solution (generated by the reaction of 270.8mg of Se powder with

152mg of NaBH₄ in 2ml water under N₂ atmosphere at 0°C) is added. Thus, CdSe precursors are formed at this stage which is accompanied by a change of the solution color, from achromaticity to orange. The precursors are converted to CdSe NCs by refluxing the reaction mixture at 100°C with a condenser attached under N₂ atmosphere. For overcoating CdSe NCs with CdS, two solutions of Cd(ClO₄)₂·6H₂O and Na₂S·9H₂O were slowly added dropwise alternately into CdSe colloid at the rate of 40 μ L/min at a medium temperature of 40-50°C.

Results and Discussions

In order to acquire high quality (narrow size distribution, good crystallinity, photo stability, desired surface properties, and high luminescence quantum yields) CdSe/CdS core/shell NCs, it is found that slow addition of the CdS precursors at low concentrations ensured that most of the CdS grew heterogeneously onto existing CdSe nuclei instead of undergoing homogeneous nucleation.1 we control the addition rate about 40μ L/min and received the good results.

Fig. 1 shows the absorption spectra of CdSe NCs (a) and CdSe/CdS core/shell NCs with the following shell thickness: (b) 0.65 monolayers (c) 1.3 monolayers (d) 2.6 monolayers (e) 5.2 monolayers. All samples show a well-resolved absorption maximum of the first electronic transition indicating a narrow size distribution of the NCs. The absorption maximum for the CdSe/CdS core/shell NCs shift slightly to longer wavelengths compared to the bare CdSe NCs. This red shift is related to the excitons partial leakage into the CdS matrix. We can observe more obvious regular shift in PL spectra.

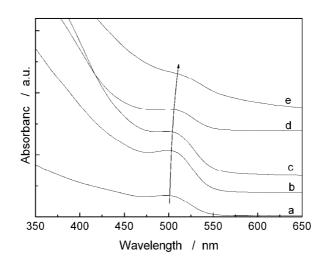


Fig. 1. Absorption spectra of CdSe NCs and CdSe/CdS core/shell NCs

Fig. 2 shows the room temperature PL spectra of these CdSe NCs before (a) and after (b-e) overcoating of CdS at the same condition under the excitation of A Xe lamp. CdS shell thickness is 0.65 monolayers (b), 1.3 monolayers (c), 2.6 monolayers (d) and 5.2 monolayers (e) respectively. The PL intensity is low due to incomplete surface passivation for CdSe NCs. PL intensity increases strongly for CdSe NCs passivated with CdS as compared to CdSe NCs. CdS shell can suppress surface states emission by passivating most of the vacancies and trap sites on the crystals surface, resulting in PL enhancement. The PL peak position of CdSe NCs is 563.8nm. As the CdS shell is over coated, the PL peak position shift to longer wavelengths. The PL integrated intensities of CdSe/CdS core/shell NCs are higher than the CdSe NCs greatly. However, NCs synthesized by the aqueous approach do not possess the narrow size distribution and the degree of crystallinity of the organometallically prepared NCs, where high annealing temperatures are used during the synthesis. The optical properties of CdSe/CdS core/shell NCs with the 2.6 monolayers CdS shell are optimal (maximal PL integral intensity and relative narrow FWHM).

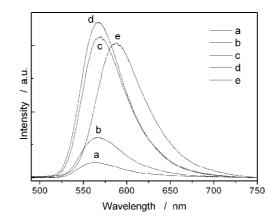


Fig. 2. PL spectra of CdSe NCs and CdSe/CdS core/shell NCs

The photo stabilities of CdSe and CdSe/CdS NCs are compared under 325nm laser irradiation, as shown in Fig. 3. 325nm laser irradiation first leads to a weak improvement of their PL intensity, followed by a gradual quenching of PL intensity in the cases of CdSe/CdS NCs. In the case of CdSe NCs the PL intensity slowly goes down during the whole irradiation. The difference between the behaviors of CdSe and CdSe/CdS NCs originates most probably from their structural difference. It takes 78s that the intensity decrease to the half for bare CdSe NCs, but 442s for CdSe /CdS core/shell NCs. The fluorescence lifetime increases about six times after overcoating, which is significative for the practical application.

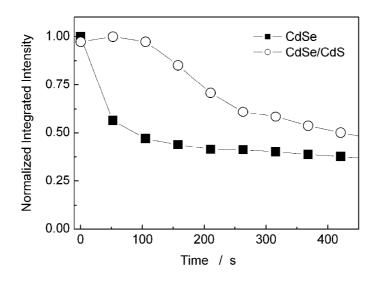


Fig. 3. Temporal evolution of PL integral intensity of CdSe and CdSe /CdS NCs

Conclusions

A simple, green, less cost and very reproducible method is employed for the preparation of CdSe/CdS core/shell NCs in aqueous solution without any poisonous materials. The synthesis condition of the optimal NCs (maximal PL intensity and relative narrow FWHM) has been achieved. The photo stability of CdSe NCs is enhanced greatly after CdS overcoating. The CdSe/CdS NCs will be useful in the practical application for their advantages in synthesis procedure and optical properties.

Acknowledgments

This paper is sponsored by the Foundation of Scientific Innovative Research Team of Education Department of Guizhou Province (201329), the Provincial Experimental Teaching Demonstration

Center of Guizhou Province (201310), Natural Science Foundation of Education Department of Guizhou Province (QJK07092), Postdoctoral Science Foundation of China (2013M541420), Natural Science Foundation of China (21173063) and Heilongjiang University Foundation (201107), Natural Science Foundation of Heilongjiang Province (A201105), Key Laboratory of Functional Inorganic Material Chemistry (Heilongjiang University), Ministry of Education (2013), the 12th Five-Year Plan for the Education Science of Heilongjiang Province (GBD1211048), Higher Education and Teaching Reform Project of Heilongjiang University under Grant (HD-028), the Second "Three Education" Research Project of Heilongjiang University (SK1216) and the Degrees and Graduate Education Reform Project of Heilongjiang University (JGXM_YJS_2012025).

- [1] B.O. Dabboüsi, J. Rodriguez-viejo, F.V. Mikulec. J. Phys. Chem. B, VOL 101(1997), P. 9463
- [2] Z.A. Peng, X. Peng. J. Am. Chem. Soc., VOL 123 (2001), p. 183
- [3] L.M. An, X.T. Han, X.L. Chen. Applied Mechanics and Materials, VOL 268-270 (2013), p. 551
- [4] L. Qu, X. Peng. J. Am. Chem. Soc., VOL 124 (2002), p. 15119
- [5] L.M. An, K.F. Chao, Q.H. Zeng, X.T. Han, Z. Yuan, F. Xie, X. Fu, W.Y. An. J. Nanosci. Nanotech., VOL 13 (2013), p. 1368
- [6] J. Yi, X.T. Han, X.L. Chen, C.X. Liu, W.Y. An, X. Dong, M.L. Liu, L.M. An, Y.M. Luo. Thin Solid Films, VOL 521 (2012), p. 112
- [7] L.M. An, Y.Q. Yang, W.H. Su, J. Yi, C.X. Liu, K.F. Chao, Q.H. Zeng. J. Nanosci. Nanotech., VOL 128 (2010), p. 2099

Advantages and Challenges Analyzed Utilizing MMA as the Printable Material to Fabricate Optical Waveguides

Li Haibao^{1, a}, Liu Hui^{1, b} Zhao Enming^{2, c}

¹College of Science, Heilongjiang University of Science and Technology, Harbin China

² Photonics Research Center, College of Science, Harbin Engineering University

^alihaibao1978@126.com, ^blhui0521@eyou.com, ^czhaoenming@hrben.edu.cn

Keywords: 3D printing, MMA, PMMA, optical waveguide

Abstract. Aimed at the professional and printable materials, the researchers involved in higher payments, a new design scheme of utilizing MMA for 3D printing has been put forward based on its proper characters. The ideas and experiment frameworks are demonstrated, as well as the challenges are discussed.

Introduction

Polymer photonics is an important branch in modern integrated optics, and provides a good platform for integrating. [1] Some polymeric materials, such as SU-8 photoresist, NOA 65, Master Bond UV15LV, etc..., which bears excellent optical properties, are widely used in the field of integrated optics. The common feature of these materials is expensive, and not easy to obtain it.

PMMA (polymethyl methacrylate), is one of the important materials for integrated optics. But in the last decades, it could be used as a kind of auxiliary materials usually. It would be founded in some optical components as the substrate material. The prominent feature of PMMA is very cheap, and easy to obtain it. It can be found in many chemical laboratories, and even in the general market.

3D printing technology is one of rapid prototyping techniques, nowadays, which are broadly used in product development process. They allow for fast and low-cost manufacturing a small series of components directly from the component geometry parameterization stored in a 3-dimensional CAD model. [2]Now, there are many scholars use 3D printing technology to fabricate optical waveguide devices. But the progress has been slowing and challenging. Two reasons to lead to such a situation, one is the minimum size of the printer can print, the other is the proper materials.

In this paper, the authors attempt to obtain a new method by using PMMA instead of expensive photoresist materials. The ideas and experiment frameworks have been put forward based on the proper characters of PMMA.

Background and Analysis

What is the Printed Optical Waveguides Technology?

As its name implies, the optical waveguides is made by printing. There are often four basic forms in the field of 3D printing in general. They are SLS(selective laser sintering), SLA(stereo lithography), FDM(fused deposition Modeling), and LOM(laminated object manufacturing). According to the property of each form and the technological requirements of optical waveguides, we choose SLA as the basic form to fabricate optical waveguides.

Comparison to the traditional forms, to fabricate optical waveguides by ink-jet printing in SLA, would bring many benefits. Now we demonstrate it based on one of the traditional fabrication form named photolithography. Fig.1 shows that the Sketch map for the manufacturing process of the optical waveguides by photolithography, and Fig.2 shows the process by inkjet printing.

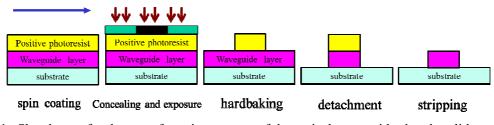


Fig.1. Sketch map for the manufacturing process of the optical waveguides by photolithography

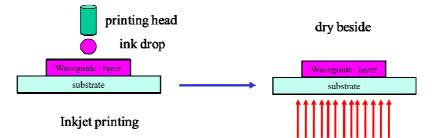


Fig.2. Sketch map for the manufacturing process of the optical waveguides by inkjet printing

We would found some advantages in the manufacturing process:

- Waveguides can be manufacture on a large scale.
- Much material is saved
- The costs is lower
- Control the material components flexibly
- Simplify the process

Utilizing MMA as 3D Printed Optical Waveguide Materials

The inkjet printing is a basic form of 3D printing technologies. Because the proper ink is one of the key issues, many researchers are trying to find the proper materials, which can be used as the ink. If the ink can be used to fabricate optical waveguide devices by printing, it should be transparent and liquefaction easily, which also bears excellent optical properties. While the PMMA is a solid at room temperature, it cannot be used as the printable materials directly. In this regime, we put forward a new method to obtain the material, which can be realized by another material named MMA (methyl methacrylate). In other words, we use MMA instead of the expensive polymeric materials. Next, we will enumerate the advantages of the scheme.

• MMA is liquid less than 15 degrees Celsius

It is the most important issue that we choose MMA as the printable material. In fact, the physical state of MMA is liquid and colorless at 15° C and 1 atm, which will become it as a natural attribute of printed material. In other words, it is a natural printable ink.

MMA is the direct material of PMMA

If the optical waveguide devices were manufactured by using 3D printing technology, PMMA should be very important component materials. It is because that MMA is the direct material of PMMA. We can obtain it using MMA by bulk polymerization in theory, shown it in Fig.3.

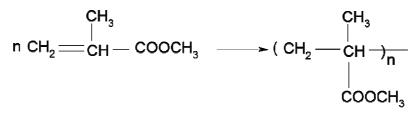


Fig.3. From MMA to PMMA by the way of bulk polymerization

• MMA is one of the cheaper polymeric materials

In comparison, MMA is one of the cheaper polymeric materials. In fact, MMA as an important but ordinary chemical material would be found in general chemical laboratory. Wide applications of this material and supply adequately determine its low price.

Many polymeric materials, SU-8, as an example, if we want to use it as the printable ink, we must obtain it from only one of the production companies.

PMMA bears excellent optical properties

Although it would be founded in some optical components as the substrate material, it is no denying the fact that PMMA bears excellent optical properties. Sometimes, researchers use it as the substrate material; they could focus the differences of refractive index between two sorts of materials.

• Can use the initiator in the polymerization process

There is a variety of polymerization in order to obtain PMMA. Based on two aspects reasons, we should choose the way named bulk polymerization. One is that it can be obtained not through any intermediate in process; the other is to initiate with the heat and radiation issues. Accordingly, we can receive two beneficial effects. One is that the finished product could be done without post processing; the other is that we could control the process by adjusting the initiator.

Thought Experiments and Challenges

Thought Experiments

Based on the five aspects discussed above, we have been putted forward a thought experiment, and the basic ideas and flow chart is demonstrated.

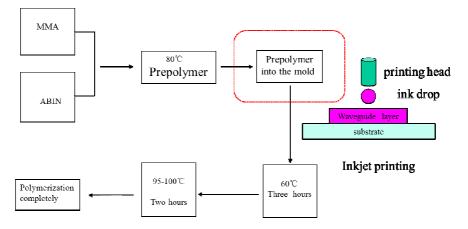


Fig.4. Route map of making PMMA in laboratory

Fig.4 shows us the brief process of manufacturing PMMA in laboratory. We would found the fact that the final product of the process is long, which does not meet the requirements of rapid prototyping technology. While we transform the technical procedure named "Prepolymer into the mold" according to technological requirements of inkjet printing, in theory we can shorten the formation time by adjustment of initiator, or adjustment of the light radiation.

The first step in printing polymer optical waveguides is to choose suitable materials for both the waveguide core and cladding layers. [3] Fig.5 shows us that the inverting ratio appears linearly and quickly in the interval of 80 to 100 minutes. When we choose the proper inkjet device, MMA acting as the ink can be utilized to manufacture the waveguides. In practice, we need to adjust the refractive index usually, which can be done by doping or by the duration and intensity of exposure. At published literatures, researchers had been obtained some optical waveguide devices with simple structure by printing, although the use of ink is not MMA. These devices include microwave lens, laser system, and thermo-optic polymer switches. [4-5]

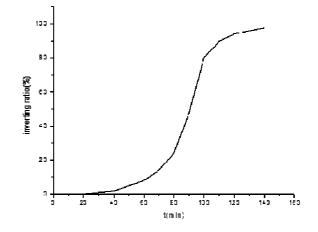


Fig.5.The transformation efficiency of PMMA with time

Challenges

Although the MMA as a printing material is very attractive, it is also faced with many challenges in the real practical process.

• Need further to explore the theory of converting MMA to PMMA

To meet the special needs of 3D printing technology, the theory of converting MMA to PMMA should be special, fast and control whenever and wherever possible. In order to achieve it, we may require a large number of experiments and theoretical analysis.

• Need further to explore and design the proper printing apparatus

The proper printing apparatus would include the high accuracy positioning translation system, high precision printing nozzle, and high precision feedback servo system. Only getting such a machine is in order to achieve micro-nano precision.

• To explore the boundary treatment technology used in conjunction with other materials

The boundary treatment technology is a key problem in field of 3D printing. In modern integrated optics, the whole optical device could involve a variety of materials. If we were going to obtain the aim ,we should research the regime of hierarchical control.

Conclusions

Through the above discussion, we put forward a new plan to utilize MMA as the printable material to fabricate optical waveguides. The basic ideas and the experiment framework have been demonstrated. In the same time, the challenges in the field have been discussed.

Acknowledgment

The authors acknowledge the support from the Education Department of Heilongjiang Province Science and Technology projects (2014): Research on Production of PMMA Planar Optical Waveguides Based on 3D Printing.

- [1] Dj.M. Maric, P.F. Meier and S.K. Estreicher: Mater. Sci. Forum Vol. 83-87 (1992), p. 119 Lin X, Ling T, Subbaraman H, et al. Optics express, 2013, 21(2): 2110-2117.
- [2] Leukers B, Gülkan H, Irsen S H, et al. Journal of Materials Science: Materials in Medicine, 2005, 16(12): 1121-1124.
- [3] Vacirca N.A, Kurzweg T.P. Inkjet printing techniques for the fabrication of polymer optical waveguides[C]//Proceedings of SPIE. 2010, 7591: 75910A.
- [4] Tien C.H, Hung C.H, Yu T.H. Journal of display technology, 2009, 5(5): 147-151.
- [5] Lin X, Ling T, Subbaraman H, et al. Optics express, 2013, 21(2): 2110-2117.

Electrical Conductivity and Breakdown Characteristics of SiC/LSR Nanocomposites at Different Temperatures

Nanqiang Shang^a, Qingguo Chen^b, Yanjun Qin^c, Minghe Chi^d and Xinlao Wei^e

Key Laboratory of Engineering Dielectrics and Its Application, MOE, Harbin University of Science and Technology, Harbin, China

^a18946057270@163.com,^bqgchen@263.net, ^cq1935657665@sina.com,

^dchiminghe1985@163.com, ^eweixinlao@hrbust.edu.cn

Keywords: SiC/LSR nanocpmposites, conductivity, electrical filed distribution, breakdown strength, temperature gradient

Abstract: In high voltage direct current (HVDC) cable accessories, there is a large difference of conductivity between crosses linked polyethylene (XLPE) and liquid silicone rubber (LSR), especially considering the presence of temperature gradient and the changing of operating temperature. In this paper, nano silicon carbide (SiC) was adopted to prepare five kinds of nanocomposites with filler fractions of 1%, 2%, 3%, 4% and 5%, respectively. The conductivity and DC breakdown strength of SiC/LSR nanocomposites were measured under different temperatures. The results show that the nano SiC doping does not has the great influence on LSR DC breakdown strength, and the nano SiC doping can improve the conductivity of LSR effectively, which can realize the conductivity matching between the LSR and XLPE to homogenize the electric field distribution in cable accessory.

Introduction

High voltage direct current transmission have been applied widely in recent years on large capacity transmission over long distance, asynchronous networking, and submarine cable transmission with many advantages, such as rapid flexible power regulation, without increase of the system short circuit capacity, improving the system transient stability, low loss, and less land occupation, etc [1].

As the indispensable equipment in high voltage direct current transmission system, HVDC cable was subjected not only the rated DC voltage, but also the polarity reversal voltage, operating impulse voltage and lighting impulse voltage in service [2]. The accessory is the key and weakest part in HVDC cable for its complex compound materials and insulation structure [3,4].

The distribution of electric field in cable accessory mainly depends on the conductivity of insulation materials under DC voltage. Because there exits the large difference of conductivity between XLPE and LSR, and also the temperature gradient during operation [5], which makes it difficult to realize the homogeneous distribution of electric field. In addition, the space charge can be accumulated in interface between XLPE and LSR [6], which will also seriously distort the electric field distribution in cable accessory, especially under the polarity reversal voltage.

To solve the above problems, LSR nanocomposites were prepared by doping different concentrations of nano SiC to realize the conductivity matching between XLPE insulation and LSR insulation under different temperature gradients.

Sample Preparation and Testing

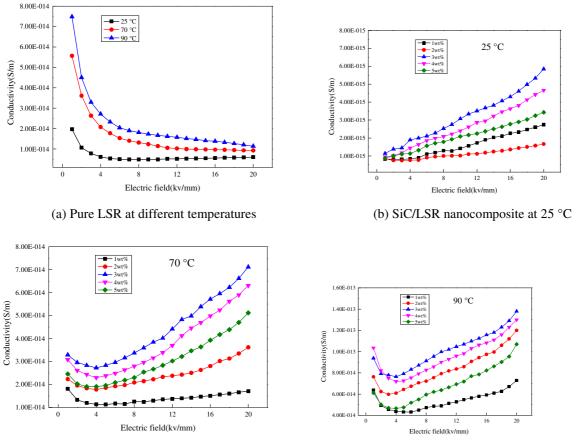
The type of LSR is POWERSIL®737 manufactured by Germany Wacker Chemical Co. LTD. For specimen preparation, a multifunctional mixing disperser was used to compound the LSR, which guarantees a uniform distribution of the filler within LSR, and the materials were vacuumed continuously. After above procedures, the samples were pressed under a plate vulcanizer at 120 °C for 10 minutes, and vulcanized at 200 °C for 4 h. Then, the samples were put in a vacuum oven at

815

25 °C for 24 h to eliminate the effect of moisture. The dimension of samples was controlled to 0.5 mm in thickness and 50 mm in radius with the LSR concentrations of 1%, 2%, 3%, 4% and 5%, respectively. The conductivity characteristics of pure LSR and SiC/LSR nanocomposites were measured under different temperatures with three-electrode system, and the DC breakdown strength of pure LSR and SiC/LSR nanocomposites were measured with two-electrode system.

Results and Discussion

Conductivity Characteristics. The conductivity of pure LSR and SiC/LSR nanocomposites under different temperatures are shown in Fig. 1.



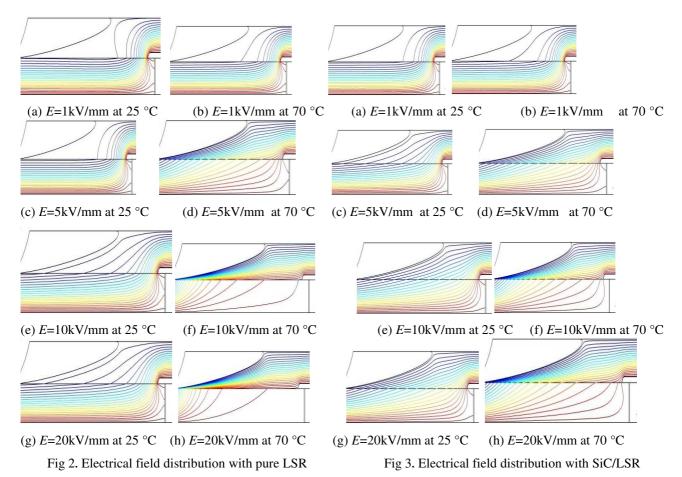
(c) SiC/LSR nanocomposite at 70 $^{\circ}$ C

(d) SiC/LSR nanocomposite at 90 °C

Fig 1. Conductivity of pure LSR and SiC/LSR nanocomposites under different temperatures

As shown in Fig. 1(a), the conductivity of pure LSR was rapidly declined at low electric field range, then the trend of decline becomes slowly at high electric field range. With temperature increasing, the conductivity of pure LSR increases. By comparison of Fig. 1(b), (c) and (d), it can be seen that the conductivity of SiC/LSR nanocomposites show similar rising tendency at different temperature with electric field increasing. At the same electric field, the conductivity of SiC/LSR nanocomposites increase with temperature increasing. Moreover, the conductivity of SiC/LSR nanocomposites is higher than that of pure LSR at the same temperature and electric field, and SiC/LSR nanocomposites with the 3wt% concentration is the highest among five concentrations in all temperature range.

Electric field homogenization. To testify the action of SiC/LSR nanocomposites on electric field homogenization for cable accessory, the electric field distribution was simulated with Comsol-Multiphysics, and the electrical field distributions in cable accessory with pure LSR or SiC/LSR nanocomposites insulation at temperature 25 °C and 70 °C are shown in Fig. 2. and Fig. 3.



From the above simulated results, it can be seen that the electrical field distribution in cable accessory with pure LSR is non-uniform, and the electrical field distribution mainly concentrates on the end of high voltage shielding layer at room temperature and on the root segment of stress cone at high temperature. The electrical field distribution in cable accessory with SiC/LSR nanocomposite insulation is more uniform than that with pure LSR insulation at room temperature. Because the SiC/LSR nanocomposites have the higher conductivity and can match the conductivity of XLPE. Comparing with the electrical field distribution at low temperature, the electrical field distribution in cable accessory with SiC/LSR nanocomposite insulation can not be homogenized well at high temperature, which is caused by the lower conductivity changing rate of SiC/LSR than that of XLPE during the temperature rising, but it is better than the electrical field distribution in cable accessory with pure LSR.

Breakdown Characteristics. The breakdown voltage and dielectric strength of pure LSR and SiC/LSR nanocomposites are shown in Table 1.

Components	Thickness [mm]	Breakdown voltage [kV]	Dielectric strength [kV/mm]
LSR	0.5	39.6	79.2
1% SiC/LSR	0.5	35.8	71.6
2% SiC/LSR	0.5	41.2	82.4
3% SiC/LSR	0.5	40.5	81.0
4% SiC/LSR	0.5	36.9	73.8
5% SiC/LSR	0.5	36.2	72.4

Table 1. Breakdown results of pure LSR and SiC/LSR

It can be seen that the nano SiC doping does not has the great influence on LSR breakdown strength, and breakdown strength increases firstly with the nano doping ratio, after reaching the peak value 82.4 kV/mm at 2%, then it decreases with the doping ratio increasing.

Conclusions

According to the experimental results and analysis, some conclusions can be summarized as follows:

(a) The nano SiC doping can improve the conductivity of LSR effectively, which can realize the conductivity matching between the LSR and XLPE to homogenize the electric field distribution in cable accessory.

(b) The nano SiC doping does not has the great influence on LSR DC breakdown strength, and breakdown strength increases firstly, after reaching the peak value at 2%, then it decreases with the doping ratio increasing.

Acknowledgements

The project was supported by the Research Found for the Doctoral Program of Higher Education (No. 20132303110006) and Natural Science Foundation of Heilongjiang Province (No.ZD201310).

- T. Shao, G. S. Sun, P. Yan, et al., "An Experimental Investigation of Repetitive Nanosecondpulse Breakdown in Air", J. Phys. D, Appl. Phys., Vol. 39, No. 10, pp. 2192-2197, 2006.
- [2] S. Ansorge, F. Schmuck, S.Aitken, and K. O. Papailiou, "Improved performance of silicone rubbers for the use in composite insulators", CIGRE Paper D1-105, 2010.
- [3] L. Meyer, S. Jayaram, and E. A. Cherney, "Thermal conductivity of filled silicone rubber and its relationship to erosion resistance in the inclined plane test", IEEE Trans. Dielectric. Electr. Insul., Vol. 11, pp. 620-630, 2004.
- [4] Samuel Ansorge, Frank Schmuck, and Konstantin O. Papailiou, "Improved Silicone Rubbers for the Use as Housing Material in Composite Insulators", IEEE Trans. Dielectr. Electr. Insul., Vol. 19, pp. 209-217, 2012.
- [5] Xinling Geng, "Development of Conductive Silicone Rubber filled with Silver-Plated Nickel Particles", China Rubber Industry, Vol. 53, No. 7, pp.417-419, 2006.
- [6] Z. Li, K. Okamoto, Y. Ohki, and T. Tanaka, "Effects of nano-filler addition on partial discharge resistance and dielectric breakdown strength of micro-al2o3/epoxy composite", IEEE Trans. Dielectric. Electr. Insul., Vol. 17, pp. 653-661, 2010.

Pre-mixed Abrasive Water Jet Cutting in the Marble

Jisheng Xia^{1, a}, Qingzhu Jia^{2,b} and Zhenzhen Sun^{3,c} ¹Yancheng Institute Of Technology Yancheng,China ^{2.3}School of Mechanical Engineering Anhui University of Science and Technology Huainan, China ^a1282907721@qq.com, ^b806271973@qq.com, ^c1040217640@qq.com

Keywords: Pre-mixed abrasive water jet, marble, cutting.

Abstract. High-pressure abrasive water jet cutting is a cold and non-traditional method, with many advantage which the traditional processing do not have. The traditional method of cutting marble have rough sections, poor dimensional accuracy, large seam, high tool cost and the processing efficiency is low. Can be considered high-pressure abrasive water jet cutting to improve its traditional cutting defects. This article explores the use of the pre-mixed abrasive water jet cutting in the marble, and its comparison with traditional methods, highlighting the advantages which the pre-mixed abrasive water jet cutting in the marble.

Introduction

High-pressure abrasive water jet technology is a cold and non-traditional methods that can be applied to cutting, cleaning, rust, detergents and so on. High-pressure abrasive water jet cutting does not cause the material deteriorated and its kerf is narrow, cutting surface is smooth and it is no dust, no pollution ,so it is applied to all kinds of metal material and non-metallic materials processing. This paper analyzes the use of pre-mixed abrasive water jet cutting process on the marble and its features.

The Traditional Method of Cutting Marble

Marble has beautiful color ,pattern, high compressive strength and good physical and chemical properties. The resources are widely distributed, which is easy to process. With economic development, applications range of marble is expanding, the amount is increasing, and the marble plays an important role in people's lives. Traditional marble cutting process is as follows: First, use a large see-saw cut the blocks, to adjust the see-saw blade between the demand and the size of the stone. The general thickness of the cut is 2cm, 1.5cm or 1.8cm; polish the large see-saw cut plate and then cut with a variety of cutting machines according to the sizes. There are many cutting machines, often there are small simple sets (small cutting machine), mainly used for cutting the small plate or sheet that below 60cm * 60cm; infrared bridge cutting machine: You can cut a variety of sheet metal; infrared in the cutting machine: for cutting thick shaped plate. Marble cutting saw cutting is shown in Fig.1.

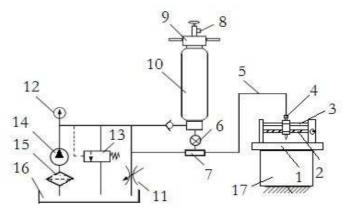


Fig 1 Marble cutting saw cutting

Pre-mixed Abrasive Water Jet Cutting in Marble

High pressure water jet cutting is the carrier carrying energy, a kind of method by water jet technology with high-speed cutting for all kinds of materials. Firstly the water pressure boosts to 300 to 1000Mpa through booster device (kinetic energy is changed into pressure energy). Then make high-pressure water erupt at $2 \sim 3$ times speed of sound through the nozzle that diameter is $0.1 \sim 0.6$ mm (Stress energy is changed into kinetic energy). When water jets impact the material being cut, if the pressure is more than the destruction strength of the material, the material is cut. Generally cutting can be divided into the pure water jet cutting taking water as energy carrier and abrasive water jet cutting taking abrasive mixture as the carrier. Because of joining the abrasive, cutting efficacy of the latter significant increases. At the same cutting speed, its pressure value can be greatly reduced, meanwhile cutting range is also widened[1].

Pre-mixed abrasive water jet has greatly improved the hybrid mechanism between the abrasive particles and water medium. In the same cutting conditions, the pressure of pre-mixed type is greatly reduced, which makes equipment power decreases, the bulk and weight of the equipment are reduced significantly and the recoil of the cutting head is also reduced. Meanwhile, pre-mixed abrasive jet also has the advantages, for example, recyclable abrasive, the lower cutting energy consumption and so on. The reliability and safety of the equipment are also improved and the service life of equipment are also further extended [2]. Water jet cutting device is shown in Fig.2[3].



1. cutting table 2. screw 3. rod guide 4. nozzle 5. pressure hose 6. abrasive cut-off valve 7. mixing chamber 8. relief valve 9. Capping 10. abrasive tank 11. relief valve 12. pressure gauge 13. valve 14. piston 15. filter 16. tank 17. cutting tank

Fig 2 The working principle of water jet cutting device

Cutting system has four parts. (1) Piston pump station Provide the pressure for The whole system. pump station is composed of tanks, related pump valve and inline horizontal three piston pump. The rated pressure of the piston pump is 40Mpa and the rated flow is 12L/min. (2) Portable abrasive happen device Use for mixing abrasive and garnet is as abrasive. Abrasive cans working pressure is less than 40Mpa and volume can be determined according to user's requirements. The bottom of the abrasive cans can be controlled abrasive circulation by abrasive globe valves. (3)Cutting nozzles Adopt prefab nozzle. Nozzle diameter is replaceable and the cutting high-pressure hose uses 0.8 mm nozzle in this experiment. (4)Cutting workbench it is mainly composed of two groups of bevel gears, wire rod, light pestle guide, cutting cistern[4].

The block of marble-like is shown in Fig.3.As shown, use pre-mixed abrasive water jet to cut specimens, use CNC2000 to program, the programing is as follows (relative coordinate programming).

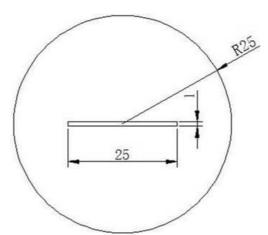


Fig 3 The block of marble-like

N0001 M07 G04 t18000 G01 x12 y0 f80 G01 x-12 y0 G00 x12 y0 G04 t10000 M08 G00 x0 y26 M07 G04 t18000 G02 x0 y0 i0 j-26 f40 G04 t80000 M08

First,input No. N0001 processing program to CNC device to trial operation, then install the plates on the machine tool and to the tool. When all is ready, open high-pressure pump to boost water, then click on the program run button of the control interface to start processing, at the same time open the valve so that water and abrasive sand after mixing through the injection nozzle to cut on the plate. After the first process close the sand value to prevent the grain of sand left in the nozzle to cause nozzle clogging, and then close the high pressure pump.

Comparison of Traditional Cutting Methods and Pre-mixedAbrasive Water Jet Cutting

Through the above comparison can be seen, because the marble is a brittle material, and the organization of coarse marble, large, hard phase and the weak interface are mixed into the matrix, the traditional processing methods for the processing is difficult to get satisfactory results [5]. The pre-mixed abrasive water jet technology with its unique processing methods, is adapted to the materials processing which have complex structure, and thus it has unique advantages in the stone processing. The pre-mixed abrasive waterjet machining technology has gradually changed the disadvatages that mosaics sections rough, size accuracy low, seam large, processing efficiency low in decorative stone processing. The equipment with this technology than traditional processing equipment that now using is low cost ,low processing cost, low power consumption and wide application and the wear materials and water are recyclable [6].

Conclusion

(1) Cutting stone with the pre-mixed abrasive water, the cutting quality is better and the size accuracy is higher compared to other processing technology.

(2) Since the pre-mixed abrasive water jet is cold technology, it does not affect the physical and chemical properties of the stone.

(3) Pre-mixed abrasive water jet cutting tool is simple and cost is low.

(4) Pre-mixed abrasive water jet technology has little environmental pollution and no dust pollution, low noise.

(5) Pre-mixed abrasive water jet has high efficiency.

In conclusion, In view of its advantages in marble cutting, it will be a promising new technology in the development of China's stone industry.

- [1] Liu Liping. high-pressure water jet cutting technology and application. Agricultural Machinery. September 2000 Vol 31, No. 5(In Chinese).
- [2] Zhang Dong-speed and so on. Test premixed abrasive water jet cutting device. Jiangsu Coal, 1999 2(In Chinese).
- [3] YE Ben, Zhang Dong-speed and so on. Portable abrasive water jet cutting device design and application. Coal Mine Machinery, November 2009(In Chinese).
- [4] Zhang Dong-speed, Dong Zuwei and so on. premixed abrasive water jet cutting in the mining of high-pressure hose. 02 years of mining machinery .2011(In Chinese).
- [5] Chen Guangming. CNC high pressure water jet cutting technique and its application. machine tools and hydraulic .2007 August 35, 8(In Chinese).
- [6] Kotwica.Influence of high-pressure water jet assistance upon the wear, load and dustiness of the tangential pick in the process of hard rock cutting. Journal of Mines, Metals and Fuels, v 51, n 7-8, p 225-228, 2003.

MgAI/PbPc/Cu Organic Thin-film Diode Preparation and Gas-sensing Characteristics Analysis

Jiabin Chen^a, Ping Yu, Yue Zhang, Yue Shan, Dongxing Wang

(Department of Electronic Science and Technology, College of Applied Science, Key Laboratory of Engineering Dielectrics and Its Application, Ministry of Education Harbin University of Science and Technology, Heilongjiang Harbin 150080, China)

^ajiabinchen1224@163.com

Keywords: lead phthalocyanine; thin-film diode; gas-sensing characteristics; NO2

Abstract. Thin-film diode structure is MgAl/PbPc/Cu if lead phthalocyanine is taken as organic semiconductor gas-sensing material with methods such as vacuum thermal evaporation or magnetron sputtering. Use Keithley 4200 semiconductor instrument and Gas-sensing measurement system to analyze gas-sensing characteristic of Schottky diode device, the sensitive degree of NO₂ with different density can be compared through theoretical analysis of measured current and voltage data. The measurement result shows: when the device is placed in 10ppm NO₂ environment, after 74 minutes, forward current is decreased by 65 times, the corresponding MgAl/PbPc Schottky barrier height rises about 20meV. Reversed current of the device is 4 times larger because the increase of minority carrier electron number in PbPc thin-film is being absorbed by NO₂.

Introduction

The first organic thin-film field effect transistor was born in 1986 [1], the core material of it is polythiophene, the research of this type of transistor keeps developing after that, it draws a lot of attention in applications such as drive display of liquid crystal display and oganic light emitting diodes [2], organic thin-film transistor with organic semiconductor material as active layer has shown good perform [3,4]. Gas sensor with organic semiconductor material also attracts more and more attentions, it has an important position in detection of toxic and harmful gas [5].

Phthalocyanines is a kind of organic small molecular materials commonly used in OTFT active layer, it has become the main material in molecular semiconductor research [6]. Phthalocyanine complexes have the characteristics of big ring conjugate structure [7]. It has high sensitivity and high selectivity to a specific kind of gas at room temperature and it's easy to be modified at the same time making it a kind of organic gas-sensing material with broad application prospect and also a kind of organic gas-sensing material with a lot of practical value which has been studied a lot and developed rapidly.

Device Structure and Fabrication

The thin-film diode in this article is consisted of MgAl/PbPc/Cu, the structure is shown in figure 1. Cu is anode, MgAl is cathode, MgAl/PbPc forms a Schottky contact, Cu/PbPc forms an ohm contact.

Using OLED multiple coating system to make vertical structure MgAl/PbPc/Cu organic thin-film diode, Cu and MgAl using magnetron sputtering deposition, sputtering time is about 20 seconds. PbPc is got by vacuum distillation method coating, time is about 50 minutes. Vacuum degree is about 6.0×10^{-4} Pa when preparing, evaporating temperature of PbPc is 330°C, and glass substrate temperature is room temperature. PbPc thin-film thickness is 50nm, evaporation rate is 0.02nm/s, and the effective area of sample is 0.06cm², respectively.

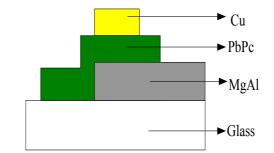


Fig. 1 Structure of MgAl/PbPc/Cu organic thin-film diode

Results and Discussion

Forward current-voltage characteristic curve of the device in air environment and 10ppm NO_2 environment is shown in figure 2, voltage range from 0V to 3V, step length is 0.2V, each step delay is 10s, from figure 2 we can see that forward I-V characteristic curve of thin-film diode has an obvious downward trend. Reversed current-voltage characteristic curve measured is shown in figure 3, voltage range from -3V to 0V, step is 0.2V, each step delay is 10s, we can see from figure 3 that reversed I-V characteristic curve has a trend to rise.

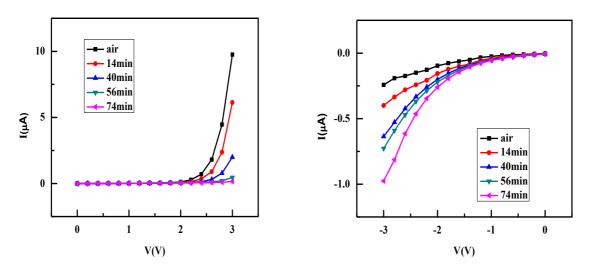


Fig. 2 Forward I-V characteristics curve when device is put in 10ppm NO₂ for 0min—74min

Fig. 3 Reversed I-V characteristics curve when device is put in 10ppm NO₂ for 0min—74min

Put the device in air environment, when forward voltage is V=3V, current value I=9.75 μ A; when the device is put in NO₂ environment for 74 minutes, when voltage is 3V, current value I=0.15 μ A, current is decreased by 65 times. For the reverse characteristics of the device, when voltage is V=-3V, current value is I=-0.24 μ A in air atmosphere; while current value is I=-0.97 μ A in NO₂ atmosphere, reversed current is increased by 4 times.

Forward Gas-sensing Characteristics of PbPc Thin-film Diode. Gas absorbed by PbPc can be divided into oxidizing gases (like O_2 or Cl_2) and reducing gases (like NH_3 or CO) when considered in chemistry theoretical knowledge of oxidation reduction view, oxidizing gases is called electron acceptor, reducing gases is electron donor.

Equation (1), (2), (3) describe the phthalocyanine lead thin-film electron producing process when absorbing reducing gas, G_{as} represents reducing gas molecule, ΔE_1 and ΔE_2 respectively represents charge transfer energy and electron delocalization energy, e represents electron produced by electron separation.

$$G_{as} + PbPc \xleftarrow{\text{physical absorption}} (G_{as} \bullet PbPc). \tag{1}$$

$$(G_{as} \bullet PbPc) \xrightarrow{\text{charge separation}} G_{as}^{+} + PbPc^{-}.$$
(2)

$$G_{as}^{+} + PbPc^{-} \xleftarrow{\text{el ect r on separat i on}}{4E_2} G_{as}^{+} + PbPc + e.$$
(3)

Therefore, it can explain the reason why MgAl/PbPc/Cu Schottky diode I-V characteristic curve forward current is decreasing in the picture, NO₂ act as reducing gas here, giving out electrons when reacts with PbPc thin-film, making majority carrier hole in PbPc thin-film smaller, as a result, forward current has an obvious descend.

Using energy change to analyze the diminish of forward current, using thermionic emission theory to analyze current transport mechanism of PbPc/MgA1 Schottky barrier. In thermionic emission theory, when the external voltage is positive, qV>>nKT, current and voltage have the following relations:

$$I = I_0 \exp(\frac{qV}{nKT})$$
(4)

$$I_0 = SA^*T^2 \exp(\frac{-q\phi_b}{KT}).$$
(5)

 I_0 is reverse saturation current, S is Active area, n is ideality factor, A* is effective Richardson constant, ϕ_b is barrier height of PbPc/MgAl.

Take natural logarithms to the equation (4), then:

$$\ln I = \ln I_0 + \frac{q}{nKT} V.$$
(6)

Figure 4 shows the Ln(I)-V relationship and linear fitting curve characteristics of the device which is placed in air environment, it's most appropriate to select external voltage that is less than the built-in electric field part of fitting. Through linear fitting, $lnI_0=-20.67$, q/nKT=2.68, in air: $I_{0air}=3.56\times10^{-9}A$, $n_{air}=14.34$.

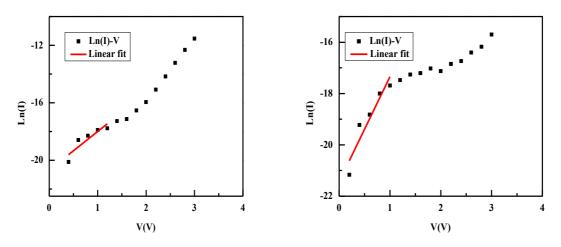


Fig. 4 Ln(I)-V characteristic relationship and linear fitting curve of the device in air environment

Fig. 5 Ln(I)-V characteristic relationship and linear fitting curve of the device in NO₂ environment

As shown in figure 5, Ln(I)-V characteristic relationship and linear fitting curve of the device in NO₂ atmosphere for 74 minutes, through linear fitting $lnI_0=-21.4$, q/nKT = 4.09. In NO₂: $I_{0NO_2}=4.68\times10^{-10}$ A, $n_{NO_2}=9.40$.

In the equation (5), $A^*=28A/(K^{2*}cm^2)$, KT=0.026eV, $S=6mm^2$, respectively. Bring the value of I_{0air} and I_{0NO2} into equation (5), then, $\varphi_{bair}=0.84eV$, $\varphi_{bNO2}=0.86eV$, Schottky barrier height rises about 20meV, device forward current decrease because of the rise of barrier height .The corresponding energy band changes are shown in figure 6.

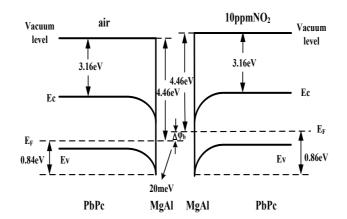


Fig. 6 Schottky barrier energy band diagram of PbPc/MgAl in air and 10ppm NO₂

Reversed Gas-sensing Characteristics of PbPc Thin-film Diode. For MgAl/PbPc/Cu Schottky diode, reverse saturation current density formula is shown as (7)

$$J_0 \equiv q \left[\frac{D_P}{L_P} p_{n0} + \frac{D_n}{L_n} n_{p0} \right].$$
⁽⁷⁾

When external voltage is reversed and |V| >> kT/q, diffusion current density $J_d=-J_0$, it has nothing to do with numerical size of reverse voltage.

For MgAl/PbPc Schottky barrier, reverse current is mainly decided by minority carrier in P area, when put in NO₂ atmosphere, number of minority carrier electron np_0 in PbPc thin-film increase, from equation (7), the increase of np_0 lead to the slight increase of J_0 , the increase of J_d makes the reverse current increase.

Conclusion

This article measurement and analyze prepared MgAl/PbPc/Cu device through Keithley 4200 semiconductor measurement analyzer and homemade gas-sensing measurement system. Experimental results show that the longer the device is put in NO₂, the more decline of forward I-V curve compared with I-V characteristic curve in air condition, the forward current is decreased by 65 times, corresponding MgAl/PbPc barrier height is 20meV higher. Reverse I-V curve has a trend to rise, the increase of minority carrier electron number in PbPc thin-film absorbed by NO₂ lead to the decrease of device reverse current by 4 times. Indicating that MgAl/PbPc/Cu Schottky diode output current has lot sensitivity to NO₂.

- [1] Seungjun Chung, Seul Ong Kim,: Electron Device letters. Vol. 32(2011), p. 1134
- [2] Zhang Wenfeng, Jie Jiansheng,: Applied Physics Letters, Vol. 92(2008), p. 153312
- [3] Kang H. S., Lee J. W., Kim M. K., Joo J.: Journal of Applied Physics, Vol. 100(2006), p. 064508
- [4] Klauk H., Gundlach D. J., Nichols J. A., Jackson T.N.: Transactions on Electron Devices, Vol. 46(1999), p. 1258
- [5] Seyama N., Sugimoto, Iwao, Miyagi T.: Sensors Journal, Vol. 2(2002), p. 422
- [6] Yu Chiang Chao, Hsin Fei Meng: space charge limited transistor, Vol. 88(2006), P. 223
- [7] Meixuer H., Lampe U.: Metal Oxide Sensors, Vol. 33(2006), p. 198

The Fabrication and Characteristics of CuPc thin film phototransistor

Yongshuang Zhang^a, Min Zhu, Dongxing Wang, Zeying Wang, Yueyue Wang, Jinghua Yin

Department of Electronic Science and Technology, School of Applied Science, Key Laboratory of Engineering Dielectrics and Its Application, Ministry of Education Harbin University of Science and Technology, Heilongjiang Harbin 150080, China

^a1181713983@qq.com

Key-words: CuPc; vertical structure; I-V characteristics; light amplification factor

Abstract. Organic transistors consist of a vertical type are promising due to their shorter channel length. We have fabricated a vertical structure thin film phototransistor: ITO/CuPc/Al/CuPc/Cu. Detected this device and then the results show that the I-V properties of the transistors exhibit unsaturated characteristics and photosensitive characteristics. When $V_{ec}=3V$, amplification factor of the device without light is 16.5 and the 625nm light amplification factor is 266.2.

Introduction

Since the 1980s, organic semiconductors device has arrested people's attention. Recently, in interest in organic thin film transistors has grown because they have potential applications to large-area devices that have low cost, light weight and flexible [1]. But organic thin film transistors in terms of performance, the service life and the production process still needs further optimization and improvement [2]. Organic materials offer a variety of advantages with respect to processing compared to conventional inorganic semiconductors [3, 4].

We have fabricated a thin film phototransistor with five layer vertical structure of indium tin oxide(ITO)/ copper phthalocyanine (CuPc)/Al/CuPc/Cu. The organic semiconductor material CuPc is a small-molecule photosensitive material which has characteristics of chemical stability, low price and easy synthesis [5, 6]. Organic transistors consist of a vertical type are promising due to their shorter channel length [7].

Device Fabrication

The vertical structure CuPc thin film phototransistor: ITO/CuPc/Al/CuPc/Cu, we fabricated on the glass substrate. To define the collector electrode, ITO was deposited by radio-frequency magnetron sputtering. The 110nm thick CuPc was deposited onto the patterned collector by vacuum evaporation. To define the base electrode, semiconductor thin film Al was deposited by direct-current magnetron sputtering. The second layer CuPc thin film thickness is 130nm and was deposited by vacuum evaporation. Then we deposited Cu as the emitter electrode by direct-current magnetron sputtering. Finally, with the method of pressing Indium, we extract electrode. The coating equipment is the OLED multifunctional coating system. And the current-voltage (I-V) characteristic was measured by using Keithley 4200 semiconductor parameter analyzer at room temperature. Figure 1 illustrates the circuit of CuPc thin film phototransistor.

The traditional structure transistor has limitation of the channel length and low carrier mobility, the device based on the traditional structure has low speed, high working voltage, and small output current and limited application. These problems can be solved by vertical structure [8]. This device uses vertical structure, carrier moving distance is the thickness of thin film which is very thin (about 200nm). The corresponding driving voltage is very low.

In the preparation process, the Al film thickness has a pretty noticeable effect on performance of the device. If the Al film is too thick, double Schottky barrier will prevent the current flowing from the emitter to the collector. If the Al film is too thin, the off state leakage current can be very high. Therefore, the thickness of the Al film should be optimized to a desired thickness. The Al film thickness of the CuPc thin film photoelectric transistor is about 20nm. Figure 2 shows the atomic force microscopy (AFM) images of the Al film.

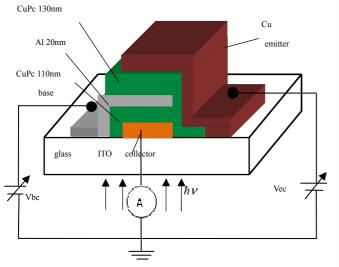


Fig.1 Circuit diagram of CuPc thin film phototransistor

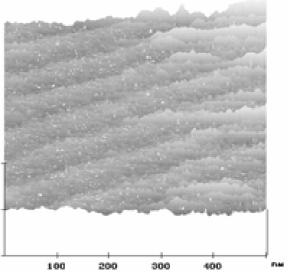


Fig.2 AFM images of the Al film electrode

Device Measurement

To measure the output characteristics of CuPc thin film phototransistor, the device characteristic is tested under 625nm light and darkness. The tested light source is using a xenon lamp, the xenon lamp produces the light whose wavelength is 625nm and intensity is 0.1648mW/cm^2 . Set the collector voltage is 0V, base-collector bias voltage (V_{bc}) is varied from 0V to 1V in 0.25V steps, emitter-collector bias voltage (V_{ec}) is stepped from 0V to 3V. The test results are shown in Figure 3. We can know that the CuPc thin film phototransistor current have unsaturated characteristic. This characteristic can be applied to photosensitive unit of image signal, it can make the image sensor gain a output signal of higher pixel. And working current I_{ec} is reduced with the increase of base voltage. This is because the base voltage controls base depletion layer thickness, the base depletion layer thickness directly controls the holes movement difficulty degree from emitter to collector. When $V_{bc}=0V$ and $V_{ec}=3V$, the relationship between I_{ec} and V_{bc} is shown in figure 4. The curves show that with V_{bc} increasing, I_{ec} gradually decreases and I_{ec} in darkness is much smaller than in 625nm light. This is because light irradiates the ITO film into the CuPc film which makes carrier density in the CuPc films increase, so I_{ec} increases from $0.41\mu\text{A}$ to $1.73\mu\text{A}$.

The CuPc thin film phototransistor current amplification factor is defined as the radio of the currents which were obtained in 625nm light and darkness. The relationship between current amplification factor and base voltage is shown in figure 5. When $V_{ec}=2V$, current amplification factor changes in 2.70–4.27. When $V_{ec}=3V$, current amplification factor changes in 1.91–3.28. The maximum value appears in Vb=0V and the minimum value appears in V_b=1V. Therefore, the bigger V_b is, the smaller current amplification factor; the bigger V_{ec} is, the smaller current amplification factor.

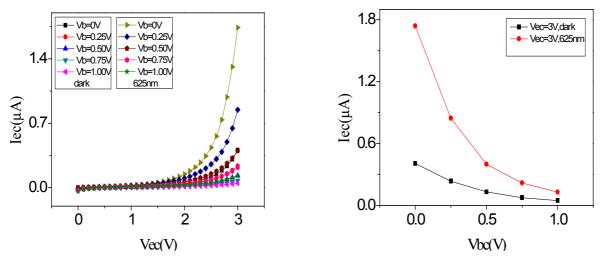
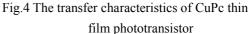


Fig.3 The output characteristics of CuPc thin film phototransistor under 625nm light and darkness



The valence band energy diagram of the device is shown in figure 6. The organic materials CuPc can be regarded as P type organic semiconductor material, its HOMO level is -5.1eV and LUMO level is -3.5eV. During the preparation process of the device, the Al should form good Schottky contact with both sides CuPc and CuPc should form good ohmic contact with Cu and ITO. When the Al film and CuPc film contact, Fermis levels are both in the same horizontal line in thermal equilibrium state, the holes moves from CuPc valence band to Al film. With Al surface accumulating positive charge and depletion layer forming equal negative charge, depletion layer barrier change is similar to unilateral p-n junction. This mechanism complies with tunneling effect rule [9], the holes overcome the double barrier and eventually reach ITO electrode.

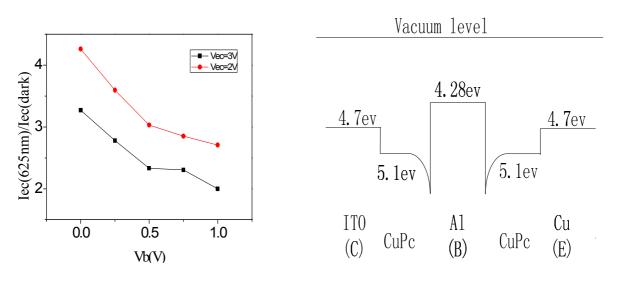


Fig.5 The relationship between current amplification factor and base voltage

Fig.6 The valence band energy diagram of the device

According to the relationship between current conversion and carrier motion, the relationship between I_b and I_{ec} in darkness is such as formula (1):

$$I_{ec} = \beta I_{b}^{\text{dark}}$$
(1)

Where β is the magnification, I_b^{dark} is base current in darkness, I_b^{625nm} is base current in 625nm light. The current in the irradiation of 625nm light relation is such as formula (2):

$$I_{ec} = \beta I_b^{\text{dark}} + I_L (1 + \beta)$$
(2)

When $V_b=0V$ and $V_{ec}=3V$, I_b , I_{ec} , β and I_L values are listed in Table (1). The magnification β can be calculated by the formula (1), then we put it into the formula (2), we can get the light current I_L . $I_L=0.0761\mu$ A and it is 2.56 times bigger than the base current.

$V_b=0V V_{ec}=3V$	I_{ec} (μA)	$I_b(\mu A)$	β	IL
Dark	0.408	0.0247	16.5	
625nm	1.739	0.0297		0.0761

Table (1) $I_b,\,I_{ec},\,\beta$ and I_L values under darkness and 625nm light

The 625nm light amplification factor β_L is defined by the formula (3):

$$\beta_{\rm L} = \frac{I_{ec}^{625\,\rm nm} - I_{ec}^{dark}}{I_{b}^{625\,\rm nm} - I_{b}^{dark}}$$

(3) The irradiated brightness of 625nm light is 1.4145 cd/m², When the 625nm light irradiated the device, light amplification factor β_L =266.2, sensitivity is 27.42A/W.

Conclusions

In a word, we successfully prepared a vertical structure CuPc thin film phototransistor and measure its light-electrical characteristics. The experiment proves unsaturated characteristics of transistor current. So CuPc thin film phototransistor can be used as a light sensor unit. The very short conductive channel structure overcomes the shortcoming of low carrier mobility and high driving voltage. When $V_{ec}=3V$ and the device under 625nm light, current amplification factor changes in 1.91-3.28, optical current $I_L=0.0761\mu A$. The β of the device in darkness is 16.5, the β_L is 266.2. The results indicate that the CuPc thin film photoelectric transistor can effective produce 625nm photosensitive current output and it is worthwhile to pursue further studies.

- [1] Sang Mi Cho, Seung Hoon Han and Jin Jang: Appl. Phys. Lett Vol. 88 (2006), p. 6951
- [2] M. Halik, H. Klauk, U. Zschieschang and C. Dehm: Nature (London) Vol. 431 (2004), p. 963
- [3] Jan Hendrik Schon and Christian Kloc: Appl. Phys. Lett Vol. 78 (2001), p.3538
- [4] C.D. Dimitrakopoulos, A.R. Brown and A. Pomp: Appl. Phys. Lett Vol. 80 (1996), p. 2501
- [5] Z.N. Bao, A.J. Lovinger and A. Dodabalapur: Appl. Phys. Lett Vol. 69 (1996), p. 3066
- [6] B. Bialek, In Gee Kim, Jae I1 Lee: Thin Solid Film Vol. 436 (2003), p. 107
- [7] Naoki Hirashima and Masaaki Iizuka: Applied Surface Science Vol. 244 (2005), p. 603
- [8] Liping Ma and Yang Yang: Appl. Phys. Lett Vol. 22 (2004), p. 5084
- [9] Mitchell A, McCarthy, Bo Liu and Andrew G. Rinzler: Nano Letters Vol. 10 (2010), p. 3467

The dynamic characteristics of AI gate CuPc Thin film transistor

Zeying Wang^a, Dongxing Wang, Yongshuang Zhang, Yueyue Wang,

Jinghua Yin, Hong Zhao

Department of Electronic Science and Technology, College of Applied Science, Key Laboratory of Engineering Dielectrics and Its Application, Ministry of Education Harbin University of Science and Technology, Heilongjiang Harbin 150080, China

^a759115167@qq.com

Keywords: organic material; Al gate electrode; CuPc; thin film transistor; Schottky barrier.

Abstract. We have fabricated Au/CuPc/Al/CuPc/Au organic thin film transistor (OTFTs) using vacuum deposition with CuPc thin films of stable chemical property and semi conductive Al gate thin film electrode. The static and dynamic characteristics were tested at room temperature. The test results show that the switching speed of the OTFT is $t_{on}=2.68ms$, $t_{off}=1.32ms$, amplification bandwidth is 400Hz, and the cutoff frequency $f_c=400Hz$ when inputting 100Hz small square wave signal. Our OTFT has submicron conductive channel, shows operation characteristics of high frequency, high speed and high current density. Good static and dynamic characteristics of OTFT can be obtained by controlling appropriate Al gate film thickness and CuPc film thickness.

Introduction

Organic semiconductor material has many advantages, such as: low cost, good flexibility, simple preparation process, easy fabrication on the substrate, good film and the fabrication of large area devices compared with the inorganic semiconductor material. Electrical properties can be obtained through the appropriate modification of organic molecular structure. Therefore organic semiconductor materials have drawn considerable attention because of their more broad prospects for development in recent years. The current extensive use of organic semiconductor materials are mainly in the following areas: readable and writable CD, organic light-emitting diodes, sensors, organic solar cell [1, 2, 3].

The structure of the device is very important in improving the performance of the device, such as the length of the conductive channel determines the working speed of device [4]. We have reported this OTFT had structure of copper phthalocyanine (CuPc) /Al/ CuPc (CuPc) [5, 6], using semi conductive Al gate electrode which was very thin and active layer used organic semiconductor material CuPc of stable chemical properties [7]. The OTFT is a vertical conductive channel device with the conductive channel of submicron level, has advantages of small conductive channel, fast operation speed, and has excellent high frequency characteristics. Measurement results confirm this device had the same electrical properties with the use of inorganic semiconductor device. In this paper, we studied the working characteristics of thin film transistor, Al gate is evaporated film in this device, whose thickness can be controlled film by adjusting the distance between aluminum evaporator source and the sample and evaporation time.

Experimental

CuPc which is a P type semiconductor material has high chemical stability and heat resistance in the OTFT. In the device structure Au/CuPc/Al/CuPc/Au, Schottky barriers were formed between Al and the two layer CuPc film, which have a decisive impact on electrical properties of OTFT. Good ohmic contact was formed between CuPc and Au film. The fabrication process was as follows: firstly, gold electrode was deposited on the glass substrate. Second, the CuPc thin film was formed. Third, semi conductive Al gate thin film was formed. Fourth, CuPc was deposited by evaporation.

Finally, the gold electrode was prepared. During the fabrication, the temperature of glass substrate was kept at room temperature. CuPc thin films were prepared at 4×10^{-5} torr vacuum environment. The evaporation temperature of CuPc was 400 °C, the evaporation rate was about 0.5 Å /s, the effective area of OTFT device is 0.025 cm^2 . Semiconductor characteristic analyzer (Keithley 4200), current amplifier (Keithley 428), function signal generator (33220A) and digital storage oscilloscope (Tektronix 3021B), were measured static and dynamic characteristics of OTFT. All electrical measurements were carried out at room temperature in the atmosphere. The sample was put in a sealed metal box to prevent the influence of the photoelectric effect which was produced when light irradiated the device. The static and dynamic measurement circuits of CuPc/Al (very thin film) /CuPc OTFT were shown in figure 1.

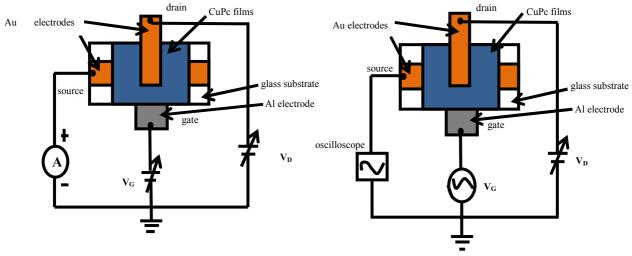


Fig.1. (a) Measuring circuit of static characteristics of the OTFT

Fig.1. (b) Measuring circuit of dynamic characteristics of the OTFT

Results and Discussion

11

In the experiment, organic semiconductor CuPc thin films is amorphous form, there are potential well which had a restrictive effect on the motion of carriers. In the gate region, the Schottky barrier was formed into the depletion layer at the interface of CuPc/Al. The Schottky barrier height was controlled by the gate voltage and the drain voltage. The average thickness of very thin Al films on CuPc film was controlled about 10~20nm. Surface morphology of Al film is observed through AFM, its surface morphology was reticular intermittent. AFM image of Al film gate electrode was shown in figure 2. The static characteristic of the CuPc/Al/CuPc OTFT was shown in figure 3. The drain / source voltage V_{DS} changed in the range of -2V~+2V, and the gate voltage V_G changed from 0V to 0.8 V, the step was 0.2. The drain / source current I_{DS} increased with the drain / source voltage of Schottky barrier height of gate area. In the experiment, saturation current of common MOSFETs was not observed. This was a remarkable characteristic of OTFT which was different from the ordinary MOSFETs. Expression of static characteristic parameter for OTFT:

$$g_m = \frac{dI_{DS}}{dV_G} \Big|_{V_{DS} = Const} \,. \tag{1}$$

$$\mathbf{r}_D = \frac{dV_{DS}}{dI_{DS}} \Big|_{V_G = Const}$$

$$\mu = -\frac{dV_{DS}}{dV_G}|_{I_{DS}=Const} .$$
(3)

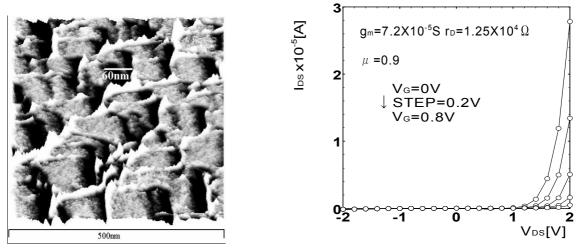


Fig.2. AFM image of Al film gate

Fig.3. Measuring results of static characteristics of the OTFT

According to the measurement results, parameters of OTFT were as follows: transconductance $g_m=7.2x10-5$ S, output resistance $r_D=1.25x10^4\Omega$, amplification factor $\mu=0.9$. The gate voltage is 0V, the drain / source voltage is 2V.

The dynamic characteristics measuring results of the OTFT were shown in figure 4. When the square wave AC signal frequency f of the gate was 100Hz, the signal amplitude was 0.2V, the response of drain / source current I_{DS} was measured. In this case, the V_{DS} remained 2V, applying a square wave AC signal on the gate electrode, the cycle T was 10ms, V_G=0.2V between t=0.25 to t=5.25ms, V_G=0V between the t=5.25 to t=10.25ms. The experimental results had good consistency with the calculated results of the static characteristics. From the dynamic characteristics switch parameters t_{on}=2.68ms, t_{off}=1.32ms could be obtained, indicated that the OTFT had characteristics of high speed. Mobility of CuPc thin film had great effect on switches of transistor.

Figure 5 showed amplitude frequency characteristic of I_{DS} as a function of frequency f of gate voltage V_G . Applying sinusoidal AC signal on the gate electrode, the signal amplitude was 0.2V, when the frequency f changed, relationship of $20log_{10}(I_{DS}/I_{DS0})$ and the f of gate voltage V_G was drawn in the graph, where I_{DS0} is the static source current, I_{DS} was drain / source current along with the change of frequency f of the gate voltage V_G , I_{DS} began to decline from the static I_{DS0} value. When $I_{DS}/I_{DS0}=\sqrt{2}$, f was defined as the cutoff frequency f_C , at this time, the I_S was reduced to -3dB, f_C was 400Hz. This was because the channel length of OTFT was very short, which could improve the working characteristics of transistors, the OTFT could obtain the higher frequency in the lower voltage.

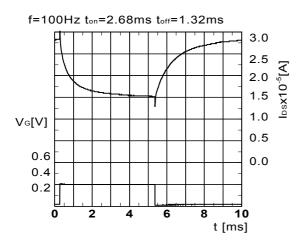


Fig.4. Measuring results of dynamic characteristics of the OTFT

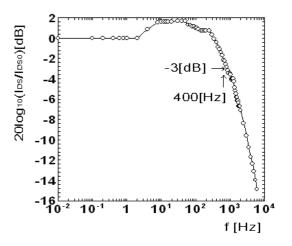


Fig.5. Amplitude frequency characteristic of I_{DS} as a function of frequency f of gate voltage V_G

Conclusion

In this study, the working principle of prepared OTFT was to modulate channel current by gate voltage changing Schottky barrier height. The experimental results showed that static output characteristics of OTFT were unsaturated, amplification bandwidth of dynamic characteristics could reach 400Hz; OTFT has advantages of low driving voltage, strong control capability of gate voltage, big working current density. The length of submicron conductive channel could be obtained by controlling the thickness of the semi conductive Al gate electrode thin film and the thickness of the CuPc film, which could improve the work current and switching speed of OTFT. Prepared OTFT of submicron vertical conductive channel structure is expected to be used in integrated circuit and LCD panel drive unit, IC smart card etc.

References

- [1] Sinha. B: Current Science Vol. 100 (2011), p. 654
- [2] Rand Barry P, Xue Jiangeng, Uchida Soichi, Forrest.S.R: Journal of Applied Physics Vol. 98 (2005), p. 124902
- [3] Marinov. O, Deen. M.J: Journal of Vacuum Science & Technology Vol. 24 (2006), p. 1728
- [4] M.S.Meruvia and M.L.Sartorelli: APPLIED PHYSICS LETTERS Vol. 84 (2004), p. 3978
- [5] Wang dong-xing, Zhu Min, Kazuhiro Kudo: CHINESE JOURNALOF ELECTRONICS, Vol.11 (2002), p. 204
- [6] Xiaolin Wang, Dongxing Wang: Measurement, Information and Control (MIC) Vol. 1 (2012), p. 432
- [7] Khasan S.Karimov, Ibrahim Qazi: Chem Solids Physics and Chemistry of Solids (Phys) Vol. 32 (2008), p. 13

The Preparation and Characteristics Analysis of ZnO/Ni/ZnO Schottky Junction TFTs

Yue Shan^a, Yanhong Wu, Dongxing Wang, Yue Zhang,

Jiabin Chen, Jinghua Yin, Hong Zhao

Department of Electronic Science and Technology, College of Applied Science, Key Laboratory of Engineering Dielectrics and Its Application, Ministry of Education Harbin University of Science and Technology, Heilongjiang Harbin 150080, China

^aShe712830@163.com

Keywords: radio frequency magnetron sputtering; ZnO TFTs; output static characteristics

Abstract. Using radio frequency magnetron sputtering deposition deposit ZnO films on SiO₂ glass, and prepare vertical structure ZnO-based thin film transistor. By means of measurement, obtain the static output characteristics, the output current can achieve the order of milliampere, get the transfer characteristics of ZnO TFTs; transconductance which get the largest value g_m =0.0061S when source-drain voltage V_{DS}=3V, source-gate V_{GS}=0.4V; output resistance and voltage amplification coefficient, the smallest voltage amplification factor is μ =1.16056,still have voltage amplification effect.

Introduction

With the rapid development of economy, the development of information technology is becoming more and more rapidly, which makes people's increasing need of high-speed, portable, high-definition flat-panel display device. Therefore, the choice of flat display device-thin film transistor (TFTs) is quite important as the driving element. At present, the commonly used TFTs is a - Si TFTs, but its carrier mobility is usually less than $1 \text{ cm}^2 \text{V}^{-1} \text{s}^{-1} [1, 2]$, this makes the output current of a - Si TFT for active matrix organic light emitting diode (AMOLED) drive unit of flat-panel display is not idea [3]. Carrier mobility of poly silicon is 2 to 3 orders of magnitude higher than a - Si, can be used in AMOLED, but poly silicon preparation need high cost, process complex and requires high temperature and is not suitable for the flexible display device, and the narrow forbidden band width, is easily affected by visible light, so it is not suitable to apply to TFT - LCD display device. In recent years, oxide semiconductor has been very extensive researched [4]. Oxide semiconductor usually has a wide band gap, low preparation temperature, high carrier mobility, low production cost, high compatible with flexible substrate, and the film transparency is higher, which can be used for transparent electronics, in addition[5], low voltage Transparent Oxide Semiconductor Thin Film Transistor (TOS-TFT) can effectively reduce the power consumption of the device, thus TOS - TFT as the active matrix switch drive of pixels, can reduce the power consumption, improve the brightness, and the process is simple [6,7]. In this paper, we studied the preparation and operation characteristics of vertical structure TFTs using ZnO as the semiconductor layer.

Device Fabrication and Results

There are many preparation methods of ZnO thin films, such as molecular beam epitaxy (MBE), pulse laser deposition (PLD), radio frequency (RF) magnetron sputtering deposition, Metal-organic Chemical Vapor Deposition (MOCVD), electron beam evaporation, electrochemical methods and so on. In this paper, using rf magnetron sputtering prepared ZnO thin film transistor at room temperature. Using SiO₂ substrate which is cleaned with deionized water, acetone, alcohol, prepare Al, ZnO, Ni, ZnO, Al 5 films in turn, ZnO thin films is prepared by RF magnetron sputtering, target material is 99.99% of the ZnO material, sputter deposition for 2 hours. Other layers are prepared by DC magnetron sputtering deposition, bottom vacuum is 6.0E-4. The sputtering gas is 99.99% high

purity argon. Argon gas pressure is 2.5Pa. Get the thin film transistor of vertical structure is shown in figure 1.

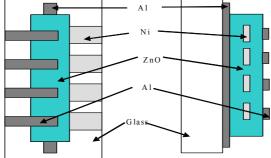


Figure 1. The vertical structure of ZnO thin film transistor (quartz glass as the substrate, Al as the source of leakage, Ni as a gate electrode, ZnO as is predestined friends the semiconductor layer)

Using Keithley 4200 - SCS semiconductor tester measure the ZnO TFTs, the test circuit is shown in figure 2, and measured static output characteristics is shown in figure 3 (a). From the figure, we can see that the opening voltage of thin film transistor is is quite low. At the same times, when drain-source voltage, V_{DS} changes in the range of 0-3V, the drain-source current I_D increases with the increase of drain-source voltage under the fixed grid voltage V_{GS} , which is shown unsaturated features. When the gate source bias V_{GS} is a constant, with the increasing of drain-source voltage, drain area ZnO semiconductor Fermi level rise. From the perspective of the electrons in the semiconductor, electronic injection barrier reduced, under the action of the drain-source voltage the number of electrons flow from semiconductor to metal increase of gate-source voltage V_{GS} , when the drain-source voltage V_{DS} is a certain value. Along with the rising of the gate-source voltage V_{GS} , the source area Fermi level of ZnO semiconductor is reduced, the barrier height between ZnO semiconductor and gate increases, the flowing of electrons from semiconductor to metal gate becomes difficult, resulting in drain source current decrease.

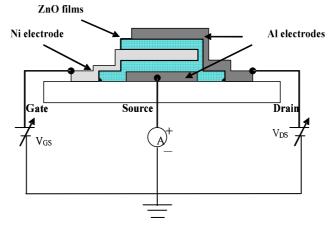


Figure2. Transistor static characteristic test circuit diagram

The current voltage characteristic between Ni-ZnO-Al is shown in figure 3(b), we can see good Schottky characteristics has been formed between Ni-ZnO from the figure. When adding positive voltage, Schottky barrier between Ni-ZnO reduced, which electrons can flow from the ZnO semiconductor to Ni easily, so as to form a larger current. The band structure of balance contact between ZnO and Ni is shown in figure 4. Schottky diode in balance, the metal Fermi energy and semiconductor Fermi energy are the same, the number of electron with enough energy in semiconductor which can cross the potential barrier to the metal side is equal to the number of electron that can cross the barrier to the side of semiconductor in metal, the net electric current is zero, cancel each other out, there will be no current outside.

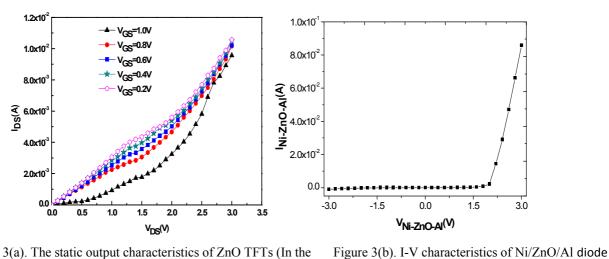


Figure 3(a). The static output characteristics of ZnO TFTs (In the condition that V_{GS} change from 0.2 V to 1 V under step 0.2 V, measured the value of I_{DS} when V_{DS} change in the range of 0 to 3 V)

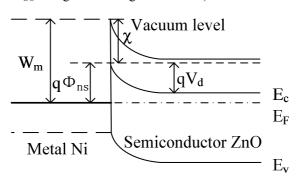


Figure 4. The band structure of balance contact between ZnO and Ni

When $V_{DS} = 3$ v, the transfer properties of ZnO-based TFTs is shown in figure 5.

The meaning of channel transconductance is when drain voltage is constant, the modulation effect of gate voltage on channel current.

$$g_m = \frac{\partial I_{\rm DS}}{\partial V_{\rm GS}}|_{V_{\rm DS}=C} \tag{1}$$

Therefore, we can get transconductance value under different gate voltages from figure 5 curve differential treatment, as shown in figure 6. From figure 6, we can see that when $V_{GS} = 0.4 \text{ V}$, transconductance is biggest, by this time, gm = 0.0061, getting the largest modulation effect of gate voltage on channel current.

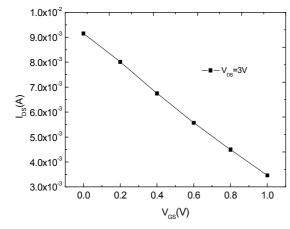


Figure 5. The transfer characteristic of ZnO TFTs (in the condition of V_{DS} =3V)

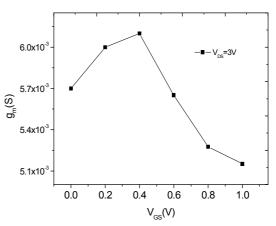


Figure 6. V_{DS} =3V, the relationship curve of transconductance g_m and gate voltage V_{GS}

The output resistance and voltage amplification coefficient are important parameters to measure the performance of TFTs.

$$\mathbf{r}_{D} = \frac{\partial V_{DS}}{\partial I_{DS}}|_{V_{GS}=C}$$
(2)

$$\mu = -\frac{\partial V_{\rm DS}}{\partial V_{\rm GS}} \Big|_{\rm I_{\rm DS}=C} \tag{3}$$

Therefore, we can get the relationship between the output resistance r_D , voltage amplification coefficient and the gate voltage V_{GS} , as shown in figure 7. By the graph, we can see that when the gate voltage is less than 0.4 V, output resistance value decreases with the increase of the gate voltage, when the gate voltage is greater than 0.4 V, output resistance increases with the increase of gate voltage. When $V_{GS} = 0.8$ V, get the minimum voltage amplification coefficient, at this time, u = 1.16056, there is still a voltage amplification effect.

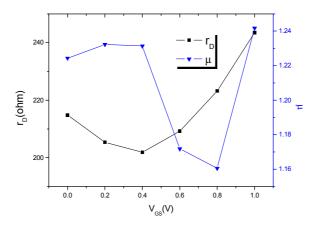


Figure 7. The relationship between output resistance r_D and voltage amplification coefficient u and the gate voltage V_{GS}

Conclusion

In this paper, using OLED multi-functional multiple coating system, prepare the vertical structure of ZnO thin film transistor by DC magnetron sputtering and RF magnetron sputtering method on quartz glass. Test basic electrical characteristics such as the static I-V, using the Keithley 4200 - SCS semiconductor thin film transistor tester. And the characteristics of the I-V characteristics of present unsaturated current increases with increasing drain voltage V_{DS} , decreases with the increase of gate voltage V_{GS} , operation current is as high as milliamperes. Analyze the static electrical properties of thin film transistors, obtain the performance parameters of the transistors, including: transistors transconductance, output resistance, voltage magnification and so on.

References

- Xin' an Zhang, Jingwen Zhang, Weifeng Zhang: Journal of Semiconductors, Vol. 29(2008), p. 859
- [2] Zhi Ye, Man Wong: IEEE ELECTRON DEVICE LETTERS, Vol. 33(2012), p. 549
- [3]HuangChung Cheng, PoYu Yang: IEEE ELECTRON DEVICE LETTERS, Vol.32(2011), p. 497.
- [4] Md Delwar Hossain Chowdhury, Sang Hyun: J. Appl. Phys., Vol.110 (2011), p. 114503
- [5] Jie Jiang, Qing Wan, Jia Sun: Appl. Phys. Lett., Vol. 95 (2009), p. 152114
- [6] R. B. Cross, M. M. De Souza: Appl. Phys. Lett., Vol. 89(2006), p. 263513
- [7]Josef W. Spalenka, Padma Gopalan, Howard E. Katz: Appl. Phys. Lett., Vol. 102(2013), p.041602

The analysis of photocurrent multiplication in organic dye CuPc transistor with wide wavelength light

Yueyue Wang^a, Dongxing Wang, Yongshuang Zhang, Zeying Wang

Department of Electronic Science and Technology, College of Applied Science, Key Laboratory of Engineering Dielectrics and Its Application, Ministry of Education Harbin University of Science and Technology, Heilongjiang Harbin 150080, China

^aqinqinxiaopang@163.com

Keywords: CuPc ; short channel devices ; organic phototransistor ; photosensitivity

Abstract. The organic photoelectric transistors using the vacuum evaporation and sputtering process are prepared in this paper. The Cu/CuPc/Al/CuPc/ITO layer based on vertical structure is grown through a CuPc active layer. The CuPc has excellent photosensitivity and it is easy to be fabricated into Short-Channel device with vertical structure. It is shown that I-V characteristics of organic photoelectric transistors are unsaturated. In this experiment the light source is the Bromine-tungsten lamp in the range of 300nm to 800nm. When the light source irradiates the device with V_{ec}=2V, the operating current is 0.155µA which has been increased to 2.3-3.6 times as compared with the dark state. Therefore, the amplification coefficient of output current I_{ec} is increasing in irradiation with smaller base voltage. As a result, the current amplification coefficient β is 5.25 and 2.14 with illumination and without illumination respectively.

Introduction

Optical sensing technology, as an important part of information technology, has extremely applications in fields of industrial production, environmental monitoring and so on. Especially the high sensitivity of photoelectric detector is a key part of the image sensor [1]. The development of inorganic lithography is nearing the peak of the miniaturization since that Gordon Moore proposed the Moore's law in 1965. The organic semiconductor is considered as a method to keep the rapid development of IC. Organic materials have the advantages of good processing performance, simple preparation, and low cost [2,3].

In recent years, with the development of organic materials, the device that uses organic materials as the active layer is widely applied to electroluminescent displays and photocells [4,5]. Among various organic semiconductor materials, Copper Phthalocyanine (CuPc) is a common choice. As a kind of organic small molecule dye, it has some excellent features, for instance, stable performance in air, simple manufacture technology, low cost and good photosensitivity. As a result, the material has promising market [6,7].

The preparation of organic pigment photomultiplier transistor is discussed in this paper. Using the vacuum coating process, the indium tin oxide (ITO), CuPc, aluminum, CuPc and copper were prepared on glass substrates in order, forming the Cu/CuPc/Al/CuPc/ITO structure. When the light signal irradiates the organic semiconductor photosensitive material layer, exciton, in organic semiconductor materials/metal built-in electric field, is separated into photocurrent and converted to the driven current which makes the output photocurrent increase using its current amplification's effect. The Schottky contact is formed between organic semiconductor materials and metal.

Experiment and measure

The preparing of organic pigment photomultiplier transistor by OLED multi-coating system was completed on a glass substrate. The purity of organic semiconductor material is 99.99%, and the effective area of the device is 30mm². The ITO electrode was firstly obtained by DC magnetron sputtering. Then, the first CuPc layer was prepared by vacuum evaporation coating of organic at 350

 $^{\circ}$ C. The preparation of base and the second layer of CuPc films were the same as above. Finally, the Cu emitter was also obtained by DC magnetron sputtering technique. The thickness of top layer and bottom layer is 130nm respectively, and the base is about 20 nm. The rate of evaporation coating is 3nm/min. The structure diagram of the vertical structure of the organic thin film transistor is shown in figure 1. There are some problems such as relatively low mobility, complicated process of the source and drain of OTFT with horizontal structure, small output current, large driving voltage, slow switching speed and other issues. As a result, it will be benefit for the lower driving voltage and the higher operating frequency by using the vertical structure to reduce the channel length of OTFT [8].

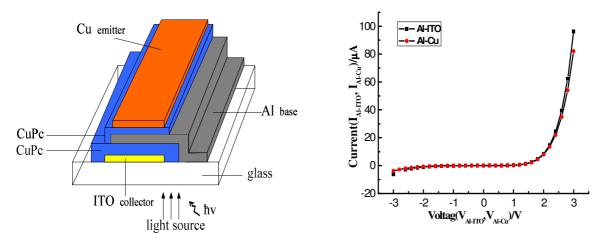


Fig.1 The vertical structure of organic thin film transistor

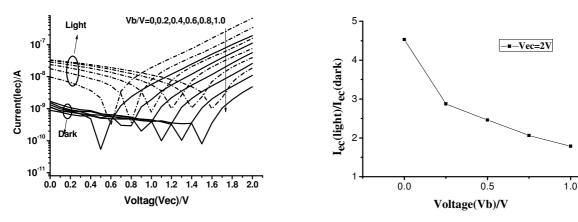
Fig.2 The Schottky I-V rectification characteristics between aluminum film and the CuPc film

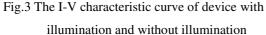
Result and analysis

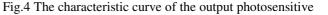
Measuring photoelectric properties of the transistor were completed in air at constant room temperature 20 °C. The measurement results of the rectification characteristics between the base of semi conductive aluminum film and the CuPc film of two sides are shown in the figure 2. The Phthalocyanine series film, taking on p-type conduction property, is forming Schottky barrier with aluminum electrode. Therefore, the experiment result is matching theoretical results [9].

Setting the step size of bias voltage V_{bc} is 0.2 at the range of 0V to 1V. The step size of bias voltage V_{ec} is 0.1 at the range of 0V to 2V, and time delay is 0.5s in each step. The I-V output characteristics of the voltage V_{ec} and the current I_{ec} are measured. The measurement results of the I-V characteristics of the device with illumination of the Bromine-tungsten lamp and without illumination are shown in the figure 3.The current I_{ec} with illumination is greater than the current I_{ec} without illumination using the Bromine-tungsten lamp with wide wavelength of 300nm to 800nm. As shown in figure 3, the illumination enlarges the current I_{ec} of the device, generates the photosensitive double current, under the same bias voltage. But the increasing of V_b will control the change of current I_{ec} , and reduces the value of current. When photon enters into the CuPc film through the ITO film, and produces the exciton pair, which spreads and disintegrates into free carrier, thus improves the carrier density of the CuPc film, the photosensitive double current is formed. The photosensitive double current, comparing without illumination, improves the value of current I_{ec} at the same V_b .

The figure 4 shows the relationship between the output current I_{ec} of the transistor with illumination and without illumination and the base voltage V_b . When V_{ec} is equal to 2V, the ratio range of the output current I_{ec} with illumination and without illumination is 2.3 to 3.6, and when base voltage V_b is equal to 0V, the ratio of the output current I_{ec} with illumination and without illumination and without illumination and sufficient of the current has the smallest magnification when V_b is equal to 1V. It can be noted that the smaller the base voltage is, the greater the ratio of output current I_{ec} with illumination and without illumination will be.







current $I_{ec}(light) / I_{ec}(dark)$ of device and V_{b}

In order to study the photomultiplier current of device and the photoelectric conversion efficiency, we assume that $V_b=0V$, and measure the relationship between the I_b , I_{ec} and the bias voltage V_{ec} of device under light and dark, V_{ec} ranges from -2V to 2V, stride length is 0.1 V, and the time delay of every step is 0.5s. The determination results are shown in figure 5.

Figure 5 shows the relationship of between the base current I_b and the collector emitter current lec and the measured bias voltage Vec with illumination and without illumination respectively at $V_b=0V$. The base current I_b is far less than the operating current lec of device, and the maximum difference even reaches to two orders of magnitude when $V_b=0V$, $V_{ec}=2V$.

The energy band diagram of metal Al contacts with P type semiconductor CuPc is shown in figure 6. When the Al film contacts with lead phthalocyanine membrane, both sides of the Fermi level are in the same level, the hole will move from lead phthalocyanine membrane's band to metal Al film to make the metal aluminum's surface form positive charge. At the same time, an amount of negative charge is formed within depletion layer. The change of the depletion layer barrier is similar to unilateral mutations p-n+. Carrier transport mechanism injected by emitter obeys the rules of the tunneling effect, and the hole overcomes double barrier to reach the collector. Then, the electron hole pairs are generated and separated to form the photocurrent which plays a role of operating current.

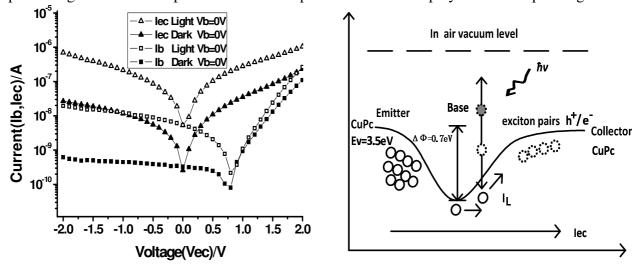


Fig.5 The characteristics curve of V_{ec} - I_{ec} , V_{ec} - I_b with illumination and without illumination

Fig.6 The energy band diagram of the CuPc transistor among aluminum electrode and both sides of CuPc

By using of the relationship between the transistor carriers and current distribution, the relation of base current I_b and collector current I_{ec} of P-m-P semiconductor without illumination is

$$I_{ec} = \beta I_b^{dark} \,.$$

(1)

Under the condition of illumination, electronic-hole pairs in the CuPc semiconductor layer are induced, and separated with built-in electric field. The electronic flows into the base area, the hole flows into the collector, and then the photocurrent I_L is generated to form a part of the device operating current. Thus, the current relationship with illumination is

$$I_{ec} = \beta I_b^{light} + I_L(1+\beta) .$$
⁽²⁾

When $V_{b}=0V$, $V_{ec}=2V$, the values of I_{ec} and I_{b} can be got by measuring. Current amplification factor β of dark state is 2.14, calculated by formula (1). Taking the value into the formula (2) and getting corresponding photocurrent $I_{L} = 0.155 \mu A$.

Amplification coefficient β_L with illumination is defined as

$$\beta_L = \frac{I_{ec}^{light} - I_{ec}^{dark}}{I_b^{light} - I_b^{dark}}.$$
(3)

Where I_{ec}^{dark} is current between the emitter and the collector in dark conditions, I_{ec}^{light} is current between the emitter and the collector in light conditions. Device light amplification coefficient $\beta_{L} = 5.25$ by calculation.

Conclusion

In this paper, the organic photoelectric transistor with vertical structure is prepared based on vacuum coating process. The structure of device is Cu/CuPc/Al/CuPc/ITO, the length of device conductive channel is reduced by the vertical structure. The results show that the base of aluminum film forms good Schottky contact with the CuPc film. In the condition of the same bias voltage, the illumination enlarges the output current I_{ec} of the device, which makes the photosensitive double current effect. When $V_{ec}=2V$, the ratio range of the output current I_{ec} with illumination and without illumination is 2.3 to 3.6. The smaller the current is, the greater the ratio of the output current I_{ec} of illumination and without illumination will be. The base current I_b of the transistor is far less than the operating current I_{ec} and the base current I_b is 100 times. The generated photoproduction current I_L is 0.155µA with illumination.

References

[1] A. V. Kosinskii, V. R. Matveevskii and A. E. Popov: Measurement Techniques Vol. 33 (1990), p. 869

[2] ZhenHua Zhang, ZhongQin Yang and JianHui Yuan: Chinese Science Bulletin Vol. 52 (2007), p. 3016

[3] D Vuillaume, S Lenfant and D Guerin: Pramana Vol. 67 (2006), p. 17

[4] ZhiGang Li, XinYan Zhao and Xin Lu: Science China Chemistry Vol. 55 (2012), p. 553

[5] B. Chandar Shekar, Jiyeon Lee and Shi-Woo Rhee: Korean Journal of Chemical Engineering Vol. 21 (2004), p. 267

[6] A. S. Komolov, E. F. Lazneva and S. A. Pshenichnyuk: Semiconductors Vol. 47 (2013), p. 956

[7] Jun Huang, Mingtian Li and Yan Tang: Journal of Wuhan University of Technology-Mater. Sci. Ed. Vol. 23 (2008), p. 606

[8] David J. Gundlach: *Electrical Behavior of Organic Transistors and Circuits* (Organic and Molecular Electronics, US 2004).

[9] Bernd Schmidt: *Ion Beams in Materials Processing and Analysis* (Springer Vienna, Germany 2013).

Research of Silicon-based Micro Direct Methanol Fuel Cell

Shanshan Cao^{1,a}

¹Department of Electrical and Information Engineering, Heilongjiang Institute of Technology, Harbin, Heilongjiang, China

^acsswy411@163.com

Keywords:MEMS; µ DMFC;ANSYS; silicon

Abstract. The objective of this study is to investigate appropriate configuration used for micro direct methanol fuel cells (DMFCs). We designed grid and spiral flow fields of electrode plate and simulated with ANSYS. Using silicon-based micro–electro–mechanical systems (MEMS) technology to fabricate the DMFCs with different flow fields and tested at room temperature. Grid flow field can effectively improve methanol mass transport performance and exhibit higher cell efficiency than spiral flow field, demonstrating 13 mAcm⁻² and 3.9 mAcm⁻² in peak current density respectively and the peak difference of power density is nearly an order of magnitude. We tested Cell performance in different concentration methanol and it shows the best performance in concentration 2M.

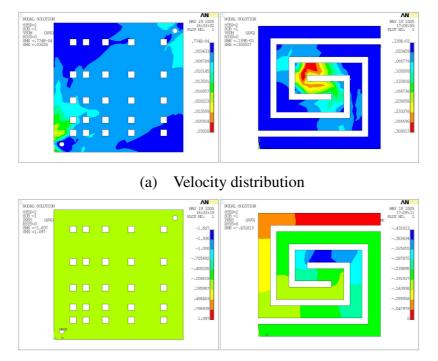
Introduction

Over the past few decades, many kinds of fuel cells based on various electrolytes and fuels have been developed, among which Micro direct methanol fuel cells (DMFCs) based on MEMS technology posses many advantages, such as high energy conversion, fuel efficiency, room temperature operation, simple structure, and high power density[1,2]. They will likely be used in portable and mobile electronic products such as laptop computers, two-way radios, and mobile phones[3].

Electrode plate is a crucial component of micro DMFCs, which not only has a principal role in transferring methanol and oxygen and removing water and CO_2 gas which are produced by the electrochemical reaction of the cells, but also provides the structural supporter for membrane electrode assembly (MEA) and collects the current[4,5]. Collector plate with appropriate channels is critical to optimize cells' performance. Bulk-silicon process based MEMS is matured, and collector plate based silicon can provide suitable configuration for micro DMFCs[6].

Structure and design

Configurations of flow fields of plates have great effects on the performance of micro DMFCs. Flow fields include channels and ribs. Channels are used for transferring methanol, which can support enough fuel for electrochemical reaction. Ribs provide the supporter for MEA which catalyze electrochemical reaction. Flow fields design needs to synthesize channels Transport function to confirm sufficient channel in electrode and ribs' enough width. Based on above principles, we designed spiral channel and grid channel. ANSYS was used to simulate flow field configuration, as illustrated in fig.1. It was concluded that distribution of grid channel's velocity was more uniform than spiral channel's, but grid channel's velocity was slow relative to spiral. Difference in pressure between import and export of grid channel was smaller than spiral channel, so methanol velocity in grid configuration was slower responding to that in spiral channel, which was considered to be more favorable to methanol redox reaction. A conclusion could be drawn that grid channel had the advantage as plate configuration.



(b) Pressure distribution Fig.1. Simulation of flow field configure

preparation process

Here silicon wafer with <100> crystal orientation was selected as current collector and fabricated by MEMS technology. Clean the silicon wafer by regular method and oxidize in oxidation oven to form 10 μ m oxidation layer. Photolithography was applied to pattern micro channels on the SiO₂. anisotropic etching process used 40% KOH solution to etch the flow channels at 40°C, which was stirred with magnetic stirring apparatus. Prepare import and export holes by electrochemical method with 40% KOH solution and tungsten probe, and holes diameter was determined by probe diameter,

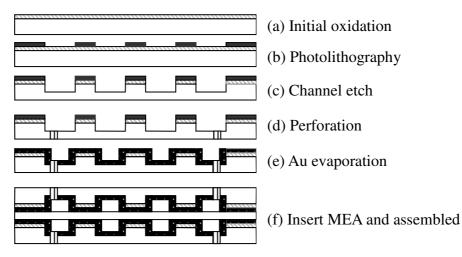
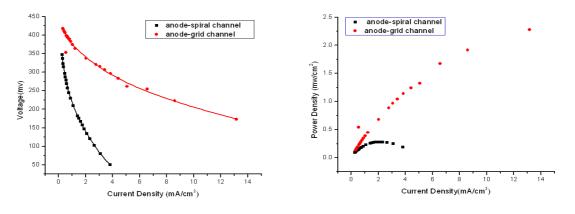


Fig.2. Fabrication steps of electrode plate channels

solution concentration and voltage. As electrode plates were used to collect electrons, Au was evaporated on plates by vacuum evaporation technology and alloyed. Finally a piece of MEA 117 was employed as catalyst layer in the micro DMFC. The fabrication steps are illustrated in fig.2.

Result and discussion

Based on the mass transfer of a single cell active material experiment, the performances of the micro DMFC with two kinds flow channels were shown in fig.3. In fig.3 (a) Current density of spiral channel was much lower than grid channel when two configures supported the same voltage and the highest current density were 3.9 mAcm⁻² and 13 mAcm⁻² respectively. As shown in fig.3 (b), the peak difference of power density is nearly an order of magnitude. The cells with grid display



(a) Characteristics of current density
 (b) Characteristics of power density
 Fig.3. Cell performance of different channel structure

more excellent performance than that with spiral channel. The reason is mainly that the rib area in grid configure are smaller relative to spiral configure, so contact area of methanol solution and MEA catalytic layer are relatively large, which can give cell bigger chemical reaction region. Then methanol utilization may be improved and performance of cell is increased. Furthermore, spiral channel configure can't ensure the reaction product CO_2 to be discharged timely and hinders fuel reaction and affect cell's productivity.

As shown in fig.4, it illustrated that the different methanol concentration had effects on the performance of the micro DMFCs. In low current density cell discharge voltage decreased by

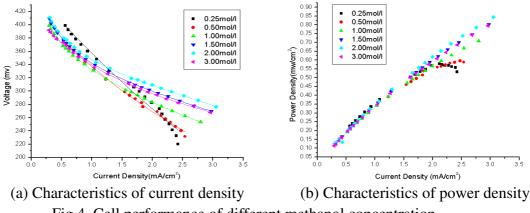


Fig.4. Cell performance of different methanol concentration

methanol concentration, but in high current density the reality was opposite. The reasons perhaps lie in that in low current density more methanol arrive at catalyst layer with concentration increase, but more methanol permeate cathode without participating in the reaction timely. Parasitic reaction of permeable methanol in cathode formed mixes potential and dropped voltage. Mass transfer limitation become the primary factor influencing the performance of the cell with concentration increasing, so high concentration of methanol has the excellent work performance at high current density. Because of MEA nature, it is impossible that methanol concentration is too high. In this paper the best concentration was 2M.

Conclusion

The micro DMFCs were designed with grid configuration and spiral configuration and fabricated using silicon –based MEMS technology. From the experimental result we can draw a conclusion that grid channel is better than spiral channel, and this corresponds to the result of ANSYS simulation. Cell performance in different concentration methanol were tested. We found that in low current density cell discharge voltage decreased by methanol concentration, but in high current density the reality was opposite. The cell shown the best performance in concentration 2M.

Acknowledgments

This work was supported by the Key Lab of Integrated Circuit of Heilongjiang University and the author would like to thank Pro.Sun at Electronics Engineering Institute of Heilongjiang University. The author is also indebted with the sponsors.

References

[1]Zhao TS, Chen R, Yang WWW, Xu C: Journal of Power Sources Vol.191 (2009), pp.185-202

- [2]Guo Z, Faghri A:J Power Sources Vol. 167 (2007), pp.378-390
- [3]Achmad F, Kamarudin SK, Daud WRW, Majlan EH: Applied Energy Vol. 88 (2011), pp.1681-1689
- [4]Wei Yuan, Yong Tang, Xiaojun Yang: Renewable Energy Vol. 50 (2013), pp.741-746
- [5]Huichao Deng, Shengtian Sang, Yufeng Zhang, Zipeng Li, Xiaowei Liu: Microelectronic Engineering Vol. 111 (2013), pp.180-184
- [6]Bo-Yan Wang, Hun-Kai Lin, Nai-Yuan Liu, K.P.P.Mahesh, Shingjiang Jessie Lue: Journal of Power Sources Vol. 227 (2013), pp.275-283

The design and characterization of three-dimension metamaterial for terahertz frequencies

QI WANG¹, YUE WANG^{1,2*}, YU LIN HE¹, WEN CHAO ZHANG¹, XUAN WANG²

¹Department of Electronic Science and Technology, Harbin University of Science and Technology, Harbin, 150080, China

²State Key Laboratory Breeding Base of Dielectric Engineering, Harbin, 150080, China

*wsbte@126.com

Keywords: Metamaterial; Terahertz frequencies; Negative refractive index; Absorption

Abstract: We present the design and characterization of a three-dimension metamaterial consisted of a Jerusalem cross unit cell on the each side of cube lattice substrate for terahertz frequencies. The retrieved effective medium parameters from scattering data prove that the three-dimension metamaterial has a negative permeability and permittivity in wide frequencies range of 1.47-1.73 THz. We demonstrate that the three-dimension can be regarded as a polarization insensitive absorber with an absorptivity of 46% at 1.49 THz. Such designed materials may find numerous applications ranging from the active element in a thermal detector to terahertz stealth technology.

Introduction

Terahertz (THz) frequency spectrum, can be defined as the portion of the sub millimeter wavelength electromagnetic (EM) spectrum between approximately 1 mm and 0.1 mm of wavelength (300 GHz-3 THz) and it has the potential of playing a major role in technological and scientific application areas. In spite of technology in these frequencies remaining relatively immature, numerous potential applications such as security detection, communications, high resolution imaging for detection of infected tissue, and chemical and biological sensing have been identified and are being pursued[1-4]. These applications may benefit greatly from materials that enhance our ability to manipulate, control, and detect THz radiation.

Artificial materials which exhibit a designed EM response have recently generated great interest.[5] This is due in part from the ability of these materials to exhibit an EM response not readily available in naturally occurring materials such as: negative refractive index, artificial magnetism, super focusing, and reduced lens aberrations[6,7]. Another advantageous and distinguishing property of EM metamaterials is that resonant structures can be designed over a large portion of the electromagnetic spectrum ranging from microwave through the THz, and higher. Thus regions devoid of natural material response, such as the so-called terahertz gap, can be targeted for metamaterial applications [8, 9]. For many potential applications it would be desirable to create metamaterials that exhibit a controlled active, dynamical, and/or tunable response.

Today's available metamaterials, based on the periodic arrangement of split-ring resonators (SRR) and continuous metallic wires, are only one-dimensional (1D), supporting left-handed properties only for propagation with fixed polarization in one direction, or two-dimensional(2D), where propagation in two directions with fixed polarization or one direction with arbitrary polarization is possible[10,11].

In this paper, we propose a three-dimensional (3D) metamaterial design that allows left-handed behavior for three direction of propagation and any polarization of the electromagnetic wave. Using CST Microwave Studio simulations, we verify the left hand transmission and absorption properties of the proposed structures.

Theory and Model

There are several methods for the extraction of effective material parameters for inhomogeneous medium[12,13]. Our method here utilizes the transmission and reflection coefficients calculated for a THz wave normally incident on a unit cell of metamaterial. We invert the scattering parameter to determine refractive index n and impedance z, from which we obtain the effective values for ε and μ . The refractive index n and impedance Z are related to ε and μ by the relations

$$\varepsilon = n/z, \quad \mu = nz. \tag{1}$$

The scattering parameters are collected in the scattering matrix [S]. For a two ports network the input and output wave can be calculated as $[O] = \begin{bmatrix} S_{11} & S_{12} \\ S_{21} & S_{22} \end{bmatrix} [I]$. The parameter S_{11} and S_{21} are related

to the reflection R and transmission T coefficients as following equations:

$$S_{11} = \frac{R(1 - T^2)}{1 - R^2 T^2}$$
(2)

$$S_{21} = \frac{T(1-R^2)}{1-R^2T^2}.$$
(3)

The reflection coefficient R in the free space and the effective medium boundary can be expressed as

$$R = \frac{z-1}{z+1} \quad , \tag{4}$$

where z is the characteristic impedance, and the transmission coefficient T is given by

$$T = e^{(-i\gamma d)} \,. \tag{5}$$

where γ and d are the propagation constant and thick of effective medium. From (2) and (3), one can obtain

$$R = \frac{S_{11}^2 - S_{21}^2 + 1}{2S_{11}} \pm \sqrt{\frac{S_{11}^2 - S_{21}^2 + 1}{2S_{11}}} - 1, \qquad (6)$$

$$T = \frac{S_{11} + S_{21} - R}{1 - (S_{11} + S_{21})R}.$$
(7)

Using (4) and (6), one can find

$$z = \pm \sqrt{\frac{(1+S_{11})^2 - S_{21}^2}{(1-S_{11})^2 - S_{21}^2}}.$$
(8)

Resolving (1) and (4) yield

$$\mathcal{E} = \frac{\ln(1/T)}{d(2\pi/\lambda_0)} \left(\frac{1-R}{1+R}\right),\tag{9}$$

$$\mu = \frac{\ln(1/T)}{d(2\pi/\lambda_0)} (\frac{1+R}{1-R}).$$
(10)

In (9) and (10), using expression $\gamma = \frac{2\pi}{\lambda_0} \sqrt{\epsilon \mu}$ and λ_0 is the wavelength of free space.

Note that while the expression for z is relatively uncomplicated, it is complex function with multiple branches, the interpretation of which can lead to ambiguities in determining the final expression for ε and μ . If the material is passive, the requirement that the real part Re (z) >0 fixes the choice of sign in (8). In (6) the \pm sign is chosen so that |R| < 1. Analyzing the expressions (8)-(10) is necessary for getting information about the optical and transport properties of a considered metamaterial medium.

The proposed metamaterial structures in this work are based upon a split-ring resonator. The Jerusalem cross unit cell and its geometrical dimensions is shown in Fig. 1(a). Fig. 1(b) shows a

three-dimensional metamaterial consisted of the Jerusalem cross unit cell made by 200nm of aluminum ($\sigma = 3.72 \times 10^7$ s/m). The unit cell are etched on each side of the GaAs ($\epsilon = 12.9$, the loss tangent value tan $\delta = 0.006$) substrates. All of unit cell structures have an outer dimension of 38µm, a cube lattice parameter of 40µm, metal line width of 2µm.

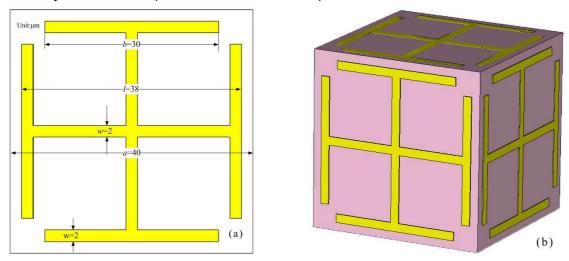
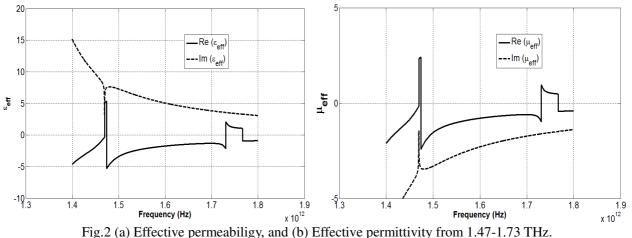


Fig. 1 (a) The unit cell of metamaterial and its geometrical dimensions, and (b) three-dimension metamaterial cell.

Results and Discussions

To obtain the final design of the three-dimension metamaterial, scattering parameter simulations were carried out on the metamaterial unit cell in Fig.1 (b). The constitutive parameters of the metamaterial can be retried from the scattering parameters by Eqs. 1-10. Fig. 2 (a) and (b) show the retrieved effective permeability and permittivity of the metamaterial, respectively. It is obverted that the electric and magnetic response occurs simultaneously from 1.47-1.73 THz, a left-handed medium (LHM) regime is achieved. It is noted that there is an anti-resonance for the effective permeability and permittivity of 1.47 THz.



A very important electromagnetic properties LHM is negative refractive index properties. This is the most intuitive LHM electromagnetic properties. Fig.3 shows the refractive index of the metamaterial. In order to verify the negative refractive phenomenon, a triangular wedge-shaped structure consist of three-dimensional unit cell have been constructed, as shown in Fig. 4(a). The angel of wedge structure is approximately 26.56° . To ensure the incident wave accumulating the structure, metal material is used on both sides of the wedge shaped structure. When the electromagnetic wave is normal incident on the structure, due to the negative refraction characteristics of the structure, the refracted wave and the incident wave locates on the same side of the normal line. As can be seen in Fig. 4(b), at the resonant frequency 1.48THz, negative refractive index phenomenon can be observed, which prove the designed three-dimensional structure is indeed a negative refractive index material.

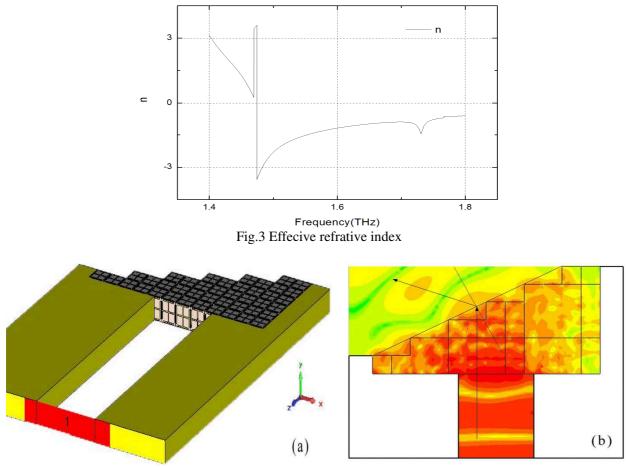


Fig.4 (a) Wedge structure and (b) schematic illustration of an incident beam refracting from the wedge structure.

In addition, we demonstrate, through simulation, that this metamaterial absorber operates over a very wide range of angles of incidence for transverse electric and transverse magnetic configuration. The amplitude of the transmission S_{21} and reflection S_{11} were obtained, and the absorption was calculated by $A = 1 - S_{21}^2 - S_{11}^2$. The absorption as a function of frequency for the optimized structure is presented in Fig. 5 for TE radiation at various angles of incidence. At normal incidence a peak absorption of 43% is obtained. With increasing angle of incidence, there are two peaks occurred, and the absorption is lower. The absorption is obtained the maximum value (46%) at the angle of incidence of 45°, and that is 61% for the transverse magnetic (Not given here). Physically, the asborption peak corresponds to strong electric field enhancement inside the metamaterial structure.

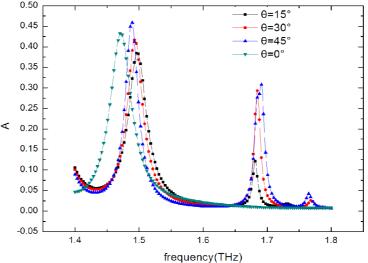


Fig. 5 The absorptivity as a function of frequency at various angles of incidence for TE radiation

Summary

In conclusion, we have demonstrated that the designed three-metamaterial can simultaneously response to electric and magnetic fields under normal incidence wave illumination. Especially, a wide range of negative permeability and permittivity can be achieved by optimized the parameters of the structures, and this allows for negative index materials at THz frequencies. The results demonstrate the fact that the magnetic permeability of optical material is unity is no longer true for the metamaterials. The simulation results suggest that three-dimension metamaterial can be regarded as an absorber that operating over a wide angular range for transverse electric wave. Such designed materials illustrate the potential of accessing a frequency range normally inaccessible to natural materials, and may find numerous applications ranging from the active element in a thermal detector to terahertz stealth technology.

Acknowledgments

The work supported by National Natural Science Foundation of China (Grant No. 61201075), and the Science and Technology Research Foundation of Heilongjiang Education Bureau of China (12521110), and by China Postdoctoral Science Foundation (2012M511507), and by Science Funds for the Young Innovative Talents of HUST (No.201302), and by Frontier Research Foundation of State Key Laboratory Breeding Base of Dielectrics Engineering (DE2012B05).

References

- [1] X. G. Peralta, E. I. Smirnova, A. K. Azad, H. T. Chen, A. J. Taylor, and J. F. O'Hara, Opt. Express, 17(2009), 773.
- [2] U. Magel, R. S. Fishman, T. Katuwai, H. Engelkamp, H. T. Yi, T. Room, Phys. Rev. Lett., (110), 2013, 257201.
- [3] H. T. Chen, J. F. O'Hara, A. J. Taylor, R. D. Averitt, Opt. Express, 15(2007), 1084.
- [4] S. G. Liu, Y. X. Zhang, Y. Yin, J. Phys. D: Appl. Phys., 44(2011), 375105.
- [5] H. Tao, C. M. Bingham, A.C. Striwerda, N. I. Landy, K. Fan, X. Zhang, W. J. Padilla, R.D. Averitt, Phys. Rev. B, 78(2008), 241103.
- [6] J. F. Wang, Sh. B. Qu, Zh. Xu, J.Q.Zhang, Photonics and nanostructures fundamentals and applications, 6(2008), 183.
- [7] X. Zhang, Nature, 480(2011), 42
- [8] R. Piesiewicz, IEEE Antennas. Propag. Mag., 49(2007), 24.
- [9] F. Sizov, Opto-Electron. Rev., 18(2010), 10.
- [10] W.J. Padilla, A.J. Taylor, C. Highstrete, M. Lee R.D. Averitt, Phys. Rev. Lett. , 96(2006), 107401.
- [11]T. Koschny, L. Zhang, C. M. Soukoulis, Phys. Rev. B, 71(2005), 121103.
- [12] T. Galek, K. Porath, Modelling Simul. Mater. Sci. Eng., 18(2010), 025015.
- [13] N. I. Landy, C. M. Bingham, Phys. Rev. B, 79(2009), 125104.

Advanced Materials Research Vol. 981 (2014) pp 851-854 © (2014) Trans Tech Publications, Switzerland doi:10.4028/www.scientific.net/AMR.981.851

The Effect of Components Based on Synchronous Radiation SAXS on Micro-structure of PI/TiO2 Nano-composite Film

Lei Yao^{1,2}, Jinghua Yin^{1,4,a}, Guangyou Li¹, Xiaoxu Liu¹, Guang Mo³ ¹Harbin University of Science and Technology, Harbin, China ²Mudanjiang Normal College, Mudanjiang, China ³Institute of High Energy Physics Chinese Academy of Sciences ⁴Key Laboratory of Engineering Dielectric and Its Application Ministry of Education, Harbin, China ^aYinjinghua1@126.com

Keyword: Nano-composite film; SAXS; Titanium dioxide nano-particle

Abstract: In this report, the micro structure of PI/ TiO₂ films with different components prepared by in-situ polymerization method is researched by XRD, TEM, synchrotron radiation SAXS. Its micro structure characteristics include nano-particles distribution, PI molecule chains spacing and interface layer thickness. The experimental result shows that after doping, particle radius is almost 10nm, and cluster of nano-particles became more serious with increase of components, however, the spacing of PI molecule chains decreases 5.238 Å-4.625 Å. The scattering curves occurs negative deflection in Debye theory, it shows that there are interface layers with thicknesses in the range 0.7nm-2.1nm between nano-particles and composite matrix. Through analyzing the three kinds of micro structure change, it shows that when the component is 15 wt.%, the micro-structure of composite film is the optimal.

Introduction

As an important super-engineering plastic, polyimide has been extensively applied in many areas such as electric industries, micro-electronics, railway transport and aerospace and so forth ^[1]. The diverse applications of Polyimide (PI) can be attributed to its outstanding electrical, mechanical, thermal, and wear-resistance properties, as well as its ability to withstand radiation ^[2]. Despite above mentioned special properties of PI; pure PI normally does not always provide reliable and long-lasting protection against high-voltage attack and stress, which can cause ionization and eventual breakdown when voltage stress reaches a critical level. Fortunately, these issues can be drastically improved by dispersing inorganic nano-particles, such as TiO₂ nano-particles ^[3], silica nano-particles ^[4], and clay nano-particles ^[5], in to PI matrix. Therefore, a polyimide-based composite ^[6] is of particular investigation interest to achieve better insulating materials.

1 Fabrication and measurement

1.1 Experimental material and fabrication composite film

TiO₂ nano-particle is anatase type, particles radius 10 nm, and purity is more than 99%.

The PI/TiO_2 nano-composite films contain TiO_2 nano-particles were prepared using in-situ polymerization method. First adding TiO_2 nano-particles and DMAC to three flask, and ultrasonic dispersion; Then adding a certain amount ODA to flask, stir in the blender; Successive join PMDA, obtain polyamide acid/TiO₂ mixed adhesive solution; Finally fabricating 30 microns thickness of imide acid membrane, into the vacuum drying oven heating with amination, get the dry and clean films.

1.2 Measurement and instruments

With transmission electron microscopy (TEM) Tecnai G2 F30, study micro-structure of TiO₂ nano-particles. Use Beijing synchrotron radiation experiment 1 W2A SAXS for small Angle X-ray scattering line, whose photon flux is 10 - 11 keV, spot size being 1.4×0.2 mm², X-ray wavelength being 0.154 nm; SAXS uses a Marresearch Company's Mar 165 type CCD imaging

detector to detect the scattering signal and the resolution of the detector is 100 microns. Experimental data remove the sample background and normalize processing of actual scattering intensity by using computer software. Use the D/Max - 2000 Ricoh X-ray diffraction meter to measure film phase structure.

2 Results and discussion

2.1 Nano-particles dispersion in the composite film

According to SAXS theory, the system with different doping components can be researched, and the micro structure of scattering material is explained, which includes the size, interface layer and fractal feature of matrix ^[7,8]. For a single scattering system, use the basic theory of Guinier. According to the Guinier draw ln [I (q)] ~ q² curve, can be directly determine dispersion of the system. Linear part of the slope can be system turning radius value of the particle ^[9]. Using tangent method step by step to make linear data fitting, by the value of the slope, the obtained particle radius of gyration R_g. Shown in table 1, doping TiO₂ radius R and R_g relations as follows:

$$R = \sqrt{3} / 5R_g \tag{1}$$

Fig. 1 shows the size distribution of particles in the sample, which includes the nano-particles, the void and the large particles formed by particle clusters. The x axis R represents the particle radius and the y axis is the percentage of the particles. The radius of the pure TiO₂ ranges from 5nm to 20nm, which could be seen in figure of the TiO₂ particles observed by the TEM, that is also Fig. 2. Fig. 1 illustrates that the particle size mainly concentrates on the range of 0-50nm. It is known that the curve peak contains certain areas in the range of 0-50nm compared with the pure TiO₂, which means that the void with the radius smaller than 5nm exists in the substrate and the void is caused by the gap and space defect in the preparation process of the film.5-20nm is the region mainly included by the curve peak, and that is also the major distribution interval of the TiO₂ particles. The curve peak arrives at 66%, 60%, 52% near the 10nm in x axis, which indicates that the number of TiO₂ particles with radius of 10nm reduces by 14% with the increase of component. 20-50nm is the cluster distribution of TiO₂ particles with small size, and the curve peak is larger in the large with the increase of the component. It could be seen from Table 1, the average radius R of TiO₂ particles with different component is 10.9nm, 11.7nm, 11.9nm respectively. With the increase of the component, the number of TiO₂ particles with the radius of 10nm reduces, the number increases with the radius larger than 20nm and the average radius of particles increase by 1nm, which shows that the nano- particles cluster becomes serious. Clustering is caused by the increase of nano-particles and incomplete dispersion.

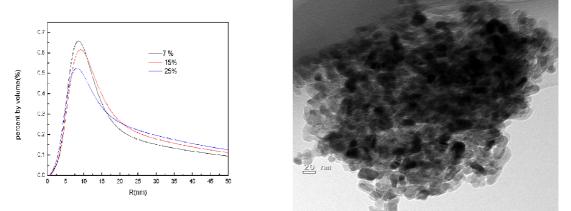


Figure 1 Composite film scattering curves Figure 2 TEM images of TiO₂ Nano-particles 2.2 PI molecular chain spacing in the composite film

The XRD patterns of different components PI/TiO_2 shown in Fig. 3, which shows that at 15 ° - 20 ° of the horizontal range 2 θ diffraction peaks appear wider; this is due to the irregular distribution of organic polymer chain in the polyimide. With component increases, polyimide

characteristic peak intensity decreased significantly; This is due to the doping of the inorganic nano-particles in the matrix component increases; Polyimide characteristic peaks move to the right: 7 wt.% peaks is 16.935 °, 15 wt.% peaks is 18.143 °, 25 wt.% peaks is 19.193 °. According to Bragg formula:

$$d = \lambda/2 \sin\theta$$
 (2)

The calculated average spacing between PI molecular chain d (λ is the X-ray scattering angle, $\lambda = 1.54E$), as shown in Table 2. At components 7-15wt.%, the molecular chain spacing down to 0.349 Å; at components from 15wt.% to 25wt.%, the molecular chain spacing reduces 0.264 Å. With component increases, the spacing reduces between the molecular chains. Nano-particles have a large specific surface area, surface energy and surface tension, PI molecular chain in the arrangement of the particles surface concentration is greater than matrix, it is the cause that PI molecular chain spacing changes in the internal microstructure of the samples, and also affect the molecular chain of morphology and orientation.

Table1 Test parameters of different components of the PI film Table 2 The molecular chains spacing of PI/TiO₂ films

component	R_g/nm	R/nm	E/nm
7 wt.%	64	10.9	07
/ WL./0	0.4	10.7	0.7
15 wt.%	6.9	11.7	1.9
25 wt.%	7.0	11 9	21

2.3 Interface layer thickness in the composite film

Fig. 4 shows that with the components increases, the negative deviation enlarges. It is seen from Table 1 that when the components increases from 7 wt.% to 25 wt.%, the interface layer thickness increased from 0.7nm to 2.1nm, which means that when the component increases, the content of nano-particles in PI substrate increases and the average thickness of interface layer increases. When the component increases from 15wt.% to 25wt.%, the average thickness of the interface layer increases from 1.9nm to 2.1nm, the thickness of the interface layer reached a relatively stable value; Referring to the average size of radius particles in table 1, after the 15-25 wt.% component doping , nano-particle cluster phenomenon becomes more serious, the contact between nano-particles in cluster and the substrate reduces, which cannot effectively form the interfacial layer. When the group reaches 15 wt.%, the interface layer thickness tends to be stable and doesn't change with the increase of the component.

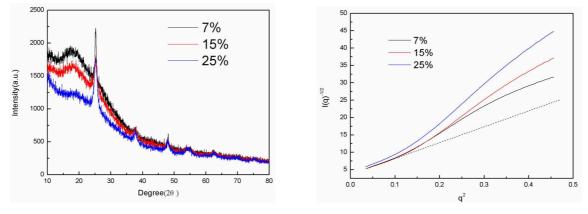


Figure 3 XRD curve of composite film

Figure 4 Debye curve of composite film

The experiment result shows that there are the interaction between polymer chains and inorganic nano-particles by anchoring effect^[10], which includes strong interaction and weak interaction. The weak interaction can cause extension of the molecule chains toward the matrix, and decrease the touch points with particle surface, it is the reason that molecule chains with circular ring type occur and form amount of interface zones. The strong interaction can bond by polymer functional groups

and particle surface activity in the middle, so that there are amount of contact points to form, and molecule chains form tightness interface layer in the particle surface. That the interaction between nano-particles and PI molecules forms interface region and tightness interface layer, dedicates the change tendency of interface layer thickness corresponds to the spacing of PI molecule chains.

3 Conclusions

The paper studied the data curves though analyzing the different components of PI/ TiO_2 film by SAXS. The result shows that:

1) The radius of TiO_2 in PI/ TiO_2 is almost 10nm. When the components increase 20 wt.%, the radius of $TiO_2(10nm)$ decrease 14%, the radius of $TiO_2(20-50nm)$ increase 14%.

2) As for PI/ TiO₂ film, with the components increase 20 wt.%, the PI molecular chain spacing decrease from 5.238 Å to 4.625 Å.

3) It can be founded the Interface layer in PI/ TiO_2 film, the thickness of interface layer is 0.7nm to 2.1nm. When the components reach 15 wt.%, the interface layer thickness becomes stable.

4) Compared the nano-particle dispersion, PI molecular chain spacing and interface layer thickness, it shows that when the component is 15 wt.%, the micro-structure of composite film is the optimal.

Acknowledgment

This article has obtained the support of the National Natural Science Foundation of China (51077028, 51307046) and Heilongjiang Natural Science Foundation of China (A201006). This work was supported by BSRF. This work was supported in part by the NSF of China (Grant No. 51307046).

References

- [1] Xiaoxu Liu, Jinghua Yin, Yunan Kong. Electrical and mechanical property study on three-component polyimide nanocomposite films with titanium TiO₂ and MMT[J]. Thin Solid Films. 2013, 544:(352-356)
- [2] Xiaoxu Liu, Jinghua Yin, Yunan Kong. The property and microstructure study of polyimide/nano-TiO2hybrid films withsandwich structures[J]. Thin Solid Films. 2013, 544:(54-58)
- [3] Zhiping S., Hui Z., and Yunhong Z. Polyimides: Promising Energy-Storage Materials[J]. Angew. Chem. Int. Ed.2010, 49(45):8444-8448.
- [4] W. WANG; X. CHEN; Q. CAI; G. MO; Z. J. CHEN, Nuclear Techniques, 2007, 30, 7, 571
- [5] Fuqiang T.,Qingquan L., Xuan W., Yi W., Effect of deep trapping states on space charge suppression in polyethylene/ZnO nanocomposite[J].Apppied Physics Letters, 2011, 99(14): 142903.
- [6] Tjong S.C. Structural and mechanical properties of polymer nanocomposites[J]. Materials Science and Engineering, 2006, 53(3-4):73-197.
- [7] Wang S.F., Wang Y.R., Cheng K.C and Hsaio Y.P, Characteristics of polyimide/barium titanate composite films[J]. Ceram. Inter, 2009, 35(1): 265-68.
- [8] Zhiping S., Terrence X., et al. Polymer–Graphene Nanocomposites as Ultrafast-Charge and-Discharge Cathodes for Rechargeable Lithium Batteries[J]. Nano Letters, 2011,12(5):2205-2211
- [9] Zhiping S., Hui Z., and Yunhong Z. Polyimides: Promising Energy-Storage Materials[J]. Angew. Chem. Int. Ed.2010, 49(45):8444-8448.
- [10] Minghua Chen, Jinghua Yin, Xiaoxu Liu. [J]. Thin Solid Films. 2013, 544:(116-119)

The Research of Trap Level Distribution of PI/AIN(treated)-MMT Films with Different Contents based on Decay Charge Theory

Liu Yuanyuan^{1,2, a}, Yin Jinghua^{1,3, b}, Lei Yao¹

¹Harbin University of Science and Technology, Harbin, China

²Harbin Cambridge College, Harbin, China

³Key Laboratory of Engineering Dielectric and Its Application Ministry of Education, Harbin, China ^aliuyuan1363@163.com, ^bYinjinghua1@126.com

Keywords: trap level distribution, AIN nanoparticle, decay charge, IDC

Abstract. Through the theoretical deviation based on charge decay theory a trap level distribution function relative to the isothermal discharge current is given in this paper. Based on that, the effect of AlN(treated)-MMT nanoparticles with different contents of 1wt%, 3wt%, 5wt% on surface trap level distribution is researched. The experimental results show that the trap level density is significantly increased compared with traditional IDC and TSC methods. Trap level density and the number of trap charges increase due to the doping AlN (treated)-MMT nanoparticles, and increase with doping contents. The maximum trap energy level density of AlN(treated)-MMT film with 5wt% is $9.14 \times 10^{24}/(eV \cdot m^3)$, which is 3.3 times compared with the PI film corresponding to the trap level in the range of $1.0 \sim 1.1eV$. The trap level density is affected by the interface trap effect caused by the AlN(treated)-MMT nanoparticles and different contents.

Introduction

Space charges and trap have important impacts on the charge transport of polymers. The investigation of trap effects on electric characteristics of conduction, ageing and breakdown of polymers based on nanocomposite, is of great practical significance and theoretical value ^[1]. It is important for charge transport of polymer to research depth and density of trap level. Isothermal discharge current method (IDC) and thermally stimulated current (TSC) with trap level density in the range of $10^{21} \sim 10^{23} \text{ eV} \cdot \text{cm}^3$ are common method on studying trap level distribution^[2]. Traditional IDC method has drawback caused by qualitative analysis and simulation, and TSC method is difficult to solve continuous energy level of polymer^[3]. This paper presents a modified isothermal discharge current method (MIDC) based charge decay theory used to study the trap characteristics of polymer matrix and form large amount of interfaces, it is the reason to form new traps. So, the MIDC method is also used to study trap level distribution of PI/AIN (treated)-MMT films with contents of 1wt%, 3wt%, 5wt%^[4]. The trap level density and number of trap charges of the nanocomposite films are given, and influence factors on trap level distribution are also discussed.

Experimental Details

PI/AIN-MMT nanocomposite films with AlN (treated)-MMT with contents of 1wt%, 3wt%, and 5wt% were prepared by in-situ polymerization method. MMT and AlN (in 1:1 ratio) inorganic composite particles were modified by coupling agent processing, where the diameter and purity of the AlN nanoparticles are 80 μ m and 99.9%, and the lamination thickness of the MMT is 25nm and its length is in the range of 2~5 μ m. The fabrication process of the films is shown in Fig.1.

After washing by acetone solution, the double surfaces of the samples were evaporated aluminum electrodes with diameter 4cm, and then treated by short circuit for 12h in the oven with constant temperature 150° C. After that, the samples treated were taken out to place in oven where temperature was increased to a constant temperature of 50° C. The sample was acted by constant DC electric field of 40kV/mm for polarization of 2h. And then, the sample is immediately short circuit, the IDC characteristic curves of the films with the thickness 100µm were measured by IDC test system, which is composed by high voltage DC source (DW-102-20f TYPE), EST122 pico-ampere ammeter and electrodes test box, as shown in Fig.2.

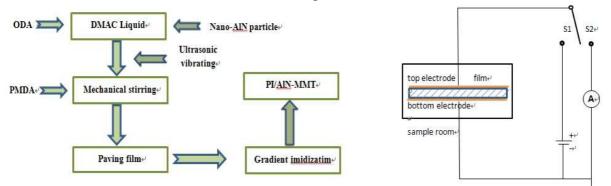
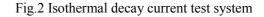


Fig.1 The fabrication process of the nanocomposite films



Theoretical Analysis

It is supposed that the interface potential barrier between metal and insulate material is ohmic contact for injected electrons, and is barrier for injected poles, which means that only the space charges and trap energy level of the electrons need to be studied. When the built-in electric field caused by the space charges in the material is enough high, all the electrons injected by isothermal decay can break away from the traps, and return to the cathode without trap again. Based on that, when it is the time t, the isothermal discharge current density caused by the electrons excited from the traps can be represented as the following^[5]

$$J_{n} = \frac{eL}{2} \int_{E_{F}}^{E_{c}} f_{0}(E) N_{t}(E) e_{n}(E) e^{-e_{n}(E)t} dE$$
(1)

where, $N_t(E)$ is the function of trap density distribution, L is the thickness of the sample, e is electronic charge, $f_0(E)$ is the probability of energy level E occupied originally by electrons, it is a constant for a certain amount of injected electrons, when the traps are full of electrons. d is the thickness of the sample. $e_n(E)$ is the probability of the electrons excited from $E_t = E - E_c (E_c)$ is the conduction band energy level) to conduction band, it is given as

$$e_n(E) = v \exp(-E_t / kT) \tag{2}$$

where k is Boltzmann Constant, ν is the escaping frequency of electrons in the range of $10^{12}s^{-1} \sim 10^{14}s^{-1}$. *T* is the absolute temperature for test. A function of $G(E,t) = e(E)\exp^{[-e(E)t]}$ is introduced to represent the weight of current density, which is caused by electrons released from traps at any time t and it should fit the following $\frac{\partial G}{\partial E}\Big|_{E=E_{\nu}} = 0$, where E_m is the energy level when *G* is extreme value. So the relation between the trap level distribution and time t is.

G is extreme value. So, the relation between the trap level distribution and time t is:

$$E_t = E_c - E_m = kT\ln(\nu t) \tag{3}$$

So, the constructor $G(E,t) = B\delta(E-E_m)$, $\delta(E-E_m)$ is impulse function. B is expressed as $B = \int_{E_v}^{E_c} G(E,t) dE$, when $t \to \infty$, $E_m \to E_F$, the temperatures are T_1 and T_2 corresponding to the time t_1 and t_2 , respectively, the escaping frequency v is 10^{12} s^{-1} [6]. So, $B \approx kT/t$, substitute B value into the Eq.(1) to integrate and apply the characteristics of impulse function, current density functions of electrons and poles are $J_n(t) = \frac{qLkT}{2t} f_0(E)N(E)$ and $J_p(t) = \frac{qLkT}{2t} (1-f_0(E))N(E)$, respectively. After that, combine the two equations, it is supposed that $f_0(E) = 1/2$, current density of the decay charges is

$$J(t) = \frac{qLkT}{4t}N(E)$$
(4)

According to $t = E_c - E_m = e^{\frac{E_c}{kT}} \cdot v^{-1}$, substitute the time t into the Eq.(4), the relation equation between the trap level density distribution and trap energy level can be given as

$$N(E) = \frac{qLkTv}{4J(t)}e^{-\frac{E_t}{kT}}$$
(5)

The Experimental Results and Discussion

When the films were acted by the constant DC electric field of 40kV/mm, respectively, Fig.4 (a) and (b) give isothermal decay current I-t characteristic curves of the PI, PI/AlN (treated)-MMT films with contents of 1wt%, 3wt%, 5wt% and their trap level distributions.

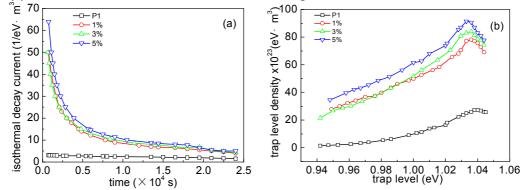


Fig.4 Curves of the PI film and PI/AlN (treated)-MMT nano-composite film with content of 5wt% for (a) isothermal decay current I-t characteristics and (b) trap level distribution

The experiment result shows that the IDC of the pure PI don't change with time, significantly, and its trap level density is $3.05 \times 10^{23}/(\text{eV} \cdot \text{m}^3)$ corresponding to the trap level in the range of $1.0 \sim 1.1 \text{eV}$ as the same as trap level measured by traditional IDC method^[7], but the trap level density is improved, significantly.

By comparing the IDC characteristics curves, the IDC current of PI/AlN (treated)-MMT film increases more than 5 times than IDC of the pure PI film in the beginning, and is also significantly high when the decay current reaches stability, furthermore, their stable state current also increases with the contents. The trap level densities of the PI/AlN (treated)-MMT films increase with contents of 1wt%, 3wt%, 5wt%, respectively, which has maximum trap energy level density of $9.14 \times 10^{24}/(eV \cdot m^3)$ and it is about 3.3 times compared with the one of the pure PI film. The trap level corresponding to their trap level density peaks is at 1.036eV.

According to the experimental results of the MIDC method, the trap level of the PI/AIN (treated)-MMT films lays in the range of 0.9eV and 1.1eV, and their trap level density increases with contents, and are closed to the factor of the order $10^{24}/(eV \cdot m^3)$ in the range of $10^{18} \sim 10^{25}/(eV \cdot m^3)$ of trap level density. Comparing with the traditional IDC results of the PI/AIN(treated)-MMT films with content of 5%, which has maximum trap level density of $7.8 \times 10^{21}/(eV \cdot m^3)$ at $1.04eV^{[7]}$, it can be found that the trap density is significantly improved by the MIDC method, but the trap level is closed. Based on the analysis of space configuration defects of polymer chains, there are amount of traps to occur in interface area of the polymer matrix inorganic nanocomposite dielectrics^[8], so the doping AIN(treated)-MMT leads to large amount of interface zones to form. Meanwhile, there are many polymer matrix with different action, density and free volume that can cause new traps to form and the trap charges increase in this interface area, which is caused by trap effect with the increase of contents.

Conclusion

A new isothermal decay current method is presented based on charge decay theory analysis, based on it the trap level density is significantly increased compared with traditional IDC method. Through the MIDC method, the effect of AlN (treated)-MMT nanoparticles with different contents of 1wt%, 3wt%, 5wt% on surface trap level distribution is researched. The experimental results show as following. 1) Due to interface effect caused by the doping, the trap level density changes with doping of the PI/AlN (treated)-MMT, and increases with doping contents compared with the PI film. 2) The maximum trap level density with 5wt% is $9.14 \times 10^{24}/(eV \cdot m^3)$, which is about 3.3 times compared with the PI trap level density of $2.74 \times 10^{24}/(eV \cdot m^3)$ in the range of $1.0 \sim 1.1eV$, but their trap levels are the closed. 3) Doping AlN(treated)-MMT nanoparticles with different contents causes amount of interfaces and decreases accumulation, the trap level density and the number of trap charges increase significantly.

Acknowledgment

This article has obtained the support of the National Natural Science Foundation of China (51077028, 51307046) and Heilongjiang Natural Science Foundation of China

References

- [1]B.X. Du, Jie Li and Wei Du. Surface Charge Accumulation and Decay on Direct-Fluorinated Polyimide/Al₂O₃ Nanocomposites[J]. IEEE Transactions on dielectrics and Electrical insulation,201220(5):1764.
- [2]Tian F., Bu W., Yang C., et al. A New Method for Direct Determination of Trap Level Distribution from TSC Measurement[C]. IEEE 9th International Conference on the Properties and Applications of Dielectric Materials, Harbin, China, 2009:980-983.
- [3]Qingquan L., Fuqiang T., Chun Y., et al. Modified Isothermal Discharge Current Theory and its Application in the Determination of Trap Level Distribution in Polyimide Films[J]. Journal of Electrostatics,2010, 68(3):243-248.
- [4]Fuqiang Tian. Investigation on the Trap Characteristics and Electrical Properties of Polyethylene Based Nanocomposite[D]. Beijing jiaotong university, 2012.42.
- [5]Wang Xia, Chen Shao-qing, Cheng xian, Tu De-min. Measuring Energy Distribution of Surface Trap in Polymer Insulation by PEA Method[J]. Proceedings of the CSEE,2009.29(1):128.
- [6]Tian F., Bu W., Shi L., et al. Theory of Modified Thermally Stimulated Current and Direct Determination of Trap Level Distribution[J]. Journal of Electrostatics, 2010, 69(1):7-10.
- [7] Bu W. Preparation and Dielectric Properties of PI/(AlN+MMT) Nanocomposite Film[D]. Harbin university of science and technology, 2012.76-77.
- [8]Tanaka T., Kozako M., Fuse N., et al. Proposal of a Multi-core Model for Polymer Nanocomposite Dielectrics[J]. IEEE Transactions on Dielectrics and Electrical Insulation, 2005, 12(4):669-681.

PIC/MCC SIMULATIONS FOR THE OXYGEN MICROWAVE BREAKDOWN AT ATMOSPHERIC CONDITIONS

Huihui Wang, Dagang Liu, Laqun Liu, Lin Meng

School of Physical Electronics, University of Electronic Science and Technology of China, Chengdu, China

Keywords: Particle-In-Cell; Monte Carlo collision; Microwave breakdown

Abstract. In this paper, the code of Particle-In-Cell/Monte Carlo Collision (PIC/MCC) for oxygen microwave breakdown is developed. This code is based on the three dimensional particle-in-cell platform CHIPIC, and with a module for increasing the charge of each super-particle. With this PIC/MCC code, the multiplication rate of the electron density and the delay time in oxygen breakdown at atmospheric conditions are researched. The results show: the multiplication rate of the electron density is periodic, and its period is the half of the electric field period; the breakdown delay time in the gas breakdown increases while the frequency of electric field or the gas pressure increases.

I. Introduction

Microwave discharge has extensive application, such as high power microwave propagation, surface treatments, biomedical application [1-6]. Recently, many scholars focus on the atmospheric pressure discharge because it do not need the large vacuum apparatus. Sometimes, the discharge gas is taken from the atmospheric directly which makes the practical application of the discharge more easily. And oxygen is the main composition of the atmosphere. Therefore, it is meaningful to figure out the property of the oxygen discharge.

The Particle-In-Cell/Monte Carlo Collision (PIC/MCC) method is one of the most valid method to simulate the gas discharge, and its accuracy is high. However, the calculation amount of PIC/MCC is very much which makes the simulation difficult. Fortunately, the boost of computers performances makes it possible to take PIC/MCC simulations. In recent decades, many scholars begin to focus on PIC/MCC simulations for gas discharges [2-3, 7-10].

In the beginning of gas discharges, the charge density grows explosively, and would signally affect the electric magnetic field eventually. This process is called gas breakdown. Ref.[5] adopted the fluid model to simulate the argon breakdown, and Ref.[11] studied the atmosphere pressure breakdown by theory and experiments. Recently, based on the PIC platform CHIPIC [7-9, 12], we developed a PIC/MCC code to simulate the argon microwave breakdown [13]. In this paper, this PIC/MCC code is introduced and enhanced in order to simulate the oxygen breakdown near the atmospheric pressure. With this code, we simulate the multiplication speed of electrons and the breakdown times at atmospheric conditions for oxygen.

II. PIC/MCC algorithm for breakdown

The PIC/MCC scheme for electric breakdown is showed in Fig.1. In the PIC/MCC simulations for oxygen, elastic collisions, ionization collisions, attachment collisions and some kinds of excitation collisions are considered, and the cross sections of collisions used for simulations are taken from Ref. [14].

The algorithms of these collisions are taken from Ref. [15]. After the elastic collision, the direction of electron scattering velocity can be expressed by Eq.(1).

$$\frac{\mathbf{v}'}{|\mathbf{v}|} = \frac{\mathbf{v}_{inc}}{|\mathbf{v}_{inc}|} \cos \chi + \left(\frac{\mathbf{v}_{inc}}{|\mathbf{v}_{inc}|} \times \mathbf{i}\right) \frac{\sin \chi \sin \varphi}{\sin \theta} + \frac{\mathbf{v}_{inc}}{|\mathbf{v}_{inc}|} \times \left(\mathbf{i} \times \frac{\mathbf{v}_{inc}}{|\mathbf{v}_{inc}|}\right) \frac{\sin \chi \cos \varphi}{\sin \theta}$$
(1)

where $\cos \chi$ is $[2+\varepsilon-2(1+\varepsilon)^R]/\varepsilon$, ε is the electron energy, φ is a uniform random number between 0 and 2π , θ is the angle between v_{inc} ands x axis direction, and v_{inc} and v' are incident velocity and scattering velocity, respectively. Besides, the amplitude of electron scattering velocity can be obtained by the energy of scattering electron which is a little less than that of the incident electron. After the excitation collision or the ionization collision, the direction of electron velocity can also be presented by Eq.(1), but the electron energy is different. For the excitation collision, the energy is reduced by the excitation collision threshold. After the ionization collision, one incident electron becomes two electrons. Therefore, besides the energy loss of the ionization collision, the attachment collision is completely different. When the attachment collision happens, the incident electron just die out without any new electrons.

When the breakdown happens, the density of electrons increases explosively. The final density is larger than 10^8 times of initial density.[10] If the charge Q of each super-particle is fixed, the number *Ns* of super-particles would become too much to simulate. In Ref.[13], We put forward a algorithm to increase Q during the simulation. This algorithm is showed in Fig.2.

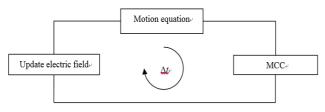


Fig. 1 PIC/MCC diagram

lr and *er* are parameters for users to adjust. *lr* is the upper limit value of N_s , and the *er* is the rate of die out super-particles. The idea of this algorithm is to increase Q by dying out a few super-particle randomly in a very low probability. The expectation of Q is expressed by Eq.(2), and the variance is expressed by Eq.(3)

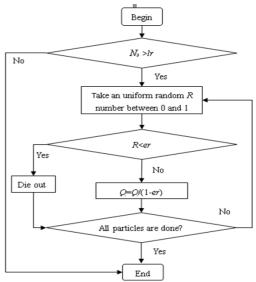


Fig. 2 Flow diagram of the Q increasing algorithm

$$E(Q_{after}) = 0 \times \varepsilon + \frac{Q_{before}}{1 - \varepsilon} \times (1 - \varepsilon) = Q_{before}$$
⁽²⁾

$$\delta(\mathcal{Q}_{after}) = \sqrt{\left[0 - E(\mathcal{Q}_{after})\right]^2 \varepsilon + \left[\frac{\mathcal{Q}_{befpre}}{1 - \varepsilon} - E(\mathcal{Q}_{after})\right]^2 (1 - \varepsilon)} = \sqrt{\frac{\varepsilon}{1 - \varepsilon}} \mathcal{Q}_{befpre}$$
(3)

Assuming that the number of the super-particles is its upper limit lr, we obtain the expectation of the total charge q expressed by Eq.(4) which shows the total charge is unchanged in statistics in this algorithm.

$$E(q_{after}) = lr E(Q_{after}) = lr Q_{before} = q_{before}$$
(4)

According to Eq.(3), the variance of the total charge q is obtained by Eq.(5). This algorithm is valid only if the variance is much less than the expectation. Eq.(6) shows that this condition is satisfied when lr is large enough and er is small enough. In the simulations of this paper, we take lr=50000 and er=0.01.

$$\delta(q_{after}) = \sqrt{lr\delta^2(Q_{after})} = \sqrt{\frac{\varepsilon}{lr(1-\varepsilon)}(lrQ_{befpre})^2} = \sqrt{\frac{\varepsilon}{lr(1-\varepsilon)}}q_{befpre}$$
(5)

$$\frac{\delta(q_{after})}{E(q_{after})} = \sqrt{\frac{\varepsilon}{lr(1-\varepsilon)}}$$
(6)

(In Section II, the subscript "before" means the physical quantity is before the module of the Q increasing algorithm, while the subscript "after" means the physical quantity is after the module of the Q increasing algorithm.)

III. Simulation results

The simulation of breakdown are carried out under a parallel plate. The gap between cathode and anode is 10mm, the voltage between cathode and anode is $V=42.3\sin(2\pi ft)kV$ (*f* is frequency and *t* is time), and the gap is filled with oxygen.

Firstly, the simulations are conducted under the condition of 500torr oxygen, and the electron transverse velocity with a 10GHz electric field is shown by Fig. 3. The multiplication speed of electrons with the 5GHz, 10GHz, 30GHz electric field are presented in Fig. 4, which shows that the multiplication speed is periodical and its period is half of the electric field. This phenomenon is consistent with the periodical electric field power, which is showed by Eq.(7) [16].

$$P_{E} = \frac{2e^{2}E_{rms}^{2}}{m} \frac{v_{m}}{(\omega^{2} + v_{m}^{2})} \left[\frac{1 - \cos 2\omega t}{2} - \omega/(2v_{m}) * \sin 2\omega t\right]$$
(7)

where P_E is electric field power, $E_{\rm rms}$ is the root-mean-square electric field, ω is $2\pi f$, v_m is the collision frequency.

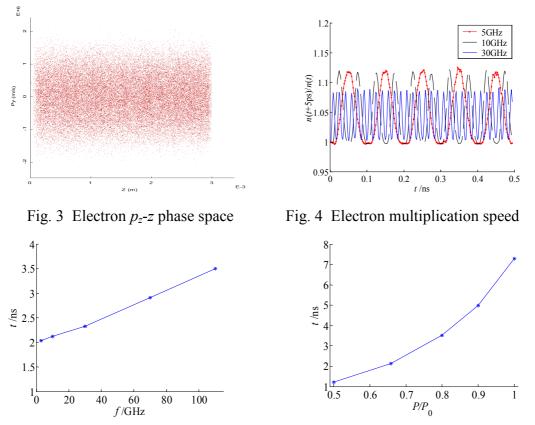


Fig. 5 Breakdown time vs. frequency at 500Torr Fig. 6 Breakdown time vs. pressure at 10GHz

Fig. 5 presents the relations between the breakdown time and electric field frequency with 500torr oxygen, which shows that the breakdown increases while the frequency increases. The average electric field power P_{Eav} can be obtained from Eq.(7).

$$P_{Eav} = \frac{e^2 E_{rms}^2}{m} \frac{v_m}{(\omega^2 + v_m^2)}$$
(8)

From Eq.(8), it is apparent to find that the increase of frequency decreases the electric field power. This is the reason why the ability of breakdown decreases while frequency increases. The results is also consistent with the results in Ref.[10].

Fig. 6 presents the relations between the breakdown time and the oxygen pressure with the frequency 10GHz and the electric field amplitude 42.3kV/cm, where P_0 represents the standard atmospheric pressure. Fig.6 shows that the breakdown time increases when the pressure increases.

Eq. (8) shows that the increase of v_m decreases P_{Eav} while v_m is larger than ω . With the atmospheric pressure and 10GHz frequency, v_m is much larger than ω . And v_m increases when pressure increases [11]. Therefore, the increase of pressure decreases P_{Eav} . Furthermore, the increase of pressure also increases the excitation collision frequency and leads to the increase of the energy loss. These may be the reasons why the ability of breakdown decreases while the pressure increases.

IV. Conclusion

The PIC/MCC algorithm for microwave breakdown is introduced. In this paper, the attachment collision and more kinds of excitation collisions are also considered for oxygen breakdown, while our previous work for argon breakdown [13] only considers the elastic collision, the ionization collision and one kind excitation collision. This PIC/MCC code, based on PIC platform Chipic, is adopt to simulate oxygen microwave breakdown at atmospheric conditions. Besides the simulations, we also qualitative analyze the breakdown discharge by previous theory [16]. The simulations show: the multiplication speed of electrons is periodical, and its period is half of the electric field period, the breakdown increases while the frequency increases, and the breakdown increases while the pressure increases. These simulation results are consistent with that of the theoretical analysis.

Acknowledgment

This paper is supported by the National Natural Science Foundation of China (Grant No.11175040)

References

- [1] Y. M. Yang, C. W. Yuan, and B. L. Qian, *Physics of Plasmas*, **19** 122101 (2012)
- [2] H. C. Kwon, I. H. Won, and J. K. Lee, Applied Physics Letters, 100 183702 (2012)
- [3] F. Iza, J. K. Lee, and M. G. Kong, Phys. Rev. Lett., 99 075004 (2007)
- [4] G. J. Kim, W. Kim, K. T. Kim, and J. K. Lee, Appl. Phys. Lett., 96 021502 (2010)
- [5] P. C. Zhao, C. Liao, D. Yang, X. M. Zhong, and W. B. Lin, Acta Phys. Sin., 62 055101 (2013)
- [6] H. H. Wang, L. Meng, D. G. Liu, and L. Q., Physics Letters A 378 810 (2014)
- [7] C. Yang, D. G. Liu, X. M. Wang, L. Q. Liu, X. Q. Wang, and S. G. Liu, Acta Phys. Sin., 61 045204, (2012)
- [8] H. H. Wang, D. G. Liu, L. Meng, L. Q. Liu, C. Yang, K. Peng, and M. Z. Xia, Acta Phys. Sin., 62 015207 (2013)
- [9] H. H. Wang, C. Yang, D. G. Liu, L. Meng, L. Q. Liu, and M. Z. Xia, Acta Phys. Sin., 62 015206, (2013)
- [10] S. K. Nam, and J. P. Verboncoeur, Applied Physics Letter, 93 151504 (2008)
- [11] G. Z. Liu, J. Y. Liu, W. H. Huang, J. S. Zhou, X. X. Song, and H. Ning, *Chinese Physics B*, 9 757 (2000)
- [12] J. Zhou, D. Liu, C. Liao, and Z. Li, IEEE Trans. Plasma Sci., 37 2002 (2009)
- [13] H. H. Wang, L. Meng, D. G. Liu, and L. Q. Liu, Phys. Plasmas, 20, 122102 (2013)
- [14] Y. Itikawa, J. Phys. Chem. Ref. Data, 38 1 (2009)
- [15] V. Vahedi, M. Surendra, Computer Physics Communications, 87 179 (1995)
- [16] L. Gould, L. W. Roberts, Journal of Applied Physics, 27 1162 (1956)
- [17] J. T. Krile, A. A. Neuber, H. G. Krompholz, and T. L. Gibson, *Applied Physics Letters*, 89 201501 (2006)

The Preparation of Alq₃/CuPc Heterojunction Organic Electroluminesence Diodes

Yanhong Wu^a, Yue Shan, Dongxing Wang, Caimin Meng, Yanwei Yang,

Jian Fu, Shikun Deng

Department of Electronic Science and Technology, College of Applied Science, Key Laboratory of Engineering Dielectrics and Its Application, Ministry of Education Harbin University of Science and Technology, Heilongjiang Harbin 150080, China

^a1712795252@qq.com

Keywords: organic electroluminescent; phthaleincyanide copper; quinoline aluminum; the device performance

Abstract. With the method of vacuum dc sputtering and vacuum evaporation, the green light double organic light-emitting devices (OLED) of ITO/CuPc/Alq3 / Al structure were prepared, the electrical characteristics and electroluminescent properties of the device were measured. Devices show good luminous performance, light intensity reaches 600000 cps, when the wavelength of luminescence spectrum is 510 nm, luminance is 2641I/a.u.

Introduction

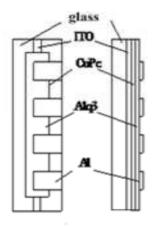
In recent years, organic electroluminescent has had great development, there are trends to replace liquid crystal display devices fully or partially. The brightness, the efficiency and lifetime of the devices have greatly improved, and they are basically close to the practical level. After recent years of research, many luminescent materials were synthesized. Now the double structure of electroluminescent device studied by most people is mostly ITO/PS: NPB/ Alq₃ / Mg: Al structure [1, 2], ITO/TPD/Alq3 / Al structure [3,4].

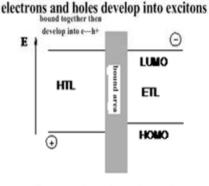
The theme of this paper is trying using the ITO/CuPc/Alq₃ / Al structure to prepare organic light emitting devices. The device is formed by CuPc and Alq₃ heterojunction, and its luminescence and electrical performance was measured and analyzed. The main purpose is to investigate whether the device of this structure has good luminescence and electrical performance or not.

Device Structure and Operating Principle

This device prepared in this experiment is ITO/CuPc/Alq₃ / Al double layer structure, as shown in figure1.

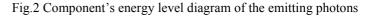
Where the CuPc is deposited as holes injection layer, Alq₃ is used as electron transport layer and the light emitting layer. ITO is used as anode of the device, Al is the cathode. When applying voltage to the device, the electrons and holes are respectively injected from the cathode and anode, when electrons and holes meet in the heterojunction barrier area, because of the coulomb force, they are bounded together and form excitons. This process of the forming excitons is different from that of forming the excitons under optical excitation, and the results are also different. Under optical excitation, the electrons and holes are produced at the same time and bound together, so the two spin states maintain the ground state, they are antiparallel, thus forming the singlet excitons. While the spins of electrons and holes injected at the electrode are random, they may be antiparallel or parallel when the two recombine; formed excitons may be the singlet, or the triplet. After exciton pairs moving to the right place in organic layer, they recombine, that is the recombination of electrons and holes, forming a bond orbital. The own energy of the exciton pairs can release in the form of radiation or radiationless. The part which releases in the form of radiation is luminescence. In organic electroluminescent devices, the injected carriers recombine to form the exciton pairs, then release luminescence. Figure 2 is the principle diagram of the light-emitting device [5].





Some excitons bound together

Fig. 1The structure of device



Experiment

Alq₃ and CuPc of 99.995% purity used in this experiment were purchased from SIGMA - ALORICH Company, ITO target of 99.99% purity, InO₃-10%SnO₂ were purchased from Beijing Union Tianrui Technology Development Center.

Before preparing the OLED devices, biological glass is cleaned using acetone solution, ethanol solution, deionized water and ultrasonic each for 10 minutes in order. First, dc sputtering method is applied to plant ITO strip electrode on biological glass; CuPc is prepared with the method of vacuum evaporation at 350 °C in organic chamber; Alq₃ is also prepared with the method of vacuum evaporation at 220 °C .Vacuum dc sputtering method is applied to prepare several aluminum electrodes. The atomic force microscope (AFM) image of CuPc surface is shown in figure 3.

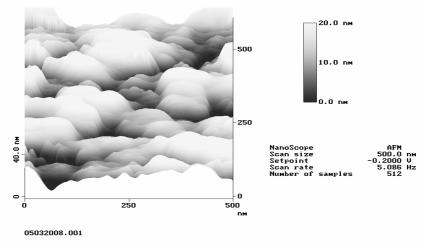


Fig.3 The AFM image of CuPc surface

In order to avoid damaging organic membrane in the process of sputtering, the discontinuous preparation method is applied in the preparation of Al electrodes. The whole sputtering process is divided into three time quantums to complete. The structure of organic devices prepared in this way is clear, its membrane layer's damage is smaller, and the damage to the performance of the devices is less.

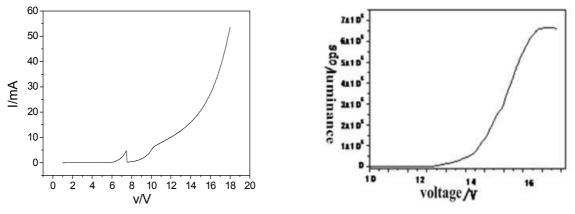
Results and Discussion

Electrical performance of the device is measured using the KEITHLEY - 4200 semiconductor characteristic analysis system, optical properties are measured using the electroluminescent equipment. Through testing I - V characteristics, spectrum and other characteristics of the device, we

found that the device we made has the typical rectification characteristics and luminescence properties of diodes, its positive light emitting threshold is around 12 V, and its luminous color is green. When applying reverse voltage to the device, reverse phase insulation of the device is good, and the device is non-luminance.

Figure 4 is I - V characteristic curve when applying 1 to 18 V positive phase voltage to the device. Where the device is applied positive scanning voltage, ITO connecting the anode, Al connecting the cathode. When voltage continue to rise, the current has a steep fall process at around 8 V, Ligong Zhang and some other people think that Alq₃ molecules have some changes of position or state when a large number of electrons and holes are injected and under the action of a high field, producing the trapping center of electrons and holes, so that the current declines greatly, and capture center may tend to occur on the Alq₃ layer interface of both sides, thus forming self-built field, film will show the rectifier features and injection luminescence[6]. Then the current grows almost linearly, and achieves 55 mA at 18 V. It has the rectification effect, which is similar to the relationship between the current density and voltage of light-emitting diodes (LEDs). It means that there is current just under the positive voltage. Under low voltage, electric current density increases slowly with increasing voltage. When it is higher than a certain voltage, current density will increase sharply. The total current of organic of light-emitting diodes (OLEDs) is composed of two parts: current of nonrecombined electrons and holes, and current of recombined electrons and holes. We can respectively name them the leakage current and the recombination current of the device. The relationship of recombined current is similar to current and voltage characteristic curve of the inorganic diode. While the leakage current performance is like current and voltage curve of pure resistance. We can know from the figure that the device's current is mainly composed of recombined current.

Applying positive voltage to the device, we measured the light intensity curve of device [7, 8] using the light intensity instrument, as shown in figure 5.



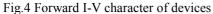
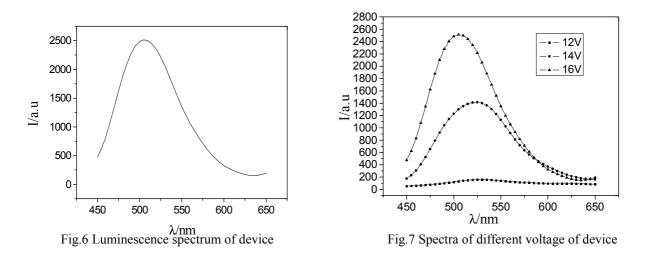


Fig.5 Luminance-voltage curves of the devices

We found that the current increases with the continuous increase of voltage. At around 12 V, devices begins to glow, then the light intensity increases continuously with increasing voltage. When the applied voltage increases to a certain extent, the increase of luminous intensity slows down and tends to be saturated. Figure 5 shows illumination intensity. We got the luminescence spectrum of device in the process of device emitting, as shown in figure 6. We can see the spectral peak is about 510 nm from the graph, and it is almost unanimously with electroluminescent spectra of single-layer Alq₃ light-emitting device. The device emitting only exists in Alq₃ layers. In the multilayer devices, operation current can also affect the recombination area of the carriers. In general, when the operation current is small, the carriers recombination probability is large in the HOMO and LUMO with small energy level gap. With the increase of operation current, the excitation density (operation current has an effect on recombination area of the device. In general, the excitation density (operation current) is large, recomination light emitting area of the device moves to the luminous color group of the HOMO and LUMO with large energy level gap. In this device, energy level gap of Alq₃ is larger, so the recombination area occurs in Alq₃ layer.



Under different voltages scanning different spectrums, under the circumstances that light intensity and voltage are different, the spectral peak is different. We got different spectrum curves under different voltages, the spectral peak is rising with the voltage increasing, from luminescence spectra under the voltage of 12, 14, 16 V, we can see that, light emitting spectra of luminous intensity increases with increasing voltage, but light emitting peak do not change, that means the relative light intensity of device is proportional to the applied voltage, as shown in figure 7.

Conclusion

We prepared the light emitting diode with of structure $ITO/CuPc/Alq_3$ / Al, the testing results show that it has good luminescence properties, light-emitting occurs only in the 8-hydroxyquinoline aluminium layer, it has nothing to do with the phthalocyanine copper layer. Phthalocyanine copper only plays a role of the auxiliary of carrier's injection or forming the stopping barrier. Device has the advantage that the structure is easy to be prepared and it has high luminous intensity, etc.

References

- [1] Tang C W, Van Slyke S A: Appl. Phys. Lett., Vol. 51(1987), p.913
- [2] M. G. Kane, J. Campi, M. S. Hammond: IEEE ELECTRON DEVICE LETTERS, Vol. 21(2000), p.534
- [3] Hisahiro Sasabe, Hiromi Nakanishi, Yuichiro Watanabe, Shogo Yano, Masakatsu Hirasawa, Yong-Jin Pu, Junji Kido: Advanced Functional Materials, Vol. 23(2013), p.5550
- [4] Serkan Zorba and Yongli Gao: Appl. Phys. Lett., Vol. 86(2005), p.193508
- [5] Jana Zaumseil, Kirk W. Baldwin, and John A. Rogers: JOURNAL OF APPLIED PHYSICS, Vol. 93(2003), p.6117
- [6] Shiu-Lun Lai, Wai-Yip Tong, Steven C. F. Kui, Mei-Yee Chan, Chi-Chung Kwok, Chi-Ming Che: Advanced Functional Materials, Vol. 23(2013), p. 5167(In Chinese)
- [7] Jiaqi Lin,Zhibai Zhong,Caixia Li etc: Journal of materials research, Vol. 20(2006), p.38(In Chinese)
- [8] Chaoyu Xiang, Wonhoe Koo, Franky So, Hisahiro Sasabe, Junji Kido: Light: Science & Applications, Vol. 74(2013), p.1038

Solute Field in Liquid Ahead of The Solid-liquid Interface During Dendritic Solidification Incorporating Relaxation Effect

Xiangzhong Jin¹, Hongyang Wang¹, Ning Wang¹, Xiaoguang Lan¹

and Shu Li^{1,a}

¹College of Applied Science, Harbin University of Science and Technology, Harbin, Heilongjiang 150080, People's Republic of China

^alishu@hrbust.edu.cn

Keywords: Rapid solidification; Dendritic growth; Solute trapping; Diffusion; Modelling

Abstract. Through solving an extended Fick's diffusion equation for the solidification front of a paraboloid of revolution, a generalized Ivantsov function is obtained. The relaxation effect of nonequilibrium liquid diffusion is taken into account. The solute profile in the interfacial region and in the bulk liquid during steady-state dendritic solidification is uniquely determined. It is concluded that the consideration of the relaxation effect and the diffuse interface of finite thickness which decreases with increasing of velocities are necessary for achieving the good model predictions.

Introduction

Modelling of solute field plays an important role in achieving predictions of the solute segregation, the morphological stability of solid-liquid interface, the migration velocities of grain boundary and phase interface, etc., in various models. A number of theoretical frameworks have been developed to describe the solute trapping; these include sharp interface methods, phase field theories, and diffuse interface approaches with solute drag treatment.

A general model of solute drag on grain boundary and phase interface migration in binary alloys was proposed by Hillert and Sundman (H-S model) [1], based on the theoretical treatments of dilute solute drag on moving grain boundary. The solute drag approach not only considers an interface of finite thickness, but also adopts relatively simple mathematical expressions. Further, Li et al. introduced the relaxation effect of nonequilibrium liquid diffusion into the H-S model to describe the complete solute trapping at finite velocities [2]. The interfacial temperature and velocity, however, do not uniquely determine the partition coefficient k in this model. More information needs to be given about C_s^* or C_L^* (C_s^* and C_L^* are the solute concentrations of solid and liquid at the interface, respectively). During steady state solidification with planar front migration, C_s^* is simply equal to the nominal (initial) solute concentration in the system, C_0 . During dendritic solidification, however, a relation between C_s^* and C_L^* should be determined by the field of local nonequilibrium diffusion in bulk liquid.

In the present, we solved an extended Fick's diffusion equation, developed by Galenko and Danilov [3], and obtained an extended relationship between C_s^* and C_L^* . This result can reduce to that derived by Ivantsov, under the condition that the relaxation effect is neglected. Finally, the composition profile through the interfacial region, as well as in the bulk phases, is determined by combining the present model and the extended H-S model developed by Li et al [2].

Model

During steady state solidification in melts of binary alloys, a model with the following characteristics is examined: an isothermal system with a solid-liquid interface of finite thickness is under study; the interface is isosolutal and exhibits a dendritic morphology with a paraboloid of

revolution (near the tip) or a planar phase boundary; solute-solvent redistribution via interdiffusion of the two species across the interface is considered; and diffusion in solid, convection in liquid and sidewise diffusion in front of the dendrite tip are negligible. Based on the last assumption, the solid phase has a constant solute concentration.

When the interfacial migration velocity V is equal to or larger than the solute diffusion velocity in bulk liquid $V_{\rm D}$, complete solute trapping occurs $(C_{\rm L}^* = C_{\rm S}^*)$ and the diffusion flux at the phase boundary in the liquid side $J|_{\eta=1}=0$. This boundary condition leads to the solute field is homogenous and thus $C = C_{\rm L}^* = C_0$ at arbitrary position in bulk liquid. Thus, in the present, we focus on the condition $V < V_{\rm D}$. Considering the relaxation effect, Galenko extended the classical Fick's diffusion equation [3] in Cartesian coordinate system (x, y, z'). In this equation an interface moving with a constant V in the z(z')-direction is assumed and a conversion z' = z - Vt is adopted (fix the reference frame on the moving interface). It is convenient to adopt the parabolic coordinate system: $\sigma = \sqrt{-z' + \sqrt{x^2 + y^2 + z'^2}}$, $\tau = \sqrt{z' + \sqrt{x^2 + y^2 + z'^2}}$, $\phi = \arctan \frac{y}{x}$. Then the

steady state diffusion equation in parabolic coordinate is given by

$$\frac{\partial^2 C}{\partial \tau^2} + \left(\frac{2}{\tau \psi} - \frac{1}{\tau} + \frac{V\tau}{D_{\rm L}\psi}\right) \frac{\partial C}{\partial \tau} = 0.$$
(1)

where $D_{\rm L}$ is the liquid diffusion coefficient and $\psi = 1 - V^2 / V_{\rm D}^2$. Above equation is easily solved by the ansatz ($\sqrt{R} < \tau < \infty$, *R* is tip radius of curvature):

$$C(\tau) = A_0 + B_0 \int_{\tau}^{\infty} x^{1-\frac{2}{\psi}} e^{-\frac{Vx^2}{2D_L\psi}} dx.$$
 (2)

The constants A_0 and B_0 can be determined by the boundary conditions, $C(\infty) = C_0$ and $C|_{\tau=\sqrt{R}} = C_L^*$, as well as transport balance of solute. Substituting the values of the constants A_0 and B_0 determined into Eq. (2) gives the solute concentration profile along z' axis (x, y = 0 and $R/2 < z' < \infty$). From the profile C(z'), C_L^* at the interface (z' = R/2) can be obtained as follows:

$$C_{\rm L}^* = \frac{C_0}{1 - (1 - k) \, \mathrm{Iv}_{\rm R}(P_{\rm c})} \,.$$
(3)

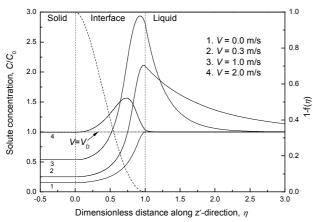
where $P_{\rm c}$ is solute Peclet number and the function $Iv_{\rm R}(P_{\rm c})$ is defined by

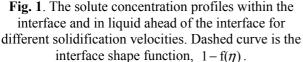
$$Iv_{R}(P_{c}) = \frac{1}{\psi} \int_{P_{c}}^{\infty} \left(\frac{P_{c}}{s} e^{P_{c}-s}\right)^{\frac{1}{\psi}} ds .$$
(4)

The function $Iv_R(P_c)$ reduces to the Ivantsov function $Iv(P_c)$ at $\psi = 1$ and then Eq. (3) reduces to Ivantsov's result. Computation shows that at a given P_c the value of the function $Iv_R(P_c)$ decreases with increasing of velocities V (i.e., with decreasing of ψ). And thus the solute concentrations C(z') and C_L^* decrease with increasing of velocities V at a given C_s^* . Therefore, the relaxation effect of the nonequilibrium liquid diffusion has been introduced into the present model.

Model predictions and discussion

The Si-As system is selected to make model predictions. Model predictions for different parameters during dendritic solidification are shown in Fig. 1 and Fig. 2. The relevant parameters can be found in reference [2].





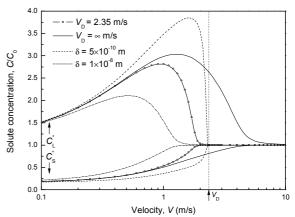


Fig. 2. The solute concentrations as a function of the interface velocity. For curves marked by $V_{\rm D} = 2.35$ m/s and $V_{\rm D} = \infty$, the interface thickness $\delta = 3.5 \times 10^{-9}$

Fig. 1 shows the solute concentration profiles in regions of the solid, interface and liquid for different interface velocities, $0 \sim V_D$, along the direction normal to the interface. The interface shape function $1 - f(\eta)$ is also illustrated, which corresponds to the variable ϕ in phase field models. The diffuse interface and the relaxation effect can be found in this figure. At $V = V_D$, the constant solute concentration, which equals to C_0 , indicates that complete solute trapping occurs due to the relaxation effect. At V = 0, from the mass conservation law for steady state solidification, $J = V(C(\eta) - C_s^*)/V_m$, the diffusive flux J = 0. As a boundary condition of the solute diffusion in bulk liquid, it leads to that the gradient of the solute concentration in bulk liquid disappears and thus $C_L^* = C_0 = 0.09$ (mole fraction). Therefore, the present model gives $C_s^* = 0.0138$ (mole fraction) and k = 0.153.

In contrast, the equilibrium solute concentrations for solid and liquid phases are 0.0379 and 0.372 in mole fraction, respectively, at 1420 K from the equilibrium phase diagram. The corresponding equilibrium partition coefficient $k_e = 0.102$. It indicates that local thermodynamic equilibrium could not be reached even though at V = 0 for Si-9 at.% As alloys during dendritic solidification. Similar predictions are also given by the non-dilute version of CGM [4] and Galenko's solute trapping model. The obvious feature of these models including the present model is that solute partitioning is also influenced by the self of the solute concentrations C_s^* and C_L^* except for the interface temperature T_I and interface velocity V. Thus, T_I and V can not uniquely determine the partition coefficient k and other factors, which influence C_s^* and C_L^* , need to be taken into account. These factors are such as the nominal composition of alloys C_0 , the interface morphology and the solute diffusion in bulk liquid ahead of the interface. Therefore, the present model gives a nonequilibrium partition coefficient k = 0.153 at V = 0 for Si-9 at.% As alloys during dendritic solidification.

In Fig. 1, it is also indicated that $C_{\rm L}^*$ increases from C_0 to its maximum and then decreases to C_0 as V increases from 0 to $V_{\rm D}$, while $C_{\rm S}^*$ monotonically increases to C_0 at $V = V_{\rm D}$. This phenomenon is more clearly shown in Fig. 2 (see the curve marked by $V_{\rm D} = 2.35$). As a comparison, the curve marked by $V_{\rm D} = \infty$ corresponds to the condition that the relaxation effect is neglected. At low velocities the influence of the relaxation effect is negligible. However, a remarkable discrepancy appears at high velocities. This implies that when the crystal growth velocity is of the order or even greater than the solute diffusive speed $V_{\rm D}$, the relaxation effect is not negligible.

In order to analyze the influence of the interfacial thickness δ on the solute partitioning, $C_{\rm s}^*$ and $C_{\rm L}^*$ as a function of V for different δ are also computed (Fig. 2). It is concluded that the behavior of solute partitioning is sensitive to δ . The parameter δ corresponds to the parameter $V_{\rm DI}$, the interfacial solute diffusive speed, in sharp interface models. Unfortunately, the experimental data of δ or $V_{\rm DI}$ are absent and they are used as fitting parameters in practice. In Fig. 2, however, there exists a qualitative relationship that the thicker the interface, the more difficult the solute redistribution.

Summary

An extended solute trapping model, which takes into account the diffuse solid-liquid interface and the relaxation effect of nonequilibrium liquid diffusion, is developed, based on Hillert-Sundman model with solute drag treatment. The interface temperature T_1 and interface velocity V can not uniquely determine the partition coefficient k in the present model. Therefore, the nominal composition of alloys, the interface morphology and the solute diffusion in bulk liquid are considered. Solving an extended Fick's diffusion equation for the solidification front of a paraboloid of revolution, which takes into account the field of local nonequilibrium diffusion, determines the generalized Ivantsov function. Finally, the composition profile through the interfacial region, as well as in the bulk phases, is obtained. A prediction is also given that local thermodynamic equilibrium could not be reached in the interfacial region even though at V = 0 for dendritic solidification. It is demonstrated that the present model is applicable to non-dilute alloys and can provide more accurate predictions. It is concluded that the relaxation effect should be considered.

Acknowledgments

The authors acknowledge the support of innovative and entrepreneurial training program for college students (Harbin university of science and technology). Shu Li acknowledges the support of National Natural Science Foundation of China (NO: 51101046), China Postdoctoral Science Foundation funded project (NO: 2012M511506).

References

- [1] M. Hillert and B. Sundman: Acta Metall. Vol. 24 (1976), p. 731.
- [2] S. Li, J. Zhang and P. Wu: Scripta Mater. Vol. 62 (2010), p. 716.
- [3] P.K. Galenko and D.V. Danilov: Phys. Lett. A Vol. 272 (2000), p. 207.
- [4] M.J. Aziz and T. Kaplan: Acta Metall. Vol. 36 (1988), p. 2335.

Study on Preparation and Refining Efficiency of AI-5Ti-1C Master Alloy Refiner

Fuiwei Kang^a, Yu Xiong, Xin Bai, Dongdong Zhang, Peng Liu, Tianlong Yang, Yicheng Feng

School of Materials Science and Engineering, Harbin University of Science and Technology, Harbin 150040, China

^afuwei_kang@163.com

Keywords: AI-5Ti-1C master alloy, refiner, microstructure.

Abstract. Al-5Ti-1C master alloy refiner was prepared by melt reaction method, and its refining efficiency was examined by purity aluminum in the paper. The microstructures under different process conditions were studied by OM, SEM and XRD. The results shown that the grains were finer, TiAl₃ and TiC phases were uniformly distributed at 900°C, held time for 15min. The refining efficiency was best at addition of 0.4% (wt.%) refiner and held time for 10min.

1. Introduction

Grain refinement is one of important methods of improving mechanical properties and workability of aluminum and its alloys. It is now a common practice to add grain refiners to molten Al before casting to produce fine grain structures in the solidified ingots or cast products. The function of grain refinement is to control the grain size and grain morphology during extrusion of billets and rolling slabs, so that good reproducible processing and mechanical properties can be achieved. At present Al-Ti-B grain refiners are the most widely used grain refiners in aluminum industry^[1]. However, they suffer from agglomeration or coalescence of borides and defects during subsequent forming operations and poisoning by certain elements such as Zr, Cr, Li and Mn^[2-5]. In the last three decades, Al-Ti-C master alloys refiner have been widely investigated to be an acceptable replacement for Al-Ti-B master alloys^[6-10]. But some issues still have to be resolved such as bad wetability of C in aluminum melt during Al-Ti-C master alloys preparation.

The present work aims at preparing the Al-5Ti-1C master alloy by the melt reaction process which add the compacted mixture of titanium, aluminum and graphite powder into molten Al at different conditions, and evaluating its refining efficiency to purity aluminum.

2. Experimental procedure

2.1 Material preparation

Commercial purity aluminum powder (99.8%, 200 grid), titanium powder (99.5%, 200 grid) and graphite powder (99.9%, 1200 grid) were used in the experiments as a source of titanium and carbon, respecitively. Melt reaction method includes three procedures. Firstly, the activated treatment of graphite powder was carried out in solution (15%HCl+15%HNO₃+70%H₂O) for 24h. Then the graphite powder was separated from the solution by vaccum separation apparatus, and dried at 80°C for 3 hours. Secondly, three powders (titanium, aluminum and graphite powder) were mixed in ball mill for an hour and compacted to a disk by pressing in a mold with diameter of 30mm at a fixed load. Lastly, an quantity of aluminum was melted in the graphite crucible at different temperatures, then the preheated compacted disk was added into the molten aluminum using a graphite rod every ten minutes. After a certain time, the crucible containning the molten alloy and salg was taken out of the furnace to separate the salg from the melt, and then the molten alloy was poured into a steel mold with a diameter of 60mm and height of 200mm. The experiment parameters are shown in the following

lable. I Experimental parameters							
sample No.	1#	2#	3#	4#	5#	6#	7#
ReactionTemperature/°C	800	850	900	950	900	900	900
Reaction Time/min	15	15	15	15	5	10	25

table 1. The prepared Al-5Ti-1C ingot was extruded to diameter of 9.5mm rod by a extrusion machine to refine purity aluminum.

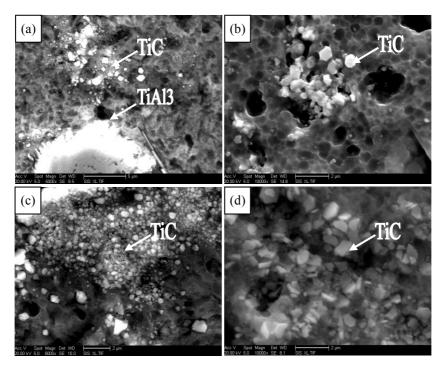
2.2 Microstructure characterization and phase identification

To reveal the microstructures of Al-5Ti-1C master alloy, the samples were polished and etch by the Keller's reagent and then analyzed by an Olympus GX-71-6230A optical microscope and an FEI Sirion SEM equipped with an energy dispersive system. X'Pert PRO XRD was employed to identify the phases present in the master alloy.

3. Results and discussion

3.1 Effect of temperature on microstructure of Al-5Ti-1C master alloy

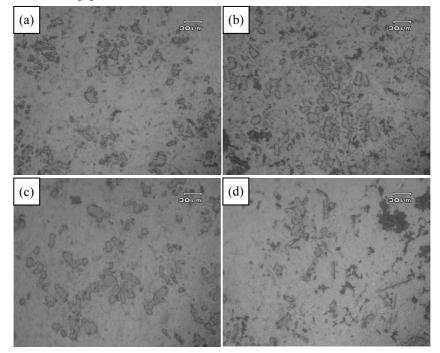
Fig.1(a)~(d) shows the state of the microstructure at temperatures between 800 and 950°C for reaction time 15min. Obvious TiAl₃ and TiC particle can be observed from Fig.1(a), and a few irregular shape TiC was distributed around TiAl₃ particle. With the rising of temperature, TiC particle appeared aggreagated at 850°C, but at 950°C the size of TiC particle grew up about 2 μ m, only at 900°C a great deal of finer TiC particle with 0.5~1.0 μ m was obtained and without aggregation, uniformly distributed in the matrix.



(a)1# 800℃ (b)2# 850℃ (c)3# 900℃ (d)4# 950℃
 Fig.1 SEM images of Al-5Ti-1C master alloy in different reaction temperatures for 15min
 3.2 Effect of reaction time on microstructure of Al-5Ti-1C master alloy

The Al-5Ti-1C master alloy prepared at 900°C and reaction time between 5min and 25min were studied. The results shown that the amount of Al₃Ti was less becasue of uncompleted reaction for 5min, as shown in Fig.2(a). The increase in reaction time from 5min to 10min resulted in the agglomeration of blocky Al₃Ti particles as clearly observed in Fig.2(b). Comparing Fig.2(a)~(d) it was clear that the Al-5Ti-1C master alloy prepared at 900°C,15min contained lots of blocky Al₃Ti particle with more homgeneous distribution when compared to other two reaction time i.e. 900°C, 20min and 900°C, 25min. From Fig.2(c)~(d), we can find that when reaction time exceed 20 minutes,

Al₃Ti particles grew along the axis direction and the shape changed gradually from blocky to bar. Since blocky TiAl₃ particles were more like equiaxed grains, the melting rate of Al₃Ti particles were same in each directions. However, the melting rate of bar Al₃Ti were fastest in the direction of crystal axis, so the effect of refining grains decreased.



(a)5# 5min (b)6# 10min (c)3# 15min (d)7# 25min Fig.2 Optical images of Al-5Ti-1C master alloy in different reaction time

Fig.3 shows the XRD pattern obtained from Al-5Ti-1C master alloy prepared at 900°C, 15min. Indexing of the XRD peaks has shown the presence of Al₃Ti and TiC phases in addition of α -Al matrix.

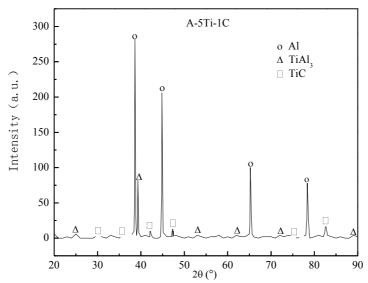


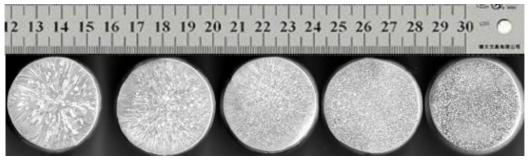
Fig.3 XRD pattern of the Al-5Ti-1C master alloy prepared at 900°C, 15min

The chemical composition of Al-5Ti-1C prepared at 900°C,15min was detected as shown in Table 2, and constrast with stnadard composition. The results show that the chemical composition of indigenous Al-5Ti-1C master alloy closed to the standard's and the absorptivity rates of Ti and C attain 90% above.

Table.2 Chemical composition of Al-5Ti-1C master alloy (wt.%)						
No.	Ti	С	Fe	Si	V	
standard content	4.5~5.5	0.9~1.1	≤0.3	≤0.2	≤0.2	
actual content	4.85	0.91	0.19	0.12	0.15	

3.5 Evaluation Refining Effect

Commercial-purity aluminum was refined by produced Al-5Ti-1C master alloy and refining effect was evaluated by average grain size. The results shown that grain size was smallest when addition of refiner was 0.4%wt. at 750°C holding time for 10 minutes in Fig.4.



(a)unrefined (b) 2min (c) 5min (d) 10min (e) 20min Fig.4 Comparison of microstructures at the different holding time

4. Conclusions

(1) Al-5Ti-1C master alloy grain refiners were successfully prepared by melt reaction at reaction temperature 900°C, holding time 15min.

(2) The optimum refining conditions for purity aluminum were at addition of 0.3%(Wt.%) and holding time for 10min.

References

- [1] Z.S.Gao: Light Metal (1999)
- [2] M.A.Doheim, A.M.Omaran, A.Abdel-Gwad: Metallurgical and Materials Transactions A(2011)
- [3] T.Sagstad, E. Bondhus: Light Metal (1999)
- [4] A.A.Rao, B.S. Mruty and M.Chakraborty : Materials Science and Technology (1997)
- [5] Q.B.Zhang, H.S.Fang, J.G.Li, H.T.Ma: Journal of Material Science Letters (2000)
- [6] D.H.Wen, M.G.Yang, H.Zhang: Light Alloy Fabrication Technology (2007)
- [7] X.C.Xu, J.S.Zhang: Materials Science and Technology (2001)
- [8] H.M.Ding, X.F.Liu, L.N.Yu: Journal of Materials Science (2007)
- [9] J.G.Li, L.Wang: Light Alloy Fabrication Technology (2003)
- [10] X.Q.Jiang,C.K. Lu: Sichuan Nonferrous Metals (2002)
- [11] P.Moldovan, G.Popescu: Journal of Metal (2004)

Optimized Technical Characteristics of Polysilicon Nanofilm

Xuebin LU^a, Linhai CUI and Mingyuan REN

Department of Integrate Circuit Design and Integrate System, Harbin University of Science and Technology, Harbin 150080, China

^alxbsw@126.com

Keywords: Polysilicon Nanofilm, Technical Characteristics, MEMS.

Abstract. In order to take good advantage of polysilicon nanofilm, optimized technical characteristics of the polysilicon nanofilm are very necessary to investigated. In this paper, the polysilicon nanofilms were prepared under different technical parameters, including thickness and doping concentration, which are very important for preparation of the nanofilm. The experimental results of piezoresistive and temperature characteristics show that the optimized technical characteristics are followed, the thickness is about 90nm, and the doping concentration is about $4.1 \times 10^{19} \text{ cm}^{-3}$ or between $2.0 \times 10^{20} \text{ cm}^{-3}$ and $4.1 \times 10^{20} \text{ cm}^{-3}$ from different point of view. The investigations of optimized technical characteristics are very useful for application of the polysilicon nanofilm to piezoresistive sensor.

Introduction

The researches about nanomaterial developed rapidly in 21st century [1]. Nanomaterial is a kind of material in which one of the material's dimensions is in nanoscale (1-100nm). Nanomaterial can be sort into three kinds, including zero dimensions, one dimension and two dimensions. Two dimension nanomaterial is a kind of film whose thickness is less than 100nm, i.e. nanofilm [2]. In this paper, polysilicon film whose thickness is under 100nm is called polysilicon nanofilm (PSNF), polysilicon film whose thickness is above 100nm is called common polysilicon film (CPSF), and the PSNF and CPSF are called polysilicon film (PSF) in a joint name. Along with the development of nanotechnology, the characteristics of PSNF received more and more attentions [3].

PSF plays an important role as a pressure-sensing material in Micro-electromechanical Systems (MEMS), and especially represents preferable properties used in high temperature piezoresistive devices. According to our previous research, the piezoresistive characteristics of PSNF exceed that of CPSF because of remarkable tunneling piezoresistive effect [4]. In order to apply of PSNF to piezoresistive sensor effectively, it is very necessary to investigate the technical parameters of preparation of PSNF. In this paper, the PSNF were prepared by low pressure chemical vapor deposition (LPCVD) under different technical parameters, including thickness and doping concentration. The experiments of piezoresistive and temperature characteristics were conducted, and optimized technical characteristics were obtained.

Preparation of PSF

PSF with Different Thickness. The 4 inch monocrystalline silicon wafers (thickness: 500µm) of <100> orientation were chosen as substrates, then a Si0₂ layer (thickness: 1µm) grown by thermal oxidation. The oxidation layer can insulate the substrate and PSF. The PSF were deposited at 620 °C with SiH₄ flow rates 50ml/min in a low pressure chemical vapor deposition system. The thicknesses of PSF are controlled by deposition time. The thickness of PSF is 29nm, 40nm, 61nm, 89nm, 123nm, 150nm, 198nm and 251nm, respectively, and error of the thickness is about \pm 3nm. Then using boron nitride of solid state, the thermal diffusion was processed at 1080°C with nitrogen protection; the doping concentration of all PSF is estimated to be 2.3x10²⁰cm⁻³ in terms of solubility of solid-state boron in silicon. In this step, the PSF finished annealing also. Because of same doping concentration and same deposition temperature of PSF, the effect of thickness on characteristics of PSF is only

taken into consideration. After that, PSF resistances were obtained through photolithography. Then the aluminum film was evaporated onto silicon wafers and photoithographed to form electrodes. Test samples of cantilever beam were obtained through photolithography. The structure of cantilever beams is of 26mm length and 4mm width, which are used in testing of PSF.

PSNF with Different Doping Concentration. Monocrystalline silicon of <111> orientation (thickness: 510µm) was chosen as substrate, then a SiO₂ layer (thickness: 860nm) was grown by thermal oxidation. PSNF of 80nm thickness were deposited at 620°C with LPCVD process onto the oxidized silicon layer. The films were doped by ion implantation of boron with energy of 20KeV and dose of 9.4×10^{13} cm⁻², 2.3×10^{14} cm⁻², 4.7×10^{14} cm⁻², 8.2×10^{14} cm⁻², 1.2×10^{15} cm⁻², 2.3×10^{16} cm⁻², 4.7×10^{16} cm⁻², 8.2×10^{15} cm⁻², 2.3×10^{16} cm⁻², 4.7×10^{16} cm⁻², 1.2×10^{15} cm⁻², 2.3×10^{15} cm⁻², 4.7×10^{15} cm⁻², 8.2×10^{15} cm⁻², 2.3×10^{16} cm⁻³, 4.1×10^{19} cm⁻³, 7.1×10^{20} cm⁻³, 2.0×10^{20} cm⁻³, 4.1×10^{19} cm⁻³, 7.1×10^{20} cm⁻³, 2.0×10^{20} cm⁻³, 4.1×10^{19} cm⁻³, 7.1×10^{20} cm⁻³, 2.0×10^{20} cm⁻³, the samples were annealed at temperature of 1080°C for half an hour with nitrogen protection. Because of same thickness and same deposition temperature of PSNF, the effect of doping concentration on characteristics of PSF is only taken into consideration. By the same way, test samples were obtained.

Experimental Results and Discussions

PSF with Different Thickness. Using the cantilever beams testing samples, the longitudinal gauge factors of PSF with different thickness were measured, and the results are shown in Fig.1. In the figure, every experimental point come from the mean of test data of over 20 same samples, respectively. Because longitudinal gauge factor is larger than transverse ones, only results of longitudinal gauge factor are shown.

In Fig.1, the longitudinal gauge factor of CPSF is between 20 and 22. For PSNF, the gauge factor is higher than that of CPSF, which is between 26 and 34. The gauge factor of 89nm PSNF is highest, 33.39; and the gauge factor of 60nm PSNF is 32.32. Because of remarkable tunneling piezoresistive effect, the piezoresistive characteristics of PSNF exceed that of CPSF [4].

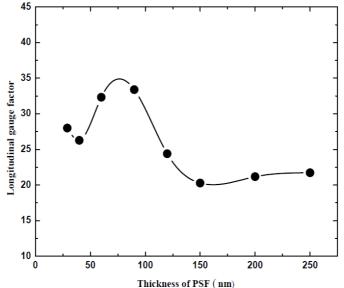


Fig.1 Longitudinal gauge factors of PSF with different thickness

For CPSF, the films thickness is larger than 150nm; the gauge factors are low and increase slightly with thickness increases. The grain size of CPSF is big and the tunneling piezoresistive effect is not significant and can be neglected (this is the reason that other researchers neglect the tunneling piezoresistive effect), so the gauge factor is low. The gauge factor slightly increasing with thickness increase may come from the grain size increasing with thickness and preferred orientation appearing gradually. For PSNF, the thickness is between 40nm and 90nm, and the grain size is very small. The gauge factors are high, because the tunneling piezoresistive effect becomes dominant. The gauge factors decrease with thickness decrease because the grains crystallization degrades. The piezoresistive property PSNF is synthesis of grain size and state of grain boundary [6].

The gauge factor of PSNF is higher than that of CPSF, which can be utilized to improve the sensitivity of MEMS piezoresistive device. According to the experimental result in Fig. 1, the optimized technical parameter about PSF thickness should be about 90nm.

PSNF with Different Doping Concentration. Using the cantilever beams testing samples, the longitudinal gauge factors of PSNF with different doping concentration were measured, and the results are shown in Fig.2. In the figure, every experimental point come from the mean of test data of over 20 same samples, respectively.

From Fig. 2, the longitudinal gauge factor of PSNF is between 33 and 40 which is larger than that of single silicon with same doping concentration, and the largest gauge factor is about 40 under 4.1×10^{19} cm⁻³. As we known, sensitivity of piezoresistive sensor is proportional to the gauge factor of piezoresistor, which ensures the achievement of high sensitivity of sensor. From this point of view about sensitivity, the optimized technical parameter about PSF doping concentration should be 4.1×10^{19} cm⁻³.

Temperature characteristic is a very important static index of piezoresistive sensor, which is related to temperature coefficient of piezoresistor. The temperature coefficients of resistivity and gauge factor of PSNF are shown in Fig. 3 and Fig. 4, respectively. Because of heavy work, only some PSNF samples under different doping concentration were test. As we known, the smaller temperature coefficient of PSNF, the better temperature characteristic of sensor. According to the experimental results in Fig. 3 and Fig. 4, the optimized technical parameter about PSF doping concentration should be between 2.0×10^{20} cm⁻³ and 4.1×10^{20} cm⁻³, which can guarantee good temperature characteristic.

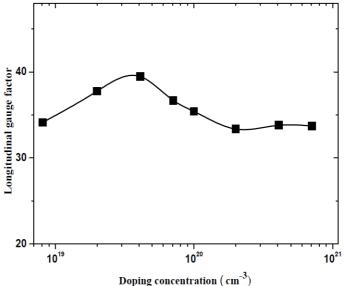


Fig. 2 Relationship between longitudinal gauge factor and doping concentration of PSNF

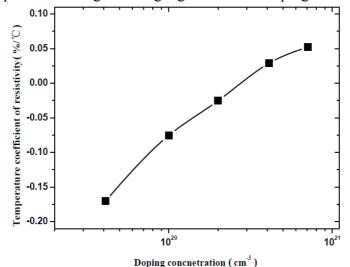
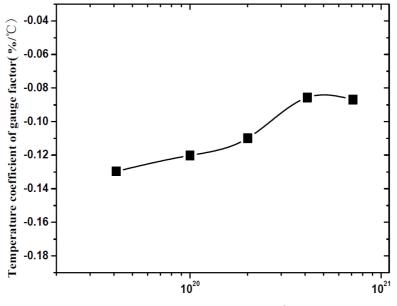


Fig. 3 Temperature coefficient of resistivity VS doping concentration of PSNF



Doping concnetration (cm⁻³)

Fig. 4 Temperature coefficient of gauge factor VS doping concentration of PSNF

From the perspective of high sensitivity, the optimized technical parameter about PSF doping concentration should be about 4.1×10^{19} cm⁻³. From the perspective of low temperature coefficient, the optimized technical parameter about PSF doping concentration should be between 2.0×10^{20} cm⁻³ and 4.1×10^{20} cm⁻³.

Conclusions

In this paper, the optimized technical characteristics of PSNF are investigated. The PSNF were prepared by LPCVD under different technical parameters, including thickness and doping concentration. The experimental results of piezoresistive and temperature characteristics show that the optimized technical characteristics are followed, the thickness is about 90nm and the doping concentration is 4.1×10^{19} cm⁻³ or between 2.0×10^{20} cm⁻³ and 4.1×10^{20} cm⁻³ from different point of view. The investigation of optimized technical process is very useful for application of the PSNF to piezoresistive sensor. Application of PSNF under optimized technical characteristics to piezoresistive sensor will be our next work.

References

[1] Zeng Wen and Liu Tian-mo: Nanotechnology and Precision Engineering. Vol. 7(2009), p. 387

[2] ZhuJing, Wenzhi Jin: Nano Materials and Devices (Tsinghua University Press, Beijing, 2003).

[3] Chuai Rong-yan, Liu Xiao-wei and Huo Ming-xue: Chinese Journal of Semiconductors. Vol. 27(2006), p.1230

[4] Lu Xue-bin, Liu Xiao-wei and Chuai Rong-yan: Advanced Materials Research. Vol. 60-61(2009), p.89

[5] J. Lindhand, M. Scharff, H. E. Schiott: Mat. Fys Med. Dan. Vid. Selsk. Vol. 33(1963), p.1

[6] Lu Xue-bin, Liu Xiao-wei, Chuai Rong-yan: Proceedings of the 2009 4th IEEE International Conference on Nano/Micro Engineering and Molecular System. (2009), p.498

[7] P. J. French: Sensors and Actuators A: Physical. Vol. 99(2002), p.3

Effect of Charge Transferring Materials on Photoluminescence Properties of CdSe/ZnS Quantum Dots

Xuanlin Chen^{1,a}, Yuqiu Qu^{1,b*}, Guifan Li^{2,c}, Hong Wei^{1,d}, Liuyang Zhang^{3,e}, Limin An^{1,f}

¹College of Physics Science and Technology, Heilongjiang University, Harbin, China

²School of Mathematical Sciences, Heilongjiang University, Harbin, China

³Department of Optoelectric Information Science and Engineering, Harbin University of Science and Technology, West campus, P. O. Box 130, Harbin 150080, China

^a1291263475@qq.com, ^bqyq0500@163.com (^{*}corresponding author), ^c670489311@qq.com, ^d752673008@qq.com, ^ejohnien@163.com, ^fanlimin@hlju.edu.cn,

Keyword: quantum dots, photoluminescence, charge transferring.

Abstract. The CdSe/ZnS core/shell quantum dots (QDs) were synthesized and characterized with absorption spectrometry, photoluminescence (PL) spectrometry and transmission electron microscopy. PL quenching of colloidal CdSe/ZnS QDs in the presence of charge transferring material was studied by means of steady-state and time-resolved PL spectroscopy. With increasing charge transferring materials concentration in the CdSe/ZnS QDs solution, the PL intensity and lifetime of CdSe/ZnS QDs decrease gradually. The quenching efficiency of CdSe/ZnS QDs decrease with increasing the oxidation potential of charge transferring materials. Based on the analysis, there are two pathways in the PL quenching process: static quenching and dynamic quenching. The dynamic quenching is correlated with hole transfer from QDs to the charge transferring materials.

Introduction

Colloidal semicondutor nanocrystals, also known as QDs, have been intensively investigated as a luminescent material in the past few decades[1]. Due to quantum confiement effects, QDs possess unique optical properties, such as size-tunable PL, narrow emission bandwidth, high PL quantum yield, broad excitation spectra. So the QDs have great potential applications in solar cells, photoelectric devices, biomarkers, immunoassay etc [2-4]. The high surface to volume ratio of QDs means the surface properties will significant influence their structural and optical properties. It has been proved that overcoating QDs with shell of wider band gap semiconductor materials can improve the PL quantum yields and photostability by passivating surface nonradiative recombination sites [5].

Since the performance of QDs are strongly dependent on their surface feature and structure, the interaction and the dynamic processes between organic molecules and QDs must be deeply investigated for improving the performance of organic/inorganic complex QDs based devices [6].

In this work, CdSe QDs were synthesised by the successive ion layer adsorption reaction (SILAR) methods and were covered by inorganic shell ZnS. With absorption spectroscopy, emission spectroscopy and time-resolved spectroscopy, the PL quenching of two charge transferring materials (CTM), NPD (N, N'- di- (1-naphthaleyl)-N,N'-diphenyl-1,1'-biphenyl-4,4'-diamine) and TPD (N,N'-Diphenyl-N,N'- bis(3-methylphenyl)-1,1'-biphenyl-4,4'-diamine), to CdSe/ZnS QDs were studied. And the mechanism of the PL quenching with the CTM was also analysised in detail.

Experiment

All reagents used here were analytical pure and bought from Sigma Corporation. Absorption spectra were obtained with a UV-3101PC UV-Vis-NIR spectrometer produce by Shimadzu Corporation. PL spectra were measured with F-4500 fluorescence spectrometer under the excitation of 485 nm. Transmission electron microscopy TEM-3010 made by JEOL Corporation were employed to view the size and surface appearance of QDs. The time-resolved measures were carried out by a time-correlated single-photo-counting detection system excited at 450 nm with the instrumental response of about 17 ps. The details of the experimental instruments can refer to [7].

CdSe/ZnS core/shell QDs were synthesized by typical SILAR methods. The detailed procedure can refer to [8]. The final products were dissolved in chloroform after removing excess ligands and synthetic byproduct. The QDs were dissolved into chloroform to form required solutions.

Results and Discussion

The absorption spectra and PL spectra of CdSe/ZnS core/shell QDs are shown in Fig. 1(a). The emission peak is at 604 nm. Overcoating with ZnS shell, CdSe QDs still have strong PL intensity. This can be owned to the passivating effect of the ZnS shell which can modify the surface nonradiative recombination sites of CdSe.

Fig. 1(b) shows the transmission electron microscope micrograph of CdSe/ZnS QDs. The image indicates that the as-prepared CdSe/ZnS QDs are homogeneous spherical particles and are well dispersive. The size of CdSe/ZnS QDs is about 4.2 nm. A calculation shows that two monolayer of ZnS are covered on the surface of CdSe.

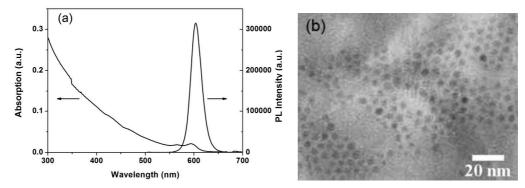


Fig. 1 (a) Absorption and PL spectra of CdSe/ZnS QDs, (b) TEM image of CdSe/ZnS QDs

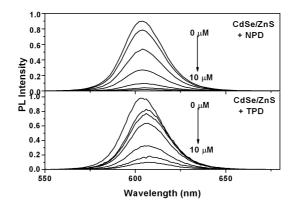


Fig. 2 PL spectra of CdSe/ZnS QDs with different concentrations of NPD or TPD

Next, we will study the PL quenching of organic molecules on QDs. We choose the two charge transferring materials: NPD and TPD which are aromatic amine polymers in which N atoms own

the strong donating electron ability. In the process of continuous electrons transporting, they show hole transporting ability. The potential of oxidation for NPD and TPD is 0.27 V and 0.48 V, respectively.

Fig. 2 shows the PL spectra of CdSe/ZnS QDs with different concentrations of NPD or TPD. With the increase of CTM, both the intensity of PL spectra decrease. It can be found that the PL quenching of CdSe/ZnS with NPD is faster than that with TPD. This indicates that the PL quenching of QDs is related to the interaction between organic molecule and the surface of QDs.

In order to further clarify the mechanism of PL quenching, we measure the time-solved spectra of the mixed solution of CdSe/ZnS QDs and CTM and fit the fluorescence decay curves. The results are listed in Table 1. When CTM are adding into the solution of QDs, the lifetime of QDs are shortened in some degree with the increase of CTM. For CdSe/ZnS QDs, the shrinkage of fluorescence lifetime is different for different CTM. The reduction of fluorescence lifetime resulting from NPD is greater than that from TPD. Combining with the value of the oxidation potential, we can conclude that the efficiency of PL quenching increases with the decrease of oxidation potential of CTM.

Concentration of Average lifetime τ_{AV} of Average lifetime	e τ_{AV} of
	<i>AY</i>
$\frac{\text{NPD/TPD} [\mu \text{mol/L}]}{\text{CdSe/ZnS} + \text{NPD} [ns]} \qquad \frac{\text{CdSe/ZnS} + \text{TP}}{\text{CdSe/ZnS} + \text{TP}}$	PD [ns]
0 12.852 12.852	
0.1 12.006 12.403	
0.5 11.089 12.291	
1 10.190 11.874	
3 7.236 8.444	
5 2.921 5.773	
10 1.669 4.514	

Table 1 Average lifetime of CdSe/ZnS QDs with different concentrations of NPD or TPD

Fig. 3 shows the relation between the PL intensity ratio (I_0/I) and average lifetime (τ_{AV0}/τ_{AV}) of CdSe/ZnS QDs with different CTM and the concentration of CTM. Here I_0 and τ_{AV0} are PL intensity and average lifetime of QDs without CTM. It is well known that most PL quenching can be explained by Stern-Volmer equation: $I_0/I = 1 + K_{sv}Q$, where K_{sv} is Stern-Volmer quenching constant, Q is the concentration of quenched material. But the results of Fig. 3 are not accord with Stern-Volmer equation. And this implies that there may be static quenching, dynamic quenching or even multiple quenching pathways [9].

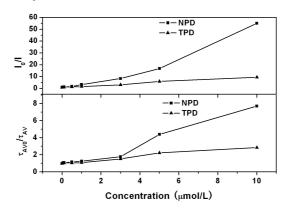


Fig. 3 I_0/I and τ_{AV0}/τ_{AV} of CdSe/ZnS QDs as functions of concentrations of NPD or TPD

In general, the PL quenching of QDs comes from two processes: static quenching and dynamic quenching [10]. Firstly, since there are many hole sites of Zn²⁺ in the shell of ZnS, CTM molecules will occupy these hole sites and then block the combination of electrons and holes. This will lead to static quenching. However, static quenching does not change the fluorescence lifetime [11]. On the other hand, there is energy difference between the valence of QDs and the HOMO energy level of the CTM. When the QDs are excited, the holes in their top valence may transmit to the HOMO energy levels of CTM. This will lead to dynamic quenching [12]. In our experiment, the excited wavelength is 480 or 450 nm at which only QDs can be excited but not CTM. And then the holes transport only happens from QDs to CTM. Meanwhile, the oxidation potential of CTM indicates that the discrepancy between the holes energy level of QDs and the HOMO energy level of CTM is different. According to the theory of hole transporting, the holes transporting probability is inverse proportional to the discrepancy between the hole energy level of QDs and the HOMO energy level of CTM. Then the holes transport from QDs to CTM leads to the dynamic quenching.

Conclusions

CdSe/ZnS core/shell QDs have been synthesized by typical SILAR methods. The QDs have strong PL intensity, homogeneous size and well monodispersity. The PL quenching of different charge transferring materials on CdSe/ZnS core/shell QDs was investigated by spectroscopy. With the increase of concentration of charge transferring material, the PL intensity of QDs decreases evidently. This PL quenching is related with oxidation potential of charge transferring material. The PL quenching of QDs can be owed to static quenching and dynamic quenching.

ACKNOWLEDGMENT

The authors thank the Science and Technology Research Program from Education Department of Heilongjiang province in China for the fund under Grant No. 12531515.

References

- [1] V. L. Colvin, M. C. Schlamp and A. P. Alivisatos: Nature, Vol. 370 (1994), p. 354.
- [2] J. Song, X. Song and T. Ling: Ind. Eng. Chem. Res., Vol. 51 (2012), p. 10074.
- [3] N. Tessler, V. Medvedev and M. Kazes: Science, Vol. 295 (2002), p. 1506.
- [4] S. Coe, W. K. Woo and M. Bawendi: Nature, Vol. 420 (2002), p. 800.
- [5] X. G. Peng, M. C. Schlamp and A. V. Kadavanich: J. Am. Chem. Soc., Vol. 119 (1997), p. 7019.
- [6] C. F. Landes, M. Braun and M. A. El-Sayed: J. Phys. Chem. B, Vol. 105 (2001): p. 10554.
- [7] D. Bebelaar: Rev. Sci. Instrum., Vol. 57 (1986), p.1116.
- [8] R. Xie, K. Ute, J. Li: J. Am. Chem. Soc., Vol. 127 (2005), p.7480.
- [9] M. Califano, A. Franceschetti and A. Zunger: Nano Lett., Vol. 5 (2005), p. 2360.
- [10] O. Schmelz, A. Mews and T. Basche: Langmuir, Vol. 17 (2001), p. 2861
- [11] A. Hagfeldt, M. Gratzel: Chem. Rev., Vol. 95 (1995), p. 49.
- [12] M. Sykora, M. A. Petruska, J. Alstrum-Acevedo: J. Am. Chem. Soc., Vol. 128 (2006), p. 9984.

Study on Photoluminescence Quenching of CdSe Core/Shell Quantum Dots with Organic Charge Transferring Material

Yuqiu Qu^{1,a*}, Liuyang Zhang^{2,b}, Limin An^{1,c}, Hong Wei^{1,d}, Guifan Li^{3,e}

¹College of Physics Science and Technology, Heilongjiang University, Harbin, China

²Department of Optoelectric Information Science and Engineering, Harbin University of Science and Technology, West campus, P.O.Box 130, Harbin 150080, China

³School of Mathematical Sciences, Heilongjiang University, Harbin, China

^aqyq0500@163.com (^{*}corresponding author), ^bjohnien@163.com, ^canlimin@hlju.edu.cn, ^d752673008@qq.com, ^e670489311@qq.com

Keywords: quantum dots; charge transferring; photoluminescence quenching.

Abstract. The effect of organic charge transferring material (CTM) on fluorescence of CdSe/ZnS and CdSe/CdS/ZnS core/shell quantum dots (QDs) are investigated by spectral methods. With the increase of organic molecular concentration, CTM can greatly quench the fluorescence of QDs and shorten the fluorescence lifetime of QDs. In the process of interacting with CTM, the efficiency of fluorescence quenching for CdSe/ZnS is significantly higher than that for CdSe/CdS/ZnS. The results of experiment show that the shell structure of QDs plays the major role in photoluminescence (PL) quenching. The mechanism of PL quenching of QDs is also analyzed.

Introduction

Fluorescent semiconductor nanocrystals known as QDs such as CdSe, CdS, ZnS and ZnSe have been extensively studied because of their unique physical and chemical properties [1,2]. For their excellent properties of high PL quantum yield, narrow emission spectral width, size-tunable PL and superior photostability, these materials are applied in thin-film light-emitting diodes (LEDs), lasers, optical amplifier media, and biology labels [3-6]. The high surface-to-volume ratio of QDs suggests that the surface properties will significantly influence their structural and optical properties, because of the large surface area and the possible presence of surface states caused by uncoordinated atoms which act as quencher of the luminescence. In recent years, the core/shell strategy has greatly been applied to enhance the PL of QDs. For example, CdSe/ZnS and CdSe/CdS have been intensively studied over the past decade. It has been proved that growing the higher band gap inorganic semiconductor materials ZnS or CdS shell on the CdSe QDs can substantially increase the PL quantum yields, chemical stability and photostabiliy by passivating surface nonradiative recombination sites [7]. However, QDs LEDs were fabricated by sandwiching QDs layer between organic charge transferring material (CTM) layers. In order to improve the performance of organic and inorganic composite quantum-dots-based optoelectronic devices, it is necessary to explore the interaction of organic molecule and the QDs with different shell structure.

In this work, the PL of CTM N,N'-bis(1-naphthyl)-N,N'-diphenyl-1,1'-biphenyl-4,4'-diamine (NPD) on CdSe/CdS/ZnS and CdSe/ZnS core/shell QDs is investigated by steady state and time-resolved spectroscopy.

Experiment

All reagents used here were analytical pure. Steady-state absorption spectra were obtained with a Cary 300 double-beam spectrometer. PL spectra were measured by the emission spectrometer of Spex Fluorolog type III under excitation at 480 nm. The time-resolved measures were carried out by a time-correlated single-photo-counting detection system excited at 450 nm.

CdSe/ZnS and CdSe/CdS/ZnS core/shell QDs were synthesized by the organometallic route [8]. The final products were dissolved in chloroform after removing excess ligands and synthetic byproduct. 2.5 mg NPD were dissolved in 1 mL chloroform to preparing the solution with 4000 μ mol/L. Different volume solutions of NPD were injected into the solutions of QDs to change the concentration of NPD in the mixed solutions.

Results and discussion

Fig. 1 shows the absorption spectra and the PL spectra of CdSe/ZnS and CdSe/CdS/ZnS QDs in chloroform with different concentration of NPD. With the increase of NPD, both absorption spectra have no significant change, however, the intensities of fluorescence decrease. Simultaneously, the PL quenching of CdSe/ZnS is faster than that of CdSe/CdS/ZnS. This illustrates that the PL quenching of QDs is strongly dependent on the shell structure, besides the interaction of organic molecules around the surfaces of QDs.

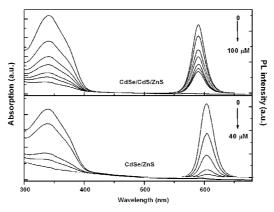


Fig. 1 Absorption and PL spectra of CdSe/CdS/ZnS and CdSe/ZnS QDs with different concentrations of NPD

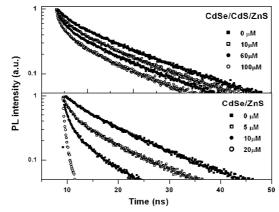


Fig. 2 Fluorescence decay curves of CdSe/CdS/ZnS and CdSe/ZnS QDs with different concentrations of NPD

In order to clarify the mechanism of PL quenching of QDs, the time-resolved spectroscopy is employed. Fig. 2 shows the time-resolved spectra of the two QDs solutions after adding NPD solutions of different concentration. Overall, the fluorescence lifetimes of QDs have been shortened in some degree. And the fluorescence lifetimes of CdSe/ZnS QDs shorten faster than that of CdSe/CdS/ZnS QDs.

Based on above experimental data, we find that the decay curves are fitted with the kinetic model of a triexponential function:

$$I(t) = A_1 \exp(-t/\tau_1) + A_2 \exp(-t/\tau_2) + A_3 \exp(-t/\tau_3).$$
(1)

where τ_j , *j*=1,2,3 are the lifetimes for the three emission components, respectively, A_j , *j*=1,2,3 are normalized amplitudes of each component.

In addition, the average lifetimes of both QDs are calculated by

$$\tau_{AV} = (A_1 \tau_1^2 + A_2 \tau_2^2 + A_3 \tau_3^2) / (A_1 \tau_1 + A_2 \tau_2 + A_3 \tau_3) .$$
⁽²⁾

Eq. (2) is from Ref. [9]. The average lifetimes are listed in Table 1.

In order to intuitively illustrate the effects of the shell structure of QDs on PL quenching, the variation of fluorescence intensities and average lifetimes of CdSe/CdS/ZnS and CdSe/ZnS QDs with the different concentrations of NPD are shown in Fig. 3.

From Table 1 and Fig. 3, it is obvious that the PL intensity and the average lifetime of QDs decrease after NPD is injected into QDs solutions. This further illustrates that the different shell structure of QDs can lead to the variation of efficiency of PL quenching.

Table	1 Average lifetime of CdSe/	CdS/ZnS and CdSe/ZnS with	th different concentrations of NP	'nD
	Concentration of NPD	Average lifetime τ_{AV} of	Average lifetime τ_{AV} of	
	[µmol/L]	CdSe/CdS/ZnS [ns]	CdSe/ZnS [ns]	
	0	15.63	6.06	
	5	14.62	5.09	
	10	14.43	3.88	
	15	14.19	2.94	
	20	13.92	0.91	
	60	13.42		
	100	13.28		
	Lo Lintensity	CdSe/CdS/ZnS (a)	—■— CdSe/CdS/ZnS (â) —◆— CdSe/ZnS	
	0.0 1.0 0.5 0.0 0.5 0.0 0.5 10 15 20 2 2	CdSe/CdS/ZnS - CdSe/ZnS - Cd	(b) 	
	Concentration (µ	mol/L)	Concentration (µmol/L)	

Fig. 3 Normalized PL intensity (a), average lifetime (b) of CdSe/CdS/ZnS and CdSe/ZnS QDs as a function of NPD concentration, and (c) schematic diagrams of PL quenching mechanisms.

In general, the PL quenching of QDs comes from two processes: static quenching and dynamic quenching [10,11]. Firstly, since there are many holes of Zn^{2+} in the shell of ZnS, charge transferring molecules will occupy these holes and then block the combination of electrons and holes. This will lead to static quenching. Secondly, the fluorescence of QDs is sensitive to its surface environment. The luminous central ions are easy to be substituted by the charge-transferring molecules adhered to its surface and this will also lead to the static quenching of fluorescence. On the other hand, there is energy difference between the valence of QDs and the HOMO energy level of the CTM. When the QDs are excited, the holes in their top valence may transmit to the HOMO energy levels of CTM, and then in the interface of QDs and CTM charge separation will happen. This will lead to dynamic quenching [12]. According to our experimental, this is the main effect lead to the decay of PL intensity and the reduction of lifetime of QDs with the increase of concentration of CTM.

A further discussion about the interaction of QDs and CTM can be developed by their electric energy levels. Fig. 3c shows the energy levels of QDs and CTM. Their energy levels illustrate that there may be electrons or holes transference between QDs and CTM. The ability of holes transference is related to the potential barrier between the shell material and CdSe, and is inverse proportional to the height of the potential barrier and the shell thickness [11].

Generally, the photoelectric devices (e.g. semiconductor based solar devices) can produce current mainly by the charge transferring between semiconductor nanocrystals and organic molecules to separate the holes and electrons produced by light exciting. According to our results, the efficiency of solar devices can be improved by using multi-shell covered QDs.

Conclusions

The effects of PL quenching of organic CTM on CdSe QDs with different shell structures are investigated by steady state and time-resolved spectroscopy. With the increase of concentration of CTM, the fluorescence of CdSe/CdS/ZnS and CdSe/ZnS QDs are effective quenched. The mechanism of PL quenching is the holes transferring originating from QDs to CTM. There are different PL quenching ways for the semiconductor nanocrystals with different shell structures. The height of potential barrier and shell thickness lead to the different degree of PL quenching.

ACKNOWLEDGMENT

The authors thank the Science and Technology Research Program from Education Department of Heilongjiang province in China for the fund under Grant No. 12531515.

References

[1] V. L. Colvin, M. C. Schlamp and A. P. Alivisatos: Nature, Vol. 370 (1994), p. 354.

- [2] R. Sakandar, G. Andrew and J. M. Cooper: Langmuir: Vol. 26 (2010), p. 16934.
- [3] W. U. Huynh, J. J. Dittmer and A. P. Alivisatos: Science, Vol. 295 (2002), p. 2425.
- [4] J. Song, X. Song and T. Ling: Ind. Eng. Chem. Res., Vol. 51 (2012), p. 10074.
- [5] Q. Sun, Y. A. Wang and L. Li: Nat. Photo, Vol. 1 (2007), p. 1.
- [6] M. Bruchez, M. Moronne and A. P. Alivisatos: Science, Vol. 281 (1998), p. 2013.
- [7] M. A. Hines, P. Guyot-Sionnest: J. Phys. Chem.B, Vol. 100 (1996), p. 468.
- [8] R. G. Xie, U. Kolb and J. X. Li: J. Am. Chem. Soc., Vol. 127 (2005), p. 7480.
- [9] G. Schlegel, J. Bohnenberger and I. Potapova: Phys Rev Lett, Vol. 88 (2002), p. 137401.
- [10] O. Schmelz, A. Mews and T. Basche: Langmuir, Vol. 17 (2001), p. 2861.
- [11] J. Müller, J. M. Lupton and A. L. Rogach: Phys. Rev. Lett., Vol. 93 (2004), p. 167402.
- [12] M. Sykora, M. A. Petruska, J. Alstrum-Acevedo: J. Am. Chem. Soc., Vol. 128 (2006), p. 9984.

Self-propagating High-temperature Synthesis of Ni-Cu-Zn Ferrites with Alternative Fuel of Carbon Powder

Zhenhua Wang^{1,a}, Jiuxing Jiang^{1,2,b}, Changlong Tan¹, Zhihan Zhu¹, Fan Xu²

¹ Harbin University of Science and Technology, Harbin, 150080, China

²Key Laboratory of Design and Synthesis of Functional Materials and Green Catalysis, College of Heilongjiang Province, Harbin Normal University, Harbin 150025, PR China

^aemail: wzhua@hrbust.edu.cn, ^bemail: jjxinghit@sina.com

Keywords: carbon content; self-propagating high-temperature synthesis; Ni-Cu-Zn ferrites; microstructure; magnetic properties;

Abstract. Ni-Cu-Zn ferrite powders were prepared by self-propagating high-temperature synthesis (SHS) using carbon powder with different mass fractions as fuel. The effects of carbon content in the raw materials on the phase composition, microstructure, density and magnetic property of the Ni-Cu-Zn powders were investigated by X-ray diffractometry(XRD), scanning electron microscope(SEM) and vibrating sample magnetometer(VSM), respectively. The results show that the use of carbon as a fuel brings no other impurities and improved the permeability. The single spinel phase powder was obtained when the precursor materials with a carbon powder of 5% in mass were used.

Introduction

The Ni-Cu-Zn ferrite powder prepared by SHS has many advantages such as high purity magnetic powder, well sintering activity, low processing cost and energy efficiency; therefore, it has great extension value [1-4]. In the process of SHS preparation, the iron powder particle-size is larger ≥ 75 μm), so after ball grinding mixture the uniformity of the hybrid materials is low. The combustion temperature of the precursor materials is higher in the area of more relative iron powder, and the products would be over burnt, discontinuous crystal grain growth coarsening tends to occur, which reduces sintering activity. In the area of deficient iron powder, the combustion temperature of the precursor materials is low; the reactants would be converted incompletely. While preparing ferrites, we have not adopted fine iron powder, because the smaller granularity is, the higher its price to be, and it is easier to be oxidized when ball-milled. If using other materials to replace the iron powder as the fuel to prepare the Ni-Cu-Zn ferrite powders, it will avoid precursor materials mixed non-uniform and sintering temperature uneven because of oversize of the iron powder particle-size [5-8]. At present it is little report in public in the study of the alternative fuel of the SHS reaction. Through the research of SHS process, in this paper, Ni-Cu-Zn ferrite powders were prepared by SHS with alternative fuel of carbon powder which is smaller in granularity and lower in cost. The products were compared with the ferrite prepared by SHS with using fine iron powder (45µm~75µm) as fuel, and discusses how carbon content in the precursor materials influences the microstructure and magnetic properties of products.

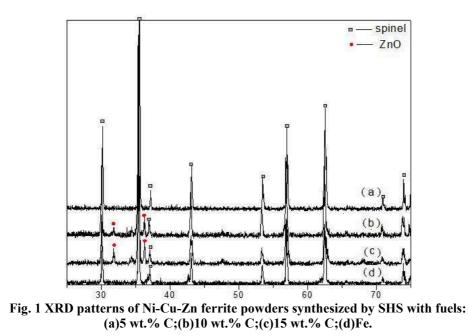
Experimental

The refinement of precursor materials particles can effectively increase the relative initial permeability of Ni-Cu-Zn ferrites and promote the solid reaction during sintering [9-12]. The raw materials used to synthesize $(Ni_{0.2}Cu_{0.2}Zn_{0.6}O)_{1.02}(Fe_2O_3)_{0.98}$ powder were nickel oxide, copper oxide, zinc oxide, iron oxide, and carbon, with the purity of 99%, respectively. The starting materials were weighed according to the required stoichiometric proportion to the addition of 5 wt.%, 10 wt.%, and 15 wt.% of carbon powder, respectively. They were mixed in de-ionized water, followed by ball milling for 2 h and then dried in a drying oven. The mixture powders were loosely packed in a quartz

container. The hybrid powders were put into the reactor to synthesize the ferrite powders under 0.2Mpa oxygen pressure. The ferrite powders prepared with different contents of carbon powder were identified by X-ray diffractometry (XRD). The microstructure of the ferrite powders was observed with a scanning electron microscope (SEM). Magnetic properties of the ferrite powders were measured on a vibrating sample magnetometer (VSM).

Results and discussion

Fig.1 shows the phase composition of the product powders prepared with different contents of carbon powder as fuel and iron powder as fuel. Spinel peaks of ferrites are observed in the X-ray pattern. The reaction products prepared with 5 wt.% carbon content and using iron powder as fuel are roughly same, indicating that the introduction of new fuel will not bring the other impurities and the reaction is relatively complete. However, as the increases of carbon powder content in the reactant powders, increases, the relative intensities of peaks belonging to ZnO, while the relative intensity of spinel peaks decreases. This indicates that the reaction proceeds are incomplete, So an excess of introduction of carbon powder will bring negative impact on the reaction. This can be explained as follow. The combustion synthesis is an oxidation reaction which controlled by the oxygen permeability, and when the oxygen pressure is determined, the oxygen permeability is certain. The oxygen permeability can fulfill requirements of the reaction when the carbon content is 5 wt.%, thus the combustion speed and combustion temperature are high. As a result, the reaction proceeded completely. However, as the carbon content in the reactants continues to increase, the release of CO₂ from the reaction is more. The CO₂ will dilute the oxidation reaction during the combustion wave propagation [13]. The dilution effect caused by the excess CO₂ will prevent the oxygen permeating, therefore the combustion speed and combustion temperature will be reduced. Consequently, the ferrite-conversion decreases.



The SEM images of the SHS products prepared with different carbon contents and using iron powder are shown in Fig. 2. Obviously, the reaction components different, the morphology and particle size are quite different. With introduction of carbon in the raw powders as fuel, contrast to using iron powder as fuel, it is clearly seen that the particle size is homogeneously fine as shown in Fig.2 (a). This will help improve the sintering activity, laying the foundation for improving magnetic properties of devices. Fig.2 (b), (c) shows that with even more carbon added, the product composed of several phases with particle size becomes a little less homogenous and bigger, as confirmed in the XRD patterns. This is not conducive to post-sintering. This phenomenon is because relative to iron

powder, the granularity of carbon powder is small; accordingly the dispersity of raw materials is better and the combustion temperature is more even. Meanwhile, the CO_2 gas escaped from the powders and left open pores during the reaction; thus the oxygen gas was easy to infiltrate through the powders to ensure the reaction taking place continuously. Hence, the homogeneously fine particles were obtained. However, with the increase of carbon concentration, the distances of Oxides were increased, which resulted in the reaction proceeded incompletely and non-uniformity of the products.

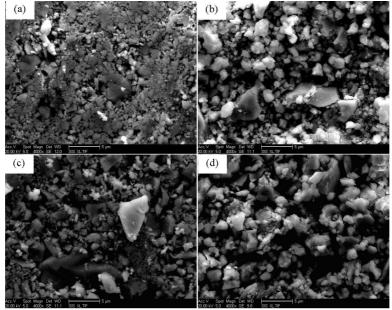


Fig. 2 SEM images of Ni-Cu-Zn ferrites prepared by SHS with fuels: (a)5 wt.% C;(b)10 wt.% C;(c)15 wt.% C;(d)Fe

Fig. 3 shows the dependence of magnetization (σ) on the applied magnetic field (H), calculated from the hysteresis curve of the Ni-Cu-Zn ferrites prepared with different carbon contents and using iron powder. The values of remanent magnetization (Mr), saturation magnetization (Ms), and coercive field (Hc) are presented in Table 1. As indicated in Fig. 3, all the products display narrow σ ×H cycles, which is a very soft material (easy magnetization and demagnetization). Apparently, Fig.3 (a) show that the value of saturation magnetization of the samples prepared with 5 wt.% carbon content, which is the highest. Fig.3 (b), (c) shows that with even more carbon added, the value of saturation magnetization of the samples prepared is the lowest due to the impurities like ZnO, as confirmed in the XRD patterns. However, all the samples prepared with using carbon powder as fuels are better than samples prepared by traditional process.

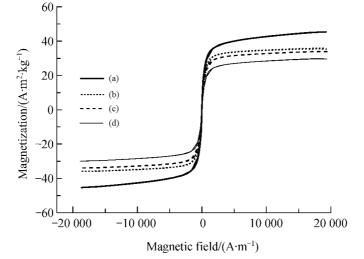


Fig. 3 Hysteresis loops of Ni-Cu-Zn ferrite prepared by SHS with fuels: (a)5 wt.% C;(b)10 wt.% C;(c)15 wt.% C;(d)Fe.

Table 1 Magne	enc data for the ferrites obtaine	a from room temperature hysic	eresis loops
Sample	$M_{\rm r}/({\rm A}\cdot{\rm m}^2\cdot{\rm kg}^{-1})$	$M_{\rm s}/({\rm A}\cdot{\rm m}^2\cdot{\rm kg}^{-1})$	$H_{\rm c}/({\rm A}\cdot{\rm m}^{-1})$
a	12.1	45.5	13.1
b	10.3	35.8	27.6
С	9.7	33.7	29.3
d	7.3	27.7	47.7

Table 1 Magnetic data for the ferrites obtained from room temperature hysteresis loops

Conclusions

The researches show that Ni-Cu-Zn ferrite powders can be prepared by SHS with alternative fuel of carbon powder. The results show that the introduction of new fuel will not bring the other impurities, but it lead to better powder sintering activity and lower costs. With increasing carbon content, the sintering activity of product powders reduces. The maximum value of saturation magnetization is obtained when the carbon content is 5 wt.%.

References

- [1] Li Guodong: New Progress of Research of Magnetic Functional Material and Application in 2004~2005, Rare Meta Materials And Engineering, Vol. 37 (2006), p. 1355.
- [2] Zhenhua Wang, Jiuxing Jiang, Changlong Tan and Zhihan Zhu: Journal of the Chinese Ceramic Society, Vol. 40 (2012), p. 888.
- [3] Keqiang Wang, Xiaodong He, Li Xiao, Jiuxing Jiang and Sun Yue: Rare Metals, Vol. 28 (2009), p. 500.
- [4] Z.H. Khan, M. Mahbubur Rahman, S.S. Sikder, M.A. Hakim and D.K. Saha: Journal of Alloys and Compounds, Vol. 548 (2013), p. 208.
- [5] Li Yao, Jiupeng Zhao, Jiecai Han and Shanyi Du: Journal of the Chinese Ceramic Society, Vol. 28 (2000), p. 427.
- [6] Youwei Du: Development of magnetic materials in recent years, Physics, Vol. 35 (2006), p. 730.
- [7] Zhigang Zheng, Dechang Zeng, Yahui Zhang and Weidong Huang: Materials Review, Vol. 27 (2007), p. 26.
- [8] Xianqing Piao, Ken-ichi Machida and Takashi Horikawa: Chem Mater, Vol. 19 (2007), p. 4592.
- [9] Li Yao, Jiupeng Zhao, Jiecai Han and Shanyi Du: Journal of the Chinese Ceramic Society Vol. 28 (2000), p. 427.
- [10] Jiuxxing Jiang, Li Yao, Xiaodong He: Journal of the Chinese Ceramic Society Vol. 21 (2003), p. 264.
- [11]T. Nakamura: J. Magn. Magn. Mater., Vol. 168 (1997), p. 285.
- [12]Mossino P.: Ceram. Int., Vol. 30 (2004), p. 311.
- [13]Peng C., Hwang C., Hong C. and Chen S.Y.: Mater. Sci. Eng. B, Vol. 107 (2004), p. 295.

Effect of PVP Hydrophilic Additive on the Morphology and Properties of PVDF Porous Membranes

Yunwei Guo^{1, a}, Weiwei Cui^{1,b}, Wenhua Xu^{1,c}, Yang Jiang^{1,d}, Huihui Liu^{1,e}, Jiayu Xu^{1,f}, Zhanqiang Gao^{1,g} and Lizhu Liu^{1,h}

¹College of Materials Science and Engineering, Harbin University of Science and Technology, Harbin, China

^a hustgyw@163.com, ^bcuiww@hrbust.edu.cn, ^cxuwenhuayi@163.com, ^dbotiluobushuo@sina.com, ^eliuhuihui935@163.com, ^fxujiayuhaha@126.com, ^ggaozhanqiangcl@163.com, ^hmrliulizhu@163.com

Keywords: Porous membranes, Polyvinylpyrrolidone (PVP), Hydrophilicity, Porosity.

Abstract. This work describes the preparation and the properties of poly(vinylidene fluoride) (PVDF) porous membranes. The porous membrane was prepared using phase-inversion method by adding hydrophilic polyvinylpyrrolidone (PVP) as hole-agent. The contrastive analysis of membrane characterizations between the membrane no PVP added and the membrane added PVP were carried out by optical microscopy analysis, scanning electron microscopy, porosity, pure water flux and water contact angle. The results showed that adding PVP can induce the building of pore structure, increase the surface roughness and hydrophilicity of PVDF membrane, and then enhance its pure water flux.

Introduction

Wastewater generated in industrial processes generally contains lots of oil/water mixtures, which will bring harm to the environment and people's health [1,2]. Separation of oil/water mixtures is always difficult and a worldwide challenge [3,4]. Poly(vinylidene fluoride) (PVDF) as one of the attractive membrane materials used in water treatment field processes many outstanding properties, including excellent chemical resistance, good mechanical properties, and having excellent resistance to most corrosive chemicals and organic compounds [5-7]. But hydrophobic PVDF membranes generally lead to the non-specific adsorption of protein in organic-containing solutions, which limited their application in the fields of biomedical uses and water treatment [8]. Intrinsic chemical composition is not the only factor affecting the suitability of the membrane, the morphological properties, too, play a significant role. By selecting the correct modified material and the fabrication parameters, the morphology and the properties of the membrane can be varied, and then the membrane can be valuable for different application.

In this paper, polyvinylpyrrolidone (PVP) possessing excellent hydrophilicity was used to change the morphology and properties of PVDF membrane, the effect of PVP on the porous structure and the hydrophilic of PVDF membranes was discussed.

Experimental

Membrane preparation. The PVDF membranes were prepared using a phase- inversion process. Amount of PVDF (KYNAR 761, ARKEMA) was dissolved in dimethylacetamide (DMAC) under continuous stirring for 2 h at 60 °C to form a transparent PVDF solution with the concentration of 17 wt %. PVP powder (Tianjin Damao Chemical Reagent, six percent of the weight of PVDF) were then added to the above solution, and kept for 6 h to form a transparent solution. After that, the mixture solutions were cast using an automatic film applicator (AFA-II, Shanghai Pushen Chemical Machinery Co, Ltd). In this experiment, the casting thickness was set to 250 μ m. The nascent membranes were then immediately immersed in a coagulation bath consisting of deionized water at room temperature for 72 h. The formed membranes were dried in the air at room temperature for 24 h, and then dried in an oven at 60 $^{\circ}$ C for 3 h.

Membrane characterization. The surface roughness of membranes was observed by Olympus GX71 Microscope. The morphologies were observed using scanning electro microscopy (Quanta 200, FEI). The water contact angle was measured by Powereach JC2000C optical contact angle meter. The porosity (P_r) was determined by weighing the dry membranes, soaking it in deionized water until attaching the swelling balance, drying the surface with filter paper, and then reweighing it. Equation (1) was used to calculate the values for P_r

$$P_r = \frac{W_1 - W_0}{\rho_{\rm w} \times S \times L} \times 100\%$$

(1)

(2)

Where P_r is the porosity of the membrane, W_1 is the weight of the wet membrane, W_0 is the weight of the dry membrane, ρ_w is the specific gravity of water, S is the area of the membrane, L is the thick of the membrane.

The flux of pure water (J_w) was measured by permeating pure water through the membrane under the pressure of 0.1 MPa and calculated as:

$$J_{w} = \frac{V_{w}}{A \times t}$$

Where J_w is the water flux (L/m²h), V_w is the permeate volume (L), A is the membrane area (m²) and t is the permeating time (h).

Results and discussions

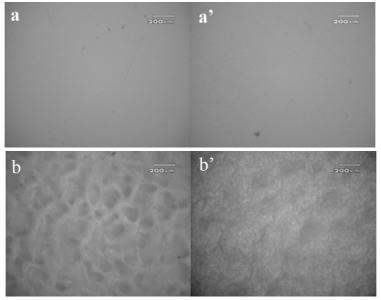


Fig.1 Surface optical images of the pure PVDF membrane, (a) top surface and (a') bottom surface, and the modified PVDF membrane with PVP, (b) top surface and (b') bottom surface.

The surface optical images of the membranes were shown in Fig.1. It can be seen that both the top and the bottom surface of the pure PVDF membrane have smooth surfaces, while the PVP modified membranes is fairly rough. The gully-like structure could be seen on the top surface of the modified membranes, and the similar structure also could be seen on the bottom surface, and the roughness is less than the top surface. These images indicated that the unmodified membrane had a denser skin, as well as smoother surface, while the modified membranes had a loose skin, as well as rougher surface.SEM was employed to investigate the effect of adding PVP on the morphology of the membranes. Fig. 2(a) and (a') show the top and the bottom surface SEM images of the pure PVDF membrane. The top surface of the membrane was smooth and flat, but almost no pore structure could be observed. The bottom surface of pure PVDF membrane is composed of discernible spherical crystalline domains. The gibbous white region was the center of the spherical crystalline. The

peripheral region was dark, and the clear grain boundary was also observed. The small folds were appeared on the spherical crystalline structure, and no pore structures were observed. The bottom surface of the membrane was denser than the top surface.

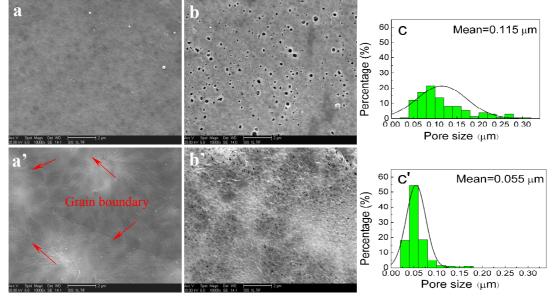
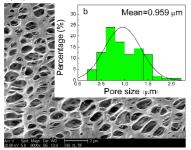


Fig.2 SEM images of surface morphology of the pure PVDF membrane, (a) top surface and (a') bottom surface, and the modified PVDF membrane with PVP, (b) top surface and (b') bottom surface. Pore size distribution of the top (c) and the bottom (c') surfaces of the modified PVDF membrane with PVP



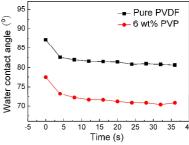


Fig.3 SEM images (a) and the pore size distribution (b) of the cross-section of the modified PVDF membrane with PVP.

Fig.4 Variation of the water contact angle of the membranes with increasing contact time

Fig. 2(b) and (b') show the top and the bottom surface SEM images of the PVP modified membranes. It can be seen that the introduction of PVP into the PVDF casting solution induced many pores both on the top and the bottom surfaces. The pore size and the size distribution were summarized in Fig. 2(c) and (c'). The pore size on the top surface (the mean value was 0.115 μ m) is larger than that one on the bottom (the mean value was 0.055 μ m). Meanwhile, the distribution of the pore size of the top surface was wider than that one of the bottom surface.

The cross-sectional micrographs of modified PVDF membrane are presented in Fig 3. Spongy-like micro-pores were uniformly distributed in the interior of the membranes. The pores were interconnected and formed a network structure. The average pore size was 0.959 μ m, which was much larger than that of the surface. This structure was obviously beneficial to reduce the resistance of the water flow and increase the pure water flux of the membrane. Meanwhile, the porous structure can act as a mechanical support. The porosity of the membranes is presented in Table 1. The porosity was evaluated by the degree of the water absorbed into the membranes[9]. The results of the porosity tests further corroborated the SEM results. Because of the dense surface structure, the porosity of the pure PVDF membrane was only 2.21%, while the porosity of modified PVDF membrane was enhanced to 11.67%. The addition of PVP caused the exchanging process between the solvent and the nonsolvent to become much faster, and thus, the membrane structure became loose, subsequently leading to higher porosity. Combined the surface optical images of the membranes, it can be concluded that the increase in pore size enhanced the surface roughness.

Water contact angles were employed to evaluate the effect of the membrane surface hydrophilicity, lower water contact angle represents higher hydrophilicity[10]. Fig.4 gives the

variation curves of the water contact angle with the contact time. The water contact angle of two membranes decreased with time. For the pure PVDF membrane, the contact angle was 87.09° at the initial time of water droplet falling, then decreased rapidly, and reached a stable value of 80.83° after 20 s. The initial angle of modified PVDF membrane was 77.44°, which was significantly lower than the pure PVDF membrane. The stable angle was 70. 84°. It showed a drop of 10 degree throughout the whole observation time. These results indicated that PVP not only induced the pore structure but also brought higher hydrophilicity to the PVDF membrane. The enhancement of the hydrophilicity may be due to the hydrogen bonding between the oxygen atom of PVP and the hydrogen atom of PVDF. The hydrogen bonding made the enrichment of PVP on the surface of the membrane during the forming process, and caused partial PVP was left in the membrane, and eventually lead to the enhancement of the hydrophilicity. The results of the pure water flux of the membranes were summarized in Table 1. Pure PVDF membrane gave the lowest flux, and almost no water flowed through the membrane. The modified membrane exhibited a substantial rise of flux up to 11.67 L/m²·h. The addition of PVP induced the pore structure of membranes. Such structure is advantageous to increase flux. Meanwhile, it is also attributed to the hydrophilicity of PVDF membrane enhanced by PVP. The excellent hydrophilicity of the membrane was helpful to overcome the hydrodynamic resistance of water, and facilitate the pass of the water through the membrane pores.

Table 1 Characteristics of pure PVDF membrane and modified PVDF membrane with PVP.

Membrane	Porosity [%]	Pure water flux $[L/m^2 \cdot h]$
Pure PVDF	2.21	0
PVDF +6% PVP	37.19	11.67

Conclusion

Porous PVDF membranes were prepared through phase-inverse process by using PVP as additive. The hydrophobicity of PVDF membrane was reduced due to the excellent hydrophilicity of PVP. The introduction of PVP facilitated the built of porous structure and the increase of porosity and pure water flux.

Acknowledgements

This work was supported by College Students' Innovative Entrepreneurial Training Plan Program of Harbin University of Science and Technology (201310214043).

References

- [1] H. Liu, R. Ramnarayanan and B.E. Logan: Environ. Sci. Technol. Vol. 38 (2004), p. 2281
- [2] G. Crini: Prog. Polym. Sci. Vol. 30 (2005), p. 38
- [3] Z. Xue, S. Wang and L. Lin: Adv. Mater. Vol.23(2011), p. 4270
- [4] Q. Zhu, Q. Pan and F. Liu: J. Phys. Chem. C, Vol. 115(2011), p. 17464
- [5] J.F. Hester, P. Banerjee and A.M. Mayes: Macromolecules Vol. 32(1999), p.1643
- [6] N. An, H. Liu and Y. Ding: Appl. Surf. Sci. Vol. 257 (2011), p.3831
- [7] Y.Y. Zhang, S.L. Jiang and Y. Yu: J. Appl. Polym. Sci. Vol. 123(2012), p. 2595
- [8] A.L. Ahmad, N. Ideris and B.S. Ooi: J. Appl. Polym. Sci. Vol.128 (2013), p. 3438
- [9] Y. Sui, X. Gao and Z. Wang: J. Membrane Sci. Vol.394–395 (2012), p.107
- [10] G. Kugel , T. Klettke and J.A. Goldberg: J. Prosthodont. Vol. 16 (2007), p. 84

Analysis to Milling Force Base on AdvantEdge Finite Element Analysis

Fucai Zhang^{1,a}, Qing Wang^{2,b}, Ru Yang^{3,c}

¹Heilongjiang University of Science and Technology, Harbin, Heilongjiang Province, China ²Shaanxi Institute of Technology, Xi'an, Shaanxi Province, China ³Harbin University of Science and Technology, Harbin, Heilongjiang Province, China ^aqingtengzfc@yeah.net, ^b510132156@qq.com, ^c78020327@qq.com

Keywords: Spherical milling cutter; Milling force modeling; Finite element analysis; Experimental verification

Abstract. Aiming at NC milling processing simulation problem, a ball-end cutter milling force model is established, the numerical simulation analysis of aluminum alloy AL2024 milling process is conducted by using the finite element analysis software AdvantEdge finite element analysis. Focus on the Milling force simulation, the size of the milling force is obtained by simulating calculation. Using the same cutting parameters for milling experiment, the results show that simulation analysis of the cutting force values are in good agreement with the experimental results, the milling force model prior established is correct. The research laid a foundation for the perfect CNC milling simulation system.

1.Introduction

The application of high speed milling becomes an increasingly widespread in process of spherical surface parts. The temperature, force, strain of milling are not easy to measure in actual process and also difficult to conduct in-depth research for cutting processing mechanism only rely on experiments. At present, Li Yang and Lou Wen Ming establish the thin-walled frame parts and studied thin frame parts by using coupling deformation model[1][2].E.Budak first establish a milling force model in the high-speed milling case and put forward dynamics model to reduce milling error in milling process [3].Du Mao Hua set establish the tool to rigid body and the machining material for milling force model[4][5]. The paper establishes a milling force model of high speed cutter and obtain the size of the milling parameters by using the finite element analysis software AdvantEdge. Conduct the experiments in the XH715 processing center, comparing the cutting force values of the simulation analysis and the experimental measurements, verify the correctness of the established model.

2 Milling Process Simulation Analysis

The work piece material is aluminum alloy (AI 2024), in which the initial temperature of 20° spindle speed 2000r/min, the feed amount 0.1524mm / r, AdvantEdge cutting parameter input interface is in Figure 3.Call the Production Module 3d (PM) module 16 milling force orthogonal simulation. As shown in Figure 1.

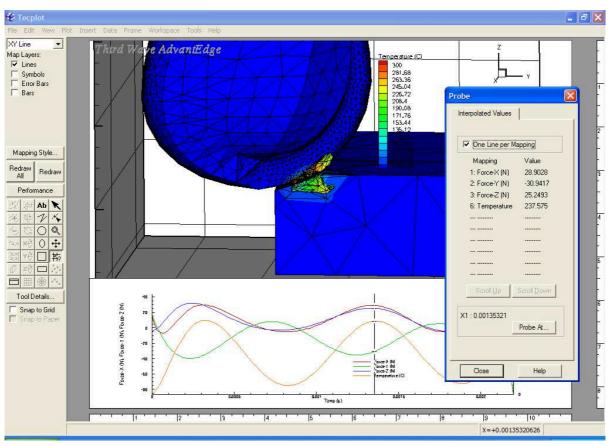


Fig. 1 The milling force orthogonal simulation experiment

In order to more intuitive to research cutting force deformation on the influence of the machining errors, you can extract tool stress changes Graphic after the end of the run. It is showed in figure 2, at the same time tool plastic strain is showed in figure 3.

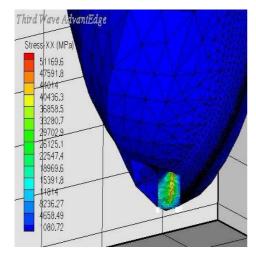


Fig. 2 Cutter stress deformation

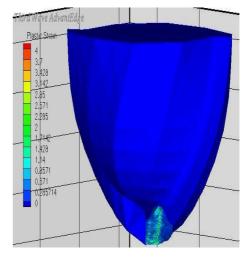


Fig. 3 Tool plastic strain

3. Milling force model experimental verification

Aluminum alloy AL2024 material has high strength and good machinability, but corrosion resistance is poor, mainly used in general machinery parts, aircraft, traffic and transportation structure tool parts. In order to improve the reliability of simulation, election of ball end cutter geometrical parameters and work piece material and simulation analysis is the same. There is a milling processing on helmet In XH715 machining center, helmet 3D graph is showed in Figure 4, Figure 5 is the experimental scene photograph[9] [10].

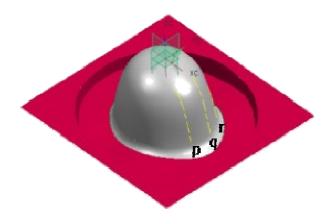


Fig. 4 Helmet 3D graph model

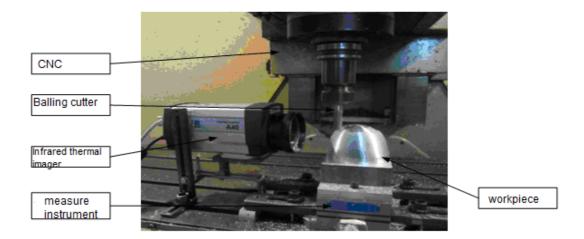


Fig. 5 The milling experiment

The simulation analysis and experimental data is shown in Table 1. The analog values relative to the experimental values obtained by simulation of certain error and mainly due to the presence of errors. firstly, set the movement of the tool and the work piece, the simulation analysis and experimental; secondly, no tool wear option set in the simulation, but it does exist in the actual cutting tool wear and tool wear measured cutting force to be larger, the third, vibration problems of the processing system is not considered in the simulation analysis process

Parameter	First	Second	Third	Fourth	Fifth
a_p/mm	0.500	0.379	0.406	0.400	0.402
F_X /N (Simulation value)	104.399	81.110	86.418	85.211	85.489
$F_{\rm y}$ /N (Simulation value)	56.615	43.779	46.696	46.034	46.185
F_X/N (experiment value)	105.47	83.476	87.125	85.693	85.739
F_{Y}/N (experiment value)	58.325	44.126	47.214	46.763	46.368

Table 1 The cutting force values of simulation analysis and experimental results

4. Conclusion

Through the study and analysis of influencing factors on spherical end milling force, established a cutting force model by using the AdvantEdge finite element analysis simulation analysis software and conduct Orthogonal cutting simulation experiment method for analysis and numerical calculation. Used XH715 processing center for experiments, the experimental results show that the simulation model can make the cutting force simulation accuracy of about 10%. This precision meet the needs of qualitative analysis, design optimization tool development process has certain reference value, and provide a theoretical basis for guiding practice.

5.References

- [1] Li Yang, Thin-walled parts milling deformation prediction. Dalian: Dalian Jiao tong University [D], 2013. (Chinese).
- [2] Lou Wenming, Study on milling process machining deformation compensation of aviation thin-wall components. Xi'an: Northwestern Poly technical University [D], 2007. (Chinese)
- [3] Budak E, Analytical models for high performance milling. Part I: Cutting forces, structural deformations and tolerance integrity. International Journal of Machine Tools& Manufacture [J], 2006,46(12/13):1478-1488.
- [4] Du Maohua, Pang Xinfu, The two dimensional orthogonal milling finite element simulation analysis, Mechanical and Electronic, 2008.
- [5] Jiang Zhitao, Liu Hongbin, Wang Fei, Two-dimensional simulation analysis of high-speed milling in ABAQUS, Modern Manufacturing Engineering, 2008.
- [6] Cai Yonglin, Huang Zehua, Thin blade machining error analysis and prediction of Beijing Jiaotong University, February, 2012.
- [7] Zhao Yunfeng, Zhang Jianhua, Shen Dongliang, Institute of aluminum alloy AL2024 milling simulation analysis and experimental study of Shandong University, Mechanical Engineering Manufacturing Technology & Machine ,2011.
- [8] Yin Li, Liu Qiang, Study on the identification of the milling force parameter model based on partial Least square regression and application [J]. Mechanical science and technology, 2005, 24(3):269-272. (Chinese)
- [9] Zhongbin Wang, Juan Xu, Yuliu Chen. Intelligent CAPP System Based on Multi-agent Architecture. Mechanical Science and Technology [J]. 2007, (06), 746-750
- [10]Longtai Wang, Denglin Zhu, Guohong Dai, Aiping Song. The Mechanical CAD/CAM Technology[M]. Beijing: Mechanical Industry Press, 2010

Research on the Effects of Ultraviolet Aging of Polyethylene Trap Distribution

Lijuan He^{1, 2}, Chao Zhu¹, Huaichong Huang¹, Shan Wang¹, Haiping Xie¹, Chuntian Chen^{1, a}

¹Harbin University of Science and Technology, Harbin, 150080, P.R.China

²Key Laboratory of Engineering Dielectric and Its Application, Ministry of Education, Harbin University of Science and Technology, 150080, China

^achenchuntian730@sohu.com

Keywords: polyethylene; space charge; charge trap; photo-stimulating discharge

Abstract. The photo-stimulating discharge (PSD) and ultraviolet-visible spectrometry were used to characterize the polyethylene (PE) and nano-hybrid PE trap before and after ultraviolet aging. In PE with the increasing of ultraviolet aging time, shallow traps reduce gradually and deep traps increase gradually, but for the nano-hybrid PE, shallow traps increase gradually and deep traps reduce gradually. Experiments show that: in the process of aging PE produces oxidation products such as carbonyl, hydroxyl etc. The incorporation of impurities can inhibit the injection of space charges, so as to achieve the purpose of improving electric field distortion in the body of the PE.

Introduction

Polymer materials represented by PE in recent years are widely used in power cable and other areas of the electrical insulation, but the trace transition metal and initiator residues remained in PE in the process of synthesis and processing make polymer chain contain a small amount of carbonyl, hydrogen peroxide groups etc, under the long-term exposure to the sun, strong fluorescent, nuclear industry, space etc, these chromophores can strongly absorb ultraviolet light and cause polymer optical oxygen degradation reaction. Ultraviolet light can cause cross-linking even fracture of molecular chain in material, thus to change the chemical properties of the materials, eventually lead to the insulation failure and the decline of electrical properties. The ultraviolet aging problems of polymer dielectric can not be ignored, so it is particularly important to do the doping modification of PE and find an effective polymer light-stability method.

Due to the various structural defects in polymer dielectric materials, the charge traps are caused by local state and doping modification introduced by the crystalline area and amorphous area interface, the charges will be captured by the traps and space charges form, space charge can change the electric field distribution making the intensity values of the local electric field exceed the designed insulator; The injection of space charge may cause electrical tree trigger and development and eventually lead to insulation failure; The accumulation of space charges makes the concentration of local energy, thus leads to aging degradation, which makes the system be at risk. A large number of studies show that, space charge traps are closely related to the aging of the insulating material, especially the space charges entering into and taking off a trap. Therefore, it is very important to research into the dynamics of space charge.

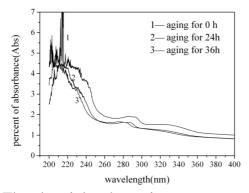
Experiments

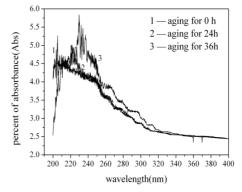
Films of PE and PE doped with 5% MgO with the thickness of 30 microns were chosen as the samples. First, the ultraviolet absorption spectrum was tested, and PSD was tested after both sides of the samples were plated with gold electrodes. The sample was charged by the method of dc

contact with the polarization field strength and charge injection time 40kv/mm and 60min respectively; The sample was irradiated uniformly for 24h with ultraviolet light bulb after the electrodes were cleaned with acetone, and the ultraviolet absorption spectrum and PSD testing were repeated; The same testing was repeated after irradiated for 36h.

The above samples were tested at room temperature, ultraviolet absorption spectrum was measured by ultraviolet-visible spectrophotometer, spectral scanning photometric mode was set as Abs (absorbance mode), spectral scanning range was set to range from 400nm to 190nm and spectral bandwidth value was set as 0.2nm. During the PSD testing, laser wavelength scanning range was set to range from 420nm to 210nm, spectral bandwidth value was set as 2nm, the time interval was set as 100s, and electrometer was connected with computer and real-time current data was obtained.

1) The ultraviolet absorption spectrum was drawn by origin software after the PE was aged for 0h, 24h and 36h as shown in Fig. 1.

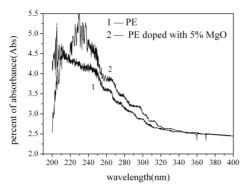




different aging time for PE

Fig. 1 The ultraviolet absorption spectrum under Fig. 2 The ultraviolet absorption spectrum under different aging time for PE doped with 5% MgO

- 2) The ultraviolet absorption spectrum was drawn by origin software after the PE doped with 5% MgO was aged for 0h, 24h and 36h as shown in Fig. 2.
- 3) The ultraviolet absorption spectrum was drawn by origin software after the PE and the PE doped with 5% MgO were aged for the same time as shown in Fig. 3.



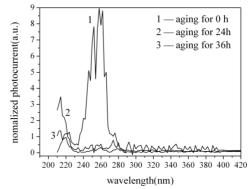
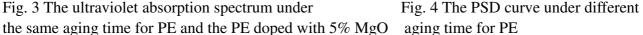


Fig. 3 The ultraviolet absorption spectrum under



- 4) The PSD curve was drawn by origin software after the PE was aged for 0h, 24h and 36h as shown in Fig. 4.
- 5) The PSD curve was drawn by origin software after the PE doped with 5% MgO was aged for 0h, 24h and 36h as shown in Fig. 5.

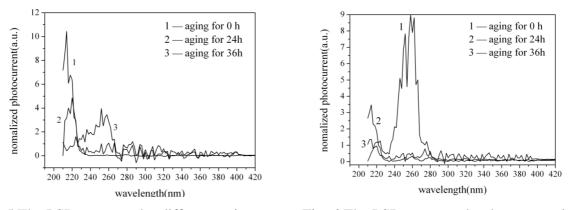
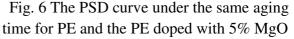


Fig. 5 The PSD curve under different aging time for PE doped with 5% MgO



6) The PSD curve was drawn by origin software after the PE and the PE doped with 5% MgO were aged for the same time as shown in Fig. 6.

Results and Discussion

As can be seen from Fig. 1, for PE aged for 0h, the peak value of maximum absorption peak is 215nm and the corresponding trap depth is 5.78eV; After aging for 24h, the peak value of maximum absorption peak is 207nm and the corresponding trap depth is 6.00eV; After aging for 36h, the peak value of maximum absorption peak is 203nm and the corresponding trap depth is 6.12eV.

As can be seen from Fig. 2, for PE doped with 5% MgO aged for 0h, the peak value of maximum absorption peak is 205nm and the corresponding trap depth is 6.06eV; After aging for 24h, the peak value of maximum absorption peak is 221nm and the corresponding trap depth is 5.62eV; After aging for 36h, the peak value of maximum absorption peak is 230nm and the corresponding trap depth is 5.40eV.

As can be seen from Fig. 3, under the same aging time, the peak value of maximum absorption peak is 229nm for PE doped with 5% MgO and the corresponding trap depth is 5.43eV. The peak value of maximum absorption peak is 203nm for PE and the corresponding trap depth is 6.12eV.

As can be seen from Fig. 4, for PE aged for 0h, the PSD is detected when scanned from 280nm to 210nm, zonal distribution is found for trap energy level on the whole and the trap depth is calculated to range from 4.4eV to 5.9eV, the maximum PSD is at 252nm and the corresponding trap depth is 4.9eV; After aging for 24h, the PSD is detected when scanned from 228nm to 210nm, and the trap depth is calculated to range from 5.4eV to 5.9eV, the maximum PSD is at 218nm and the corresponding trap depth is 5.7eV; After aging for 36h, the PSD is detected when scanned from 275nm to 210nm, and the trap depth is calculated to range from 4.5eV to 5.9eV, the maximum PSD is at 214nm and the corresponding trap depth is 5.8eV.

As can be seen from Fig. 5, for PE doped with 5% MgO aged for 0h, the PSD is detected when scanned from 228nm to 210nm and the trap depth is calculated to range from 5.4eV to 5.9eV, the maximum PSD is at 214nm and the corresponding trap depth is 5.8eV; After aging for 24h, the PSD is detected when scanned from 228nm to 210nm, and the trap depth is calculated to range from 5.4eV to 5.9eV, the maximum PSD is at 220nm and the corresponding trap depth is 5.6eV; After aging for 36h, the PSD is detected when scanned from 266nm to 210nm, and the trap depth is calculated to range from 4.7eV to 5.9eV, the maximum PSD is at 252nm and the corresponding trap depth is 4.9eV.

As can be seen from Fig. 6, during the PSD testing under the same aging time, the peak value of maximum PSD peak for PE doped with 5% MgO is 252nm and the corresponding trap depth is

4.9eV; The peak value of maximum PSD peak for PE is 214nm and the corresponding trap depth is 5.8eV.

Conclusions

The results show that with the increasing of aging time, the maximum absorption peak of PE moves towards short wave direction and blue shift happens, the shallow traps gradually reduce and deep traps increase. As can be seen from the PE doped with nanometer particles, with the increase of aging time, the peak moves towards long wave direction as a whole and red shift happens, the deep traps gradually reduce and shallow traps increase; Under the same aging time, the peak of PE doped with impurities moves towards long wave direction and the red shift happens, shallow traps increase.

Experiments show that: in the process of aging, PE produces oxidation products such as carbonyl, hydroxyl etc. The incorporation of impurities can inhibit the injection of space charge, the energy needed for positive and negative charges to take off from trap reduce, so as to achieve the purpose of improving electric field distortion in PE.

Acknowledgments

The authors would like to express sincere gratitude to all the colleagues in our project group. This work is the program supported by Natural Science Foundation of Heilongjiang under Contract No. E200720, F201301, the program of Educational Commission of Heilongjiang Province under Contract No. 12521079 and Heilongjiang Province graduate entrepreneurship research project in 2012 under Contract No. YJSCX2012-119HLJ.

References

[1] A. Petre, D. Mary, C. D. Pham and L. Berquez: 3D Cartography of Space Charges Induced by UV Irradiation. Annual Report - Conference on Electrical Insulation and Dielectric Phenomena, (2007), p. 496.

[2] Y. Maeno, N. Hirai, Y. Ohki, T. Tanaka, M. Okashita and T. Maeno: Effects of Crosslinking Byproducts on Space Charge Formation in Cross Llinked Polyethylene. IEEE Transactions on Dielectrics and Electrical Insulation, vol.12(1) (2005), p. 90.

[3] J. Castellon, H. N. Nguyen, S. Agnel, A. Toureille and M. Frechette: Electrical and Thermal Aging of Micro-composite Nano-filled Epoxy: Influence on Space Charge Accumulation, IEEE Conference on Electrical Insulation and Dielectric Phenomena - CEIDP, (2009), p. 715.

[4] G. Chen, et al.: Effect of Polyethylene Interface on Space Charge Formation. Dielectrics and Electrical Insulation, IEEE Transactions on, vol. 11(1) (2004) p. 113.

[5] X. Wang: The Study on United Spectrum Instrument for Thermo Luminescence and Thermally Stimulated Current in Polymer. Xi'an Jiao tong University, (1999) p. 1.

[6] Masayuki Ieda: Dielectric Breakdown Process of Polymers, IEEE Trans. on EI. vol15(3) (1980) p. 206.

[7] L. J. He, L. Dai, C. Yang, F. Q. Tian, L. Zhao, J. L. Cao, X. Wang and Q. Q. Lei. Study on Deep Trap States in Polymers by Photo-stimulated Discharge Based on the OPO Laser. Modern Physics Letters B. Vol. 24(18) (2010) p. 1933.

Characteristics Research of New Type Silicon Magnetic Sensitivity Transistor Differential Structure by ATLAS

Zhao Xiaofeng^a, Guan Hanyu^b, Sui Huan, Wen Dianzhong^{c*}

Key Laboratory of Electronics Engineering, College of Heilongjiang Province, Heilongjiang University, Harbin, 150080

^azhaoxiaofeng@hlju.edu.cn, ^bguan.han.yu@163.com.cn, ^{c*}wendianzhong@hlju.edu.cn

Keywords: new type silicon magnetic sensitivity transistor; differential structure; magnetic characteristics; temperature characteristics; ATLAS.

Abstract. According to the experimental results of new type silicon magnetic sensitivity transistor (SMST), the simulation models of new type SMSTs with different base region lengths and widths were established by ATLAS software. The simulation results of optimizing the geometric parameters demonstrate that the max collector current relative magnetic sensitivity can be achieved when the base region length and width are 170 μ m and 30 μ m, and the simulation model of the differential structure of new type SMST was established based on it. The simulation results indicate that the max collector current relative magnetic sensitivity is 322%/T for new type SMST differential structure when the base currents are 5.0 mA and the collector voltages are 5.0 V, and it can improve the magnetic sensitivity and ameliorate temperature characteristics.

Introduction

In the 1970s, the junction type magnetic sensitivity device mainly concluded cubic structure germanium magnetic sensitivity transistor and silicon magnetic sensitivity diode.^[1,2] With the development of micro electromechanical system (MEMS) technology, the fabricating process for junction type devices based on the double injecting effect have been developed to the cubic process technology.^[3] In 2003, a new type n^+pn^+ SMST which had the rectangular three-dimensional cubic structure was fabricated in Heilongjiang University, it can achieve the maximum relative magnetic sensitivity 227%/T for collector current, and it has negative temperature coefficient.^[4-10]

Based on the characteristics of new type SMST, this paper adopts ATLAS software to establish the simulation model of new type SMST to have an optimization research of geometric parameters. The current-voltage characteristics, magnetic characteristics and temperature characteristics of new type SMST differential structure are studied by establishing the simulation model, which lays foundation for further applications of SMSTs in magnetic sensors.

The basic structure of the new type SMST

Figure 1 shows the basic structure of new type SMST, this long-base transistor was fabricated on the C type silicon cup which has p-type silicon substrate with the <100> orientation high resistivity (resistivity $\rho \ge 100 \ \Omega \cdot cm$), and the thickness of the silicon diaphragm is d ($d=30 \ \mu m$). The emitter, base and collector of SMST are represented by E, B and C, and the base region length and width are represented by L and w as the figure shows. The magnetic sensitive direction for new type SMST is along the z axis direction which is shown as coordinate system in Figure 1.

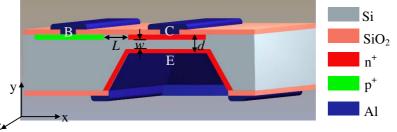
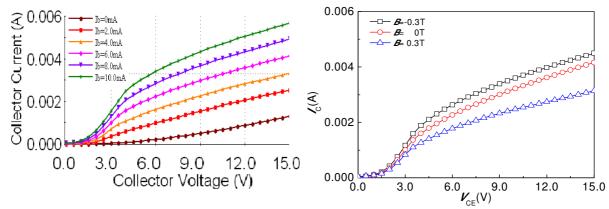


Figure 1. Basic structure of new type silicon magnetic sensitivity transistor (SMST)

The current-voltage characteristics of SMST

The current-voltage characteristics of new type SMST were tested by KEITHLEY 4500-SCS semiconductor characteristic testing system and the CH-1 magnetic field generator. At room temperature, the collector voltage V_{CE} ranges from 0 to 15.0V with the step of 0.5 V.





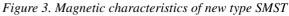


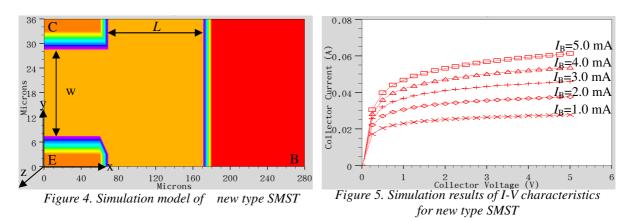
Figure 2 shows the current-voltage characteristics of new type SMST without external magnetic field, where the base current I_B ranges from 0 to 10.0 mA with the step of 2.0 mA. The experimental results show that current-voltage characteristics of the new type SMST are similar to the thin-base transistor, but the current gain β of the new type SMST is less than 1, while the thin-base transistor is much higher than 1.

When the collector current I_C is decreased, the external magnetic field is defined the positive direction for new type SMST. Figure 3 shows the magnetic characteristics of new type SMST under different the external magnetic fields (-0.3 T, 0 T and 0.3 T), where the base current I_B is 6.0 mA. When V_{CE} is constant, I_C is decreased under the positive external magnetic field direction, while increased under the negative external magnetic field, so it is easy to realize the measurement of the magnetic field.

The characteristics simulation of the new type SMST

The simulation model of new type SMST was established with the aid of ATLAS software in this paper shown as Figure 4, where L ($L=120 \mu$ m) and w ($w=30 \mu$ m) are present the base region length and width, the simulation model comprises the emitter (E), the base (B) and collector (C). The n⁺ impurity concentration of the emitter is 1E17 cm⁻³, the p⁺ impurity concentration of the base is 1E19 cm⁻³, and the n⁺ impurity concentration of the collector is 1E19 cm⁻³.

Figure 5 indicates the simulation results of current-voltage characteristics for new type SMST without the external magnetic field, where the base current $I_{\rm B}$ ranges from 1.0 to 5.0 mA with the step of 1.0 mA, and the collector voltage $V_{\rm CE}$ ranges from 0 to 5.0V with the step of 0.25 V.



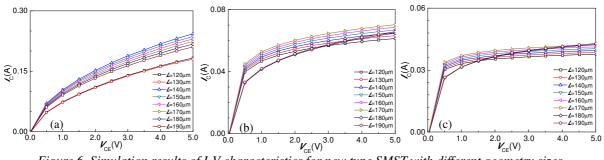


Figure 6. Simulation results of I-V characteristics for new type SMST with different geometry sizes (a) $w=20 \ \mu m$ (b) $w=30 \ \mu m$ (c) $w=40 \ \mu m$

In order to optimize the size parameters of new type SMST, ATLAS was utilized to simulate SMST, where the base length ranges from 120 μ m to 190 μ m with the step of 10 μ m, and the base width is 20 μ m, 30 μ m and 40 μ m. Figure 6 indicates the simulation results of current-voltage characteristics for new type SMST without the external magnetic field, where the base current I_B ranges from 1.0 to 5.0 mA with the step of 1.0 mA, and the collector voltage V_{CE} ranges from 0 to 5.0 V with the step of 0.5 V. According to the simulation results from Figure 6, when the base length *L* and collector voltage V_{CE} are constant, the collector currents I_C decrease with the increment of the base width *w*. Additionally, when the base width *w* and collector voltage V_{CE} are constant, the collector currents I_C changes with the variation of the base length *L*, and when the base width and length are 20 μ m and 140 μ m, the collector currents I_C can achieve the maximum value.

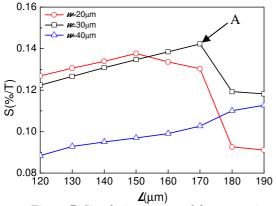


Figure 7. Simulation curves of the magnetic sensitivity and the base region length for new type SMST with different base region width

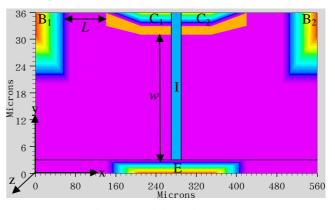


Figure 8. Simulation model of the of new type SMST differential structure

Based on the size parameters in Figure 6, the simulation results under different magnetic fields (-0.3 T, 0 T and 0.3 T) were calculated as Figure 7, where the base current I_B is 5.0 mA and the collector voltage V_{CE} is 5.0 V. Figure 7 indicates the simulation curves of the collector current relative magnetic sensitivity S and base region length L for new type SMST with different base region width, where the base length ranges from 120 µm to 190 µm with the step of 10µm, and the base width w are 20 µm, 30 µm and 40 µm. From Figure 7 it is easy to draw a conclusion that the max collector current relative magnetic sensitivity is 142%/T represented as the point A (L=170 µm and w=30 µm).

The characteristics simulation of the new type SMST differential structure

The simulation model. In order to further improve the magnetic sensitivity of new type SMST, the differential structure was adopted to establish the simulation model with the aid of ATLAS. Figure 8 shows the simulation model of new type SMST differential structure, where L (L=170 µm) and w (w=30 µm) are represent the base length and width, the simulation model comprises the common emitter (E), the left base (B₁) and collector (C₁), the right base (B₂) and collector (C₂), the two SMSTs in the simulation model are defined as SMST-1 and SMST-2 respectively, and they have opposite magnetic sensitivity directions that the z axis direction shown as coordinate system in Figure 8. The n⁺ impurity concentration of the common emitter is 1 E17cm⁻³, the p⁺ impurity

concentration of the bases are 1 $E19cm^{-3}$, the n⁺ impurity concentration of the collectors are 1 $E19cm^{-3}$, and region I is insulation layer.

The current-voltage characteristics. Figure 9 (a) and (b) illustrate the simulation results of current-voltage characteristics for SMST-1 and SMST-2 in the differential structure without the external magnetic field, where the base current $I_{\rm B}$ ranges from 1.0 to 5.0 mA with the step of 1.0 mA, and the collector voltage $V_{\rm CE}$ ranges from 0 to 5.0 V with the step of 0.25 V.

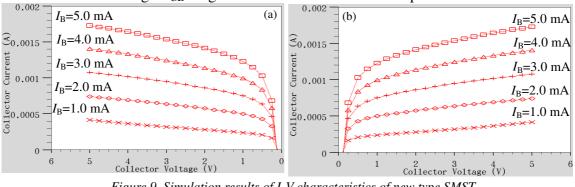


Figure 9. Simulation results of I-V characteristics of new type SMST differential structure (a) SMST-1 (b) SMST-2

In this simulation model, when the collector current $I_{\rm C}$ for SMST-1 is decreased, the external magnetic field is defined as the positive direction. Figure 10 (a) and (b) show the magnetic characteristics for SMST-1 and SMST-2 in the differential structure under the different external magnetic field *B* (-0.3T, 0T and 0.3T), where the base current $I_{\rm B}$ is 5.0 mA, the collector voltage $V_{\rm CE}$ ranges from 0 to 15.0V with the step of 0.25 V. According to Figure 10, when $V_{\rm CE}$ is constant, the collector current for SMST-1 $I_{\rm C1}$ is decreased while the collector current for SMST-2 $I_{\rm C2}$ is increased (*B*=0.3 T), $I_{\rm C1}$ is increased while $I_{\rm C2}$ is decreased (*B*=-0.3T), they indicate that the magnetic sensitivity directions of the SMST-1 and SMST-2 are opposite.

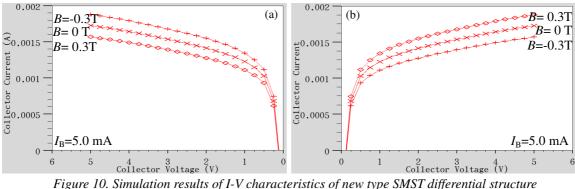


Figure 10. Simulation results of I-V characteristics of new type SMST differential structur under external magnetic field (a) SMST-1 (b) SMST-2

The magnetic characteristics. Figure 11 (a) and (b) show the relation curves of collector current $I_{\rm C}$ and external magnetic field *B* for SMST-1 and SMST-2 in the differential structure, where the base current $I_{\rm B}$ ranges from 1.0 to 5.0 mA with the step of 1.0 mA, the collector voltage $V_{\rm CE}$ is 5.0 V, and the external magnetic field *B* ranges from -0.3 to 0.3 T with the step of 0.1 T. In this paper, $\Delta I_{\rm C1}$ and $\Delta I_{\rm C2}$ are defined as the variable quantity of collector current for SMST-1 and SMST-2 under the changing magnetic field.

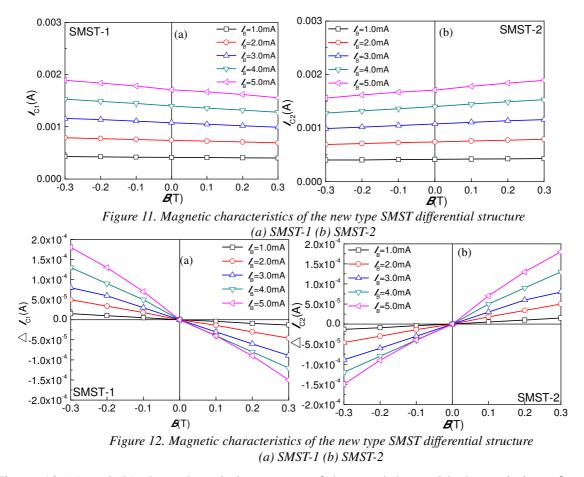
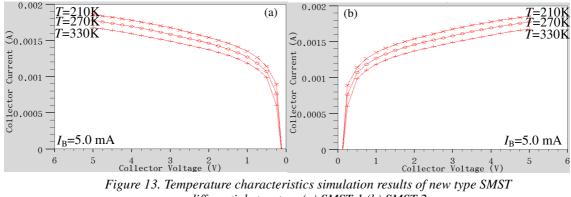


Figure 12 (a) and (b) show the relation curves of ΔI_{C1} and ΔI_{C2} with the variation of external magnetic field *B*, where the base current I_B ranges from 1.0 to 5.0 mA with the step of 1.0 mA, the collector voltage V_{CE} is 5.0 V, and the external magnetic field *B* ranges from -0.3 to 0.3 T with the step of 0.1T. When I_B is constant, ΔI_{C1} and ΔI_{C2} are increased with the increment of both the positive and the negative external magnetic field *B*; while ΔI_{C1} and ΔI_{C2} are increased with the increment of both the increment of I_B . According to Figure 7 and Figure 8, it is easy to calculate the max collector current relative magnetic sensitivity is 322%/T for the differential structure of new type SMST when the base current I_B is 5.0 mA and the collector voltage V_{CE} is 5.0 V, the analysis of simulation results show that the magnetic sensitivity of the differential structure is the summation of SMST-1 and SMST-2, the magnetic sensitivity is improved.



differential structure (a) SMST-1 (b) SMST-2

The temperature characteristics simulation results. Figure 9 (a) and (b) show the temperature characteristics simulation results of SMST-1 and SMST-2 in the differential structure without external magnetic field, where the base current I_B is 5.0 mA, the collector voltage V_{CE} is 5.0 V, and the temperatures are 210 K, 270 K and 330 K. According to Figure 13, when V_{CE} is constant, I_C is decreased with the increment of the temperatures, so the new type SMST differential structure has

the negative temperature coefficient which equals to the difference of SMST-1 and SMST-2, so it can realize compensation of temperature.

Conclusion

In this paper, we have proposed a differential structure magnetic sensor composes two new type SMSTs with opposite magnetic sensitivity direction. A single SMST, fabricated on the <100> orientation double side polished silicon with high resistivity by MEMS technology, was tested by KEITHLEY 4500-SCS semiconductor characteristic testing system and the magnetic field generator to research the magnetic characteristics. According to the experiment results, the simulation models of SMST with different geometric parameters were established by ATLAS software, when the base region length and width are170 μ m and 30 μ m, the max collector voltage V_{CE} is 5.0 V. In terms of it, the simulation model of the new type SMST differential structure was established by ATLAS software, where the differential structure magnetic sensor composes two new type SMSTs with opposite magnetic sensitivity directions, and the max collector current relative magnetic sensitivity is 322%/T for the differential structure when the base currents I_B are both 5.0 mA and the collector voltages V_{CE} is 5.0 V. The experiments and simulation results lay the foundation for further analysis of SMSTs in magnetic sensors.

Acknowledgements

This work is supported by the National Natural Science Foundation of China (Grant No. 61006057), the China Postdoctoral Science Foundation (Grant No.2013M530163), the Heilongjiang Postdoctoral Science Foundation (Grant No.LBH-Z12225), the Modern Sensor Technology Innovation Team for College of Heilongjiang Province(Grant No.2012TD007).

- [1] Victor Zieren, Bart P.M. Duydam. Magnetic-field-sensitive multicollector n-p-n transistors[J]. IEEE Transactions on Electron Devices, 1982, 29(1):83-90.
- [2] Agnes Nagy, Hector Trujillo. Highly sensitive magneto transistor with new topology[J]. Sensors and Actuators, 1998, 65:97-100.
- [3] Wen Dianzhong, Mu Changsheng, Zhao Xiaofeng. Silicon magneto transistor by MEMS technology silicon transistor[J]. Journal of Transducer Technology,2001,20(5):49-52.
- [4] Wen Dianzhong. Study on laser etching emitter region-groove approach of magnetic-sensitive silicon transistor[J]. Chinese Journal of Lasers, 2003, 30(5):454-456.
- [5] Zhao Xiaofeng, Wen Dianzhong. Negative-resistance oscillations characteristics of a new type silicon magnetic sensitive transistor on MEMS [J]. Chinese Journal of Semiconductor, 2005,26(6):1214-1219.
- [6] Tian Fengjun, Wen Dianzhong. New type of P⁺-I-N⁺ double injection magneto-sensitive difference circuit developted on SOI[J]. Journal of Transducer Technology.2005,24(4):84-86.
- [7] Zhao Xiaofeng, Wen Dianzhong. Fabrication-technology research of new type silicon magnetic-sensitive transistor[J].Rare Metal Materials and Engineering,2006,35(12):492-494.
- [8] Wen Dianzhong. Study on a new magnetic-transistor on a SOI substrate[J]. Chinese Journal of Electron Devices,2006,29(3): 609-612.
- [9] Zhao Xiaofeng, Li Lei, Wang ping, et al. Simulation research of the long-base silicon magnetic sensitive diode negative-resistance characteristics on the base of ATLAS[J]. Key Engineering Materials,2013.562-565:465-470.
- [10] Zhao Xiaofeng, Wen Dianzhong, Pan Dongyang, et al. Differential structure and characteristics of a new-type silicon magnetic sensitivity transistor[J]. China Physics Letter ,2013,30(8) : 088501(1-4).

Fast Solidification and Electrical Conductivity of Apatite-type Nanoceramics

Qin Li^{1, a}, Limin Dong¹

¹College of Materials Science and Engineering, Harbin University of Science & Technology, Harbin, China

Unina

^aqinalily@hotmail.com

Keywords: Nanostructured materials; Sintering; Microstructure; Electrical Conductivity

Abstract. Apatite oxides electrolytes $La_{9,33}(SiO_4)_6O_2$ was prepared following the Sol-Gel aqueous route. The structure of $La_{9,33}(SiO_4)_6O_2$ was evaluated using the X-ray diffraction patterns (PXRD). The main phase is $La_{9,33}Si_6O_{26}$ with the Minor impurity phase of La_2SiO_5 as a secondary phase. And dense $La_{9,33}(SiO_4)_6O_2$ nanoceramics with grain size of smaller than 100 nm were fabricated by high-pressure sintering, the pressure of 4.5 GPa, the sintering temperature of 1200 °C and dwelling time of 10 min were used. The ionic conductivity of the samples is evaluated by AC impedance spectroscopy. The conductivity of dense $La_{9,33}(SiO_4)_6O_2$ nanoceramics. The activation energy in the samples by high-pressure densification and conventional sintering method was 1.06 eV and 1.44 eV, respectively.

Introduction

Materials that exhibit good oxide ion conductivity are of considerable interest for a range of "clean" electrochemical applications including solid oxide fuel cells and separation membranes. Apatite oxides based on $RE_{9.33}(SiO_4)_6O_2$ (RE: rare earth) compounds have recently attracted considerable attention [1, 2]. These compounds exhibit higher conductivity compared to that required for ZrO_2 solid electrolytes. Conduction mechanism on this type of compounds has been ascribed to migration of oxide ions running through the hexagonal channel along the c-axis [3].

The apatite has been prepared by solid-state reaction between La₂O₃ and SiO₂ in high temperature above 1600 °C [1, 2]. Such high sintering temperature made it difficult to control the microstructure of the resultant ceramics. It is predicted by Herring's scaling law [4] that nanocrystalline powders provide faster densification kinetics and lower sintering temperatures. And the dense ceramics have been prepared by using nanocrystalline powders La_{9.33}Si₆O₂₆ synthesized from new chemical route based on sol–gel process, which decreased the sintering temperature of these materials really down to 1500 °C by adjusting, in particular, agglomerates size and heating profile [5]. However, the sintering temperature was still high, and the high temperature produced a significant grain growth that results into the destruction of the nanostructure. In order to further decrease the sintering temperature, the study on the film of apatite has been done [6]. The use of thin film electrolytes reduced the overall device resistance and the operation temperature, and was considered a promising approach to improving fuel cell performance. However, few reports have been made on the apatite bulk materials. High-pressure compaction applied a pressure during heating, which made it possible to obtain full densification in a few minutes at relative low temperatures with very limited grain growth. Fast low temperature consolidation of the ceramics could be carried out through it.

In this work, the pressure with a superhigh value of about 4.5 GPa was applied, while the dense apatite ceramic with the average grain size smaller than 100 nm was obtained.

Experimental

The apatite powder was prepared following the Sol-Gel aqueous route. As precursors, TEOS (tetraethyl orthosilicate, 28%) and lanthanum oxide (La₂O₃, 99.99%) were used. A solution of lanthanum nitrate was obtained by dissolving La₂O₃ into nitric acid, and then mixed with ethanol and

acetic acid. Then TEOS was added to the mixture, and stirred. The solution transformed into a rigid white gel after several hours at 80 $^{\circ}$ C. Then the gel was dried at 100 $^{\circ}$ C and finally calcinated at 1000 $^{\circ}$ C to obtain the apatite powders.

The obtained powder was first pressed into a cylindrical pellet under a pressure of 200 MPa, and then sintered by conventional sintering methods and high-pressure densification, respectively. For the conventional sintering methods, very high sintering temperatures (1700 or 1800°C) for such a material were suggested [7, 8]. Nevertheless, The presence of secondary phases leads to the formation of a liquid phase at temperatures above 1600 °C [9]. So further samples were sintered at lower temperature of 1500°C. And the sintered pellet with nominal dimensions of Φ 9.1×3.0 mm³ was obtained. Whereas, the high-pressure experiments were conducted on a cubic-type high-pressure apparatus with six WC anvils (DS-029C, China). The green compacts were placed into an anvil cell with a graphite sleeve heater, and then the remaining room was occupied by h-BN as heat-transmitting medium. Annealing under high pressure was achieved by loading first and then heating to a certain temperature, keeping it constant for 10 min, then cooling down and unloading. The temperature was controlled by Pt·30%Rh-Pt·6%Rh thermal couple. The schematic diagram of high-pressure cell was shown in Fig.1. After the high-pressure experiment, the green compact was sintered into a pellet with nominal dimensions of Φ 7.8×1.3 mm³ under a high pressure (4.5 GPa) at 1200 °C for a short time of 10 minutes.

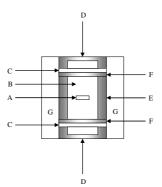


Figure 1. Schematic diagram of high-pressure cell. A, sample; B, BN; C, Titanium disc; D, conductive ring; E, graphite tube; F, graphite disc; G, pyrophylite.

X-ray diffraction (XRD) patterns were collected on a Rigaku D/Max-IIB diffractometer with Cu-K α radiation. Microstructure was controlled on fractured pellets by the environmental scanning electron microscope (Philips, XL30). The grain size can be obtained from the SEM photos. The apparent density of the as-sintered pellet was estimated from its mass and geometric dimensions, and also determined by the Archimedes method using distilled water as an intrusion medium. The results from the two methods are coincident. For AC impedance measurement, a Solartron SI 1255 High Frequency Response Analyzer coupled with a SI 1287 Electrochemical Interface controlled by Zplot electrochemical impedance software was used over the frequency range of 1 MHz to 0.1 Hz. Platinum electrodes were used for the electrical measurements.

Results and Discussion

The Characterization of the Powder

The XRD pattern of apatite nanopowder calcined at 1000 oC is shown in Fig. 2. The crystalline phases were identified from a comparison of the registered patterns with the international center for diffraction data (ICDD) powder diffraction files (PDF). It can be seen that the main phase is $La_{9.33}Si_6O_{26}$ with the Minor impurity phase of La_2SiO_5 as a secondary phase.

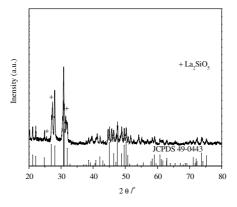


Figure 2. The X-ray powder diffraction patterns of La_{9.33}Si₆O₂₆ nanopowder.

Densification of the Nanopowders

Table 1 Characterization of Apatite Preapared by Different Methods	Table 1	Characterization	of Apatite	Preapared b	y Different Methods
--	---------	------------------	------------	-------------	---------------------

Preparation methods	Temperature	Dwelling time	Grain size	Relative density
Conventional Sintering Method	1500 °C	12 h	1-2 μm	78%
High-pressure Densification	1200 °C	10 min	80 nm	94%

Relative density and grain size of the ceramics isothermally sintered by various methods are shown in Table.1. The conventional sintering method for the pellets led to the specimens not fully dense with compactions ranging between 70 and 80% of the theoretical value. However, dense sample with the relative density above 90% was obtained by high-pressure densification despite of low dwell temperature and short dwell time. The densification temperature is 400 °C lower than that for conventional sintering method reported before [1, 2, 5]. Fig.3 shows the typical scanning electron microscopy (SEM) micrographs of the sample densified by different methods. The sample by high-pressure densification shows that the sample was well sintered and has a uniform microstructure with a grain size smaller than 100 nm as seen in Fig.3a. Whereas the sample by conventional sintering methods is porous and has the grain size of about 2 μ m as seen in Fig.3b and c. High-pressure compaction applied the pressure on the compact during sintering, improved the density, reduced the sintering temperature and sintering time, and further significantly restrained the grain growth.

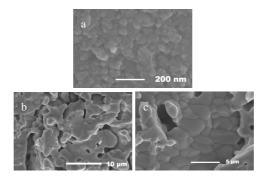


Figure 3. SEM micrographs of apatite: (a) for the sample by high-pressure densification; (b) and (c) for the sample by conventional sintering method.

The sample after high-pressure densification has a dark-grey color while it is white before densification. When annealed at 800°C in air, the sample turned back to be white. The similar discoloration phenomena had also been observed previously in yttria-stabilized zirconia and 30 mol% samaria-doped ceria densified in the SPS apparatus [10, 11], and it was attributed to oxygen deficiency resulting from the exceedingly low oxygen partial pressure in the graphite die at high temperatures [10, 11].

Electrical Characterization

To check the different possible contributions to the electrical response, the apatite ceramic underwent impedance spectroscopy analysis. The complex impedance spectra were analyzed with equivalent circuits, using the software ZView [12]. In the low temperature, the slightly depressed impedance spectra show three different processes. The two processes at high frequency are overlapped and can be ascribed to the bulk and grain boundary. The third contribution at low frequency is ascribed to the electrode process. These parameters have been determined for the samples. The calculated spectra (solid line) for high-pressured apatite ceramic at 450 °C are shown in Fig. 4a as an example of this type of fits. The equivalent circuit was seen in the insert in Fig. 4a. The fitting parameters are the resistances (R), CPE-T and CPE-P. The resistance R1, Rb, Rgb, Re stands for the resistance for contact, bulk, grain boundary and the resistance correlative to electrode, respectively. The constant phase element (CPE) is defined by two values, CPE-T and CPE-P. CPE-P stands for a pseudo-capacitance.

$$Z = 1 / [1(1 \times \omega)^{2}].$$
(1)
According to the equation [13]

(2)

According to $C=R^{(1-P)/P} \times T^{1/P}$

-20000

-15000

-50000

(a)

25118 9 F

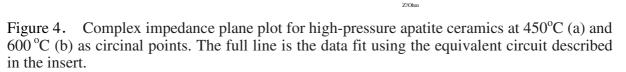
the capacitances obtained are 2.87 pF, 22.8 nF, 113 μ F, which are in good agreement, respectively, with bulk capacitance (high frequency), grain boundary capacitance (intermediate frequency) and electrode capacitance (low frequency). When the temperatures increase, the semicircle that stands for bulk process disappeared, for example, the impedance spectra of high-pressured apatite ceramic at 600 °C in Fig. 4b shows two semicircles corresponding to grain boundary resistance and electrode reaction impedance, respectively.

The resistances are obtained from the intercept of the spectra on the Z' and also obtained by fitting, and the results densification and conventional sintering method was 1.06 eV and 1.44 eV, respectively.

-20000

(b)

6000



The conductivity of a pellet pressed from this sample and sintered at 1500 oC for 12 h showed a low conductivity value of $3\times10-5$ S cm-1 at 800 oC, consistent with the presence of insulating La2SiO5 phase. The total ionic conductivity for the specimens by high-pressure densification is one multiple higher compared with that of the microcrystalline ceramics. It can be attributed to the high relative density of the sample compared with those of samples by conventional sintering method.

Morever, maybe the improvement of the purity of the samples will contribute to the improvement of their electrical conductivity.

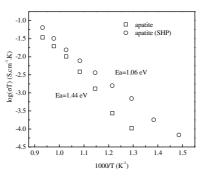


Figure 5. Arrhenius plots of electrical conductivities of apatite prepared by high-pressure densification and conventional sintering methods.

Conclusions

Nanometric powders of apatite synthesized by a sol-gel method were successfully consolidated by high-pressure densification. Relative density of 92% could be obtained by the use of high pressure of 4.5 GPa and shorter sintering time of 10 min. In these conditions the sintering temperatures are much lower than the temperatures used in conventional sintering methods. Also, the grain growth is very limited. Due to a dependence of electrical conductivity on densification this method led to the improvement of the electrical conductivity.

Acknowledgment

This work was financially supported by Educational Commission of Heilongjiang Province of China (No.12531117). We also would like to thank Chang Chun Institute of Applied Chemistry, Chinese Acadamy of Sciences.

- [1] S. Nakayama, T. Kageyama, H. Aono, Y. Sadaoka, J. Mater. Chem. 5 (1995) p1801.
- [2] S. Nakayama, M. Sakamoto, J. Eur. Ceram. Soc. 18 (1998) 1413.
- [3] M. S. Islam, J. R. Tolchard, P. R. Slater, Chem. Commun. 13 (2003) 1486.
- [4] K. Higashi, K. Sonoda, H. Ono, S. Sameshima, Y. Hirata, J. Mater. Res. 14 (1999) 957.
- [5] S. Celerier, C. Laberty-Robert, F. Ansart, C. Calmet, P. Stevens, J. Eur. Ceram. Soc. 25 (2005) 2665.
- [6] Y. Masubuchi, M. Higuchi, T. Takeda, S. Kikkawa, J. Alloys Compd. 408–412 (2006) 641.
- [7] E. J. Abram, D.C. Sinclair, A. R. West, J. Mater. Chem. 11 (2001) 1978.
- [8] J. E. H. Sansom, D. Riching, P.R. Slater, Solid State Ionics 139 (2001) 205.
- [9] P.J. Panteix, I. Julien, D. Bernache-Assollant, P. Abélard, Mater. Chem. Phys. 95 (2006) 313.
- [10] U. Anselmi-Tamburini, J. E. Garay, Z. A. Munir, A. Tacca, F. Maglia, G. Chiodelli, G. Spinolo, J. Mater. Res. 19 (2004) 3263.
- [11] U. Anselmi-Tamburini, F. Maglia, G. Chiodelli, A. Tacca, G. Spinolo, P. Riello, S. Bucella, Z. A. Munir, Adv. Funct. Mater. 16 (2006) 2363.
- [12] D. Johnson, Zview Program, Version 2.4a, Scribner Associates, Inc., 1990–2001.
- [13] Q. Li, T. Xia, X. D. Liu, X. F. Ma, J. Meng, X. Q. Cao, Mater. Sci. Eng. B 138 (2007) 78.

Particle Size Effect on the Corona Resistant Properties of PI/TiO₂ Composite Films

Guangyou Li^{1,a}, Jinghua Yin^{1,2}, Lei Yao¹, Xing Zhao¹

¹School of Applied Science, Harbin University of Science and Technology, Harbin 150080, PR China

²Key laboratory of Engineering Dielectrics and Its Application, Ministry of Education, Harbin University of Science and Technology, Harbin 150080, PR China

^a249607492@qq.com

Keywords: Polyimide; dioxide titanium; sizes; trap; corona-resistant

Abstract: Polyimide-based (PI) nanocomposites possess excellent electrical and thermal performance, widely used in inverter motor. In the paper using different particle sizes made polyimide/titania (PI/TiO2) nano composite films in situ polymerization, including 20nm A series and 50nm B series. The results shows that A series have a larger specific surface, combination of the film and matrix is closer without affecting the imidization of PI, and there is a clear interface layer and the structure is more stable. According to the time of corona-resistant A Series films is significantly longer than B Series films, especially the A series films with 15% of which corona-resistant time is 15h, five times than the pure PI. By both SAXS and XRD particle size in the matrix can be calculated, proving small particles can be better combination of the matrix of PI, increasing the number of traps, more effectively cutting off charge corrosion and making corona resistance greater performance.

Introduction

Frequency motor has easy control, efficiency and convenience to governor and other features, which are more widely used, but the high power frequency conversion motor is easily destroyed because of corona corrosion, which greatly reduced reliability and life [1-4], so it is the urgent need that traditional insulation materials can be improved and new insulating materials is developed [5-6]. Polyimide nanocomposite as a novel nano-dielectrics, by doping nanoparticles greatly improves its dielectric properties and Corona-resistant performance.

This article describes that PI/TiO_2 nano-composite films are prepared in situ polymerization by changing the particle size to change the degree of integration of PI and nano-particles and increasing the number of traps, and particle size has an effect on the electrical properties of polyimide through the corona resistance research.

Experiment Preparation and Characterization

The experiment maerials and equipments. 1) Experimental materials: pyromellitic dianhydride (PMDA)(CP); N, N–dimethylacetamide (DMAC)(AP); 4, 4'- diamino diphenylether (ODA)(CP); Anatase nano-TiO₂ (20nm and 50nm). 2) Experimental equipment: JJ-1 precision electricblender; DHG-9140A high temperature drying oven; SK3300H ultrasonic cleaning machine; SDZF-6020 vacuum oven.

Preparation of PI/TiO₂ nano-composite films. Anatase nano-TiO₂ is accurately weighed according to the proportion of complex, then weighing recipe ratio of ODA monomer is mixed in a

certain DMAC and the reagent bottle is sealed, Using the ultrasonic dispersion equipment to scatter nanoparticles, for a while the container was cooled with stirring, next putting PMDA(with ODA mole ratio was 1.01:1) into mixed solvent. Standing for a period of time, the nanocomposite solution is coated on the flat glass, vacuumed in the vacuum oven, and then heatted with a stepwise manner, to make it iminated and PI/ TiO_2 nanocomposite films are prepared. the types of films in the paper are shown in Table I.

TABLE ITHE TYPE AND NUMBER OF FILM

Constituent Particle size	7wt%	15 wt %	25 wt %
20nm	Al	A2	A3
50nm	B1	B2	В3

Characterization of PI/TiO₂ nanocomposite films. The distribution of Nano-TiO₂ In the PI matrix and films after corona breakdown are characterized by scanning electron microscopy (SEM, FEI Quanta200), then finding the factors affecting corona resistance by comparative analysis. The struction of films, particle types and absorption peaks are texted by X diffraction (XRD) and synchronous small-angle X-ray scattering (SAXS).

Results and Discussion

Electron microscopy analysis. Fig. 1 is the surface morphology of PI/TiO_2 nano-composite film with 15%, which shows that the size of TiO_2 nano-particles is very small, and nano-particles uniformly distribute in the matrixal. though there is a small amount together, the combination PI matrix with nano-particles is still very tight.

Fig. 2 is the surface morphology after corona breakdown of PI/TiO_2 nanocomposite films with 15%, which shows that polyimide is destroyed, some TiO_2 particles exposes outside and are separated with matrix, resulting clusters. PI/TiO_2 composite films have a longer Corona-resistant time than pure PI, which illustrates that TiO_2 particles with high performance of Corona-resistant gradually accumulate form clustered state on the surface of films because of erosion from the discharge, the gap of particles can be effectively reduced, and it reduces electronics because of discharge or the chance to accelerate.

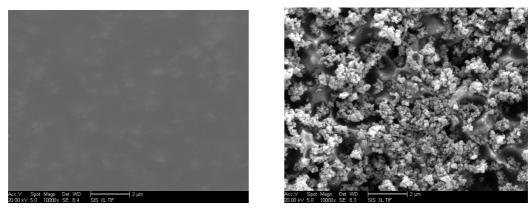
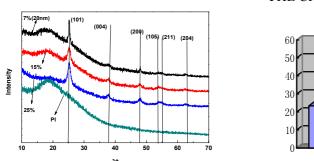
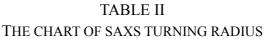


Fig.1 Surface morphology of A2 film Fig.2 Surface morphology after corona breakdown **The XRD analysis.** Fig.3 shows XRD spectrum of 20nm PI/ TiO₂ nano-composite films, which shows that pure PI films appear the broad diffraction peaks in the vicinity of $2\theta = 19^{\circ}$, because the polymer chain Randomly distributes in the polyimide film. PI/ TiO₂ composite films havn't only the same position of diffraction peaks as pure PI, still nearby $2\theta = 25^{\circ}$, 37.5° , 47.5° , 53° , 55° , 63°

occur six peaks, consistent with XRD diffraction peaks of Anatase TiO_2 nanoparticles, which proves that Anatase TiO_2 nanoparticles have been incorporated into polyimide, forming inorganic/organic composite structure.





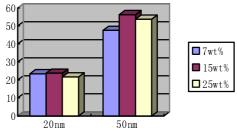


Fig.3 XRD spectrum of nanocomposite films

SAXS test analysis. Particle diameter is calculated by SAXR radius of gyration, as shown in Table II. 20nm and 50nm particles are of slightly different with different compositions and there is no significant clusters, which indicates that the measured nanoparticle size matchs with the information given.

Film corona characterization. According to national standards IEC60343 corona device is produced as is shown in Fig.4, the frequency of the test voltage is operating frequency and a waveform is a sine wave and in the test circuit the regulator linked into is stable waveform. Between the upper and lower electrode voltage is 1600V and the distance between the electrode and the sample is $100\mu m$.

As shown in Table 3, we can see from the table corona resistant time of composite films with different components, increasing component, first increases then decreases, and particles added enhance activity level of the film at high temperatures to ensure probability of collisions reduced. Particle size has an large effect on the corona-resist-

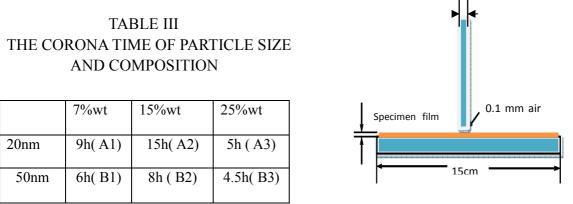


Fig. 4 Corona resistant electrode system

ant properties of the film, and 20nm nanoparticles under the same components have a higher resistance to corona time than 50nm, which describes the combination of small size particles and the matrix is better and the specific surface area can greatly bear and laterally spread charge to separate the breakdown of electric field and ensure that the base is relatively slowly mortared in the electric field.

Conclusions

In this paper, the different particle size of PI/ TiO2 nanocomposite films were tested and analyzed following conclusions: By XRD spectrum we can judge that particles are Anatase TiO₂, nanoparticles disperse in the polyimide and polyimide structure isn't destroyed, after calculations and analysis grain size is consistent with actual size. Under the SEM particles uniformly distribute in the matrix. Particle diameter is calculated by SAXS radius of gyration, which shows the measured nanoparticle size matchs with actual size. By the corona resistance time of the composite films, small nanoparticles have a longer corona resistance time, on the one hand increasing the surface area can better lateral release charge and make corona resistant of films strengthen, on the other hand a large number of traps generated trapped charge to reduce the chance of breakdown, Particles added increase thermal stability of the film to reduce the erosion of films.

- [1] Bonnet A. H. Transaction on Industrial Applications, Vol. 33(1997), p.1331-1334
- [2] Yin W J. Electrical Insulation Magazine, Vol. 13(1997), p. 18-23
- [3]Kaufhold M, Auinger H, Berth M, et al. Transaction on Industrial Electronics, Vol. 47(2000), p. 396-402
- [4]Kaufhold M, Borner G, Eberhardt M, et al. Electrical Insulation Magazine, Vol. 12(1996), p. 9-16
- [5] Tu Demin. China Electrotechnical Society, Vol. 20(2005), p. 8-15
- [6] Tsai M H, Lin S J, Chiang P C. Thin Solid Films, Vol. 515(2006), p. 1126-1131

Structure and Property Stability of Rapidly Solidified In-Sn γ-Phase Alloy

Jing-ze Wang^{1,a}, Ming-lu Liu¹, Da-yong Li¹

¹Harbin University of Science and Technology, Harbin, 150080, China.

^awjz_hit@sina.com

Keywords:In-Sn y-phase IMC, rapid solidification, metastable structure, thermal stability.

Abstract. The crystallization characteristics of the binary alloys which have $InSn_4$ intermetallic compounds(IMC) were investigated. The influence which high undercooling had caused to the process of lattice formation, the lattice evolution in the later period of solidification, the stabilization process of the alloy property were mainly studied. The results show that the solute redistribution is restrained intensely in the rapidly solidified condition, the components of $InSn_4$ IMC distribute uniformly, the highly undercooling structure have small sub-grain structure. X-ray diffraction analysis show that strong (0001) texture is formed in the alloys, EBSD analysis show that many sub-boundaries exist in the grains. While these unstable structures have an isothermal annealing between $20 \sim 140^{\circ}$ C, the texure feature of the alloys weaken, and at the same time the microhardness lower in varying degrees.

Introduction

In-Sn alloy is one of the few alloys which can satisfy the packaging of semiconductor devices which have high-power and highly integrated density. This kind of semiconductors need solve the problems like excessive packaging temperature, thermal diffusion, thermal stress and biotoxicity,etc.In-Sn alloys have low melting point,low strength and good surface wettablity.Related studies show that Sn can improve the bonding reliability of solder with the addition of a certain amount of In.For high-power semiconductor lasers, mainly using pure In and In-Sn eutectic alloy to package can prevent Smile-effect of laser bars. The reduction in the content of In can lower the cost. The direction which is more promising is to add another element based on In-Sn y-phase(Sn content:70~85%)¹⁻⁴. Most of the studies concentrate on the influence of the third component and the problems between solder and substrate, the process, in which alloy solidify and form small brazing joint on the Cu surface, is actually a more complicated process. Among of them, the solid non-equilibrium structure, which is the result of non-equilibrium solidification caused by highly solidified speed, can influence the packaging property obviously. Owing to the limitation of the packaging sample structure and the complexity of the non-equilibrium crystallization process, this kind of studies had been rarely involved. Relevant rapidly solidified studies (The structures and property studies of other rapidly solidified alloys) show that the micrograin and the texture which appeared in the rapidly solidified structure can change the features of the material⁵⁻⁸.

This research analyze the rapidly solidified structure and the property stabilbity of In-Sn γ -phase alloy(Sn content:70~85%). To this end, this research focus on the structural morphology and the substructural features in rapidly solidified condition, which includes the state of texture formation and the defects in grains, the property stability reflected by varying microhardness. The analysis methods which need to be used include scanning electron microscope analysis(SEM), energy dispersive x-ray analysis(EDS), electron back-scattered diffraction analysis(EBSD), x-ray diffraction analysis(XRD) and the microhardness measurement, etc.

Experiment Process

According to the phase diagram, In-Sn γ -phase(Sn content:70~85%) is the binary alloys which have InSn₄ IMCs.In and Sn can be uniformly miscible when they are in this composition range, and show relative consistency⁹. This research study the composition of Sn-28In, Sn-25In, Sn-20In, Sn-15In, etc.

In and Sn was used as raw material,the purity was not less than 99.995%. According to the composition proportion, master alloy was smelted by using electric furnace, and solidified into ingots in the speed less than 10^{-2} K/S. About 2g master alloy was cut down, and melted by quartz tube. A foil which is less than 50μ m was produced by melt-spun method. According to the calculation, the alloy cooling velocity was not less than 10^{6} K/s. The surface where the foil contacted with the copper mould was a smooth surface(surface A), some elongated acicular pores appeared in the relative surface(surface B). The foil was cut into specimen of 10×10 mm. For confirming the texture formation of the rapidly solidified materials, using x-ray diffraction analysed the diffraction strength of the specimen surface of A and B, and the arithmetic mean was used as a reference. For analysing the solute redistribution in the crystallization process, the line distribution of In on the substrate was confirmed by energy dispersive x-ray analysis(EDS); For confirming the process of nucleation and growth, the surface A of the specimens were analysed by scanning electron microscope(SEM); In order to further confirm the distribution state of the defects in grains, the distribution of the subgrain boundaries and the feature of intergranular angles was analysed by electron back-scattered diffraction(EBSD).

Owing to the rapidly solidified material was inhibited severely,the material was still in metastable state, under certain thermaldynamic condition, the situation like atomic diffusion, residual stress releasing, disloctaion climb, etc. still can happen, which will lead to the change of material structure and the property. For studying the solidified features and the stabillization process of In-Sn γ -phase alloys, a consecutive experiment which lasted for 7 hours and had a 1 hour interval was conducted by microhardness tester. In the further experiment, isothermal annealing was conducted to the material, the temperature was between 40~140°C and had a 20°C interval, the unit of annealing time was 20min, the stabillized process was reflected by the microhardness and the change of x-ray diffraction characteristics.

Experiment Result and Discussion

 γ -phase is the IMC which have close-packed hexagonal structure. The microhardness analysis result of the equilibrium structures of these alloys is in figure 1a.Overall, the alloy microhardness is close to Sn, much higher than In, with the increase of In, the alloy microhardness increase, but have no significant change. As shown in figure 1b, the different components of rapidly solidified foils were analysed by energy-dispersive x-ray analysis (EDS), which discover that the foils have uniform distribution of In and Sn, and that rapid solidification have effectively restrained the solute redistribution in the solidified process. The constant of the rapidly solidified lattice is defenitely measured by x-ray diffraction. The results are shown in Table 1. With the In content increase, the lattice constants of a and c have a certain increase, correspondingly, the unit cell volume increase, but a/c value stay the same.

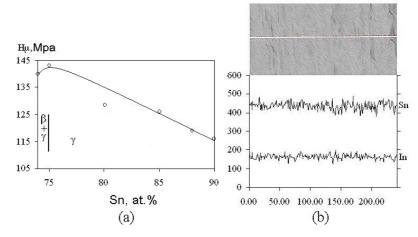


Fig. 1 (a)The mircrohardness curve of In-Sn γ-phase alloys,(b)The component distribution of rapidly solidified In-Sn γ-phase alloy.

Sm			Lattice	Constant		Microhardness
Sn at.%	Phase Type	a [nm]	c [nm]	a/c	V 10 ⁻⁵ ,nm ³	Hµ/Mpa (Foil)
75	γ	0.3213	0.2977	0.927	7986	134
76	γ	0.3213	0.2978	0.927	7988	137
80	γ	0.3216	0.2980	0.927	8006	130
85	γ	0.3219	0.2983	0.927	8029	126

Table 1 Using x-ray diffraction defenitely measured the lattice constant of a,c,a/c,V.

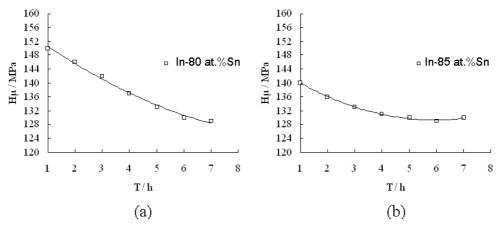


Fig 2. The microhardness changing curve of rapidly solidified In-Sn γ-phase foils:(a)In-80at%Sn,(b)In-85at.%Sn.

After a few hours, when rapid solidification ended, In-Sn γ -phase alloys was in unstable state. Through consecutive measurement which lasted 7 hours, the results are shown in figure 2, the initial microhardness of rapidly solidified structures are all obviously higher than the corresponding equilibrium alloy.

The distribution state of grain boundaries and the feature of intergranular angles were analysed by electron back-scattered diffraction(EBSD),the results are shown in figure 3,rapid solidification don't make the grains become refined obviously,but many subboundaries is formed,and at the same time, measuring the intergranular angles discover that the intergranular angles of grain boundaries are 5~6 degrees, and the angles between the sub-grains are less than 3 degrees. The grain boundary thickness and the interfacial energy of these kind of small-angle subboundaries are relatively small, so the energy barriers are relatively small in the process of the grain growth, which may not stop the further growth of the grains, the distortion energy produced in the rapidly solidified process make many subboundaries emerge.

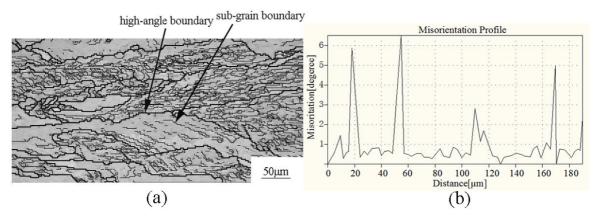


Fig 3. Grain boundary analysis:(a)electron back-scattered diffraction(EBSD) image,(b)characteristic graph of intergranular angle.

The material metastructure was further analysed by x-ray diffraction analysis, as shown in Table 2, which discover that (0001) texture exist inside the In-Sn γ -phase foils. Through the analysis after isothermal annealing, while the isothermal annealing is under 100°C, there aren't any influence on the texture weakening, but while the temperature is 100~140°C, the texture strength of the foils become weakened obviously. The change of the corresponding microhardness is shown in Figure 4, with the increase of annealing temperature, the material microhardness decrease gradually, which tend toward the corresponding equilibrium structural property.

Diffraction				In, at.%			
Paremeters	10	12	15	20	25	28	30
1011	0.6	0.7	0.6	0.4	0.8	0.8	1.3
$11\overline{2}0$	1.2	0.5	0.6	0.7	0.4	0.8	0.2
0002	3.0	3.6	3.3	4.0	3.2	2.8	3.5
1121	0.2	0.2	0.5	0.1	0.1	0.6	0.1
$20\overline{2}0$	1.1	0.8	1.1	0.8	0.7	0.8	0.6
1012	0.3	0.7	0.6	0.5	1.1	0.6	1.2
2021	0.7	0.5	0.3	0.5	0.7	0.6	0.1

Table 2 Diffraction peak distribution of the rapidly solidified In-Sn γ-phase alloy x-ray diffraction

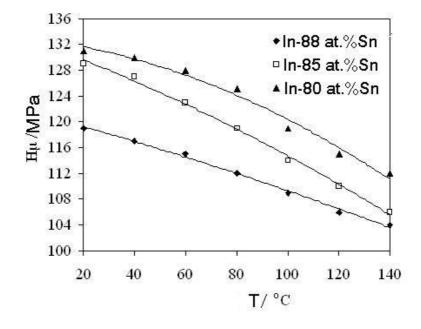


Fig 4. The microhardness changing curve of the rapidly solidified In-Sn γ -phase isothermal annealing structures.

Discussion

The rapidly solidified In-Sn γ -phase alloys have the unit cell which is relatively stable. The change of chemical components lead to the change of unit cell volume without affecting the a/c value. The effect of In isn't obvious to the solid solution strengthening of the materials. One of the possible reasons is that the atomic diameter of In and Sn are relatively close, or the atomic arrangement order are relatively regualr. Rapid solidification is beneficial to the homogenization of IMCs. The small angle grain boundaries, which was formed in the rapidly solidified process, which have relatively small grain boundary thickness and interfacial energy, may not stop the further growth of the grains. The distortion energy that is formed in the rapidly solidified process lead to the emergence of many subboundaries. Sub-grain structure might have a certain effect on the material microhardness, but it stay in metastable state in itself and can lead to the change of material properties in ambient temperature. Texture formation can be considered having a link with the solidified process of the alloys. The high undercooling make the process of the solute distribution inhibited, and force the liquid-solid interface advance in the most convenient way and absorb the most liquid atoms. One of the way for growth is that the atoms grow into liquid phase with the maximum lattice spacing in the direction which is prependicular to the solid-liquid interface, and at the same time keep the maximum atom arrangement density in the surface which is parallel to the phaseboundary plane. The (0001) texture in the rapidly solidified alloys are considered to improve the microhardness dramaticlly and stay in the material in its relatively high heat stability.

Conclusions

- [1] In-Sn γ -phase have the unit cell structure which is relatively stable, the component change of the alloy can lead to the change of unit cell volume, but a/c-value don't change;
- [2] In the rapidly solidified condition, the metastrucutre, which includes the intracrystalline high density sub-boundaries and the stable (0001) texture, is formed inside the In-Sn γ -phase alloys;
- [3] Rapid solidification make the microhardness of the In-Sn γ -phase change,the material microhardness tend towards stability after 7 hours aging, and tend towards the corresponding equilibirium state when the isothermal annealing temperature is beyond 100°C.

Acknowledgements

The work was supported by the Provincial Education Foundation of China under grant 4101-430010065.

- [1] K.O.LEE, J.W.MORRIS Jr., FAY Hua: *Martenstic Transformation in Sn-rich SnIn Solder Joints* (Journal of ELECTRONIC MATERIALS, Vol 41.No2, 2012).
- [2] K.O.LEE, J.W.MORRIS Jr., FAY Hua: *Transformation-Induced Plasticity in Sn-In Solder Joints*. (Journal of ELECTRONIC MATERIALS, Vol 41.No1, 2013).
- [3] Zhongnan Guo, Michael Hindler, Wenxia Yuan Adolf Mikula: *The Density and Surface Ten* sion of In-Sn and Cu-In-Sn Alloys (Monatsh Chem, 142, 579-284, 2011).
- [4] Z.Moser, W.Gasior, J.Pstrus. I.Kaban. W.Hoyer: *Thermalphysical Properties of Liquid In-Sn Al loys* (Int J Thermophys, 30, 1811-1822, 2009).
- [5] R.DASGUPTA,S.K.BOSE:*High Temperature Stability of Rapidly Solidified Al-Mn-Ni allo ys*(Journal of MATERIALS SCIENCE LETTERS,15,366-367,1996).
- [6] SOON-GUN KIM, SUNG H. WHANG: Grain Refinement in Rapidly Solidified W-Si alloys (Journal of MATERIALS SCIENCE LETTERS, 26, 5911-5914, 1991).
- [7] S.H.LO,W.MGIBBON: *Thermal Effect on Rapidly Solidified Cu-10Ni-8Fe alloy*(Journal of MATERIALS SCIENCE LETTERS,6,441-443,1987).
- [8] M.FASS, D.ELIEZER, E.AGHION: *Hardening and Phase Stability in Rapidly solidified Al-Fe-Ce alloys*(Journal of MATERIALS SCIENCE, 33, 833-837, 1998)
- [9] T.B.Massalski: *Binary Alloy Phase Diagrams* (Materials Park: American Society for Metals, 1987).

Influcing Factor Research of Kerr Effect

Runlin Guo¹, Ningning Sun¹, Mingxin Song^{1, a}, Qian Liu¹

¹College of Applied Science, Harbin University of Science and Technology, Harbin 150080, China

^asongmingxin@126.com

Keywords: Kerr effect; Kerr cell voltage; Duration time; Electrode material;

Abstract. This paper presents a model of Kerr effect for the influencing factors research. The influencing factors proposed are Kerr cell voltage, charging duration time and electrode material. The experimental results show that refractive index of transformer oil will rise when Kerr cell voltage become larger; There is a period of 15 minutes called 'polarization time' after the beginning of the experiment and electrode material indeed has an obvious effect on the transformer oil.

Introduction

Electrooptical Kerr effect is a kind of phenomenon that the refractive index of a medium changes under the effect of electric field. Generally, light will not produce birefringent phenomenon when it travels along the optical axis in isotropic medium or piezoelectric crystal, but some isotropic transparent media do in a strong electric field, namely optical anisotropy[1]. Then, the difference of refractive indexes parallel and perpendicular to the direction of the electric field is proportional to the square of Kerr cell voltage. The research results show that electrooptical Kerr effect is very important to measure space charge and study electric field distortion mechanism.

Kerr effect principle is shown in Fig. 1. The light from the light source *S* enters the Kerr cell through the polarizer and the analyzer; The applied electric field between parallel electrode plates in the Kerr cell is perpendicular to the direction of optical axis.

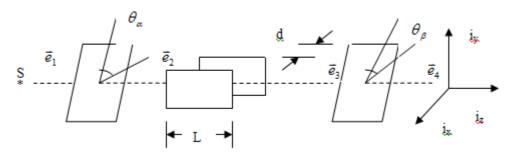


Fig. 1 Kerr effect principle

When there is no applied voltage, the optical axis of the polarizer is perpendicular to that of the analyzer. The Kerr cell is in the so-called 'off' state and impenetrable to light. Applied voltage changes the polarization of the incident light, producing a portion of the light which can pass through the analyzer; The Kerr cell is in the so-called 'open' state. The author has studied Kerr effect from different sides such as Kerr cell voltage, charging duration time and electrode material.

Test of Experiment Stability

Fig. 2 shows the block diagram of measuring devices for Kerr effect. He-Ne gas laser produces the laser light whose wavelength is 632.8 nm with good optical homogeneity, monochromaticity and spatial coherence[2], as a light source (the maximum output power is 10 mW). The polarizer is used to generate the polarized light, iris diaphragm to shrink light beam and analyzer to receive light. The transformer applies $0 \sim 50$ kV step-less adjustable dc voltage on the parallel electrodes in Kerr cell. Luminous power meter acts as the luminous power measurement device.

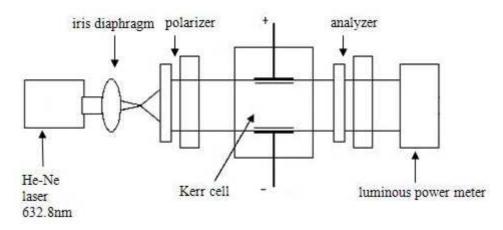
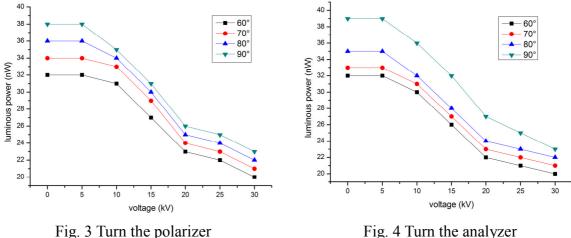
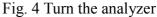


Fig. 2 Block diagram of test system

Transformer oil has so large resistivity $(10^8 \sim 10^{12} \ \Omega \cdot m)$ and small conductivity current (Kerr cell steady-state current is less than 0.2 mA) that there is almost no heat produced in the measurement process. And the oil is reusable when filtered by the filter paper under normal temperature and atmospheric pressure[3]. When the experiment is running, adjust the light path to minimize the measurement data of the luminous power meter. Respectively turn the polarizer and the analyzer to 60°, 70°, 80° and 90°; The Kerr cell voltage is set orderly to 0 kV, 5 kV, 10 kV, 15 kV, 20 kV, 25 kV and 30 kV. The relationship of luminous power and Kerr cell voltage is shown in Fig. 3 and Fig. 4.





From Fig. 3 and Fig. 4, conclusions come out that the change trend of the experimental data producing by adjusting the polarizer is as same as that by adjusting the analyzer, so the experimental light path is enough stable to take the next step of the experiment. Fig. 3 and Fig. 4 also show that with the increase of Kerr cell voltage, the luminous power detected gets weaker. The reason for this result is that He-Ne laser beam is assumed to propagate along a straight line[4], but the larger Kerr cell voltage becomes, the greater refractive index of transformer oil changes, the more laser beam deflecting loss is and the less luminous power detected gets. So the curves in Fig. 3 and Fig. 4 are on the decline.

Influence of Charging Duration Time

Choose 15 kV as Kerr cell voltage and 50 nW as the initial luminous power for this experiment. Turn the polarizer to 0°, 15°, 30° and 45° respectively, record the luminous power in 5 minutes, 10 minutes, 15 minutes, 20 minutes, 25 minutes and 30 minutes in sequence. The relationship of the luminous power and the duration time of Kerr cell voltage is shown in Fig. 5.

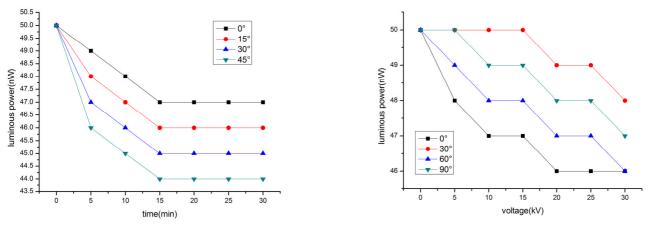
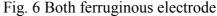


Fig. 5 The influence of charging duration time



It can be seen from Fig. 5 that when the Kerr cell voltage is fixed, within a certain period of time, as the time extended, the luminous power tends to be weaker; Over the period of time, the luminous power will no longer change. The first 15 minutes is be definited as 'polarization time' during which the transformer oil is polarized. When the polarization is completed, the refractive index of transformer oil changes no longer, so does the luminous power detected.

Influence of Different Electrode Materials

First, use two pieces of iron plates as electrodes (the sizes of both plates are the same), Kerr cell voltage goes from 0 kV to 30 kV with a step-length of 5 kV; The range of polarizer turning angle is from 0° to 90° with a step-length of 30° and the initial luminous power is 50 nW. Fig. 6 is the relationship of the luminous power and Kerr cell voltage. Turn plates combination respectively into 'ferruginous cathode, aluminous anode', 'ferruginous cathode, brass anode', 'ferruginous anode, aluminous cathode' and 'ferruginous anode, brass cathode' to get Fig. 7, Fig. 8, Fig. 9 and Fig. 10.

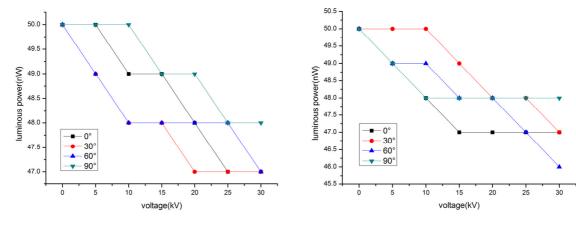
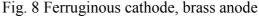


Fig. 7 Ferruginous cathode, aluminous anode



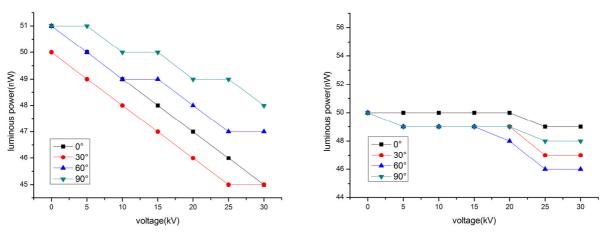


Fig. 9 Ferruginous anode, aluminous cathode

Fig. 10 Ferruginous anode, brass cathode

By comparing Fig. 6 with subsequent four pictures, it can be seen that if anode and cathode have the same material, difference angles have less influence on the trend of curves; Four curves decline or keep stable almost at the same time; But the influence of different angles is larger on the absolute value of luminous power. When materials of anode and cathode are different, changes of the four curves seem not to be in noteworthy synchronization; The fluctuations of curves are so weak that most parts of the four curves are overlapped. When the cathode material is iron, regardless of anode material is aluminum or brass, the curves show little change. When the anode material is iron, if cathode material is aluminium, with the rise of the Kerr cell voltage, the luminous power decreases significantly; If cathode material is brass, luminous power changes little.

Conclusions

Electrooptical Kerr effect has a good prospect, but it has not been controlled exactly. This paper studies the influence of Kerr cell voltage, charging duration time and electrode material. At the same time, 'polarization time' and the trend of voltage-luminous curves are confirmed.

Acknowledgements

The work is supported by the Project of Student Innovation Fund in Harbin University of Science and Technology Harbin.

- [1] Dj.M. Maric, P.F. Meier and S.K. Estreicher: Mater. Sci. Forum Vol. 83-87 (1992), p. 102
- [2] P.G. Clem, M. Rodriguez, J.A. Voigt and C.S. Ashley, U.S. Patent 6,231,666. (2005)
- [3] R.J. Ong, J.T. Dawley and P.G. Clem: submitted to Journal of Materials Research (2007)
- [4] Yeh,Y.,Cummins,H.Z.:Localized Fluid Flow Measurements with an He-Ne Laser Spectrometer. Applied Physics Letters. Vol. 4, p. 176-178. (2009)

Type Conversion of Undoped NiO Thin Films Fabricated by Electron Beam Evaporation Technique

Qingcheng Liang^{1,a}, Man Zhao^{2,b}, Dayong Jiang¹, Xin Wang^{3,c}, Jianxun Zhao¹, Shang Gao¹, Jieming Qin¹, Jianhua Hou¹ and Yuan Cui¹

¹ School of Materials Science and Engineering, Changchun University of Science and Technology, Changchun 130022, China

² Special Service Department, Aviation University of Air Force, Changchun 130000, PR China

³ School of Science, Changchun University of Science and Technology, Changchun 130022, China

^aliangqingcheng@cust.edu.cn, ^bzhaoman@126.com, ^cwangxin@cust.edu.cn

Keywords: NiO; thin film; electron beam evaporation

Abstract. As an important semiconductor, nickel oxide (NiO) films deposited by electron beam evaporation are reported scarcely. In this study, undoped NiO films were deposited on quartz by electron beam evaporation technique, and annealed at different temperature in a pure oxygen atmosphere. The electrical characterization of NiO films were investigated using Hall effect measurements. The results show that the film conduction types of n, p, and high resistivity appear in proper order with the increasing temperature. The mechanism is further explicated by the SEM and Raman measurements. The oxygen atoms are introduced by the thermal treatment under oxygen ambience. The amount of atoms is more and more with the increasing temperature and it results in becoming larger grain size of the film while the conduction type converting. High resistivity of the film reveals that some oxygen atoms will be out of the film at a higher annealing temperature. So the amount of oxygen atoms in the film plays a key role in the conduction behavior of NiO film. Our results provide important information for the improved understanding of the conduction mechanism.

Introduction

Nickel oxide (NiO) has recently become the focus of many studies since a wide range of application are possible due to its excellent characteristics [1-9]. In particular, NiO is a good example for p-type semiconductor [10,11]. Furthermore, non-stoichiometric NiO was a p-type semiconductor with nickel deficiencies, which comes to an agreement. This view point assigns basal ideas to obtain p-type NiO without doping such as heat treatment in oxygen ambience. NiO thin films are fabricated by many techniques such as reactive sputtering [12], spray pyrolysis [13], sol-gel [14], plasma enhanced chemical vapor deposition [15]. However, the report about the fabrication of NiO films deposited by electron beam evaporation is scarcely. It is quite suitable for fabricating high purity materials, which are hardly melted.

In this study, an attempt has been made to fabricate non-stoichiometric NiO thin films by electron beam evaporation technique, and all the films were annealed in a thermal treatment furnace. The ordinal type conversion of n, p, and high resistivity is observed with the annealing temperature in oxygen ambience. The mechanism which influences the conduction properties of NiO is investigated.

Experiments

The target used to fabricated NiO thin films on quartz (SiO₂) substrate by electron beam evaporation technique was a high purity (99.99 %) polycrystalline NiO source. The vacuum chamber was evacuated, using a primary and a diffusion pump, to a pressure below 10^{-6} Torr. The

distance between the substrate and the evaporation source was approximately 30 cm, and the substrate temperature was maintained at 673 K by a resistance heater. Before deposition, the substrate was cleaned successively with degreaser in an ultrasonic cleaner, and then rinsed in distilled water and alcohol. The electron beam evaporation voltage and current were constant at 12 KV and 55 mA, respectively. The thickness of NiO thin film was about 500 nm with the deposition ratio of 30 nm/min. The as-grown film on SiO₂ substrate was cut into smaller pieces and transferred into a standard diffusion furnace for annealing. The samples were annealed at 773, 873, 973, 1073, and 1173 K, respectively, for 30 min with an oxygen flux of 1 liter/min.

Scanning electron microscopy (SEM) of Hitachi S-4800 was used for the observation of the films surface. To investigate the effect of the annealing temperature on the vibration modes, Raman spectra were obtained using the 325 nm line of a He–Cd laser under back-scattering configuration. The electrical properties of the films were measured in Van der Pauw configuration by a Hall analyzer (Lakeshore 7707) at room temperature.

Results and discussion

Table 1 lists the Hall measurement results for the as-grown sample (A) and samples annealed at 773 (B), 873 (C), 973 (D), 1073 (E), and 1173 K (F).

Sample	Туре	Mobility	Resistivity	Concentration
		$[cm^2V^{-1}s^{-1}]$	[Ωcm]	$[cm^{-3}]$
А	n	20	3.0×10^{1}	5.0×10 ¹⁸
В	n	3	5.2×10^{2}	6.6×10 ¹⁶
С	р	0.3	1.3×10^{3}	2.1×10^{15}
D	р	0.8	5.7×10^{3}	8.9×10 ¹⁵
Е	р	0.4	1.6×10^4	3.1×10^{14}
F	High resistivity	_	_	_

 Table 1 Conductivity type, carrier mobility, resistivity, and carrier concentration of the as-grown sample and the samples annealed at different temperature

As can be seen from the table, samples A and B show n-type conduction, while samples C, D and E show p-type conduction, and sample F shows high resistivity, implying that the conduction type of the sample is related to oxygen ambience. In equilibrium defect chemistry, NiO usually has an oxygen excess accommodated by nickel vacancies. The radius of Ni²⁺ (0.69 Å) is much smaller than that of O^{2-} irons (1.32 Å). That means the NiO films can contain little oxygen atoms in the interstitial spaces. As a result, excess of oxygen in NiO will create vacancies in the normally occupied Ni sites. In order to keep electric balance in the film, two Ni²⁺ ions must be converted to Ni³⁺ for every vacant Ni²⁺ site. Thus, Ni³⁺ ions can be considered to be positive centre capable of jumping from one Ni²⁺ site to another. Thus, NiO with excess of oxygen is a p-type semiconductor. However, the p-type conduction has not found in samples A, B, and F. It is necessary to point out that there is no report about n-type NiO. Hence, the mechanism of the type conversion should be discussed.

Fig. 1 shows the SEM micrographs of NiO annealed at different temperatures.

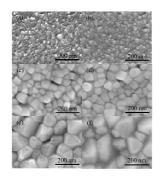


Fig. 1. SEM images of all the samples.

It can be observed that the grain size is enlarged by the increasing annealing temperature obviously. As is well known that the SEM only provides the information about the morphological studies, and it is too hard to explain the n or p types conduction from the morphological studies. However, some details of the SEM micrographs can be indirectly related with table 1 more or less. Fig. 1(a) presents the smallest grain size of the as-grown sample. Surprisingly, the as-grown sample shows many small particles in some regions. We found there is only one peak in the XRD spectrum for the as-grown sample (not shown here), and this peak origins from nickel atoms. This phenomenon may be due to some nickel atoms did not locate at the normal lattice points. That means some nickel atoms will stay at the surface or become interstitial atoms. The formation of these metallic nickel atoms can be attributed to high energy of the electron beam and the film will loss some oxygen atoms during the process. As a result, this will produce n type samples. The oxygen atoms will be introduced by the thermal treatment under oxygen ambience. The amount of atoms will be more and more with the increasing temperature and it results in becoming larger grain size of the film. However, excess oxygen atoms will occupy the nickel sites, which will be responsible for the p-type conduction in NiO. It should be noted that oxygen atoms in the film will be saturated at some temperature. As can be seen from Fig. 1(e), the crystal grain size was grown very slowly. According to our experience, some oxygen atoms will be separated out from the NiO film at high temperature. The variation of the oxygen atoms in the film will be investigated by Raman spectra in below.

Raman scattering spectra of the samples are collected in a backscattering geometric configuration at room temperature. All the samples show intense multi-phonon scattering in the range from 400 to 2000 cm⁻¹. Fig. 2 shows a typical resonant Raman scattering spectrum of all the samples. The Raman spectrum is composed of two lines at frequency shifts that are multiples of the 1-longitudinal optical (LO) zone-center frequency of 545 cm⁻¹. Compared to the predicted data of cubic NiO single crystal, we can note that all the samples mainly kept cubic structure.

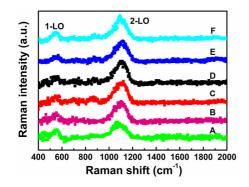


Fig. 2. Raman scattering spectrum of the samples.

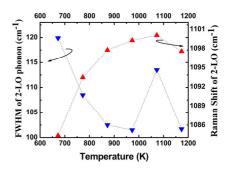


Fig. 3. Variations of FWHM and Raman shift of 2-LO phonon with the annealing temperature.

The variations of FWHM and the frequency of the 2-LO phonons versus annealing temperature are shown in Fig. 3.

As can be seen from Fig. 3, the FWHM of the 2-LO phonons decreases with the increase of the annealing temperature until 1073 K, which indicates the improvement of the NiO crystal quality. On the other hand, this means oxygen will be introduced into the normal lattice sites or occupy the nickel sites with the increasing temperature. However, the FWHM of the 2-LO phonons broadened at the annealing temperature of 1073 K. This indicates that there were some new defects in the crystal lattice, which may be due to the over-saturation of oxygen atoms in the film. Surprisingly, the FWHM of the 2-LO phonons shrinks again at the annealing temperature of 1173 K, indicating that the defects in the film will be smaller. The same conclusion can be conformed by the other hand. The data shows that annealing has caused the increase of the 2-LO phonon peak value from 1084 to 1100 cm⁻¹, the corresponding samples are A, B, C, D, and E, respectively. This confirms that the annealing led to a change in the composition of the film from Ni-rich to the excess of oxygen (Ni₂O₃) [17]. Sample F shows blue shift of the 2-LO phonon, this can be explained by the loss of oxygen from NiO film, which is according with the above discussions.

Conclusion

In this study, non-stoichiometric NiO films were deposited by electron beam evaporation technique and annealed at different temperature. With the increasing temperature, the conduction types of n, p, and high resistivity appear in series. The mechanism is further explicated by the SEM and Raman measurements. All characterizations indicate that interstitial nickel atoms will exist in the film when deposited on the substrate, which is related to the n type conduction. Oxygen atoms will be introduced into the film when annealed, as a result, the thermal treatment will affect the electricity of the NiO film. The appearance of p type conduction originates from the oxidation of Ni²⁺ irons. High resistivity of the film reveals that some oxygen atoms will be out of the film at high annealing temperature, and the ratio between nickel and oxygen will achieve the stoichiometric proportion. Thus, the NiO film is hard to be conductive for an intrinsic crystal. These results indicate that the conduction types of NiO films can be adjusted by annealing in oxygen ambience.

Acknowledgements.

We are grateful to the National Natural Science Foundation of China (no. 61106050, 21201022, 61205038), the Scientific and Technological Development Project of Jilin Province (no. 201201121, 20120435, 20130204033), and the Specialized Research Fund for the Doctoral Program of Higher Education (New Teachers, no. 20122216120001).

References

[1] J. Choi, S. Das and J. Myoung, et al.: Appl Phys Lett Vol. 95 (2009), p.062105

- [2] S. Seo, M. Lee and D. Seo, et al.: Appl Phys Lett Vol. 86 (2005), p. 093509
- [3] J. Son, Y. Shin: Appl Phys Lett Vol. 92 (2008), p. 222106
- [4] D. Kim, M. Lee and S. Ahn, et al.: Appl Phys Lett Vol. 88 (2006), p. 232106.
- [5] R. Eder, H. Winter: Physica B Vol. 359 (2005), p. 819-821
- [6] T. Schuler, D. Ederer and S. Itza-Ortiz, et al.: Phys. Rev. B Vol. 71 (2005), p. 115113
- [7] S. Noh, E. Lee and J.H. Seo, et al.: Sens. Actuators A Vol. 125 (2006), p. 363-366

- [8] J. Nel, F. Auret and L. Wu, et al.: Sens. Actuators B Vol. 100 (2004), p. 270-276
- [9] A. Neubecker, T. Pompl and T. Doll, et al.: Thin Solid Films Vol. 310 (1997), p. 19-23
- [10] H. Sato, T. Minami and S. Takata, et al.: Thin Solid Films Vol. 236 (1993), p. 27-31
- [11] A. Atkinson, R. Taylor and A. Hughes: Philos. Mag. A Vol. 45 (1982), p. 823-833
- [12] M. Bogner, A. Fuchs and K. Scharnagl, et al.: Sens. Actuators. B. Vol. 47 (1998), p. 145-152
- [13] P. Puspharajah, S. Radhakrishna and A. Arof: J. Mater, Sci. Vol. 32 (1997), p. 3001-3006
- [14] R. Young, J. Kwang: J. Crys. Growth Vol. 258 (2003), p. 380-384
- [15] W. C. Yeh and M. Matsumura: Jpn. J. Appl. Phys. Vol. 36 (1997), p. 6884-6887
- [16] W. Wang, Y. Liu and C. Xu, et al.: Chem. Phys. Lett. Vol. 362 (2002), p. 119-122
- [17] R. Srnanek, I. Hotovy and V. Malcher, et al.: ASDAM (2000), p.303-306.

A New Type of EO Polymer Based on Polyphosphazenes

ZHANG Ying¹, QIU Chengjun^{1,a}, Li You², ZHANG Wenlong³, WANG Xuan³

¹Electronic Engineering College of Heilongjiang University, Harbin, 150080, China;

²Harbin Research Institute of Electrical Instrument, Harbin, 150028, China;

³State Key Laboratory Breeding Base of Dielectric Engineering, Harbin, 150080, China ^awaterunderbridge@163.com

Keywords: polyphosphazenes; EO property; photoconductive property; THz wave

Abstract: Polyphosphazenes containing carbazole grafted by azo nitrobenzene is synthesized by microwave method in this paper. Its structure is characterized by infrared (IR) spectroscopy and UV-visible spectroscopy. This new polymer, with both electro-optic(EO) property and photoconductive property, has unique stability and can be easily processed. Terahertz(THz) wave can be detected using the device which is made with our new polymer. The time domain waveform and frequency spectrum of the THz wave are obtained.

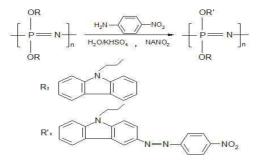
Introduction

Polyphosphazenes is one of the three kinds of inorganic polymeric functional materials. Phosphorus atoms alternate with nitrogen atoms along the main chain. There are two side groups connected to every phosphorus atoms. The materials could have different properties for different side groups [1]. Nowadays, polyphosphazenes has been the research focus of most scholars and widely applied in liquid crystal, aerospace, energy storage and so on [2, 3].

A new kind of EO polymer material, polyphosphazenes containing carbazole grafted by azo nitrobenzene, is introduced in this paper. Under the condition of the microwave radiation, polyphosphazenes containing carbazole grafted by azo nitrobenzene was synthesized for one step. Its structure is characterized by infrared (IR) spectroscopy and UV-visible spectroscopy. EO coefficient and photoconductivity are tested. These experiments show that this new polymer has unique stability and can be easily processed. The polymer have both EO property and photoconductive property, and its EO coefficient is 35 pm/V. Terahertz (THz) wave can be detected using the device which is made with our new polymer. The time domain waveform and frequency spectrum of the THz wave are obtained. Owing to these unique properties, this new type of EO polymer might be widely used in military manufacturing, medical science and ordinary life fields [4, 5, 6], as well as the emission and detection of THz radiation [7].

Synthesis of the Material

The polyphosphazenes containing carbazole grafted by azo nitrobenzene is synthesized by chemical reactions with polyphosphazenes containing carbazole, potassium bisulfate, P-nitroaniline and sodium nitrite as raw materials, while heated by microwave oven. The material is obtained by only one step, which is fast and time saving. The chemical reaction is shown in equation 1.



Structure Characterization

The structure of the new polymer is characterized by infrared (IR) spectroscopy and UV-visible spectroscopy. The result is shown in Fig.1.

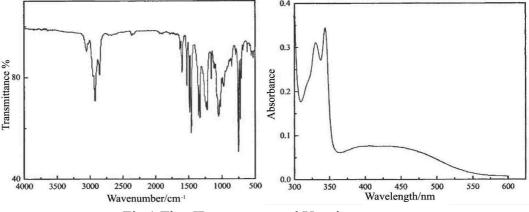


Fig.1 The IR spectrum and Uv-vis spectrum

For the IR spectrum, the characteristic absorption peaks of the carbazole appear at 3050 cm⁻¹, 1600 cm⁻¹, 1484 cm⁻¹, 1450 cm⁻¹. The stretch absorption peak of the C-H on fatty chain is obtained at 2930 cm⁻¹. The characteristic absorption peaks of the P-O-C appear at 1050 cm⁻¹ and 926 cm⁻¹, while the peaks of the P=N appear at 1320 cm⁻¹, 1240 cm⁻¹. The stretch absorption peak of P-N is obtained at 750 cm⁻¹ and 723 cm⁻¹. These evidence indicate that the carbazole is grafted on the polydichlorophosphazene successfully. For the Uv-vis spectrum, There is no absorption in the visible light region. The peaks obtained at 330nm and 343nm are the absorption peaks of carbazole groups, which are the results of the π - π * transition.

Property Tests

EO property. The EO coefficient of the new polymer film, the thickness of which is more than $200\mu m$, is tested by simple reflection method [8, 9]. The principle of the test is as fig.2.

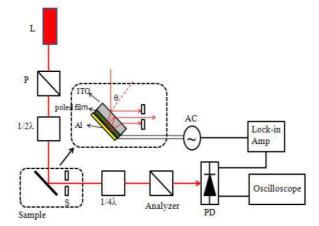


Fig.2 Principle scheme of the simple reflection method

The wavelength of the laser is 632.8nm, while the voltage peak is 16.5V. The EO coefficient γ_{33} =35pm/V when the grafting rate is 18.8wt%.

Photoconductivity. The polymer has the photoconductivity because of the carbazole group. The result is shown in Fig.3 under different luminous power when the grafting rate is 18.8wt%.

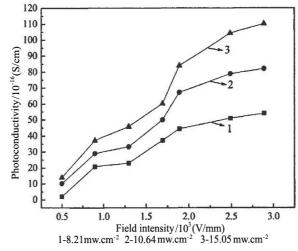


Fig.3 Characteristic curve of photoconductivity

With the same luminous power, the photoconductivity increase as the field intensity become larger, which indicate that the carrier mobility is improved so as that the electrical conductivity is improved because of the improvement of the electric field intensity. With the same field intensity, the photoconductivity increase as the luminous power intensity become larger, which indicate that the optical carrier increase because of the increase of the light intensity.

THz Characters. Terahertz(THz) wave can be detected using the device which is made with our new polymer. The time domain waveform and frequency spectrum of the THz wave are shown in Fig.3.

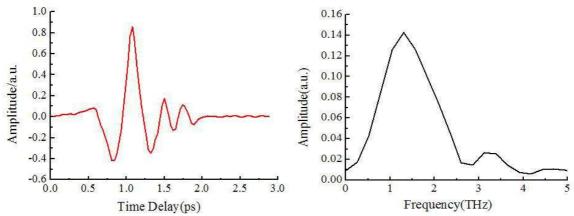


Fig.3 Time domain waveform of THz wave and Frequency spectrum of THZ wave

Conclusions

Under the condition of the microwave radiation, polyphosphazenes containing carbazole grafted by azo nitrobenzene was synthesized for only one step. Its structure is characterized by infrared (IR) spectroscopy and UV-visible spectroscopy. This new polymer has unique stability and can be easily processed. Experiments show that when the grafting rate is 18.8wt%, the EO coefficient is 35pm/V. The polymer have both EO property and photoconductive property. Under certain luminous power intensity, the photoconductivity increase as the field intensity becomes lager. Under certain field intensity, the photoconductivity increase as the light intensity becomes lager. Terahertz(THz) wave can be detected using the device which is made with our new polymer. The time domain waveform and frequency spectrum of the THz wave are obtained.

Acknowledgments

The work is supported by the National Natural Foundation of China (60871073) and the Research Foundation of Education Bureau of Heilongjiang Province (11551076, 12511078)

- HARRY R. Generation of structural diversity in polyphosphazenes [J]. Applied Organometallic Chemistry, 2013, 27(11):620~629.
- [2] Zhou Lintao, Su Yi, Zha Zuotong. Research on application and synthesis of polyphophazene [J]. Science and Technology In Chemical Industry, 2012, 20(4):68~72.
- [3] HARRY R. New developments in the science and applications of polyphosphazenes [J]. American Chemical Society, Polymer Preprints, Division of Polymer Chemistry, 2000, 41(1):553.
- [4] Helena Henke, Sandra Wilfert, Aitziber Iturmendi. Branched polyphosphazenes with Controlled Dimensions [J]. Journal of Polymer Science Part A-Polymer Chemistry, 2013, 51(20):4467~4473.
- [5] Muhsin Eralp, Jayan Thomas, Savas Tay. High performance photorefractive polymer operating at 975nm [J]. Applied physics letters, 2004, 85(7):1095~1101.
- [6] Zhang Wenlong, Zhao Chenglong, Jiang Qiang. Photoelectric performance of polyphophazene grafted functional group [J]. Journal of Functional Materials, 2012, 43(24): 3386~3392.
- [7]HARRY R. Recent developments in poly- phosphazene materials science [J]. Current Opinion in Solid State and Materials Science, 2006, 10(12):231~240.
- [8]Alexander M, Sinyukov, L. Michael Hoyden. Generation and detection of terahertz radiation with multilayered electro-optic polymer films [J]. Optics letters, 2002, 27(1):55~64
- [9]Yu, Feng, Spring, Andrew M, Li, Lu. An enhanced host-guest electro-optical polymer system using poly(norbornene-dicarboximides) via ROMP [J]. Journal of Polymer Science, Part A: Polymer Chemistry, 2013, 51(6):1278~1284.
- [10]F. Michelotti, E. Toussaere, R. Levenson Real-time pole and probe assessment of orientational processes in electro-optic polymers [J]. Applied physics letters, 1995, 67(19):2765~2773.
- [11]Wang Xibin. Basic Research on Electro-Optic Characteristics of Poled Polymer Thin Films [D]. Jilin University, 2010: 20~31.

The Stress Distribution and Influence of VDMOS Device Based On ANSYS

Jinghua Yin^{1,a}, Shuting Gao^{1,b}, Minghua Chen^{1,c}

¹Department of Electronic Science and Technology, College of Applied Science, Harbin University of Science and Technology, Harbin, 150080, China

^ayinjinghua1@126.com, ^b13703635425@163.com, ^ccmh.007@163.com

Keywords: VDMOS, stress distribution, finite element, reliability

Abstract In this paper, the device of VDMOS packaged in a TO-220C power is acted as research object. ANSYS finite element software simulation is used to build the three dimension model, the software is also used to imitate the stress distribution under the frequency of 220Hz ~ 400Hz. The simulation result shows that the stress of the chip of corresponding to the empty space is bigger than the others as the increasing frequency on the boundary of bonding layer and the chip, which easily leads to micro deformation of the bonding layer and the micro crack of the chip. The value of stress effects by changing the bonding layer material and layer thickness, the simulation results show that the bigger heat conductivity coefficient and the thinner thickness of bonding layer is the smaller stress, Which the design of the bonding layer can be optimized. The results of the study provide the theoretical basis for the structural design of the device, founding the weakness of structure design, having guiding significance for improving the reliability of the device.

Introduction

VDMOS device^[1] with the advantages of bipolar transistor and common power MOS device, which is the mainstream of current power semiconductor devices, it has low price, high input resistance, fast switching speed, good thermal stability and other characteristics, and it is also used in the civilian and military electronics industry widely. However, in the actual process of service, the failure distribution of VDMOS are not only affected by the failure modes, the failure mechanisms and the structures of device, but also by the sustained stress, its working environment and many other factors. The device of VDMOS has to withstand the combined harsh working conditions of shock and temperature. And, vibration has become a key factor affecting the reliability of electronic products in the areas of aerospace and military. So it is necessary to carry out the research of the reliability of the device to avoid the device failure in the process of actual use. At home and abroad has done a lot of reliability related test of power device, such as simulating the stress distribution of device under the conditions of temperature cycling. The beginning location of failure is found from these experiments, then evaluating the property of resist and the ability of work for the device during the changes of temperature. Other study caused the failure of device by the environment is also carried out in different levels, like, humidity, pressure, gravity field, sunlight and so on. The finite element software is used to simulate the stress for the power VDMOS device to avoid the high experimental cost and provide valuable theory data to improve the structural design continuously, according to the distribution of stress and strain, finding the weakest link of the device. The failure discipline of the device was analysis caused by the stress distribution, the device in order to improve the performance and reliability.

Finite element procedure implementation

Building the model of the power VDMOS. The model of device is comprised by five parts, such as the lead frame, the bonding layer, chip, pins and plastic body, packaging in the form of TO-220C. The bonding wire between the chip and the left and right pin is ignored, the chip is connected with the bonding layer and the lead frame, this section assumes that the bonding layer hollow has empty

hollow and the hollow is circular. The bonding layer is simulated by the 8node plas107 of Visco Solid unit, and the other part of the device is simulated by the Brick 8node 45 of structural solid unit. By measuring the dimension of the device, the size of each part of the device structure is shown in Table 1, Material parameters of the device is shown in Table 2.

Table.1 Model dimension						
Model components	length(mm)	width(mm)	height(mm)			
Lead frame (above)	10	6.75	1.5			
Lead frame (below)	8	6.75	1.5			
Bonding layer	3.5	3	0.25			
Chip	3.5	3	0.5			
Plastic body	10	9	4.5			

Table 7	Matarial	noromotoro

Model	Material	EX(GPa)	P RXY	ALPX(1/K)	Density(1/g/cm ³)
components	composition				
Lead frame	Cu	120	0.345	17.0E-6	8.9
Bonding	63Sn37Pb	43.25	0.363	21.0E-6	174.35
layer					
Chip	Si	130	0.3	2.8E-6	2.34
Pin	Cu	120	0.345	17.0E-6	8.9
Plastic body	Epoxy	26	0.3	7.0E-6	1.1

The model of device is built by ANSYS10.0 finite element software^[2], building the modle of the device after selecting the Element Type and setting the Material Props, Applying the analysis of Structural Dynamics, the model of bonding layer and chip is shown in Fig.1, the model of the whole device is shown in Fig.2.

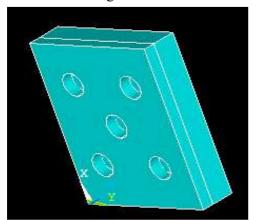


Fig.1 The model of bonding layer and chip

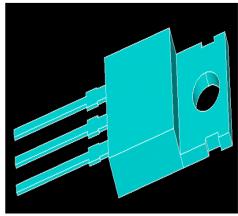
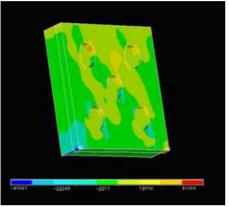


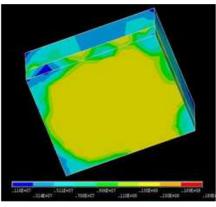
Fig.2 The model of the whole device

Define loads and Solution Applying the Displacement to the model of device after meshing the model. Meshing of the device choosing the shape of Hex and adopting the way of mapped. The whole Displacement imposed on the modle of bonding and chip, external underside pin of model. After that when solving with simulation using full N-R, open the Large Deflection Option, assuming that the temperature is 20°C, the range of the freqency between 220Hz and 400Hz, the internal model has zero stress. Solving is done after define loads^[3,4].

View Results The device model is loaded for calculation after the pre-processing change. The results are checked by the regular post-processor. The result shows in a way of contours, where the value of the stess can be displayed. The stress distribution of the bonding layer and the chip are shown in

Fig.3, where the intensity of the hollow's edge as well as that lies between the border of the hole and the chip are pretty strong.







As to the empty hollow produces different asymmetrical stress, the stress of empty hollow at edge is greater than the peripheral portion. At the same time, with the change of the frequency, the phenomenon of stress concentration on the bonder intensifies. The chip is easy to produce deformation when the stress reaches its maximum strength, which appears micro-cracks. When design the device should avoid the defect.

The stress distribution of the whole device is shown in Fig.4. The value of stress distribution in the figure reveals that the stress intensity on chip and external pin is larger than other location.

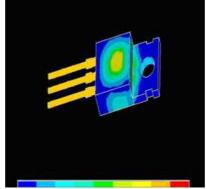


Fig. 4 The vibration stress distribution of the whole device

The different frequencies produce different shear stresses, as the external device pin contacts with the outside space, the external pin exists stress concentration, which value is obvious larger than other location, then, it appears fatigue cracks. When stress reaches maximum intensity for the pin, the pin appears fracture. When the device is used in actual environment, the stress value on the boundary of the chip and the bonding layer and the location of the external pin is bigger than the result of simulation, it can be effected not only the frequencies but also other factors^[5].

Results and discussion Keeping other parameters of the device unchanged, the different materials of the bonding layer are selected and its thickness of the bonding layer is changed from 0.1mm to 0.5mm. Conducting the stress analysis after changing the model, different thickness of the bonding layer has different stress results. The result is shown in Fig.5, with the thickness of bonding layer increases, the maximum stress of the different material of the devices all have more obviously rising trend, the stress of the Au80Sn20 is biggest, 63Sn37Pb is followed and the conductive adhesive has minimum stress. The result shows that the thinner thickness and the bigger heat conductivity coefficient of the bonding layer have high stress.

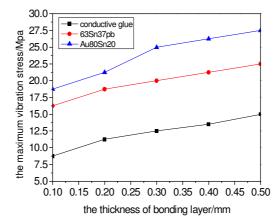


Fig.5 Relationship of device stress bonding material and thickness

The structure and material parameters of the device effects the value of stress, adopting the most optimal parameters provide the data for the structural design and improve the service life of the device in actual environment.

Conclusions

The stress distribution of power device is studied under the frequency between 220Hz and 400Hz with the theory simulation of finite element software, the location of the stress distribution reveals that the device of power VDMOS suffer different shear stresses under the environment, and the stress between the chip and the pin is more concentrated. When the stress reaches maximum intensity for the chip and the external pin, the chip appears fatigue crack, and the fatigue crack of the chip likely extends to the micro-cracks, the pin easily creates fatigue fractures. The device is optimized by selecting the appropriate thickness and materials of the bonding layer. Finite element method is used to calculating with high precision, short development cycle, which having guiding significance for optimizing the design and improving the reliability of the devices The three typical bonding layer materials of conductive adhesive, 63Sn37Pb and Au80Sn20 change the thickness. The result shows that the thinner thickness and the bigger heat conductivity coefficient of the bonding layer have high stress.

Acknowledgment

This work was supported by the science and technology research project of Heilongjiang Province Education Department (11551100).

- [1] Y. Rey-Tauriac, et al. *Reliability oriented process and device simulations of power VDMOS transistors in Bipolar/CMOS/DMOS technology*. Physical and Failure Analysis of Integrated Circuits, 2003. Proceedings of the 10th International Symposium on the. IEEE, 2003: 29-35.
- [2] Z. Yingqian, Z. Hongcai, *ANSYS10.0 finite element software* [M]. BeiJing: The People's Posts and Telecommunications Press, 2010: 95-400.
- [3] M. Weihua, X. Bingrong, et al. *Research of Atigue Life Simulations Applied to Complex Structure by MBS-FEM* [J]. Journal of Mechanical Strength, 2008, 30(1): 137-143.
- [4] Z. Yuan, Z.L. Sun, et, al, *Sensitivity Analysis of Gear Structures Vibration with Random Parameters*, Machinery and Electronics, 2009: 16-17.
- [5] J. Zhao, H. C. Wu, J. Tang: A Reliability Assessment Method in Strain-based Fatigue Life Analysis [J]. Journal of Pressure Vessel Technology ASME, 1998.120(1): 99-104.

Analysis of Electric Field Homogenization of Converter Transformer Barrier System based on Nano Modification of Pressboard

Qingguo Chen^a, Heqian Liu^b, Xiangli Zhuge^c, Minghe Chi^d and Xinlao Wei^e Key Laboratory of Engineering Dielectrics and Its Application, MOE, Harbin University of Science and Technology, Harbin, China

^aqgchen@263.net, ^bheqian_liu@163.com, ^c757450371@qq.com,

^dchiminghe1985@163.com, ^eweixinlao@hrbust.edu.cn

Keywords: converter transformer, barrier system, non-linear, nano-modification, electrical field distribution

Abstract. In order to solve the problem of non-uniform electric field distribution in converter transformer barrier system caused by conductivity difference between the transformer oil and pressboard, the SiC(silicon carbide) modified pressboard was developed by nano doping method. The conductivity of modified pressboard was measured. The measuring results show that the conductivity of modified pressboard increases exponentially with the increase of nano SiC doping ratio. The electric field strength has obvious influence on conductivity at high nano doping ratio, which shows great nonlinear characteristic. Based on the nonlinear conductivity characteristic of modified pressboard, the homogenizing effect of the nano modified pressboard on electric field distribution was verified by simulation. The simulation results show that the electric field distribution under DC and polarity reversal voltage in barrier system can be well homogenized by using the nonlinear characteristic of nano modified pressboard.

Introduction

As mainly equipment used in HVDC transmission system, the reliability of converter transformer will directly influence the safe operation of the whole power system. The barrier system is the important part of convert transformer, whose insulation structure will undertake the DC superimposed AC voltage and polarity reversal voltage during operation [1].

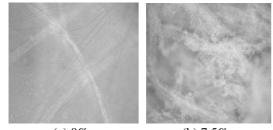
In oil/pressboard insulation structure, the distribution of electric field under DC voltage mainly depends on the conductivities of oil and pressboard. For there exists large difference in electrical conductivity between pressboard and oil, and it also depends on many other factors, such as temperature, electric field strength and moisture content, which possibly makes the conductivity of pressboard be 10 to 1000 times lower than the conductivity of oil. The large conductivity difference between pressboard and oil can lead to extremely high electric field strength in pressboard and low electric field strength in oil under DC voltage. To solve above problem of electric field concentration in pressboard under DC voltage, the pressboard modification method is proposed to realize the conductivity matching between pressboard and oil by using nonlinear characteristic of nano modified pressboard. So, the SiC modified pressboard was developed by nano doping method in this paper. The conductivity characteristic of modified pressboard under DC voltage was measured, and the homogenization effect on electric field distribution in oil/pressboard insulation structure was studied by software simulation.

Experimental Method

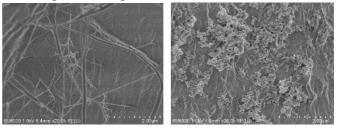
The nano modified pressboard sample is made of industrial grade unbleached coniferous kraft pulp, SiC nanoparticles and distilled water. According to industrial manufacture process of insulation pressboard, sample preparation process includes the following six steps, such as pulping, nano doping, shaping, compressing, drying and oil impregnation. The paper pulp fiber and the SiC nanoparticles are mixed uniformly by standard mixing agitator with the given nano doping ratio (in mass fraction). The conductivity characteristic of modified pressboard was studied by measuring leakage current with the three terminal electrode system.

Results and Discussion

Microscopic structure. Microscopic structures of paper pulp and surface of modified pressboard with nano doping radio of 0% and 7.5% are shown in Fig. 1 and Fig. 2.



(a) 0% (b) 7.5% Fig. 1 Microscopic structure of paper pulp



(a) 0% (b) 7.5% Fig. 2 SEM images of modified pressboard surface

By the comparison between Fig. 1(a) and Fig. 1(b), it can be observed that the nano-particles overlay uniformly at pulp fiber. Fig. 2 shows that the nanoparticles are dispersed uniformly in gaps of paper fibers after shaping, and the nano SiC particle doping in the pressboard does not lead to obvious change of microstructure of pressboard.

Effect of modification on conductivity of pressboard. The conductivity characteristic of modified pressboard with different nano doping ratios under 13kV/mm DC electric field strength is shown in Fig. 3. The relationships between conductivity of pressboard and electric field strength with different nano SiC doping ratios are shown in Fig. 4.

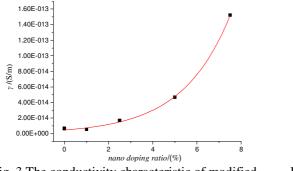


Fig. 3 The conductivity characteristic of modified pressboard with different nano doping ratios

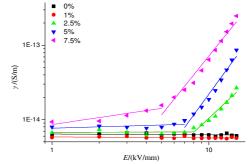


Fig. 4 The relationship between conductivity of modified pressboard and electric field strength

It can be seen that the conductivity of modified pressboard increases exponentially with the nano SiC doping ratio. The relationship between the conductivity γ and the nano doping ratio *a* can be fitted as:

 $\gamma = 4.717 \times 10^{-15} \times e^{0.46307a}$

(1)

The conductivity of pressboard increases significantly with electric field strength at high nano doping ratio. At low nano doping ratio, the distance between nano SiC particles is long, and the particles cannot contact with each other, which makes it difficult for carriers to migrate. Also, the carriers will be captured by the traps provided by SiC particles. So within certain nano doping range, the SiC doping has little influence on conductivity characteristic of the modified pressboard. However, as nano doping ratio increasing, conductive channel is easy to form due to the decrease of average distance between SiC particles. With the tunnel effect intensifying, the change of conductive mechanism occurs, which makes conductivity of modified pressboard show nonlinear characteristic under higher electric field strength[2,3].

The relationship between the conductivity of modified pressboard and electric field strength can be expressed by Eq. 2:

 $\gamma = \mathbf{A}E^{\beta} \tag{2}$

in which A is a constant relate to material properties, β is the non-linear conductive coefficient. $\beta=0$ equals to that the material is defined as linear material; when $\beta>0$, the material is defined as nonlinear material.

By logarithmic transformation of Eq. 2, there is:

 $\lg \gamma = \lg A + \beta \lg E$

here, the slope of changing curve β represents the degree of nonlinear characteristic[4].

The threshold electric field can be defined as E_c at which the non-linear conductive coefficient changes, and the non-linear conductive coefficient β_1 (below E_c) and β_2 (upon E_c) are shown in Table 1.

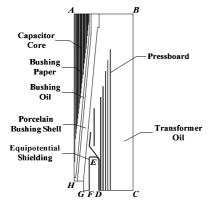
nano doping ratio [%]	E _c [kV/mm]	eta_1	β_2	
0.0	_	0.00	0.00	
1.0		0.00	0.00	
2.5	8.0	0.01	1.98	
5.0	6.0	0.06	2.90	
7.5	5.0	0.31	2.62	

As shown in Table 1, the modified pressboard shows no nonlinear characteristic until the nano doping ratio reaches 2.5%. Above this ratio, the modified pressboard shows more obvious nonlinear characteristic, and the threshold electric field E_c will decrease with nano doping ratio increasing.

Effect of modification on electric field distribution. The simulation model is built (shown in Fig. 5) according to the real structure of barrier system, in which some simplification is made considering the calculation speed.

In the model, the line A-H expresses the guide rod; the line F-E-D expresses equipotential shielding. The potential of the line B-C is set at 0V, and line F-E-D and line H-G-F are set at high voltage. The conditions of the boundary A-B and D-C coincide with the Neumann boundary condition[5].

The amplitude of applied DC voltage is 1691kV. The waveform of applied polarity reversal voltage is shown in Fig. 6, in which U_{pr} is 1306 kV, t_{pr} is 2min.



-Upr 90min

(3)

Fig. 5 Simulation model

Fig. 6 The waveform of applied polarity reversal voltage

The parameters of modified pressboard with nano doping ratio of 7.5% is applied to the simulation model, as its conductivity shows more obvious nonlinear characteristic than other contents. The relationship between conductivity γ and electric field strength *E* can be expressed by Eq. 4:

$$\gamma = \begin{cases} 8.692 \times 10^{-15} \times E^{0.31}, & E \le 5 \text{kV/mm} \\ 1.668 \times 10^{-16} \times E^{2.62}, & E > 5 \text{kV/mm} \end{cases}$$
(4)

The electric field distributions in barrier system with non-modified pressboard and modified pressboard under DC voltage are shown in Fig. 7.

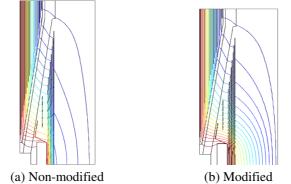


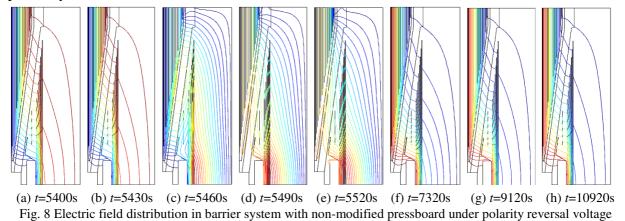
Fig. 7 Electric field distribution in barrier system under DC voltage

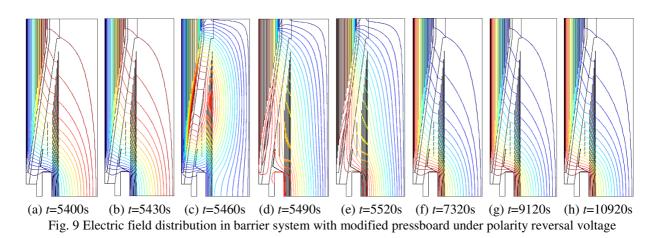
The maximum electric field strength E_{omax} in oil and E_{pmax} in pressboard under DC voltage are shown in Table 2.

Table2 The maximum electric field strength E_{omax} and E_{pmax}						
Pressboard type	E _{omax} [kV/mm]	E _{pmax} [kV/mm]	$E_{\rm pmax}$ / $E_{\rm omax}$			
Non-modified	4.41	134.37	30.47			
Modified	6.87	17.17	2.50			

The simulation result shows that the E_{pmax} appears on the surface of equipotential shielding, and the ratio of E_{pmax}/E_{omax} decreases obviously by adopting the modified pressboard. This can be contributed to the good non-linear characteristic of modified pressboard. When the electric field strength reaches a certain level, the conductivity difference between pressboard and oil becomes small, which leads to the homogenization of electric field in oil/paper insulation structure under DC voltage.

The electric field distributions in barrier system with non-modified pressboard and modified pressboard under polarity reversal voltage at several typical times are shown in Fig. 8 and Fig. 9, respectively.





As shown in Fig. 8 and Fig. 9, the electric field concentrates in the pressboard during DC steady state before 5400s. And the electric field concentration shifts from pressboard to oil in process of polarity reversal from 5400s to 5520s. It can be observed that the shape of contours appears reverse and tortuous. In transition process from 5520s to 10920s, the electric field distribution changes contrary to that in process of polarity reversal, and finally tends to the condition under DC steady state. From the comparison between Fig. 8 and Fig. 9, it can be seen clearly that number of contours in oil in Fig. 9 is more than that in Fig. 8 at same typical time. It represents that the electric field strength increases in oil and decreases in pressboard. The E_{omax} appears in oil gap between equipotential shielding and pressboard molding, and increases from 9.51kV/mm to 23.33kV/mm by adopting modified pressboard. The E_{pmax} decreases from 107.97kV/mm to 38.25kV/mm, appears on the surface of equipotential shielding. That indicates electric field distribution is homogenized.

The electric field is produced by combined action of external voltage and space charge. The conductivity difference between pressboard and oil decreases through modification, leading to the homogenization of electric field in oil/paper insulation structure. Also the space charge accumulation is weakened on the interface between pressboard and oil. So the electric field distribution can be well homogenized by adopting nano-modified pressboards in barrier system under polarity reversal voltage[6].

Conclusions

From the investigation mentioned above, some conclusions can be drawn:

(a) The conductivity of modified pressboard does not show nonlinear characteristic at low nano doping ratio. However, it increases exponentially with enhancement of electric field strength at higher nano doping ratio, which shows good nonlinear characteristic.

(b) The electric field distribution under DC and polarity reversal voltage in barrier system can be well homogenized by using the nonlinear characteristic of nano-modified pressboard.

Acknowledge

This project was supported by the Research Found for the Doctoral Program of Higher Education (No. 20132303110006) and Natural Science Foundation of Heilongjiang Province (No.ZD201310).

References

- Yan Li, Xiaohui Li, Cong Tang and Dongxue Li: High Voltage Engineering. Vol. 38, No. 11 (2012), p. 2797-2804(In Chinese).
- [2] J. Robertson, B. R. Varlow: IEEE Transactions on Dielectrics and Electrical Insulation. Vol. 12, No. 4 (2005), p. 779-790.
- [3] Wenmin Guo: "Research on non-linear conductive characteristics and mechanisms of polyethylene composites filled with inorganic filler" (In Chinese). Harbin: Harbin University of Science and Technology. p. 27-34 (2010).
- [4] Baozhong Han, Wenmin Guo and Zhonghua Li: Functional Materials. Vol. 9, No. 39 (2008), p. 1490-1493 (In Chinese).
- [5] Qingguo Chen, Jie Zhang, Yuan Gao and Xinlao Wei: High Voltage Engineering. Vol. 34, No. 3 (2008), p. 484-488 (In Chinese).
- [6] Yuan Gao, Qingguo Chen, Guangjun Li, Xinlao Wei and Yonghong Wang: "Analysis of electrical field on valve side winding of converter transformer". Proceedings of the 9th International Conference on Properties and Applications of Dielectric Materials. p. 85-88 (2009).

Experimental Investigation of Emulsifying Viscosity Reduction of a New Viscosity Breaker

Feng Wang^{1,2} Chi Ai¹ Dandan Yuan³ Shuang Liang⁴ Guangmiao Qu^{4,a} ¹Key laboratory of Education Ministry for Enhanced Oil Recovery Northeast Petroleum University 163318 China

²Jilin Oilfield Limited Company of Petrochina 138001 China

³Engineering and Technology Research Institute of Xinjiang Oilfield Company 834000 China

⁴College of chemistry and chemical engineering Northeast Petroleum University 163318 China

^aqugm110@126.com

Keywords: heavy crude oil, water soluble viscosity reducer, viscosity reduction rate

Abstract: In this paper, alkyl polyglucoside (APG) and fatty alcohol polyoxyethylene ether (AEO₃) were prepared to obtain a new type of soluble viscosity reducer which can change the rheological behavior of the crude oil and reduce its viscosity using method of emulsification viscosity reduction. The typical sample of heavy oil produced in Jilin oilfield was analyzed to figure out the key factors of influencing the viscosity of this heavy oil and the static evaluation experiments were carried out to investigate the reducing performance of the viscosity breaker. The viscosity breaker can lower the interfacial tension between oil and water to some extent, and the stability of emulsion between the oil and water is relatively good, in addition, it can provide high viscosity reduction rate and detergent factor of oil to produce a good viscosity reduction performance.

Introduction

In development of heavy oil reservoir, if they are relatively small or thin, they are not good candidates for thermal methods, so non-thermal techniques are required to recovery the remaining oil in place (Mai and Bryan, 2009). Water flooding are relatively inexpensive and easy to control, therefore they are still often employed even in heavy oil fields. But some of the mechanisms differ from the conventional fractional flow theory [1]. In heavy oil reservoirs, water flooding may not be successful due to extremely high oil viscosity, so there is a need to reduce the viscosity of the heavy oil [2].

At present, the common methods of reducing oil viscosity include heating, mixing thin oil, upgrading heavy oil, chemical viscosity reduction etc[3]. Duo to its widely application range, simple process and low cost, the method of chemical agent viscosity reduction has advantages over other technologies.

This paper used alkyl polyglucoside (APG) and fatty alcohol polyoxyethylene ether (AEO_3) to combine a new water soluble viscosity breaker which follows the emulsification rule. This viscosity reducer can change the heavy oil or w/o emulsion into o/w emulsion and turn the friction among oil slicks into the friction among water films, thus the viscosity of heavy oil decreases greatly, so does the flow resistance of it [4].

Experiment

Experiment agent: viscosity breaker, formation water, crude oil. Experimental apparatus: electron microscope, Zeta electric potential nm-zetasizer tester, interfacial rheometer.

This chemical system is prepared of alkyl polyglucoside (APG) and fatty alcohol-polyoxyethylene ether (AEO₃) in the ratio of 2:1, with the 20% of triethanolamine as the solubilizer and fatty acid amides two ethanol as the synergist.

Experimental method

The determination of emulsion stability This work utilized natural subsidence diversion rate of water as evaluation criterion of the emulsion stability. The diversion rate of water is the percentage of water volume in emulsion. Viscosity breaker solution in concentration of 0.1%, 0.2%, 0.3% and 0.5% were prepared to carry out the natural sinking experiments according to the o/w ratio of 7/3 to investigate the effect of concentration of viscosity breaker on diversion rate.

The determination of interfacial tension The interfacial tension between the solution and heavy crude oil was measured using surface tensionmeter. Each test lasted 120 minutes, taking average value of stable stage as the balance interfacial tension [5].

The determination of viscosity reduction rate The viscosity reduction rate is the percentage of viscosity decline size. According to the enterprise standard of SINOPEC (Q/SH0055-2007), the heavy oil was placed in waterbath at 50°C to be preheated for 1 hour, wiping out the free water and bubble, and the viscosity of it was measured at 50°C; The emulsion was prepared according to the mass ratio of oil/water of 7:3, and was left at constant temperature for 1 hour, after mixing for 2 minutes, the viscosity was tested instantly.

The determination of detergent factor of oil 50 g oil (marked as m_1) sand and 100 g viscosity reducer solution of 0.2% were placed in beaker. Subsequently, the beaker was put into waterbath at 50°C, and was stirred for 2 hours [6]. The system was left for 1 day, from which the oil sand and emulsion were obtained. The oil sand, after removing the emulsion, was placed in forced air drying at 115°C until the mass of it did not decrease. The detergent factor of oil was calculated according to following formula. Where m_1 —the mass of oil sand before washed, g; m_2 —the mass of oil sand after washed, g; X/Y—water content/oil content before washed, %.

$$D = \frac{m_2 (1 - X) - m_2}{m_2 Y}$$
(1)

Results and discussion

Analysis of oil component The composition of heavy oil in table 1 shows that there is more wax in the oil than colloid and asphaltene. Theoretically, when the intermolecular relative displacement takes place, the internal friction should be small, and the viscosity of the crude oil was not supposed to be high. However, the viscosity of Jilin crude oil is 301 mPa·s at 30°C. The reason may be as follows: the heavy oil is rich in wax, and it will dissolve in the oil at high temperature. When the oil cools down to certain temperature, the aggregation stability of oil starts to decrease, leading to the separation out of the solid state hydrocarbon which increases as the temperature gets down. Meanwhile, disperse phase (wax crystal particle) turns into continuous phase gradually to form wax crystal network wrapping up the oil. The crystallization and separation in heavy oil make the viscosity get larger. Asphaltene can play a role of crystal nucleus to form many minute wax crystal dispersing in oil, so the viscosity is relatively small apparently. Thus colloid and asphaltene are naturally crystallization inhibitor of wax. The heavy oil is low in colloid and asphaltene, so it presents relatively high viscosity due to lack of inhibitor.

Table 1 Analysis of on componet						
Component	asphaltene	colloid	wax			
Content (%)	0.62	5.78	14.70			

Table 1 Analysis of oil componet

Stability of emulsion Stability of emulsion is foremost in viscosity reduction. In this work, The smaller the diversion ratio is, the more stable the emulsion is, which is in favor of viscosity reduction by emulsification. As shown in Fig 1, the diversion rate (η) decreases as the concentration of viscosity breaker increase, which means the emulsion are getting more stable. When the mass

concentration soars to 0.2%, the diversion rate reduces greatly but declines slightly as the concentration keeps increasing. The above analysis indicates that the viscosity reducer can provide good emulsification performance to heavy oil.

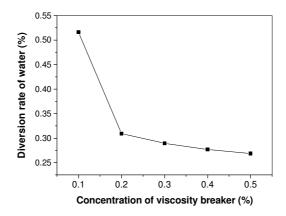
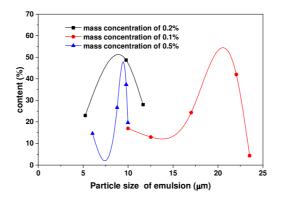
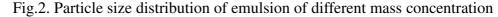


Fig.1. Effect of mass concentration of viscosity breaker on diversion ratio

Particle size distribution of emulsion To further illustrate the stability of emulsion, dynamic light scattering method was used to test the particle size distribution of emulsion produced by heavy oil and viscosity breaker at concentration of 0.1%, 0.2%, 0.5%. As shown in Fig 2, the particle size of water-in-oil emulsion reducer range from 5µm to 50µm with average grain diameters of 18.8µm, 10.3μ m, 9.6μ m. The size distribution of concentration of 0.5% and 0.2%, with narrow peak width and uniform grain size, is comparatively concentrated, so the emulsion is stable. But that with concentration of 0.1% ranges widely and the emulsion system is relatively unstable. Thus the size distribution also demonstrates the viscosity breaker has good emulsifying performance to heavy oil.





Interfacial tension If combined system containing surfactant can bring down the interfacial tension between oil and water to ultra-low (10^{-3}mN/m) , high oil recovery rate can be gain, so whether the interfacial tension can reach the ultra-low is an important criterion in screening system [7,8]. For chemical viscosity reduction, lowering the interfacial tension is good for the stability of emulsion. The dynamic interfacial tension between viscosity breaker with the mass concentration of 0.2% and the heavy oil is shown in Fig 3. The ITF decreases and gets stable gradually over time, and the balanced ITF is 2.5×10^{-2} mN/m. When the emulsifying viscosity reducer is added into heavy oil, absorbed film with certain strength is formed at the oil-water interfaces to protect the dispersive liquid drop from coalescence because of Brownian motion. If the viscosity reducer is not enough, the interfacial film is weak, which will cause the combination of liquid drop and weaken the stability of the emulsion. When adequate viscosity reducer is mixed into the heavy oil, it will

compactly arranges in the surface to not only strengthen the intension of surface film but also lower the interfacial tension, therefore, the liquid drop is not prone to combine.

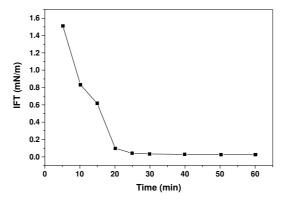


Fig.3 Dynamic interfacial tension

Viscosity reduction rate Viscosity reduction rate is the primary index in evaluating the performance of the viscosity reducer. The viscosity reduction rate of viscosity breaker with the mass concentration of 0.2% at 50°C is shown in Table 2. The viscosity reduction rate increases with the decline of the oil-water ratio. This is because the new viscosity breaker is the water soluble system, and low oil-water ratio makes it easier to form oil in water type emulsion and lower the viscosity of heavy oil.

Table 2 Viscosity reduction rate

Oil-water ratio	7:3	6:4	5:5
Viscosity reduction rate (%)	85.5%	90.3%	92.1%

Detergent factor of oil First, oil content and the water content of the oil sands in Jilin oilfield were measured. The measuring method is the standard method of *Dean-Stark* toluene extraction recommended by Alberta Oil Sands Technology Research Administration (AOSTRA) in Canada [9], and the same experiment of testing the detergent factor of oil sand was repeated 3 times according to above method. The results are shown in table 3. The viscosity reducer performs well in washing the heavy oil. Meanwhile, although the interfacial tension is not ultra-low (10^{-3} mN/m) , it does not affect its oilwashing effect, which shows that there is no specific corresponding relation between the interfacial tension and detergent factor.

14010 0	The measuring results	or on sands in thin childre
Oil content (%)	Water content (%)	Detergent factor of oil (%)
9.54	2.97	61.06

Table 3 The measuring results of oil sands in Jilin oilfield

Conclusions

1. The heavy oil in Jilin oilfield is rich in wax which will crystallize and separate out at low temperature to make the oil present high viscosity, but is poor in colloid and asphaltene that are the naturally crystallization inhibitor of wax.

2. The diversion rate of water in emulsion is small, and the emulsion stability is good. The particle size distribution of the emulsion is relatively uniform which represents the good stability of emulsion. This new viscosity reducer can lower the IFT to some degree, which is helpful for keeping the stability of emulsion.

3. The detergent factor of oil of the new viscosity reducer is relatively high, presenting high capability of elution. The viscosity reducer can provide high viscosity reduction rate which increases as the decline of the oil-water ratio.

Acknowledgement

This work was sponsored by the Department of Education of Heilongjiang Province (12521046).

References:

- [1] Brook, G. and A. Kantzas. Evaluation of Non-Thermal Eor Techniques for Heavy Oil Production. In Annual Technical Meeting. 1998. Calgary, Alberta: Petroleum Society of Canada.
- [2] Mai, A., J.Bryan, N. Goodarzi, and A. Kantzas, (2009). Insights into Non-Thermal Recovery of Heavy Oil.(3): p. 27-35.
- [3] Mc. C., Gifford. Method of Transporting Viscous Hydrocarbons[P].US,1979.
- [4] Wu B. F., Guo J. B. Technology of Emulsification Viscosity Reduction of Crude Oil [J]. Journal of Luo Yang Normal Institute,2002(5).
- [5] Li G. Z., Mou J. H., Sui H.. Study of Dynamic Interfacial Tension and Adsorption Dynamics of Surfactant Solution (to be continued) [J]. China Surfactant Detergent & Cosmetics.1999(4).
- [6] Brice, B.W. and G. Renouf. Increasing Oil Recovery from Heavy Oil Waterfloods. In International Thermal Operations and Heavy Oil Symposium. 2008. Calgary, Alberta, Canada: 2008, SPE/PS/CHOA International Thermal Operations and Heavy Oil Symposium.
- [7] Lin M. Q., Li M. Y., Wu Z. L.. Experimental Study of Interfacial Tension Between HABS Solution and Crude Oil [J]. Journal of Petroleum University:Natural Science Edition, 2002,26(5):55~57.
- [8] Hou J. R., Liu Z. C., Yue X. A. et al. The Adaptive Limits Analysis of ASP FLooding with Little Alkali [J]. Journal of Petroleum University: Natural Science Edition, 2003,27(3):46~49.
- [9] Hepler L G, His C.AOSTRA. Technical Manual of Oil Sand, Asphalt and Heavy Oil [M]. Dong Ying: Petroleum University Press, 1992:1~12/34~35.

The photocurrent characteristic analysis of the copper phthalocyanine organic thin film transistor irradiated by 700 nm monochromatic light

Yue Zhang^a, Dongxing Wang, Jiabin Chen, Yue Shan, Jinghua Yin, Hong Zhao

College of Applied Science, Key Laboratory of Engineering Dielectrics and Its Application, Ministry of Education, Harbin University of Science and Technology, 150080, Harbin, China

^a776703122@qq.com

Keywords: CuPc; Thin film transistor; Organic semiconductor; Photoelectric properties

Abstract. By using organic semiconductor CuPc as photosensitive materials, we prepared an organic thin film transistor with the vertical structure consisted of metal Cu/ organic semiconductor CuPc/ Al/ organic semiconductor CuPc/ indium tin oxide ITO. CuPc semiconductor material has good photosensitive properties in the 700 nm light. When the light signal irradiates organic semiconductor photosensitive material, the electron-hole exciton is separated into photocurrent in built-in electric field produced by organic semiconductor material/ metal schottky contact. It transforms into the driving current of organic photoelectric triode. By using its current amplification effect, the output current increase obviously. The test result shows that the I-V characteristics of the transistor are obvious unsaturated triode characteristics. When using 700 nm light to irradiate the device, the working current of the device increases obviously.

Introduction

Since the advent of semiconductor device, microelectronics technology occupies a quite important position in the new technology industry. At present, inorganic lithography has close to the natural limit of device miniaturization. Because of the smaller components, the thinner conductor, therefore, the resistance will be bigger, and the heating effect will be more and more obvious, which limit the performance of the integrated block.

Organic electronic material is a new type of electronic material. Organic electronic material not only has the semiconductor optical and electrical properties, but also keeps some of the good qualities of organic matter[1,2,3,4], such as the rich variety, easy processing and so on. Due to the advantages, such as its low cost, light quality, folding bending and it can be used to make large area components, so it obtains the widespread attention [5,6,7,8]. Organic electronic materials can be used to manufacture the organic photoelectric sensor, organic electroluminescent display, organic solar cells, organic field-effect transistor and so on [9,10,11].

In this paper we study the vertical structure of metal Cu/organic semiconductor CuPc/ Al / CuPc/ indium tin oxide ITO organic photoelectric triode. Through the design of the device structure and organic photoconductive function layer, when the light signal irradiates to organic semiconductor photosensitive material layer, the electron-hole exciton is separated into photocurrent in built-in electric field produced by organic semiconductor materials/metal schottky contact. It transforms into the drive current of organic photoelectric triode. By using its current amplification effect, the output current increase obviously.

Experiment

Device Preparation. The device is composed of Cu/ CuPc/ Al/ CuPc/ ITO five layers thin films. It was made by using OLED multi-functional coating system prepared by Shen Keyi. CuPc thin film

layer is prepared through the traditional vacuum evaporation method with a purity of 99.9% CuPc powder. Evaporation temperature is controlled at 350°C. The preparation of the base electrode Al and the collector electrode Cu both use dc magnetron sputtering. We use RF magnetron sputtering to prepare the emitter electrode ITO. The production order is as follows. First of all, we prepare collector electrode indium tin oxide ITO in the glass substrate, and then the first layer CuPc, then base electrode Al thin film and the second layer CuPc evaporation film, and finally the emitter electrode Cu thin film. CuPc evaporation temperature is 350°C and substrate temperature is 20°C. The thickness of two layers CuPc thin film up and down is controlled by evaporation time, and the evaporation rate is about 3 nm/ min. The thickness of two layer CuPc thin film is about 130 nm and 70 nm, respectively. The thickness of base electrode Al thin film is about 20 nm.

The Photosensitive Properties Measurement of the Organic Photoelectric Triode. In the air environment, we use semiconductor characteristic analyzer Keithley-4200scs to test I-V characteristics of CuPc thin film transistor. Then place the device into the sample room located in the light exit of the LP-130 Xe type adjustable wavelength light source. Make 700 nm monochromatic light irradiate the device from the ITO side. Open the wavelength tunable monochromatic light source and semiconductor testing system, and then test photosensitive output I-V characteristic curve of the organic photoelectric transistor.

Results and Discussion

Photosensitive Properties of the Copper Phthalocyanine Thin Film Transistor. The determination conditions of the device for dc operating characteristics is to make the base bias voltage V_b increase from 0 V to 1 V, 0.25 V in step and emitter-collector bias voltage V_{ec} from 0 V to 3 V, 0.25 V in step. We measure change relationship of emitter-collector current I_{ec} and emitter-collector voltage V_{ec} in dark and in 700 nm light, respectively. The I-V characteristics curve is shown in Fig. 1.

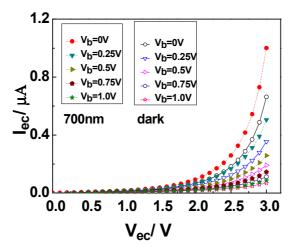


Fig. 1 The I-V characteristic curve of the device under the condition of dark and 700 nm light

From Fig. 1 we can see that I-V characteristics curve is obviously unsaturated. When V_b is a constant value, I_{ec} increases with the increasing of the V_{ec} . While V_{ec} is constant, I_{ec} decreases with the increasing of V_b . In the constant base voltage, the output current I_{ec} in 700 nm wavelength light increases dramatically, which proves that the device is sensitive for 700 nm light. But in 700 nm light, the increasing of the V_b will still control the change of the output current I_{ec} , and reduce the output current I_{ec} . When $V_b=0$ V, $V_{ec}=3$ V, under the dark condition, $I_{ec}=0.66 \mu$ A. However, it is 1.0 μ A in 700 nm light. The output current is amplified about 1.51 times.

The Analysis of Amplification Mechanism of Photosensitive Output Current of Copper Phthalocyanine Thin Film Transistor. When the light irradiates the CuPc through the ITO thin film, carriers in CuPc absorb the light energy and generate electron-hole exciton. Then exciton spreads and separates into free carriers, which lead to the increasing of carrier density in the CuPc thin film. Such there are two different current I_{ec} curves for 700 nm light and dark with the same V_b .

For the current transport mechanism, the thermionic electron emission theory is considered to go on the analysis. According to the thermionic electron emission theory, there exits following relationship between the current I and bias V:

$$I = I_0 \left[\exp(\frac{qV}{nKT}) - 1 \right]$$
(1)

$$I_0 = \mathrm{SA}^* T^2 \exp(\frac{-\mathrm{q}\varphi_{\mathrm{b}}}{KT})$$
(2)

 I_0 is the reverse saturation current. n is the ideal factor. S is the headwater area. A* is valid Richardson constant. φ_b is barrier height. Positive qV >> nKT, so formula (1) can be written as:

$$I = I_0 \exp(\frac{qV}{nKT})$$
(3)

Take the natural logarithm of the formula above:

$$\ln I = \ln I_0 + \frac{q}{nKT}V \tag{4}$$

Fig. 2 shows Ln (I)-V characteristics relationship and linear fitting curve of the device in the

dark state. We can obtain $\ln I_{0 (dark)} = -20.45$, $\frac{q}{nKT} = 2.0413$. Fig. 3 shows Ln (I)-V characteristics relation and linear fitting curve of the device in the 700nm light state. We can obtain $\ln I_{0(700nm)} = -20.02$, $\frac{q}{nKT} = 1.9871$. Transform formula (2), and we can obtain:

$$\varphi_{\rm b} = KT \frac{\ln(SA^*T^2) - \ln I_0}{q} \tag{5}$$

Among them, $A^* = 28 \text{ A/ K}^2 \text{ *cm}^2$, KT = 0.026 eV, $S = 2\text{mm}^2$. Take $\ln I_0 \text{ (dark)}$ value, $\ln I_0 \text{ (700 nm)}$ value into the formula (5) respectively, and we can get $\phi_b \text{ (dark)} = 0.81 \text{ eV}$, $\phi_b \text{ (700nm)} = 0.80 \text{ eV}$. We can see that compared with the dark state, CuPc/A1 schottky barrier height has decreased 10meV when the device is under the condition of 700 nm light.

Conclusion

Based on CuPc organic semiconductor materials, we prepared an organic thin film transistor with Cu/ CuPc/ Al/ CuPc/ ITO in vertical structure. The test result shows that the I-V characteristics of transistor are obvious unsaturated characteristics. Phthalocyanine copper semiconductor material has good photosensitive characteristic. When using 700 nm light to irradiate the device, the working current of the device increases obviously. We use Ln (I)-V curve and the fitting results, which demarcate CuPc/ Al schottky barrier height and know that the barrier height of the device is $\varphi_b = 0.81$ eV in dark condition, while $\varphi_b = 0.80$ eV in 700 nm light. The barrier height decreased 10 meV by light. Because of lower hole injection barrier, the photosensitive output current increases. The experimental result shows that device we prepared can realize amplifier output of photosensitive current and it could be used for photoelectric sensors, such as images or fingerprint identification and so on.

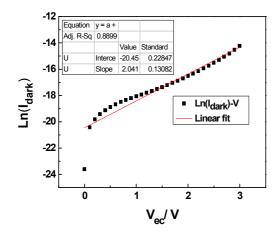


Fig. 2 When $V_b = 0$ V, Ln (I)-V characteristics relation and linear fitting curve in dark

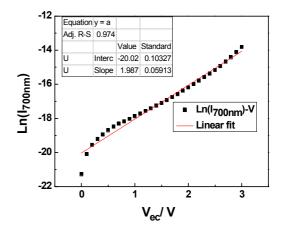


Fig. 3When $V_b = 0$ V, Ln (I)-V characteristics relation and linear fitting curve in 700nm light

References

- C. Schuster, M. Kraus, A. Opitz, W. Brutting, and U. Eckern: Eur. Phys. Vol. 180 (2010), p. 117–134,
- [2] K. Fujimoto, T. Hiroi, K. Kudo, and M. Nakamura: Adv. Mater. Vol. 19 (2007), p. 525–530
- [3] Z. Y. Ji, L.W. Shang, C.Y. Lu, L.Wang, J. W. Guo, H. Wang, D. M. Li, M. Liu: IEEE ELECTRON DEVICE LETTERS. Vol. 33 (2012), p. 1619~1621.
- [4] X. J.Wang, Z. H. Huang, Z. M. Su, R. S. Wang: Chemical Journal of Chinese Universities. Vol. 18 (1997), p. 1847-1850
- [5] J. M. Tang, W. M. Shi, L. J. Wang, W. J. Zhou, W. Q. Zhu, Y.B. Xia: Journal of Shanghai University. Vol.16 (2010), p. 38-41
- [6] J. Z. Sun, M. Wang and C. Zhou: Chemical Journal of Chinese Universities. Vol.22 (2001), p. 498-505
- [7] X. Dai, F. S. Liu, K. Li and Y. M. Sun: Chemical Industry Times. Vol. 18 (2004), p. 5-8
- [8] K. N. N. Unni, Remi .D. Bettignies, Sylvie Dabos-Seignon: Applied Physics Letters. Vol. 85 (2004), p. 1823-1824
- [9] G. H. Gelinck, H. E. A. Huitema, E. V. Veenendaal, E. Cantatore and L. Schrijnemakers: Nature Mater. Vol. 3 (2004), p. 106-110
- [10]E.J. Meijer, D.M. Deleeuw, S. Setayesh, E. Van Veenendaal and B.H. Huisman: Nature Mater. Vol. 2 (2003), p. 678-82
- [11] Y. Bai, D. H. Fan, W.Xu, Y. Wang: Journal of Wuyi University. Vol. 24 (2010), p. 19-23

CHAPTER 12:

Engineering Management and Logistics

Order batching picking based on activity based classification storage

Lin Guo^{1, a}, Xiaojun Yang²

¹ The Department of Computer and EEE, Oxbridge College Kunming University of Science and Technology, Kunming, China

² Kunming Shipbuilding Equipment Co.Ltd, Kunming, China

^aguolin0114@163.com

Keywords: picking strategy, distribution center, order batching, activity based classification

Abstract. Warehouse shelves were quantified and partitioned based on activity based classification storage. In the warehouse, order batching method based on activity based classification storage was adept to batch orders. After finished batching, goods mainly concentrated on A, B and C area. Traversal strategy, return strategy, midpoint strategy and largest gap strategy was compared with each other according to the orders belong to different areas. Mid-point strategy and traversal strategy would make picking easy and efficient on the basis of order bathing result.

Introduction

Distribution center is an important part of logistics supply chain. The order picking planning in distribution center directly affects the performance and further affects the operational efficiency of the whole supply chain. Oder picking is the most labor-intensive activity and its workload account for about 60% of the entire workload [1]. In terms of cost, order picking cost is 9 times stacking, handling and transportation cost, and is the great majority of logistics handling cost [2]. It is very important to cost reduction and customer satisfaction improvement that improve picking efficiency. The influence factors of picking method, picking route and so on. Picking efficiency can be improved by optimizing main operation strategies such as order batching, route strategies, storage strategies and so on [3]. This paper optimizes location distribution method, order assignment principle and picking strategy to improve picking efficiency.

Organization of the Text

Storage strategy is that how to assign location to storage unit. A well strategy can make travel distance of picking short and decrease time. The main strategies are shown as follows.

A. Random storage. This strategy is to assign an available random location to each goods in storage area according to the only assignment basis that goods location is available. It is the simplest strategy which comes with a big price that is picking travel time increasing. Thus, it is rarely used in real environment.

B. Fixed storage. Each goods which needs to be stored has a fixed location and cannot use other goods location. For the minimum travel distance, goods with high outbound frequency and small volume are usually placed in the location near exit and entrance. The original form of location storage is based on COL (Cub-per-Order-Index) storage strategy. The COL means that the ratio of the total storage space which some goods storage requires in some time and the goods turnover rate. The goods with a minimum COL value are placed in the location near exit and entrance, and then the goods with second-minimum COL value and so on. But in some environment, because of quick goods classification, it is difficult to get a lot of accurate information to build statistical data, which brings about wrong location assignments.

C. Classified storage. In stock control, the classic classification method is based on Pareto method, which is to consider goods of which shipments accounts for 85% of total shipments and stock class accounts for 15% of total stock class as the same class which is the focus of management.

In classification storage, there are several goods classifications according to some standards. Each classification goods have a fixed storage area, but in the area, each location is distributed to each goods randomly. Based on commerce (EIQ analysis) and logistics (stock turnover rate), salable and high stock turnover rate goods are classified as A classification, inversely, unsalable and low stock turnover rate are C classification and goods between A and C are B classification. It is called activity based classification storage that divides storage area according to activity based classification.

Activity based classification storage is an analysis and comparison result of stock goods. The enterprises base proportion of each classification goods on their sales policy and stock management strategy. Usually, A classification goods account for 15% to 20% of total goods classifications, B classification goods account for 30% to 40% and 60% to 70% for C classification goods. Activity based classification of goods is changing with market and sales policy. Activity based classification, of which generality, good usability and optimization is better than random storage and location storage, can be a basis to divide warehouse space in logistics center. Considering convenience of picking and shipments, A classification storage area accounts for 20% of total storage area, B accounts for 30% and C for 50%, which is shown in Fig.1.

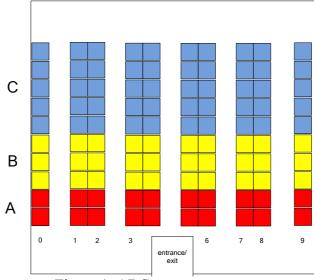


Figure 1 ABC storage area

Order batching strategy based on ABC storage area

In traditional picking, First come first service (FCFS) is a common way to handle order. It will waste a lot of manpower and material and make the average travel distance long. For the sake of picking efficiency improvement, merge several orders into one batch, which purpose is that shorten the average travel distance and time. Pickers or picking equipment can handle several orders in the same time to improve picking efficiency. It is batch picking that pick after calculate total amount of same goods in each batch, and then the goods picked are distributed to each order in the batch again when picking finished, which not only shortens average travel distance but also avoids picker looking for the same location repeatedly, bringing about picking efficiency improvement. Batch picking is more effective to the orders with little item number but large goods number. During order batching, for the different order rules and applied conditions, to batch order, the first thing need to do is that get the right way according to the real situation [4]. This paper batches orders according to location distribution based on activity based classification. There is T-classification order and M-classification order. T stands for travel and M stands for midpoint. The batch rule is shown as fellows.

1. Get all the orders

2. Analyze the proportion which all required goods in each order account for in ABC storage area.

1) If the goods in the order account for more than 60% of both A and B area, the order is M-classification order.

2) If the goods in the order account for more than 60% of C area, the order is M-classification order.

- 3) Except for 1) and 2), others is T-classification order.
- 3. All order classifications are finished.

After classification finished, picking can be implemented with some strategies to reduce picking travel distance.

Comparison and analysis on picking strategy

Petersen proposed 5 algorithms [5] including traversal strategy, return strategy, midpoint strategy, largest gap strategy and composite strategy. Traversal strategy, return strategy and midpoint strategy are easier to implement than largest gap strategy and composite strategy.

1. Traversal strategy

The route of traversal strategy is simple, easy to perform and especially appropriate for high picking density situation, thus many warehouses choose it. Pickers get in the roadway from one end, picking the goods on shelves on both side of the roadway and leaving from the other end of the roadway. Before leaving, pickers will travel all roadways where there are goods need to pick. Because of the "S" shape of travel route, it is also called "S" strategy. The travel route is shown in Fig.2.

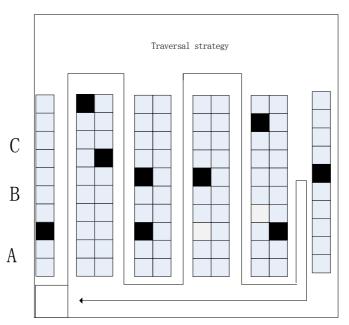


Figure 2 Traversal strategy

Traversal strategy is appropriate for scattered pickings in warehouse and has a shorter picking route than return strategy and midpoint strategy. In storage area based on activity based classification, if orders belong to T-classification, it means that picking operation scatter in A, B and C area uniformly. Traversal strategy is the one to improve picking efficiency.

2. Return strategy

In return strategy, if there are goods to be picked in shelves, pickers get in the roadway, picking the goods on the shelves on both side of roadway and leaving from the other end of roadway. The roadway where there is no goods to be picked should be skipped over.

3. Midpoint strategy

Midpoint strategy divides the picking area into front and back part from midpoint of the roadway. Pickers get in the roadway from one end, picking and returning and the farthest point is the roadway midpoint. After pickers finish picking goods in front part of picking area, they should get in the back part. When they finish picking in back part, they should return to the nearest entrance or exit and picking process is over. It not only has all the advantages that belong to return strategy but also is the improvement of it and always better than it. Midpoint strategy is shown in Fig.3.

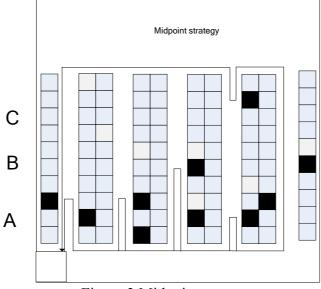


Figure 3 Midpoint strategy

It is especially appropriate for the pickings with most pickings concentrating in front part or back part of storage area and is better than traversal strategy. In storage area based on activity based classification, if order batching belongs to M-classification, it means that pickings concentrate in front or back part of the storage area, and midpoint strategy gets a shorter travel route.

Conclusion

This paper analyzed and optimized storage strategy, order batching and picking strategy. Based on quantifying and partitioning storage area in distribution center by using activity based classification storage, classify the orders into T-classification and M-classification combining with order batching strategy and storage area traits. Use traversal strategy and midpoint strategy to pick goods in order to get a shorter route when pick a batch of orders.

References

[1] Rene de Koster, Edo van der Poort : IIE Transaetions, J. 30(1998), 468-480.

[2] Chen Hui-juan, The operating system of logistics center [M].Taipei: Institute of Mechanical Industry of Industrial Technology Research Institute publishing,1997. In Chinese

[3] Caron F, Marchet G, Perego A: INT.J.PROD.RES, J. 36(1998) 713-732.

[4] Gademann, A. J. R. N., VandenBe, B, J. P. and Van der Hoff, H.H.: IIE Transactions, J. 33(2001) 385-398.

[5] Petersen,e.G. : International Journal of Operations & Production Management, J. 17(1997) 1098-1111

Analysis of financial agglomeration effect on corporate financing behavior

Fei-fei Li^a, Jie-yu Huang

Economy and Management Department, Yuncheng College, Yuncheng 044000, China ^a511935220@qq.com

Key words: financial agglomeration; financing cost

Abstract: Financial agglomeration is the transfer and concentration of financial resources in space, this transfer and concentration can make the zone enterprises obtain financing at lower cost, particularly financial agglomeration can reduce the enterprise financing cost, time cost, and unstable financial risk cost; then this paper uses the listing Corporation and the various provinces and cities in 2011 which issued A shares of the financial as the sample data, starting from the financial agglomeration effect on the enterprises' financing behavior as the point of empirical analysis, the results show that: the financial agglomeration degree and the enterprise financing cost is negatively related, namely the financial agglomeration reduces the financing cost.

Introduction

In the area of financial industry, starting from the 70 's of the last century, more and more financial institutions began with coordinated ways to organize transactions between enterprises and production activities,today, the cluster has become the basic form of the modern financial industry organizations. Financial industry cluster can be defined as a high concentration in a geographical of financial institutions, financial companies, financial intermediaries, financial regulators and multinational financial institutions , through market and non-market linkages, formation of industry groups compete with each other, mutual cooperation. Since 1974 Kindle Berger study after the financial center, a growing number of scholars began to study the financial gathering, and to further study the impact of financial concentration on the real economy. While,financial concentration has what impact on enterprise's financing behavior ? Currently, the study of this issue basically has not dabbled in at home and abroad, mainly focused on financial accumulation associated with this impact on the regional economy.

The literature review

In the foreign country, King and Levine[1] by using cross-country data for empirical analysis concluded that financial development can contribute to economic growth. Rajan and Zingales[2] from the microscopic point of view shows the financial development can contribute to economic growth. Arestis and Demetriades[3] by study found that financial development has an impact on economic growth, but this effect has different manifestations in different countries; At present,the research on this issue in China are mainly as follows:Liu June, Huang Jieyu [4] shows that through the effect of financial agglomeration and financial diffusion,the financial accumulation can promote the growth of the real economy. Liu [5] identified by studies that financial accumulation can make the core area access much higher growth rates, and financial concentration have effects on the region's economy. Yang Qi [6] in theory deals with the mechanism of financial industry cluster affecting regional economic development, But none of these documents further study the impact of financial concentration on the enterprise's financing behavior.

Based on the above literature, at present, the research on the effect of financial agglomeration to enterprise' financing acts are also almost no, and the research related to this problem are mainly the financial agglomeration' effect on regional economic growth .Overall, these literature has guidance significance to solve this problem, but these research general lack an empirical data to do

support. Therefore, based on the predecessors'research,first,i will make a theory analysis between financial agglomeration and enterprise financing. And then i will make an empirical test of the financial agglomeration's effect on enterprise financing, and, accordingly, draw appropriate conclusions.

Theoretical analysis of financial agglomeration effect on corporate finance

Traditional financial industry distribution in the past and the future still plays an important part to promote domestic economic development. However ,throughout economic power, their financial industry has experienced or is experiencing financial agglomeration process to form powerful financial center, in order to play the support role of the finance on economic development through market competition mechanism. Through market this only "intangible of hand" ,different financial institutions for financial resources of leveling reached optimization integration, providing facilitate for enterprise in maximum degree, and reducing its long plagued enterprise of financial region can establish the geographical affinity easily, allowing enterprises to give full play to its geographical advantages, strengthen their communication between financial units and financial supervision, promote financial district can reduce the cost of risk which is produced by enterprises to cope with financial instability. Generally speaking, the security operations are along with the economic security of the financial system ,and the increase and spread of the instability of financial system will affect the normal development of the real economy, even on their serious wounds.

Therefore, based on the analysis we can propose the hypotheses: financial concentration levels affect enterprise funding costs, namely the financial gathering more, lower the cost of financing.

Empirical test of the financial agglomeration effect

Based on the theory analysis, this article will study on the relationship between financial agglomeration and financing costs.

The variable design:

(1) explanatory variable-----financing costs

Financing costs are all the costs of the enterprises in the process of financing, such as interest paid to banks and dividends paid to shareholders.

Financing costs include the cost of equity financing and debt financing . Equity financing can be divided into ordinary shares and preferred shares , Because China has not issued preferred stock, therefore here consider only ordinary shares. Debt financing consists mainly of corporate bonds and bank loans.

(1) equity financing costs

Equity financing costs can be calculated from the capital asset pricing model as Eq.1:

$$R_E = R_F + \beta (R_M - R_F) \tag{1}$$

Among them, R_F is the risk-free rate, R_M is the market risk on average, β is the systemic risk factor of the enterprise, specially the larger the coefficient, it indicates that the enterprise have the greater system risk.

The determined of the risk-free rate: under current conditions in China's stock market, actually, there is no uniform standard about the choice of risk-free rate.

Taking into account the perspective of listed companies, we can use the internal rate of the longest term bond listed in Shanghai Stock Exchange as the standard.

Determination of average market yields on risk: determined by the 1-3 years of the people's bank loan interest rates

Determination of β : yield on stock returns relative to the stock market.

(2) debt financing costs

Debt financing costs can be depressed as Eq.2:

$$D = D_1 + D_2 + LD \tag{2}$$

Among them, D is total debt financing costs, D_1 is short-term borrowings, D_2 is long-term borrowings within one year, LD is total long-term liabilities.

Debt financing costs are calculated as Eq.3:

Debt financing costs R_D = Interest expense/cost of debt financing (3)

(3) the total financing costs

Total costs for listed companies is the weighted average cost of debt financing and equity financing as Eq.4:

$$R_{W} = \frac{E}{V} \times R_{E} + \frac{D}{V} \times R_{D} \times (1 - T)$$
(4)

 R_W represents the weighted average cost of capital enterprises, E_{∞} D respectively represents the common shares and market value of corporate bonds .V is the total market value of enterprises. R_E_{∞} R_D are on behalf of common shareholders and debt financing required yield, T is the corporate income tax rate.

(2) the explanatory variables

Most literature about financial agglomeration at home and abroad used the location quotient as agglomeration factors, this article also draws on the location quotient analysis mode.

Various provincial and municipal finance location quotient can be expressed as Eq.5:

a province's location quotient (Q) =
$$\frac{the \ province's \ total \ loans \ of \ financial \ institutions/total \ loans \ of \ all \ financial \ institutions/total \ loans \ of \ all \ financial \ institutions/total \ loans \ of \ all \ financial \ institutions/total \ loans \ of \ all \ financial \ institutions/total \ loans \ of \ all \ financial \ institutions/total \ loans \ of \ all \ financial \ institutions/total \ loans \ of \ all \ financial \ institutions/total \ loans \ of \ all \ financial \ institutions/total \ loans \ of \ all \ financial \ institutions/total \ loans \ of \ all \ financial \ institutions/total \ loans \ of \ all \ financial \ institutions/total \ loans \ of \ all \ financial \ institutions/total \ loans \ of \ all \ financial \ institutions/total \ all \ al$$

(5)

(3) control variables

Based on the research results, this article selects the asset-liability ratio (leverge), company size (size), operational risks (VOE), asset turnover (turnover), return on assets (ROA), ownership concentration (OC), company growth (grow), fixed assets ratio (fixass) as well as the type of industry (industry) as the control variables in the analysis.

All of the variables in this article covered are shown in the Table.1:

1403	· · · · · · · · · · · · · · · · · · ·
variable names	variable definitions
cost of equity financing	$R_E = R_F + \beta (R_M - R_F)$
debt financing cost	$R_D = \frac{\text{int} erest \exp ense}{average \ total \ debt}$
total finance costs	$R_{W} = \frac{E}{V} \times R_{E} + \frac{D}{V} \times R_{D} \times (1 - T)$
leverage	Total liabilities divided by total assets
financial agglomeration degree	A province's location quotient
size	Logarithm of total assets
voe	Net profit divided by the standard deviation of net profit
turnover	Operating income divided by average assets
roa	Net profit divided by average total assets
oc	Total equity divided by the number of shares held by board of directors, senior management
grow	The growth rate of company main business income over the previous year
fixass	Book value of fixed assets divided by total assets
industry	Accordance with the "national industry classification and code"

Determination of average market yields on risk: use the people's Bank of 1-3-year lending interest rate 6.15%.

Treasury bill rate: 5.41%

Study sample:

Study sample data in this article come from Taian, China Statistical Yearbook, state database, annual reports of listed companies, covering 31 provinces, autonomous regions and municipalities across the country, selecting the financial date of listed companies which have issued A shares as sample.

(1)Because listed financial companies's accounting methods are different from ordinary companies, and also there is a big difference on the financial characteristics, as well as this article is mainly studying on the relationship between financial agglomeration and non-financial enterprises ' financing activities, so we must exclude the date of listed financial companies.

(2)As in the calculation of companies risk it need to use the standard deviation of the net profit, so it requires at least three years of date, that is date 2009,2010,2011, if the company listed in 2009 and beyond, there will be lake of date, so we should weed out the date of company listed in 2009 and beyond.

(3)Taking into the availability of each variable, we should weed out incomplete data samples.

After the screening according to the standard, there are 1074 listed companies to meet the requirements and large sample requirements are met.

Empirical analysis:

(1)variable descriptive statistics as Table.2:

Tab.2Variable descriptive statistics

	mean	median	Standard deviation	maximum	min
Re	9.121	9.133	0.900	11.816	-5.964
Rd	6.213	4.273	4.334	19.975	4.451
Rw	7.775	7.294	2.528	16.041	-2.892
leverage	0.545	0.553	0.184	0.996	0.048
Q	1.118	0.997	0.427	2.090	0.121
size	22.276	22.112	1.259	28.282	19.666
voe	0.384	0.305	0.324	2.449	0.014
turnover	0.755	0.617	0.602	7.518	0.011
roa	0.039	0.033	0.064	0.864	-0.300
oc	0.066	3.481	0.224	2.909	0.000
grow	15.104	16.560	0.443	25.786	-0.7351
fixass	0.255	0.220	0.187	0.971	0.000

Firstly, this paper made a descriptive statistics about the various relevant variables, it can be seen from the table:

(1)most relevant variables are largely stable, the mean and median are roughly equal.

(2) the mean of the debt financing costs is6.213317, but its fluctuation is severe, and the maximum is 19.97495, the minimum is 4.451, all of these show that the level of debt financing cost of China's listed companies is vary greatly.

(3) the standard deviation of the total cost of financing is 2.528478, the volatility is also large, which is mainly due to the the instability of the debt financing.

(2)Regression analysis

This paper introduces the various relevant control variables, and then establishes a regression model to study the financial agglomeration's effect on the financing costs, it can be shown as Eq.6:

$$RW = \alpha_0 + \alpha_1 Q + \alpha_2 leverge + \alpha_3 size + \alpha_4 voe + \alpha_5 turnover + \alpha_6 roa + \alpha_7 oc + \alpha_8 grow + \alpha_9 fixass + \alpha_{10}H_1 + \dots + \alpha_{20}H_{11} + \varepsilon$$
(6)

Among them, α_0 is a constant term, α_i (*i* = 1,2...) are the regression coefficients of the model, ε is the error term.

	rab.5 (a) Regression results													
va	riable	le Constant term		Constant term Q		Q	b	eta		size	le	v	tu	r
coet	fficient 25.311		25.311	-3.227	1.	589	-().934	-4.7	70	0.0	94		
	+	8.301 -		-1.438	438 5.9		-6.82		2 -11.549		0.85	3		
t		(0.000)		(0.044)	(0.000)		(0	(000)	(0.000)		(0.39	4)		
R-so	R-squared=0.366 Adjusted-squared=0.352 F-statistic=27.474													
	Tab.3 (b)Regression results													
i			1	•										
variable roa gr		grow		fixas	S	0	c	V	<i>loe</i>					

0.081

0.206

(0.036)

-0.094

-0.330

(0.077)

0.291

1.364

(0.172)

0.001

3.588

(0.000)

Regression results are shown as Table.3 (1), (2):

Tab.3 (a) Regression results

Note: figures in brackets is the P-value

-0.142

-0.127

(0.099)

coefficient

t

Analysis:It can be seen from the table that all the variables are basically adopted t-test,the explanatory variable's t-test is 0.044,and it is adopted on 5% level of significance test,and the coefficient is -1.438.It is indicated that financial agglomeration and total cost of corporate fiance have a negative correlation,that is,the higher the degree of financial agglomeration ,the lower the cost of corporate financing, and financial agglomeration reduces the company's financing costs.

Conclusion

This article first makes a theoretical analysis of the relations between the financial agglomeration and corporate financing cost, and it shows that the financial agglomeration can improve the efficiency of financial service and reduce financing costs. Then the article draw the conclusion: the higher of the financial agglomeration degree, the lower the cost of corporate finance. This shows that financial agglomeration is able to promote domestic financing environment and have a profound impact on corporate financing behavior.

Acknowledgements

This paper is supported by study plan of Humanities and social sciences in Ministry of Education foundation(No.12YJA790050).

References

- [1] King R G, Levine R. Finance and Growth: Schumpeter Might Be Right[J]. Quarterly Journal of Economics, 1993,108(3):717-737.
- [2] Rajan R G, Zingales L. Financial Dependence and Growth[J]. The American Economic Review, 1998,88(3):559-586.
- [3] Arestis P, Demetriades P. Financial Development and Economic Growth: Assessing the Evidence[J]. The Economic Journal, 1997,107(442):783-799.
- [4] Liu jun, Huang Jie yu. The mechanism of financial agglomeration's effect on the real economy[J]. Management Word, 2007(4):152-153.
- [5] Liu.Financial agglomeration on regional economic growth and Radiation Research [J]. Shanghai Finance, 2008 (6) :14-19.
- [6] Young Kor. The financial agglomeration's impact on the economic development in the Yangtze River Delta[J].Zhejiang Academic Journal,2009(6):184-188.

Research on Seasonal Index Based on Dynamic Clustering of the Daily Railway Passenger Flow Title

WEI Zhengzheng^{1, a}, WANG Fuzhang^{1,b}

¹Institute of Computing Technologies, China Academy of Railway Science, Beijing 100081, China ^aninna.weina@163.com, ^bwfzh@rails.cn.

Keywords: Seasonal index, Passenger flow forecast, Dynamic time warping distance, Clustering.

Abstract. The railway passenger flow is greatly impacted by different months and weeks of the season, and the impact is periodic. Accurate evaluation of the seasonal index for predicting the railway passenger flow is of key importance. Based on this background, the paper proposes an algorithm for calculating the seasonal index which is impacted by both months and weeks. The railway passenger flow between different OD(Origination Destination) is affected by months and weeks quite different. Therefore the paper focuses on the method for effective calculation of the month index and week index on the basis of time series clustering. When adopting hierarchical cluster, general Euclidean distance and its expansion used as a similarity metric is widely applied in time series comparison, however, this distance measurement is not robust enough for the processed data. Dynamic time warping is a pattern matching algorithm based on nonlinear dynamic programming technique. It is applied to calculate month and week index to get seasonal index that defined in this paper, which has good application value for predicting the passenger flow.

Introduction

Passenger flow seasonal index is various and complicated between OD(Origination Destination). Reference [1] takes seasonal index as the season that has significant different of observed value compared to other seasons. In reference [2], it studied a method calculating seasonal index based on months and four seasons. For reference [3], week index has been researched on for calculation seasonal index. These papers have one common flaw. They only take one aspect into consideration for calculating the seasonal index. For railway commercial operation, the passenger flow is affected by various factors. Based on this fact, the paper defines the seasonal index: Economic phenomena that has significant different characteristic in the time domain during a certain period of time compared to other observed period. This paper also proposed a method for calculating seasonal index by taking both week and month into consideration and adopting similar time sequence to eliminate random factor that affect seasonal index calculated results. Dynamic time warping is introduced when sequential clustering OD daily passenger flow, which enhances the robust against amplitude difference, noises and linear drift.

1. Time sequence pre-process

Time sequence pre-process is a method for eliminating the noise data in the time sequence. The noise data can be the random error data or the offset data that get from the measurement. When process the data of passenger flow statistic, this noise are mainly generated by the following two reasons: .

- a. The hardware for collecting data is in false state which causes the statistical passenger flow is much lower than the real one.
- b. Outburst passenger flow around holidays causes the statistical passenger flow is much higher than the average one.

These kinds of data are considered as abnormal data or outlier. If these data is not appropriately processed, the calculated seasonal, weekly index will not be accurate. Thus, identify the abnormal data, replace it with valid passenger flow distribution is the precondition for calculating the seasonal index accurately. In the research of identifying isolate point in time sequence, there are methods

based on likelihood ratio[5], based on statistic[6] and based on wavelet transformation[7]. This paper compare the number in the sequence to evaluate whether or not it is a outlier.

 \overline{X}_{t}^{2} presents smoothing X_{t} and then calculating its square value. \overline{X}_{t}^{2} presents calculating the square value of X_{t} and then smooth it. $S_{t}^{2} = \overline{X}_{t}^{2} - \overline{X}_{t}^{2}$ presents variance of sample points, S_{t} presents the standard deviation. If the Eq. 1 is set up.

$$X_{t} - kS_{t} < X_{t+1} < X_{t} + kS_{t}$$
(1).

 X_{t+1} can be considered as normal, or it will be considered as a outlier. Normally, The number of k is a integer between 3 and 9, it can be valued as 6.

If X_{t+1} is a outlier, it can be replaced based on the other data in the same month, which is the passenger average flow and median number of the month.

2. Dynamic time warping

Set two time sequence as Q and C, the length of them are n and m as Eq. 2 shows: .

$$Q = q_1, q_2, ..., q_n$$

$$C = c_1, c_2, ..., c_m$$
(2)

In order to synchronize time sequences, define a matrix with different distance.

Define 1: A matrix with n rows and m columns. The element in the matrix is Euclidean distance between different time sequences, namely $D_{-}matrix$ is the Euclidean distance.

$$D_{matrix} = \begin{pmatrix} d(q_{1}, c_{m}) & d(q_{2}, c_{m}) \dots & d(q_{n}, c_{m}) \\ \vdots & \ddots & \vdots \\ d(q_{1}, c_{1}) & \cdots & d(q_{n}, c_{1}) \end{pmatrix}$$
(3)

In the matrix of Eq. 3, $d(q_i, c_j)$ is the distance between two time sequences of the data, which can be seen as the quantization of element q and element c differences. When the element q and c are similar, the value of d is kin to 0; the less the same of element q and c, the bigger is value d. This is the basis of clustering algorithm.

Define 2: In two different distance matrix of time sequence, define the continuous collection of matrix element which present the time sequence differences as warping path.

$$W = w_1, w_2, \dots, w_k \dots w_K \tag{4}$$

 $w_1 = D_{matrix(q_i,c_i)}$ and $w_k = D_{matrix(q_n,c_m)}$ are the starting and ending elements at warping path in Eq. 4. They are also at the diagonal ends in the matrix. Fig. 1 shows the distance based on dynamic time warping value: Dynamic time warping schematic plot

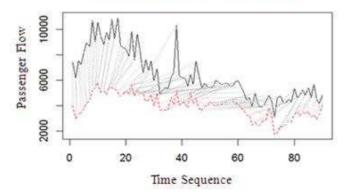


Figure 1 Dynamic time warping schematic plot

Matrix analysis shows that there are multiple solution for warping path. However, we care about the one with the least warping path value. Tow data similar to each other most (with the least distance value) are set as the basis of similarity search:

$$DTW(Q,C) = \min(\frac{1}{K}\sum_{k=1}^{k} w_k)$$
(5)

In Eq. 5, K is a parameter for drawing out unified standard when comparing the distance in different paths. To solve the Eq. 5, dynamic plan is taken into consideration.

$$S_{1,1} = d(q_1, c_1);$$

$$S = d(q_i, c_j) + \min\{S(i-1, j); S(i-1, j-1); S(i, j-1)\}$$
(6)
(7)

By using recursive search as shows in Eq. 6 and Eq. 7, the partial optimized value between two points is found out, the warping path has also been found out.

3. Seasonal Index

Clustering is a process that classifies dataset into several groups or clusters. The data in the same cluster are similar to each other while the data in different cluster has low similarity. The key to clustering is to classify the data that similar to each other together for future calculation. Reference [8] and [9] discuss in detail the method of clustering in data mining. When calculating the distance of two clustering, there are three options:

- a. Single connected method. Chose the nearest distance of the two clustering as the final distance.
- b. Complete connected method. Chose the farthest distance of the two clustering as the final distance.
- c. Average connected method. Calculate the average distance of the two clustering as the final distance.

The paper adopts hierarchical clustering by using the dynamic time warping distance method to get similar matrix. and calculates monthly index and monthly index in each OD. Set monthly index as S_{MONTH} and weekly index as S_{WEEK} . The integrated effects of these two factors can be displayed as Eq. 8.

$$S_{SEASON} = S_{MONTH} \times S_{WEEK}$$

In it, S_{WEEK} can be calculated by Eq. 9:

$$S_{WEEKi} = \frac{\overline{\sum SS}_{WEEKi}}{\overline{\sum SS}_{WEEK}}$$
(9)

i = 1,2,3..7. $\sum SS_{WEEKi}$ means the average passenger flow in one week during a period of time of a classified clustering OD time sequence. means the overall average passenger flow during this period of time. Monthly index S_{MONTH} can be derived using the same method as shows in Eq. 10.

$$S_{MONTHj} = \frac{\sum SS_{MONTHj}}{\sum SS_{MONTH}}$$
(10)

j = 1,2,3...12. As the weekly index, 12 months is applied to get the monthly index which can be used to get the daily seasonal index.

4. Simulation and analyses

To model this algorithm, the processed data is chosen from the passenger flow of Jin Hu dedicate passenger line, from July 1st of year 2011 to July 1st of year 2013 with seven ODs, set as A, B, C, D, E, F and G. Firstly, analyze the distribution of each OD and detect the outliers, and replace them with estimated value. Then, process time sequence in each OD by using hierarchical clustering. Dynamic time warping distance and Euclidean distance are introduced to calculate the similarity between time sequences as well as comparing the differences. Using average connecting method to calculate the distance whose diagram displayed in Figure 2. It shows that this method superior to Euclidean method.

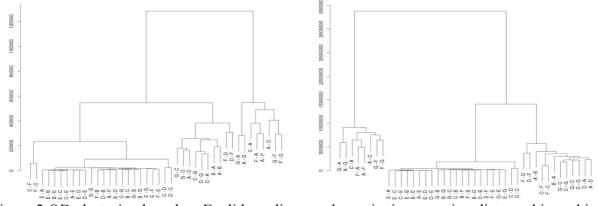


Figure 2 OD clustering based on Euclidean distance dynamic time warping distance hierarchical clustering

It can be inferred from Fig. 2 that some of the OD clustering results using these two methods are the same while others are different. Analyze the different ones to determine which method surpasses the other one. Take OD"C-F", "F-C", "E-A", "B-A" for example, in dynamic time warping distance hierarchical clustering, "C-F", "F-C", "B-A" are the close one. In Euclidean hierarchical clustering, "C-F", "F-C", "B-A" are the shows the passenger flow between ODs from July 2011 to February 2012.

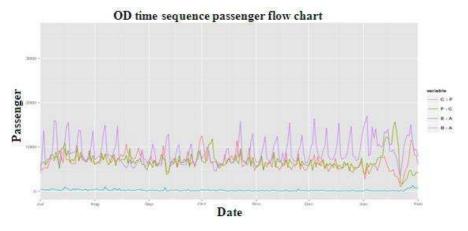


Figure 3 OD time sequence passenger flow chart

Fig. 3 and Fig. 4 show that classify "C-F", "F-C", "B-A" as a similar group is more appropriate than "C-F", "F-C", "E-A". The OD that clustered by dynamic time warping distance as similar matrix of hierarchical clustering is better than that of Euclidean distance. When determine the clustering number, take dynamic time warping distance, the red line passes through three clustering while the blue line passes through five.

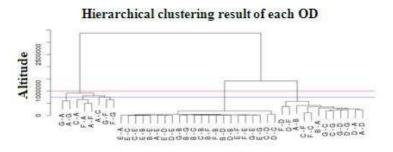


Figure 4 Hierarchical clustering result of each OD

Analyzing the clustering get from the blue line to calculate "A-C", "G-F", "F-G" seasonal index. Fig. 5 shows the passenger flow of these three ODs in two years. It also shows the passenger flow of these three ODs and weekly average value. Weekly index can be derived by dividing weekly average passenger flow by daily passenger flow. The same procedure can be applied to monthly index. Then, seasonal index can be calculated by multiplying monthly index vector and weekly index vector.

> 1	Fri Mon Sat Sun Thu Tue Wed G - F 618743 486023 476902 470575 501511 475473 488772 F - G 649946 422982 435387 586247 504188 441685 488866 A - C 647944 468893 475432 507165 516364 469604 490967 weeke Mon Tue Wed Thu Fri Sat Sun
0.9	9041996 0.9187665 0.9729896 1.0084070 1.2577265 0.9106456 1.0263143
> monthe	
Jan Fel	o Mar Apr May Jun Jul Aug Sep Oct Nov
0.8659223 0.7743122	2 0.9658223 0.9545369 0.9545369 0.9971024 1.1571065 1.1973988 0.8968698 0.9859486 0.9343394
Dec	
0.9238548	
	Mon Tue Wed Thu Fri Sat Sun
	Jan 0.7829666 0.7955804 0.8425334 0.8732021 1.0890934 0.7885484 0.8887085
	Feb 0.7001328 0.7114121 0.7533977 0.7808218 0.9738729 0.7051240 0.7946877
	Mar 0.8732962 0.8873652 0.9397351 0.9739419 1.2147403 0.8795219 0.9912373
	Apr 0.8630919 0.8769965 0.9287545 0.9625617 1.2005464 0.8692449 0.9796549 May 0.8630919 0.8769965 0.9287545 0.9625617 1.2005464 0.8692449 0.9796549
	Tup 0.9015796 0.9161043 0.9701703 1.0054850 1.2540821 0.9080070 1.0233405
	Jul 1.0462553 1.0631107 1.1258526 1.1668343 1.4553235 1.0536740 1.1875550
	Aug 1.0826875 1.1001299 1.1650566 1.2074653 1.5060002 1.0904060 1.2289075
	Sep 0.8109493 0.8240139 0.8726450 0.9044098 1.1280169 0.8167306 0.9204703
	Oct 0.8914944 0.9058566 0.9593178 0.9942375 1.2400537 0.8978498 1.0118932
	Nov 0.8448293 0.8584397 0.9091025 0.9421943 1.1751434 0.8508521 0.9589259
	Dec 0.8353492 0.8488069 0.8989012 0.9316217 1.1619567 0.8413044 0.9481655
	Figure 5 Passenger flow of ODs

Figure 5 Passenger flow of ODs

Conclusions

This paper proposes a new method for calculating seasonal index that affect passenger flow: taking both week and month into consideration. When pre-process data of each OD, dynamic time warping is introduced to calculate similar time sequence. General Euclidean distance and its expansion used as a similarity metric is widely applied in time series comparison. It shows that dynamic time warping performs well when calculating similar time sequence of passenger flow of each OD. Based on this fact, the paper proposed a method for calculating seasonal index by taking both week and month into consideration. Calculation shows that this method is of key guiding significance for railway passenger prediction.

References

- [1] Philidep, Hanse Francis. Translated by Feng Jianqiang. Time sequence model in business and economical prediction. [M]. Beijing. China Renmin University Press. 2002.12
- [2] Chang Linxing. Research on railway passenger flow based on seasonal index. Railway transportation and ecomomic. 2006.7
- [3] Pan Xiaowei. Multiple regression and time series analysis in application of passenger flow prediction in the expo. Economic research
- [4] Weng Yingjun, Zhu Zhongying. Time-series data clustering algorithm based on dynamic time warping. computer simulation. 2004.3
- [5] Lv Qingji. Two kinds of time series comparison of outlier mining method. Journal of statistics, 2005.1.
- [6] Feng Hongwei. The research and application of data mining technology. Ph.D. Dissertation, northwestern polytechnical university. 2004.7.
- [7] Wang Jianzhou, Yang Yong. Outlier data identification and mining based on the statistical distribution of the wavelet analysis of time series. Journal of northwest normal university (natural science edition). 2004.2.
- [8] He Lin, Wu Lingda, Cai Yinchao. Clustering algorithm in data mining. Computer application research. 2007. Volumn 1.
- [9] R O Duda, P E Hart, D G Stork. Pattern Classification(2nd Edition) [M].New York:Wiley,2001.

Evolving Model Research of Layered Agri-food Supply Chains Weighted Complex Networks

LI Yang^{1, a}, Du Ziping^{2, b}, Zhang Liang^{2, c}

¹ College of Economics and Management, Food Safety Strategy and Management Research Center, Tianjin University of Science and Technology, Tianjin dagunanlu 1038, China

² College of Economics and Management, Tianjin University of Science and Technology, Tianjin dagunanlu 1038, China

^aerlee@tust.edu.cn, ^bduziping@tust.edu.cn, ^czhangliang@tust.edu.cn

Keywords: agri-food supply chain network; evolving model; complex network.

Abstract. In this paper, we analyzed the characteristics of the agri-food supply chain network, described the reasons of the network hierarchy generated. Based on the analysis we proposed a layered agri-food supply chains weighted complex network model. This model possess topological characteristics of the real network, and effectively depicted the mechanism of formation and evolution of the agri-food supply chain network. This has important practical and theoretical significance for the rational design of agri-food supply chain network.

Introduction

With the liberalization of trade in agri-food products, in-depth development of globalization, and the trends of agri-food industry conversion from supply chain to supply chain network has become increasingly evident, the agribusiness management from agricultural products to consumers has become increasingly complex. How to establish an effective supply chain from agricultural producers to consumers has become the focus of government, business and academia.

Food supply chain management has proven to be a very effective method to improving the performance and optimization all the processes of the supply chain network [1]. Supply chains involve complex webs of interactions among suppliers, manufacturers, distributors, third-party logistics providers, retailers, and customers [2]. Because of the complex net configuration of the agri-food supply chain, the disturbance events of supply chain steady state occur frequently in the field of the food supply chain. How to analyze, evaluate, monitor, control and improve the agri-food supply chain network risk (FSCNM) is gaining more and more attention. In recent years, more and more researchers began to focus on the supply chain network modeling of complex networks. Jin-Li Guo proposed that the supply chain networks bilateral power-law distributions model and calculate the degree distributions and stationary average degree distributions of the network model [3]. GREGORY's study suggests, Globalization has increased the complexity of the supply chain network, And that the complexity of the supply chain network depends on the adaptability of its structure [4]. BALAN S developed a dynamic model of a supply chain network based on Multiple Attribute Decision Making for supply chain network risk assessment consists of five layers of suppliers, manufacturers, distribution, retailers and multinational consumer [5]. However, as a network system the study of agri-food supply chain network are still some knowledge gaps. Most researches focused on in the methods of the qualitative research of the supply chain system complexity, but it is not enough that to research the real-world complex networks rely solely on the topological characteristics of nodes and edges formed.

The supply chain complexity depends on the suitability of network structure, to explain the behavior of evolving complex supply chain network dynamic, non- deterministic methods must be selected. In this paper, based on complex network, we analyzed of the statistical distribution of agri-food supply chain network nodes in the evolution of behavior exhibited.

Agri-food Supply Chain Network

Food supply chains are distinct from other product supply chains [6]. Agri-food supply chain is a network of food-related business enterprises from production to consumption, including pre-production and post-consumption activities, its numerous links are cause of the massive growth of agri-food supply chain information. As a result of the complexity of agri-food supply chain network, the difficulty of Supply chain management is also increasing. Furthermore, agri-food supply chain network information has strong timeliness, circulation of agricultural products information acquisition is not timely, and the defective information exchange, caused agri-food supply chain network became more vulnerable.

Compared with industrial manufactured products, agricultural growth cycle is longer, and the production has a certain seasonality, different seasons suitable for planting different varieties of agricultural products. The quality of food products is decreasing with time, even with the utilization of the most advanced facilities and conditions [7], the continuous and significant change in the quality of food products throughout the entire supply chain until the points of final consumption that make agri-food supply chain has more market risk. Van der Vorst et al. [8] supposed an extend this to an FSN(Fig. 1), referring to an interconnected system with a large variety of complex relationships such as alliances, horizontal and vertical cooperation, forward and backward integration in supply chains.

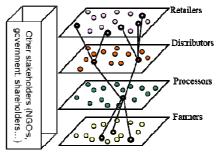


Fig 1. Schematic Diagram of a Food Supply Chain Network (Van der Vorst et al., 2005).

Model of Agri-food Supply Chains Networks

In the agri-food supply chain network structure different types of businesses constitute the network of different organizational structures, reflects the hierarchy of the network (Fig. 1). Because of the time a great impact on the quality of agricultural products, every node in the agri-food supply chain network are very seriously to the timeliness requirements, and special control measures are required in the whole process of production and distribution. For this reason circulation of agricultural products has stronger asset specificity than industrial products circulation, entering or leaving agri-food supply chain network has the larger resistance. In the agri-food supply network, supplier have proprietary sales channels and distributors have the proprietary supply, the partnership based on the mutual trust mechanism and the same product standards. The presence of competition between companies in the same layer, and cooperation between the other enterprises upstream and downstream. Therefor we assume that links between the nodes occurs only between the layers.

In the design of evolutionary mechanism of the supply chain, most researches constructed undirected and unweighted network, there is relatively few research considered the weight and the direction. But agri-food supply chain network is a scale-free network this means that there are a few nodes that have very many edges, whereas most of the nodes have very few. Those nodes have very many edges are the core enterprise of agri-food supply chain network, obviously it has more significance for the supply chain. Connection between the member companies in the agri-food supply chain network is multifaceted. To establish a network model should consider not only whether the connection between the nodes, but also the number, property and strength of the connection. The connection strength has the decisive significance for the network structure, while the agri-food supply chain network the trading volume among member companies precisely reflects the importance of the connection. Trading volume reflects the status of enterprises in the supply chain network, the greater the trading volume, the more important status. For this reason, we established a layered agri-food supply chains weighted network model.

Agri-food supply chain network is described by a set G = (V, W), where $V = \{v_1, v_2, \dots, v_N\}$ is the set of nodes expressed the enterprises involved in the agri-food supply chain network. These node is divide into four classification, include the suppliers, the manufacturers, the distributors and the retailers. $W = \{w_{11}, w_{12}, \dots, w_{ij}\}$ is the set of weighted edges, represent of the various relationships among various enterprises, where w_{ij} is the edge weight from enterprise *i* to enterprise *j* (trading volume). Considering the reciprocity of transaction, we assumed that the agri-food supply chain network is undirected network.

Evolutionary rules of the Layered Agri-food Supply Chains Weighted Complex Networks model presents in this paper described follow:

(1) Initial: network G is a BA complex network, composed by m_0 nodes, w_0 is the initial weight value between nodes.

(2) Increase: Each interval the number of new nodes obey Poisson process with parameters of λ . Each node has a layer properties I ($I \in (0,4]$), links between the nodes occurs only between the adjacent layers, eI is used to distinguish the layer new node belongs to. Where is the probability of new nodes belonging to different layer, its value reference to the existing supply chain data (Reference to a mid-size Italian supermarket food supply chain[9] and the U.S. military adopted UltraLog plan to get the logistics network[3]). Connecting probability as fallow:

$$\prod_{i} (k_{i}, d_{in}, \boldsymbol{\alpha}, \boldsymbol{\beta}) = \frac{k_{i}^{\boldsymbol{\alpha}} d_{in}^{-\boldsymbol{\beta}}}{\sum_{j} k_{i}^{\boldsymbol{\alpha}} d_{jn}^{-\boldsymbol{\beta}}}$$
(1)

(3) Evolution of the weight value: Each new node with $m(m \le m_0)$ edges connected to different nodes in the network that already exists, W_0 is initial weight of the new edge. If the edge already exists between the new node and the old node, then W_t the weight of the edge already exists: $W_t = W_{t-1} + W_0$.

(4) Termination: The number of nodes in the network to achieve the desired N.

Numerical simulation analysis

Set the initial network constituent by 10 nodes, $m_0 = 10$ including 3 supplier nodes, 2 manufacturer nodes, 1 distributor nodes and 4 retailer nodes. Network simulation set N is the number of time intervals, where $N = 500 \sim 2000$. Set initial weight $w_0 \in (0,1)$. In order to eliminate the influence of random factors during simulation generated, each simulation is carried out 10 times, and the results were averaged.

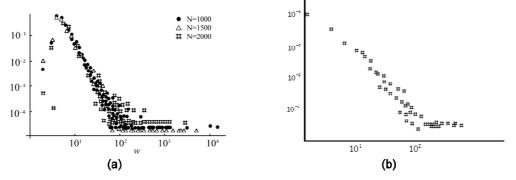


Fig2. Weights probability distributions (a) and degree distribution (b)

The degree distribution statistics of nodes in the network, the results are shown in Figure 2(a), network nodes degree distribution follows a power-law distribution of basic, the network characteristic exhibited "scale-free " feature. The statistics of network edge weights probability distributions, the results are shown in Figure 2(b), from the experimental results can be seen, weights obey a power law distribution of basic and more consistent weight distribution.

Conclusions

The main aim of this paper is to model agri-food supply chain network and analyze their behaviors based on complex network theory. In this paper, we analyzed the characteristics of the agri-food supply chain, in the agri-food supply chain network different types of businesses constitute the network of different organizational structures, reflects the hierarchy of the network. Because of agri-food supply chain network is a scale-free network, the core enterprise in agri-food supply chain network are the nodes have very many edges, it is more significance to the supply chain. Based on the analysis we proposed a layered agri-food supply chains weighted complex network model. This model possess topological characteristics of the real network, and effectively depicted the mechanism of formation and evolution of the agri-food supply chain network. This has important practical and theoretical significance for the rational design of agri-food supply chain network.

Acknowledgment

The authors would like to thank peer reviewers for commenting this article. This work is supported by the Tianjin Science and Technology Development Strategy Research Program (Grant No.13ZLZLZF) and Humanities and Social Sciences Projects of Tianjin universities and colleges (Grant No.20132155).

References

- [1] Li Hong. Chinese food supply chain risk and critical control point's analysis [J]. Jiangsu Agricultural Sciences, 2012, 40(5): 262-64.
- [2] Thadakamaila, H. P., et al. "Survivability of multiagent-based supply networks: a topological perspect." Intelligent Systems, IEEE 19.5 (2004): 24-31.
- [3] Jin-Li Guo. "The bilateral power-law distribution model of supply chain networks." (2006): 3916-3921.
- [4] Sun, Huijun, and Jianjun Wu. "Scale-free characteristics of supply chain distribution networks." Modern physics letters B 19.17 (2005): 841-848.
- [5] Balan S, Vrat P, Kumar P. Risk analysis in global supply chain network environments[J]. European Journal of Operational Research, 2006, 174(3): 1353-1367.
- [6] Yu, Min, and Anna Nagurney. "Competitive food supply chain networks with application to fresh produce." European Journal of Operational Research (2012).
- [7] Zhang, Guimei, Walter Habenicht, and Walter Ernst Ludwig Spieß. "Improving the structure of deep frozen and chilled food chain with tabu search procedure." Journal of Food Engineering 60.1 (2003): 67-79.
- [8] Van der Vorst, J. G. A. J., 2000. Effective food supply chains: Generating, modelling and evaluating supply chain scenarios. Ph.D. thesis, Wageningen University, The Netherlands.
- [9] Pietro Vecchiato, Maurizio Faccio, Emilio Ferrari, Alessandro Persona. "Apply lean distribution principles to food logistics" Proceedings of the 1st International Workshop on Food Supply Chain (2011):71-90.

Affective Identification Motivation Mechanism of Sino-Japanese Bi-Cultural Teleworking Teams

Bin He^a, Siying Li^b, Hong Zheng^c, Changzhi Ma^d, Xing Tang^e Management School, Guangdong University of Technology, Guangzhou, Guangdong, China,

510520

^arivergdut@163.com, ^b263412633@qq.com, ^c254081630@qq.com, ^d24710879@qq.com, ^e337980045@qq.com

Key words: affective identification motivation, motivation mechanism, cross-cultural management, experiment research

Abstract. Under the background of economic globalization and cross-cultural management, this paper proposes hypothesis and model of affective identification motivation mechanism in Sino-Japanese bi-cultural teleworking (BCT) teams, based on ample resources of literature and system rational analysis thinking. This paper firstly studies the working process of Sino-Japanese BCT teams by management experimental methods. And then the experiment data and proposed hypothesis are analyzed and verified statically. Finally, a conclusion is obtained that in Sino-Japanese BCT teams, team's affective support, work attitude identification, cultural affective identification can enhance team identification, moderated by team members' perception level.

Introduction

As a form of cross-cultural teleworking team, bi-cultural teleworking team (shorted for BCT team) has the advantage of bi-cultural resources, remote technical resources and virtual organization[1]. However, to some extent, potential cross-cultural conflicts, remote communication difficulties, organizational slack and the problem of mixed information keep hinder BCT team from developing. Faced with numerous challenges, in order to create greater team effectiveness, the problem of how to carry out effective incentives to the members of BCT team has become an important research content that cannot be ignored.

Most of the Sino-Japanese BCT team's members are knowledge-based talent. They master professional knowledge, independent and have a strong sense of innovation, good communication skills and high achievement motivation[2]. In academia, the research on motivating knowledge talented persons gradually goes deeper from the material incentive level into the affective motivation level. In this perspective, Gan et al [3] put forward that implementing affective identification motivation can increase team identification and work engagement, and contribute to team performance. With different cultural background and means of communication, will affective identification motivation continue to play a role in Sino-Japanese BCT teams? By utilizing the methods of questionnaire survey and managerial experiment, this paper will explore the positive impact of affective identification motivation on team identification, which then enhance team performance in Sino-Japanese BCT teams.

The analysis and hypothesis

From affective identification motivation to team identification

In dictionary, identification is regarded as the process of naturalization of emotion, attitude and cognition[4]. Affective identification means man's emotional acceptance about things perceived. To implement affective identification on teams, it's needed to enhance the acceptance and affiliation to the team from members by some emotional encouragement measures, which help improve members' engagement and team performance. Meanwhile, when team members regard themselves as a part of the team, and view team's aim, benefit and norms as their own characteristics, they form the strong feelings of team-belongings, which is generally call team identification. Therefore, affective

identification motivation should be adopted to improve the team performance through team identification.

In the study of organization identification, Bao(2006) concluded that, organization image, organization atmosphere, assignment and culture characteristic can have an impact on organization identification. While organization encompasses the form of team, so the factor of organization, working and culture can have a significant impact on team identification. Ashforth(1992) and Morgan(2004) point out that, it can facilitate the team member's sense of identification when the members are given appropriate team's affective support. Concern, trust and timely communication from team leaders to team members will help satisfy the emotional demand of members, which lead to the formation of team identification atmosphere and increment of team-belonging in the practical working process. Iver(2002) suggested that, the commitment to the work attitude may also contribute to the increment of members' team identification. When members with good attitude are given identification. For the aim of this paper, hypotheses are put forward as follows:

H1 : Team's affective support has positive function on Sino-Japanese BCT team member team identification.

H2 : Work attitude identification has positive function on Sino-Japanese BCT team member team identification.

Schrodt(2002) also argued that, respect and identification to team members' cultural background and practices can result in a rise on the team identification. China and Japan have had profound cultural ties and upheld Confucian culture for long time in history. In terms of teamwork culture, Chinese value harmony most, while Japanese attach importance to the culture of family and connect the family with team strongly. On the whole, the Chinese teamwork culture shed light on emotion, meanwhile Japanese pay more attention on loyalty. As the team member of the Sino-Japanese BCT teams coming from different culture background, clashed is easy to burst. It is of great importance for the two side to attach mutual respect and identification before team working. Cultural affective identification is an important part when affective identification motivation are implemented into Sino-Japanese BCT teams. Therefore, a hypothesis is raised as follows:

H3 : Cultural affective identification has positive function on Sino-Japanese BCT team member team identification.

Adjustment of perception level of members

In Sino-Japanese team, members from China and Japanese have different comprehension and acceptance on the same system. Gundlach and Zivnuska (2006) pointed out that members' individual characteristic of sense have a great effect on team identification. Hofstede's study[5] has analyzed the difference between Chinese and Japanese on the perceptive of five culture dimension. Firstly China and Japan are collectivism country, while Chinese values consanguinity and Japan pay attention on loyalty. On the power ascription, Chinese believe power belongs to person, just like they regard official rank is the sole criterion, whereas the power is publicly owned in the eyes of Japanese in the background of Seniority-based Wage System. Chinese appear to be in the exclusive culture and Japanese to be compatible culture on uncertain circumvention. Japanese has more attention on the value of male chauvinism then Chinese. Consequently, the difference of perception level result in different perception level on team implementation of affective identification motivation between Chinese and Japanese members, which may have significant effect on the function of affective identification motivation on team identification. The Sino-Japanese BCT team members' perception level of the affective identification motivation is an important regulated variable. Therefore, a hypothesis is raised as follows:

H4: Team members' perception level has regulating effect on the function of affective identification motivation on Sino-Japanese BCT team identification.

The mediator effect of team identification

Gundlach and Zivnuska(2006) suggested that, team performance is the outcome variable of team identification.

Based on the analysis before, team's affective support, work attitude identification, cultural affective identification have an effect on team identification under the regulation effect by perception level of team members, which will lead to an effect on team performance. Based on this affective identification motivation pattern, a hypothesis is raised as follows:

H5: Team's affective support, work attitude identification and cultural affective identification have an effect on team performance through team identification thoroughly.

Based on the raised hypothesis above, the affective identification motivation model of Sino-Japanese BCT team is presented in Fig.1.

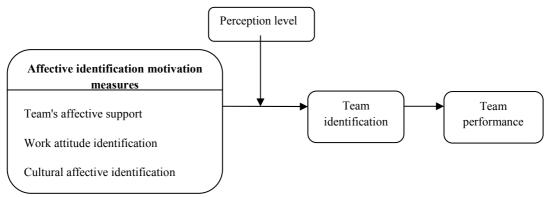


Fig.1: Affective identification motivation model of Sino-Japanese BCT team

Research method and results analysis

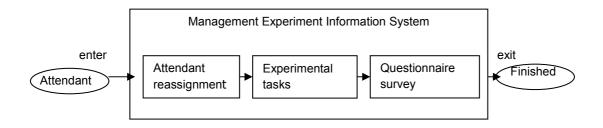
Research method

Research methods including questionnaire and management experiments[6] are adopted in this paper to study affective identification motivation of Sino-Japanese BCT teams.

592 attendants participated in the experiment and were reassigned into groups which were comprised of random proportions of Chinese and Japanese. All groups are divided into experimental group and control group. Each group had 4 members. All attendants complete tasks on the experimental information system, so as to simulate team members' communication and operation of Sino-Japanese BCT teams.

The experiment includes three parts: preliminary experiment, first-stage experiment and secondstage experiment. In preliminary experiment, experimenters check the managerial experiment information system and make sure the system's proper function can run well, and collect primary experiment data to improve experiment design. First-stage experiment and second-stage experiment converge at collecting data.

Experimental procedure includes three parts: attendant reassignment, experimental tasks and questionnaire survey, which is shown in Fig.2.



Research results analysis

Reliability of experimental data

592 attendants in 148 groups took part in the experiment. Data which doesn't meet experiment specification was weeded out, and 126 groups of data are available. SPSS was employed to analyze the data. The value of Cronbach α of experiment data is 0.806, and more than 0.8, which means the reliability of experimental data is acceptable.

The research of affective identification motivation of Sino-Japanese BCT teams is on team level. However, the subjects whom were measured in the experiment were team members, and it needs the individual data integrated up to the level of team to continue the analysis. The paper uses R_{WG} (Group internal consistency) to test the consistency of team members' reaction in each group for detecting consistency for each subject. It is considered that when R_{WG} more than 0.7 is qualified[7]. Table 1 shows that measurement data can reflect the consistency within group so that the data can be integrated from individual level to team level.

Variable	Affective identification motivation	Work attitude identification	Cultural affective identification	Perception level	Team performance		
R _{WG}	0.83	0.81	0.71	0.75	0.76		

Table 1: Average of variable R _w	/G
---	----

Relationship analysis between affective identification motivation and team identification

This paper uses the method of correlation analysis, regression analysis and variance analysis to analyze the data of experiment groups and control groups of Sino-Japanese BCT teams. Table 2 shows the results.

Table 2: Relationship analysis between affective identification motivation and team

identification

	Correlation	analysis	Regre	ssion anal	ysis		Variance	analysis	
Affective identification motivation	Correlation index	Sig.	F	Sig.	R ²	Equal variance	Т	Sig.	Mean differ- ence
Team's affective support	0.486**	0.000	148.155	0.000	0.235	yes	12.172	0.000	4.794
Work attitude identification	0.695**	0.000	171.567	0.000	0.263	yes	13.098	0.000	6.010
Cultural affective identification	0.843**	0.000	191.751	0.000	0.707	yes	13.847	0.000	6.625

note: ** significantly correlated(bilateral) in level 0.01

The data shows that team's affective support, work attitude identification and cultural affective identification have significantly correlated relationships with team identification. Besides, the mean difference between experiment groups and control groups are significant differences, which means team's affective support, work attitude identification and cultural affective identification have positive effects on team identification. Assumptions H1, H2, H3 are all verified.

Analysis of the effect of moderated variable

The paper assumes that the effect of affective identification motivation on Sino-Japanese BCT team identification will change due to team members' perception level. According to the study of moderated variable measurement[8,9], this paper uses multiple regression method to verify whether the team members' perception level is moderated variable. First we use team's affective support as independent variable, team identification as dependent variable to make regression analysis. Second we make regression analysis by using team's affective support and team members' perception level as independent variable, and team identification as dependent variable to make regression analysis.

Third we make regression analysis by using team's affective support, team members' perception level and product of team's affective support and team members' perception level as independent, and team identification as dependent variable. The methods to verify the moderating role of members' perception level in the relationship between work attitude identification, cultural affective identification and team identification are the same as above. If product of affective identification, the moderated variable works. If the difference of R^2 between the third step and other steps are significant, the moderated effects exist[8]. Table 3 shows the analysis results.

		i moderated variable
Independent variable × Moderated	Dependent variable	Difference of R ²
variable		
affective identification motivation × team	team identification	0.18**
members' perception level		
work attitude identification × team	team identification	0.23**
members' perception level		
cultural affective identification × team	team identification	0.12**
members' perception level		

Table 3: Interaction between affective identification motivation and moderated variable

note: ** significantly correlated(bilateral) in level 0.01

The results shows that the standardized regression coefficient of interactions between affective identification motivation and team members' perception level are significant in level 0.01, which means these interactions have significant effect on team identification. Team's affective support, work attitude identification and cultural affective identification can influence Sino-Japanese BCT teams' identification, which can be moderated by team members' perception level. Assumption H4 is verified.

Analysis of the effect of mediated variable

This paper uses multiple regression method to verify whether the team identification is mediated variable. First we use team's affective support as independent variable, team identification as dependent variable to make regression analysis. Second we use team identification as independent variable, team performance as dependent variable to make regression analysis. Third we use team's affective support as independent variable, team performance as dependent variable, team performance as dependent variable, team performance as dependent variable by controlling team identification to make regression analysis, which can tell whether the team identification is mediated variable. The methods to verify the mediating role of team identification in the relationship between work attitude identification, cultural affective identification and team performance are the same as above. Table 4 shows the analysis results.

	regression 1	regression 2	regression 3 (team performance)	
Independent variable	team	team	First	Second
	identification	performance		
team's affective	0.813*		0.634*	
support				
team identification		0.786^{*}		
team's affective				0.571*
support				
team identification				0.408*

Table 4: Results of the effect of mediated variable

note: * significantly correlated(bilateral) in level 0.05

The results of regression 1 and regression 2 shows that team's affective support has significant effect on team identification and team identification has significant effect on team performance. Regression 3 shows that although standardized regression coefficient between team's affective support and team performance are significant in level 0.05 while team identification was controlled, the effect has reduced, which means team identification is partial mediation between team's affective support and team performance of Sino-Japanese BCT team. Assumption H5 is not true. The effect of team's affective support, work attitude identification and cultural affective identification on team performance can be partial passed by team identification.

Conclusion

The main purpose of this study is to explore how affective identification motivation has an effect on team performance in Sino-Japanese BCT teams, which is moderated by members' perception level and mediated by team identification. The results show that team's affective support, work attitude identification, and cultural affective identification can have a significant impact on Sino-Japanese BCT team identification. The impact is moderated by the members' perception level. Different levels have different influence on the impact. Therefore, team leaders should pay attention to the effects of team's affective support, work attitude identification, and cultural affective identification on team identification in the team management, and take into account the ways and strength of team's affective support, the role of work attitude identification and members' cultural background when developing the encouraging measures for a team. At the same time, leaders should also notice that the difference of perception level and acceptance of members will lead the envisioned impact to other undesired direction. Leaders should care and trust members more, build a good communication access to members, praise and encourage their fine productivity, lead them to respect each other's culture. These are the ways to form a good atmosphere in the team. To further increase member's enthusiasm and satisfaction as well as enhance the ability of members and team performance, leaders should improve communication among members and promote the cultural integration of the two sides.

Acknowledgements

This work is supported partly by Humanities & Social Science Project from Chinese Ministry of Education (No.10YJA630054), National Natural Science Fund (No.70671029) and Natural Science Found of Guangdong Province (No.9151009001000054). We are also indebted to other members in our research group.

References

- [1] Jing Sun, In Chinese: Research on Bi-cultural Telework Team Management Experiment, Guangdong university of technology, 2010.
- [2] Qiusheng Liu, Ling Zhu, In Chinese: China Management Informationization, 12(3), 2009, pp:72-75.
- [3] Weiyu Gan, Xixiong Xu, Juan Yi, In Chinese: Industrial Engineering Journal, 14(4), 2011, pp:82-86.
- [4] Suiyu Fei, Panshi Zhang, In Chinese: Social Psychological Dictionaries, Hebei People's Publishing House, 1998.
- [5] Geert Hofstede, Gert Jan Hofstede, Cultures and Organizations: Software of the Mind (Second Edition), Renmin University of China Press, 2010, pp:43-294.
- [6] Bin He, Zeying Li, Xueli Wang, In Chinese: Management Experiments and Experimental Management Science, Tsinghua University Press, 2010, pp59-87.
- [7] James, L.R., Demaree, R.G., Wolf, G, Journal of Applied Psychhology, 78(2), 1993, pp:306-309.
- [8] Xiaoping Chen, Shuying XU, Jingli Fan, In Chinese: Empirical Methods in Organization and Management Research, Peking University Press, 2008, pp:316-324.
- [9] Baron, R.M., & Kenny, D.A, Journal of Personality and Social Psychology, 51, 1986.
- [10]Bin He, Zeying Li, In Chinese: International Journal of Information Technology and Decision Making, 7(3), 2008.
- [11]Bin He, Jing Sun and Hans Olav Omland(2009), Cross-cultural Teleworking Virtual Team and Its Management. The 5th International Symposium For Corporate Governance, Tianjin, China, 2009, pp:5-6.
- [12]Bin He, Jing Sun, LiLi Li, Baozhen Liu (2010), Management Mechanisms of BCT Teams: A Comparative Study between China and Norway, The International Conference on E-Product, E-Service and E-Entertainment (ICEEE2010), VOL 1, 2010.

1/f Fluctuation	17, 50
2-2 Mash	121
2-Tuple	267
3D HOG	331
3D Model	213
3D Printing	810
Σ - Δ Modulator	121

A

Absorption	846
Absorption Sensor	624
Accelerometer	522
Accuracy Rate	157
Achromatic Phase Matching	774
Action Recognition	331
Activity Based Classification	957
Ad Hoc Network	490
AD7742	589
Adaptive LMS	40
ADC	121
Adjacent Strong Edge Chromatic Number	474
ADS8364	653
Affective Identification Motivation	976
Aggregation Operator	267
Agri-Food Supply Chain Network	972
Al-5Ti-1C Master Alloy	871
Al Gate Electrode	830
Algorithm	743
Aliasing Problem	11
AlN Nanoparticle	855
Ambiguous Word	157
Amplifie	31
Amplifier	90
Analog Fault Diagnosis	3, 11
Analog Switches	594
Analysis of Energy Efficiency	769
Android	161, 227
ANSYS	842
Anti-Noise Property	786
Aqueous Solution	806
Area Estimation	94
ARM	17
Armored Mechanized Forces	724
Athermalization	295

ATLAS	903
Augmented Reality	196
Automatic Monitoring	501

B

Bacterial Foraging Optimization	668
Bacterial Foraging Optimization Algorithm	673
Ball Grid Array	137
Ballistic Missile	743
Bandgap Reference	66, 90
Barrier System	940
BDM	25
Behavior Recognition	542
Beidou(BD) Satellite Navigation and Orientation System	381
Bit Error Rate	444
Boosting Algorithm	258
Brain Computer Interface (BCI)	171
Breakdown Strength	814
Breakdown Voltage	683
BSNs	542

С

C-Means	344
Cable Insulation	653
Capacitance Measurement Method with Comparison	594
Capacitance Measurement Method with Reference	594
Carbon Content	887
Carrier Tracking	392
Cascade Fuzzy	555
Cascade Structure	121
CC2430	501
CCD Measurement System	598
CdSe	801, 806
CdSe/CdS	806
Center Window	157
Cepstrum	786
Channel Error	636
Channel Estimation	457
Chaotic Systems	327
Charge Transfer	801
Charge Transferring	879, 883
Charge Trap	899

СНР	668	Cross Beam	402
CHP Microgrid	673	Cross-Cultural Management	976
Cigarette Production	231	Cross-Platform	196
Classification Labels	153	Crypt-Analysis	372
Clock Optimization	315	CuPc	826, 830, 838,
Closed-Loop	526		951
Cloud Computing	218	Current Transformer	589
Cloud Storage	205	Curve Fitting	376
Cluster Analysis	344	Custom Instruction	94
Clustering	966	Cutting	818
Clustering Algorithm	494		
CMOS	66, 107	D	
Coal Mine Main-Fan	501	Data Mining (DM)	258, 641
Coal Mining Equipment	778	Data Pretreatment	530
Code Tracking	392	Data Process	192
Coded Structured Light	319, 348	Data Processing	647
Coherent Signal	386	Database	546
Collaborative Command	509	Davenport's Constant	255
Color	602	DC Electric Field	598
Color Correction	319	DCT	323
Combinatorial Techniques	275	Decay Charge	855
Common Neighbors Similarity	222	Decision Tree	701
Common Spatial Patterns (CSP)	171	Defect	304
Common-View	381	Deformable Parts	331
Community Discovery	222	Degaussing	579
Complex Network	972	Delay Feedback Control	463
Conception Model	754	Dempster-Shafer Evidence Theory	360
Conception System	754	Dendritic Growth	867
Conductivity	814	Detecting Device	602
Conductivity Measuring	628	Detection	663, 730
Conical Form	469	Device Performance	863
Context-Modeling	240	DFE-MMSE	444
Control Points	352	DFT	457
Control System	509	Differential Structure	903
Control Unit	58	Diffusion	327, 867
Conventional Weapons Proving	717	Digital Communications	398
Ground	0.40	Digital Filter	576
Converter Transformer	940	Digital Integrator	589
Cooperative Combat	505 725	Digital Zooming	315
Cooperative Jamming	735	Dioxide Titanium	914
Cooperative Penetration Attack Corona-Resistant	735 914	Distortion	116
Corrected Differential Evolution	914 422	Distribution Center	957
Correction Factor	422 444	Distribution Simulation	200
Correlation Deltection	133	DMD	364
	209	Domination	175
Cournot Equilibrium Sharing Coverage	103	Doppler Frequency	743
COVERAGE	103 74	Downlink	440
CPM Signal	417	Driver Transplant	227
CPU CPU	417 58	DSP	398, 653
	50		

DSP Builder	793
Duration Time	923
Dynamic Balanced Scorecard	249
Dynamic Characteristic	62
Dynamic Compensation	517
Dynamic Programming	352
Dynamic Time Warping Distance	966

E

E-Government	192
E-L _p Metric	279
Effectiveness Evaluation	509
Efficiency Power Plant	695
Electrical Conductivity	909
Electrical Experiments	196
Electrical Field Distribution	814, 940
Electrical-Stimulation Adaptability	17
Electroacupuncture	50
Electrode Material	923
Electron Beam Evaporation	927
Electronic Compass	522
Electronic Engineering Design	275
Elementary Cellular Automata	372
Embedded	50
Embedded System	522
Embedded Technology	227
EMI	103
Empirical Mode Decomposition (EMD)	340
End Support	778
Energy Acceleration Parameter	287
Energy Harvesting Rate	482
Energy Storage	585
Energy Transfer	797, 801
Enhanced Detection	161
Enterprise Informatization Performance Evaluation	249
Environment Awareness	240
EO Property	932
Equal Precision Measurement	647
Equipment Selection	765
Equipment Support	724
Equivalent Capacitance	36
Equivalent Energy Function	695
Erase	25
Erbium-Doped Fiber Amplifier	54, 129
Error Analysis	647
Evaluation	713
Evanescent Field	624

Evolving Model	972
Experiment Research	976
Experimental Verification	895
Extension of Structure Query	167
Exterior Trajectory Differential Equations	758
External Parameters Calibration	364

F

Failure Prognosis	86
Faint Current Measurement	620
Faraday Effect	133
Fault Diagnosis	701
Fault Feature	3
Fault Modeling	3, 11
FBG	413
Feature Dependent Graph	149
Feature Extraction	786
Federation Member	717
FFT	426
Fiber Amplifier	54
Fiber Length	54
Fiber-Optic Transformer	133
Fiber Raman Amplifier	141, 409
FIFO	315
Financial Agglomeration	961
Financing Cost	961
Finite Element (FE)	936
Finite Element Analysis (FEA)	895
Fire Detection	657
Fire Distribution	709
Fluorescence Life	801
Fluxgate Sensor	107
Focal Plane Array	46
Folded Cascode	31
Formal Concept Analysis	187
Forth-Order Runge-Kutta Algorithm	758
Forward Looking Sonar Image	368
FPGA	82, 94, 299,
	323, 398, 426, 612
Freescale HCS12	25
Frequency Compensation	111
Frequency Domain	641
Full Scan Structure	78
Fuzzy Algorithm	304
Fuzzy Number	279
Fuzzy Rough Set	701
Fuzzy Structured Element	279

G

G Language	647
Gain-Flatness	141, 409
Galois Lattice	187
Game Theory	209
Gas-Sensing Characteristics	822
Geomagnetic Simulation	579
Geometric Constraints	149
GPS	653
GPS L2C Signal	392
Grid	200

H

Hadoop	205
Hadoop System	262
HDFS	205
Heavy Crude Oil	946
Henon Map	793
HHT	663
High-Frequency	683
High Level Architecture (HLA)	717, 724
High Performance	31
High-Precision Timing Transfer	381
High Relative Humidity	616
High-Speed Downloading	25
High-Voltage Pulse Voltage	683
Home Wireless Network	542
Human Visual System	310
Humidity Sensor	616
Hybrid Routing Protocol	490
Hydrogel	616
Hydrophilicity	891
Hypersonic	730

I

I-V Characteristics	826
Ice Lantern	571
IDC	855
IDCT	323
IEEE 1801	21
IGBT	86
Image Encryption	327, 372
Image Frequency	310
Image Fusion	299
Image Processing	299
Image Retrival	360
Image Segmentation	344, 368, 376

Imaging Model	348
Imbalanced Voltage	688
Impact Velocity	560
Impedance Transformation	36
In-Sn γ-Phase IMC	918
Incentive Mechanism	209
Independent Component Analysis (ICA)	340
Induced Magnetic Field	579
Information	717
Information Entropy	509
Information Model	244
Information Monitoring System	231
Information Platform	218, 244
Information Retrieval	167
Infrared Image	304
Infrared Optical System	295
Infrastructure	200
Input Delay	551
Installation Error	782
Integrated Gasification Combined	677
Cycle	077
Intelligence Application Platform	192
Intelligent Control	542
Intelligent Inspection	235
Interface Circuit	107
Internal	364
IP	426
IPC	161
ISP	315
IT Alliance	218
J	
Jamming Troop	735
Jerk Model	463
Join Graph	474
John Gruph	171
Κ	
K-Means Clustering Algorithms	262
Kalman Filtering	743
Kerr Cell Voltage	923
Kerr Effect	923
Kerr Electro-Optic Effect	598
KGS-20	608
KIPSO (K-Means Immune Particle Swarm Optimization)	534
Kirsch Edge Detection	335
Knowledge Extracting	187

L

Latent SVM	331
Lead Phthalocyanine	822
LED Display	571
Level Set	368
Lifetime	482
Light Amplification Factor	826
Link Similarity	474
Linux	513
Liquid	602
Liquid Food	628
Load Management	673
Long Baseline	435
Long Period Grating	616
Low Cost Online Real Estate Display System	213
Low Frequency Oscillation	663
Low Pass Filter	74
Low Power	21
LS	40
LTE-A	457

Μ

Machine Learning Methods	258
Machine Translation	153
Magnetic Characteristics	903
Magnetic Field Measurement	579
Magnetic Properties	887
Management System	546
MapReduce Module	262
Marble	818
Master-Slave Control System	530
Matching	546
Material	213
Mathematical Model	505
MATLAB	576
MATLAB Software	413
Matrix Decomposition	323
Maximum Channel Capacity	450
MCU	78, 99
MCU Control	571
μDMFC	842
Measurement	275
Mechanical Design	765, 778
MEMS	842, 875
Metamaterial	846
Metastable Structure	918
Methane Concentration	608

Micro-Current Detection	62
Microbolometer	46
Microcrystalline Alloy	620
Microelectronic Packaging	137
Microgrid	668
Micromechanical Gyroscope	125, 526
Microstrip Antenna Array	486
Microstructure	137, 871, 887, 909
Microwave Breakdown	859
Microwave Performance	564
Milling Force Modeling	895
Minimum Bias-Normal Distribution Index	304
Mining Machinery	765
Mission-Critical Systems	240
MMA	810
Mobile	235
Mobile Prediction	494
Model Driven Architecture	183
Modeling	867
Modified Fast Directional Multilevel Algorithm	486
Modified Proportional 2-Tuple	267
Monitor System	612
Monitoring System	653
Monte Carlo Collision	859
Morphological Operations	368
Motivation Mechanism	976
Moving Target Detection	335
MRI	538
MSP430 Microcontroller	74
Multi-Features Fusion	360
Multi-Points Sources Power Synthesis	402
Multi-Relational Social Network	222
Multi-Scale Gabor Wavelet	360
Multi-Stage Amplifier	111
Multi-Wavelength Pump	141
Multiple Attribute Decision Making	267
Multiply Routing Algorithm	431
Multivibrator	594
Music Electro-Acupuncture Apparatus	17
Music Therapy	50
Mutual Information (MI)	171

Ν

Namenode	205
Nano-Composite Film	851

Nano-Modification	940
Nanocrystals (NCs)	806
Nanostructured Materials	909
Nash Equilibrium Sharing	209
Natural Language Processing	157
Naval Gun Weapon System	754
NC Cutting Tool	546
Near Space	730
Negative Refractive Index	846
Neural Net	376
New Type Silicon Magnetic Sensitivity Transistor	903
Ni-Cu-Zn Ferrites	887
NiO	927
NO ₂	822
NoC	431
Noise Figure	129
Noise Power Estimation	457
Non-Contact Detection	620
Non-Ideal Factors	121
Non-Linear	125, 940
Non-Linear Observer	517
Non-Redundant Scale	275
Nonlinear Filtering	422
Nonlinearities	40
Normal Sequence	255
NPs	797
Nuclear Power Plant (NPP)	701

0

Objective Optimization	505
OFDM	440, 450
On-Line Measurement	636
Open Loop Gain	116
Open Numerical Control System	530
Operational Capability	713
Oppressive Fire	709
Optical Design	295, 774
Optical Fiber Communication Systems	54, 129
Optical Waveguide	810
Optimization	275, 409, 474,
	673
Order Batching	957
Organic Electroluminescent	863
Organic Material	830
Organic Phototransistor	838
Organic Semiconductor	951
Orthogonal Gray Code	319
Orthogonal Phase Shift	348

Orthogonality	641
OTFT	62
Output Static Characteristics	834
Output Translation	153
Overlap Degree	435
Overlap Energy	435
1 05	
Р	
P2P Networks	209
Particle Filter	86, 422
Particle-In-Cell	859
Passenger Flow Forecast	966
Path Planning	735
PCI Bus	513
PCI9052	513
Penetration Attack	735
Performance	730
Petri Net	179, 183
Phase Detecting	386
Phase Locked Loop	70
Phase Noise	70, 526
Phase Smoothing	417
Phase Space Differentiate Area	463
Photo-Stimulating Discharge	899
Photoconductive Property	932
Photoelectric Properties	951
Photoluminescence	797, 879
Photoluminescence Quenching	883
Photosensitivity	838
Photovoltaic	673
Phthaleincyanide Copper	863
Picking Strategy	957
PID Controller	534
Piezoelectric	632
Piston Type Air Compressor	769
Pixel Crosstalk Compensation	310
Plumpness	376
PMMA	810
Polyaniline (PAni)	801
Polyethylene	899
Polyimide	914
Polyphosphazenes	932
Polysilicon Nanofilm	875
Polyvinylpyrrolidone (PVP)	891
Porosity	891
Porous Membranes	891
Positioning Accuracy	435
Positron Emission Tomography	340
Power Amplifier	40

Power Consumption	21
Power-Line Channel	450
Power Spectrum	417
Power Supply Efficiency	677
Power Supply System	585
Power Transformer	636
PR-Quadtree	175
Pre-Mixed Abrasive Water Jet	818
Predistortion	40
Prefetch	205
Probabilistic Production Simulation	695
Process Model	179
Processing	576
Processor	58
Programmable	36
Programmer	25
Projector Calibration	348, 364
Pseudo-Randomness	793
PSRR	90
PTAT	66
Ptimal Operation	668
Public Security System	192
Public Service Network	244
Pulse Coefficient	683
Pulse Delay Time	683
Pulse Response Method	628
Pulse Wave	576

Q

QoS Strategy	450
QPSK	398
Quadrature Error	356
Quantization Noise	356
Quantum Dot (QD)	879, 883
Query of Content	167
Quinoline Aluminum	863

R

Radial Distortion	356
Radiation	486
Radio Frequency Magnetron Sputtering	834
Random Space Disposal	402
Rapid Solidification	867, 918
Readout Circuit	125
Real-Time Monitoring	99
Refiner	871
Registration Target	319

Reliability	936
Resampling Optimization	422
Resolving Ability	275
Resonant	632
Resource Block	478
Reusable Software Process	179
RF-MEMS Switch	560, 564
RFID	235
Ring Voltage Controlled Oscillator	70
RISC	58
Robot	538
Rogowski Coil	585, 589, 620
Router	431
Routing	657
RTI	200
RUL	86

S

Sampled-Data Control	551
SAXS	851
Schottky Barrier	830
Seasonal Index	966
Second Harmonic Generation	774
Security	218
Self-Configuration	240
Self-Propagating High- Temperature Synthesis	887
Semantic Feature Modeling	149
Semiconductor Nano Crystals (NCs)	801
Service Model	183
Service Oriented Architecture	183
Servo Control Card	513
Servo-System Friction	517
Ship-To-Air Missile	713
Shipboard-Gun	709
Short Channel Devices	838
Short-Circuit Reactance	636
SiC/LSR Nanocpmposites	814
Sideband Filter	413
Signal Aliasing	435
Signal Generator	74
Signal Simulation	133
Signal Sorting	386
Signal-to-Noise Ratio (SNR)	392
Silicon	842
Simulation	137, 141, 409, 555, 743, 758
Sine Function	417
Sine Wave Generator	116

Single Miller Capacitor	111	TD-LTE	478
Feedforward Compensation	(20)	Technical Characteristics	875
Single-Turn Cored Clamp-Type	620	Techno-Economic Evaluation	677
Sintering	909	Temperature	99
Sinuous Antenna	469	Temperature Characteristics	903
Sizes	914	Temperature Coefficient	90
Skyline Query	175	Temperature Control	555
Slenderness of Tongue	376	Temperature Gradient	814
Small Capacitor Testing	594	Temperature Sensor	632
Small File	205	Terahertz Frequencies	846
Small-Signal Gain	54	Test Bench	46
Smart Home	542	Testability Design	78
Sn-5mass%Pb	137	Texture	213
Social Network	222	The Medical Robotics	538
Software Radio	398	Thermal Imaging	299
Solar Tracking	522	Thermal Insulating Door	782
Solder Ball	137	Thermal Sensing	632
Solute Trapping	867	Thermal Stability	918
Space-Based Radar	730	Thermoelectric Cooler	99
Space Charge	899	Thin Film	927
Spatial Power Combination	402	Thin-Film Diode	822
Special Optical Fiber	624	Thin Film Transistor	830, 951
Specific Power	769	Three-Frame Difference	335
Spectrum Analysis	641	Three-Phase Four-Leg Inverter	688
Spherical Milling Cutter	895	Throughput Capacity	482
Stability	494	THz Wave	932
Statistical Characteristics	793	Time Domain	641, 709
Statistics	743	Time Domain Recognition	386
Steam Generator (SG)	534	Time-Varying Delay	551
Stereo Matching Algorithm	352	Timing Sequence	82
Stress Distribution	936	Titanium Dioxide Nano-Particle	851
Structure	167	Tolerance	3, 11
Structure Entropy	509	Track Control	463
Subcarriers	440	Tracking Algorithm	392
Submarine	579	Training	724
Substitution	327	Transaction	103
Super Capacitor	585	Transformer Oil	598
Super-Heater	555	Transistor Modeling	62
Support Vector Machine (SVM)	171, 287	Translation Quality	153
Swarm Intelligence	440	Trap	914
System Dynamics (SD)	249	Trap Level Distribution	855
System Precision	782	Turbo Equalization	444
Systematic Demonstration	754		
Systematic Method	754	U	
SystemVerilog VMM	103		624
		U Shaped Ultra-Wideband	624 469
Τ			409

Ultrashort Pulses

Unbalanced Load

Uncertain Linguistic

774

688

267

Т

Tangential Distortion	356
Task Model	505

Uncertainty	551
Unified Architecture	323
University-Enterprise Cooperation	244
Untiy 3D Platform	213
UPF	21
User Interface	530
User Rate	478

V

Value Petri Net	179
VDMOS	936
VENSIM	249
Verification	103
Verilog HDL	58
Vertical Structure	826
VFC	589
VGA	612
VGA Controller	82
VI	647
Video Segmentation	335
Video Stabilization	299
Virtual Reality (VR)	196
Virtual Reality Technology	213
Viscosity Reduction Rate	946
Visual Navigation	352
Voice Activation Detection	287

W

Water Level Control	534
Water Soluble Viscosity Reducer	946
Wavelength Demodulation	413
Weapon System	713
Web Page Mining	187
Web Terms	187
Weighted Function	279
Whole Producing Process	231
Wide Field	295
Wien Bridge Oscillation Circuit	116
WIFI Network	227
Win-Win Situation	244
Wind Control	571
Wind Power System	663
Wireless Communication	235
Wireless Sensor Network (WSN)	474, 482, 501
Wireless Video	612
Write	25

X

Xbee	657
XML Retrieval	167

Z

688
774
255
364
608, 657
834
490

Α		Chen, Z.Q.	735
Abdo, A.A.	372	Chen, Z.Y.	222
Ai, C.	946	Chi, J.G.	801
Amin, M.	327	Chi, M.H.	814, 940
An, L.M.	463, 797, 801,	Chi, S.M.	315
7 m, 12.1vi.	806, 879, 883	Chi, X.M.	310
An, W.Y.	797	Cui, L.H.	111, 431, 875
		Cui, L.J.	179, 183
В		Cui, P.Z.	200
	071	Cui, S.P.	21
Bai, X.	871	Cui, W.W.	891
Bao, L.	360	Cui, Y.	927
Bi, S.Z.	17		
Bian, H.Y.	368	D	
С		Dai, W.J.	806
Cai, T.	801, 806	Deng, L.	153
Cai, X.P.	801	Deng, S.K.	863
Cao, D.S.	494	Deng, Y.	450
Cao, D.Y.	175	Ding, C.H.	376
	435	Ding, Q.	793
Cao, J.	571	Dong, C.C.	103, 107, 431
Cao, J.M.	842	Dong, H.G.	58, 227, 657
Cao, S.S.		Dong, L.M.	909
Cao, Y.J.	31, 571	Dong, W.F.	352, 364
Chen, C.	161	Dong, W.N.	641
Chen, C.J.	530	Dong, X.N.	513
Chen, C.T.	899	Dong, Y.H.	482
Chen, C.X.	743	Dou, J.H.	713
Chen, C.Y.	335	Du, J.L.	258
Chen, H.	299, 486	Du, J.Q.	50, 376
Chen, H.Y.	632	Du, N.	657
Chen, J.	474	Du, Z.P.	972
Chen, J.B.	822, 834, 951	Duan, Y.F.	797
Chen, J.X.	167		
Chen, M.H.	936	Ε	
Chen, Q.G.	814, 940		222 222
Chen, Q.J.	402	El-Latif, A.A.A.	327, 372
Chen, W.W.	196		
Chen, X.	360	F	
Chen, X.F.	616	Fan, H.	58
Chen, X.L.	806, 879	Fan, L.Y.	551
Chen, X.Q.	46	Fan, Y.J.	299
Chen, X.Y.	392	Fan, Z.W.	171
Chen, Y.	806	Feng, C.	352
Chen, Y.J.	175	Feng, J.M.	31
Chen, Z.G.	490, 494		

Feng, Y.	129	Huang, J.W.	137
Feng, Y.C.	871	Huang, J.Y.	961
Feng, Y.M.	356	Huang, J.Z.	774
Fu, J.	863	Huang, L.	360
		Huang, W.Z.	231
G		Huang, X.B.	806
Gao, S.	927	Huang, Z.	36
Gao, S.H.	801	Huang, Z.J.	538
Gao, S.T.	936	Huang, Z.Y.	769
Gao, X.Y.	149, 153, 157		
Gao, Y.	3, 11	J	
Gao, Z.Q.	891	Ji, M.	360
Gao, 2.Q. Ge, W.Q.	304	Jia, Q.Z.	818
Guan, H.Y.	903	Jiang, D.Y.	927
Guan, S.Y.	192	Jiang, J.X.	887
Guang, Y.	82, 90, 111	Jiang, P.P.	287
Guaig, T. Guo, H.W.	440	Jiang, R.	213
	641	-	891
Guo, J.Y.		Jiang, Y. Jiang, Z.D.	
Guo, L.	957	Jiang, Z.P.	103, 107, 431
Guo, L.L.	153, 157	Jiao, B.	522
Guo, L.R.	386	Jie, F.Y.	486
Guo, R.L.	923	Jin, X.	78
Guo, S.Z.	279	Jin, X.Z.	867
Guo, W.L.	513, 538	Jin, Z.X.	235
Guo, X.P.	218	Jing, Z.H.	62
		-	
Guo, Y.W.	891		
Guo, Y.W.		K	
		K Kang, F.W.	871
Guo, Y.W.			
Guo, Y.W. H	891		
Guo, Y.W. H Hai, H.	891 90	Kang, F.W. L	871
Guo, Y.W. H Hai, H. Han, J.N.	891 90 74	Kang, F.W. L Lan, L.	871 571
Guo, Y.W. H Hai, H. Han, J.N. Han, X.T.	891 90 74 801	Kang, F.W. L Lan, L. Lan, X.G.	871 571 867
Guo, Y.W. H Hai, H. Han, J.N. Han, X.T. He, B.	891 90 74 801 976	Kang, F.W. L Lan, L. Lan, X.G. Lei, Y.	871 571 867 855
Guo, Y.W. H Hai, H. Han, J.N. Han, X.T. He, B. He, L.J.	891 90 74 801 976 295, 899	Kang, F.W. L Lan, L. Lan, X.G. Lei, Y. Li, D.	871 571 867 855 310, 315
Guo, Y.W. H Hai, H. Han, J.N. Han, X.T. He, B. He, L.J. He, L.Z.	891 90 74 801 976 295, 899 797	Kang, F.W. L Lan, L. Lan, X.G. Lei, Y. Li, D. Li, D.H.	871 571 867 855 310, 315 463
Guo, Y.W. H Hai, H. Han, J.N. Han, X.T. He, B. He, L.J. He, L.Z. He, M.H.	891 90 74 801 976 295, 899 797 386	Kang, F.W. L Lan, L. Lan, X.G. Lei, Y. Li, D. Li, D.H. Li, D.X.	871 571 867 855 310, 315 463 602
Guo, Y.W. H Hai, H. Han, J.N. Han, X.T. He, B. He, L.J. He, L.Z. He, M.H. He, S.X.	891 90 74 801 976 295, 899 797 386 769	Kang, F.W. L Lan, L. Lan, X.G. Lei, Y. Li, D. Li, D.H. Li, D.X. Li, D.Y.	871 571 867 855 310, 315 463 602 918
Guo, Y.W. H Hai, H. Han, J.N. Han, X.T. He, B. He, L.J. He, L.Z. He, M.H. He, S.X. He, W.	891 90 74 801 976 295, 899 797 386 769 450	Kang, F.W. L Lan, L. Lan, X.G. Lei, Y. Li, D. Li, D.H. Li, D.Y. Li, D.Y. Li, E.T.	871 571 867 855 310, 315 463 602 918 624
Guo, Y.W. H Hai, H. Han, J.N. Han, X.T. He, B. He, L.J. He, L.Z. He, M.H. He, S.X. He, W. He, Y.L.	891 90 74 801 976 295, 899 797 386 769 450 846	Kang, F.W. L Lan, L. Lan, X.G. Lei, Y. Li, D. Li, D.H. Li, D.Y. Li, D.Y. Li, E.T. Li, F.F.	871 571 867 855 310, 315 463 602 918 624 961
Guo, Y.W. H Hai, H. Han, J.N. Han, X.T. He, B. He, L.J. He, L.Z. He, M.H. He, S.X. He, W. He, Y.L. He, Y.Z. He, Z.L.	891 90 74 801 976 295, 899 797 386 769 450 846 40	Kang, F.W. L Lan, L. Lan, X.G. Lei, Y. Li, D. Li, D.H. Li, D.Y. Li, E.T. Li, F.F. Li, G.F.	871 571 867 855 310, 315 463 602 918 624 961 879, 883
Guo, Y.W. H Hai, H. Han, J.N. Han, X.T. He, B. He, L.J. He, L.Z. He, M.H. He, S.X. He, W. He, Y.L. He, Y.Z. He, Z.L. Hou, G.Z.	891 90 74 801 976 295, 899 797 386 769 450 846 40 426	Kang, F.W. L Lan, L. Lan, X.G. Lei, Y. Li, D. Li, D.H. Li, D.Y. Li, E.T. Li, F.F. Li, G.F. Li, G.Y.	871 571 867 855 310, 315 463 602 918 624 961 879, 883 851, 914
Guo, Y.W. H Hai, H. Han, J.N. Han, X.T. He, B. He, L.J. He, L.Z. He, M.H. He, S.X. He, W. He, Y.L. He, Y.L. He, Z.L. Hou, G.Z. Hou, J.H.	891 90 74 801 976 295, 899 797 386 769 450 846 40 426 490 927	Kang, F.W. L Lan, L. Lan, X.G. Lei, Y. Li, D. Li, D.H. Li, D.Y. Li, E.T. Li, F.F. Li, G.F. Li, G.Y. Li, H.B.	871 571 867 855 310, 315 463 602 918 624 961 879, 883 851, 914 810
Guo, Y.W. H Hai, H. Han, J.N. Han, X.T. He, B. He, L.J. He, L.Z. He, M.H. He, S.X. He, W. He, Y.L. He, Y.L. He, Z.L. Hou, G.Z. Hou, J.H. Hu, C.	891 90 74 801 976 295, 899 797 386 769 450 846 40 426 490	Kang, F.W. L Lan, L. Lan, X.G. Lei, Y. Li, D. Li, D.H. Li, D.Y. Li, E.T. Li, F.F. Li, G.F. Li, G.Y. Li, H.B. Li, H.X.	871 571 867 855 310, 315 463 602 918 624 961 879, 883 851, 914 810 231, 235
Guo, Y.W. H Hai, H. Han, J.N. Han, X.T. Han, X.T. He, B. He, L.J. He, L.J. He, L.Z. He, M.H. He, S.X. He, W. He, Y.L. He, Y.L. He, Y.Z. Hou, G.Z. Hou, J.H. Hu, C. Hu, J.W.	891 90 74 801 976 295, 899 797 386 769 450 846 40 426 490 927 133, 598	Kang, F.W. L Lan, L. Lan, X.G. Lei, Y. Li, D. Li, D.H. Li, D.Y. Li, E.T. Li, F.F. Li, G.F. Li, G.Y. Li, H.B. Li, H.X. Li, L.	871 571 867 855 310, 315 463 602 918 624 961 879, 883 851, 914 810 231, 235 422
Guo, Y.W. H Hai, H. Han, J.N. Han, X.T. Han, X.T. He, B. He, L.J. He, L.J. He, M.H. He, S.X. He, M.H. He, Y.L. He, Y.L. He, Y.L. He, Z.L. Hou, G.Z. Hou, J.H. Hu, J.W. Hu, W.T.	$\begin{array}{c} 99\\ \\ 90\\ \\ 74\\ \\ 801\\ \\ 976\\ \\ 295, 899\\ \\ 797\\ \\ 386\\ \\ 769\\ \\ 450\\ \\ 846\\ \\ 40\\ \\ 426\\ \\ 490\\ \\ 927\\ \\ 133, 598\\ \\ 200\\ \\ 594\end{array}$	Kang, F.W. L Lan, L. Lan, X.G. Lei, Y. Li, D. Li, D.H. Li, D.H. Li, D.Y. Li, E.T. Li, F.F. Li, G.F. Li, G.Y. Li, H.B. Li, H.X. Li, L.	$\begin{array}{c} 871\\ \\571\\ \\867\\ \\855\\ 310, 315\\ \\463\\ \\602\\ \\918\\ \\624\\ \\961\\ \\879, 883\\ \\851, 914\\ \\810\\ 231, 235\\ \\422\\ \\683\end{array}$
Guo, Y.W. H Hai, H. Han, J.N. Han, X.T. Han, X.T. He, B. He, L.J. He, L.Z. He, M.H. He, S.X. He, W. He, Y.L. He, Y.L. He, Y.Z. Hou, G.Z. Hou, J.H. Hu, C. Hu, J.W. Hu, W.T. Hu, W.T. Hu, Z.P.	$\begin{array}{c} 99\\ 74\\ 801\\ 976\\ 295, 899\\ 797\\ 386\\ 769\\ 450\\ 846\\ 40\\ 426\\ 490\\ 927\\ 133, 598\\ 200\\ 594\\ 381\end{array}$	Kang, F.W. L Lan, L. Lan, X.G. Lei, Y. Li, D. Li, D.H. Li, D.H. Li, D.Y. Li, E.T. Li, F.F. Li, G.F. Li, G.Y. Li, H.B. Li, H.X. Li, L. Li, L. Li, M.	$\begin{array}{c} 871\\ \\571\\ \\867\\ \\855\\ 310, 315\\ \\463\\ 602\\ \\918\\ 624\\ \\961\\ \\879, 883\\ \\851, 914\\ \\810\\ 231, 235\\ \\422\\ \\683\\ \\86\end{array}$
Guo, Y.W. H Hai, H. Han, J.N. Han, J.N. Han, X.T. Han, X.T. He, B. He, L.J. He, L.J. He, L.Z. He, M.H. He, S.X. He, M.H. He, S.X. He, Y.L. He, Y.L. He, Z.L. Hou, G.Z. Hou, J.H. Hu, C. Hu, J.W. Hu, Z.P. Hua, Y.	$\begin{array}{c} 99\\ \\ 90\\ \\ 74\\ \\ 801\\ \\ 976\\ \\ 295, 899\\ \\ 797\\ \\ 386\\ \\ 769\\ \\ 450\\ \\ 846\\ \\ 40\\ \\ 426\\ \\ 40\\ \\ 426\\ \\ 490\\ \\ 927\\ \\ 133, 598\\ \\ 200\\ \\ 594\\ \\ 381\\ \\ 381\end{array}$	Kang, F.W. L Lan, L. Lan, X.G. Lei, Y. Li, D. Li, D.H. Li, D.H. Li, D.Y. Li, E.T. Li, F.F. Li, G.F. Li, G.Y. Li, H.B. Li, H.X. Li, L. Li, L. Li, M. Li, P.	$\begin{array}{c} 871\\ \\571\\ \\867\\ \\855\\ 310, 315\\ \\463\\ 602\\ \\918\\ 624\\ \\961\\ \\879, 883\\ \\851, 914\\ \\810\\ 231, 235\\ \\422\\ \\683\\ \\86\\ 275, 668, 673\end{array}$
Guo, Y.W. H Hai, H. Han, J.N. Han, X.T. Han, X.T. He, B. He, L.J. He, L.Z. He, M.H. He, S.X. He, W. He, Y.L. He, Y.L. He, Y.Z. Hou, G.Z. Hou, J.H. Hu, C. Hu, J.W. Hu, W.T. Hu, W.T. Hu, Z.P.	$\begin{array}{c} 99\\ 74\\ 801\\ 976\\ 295, 899\\ 797\\ 386\\ 769\\ 450\\ 846\\ 40\\ 426\\ 490\\ 927\\ 133, 598\\ 200\\ 594\\ 381\end{array}$	Kang, F.W. L Lan, L. Lan, X.G. Lei, Y. Li, D. Li, D.H. Li, D.H. Li, D.Y. Li, E.T. Li, F.F. Li, G.F. Li, G.Y. Li, H.B. Li, H.X. Li, L. Li, L. Li, M.	$\begin{array}{c} 871\\ \\571\\ \\867\\ \\855\\ 310, 315\\ \\463\\ 602\\ \\918\\ 624\\ \\961\\ \\879, 883\\ \\851, 914\\ \\810\\ 231, 235\\ \\422\\ \\683\\ \\86\end{array}$

Li, R.	275, 668, 673	Liu, X.W.	125, 526
Li, R.H.	585, 589, 653	Liu, X.X.	851
Li, S.	137, 867	Liu, X.Y.	546
Li, S.F.	381	Liu, Y.	17, 200
Li, S.Y.	976	Liu, Y.J.	774
Li, T.	478	Liu, Y.Y.	855
Li, W.H.	192	Liu, Z.L.	657
Li, X.G.	797	Long, B.	86
Li, Y.	469, 932, 972	Long, J.	99
Li, Y.B.	444, 457	Lu, K.	717, 724
Li, Y.C.	141, 409	Lu, X.B.	103, 111, 323, 875
LI, Y.L.	628	Lu, Y.H.	713
Liang, D.Q.	709, 754	Luan, Z.H.	295
Liang, Q.C.	927	Lv, Q.	46
Liang, S.	946	Δ, χ.	10
Liang, Y.C.	304	Μ	
Liang, Y.Q.	222		
Liao, D.	209	Ma, C.	426
Lin, J.Q.	196	Ma, C.Z.	976
Liu, C.	319	Ma, H.H.	717, 724
Liu, C.L.	624	Ma, J.	632
Liu, C.X.	141, 463, 797	Ma, X.Y.	688
Liu, C.Y.	409	Ma, Y.	141, 409, 522
Liu, D.G.	859	Ma, Z.Y.	413
Liu, D.Y.	175	Manhrawy, I.M.	372
Liu, G.Y.	368	Mao, Y.Y.	769
Liu, H.	797, 810	Meng, C.M.	863
Liu, H.H.	891	Meng, L.	859
Liu, H.M.	94	Meng, S.	54
Liu, H.Q.	940	Meng, X.L.	348
Liu, J.B.	801	Meng, X.Y.	141
Liu, J.M.	323	Min, Z.	231
Liu, L.F.	602	Mo, G.	851
Liu, L.L.	54	Mu, X.F.	555
Liu, L.Q.	859	Mu, Y.	701
Liu, L.Z.	891		
Liu, M.L.	918	Ν	
Liu, P.	871	Nie, P.Y.	54
Liu, Q.	287, 340, 923	Nie, Z.L.	25
Liu, Q.B.	402		
Liu, R.T.	175	0	
Liu, S.C.	616		725
Liu, T.	585, 589, 653	Ou, J.J.	735
Liu, T.L.	522	D	
Liu, W.	137	Р	
Liu, W.D.	161	Pan, H.B.	78
Liu, W.S.	594	Pan, J.	793
Liu, X.	608	Pang, B.	585, 589, 653
Liu, X.C.	62	Pang, Y.J.	368

		Sun, D.J.	435
0		Sun, D.J.	70, 116, 121
Q		Sun, N.N.	923
Qi, L.J.	360	Sun, P.N.	701
Qian, J.	235	Sun, X.M.	348, 360
Qian, Y.	258, 701		
Qin, J.M.	927	Sun, X.W.	709, 754, 758
Qin, Y.	602, 641	Sun, Y.	594, 688
Qin, Y.J.	814	Sun, Z.J.	474
QIU, C.J.	932	Sun, Z.Z.	818
Qiu, L.Q.	222	Т	
Qiu, Z.M.	509	Τ	
Qu, G.M.	946	Tan, C.L.	129, 887
Qu, Y.Q.	806, 879, 883	Tan, X.S.	730
		Tang, G.Y.	179, 183, 187
R		Tang, X.	976
	66 075	Teng, Y.	546
Ren, M.Y.	66, 875	Tian, F.	709, 754, 758
Ren, N.K.	413	Tian, J.Y.	463
Rhouma, R.	372	Tian, L.	319
Rublev, V.	398, 417	Tian, L.Q.	490
C		Tian, S.L.	3, 11
S		Tian, S.Q.	555
Sha, C.M.	612		
Shan, H.Y.	754, 758	W	
Shan, L.J.	304		
Shan, Y.	822, 834, 863,	Wan, L.Y.	167
	951	Wang, B.Q.	386
Shang, N.Q.	814	Wang, B.S.	36
Shang, Q.H.	36	Wang, B.Y.	319
Shang, W.J.	398, 417	Wang, C.H.	17, 50, 376
Shao, T.J.	494	Wang, C.Y.	542
Shen, B.	196	Wang, D.	546, 641
Shen, F.	392	Wang, D.D.	769
Shen, T.	54, 129, 133,	Wang, D.H.	709
	598	Wang, D.X.	822, 826, 830,
Sheng, G.M.	534, 701		834, 838, 863, 951
Sheng, X.	36	Wang, F.	137, 946
Shi, J.	376	-	966
Shi, Z.S.	505, 509	Wang, F.Z.	
Song, B.B.	793	Wang, G.Q.	227
Song, J.X.	161	Wang, G.S.	125, 526
Song, M.X.	70, 78, 116,	Wang, H.	364, 730
	121, 133, 560, 564, 598, 923	Wang, H.C.	709
Song S		Wang, H.H.	859
Song, S. Song, V	469 99	Wang, H.J.	717, 724
Song, Y.		Wang, H.Y.	867
Su, M.	688	Wang, J.	240, 440
Sui, H.	903 546	Wang, J.X.	287
Sui, X.L.	546	Wang, J.Z.	918
Sun, B.W.	196		

Wang, L.	171, 348, 444, 457	Xia, Y.	444, 457
Wang, L.J.	641, 758	Xiao, D.H. Viao	806
Wang, L.Z.	517	Xiao, J. Vice S	801 730
Wang, M.J.	287	Xiao, S.	
Wang, N.	398, 417, 867	Xiao, Y.J.	505, 509
Wang, P.Y.	797	Xie, B. Via C	352
Wang, Q.	846, 895	Xie, C. Via C.S.	21
Wang, S.	209, 585, 589,	Xie, C.S.	677, 695 663
6,	653, 899	Xie, H.L. Xie, H.P.	899
Wang, S.S.	70, 116	Xing, H.J.	513
Wang, S.Y.	647	Xing, 11.5. Xiong, Y.	871
Wang, W.	469	Xiong, Y.L.	295, 413
Wang, X.	846, 927, 932	Xiolig, T.L. Xu, F.	887
Wang, X.D.	99	Xu, H.	413
Wang, X.H.	463	Xu, J.	632
Wang, X.L.	315	Xu, J.J.	222
Wang, X.P.	769	Xu, J.Y.	891
Wang, X.T.	469	Xu, J. I. Xu, L.	891
Wang, Y.	192, 227, 319,	Xu, L. Xu, R.	103, 431
XX7 X7	846	Xu, W.H.	891
Wang, Y.L.	683	Xu, W.II. Xu, W.Z.	249
Wang, Y.P.	235	Xu, W.Z. Xu, Y.Q.	249
Wang, Y.Y.	826, 830, 838	Xu, 1.Q. Xue, Y.C.	534
Wang, Z.F.	31	Aut, 1.C.	554
Wang, Z.H.	887		
	101	V	
Wang, Z.M.	121	Y	
Wang, Z.M. Wang, Z.Y.	310, 319, 826,	Yan, W.	310
Wang, Z.Y.	310, 319, 826, 830, 838	Yan, W. Yang, B.	315
Wang, Z.Y. Wei, H.	310, 319, 826, 830, 838 806, 879, 883	Yan, W. Yang, B. Yang, C.L.	315 3, 11
Wang, Z.Y. Wei, H. Wei, J.Z.	310, 319, 826, 830, 838 806, 879, 883 352, 356	Yan, W. Yang, B. Yang, C.L. Yang, D.R.	315 3, 11 392
Wang, Z.Y. Wei, H. Wei, J.Z. Wei, L.	310, 319, 826, 830, 838 806, 879, 883 352, 356 218, 249	Yan, W. Yang, B. Yang, C.L. Yang, D.R. Yang, H.	315 3, 11 392 40
Wang, Z.Y. Wei, H. Wei, J.Z. Wei, L. Wei, Q.	310, 319, 826, 830, 838 806, 879, 883 352, 356 218, 249 340, 555	Yan, W. Yang, B. Yang, C.L. Yang, D.R. Yang, H. Yang, H.D.	315 3, 11 392 40 683
Wang, Z.Y. Wei, H. Wei, J.Z. Wei, L.	310, 319, 826, 830, 838 806, 879, 883 352, 356 218, 249 340, 555 133, 585, 589, 598, 620, 628,	Yan, W. Yang, B. Yang, C.L. Yang, D.R. Yang, H. Yang, H.D. Yang, H.J.	315 3, 11 392 40 683 58
Wang, Z.Y. Wei, H. Wei, J.Z. Wei, L. Wei, Q. Wei, X.L.	310, 319, 826, 830, 838 806, 879, 883 352, 356 218, 249 340, 555 133, 585, 589, 598, 620, 628, 653, 814, 940	Yan, W. Yang, B. Yang, C.L. Yang, D.R. Yang, H. Yang, H.D. Yang, H.J. Yang, H.Y.	315 3, 11 392 40 683 58 54
Wang, Z.Y. Wei, H. Wei, J.Z. Wei, L. Wei, Q. Wei, X.L. Wei, Y.B.	310, 319, 826, 830, 838 806, 879, 883 352, 356 218, 249 340, 555 133, 585, 589, 598, 620, 628, 653, 814, 940 636	Yan, W. Yang, B. Yang, C.L. Yang, D.R. Yang, H. Yang, H.D. Yang, H.J. Yang, H.Y. Yang, J.R.	315 3, 11 392 40 683 58 54 141, 409
Wang, Z.Y. Wei, H. Wei, J.Z. Wei, L. Wei, Q. Wei, X.L. Wei, Y.B. Wei, Z.Z.	310, 319, 826, 830, 838 806, 879, 883 352, 356 218, 249 340, 555 133, 585, 589, 598, 620, 628, 653, 814, 940 636 966	Yan, W. Yang, B. Yang, C.L. Yang, D.R. Yang, H. Yang, H.D. Yang, H.J. Yang, H.Y. Yang, J.R. Yang, M.	315 3, 11 392 40 683 58 54 141, 409 331
Wang, Z.Y. Wei, H. Wei, J.Z. Wei, L. Wei, Q. Wei, X.L. Wei, Y.B. Wei, Z.Z. Wen, D.Z.	310, 319, 826, 830, 838 806, 879, 883 352, 356 218, 249 340, 555 133, 585, 589, 598, 620, 628, 653, 814, 940 636 966 903	Yan, W. Yang, B. Yang, C.L. Yang, D.R. Yang, H. Yang, H.D. Yang, H.J. Yang, H.Y. Yang, J.R. Yang, M. Yang, Q.R.	315 3, 11 392 40 683 58 54 141, 409 331 129, 133, 598
Wang, Z.Y. Wei, H. Wei, J.Z. Wei, L. Wei, Q. Wei, X.L. Wei, Y.B. Wei, Z.Z. Wen, D.Z. Wen, L.	$\begin{array}{c} 310, 319, 826, \\ 830, 838 \\ 806, 879, 883 \\ 352, 356 \\ 218, 249 \\ 340, 555 \\ 133, 585, 589, \\ 598, 620, 628, \\ 653, 814, 940 \\ 636 \\ 966 \\ 903 \\ 364 \end{array}$	Yan, W. Yang, B. Yang, C.L. Yang, D.R. Yang, H. Yang, H.D. Yang, H.J. Yang, H.Y. Yang, J.R. Yang, M. Yang, Q.R. Yang, R.	315 3, 11 392 40 683 58 54 141, 409 331 129, 133, 598 895
Wang, Z.Y. Wei, H. Wei, J.Z. Wei, L. Wei, Q. Wei, X.L. Wei, Y.B. Wei, Z.Z. Wen, D.Z. Wen, L. Wen, Q.Y.	$\begin{array}{c} 310, 319, 826, \\ 830, 838 \\ 806, 879, 883 \\ 352, 356 \\ 218, 249 \\ 340, 555 \\ 133, 585, 589, \\ 598, 620, 628, \\ 653, 814, 940 \\ 636 \\ 966 \\ 903 \\ 364 \\ 205 \end{array}$	Yan, W. Yang, B. Yang, C.L. Yang, D.R. Yang, H. Yang, H.D. Yang, H.J. Yang, H.Y. Yang, J.R. Yang, M. Yang, Q.R. Yang, R. Yang, S.C.	315 3, 11 392 40 683 58 54 141, 409 331 129, 133, 598 895 364
Wang, Z.Y. Wei, H. Wei, J.Z. Wei, L. Wei, Q. Wei, X.L. Wei, Y.B. Wei, Z.Z. Wen, D.Z. Wen, L. Wen, Q.Y. Wu, H.B.	$\begin{array}{c} 310, 319, 826, \\ 830, 838 \\ 806, 879, 883 \\ 352, 356 \\ 218, 249 \\ 340, 555 \\ 133, 585, 589, \\ 598, 620, 628, \\ 653, 814, 940 \\ 636 \\ 966 \\ 903 \\ 364 \\ 205 \\ 319, 348, 356 \end{array}$	Yan, W. Yang, B. Yang, C.L. Yang, D.R. Yang, H. Yang, H.D. Yang, H.J. Yang, H.Y. Yang, J.R. Yang, M. Yang, Q.R. Yang, R. Yang, S.C. Yang, T.L.	315 3, 11 392 40 683 58 54 141, 409 331 129, 133, 598 895 364 871
Wang, Z.Y. Wei, H. Wei, J.Z. Wei, L. Wei, Q. Wei, X.L. Wei, Y.B. Wei, Z.Z. Wen, D.Z. Wen, L. Wen, Q.Y. Wu, H.B. Wu, J.	$\begin{array}{c} 310, 319, 826, \\ 830, 838 \\ 806, 879, 883 \\ 352, 356 \\ 218, 249 \\ 340, 555 \\ 133, 585, 589, \\ 598, 620, 628, \\ 653, 814, 940 \\ 636 \\ 966 \\ 903 \\ 364 \\ 205 \\ 319, 348, 356 \\ 244, 490, 494 \end{array}$	Yan, W. Yang, B. Yang, C.L. Yang, D.R. Yang, H. Yang, H.D. Yang, H.J. Yang, H.Y. Yang, J.R. Yang, M. Yang, Q.R. Yang, R. Yang, S.C. Yang, T.L. Yang, X.B.	315 3, 11 392 40 683 58 54 141, 409 331 129, 133, 598 895 364 871 713
Wang, Z.Y. Wei, H. Wei, J.Z. Wei, L. Wei, Q. Wei, X.L. Wei, X.L. Wei, Z.Z. Wen, D.Z. Wen, L. Wen, Q.Y. Wu, H.B. Wu, J. Wu, M.Z.	$\begin{array}{c} 310,319,826,\\ 830,838\\\\ 806,879,883\\\\ 352,356\\\\ 218,249\\\\ 340,555\\\\ 133,585,589,\\598,620,628,\\653,814,940\\\\ 636\\\\ 966\\\\ 903\\\\ 364\\\\ 205\\\\ 319,348,356\\\\ 244,490,494\\\\ 413\\\end{array}$	Yan, W. Yang, B. Yang, C.L. Yang, D.R. Yang, H. Yang, H.D. Yang, H.J. Yang, H.Y. Yang, J.R. Yang, J.R. Yang, Q.R. Yang, R. Yang, S.C. Yang, T.L. Yang, X.B. Yang, X.H.	$\begin{array}{c} 315\\ 3,11\\ 392\\ 40\\ 683\\ 58\\ 54\\ 141,409\\ 331\\ 129,133,598\\ 895\\ 364\\ 871\\ 713\\ 624\end{array}$
Wang, Z.Y. Wei, H. Wei, J.Z. Wei, L. Wei, Q. Wei, X.L. Wei, Y.B. Wei, Z.Z. Wen, D.Z. Wen, D.Z. Wen, L. Wen, Q.Y. Wu, H.B. Wu, J. Wu, M.Z. Wu, Q.	$\begin{array}{c} 310, 319, 826, \\ 830, 838 \\ 806, 879, 883 \\ 352, 356 \\ 218, 249 \\ 340, 555 \\ 133, 585, 589, \\ 598, 620, 628, \\ 653, 814, 940 \\ 636 \\ 966 \\ 903 \\ 364 \\ 205 \\ 319, 348, 356 \\ 244, 490, 494 \\ 413 \\ 94 \end{array}$	Yan, W. Yang, B. Yang, C.L. Yang, D.R. Yang, H. Yang, H.D. Yang, H.J. Yang, H.Y. Yang, J.R. Yang, J.R. Yang, Q.R. Yang, R. Yang, S.C. Yang, T.L. Yang, X.B. Yang, X.H. Yang, X.H. Yang, X.J.	$\begin{array}{c} 315\\ 3,11\\ 392\\ 40\\ 683\\ 58\\ 54\\ 141,409\\ 331\\ 129,133,598\\ 895\\ 364\\ 871\\ 713\\ 624\\ 957\end{array}$
Wang, Z.Y. Wei, H. Wei, J.Z. Wei, L. Wei, Q. Wei, X.L. Wei, X.L. Wei, Z.Z. Wen, D.Z. Wen, D.Z. Wen, L. Wen, Q.Y. Wu, H.B. Wu, J. Wu, M.Z. Wu, Q. Wu, R.	$\begin{array}{c} 310,319,826,\\ 830,838\\\\ 806,879,883\\\\ 352,356\\\\ 218,249\\\\ 340,555\\\\ 133,585,589,\\598,620,628,\\653,814,940\\\\ 636\\\\ 966\\\\ 903\\\\ 364\\\\ 205\\\\ 319,348,356\\\\ 244,490,494\\\\ 413\\\\ 94\\\\ 560,564\end{array}$	Yan, W. Yang, B. Yang, C.L. Yang, D.R. Yang, H.N. Yang, H.J. Yang, H.J. Yang, J.R. Yang, J.R. Yang, Q.R. Yang, R. Yang, S.C. Yang, T.L. Yang, X.B. Yang, X.H. Yang, X.J. Yang, X.S.	$\begin{array}{c} 315\\ 3,11\\ 392\\ 40\\ 683\\ 58\\ 54\\ 141,409\\ 331\\ 129,133,598\\ 895\\ 364\\ 871\\ 713\\ 624\\ 957\\ 255\end{array}$
Wang, Z.Y. Wei, H. Wei, J.Z. Wei, L. Wei, Q. Wei, X.L. Wei, Y.B. Wei, Z.Z. Wen, D.Z. Wen, D.Z. Wen, L. Wen, Q.Y. Wu, H.B. Wu, J. Wu, M.Z. Wu, Q.	$\begin{array}{c} 310, 319, 826, \\ 830, 838 \\ 806, 879, 883 \\ 352, 356 \\ 218, 249 \\ 340, 555 \\ 133, 585, 589, \\ 598, 620, 628, \\ 653, 814, 940 \\ 636 \\ 966 \\ 903 \\ 364 \\ 205 \\ 319, 348, 356 \\ 244, 490, 494 \\ 413 \\ 94 \end{array}$	Yan, W. Yang, B. Yang, C.L. Yang, D.R. Yang, H. Yang, H.D. Yang, H.J. Yang, H.Y. Yang, J.R. Yang, J.R. Yang, Q.R. Yang, R. Yang, R. Yang, S.C. Yang, T.L. Yang, X.B. Yang, X.H. Yang, X.J. Yang, X.S. Yang, Y.	$\begin{array}{c} 315\\ 3,11\\ 392\\ 40\\ 683\\ 58\\ 54\\ 141,409\\ 331\\ 129,133,598\\ 895\\ 364\\ 871\\ 713\\ 624\\ 957\\ 255\\ 121,331,392 \end{array}$
Wang, Z.Y. Wei, H. Wei, J.Z. Wei, L. Wei, Q. Wei, X.L. Wei, X.L. Wei, Z.Z. Wen, D.Z. Wen, D.Z. Wen, L. Wen, Q.Y. Wu, H.B. Wu, J. Wu, M.Z. Wu, Q. Wu, R. Wu, Y.H.	$\begin{array}{c} 310,319,826,\\ 830,838\\\\ 806,879,883\\\\ 352,356\\\\ 218,249\\\\ 340,555\\\\ 133,585,589,\\598,620,628,\\653,814,940\\\\ 636\\\\ 966\\\\ 903\\\\ 364\\\\ 205\\\\ 319,348,356\\\\ 244,490,494\\\\ 413\\\\ 94\\\\ 560,564\end{array}$	Yan, W. Yang, B. Yang, C.L. Yang, D.R. Yang, H.N. Yang, H.D. Yang, H.J. Yang, H.Y. Yang, J.R. Yang, M. Yang, Q.R. Yang, R. Yang, S.C. Yang, T.L. Yang, X.B. Yang, X.B. Yang, X.H. Yang, X.J. Yang, X.S. Yang, Y. Yang, Y.W.	$\begin{array}{c} 315\\ 3,11\\ 392\\ 40\\ 683\\ 58\\ 54\\ 141,409\\ 331\\ 129,133,598\\ 895\\ 364\\ 871\\ 713\\ 624\\ 957\\ 255\\ 121,331,392\\ 863\end{array}$
Wang, Z.Y. Wei, H. Wei, J.Z. Wei, L. Wei, Q. Wei, X.L. Wei, X.L. Wei, Z.Z. Wen, D.Z. Wen, D.Z. Wen, L. Wen, Q.Y. Wu, H.B. Wu, J. Wu, M.Z. Wu, Q. Wu, R.	$\begin{array}{c} 310,319,826,\\ 830,838\\\\ 806,879,883\\\\ 352,356\\\\ 218,249\\\\ 340,555\\\\ 133,585,589,\\598,620,628,\\653,814,940\\\\ 636\\\\ 966\\\\ 903\\\\ 364\\\\ 205\\\\ 319,348,356\\\\ 244,490,494\\\\ 413\\\\ 94\\\\ 560,564\end{array}$	Yan, W. Yang, B. Yang, C.L. Yang, D.R. Yang, H.N. Yang, H.D. Yang, H.J. Yang, H.Y. Yang, J.R. Yang, J.R. Yang, Q.R. Yang, R. Yang, R. Yang, S.C. Yang, T.L. Yang, X.B. Yang, X.B. Yang, X.H. Yang, X.J. Yang, X.S. Yang, Y. Yang, Y.W. Yao, D.J.	$\begin{array}{c} 315\\ 3,11\\ 392\\ 40\\ 683\\ 58\\ 54\\ 141,409\\ 331\\ 129,133,598\\ 895\\ 364\\ 871\\ 713\\ 624\\ 957\\ 255\\ 121,331,392\\ 863\\ 179,183,187\end{array}$
Wang, Z.Y. Wei, H. Wei, J.Z. Wei, L. Wei, Q. Wei, X.L. Wei, X.L. Wei, Z.Z. Wen, D.Z. Wen, D.Z. Wen, L. Wen, Q.Y. Wu, H.B. Wu, J. Wu, M.Z. Wu, Q. Wu, R. Wu, Y.H.	$\begin{array}{c} 310,319,826,\\ 830,838\\\\ 806,879,883\\\\ 352,356\\\\ 218,249\\\\ 340,555\\\\ 133,585,589,\\598,620,628,\\653,814,940\\\\ 636\\\\ 966\\\\ 903\\\\ 364\\\\ 205\\\\ 319,348,356\\\\ 244,490,494\\\\ 413\\\\ 94\\\\ 560,564\end{array}$	Yan, W. Yang, B. Yang, C.L. Yang, D.R. Yang, H. Yang, H.D. Yang, H.J. Yang, H.Y. Yang, J.R. Yang, J.R. Yang, Q.R. Yang, R. Yang, S.C. Yang, T.L. Yang, X.B. Yang, X.B. Yang, X.H. Yang, X.H. Yang, X.J. Yang, X.S. Yang, Y. Yang, Y.W. Yao, D.J. Yao, L.	$\begin{array}{c} 315\\ 3,11\\ 392\\ 40\\ 683\\ 58\\ 54\\ 141,409\\ 331\\ 129,133,598\\ 895\\ 364\\ 871\\ 713\\ 624\\ 957\\ 255\\ 121,331,392\\ 863\\ 179,183,187\\ 851,914\end{array}$
Wang, Z.Y. Wei, H. Wei, J.Z. Wei, L. Wei, Q. Wei, X.L. Wei, Y.B. Wei, Z.Z. Wen, D.Z. Wen, D.Z. Wen, L. Wen, Q.Y. Wu, H.B. Wu, J. Wu, M.Z. Wu, Q. Wu, R. Wu, Y.H. X	$\begin{array}{c} 310,319,826,\\ 830,838\\\\ 806,879,883\\\\ 352,356\\\\ 218,249\\\\ 340,555\\\\ 133,585,589,\\ 598,620,628,\\ 653,814,940\\\\ 636\\\\ 966\\\\ 903\\\\ 364\\\\ 205\\\\ 319,348,356\\\\ 244,490,494\\\\ 413\\\\ 94\\\\ 560,564\\\\ 834,863\\\end{array}$	Yan, W. Yang, B. Yang, C.L. Yang, D.R. Yang, H.N. Yang, H.D. Yang, H.J. Yang, H.Y. Yang, J.R. Yang, J.R. Yang, Q.R. Yang, R. Yang, R. Yang, S.C. Yang, T.L. Yang, X.B. Yang, X.B. Yang, X.H. Yang, X.J. Yang, X.S. Yang, Y. Yang, Y.W. Yao, D.J.	$\begin{array}{c} 315\\ 3,11\\ 392\\ 40\\ 683\\ 58\\ 54\\ 141,409\\ 331\\ 129,133,598\\ 895\\ 364\\ 871\\ 713\\ 624\\ 957\\ 255\\ 121,331,392\\ 863\\ 179,183,187\end{array}$

V: I	462 570 707	Zhang T I	277 272
Yi, J.	463, 579, 797	Zhang, T.J. Zhang, W.C	327, 372 846
Yin, J.H.	78, 826, 830, 834, 851, 855,	Zhang, W.C. Zhang, W.I.	932
	914, 936, 951	Zhang, W.L. Zhang, W.Y.	218, 249
Yin, J.Y.	641	Zhang, W.X. Zhang, X.	54, 129, 171,
Yu, B.	82, 90, 187, 323	Zhang, A.	450, 758
Yu, B.Y.	364	Zhang, X.D.	482
Yu, C.B.	806	Zhang, X.J.	612, 754
Yu, C.L.	386	Zhang, X.Y.	717, 724
Yu, G.	364	Zhang, Y.	538, 822, 834,
Yu, P.	822	7hana VD	932, 951
Yu, S.C.	352, 356	Zhang, Y.P. Zhang, V.S.	196
Yu, X.J.	616	Zhang, Y.S.	826, 830, 838
Yu, X.Y.	149, 348	Zhang, Y.W. Zhang, V.V.	356
Yu, Y.	632	Zhang, Y.X. Zhang, Z.U.	594
Yuan, D.D.	946	Zhang, Z.H. Zhang, Z.P.	501, 608 522
Yue, T.	663	Zhang, Z.R. Zhang, Z.V.	579
Yue, Y.J.	612	Zhang, Z.Y.	
,		Zhao, C.C. Zhao, C.R.	677, 695 310, 315
Z		Zhao, E.M.	66, 368, 624,
	207	Zhao, E.Ivi.	810
Zaghloul, A.	327	Zhao, F.	279
Zeng, F.L. Zong, V	402	Zhao, G.S.	240
Zeng, Y. Zhan S	482	Zhao, H.	830, 834, 951
Zhan, S. Zhan, T. I	786	Zhao, J.X.	927
Zhan, T.J. Zhang A	267 735	Zhao, L.	129, 295
Zhang, A. Zhang, A.P.	267	Zhao, M.	927
Zhang, B.Y.	534	Zhao, M.Y.	335
-	149, 153, 157	Zhao, Q.Y.	129
Zhang, C.X. Zhang, C.Z.	74, 422	Zhao, X.	914
Zhang, D.	636	Zhao, X.F.	903
Zhang, D.D.	871	Zhao, Y.	116
Zhang, D.L.	435	Zhao, Z.N.	440
Zhang, D.X.	505	Zheng, H.	976
Zhang, F.C.	895	Zheng, S.L.	769
Zhang, G.L.	576	Zheng, W.L.	620
Zhang, H.L.	50, 576	Zheng, Z.Y.	769
Zhang, H.Q.	501, 608	Zhong, P.Y.	677, 695
Zhang, H.W.	530	Zhong, X.F.	171
Zhang, H.Y.	255	Zhou, A.	624
Zhang, J.	25, 542	Zhou, C.Y.	677, 695
Zhang, J.T.	616	Zhou, D.Y.	743
Zhang, K.	376, 576	Zhou, H.W.	765, 778, 782
Zhang, L.	972	Zhou, H.X.	205
Zhang, L.F.	647	Zhou, K.	450
Zhang, L.Y.	774, 879, 883	Zhou, L.S.	797
Zhang, L.Z.	594	Zhou, S.G.	398, 417
Zhang, Q.F.	209	Zhou, W.L.	801, 806
Zhang, T.F.	344	Zhou, Z.	602, 641
C ,			

Zhu, B.	585, 589, 653
Zhu, C.	899
Zhu, C.W.	713
Zhu, J.J.	86
Zhu, M.	62, 826
Zhu, X.F.	392
Zhu, Y.	74
Zhu, Z.H.	887
Zhuge, X.L.	940
Zou, J.Y.	413
Zuo, Z.F.	730